

AD-A094 826

ROCKWELL INTERNATIONAL THOUSAND OAKS CA SCIENCE CENTER F/8 11/2
PROCEEDINGS OF THE DARPA/AFML REVIEW OF PROGRESS IN QUANTITATIV-ETC(U)

JUL 80 D O THOMPSON, R B THOMPSON

F33615-74-C-5180

UNCLASSIFIED

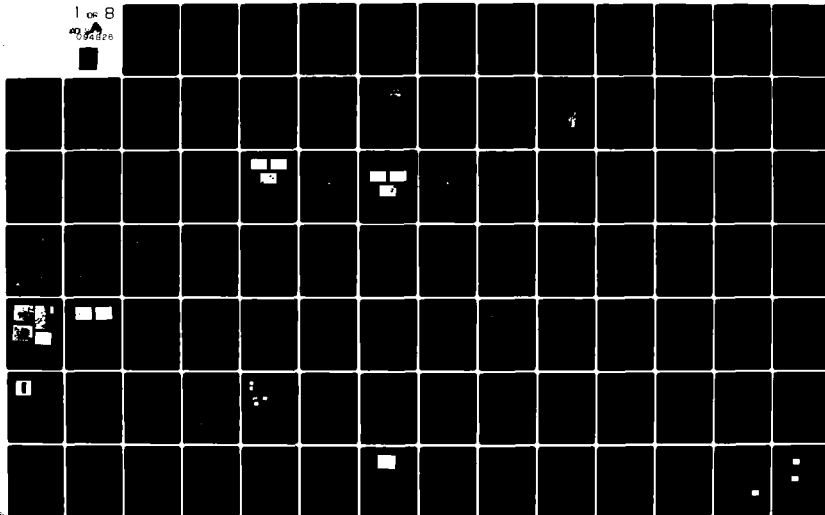
SC595.70AR

AFWAL-TR-80-4078

NL

1 of 8

000000



AD A094826

AFWAL-TR-80-4078 ✓

17 071047

②

LEVEL III

PROCEEDINGS OF THE DARPA/AFML REVIEW
OF PROGRESS IN QUANTITATIVE NDE

Rockwell International, Science Center
1049 Camino Dos Rios
Thousand Oaks, California 91360

July, 1980

Fifth Annual Report 1 July 1978 - 30 September 1979

DTIC

1331

E

Approved for Public Release; Distribution Unlimited.

Prepared for:

DEFENSE ADVANCED RESEARCH PROJECTS AGENCY
1400 WILSON BOULEVARD
ARLINGTON, VIRGINIA 22209

MATERIALS LABORATORY
AIR FORCE WRIGHT AERONAUTICAL LABORATORIES
AIR FORCE SYSTEMS COMMAND
WRIGHT-PATTERSON AIR FORCE BASE, OHIO 45433

81 2 09 041

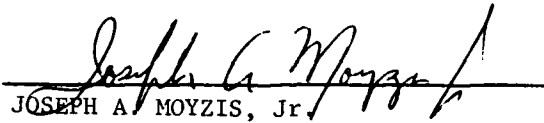
× DDC FILE COPY

NOTICE

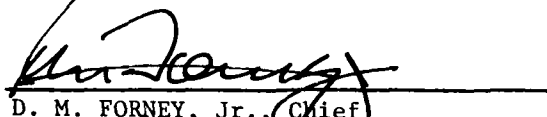
When Government drawings, specifications, or other data are used for any purpose other than in connection with a definitely related Government procurement operation, the United States Government thereby incurs no responsibility nor any obligation whatsoever; and the fact that the government may have formulated, furnished, or in any way supplied the said drawings, specifications, or other data, is not to be regarded by implication or otherwise as in any manner licensing the holder or any other person or corporation, or conveying any rights or permission to manufacture use, or sell any patented invention that may in any way be related thereto.

This report has been reviewed by the Office of Public Affairs (ASD/PA) and is releasable to the National Technical Information Service (NTIS). At NTIS, it will be available to the general public, including foreign nations.

This technical report has been reviewed and is approved for publication.


JOSEPH A. MOYZIS, Jr.
Project Engineer

FOR THE COMMANDER


D. M. FORNEY, Jr., Chief
Nondestructive Evaluation Branch
Metals and Ceramics Division

"If your address has changed, if you wish to be removed from our mailing list, or if the addressee is no longer employed by your organization please notify AFWAL/MLLP, W-PAFB, OH 45433 to help us maintain a current mailing list".

Copies of this report should not be returned unless return is required by security considerations, contractual obligations, or notice on a specific document.

UNCLASSIFIED

SECURITY CLASSIFICATION OF THIS PAGE (When Data Entered)

REPORT DOCUMENTATION PAGE		READ INSTRUCTIONS BEFORE COMPLETING FORM
1. REPORT NUMBER AFWAL-TR-80-4078	2. GOVT ACCESSION NO. AD-A094 826	3. RECIPIENT'S CATALOG NUMBER
4. TITLE (and Subtitle) PROCEEDINGS OF THE DARPA/AFML REVIEW OF PROGRESS IN QUANTITATIVE NONDESTRUCTIVE EVALUATION		5. TYPE OF REPORT & PERIOD COVERED Fifth Annual Report 07/01/78 through 09/30/79
7. AUTHOR(s) Donald O. Thompson R. Bruce Thompson Program Managers		6. PERFORMING ORG. REPORT NUMBER SC595.70AR
9. PERFORMING ORGANIZATION NAME AND ADDRESS Rockwell International, Science Center 1049 Camino Dos Rios Thousand Oaks, California 91360		10. PROGRAM ELEMENT PROJECT, TASK AREA & WORK UNIT NUMBERS 7351
11. CONTROLLING OFFICE NAME AND ADDRESS Defense Advanced Research Projects Agency 1400 Wilson Boulevard Arlington, Virginia 22209		12. REPORT DATE July 1980
14. MONITORING AGENCY NAME & ADDRESS (if different from Controlling Office) Air Force Wright Aeronautical Laboratories Air Force Systems Command Wright-Patterson Air Force Base Dayton, Ohio 45433		13. NUMBER OF PAGES 740
		15. SECURITY CLASS. (of this report) UNCLASSIFIED
16. DISTRIBUTION STATEMENT (of this Report) Approved for Public Release: Distribution Unlimited		15a. DECLASSIFICATION DOWNGRADING SCHEDULE
17. DISTRIBUTION STATEMENT (of the abstract entered in Block 20, if different from Report)		
18. SUPPLEMENTARY NOTES		
19. KEY WORDS (Continue on reverse side if necessary and identify by block number) nondestructive evaluation; nondestructive testing; quantitative ultrasonics; eddy currents; signal processing; acoustic emission, adhesive bonds; reliability; failure mechanisms; accept/reject criteria		
20. ABSTRACT (Continue on reverse side if necessary and identify by block number) The edited transcripts of the DARPA/AF Review of Progress in Quantitative Nondestructive Evaluation (NDE) held on July 8-13, 1979, at Scripps Institution of Oceanography, La Jolla, California, are presented in this document. Several key topics form the core of these presentations and discussions. They include quantitative ultrasonics, eddy currents, emissions related to failure prediction, and reliability of metals and ceramics. It is believed that this document provides a reasonable summary of NDE research and development currently underway.		

DD FORM 1 JAN 73 1473

EDITION OF 1 NOV 65 IS OBSOLETE

UNCLASSIFIED

SECURITY CLASSIFICATION OF THIS PAGE (When Data Entered)

PREFACE

This report contains the edited transcripts of the Review of Progress in Quantitative NDE held at the Scripps Institution of Oceanography, July 8-13, 1979. The Review was sponsored by the Advanced Research Projects Agency and the Air Force Materials Laboratory as a part of the Interdisciplinary Program for Quantitative Flaw Definition, Contract No. F33615-74-C-5180. Arrangements for the Review were made by the Science Center, Rockwell International, host organization for the Interdisciplinary Program, and the Scripps Institution of Oceanography, Dr. William A. Nierenberg, Director.

The format selected for this review was the same as that adopted for previous meetings at Cornell University and at the Scripps Institution of Oceanography. This format included a number of poster sessions in addition to the more traditional technical sessions. It has been found that the poster sessions provide a good way to accommodate the increased activity in this field while maintaining a forum that is highly conducive to technical interchange. As a further means of stimulating this exchange, a number of papers were included which are directly related to the principal technical interests of ARPA/AFML program even though they were not directly sponsored by ARPA/AFML.

The program emphasized several areas of progress in quantitative NDE. In addition to the work in quantitative ultrasonics, which has been a main program activity, new work in quantitative eddy current research and the methodology for the generation of rational accept/reject criteria were reported. In all these areas, strong emphasis is placed upon the physical interpretation of the quantitative measurements and their evaluation in terms of appropriate failure models. Emphasis is also given in the program to presentations and discussions which address state-of-the-art knowledge related to the development of failure models for both ceramic and metallic materials, and the difference in such models required by the nature of the materials.

Prof. J. E. Gordon, University of Reading, England, provided an excellent paper on structural design concepts and comments upon improved design concepts which incorporate early awareness of NDE advances. Prof. Gordon is well known for his humorous and witty books which compare modern design practices with those "structures" provided by nature.

The organizers of the Review wish to acknowledge the financial support and encouragement provided by the Advanced Research Projects Agency and the Air Force Materials Laboratory and the technical participation of members of the Materials Research Council. Special thanks are due to Prof. Gordon for his overview. The organizers also wish to thank speakers, session chairmen, authors of poster presentations, and participants who collaborated to provide a stimulating meeting. They wish to acknowledge with thanks the assistance of Mrs. Diane Harris who managed the organizational matters of the meeting and who organized these Proceedings, and Mrs. Pat Apadoca for her assistance at the meeting. They are also indebted to the management of the Scripps Institution of Oceanography, particularly Dr. William Nierenberg and Mrs. Shirlee Long, UCSD, for their cooperative support in the conduct of the meeting.

Accession for
NTIS (GPO)
RILEY
U.S.
S
P
L
A
List

DEFENSE ADVANCED RESEARCH PROJECTS AGENCY/AIR FORCE MATERIALS LABORATORY

REVIEW OF PROGRESS
IN
QUANTITATIVE NDE

July 8 - 13, 1979
Scripps Institution of Oceanography
University of California
La Jolla, California

TABLE OF CONTENTS

SESSION I - INTRODUCTORY	D. O. Thompson, Chairman	PAGE
INTRODUCTORY COMMENTS		
D. O. Thompson Rockwell International Science Center		1
CATASTROPHIC DESIGN, OR, HOW TO BEHAVE LIKE A WORM		
J. E. Gordon University of Reading, England		5
SESSION II - EDDY CURRENTS	D. M. Forney, Jr., Chairman	
MICROWAVE EDDY-CURRENT TECHNIQUES FOR QUANTITATIVE NDE		
A. J. Bahr Stanford Research Institute International		12
FINITE ELEMENT ANALYSIS OF AXISYMMETRIC GEOMETRIES IN QUANTITATIVE NDE		
R. Palanisamy and W. Lord Colorado State University		25
SURFACE FLAW DETECTION WITH FERROMAGNETIC RESONANCE PROBES		
B.A. Auld, A. Ezekiel, D. Pettibone and D.K. Winslow Stanford University		33
TWO APPROACHES TO SOLVING THE INVERSION PROBLEM FOR EDDY-CURRENT NDE		
T.G. Kincaid, M.V.K. Chari, Z.J. Csendes, K. Fong and R.O. McCary General Electric Company		46
OVERVIEW OF EDDY CURRENT RESEARCH AT SAARBRUCKEN		
P. Holler, R. Becker and K. Betzold Fraunhofer-Institut fur Zerstorungsfreie Prufverfahren		54
SESSION III - EDDY CURRENTS, TECHNIQUES AND PHENOMENA (Posters)		
DESIGN OF A TEMPERATURE-COMPENSATED INDUCTION EXTENSOMETER		
W.E. Deeds and A.R. Yazdi, University of Tennessee C. V. Dodd, Oak Ridge National Laboratory		62
AC MAGNETIC FIELDS IN THE VICINITY OF A CRACK CALCULATED BY ANALYTIC AND NUMERICAL METHODS		
A.H. Kahn and R. Spal National Bureau of Standards		65
IMPEDANCE OF A LOOP WITH A CYLINDRICAL CONDUCTING CORE		
S.A. Long, C.G. Gardner, A. Zaman and S. Toomsawadi University of Houston		69

	PAGE
MATERIALS CHARACTERIZATION BY TIME DELAY SPECTROMETRY ULTRASOUND <i>P.M. Gammel and M.H. Leipold</i> <i>Jet Propulsion Laboratory</i>	74
ACOUSTIC EMISSION SOURCE CHARACTERIZATION THROUGH DIRECT TIME-DOMAIN DECONVOLUTION <i>N.N. Hsu and D.G. Eitzen</i> <i>National Bureau of Standards</i>	81
IDENTIFICATION OF ACOUSTIC EMISSION SOURCE MECHANISMS <i>C. K. Heiple, Rockwell Intl-Rocky Flats Plant</i> <i>S. H. Carpenter, Denver University</i>	85
INVESTIGATION OF NUCLEAR ACOUSTIC RESONANCE FOR THE NONDESTRUCTIVE DETERMINATION OF RESIDUAL STRESS <i>G. A. Matzkanin, Southwest Research Institute</i> <i>R. J. Leinane and P. K. Hsu, Colorado State University</i>	92
NONDESTRUCTIVE EVALUATION OF BULK STRESSES IN ALUMINUM AND COPPER <i>K. Sakuma and C.K. Ling</i> <i>University of Houston</i>	96
TRIBOSTIMULATED EMISSION OF ELECTRONS AND NEUTRAL PARTICLES FROM ANODIZED ALUMINUM <i>J. T. Dickinson and P. Brunlich</i> <i>Washington State University</i>	102
A REVIEW OF RECENT POSITRON ANNIHILATION NDE APPLICATIONS <i>S. Ramchandrasekaran, Io-Wu Kuo, H.W. Yee, Jr., and C.L. Farn</i> <i>University of Utah</i>	109
ASSESSMENT OF POSITRON ANNIHILATION AS A POTENTIAL NON-DESTRUCTIVE EXAMINATION TECHNIQUE <i>W.B. Jones, J.A. Van Den Auyle, W.B. Bauster and W.E. Kumpier</i> <i>Sandia Laboratories</i>	115
SESSION IV - ULTRASONIC TRANSDUCERS	D. Eitzen, Chairman
DEVELOPMENT OF TRANSDUCERS FOR NDE <i>G.S. Kino, B.T. Khuri-Yakub, A. Selfridge and H. Tarn</i> <i>Stanford University</i>	120
NDE APPLICATIONS OF THIN FILM ULTRASONIC TRANSDUCER ARRAYS: PROGRAMMABLE FILTER, SCANNED RECEIVER, AND POWER TRANSDUCER <i>K. Chuang, A. Lee and R.M. White</i> <i>University of California, Berkeley</i>	127
ABSOLUTE ULTRASONIC MEASUREMENTS WITH PIEZOELECTRIC TRANSDUCERS <i>W. Sachse</i> <i>Cornell University</i>	133
EMAT RADIATION PATTERNS <i>W. Pardee and R. B. Thompson</i> <i>Rockwell International Science Center</i>	139
PVF ₂ TRANSDUCERS FOR NDT <i>E. Tureme, K. Fessler, H.J. Shaw, D. Weinstein, and L.T. Titelli</i> <i>Stanford University</i>	153
SESSION V - FAILURE MECHANISMS FOR METALS	R. Thomson, Chairman
UNDERSTANDING MATERIALS RELIABILITY - THE MECHANISMS OF FAILURE <i>R. M. Thomson</i> <i>National Bureau of Standards</i>	159

	PAGE
SUBCRITICAL CRACK GROWTH AND ITS RELATION TO PREDICTIVE ANALYSIS <i>H. L. Marcus</i> <i>The University of Texas at Austin</i>	167
ELASTIC PLASTIC CRACK MECHANICS <i>J. R. Rice</i> <i>Brown University</i>	172
MICROCRACK INITIATION AND GROWTH <i>W. L. Morris and M. R. James</i> <i>Rockwell International Science Center</i>	174
J-INTEGRAL ELASTIC-PLASTIC FRACTURE MECHANICS TECHNOLOGY IN THE U. S. NAVY <i>J. P. Gudas, David W. Taylor Naval Ship R&D Center</i> <i>J. A. Joyce, United States Navy Academy</i> <i>H. H. Vanderwelt, Naval Sea Systems Command</i>	181
TURBINE DISK RETIREMENT-FOR-CAUSE: MEASUREMENT OF INSPECTION UNCERTAINTY FOR DISK EDDY CURRENT INSPECTIONS <i>C.A. Rau, Jr., S.W. Hopkins, J.W. Eischen and D.E. Allison</i> <i>Failure Analysis Associates</i>	182
SESSION VI - NON-METALLIC NDE, ACOUSTIC MICROSCOPY (Posters)	
ULTRASONIC INSPECTION OF RUBBER SONAR DOME WINDOWS <i>G. A. Alers and C. M. Fortunko</i> <i>Rockwell International-Albuquerque Development Laboratory</i>	188
APPLICATION OF NONDESTRUCTIVE EVALUATION (NDE) IN ASSESSING THE STATE-OF-HEALTH OF PHOTOVOLTAIC SOLAR ARRAYS <i>C. D. Coulbert and J. C. Arnett</i> <i>Jet Propulsion Laboratory</i>	191
POLYMER COMPOSITE RELIABILITY REQUIREMENTS FOR LARGE SPACE STRUCTURES <i>J. Moacanin</i> <i>Jet Propulsion Laboratory</i>	197
NONDESTRUCTIVE MONITORING OF FLAW GROWTH IN GRAPHITE/EPOXY LAMINATES UNDER SPECTRUM FATIGUE LOADING <i>I.M. Daniel and S.W. Schramm, IIT Research Institute</i> <i>T. Liber, Travenol Laboratories</i>	201
IMPLEMENTATION OF AN ULTRASONIC, ADHESIVE BOND TEST BED: SAMPLE PROBLEMS: ALUMINUM TO ALUMINUM AND HONEYCOMB STRUCTURES <i>E. Segal, G. Thomas and J. Rose</i> <i>Prexel University</i>	209
NONDESTRUCTIVE EVALUATION OF FLAW CRITICALITY IN GRAPHITE-EPOXY LAMINATES <i>S.N. Chatterjee and Z. Hashin, Materials Sciences Corporation</i> <i>R. B. Pipes, University of Delaware</i>	219
X-RAY STRESS MEASUREMENT IN GRAPHITE/EPOXY COMPOSITES <i>P. Predecki and C. S. Barrett</i> <i>University of Denver Research Institute</i>	225
STATISTICAL EVALUATION OF SOURCES OF ACOUSTIC EMISSION IN COMPOSITES <i>L. J. Graham</i> <i>Rockwell International Science Center</i>	228
DIGITAL DISPLAY OF ACOUSTIC HOLOGRAPHIC IMAGES <i>J.W. Brophy, A.E. Holt and J.H. Flora</i> <i>Babcock & Wilcox Company</i>	235

	PAGE
ACOUSTIC MICROSCOPY VIA SCANNING <i>A. Atakan and A. E. Quate</i> <i>Stanford University</i>	241
FURTHER PROGRESS ON NONDESTRUCTIVE DIAGNOSIS OF HYBRID MICROELECTRONIC COMPONENTS USING TRANSMISSION ACOUSTIC MICROSCOPY <i>J. K. King, C. C. Lee and C. B. Teal</i> <i>Carnegie-Mellon University</i>	247
NONDESTRUCTIVE SUBSURFACE IMAGING WITH THE REFLECTION ACOUSTIC MICROSCOPE <i>R. D. Korpeln, Hughes Research Laboratories</i> <i>D. A. Bergman, Hughes Aircraft Company</i>	253
SESSION VII - VISUALIZATION PROCEDURES G. C. Posakony, Chairman	
A COMPARISON OF ACOUSTIC MICROSCOPY, IMAGING, HOLOGRAPHIC AND TOMOGRAPHIC PROCEDURES <i>A. E. Quate</i> <i>Stanford University</i>	254
DIGITAL SYNTHETIC-APERTURE ACOUSTIC IMAGING SYSTEM <i>D. Aert, J. B. Kins, D. Bohar, B. Olafsen and P. Titchener</i> <i>Stanford University</i>	264
WAVEFRONT RECONSTRUCTION ACOUSTIC IMAGING USING TWO-DIMENSIONAL ARRAYS <i>K.M. Lukin, W.H. Sheppard and R. Tan</i> <i>University of Southern California</i>	272
PROGRESS REPORT ON VARIAN ULTRASOUND IMAGING SYSTEM FOR NDE <i>A. Fahn and G. Schleich</i> <i>Varian Associates, Inc.</i>	280
MAPPING OF MATERIALS STRESS WITH ULTRASONIC TOMOGRAPHY <i>R. E. Hildebrand, Spectron Development Laboratories, Inc.</i> <i>T. D. Harrington, Battelle, Pacific Northwest Laboratories</i>	283
APPLICATIONS OF TOMOGRAPHY TO THE NUCLEAR INDUSTRY <i>B.A. Morris, R.P. Kruger and J.W. Wozniak</i> <i>Los Alamos Scientific Laboratory</i>	295
SESSION VIII - ULTRASONICS-BULK WAVES J. A. Krumhansl, Chairman	
OVERVIEW OF ULTRASONIC DEVELOPMENTS <i>R. E. Thompson</i> <i>Rockwell International Science Center</i>	301
FINITE DIFFERENCE METHODS APPLIED TO ULTRASONIC NON-DESTRUCTIVE TESTING PROBLEMS <i>L. J. Bond</i> <i>The City University, London</i>	310
APPLICATION OF MOOT TO SCATTERING OF ELASTIC WAVES FROM INCLUSIONS AND CRACKS <i>W. M. Hingor</i> <i>Los Alamos Scientific Laboratory</i>	323
MATRIX THEORY OF ELASTIC WAVE SCATTERING: APPLICATION TO SCATTERING OF TRANSVERSE WAVES <i>A. L. Gurt</i> <i>Los Alamos Scientific Laboratory</i>	328
AN APPLICATION OF PADE APPROXIMANTS TO ELASTIC WAVE SCATTERING <i>A. E. Adamantia</i> <i>Los Alamos Scientific Laboratory</i>	334

	PAGE
ELASTIC WAVE SCATTERING BY GENERAL SHAPED DEFECTS: THE DISTORTED WAVE BORN APPROXIMATION <i>D. Jaramay, R.M. Gorman and D. J. Eick</i> <i>University of Washington</i>	341
ELASTIC WAVE SCATTERING BY ROUGH FLAWS AND CRACKS <i>L. E. Lindholm and V. K. Ramanani</i> <i>McGill University</i>	348
MEASUREMENTS OF ULTRASONIC SCATTERING FROM BULK FLAWS OF COMPLEX SHAPE <i>B. Hargrave, R. Halsey and V. Eaton</i> <i>Rockwell International Science Center</i>	359
DIRECT AND INVERSE METHODS FOR SCATTERING BY CRACKS AT HIGH FREQUENCIES <i>C. D. Achenbach</i> <i>The Technological Institute, Northwestern University</i>	367
DIFFRACTION OF ULTRASONIC WAVES BY ELLIPTICAL CRACKS IN METALS <i>L. Adler and D. E. Lewis</i> <i>The University of Tennessee</i>	377
SESSION IX - ULTRASONICS, SURFACE WAVES E. A. Kraut, Chairman	
LASER DETECTION AND IMAGING TECHNIQUES FOR SURFACE EXAMINATION <i>J. Amodei, F.A. Ash, C. Hoo, D. Marmy and H.K. Wickramasinghe</i> <i>University College, London</i>	384
ON THE RESONANCES OF SURFACE BREAKING CRACKS <i>C. Apter and H. A. Auld</i> <i>Stanford University</i>	394
LIFE PREDICTION FOR A1 IN THE MICROCRACK REGIME USING SAW NDE <i>C. Back, W.L. Morris, M.R. James and R.J. Richards</i> <i>Rockwell International Science Center</i>	403
FATIGUE LIFETIME PREDICTION WITH THE AID OF SAW NDE <i>R. R. Eitzmann and C. Back</i> <i>Rockwell International Science Center</i>	411
SESSION X - ULTRASONICS, MATERIAL PROPERTIES P. Holler, Chairman	
THE USE OF ACOUSTOELASTIC MEASUREMENTS TO CHARACTERIZE THE STRESS STATES IN CRACKED SOLIDS <i>J. Bolton, R. King, J. King, P.M. Barnett, J. Herrmann and D. Ilic</i> <i>Stanford University</i>	422
ACOUSTIC MEASUREMENT OF MICROSTRUCTURES IN STEELS <i>M. Ingelli, D.B. Ilic, P. Stanke, J.J. King and J.C. Shyne</i> <i>Stanford University</i>	429
FAST SIGNAL-AVERAGING UNIT FOR ULTRASONIC TESTING. CHARACTERIZATION OF MATERIALS PROPERTIES AND SNR-IMPROVEMENT FOR COARSE-GRAINED MATERIALS <i>K. Ischler, B. Kraus, R. Neumann</i> <i>Forschungsinstitut für Gestaltungslehre und Fertigungstechnik</i>	437
DEFECT IDENTIFICATION AND SIZING BY THE ULTRASONIC SATELLITE-PULSE TECHNIQUE <i>G. J. Under</i> <i>Rockwell Research Institute</i>	445
INTERROGATION OF VOIDS IN SOLIDS UTILIZING RAMP FUNCTION ULTRASONIC PULSES <i>K. D. Cook</i> <i>University of Houston</i>	454

	PAGE
SESSION XI - INVERSION PROCEDURES	
B. DeFacio, Chairman	
MATHEMATICAL PRINCIPLES OF DATA INVERSION	
L. A. Lee Air Force Institute of Technology, WPAFB	459
APPLICATIONS OF IMAGE RECONSTRUCTION IN NDE	
B. D. Linton and J. Miller Systems Control, Inc.	468
PROGRESS ON A MATHEMATICAL INVERSION TECHNIQUE FOR NON-DESTRUCTIVE EVALUATION	
T. Pleschke and J. E. Cohen Dow Chemical Company	475
APPLICATION OF ADAPTIVE LEARNING NETWORKS FOR THE CHARACTERIZATION OF TWO-DIMENSIONAL AND THREE-DIMENSIONAL DEFECTS IN SOLIDS	
R. E. Whalen, L. J. O'Brien and A. N. Mucciardi Alphatronics, Inc.	482
TESTING THE INVERSE BORN PROCEDURE FOR SPHEROIDAL VOIDS	
J. H. Rose, University of Michigan T. V. Vavilam and V. K. Varadan, Ohio State University R. E. Hsieh and B. R. Tittmann, Rockwell Intl. Science Center	509
DETERMINISTIC AND PROBABILISTIC INVERSION AT LONG WAVELENGTHS	
J. Richardson Rockwell International Science Center	514
ULTRASONIC CAUSTICS AND THE INVERSE SCATTERING PROBLEM IN NDE	
P. A. Doyle Aeronautical Research Laboratories, Australia	521
INVERSE SCATTERING AT LOW AND INTERMEDIATE FREQUENCIES	
R. W. Fertig and J. M. Richardson Rockwell International Science Center	528
SESSION XII - NEW TECHNOLOGY APPLICATIONS (Posters)	
RADIOGRAPHIC INSPECTION OF WELDS	
R. L. Buckrop U. S. Army Armament Material Readiness Command	541
WELD INSPECTION WITH SHEAR HORIZONTAL ACOUSTIC WAVES GENERATED BY EMATS	
J. M. Fortunko, Rockwell Intl.-Albuquerque Development Laboratory W. E. Lawrence, Rockwell International Science Center	549
DEMONSTRATION OF THE ALN 4000 MULTI PURPOSE PROCESSING SYSTEM FOR ULTRASONIC AND EDDY CURRENT QUANTITATIVE NDE	
A. N. Mucciardi Alphatronics, Inc.	553
PORTABLE INSTRUMENT FOR DETECTION OF SURFACE FLAWS USING EMATS	
C. E. Visile, R. B. Houston and E. Pongraz-Bartha, Rockwell Intl. Science Center R. E. Lee, Rockwell Intl.-Albuquerque Development Laboratory	555
CODED APERTURE IMAGING IN NDE	
T. M. Cannon and E. E. Fenimore Los Alamos Scientific Laboratory	558
ACOUSTIC EMISSION MONITORING OF IN-FLIGHT CRACK GROWTH IN AIRCRAFT STRUCTURES	
L. B. Hutton and J. R. Skorpik Battelle Northwest Laboratories	559
EMAT SYSTEM FOR DETECTING FLAWS IN STEAM GENERATOR TUBES	
R. E. Thompson, R. E. Hsieh, W. Petersen and C. Visile Rockwell International Science Center	562

	PAGE
INSPECTION OF LOWER HALF OF WING LAP JOINTS WITH EMATs J.E. Martin, P.F. Bolger, B. Houston, R.L. Thompson, and L.L. Thompson Naval International Defense Center	568
DETECTION OF BENDING STRESSES IN BURIED PIPELINES J. A. Alora, Rockwell Intl.-Allbuquerque Development Laboratory, B. B. Thompson, Rockwell International Defense Center	572
ON DETERMINING STRESS IN BOLTS ULTRASONICALLY J. L. MacDonald National Bureau of Standards	576
RAPID ULTRASONIC INSPECTION OF ARMY PROJECTILES J. L. Dingus Rockwell Intl.-Allbuquerque Development Laboratory	581
STRONG NEED FOR IMPROVED ULTRASONIC STANDARDS FOR INSPECTION OF ARTILLERY SHEEL METAL BODIES J. M. Smith Army Materials and Mechanics Research Center	583
A BASIS FOR TRACEABLE NDE STANDARDS J. L. Eitzen, H. Berger, and J. Emdin National Bureau of Standards	586
SESSION XIII - TEST BEDS	J. A. Brinkman, Chairman
TEST BED FOR QUANTITATIVE NDE J. L. Allen, B.B. Houston, J.M. Martin, and R.P. Thompson Naval International Defense Center	590
AUTOMATIC INTERPRETATION OF ULTRASONIC IMAGING J. L. Lee, Aluminides, Inc. D. E. Leroy, Battelle Northwest Laboratories	599
DEVELOPMENT OF ADVANCED NDE ULTRASONIC EQUIPMENT J. L. Allen and J. L. Lee Battelle Northwest Laboratories	605
AUTOMATED INSPECTION DEVICE FOR EXPLOSIVE CHARGE IN SHELLS-AIDECS B. Weber, A.E. Trapp, D. Battelle, J.C. Young, L.A. Parks, J.L. Brinkitt and J. John, IIT Corporation	612
SESSION XIV - FAILURE MODES, DEFECT CHARACTERIZATION, AND ACCEPT/REJECT CRITERIA	A. G. Evans, Chairman
STRUCTURAL AND MICROSTRUCTURAL DESIGN IN BRITTLE MATERIALS A. L. Evans University of California, Berkeley	619
PROBABILISTIC MODELS FOR DEFECT INITIATED FRACTURE IN CERAMICS A. L. Evans, University of California, Berkeley M.F. Meyer, E.W. Fentley, and B.L. Davis, Rockwell Intl. Defense Center B. B. Buchanan, Norton Company	636
CONDITIONAL PROBABILITY OF FAILURE AND ACCEPT/REJECT CRITERIA A. L. Evans and K. Fentley, Rockwell Intl. Defense Center A. L. Evans, University of California, Berkeley	646
LONG WAVELENGTH ULTRASONIC CHARACTERIZATION OF INCLUSIONS IN SILICON NITRIDE J.L. Allen, D. Allen, B.B. Houston, and J. L. Allen Rockwell International Defense Center	656
HIGH-FREQUENCY BULK WAVE MEASUREMENTS OF STRUCTURAL CERAMICS J.L. Allen, D.L. Allen, B.B. Houston, and J.L. Allen Rockwell International	663

	PAGE
ACOUSTIC SURFACE WAVE PROBING OF CERAMICS <i>C. Elly, E. Khuri-Yakub and G. G. Kino</i> <i>Stanford University</i>	671
DIFFERENTIATION OF VARIOUS FLAW TYPES IN CERAMICS USING THE SCANNING LASER ACOUSTIC MICROSCOPE <i>D.E. Yuhas, T.E. Mooney and L.W. Kessler</i> <i>Amesbury, Ind.</i>	678
SCANNING LASER ACOUSTIC MICROSCOPE VISUALIZATION OF SOLID INCLUSIONS IN SILICON NITRIDE <i>D.E. Yuhas, T.E. Mooney and L.W. Kessler</i> <i>Amesbury, Ind.</i>	683
ULTRASONIC DETECTION OF SURFACE FLAWS IN GAS TURBINE CERAMICS <i>E. Parkins and I. M. Matay</i> <i>ESA, Ind.</i>	691
NONDESTRUCTIVE EVALUATION TECHNIQUES FOR SILICON CARBIDE HEAT- EXCHANGER TUBING <i>L.H. Egermann, W.D. Deininger, N.P. Lapinski, C. Solarmarella and D. Yuhas</i> <i>Argonne National Laboratory</i>	700
CHARACTERIZATION OF DEFECTS AND HETEROGENEITIES IN SILICON NITRIDE AND SILICON CARBIDE BY DIFFERENT NDE METHODS <i>E. Koelbeis and E. Reiter</i> <i>Forschungsinstitut für Zerstörungsfreie Prüfverfahren, Germany</i>	713
APPENDIX - SPECIAL REPORT	
PLANNING ACTIVITY REPORT FOR NDE OF ADHESIVE BONDED STRUCTURES <i>F. N. Kelley, University of Akron</i> <i>W. G. Knuss, California Institute of Technology</i> <i>D. H. Kaelble, Rockwell International Science Center</i>	719
ATTENDEES LIST	731

INTRODUCTORY COMMENTS

D. O. Thompson*
Science Center, Rockwell International
Thousand Oaks, Calif. 91360

ABSTRACT

I'd like to take a few minutes at the outset of this meeting to welcome you to the sixth annual review of research Progress in Quantitative NDE and to provide you with some perspective for the program that you will hear and participate in this week. As you know, the review is centered upon research work sponsored by the Defense Advanced Research Projects Agency and the Air Force (Drs. Michael Buckley and Joseph Moyzis, Program Managers). In order to further promote technical interchange, however, we have included related research efforts in this meeting that are sponsored by agencies other than DARPA and the Air Force. I'll focus my remaining remarks on three topics - the DARPA/AF goals, our approach for the attainment of those goals, and some accomplishments to date. I hope that these comments will provide you with a perspective of the week's program.

GOALS

The goals of the DARPA/AF Program Quantitative NDE may be stated as follows:

- * To pursue advanced research in quantitative techniques for NDE.
- * To establish a focal point for NDE research.
- * To enhance communication between the research community and the NDE user.
- * To improve the scientific base for NDE in selected areas.

In order to clarify and enhance the meaning of these goals, it is worthwhile to comment upon our definition of NDE. Although the definition is still in somewhat of a state of evolution, we have adopted an operational definition which is both functional and ambitious. It is:

"Non-destructive evaluation (NDE) represents the capability to assess the state of a material, a component, or a structure from a series of quantitative non-destructive measurements, and to predict the remaining serviceability of the item in question from these measurements and their evaluation in the context of appropriate failure models."

I would like to call to your attention and to emphasize one of the key differences involved in this definition for NDE and that which is in more common useage for non-destructive testing (NDT). As noted above, NDE involves the concept of failure prediction, i.e. the capability to predict the remaining serviceable life of the item. This capability can only result when quantitative measurements of a flaw are available - it is not a capability found in current NDT field practices. The difference between NDE and NDT as implied by this single concept is rather enormous - both in potential benefit to the user and in the scientific content required to achieve that capability.

APPROACH

I would now like to discuss with you our approach for the achievement of a quantitative NDE capability. It is my hope that it will help you to place in perspective the various presentations that you will hear this week and to realize that the achievement of a quantitative NDE capability, as defined above, represents the development of an integrated scientific structure as well as the achievement of individual research results. It is indeed a "team" effort.

The various elements of quantitative NDE are shown in Figure 1, and labeled on the figure. This is a "modular" view in which not only the "modular" elements of work are shown but also the principal directions of work flow and integration. As noted earlier, this integration is essential to the achievement of a working NDE technology. In this figure, the three principal research "modules" are shown in the "northwest" quadrant of the roadmap and are entitled "Quantitative Measurement Techniques," "Probabalistic Failure Models," and "Life Prediction and Quantitative Decision Processes." The first of these is aimed at the development of quantitative inspection techniques, the second of these is concerned with the adaptation and development of failure models that are heavily materials-oriented, and the third is devoted to the development of techniques that are suitable for the combination of results of the first two modules into a probabalistic service-life prediction. Most of the presentations that you will hear this week represent building blocks that fit into one of these modules. The two boxes at the right margin of the figure represent the engineering outputs of this approach. They represent the "tools" and the "rules" of an operating NDE Technology - i.e. quantitative inspection hardware and probabalistically based accept/reject criteria. Both of these are essential for an efficient, operating NDE Technology.

* Now at Ames Laboratory, Iowa State University, Ames, Iowa 50011.

Also shown on the figure are two other entries - management options and a priori knowledge. Management options refers to choices that management wishes to exercise in regard to cash/risk tradeoffs, and which sets the "bias" on the accept/reject criteria. We believe that the approach developed here represents the first time that such management choices can be traced in detail back to fundamental materials and measurement knowledge, and in which cause-effect relationships between the two can be demonstrated. The final box, a priori knowledge, represents the body of historical knowledge and data that may exist about a material or a component that can also be inputted usefully into the life prediction capability. Details of work related to these latter modules will not be presented in this program.

Now, we found that each one of these elements or modules, if you will, is a subsystem of building blocks itself, and I would like to say a few words about the nature of the work that is contained in the research modules.

In Figure 2 are shown the building blocks of the measurement module, that is, those steps that we have found to be necessary in order to achieve a quantitative flaw characterization capability. First of all, it is important to understand, at least approximately, the theoretical interaction of the probing energy with a flaw. Besides providing an understanding of the interaction, these theories provide useful hardware design guidelines. Secondly, these theories must be compared with experimental results both to guide the theoretical developments and also to verify the theoretical developments. Having done this, then, one can use these approximate theories for inverse procedures which are the necessary steps that are used to extract quantitative flaw information from the measurements. With this information various fracture-related parameters (such as stress intensity factors) can then be derived. The output of this development can then be fed into the life-prediction modules.

The second important module of work is that of the development of probabilistic failure models to go with these measurements. Building blocks of this module are shown in Figure 3. Failure models have a generic base in fracture mechanics, of course; as it turns out, however, many materials and components have specific requirements as far as the development of failure models is concerned. These depend upon the usage cycle, the brittle/ductile nature of the materials and so on. Thus, some specificity must be employed in the development of useful failure models.

The first step of major importance in this area is to identify and to prioritize these flaws which are serious in a failure-initiating sense. Of the multitudinous flaws that are possible, it is our estimate that one needs to deal with those which can be identified as important to the actual field failure conditions, and to develop the statistical failure models according to those identified flaws. Please note these are statistical in nature. At our current level of knowledge of materials preparation and processing, all materials exhibit a variance in their failure

modes and rates. Thus, statistical representations are essential. Again, as with the measurement modules, these failure models need to be verified with experimental characterization and statistical analysis of the failure itself. The output of this module is incorporated into the life prediction module, along with the results of the first module. Again, that leads into the life-prediction box.

Building blocks of the third research module, Life Prediction and Quantitative Decision Processes, are represented in Figure 4. Individual research topics in this module are devoted primarily to the mathematical development of appropriate probabilistic formats which must incorporate the outputs of modules 1 and 2 to provide probabilistic predictions of failure. This module must make provision also for the coupling of cost/risk choices and any a priori history.

As I noted earlier, the development of a non-destructive evaluation capability is not a one-shot problem. It is, rather, a systematic and logical system build-up which includes quantitative measurements, materials performance, and a mathematical treatment of appropriate probabilities in order to produce a predictive NDE Technology.

ACCOMPLISHMENTS

Although the development of a complete NDE Technology is not complete, remarkable progress has been made toward this goal in the relatively short span of the DARPA/AF program. Some of these accomplishments will be given in this section in order to provide you with a further perspective of the meeting. Highlights that are given here are necessarily much abbreviated and cannot convey the credits that are due to the individual program participants. Rather, they highlight the nature of the team effort.

A number of important advances have been made in what may be called research accomplishments. These include:

- * Demonstration of all phases of a quantitative ultrasonic technology with current applications to eddy current measurements (Module 1).
- * Demonstration of failure mode analyses for structural ceramics and initial insights of analyses for metallic materials (Module 2).
- * Demonstration of failure predictive technology for structural ceramics (Module 3).
- * Many stand-alone spinoffs.

SC79 5117

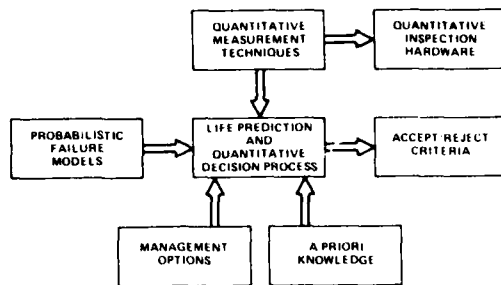
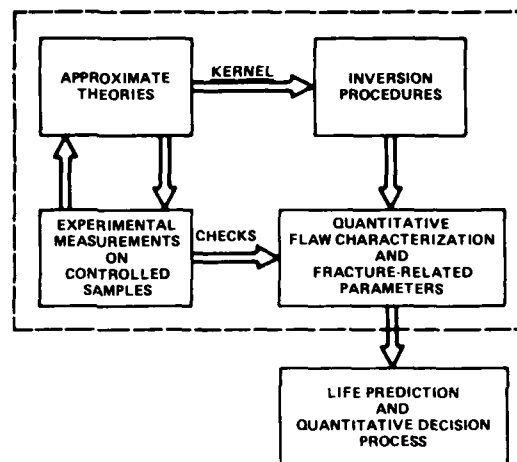
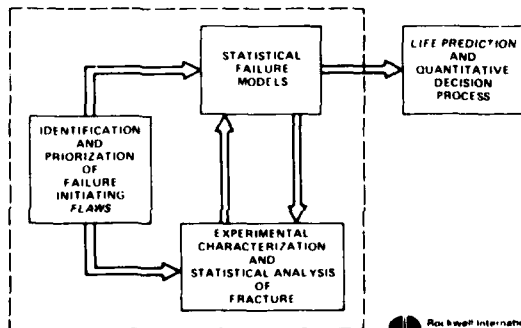


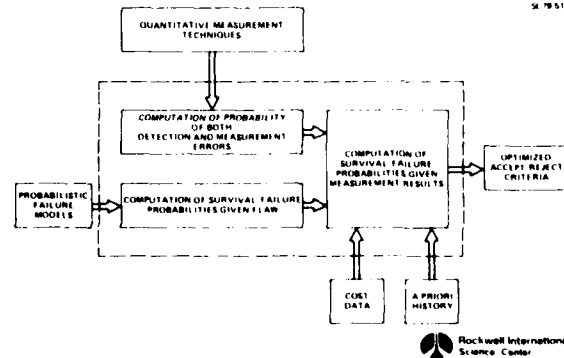
Fig. 1 Elements of Quantitative NDE

Rockwell International
Science CenterFig. 2 Quantitative Measurement Technique
Module 1

SC79 5116

Rockwell International
Science CenterFig. 3 Probabilistic Failure
Module - Module 2

SC 79 5118

Rockwell International
Science CenterFig. 4 Life Prediction and
Quantitative Decision
Processes - Module 3

In addition, several important advances have also been made in the reduction to practice of new research results generated in the DARPA/AF program. These include:

- * Electromagnetic Acoustic Transducer (EMAT) Technology
 - Initiation of Albuquerque Development Laboratory
 - Air Force Cracks under Fasteners
 - Army Projectiles
 - Navy Sonar Domes
 - Railway Inspection
 - Pipeline Inspection
 - EPRI Steam Generator Tubing
- * DARPA Test Bed
 - Integration of Research Results
 - Expected Impact on Retirement for Cause Strategies.

J. E. Gordon
Department of Engineering
University of Reading
England

1. INTRODUCTION

The number of accidents which are caused by the existence of defects in engineering structures can be reduced in two ways,

- (1) By diminishing the number and size of the defects, either by making the structure more carefully in the first place or by using better inspection methods in service - or by some combination of the two.
- (2) By designing structures which are inherently safer - that is to say less susceptible to the presence of defects. An 'ideal' structure could be shot full of holes and still not break.

In fact there will always be some defects in every structure for no manufacturing process and no inspection procedure can be perfect. Furthermore defects will accumulate in a structure between inspections due to fatigue, corrosion, accidental impacts, bad servicing, enemy action and so on. This paper is therefore about the philosophy of the imperfect structure. Since Nature has to deal with similar problems - because no plant or animal is perfect - I am making no apology for using analogies and examples from the new and expanding and exciting discipline of biomechanics. That is to say from the science of the mechanical strength of living structures.

First of all I am going to stick my neck out and say that we know almost nothing about designing structures. Of course there are hundreds of text-books on the subject and people like me give the Lord knows how many lectures about the properties of materials and about the strength of what we choose to call 'structures'. But I think that what we and the text-books - are really teaching is not so much the design of structures as the design of components. Analytical engineers are enormously clever about this and, very often, they can predict the strength of comparatively simple components within a few percent. In the universities, of course, such problems furnish heaven-sent examination questions containing lots of lovely juicy mathematics. Contrariwise, 'design' is difficult to teach and still more difficult to examine.

But real structures - aircraft, bridges, ships and so on - consist of assemblages of components which interact with each other in very complicated ways: too complicated, very often, for the designer to predict with any approach to accuracy. And, in fact, designers are not very good at it. Looking at the question historically - I am speaking of England, but I doubt if the situation was much different in America - airframes designed by the most eminent designers and stressed by the most experienced teams of stressmen have failed initially on the test-frame at loads which have varied, quite randomly, between rather less than 50% and rather over 150% of the fully factored load. This represents a factor of ignorance or mis-design of something over 3.0. I sometimes think that what keeps aeroplanes in the air is not the skill of the designers but the fact that, to a considerable extent, airframes are designed to stiffness rather than to strength criteria - and the stiffness of a structure is,

of course, much easier to predict than its strength. In other words, if such structures are sufficiently stiff, they will with luck be sufficiently strong.

One cannot really speak of the efficiency of the design process with things like ships and bridges because these structures are almost never broken under controlled laboratory conditions - which is perhaps as well for the reputation of their designers for it is reasonable to suspect that the variation is even greater than it is in aircraft. All we really know is that the number of structural failures in ships and bridges is quite high - and may well be increasing. In other words it may be that we know a good deal about the exact design of components but far too little about putting components together to make complicated structures.

Yet, paradoxically, the very ignorance of designers may contribute to the safety of their structures. For, if an inefficient structure reaches the required load on the test-frame it will have failed at its weakest point and it is certain that the rest of the structure is stronger - perhaps much stronger. Thus most of the structure is understressed, perhaps grossly so. Now the length of a critical Griffith defect varies as the reciprocal of the square of the stress and so, over large areas, we can perhaps put up with quite serious defects - we are really only seriously concerned with faults in certain critical regions of the structure. Although we may not know which these regions are, yet statistics are, so to speak, on our side. The more nearly we approach the ideal of a uniformly stressed structure - the 'one-hoss shay' in fact - the more dangerous the situation becomes. Because the one-hoss shay is the aim for which all designers are striving and because in this computer age there is some danger that they might reach it, it seems to me very necessary to consider the problem of reducing the vulnerability of the structure to unavoidable defects.

2. STRUCTURES AS 'SYSTEMS'

The fact that complicated structures are made up of components whose interaction is difficult to predict naturally leads us to look at structures as 'systems'. For one thing 'systems approaches' are very fashionable just now, understandably so, since the success of such methods in non-structural applications has sometimes been remarkable.

But such an approach to the design of structures raises a number of problems. The text-book case of a 'sufficient' structure provides perhaps the simplest example of a structural 'system'. It is equivalent to a chain with a number of links in series where we can hope to know both the mean and the standard deviation of the strength of each link - from which, no doubt, the probability of failure of the whole chain can be calculated. As this will be markedly worse than that of any individual component in the system there is a strong motive to make the structure redundant - that is to introduce several components or elements in parallel. We want to use both a belt and suspenders - and perhaps pieces of string as well - for surely this will be safer?

The reliability of analogous systems in electrical or hydraulic circuitry (about which I know nothing whatever) may or may not be calculable, but it seems to me that the difficulties which arise in calculating the behaviour of a redundant structural 'circuit' are very great. For a start we have the fact, which is well-known to engineers, that redundancy in a structure can, in some cases, be very dangerous. For, if the load distribution in the system is such that one link can be pushed beyond its yield-point while the system as a whole is still within its working range, then, when the load is reduced, this stretched component may be strained back plastically in the reverse direction by reason of the elastic forces of recovery which are stored in the system. Thus high-strain, low-cycle fatigue may be induced in a very short time. I have seen a pressure vessel which failed in this way after only an hour or two in service - as a consequence a man was killed by boiling oil.

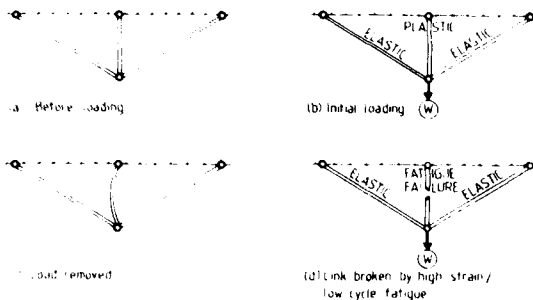


Figure 1: The danger of a redundant structure

3. FRACTURE MECHANICS IS ABOUT COMMUNICATION BETWEEN THE PARTS OF A STRUCTURE

But in reality all structures are redundant, if only because every material contains millions of interatomic bonds a great many of which act in parallel. Or, if we like, we can consider a continuous material, like a metal, as being made up of many parallel elements or strips. As we all know, when a crack starts in a material, the strain energy which is released when one bond or one element breaks is supposed to make its way to the fracture zone where it provides the 'work of fracture', that is the energy which is needed if the breaking process is to be able to continue. This is the Griffith or 'domino', or 'one thing leads to another' theory of fracture.

In modern engineering structures the accepted way of preventing things from breaking is to use a material with a high work of fracture - hence the use of ductile metals like mild steel. But, of course, this approach almost rules out the use of really strong materials because they are nearly always brittle. Another way of ensuring safety is possibly simpler; it is to prevent the released strain energy from getting access to the fracture zone. In other words to interrupt or to control the elastic communication between the appropriate parts of the system.

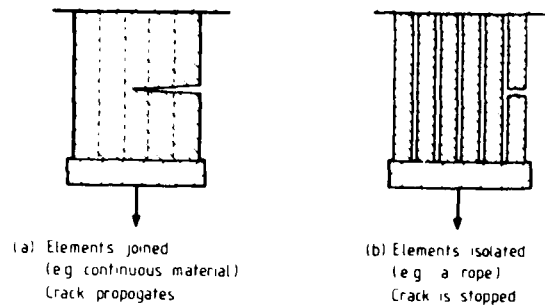


Figure 2: Effect of 'communication' between parts of a structure

This is what commonly happens in ropes and it is what we do in modern suspension bridges. In the older suspension bridges the cables consisted of chains with simple plate links made from wrought iron or mild steel; both of which had a high work of fracture but were consequently quite weak. But in modern bridges the cables are made from many thousands of strands or elements of high tensile steel wire which is very strong but also very brittle. The whole safety of the bridge depends upon the fact that there is virtually no shear connection between the various wires. If one wire breaks its strain energy is released but there is no path by which this released energy can reach the other intact wires and so cause them to break - and so Saint Griffith is frustrated. (Also see Cook & Gordon, 1964, ref. 1). But, if the wires were connected to each other in shear by solder or glue the bridge might become very dangerous; almost as dangerous as if the cable were made from a single solid rod of brittle steel - or indeed of glass.

It is the lack of communication between the elements or components of the bridge which enables brittle high-tensile steel to be used in place of weak, but tough, mild steel - with a very great increase in safety and a very great reduction in weight and cost. Thus we can build, with confidence, bridges from 'dangerous' materials which are around ten times as long as those which can be built from what engineers consider to be 'safe' materials.

At the other end of the scale, if you like, we have monocoque or plate construction which, of course, is particularly fashionable for aircraft and ships. Such metal plates might be considered as an infinitely redundant system of strips or elements which are connected to each other by means of a shear modulus - by virtue of which strain energy can be transmitted from one element to the next. And, as we all know, monocoques tear quite easily - in fact much too easily.

Various intermediate systems can, of course, be made; space-frames for instance. During the war Sir Barnes Wallace's 'geodetic' or lattice construction - used in the Wellington bomber and other aircraft - proved to be exceptionally resistant to damage by 'flak'. And, many years ago, American battleships were fitted with lattice masts - which were supposed to be moderately indestructible by shell-fire. But we cannot entirely escape from Griffith simply by turning a continuous material

into a network or lattice. The problem of 'vulnerability' is not so much a question of whether we use a monocoque or a space-frame as a question of defining and controlling the degree of elastic intercommunication between the various parts of the structure; whether these parts consist of geometrically discrete members, hypothetical strip-like elements in a continuous solid, or interatomic bonds. Thus, in a 'systems approach' to the safety of structures we shall have to be able to:

- (1) Model the elastic interaction which exists between the various units or components in the system.
- (2) Decide what we really mean by a 'unit' or 'component' in the system. Is a single sheet of aluminium, for instance, to be regarded as one single unit or element or as many? If so, how many? I do not see that there can be a rigorous solution to this problem above the atomic or molecular level - but can we approximate, and if so, how?

In fact I do not think that the fracture mechanics of networks has ever been tackled at all seriously. It is clearly very important; but it is also clearly an exceptionally difficult job.

4. PRACTICAL 'SAFE SYSTEMS' IN ENGINEERING AND IN BIOLOGY

4.1 'Uni-directional' systems

The principle of 'isolating' the elements of a structure, that is, making them act independently, is perhaps most easily applied in uni-axial tension; in technology in ropes and suspension bridges. Nature uses this principle in exactly the same way as the bridge-builders when she makes a tendon,

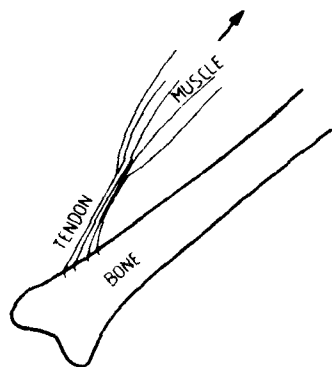


Figure 3

It will be seen that, not only is the middle part of the tendon constituted from many parallel strands of collagen fibre, which are very easily split up or separated - so that there is little or no lateral elastic communication - but that the end attachments are subdivided and multiplied in such a way that the failure of any one joint is not catastrophic - though it is, probably purposely, painful. Nature got there first, but the use of such devices in technology is very old. Rope has been in existence for a long time (it is ruined by closing the strands together) and, in a more sophisticated way, this approach to safety has been used for the main shrouds of sailing ships at least since Roman times.

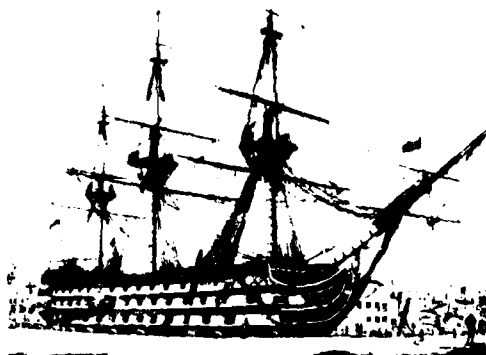


Figure 4: H.M.S. 'Victory'

In compression 'totally isolated systems' are generally impracticable - because of Dr. Euler.

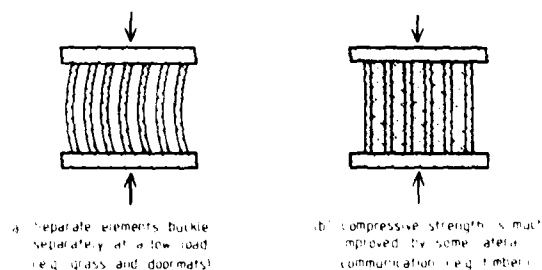


Figure 5: In compression some 'communication' is needed

As a rule lateral communication between the members (e.g. cross-bracing) is necessary in compression structures. Nature uses a 'weak interface' method to ensure the toughness and safety of wood - but it gets Nature into very considerable complications - though in the end Nature wins, hands down. (Cook & Gordon, ref. 1, Jeronimidis & Gordon, ref. 2, ditto, ref. 3). Most fibrous compression systems are provided with 'weak interfaces' and, when we are dealing with weak interfaces we have to distinguish clearly between the strength and the stiffness of the interface,

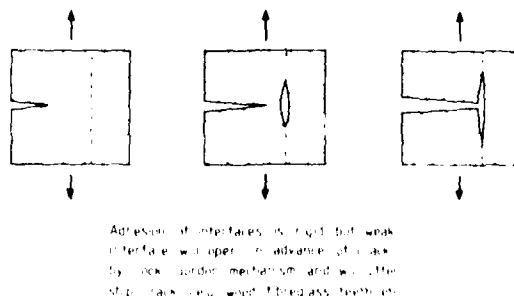
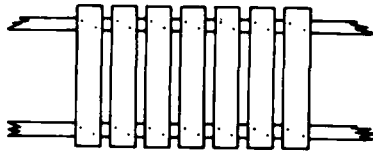


Figure 6: Effect of 'weak interface' or limited communication

I do not know how this is to be modelled.

When we come to bending the problem is simpler and 'total isolation' of the elements is often beneficial. This of course, is what we do when we make a tiled roof (might it be an interesting exercise for the neophyte to calculate the best size of a roof-tile on 'structural-systematic' principles?). It is also what we do with the decking of simple wooden bridges,



Ordinary slatted decking of simple wooden bridges is example of 'isolated' structure in bending. If one plank breaks little harm is done and damage may not spread.

Figure 7

The aerodynamic surfaces of birds are not constructed from aluminium plates but from many cantilevers made from keratin - in other words feathers. Both the individual barbs on the feathers and also the feathers themselves are only connected to each other laterally in the weakest possible way. Thus the spread of damage is almost wholly prevented and it is quite common to see birds flying about with one or more feathers missing. No doubt the air safety authorities would be horrified.

The isolation of the individual feathers goes a long way to account for the effectiveness of feathers as armour - both on birds and on Japanese warriors. Until the late 1930s the hardened steel armour with which the sides of battleships were protected was mounted on the ship's side rather like tiles on a roof. Intentionally, there was little or no structural connection between the plates.

4.2 Multi-dimensional fibrous systems

The problem of isolating the members or units or cords of a structure is clearly easiest when the applied load is unidirectional - but very frequently this is not the case. Often we have to provide a sheet or membrane of one kind or another which has to sustain, with safety, loads coming from at least two directions. For certain applications cloth is extremely effective. For important engineering uses like sails and the covering of airships - where it is essential to avoid tearing or splitting - cloth provides the only satisfactory solution. One can hardly think of a worse or more dangerous sail than one made from metal foil or sheet. Furthermore, it will be remembered that the loss of the R101 airship in 1931 was due to the improper doping of the covering fabric.

Where the stiffness requirements are more severe the problem becomes more difficult - this is what composites made with glass or boron or carbon fibres are about. The design of these materials is a very sophisticated business. But the same principles, of course, can be applied to metals. I remember that one of the large spherical pressure vessels in the German V2 rocket was made by

winding a kind of ball from high-tensile steel tape, the strips being only loosely connected to each other. This was a very clever piece of design which is worthy of imitation.

And Nature does much the same thing when she wants to provide 'rigid' shells; for instance in the cuticle of beetles which are made from crossed layers of chitin fibres, rather badly stuck together by means of a resin-like substance called sclerotin. The shells of shellfish, such as oysters, consist of brittle layers of mineral material separated by weak interfaces.

5. SYSTEMS WITH NON-LINEAR INTERCOMMUNICATION

So far we have dealt with systems where the intercommunication between the parts or elements of the structure is,

- (a) Linear or Hookean - as in modern metal structures. As we have seen such systems are particularly vulnerable and form the foundation of the classical Griffith theory of fracture.
- (b) Systems where the components are almost totally isolated - as with traditional ropes, the cables of modern suspension bridges, natural tendons and so on. Such a system completely frustrates Griffith and is generally very safe indeed, but it is often impracticable.
- (c) Systems containing 'weak interfaces': that is interfaces where the components are 'rigidly' attached to each other initially, but the adhesion fails at a low load. These occur in timber, in teeth and in modern artificial fibre composites.

But none of these systems may be very suitable when what is wanted is a continuous, highly extensible membrane which may have to be watertight or gas-tight.

5.1 Natural membranes with non-linear communication systems

This latter requirement is particularly common in animal membranes where, as usual, Nature has at least one very clever trick up her sleeve. Anyone who has ever tried to gut a rabbit with a blunt knife will be aware that skin and stomach membranes and artery walls are curiously difficult to tear - yet there is no question of any weak interfaces in them. Furthermore, if you stick a pin into a blown-up rubber balloon it will burst with a loud pop. If you stick a fish-hook into a worm or a hypodermic needle into a distended human bladder nothing of the sort will happen. There will certainly not be the sort of explosion which occurred when the fuselages of three Comet aircraft disintegrated in 1954.

In the Biomechanics Group at Reading University our first reaction when we became aware of the toughness of animal membranes was to suppose that the work of fracture of these tissues must be very high. But it is not especially so. My colleague, Peter Purslow, has recently measured the work of fracture of a considerable number of animal membranes; it is usually between 10^3 and 10^4 Joules/m². This is perhaps an order of magnitude below the value for aluminium foil which, in comparable thicknesses, tears very easily indeed.

Where rat skin, or worm cuticle, or human arteries differ from metal sheet - or for that matter from

rubber - is not so much in the work of fracture as in the shape of the stress-strain curve,

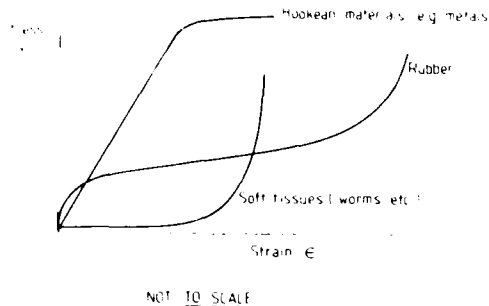


Figure 8

Egg membranes and amniotic membranes are exceptions. They have an almost Hookean stress-strain curve, much like a metal, and they tear quite easily, as they are meant to.

But, as far as I know, virtually all tough natural membranes have the J-shaped stress-strain curve indicated in figure 8. This type of curve has two consequences, I think. In the first place it diminishes the amount of strain energy which can be stored in the material at moderate stresses; more importantly, it limits the elastic shear communication which can take place between the various elements or parts of the material.

In a fracture situation we have to remember that, although the stress is high at the stress-concentration, that is at the point of fracture, it is very much lower throughout most of the material. The strain energy which is released to cause fracture is in fact, so to speak, low-grade strain energy, coming from comparatively lightly stressed regions. In predicting fracture therefore we are mostly concerned with the bottom rather than the top part of the stress-strain curve. But, in many animal tissues, the bottom part of the stress-strain curve is almost horizontal and so the shear modulus at low stresses will be very low. In fact, in this region, the material will behave rather like the surface of a liquid, which has surface tension but no shear modulus. In these conditions it will be difficult to transport strain energy from one part of the tissue to the next - so the material will be difficult to tear. Artificial knitted fabrics have the same sort of stress-strain curves as animal tissues (which is why they fit the human body) - they also are very difficult to tear.

Conversely, unreinforced rubber has a high shear modulus at low stresses; thus intercommunication between the elements of a rubber sheet are good and so the rubber is easily torn - even though its work of fracture is high.

In the wild, most animals live more difficult lives than do most engineering structures. They are continually acquiring wounds, scratches, sores, ulcers and all sorts of defects which no aircraft inspector would dream of passing. Of course wild animals die for all sorts of reasons, but they seldom die because dangerous cracks and tears spread from defects in their soft membranes. (The bursting of cerebral aneurysms in human

beings is an exception - we do not understand why. I understand that, as a cause of death, it is virtually confined to human beings living in sophisticated countries).

5.2 Traditional artificial structural systems with non-linear intercommunication

Modern engineers are very apt to look down on traditional artificial structures such as wooden ships fastened with treenails or carts or buggies which are more or less pegged together. These structures creaked and groaned - and wooden ships leaked and leaked - but they practically never disintegrated quite suddenly and without warning like the one-hoss shay or modern monocoque aircraft or welded steel tankers. In fact, according to their lights, these despised traditional structures were very safe. When they did finally disintegrate, it was nearly always the last stage of a long process of attrition. And they gave ample warning.

The safety of these structures depended, paradoxically upon the wobbliness of their joints. A pegged or lashed or sewn joint has a shear stiffness which is non-linear, something like figure 9.

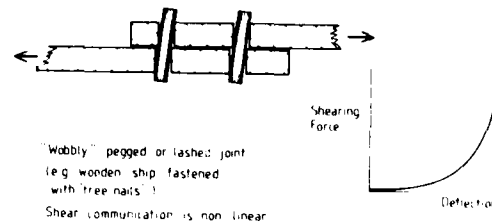


Figure 9

This is very much like the shear stiffness of a natural membrane. Thus a wooden ship, for instance, consists of a system of planks and ribs which are stiff and Hookean in themselves but are connected to each other by non-linear shear connections. The result is a very tough (though leaky) structure and this is no doubt one reason why the world could be explored by incredibly brave men sailing what appear to the modern engineer to be incredibly frail ships. But, if the joints of ships like the Santa Maria had not been wobbly America might not have been discovered until much later.

6. CONCLUSIONS

I think it is fair to say that we do not really understand how to design 'efficient' structures: still less do we know how to minimise the consequences of defects in a structure. It seems to me that there is a good case for doing some sort of 'systems analysis' but,

- (1) It will be difficult to decide what the components or elements of the system consist of.
- (2) It will be essential to model with accuracy the 'elastic communication' between the elements in the system - for this is at the root of the whole question of mechanical failure.

Judging by analogy with traditional structures and with animals a fairly high degree of sub-division will be beneficial. Furthermore it looks to me as though there might be very great advantages in

safety from introducing a non-linear - that is a non-Hookean - connection between the parts of a structure. No engineer, certainly no inspector, could be brought to accept loose or 'wobbly' joints - but is there a case for considering the design of engineering joints with a non-linear response to load? Can all this be explored on the computer?

I am acutely aware that most of what I have said is highly heretical and will perhaps arouse the strongest emotions in many of those present. But let us think for a moment about the conventional engineer's ideal of a respectable modern structure. Broadly speaking this tends to the one-hoss shay and very often to some kind of shell or monocoque. It is true that mathematical analysis often reveals that such structures are lighter and cheaper than what the engineer might consider as Heath-Robinson solutions. But a high proportion of the accidents in the world are caused by mathematicians - not because their mathematics are wrong but because their assumptions are. What the sums about modern structures do not take into account is the interdependence between that unholy trinity, the structure, the material and the defects.

Let us consider the penalties which we incur when we commit ourselves to a conventional modern shell structure made, for instance, from steel. Because of the danger from cracks - that is for reasons of fracture mechanics - we rightly insist on a high work of fracture. In other words we have to use a ductile mild steel. But such a steel is limited to a strength which is probably not much above 60,000 p.s.i. (400 MN/m^2) which is about one eighth of the strength of the highest tensile steel and not much over one hundredth of the theoretical strength of iron. But, even so, we do not dare to stress the steel in a large structure to anything like 60,000 p.s.i.; in many cases we probably put a stress-factor of five into our calculations, ending up with a nominal working stress of possibly 12,000 p.s.i. Even so, such structures often break.

What we may hope to do by re-designing our structures on what we might call 'biological' lines is to be able to make profitable use of stronger but more brittle materials while, at the same time, reducing the vulnerability of the structure to defects - thus possibly working without danger at a lower factor of safety with a consequent reduction in weight and cost. Bridge-builders are conservative folk but even they stress their suspension wires to about 85,000 p.s.i. which is about seven times the stress in steel shell structures.

We do not know very much about the factors of safety in animals but, in the few cases in which we can calculate them, they seem to be very low. In one instance, a colleague tells me, about 1.2. Thus, even if the materials used by the animal were worse, specifically, than the materials of the engineer there is a good chance that the animal's structure will be lighter with regard to the service which it has to perform than the engineer's structure. But it must be remembered that many animals also incorporate load-limiting devices of one kind or another.

In fact my respectable friend the worm (with whom I include a great host of soft and wriggly animals) possesses a geodetic structure consisting of a lattice or network of collagen fibres covered by a continuous skin or membrane whose principle virtue is that it does not obey Hooke's law. When such

creatures want a smooth surface they get it by padding themselves out with soft tissue or by blowing themselves up like a motor-tyre.

When Nature wants a more rigid animal she has, of course, to provide a bony framework - that is a skeleton - which is, to some extent, vulnerable. It is noticeable that one of the penalties which animals seem to have to pay for this engineering convenience of brittle bones is an enhanced sense of pain - which has, of course, a protective function.

It can be argued that many engineering structures are designed to pretty exacting stiffness requirements. If we are enabled to reduce the amount of structural material - such as steel - which is needed to provide strength and safety, then we may not be able to provide the necessary stiffness. Since it is much easier to increase the strength than the stiffness of an engineering material this may be a valid objection in some cases.

However, since animals, whether soft or vertebrate, seldom seem to have to provide much stiffness there may be valid biomechanical ways round this difficulty - but that is another story.



Figure 10

1. COOK, J. & J.E. GORDON (1964). A mechanism for the control of crack propagation in all-brittle systems. *Proc. Roy. Soc. A282*, 508.
2. GORDON, J. E. & G. JERONIMIDIS (1974). Work of fracture of natural cellulose. *Nature, Lond.*, 252, 116.
3. GORDON, J. E. & G. JERONIMIDIS (1978). Composites with high work of fracture. *Phil. Trans. Roy. Soc. Lond.* (in press).

SUMMARY DISCUSSION
(J. E. Gordon)

Don Thompson (Science Center): Thank you, Professor Gordon. We have time for a few questions.

Frank Kelley (University of Akron): I wonder if the principles you have mentioned about the nonlinear shear coupling have been applied successfully in composite structures of filamentary reinforcement module structures in terms of the interaction between the matrix and the fibers. That is, has anyone deliberately put in any connection in order to achieve the results which you suggest through biological membrane?

Professor Gordon: As far as I know, no, but they're only looking at biologic soft tissues on this model. That is to say, in soft tissue, such as an artery wall, there is a very complicated morphology which I think is influencing this area. I haven't time now to talk about some interesting diagrams that can be used to help interpret this cycle, but I don't think it's used in traditional, respectable aerospace circles.

Paul Jammell (Jet Propulsion Lab): How do your composite materials compare with the biological as far as the stress-strains, as far as getting closer to the ultimate tolerances?

Professor Gordon: Well, of course, you better talk to the aircraft structures people. The short answer is, I don't know, but I think we all tend to run composite structures at lower design stresses, perhaps, than metal ones. Perhaps justifiably. If you look at the sort of composite you get in (inaudible) I believe they are now illegal in this country because it was too low. It isn't because you can't make it with (inaudible) I mean, I have seen a plastic sports car that we have now driven into a lamppost which was no bigger than about that. I mean, it's not so much can you do it as will you do it. But I may be wrong about all this.

Dave Kaelble (Science Center): In cases of biological membrane, I would presume the uncoiling of the individual protein chain may be a factor in the stiffening, and it seems to me nonessentially difficult to translate this into a very normal composite-type response, to put the limits on sheer stress transmission.

Professor Gordon: I'm sure it is. Whether you need to do this in a material, I'm not sure because I think the moral is that although the components are more or less (inaudible) against the wood, the communication between is highly (inaudible). I'm not suggesting we should try to get aircraft inspectors to pass wobbly joints. (Inaudible) sources of the assembled intellects of the computer to design communication of joints which are in fact not linear. Conceivably a rubbery glue is a sort of example of this. And of course you get into some extent the sort of woven sticking plaster you put on your cut finger. Incidentally, a thing we ought to go back and look at is skin. This is made from (inaudible) but it was used in enormous quantities in airships as a lining for gas tanks. And it has quite exceptional resistance to hydrogen and helium combined with extraordinary high resistance to tear (inaudible). But this happened 50 years ago, and nobody seems to know anything about it. But it might be worth having a look at.

#

MICROWAVE EDDY-CURRENT TECHNIQUES FOR QUANTITATIVE NDE

A. J. Bahr
Stanford Research Institute International
Menlo Park, CA 94025

ABSTRACT

The objectives of this work are to develop an electromagnetic scattering model that can be used to predict the scattering from a crack in a conducting surface and to evaluate the feasibility of using this model in conjunction with microwave-measurement techniques to determine the dimensions of such a crack. Such a theory has been developed, and its derivation is presented. Theory and experiment are compared for rectangular slots measured at 100 GHz, and the agreement is found to be good. The necessary measurement protocol for determining the dimensions of a crack is discussed, and an example of inverting the measured data to determine the dimensions of a rectangular slot is presented.

INTRODUCTION

In the low-frequency eddy-current testing of metals, currents are caused to flow in a test specimen by placing it in the magnetic field of an induction coil. The flow of currents is affected by the electrical properties and shape of the test specimen, and by the presence of discontinuities and defects. In turn, these currents react on the exciting coil and affect its impedance. Thus, the presence of a defect is determined by monitoring the test coil impedance.

Such eddy-current tests are typically conducted at frequencies of less than 1 MHz where induction fields predominate and the electromagnetic wavelength is greater than 300 m. However, in quantitative NDE, where it is desired to obtain the defect dimensions from an analysis of the measured data, the use of such low frequencies does not provide the degree of sensitivity to changes in defect dimensions that is necessary for obtaining an accurate determination of these dimensions from an inversion of the eddy-current data. The problem of obtaining sufficient accuracy becomes more difficult as the flaws of interest become smaller.

This problem would be alleviated if higher frequencies were to be used in eddy-current inspection. Thus, the work reported here addresses the possibility of conducting eddy-current measurements in the microwave frequency regime (1 GHz to 100 GHz). Previous work^{*} using frequencies in the range 10 GHz to 30 GHz has shown that good sensitivity to small cracks can be obtained, and that there is a clear correlation between crack depth and the detected signal.

In using microwave frequencies, the radiation fields associated with the sensors become an important consideration, and the physics involved is best described in terms of fields and waves. For example, a defect should be thought of as producing a change in the scattering of electromagnetic waves from the metal surface. It should also be noted that, since the use of microwave frequencies causes the currents induced in the test object to flow essentially on the surface (i.e., the skin depth is typically less

than 1 μ m at 100 GHz), microwave eddy-current techniques are limited in metals to surface inspection, e.g., to detection and characterization of surface-breaking cracks.

In order to invert the measured microwave eddy-current data to obtain crack dimensions, it is necessary to have a theoretical model that relates the electromagnetic scattering from a crack to the crack dimensions. The requisite theory should be variational so that approximate solutions for irregular crack geometries can be obtained. In addition, the theory should not be restricted to any particular frequency range so it can be used to clarify any distinctions between conventional (low-frequency) and microwave (high-frequency) eddy-current techniques. Finally, such a model would be useful for establishing an optimum measurement protocol.

A suitable general theory has been developed, and its derivation is outlined below. Then, as an example, the theory is applied to cross-polarized backscattering of a plane wave from a rectangular slot in an aluminum plate, and the measurement protocol necessary to determine the slot dimensions is discussed. The results of this theoretical example are compared with experimental results obtained at 100 GHz and are found to be in good agreement. Finally, graphical inversion of the theoretical electromagnetic scattering from the slot is performed to illustrate the process of obtaining the slot dimensions from the measured data.

A THEORETICAL MODEL FOR ELECTROMAGNETIC SCATTERING FROM SURFACE-BREAKING CRACKS IN METALS

A general electromagnetic scattering-measurement system is shown schematically in Fig. 1, which illustrates the general bistatic case where the transmitter and receiver are separated. The probes are arbitrary, but it is assumed that a single electromagnetic mode propagates at some point in the transmission line(s) {waveguide(s)} that connect the probe(s) to the transmitter and receiver. It is also assumed that the metal shields and test body exhibit finite conductivity.

*References are listed at the end of the paper.

The starting point of the theory is the Lorentz reciprocity theorem, which involves an integral

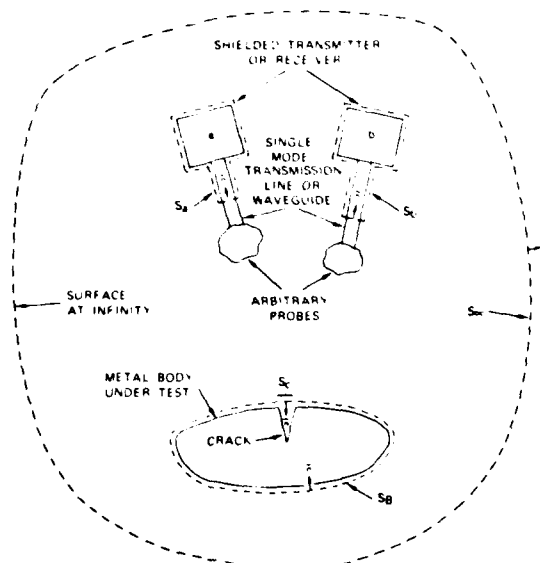


FIGURE 1 GENERAL ELECTROMAGNETIC SCATTERING-MEASUREMENT SYSTEM

over the closed surface, S , equal to $S_a + S_b + S_c + S_0$. If there are no sources enclosed within the volume defined by S , the theorem takes the following form:

$$\iint_S (\vec{E} \times \vec{H}' - \vec{E}' \times \vec{H}) \cdot \vec{n} dS = 0 \quad (1)$$

where \vec{n} is a unit vector that points outward from the enclosed volume. The quantities \vec{E} and \vec{H} are the electric and magnetic fields, respectively, that exist on the surface S . The unprimed and primed fields are defined by the following conditions:

- Unprimed field--no crack is present, "a" is a receiver, "b" is a transmitter.
- Primed field--a crack is present, "a" is a transmitter, "b" is a receiver.

In addition, if gyromagnetic media exist within the closed volume, all dc magnetic fields within the volume must be reversed in the two cases."

The evaluation of the surface integral in Eq. (1) requires a knowledge of the fields on the various parts of the surface S . First, on all the metal surfaces the tangential electric field can be related to the surface magnetic field by means of a surface impedance, Z_s :

$$\vec{E}_t = -Z_s(\vec{n} \times \vec{H}) \quad (2)$$

For the plane waves, Z_s is related to the skin depth, δ , by the well-known formula

$$Z_s = \frac{1+j}{\sigma \delta} \quad (3)$$

where σ is the conductivity of the metal. Second, on the surface at infinity one has the following radiation condition:

$$\vec{E} = j\omega \vec{A} \quad (4a)$$

$$\vec{H} = -j \frac{1}{\mu_0} (\vec{n} \times \vec{A}) \quad (4b)$$

where ω is the radian frequency, μ_0 is the intrinsic impedance of free space, and \vec{A} is the vector potential. Third, since single modes are assumed to propagate in the transmission lines, it can be shown that the integrals over the transmission-line cross sections reduce to the following form:

$$\iint_{S_a} (\vec{E} \times \vec{H}' - \vec{E}' \times \vec{H}) \cdot \vec{n} dS = -4P_A \Gamma_a \quad (5a)$$

$$\iint_{S_b} (\vec{E} \times \vec{H}' - \vec{E}' \times \vec{H}) \cdot \vec{n} dS = 4P_A \Gamma_b \quad (5b)$$

where P_A is the power available from the transmitter and Γ is the reflection coefficient of the propagating mode in the transmission line. Finally, the unknown electric field in the crack mouth can be expressed as a fictitious magnetic current, \vec{M}' , viz.,

$$\vec{M}' \triangleq \vec{n} \times \vec{E}' \quad (6)$$

By using Eqs. (2), (4), (5), and (6), one can convert Eq. (1) into the following form:

$$4P_A(\Gamma_b - \Gamma_a) = -Z_s \iint_{S_c} (\vec{H}_t' \times \vec{H}) \cdot \vec{n} dS + \iint_{S_c} (\vec{M}' \times \vec{H}) \cdot \vec{n} dS \quad (7)$$

Equation (7) expresses the difference between the scattering coefficients measured with probes "a" and "b" in terms of fields that exist in the crack mouth when it is either open or covered by a conductor having surface impedance Z_s . Hence, to relate this theoretical result to an experimental measurement, the measurement system must be capable of measuring this difference in scattering coefficients.

In conventional eddy-current systems, one usually measures the change in impedance, $Z' - Z$, of a probe as it passes over a crack, rather than the change in scattering coefficient. In the monostatic case, the distinction between "a" and "b" disappears, and one finds from transmission-line theory that the change in scattering coefficient and the change in impedance are related by

$$4P_A(\Gamma' - \Gamma) = I I' (Z' - Z) \quad (8)$$

where I and I' are the total currents flowing in the transmission line without and with a crack present, respectively. However, the scattering coefficients will be retained in the present development because they are more fundamental to a wave analysis.

Equation (7) is a linear integral equation that relates the unknown reflection coefficient, Γ , to the unknown tangential magnetic field, \vec{H}_t' , and magnetic current, \vec{M}' , in the crack mouth. The quantity \vec{H} is the magnetic field that exists on the surface of the metal test object in the absence of a crack. One way of solving this equation is to use the method of moments. Such a solution possesses the variational characteristics that are desired.

In the moment-method solution, one expands \vec{M}' in a set of basis functions, \vec{M}_n :

$$\vec{M}' = \sum_{n=1}^N V_n \vec{M}_n \quad (9)$$

The only conditions on the \vec{M}_n are that they be linearly independent, and that their superposition approximate \vec{M}' "reasonably well" (herein lies the "art" in the method of moments). One also needs to invoke the condition that the tangential magnetic field be continuous across the crack mouth; i.e.,

$$\vec{H}_t^i = \vec{H}_t^i + \vec{H}_t^r(\vec{M}') = \vec{H}_t^c(-\vec{M}') \quad (10)$$

where \vec{H}_t^i is the incident magnetic field, $\vec{H}_t^r(\vec{M}')$ is the induced magnetic field just outside the crack mouth, and $\vec{H}_t^c(-\vec{M}')$ is the induced magnetic field just inside the crack mouth. \vec{H}_t^c is a function of $-\vec{M}'$ rather than of \vec{M}' because of the equivalence principle. Also, because the \vec{H}_t operators are linear, Eq. (9) can be substituted into Eq. (10) to give the result

$$\sum_{n=1}^N V_n \vec{H}_t^r(\vec{M}_n) + \sum_{n=1}^N V_n \vec{H}_t^c(\vec{M}_n) = -\vec{H}_t^i \quad (11)$$

Next, one chooses a set of testing functions, \vec{W}_m , that are similar (but not necessarily equal) to the \vec{M}_n . By taking the dot product of each \vec{W}_m with Eq. (11) and integrating that product over the crack mouth, one obtains the following result:

$$\begin{aligned} & \sum_{n=1}^N V_n \iint_{S_c} \vec{W}_m \cdot \vec{H}_t^r(\vec{M}_n) dS \\ & + \sum_{n=1}^N V_n \iint_{S_c} \vec{W}_m \cdot \vec{H}_t^c(\vec{M}_n) dS \\ & = - \iint_{S_c} \vec{W}_m \cdot \vec{H}_t^i dS \end{aligned} \quad (12)$$

Thus, Eq. (10) has been converted into a set of scalar inhomogeneous linear equations, which thus can be solved for the unknown coefficients, V_n .

The result of eliminating the V_n in Eq. (9) and substituting the result into Eq. (7) is best expressed in matrix form:

$$\begin{aligned} \begin{Bmatrix} b \\ b \end{Bmatrix} &= \begin{Bmatrix} a \\ a \end{Bmatrix} - \frac{F_{LFFCO}}{0} \begin{Bmatrix} -Z_s \\ -Z_s \end{Bmatrix} \begin{Bmatrix} c \\ c \end{Bmatrix} \\ &+ \frac{1}{0} [Y_r + Y_c]^{-1} \begin{Bmatrix} c \\ c \end{Bmatrix} \\ &+ \frac{1}{0} [Y_r + Y_c]^{-1} \begin{Bmatrix} c \\ c \end{Bmatrix} \end{aligned} \quad (13)$$

where the normalized coefficients and matrix elements are given by

$$F_{LFFCO} = \frac{\iint_{S_c} (\vec{a}_M \cdot \vec{H})(\vec{a}_W \cdot \vec{H}_t^i) dS}{4P_A} \quad (14a)$$

$$C_c = \frac{\iint_{S_c} (\vec{H}_t^i \cdot \vec{H}) dS}{\iint_{S_c} (\vec{a}_M \cdot \vec{H})(\vec{a}_W \cdot \vec{H}_t^i) dS} \quad (14b)$$

$$Y_r = \frac{\iint_{S_c} \vec{H}_t^r(\vec{M}_n) \cdot \vec{H} dS}{\sqrt{\iint_{S_c} (\vec{a}_M \cdot \vec{H})(\vec{a}_W \cdot \vec{H}_t^i) dS}} \quad (14c)$$

$$Y_{mn}^r = \frac{\iint_{S_c} \vec{W}_m \cdot \vec{H}_t^r(\vec{M}_n) dS}{\iint_{S_c} (\vec{a}_M \cdot \vec{H})(\vec{a}_W \cdot \vec{H}_t^i) dS} \quad (14d)$$

$$Y_{mn}^c = \frac{\iint_{S_c} \vec{W}_m \cdot \vec{H}_t^c(\vec{M}_n) dS}{\iint_{S_c} (\vec{a}_M \cdot \vec{H})(\vec{a}_W \cdot \vec{H}_t^i) dS} \quad (14e)$$

$$C_m^i = \frac{\iint_{S_c} (\vec{W}_m \cdot \vec{H}_t^i) dS}{\sqrt{\iint_{S_c} (\vec{a}_M \cdot \vec{H})(\vec{a}_W \cdot \vec{H}_t^i) dS}} \quad \text{and} \quad (14f)$$

$$C_n = \frac{\iint_{S_c} (\vec{M}_n \cdot \vec{H}) dS}{\sqrt{\iint_{S_c} (\vec{a}_M \cdot \vec{H})(\vec{a}_W \cdot \vec{H}_t^i) dS}} \quad (14g)$$

Here, \vec{a}_M and \vec{a}_W are unit vectors pointing along \vec{M} and \vec{W} , respectively.

Equation (13) applies to all electromagnetic eddy-current measurements of cracks. At this stage, no restrictions have been made on the operating frequency or the distance between the probe(s) and the sample. The first term in the equation--i.e., the one involving Z_c --can be interpreted as the change in scattering caused by removing a small volume (the crack) of metal that has finite conductivity. The second term can be interpreted as the change in scattering caused by energy being stored in the crack and being reradiated. The coefficient F_{LFFCO} contains the effects of changing the distance between the probe and the sample surface (lift off), and of the crack orientation. At low frequencies, one finds that the finite-conductivity term dominates; at high frequencies, where the crack becomes resonant, the effects of energy storage become predominant. Thus, the theory provides a clear distinction between conventional and microwave eddy-current techniques.

AN EXAMPLE

To illustrate how Eq. (13) can be evaluated in a specific case, consider the simple case of perpendicular plane-wave excitation of a rectangular slot cut in a perfectly-conducting plane. The geometry of such a slot is shown in Fig. 2. Assuming the receiver is cross-polarized to the transmitter, $a = 0$ and Eq. (13) becomes

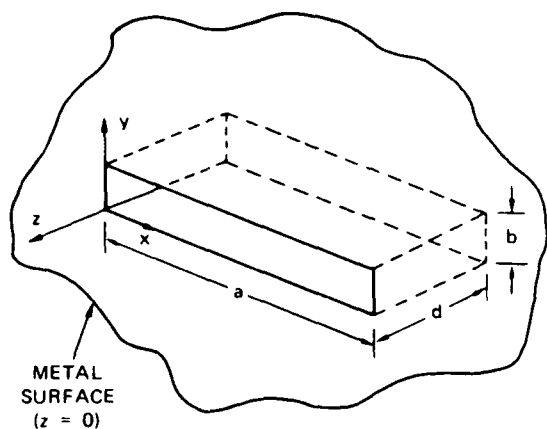


FIGURE 2 RECTANGULAR SLOT GEOMETRY

$$\vec{b} = F_{LF} F_{CO} C_1 \vec{c}_1 \left[1 / (\epsilon_0 Y_s) \right] \quad (15)$$

where the slot admittance is $Y_s = Y_r + Y_c$ and it has been assumed that only one basis function is needed to approximate the fields in the slot mouth.

In this case, one can take advantage of the knowledge that exists concerning the solution for the fields in the aperture of a narrow-slot antenna.¹¹ This solution should provide a good resonance-region* approximation to the fields in the mouth of a slot that is deeper than it is wide. Hence, one chooses the basis function and test function to be

$$\vec{M}_1 = \vec{a}_x \frac{1}{b} \sin \left[k \left(\frac{a}{2} - \left| x - \frac{a}{2} \right| \right) \right] = \vec{W}_1 \quad (16)$$

where \vec{a}_x is a unit vector along the x-axis, k is the wave number, and the slot dimensions and coordinate system are defined in Fig. 2. Use of this approximate function converts the moment-method solution to a perturbation solution.

Now, for a plane incident wave with magnetic field H_0 , one has

$$\vec{a}_x \cdot \vec{H}_t^i = H_0 \cos \theta \quad (17)$$

and

$$\vec{a}_x \cdot \vec{H} = 2H_0 \sin \theta \quad (18)$$

where θ is the angle between \vec{H}_t^i and the x-axis and it has been assumed that there are no reflections from the probe. Thus, using Eqs. (16), (17), and (18) the coefficients of the normalized slot impedance $(1/\epsilon_0 Y_s)$ in Eq. (15) become

$$F_{LF} = \frac{\eta_0 H_0^2 ab}{4P_A} \quad (19a)$$

*The term resonance region refers to frequencies where the slot length is equal to or greater than one-half wavelength.

$$F_{CO} = \sin 2\theta \quad (19b)$$

$$C_1 = \sqrt{2} \tan \theta - \frac{4}{k\sqrt{ab}} \sin^2 \left(\frac{ka}{4} \right) \quad \text{and} \quad (19c)$$

$$C_1^i = \frac{1}{\sqrt{2} \tan \theta - \frac{4}{k\sqrt{ab}}} \sin^2 \left(\frac{ka}{4} \right) \quad (19d)$$

Here, the quantity $C_1 C_1^i$ is a slot coupling factor that gives the frequency dependence of the coupling between the slot and the incident field. The normalized slot admittance, $\eta_0 Y_s$, is a slot parameter that is independent of the excitation. It is important to note that Y_s is the sum of a radiation admittance, Y_r , that depends on the boundary conditions external to the slot, and a cavity admittance, Y_c , that depends on the geometry inside the slot. Thus, if the geometry of the slot cavity changes, but not the geometry of the slot mouth, only the cavity admittance needs to be recalculated.

To calculate the cavity admittance for a rectangular slot, one can expand $H_z^i(\vec{M}_1)$ in transverse-electric waveguide modes. Then Eq. (14e) becomes

$$Y_c = -j \sum_{q \text{ odd}} 8 \frac{a}{b} \frac{\text{ctnh}(\Gamma_q d)}{\Gamma_q} \frac{ka}{(\Gamma_q a)^3} \cos^2 (ka/2) \quad (20)$$

where

$$\Gamma_q^2 = (q\pi/a)^2 - k^2 \quad (21)$$

This result differs slightly from that obtained in Ref. 5 because of a difference in the definition of slot voltage.

The radiation admittance Eq. (14d) can be calculated by expanding the aperture fields in a plane-wave spectrum.^{9,10} Assuming $kb \ll 1$, one has

$$\begin{aligned} \text{Re}(Y_r) = (1/\pi\eta_0) \{ & \text{Cin}(ka) \\ & + [\text{Cin}(ka) - 1/2 \text{Cin}(2ka)] \cos ka \\ & - [\text{Si}(ka) - 1/2 \text{Si}(2ka)] \sin ka \} \end{aligned} \quad (22a)$$

and

$$\begin{aligned} \text{Im}(Y_r) = (1/\pi\eta_0) \{ & \text{Si}(ka) \\ & + [\text{Si}(ka) - 1/2 \text{Si}(2ka)] \cos ka \\ & + [\text{Cin}(ka) - 1/2 \text{Cin}(2ka)] \\ & - \ln \left(\frac{e^{3/2} a}{2b} \right) \sin ka \} \end{aligned} \quad (22b)$$

where

$$\text{Cin}(x) \triangleq \int_0^x \frac{1 - \cos u}{u} du \quad \text{and} \quad (23a)$$

$$\text{Si}(x) \triangleq \int_0^x \frac{\sin u}{u} du \quad (23b)$$

Equations (19), (20), and (22) show explicitly how slot coupling and slot admittance depend on the frequency and the dimensions of the slot. In order

to show explicitly how the liftoff factor [Eq. (19a)] depends on these parameters, it is necessary to relate H_0 and P_A . For example, if the source antenna were equivalent to a magnetic dipole located at a large distance, R , from the slot, one would have

$$F_{LF} = \frac{-3}{16\pi} \frac{ab}{R^2} e^{-j2kR} \quad (24)$$

Hence, if k is large (wavelength is small), the dominant effect of changing R will be to change the phase of the reflection coefficient. Thus, the locus of the reflection coefficient in the reflection-coefficient plane as R is changed will be a nearly circular arc. This behavior can be used to discriminate between the signals produced by variations in liftoff and by a bonafide crack.

Having obtained Eqs. (19), (20), and (22), it is now possible to calculate the cross-polarized scattered power given by

$$P_{HV} = \left| \frac{1}{b} \right|^2 P_A \quad (25)$$

as a function of the frequency and slot dimensions. It is convenient, however, to normalize the scattered power first to suppress the dependence of the result on the characteristics of the probe and slot orientation, viz.,

$$\begin{aligned} & P_{HV} (P_A / \frac{1}{4} a^2 b^2 |H_0^4| \sin^2 2\alpha) \\ &= \frac{64}{k^4 a^2 b^2} \sin^8 \left(\frac{ka}{4} \right) \frac{1}{|H_0^4| \sin^2 2\alpha} \end{aligned} \quad (26)$$

The right-hand side of this equation is plotted (in dB) in Fig. 3 as a function of the product of frequency and slot length, with the ratios of slot width and depth to slot length as parameters. In this figure, $ka/b \geq 1$ defines the resonance region where electromagnetic energy can propagate into the slot with low attenuation. In this region, the scattering is seen to be a strong function of slot depth, which is a desirable characteristic from the standpoint of obtaining an accurate determination of depth from a scattering measurement. For frequencies below the resonance region, the fields inside the slot are evanescent, and so the sensitivity of the scattering to changes in slot depth decreases rapidly as the slot approaches one slot length in depth. Thus, eddy-current measurements for determining slot depth quantitatively are best conducted in the resonance region. It should be noted, however, that more than one slot depth can give the same value of scattered power in this frequency region, and so it may be necessary to conduct measurements at more than one frequency to resolve this ambiguity.

So far, this example has neglected the contribution of the surface-impedance term to the scattering. Indeed, in the cross-polarized case, $C_c = 0$ in Eq. (13), and the other term containing Z_s is small for most metals. On the other hand, in the co-polarized case, $C_c = 1$, and $F_{CO} = 2 \cos^2 \alpha$. At very low frequencies, $1/Y_s \rightarrow 0$, and the quasi-static scattered power, P_Q , is determined entirely by the surface impedance:

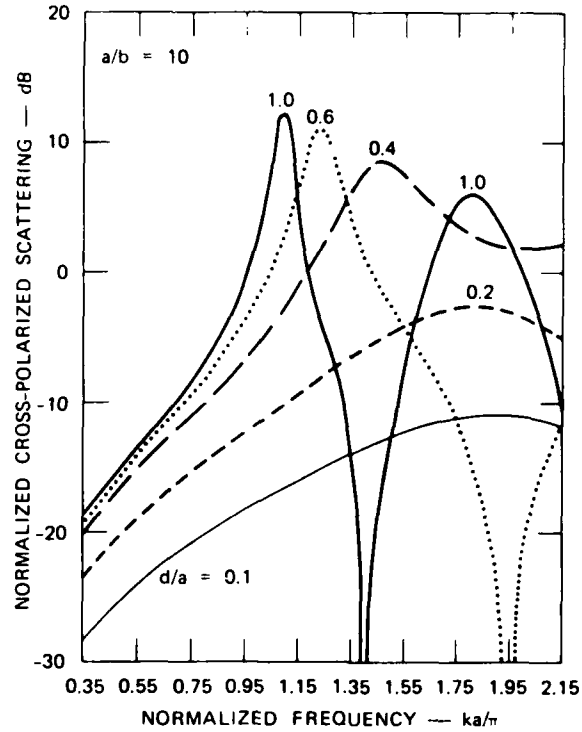


FIGURE 3 NORMALIZED CROSS-POLARIZED POWER SCATTERED FROM A SLOT AS A FUNCTION OF NORMALIZED FREQUENCY

$$P_Q (P_A / \frac{1}{4} a^2 b^2 |H_0^4| \cos^4 \alpha) \cong \frac{|Z_s|^2}{4 \frac{1}{4} a^2 b^2} \quad (27)$$

Of course, as the frequency is increased from zero, the energy stored in the slot also contributes to the scattering. For a deep slot ($d/a \gg 1$), the Rayleigh scattering term, P_R , can be approximated by expanding Eq. (15) for small ka . The result is

$$P_R (P_A / \frac{1}{4} a^2 b^2 |H_0^4| \cos^4 \alpha) \cong \frac{6}{16^4} (ka)^2 \quad (28)$$

These two normalized scattered powers are plotted as functions of frequency in Fig. 4. In making the computations it was assumed that $a = 2.5$ mm and that the material was aluminum with $Z_s = 3.26 \cdot 10^{-7} \sqrt{f(1+j)}$ ohms, where f is the frequency. This figure clearly shows the dominance of the surface-impedance term (quasi-static term) at low frequencies, and the dominance of the energy-storage term (Rayleigh term) at high frequencies. The crossover occurs in this example at about 10 kHz. It is important to note that neither of these low-frequency approximations to the slot scattering contains any depth information. Hence, one concludes from this example that eddy-current measurements of crack depth are best conducted at frequencies where the wavelength is commensurate with the crack length.

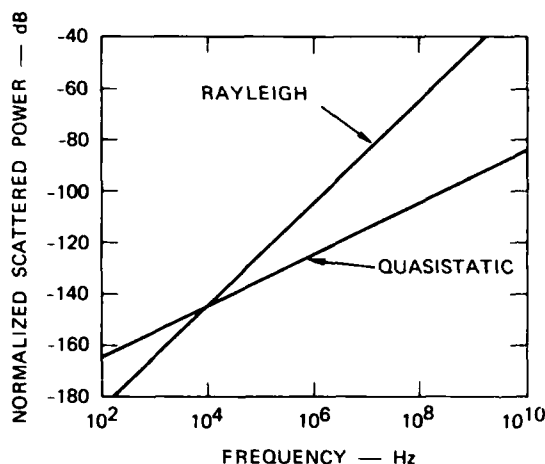


FIGURE 4 COMPARISON OF RAYLEIGH AND QUASI-STATIC SCATTERING FOR A DEEP SLOT

AN IDEALIZED MEASUREMENT PROTOCOL

Equation (13) provides the basis for defining an idealized eddy-current measurement protocol for determining crack dimensions. This protocol can be divided into four main steps:

- (1) Calibrate the system at each measurement frequency using a "standard crack" to determine the lift-off factor,
- (2) Detect the real crack while keeping the distance between the probe and the specimen the same as in the calibration,
- (3) Measure the crack in at least two different orientations to determine the orientation factor (assuming the crack length is much larger than the crack width),
- (4) Collect sufficient data to permit unambiguous inversion using the model to obtain the crack dimensions. (Ideally, a minimum data set would consist of amplitude and phase at two frequencies--the use of more frequencies may be required in the resonance region in order to resolve ambiguities).

Since the data will not be perfectly accurate and the crack geometry will not be known precisely, it is likely that statistical techniques, adaptive learning techniques, or both, will be required to obtain sufficient accuracy for crack dimensions determined from eddy-current measurements. In any case, Eq. (13) should provide a useful basis for designing experiments.

EXPERIMENT

The amplitude and phase of the cross-polarized backscattering from a series of rectangular slots in an aluminum plate were measured using the microwave system whose schematic diagram is shown in Fig. 5. This system uses an orthomode coupler to discriminate against co-polarized backscatter, and a homodyne detection system to provide in-phase (I) and quadrature (Q) output signals. The sensitivity of this

system is currently about -75 dBm; this sensitivity is determined by the degree to which the transmitting and receiving portions of the system can be isolated in the absence of a crack by the orthomode coupler. The antenna used in the system is a lens-focused horn with a beamwidth at its focal point of about 3.5 mm at the operating frequency of 100 GHz.

An aluminum plate with six slots of different sizes electrodischarge-machined into its surface was prepared according to the layout shown in Fig. 6. Slots 1, 2, and 3 have a cross section ($a \times b$) of 2.54 mm \times 0.25 mm; slots 4, 5, and 6 have a cross section of 1.27 mm \times 0.25 mm. Thus, $a/b = 10$ for the first set of slots, and $a/b = 5$ for the second set of slots. Also, at 100 GHz, $ka/\pi = 1.7$ for the first set, and $ka/\pi = 0.85$ for the second set. Finally, slots 1 and 4 were specified to be 0.25 mm deep, slots 2 and 5, 0.5 mm deep, and slots 3 and 6, 1.0 mm deep.

The measured in-phase and quadrature voltages obtained at 98 GHz by translating the slots through the microwave beam are shown in Fig. 7. The plate was aligned perpendicularly to the microwave beam and was positioned so that a linear translation of the plate caused the centers of the slots to pass through the center of the beam, thereby maximizing the peak signal obtained from each slot. The slots were aligned with their lengths at an angle of about 60° to the electric polarization vector, thus ensuring that some of the incident energy would be coupled into the cross-polarized mode by each slot.

The in-phase and quadrature voltages were combined to form a polar display on a storage oscilloscope--common practice in low-frequency eddy-current work. The corresponding polar display for slots 1, 2, and 3 (the 2.5 mm-long slots) is shown in Fig. 7(c). This type of display clearly shows the differences in the amplitudes and phases of the scattered signals produced by the different-depth slots. In this case, the signal produced by slot 3 (1.0 mm deep) is very different from the signals produced by the other slots. However, all three signals are clearly distinguishable.

The approximate model (described previously) that assumes a sinusoidal distribution of electric field in the slot mouth can be used to calculate the theoretical slot response for the parameters used in the experiment. For a focused microwave beam, the change in excitation of the slot caused by moving the slot through the beam can be approximated by setting

$$F_{LF} = e^{-jkx'^2/R_0} \frac{2J_1(kx'/2)}{kx'/2} \quad (29)$$

where k is the wave number, x' is distance along the scanning direction measured from the center of the slot, R_0 is the distance between the microwave lens and the aluminum plate, and J_1 is the Bessel function of first kind and first order. Also, in this simple model, it is necessary to assume that the incident field is constant over the slot mouth for each position x' .

* This test plate was prepared under the direction of Dr. O. Buck of the Rockwell International Science Center, Thousand Oaks, California.

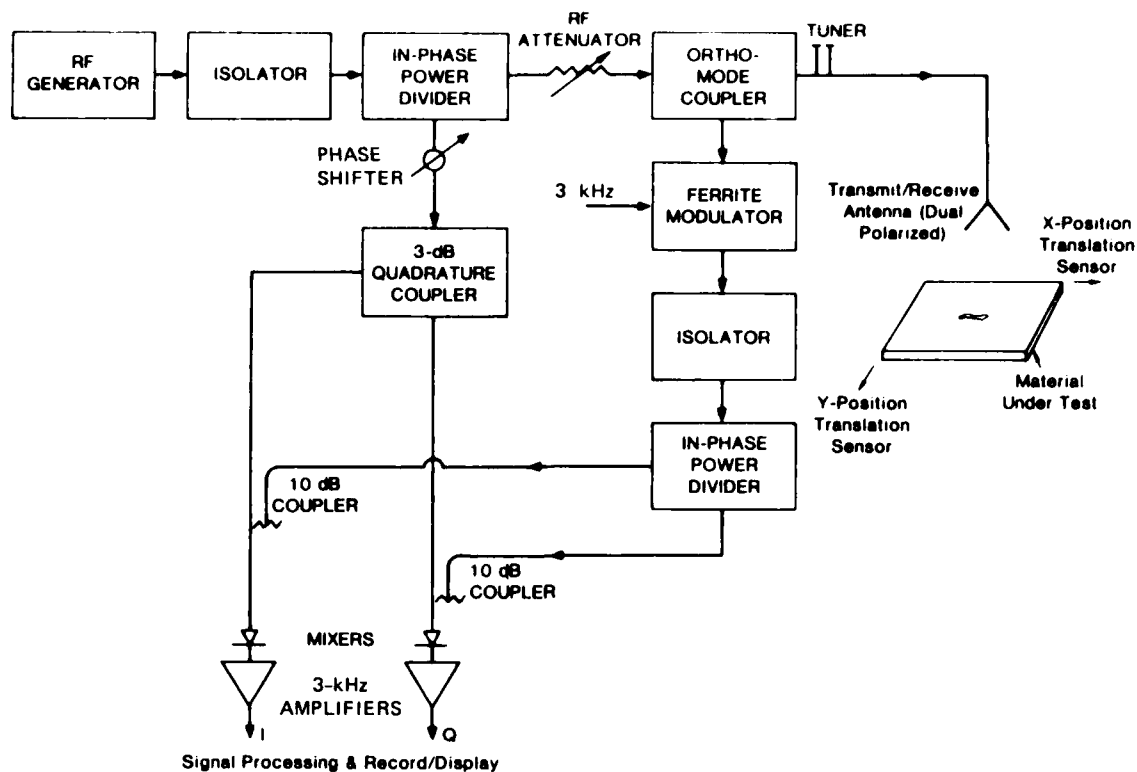


FIGURE 5 MICROWAVE SYSTEM FOR MEASURING CROSS-POLARIZED BACKSCATTER USING HOMODYNE DETECTION

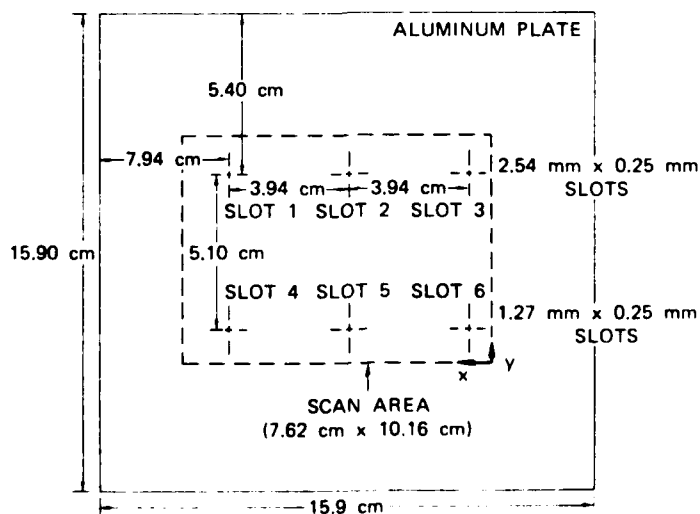


FIGURE 6 LAYOUT OF SLOTTED ALUMINUM PLATE (slots are aligned in the x-direction)

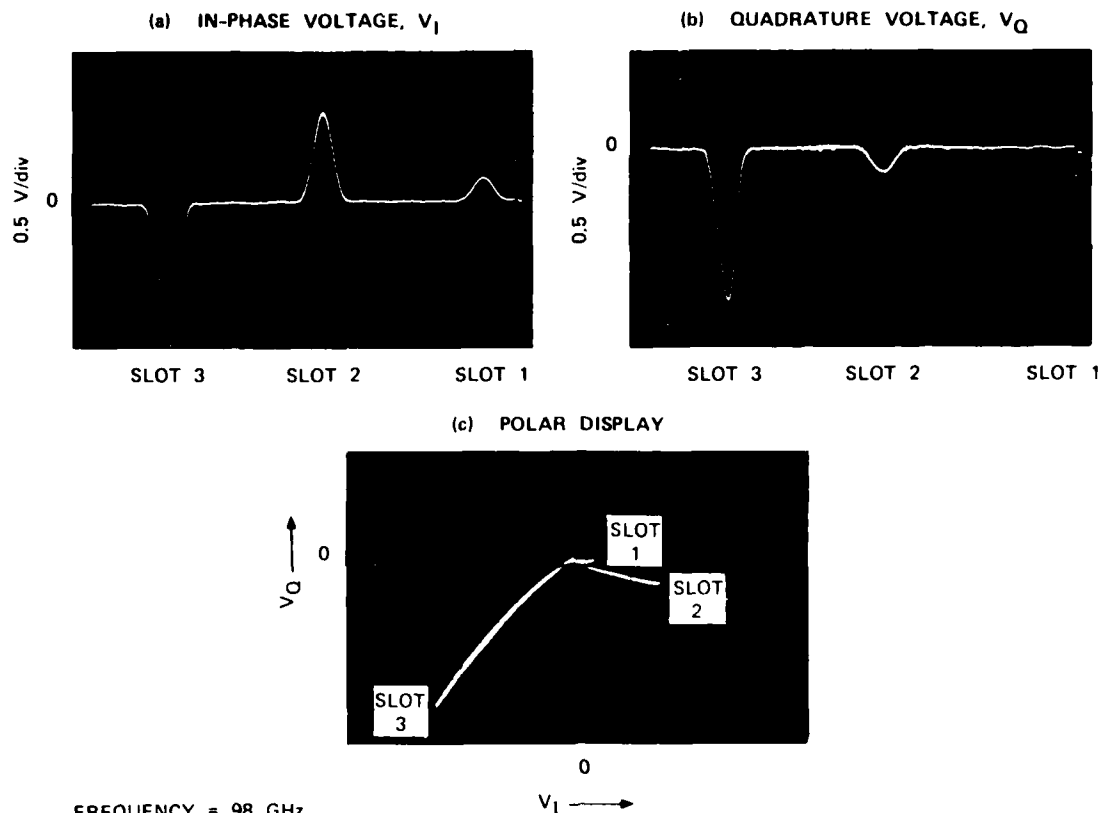


FIGURE 7 MEASURED SLOT RESPONSE FOR SLOTS 1, 2, AND 3

The result of the calculation for slots 1, 2, and 3 is shown in Fig. 8. The absolute amplitude and phase is undetermined in this calculation; therefore, the theoretical plot has been normalized so that the peak response for slot 3 matches the experimental value for that slot. The experimental peak values of each slot response are indicated by Xs. A comparison of Figs. 7(c) and 8 shows remarkable agreement, considering the approximate nature of the model.

The experimental results obtained for slots 4, 5, and 6 are shown in Fig. 9. In that measurement, the gain was increased over that used for the larger slots and, as a result, liftoff effects became noticeable, as is evidenced by the high background or clutter in Figs. 9(a) and (b). However, as expected, the polar display [Fig. 9(c)] allows the slot signals to be clearly distinguished from the liftoff signal because the two types of signals are nearly orthogonal.

In this case, the length of the slots (1.27 mm) causes the operating frequency of 98 GHz to lie below the resonance region, with the result that changes in slot depth produce relatively little change in the phase of the scattered signal.

The corresponding theoretical response for these smaller slots is shown in Fig. 10. In this case, the theoretical plot was normalized to the experimental peak value for slot 6 after the clutter (liftoff signal) had been subtracted. Again, agreement between theory and experiment is fairly good.

INVERSION

In view of the good agreement between theory and experiment, it appears worthwhile to examine the measurement-error sensitivity of an inversion process that is based on the simple model. Since all the slots were located at the same distance from the microwave lens and had the same orientation relative to the polarization of the incident wave, it was simplest to use one of the slots (slot 3) as a reference slot for calibrating the system via the model. Slot 2 was chosen as the unknown slot whose dimensions were being sought. Hence, the ratio of the measured complex signal for slot 2 to that for slot 3 was compared to the same ratio obtained from theory.

Ideally, measurements at two frequencies that are far enough apart to produce measureable changes in scattering are needed in order to determine all three dimensions of a slot, as was mentioned in the section on measurement protocol. However, the existing experimental system did not permit significant changes in operating frequency to be made; therefore it was necessary to assume that one of the slot dimensions was known. The slot length, a , was chosen for this dimension, as it is the most likely to be known.

The amplitude and phase of the relative scattering from slot 2 at 99.9 GHz are shown in Fig. 11 as functions of slot depth, with slot width as a parameter. It is assumed that $a = 2.5$ mm. Also indicated in the figure are the estimated ranges for

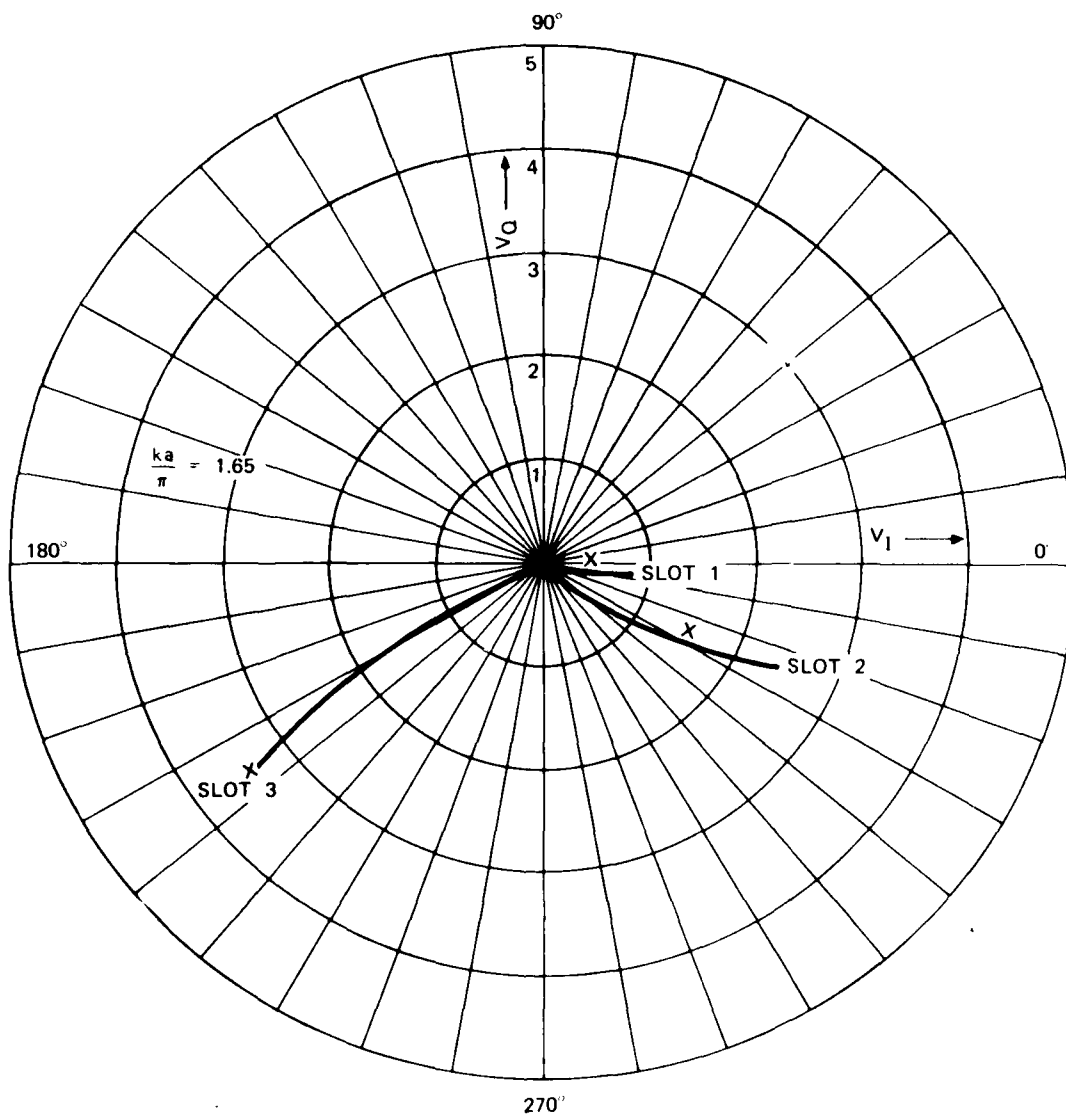


FIGURE 8 THEORETICAL SLOT RESPONSE FOR SLOTS 1, 2, AND 3 (x indicates measured peak value)

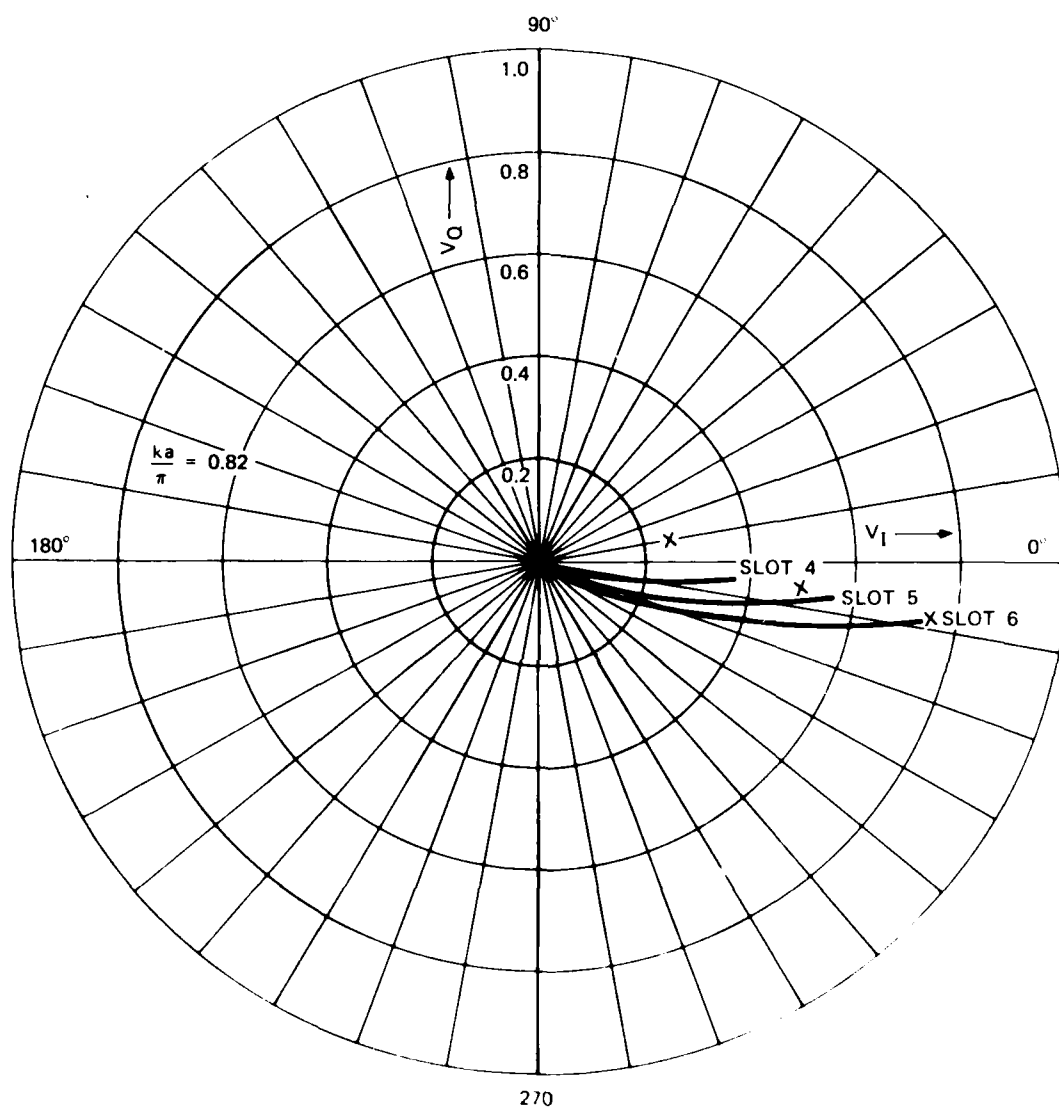


FIGURE 10 THEORETICAL SLOT RESPONSE FOR SLOTS 4, 5, AND 6 (x indicates measured peak value)

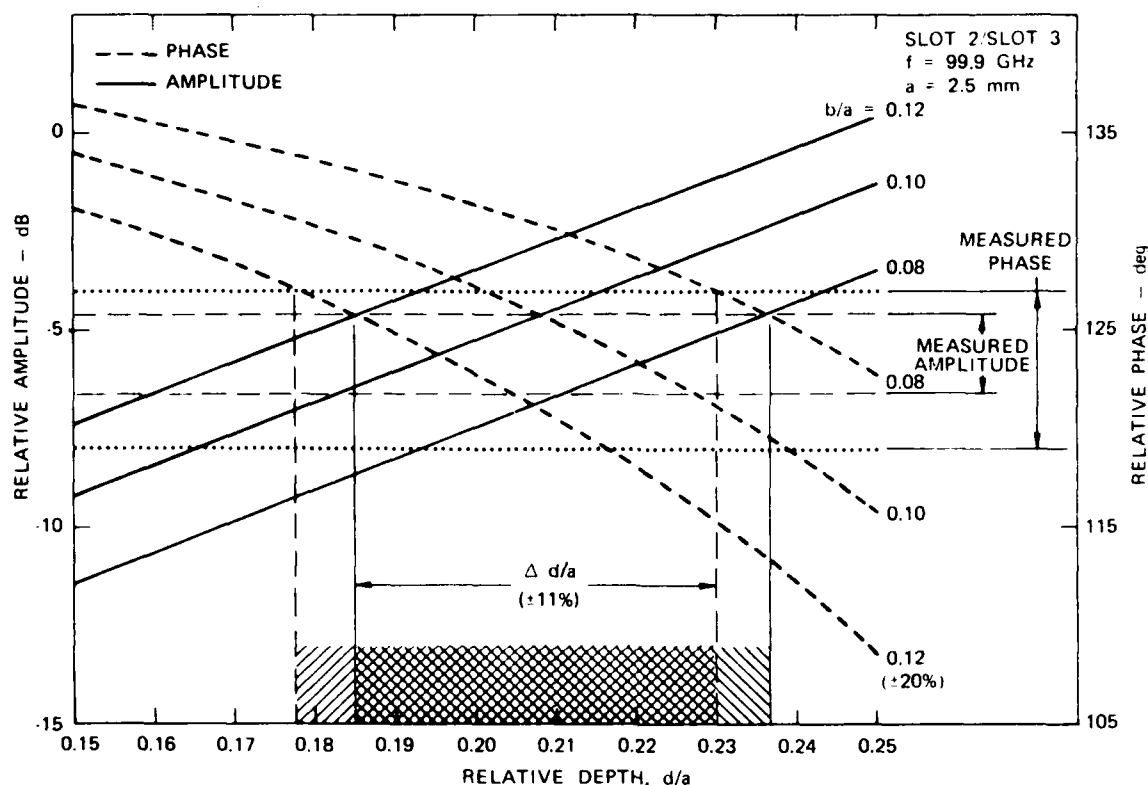


FIGURE 11 AMPLITUDE AND PHASE OF THE SCATTERING FROM SLOT 2 (relative to slot 3) AS FUNCTIONS OF SLOT DEPTH

the measured data. The measurement errors corresponding to these ranges are: amplitude ± 1 dB; phase, $\pm 4^\circ$. One can see from the figure that, if the slot width can be estimated to within $\pm 20\%$, the measured data determines the slot depth to within $\pm 11\%$ (the cross-hatched area).

It is interesting to note that, in this case, the use of amplitude data alone would only increase the uncertainty in the depth determination by a small amount, namely to $\pm 14\%$. The slot depth measured from a scanning electron micrograph of a rubber replica of slot 2 is $d/a = 0.21$. This value lies approximately in the center of the cross-hatched slot-depth range shown in Fig. 11.

If the cross-sectional dimensions of a crack cannot be obtained by microscopic examination or by some other means, all three of the crack dimensions must be obtained from the eddy-current measurement alone. The accuracy of the required inversion solution will depend on how sensitive the scattering is to changes in each crack dimension. Calculations using the model developed here show that this sensitivity depends on the product of crack length and operating frequency, with maximum sensitivity obtained in specific portions of the resonance region. Thus, obtaining maximum accuracy in determining crack size will necessitate the use of a frequency that is appropriate to the size range being measured.

SUMMARY

A general theory for the electromagnetic scattering from a surface-breaking crack in a conducting material has been developed. The theory is valid for any frequency, and provides a basis for defining a measurement protocol for the purpose of determining crack dimensions from eddy-current measurements. The theory also shows that, at low frequencies, eddy-current measurements of cracks are dominated by effects of finite conductivity while, at high frequencies, the measured signals are determined mostly by energy storage in the crack.

Approximate numerical results have been obtained for the case of a rectangular slot. This example reveals all of the essential characteristics of the backscattering as a function of frequency and slot dimensions, and gives insight into what can be expected for the behavior of a signal scattered by a real crack. For example, when the slot length is greater than one-half wavelength, resonances can occur; these resonances make the determination of slot depth from measured scattering accurate but introduce ambiguities. For smaller slot lengths, there is a one-to-one relation between slot depth and scattered signal, but the amplitude of the scattered energy is smaller and slot depths that are greater than one slot length are not well resolved. The effects of liftoff and slot orientation are also elucidated in the example.

Experimental results obtained at 100 GHz using electrodischarge-machined slots in an aluminum plate were found to be in good agreement with theory. The smallest available slot, which was 1.27 mm long, 0.25 mm wide, and 0.25 mm deep, could be distinguished from clutter (liftoff) by using phase-sensitive detection and a polar display. An example of using the measured data and the theoretical model to determine slot depth was given.

One can conclude that it should be possible to obtain an accurate determination of the dimensions of a surface-breaking crack from microwave scattering measurements. Although further improvements in the theory are possible, questions concerning the practical and economic realization of the technique should be addressed first.

ACKNOWLEDGEMENT

Technical discussions with Dr. B. A. Auld of Stanford University and Dr. R. B. Thompson of Rockwell International Science Center were most helpful in this work. Thanks are also due to Dr. A. C. Phillips of SRI for designing the 3-kHz portion of the phase-sensitive detection system used in the measurements.

This work was sponsored by the Center for Advanced NDE operated by the Rockwell International Science Center under Contract F33615-74-C-5180.

REFERENCES

1. R. J. Hruby and L. Feinstein, "A Novel Nondestructive, Noncontacting Method of Measuring the Depth of Thin Slits and Cracks in Metals," The Review of Scientific Instruments, Vol. 41, pp. 679-683 (May 1970).
2. A. Hussain and E. A. Ash, "Microwave Scanning Microscopy for Nondestructive Testing," Proceedings of the 5th European Microwave Conference, Hamburg, Germany, pp. 213-217 (September 1975).
3. R. E. Collin, Field Theory of Guided Waves (New York: McGraw-Hill, 1960).
4. P. R. McIsaac, "A General Reciprocity Theorem," IEEE Trans. Microwave Theory Tech., Vol. MTT-27, pp. 340-342 (April 1979).
5. A. J. Bahr, "Using Electromagnetic Scattering to Estimate the Depth of a Rectangular Slot," IEEE Trans. Antennas Propagat., to be published.
6. R. F. Harrington and J. R. Mautz, "Computational Methods for Transmission of Waves Through Apertures," Electromagnetic Scattering, P.L.E. Uslenghi, Ed. (New York: Academic Press, 1978).
7. R. F. Harrington, Field Computation by Moment Methods (New York: Macmillan Company, 1968).
8. R.W.P. King and C. W. Harrison, Jr., Antennas and Waves: A Modern Approach (The M.I.T. Press, Cambridge, Mass., 1969).
9. D. R. Rhodes, "On a Fundamental Principle in the Theory of Planar Antennas," Proc. IEEE, Vol. 52, pp. 1013-1021 (Sept. 1964).
10. D. R. Rhodes, "On the Stored Energy of Planar Apertures," IEEE Trans. Antennas Propagat., Vol. AP-14, pp. 676-683 (Nov. 1966).

FINITE ELEMENT ANALYSIS OF AXISYMMETRIC GEOMETRIES IN QUANTITATIVE NDE

R. Palanisamy and W. Lord
Department of Electrical Engineering
Colorado State University
Fort Collins, Colorado 80523

ABSTRACT

Solution of the inversion problem in quantitative eddy current NDE requires an adequate mathematical model to describe the complicated interactions of currents, fields and flaws in materials. Existing analytical techniques are not capable of accommodating materials with nonlinear magnetic characteristics or awkward flaw shapes.

This paper describes a finite element computation of the complex impedance of an eddy current sensor in axisymmetric testing configurations, some with defects and gives the corresponding magnetic flux distributions. The authors suggest that, because finite element analysis techniques are not limited by material nonlinearities and complex defect geometries, they can be applied to the development of computer based defect characterization schemes for realistic eddy current NDE applications.

INTRODUCTION

Nondestructive testing and evaluation play an important role in the design, fabrication and day-to-day maintenance of military, aerospace, electric power and transportation industry equipment. The economic impact of component failure in these industries is well documented¹⁻⁴ and, together with the obvious human and environmental implications, provides a major impetus to improve all aspects of the nondestructive testing art. Progress has been made toward this end through such efforts as the DARPA/AFML program⁵. Although the work has concentrated primarily on ultrasonic techniques, much of the research philosophy developed for the program with regard to the study of basic phenomena⁶, development of models⁷, signature identification by signal processing⁸ and the subsequent accept/reject decision founded on a knowledge of fracture mechanics and related failure probabilities could and should be applied to other nondestructive testing techniques. The cornerstone of such an approach is the development of an adequate mathematical model for the study of basic field/defect interactions. Such a model is needed in order to develop a defect characterization scheme and to identify suitable parameters for signal processing.

In eddy current methods of nondestructive testing, alternating current excitation is used to induce secondary currents and fields in the specimen undergoing inspection. Defects in the specimen cause changes in both induced current and fields, resulting in measurable impedance variations in a nearby search coil. Despite recent developments in automatic defect characterization associated with eddy current and leakage flux methods of nondestructive testing⁹⁻¹¹, the subject of electromagnetic methods of nondestructively testing ferromagnetic materials is characterized largely by empirical knowledge. Where closed form mathematical solutions do exist, describing electromagnetic field/defect interactions, the underlying assumptions of the theories tend to invalidate any realistic application of the results to the problem of defect characterization.

The problem of modeling electromagnetic field/defect interactions in materials is complicated by any nonlinear magnetization characteristic of the material and awkward defect boundaries. For this reason, much of the existing literature associated with eddy current phenomena is concerned with making simplifying assumptions so that, for a given eddy current situation, closed-form expressions can be obtained for the normalized impedance of the search coil. Scott¹² gives an overview of the numerous mathematical approaches which lead to closed-form solutions of eddy current problems and references 13 through 26 describe these various classical approaches in more detail. Despite the apparent plethora of analysis techniques including wave theory, integral, network and finite difference formulations, the basic problem of developing a defect characterization scheme for realistic defects in nonlinear ferromagnetic materials still remains.

An approach which does show promise of providing the basis of defect characterization schemes for all electromagnetic NDE methods (i.e., residual and eddy current forms) is the finite element analysis technique which was originally developed for the study of magnetic fields in electrical machinery.²⁷⁻³⁰ Lord and Ward³¹ have subsequently applied this technique^{32,33} to the development of a defect characterization scheme for active leakage field methods of nondestructive testing. More recently, Lord and Ward³⁴ building on work relating to eddy current methods^{35,36} have demonstrated how that finite element NDE techniques for both active and the finite element approach.

The main purpose of this paper is to give a further overview of the authors' method to extend the finite element approach to the analysis of eddy current NDE problems, and to describe the basic principles of the finite element approach.

THE FINITE ELEMENT APPROACH

The finite element approach is a numerical technique for solving problems in engineering and science. It is based on the idea of approximating a continuous domain by a discrete set of elements, each of which is assumed to have a constant value of the field variable.

in the r, z plane as shown in Fig. 1.

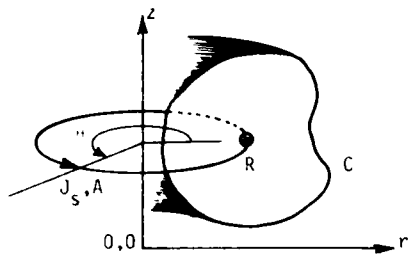


Fig. 1. Axisymmetric Geometry Showing the Direction of J_s and A .

The sinusoidal source current density J_s (amps/m²) and hence the complex magnetic vector potential A (Webers/m) have components only along the positive θ direction. That is, both J_s and A are a function of r and z only. This situation can be modeled by a Poisson type of nonlinear diffusion equation³⁷

$$\frac{\partial^2 A}{\partial r^2} + \frac{1}{r} \frac{\partial A}{\partial r} + \frac{\partial^2 A}{\partial z^2} - \frac{A}{r^2} = -\mu J_s + j\omega\sigma\mu A \quad (1)$$

where μ = nonlinear magnetic permeability (Henry/m)

ω = angular frequency (rad/sec)

σ = electrical conductivity (mhos/m)

$j = \sqrt{-1}$, complex operator.

The eddy current density J_e (amps/m²) is given by

$$J_e = -j\omega A \quad (2)$$

From the principles of variational calculus, it can be shown that a correct solution of Eq. 1 can be obtained by minimizing the nonlinear energy functional

$$F = \iiint_V \left[\frac{1}{\mu} B dB + \frac{1}{2} j\omega\sigma |A|^2 - J_s \cdot A \right] dv \quad (3)$$

where B = flux density (Webers/m²), over the entire region of interest.

Finite Element Formulation - The very basis of finite element analysis is to search for a function A such that the energy functional F of Eq. 3 is minimized, instead of solving Eq. 1 directly.

The region R of Fig. 1 which contains the area of interest (including current sources, ferromagnetic material, etc.) must be of finite size if Eq. 3 is to be solved numerically. The boundary of the region is chosen such that the magnetic vector potential A is either zero along the boundary or the gradient of A is negligibly small along the boundary compared to the value elsewhere in the region. Discretization of this region is achieved as follows (see Fig. 2)³⁴:

The chosen solution region (finite element region) is subdivided into triangles. The number, shape and size of these triangles

are not restricted in any way.

- Interfaces between different materials must be formed by the sides of the triangles.
- In order to ensure a reasonable accuracy of the numerical solution, the triangles must be smaller in a region where the gradient of the magnetic flux density is larger.
- All the elements have the same unit depth of one radian in the θ direction.
- The current density, permeability and flux density are assumed to be constant within each triangular element.
- Along the boundary C , the magnetic vector potential is zero.

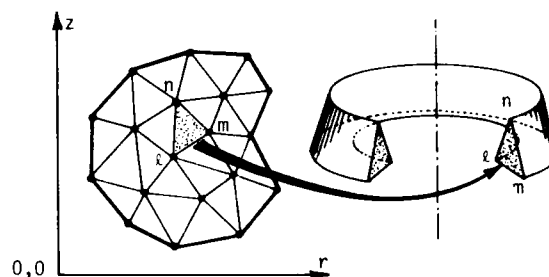


Fig. 2. Discretization of the Finite Element Region R , and a Typical Axisymmetric Finite Element lmn .

In order to set up the local element matrix equation the variation of function A within each element is assumed to be linear and dependent only on the values of A at the vertices. For example, the value of $A_p(r, z)$ at the point $P(r, z)$ within the element lmn in Fig. 3 is given by

$$A_p(r, z) = \frac{1}{2\Delta} \sum_{i=l,m,n} (a_i + b_i r + c_i z) A_i \quad (4)$$

where

$$a_l = r_m z_n - z_m r_n \quad (5)$$

$$b_l = z_m - z_n \quad (6)$$

$$c_l = r_m - r_n \quad (7)$$

Δ is the area of the element lmn , and A_l , A_m and A_n are the values of A at the vertices l , m and n . Extending this approximation to all the elements in the region R , we obtain an approximate representation for A throughout the region. All the vertex (nodal) values of A in the region are varied simultaneously until the energy functional F given in Eq. 3 reaches a minimum, resulting in the final solution for A at all the nodes in the region.

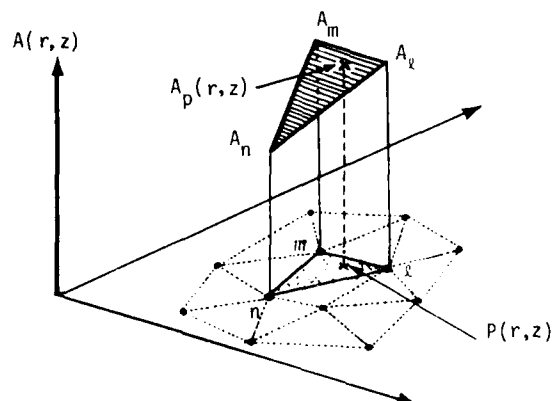


Fig. 3. Linear Approximation of Function A within a Triangular Finite Element, Δ_{mn} .

Minimization of the energy functional F is achieved by setting the first derivative of F with respect to every vertex value equal to zero. That is

$$\frac{\partial F}{\partial A_k} = 0, \quad k=1,2,\dots,N \quad (8)$$

where N = total number of nodes in the region. Instead of performing the minimization node by node in sequence, for convenience, we perform it element by element. Substituting $A_p(r, z)$ from Eq. 4 in Eq. 3 and performing the following three operations simultaneously, i.e.

$$\frac{\partial F}{\partial A_i} = 0, \quad i=l,m,n \quad (9)$$

we obtain three equations in three unknown vector potential values (A_l , A_m and A_n) for the element Δ_{mn} .

After some algebra these equations are represented in the final matrix form as³⁷

$$([S]_e + j[R]_e)\{A\}_e = \{Q\}_e \quad (10)$$

where $[S]_e$ is a 3×3 'element matrix' formed from the r and z values of the three vertices l , m and n and the area Δ in an element Δ_{mn} , μ value associated with the element Δ_{mn} , and the centroid of the element r_c from the z axis,

$$= \frac{r_c}{4\Delta\mu} \begin{bmatrix} (b'_l b'_l + c'_l c'_l) & (b'_l b'_m + c'_l c'_m) & (b'_l b'_n + c'_l c'_n) \\ (b'_m b'_l + c'_m c'_l) & (b'_m b'_m + c'_m c'_m) & (b'_m b'_n + c'_m c'_n) \\ (b'_n b'_l + c'_n c'_l) & (b'_n b'_m + c'_n c'_m) & (b'_n b'_n + c'_n c'_n) \end{bmatrix}$$

$$b'_k = b_k + \frac{2\Delta}{3r_c}, \quad k = l, m, n$$

$[R]_e$ is a 3×3 'element matrix' formed from the angular frequency ω , electrical conductivity σ

associated with the element Δ_{mn} and the centroid r_c and area Δ of the element Δ_{mn} ,

$$= \frac{\omega\sigma\Delta r_c}{12} \begin{bmatrix} 2 & 1 & 1 \\ 1 & 2 & 1 \\ 1 & 1 & 2 \end{bmatrix}$$

$\{Q\}_e$ is a 3×1 'element matrix' formed from the complex current density J_s within an element Δ_{mn} ,

$$= \frac{J_s \Delta r_c}{3} \begin{bmatrix} 1 \\ 1 \\ 1 \end{bmatrix}$$

$\{A\}_e$ is a 3×1 'element matrix' formed from the unknown complex vector potentials A_l , A_m and A_n of an element Δ_{mn} ,

$$= \begin{bmatrix} A_l \\ A_m \\ A_n \end{bmatrix}$$

This is the finite element representation of the energy functional of Eq. 3 for a typical triangle Δ_{mn} in the region R . This approach now has to be extended to cover all the elements of region R to form the global matrix equation.

Element matrix equations corresponding to Eq. 10 can be formed separately for all the elements in the finite element region. These individual element equations are then combined into a single 'global matrix' equation

$$[G]\{A\} = \{Q\} \quad (11)$$

where $[G]$ is a $(N \times N)$ banded symmetric complex matrix, and $\{Q\}$ and $\{A\}$ are $(N \times 1)$ complex column matrices. The expanded form of equation 11 is

$$\begin{bmatrix} \text{Semibandwidth} \\ \vdots \\ \vdots \\ \vdots \end{bmatrix} \begin{bmatrix} A_1 \\ A_2 \\ A_3 \\ \vdots \\ \vdots \\ \vdots \\ A_N \end{bmatrix} = \begin{bmatrix} Q_1 \\ Q_2 \\ Q_3 \\ \vdots \\ \vdots \\ \vdots \\ Q_N \end{bmatrix} \quad (12)$$

$N \times N \quad N \times 1 \quad N \times 1$

Any of the direct solution techniques (e.g. Gaussian elimination⁴⁵), utilizing the banded symmetry and sparse nature of the global matrix, [G], can be applied to solve for the unknown vector potentials, A. Because of symmetry, it is sufficient to store only the elements in the semibandwidth of the matrix [G], and this brings down the computer storage requirement considerably.

Calculation of Flux Density - The relationship between the magnetic flux density B and the magnetic vector potential A is

$$\mathbf{B} = \nabla \times \mathbf{A} \quad (13)$$

Remembering that A has a component only along the positive z direction, we obtain

$$B_r = -\frac{\partial A}{\partial z} \quad (14)$$

$$B_z = \frac{A}{r} + \frac{\partial A}{\partial r} \quad (15)$$

$$B_\theta = 0 \quad (16)$$

Within each finite element a linear variation of A is assumed⁴⁰.

$$A = \alpha_1 + \alpha_2 r + \alpha_3 z \quad (17)$$

Therefore,

$$B_r = -\alpha_3 \quad (18)$$

$$B_z = \frac{A}{r} + \alpha_2 \quad (19)$$

Taking A_c as the value of A at the centroid r_c (Fig. 4)^c of a triangular element, without loss of accuracy, we obtain

$$B_z = \frac{A_c}{r_c} + \alpha_2 \quad (20)$$

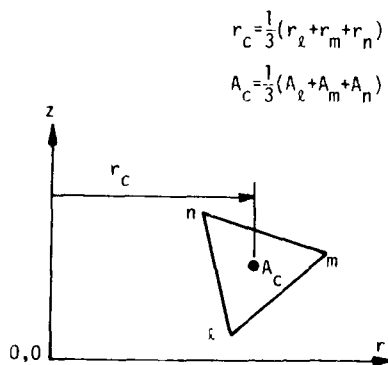


Fig. 4. Approximate values of r_c and A_c in an Element kmn .

The expressions for α_2 and α_3 can be obtained by simultaneously solving the three equations written for A_k , A_m and A_n using Eq. 17. A_c and r_c can be calculated either as indicated in Fig. 4, or by using area coordinates for better accuracy⁴⁶. That is,

$$r_c = \left[\frac{1}{12} (r_k^2 + r_m^2 + r_n^2 + (r_k + r_m + r_n)^2) \right]^{1/2} \quad (21)$$

and

$$A_c = \left[\frac{1}{12} (A_k^2 + A_m^2 + A_n^2 + (A_k + A_m + A_n)^2) \right]^{1/2} \quad (22)$$

Hence the final expression for the flux densities are

$$B_r = -\frac{1}{2\Delta} [A_k(r_n - r_m) + A_m(r_k - r_n) + A_n(r_m - r_k)] \quad (23)$$

$$B_z = \frac{A_c}{r_c} + \frac{1}{2\Delta} [A_k(z_m - z_n) + A_m(z_n - z_k) + A_n(z_k - z_m)] \quad (24)$$

Resultant flux density

$$B = (B_r^2 + B_z^2)^{1/2} \quad (25)$$

The simplified flow chart of Fig. 5 outlines the computational steps involved in the finite element analysis of eddy current problems.

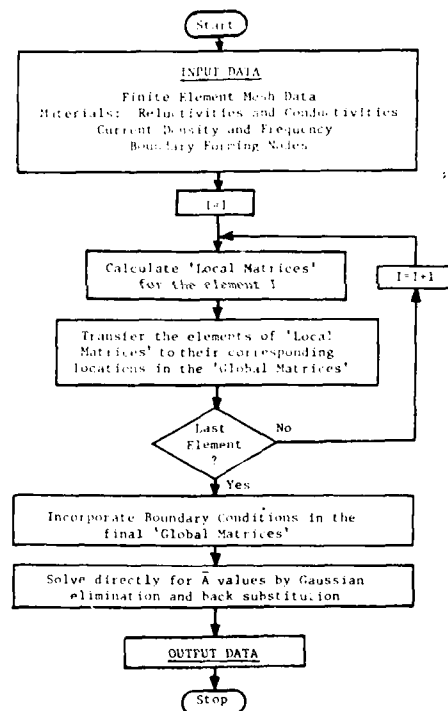


Fig. 5. Simplified Flow Chart for the Finite Element Analysis of Eddy Current Problems.

Normalized Complex Impedance (Z_n) of a Coil - The complex impedance of a circular coil can be calculated from the complex magnetic vector potential values. That is

$$Z = -\frac{j\omega 2\pi N}{I_s} \sum r_c A_c \quad (26)$$

where N is the turn density (turns/m²) in the coil, I_s is the source current (amps), r is the centroidal distance as a triangular element from the z axis (meters), A_c is the complex magnetic vector potential

at the centroid of an element, and the summation is taken over all the elements forming the coil cross-section in the finite element region.

The normalized impedance, Z_n , useful for the complex impedance plane plot, is obtained by dividing Z with the reactance of the coil, ωL_0 , where L_0 is the self inductance of the coil in air. That is,

$$Z_n = \frac{Z}{\omega L_0} \quad (27)$$

RESULTS

Initial emphasis in this work was placed on studying those eddy current geometries for which analytical solutions existed. Reference 44 describes the application of finite element analysis techniques to the problem of predicting the current density in a metal slab lying under a conductor carrying an alternating current. As the results agreed well with the analytical predictions of Stoll¹⁴ the finite element studies were then extended to the axisymmetric geometries described in this paper. For the first three cases results are compared with those predicted by an ORNL program²⁶ based on integral equation concepts. Values of conductivity chosen for the aluminum copper and iron used in these studies were 28.6×10^6 , 57.7×10^6 and 10×10^6 mhos/m respectively. Relative permeability values were 1.0 for aluminum and copper, and 100 for iron.

Case 1: - coil in air. Figures 6a), b) and c) show the geometry, finite element mesh and predicted flux distribution. The corresponding inductance values obtained using finite element (FE) and ORNL code are given in Table 1.

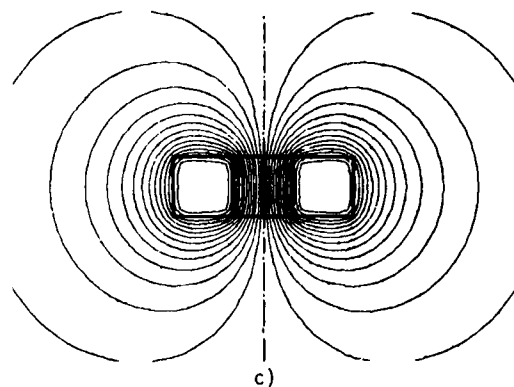
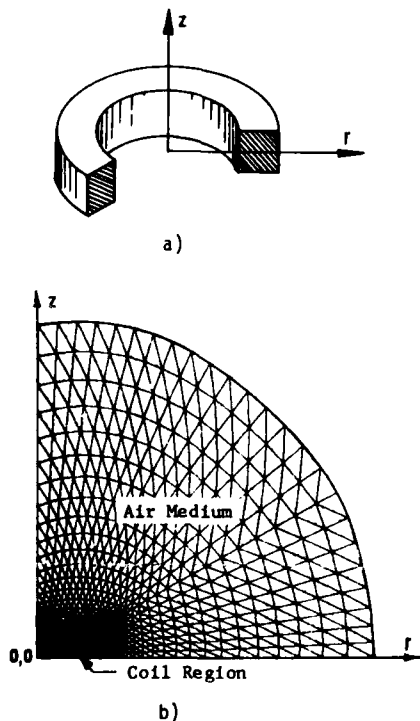


Fig. 6. Circular eddy current coil: a) geometry, b) finite element mesh, c) predicted flux distribution.

Case	FE Code	ORNL Code
1. (Fig. 6). Self Inductance	$3.216 \times 10^{-4} \text{H}$	$3.217 \times 10^{-4} \text{H}$
2. (Fig. 7). Normalized Impedance	$0.101 + j0.723$	$0.101 + j0.737$
3. (Fig. 8). Normalized Impedance	$0.109 + j0.649$	$0.108 + j0.647$

Table 1. Estimated inductance values for cases 1, 2 and 3.

Case 2: - coil on a copper slab. Figure 7 shows the predicted flux distribution for a circular coil supplied at 1250Hz lying on a copper slab. The corresponding normalized impedance values are given in Table 1.

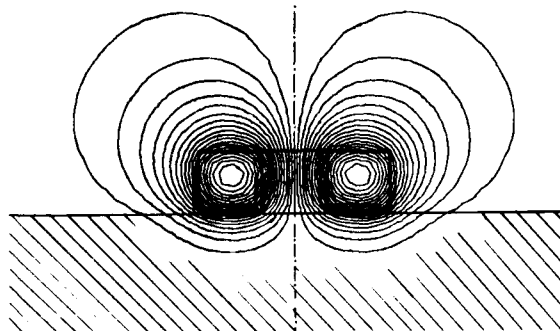


Fig. 7. Flux distribution for a coil on a copper slab at 1250Hz.

Case 3: - coil encircling a two conductor rod. Figure 8 shows the finite element predicted flux distribution for this case with the corresponding normalized impedance values given in Table 1 at

1250 Hz.

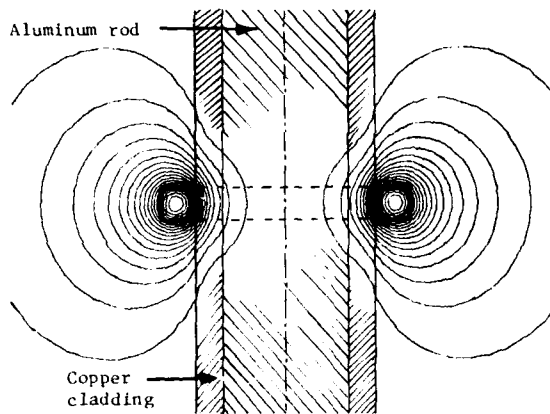


Fig. 8. Flux distribution for coil encircling a two-conductor rod.

Case 4: - coil centered over a flat-bottomed hole in a copper slab. Figures 9a) and b) show the finite element predictions of flux lines for excitation frequencies of 500 and 5,000Hz respectively, the depth of penetration effects are clearly visible.

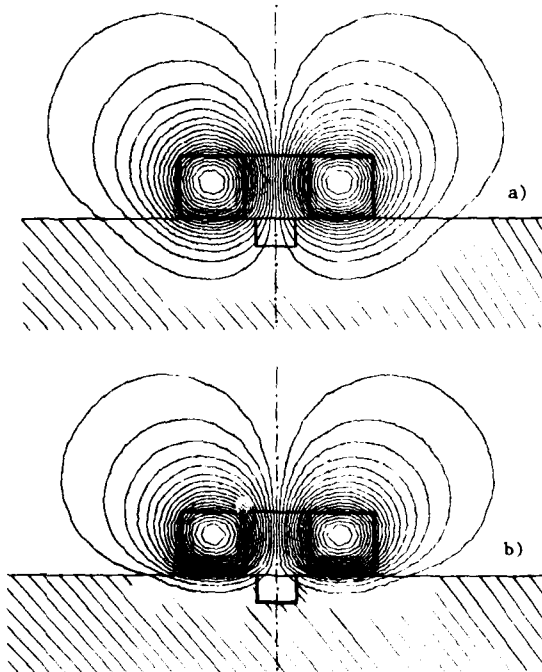


Fig. 9. Flux distribution at a) 500Hz and b) 5,000Hz for a coil lying on a copper slab with a flat bottomed hole.

Case 5: - coil inside a copper tube with an axisymmetric slot. Figures 10a) (copper tube) and b) iron tube) show the effect of tube permeability on the predicted flux distribution. Both plots are

for an excitation frequency of 500Hz and the "shielding" effect of the higher permeability iron tube is clearly visible.

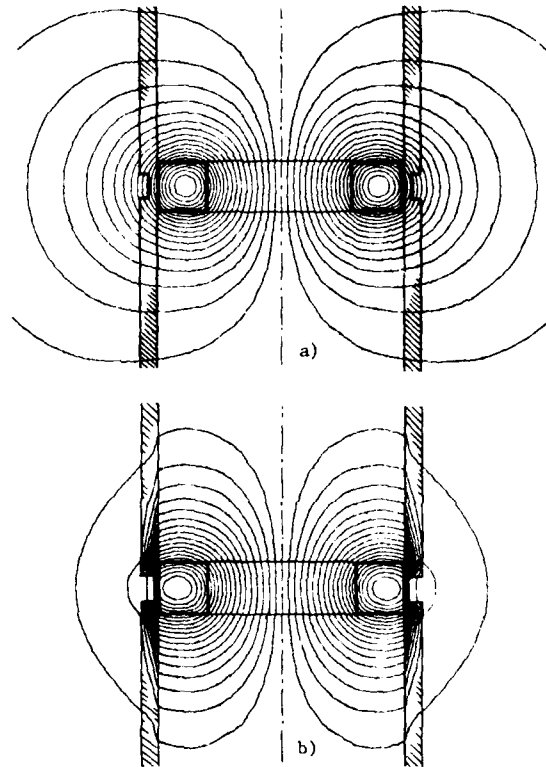
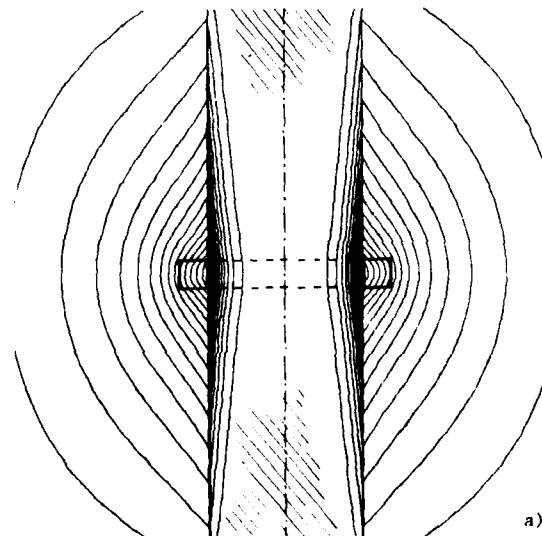


Fig. 10. Flux distribution around a coil in a) a copper tube and b) an iron tube at 500Hz.

Case 6: - coil encircling an iron rod. Figures 11a) and b) show the effect of an axisymmetric slot on the flux distribution in an iron rod encircled by a coil carrying current at 500Hz.



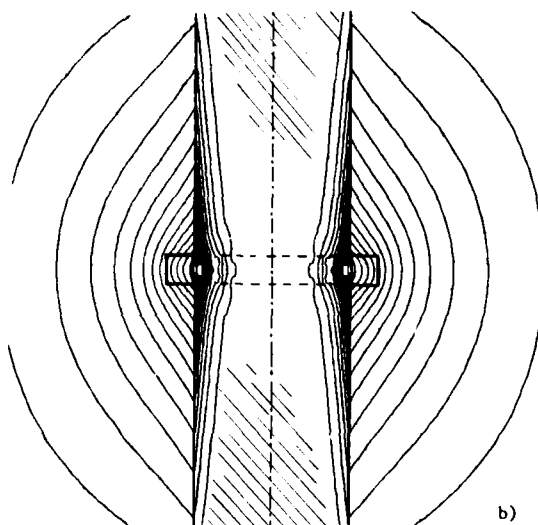


Fig. 11. Flux distribution around a coil encircling a) a plane iron rod and b) an iron rod with an axisymmetric defect.

DISCUSSION

Initial finite element studies of eddy current geometries appear promising. Where corresponding analytical and/or other numerical models exist, good agreement has been obtained with the finite element predictions. This observation is not surprising in that such methods have previously been used with success in the study of eddy current phenomena in electrical machinery. Indeed, if recent progress in the general area of finite element analysis is any yardstick, it should be reasonably safe to predict the solution of nonlinear, 3-dimensional, moving probe eddy current problems within the foreseeable future.

ACKNOWLEDGMENTS

This work is supported by the Electric Power Research Institute under contract RP1395-3 and the Army Research Office under grant DAAG29-76-G-0249.

REFERENCES

1. Bray, D. E. "Railroad Accidents and Nondestructive Inspection". Presented at the ASME Winter Annual Meeting, Paper No. 74-WA/RT-4, November 17, 1974.
2. Darcy, G. "Economic Motivation and Potential Impact of NDE in DOD, Proceedings of the Interdisciplinary Workshop for Quantitative Flaw Definition". AFML publication TR-73-238, June 1974, pp. 68-84.
3. Knight, S. R. "NDT for Nuclear Power". *Materials Evaluation*, May 1973, pp. 19-24.
4. Dau, G. J. "Rationale for Inservice Inspection During Nuclear Power Plant Design/Fabrication". Presented at the American Nuclear Society 23rd Annual Meeting, New York, June 1977.
5. Thompson, R. B. "Overview of the ARPA/AFML Program for Quantitative Flaw Definition". *Proceedings of the ARPA/AFML Review of Progress in Quantitative NDE*, AFML publication TR-77-44, September 1977, pp. 109-115. (Several papers relating to this work appeared in the first edition of the quarterly Research Supplement to *Materials Evaluation*, April 1977).
6. Adler, L. and Lewis, D. K. "Models for the Frequency Dependence of Ultrasonic Scattering from Real Flaws". *ibid.*, pp. 180-186.
7. Krumhansl, J. A. "Interpretation of Ultrasonic Scattering Measurements by Various Flaws from Theoretical Studies". *ibid.*, pp. 164-172.
8. Mucciardi, A. N. "Adaptive Nonlinear Modeling for Ultrasonic Signal Processing". *Proceedings of the Interdisciplinary Workshop for Quantitative Flaw Definition*. AFML publication TR-74-238, June 1974, pp. 194-212.
9. Stumm, W. "Multiparameter-Methoden in der Zerstörungsfreien Werkstoffprüfung". *Materialprüfung*. Vol. 19, April 1977, pp. 131-136.
10. Sukhorukov, V. V., Ullitin, Y. M., Chernov, L. A. "Feasibility of Determining Defect Parameters by Eddy Current Modulation Defectoscopy." *Defektoskopiya*. No. 1, January-February, 1977.
11. Brown, R. L., "Investigating the Computer Analysis of Eddy Current NDT Data", Hanford Engineering Development Laboratory Report, HEDL-SA-1721, February 1979.
12. Scott, I. G. "Eddy Current Problems in Non-destructive Testing", *The Institution of Engineers, Australia Electrical Engineering Transactions*, Vol. EE10, No. 1, 1974, pp. 46-53.
13. Lammeraner, J. and Staf1, M. "Eddy Currents", Iliffe Books, Ltd., 1966.
14. Stoll, R. L. "The Analysis of Eddy Currents", Clarendon Press, 1974.
15. Stoll, R. L. "Solution of Linear Steady State Eddy Current Problems by Complex Successive Overrelaxation", *Proceedings IEE*, Vol. 117, No. 7, July 1970, pp. 1317-1323.
16. Zhukov, V. K. and Zabiroy, R. M. "Conductive Elliptical Cylinder in a Cross-sectionally Varying Uniform Magnetic Field", *Defektoskopiya*, No. 5, September-October 1970, pp. 102-109.
17. Schieber, D. "Transient Eddy Currents in Thin Metal Sheets", *IEEE Transactions on Magnetics*, Vol. MAG-8, No. 4, December 1972, pp. 775-779.
18. Carpenter, C. J. "A Network Approach to the Numerical Solution of Eddy Current Problems", *IEEE Transactions on Magnetics*, Vol. MAG-11, No. 5, September 1975, pp. 1517-1522.

19. Demirchian, K. S. et al, "Scalar Potential Concept for Calculating the Steady Magnetic Fields and Eddy Currents", IEEE Transactions on Magnetics, Vol. MAG-12, No. 6, November 1976, pp. 1045-1046.
20. Freeman, E. M. "Computer-aided Steady-state and Transient Solutions of Field Problems in Induction Devices", Proceedings IEE, Vol. 124, No. 11, November 1977, pp. 1057-1061.
21. McWhirter, J. H. et al, "A Computational Method for Solving Eddy Current Problems via Fredholm Integral Equations", submitted for publication in the IEEE Transactions on Magnetics.
22. Burrows, M. "Theory of Eddy Current Flaw Detection", Ph.D. Thesis, University of Michigan, 1964.
23. Dodd, C. V. "A Solution to Electromagnetic Induction Problems", M.S. Thesis, University of Tennessee, 1965.
24. Dodd, C. V. "Solutions to Electromagnetic Induction Problems", Ph.D. Thesis, University of Tennessee, 1967.
25. Dodd, C. V. et al, "Some Eddy Current Problems and their Integral Solutions", Oak Ridge National Laboratory, Contract No. W-7405-eng-26, April 1969.
26. Luquire, J. W. et al, "Computer Programs for some Eddy Current Problems", Oak Ridge National Laboratory, Contract No. W-7405-eng-26, August 1969.
27. Lord, W., Bridges, J. M., Yen, W., Palanisamy, R. "Residual and Active Leakage Fields Around Defects in Ferromagnetic Materials", Materials Evaluation 36, no. 8, (1978): 47.
28. Winslow, M. A. "Numerical Solution of the Quasilinear Poisson Equation in a Nonuniform Triangle Mesh". Journal of Computational Physics, Vol. 2, 1967, pp. 149-172.
29. Chari, M. V. K., and Silvester, P. "Finite Element Analysis of Magnetically Saturated dc Machines". IEEE Transactions on Power Apparatus and Systems, Vol. 90, 1971, pp. 2362-2372.
30. Anderson, O. W. "Transformer Leakage Flux Program Based on the Finite Element Method". IEEE Transactions on Power Apparatus and Systems, Vol. 92, 1973, pp. 682-689.
31. Lord, W., and Hwang, J. H. "Finite Element Modeling of Magnetic Field/Defect Interactions". ASTM Journal of Testing and Evaluation, Vol. 3, No. 1, January 1975, pp. 21-25.
32. Hwang, J. H., and Lord, W. "Magnetic Leakage Field Signatures of Material Discontinuities". Proceedings of the Tenth Symposium on Nondestructive Evaluation, San Antonio, April 1975, pp. 63-76.
33. Lord, W., and Hwang, J. H. "Defect Characterization from Magnetic Leakage Fields", British Journal of Nondestructive Testing, Vol. 19, No. 1, January 1977, pp. 14-18.
34. Chari, M. V. K. "Finite Element Solution of the Eddy Current Problem in Magnetic Structures". IEEE Transactions on Power Apparatus and Systems, Vol. 93, No. 1, January-February 1974.
35. Okuda, H. "Finite Element Solution of Traveling Wave Magnetic Field and Eddy Current". Electrical Engineering in Japan, Vol. 96, No. 4, 1976, pp. 75-82.
36. Sato, T., et al, "Calculation of Magnetic Field Taking into Account Eddy Current and Nonlinear Magnetism". Electrical Engineering in Japan, Vol. 96, No. 4, 1976, pp. 96-102.
37. Brauer, J. R. "Finite Element Analysis of Electromagnetic Induction in Transformers". Presented at the IEEE Winter Power Meeting, New York, January 1977.
38. Anderson, O. W. "Finite Element Solution of Skin Effect and Eddy Current Problems". Presented at the IEEE PES Summer Meeting, Mexico City, July 1977.
39. Csendes, Z. J. and Chari, M. V. K. "Finite Element Analysis of Eddy Current Effects in Rotating Electric Machines". Presented at the IEEE PES Summer Meeting, Mexico City, July 1977.
40. Chari, M. V. K., and Csendes, Z. J. "Finite Element Analysis of the Skin Effect in Current Carrying Conductors". IEEE Transactions on Magnetics, Vol. 13, No. 5, September 1977, pp. 1125-1127.
41. Demerdash, N. A. and Nehl, T. W. "Solution of Nonlinear Eddy Current and Loss Problems in the Solid Rotors of Large Turbogenerators using a Finite Element Approach". Presented at the PES Winter Meeting, January 1978.
42. Aldefeld, B. "Electromagnetic Field Diffusion in Ferromagnetic Materials". Proceedings IEE, Vol. 125, No. 4, April 1978, pp. 278-282.
43. Chari, M. V. K. and Kincaid, T. G., "The Application of Finite Element Method Analysis to Eddy Current NDE", ARPA/AFML Review of Progress in Quantitative NDE, July 1978.
44. Palanisamy, R. and Lord, W., "Theoretical Aspects of Eddy Current Testing", ASNT National Spring Conference Paper Summaries, April 1979, pp. 138-143.
45. Isaacson, E. and Keller, H. B., Analysis of Numerical Methods, John Wiley & Sons, Inc., New York, 1966.
46. Segerlind, L. J., Applied Finite Element Analysis, John Wiley & Sons, Inc., New York, 1976.

SURFACE FLAW DETECTION WITH FERROMAGNETIC RESONANCE PROBES

B. A. Auld, A. Ezekiel, D. Pettibone, and D. K. Winslow
Ginzton Laboratory
Stanford University
Stanford, California 94305

ABSTRACT

Ferromagnetic probes resonating at microwave frequencies have previously been shown to function as sensitive detectors of surface breaking flaws in metals. A swept frequency mode of operation was used, with the resonance line of the probe displayed on an oscilloscope and the presence of a flaw indicated by a shift of the resonance line. This type of presentation lacks good discrimination between lift-off and flaw signals and also reduces the probe scanning speed because the entire resonance line must be swept at each measurement point on the test specimen. Our new system operates under cw conditions, with a network analyzer type of display giving the probe input impedance in polar coordinates. This provides lift-off discrimination and also enhances sensitivity. Experimental curves and their theoretical interpretations will be presented, and a portable prototype instrument will be described.

INTRODUCTION

The ferromagnetic resonance (FMR) eddy current probe is a miniature microwave resonator consisting of a single crystal yttrium iron garnet (YIG) sphere, less than a millimeter in diameter (Fig. 1).

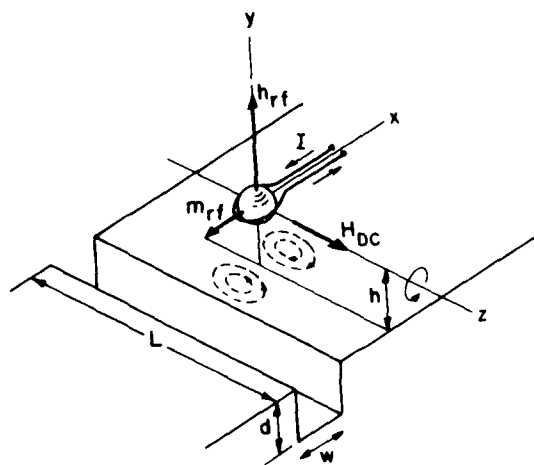


Fig. 1 General schematic of FMR probe interaction with a surface slot.

Its resonant frequency is determined not by its size, as in the case of an electromagnetic or acoustic resonator, but by the strength and direction of an applied dc magnetic field. Like an acoustic resonator, a YIG sphere has many modes of resonance and, when coupled to an external source, can be represented by the same type of equivalent circuit. With ferromagnetic resonance, the magnetization of the resonator material precesses like a spinning top about the applied dc field. For this reason, the resonant frequency is controlled by the applied field. In each mode of resonance the magnetization moves in a characteristic spatial pattern, the most important and easily excited being the one illustrated in Fig. 1, where the precession processes uniformly about the dc field.

The position of the tip of the precessing magnetization vector in Fig. 1 is described by the transverse circularly polarized magnetization m_{rf} , and it is the interaction of this rotating magnetic dipole with the test piece that generates microwave frequency (700 - 4000 MHz) eddy currents on the surface. By contrast with conventional eddy currents in the hundreds of kilohertz frequency range, these microwave eddy currents penetrated only a few microns into the surface. Nevertheless, surface breaking flaws may be detected, as in standard eddy current technology, by passing the probe over the test surface and observing the change in input impedance resulting from perturbation by the flaw of the magnetically induced surface currents. The microwave flaw signal results from the interruption of the surface currents and/or the flow of these currents into the flaw. Because of the stronger concentration of the eddy currents at the surface and also because of the resonant nature of the probe, it is expected that microwave FMR probes should have greater sensitivity to very small surface breaking cracks. A detailed analytical study of the basic probe theory presented a year ago¹ estimated that a surface breaking crack of 0.002" length should be detectable with this system. Such an estimate is, of course, incomplete in that it ignores the effects of spurious signals arising from surface roughness and lift-off variations. For this reason our top priorities this year have been to study lift-off variations and to construct a portable instrument for performing experiments under more realistic environmental conditions.

In addition to its potential advantages with regard to sensitivity the YIG probe, because of its very small size, promises to provide excellent spatial resolution, discrimination against edge effects, and accessibility to restricted corners. Figure 2 illustrates the geometries of our present generation of probes, one for surface probing and the other for the interiors of holes and corners. Our current philosophy is to apply the dc magnetic field from a separately-mounted samarium cobalt permanent magnet having dimensions in the order of a fraction of an inch. This technique, illustrated in Fig. 3, allows accessibility to flaws to be

determined by the probe size rather than the magnet.

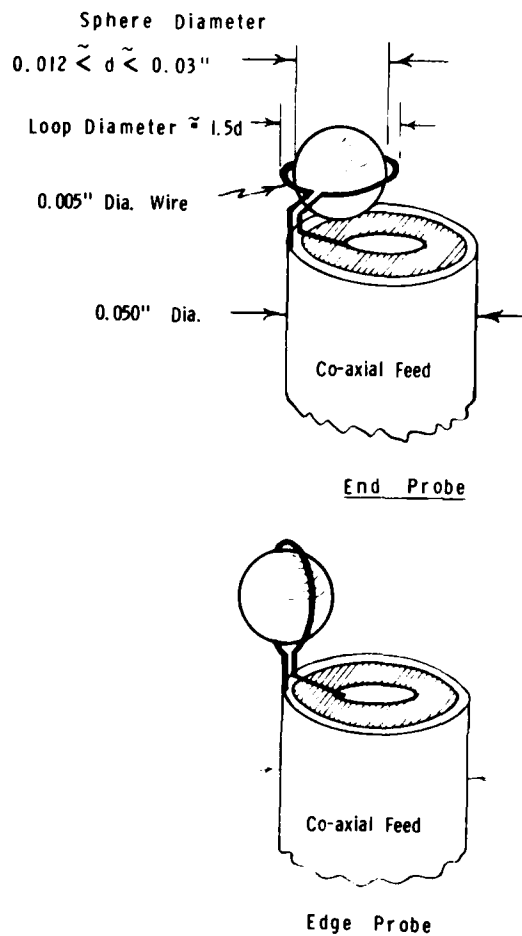


Fig. 2 Detail of currently used probes. (a) End probe. (b) Edge probe.

Unlike lower frequency eddy current probes the coil in Fig. 2 requires only a single turn, which simplifies fabrication in miniature sizes. YIG resonator technology has been an established industrial process for many years, being used for tunable microwave filter and oscillator applications. Reproducibility has therefore already been realized. At the present time the smallest YIG spheres available commercially are 0.012 inch diameter, but the fabrication of even smaller spheres appears feasible. This is one possible direction for further improving the edge discrimination characteristics of these probes. Another is the use of shielding, as currently applied in low-frequency probes. The lowest operating frequency in our current experiments is slightly below 800 MHz, but this is not a limit, even for the present generation of probes. Also, use of resonator shapes other than a sphere and choice of other magnetic materials offer possibilities for a very substantial lowering of the resonant frequency.

Samarium Cobalt
Permanent Magnet

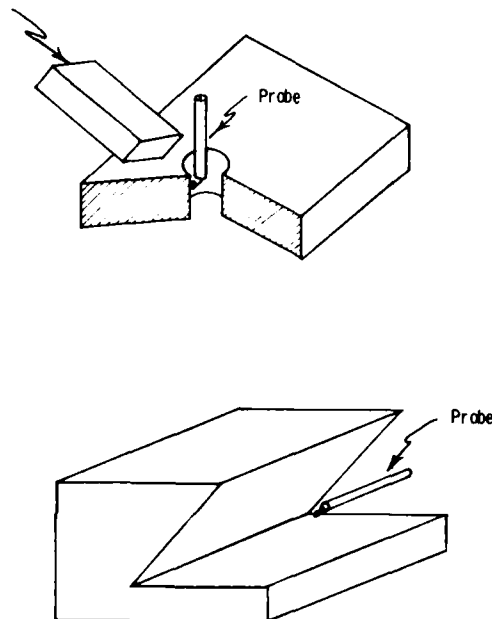


Fig. 3 Typical positioning of the edge probe relative to a test piece.

LIFT-OFF DISCRIMINATION AND FLAW SIGNAL PRESENTATION

In the last year's work the change in the input impedance due to the presence of a flaw was detected by observing the shift in the magnetic resonance frequency due to perturbation of the eddy currents. Initially the resonance line was displayed on an oscilloscope by exciting the probe at a fixed frequency and then sweeping the probe resonance by applying a swept magnetic field (Fig. 4). This was a bulky and inconvenient technique, and later experiments were performed with a fixed magnetic field and a swept frequency source. Active probes were also constructed, in which the YIG probe controlled the frequency of a transistor oscillator. The disadvantage of these methods is that they utilize only the amplitude of the flaw signal, whereas it is well-known in low-frequency eddy current applications that the phase information provides lift-off discrimination (Fig. 5(a) and (b)), as well as flaw depth information. An improved type of probe operation, giving the required phase information, is therefore being used this year. Basically, a small dedicated network analyser provides a measure of the complex input impedance of the probe, in either fixed or swept frequency operation, and this complex impedance information is displayed on an image storage tube.

In conventional low-frequency eddy current testing the curve traced in the complex impedance plane by a variation in lift-off follows a different path than the curve traced by traversing a flaw.^{2,3} Figure 5(a) and (b) compares the lift-off curves

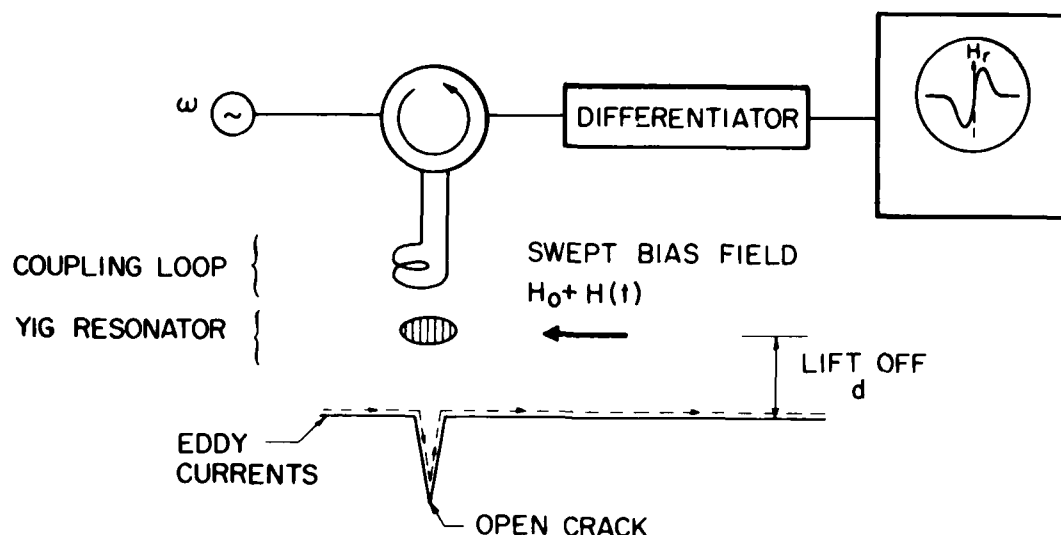


Fig. 4 Original method of flaw detection by observation of the ferromagnetic resonance frequency shift.

(dashed) with flaw signal curves (solid) for single coil and differential coil versions of a low-frequency probe. The figure-eight characteristic of the differential coil can be easily visualized by superposing two single coil responses that are 180° out of phase and occupy displaced but overlapping responses in space. In both of these figures the flaw signal has a component orthogonal to the lift-off curve, and this effect is exploited in eddy current instruments by designing the electronics so that one can select this orthogonal signal component for presentation. Corresponding impedance plane curves for the FMR probe are shown in Fig. 5 (c). As was noted in our February 1979 report,⁴ the lift-off curve now follows a closed circle because of the resonance phenomenon and, with proper adjustment of the probe, the flaw curve is a teardrop more or less aligned along the lift-off curve. To obtain this type of response it appears that excitation of a second (or spurious) FMR mode, in addition to the uniform precession mode of Fig. 1, is required. Deliberate excitation of such a mode is something to be avoided in YIG filter and oscillator design, and marks a distinct difference between the operation of the YIG probe and earlier YIG devices.

The effect of spurious mode coupling on the complex impedance versus frequency curve of the YIG probe depends on the nature of the coupling. This can be best illustrated by looking at equivalent circuit models. Figure 6 shows the usual equivalent circuit representation of a low-frequency probe, where lift-off is modeled as a change in mutual inductance and conductivity changes or flaws in the test piece by changes in the load resistance. Straightforward circuit analysis shows that this circuit gives impedance curves of the type illustrated in Figs. 5(a) and (b). The FMR (or YIG) probe, on the other hand, has a main internal resonance (uniform precession) that is coupled to both the input excitation and the test piece, represented by R in Fig. 7. Coupling to a spurious mode may occur either directly from the excitation coil or indirectly through the uniform precession modes, as noted schematically in the figure by the two mutual couplings to the dashed spurious resonant circuit.

The complexity of the FMR resonator response can be appreciated by examining Fig. 8, which shows tuning curves (frequency versus magnetic field) for some of the modes of a magnetic sphere, including as a heavy line the uniform precession mode and a spurious mode of the same frequency. Spatial variations of the model fields are identified by a three-subscript system.⁵ The uniform precession mode (110), shown in Fig. 9 for the tilted dc field arrangement that is found to give the best operating characteristics, has a uniform magnetization that precesses around H_{DC} . The corresponding RF component of magnetization m_{RF} in the figure is uniform and circularly polarized in the plane normal to H_{DC} . The RF magnetization therefore has one polar variation, one azimuthal variation and no radial variations. Since the entire resonator structure is small compared to a wavelength, the input impedance can be obtained by a simple flux linkage calculation - leading to the coil inductance and coupled resonance terms shown in the figure. The degenerate mode illustrated in Fig. 10 is much more complicated and more difficult to couple, because of spatial cancellation of flux linkages. This mode was selected for illustrative purposes only, since it is unlikely that it is the one responsible for our experimental observations.

From the input impedance expression for the uniform precession mode in Fig. 9, it is easy to show that the corresponding equivalent circuit has an inductor in series with a parallel resonant circuit (Fig. 11). This is completely analogous to the equivalent circuit of an acoustic resonator or transducer, but with a coupling inductor instead of a coupling capacitor. Consequently, the complex impedance versus frequency curve is the offset circle diagram shown at the bottom of the figure. Regarding spurious mode coupling, one may consider separately the cases of direct coupling to the excitation loop and indirect coupling through the uniform precession mode. Simple flux linkage considerations show that these cases correspond to the equivalent circuits of Fig. 12, and a qualitative examination of the behavior of these circuits shows that the resistance, reactance and complex frequency versus frequency curves are as illustrated. As

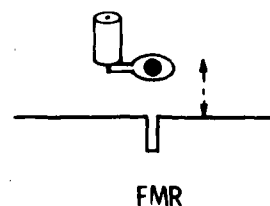
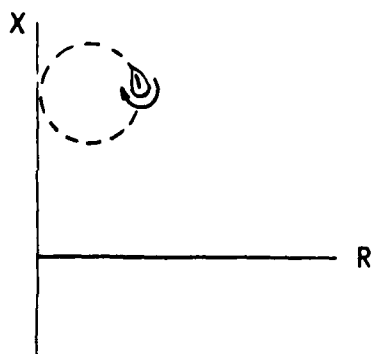
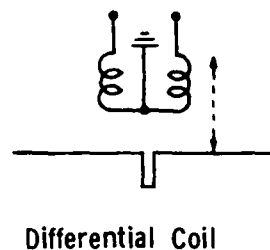
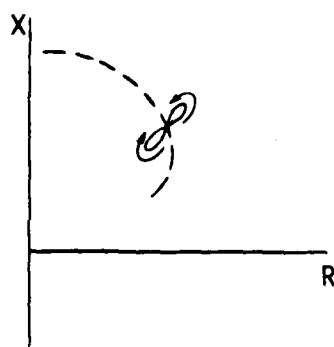
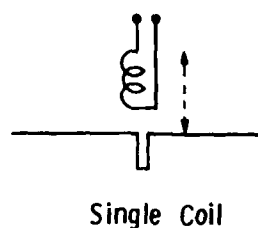
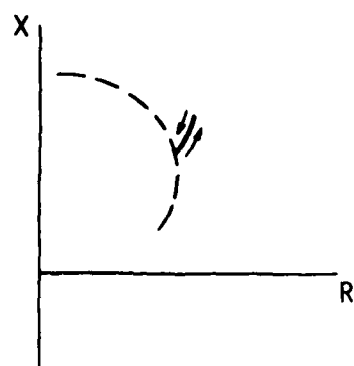


Fig. 5 Discrimination between lift-off response (dotted curve) and flaw response (solid curve) in (a) standard single coil probe, (b) standard differential coil probe, (c) FMR probe.

will be seen below, our experimental complex impedance displays correspond to the case of indirect coupling, and we therefore conclude that this is the relevant coupling mechanism. Spurious coupling in YIG filters is generally attributed to the same mechanism.

INSTRUMENTATION

As was noted above, the electronics used previously with the probe (a swept frequency source and resonance line display on an oscilloscope (Fig. 13)) does not provide the phase information necessary for lift-off discrimination. At microwave fre-

quencies, the required complex input impedance information can be obtained by using the polar phase discriminator circuit illustrated in Fig. 14. This unit, which is the central element in commercial network analyser instruments, has as its signal input the reflected wave from the load impedance to be analysed. In the figure this is provided by the directional coupler shown at the left. The reflected microwave signal is then split and the two parts are mixed separately with a reference signal from the source, shifted 90° in phase at one of the mixers. The dc outputs of the mixers are then proportional to components of the reflected signal 90° out of phase with each other. Application of these

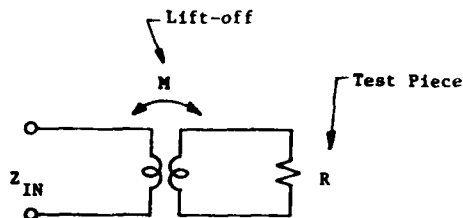


Fig. 6 Equivalent circuit model of the standard single coil probe.

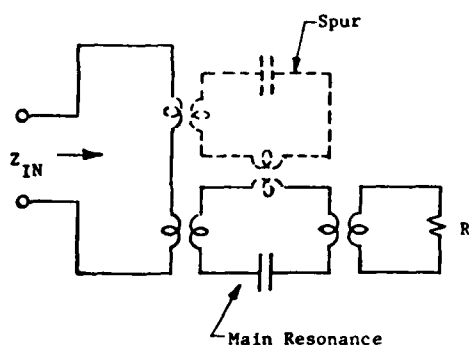


Fig. 7 Equivalent circuit model of the FMR probe.

signals to the x and y axes of an oscilloscope gives a complex display of the reflected signal and therefore of the reflection coefficient Γ_{IN} , with an arbitrary amplitude scaling and phase rotation. The relation of this display to input impedance Z_{IN} can be deduced by inverting the complex reflection coefficient relation

$$\Gamma_{IN} = \frac{Z_{IN} - Z_0}{Z_{IN} + Z_0}$$

or, better, by constructing the contours of constant R and constant X in the complex reflection coefficient plane. This leads to a system of orthogonal circular contours, known as a Smith Chart. Figure 15 compares the impedance versus frequency trajectories for the uniform precession mode coupled with a spurious mode, as displayed on a rectangular display and a Smith Chart display.

The block diagram of the dedicated network analyser constructed for use with our FMR probes is

shown in Fig. 16. A small varactor-tuned transistor oscillator capable of operating from 800 to 1600 MHz serves as the source and the phase discriminator is a compact commercial unit. Use of miniature directional couplers allows the whole system to be assembled in a portable unit (Figs. 17 and 18). The electronics provides for rotation of the impedance display on the screen so that the part of the flaw signal orthogonal to the lift-off curve appears on only one axis. Gain and offset controls are also provided for magnifying the important part of the impedance curve.

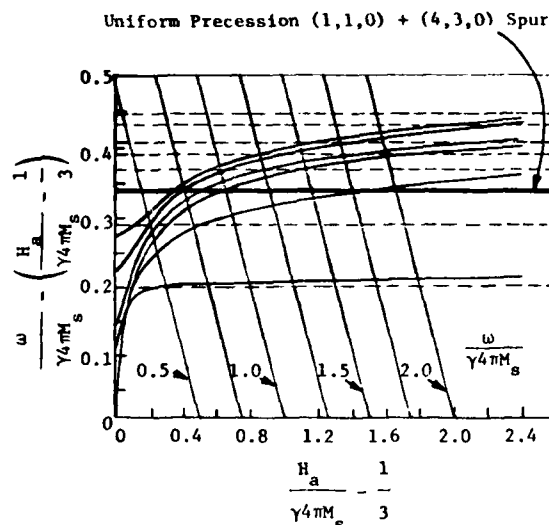


Fig. 8 Chart showing the ferromagnetic resonance frequencies of a spherical resonator as a function of the applied dc field H_a . The dashed lines represent tracking modes and the solid lines nontracking modes.

EXPERIMENTAL RESULTS

The experimental results obtained with our new instrumentation and probe configurations are not substantially different than those presented in our February report⁴ and measured with a commercial network analyser. We now have a lower noise level and better display capabilities because of the offset controls available in our electronics. The same micromanipulator is used for lift-off and scan control, but the new magnet mounting allows more flexible magnetic field adjustment (Fig. 19).

Figure 20 shows a Smith Chart display of the probe input impedance, with the magnetic field adjusted for simultaneous coupling to many spurious modes. The similarity to the indirect coupling curves of Fig. 12 should be noted. Measurements with our new system of two samples discussed in our February report are shown in Figs. 21 and 22. These were both stored on the CRT before photographing. The improvement in signal-to-noise is especially notable in the second sample, although no special filtering has been used.

DIRECTIONS FOR FUTURE DEVELOPMENT OF PROBE THEORY

In Reference 1 the general theory of an FMR probe operating in the uniform precession mode was

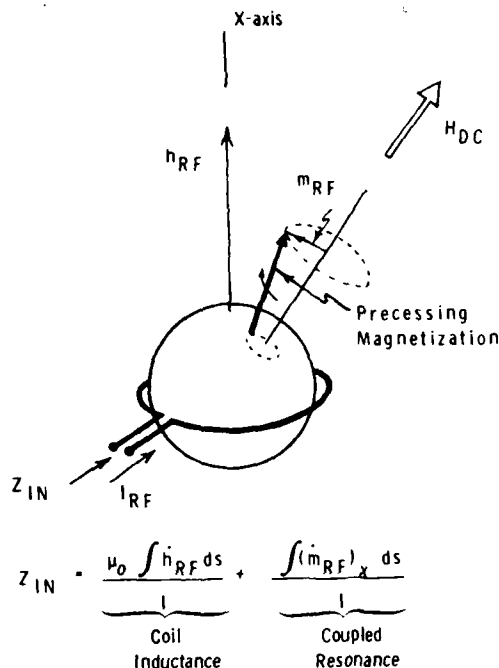


Fig. 9 Impedance at the input to the coupling coil for the uniform precession (110) mode, with the applied magnetic field at an angle.

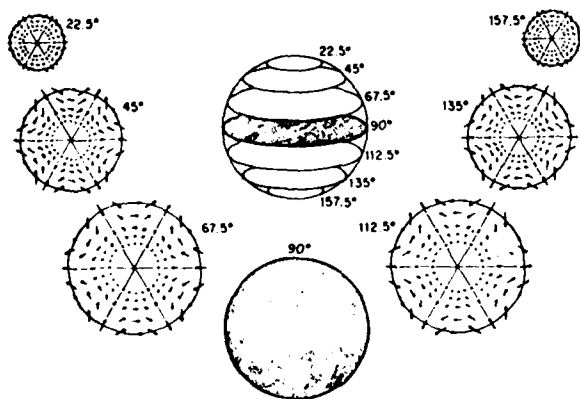


Fig. 10 Spatial distribution of the precessing magnetization in the (430) mode.

developed on the basis of a Lorentz reciprocity relation adapted to gyromagnetic materials. This theory, which was formulated for one terminal-pair probes such as the ones used here and also for two terminal pair probes having both an input and an output, is easily adapted to conventional low-frequency probes. To do so it is only necessary to reduce the gyromagnetic form of the Lorentz reciprocity relation to its ordinary form and to eliminate use of the quasistatic approximation.

This theory was applied previously only to the calculation of the frequency shifts produced by the influence of a flaw on a probe operating in the

the uniform precession mode. One is led naturally to ask if it can also be used to predict the results shown in Figs. 21 and 22, or to shed some light on the principles of multimode probe operation.

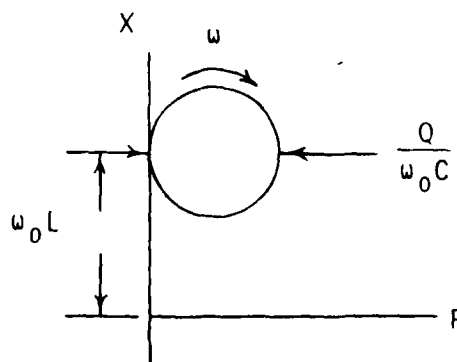
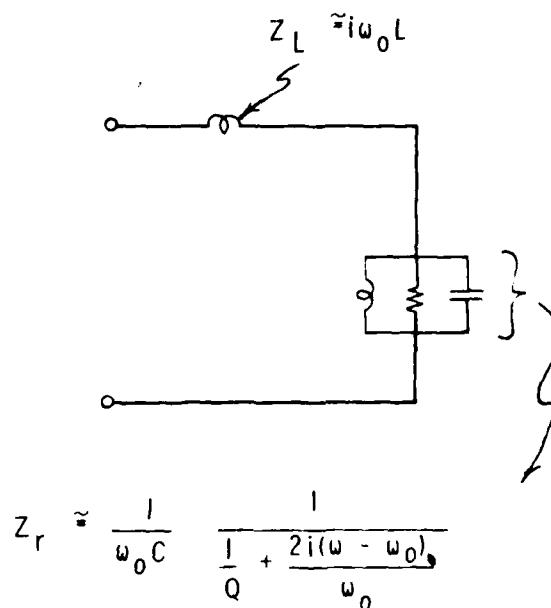
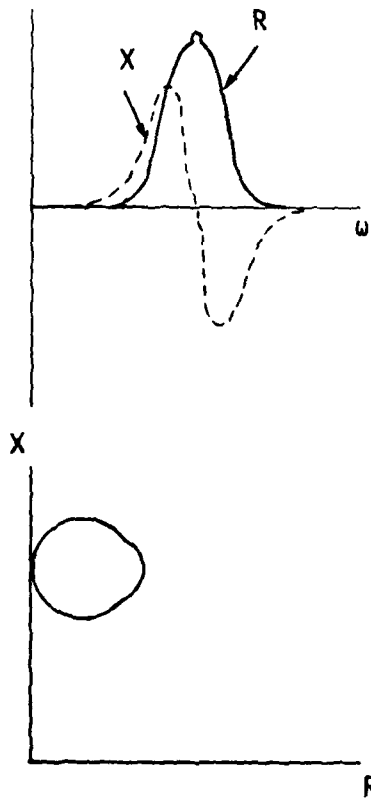
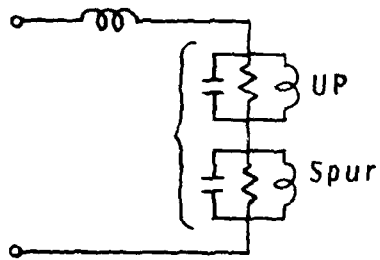


Fig. 11 Equivalent circuit and complex impedance versus frequency display for the uniform precession mode.

The previous theory was based on the construction shown in Fig. 23. Integration of the gyro-magnetic Lorentz reciprocity relation over the volume enclosed by the dashed lines - taking one of the solutions in the relation to be in the presence of the flaw, the other in the absence of the flaw - gave an expression for the change in Z_{IN} at the plane S_C in terms of an integral of perturbed and unperturbed fields over the mouth of the flaw. This method does not appear to be easily adaptable to the case of a probe operating in two coupled modes.

An alternative approach would be to find for the equivalent circuit (Fig 7) perturbations of frequency and mode coupling due to the presence of a flaw. The complex impedance curves could then be obtained from the equivalent circuit. This method

Direct Coupling



Indirect Coupling

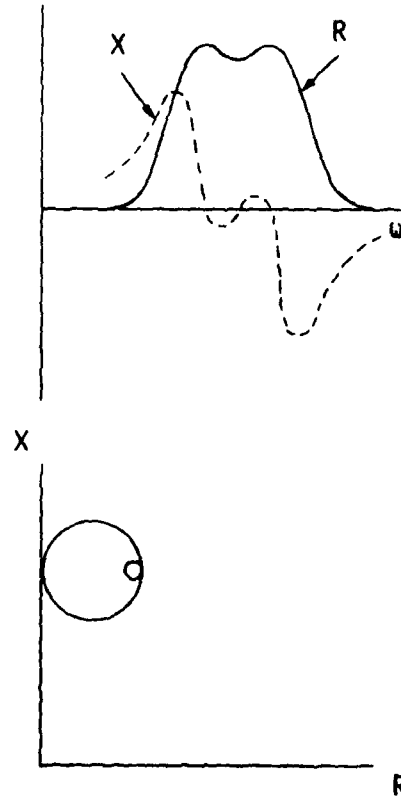
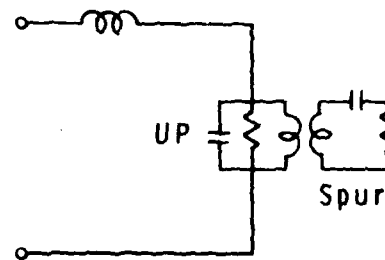


Fig. 12 Equivalent circuits and complex impedance plane displays for coupled ferromagnetic resonance modes.

might be implemented in the following way. We suppose that the plane S_c is sufficiently close to the loop that the quasimagnetostatic approximation is applicable to the entire region comprising the loop, the YIG sphere and the test piece surface. The uncoupled resonator is defined as having a short circuit at the plane S_c . Orthogonality relations for the magnetic resonance modes of this system can be derived from the quasimagnetostatic form of the complex reciprocity relation

$$\nabla \cdot (\mathbf{B}_1^* (i\omega_2 \mathbf{B}_2) + \mathbf{B}_2 (i\omega_1 \mathbf{B}_1)^*) = 0,$$

analogous to the corresponding relation applied to piezoelectric resonators.⁶ Similarly one can develop, just as in the piezoelectric case, a modal theory for excitation of the resonator by an applied voltage at the terminal plane S_c . As in the piezoelectric case perturbation formulas may be developed for changes in the modal resonant frequencies

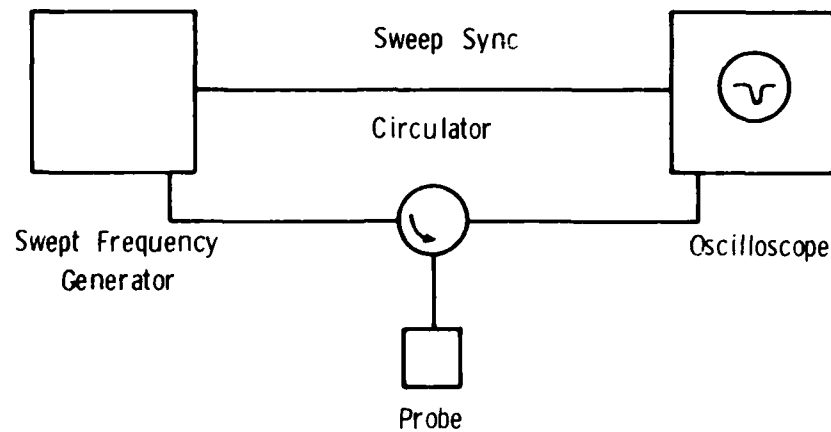


Fig. 13 Block diagram of electronics used for flaw detection by observing changes in the resonant frequency of the FMR probe.

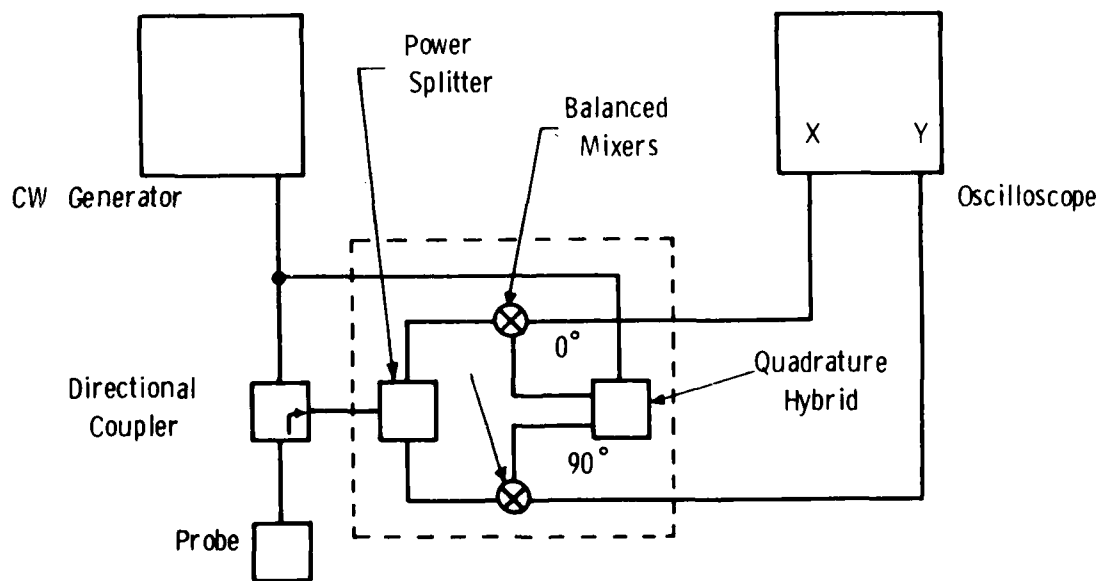


Fig. 14 Schematic of the polar phase discriminator circuit used for measuring the complex input impedance of the FMR probe.

as a function of the flaw perturbation,⁷ and expressions of the same type can be formulated for mode coupling introduced by the flaw. Perturbation theory provides a useful tool for evaluating the effect of crystalline anisotropy on the probe behavior and possibly also for the effect of a nonuniform magnetic field.

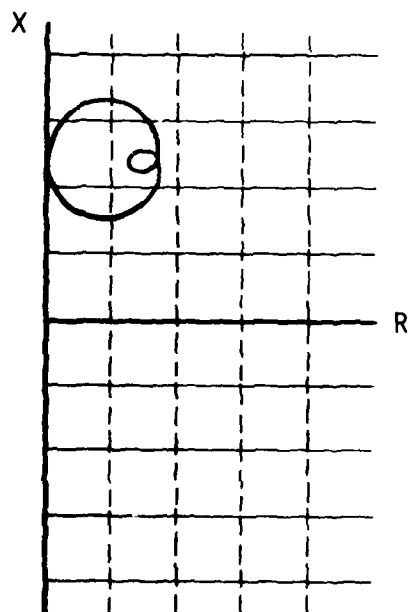
SUMMARY

A portable instrument has been developed for measuring the complex input impedance of an FMR probe and displaying it on a storage image tube. This instrument has an improved signal-to-noise performance and gives clearer and larger displays than those reported previously. Coupling with spurious modes has been identified as probably taking place through the uniform precession mode, but this remains to be confirmed by further experi-

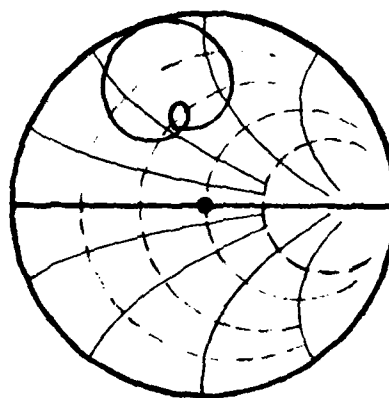
ment. The basic elements of a theory for this type of probe operation have been established.

The highest priority tasks for future work are (1) development of more stable probe support and scanning mechanisms, especially for test pieces of complicated shapes, (2) measurements on fatigue cracks under tightly closed and partly opened conditions, (3) quantitative definition of operating conditions for optimum lift-off discrimination, (4) development of a theoretical base for multimode probe operation.

Acknowledgments are due to R. A. Craig and C. Fortunko for their advice and suggestions, to J. James for his expert assistance with the electronics, and to D. Walsh for probe fabrication.



Rectangular



Smith Chart

Fig. 15 Comparison of rectangular and Smith Chart complex impedance displays. Dashed lines are constant R and solid lines constant X .

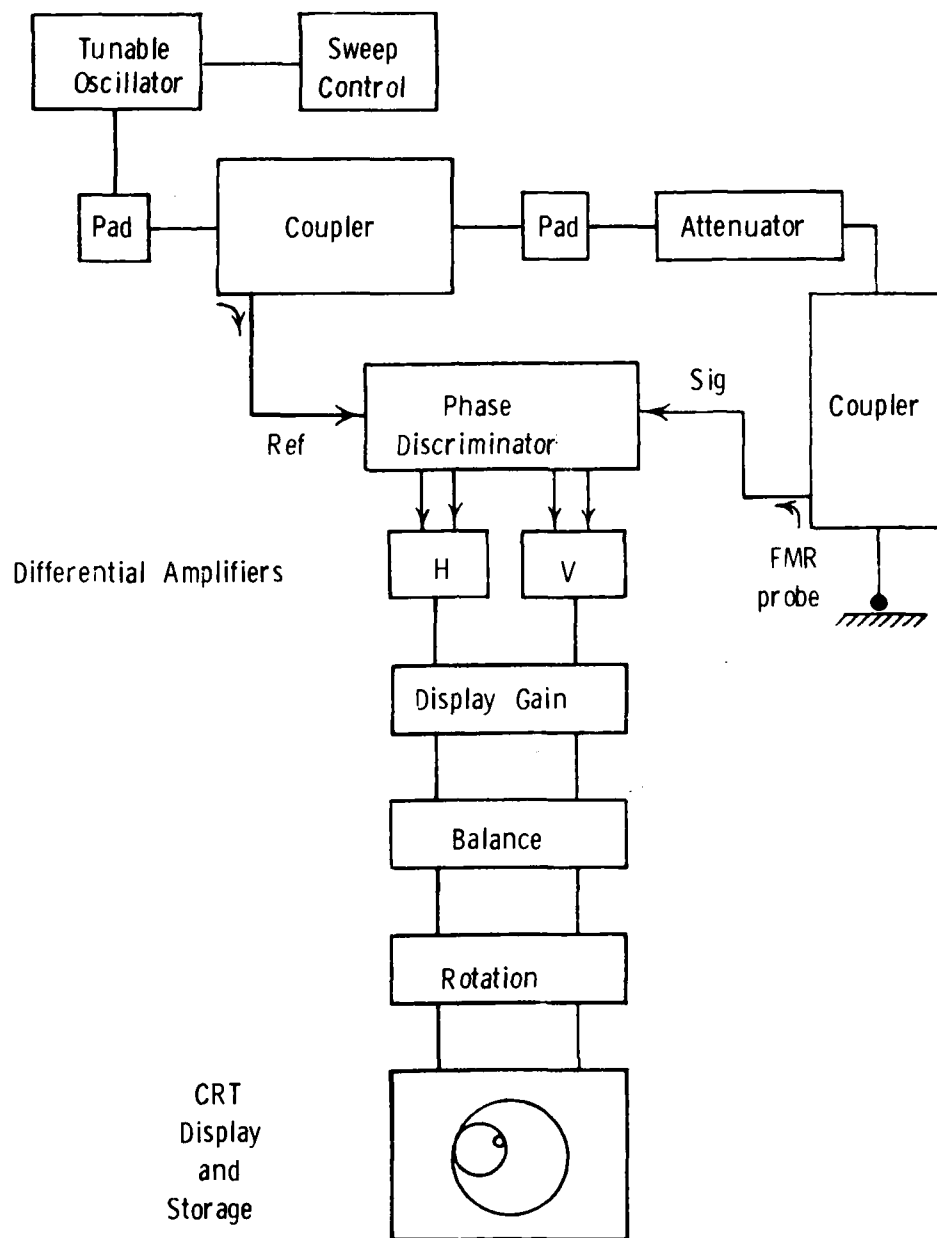


Fig. 16 Block diagram of the small dedicated microwave network analyser constructed for use with the FMR probe.

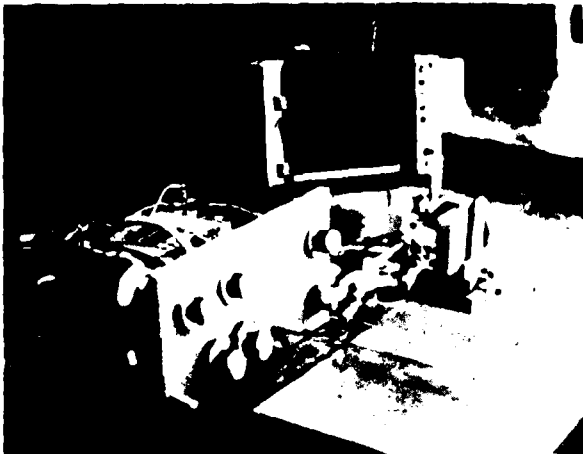


Fig. 17 Test setup, showing network analyser with case removed and storage tube for recording data.

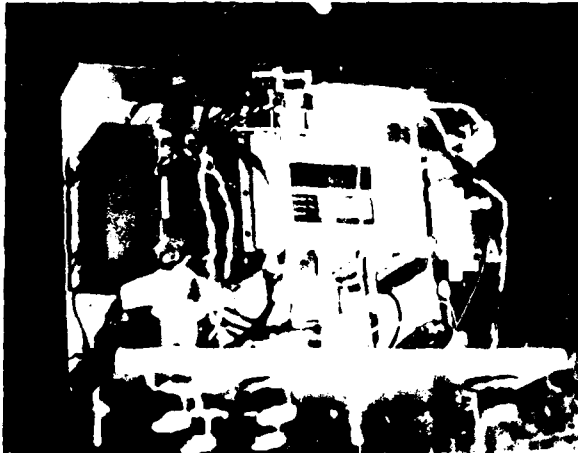


Fig. 18 Detail of network analyser circuitry.

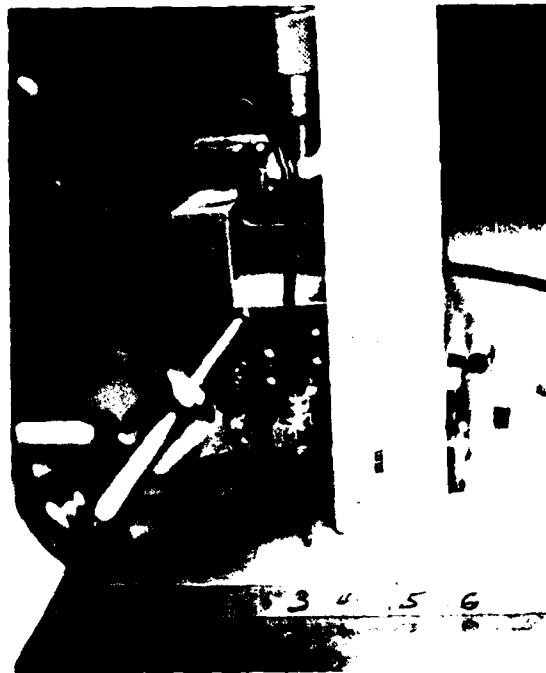


Fig. 19 Detail of probe and magnet assembly.

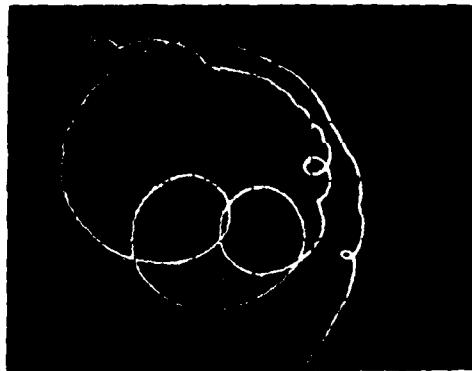


Fig. 20 Smith Chart display of probe input impedance adjusted to show many spurious mode couplings. The trace shows impedance versus frequency of the probe placed in proximity to the test piece surface.

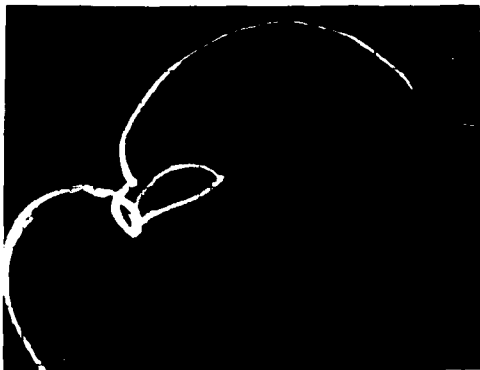


Fig. 21 Observation on test slot B-4 with length = 2", depth = 0.010" and width = 0.012", in aluminum (Fig. 19). The outer scalloped curve gives impedance versus frequency and shows an open loop corresponding to spurious mode coupling. Scanning the probe over the test slot at a fixed frequency (~ 850 MHz) produces the elliptical trace coming out of the side of the spurious mode loop.



Fig. 22 Traces analogous to those of Fig. 21, but for an EDM notch (length = 0.105", depth = 0.024", width = 0.10") in titanium G-4.

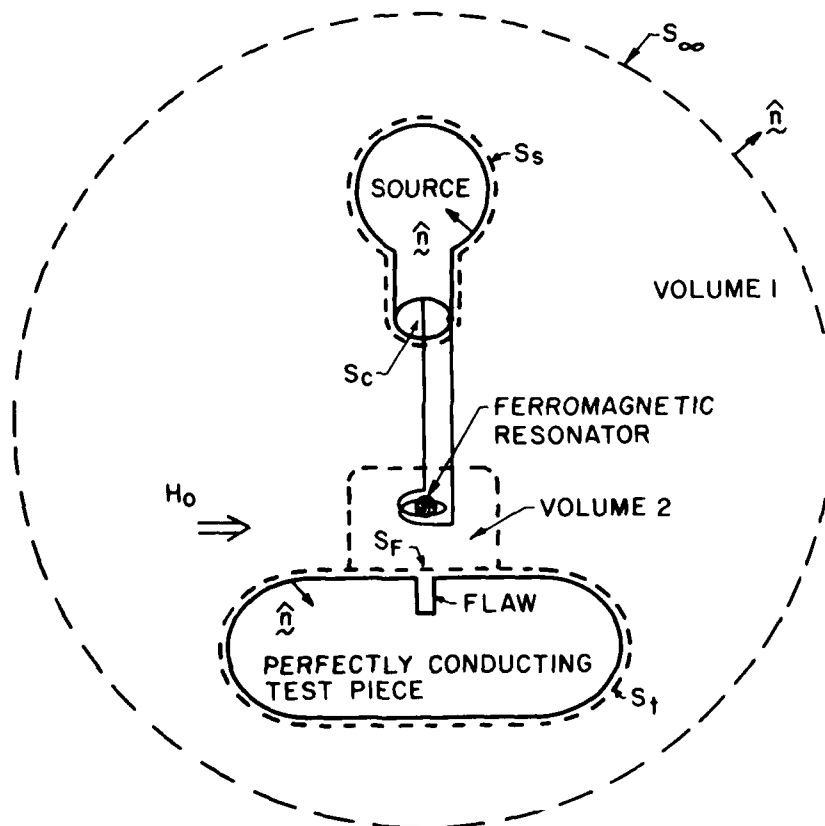


Fig. 23 Construction for the development of FMR probe theory from the reciprocity relation for gyrotropic materials.

This research was sponsored by the Center for Advanced NDE operated by the Science Center, Rockwell International, for the Advanced Research Projects Agency and the Air Force Materials Laboratory under Contract F33615-74-C-5180.

REFERENCES

1. B. A. Auld, "Theory of Ferromagnetic Resonance Probes for Surface Cracks in Metals," Ginzton Lab Report No. 2839, Contract (CMR) NSF DMR76-00726, Stanford University (July 1978).
2. H. Libby, "Introduction to Electromagnetic Non-destructive Test Methods," Wiley-Interscience, New York (1971).
3. T. J. Davis, "Multifrequency Eddy Current Inspection with Continuous Wave Methods," Proc. ARPA/AFML Review of Progress in Quantitative NDE, pp. 109-116, Science Center, Rockwell International (January 1979).
4. B. A. Auld, C. Eberspacher, A. Ezekiel, and D. Winslow, "Surface Flaw Detection with Ferromagnetic Resonance Probes," Ginzton Lab Report No. 2928, Rockwell International Science Center Grant 77-70946 (February 1979).
5. B. Lax and K. Button, "Microwave Ferrites and Magnetism," Section 4.6, McGraw-Hill, New York (1962).
6. B. A. Auld, "Acoustic Fields and Waves in Solids, Volume II," pp. 250-262, Wiley-Interscience (1973).
7. Ibid., pp. 315-324.

TWO APPROACHES TO SOLVING THE INVERSION PROBLEM FOR EDDY CURRENT NDE

T. G. Kincaid, M.V.K. Chari, Z. J. Csendes
K. Fong and R. O. McCary
General Electric Company
Schenectady, N. Y. 12345

ABSTRACT

The eddy current NDE inversion problem is to determine flaw parameters from eddy current sensor impedance changes. Two approaches to solving this problem are discussed for geometries with two components of eddy current. The first is to use the Finite Element Method of numerical analysis to compute the sensor impedance change for each flaw parameter value. The second approach is to combine the Finite Element Method with an analytical scattering technique. These two approaches are applied to the problem of an infinitely long coil surrounding an infinitely long conducting bar with an infinitely long surface crack. The calculated impedance changes show good agreement with known analytical and experimental results.

INTRODUCTION

The eddy current NDE inversion problem is to determine flaw parameters from the measured changes in the eddy current sensor impedance. This is equivalent to determining the transformation between the flaw parameters and the impedance changes of the sensor caused by the flaw. A method of obtaining this transformation is to find the electromagnetic fields induced in the material by the sensor, with and without the flaw, and use these fields to calculate the change in sensor impedance. The principal difficulty is solving Maxwell's equations in the complex geometries involved. Two approaches to overcoming this difficulty are shown for problems with two component eddy current fields, and both are applied to an infinitely long coil surrounding an infinitely long conducting bar with an infinitely long radial surface crack. The results are compared to previous analytical and experimental work.

The first approach is to use the Finite Element Method (FEM) to compute the sensor impedance with and without the flaw. The impedance change can then be found by subtracting the two. An example of the use of this method has been previously reported for a problem with a one component eddy current field. [1]. The FEM approach has the advantage that it can be applied to almost any geometry and is capable of very high accuracy. The disadvantage is that a separate computation must be made for each flaw parameter, which can be expensive. In addition, the lack of an analytical transformation equation hinders "understanding" of the relationship between the flaw parameters and the sensor impedance changes.

The second approach is to combine the FEM with analytical scattering theory. In this approach, the eddy current field in the unflawed material is computed using the FEM. Scattering theory is then used to compute the fields resulting from the introduction of the flaw into this incident field. A formula is then derived for the sensor impedance change as a function of the flaw parameters and the incident field. This combined approach has the advantages that the FEM computation needs only to be made once and that

the impedance change formula enhances "understanding" of the relationship between the flaw parameters and the impedance change. The disadvantage is that the formula can only be applied to flaws which fit the scattering model flaw geometry.

TWO COMPONENT FINITE ELEMENT ANALYSIS

This section outlines the analysis required for computing two component eddy current fields by the finite element method. The two component eddy current problem can be formulated directly in terms of a single component diffusion equation in the magnetic field intensity H . Thus the formulation follows closely that previously presented by the authors [1], requiring only some notational changes.

Assumptions Underlying the Analysis

The following assumptions are made in modeling the eddy current problem and obtaining the field solution.

1. Displacement currents are neglected and the problem is treated as quasi-stationary.
2. The source current is assumed to be free of eddy current and proximity effects.
3. The resistivity of the conducting parts is constant and single valued.
4. The problem is assumed to be two-dimensional and linear and all field quantities are considered to be harmonic functions of time.
5. The current density is assumed to have components along the x and y directions, while the magnetizing field H has only one component along the z direction.

Linear Diffusion Equation

For the two-component linear eddy current field problem, subject to the assumptions stated above, the magnetic field intensity vector H is a single component vector given by the solution to the linear diffusion equation,

$$\frac{1}{\sigma} \nabla^2 \vec{H} = j\omega \mu \vec{H} \quad (1)$$

where: σ = conductivity
 μ = permeability
 ω = radian frequency

Finite Element Representation

Equation (1) can be reformulated in variational terms by energy expressions called functionals. The finite element method consists of discretizing the field region into sub-regions or elements and projecting approximations to the solutions H which minimize the corresponding functionals. This process results in a matrix equation, which when solved yields the solution to the eddy current problem. The accuracy of the solution depends largely on the discretization of the field region and the prescription of a good solution approximation. For the sake of completeness, the salient steps of the finite element method are presented below, using a second order approximation to the field solution.

Representing the diffusion equation formulation (1) in terms of a single differential equation

$$D\psi = f \quad (2)$$

where D = the differential operator
 ψ = the potential function
 f = the source or forcing function,

the expression for the energy functional is obtained as

$$F = \langle \psi | D\psi \rangle - 2 \langle \psi | f \rangle \quad (3)$$

where the inner product $\langle \cdot \rangle$, represents volume integration of dot product of the variables.

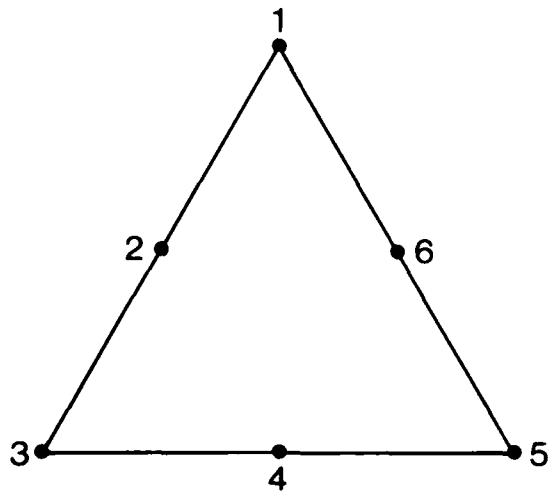


Fig. 1 Second Order Triangular Element

We now sub-divide the field region into triangular elements as shown in Fig. 1 and prescribe the potential function ψ in each element in terms of interpolation polynomials called shape functions, weighted by function values at the nodes.

Thus we may write

$$\psi = \sum_{k=1}^n \zeta_k \psi_k \quad (4)$$

For the second order approximation, the shape functions are given as

$$\zeta_k = \zeta_k (2\zeta_k - 1) \text{ for } k = 1, 3 \text{ or } 5 \quad (5)$$

$$\zeta_k = 4\zeta_p \zeta_q \text{ for } k = 2, 4 \text{ or } 6 \quad (6)$$

with p, q respectively (1,3), (3,5), (5,1), and

$$\zeta_k = \frac{(a_k + b_k x + c_k y)}{2\Delta} \quad (7)$$

where Δ is the element area, and a_k , b_k and c_k are defined in progressive modulo 3 as

$$a_k = \begin{vmatrix} x_\ell & x_m \\ y_\ell & y_m \end{vmatrix}; \quad b_k = (y_\ell - y_m); \quad c_k = (x_m - x_\ell) \quad (8)$$

Thus the final set of complex linear equations is expressed in matrix form in terms of the coefficient matrix $[S]$ and the related numerical matrix $[T]$, as

$$K_1 [S] [\psi] + j\omega k_2 [T] [\psi] = [T] [f] \quad (9)$$

where $k_1 = \frac{1}{\sigma}$; $k_2 = \mu$; $\psi = \bar{H}$

Equation (9) is readily recognized as identical to equation (16) of reference [1].

Boundary Conditions and Forcing Function

For the two-component eddy current field problem described above, with a single component magnetic field H , the field external to the infinitely long coil is zero. Also, the magnetic field distribution in the coil is unaffected by the circulating currents in the conducting bar.

The value of the forcing function H on the inner surface of the coil is related to the coil current density J which is uniform such that

$$H_{T1} - H_{T2} = J \quad (10)$$

Winding Resistance and Inductance

The total energy stored in the system is obtained by integrating the product of free space permeability and the square of the magnetic field H over the volume. Thus the energy per unit length is

$$W_s / \ell = 1/2 \mu_0 |H|^2 \Delta \quad (11)$$

where ℓ is the length of the bar or solenoid.

Equating the above expression to the well known stored energy in the terminal inductance, and dividing by the square of the bar coil current, I , we have

$$L / \ell = \frac{\mu_0 |H|^2 \Delta}{I^2} \quad (12)$$

The power dissipated per unit length in the bar resistance is obtained by integrating the ohmic losses over the volume, giving

$$P_d/l = 1/2 \sum J_e^2 \rho \Delta \quad (13)$$

where the sum is over all triangles, and

J_e = eddy current density

ρ = resistivity of the bar

Note that J_e can be calculated from H by Maxwell's equation

$$\nabla \times \vec{H} = \vec{J}_e \quad (14)$$

Equating the above power loss to the $I^2 R$ product one obtains

$$R/l = \frac{\frac{1}{2} \sum J_e^2 \rho \Delta}{I_p^2} = \frac{\sum J_e^2 \rho \Delta}{I_p^2} \quad (15)$$

The results of applying the FEM analysis to the problem of the infinitely long conducting bar surrounded by an infinitely long coil are shown in Figs. (2) through (7). The eddy current density profiles in the bar cross-section without and with a crack are shown in Fig. (2) through (5). The corresponding impedance plane diagrams are illustrated in Figs. (6) and (7). The experimental results in Fig. 7 are those of Forster [4].

CONTOUR DIVISIONS = 0.4988E 00
NO. OF CONTOURS = 24

MU = 0.1257E-05
RHO = 0.5000E-06
FREQ = 0.1470E 03



Fig. 2 Real Part Eddy Current Profile in Cross-Section of Round Bar Without Crack

CONTOUR DIVISIONS = 0.9011E-01
NO. OF CONTOURS = 24

MU = 0.1257E-05
RHO = 0.5000E-06
FREQ = 0.1470E 03

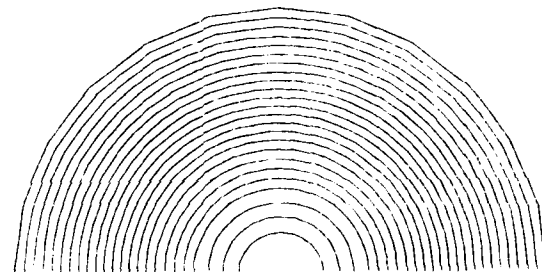


Fig. 3 Imaginary Part Eddy Current Profile in Cross-Section of Round Bar Without Crack

CONTOUR DIVISIONS = 0.4919E 00
NO. OF CONTOURS = 24

MU = 0.1257E-05
RHO = 0.5000E-06
FREQ = 0.1470E 03

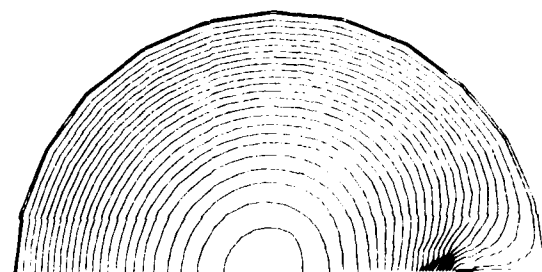


Fig. 4 Real Part Eddy Current Profile in Cross-Section of Round Bar With Crack

CONTOUR DIVISIONS = 0.8632E-01
NO. OF CONTOURS = 24

MU = 0.1257E-05
RHO = 0.5000E-06
FREQ = 0.1470E 03

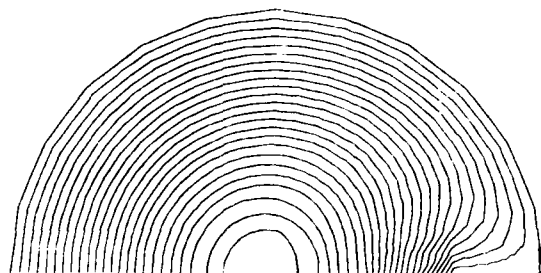


Fig. 5 Imaginary Part Eddy Current Profile in Cross-Section of Round Bar With Crack

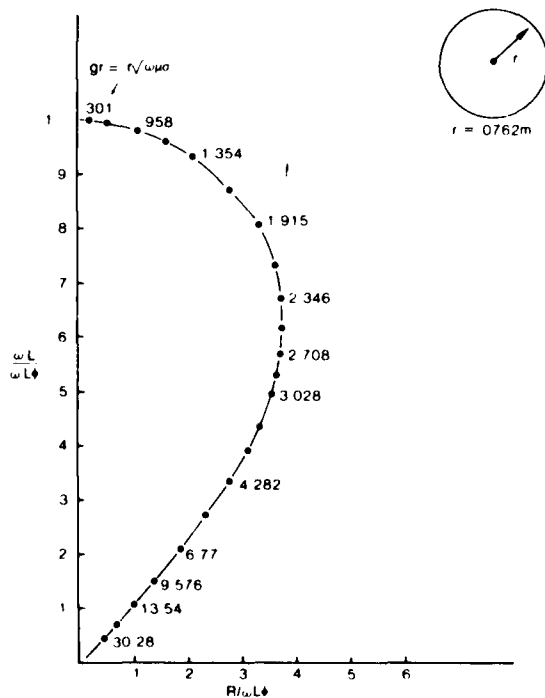


Fig. 6 Normalized Impedance Plane Diagram for Circular Cross-Section

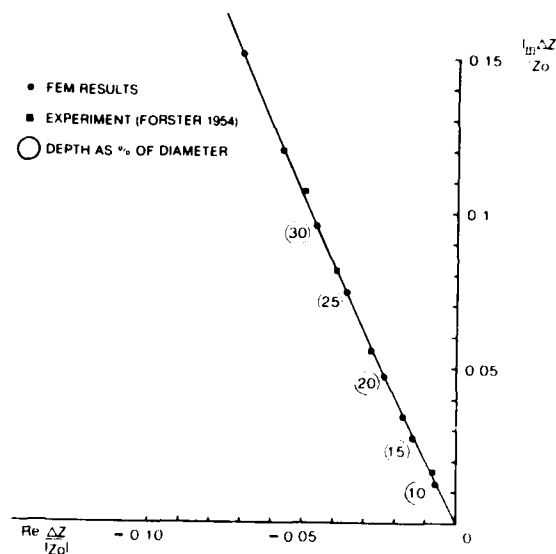


Fig. 7 Comparison of Finite Element Results with Experiment for a Crack in a Bar with Circular Cross-Section

TWO COMPONENT SCATTERING THEORY

The Scattering Model

In the scattering theory approach, the change in sensor impedance is found from the incident and scattered fields of the flaw by using the reciprocity theorem, as explained by Auld [5]. For a void flaw in a homogeneous, isotropic, conducting medium with permittivity ϵ_0 and permeability μ_0 , the change ΔZ in sensor impedance is given by

$$\Delta Z = \frac{1}{I^2} \int_{V_f} (\vec{E} \cdot \vec{E}') dv \quad (16)$$

where: I = the sensor terminal current

\vec{E} = the electric field without the flaw

\vec{E}' = the electric field with the flaw

V_f = the volume of the flaw.

Therefore, to compute the sensor impedance change, it is necessary to compute the electric fields within the boundaries of the flaw both when the flaw is present and when it is not.

The strategy for computing these electric fields is to approximate the incident field (i.e. the field without the flaw) by a constant plus a linearly varying component, as shown in Fig. 8. The respective scattered fields can then be computed for an elliptic cylinder flaw by assuming dipole and quadrupole scattered fields,

and matching boundary conditions at the flaw. The resultant field (i.e. the field with the flaw) is then the sum of the incident and scattered fields. (Figs. 9 and 10)

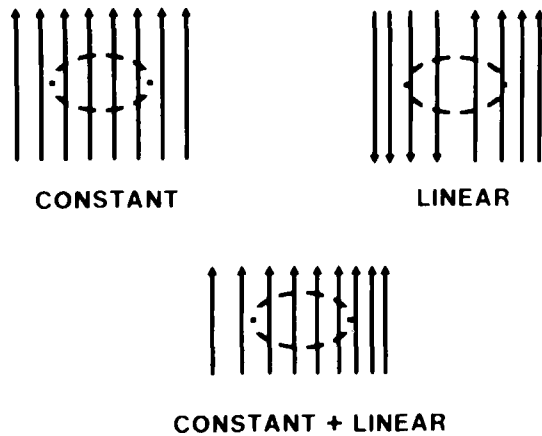


Fig. 8 Incident Eddy Current Fields

In cartesian coordinates, the constant component of the incident eddy current field is given by

$$\vec{J}_{ci} = \vec{i}_y J_{ci} \quad (17)$$

The associated scattered current field is a dipole field. The resultant sum field satisfies the static form of Maxwell's equations and matches the current boundary condition for a void i.e. zero current normal to the flaw boundary $\rho = \rho_0$.

The important field for the sensor impedance change calculation is the electric field interior to the flaw boundary with and without the flaw. When there is no flaw, the interior electric field is the incident current density field divided by the conductivity

$$\vec{E}_c = \vec{i}_y \frac{J_{ci}}{\sigma} \quad (18)$$

When there is a flaw, the electric field inside the flaw is the constant field

$$\vec{E}'_c = \vec{i}_y \frac{J_{ci}}{\sigma} \frac{a+b}{b} \quad (19)$$

where a and b are the major and minor axes of the ellipse. This field satisfies the static form of Maxwell's equations and matches the boundary condition for the electric field i.e. no change in the tangential electric field across the flaw boundary.

Similarly, the linearly varying component of the incident eddy current field is given by

$$\vec{J}_{vi} = \vec{i}_y M x \quad (20)$$

The associated scattered current field is a quadrupole field. When there is no flaw, the electric field interior to the flaw boundary is the linearly varying incident current field (20) divided by the conductivity.

$$\vec{E}_v = \vec{i}_y \frac{M}{\sigma} x \quad (21)$$

When there is a flaw, the electric field inside the flaw is the sum of a linearly varying and a "saddle" electric field.

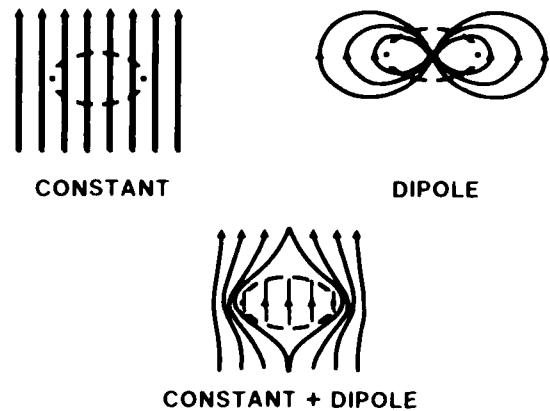


Fig. 9 Electric Fields for Dipole Scattering

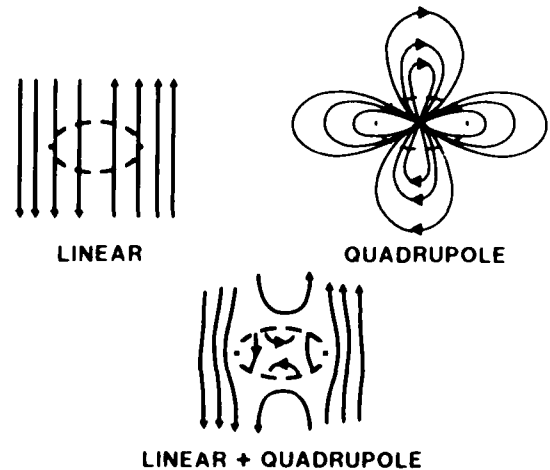


Fig. 10 Electric Fields for Quadrupole Scattering

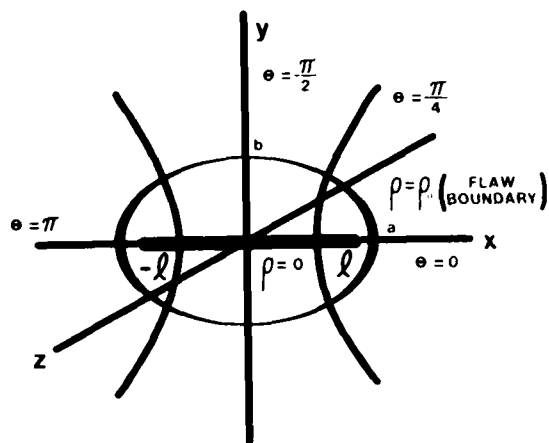


Fig. 11 Elliptic Cylinder Coordinates

In elliptic cylinder coordinates (see Fig. 11), this field is given by

$$\begin{aligned} \bar{E}_y = & \bar{I}_y \frac{M}{2\sigma} \frac{a}{h} \cosh^2 \rho_0 \sin 2\theta \\ & + \bar{I}_\theta \frac{M}{2\sigma} \frac{a}{h} \sinh \rho_0 \cosh \rho_0 (1 + \cos 2\theta) \\ & + \bar{I}_x \frac{M}{2\sigma} e^{-2\rho_0} \cosh^2 \rho_0 e^{2\rho} \sin 2\theta \\ & + \bar{I}_\theta \frac{M}{2\sigma} e^{-2\rho_0} \cosh^2 \rho_0 e^{2\rho} \cos 2\theta \end{aligned} \quad (22)$$

where h is the metric coefficient for elliptic cylinder coordinates. Note that the first two terms are the linearly varying field \bar{I}_y ($m/2\sigma$) x in elliptic cylinder coordinates.

Computation of the Change in Sensor Impedance

The change in sensor impedance due to the flaw can be calculated from (16). For the sinusoidal steady state, the electric fields are complex quantities.

$$\begin{aligned} \bar{E} &= \bar{E}_p + j \bar{E}_q \\ \bar{E}' &= \bar{E}'_p + j \bar{E}'_q \end{aligned} \quad (23)$$

Then the dot product in (16) is given by

$$\bar{E} \cdot \bar{E}' = (\bar{E}_p \cdot \bar{E}'_p - \bar{E}_q \cdot \bar{E}'_q) + j(\bar{E}_p \cdot \bar{E}'_q + \bar{E}_q \cdot \bar{E}'_p) \quad (24)$$

The procedure from here for finding ΔZ is to substitute the expressions for the various electric fields into the right side of (24), and perform the integration indicated in (16).

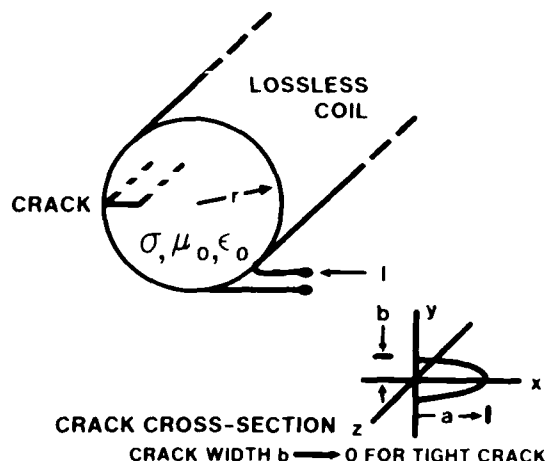


Fig. 12 Conducting Cylinder with Tight Surface Crack

The problem to be solved here is shown schematically in Fig. 12. The change in impedance of the lossless coil wrapped tightly around the cylinder is to be found as a function of the tight surface crack depth. The crack cross-section is assumed to be a semi-ellipsoid as shown. By letting the minor axis b approach zero, the ellipsoid becomes a tight crack.

The distribution of the eddy current density in a conducting cylinder with no crack is well known [6], or can be computed by FEM analysis as shown above. The real and imaginary parts of this distribution are shown in Fig. 13 for $gr = \sqrt{5}$, normalized to the eddy current density $J(0)$ at the surface of the cylinder. The constant plus linearly varying approximations to this normalized incident eddy current field at the surface of the cylinder are shown as dashed lines in Fig. 13. The real part is approximated by the constant 1 plus a linearly varying field with slope A. The imaginary part is approximated only by the linearly varying field with slope B.

Thus, when there is no flaw, the approximations to the real and imaginary parts of the electric field inside the flaw boundaries is given by appropriate combinations of (18) and (21).

$$\bar{E}_p = \frac{J(0)}{\sigma} [\bar{I}_y + \bar{I}_y A \frac{x}{r}] \quad (25)$$

$$\bar{E}_q = \frac{J(0)}{\sigma} [\bar{I}_y B \frac{x}{r}] \quad (26)$$

when there is a flaw, the electric field inside the flaw is given by appropriate combinations of (19) and (22).

$$\bar{E}'_p = \frac{J(0)}{\sigma} \left[\bar{I}_y \frac{a+b}{b} + \bar{I}_y \frac{A}{2} \frac{x}{r} \right] \quad (27)$$

$$+ \bar{I}_p \frac{A}{2r} e^{-2\rho_0} \cosh^2 \rho_0 e^{2\rho} \sin 2\theta$$

$$+ \bar{I}_\theta \frac{A}{2r} e^{-2\rho_0} \cosh^2 \rho_0 e^{2\rho} \cos 2\theta]$$

$$\bar{E}'_q = \frac{J(0)}{\sigma} \left[\bar{I}_y \frac{B}{2} \frac{x}{r} \right] \quad (28)$$

$$+ \bar{I}_p \frac{B}{2r} e^{-2\rho_0} \cosh^2 \rho_0 e^{2\rho} \sin 2\theta$$

$$+ \bar{I}_\theta \frac{B}{2r} e^{-2\rho_0} \cosh^2 \rho_0 e^{2\rho} \cos 2\theta]$$

The change in impedance ΔZ can now be found by substituting (25) through (28) into (24), and performing the integration (16) over the semi-elliptical cylinder volume, and letting the crack width b go to zero.

It has been implicitly assumed up to this point that the scattering model is valid for the semi-ellipse. This is exactly true for the dipole field, since there is no current normal to the y-axis. The quadrupole field, however, does have a component normal to the y-axis as shown in Fig. 10. This component is very small compared to the total current density in the region, and is simply ignored. The placing of a boundary along the y-axis should not significantly change the distribution of the scattered field.

Carrying out the integration in (16), and letting b go to zero, gives for the change in impedance per unit length

$$\Delta Z = - \frac{J(0)^2}{\sigma l^2} a^2 \left[\left(\frac{\pi}{2} + \frac{2}{3} A \frac{a}{r} \right) + j \frac{2}{3} B \frac{a}{r} \right] \quad (29)$$

It is customary in the literature to normalize this change in impedance to the magnitude of the impedance of the coil with no conducting bar inserted. The magnitude of the impedance per unit length is given by the well known expression

$$|Z_0| = \omega \mu_0 N^2 \pi r^2 \quad (30)$$

where N is the number of turns per unit length, and ω is the radian frequency of the excitation.

The expression for $J(0)$ is given by Hochschild [6].

$$J(0) = \frac{g}{\mu_0} B_r G e^{j\gamma} \quad (31)$$

where:

$$\gamma = [\theta_1(qr) - \theta_0(qr) - \frac{3\pi}{4}] \quad (32)$$

$$G = [M_1(qr) / M_0(qr)] \quad (33)$$

In these equations, the functions M_0 , M_1 and θ_1 are respectively the moduli and phases of the Kelvin functions of orders 0 and 1. The constant B_r is the magnetic flux density at the surface

of the conducting cylinder, and is given by the well known expression

$$B_r = \mu_0 NI \quad (34)$$

Combining (29) through (32) gives change in normalized impedance of the coil as a function of the crack depth a .

$$\frac{\Delta Z}{|Z_0|} = - \frac{1}{2} (Ge^{j\gamma})^2 \left(\frac{a}{r} \right)^2 \left[\left(1 + \frac{4}{3} A \frac{a}{r} \right) + j \left(\frac{4}{3} B \frac{a}{r} \right) \right] \quad (35)$$

Since Z is a single valued function of the crack depth a , this equation is also a solution to the inversion problem for the given conditions.

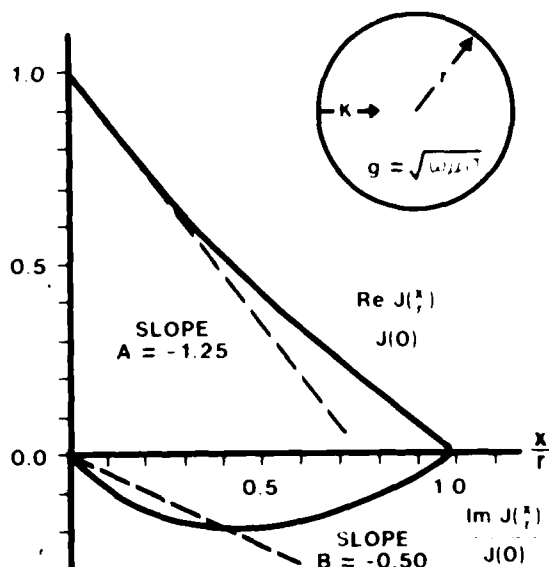


Fig. 13 Eddy Current Density in a Cylinder for $qr = \sqrt{5}$

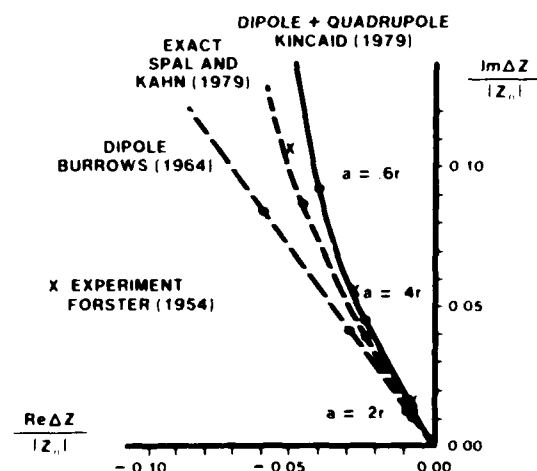


Fig. 14 Comparison of Theory and Experiment

Comparison With Other Theory and Experiment

A comparison of the normalized impedance with other theoretical and an experimental result is shown in Figure 14 for $ga = \sqrt{5}$. The theoretical results are those Burrows [2] and Spal and Kahn [3]. The experimental result is due to Forster [4]. Burrows dipole model shows good agreement with experiment only for crack depths small compared to the skin depth, as he predicted.

The dipole plus quadrupole model derived here compares favorably with experiment for crack depths up to one half skin depth. The departure of the model from experiment for greater depths is due to the large error in the linear approximation to the imaginary part of the incident field beyond one half skin depth. The exact theoretical model of Spal and Kahn follows the phase of the experimental result more closely than the others, but has about the same difference in magnitude. This suggests that the experimental conditions deviated from the model assumptions.

ACKNOWLEDGEMENT

This work was sponsored by the Center for Advanced NDE operated by the Science Center, Rockwell International, for the Advanced Research Projects Agency and the Air Force Materials Laboratory under Contract F33615-74-C-5180.

REFERENCES

- [1] Kincaid, T.G., and Chari, M.V.K., "The Application of Finite Element Method Analysis to Eddy Current NDE", Proceedings of the ARPA/AFML Review of Progress in Quantitative NDE, Rockwell International Report to Air Force Materials Laboratory, AFML-TR-78-205, January 1979.
- [2] Burrows, M.L., A Theory of Eddy-Current Flaw Detection, University of Michigan PhD. Thesis, 1964, University Microfilms, Ann Arbor, Mich.
- [3] Spal, R., and Kahn, A.H., "Eddy Currents in a Conducting Cylinder with a Crack", National Bureau of Standards, (to be published).
- [4] Forster, F., Z. Metal., Vol. 45, No. 4, 1954 pp.
- [5] Auld, B.A., "Quantitative Modeling of Flaw Responses in Eddy Current Testing", Fourth Monthly Report, Electric Power Research Institute Contract No:RPI395-3, February 1979.
- [6] Hochschild, R., "Electromagnetic Methods of Testing Metals", Progress in Non-destructive Testing, E.G. Stanford, and J.H. Fearon, Ed., MacMillan, 1959.

OVERVIEW OF EDDY CURRENT RESEARCH AT SAARBROCKEN

P. Höller, R. Becker, K. Betzold
 Fraunhofer-Institut für zerstörungsfreie Prüfverfahren
 D-6600 Saarbrücken 11, Germany

ABSTRACT

The development of an eddy current testing system is described which encloses a 4-frequency test device as well as extensive computer programs to optimize layout and adaptation to practical problems. Results obtained on the testing of welds and heat exchanger tubes are presented. The testing aim is to detect defects and to determine their type and size.

PHYSICAL BASIS

Starting our investigations in the field of eddy current testing we had to learn and then to enlarge the physical basis of the method. We studied the correlation between the impedance of the coil and the test parameters such as the metallurgical and geometrical properties of the specimen as well as the test frequency and the data of the coil itself. We had in hand the results of the work done by Förster /1/ and the theoretical approaches going back to Dodd, Deeds et al. /2/. So we built up a computer program system which allows the numerical evaluation of those test situations where all bordering areas of the coils and the specimens correspond with coordinate planes of the cylindrical coordinate system. Therewith the most important practical test situations can be treated:

- coaxial encircling coil for a bar or a tube
- coaxial inside coil in a tube
- pick-up coil above a plate.

The specimens can consist of one or two layers whereby the electric conductivity, the magnetic permeability and the thickness of the layers are the input parameters of the program. The cross section of the cylinder shaped winding is assumed to be rectangular and its outer and inner diameter as well as its height can be varied.

The numerical algorithm is based on the formulae published by Dodd, Deeds et al. The coil is composed of infinitesimal current loops. The Maxwell equations give the vector potential of the problem reduced to a single current loop. The vector potential of the real coil and therewith its impedance is obtained by integrating the vector potential of the single current loop over the cross section of the coil.

In the following some results got by this proceeding are shown /4,5/. Figure 1 represents an impedance diagram for the problem of testing the walls of a reactor pressure vessel. The thickness of the cladding is about 6 mm; the ferrite content of the cladding causes a magnetic permeability of 2; the base material is ferrite. The dimensions of the pick-up coil are listed on the right side of Fig. 1. The abscissa and the ordinate axes represent the real and imaginary part of the coil impedance in presence of the test specimen, normalized by the inductance of the coil in air. The tips of the impedance vectors are moving as a function of the test parameters on locus curves in the impedance plane.

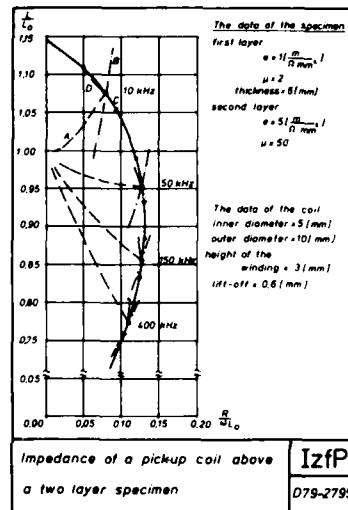


Fig. 1

At four frequencies 10, 50, 150 and 400 kHz the effects on the coil impedance caused by variations of the material data of the cladding are calculated. The dotted lines (marked with A) are corresponding to a lift-off of the coil; The lines marked with B represent the variation of the magnetic permeability from 1 to 3; curve C shows the effect of the increase and decrease of the electric conductivity of the upper layer. In addition to these effects the measured impedance of a slit in the surface of the plate is plotted (D). The upper starting point of the locus curve, representing low frequencies, is typical for the special test configuration. Therefore testing of different specimens with the same coil at low frequencies allows to correlate the ordinate value with the magnetic permeability.

Figure 2 represents calculated results for a coil in presence of an austenitic (lower curve) and a ferritic (upper curve) material. At the aforementioned frequency points the lift-off signals and the measured signals of defects are plotted. The low frequency values on the ordinate axis are 1 for the austenitic specimen and about 1,28 for the ferritic material.

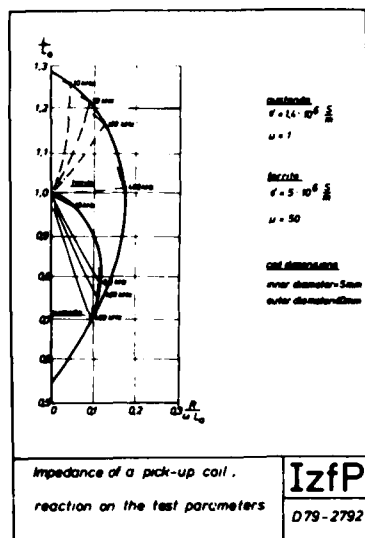


Fig. 2

Figure 3 allows the comparison between two different coils above a two layer specimen. The increase in the coil diameter is correlated with greater real and imaginary parts of the impedance representing a stronger reaction between coil and material. Besides that there arise other phase angles between the different test parameters. These phase angles are, as we can see, a function of the test frequency and of the coil dimension and they are the basis of the later on explained multifrequency method. The eddy current computer-program system allows a short and fast overview of the effects and at least the optimization of the choice of frequencies.

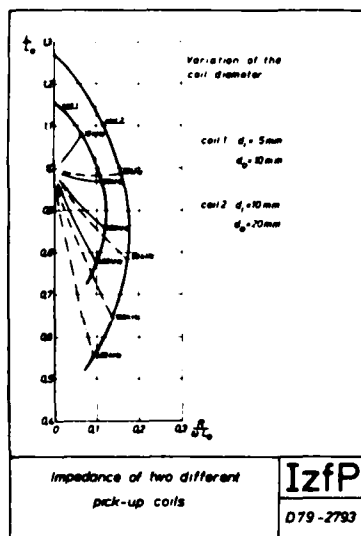


Fig. 3

To demonstrate the penetration of eddy currents into the test specimen the figures 4 and 5 show the calculated amplitude of the eddy

current density of a pick-up coil in two different depths. The winding of the coil is above the maximum value. One can recognize that the decrease of the current amplitude in the radial direction of the coil is near the surface steeper than deeper below the surface.

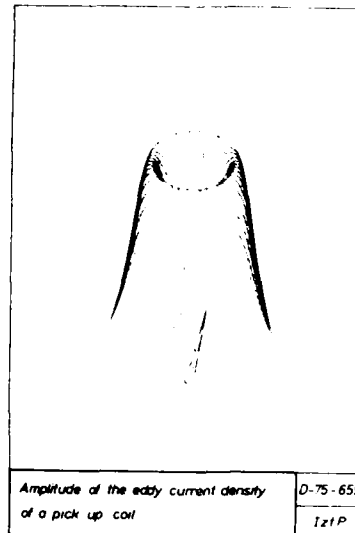


Fig. 4

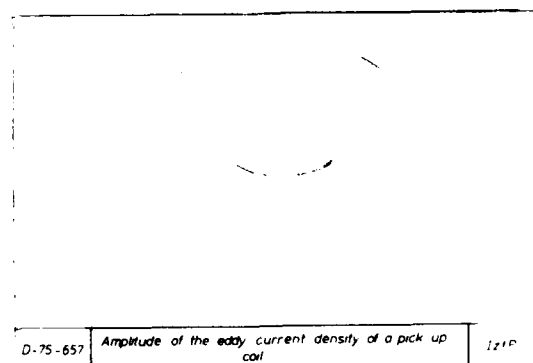


Fig. 5

In Fig. 6 equivalent evaluations for coaxial outside coils are demonstrated. The lines marked with A are corresponding to an austenitic tube with a wall thickness of 1.2 mm while the curves marked with B are corresponding to an austenitic bar. For the input data of the program therefore follows that the electrical conductivity of region 1 in the upper part of Fig. 6 must be 0 in the first case (tube) and 1,1 m/Ωmm² in the second (bar).

At lower frequencies there is an obvious difference between the eddy current density in tubes and in bars; the difference decreases with increasing frequency.

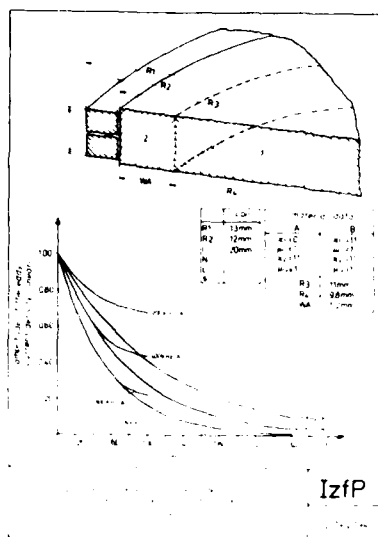


Fig. 6

At least one representative plot shows in Fig. 7 the effects and the problems concerning the testing of built-in heat exchanger tubes with inside coils.

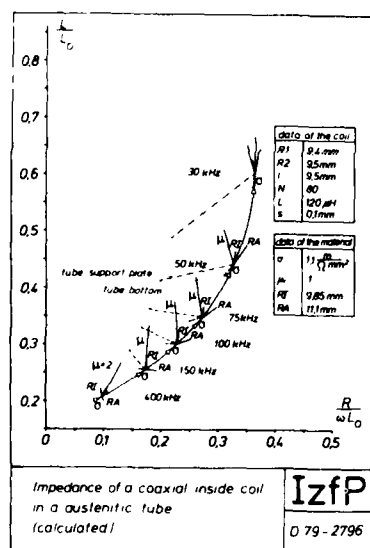


Fig. 7

At six frequencies in the range of 30 kHz to 400 kHz the changes of impedance caused by variations of the following parameters has been calculated: electric conductivity, magnetic permeability, inner and outer diameter of the tube. The effects of the ferritic tube plate and of a ring shaped austenitic tube support plate can be simulated in the computer program by the material data of a second layer. All parameters standing in the schedule in the right half of Fig. 7 (R1, R2 inner and outer radius of the coil; L length of the coil; N number of turns; L inductance, s diameter of the wire) are input parameters and they can be varied

to get a complete overview of static effects in tube testing.

In order to know the capability of the theoretical and numerical results for the application on real problems a measuring device has been built up. There was a good agreement between predicted and experimental locus curves.

THREE MAIN PROBLEMS OF THE EDDY CURRENT METHOD

As demonstrated by the examples the impedance of the coil carries the information about the test parameters; it is measured and interpreted. But generally, the impedance simultaneously is affected by several parameters, also by those which not at all are the subject of the testing. The type of the parameter which has caused the detected variation of the impedance cannot be recognized at once. Therefore, the first of the problems applying the eddy current test method is to eliminate the contributions of the parameters to the impedance and to suppress the contributions caused by undesired or disturbing parameters.

In this connection the detection limit for the different parameters is important. Related to defects the detection limit indicates how great the defect size must be that the variation of the impedance caused by the defect is just as strong as the maximum of the disturbing background. Principally, the detection limit is decreased to more advantageous small values by the suppression of the signals caused by the disturbing parameters. But generally, the suppression succeeds not completely, additionally the contributions of the interesting parameters do not remain unaffected by the procedures applied to realize the suppression of the disturbing parameters. Therefore the second of the problems is the optimization of the detection limit of the interesting parameters.

Finally after the suppression of the disturbing signals, as the third of the problems remains the classification and interpretation of the variation of the impedance. Especially for the testing of defects it is necessary to distinguish which type of defect has caused the measured change of impedance before the defect size can be determined.

MULTIFREQUENCY TEST EQUIPMENT /6/

At an early state we understood that the described problems only could be solved by a multifrequency or multiparameter approach originally published by Libby /3/. Therefore, we developed and built a multifrequency equipment. After a first simple laboratory device at present a fully developed prototype exists which is suitable to application in the field. Figure 8 shows the prototype.

In contrast to the common concept where the several test frequencies are fed simultaneously into the coil and processed in parallel channels, we have realized the multiplexing concept. The principle is shown in Fig. 9. The frequency is changed sequentially step by step so fast that the time needed for one cycle is so small that, depending on the scanning speed the test parameters remain unchanged. The lowest frequency limits testing speed.

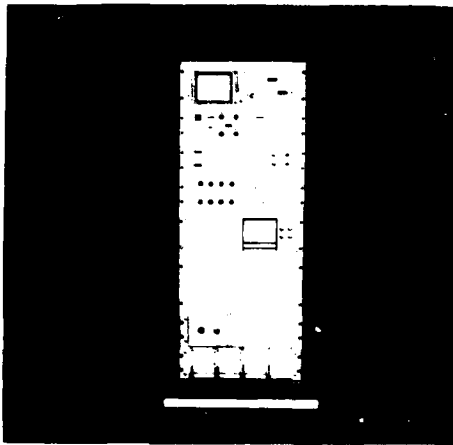


Fig. 8

Under the condition that the clock frequency is sufficiently high, both concepts yield the same results. But concerning the realization and the universal and flexible applicability the multiplex concept has some advantages:

- the electronic expense is independent of the number of frequencies,
- the frequencies can be tuned continuously and in a wide range; there is no need for band filters,
- cross talk between the frequency channels does not exist.

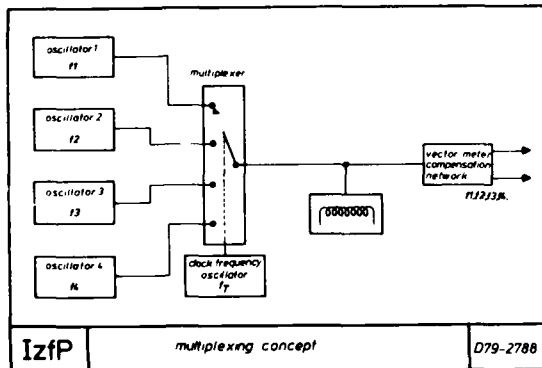


Fig. 9

Figure 10 shows a simplified block diagram of the prototype.

In Fig. 11 the frequency control is drawn separately. Four variable DC-voltages are fed into the VCO-input of a generator. Varying the voltages the 4 test frequencies can be adjusted in the range of 50 Hz to 1 MHz. The test frequency generator yields two output voltages with 90° phase shift one against the other. The multiplexer is controlled by the clock frequency oscillator.

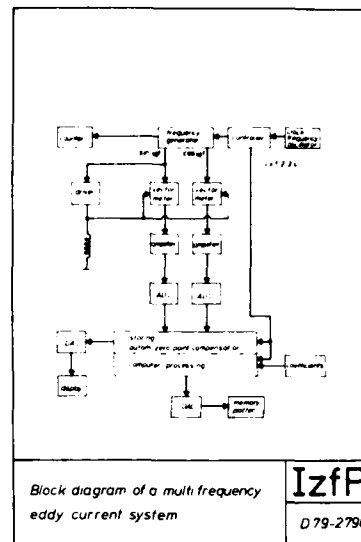


Fig. 10

The output voltage of the test frequency generator drives a current source which impresses a constant current into the coil. The amplitude and the phase of the voltage at the coil is affected by the properties of the specimen. The complex voltage at the coil is splitted into a real and an imaginary part.

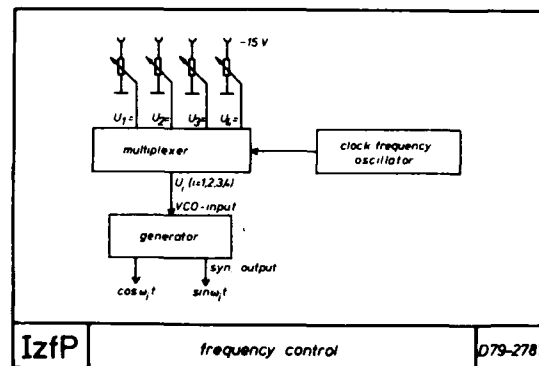


Fig. 11

The further processing of the two components of the voltage at the coil is performed digitally. At first, there is a network to compensate a given voltage at the coil and to fix any zero point in the impedance plane. The following network performs the suppression of the disturbing signals. This network is controlled by a μ -Processor and composed of fast computer modules to execute additions and multiplications.

MULTIFREQUENCY APPROACH /7/

The algorithm applied to suppress the disturbing signals is described in Fig. 12 for a particular example.

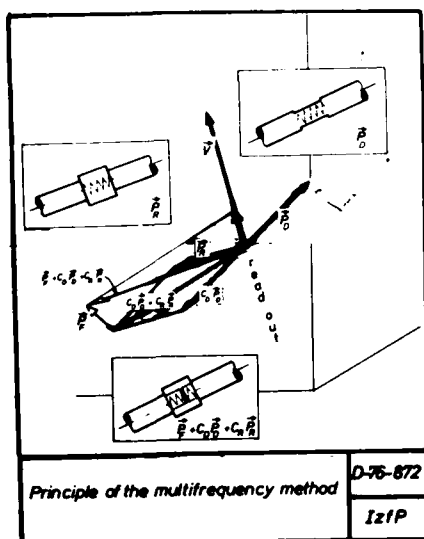


Fig. 12

The task shall be to detect defects in a heat exchanger tube. Disturbing signals are caused by the tube sheet and by variations of the diameter of the tubes. A general rule says that to suppress the signals of n disturbing parameters at least $n+1$ independent measured values are necessary. Therefore in our example we need three independent measured values which can be the real and imaginary part of the voltage at the first frequency and the real or imaginary part of the voltage at the second frequency. These measured values produce a 3-dimensional vector space; its coordinate system is plotted in Fig. 12. In a first step the calibration of the multifrequency system must be performed. The reference point of the measurement is a defined position on the tube where no disturbances exist. Now the coil is brought at a position below the tube sheet, outlined at the left of Fig. 12. The alterations of measured values related to the reference point form the 3-dimensional vector \vec{P}_R . In the same way the measured values at a position shown at the top of Fig. 12, where the diameter of the tube is decreased, give the vector \vec{P}_D . Both vectors spread out in the 3-dimensional space a plane grey-coloured in Fig. 12. In this plane lie all measured vectors which are caused by the two disturbing parameters in each combination and superposition. The strength of the alteration of the disturbing parameters is expressed in the coefficients c_R and c_D . Obviously the coefficient c_R only can have the two values 0 or 1. In a computing step consisting in solving a linear equation system the read-out vector \vec{V} is determined in such a manner that it is perpendicular to the plane of the disturbing parameters.

The diagram illustrates the relationship between the number of combinations of test frequencies in tube testing and the number of inner code frequencies. It features a large central area with many small text boxes and arrows, and a smaller area on the right with a table-like structure.

Table 1: Relationship between the number of combinations of test frequencies in tube testing and the number of inner code frequencies

Number of combinations of test frequencies in tube testing	Number of inner code frequencies
1	1
2	2
3	3
4	4
5	5
6	6
7	7
8	8
9	9
10	10
11	11
12	12
13	13
14	14
15	15
16	16
17	17
18	18
19	19
20	20
21	21
22	22
23	23
24	24
25	25
26	26
27	27
28	28
29	29
30	30
31	31
32	32
33	33
34	34
35	35
36	36
37	37
38	38
39	39
40	40
41	41
42	42
43	43
44	44
45	45
46	46
47	47
48	48
49	49
50	50
51	51
52	52
53	53
54	54
55	55
56	56
57	57
58	58
59	59
60	60
61	61
62	62
63	63
64	64
65	65
66	66
67	67
68	68
69	69
70	70
71	71
72	72
73	73
74	74
75	75
76	76
77	77
78	78
79	79
80	80
81	81
82	82
83	83
84	84
85	85
86	86
87	87
88	88
89	89
90	90
91	91
92	92
93	93
94	94
95	95
96	96
97	97
98	98
99	99
100	100

Fig. 13

THE OPTIMIZATION OF THE TEST FREQUENCIES /8/

It can be seen from Fig. 12 that the described algorithm not only suppresses the signals caused by the disturbing signals but also reduces more or less the defect signals. A measure for the projection losses is the angle α between the defect vector $\vec{P}\vec{F}$ and the read-out vector \vec{V} . This angle is a function of the applied test frequencies. Therefore a frequency combination is optimal when the angle α is as different to 90° as possible. Especially when the quantity of the needed frequencies is high there are many frequency combinations which must be examined. Therefore we have developed a computer program which performs the choice of the frequencies automatically. Applying the method described in the first section we determine numerically the relevant disturbing vectors as a function of the test frequency and the coil dimensions. Therewith and with the measurement of a reference defect vector the angle α is computed for all possible frequency combinations. Figure 13 shows the result for a particular example in the field of heat exchanger testing. To suppress the disturbing signals caused by the tube plate, tube support plate, by variation of conductivity of the tubes we must apply 3 frequencies. In the suitable frequency range of 30 to 400 kHz we designate the 9 frequencies coming into account and listed at the right of Fig. 13. Beside the frequency table the material properties and the coil data are described (σ electric conductivity, μ relative magnetic permeability, R_1 and R_2 inner and outer diameter of the tubes, R_1 and R_2 inner and outer diameter of the coaxial coil, l length of the coil, N number of turns, L inductance, s diameter of the wire). Diagonally through the picture tables with squares are depicted. The triples of numbers in the squares characterize the frequencies of the corresponding combinations.

The table at the left contains all combinations with the first frequency, the following table the combinations with the second frequency etc. Beside the numbers in each square a sign is written which weights the ability of the appertaining frequency combinations. The signs are declared at the left at the top in Fig. 13 and correspond to the angle α . The test frequencies with the smallest projection losses and therefore with the best defect detection limit are marked by crosses. The result shown in Fig. 13 is valid for an artificial slit at the

outside of the tubes and a depth of 0.7 mm. The wall thickness of the tube is 1.3 mm.

SEVERAL APPLICATIONS

Testing of welds - In Figure 14 on the right, a ferritic specimen is outlined which is clad by an austenitic steel. In the welding two pulsed fatigue cracks are present. Just there, the distortions caused by material alterations (σ and μ) and lift-off are especially strong. The testing is made with an absolute pick-up coil which is moved in several traces over the surface.

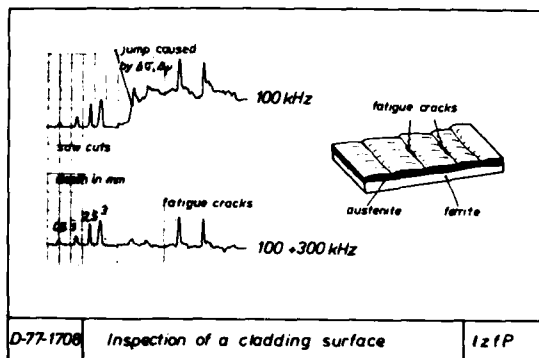


Fig. 14

In Fig. 14 on the left the results of testing with one frequency (100 kHz) and with two frequencies (100 and 300 kHz) are compared. Slits with different depths are used to weight the defect depths. The signals caused by these slits are shown on the left of the plots, followed by signals which appear along an inspection trace over the actual specimen. It can be seen that at the bottom of the plot the disturbing signals are reduced strongly; the remaining signals have the same indication peak as a slit of 0.5 mm depth. The pulsed fatigue cracks give signals which correspond to a slit of 3 mm depth.

Figure 15 describes the results of testing an austenitic welded joint. The material properties between the welding and the basic material differ. The two outlined pulsed fatigue cracks in the welded joint are measured. At first the signals caused by saw cuts are shown on the left of the plots, followed by signals along an inspection trace which meet both cracks in the welded joint.

The signals caused by the cracks are totally masked if the testing is performed by means of one frequency (100 kHz), whereas they are clearly read out if the testing is performed by means of two frequencies (100 and 300 kHz). The disturbing signals caused by the welding are suppressed as well as those caused by lift-off. The remaining disturbing signals have the same indication peak as a saw cut of 0.5 mm depth. The pulsed fatigue cracks are indicated with different height related to their different depth; they produce the same signals as slits of 2 mm and 3 mm depth.

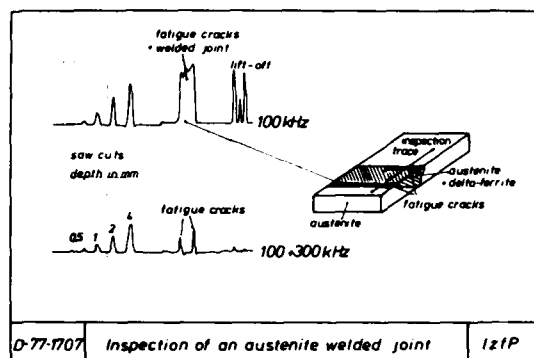


Fig. 15

Figure 16 shows the testing results of a ferritic welded joint, in which two natural surface cracks are present. In the area of the welding the specimen is scanned in several traces. The plots demonstrate on the left the signals caused by the slits, followed on the top by the signals caused by the defect 1, which is indicated four times corresponding to the four traces meeting this defect. Subsequently one can see the defect 2, which is indicated at first with increasing and then with decreasing depth. The plot on the top is the result of testing by means of two frequencies. In contrast, if the testing is performed by means of one frequency, as shown at the bottom of the plots, the defect depths are read out falsely and defect responses appear, where no defects are present. So the defect 1 is read out with the same height as a saw cut of 4 mm depth, whereas, if working by means of two frequencies, it is weighted as a slit of 1.5 mm depth.

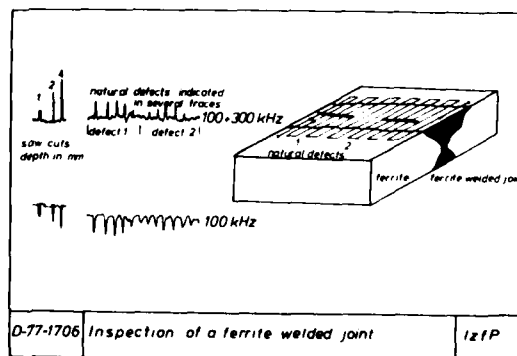


Fig. 16

Testing of heat exchanger tubes - The testing is performed with an absolute coaxial inside coil which is moved through the tubes. Figure 17 shows the testing result obtained with the three frequencies 75, 200 and 400 kHz. At the bottom of Fig. 17 the defect signals are superimposed by disturbing signals caused by the tube sheet, by the tube support plate, by variations of the inner and outer diameter of the tubes and by coil wobble. After the processing of the signals

obtained at the three frequencies the upper plot in Fig. 17 indicates only defect signals.

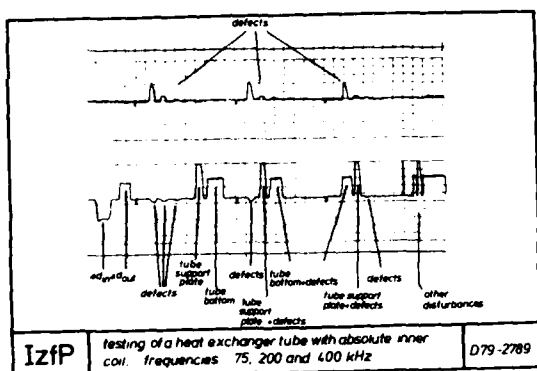


Fig. 17

One can recognize three times the indications of three slits (0.85, 0.7 and 0.4 mm depth, 0.5 mm width, 1.2 mm wall thickness of the tubes) which are located as well in the free part of the tubes as below the tube sheet and tube support plate.

Figure 18 indicates the defect detection limit for the same application. The plots show

- 1a: disturbing signals caused by the tube sheet, the ring shaped and the grid shaped tube support plate;
- 1b: the remaining underground of the disturbing signals after the processing;
- 2a: disturbing signals as in 1a but superimposing defect signals;
- 2b: the same signals as in 2a but after the suppression of the disturbing signals. The defects are outside slits in the axial direction of the tubes; their depth related to the wall thickness is marked in the Fig. 17;
- 3: defect signals of outside slits in the azimuthal direction of the tubes.

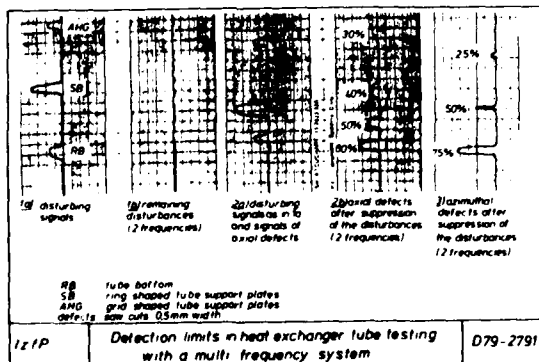


Fig. 18

The results show that the 30 % axial and the 25 % azimuthal slit can be detected certainly even when they are located below the tube sheet or tube support plate. It shall be emphasized that in all cases an absolute coil is used.

INTERPRETATION AND CLASSIFICATION OF THE DEFECT SIGNALS

The multifrequency algorithm described in chapter 4 yields a one-dimensional read-out value. As be done in the preceding chapter the read-out value can be weighted by artificial reference defects with known depths and equivalent indication peaks. But it is not possible to distinguish which type of defect has really caused the read-out value. It is obvious that before the defect size can be determined it is necessary to know the defect type. To enable this we apply the following method. By means of adding at least one additional measured value (this can be the real or imaginary part of a new test frequency) or replacing the test frequencies by completely new ones the multifrequency algorithm is applied two times. In both parallel channels the signals caused by the disturbing parameters are suppressed. Under the condition that the two combinations of the processed measured values react in a different manner upon the different types of defects one obtains a two-dimensional read-out value. Displaying the two channels on the horizontal and vertical deflection of an oscilloscope one achieves the results:

- the disturbing signals are suppressed and concentrated in the zero point of the screen;
- the defects give indications with different phase angles corresponding to the different defect types;
- the peaks of the defect indications are correlated with the defect size.

Using a computer program similar to that described in an earlier chapter, the angles between the phase directions belonging to the different defect types can be optimized.

In the middle of Fig. 19 a heat exchanger tube with the tube sheet, the tube support plate and several types of defects is outlined. Realizing the above described method and processing the two frequency combinations 200/340 kHz and 100/200 kHz one obtains at the right of Fig. 19 the indications caused by the named defect types.

Displaying both read-out values in the described manner on an oscilloscope one obtains the deflections shown at the left of Fig. 19. The upper picture differs from the lower in the depth of the outside notch (60 % and 90 % of the wall thickness) and in the diameter of the hole (0.8 mm and 1.5 mm, both 100% of the wall thickness deep). Both times the alterations of the diameters are the same.

Figure 20 shows for the same test situations the indications for some other type of defects. In each case the plot and the picture beside them belong together.

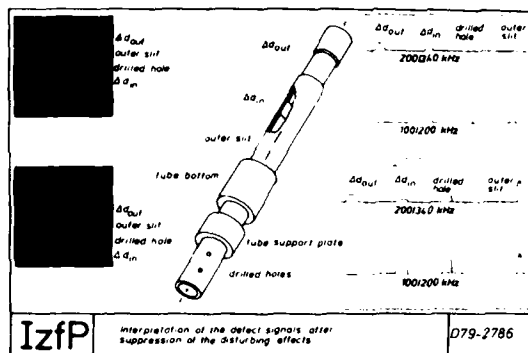


Fig. 19

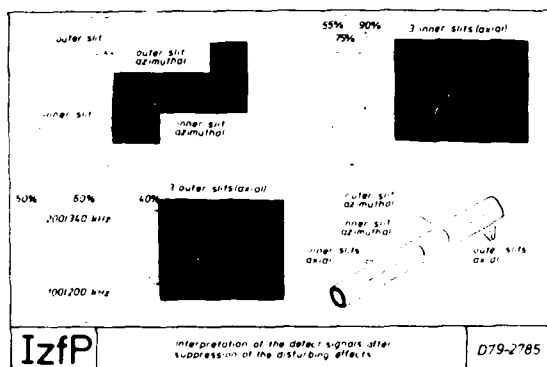


Fig. 20

Summarizing Fig. 19 and 20 one can see that applying the described procedure it is possible to determine uniquely the types of the defects detected after the suppression of the disturbing signals. In the case of simple defect structures the obtained induction peaks are a measure for the defect size.

REFERENCES

- /1/ F. Förster, K. Stambke: "Theoretische und experimentelle Grundlagen der zerstörungsfreien Werkstoffprüfung mit Wirbelstromverfahren. III. Verfahren mit Durchlaufspule zur quantitativen zerstörungsfreien Werkstoffprüfung". Z. Metallkde. 45 (1954), p. 166-179
- /2/ C.V. Dodd: "Integral solutions to some eddy current problems." International Journal of Nondestructive Testing 1 (1969), p. 29-90
- /3/ H.L. Libby: "Multiparameter eddy current concepts". Research Techniques in Nondestructive Testing. Volume 1 (R.S. Sharpe, Ed.), Chapter 7. Academic Press, London 1970
- /4/ K. Betzold, R. Becker: "Theoretische und numerische Untersuchungen zur Wirbelstromprüfung geschichteter Materialien mit Abtastspulen gegebener Abmessungen". IzfP-Bericht Nr. 760501-TW, Saarbrücken, 1976
- /5/ K. Betzold: "Theoretische und numerische Untersuchungen zur Wirbelstromprüfung geschichteter Materialien mit coaxialen Innenspulen und Außenspulen". IzfP-Bericht Nr. 780725-TW, Saarbrücken, 1978
- /6/ R. Becker, L. Regneri, R. Rüdiger: "Mehrfrequenz-Wirbelstromprüfung; Phase 1 Aufbau eines Mehrfrequenz-Geräteprototyps". IzfP-Bericht Nr. 780120-TW, Saarbrücken, 1978
- /7/ R. Becker, L. Regneri: "Anpassung des Wirbelstromverfahrens für den Einsatz an Reaktoren". IzfP-Bericht Nr. 780832-TW, Saarbrücken, 1978
- /8/ K. Betzold: "Mathematische Modelle zur Auslegung der Spulen und Wahl der Frequenzen bei der Mehrfrequenz-Wirbelstrom-Methode". Neuere Entwicklungen und besondere Verfahren der zFP. Europäische Tagung für zerstörungsfreie Materialprüfung, Mainz, 1978

DESIGN OF A TEMPERATURE-COMPENSATED INDUCTION EXTENSOMETER

W. E. Deeds and A. R. Yazdi
Department of Physics and Astronomy, University of Tennessee
Knoxville, Tennessee 37916

C. V. Dodd
Metals and Ceramics Division, Oak Ridge National Laboratory
Oak Ridge, Tennessee 37830

ABSTRACT

By proper choice of materials, dimensions and circuit parameters, it is possible to design a linear displacement transducer, or extensometer, to have zero net thermal drift over any given temperature range. The chief limitation is the inability of wires and insulation to withstand very high temperatures. An extensometer has been designed and tested which could theoretically measure displacements up to 150 mm with a maximum error of ± 0.15 mm caused by thermal effects over the temperature range from 0° to 1000°C . Experimental limitations prevented testing at temperatures higher than 500°C , but measured and theoretical results were in good agreement over that range. The principles involved in the temperature compensation will be discussed.

When eddy current tests must be made over a range of temperatures, there are several possible thermally-caused errors. The resistance of the coils may change; the resistivity of the samples may change; thermal expansion may change all of the dimensions, and, at very high temperatures, the structural integrity of the coils may fail.

In the design of an induction extensometer to be used at high temperatures,¹ ways were found to compensate for all of these sources of error, except the last. The extensometer coils were wound of Secon alloy wire with baked-ceramic insulation on a fused quartz coil form and should be usable to 1000°C . The driver and pickup coils were interwound as a bifilar coil with a common ground, as shown in Fig. 1. The associated electrical circuit is shown in Fig. 2, where Z_D is the driver coil impedance, Z_{PU} is the pickup coil impedance, and M is their mutual inductance. The discriminator measures the phase difference between the driving current I_1 and the output current I_4 . Actually, changes in the phase difference from the value when the coils were in air were measured and called the "phase shift."

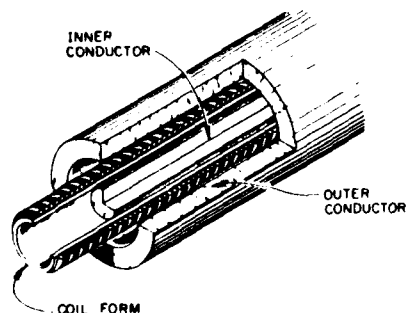


Fig. 1. Cutaway drawing of solenoidal coil coaxial with inner and outer conductors.

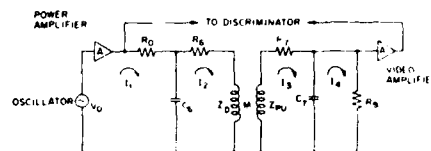


Fig. 2. Designation of various components and connection to measuring equipment. Designations and values: $V_0 = 10$ V, $C_1 = C_2 = 150$ pF, $R_0 = R_1 = 681.5 \Omega$, $R_2 = R_3 = 37 \Omega$, $TN = 300$ turns.

The performance of the system was calculated using computer programs² developed at Oak Ridge National Laboratory. If the coils are wound on a coil form of negligible thermal expansion (such as fused quartz) and are inside a conducting tube, the tube will expand away from the coils as the temperature is raised, decreasing the "fill factor" (or increasing the "lift-off"), and producing a decrease in the phase change, as shown in Fig. 3. On the other hand, if the coils encircle an inner conducting rod or tube, the inner conductor will expand toward the coil, increasing the "fill factor" and increasing the phase difference, as shown in Fig. 4. Since the expansions of the inner and outer conductors produce phase shifts in opposite directions, the combination can be made to produce zero phase shift over a given temperature range if the coil is sandwiched between an inner conductor and an outer tube, as shown in Fig. 1 and the top part of Fig. 5. The inner radius of the outer conductor necessary to compensate for the thermal expansion effect is plotted as the curve marked R in the lower part of Fig. 5 as a function of the outer radius of the inner conductor. Both radii have been "normalized" by dividing by the mean coil radius, \bar{r} , and the point marked "A" indicates the combination of radii for the extensometer as constructed.

The dimensionless quantity $r^2 \omega \mu$, where ω is the angular frequency, μ and σ the permeability and conductivity of the metal, respectively, describes the dimensions of the coil in terms of the penetration depth of the eddy currents at the given frequency. For given geometrical dimensions and material properties, there will be an operating frequency, $\omega/2\pi$, for which the total phase shift produced when the coil is inserted between the

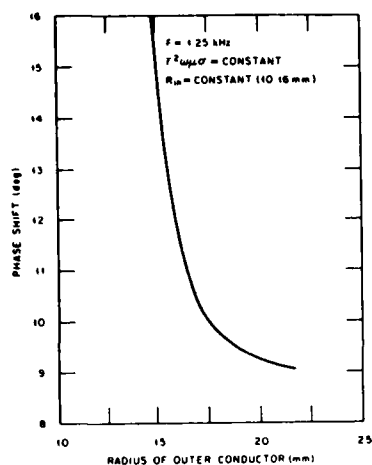


FIG. 3. Phase shift versus radius of outer conductor for constant R_{in} .

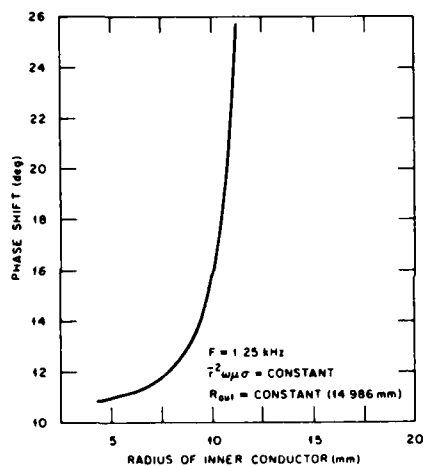


FIG. 4. Phase shift versus radius of inner conductor for constant R_{out} .

conductors (or withdrawn from them) will be a maximum. Figure 6 shows the variation in this total phase shift for various values of $r^2_{\omega\mu\sigma}$ near the maximum. From this we see that, if the conductivity σ and permeability μ of the material change over the prescribed temperature range, the value of ω can be chosen so that the extreme values of $r^2_{\omega\mu\sigma}$ will be equally spaced on opposite sides of the maximum, for example, at the points marked $\Delta\phi_{20}$ and $\Delta\phi_{1000}$ in Fig. 6, corresponding to phase shifts at 20°C and 1000°C, respectively. Thus, the phase shifts at the extremes of temperature will be the same, and the errors at intermediate temperatures will be very small. The curve marked $r^2_{\omega\mu\sigma}$ in Fig. 5 gives the value of that quantity producing the maximum phase shift as the coil is withdrawn from between the conductors; it is shown as a function of the normalized radius of the inner conductor, and the point marked "C" is the value corresponding to the radii designated by the point "A" (in this case, $r^2_{\omega\mu\sigma} = 9.34$). Using the frequency necessary to produce this "optimum" value of $r^2_{\omega\mu\sigma}$, the phase shift that will be produced is shown by the curve marked "PHASE SHIFT." For this example (and the

extensometer actually constructed), the point marked "B" corresponds to the same inner conductor radius as the points "A" and "C" and indicates that there should be a phase shift of 25.48° as the coil is withdrawn from the conductors. Figure 7 shows the measured phase shift versus displacement for the actual coil, which was 150 mm long; the non-linearity was caused by end effects and was quite reproducible.

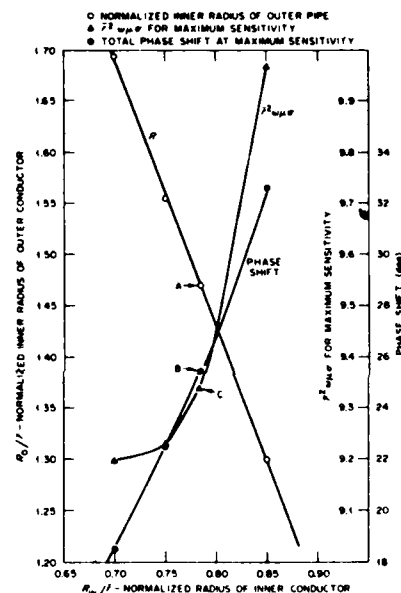
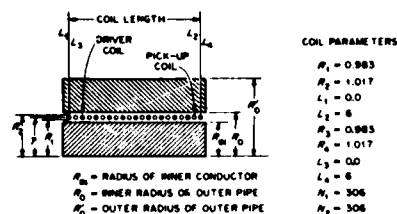


FIG. 5. Outer conductor radius, optimum $r^2_{\omega\mu\sigma}$, and phase shift as functions of inner conductor radius.

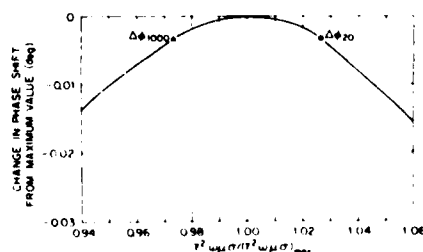


FIG. 6. Change in phase shift versus relative value of $r^2_{\omega\mu\sigma}$.

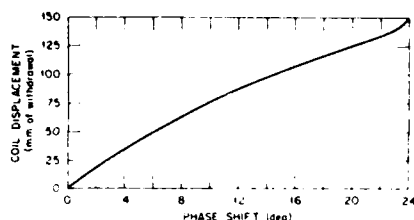


FIG. 7. Phase shift versus coil displacement.

The final source of thermal drift to require compensation is the change in DC resistance of the coils. If the series resistance R_0 in the driver circuit and the shunt resistor R_9 in the pickup circuit have the proper relationship to the other circuit parameters in Fig. 2 (the cable capacitances, C_6 and C_7 , the coil resistances, R_6 and R_7 , and the coil inductances, Z_D , Z_{PJ} and M), then the output phase shift can be made to have zero net change as the coil resistances are changed from their minimum to their maximum values, thus compensating for the final source of possible thermal error.

The extensometer design indicated by the values listed in Table I was constructed using Inconel for the conductors and Secon alloy wire for the coils on a quartz coil form 150 mm long. It could only be tested to 500°C, but the measurements accurately confirmed the theoretical predictions. If the values of R_0 and R_9 had been chosen properly, the maximum thermally caused error of displacement measurements would have been 0.1% of full scale over the full temperature range from 0° to 1000°C.

TABLE I. Dimensions of Inconel extensometer

	Actual (mm)	Normalized
Mean coil radius	6.07	1.000
Inner radius of inner conductor	0.00	0.00
Outer radius of inner conductor	4.76	0.784
Inner radius of outer conductor	8.93	1.471
Outer radius of outer conductor	10.2	1.673

We wish to thank the Metals and Ceramics Division of Oak Ridge National Laboratory for use of their facilities during the course of this investigation and the Computer Center of The University of Tennessee for much of the computer calculations.

REFERENCES

1. A. R. Yazdi, W. E. Deeds, and C. V. Dodd, "Temperature-Compensated Induction Extensometer," Rev. Sci. Instrum. 49, 1684-1687 (1978).
2. C. W. Nestor, Jr., C. V. Dodd, and W. E. Deeds, "Analysis and Computer Programs for Eddy Current Coils Concentric with Multiple Cylindrical Conductors," ORNL-5520 (to be published).

AC MAGNETIC FIELDS IN THE VICINITY OF A CRACK CALCULATED BY ANALYTIC AND NUMERICAL METHODS

A. H. Kahn and R. Spal[†]
National Bureau of Standards
Washington, DC 20234

ABSTRACT

We report calculations of the impedance of a long solenoid which surrounds a cylinder of conducting material containing a radial surface crack. The calculation is accomplished by two independent methods. The first method expresses the field in the interior of the "cracked" cylinder as an infinite series of cylindrical Bessel functions. The coefficients in the series are determined in principle by boundary conditions; the most significant terms are calculated by solving the finite set of equations obtained by truncation of the series. The second method, applicable to any uniform geometric cross-section, obtains the impedance from the normal derivative of the field on the boundary of the conductor. This normal derivative satisfies a (boundary) Fredholm integral equation of the first kind; a solution is obtained by discretizing and solving the resulting linear system of algebraic equations. The impedance is calculated for a wide range of values of the ratios of crack depth-to-radius and radius-to-skin depth. The results are displayed in graphical form giving the fractional charges of the real and imaginary parts of the complex impedance induced by the presence of the crack.

We consider an infinitely long conducting cylinder with a thin radial crack as shown in Fig. 1 and Fig. 2. The goal of the calculation is to obtain the familiar impedance diagram, i.e., a plot of imaginary versus real part of the impedance of a surrounding coil (with unity filling factor), when the ratio of radius to electromagnetic skin-depth is varied. The eddy current equation shown in Fig. 3 must be solved for the field in order to obtain the impedance.

An analytic solution can be obtained by a generalization of a closed form expression for the case when the crack depth is equal to the radius. To apply the boundary conditions on the circumference, it is necessary to transform coordinates through use of the Bessel function addition theorem. The form of the solution is shown in Fig. 4. The coefficients A_n are obtained by truncating the series at 30 to 40 terms and solving numerically. Accuracy of the impedance is estimated as better than 0.05% in the range covered.

An alternate approach is to use Green's theorem to recast the differential equation of Fig. 1 into integral equation form. This approach has the advantage of being applicable to any shape of cross-section, although here it is used only for the circular cylinder with a crack. In Fig. 5 we show the integral equations which apply with and without the crack. Subtraction of the two provides simplification and yields an equation for the perturbation of the normal derivative of the field at the surface, induced by the crack. The change of normal derivative is calculated numerically by discretizing, applying approximation techniques, and solving the resultant linear equations. With 64 collocation points agreement with the eigenfunction method is within 1%.

The resulting impedance plot is shown in Fig. 6, where arrows indicate the shift of points, induced by the crack, corresponding to representative values of a/δ (the ratio of radius to skin-depth). We see that the shape of the impedance curve is changed only slightly, but that representative points are shifted significantly along the curve. At low frequencies the crack impedes the flow of penetrating eddy currents, decreasing the loss; at high frequencies the current is confined to the surface and the crack increases the loss through the increased surface area. At all frequencies the inductance is increased by the crack, corresponding to enhanced magnetic flux penetration. In Fig. 7 and Fig. 8 we show numerical results for the fractional change of the real and imaginary parts of the impedance as a function of crack depth for a representative range of values of a/δ .

[†]Mailing address: Department of Physics, University of Pennsylvania, Philadelphia, PA 19104.

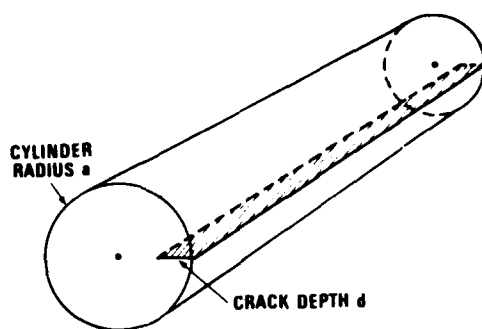


Fig. 1. Segment of an infinite conducting cylinder with a radial surface crack. The cylinder is placed in a coaxial solenoid and the change of impedance due to the crack is calculated.

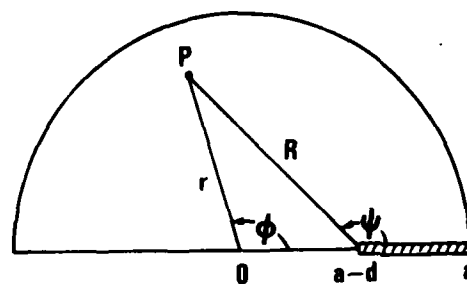


Fig. 2. Cross-section of the cylinder showing coordinate systems used in the analysis. Point P is a general point which may be expressed by (r, ϕ) measured from the center, or by (R, ψ) from the crack tip.

$$(\nabla^2 + k^2) H(r) = 0$$

$$k^2 = i\sigma\omega\mu$$

$$k = (1 + i)/\delta$$

$$\text{Time factor} = e^{-i\omega t}$$

$$\text{Boundary condition: } H = H_0 \text{ on surface}$$

Impedance:

$$Z = \frac{Lk^2 n'^2}{\sigma} \iint r dr d\phi H(r)/H_0$$

or

$$Z = \frac{L n'^2}{\sigma} \frac{1}{H_0} \oint \frac{\partial H}{\partial n_0} dS_0$$

L = length of solenoid

n' = reciprocal of pitch

H = magnetic field

σ = conductivity

ω = angular frequency

μ = permeability

δ = skin depth

k = propagation constant

Fig. 3. Eddy current differential equation and related quantities for two-dimensional problems.

Eigenfunction Expansion

$$H(\vec{r})/H_0 = \cos(kR \sin \psi) + \sum_{n=0}^{\infty} A_n \frac{J_{n+\frac{1}{2}}(kR)}{J_{n+\frac{1}{2}}(ka)} \sin(n+\frac{1}{2})\psi$$

$$= \cos(kr \sin \phi) + \begin{cases} \sum_{\ell=-\infty}^{\infty} \sum_{n=0}^{\infty} A_n (-1)^n \frac{J_{n+\frac{1}{2}+\ell}(k(a-d))}{J_{n+\frac{1}{2}}(ka)} J_{\ell}(kr) \cos \ell \phi & \text{for } r < a-d \\ \sum_{\ell=-\infty}^{\infty} \sum_{n=0}^{\infty} A_n \frac{J_{\ell-n}(k(a-d))}{J_{n+\frac{1}{2}}(ka)} J_{\ell+\frac{1}{2}}(kr) \sin(\ell+\frac{1}{2})\phi & \text{for } r > a-d. \end{cases}$$

Fig. 4. Form of solution for a crack in a circular cylinder. The second version, obtained by the application of the Bessel function addition theorem, allows application of the boundary conditions at $r = a$.

Integral Equation Formulation

With crack:

$$H(\vec{r}) = \frac{1}{4\pi} \int_{\odot} G(r, S_0) \frac{\partial H}{\partial n_0} dS_0 - \frac{1}{4\pi} \int_{\odot} \frac{\partial G(r, S_0)}{\partial n_0} H(S_0) dS_0$$

where

$$G(r, r') = i\pi H_0^{(1)}(k|r-r'|)$$

without crack:

$$H(r) = \frac{1}{4\pi} \int_{\odot} G(r, S_0) \frac{\partial H}{\partial n_0} dS_0 - \frac{1}{4\pi} \int_{\odot} \frac{\partial G(r, S_0)}{\partial n_0} H(S_0) dS_0$$

$$= H_0 J_0(kr)/J_0(ka)$$

Subtract, let $r \rightarrow S$, simplify:

$$\frac{1}{4\pi} \int_{\odot} G(S, S_0) \Delta \frac{\partial H}{\partial n_0} dS_0 = \begin{cases} 0 & S \text{ on circle} \\ H_0 [1 - \frac{J_0(kr)}{J_0(ka)}] & S \text{ on crack} \end{cases}$$

Fig. 5. Integral equation formulation for two-dimensional eddy current problems. In the last equation Δ represents the perturbation of the normal derivative of H , on the boundary of the conductor, produced by the crack.

IMPEDANCE DIAGRAM FOR A CYLINDER
WITH CRACK DEPTH EQUAL TO 0.5 X RADIUS

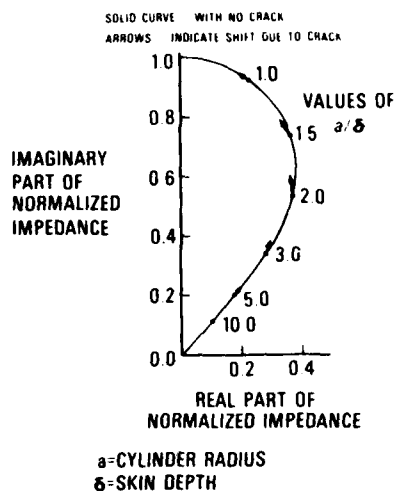


Fig. 6. Impedance diagram for a demonstrative case. Arrows drawn to scale, show the shifts of selected a/δ points induced by the presence of the crack.

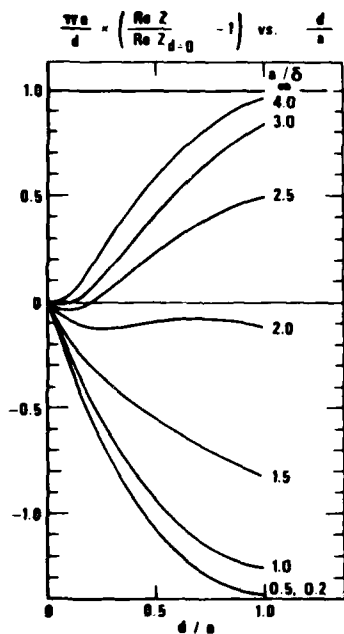


Fig. 7. Fractional change due to the crack, of the real part of the impedance as a function of d/a for selected values of a/δ .

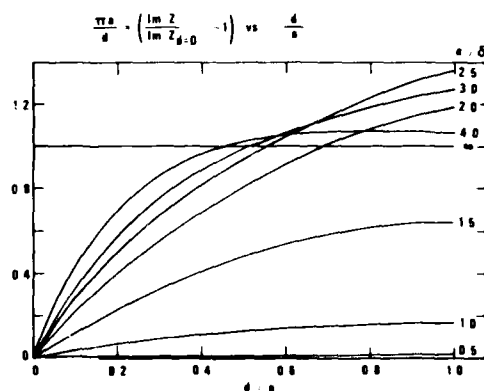


Fig. 8. Fractional change, due to the crack, of the imaginary part of the impedance as a function of d/a for selected values of a/δ .

IMPEDANCE OF A LOOP WITH A CYLINDRICAL CONDUCTING CORE

S.A. Long, C.G. Gardner, A. Zaman, and S. Toomsawadi
Electrical Engineering Department
University of Houston
Houston, Texas 77004

ABSTRACT

The change in complex impedance between an ideal one-turn coil surrounding and coaxial with an infinitely long circular cylinder of conductivity σ and permeability μ and a similar coil without the core has been calculated. From the exact expression a power series in (δ/b) (δ = skin depth; b = radius of core) has been developed. From this result the change in impedance of a physically realistic multi-turn coil can be estimated with reasonable accuracy. The theory permits a rational approach to optimization of the design of eddy current test coils and provides a basis for the later calculation of the effects of discontinuities in the core.

INTRODUCTION

A notable omission to the present body of knowledge dealing with eddy current testing is the lack of an adequate theoretical basis for the interpretation of changes in the impedance of the test coil. This deficiency remains, even though the fundamental theory is well established, owing to the mathematical difficulties involved in solving the equations for practical test-coil and specimen configurations. A complete solution in analytical form seems to exist for only a few idealized cases which do not necessarily approximate practical problems of current interest.

The program selected for study in this investigation is that of an idealized one-turn coil (or loop) around and coaxial with a long, solid, electrically conducting cylinder. This arrangement is illustrated in Fig. 1 and shows the loop with radius a and the core with radius b and conductivity σ . The theoretical treatment will assume that the core is infinitely long. (This approximation should produce very small errors as long as the distance from the position of the loop to either end of the core is large compared to the dimensions of the loop itself). This problem has the advantage of being simple enough to permit a meaningful approximate solution to be found while still corresponding to a practical eddy current testing situation. The results show how the complex impedance of the test coil changes when a cylindrical specimen is placed inside the loop and how this impedance is a function of the geometrical and material parameters of the cylindrical core.

THEORY

A theoretical treatment of a geometrically similar problem has been previously reported by Islam.⁽¹⁾ In this work, however, the emphasis was on the radiation properties of the configuration and thus only a high frequency approximation was attempted for the case of a magnetically permeable cylindrical core. The case of interest in this work, that of an electrically conducting core at much lower frequencies, may be attacked in a similar fashion but is essentially a completely different problem. From Maxwell's equations for time-harmonic fields one may derive the wave equation for the

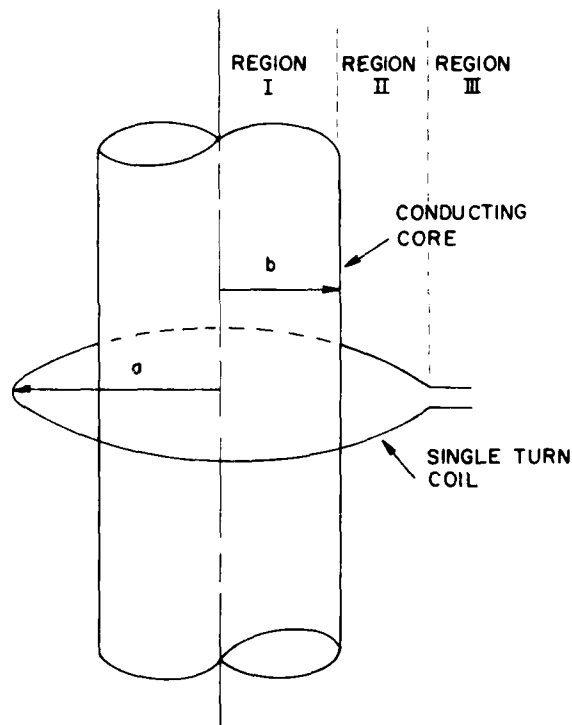


Fig. 1 Loop with Cylindrical Core

magnetic vector potential \vec{A} in terms of the impressed current density \vec{J} .

$$\nabla^2 \vec{A} + k^2 \vec{A} = -\mu \vec{J}$$

Using the standard eddy current approximation of neglecting the displacement current terms and recognizing that the vector potential has only a ϕ component which depends on r and z , the left hand side of the equation becomes

$$\begin{aligned} \nabla^2 \vec{A} &= \hat{\phi} (\nabla^2 A_\phi - \frac{A_\phi}{r^2}) = \hat{\phi} [\frac{1}{r} \frac{\partial}{\partial r} (r \frac{\partial A_\phi}{\partial r}) + \frac{\partial^2 A_\phi}{\partial z^2} - \frac{A_\phi}{r^2}] \\ &= \hat{\phi} [\frac{\partial^2 A_\phi}{\partial r^2} + \frac{1}{r} \frac{\partial A_\phi}{\partial r} - \frac{A_\phi}{r^2} + \frac{\partial^2 A_\phi}{\partial z^2}] \end{aligned}$$

Equating this expression to the source terms due to the loop current and the induced eddy currents one obtains the equation for the vector potential in each of the regions shown in Fig. 1.

$$\frac{\partial^2 A_\phi}{\partial r^2} + \frac{1}{r} \frac{\partial A_\phi}{\partial r} - \frac{A_\phi}{r^2} + \frac{\partial^2 A_\phi}{\partial z^2} = \begin{cases} -\mu_0 i_0 \delta(z) \delta(a-r); & r > b \\ j\omega\mu\sigma A_\phi; & r < b \end{cases}$$

where μ_0 is the permeability of free space, i_0 is the magnitude of the impressed loop current, ω is the angular frequency of the time-harmonic fields, and μ and σ are the permeability and conductivity of the core. The presence of the impressed loop current at $z=0$, $r=a$ is represented by the two δ -functions.

The solution to the equation may be found using a cosine transform.

$$A_\phi(r, z) = \frac{1}{\pi} \int_0^\infty g(r, k) \cos kz \, dk$$

with the following functions defined for each of the three regions.

$$g(r, k) = \begin{cases} C_1 I_1[\sqrt{(k^2 + j\kappa^2)}r] & r < b \\ C_2 I_1(kr) + C_3 K_1(kr) & b < r < a \\ C_4 K_1(kr) & r > a \end{cases}$$

where I_1 and K_1 are the modified Bessel functions of order one, $\kappa^2 = \omega\mu\sigma$, and C_1, C_2, C_3 , and C_4 are constants to be determined by the boundary conditions.

Since the quantity of primary interest is the vector potential in the vicinity of the loop, the simplest expression is that for Region III for which only C_4 needs to be found from the standard boundary conditions.

$$C_4 = \mu_0 i_0 a \{ I_1(ka) + [\frac{kb I_0(kb) I_1(\gamma) - r I_0(\gamma) I_1(kb)}{ka I_1(\gamma) K_0(kb) + \gamma I_0(\gamma) K_1(ka)}] K_1(ka) \}$$

where I_0 and K_0 are the modified Bessel functions of order zero and $\gamma = \sqrt{(kb)^2 + j\kappa^2}$. Using this expression the value of A_ϕ along the loop at $z=0$, $r=a$ can be found.

$$A_\phi(a, 0) = \frac{\mu_0 i_0 a}{\pi} \int_0^\infty I_1(ka) K_1(kr) dk + \frac{\mu_0 i_0 a}{\pi} \int_0^\infty [\frac{kb I_0(kb) I_1(\gamma) - \gamma I_0(\gamma) I_1(kb)}{kb I_1(\gamma) K_0(kb) + \gamma I_0(\gamma) K_1(kb)}] K_1^2(ka) dk$$

The first of these integrals can be shown to be exactly the contribution to the vector potential due to the loop itself if the core were not present at all. (This term is singular in nature.) The second integral is the contribution due to the eddy currents and thus represents the difference in the vector potential with and without the core present. This term now called ΔA_ϕ may be expanded as an asymptotic series.

$$\Delta A_\phi = \frac{\mu_0 i_0 a}{\pi} [- \int_0^\infty \frac{I_1(kb) K_1^2(ka)}{K_1(kb)} dk + \int_0^\infty \frac{T(\gamma) K_1^2(ka)}{K_1^2(kb)} dk - \int_0^\infty \frac{T^2(\gamma) kb K_0(kb) K_1^2(ka)}{K_1^3(kb)} dk + \dots]$$

$$\text{where } T(\gamma) = \frac{1}{\gamma} \frac{I_1(\gamma)}{I_0(\gamma)}.$$

It should be noted that the dependence of ΔA_ϕ on the material parameters μ and σ of the core is completely contained in the $T(\gamma)$ term. Using the asymptotic series for the modified Bessel functions the following expressions can be found.

$$T(\gamma) = \frac{1}{\gamma} - \frac{1}{2\gamma^2} + \dots$$

$$\text{and } \gamma = \sqrt{j\kappa}b = (1+j) \frac{b}{\delta}$$

where the skin depth is given by $\delta = \sqrt{2/\omega\mu\sigma}$. One may then divide the contributions to A_ϕ into real and imaginary parts.

$$\begin{aligned} \Delta A_\phi &= \frac{\mu_0 i_0 a}{\pi b} \{ -N_0(\frac{a}{b}) + \frac{1}{2}(\frac{\delta}{b}) N_1(\frac{a}{b}) - \frac{1}{4}(\frac{\delta}{b})^3 [N_2(\frac{a}{b}) \\ &+ N_3(\frac{a}{b})] \} - j \frac{\mu_0 i_0 a}{\pi b} \{ \frac{1}{2}(\frac{\delta}{b}) N_1(\frac{a}{b}) - \frac{1}{2}(\frac{\delta}{b})^2 [\frac{1}{2} N_1(\frac{a}{b}) \\ &+ N_2(\frac{a}{b})] + \frac{1}{4}(\frac{\delta}{b})^3 [N_2(\frac{a}{b}) + N_3(\frac{a}{b})] \} \end{aligned}$$

where the following integrals have been defined and are seen to be only a function of the ratio a/b . ($\eta = kb$)

$$N_0(\frac{a}{b}) = \int_0^\infty \frac{I_1(\eta) K_1^2(\eta \frac{a}{b})}{K_1(\eta)} d\eta$$

$$N_1(\frac{a}{b}) = \int_0^\infty \frac{K_1^2(\eta \frac{a}{b})}{K_1^2(\eta)} d\eta$$

$$N_2(\frac{a}{b}) = \int_0^\infty \frac{\eta K_0(\eta) K_1^2(\eta \frac{a}{b})}{K_1^3(\eta)} d\eta$$

$$N_3(\frac{a}{b}) = \int_0^\infty \frac{\eta^2 K_0(\eta) K_1^2(\eta \frac{a}{b})}{K_1^4(\eta)} d\eta$$

The apparent change in the driving point impedance of the loop is

$$\Delta Z = \Delta R + j\omega \Delta L = \frac{j\omega \Delta A_\phi 2\pi a}{i_0}$$

From the previous expressions the changes in inductance and resistance can be found to third order in δ/b .

$$\Delta L = -2\mu_0 \frac{a^2}{b} \left(N_0 \left(\frac{a}{b} \right) - \frac{1}{2} \left(\frac{\delta}{b} \right) N_1 \left(\frac{a}{b} \right) + \frac{1}{4} \left(\frac{\delta}{b} \right)^2 \left[N_2 \left(\frac{a}{b} \right) + N_3 \left(\frac{a}{b} \right) \right] \right)$$

$$\Delta R = 2\omega\mu_0 \frac{a^2}{b} \left(\frac{1}{2} \left(\frac{\delta}{b} \right) N_1 \left(\frac{a}{b} \right) - \frac{1}{2} \left(\frac{\delta}{b} \right)^2 \left[\frac{1}{2} N_1 \left(\frac{a}{b} \right) + N_2 \left(\frac{a}{b} \right) + \frac{1}{4} \left(\frac{\delta}{b} \right)^2 \left[N_2 \left(\frac{a}{b} \right) + N_3 \left(\frac{a}{b} \right) \right] \right] \right)$$

To obtain numerical values for ΔL and ΔR it is first necessary to evaluate the integrals N_0 , N_1 , N_2 and N_3 . Although they cannot be evaluated analytically they can be found numerically for fixed values of the geometrical parameter a/b . Once these integrals are evaluated the expressions are each seen to be a power series in the parameter δ/b which contains the electrical properties of the core material. One should note that for the case of a perfectly conducting core (i.e. $\delta/b = 0$)

$$\Delta L = \frac{-2\mu_0 a^2}{b} N_0 \left(\frac{a}{b} \right)$$

and $\Delta R = 0$.

This is a reasonable results which shows a decrease in the inductance but no change in the resistance since no losses are possible. The effect of a large but finite conductivity is seen to diminish the amount of decrease found for the perfectly conducting case and to add a finite, positive apparent resistance.

RESULTS

To facilitate the evaluation of ΔL and ΔR for practical cases the integrals N_0 , N_1 , N_2 , and N_3 were evaluated for several values of a/b varying from a value of 1.05 to 2.0. Using these results the values of ΔR and ΔL can be calculated through terms of order $(\delta/b)^3$. Accuracy of the results depends critically on the assumption that δ/b remains small with respect to one.

For the case of an aluminum core with a 3/4" diameter we find $\delta = .0826/\sqrt{f}$ which for $f = 50$ KHz yields a skin depth $\delta = 0.37$ mm resulting in a value of $\delta/b = .0388$. Thus for this practical case we are well within the assumptions used in the derivations.

To generalize the results somewhat the normalized quantities $\Delta R/\omega\mu_0 a$ and $\Delta X/\omega\mu_0 a$ have been plotted in the remaining figures ($\Delta X = \omega\Delta L$). It should be noted that each of these quantities are dimensionless. The most obvious graphical presentations are those of ΔR and ΔL versus the geometrical parameter a/b and the material parameter δ/b . Unfortunately, this direct approach does not correlate the physical parameters which may be subject to change. It is noted that the practical testing involves a cylindrical sample moving through the quantities which may change

are actually the radius of the core b and the conductivity of the core material σ . To illustrate the changes in impedance for variations in b about a nominal radius b_0 , the graphs in Fig. 2 and 3 are shown. In Fig. 2 the normalized change in resistance is shown versus the quantity b/b_0 . The nominal radius b_0 may be any value as long as our restriction of $\delta/b_0 \ll 1$ is satisfied. The value of $a/b_0 = 1.25$ was chosen to be representative of a real coil design which couples strongly with the core. A family of curves is also shown for several values of δ/b_0 . It is noted that all the curves approach zero as b/b_0 is decreased and become very large as b/b_0 approaches 1.25 which is the position of the driving loop. A similar set of curves is shown in Fig. 3 for the change in reactance. Again as expected the change in reactance approaches zero as the core radius decreases and becomes a very large negative value for b/b_0 near 1.25. It should be noted that changes in the parameter δ/b_0 have a relatively small effect on ΔX as compared to their effect on ΔR . The same functional dependence is also illustrated in Fig. 4. The solid curves show the normalized resistance plotted versus the normalized reactance as b/b_0 is varied. Changes in the complex impedance can be seen for varying radii for each of four values of δ/b_0 .

The effect of changes in conductivity of the core on the resistance and the reactance are shown in Figs. 5 and 6. The conductivity is again normalized with respect to σ_0 near that of aluminum. (However, σ_0 is actually arbitrary as long as the condition that $\delta/b \ll 1$ is still satisfied). The limiting behavior is again logical showing the resistance approaching zero for large conductivities and zero for very small values. The reactance is seen to approach the "perfect conductor" case as σ increases. The region where σ becomes small violates the assumption on δ/b and therefore the behavior of these curves then has no meaning. The resistance versus the reactance is shown in the solid lines of Fig. 7. As the conductivity decreases from the perfect conductor case ΔR is seen to increase while ΔX becomes less negative. Each of these curves terminates in the region where the assumption that $\delta/b \ll 1$ begins to break down.

With the aid of Figs. 4 and 7 one may ascertain the behavior of changes in both the resistance and reactance for any percent change in either the radius of the core or its conductivity. The functional change in impedance is quite different for the two parameters. This characteristic may therefore be utilized in practical testing to determine changes in sample radius and conductivity.

ACKNOWLEDGEMENT

This work was supported in part by the U. S. Air Force Office of Scientific Research under Grant 77-3457.

REFERENCE

- (1) Islam, A. M., "A Theoretical Treatment of Low-Frequency Loop Antennas with Permeable Cores", IEEE Trans. on Antennas and Propagation, Vol. AP-11, No. 2, March 1963, pp. 162-169.

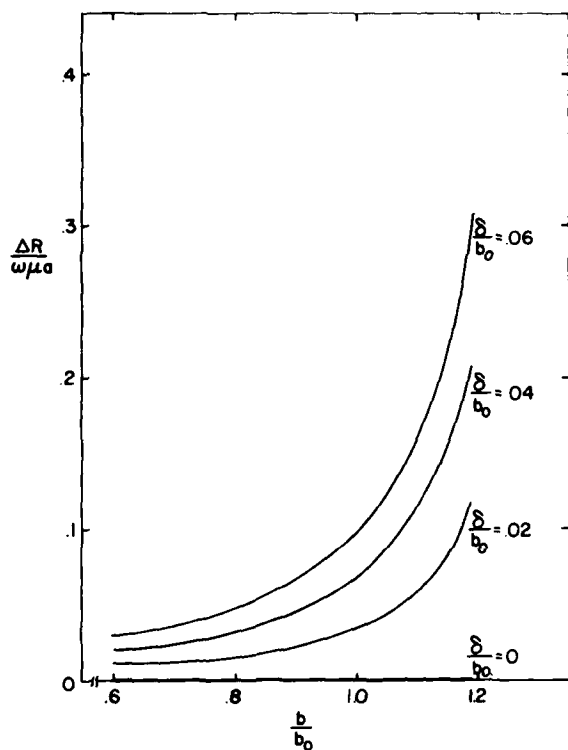


Fig. 2 Normalized Resistance Versus Core Radius

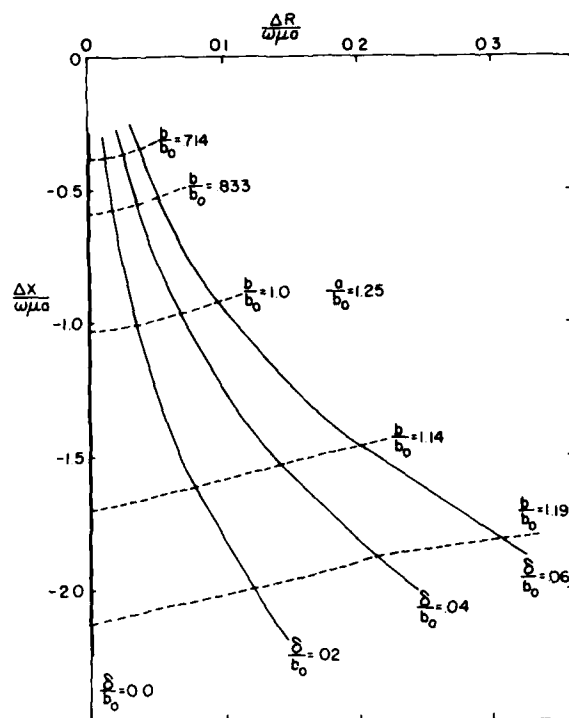


Fig. 4 Resistance Versus Reactance as Core Radius Changes

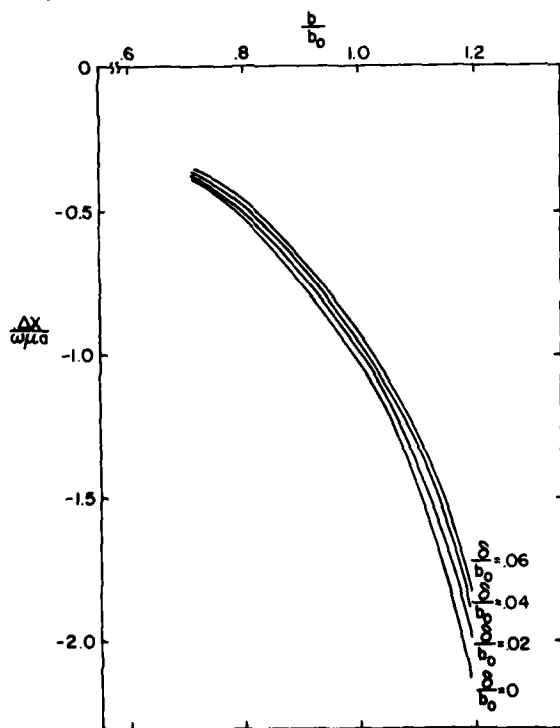


Fig. 3 Normalized Reactance Versus Core Radius

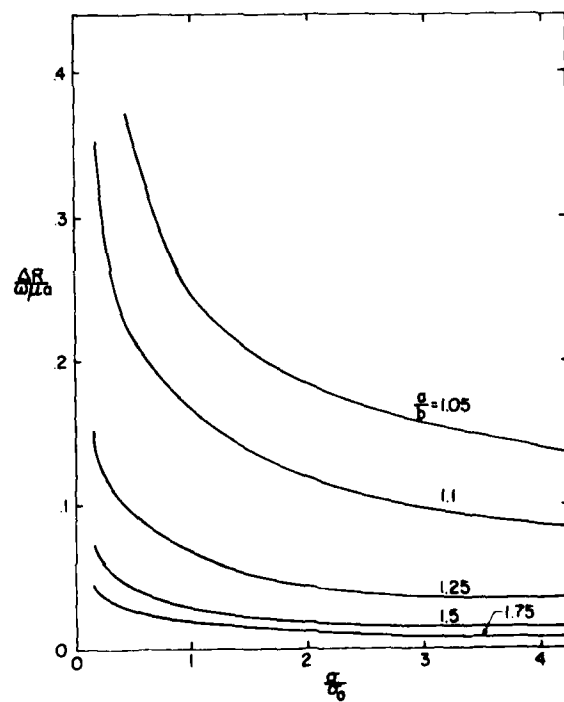


Fig. 5 Normalized Resistance Versus Conductivity

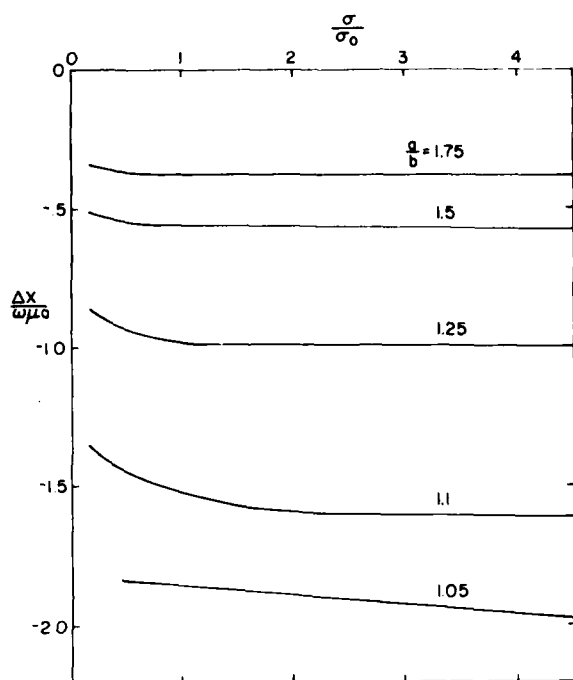


Fig. 6 Normalized Reactance Versus Conductivity

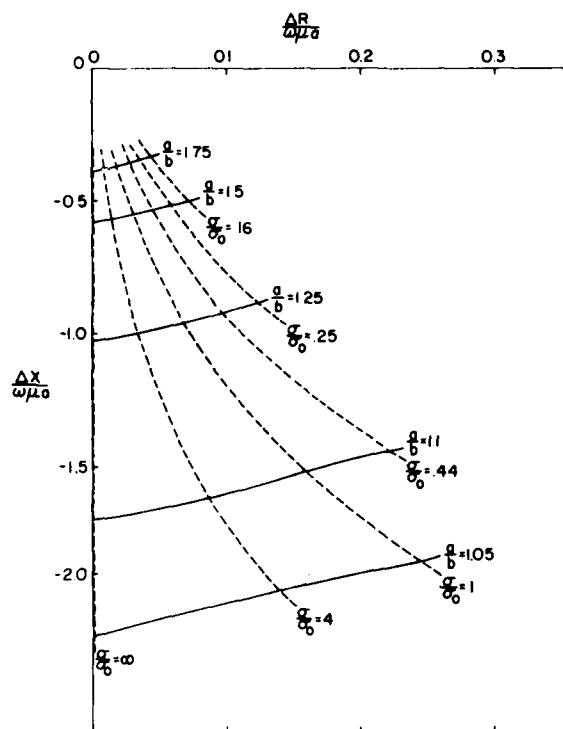


Fig. 7 Resistance Versus Reactance as Conductivity Changes

MATERIALS CHARACTERIZATION BY TIME DELAY SPECTROMETRY ULTRASOUND

P. M. Gammel and M. H. Leipold
Jet Propulsion Laboratory
California Institute of Technology
Pasadena, CA 91103

ABSTRACT

A technique known as Time Delay Spectrometry (TDS), which has been used at JPL for ultrasonic tissue characterization, has promise for similar application in materials characterization as well. This technique differs from the approaches based on pulse-echo techniques which are used by other workers.

Time Delay Spectrometry operates in the frequency domain directly. The transducer is excited by a rapidly swept frequency source and a tracking receiver is used to select signals arriving during a narrow time interval. In the reflection mode this time interval represents the range of the reflecting surface. In the transmission mode this time interval is adjusted to the desired acoustic delay, causing rejection of signals which follow extraneous paths. This swept frequency implementation makes coherent processing of the full analytic signal possible, which in turn allows more representative signatures to be obtained. In the reflection mode, for example, a better indication is obtained of the true strength of an interface or scatterer because the response can be made less dependent on the interference effects that so greatly alter the amplitude peaks of the conventional echo. This technique also permits an enhanced dynamic range to be obtained by applying frequency compensation directly to the transmitted signal. An added bonus is the ability to use data logging systems at rates commensurate with microprocessor operation in place of more expensive high speed transient recorders with limited memory capacity.

Attenuation spectra taken on tissue specimens and on a few material samples will be presented. These data will demonstrate the ability of Time Delay Spectrometry to either minimize reverberation artifacts or to make use of the information contained in the artifact.

INTRODUCTION

Time Delay Spectrometry* (TDS) is an anechoic ultrasonic measurement technique which operates in a domain that is intermediate between the time domain and the frequency domain. This technique has been used in many other fields and is a potential method for directly measuring a "materials signature".

Time Delay Spectrometry was originally developed for loudspeaker testing, where it allows an ordinary room to be used and yet achieves results superior to those obtained by other electronic techniques, even when they are aided by the use of an expensive anechoic chamber. (1,2) This technique was later applied to ultrasonic tissue characterization where it has been used to measure the ultrasonic attenuation coefficients, reflectivity, and velocity of biological specimens as a function of frequency. (2,3,4,5,6) Most recently it has been applied for imaging undersea sediments by ultrasonic reflection, with a resolution and discrimination superior to that of pulse-echo techniques. (7)

PRINCIPLES OF TDS

TDS consists of a swept source frequency and a tracking filter. The received signals arrive at the receiver with a time delay that depends on the pathlength and the propagation velocity. Since the transmitter frequency is swept, the time delay is equivalent to a frequency offset. Thus, by

selecting an appropriate offset frequency and bandwidth for the tracking filter, an equivalent time interval is selected. For the case of a linear sweep, (1) discrimination of arrival times is related to the filter bandwidth by:

$$\Delta T = \frac{B}{(dF/dT)} \quad (1)$$

Where ΔT = Time Discrimination
B = Receiver Bandwidth
 dF/dT = Sweep Rate, Hz/Sec.

This chirp technique is not pulse compression since the frequency information is preserved instead of being "collapsed" to provide improved time resolution.

The principles of operation of TDS are in one earlier paper (3) and equation (1) derived in another (1). The interchange of the time and the frequency domains by TDS and the effect of applying a Fourier Transform to the TDS output or mixing the received signal with a coherent reference has been treated rigorously (4). The significance of processing the full analytic signal, as opposed to only one of the quadrature components, has been discussed. (2)

TDS is well suited for advanced signal processing. The large (around 200,000) time-bandwidth product permits significant signal to noise enhancement.

*Time Delay Spectrometry is an invention of Richard C. Heyser, U.S. Patent No. 3,466,652, assigned to the California Institute of Technology.

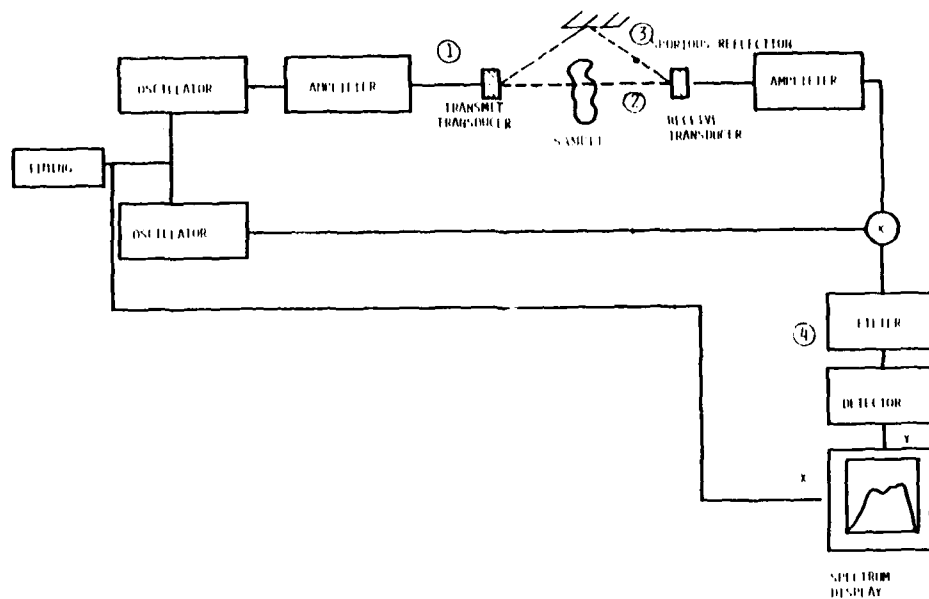


Fig. 1a. TDS instrumentation.

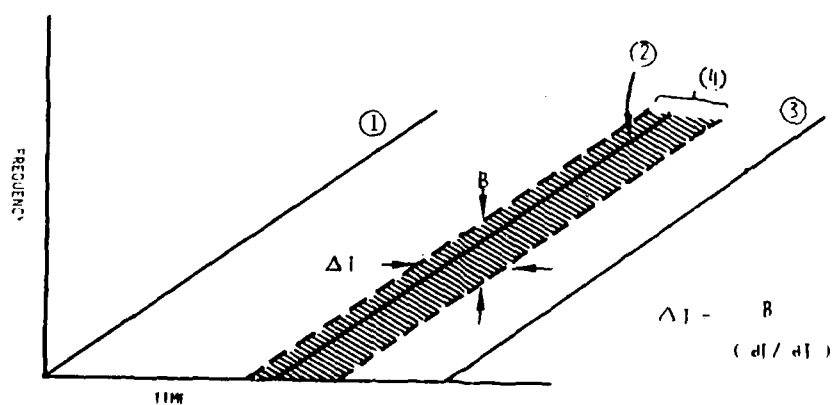


Fig. 1b. TDS signals

A delayed reference is available for coherent detection of both quadrature components. This permits pulse compression for high time domain resolution, true measure of the received energy vs time which is not modulated at the ultrasonic frequency, and phase-of-arrival information for very precise velocity measurements.

A selected portion of the spectrum can be used to produce a raster scan of attenuation, velocity, or reflectivity (3).

TDS TRANSMISSION MODE RESULTS

An example of TDS capability is shown by the test object in Fig. 2, which produces multiple reflection and therefore has a continuous wave (c.w.) transmission spectrum that consists of maxima and minima as determined by the interference of these multiple reflections. The transmission spectrum of the object was measured using the TDS system shown in Fig. 1 with two extreme settings of the filter bandwidth. One of these settings produced results similar to the cw case whereas the other discriminates signals of differing arrival times. In both cases the system was swept from 0 to 10 MHz at the rate of 500 MHz/sec. The TDS transmission response with a bandwidth of 3,000 Hz which results in acceptance of signals arriving within a 7 μ s time window is shown in Fig. 3. Since the aluminum-water interface is strongly reflecting and many such interfaces are present, appreciable energy is transmitted only at those frequencies where constructive interference of several such reflections occur. The TDS transmission response with the bandwidth reduced to 340 Hz, which reduced the width of the time acceptance window to 0.7 μ s, is shown in Fig. 4. This enables successive arrivals of the ultrasonic energy to be distinguished, as can be seen along the 2 MHz cut in the spectra. The spectra with different time delays are displayed along the delay axis. Since only the energy which arrives within a time interval 0.7 μ s wide is considered in producing the swept spectra, the interference of energy from successive reflections is eliminated. The slight remaining irregularity in the spectra (± 1 dB) is probably due to complicated surface interactions. This improvement in the time resolution has resulted in a "smearing" of the frequency resolution, which is

about 2 MHz in Fig. 4, in contrast to 0.2 MHz in Fig. 3.

TDS has been used extensively for biological tissue characterization at ultrasonic frequencies at the Jet Propulsion Laboratory as part of the biomedical program. A few examples of the results obtained are shown in Fig. 5 and Fig. 6. In both of these figures the attenuation was measured by a substitution technique: the spectrum of the ultrasonic energy through the water path between the transducers in the water tank was recorded with various calibrated electronic attenuators in the system. Typically, these calibration spectra are taken for 0, 5, 10, ..., 40 dB attenuation. The specimen is inserted and the spectra again recorded. From this composite spectrum the attenuation can be interpolated to around 1 dB.

Figure 5 demonstrates the frequency range that can be covered by TDS. These data are the composite of several measurements, each over a frequency sweep of less than 10 MHz.

Figure 6 demonstrates measurements obtained on one specimen, human breast, which is of great biomedical interest. Good agreement was obtained with other published data (8). Research on a larger population of specimens must be conducted before this can be considered useful for medical diagnosis.

REFLECTION MODE TDS

Reflection signatures have also been obtained with TDS using both double and single transducer techniques.

Two transducer reflection measurements can readily be made with the system shown in Fig. 1 by placing the transducers on the same side of the sample. The range is selected by a change of the offset of the oscillator sweep and the width of the range window is selected by the filter bandwidth or by the sweep rate.

Single transducer measurements can be made using a heterodyne technique (9) as shown in Fig. 7. This consists of mixing the transmitted and received signals. If the frequency is swept linearly in time, the difference frequency is proportional to

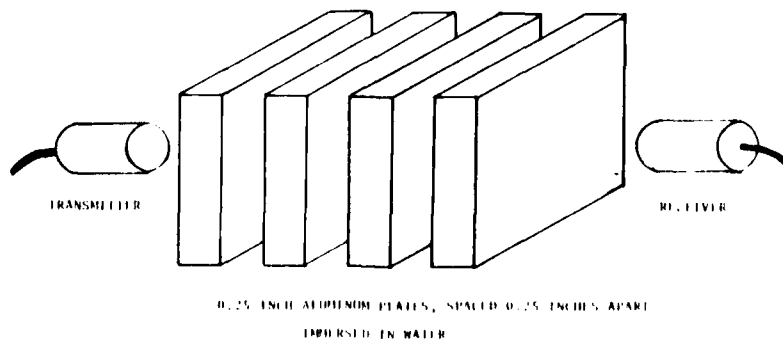


Fig. 2. Reverberant test object.

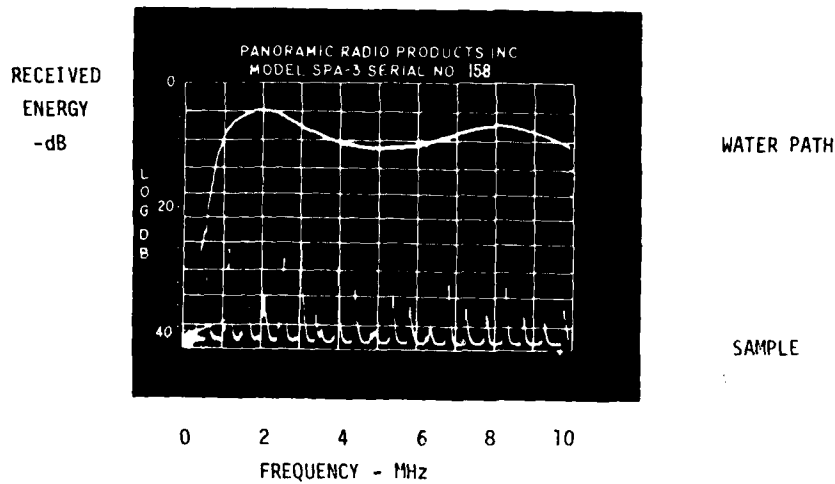


Fig. 3. Spectral response of reverberant test object with nearly c.w. response (time acceptance window 6 μ s.)

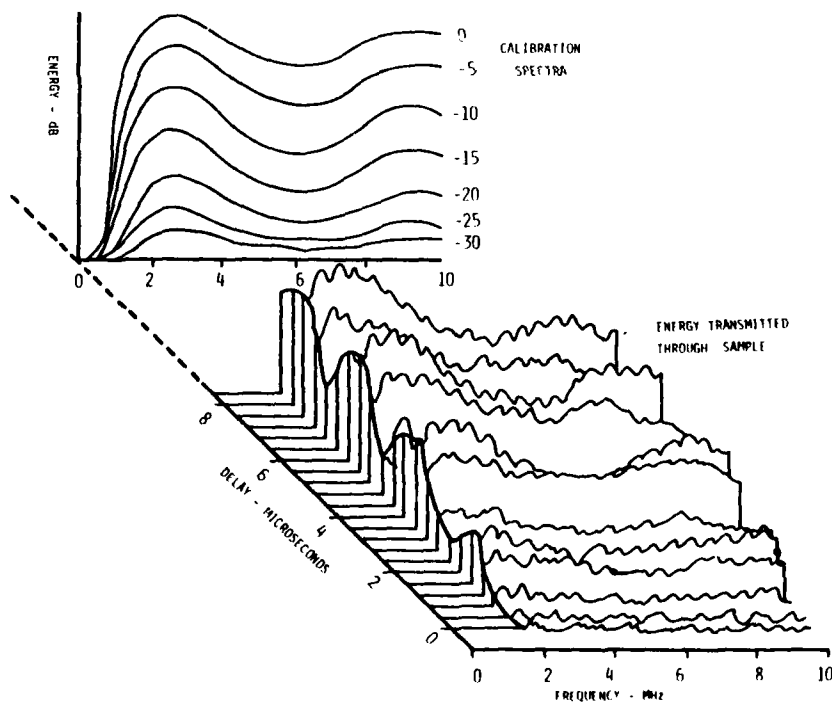


Fig. 4. Received energy vs frequency and arrival time for a reverberant object.

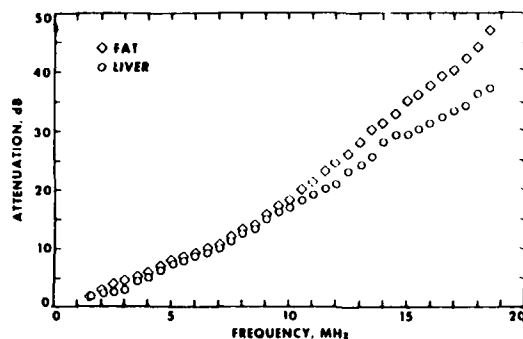


Fig. 5. Attenuation vs frequency for excised hog specimens (formalin fixed, 14 mm thick) over the frequency range 1.5 to 17.5 MHz.

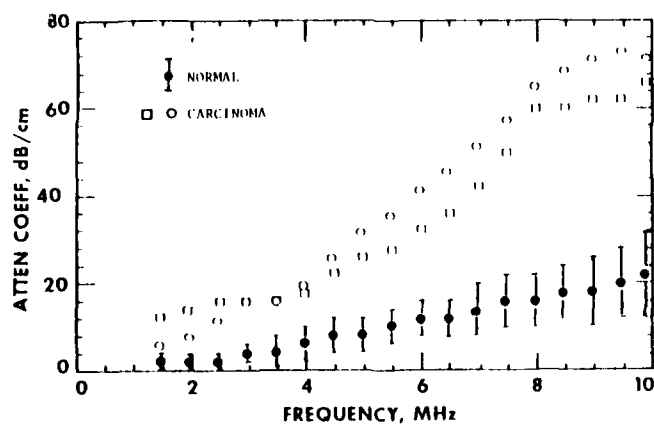


Fig. 6. Ultrasonic attenuation vs frequency in breast tissue.

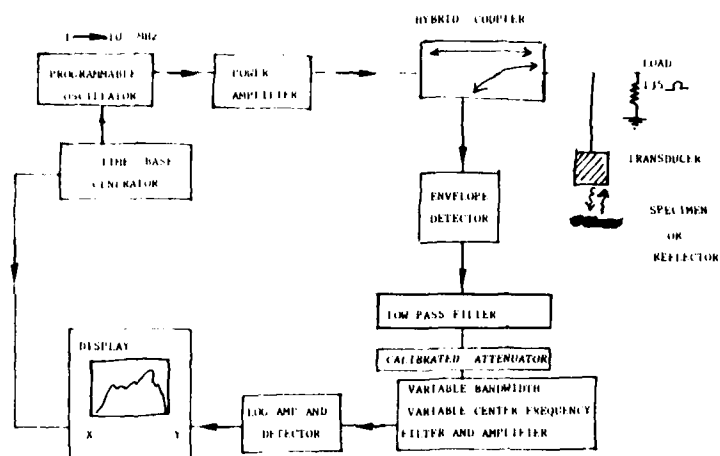


Fig. 7. Block diagram of system for single transducer reflection measurements.

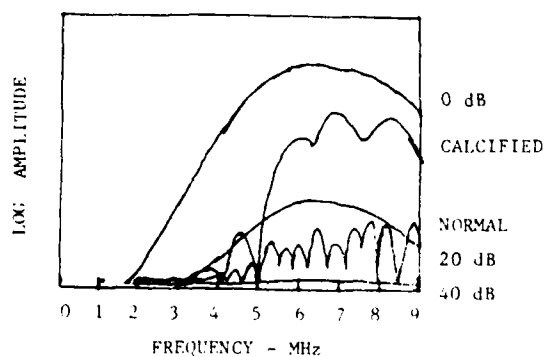


Fig. 8. Reflection spectra from regions of flattened human aorta and from plane reflector with calibrated electronic attenuation.

the range of the reflector. Thus the desired range is selected by varying the receiver frequency and the width of the range gate by the receiver bandwidth.

Among the advantages of TDS for reflection mode measurements are that surface and interior reflections are readily separated and it produces a direct spectral display. TDS appears to have great promise for characterizing materials. Internal flaws and distributed properties of materials could be characterized by TDS reflection spectra. Characterization of distributed material properties by ultrasonic backscatter has been treated elsewhere in the literature (10).

One application of TDS in the reflection mode is demonstrated in Fig. 8. The reference spectra are the reflected energy from a plane reflector with the receiver gain reduced by the indicated number of dB. These were obtained with a 10 MHz, 0.5-inch diameter transducer with a 3-inch focus. The reflectivity spectrum of a calcified region in an excised human aorta is shown to be around 5 dB below that of a plane reflector, whereas the reflectivity of a normal section of the same aorta is shown to be around 30 dB lower. Irregularity in the spectra is due to interference of reflections from the two walls (adventitial and intimal surfaces), which exists in all specimens studied. Calcium deposits cause further interference effects.

SUMMARY

Time Delay Spectrometry (TDS) consists of a swept frequency transmitted signal and a tracking receiver which is adjusted to receive only signals with the desired propagation time delay. TDS can be operated in either the transmission mode or in the reflection mode. It can produce time or frequency domain information that is equivalent to that of pulse-echo systems. In addition, it is especially suited to processing the full analytic signal, which provides a better measure of the arriving energy than does processing the real portion of the waveform alone, as is usually carried out in pulse-echo systems (2). Other advantages are that it allows signal-to-noise enhancement through coherent processing, optimization of time or frequency resolution is straightforward and naturally apodized, and conversion between time and frequency domains is readily implemented by analog as well as by digital techniques.

Time Delay Spectrometry has several unique features. TDS can operate intermediately between the pure time domain and the pure frequency domain, providing optimal characteristics for otherwise difficult applications, such as loudspeaker evaluation in an actual room. Continuous adjustment is possible, giving time domain response at one extreme and frequency domain response at the other. The time domain sampling is apodized by the smooth receiver passband, rather than being abruptly chopped off by a gate. After the time and frequency domains are interchanged by TDS, the time window is selected by a tracking filter. The apodization is produced by the roll-off characteristics of this filter. A slower data rate aids digital sampling since the data rate is determined by the sweep rate, rather than by the speed of sound and frequency alone. If the velocity

dispersion is known, compensation can be effected by dynamically programming the sweep offsets. Pre-whitening the transmitted signal to improve the dynamic range at the receiver is practical.

ACKNOWLEDGEMENTS

This paper presents the results of one phase of research carried out at the Jet Propulsion Laboratory, California Institute of Technology, under Contract No. NAS7-100, sponsored by the National Aeronautics and Space Administration.

The authors wish to thank David H. Blankenhorn, M.D., Chief of Cardiology at the University of Southern California-Los Angeles County Hospital, for the preparation and use of the aorta specimen.

REFERENCES

1. Heyser, R. C., "Acoustical measurements by time delay spectrometry", *J. Audio Eng. Soc.*, **15**, 370-382 (1967).
2. Heyser, R. C., "Determination of loudspeaker signal arrival times", *J. Audio Eng. Soc.*, Part I: 19, 734-743 (1971); Part II: 19, 829-834 (1971); Part III: 19, 902-905 (1971).
3. Heyser, R. C., and Le Croisette, D. H., "A new ultrasonic imaging system using time delay spectrometry" *Ultrasound in Med. and Biol.*, **1**, 119-131 (1974).
4. Le Croisette, D.H. and Heyser, R.C., "Attenuation and velocity measurements in tissue using time delay spectrometry" *Proceedings of Seminar on Tissue Characterization: NBS Special Publication 453*, 81-95 (1976).
5. Gammell, P.M., Le Croisette, D.H., and Heyser, R.C., "The temperature and frequency dependence of ultrasonic attenuation in selected tissues", *Ultrasound in Med. and Biol.* (in press, 1979).
6. Rooney, J.A., Gammell, P.M., Hesteres, J.D., Blankenhorn, D.H., and Chin, H.P., "Velocity of sound in arterial tissue", 97th Meeting of the Acoustical Society of America, June 11-15, 1979, Boston, MA., Abstract in *J. Acoust. Soc. Am.* **65**, Supp. 1, Spring 1979.
7. Richard C. Heyser, work in progress at The Jet Propulsion Laboratory (1979).
8. Calderon, C., Vilkomerson, D., Mezrich, R., Etzold, K.F., Kingsley, B., and Haskin, M., "Difference in the attenuation of ultrasound by normal, benign, and malignant breast tissue", *J. Clin. Ultrasound* **4**, 249-254 (1976).
9. Gammell, P.M. "Single transducer swept frequency ultrasonic reflection measurements", *Ultrasonics* (in press, 1979).
10. Gericke, O.R. "Ultrasonic Spectroscopy", in *Research Techniques in Nondestructive Testing*, R. S. Sharpe, Ed., London: Academic Press, 31-61 (1970).

ACOUSTIC EMISSION SOURCE CHARACTERIZATION THROUGH DIRECT TIME-DOMAIN DECONVOLUTION

N. N. Hsu and D. G. Eitzen
National Engineering Laboratory
National Bureau of Standards
Washington, D.C.

ABSTRACT

While detected acoustic emission (AE) signals contain potentially useful information about the deformation source mechanisms of a structure under load, signal processing techniques such as threshold counting, RMS recording, energy measurement, peak detection, and spectral analysis often fail to extract such information unambiguously. The difficulty lies both in the inherent complexity of the deformation mechanism and in the lack of understanding of the source mechanism, the wave propagation details, and the physics of the sensor's mechanical-to-electrical conversion process.

Instead of taking an empirical approach to establish the correlations between the detected AE and the observed possible deformation mechanism, we approach the problem by constructing a simple test system which consists of three main ingredients: a true displacement sensor (capacitive transducer), a simple structure (either a large block or a plate), and known theoretical impulse-response functions for specific sensor-source relative locations. We first establish the validity of these ingredients by testing with simulated AE of known step-function time dependency generated by breaking glass capillaries. Unknown sources are then introduced, one at a time, into the system for determination of their time functions. The time function at the source is determined by a deconvolution process from the known impulse response and the detected displacement. Furthermore, we show the existence of the inverse of the impulse-response function with respect to convolution for at least two extreme cases. Consequently, the source function can be obtained simply by convolving the detected signal with the inverse function. Applications to AE system calibration, sensor characterization, wave propagation studies, and brittle crack opening signature analysis will be demonstrated.

INTRODUCTION

The objective of our study is to determine AE source characteristics at the source by analyzing detected AE signals. As shown in Fig. 1 the evolution of AE signals are rather complex; the evolution can be broadly divided into three steps and associated with them, three analytical problems. The first is the description of the deformation mechanism of generating AE at the source location, second is the transient stress wave propagation through the structure, and third is the sensor transduction process which converts a local disturbance into a measurable voltage signal. The goal of AE signal analysis is to extract the information of the source mechanism from the detected voltage signals.

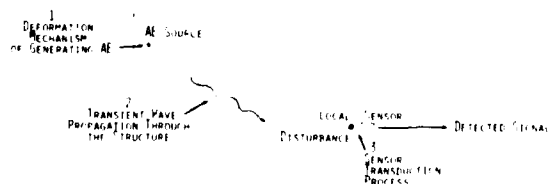


Fig. 1. The evolution of an AE signal and its associated analytical problems.

Our approach to the problem is based upon a simple experimental system consisting of a large plate (or a large block) as the structure and a capacitive displacement transducer as the sensor (Fig. 2).^{1,2} The transfer function (impulse response) of the plate in terms of displacements at arbitrary points due to an impulsive force can be

theoretically computed; thus it provides a basis for detailed analysis. It has been shown that the capacitive transducer measures true displacement so that the transducer transfer function is trivial. The AE source, for the time being, is modeled as a force-drop whose time dependence is to be determined from the displacement measurements and the known response of the plate.

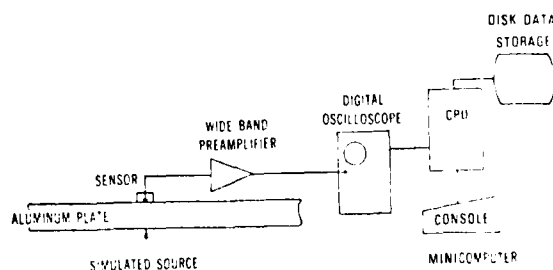


Fig. 2. An experimental system for AE source analysis.

THEORY

The method of time domain deconvolution for AE signal analysis is summarized in Fig. 3. The detected displacement $U(t)$ is the convolution of the system impulse response with the source function. The conceptual solution to the inverse problem, i.e., to find the source function from the detected displacement, can be formulated as a convolution integral of the detected displacement $U(t)$ with the inverse function $G^{-1}(t)$ of the impulse response of the system. Here $G^{-1}(t)$ is defined by the convolution integral so that when $G^{-1}(t)$ convolves with the impulse response $G(t)$, a delta function is produced. If it exists, $G^{-1}(t)$

can be computed numerically. The algorithm for computing $G^{-1}(t)$ is shown in Fig. 4.

METHOD OF TIME DOMAIN DECONVOLUTION

DESCRIPTION OF A LINEAR SYSTEM:

$$U(t) = \int_0^t F(\tau) G(\tau-t) d\tau$$

G = IMPULSE RESPONSE
 U = OUTPUT
 F = INPUT

CONCEPTUAL SOLUTION TO THE INVERSE PROBLEM:

$$F(t) = \int_{-\infty}^{\infty} U(\tau) G^{-1}(\tau-t) d\tau$$

G^{-1} IS DEFINED BY

$$\int_{-\infty}^{\infty} G(\tau) G^{-1}(\tau-t) d\tau = \delta(t)$$

Fig. 3. Method of time domain deconvolution

NUMERICAL METHOD:

$$\text{DISCRETIZE: } \begin{cases} U(I) = u(I\Delta t) \\ F(I) = f(I\Delta t) \\ G(I) = g(I\Delta t) \end{cases} \quad I = 0, 1, 2, \dots$$

WRITE IN MATRIX FORM:

$$\begin{bmatrix} U(0) \\ U(1) \\ U(2) \\ \vdots \end{bmatrix} = \begin{bmatrix} G(0) & 0 & 0 & 0 \\ G(1) & G(0) & 0 & 0 \\ G(2) & G(1) & G(0) & 0 \\ \vdots & \vdots & \vdots & \vdots \end{bmatrix} \begin{bmatrix} F(0) \\ F(1) \\ F(2) \\ \vdots \end{bmatrix}$$

$$\mathbf{U} = \mathbf{G} \mathbf{F} \longrightarrow \mathbf{F} = \mathbf{G}^{-1} \mathbf{U}$$

$$\text{or } U(I) = \sum_{k=0}^I F(k) G(I-k)$$

$$F(I) = [U(I) - \sum_{k=0}^{I-1} G(I-k)F(k)]/G(0)$$

Fig. 4. An algorithm for computing the inverse function $G^{-1}(t)$. If G^{-1} exists, the unknown force function may be computed directly by the last two equations.

RESULTS

We have computed explicitly $G^{-1}(t)$ for two cases. One is when the sensor is on one side of a large plate and the source is at the other side of the plate directly opposite the sensor location (the epicenter). The other is when the sensor and the source are on the same side of the plate (or a

large block) but reflected rays from the opposite free surface, which arrive at a later time, are not included. Shown in Fig. 5 through 8 are the impulse responses and their inverses for the two cases.

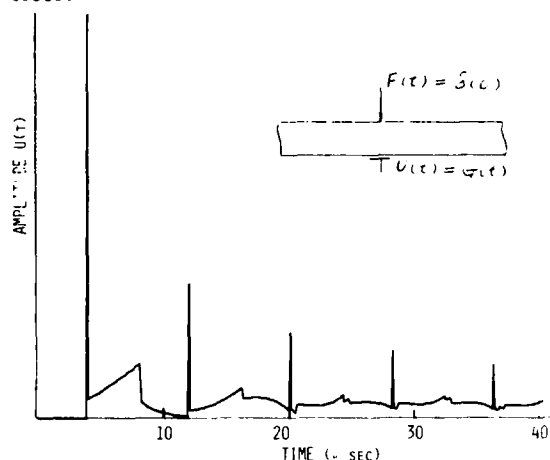


Fig. 5. Impulse response at the epicenter of a large plate. Physically the curve is the vertical displacement as a function of time at the epicenter due to a vertical force function of delta function time dependency.

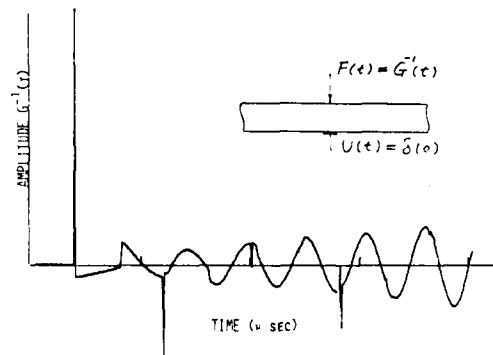


Fig. 6. Inverse function $G^{-1}(t)$ at the epicenter of a large plate. The curve is obtained by direct inversion of the function shown in Fig. 5. Physically the curve is the force function required to produce a displacement at epicenter of delta function time dependency.

The signatures of many simulated AE sources have been determined in terms of a force time function for the source. These signatures were obtained by direct convolution of the detected displacement at the epicenter with the inverse impulse response function G^{-1} shown in Fig. 6. The breaking glass capillary signature is a step function with a rise time of less than 0.5 μ sec. The breaking pencil lead source has a small yet noticeable dip before the step; its rise time is less than one μ sec and the magnitude of the step has been calibrated from 1 to 7 newtons depending on the particular size of lead used. The dropping ball contact force function also compares well with elasticity theory (Fig. 9-11).

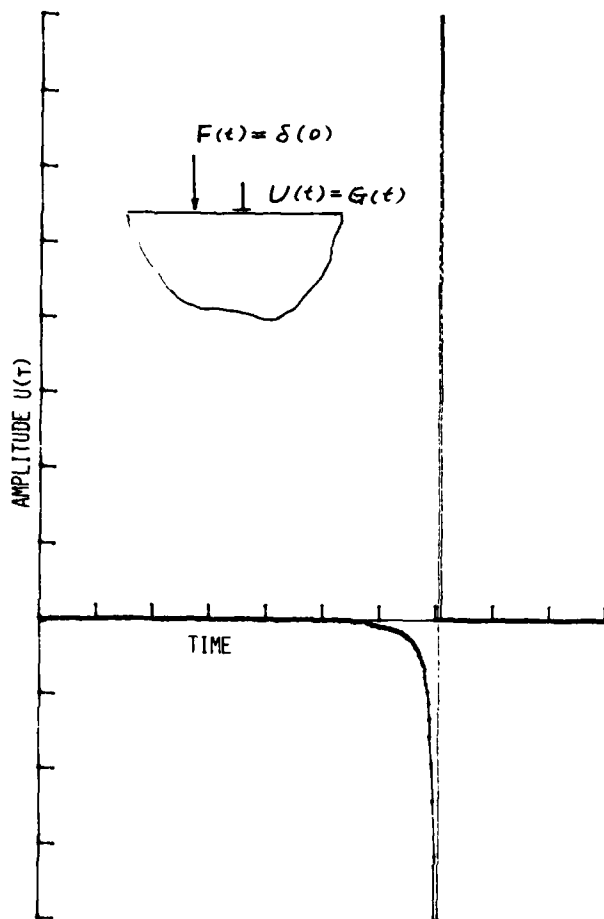


Fig. 7. Impulse response of a surface pulse. The curve shows the vertical displacement on the surface of a large block due to a vertical force of delta function time dependency applied on the same surface.

AE signals induced in glass plates by dynamic impact have also been recorded using a capacitive transducer located at the epicenter. The signals are very reproducible. The source signatures of such brittle fracture resembles a step-function at least at the initial part of the waveform (Fig. 12).

In addition to the examples given, the simple test system has many potential applications. Many unknown elements in an AE system such as sensors or structure transfer functions may be substituted into the controlled system, one at a time, and be analyzed in detail.

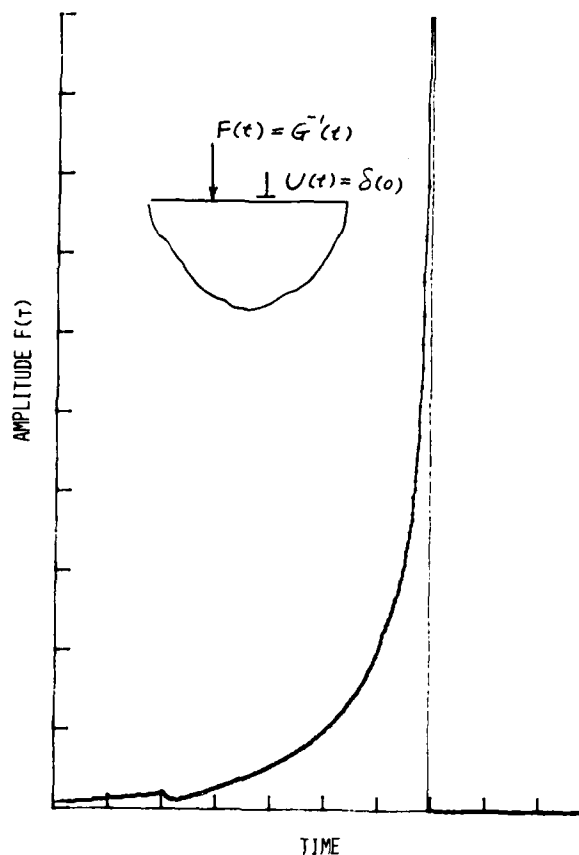


Fig. 8. Inverse of the function shown in Fig. 7. Physically it is the vertical force required to generate a vertical displacement of delta function time dependency.

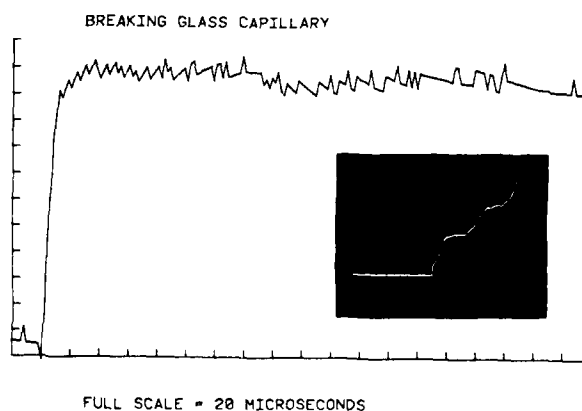
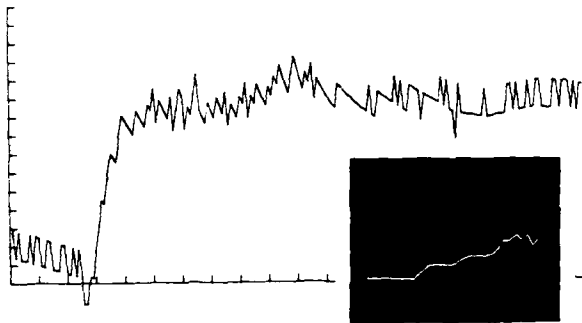


Fig. 9. Source force-time function of breaking glass capillary obtained by time-domain deconvolution of recorded epicenter displacement. Inset trace is the recorded epicenter displacement.

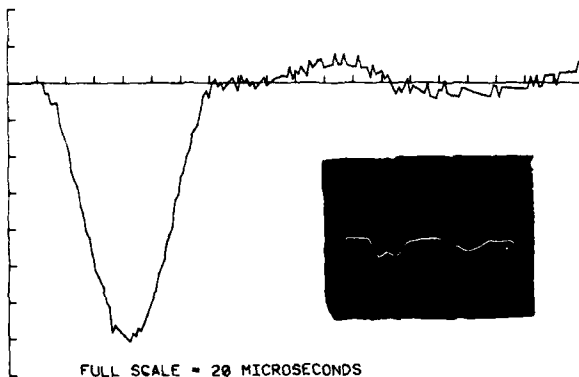
BREAKING 0.5 mm LEAD



FULL SCALE = 20 MICROSECONDS

Fig. 10. Source force-time function of breaking 0.5 mm pencil lead. Inset trace is the recorded epicenter displacement.

DROPPING 1.54 mm STEEL BALL



FULL SCALE = 20 MICROSECONDS

Fig. 11. Source force-time function of dropping ~1.5 mm steel ball from 5 cm height. Inset trace is the recorded epicenter displacement.

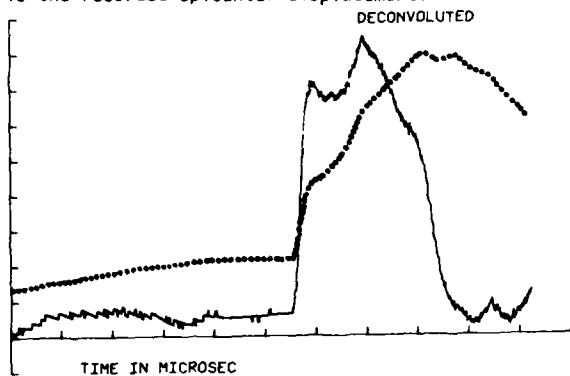


Fig. 12. Source signature of a brittle fracture produced on a glass plate by impact of a diamond indenter. The dotted line is the recorded epicenter displacement. The solid line is the deconvoluted source force-time function. Note that the initial part of the source function resembles a step function.

ACKNOWLEDGEMENT

This work has been partially supported by the Electric Power Research Institute through the EPRI/NBS AE Program.

REFERENCES

1. N. N. Hsu, J. A. Simmons and S. C. Hardy, *Materials Evaluation*, **35** (11), October 1977, pp. 100-106.
2. N. N. Hsu and S. C. Hardy, *AMD 29*, ASME New York, 1978, pp. 85-106.

AD-A094 826

ROCKWELL INTERNATIONAL THOUSAND OAKS CA SCIENCE CENTER F/8 11/2
PROCEEDINGS OF THE DARPA/AFML REVIEW OF PROGRESS IN QUANTITATIV--ETC(U)
JUL 80 D O THOMPSON; R B THOMPSON F33615-74-C-5180
SC595.70AR

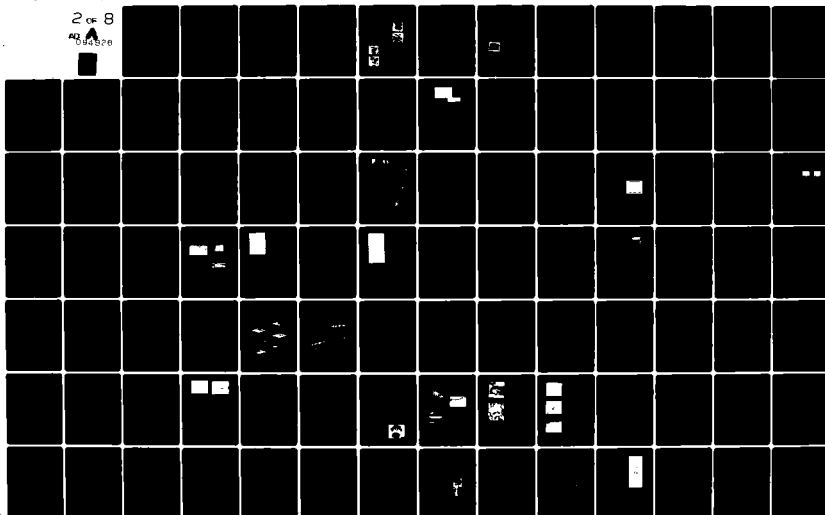
UNCLASSIFIED

AFWAL-TR-80-4076

NL

2 of 8

AD
644576



IDENTIFICATION OF ACOUSTIC EMISSION SOURCE MECHANISMS

C. R. Heiple
Rockwell International-Rocky Flats Plant
Golden, CO 80401

S. H. Carpenter
Denver University
Denver, CO 80208

ABSTRACT

Identification of mechanisms generating acoustic emission during deformation of materials is often difficult because several mechanisms may be potentially or actually operating simultaneously. Identification of sources which are actually contributing significantly to the acoustic emission can often be accomplished by testing material with different process histories, by microstructural examination before and after deformation, and by using different stress states. Mechanisms which operate simultaneously in one stress state may operate predominantly in different strain ranges in another stress state. Further confirmation of the mechanisms involved can be obtained by measurement of physical parameters, other than acoustic emission, during deformation which are sensitive to the proposed generation mechanisms for the acoustic emission.

Several examples of the use of these techniques will be shown. The sources of acoustic emission in 7075 aluminum were identified by testing in the T6 and T651 tempers, by testing in both tension and compression, and by measurement of internal friction as a function of strain. Dislocation motion was shown to be the major source of acoustic emission in beryllium by testing beryllium of different purity, heat treatment, and origin (powder metallurgy or cast and worked) in both tension and compression combined with microstructural observations. Confirmation that the source was dislocation motion and identification of the type of dislocation activity involved was made by internal friction measurements during deformation. Acoustic emission from hydrogen assisted crack growth in an austenitic stainless steel was separated from other sources of emission by holding at constant load. Cracking was also monitored by observing changes in the apparent elastic modulus of a sample as hydrogen-assisted cracks propagated in it.

7075 ALUMINUM

The mechanisms responsible for the acoustic emission generated during the plastic deformation of 7075 aluminum have been identified by testing the material in two different tempers, testing in both tension and compression and by measuring the internal friction or damping during deformation. When the acoustic emission from 7075 aluminum was first investigated some years ago, it was proposed that the acoustic emission was generated entirely from dislocation motion. The major apparent problem with this interpretation was that the acoustic emission maximum occurs at approximately 2.5% strain. It is difficult to understand why the maximum should not occur near the onset of plastic flow if it is due to dislocation mechanisms. Testing of 7075 aluminum in the T-6 and T-651 tempers revealed a second acoustic emission peak in the T-6 temper centered at yield, as shown in Poster 1. The peak at yield is in addition to the previously reported peak at 2.5% strain. The difference between the T-6 and T-651 tempers is that the material in the T-651 condition is given a stress relief stretching of up to 3% plastic strain following solution heat treatment in order to improve flatness. This mechanical treatment suppresses the acoustic emission peak at yield but does not affect the peak occurring at higher strains. When deformed in uniaxial compression, the peak at yield (T-6 temper) is unaffected, however, the peak at higher strains disappears. Analysis of these results suggests that the acoustic emission peak at yield is due to a dislocation motion or break-away phenomena and that the peak at higher strains originates from some other source. Confirmation of this interpretation is provided by amplitude independent internal friction measurements. The magnitude of the amplitude independent internal

friction is sensitive to both the dislocation density and the average dislocation loop length. An increase in either will cause an increase in the internal friction, although the magnitude is more sensitive to the average loop length. Internal friction measurements during deformation of 7075 aluminum in the T-6 temper showed an internal friction peak which corresponded closely with the acoustic emission peak observed at yield. There was no measurable internal friction at the location of the second peak (Poster 1). Measurements of the internal friction in the T-651 temper showed no internal friction above the background level of our instrumentation throughout the entire test. Work at our laboratories² and work by other investigators^{3,4} has shown conclusively that the second acoustic emission peak arises from the fracture of inclusions within the aluminum matrix.

BERYLLIUM

There are many potential sources of acoustic emission during deformation of beryllium. Dislocation motion, twinning, grain cleavage, inclusion (primarily BeO) fracture or decohesion, and precipitate fracture or decohesion are all reasonable possibilities. The general characteristics of acoustic emission from beryllium are shown in the top figure of Poster 2. Beryllium from powder metallurgy stock, from rolled ingot, and from special high purity powder metallurgy stock was tested. Material was tested after several different heat treatments, and measurements were made in both tension and compression. Details of the heat treatments used are given in Reference 5. The response of the magnitude of the two peaks to these experimental parameters is summarized on

Poster 2. (The locations of the peaks were the same for all tested conditions.) The variation in peak size with heat treatment, purity, material origin (powder source or ingot source), and testing mode (tension or compression) combined with metallographic observations exclude grain cleavage, twinning, beryllium oxide fracture or decohesion, and precipitate fracture or decohesion as significant contributors to the observed acoustic emission, as indicated in Poster 2. All results are consistent with dislocation motion as the source of both acoustic emission peaks. The observations cannot, however, distinguish between sudden breakaway of dislocation avalanches from pins or rapid generation of new dislocations as the type of dislocation activity responsible for the acoustic emission. This separation is achieved by internal friction measurements during deformation. As mentioned previously, amplitude independent dislocation damping is sensitive to both dislocation density and average dislocation loop length. More specifically, the damping is proportional to the fourth power of the average loop length and the first power of the dislocation density. Thus a breakaway process which increases the average loop length should produce a larger change in damping than the generation of new dislocations, which primarily increases the dislocation density. The internal friction measurements indicate that the acoustic emission peak at the onset of plastic flow is most probably due to the generation of new dislocations, and the peak at 1 pct plastic strain is most probably due to breakaway of dislocations from pins. The validity of the internal friction interpretation is supported by tests in iron where the yield point is known to arise from breakaway of dislocations from carbon atmospheres. There is a corresponding internal friction peak, as expected.

STAINLESS STEELS IN A HYDROGEN ENVIRONMENT

Acoustic emission is a potential technique for monitoring stainless steels for hydrogen-assisted crack growth. Acoustic emission was monitored from 21-6-9 stainless steel (nominally 21 pct Cr, 6 pct Ni, 9 pct Mn, 0.25 pct N) stressed biaxially in hydrogen and inert environments. The first observation was that the amount of emission from a sample loaded biaxially was substantially greater than in uniaxial tension, as shown in Poster 3. The sample volumes and strain rates were different for the two tests, so the rms has been normalized to the same volume and strain rate using the well established proportionality between rms and the square root of strain rate or sample volume. No detectable difference in the amount or strain dependence of acoustic emission during loading was seen between hydrogen and inert environments, although hydrogen-assisted crack growth clearly occurred in a hydrogen environment. A typical surface crack and a fracture surface from a sample tested in a hydrogen environment are compared with a surface and fracture occurring in an inert environment in Posters 3 and 4. Furthermore, the amplitude distributions of acoustic emission bursts from samples tested in hydrogen and inert environments were similar, as shown in Posters 5 and 6, although a major shift in amplitude

occurred from loading to holding at constant load (beyond the yield stress).

Acoustic emission from hydrogen-assisted crack growth can be distinguished from other sources of emission by holding the sample at constant load and measuring the emission as a function of time. Acoustic emission associated with plastic flow should decline rapidly with time at constant load as plastic deformation producing stress relaxation ceases. Hydrogen-assisted crack growth, however, should not decrease significantly with time and will provide an acoustic emission source after stress relaxation has ended. The predicted difference in acoustic emission versus time between samples stressed and held in hydrogen or helium was observed (Poster 5).

The presence of cracks or voids in a test sample will cause a decrease in the measured elastic modulus when compared to a defect free sample. A simple first order theory showing that the apparent or effective elastic modulus is dependent on the volume of cracks in the material is given in Poster 7, i.e. $Y_{eff} = Y(1 - V/V_0)$. Clearly changes in the apparent modulus will be small since in most cases V/V_0 will be small. Certainly, the changes in apparent modulus cannot be detected from typical load deflection curves. In order to effectively use modulus change measurements as a tool to study crack initiation, growth, etc., it is necessary that techniques be used which can detect small changes in the modulus to a very high degree of accuracy and precision.

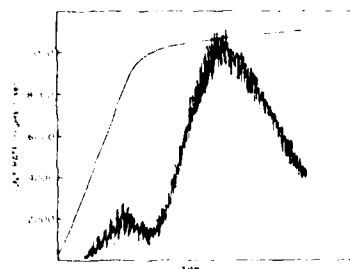
A technique meeting these requirements is measuring the resonant frequency of a sample vibrating in a standing longitudinal wave. A Marx composite oscillator operating in a longitudinal mode at a resonant frequency of approximately 50,000 Hz has been used. A schematic of the system is shown in Poster 8. The resonant frequency of the total wave train is the measured quantity from which the resonant frequency of the sample is easily calculated. The sample tested is one-half wave length in length so that the center of the sample is at a displacement node. The necessary electrical connections can be made at this point without disturbing the standing wave.

Data for a high purity Armco iron and for 304 stainless steel are shown in Poster 8. The samples were charged in an electrolytic solution of 1 normal H_2SO_4 with slight additions of CS_2 and As_2O_3 . The data show no change in the resonant frequency for the first 10² seconds. At this point, the resonant frequency of the pure iron begins to decrease giving a negative change in the resonant frequency as plotted. No change in the resonant frequency of the 304 stainless steel was observed on charging to nearly 10⁵ seconds. This result is expected since the 304 should not crack with zero applied stress. A micrograph showing cracks which developed in the pure iron is shown in Poster 7. No cracks could be found in the 304 sample. An attempt was made to correlate the measured crack volume with that predicted by the change in apparent modulus. It was found that the measured modulus change is greater than that predicted from measured crack volume by approximately 40 times. It is unclear whether this disagreement is due to the elementary nature of the theory or whether there are other mechanisms which might cause changes in the modulus. More work is necessary to answer this question, although recent data suggest additional mechanisms are involved.

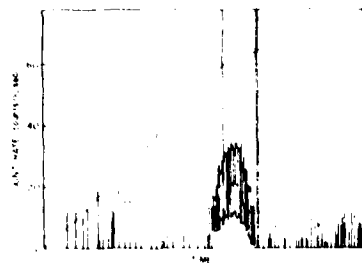
REFERENCES

1. H. L. Dunegan and D. O. Harris, "Acoustic Emission--A New Nondestructive Testing Tool," Ultrasonics 1, 1969, pp. 160-166.
2. S. H. Carpenter and F. P. Higgins, "Sources of Acoustic Emission Generated During the Plastic Deformation of 7075 Aluminum Alloy," Met. Trans. A, 8A, 1977, pp. 1629-1632.
3. M. A. Hamstad and A. K. Mukherjee, "A Comparison of the Acoustic Emission Generated by Tensile and Compressive Testing of 7075 Aluminum," UCID 17787, Lawrence Livermore Laboratory, Livermore, CA (April 1978).
4. R. Bunch, M. A. Hamstad, and A. K. Mukherjee, "Correlation Between Acoustic Emission and Microstructure in Aluminum Alloys," UCRL 31879, Lawrence Livermore Laboratory, Livermore, CA (December 1978).
5. C. R. Heiple and R. O. Adams, "Acoustic Emission from Beryllium," Proceedings of the Third Acoustic Emission Symposium, Japan Industrial Planning Association, Tokyo, Japan, 1976, pp. 342-359.

7075 ALUMINUM



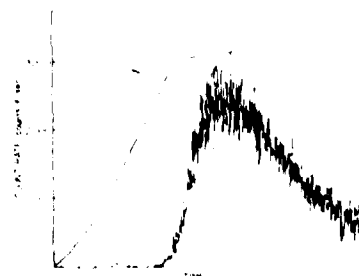
ACoustic Emission Rate vs. Time for 7075 Aluminum



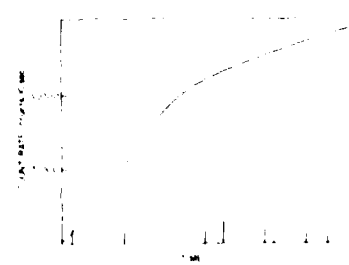
ACoustic Emission Rate vs. Time for 7075 Aluminum

THE ACoustic Emission Rate vs. Time for 7075 Aluminum is shown in the figure. The rate increases sharply after 10 minutes, peaking at approximately 1000 counts/min around 20 minutes, and then decreases.

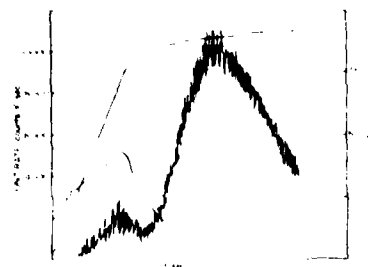
THE ACoustic Emission Rate vs. Time for 7075 Aluminum is shown in the figure. The rate remains low until about 15 minutes, then rises to a peak of about 400 counts/min at 20 minutes, before declining.



ACoustic Emission Rate vs. Time for 7075 Aluminum

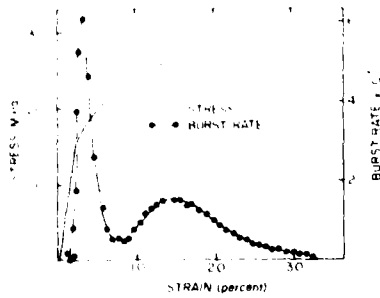


ACoustic Emission Rate vs. Time for 7075 Aluminum

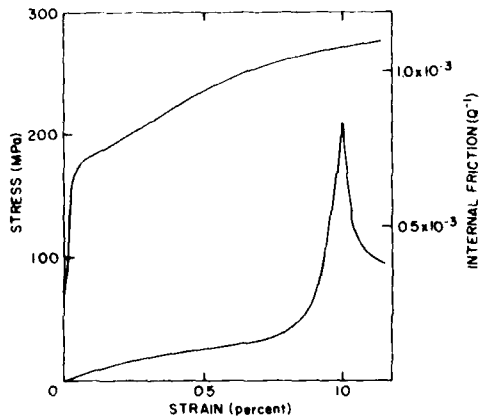


THE ACoustic Emission Rate vs. Time for 7075 Aluminum is shown in the figure. The rate increases sharply after 10 minutes, peaking at approximately 1000 counts/min around 20 minutes, and then decreases.

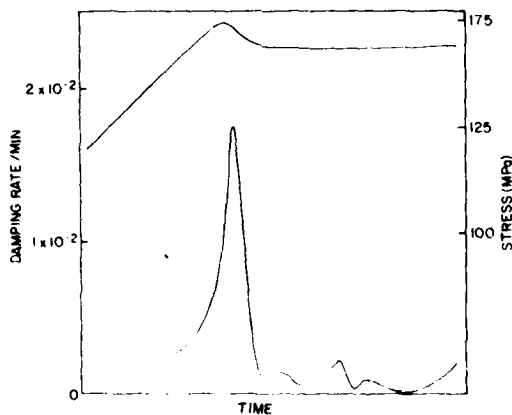
BERYLLIUM



ACoustic EMISSION BURST RATE AND STRESS VERSUS STRAIN FOR A CUMULATIVE DEFORMATION OF 10% IN BERYLLIUM



THE INCREASE IN INTERNAL FRICTION VERSUS STRAIN IN TENSION FOR A CUMULATIVE DEFORMATION OF 10% IN BERYLLIUM



CHARACTERISTICS OF THE ACOUSTIC EMISSION PEAK AT THE ONSET OF PLASTIC FLOW

- 1. MAXIMUM BURST RATE OCCURS AT THE ONSET OF PLASTIC FLOW
- 2. BURST RATE AFTER THE MAXIMUM BURST RATE IS INVERSELY RELATED TO THE BURST RATE
- 3. BURST RATE AFTER THE MAXIMUM BURST RATE IS INVERSELY RELATED TO THE BURST RATE
- 4. BURST RATE AFTER THE MAXIMUM BURST RATE IS INVERSELY RELATED TO THE BURST RATE
- 5. BURST RATE AFTER THE MAXIMUM BURST RATE IS INVERSELY RELATED TO THE BURST RATE
- 6. BURST RATE AFTER THE MAXIMUM BURST RATE IS INVERSELY RELATED TO THE BURST RATE
- 7. BURST RATE AFTER THE MAXIMUM BURST RATE IS INVERSELY RELATED TO THE BURST RATE
- 8. BURST RATE AFTER THE MAXIMUM BURST RATE IS INVERSELY RELATED TO THE BURST RATE
- 9. BURST RATE AFTER THE MAXIMUM BURST RATE IS INVERSELY RELATED TO THE BURST RATE
- 10. BURST RATE AFTER THE MAXIMUM BURST RATE IS INVERSELY RELATED TO THE BURST RATE

CHARACTERISTICS OF THE ACOUSTIC EMISSION PEAK CENTERED AT ONE PERCENT PLASTIC STRAIN

- 1. BURST RATE AFTER THE MAXIMUM BURST RATE IS INVERSELY RELATED TO THE BURST RATE
- 2. BURST RATE AFTER THE MAXIMUM BURST RATE IS INVERSELY RELATED TO THE BURST RATE
- 3. BURST RATE AFTER THE MAXIMUM BURST RATE IS INVERSELY RELATED TO THE BURST RATE
- 4. BURST RATE AFTER THE MAXIMUM BURST RATE IS INVERSELY RELATED TO THE BURST RATE
- 5. BURST RATE AFTER THE MAXIMUM BURST RATE IS INVERSELY RELATED TO THE BURST RATE
- 6. BURST RATE AFTER THE MAXIMUM BURST RATE IS INVERSELY RELATED TO THE BURST RATE
- 7. BURST RATE AFTER THE MAXIMUM BURST RATE IS INVERSELY RELATED TO THE BURST RATE
- 8. BURST RATE AFTER THE MAXIMUM BURST RATE IS INVERSELY RELATED TO THE BURST RATE
- 9. BURST RATE AFTER THE MAXIMUM BURST RATE IS INVERSELY RELATED TO THE BURST RATE
- 10. BURST RATE AFTER THE MAXIMUM BURST RATE IS INVERSELY RELATED TO THE BURST RATE

POSSIBLE MECHANISMS

- 1. BURST RATE AFTER THE MAXIMUM BURST RATE IS INVERSELY RELATED TO THE BURST RATE
- 2. BURST RATE AFTER THE MAXIMUM BURST RATE IS INVERSELY RELATED TO THE BURST RATE
- 3. BURST RATE AFTER THE MAXIMUM BURST RATE IS INVERSELY RELATED TO THE BURST RATE
- 4. BURST RATE AFTER THE MAXIMUM BURST RATE IS INVERSELY RELATED TO THE BURST RATE
- 5. BURST RATE AFTER THE MAXIMUM BURST RATE IS INVERSELY RELATED TO THE BURST RATE
- 6. BURST RATE AFTER THE MAXIMUM BURST RATE IS INVERSELY RELATED TO THE BURST RATE
- 7. BURST RATE AFTER THE MAXIMUM BURST RATE IS INVERSELY RELATED TO THE BURST RATE
- 8. BURST RATE AFTER THE MAXIMUM BURST RATE IS INVERSELY RELATED TO THE BURST RATE
- 9. BURST RATE AFTER THE MAXIMUM BURST RATE IS INVERSELY RELATED TO THE BURST RATE
- 10. BURST RATE AFTER THE MAXIMUM BURST RATE IS INVERSELY RELATED TO THE BURST RATE

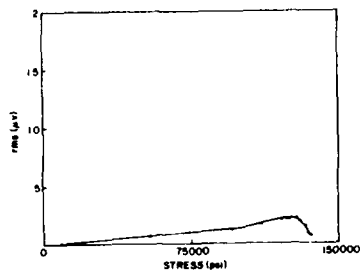
BURST RATE AFTER THE MAXIMUM BURST RATE IS INVERSELY RELATED TO THE BURST RATE

INTERNAL FRICTION MEASUREMENTS CONFIRM POSTULATED MECHANISMS

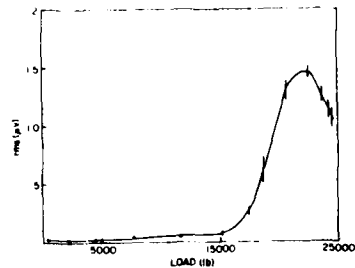
- 1. BURST RATE AFTER THE MAXIMUM BURST RATE IS INVERSELY RELATED TO THE BURST RATE
- 2. BURST RATE AFTER THE MAXIMUM BURST RATE IS INVERSELY RELATED TO THE BURST RATE
- 3. BURST RATE AFTER THE MAXIMUM BURST RATE IS INVERSELY RELATED TO THE BURST RATE
- 4. BURST RATE AFTER THE MAXIMUM BURST RATE IS INVERSELY RELATED TO THE BURST RATE
- 5. BURST RATE AFTER THE MAXIMUM BURST RATE IS INVERSELY RELATED TO THE BURST RATE
- 6. BURST RATE AFTER THE MAXIMUM BURST RATE IS INVERSELY RELATED TO THE BURST RATE
- 7. BURST RATE AFTER THE MAXIMUM BURST RATE IS INVERSELY RELATED TO THE BURST RATE
- 8. BURST RATE AFTER THE MAXIMUM BURST RATE IS INVERSELY RELATED TO THE BURST RATE
- 9. BURST RATE AFTER THE MAXIMUM BURST RATE IS INVERSELY RELATED TO THE BURST RATE
- 10. BURST RATE AFTER THE MAXIMUM BURST RATE IS INVERSELY RELATED TO THE BURST RATE

CONFIRMATION OF THE VALIDITY OF THE INTERPRETATION OF THE INTERNAL FRICTION RESULTS

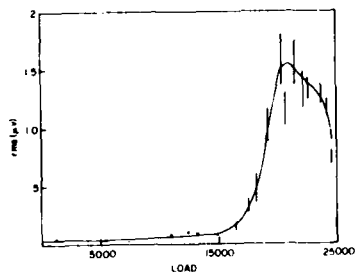
BURST RATE AFTER THE MAXIMUM BURST RATE IS INVERSELY RELATED TO THE BURST RATE



RMS ACOUSTIC EMISSION VS LOAD FOR 2188 STAINLESS STEEL LOADED IN TENSION IN AIR. MEASURED RMS VALUES SCALED TO APPROXIMATELY THE SAME SAMPLE VOLUME AND STRAIN RATE AS THE BIAXIAL TESTS. TEST DATA FROM A. HAMSTAD, LAWRENCE LIVERMORE LABORATORY.



RMS ACOUSTIC EMISSION VS LOAD FOR 2189 STAINLESS STEEL LOADED IN BIAXIAL TENSION IN AIR-TIN ENVIRONMENT.



RMS ACOUSTIC EMISSION VS LOAD FOR 2188 STAINLESS STEEL LOADED IN BIAXIAL TENSION IN AIR-TIN ENVIRONMENT.



SURFACE CRACKS COMMONLY FOUND ORIGINATING AT INCLUSIONS FOR STEEL LOADED IN AIR-TIN ENVIRONMENT.

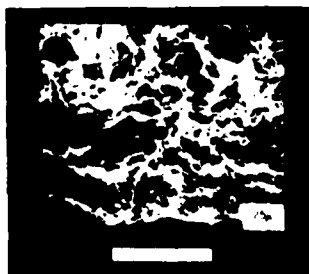


NO SURFACE CRACKS IN STEEL LOADED IN AIR-TIN ENVIRONMENT.

Poster 3



FRacture SURFACE FOR CRACK PROPAGATED IN AIR ENVIRONMENT.

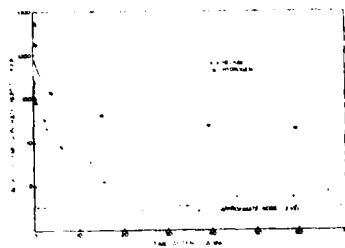


FRacture SURFACE FOR CRACK PROPAGATED IN AIR ENVIRONMENT.

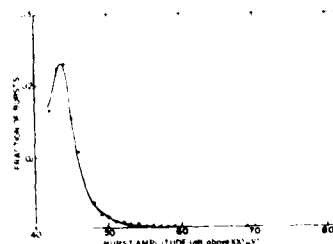
●BIAXIAL STRESS INCREASES AMOUNT OF OBSERVED ACOUSTIC EMISSION

●MATERIAL CRACKS WHEN LOADED IN A HYDROGEN ENVIRONMENT BUT DOES NOT CRACK IN AN INERT ENVIRONMENT. THERE IS NO APPARENT DIFFERENCE IN ACOUSTIC EMISSION DURING LOADING IN THE TWO ENVIRONMENTS

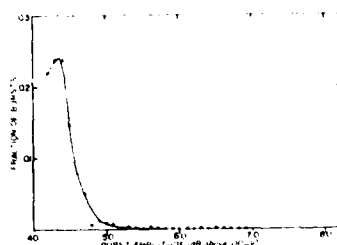
Poster 4



ALIGNED BURST AMPLITUDE DISTRIBUTION
FOR BURST AMPLITUDES ABOVE 40 DB
THAN BURST AMPLITUDES ABOVE 40 DB
FOR BURST AMPLITUDES ABOVE 40 DB

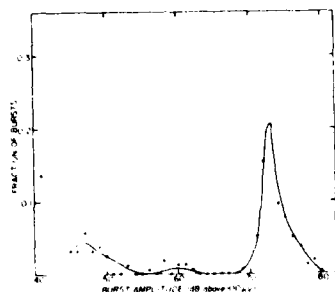


ALIGNED BURST AMPLITUDE DISTRIBUTION
FOR BURST AMPLITUDES ABOVE 40 DB
THAN BURST AMPLITUDES ABOVE 40 DB
FOR BURST AMPLITUDES ABOVE 40 DB

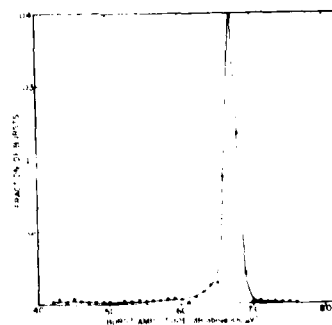


ALIGNED BURST AMPLITUDE DISTRIBUTION
FOR BURST AMPLITUDES ABOVE 40 DB
THAN BURST AMPLITUDES ABOVE 40 DB
FOR BURST AMPLITUDES ABOVE 40 DB

Poster 5



ALIGNED BURST AMPLITUDE DISTRIBUTION
FOR BURST AMPLITUDES ABOVE 40 DB
THAN BURST AMPLITUDES ABOVE 40 DB
FOR BURST AMPLITUDES ABOVE 40 DB



ALIGNED BURST AMPLITUDE DISTRIBUTION
FOR BURST AMPLITUDES ABOVE 40 DB
THAN BURST AMPLITUDES ABOVE 40 DB
FOR BURST AMPLITUDES ABOVE 40 DB

● THE BURST AMPLITUDE DISTRIBUTIONS
ARE DIFFERENT DURING LOADING
AND HOLDING AT CONSTANT LOAD
BUT THE BEHAVIOR IN HYDROGEN
AND HELIUM ENVIRONMENTS IS SIMILAR

● CRACKING CAN BE DETECTED BY MEASURING
THE TIME DEPENDENCE OF THE ACOUSTIC
EMISSION BURST RATE AT CONSTANT LOAD

Poster 6

● PROBABLE MECHANISM

THE BURST AMPLITUDE DISTRIBUTION
FOR BURST AMPLITUDES ABOVE 40 DB
THAN BURST AMPLITUDES ABOVE 40 DB
FOR BURST AMPLITUDES ABOVE 40 DB

41

INVESTIGATION OF NUCLEAR ACOUSTIC RESONANCE FOR THE
NONDESTRUCTIVE DETERMINATION OF RESIDUAL STRESS

G. A. Matzkanin
Southwest Research Institute
San Antonio, Texas

and

R. G. Leisure and D. K. Hsu
Colorado State University
Fort Collins, Colorado

ABSTRACT

Nuclear acoustic resonance has been studied in cylindrical specimens of polycrystalline aluminum deformed in compression and tension. The acoustic absorption lineshape is found to be asymmetric and dependent on the amount of deformation. Analysis of the signals in terms of an admixture of the real and imaginary parts of the nuclear susceptibility has been performed. The linewidth measured from the experimental signals varies with deformation exhibiting a minimum between twelve and fifteen percent strain.

INTRODUCTION

As is well known, residual stresses and internal strains play important roles in determining the service behavior of many materials, components and structures. As such, the detection and quantitative characterization of residual stresses and internal strains are crucial factors in the rational assessment of the serviceability of structural materials. The present program was initiated in response to the important need for a practical method of making residual stress measurements in nonferromagnetic materials. One of the methods under investigation is nuclear acoustic resonance (NAR) in which changes in acoustic absorption due to nuclear magnetic resonance (NMR) are measured. The advantage of this approach for NDE over the conventional inductive NMR method is that the acoustic approach is sensitive to the interior of bulk metal specimens whereas the inductive approach is limited to the electromagnetic skin depth which is typically only 10 to 100 microns at the radio-frequencies usually employed.

The effect of residual stress and internal strain on the nuclear resonance signal (either inductive or acoustic) is associated with the interaction between the nuclear quadrupole moment and the electric field gradient (EFG) determined by other ions and electrons. For cubic symmetry the EFG normally vanishes, however, lattice distortion associated with stress-strain fields can produce EFG's in nominally cubic materials (Figs. 1 and 2). The resulting quadrupole interaction perturbs the magnetic energy levels thus modifying the detected nuclear resonance signal.

EXPERIMENTAL

The NAR approach, illustrated in Fig. 3, involves coupling ultrasonically to a specimen which is subjected to a static magnetic field. In the experiments reported here, a continuous wave (cw) transmission method was used.⁽¹⁾ Acoustic standing waves of approximately 60 MHz were established by means of a transducer bonded to one end of a cylindrical specimen. Changes in acoustic

attenuation as the applied magnetic field was slowly swept through the resonance condition were measured by means of a second transducer bonded to the other end of the specimen. To enhance the signal-to-noise ratio, synchronous detection and signal averaging were used. Experimental conditions are detailed in Table I.

RESULTS

Typical NAR signals obtained from aluminum specimens subjected to various amounts of compressive deformation are shown in Fig. 4. The indicated strain values were determined from the changes in specimen length after deformation. The displayed NAR signals are the first derivatives of the acoustic absorption. The amplitudes of these signals cannot be directly compared since this parameter is affected by the bonding characteristics of the transducers among other factors. However, all of the detected NAR signals were found to be asymmetric in agreement with previously reported results for single crystal aluminum.⁽²⁾ This asymmetry has been shown both experimentally⁽³⁾ and theoretically⁽⁴⁾ to be associated with an admixture of χ' and χ'' (the real and imaginary parts, respectively, of the complex nuclear susceptibility) according to the following expression for the resonant acoustic absorption

$$A\omega \propto [(1 - R^2)\chi'' - 2R\chi'] \quad (1)$$

where R is a factor depending on the acoustic velocity and electrical conductivity.

The relative amplitudes of the peaks of the NAR first derivatives are a measure of the asymmetry of the acoustic absorption lineshape and can be used to determine the percentages of χ' and χ'' based on the assumption of a Gaussian lineshape. The amounts of χ'' determined in this way are listed in the second column of Table II, while similar results obtained by analyzing the experimental acoustic absorption second derivatives are listed in the third column. No consistent variation of χ'' with strain was found and except for the undeformed specimen, the χ'' components computed from the two derivatives are quite

different. The implication of these results is that the assumption of a Gaussian lineshape for acoustic absorption from deformed aluminum may not be valid. Indeed, comparisons between the experimental signals and Gaussian lineshapes (shown by open circles in Fig. 4) show that the deviation from a Gaussian lineshape increases with increasing deformation.

In addition to determining χ'' , the NAR signals from deformed aluminum were analyzed to obtain information on the acoustic absorption linewidth. The linewidths determined by measuring the peak-to-peak separations of the experimentally recorded signals are tabulated in columns 2 and 3 of Table III for the first and second derivatives, respectively. Determined in this way, the experimental linewidth initially decreases with plastic deformation and then increases for strains greater than approximately 15 percent. Although a change in resonance linewidth is expected for quadrupole perturbed energy levels, the results presented here are difficult to interpret analytically since the variation of the admixture of χ' and χ'' with strain also affects the linewidth. Thus for comparison with theory, the linewidth in terms of the χ'' component must be extracted from the experimental NAR signals.

Interesting results have been obtained indicating that the acoustic absorption lineshape for the deformed aluminum specimens is dependent on the frequency used to modulate the static magnetic field for synchronous detection. As shown in Fig. 5, for a lightly deformed specimen (5% tensile strain), the NAR lineshape is essentially independent of modulation frequency (results were obtained in the 25-100 Hz range) whereas for a highly deformed specimen (25% tensile strain) the lineshape changes substantially with modulation frequency. In fact, as the modulation frequency is decreased from 100 Hz to 35 Hz, the lineshape for the 25% tensile strain specimen changes from approximately 50% or 60% χ'' to approximately 20% χ'' . Since the modulation frequency determines the depth of penetration of the magnetic field into the specimen, a possible interpretation of these results is that the change in lineshape observed for the 25% deformed specimen may be associated with inhomogeneous deformation existing in this specimen.

CONCLUSIONS

As a consequence of the results obtained to date, the following conclusions are reached:

- (1) Nuclear acoustic resonance signals observed in polycrystalline aluminum are quantitatively similar to NAR signals in single crystal aluminum.
- (2) The NAR signals are asymmetric due to an admixture of χ' and χ'' .
- (3) The NAR linewidth and admixture of χ' and χ'' vary with plastic deformation.
- (4) The NAR lineshape for plastically deformed aluminum does not fit a Gaussian function.
- (5) The effect of modulation frequency on lineshape depends on the amount of plastic deformation.

ACKNOWLEDGEMENTS

The assistance of Don Allred and Gary Asnton at Colorado State University in performing the experimental measurements is gratefully acknowledged. The research was supported by the Air Force Office of Scientific Research (AFSC) under Contract #F44-20-76-C-0114.

REFERENCES

1. Leisure, R. G. and Balef, D. I., "CW Microwave Spectrometer for Ultrasonic Paramagnetic Resonance," Rev. Sci. Instrum. **39**, 199 (1968).
2. Buttet, J., Gregory, E. H., and Bailey, D. K., "Nuclear Acoustic Resonance in Aluminum Via Coupling to the Magnetic Dipole Moment," Phys. Rev. Lett. **23**, 1030 (1969).
3. Leisure, R. G., Hsu, D. K., and Seiber, B. A., "Nuclear-Acoustic-Resonance Absorption and Dispersion in Aluminum," Phys. Rev. Lett. **30**, 1326 (1973).
4. Fedders, P. A., "Acoustic Magnetic Resonance in Metals via the Alpher-Rubin Mechanism," Phys. Rev. **B8** 5156 (1973).

Table I.
Experimental Conditions

SPECIMENS:	99.999% PURE POLYCRYSTALLINE ALUMINUM
CYLINDERS:	1/2-IN. LONG BY 1/2-IN. DIAMETER
FREQUENCY:	60 MHz
MAGNETIC FIELD:	54 kG
TEMPERATURE:	4.2°K & 65°K
ACOUSTIC MODE:	SHEAR

Table II.

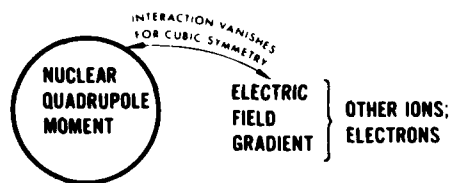
The Imaginary Component, χ'' , of the Complex Nuclear Susceptibility for Plastically Deformed Aluminum Based on Measurements of Experimental Curves and Gaussian Lineshape Assumption

Strain (%)	χ'' (%)	
	First Derivative	Second Derivative
0	84	89
4.8	49	88
9.8	82	63
14.9	53	71
19.8	48	77
25.0	66	51

Table III.

The Acoustic Absorption Linewidth for Plastically Deformed Aluminum Measured from Experimental Curves

Strain (%)	Linewidth (Gauss)	
	First Derivative	Second Derivative
0	9.3	10.5
4.8	8.0	11.3
9.8	7.3	9.7
14.9	7.2	8.5
19.8	8.9	9.3
25.0	8.0	10.5



EFG IN CUBIC CRYSTALS CAUSED BY:

1. Stress-Strain Fields Produced by External Loads or Lattice Defects
2. Charge Difference Between Point Defects and Host Ions
3. Redistribution of Conduction Electrons Around a Defect in the Case of Metals

Fig. 1. Schematic Illustration of Nuclear Quadrupole Interaction

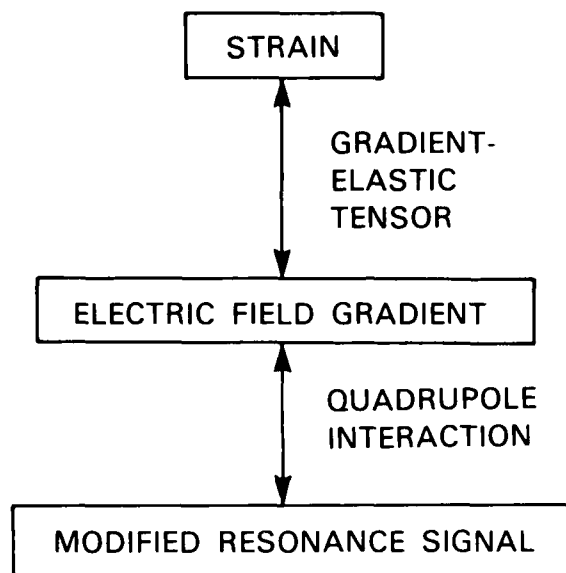


Fig. 2. Relationship Between Lattice Strain and Nuclear Acoustic Resonance

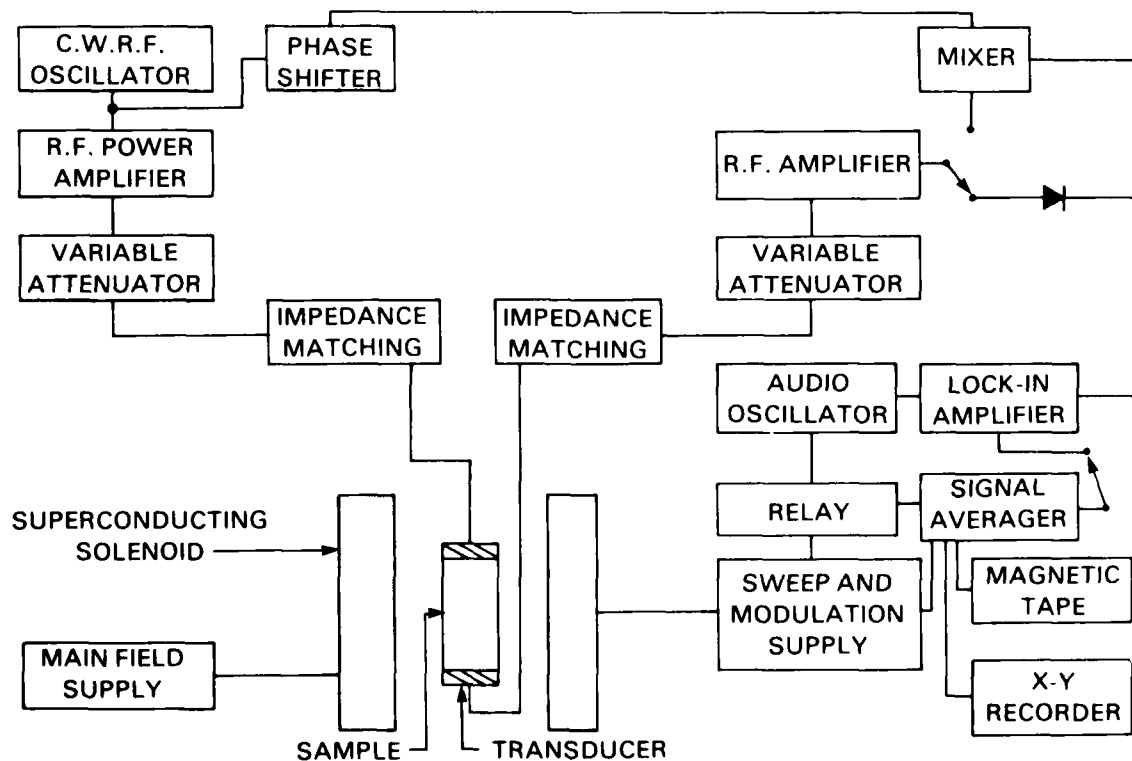


Fig. 3. Block Diagram of Nuclear Acoustic Resonance Approach

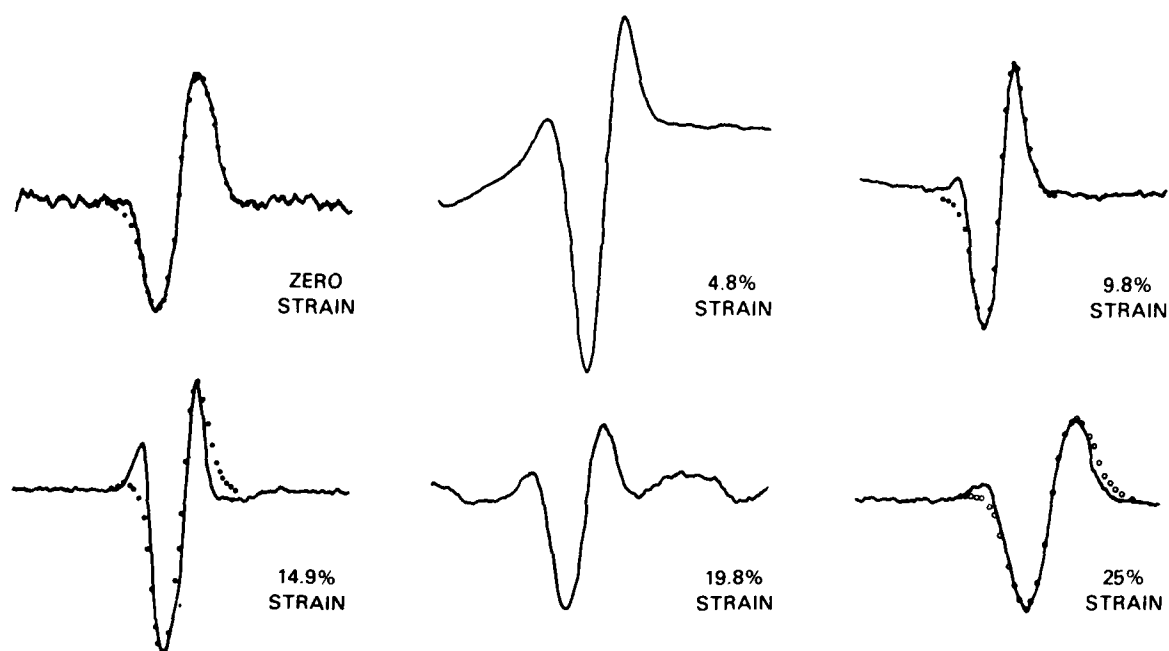


Fig. 4. Dependence of Aluminum Acoustic Absorption First Derivative on Compressive Strain

Open Circles Represent the Gaussian Lineshape; The Solid Line Shows the Experimental NAR Signals

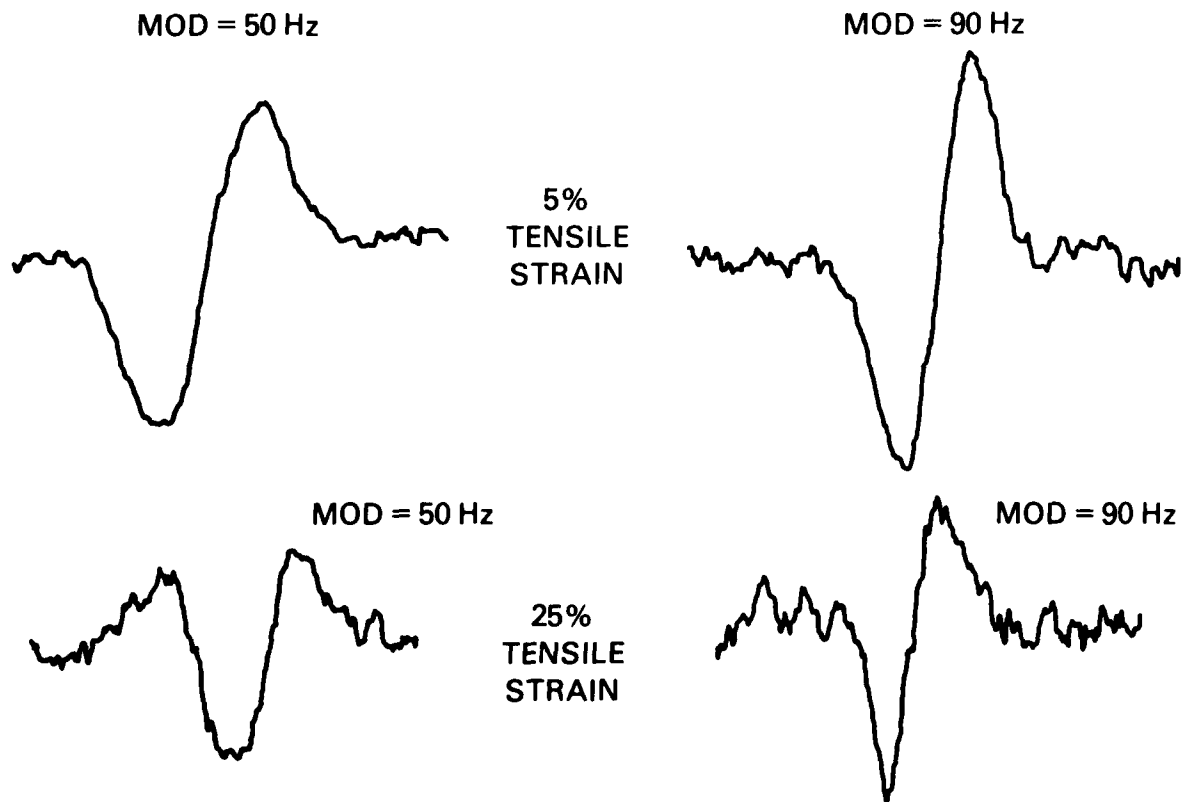


Fig. 5. Effect of Modulation Frequency on NAR Lineshape as a Function of Plastic Deformation in Polycrystalline Aluminum

NONDESTRUCTIVE EVALUATION OF BULK STRESSES IN ALUMINUM AND COPPER

K. Salama and C. K. Ling
Department of Mechanical Engineering
University of Houston
Houston, Texas 77004

ABSTRACT

The effect of applied stress on the temperature dependence of the longitudinal ultrasonic velocity has been investigated in commercial aluminum and copper. Velocities of 10 MHz longitudinal waves as a function of temperature were measured on ten specimens of these metals while they were subjected to external compressive stresses. In all measurements, the velocity increased linearly as the temperature was lowered in the temperature range between 280 and 200 K. Furthermore, the slope of this linear relationship was found to decrease linearly as the amount of applied compressive stress was increased within the elastic limit of the specimen under investigation. The maximum decrease in the temperature dependence of aluminum and copper were respectively 23% which occurred at a stress of 96 MPa, and 6% which occurred at 180 MPa. The linear relationship between the temperature dependence of the ultrasonic velocity and the applied stress was then used to determine the change as a function of distance of the tangential component of the stresses developed when an aluminum rod was shrink fit into a slightly smaller hole drilled in an aluminum disc. Excellent agreement was obtained between the computed stress distribution, and that measured using the temperature dependence method.

INTRODUCTION

Only in the case of surface stresses in components made of crystalline materials, can nondestructive evaluation of stresses be performed by the X-ray diffraction method. Although considerably improved in the last ten years, this method still suffers from serious problems which severely restrict its applications^{2,3}. Ultrasonic methods appear to hold the best promise in measurements of bulk stresses in both crystalline and non-crystalline materials⁴. All these methods are believed to utilize the anharmonic properties in solids; however, the exact mechanism in each is not yet established.

These anharmonic properties can be described in terms of changes in the elastic constants or velocities of ultrasonic waves when stresses are applied to the solid. Calculations have shown that these velocity changes are linear functions of applied stresses, and combinations of second- and third-order elastic constants⁵. In the application of these calculations to determine unknown stresses, both the velocity in the absence of stress as well as third-order elastic constants have to be known independently⁶. In addition, the measured velocity strongly depends on microstructural features which makes it necessary to develop a calibration between velocity and stress in order to be used in the determination of unknown stresses. Development of preferred orientations (texture) during deformation or fatigue, severely modify the third-order elastic constants. These problems can be solved when the differences between velocities of shear waves polarized perpendicular and parallel to stress direction are used⁷. Due to these differences, a shift in phase will occur, and the out-of-phase components will interfere and cause a change in intensity. This method, however, does not have at present enough sensitivity, and requires an accurate determination of the shear velocity in the absence of stress⁸.

Basically, the temperature dependences of the elastic constants of a solid are due to the anhar-

monic nature of the crystal lattice, and are directly related to the coefficients of higher-order terms in the strain energy function^{9,10}. A measure of the temperature dependence of the ultrasonic velocity can, therefore, be used to evaluate bulk stresses. Experiments undertaken on pure aluminum¹¹ and copper¹² plastically deformed in compression showed that the ultrasonic velocity, in the vicinity of room temperature, changed linearly with temperature, and the slope of the linear relationship changed considerably as the amount of prestrain was varied. In aluminum, the relative changes of the temperature dependences of both longitudinal and shear velocities increased by as much as 23% at a prestrain of approximately 13%.

In this paper, the effects of compressional elastic stresses on the temperature dependence of the longitudinal ultrasonic velocity have been studied in commercial aluminum and copper. The results obtained on these two metals show that the relative change in the temperature dependence is a linear function of the elastic stress applied. The linear relationship for aluminum was used to determine the stress distributions generated by an aluminum rod which was shrink fit into a smaller hole drilled into an aluminum disc. The agreement between stresses measured by the temperature dependence method and those calculated was very good.

EXPERIMENTAL

Five aluminum and five copper specimens were used in this investigation. The specimens were machined in the form of rods of 0.95 cm in diameter and 1.29 cm in length, to be suitable for ultrasonic measurements. Three of the aluminum specimens were of the type 2024-O, which were annealed for four hours at 400°C in a vacuum of 10^{-6} torr. The other two specimens were made of Aluminum 6063-T4, and were used as received. The copper specimens were all of the type CDA 110, where two of them were annealed in the same way the aluminum specimens were.

and the other three were used as received. The system used to apply external stresses on the specimens is shown in Fig. (1). It consists of a split collar of inner diameter and height closely equal to those of the specimens used. The collar was made of brass in order to minimize the effect of differences in thermal expansion during the temperature range (280-200) covered in the temperature dependence measurements. In addition, high viscosity oil (46,500 cs.) was put between the screws and the collar, which proved to be effective in keeping the stress applied uniform and constant during measurements. The stress was applied by tightening the screws of the collar, and simultaneously measuring the change in the diameter of the specimen. This change was measured by a shadow-graph capable of measuring changes in diameter with an accuracy of $\pm 5\%$. Values of applied stress were computed from the product of strain and the appropriate elastic modulus. In order to ensure that the stress applied was elastic, the diameter of the specimen was measured after ultrasonic measurements were finished, and the stress applied was removed.

The ultrasonic velocity was measured using the pulse-echo-overlap method which has been fully described elsewhere¹³. Figure 2 displays the experimental system used in this investigation. A pulse of approximately, 1 μ sec duration of variable pulse-repetition rate is generated by the ultrasonic generator and impressed on a transducer of a fundamental frequency of 10 MHz which is acoustically bound to the specimen. The reflected rf echoes are received by the same transducer, amplified and displayed on the screen of an oscilloscope. Two of the displayed echoes are then chosen and exactly overlapped by critically adjusting the frequency of the C.W. oscillator, and the division factor on the decade divider. This frequency f , accurately determined by the electronic counter, is employed to compute the ultrasonic velocity using the relation $V = 2lf$, where l is the length of the specimen. X-cut transducer is used for the generation of the longitudinal waves. A continuous flow cryostat in conjunction with a temperature control arrangement is used to maintain the temperature of the specimen at any desired value between 300 and 200 K. The system is capable of measuring changes in the ultrasonic velocity to an accuracy of better than 1 part in 10^5 , and the temperature of the specimen to within $\pm 0.1^\circ\text{C}$.

RESULTS

The velocity of longitudinal ultrasonic waves was measured as a function of temperature on five aluminum specimens denoted A, B, C, D and E. The measurements were undertaken while the specimens were subjected to various amounts of compressional stresses applied in a plane perpendicular to the direction of propagation of the ultrasonic waves. Typical examples of the results obtained on specimen E are shown in Fig. 3, where the longitudinal velocity V_L is plotted vs temperature T , at the stresses 0, 27.6, 46.2 and 75.8 MPa. From these data, one can see that the longitudinal velocity increases linearly with the lowering of temperature, and the slope of this linear relationship dV_L/dT decreases as the applied stress σ is increased. The absolute value of the velocity, however, is increased with the increase of the applied stress, indicating that the specimen becomes stiffer when

it is subjected to compressional stresses. The least mean square method was used to determine the slope of the straight line (dV_L/dT) which best fit the experimental data representing V vs T . The accuracy in determining dV_L/dT by this method was estimated to be $\pm 2\%$.

Table I lists the results obtained on the five aluminum specimens investigated in this work. The table includes the values of the temperature dependence of the longitudinal velocity, measured at stresses ranging between zero and the yield stress of the specimen. Because the values of dV_L/dT at zero stress were found to vary among specimens investigated, the relative change in the temperature dependence, Δ , due to the application of stress was calculated, and its values are listed in column 4 of table I.

TABLE I.

Effect of applied compressive stress on the temperature dependence of ultrasonic longitudinal velocity in aluminum. Stress is applied in a plane perpendicular to the waves propagation direction.

Specimen	Applied Stress (MPa)	$-dV_L/dT(\text{m/S.K})$	$\Delta\%$
A (2024-0)	0.0	0.923	0.0
	21.4	0.878	4.9
B (2024-0)	0.0	0.957	0.0
	37.2	0.856	10.6
C (2024-0)	0.0	1.007	0.0
	44.1	0.908	9.8
D (6063-T4)	0.0	1.111	0.0
	94.5	0.866	22.1
E (6063-T4)	0.0	1.066	0.0
	27.6	1.008	5.5
	46.2	0.955	10.4
	75.8	0.875	17.9
Pure, Annealed	0.0	0.847	

These values of Δ are calculated from the relationship,

$$\Delta = \frac{(dV_L/dT)_0 - (dV_L/dT)_\sigma}{(dV_L/dT)_0} \quad (1)$$

The variations in the temperature dependence measured on these specimens at zero stress are believed to be due to the differences in residual stresses in these specimens, even after annealing. Also included in this table, is the value of $(dV_L/dT)_0$ obtained on annealed pure aluminum¹¹ (99.99%) which is smaller than any of the temperature dependences measured on these commercial specimens at zero stress.

The results in table I indicate that the temperature dependence of longitudinal velocity decreases as the amount of compressional stress is increased. The relative changes in the temperature dependence, obtained on all five specimens investigated, are plotted in Fig. 4, as a function of stress applied. The plot shows that all data points lie on a straight line which passes through the origin. This indicates that, regard-

less of the type of aluminum used, the relative change in the measured temperature dependence is a linear function of the applied stress. The slope of this linear relationship is 2.4×10^{-3} per MPa, which yields a maximum change of 23% at a stress of 96 MPa.

Table II contains the results of the temperature dependence of ultrasonic longitudinal velocity obtained on five copper specimens designated A, B, C, D and E when they were subjected to compressional stress applied in a plane perpendicular to the direction of wave propagation. Two of these five specimens were in the annealed state, before any velocity measurements were undertaken, while the other three were used as received. Also included in this table is the value of $(dV_L/dT)_0$ measured on pure annealed copper¹². In this case, (99.999%) $(dV_L/dT)_0$ is approximately equal to those obtained on commercial annealed specimens, but considerably lower than the temperature dependence determined on the as received specimens.

TABLE II

Effect of applied compressive stress on the temperature dependence of ultrasonic longitudinal velocity in copper. Stress is applied in a plane perpendicular to the waves propagation direction.

Specimen	Applied Stress (MPa)	$-dV_L/dT$ (m/S.K)	$\Delta\%$
A (annealed)	0.0	0.487	0.0
	23.4	0.484	0.7
	205.4	0.463	4.9
B (annealed)	0.0	0.486	0.0
	117.2	0.468	3.6
C (CDA 110)	0.0	0.557	0.0
	100.7	0.541	2.9
	179.9	0.523	6.1
D (CDA 110)	0.0	0.509	0.0
	59.3	0.502	1.4
	131.0	0.496	2.5
E (CDA 110)	0.0	0.497	0.0
	124.1	0.485	2.9
Pure, Annealed	0.0	0.495	

Similar to the behavior observed in aluminum, the temperature dependence of the ultrasonic longitudinal velocity in copper is found to decrease as the applied stress is increased. The decrease in the temperature dependence for the same stress is, however, much smaller in copper than in aluminum. A plot of the relative change in (dV_L/dT) as a function of stress for all five copper specimens, is shown in Fig. 5. Again, a straight line which passes through the origin, is found to represent the relative changes in (dV_L/dT) vs stress. The maximum value of Δ obtained is about 6% at a stress of 180 MPa. The slope of the straight line is 0.25×10^{-3} per MPa which is approximately an order of magnitude smaller than that calculated from aluminum data.

When the stress applied to the specimen was high enough to cause yielding, the temperature

dependence of the velocity was found to increase instead of further decreasing. This occurred in both aluminum and copper specimens, where the increase in (dV_L/dT) is increased as long as the stress applied on the specimen was beyond the elastic limits. These results are consistent with those obtained by Salama and Ippolito¹⁴ in their study on the effect of plastic deformation on the temperature dependence of the ultrasonic velocity.

The data plotted in Figs. 4 and 5 suggest that the temperature dependence of the ultrasonic velocity measured at an applied compressional stress σ , can be represented by

$$\frac{(dV/dT)_\sigma - (dV/dT)_0}{(dV/dT)_0} = -K\sigma \quad (2)$$

where $(dV/dT)_0$ is the temperature dependence at zero stress, and K is a constant equal to 2.4×10^{-3} or 0.25×10^{-3} per MPa for aluminum or copper respectively. Equation 2 relates the relative difference of the temperature dependences of the velocity with and without stress as a function of the applied stress.

The use of equ. 2 in the determination of unknown stresses in a specimen, requires the knowledge of the temperature dependence of the ultrasonic velocity at zero stress in the material from which the specimen was made. Theoretical calculations of $(dV/dT)_0$ are not available at present. This means that values of this parameter should be either determined independently by a separate experiment, or estimated from other appropriate results. Measurements of (dV/dT) at zero stress, made on different types of specimens (Tables I and II) have shown that this quantity differs considerably with heat treatment, and to a lesser extent from one specimen to the other. These differences are mainly due to the variations of residual stresses in specimens, even when they are given the same heat treatment. This, of course, limits the use of equ. 2 in the determination of the absolute values of unknown stresses. However, as will be shown in the next section, a reasonable estimate of the stress at any location on the specimen, will make it possible to determine bulk stresses at other locations on that specimen using equ. 2.

STRESS DETERMINATION

In order to examine the possibility of using equ. 2 to determine unknown stresses, the shrink fit method was employed to introduce known stress distributions in a disc made of type 6063-T4 aluminum. The diameter of the disc was 3.50 cm while its thickness was 0.79 cm. An aluminum rod of the same material was shrunk fit into a hole drilled in the center of the disc. The diameter of the hole was 0.50 cm, while that of the rod was 0.0064 cm larger. In order to fit into the cryogenic system employed to control the temperature of the system, the disc was then machined to its final shape shown in Fig. 6.

The stresses generated in the disc due to the presence of the rod can be represented by an axial component σ_a , a radial component σ_r , and a tangential component σ_t , which are related by the relationship, $\sigma_a = \nu(\sigma_r + \sigma_t)$, where ν is the Poisson's ratio. Three independent measurements are then required to determine the values of these components: the temperature dependences of the longitudinal and the two shear velocities of the ultrasonic waves propagating along the thickness of the disc. The two shear

velocities will be measured with the polarization vector parallel to and perpendicular to the radial line connecting the center of the rod and the tip of the circumference of the disc. These measurements, will evaluate the resultant of the stress components acting in a cylinder of cross-sectional area equal to that of the transducer used in the measurements (0.08 cm^2), and of length equal to the thickness of the disc (0.79 cm). The results of the temperature dependences of the longitudinal and the two shear velocities (dV_L/dT) , $(dV_S/dT)_{||}$ and $(dV_S/dT)_{\perp}$, function of distance between 0.45 and 1.60 cm are listed in table III. These distances are measured between the centers of the rod and the transducers. From this table one can see that the values of (dV_L/dT) at the four locations are equal to within $\pm 2\%$. This shows that the stress component measured by the temperature dependence of the longitudinal velocity, remains unchanged over the distance where the measurements were performed. Analysis of stresses in the disc used in the present investigation, indicates that only the axial component remains constant over that distance.

TABLE III

The temperature dependences of the ultrasonic longitudinal velocity (dV_L/dT) , the ultrasonic shear velocity polarized parallel to the radial direction $(dV_S/dT)_{||}$, and the ultrasonic shear velocity polarized perpendicular to the radial direction $(dV_S/dT)_{\perp}$, as a function of the radial distance R in the aluminum disc shown in Fig. 6.

Radial Distance $R \text{ (cm)}$	Temperature dependence of ultrasonic velocity (m/S.K)		
	$-(dV_L/dT)$	$-(dV_S/dT)_{ }$	$-(dV_S/dT)_{\perp}$
0.45	1.123	0.821	0.831
0.70	—	0.770	0.756
0.95	1.088	0.868	0.849
1.15	1.113	—	—
1.60	1.107	0.914	0.899

The data listed in table III, also show that the values of the temperature dependences of the two shear velocities obtained at the same distance, are equal to within $\pm 1\%$. This indicates that the stress components measured by these two temperature dependences at the same distance from the center of the rod should be equal. As a function of distance, however, the values of either of the shear temperature dependences change considerably. Close to the edge of the disc, where the radial or the tangential stress component is small, the temperature dependence is the largest, and equal to about -0.9 m/S.K . This value decreases as the distance from the center of the rod is decreased, and reaches a minimum around 0.7 cm. As the distance from the rod is further decreased, the value of (dV_S/dT) is increased again.

The stress distribution in the disc shown in Fig. 6, may be approximated by that generated in a circular plate of 2.3 cm in diameter, with an eccentric hole of 0.5 cm in diameter and at distance 0.6 cm from the center of the plate. The hole is subjected to inside radial pressure. Savin¹⁵ calculated the distribution of the tangential stress component in this case, and his calculations are shown in the Appendix. Using the dimensions shown

in Fig. 6, along with a shear modulus $\mu = 0.26 \times 10^5 \text{ MPa}$ and a Poisson's ratio $\nu = 0.346$, the tangential component of the stress was calculated as a function of the radial distance, and plotted in Fig. 6. From this plot, one can see that the tangential component in this disc is compressive near the rod, equal to zero at approximately 0.4 cm, and becomes tensile at larger distances. Between 0.4 cm and the circumference of the disc, this component has a maximum at 0.6 cm of approximately 95 MPa, which decreases to 1.4 MPa at the circumference. The values of the tangential stress component at the locations where ultrasonic measurements were undertaken, are listed in table IV.

TABLE IV

Radial Distance	$-(dV_S/dT)_{\perp} \text{ (m/S.K)}$	Applied Stress* (calculated in MPa)	Applied Stress measured in MPa)
0.45	0.831	34.0	44.8
0.70	0.756	74.4	69.0
0.95	0.849	22.8	22.1
1.60	0.899	1.4	1.4

*G.N. Savin, "Stress Concentration Around Holes, Pergamon Press (1961), p. 116.

Also included in this table, were the values of the temperature dependence of the shear velocity measured when the polarization vector was perpendicular to the radial direction. At 1.6 cm (close to the circumference of the disc), $(dV_S/dT)_{\perp}$ is -0.899 m/S.K and the value of the tangential component is 1.4 MPa. Assuming this value of temperature dependence corresponds to the stress calculated at this point, values of the tangential component at the other three locations were calculated using equ. 2, and the measured values of the temperature dependence. These values are included in column 4 of table IV. The agreement between these values of the tangential component, and those calculated using Savin's equations is very good considering the approximations made in calculating these stresses.

Unfortunately, no comparison could be made between radial stresses determined from the temperature dependence measurements and those calculated from elasticity theory, which are difficult to compute for an eccentric hole in a disc. Nevertheless, the values of $(dV_S/dT)_{||}$ listed in table III, indicate that the distribution of the radial stress component along the axis OX will be similar to that of the tangential component. At the circumference, σ_r will be equal to zero, increases to a maximum compressive value at $R = 0.7 \text{ cm}$, and then drops sharply to zero at $R = 0.4 \text{ cm}$. As a function of distance, the sum of the tensile tangential and the compressive radial components $(\sigma_t + \sigma_r)$ should be constant, as indicated from the small variations found in the measurements of (dV_L/dT) listed in table III. Values of this quantity determine the axial component of the stress σ_a which is equal to $\nu(\sigma_t + \sigma_r)$. The sum of the tangential and the radial stress components are expected to be small, as the values of (dV_L/dT) listed in table III are very close to those measured on specimens D and E of table I at zero stresses.

ACKNOWLEDGMENT

The authors would like to thank the Air Force Office of Scientific Research for their financial support of this investigation under Grant No. 77-3457. The authors also wish to acknowledge very useful discussions with Drs. B.D. Cook and K.J. Waldron from the Mechanical Engineering Department at the University of Houston.

REFERENCES

1. Proceedings of the Annual Conference on Application of X-ray Analysis, Denver, Advances in X-ray Analysis, 20 (1977).
2. Cullity, B.D., Advances in X-ray Analysis, 20, 259 (1977).
3. James, M.R. and Buck, O., Quantitative Nondestructive Measurements of Residual Stresses, Technical Report, Science Center, Rockwell International (1978).
4. Proceedings of Workshop on Nondestructive Evaluation of Residual Stress, NTIAC-76-2 (1976).
5. Thruston, R.N. and Brugger, K., Phys. Rev. 133, A1604 (1964).
6. Alers, G.A., Proceedings of Workshop on Nondestructive Evaluation of Residual Stress, p. 166, NTIAC-76-2 (1976).
7. Noronha, P.J., Chapman, J.R., and Wert, J.J., Testing and Evaluation, 1, 209 (1973).
8. Hsu, N.N., Exp. Mech. 14, 169 (1974).
9. Stern, E.A., Phys. Rev. 111, 786 (1958).
10. Garber, J.A., and Granato, A.V., Phys. Rev. 131, 3990 (1975).
11. Ippolito, R.M. and Salama, K., Proc. 11th Symposium on NDE, p. 62 (1977).
12. Ippolito, R.M. and Salama, K., Advances in Test Measurements, Vol. 15, 403 (1978).
13. Papdakis, E.P., J. Acoust. Soc. Amer. 42, 1045 (1967).
14. Salama, K., and Ippolito, R.M., Proceedings of First International Symposium on ultrasonic Materials Characterization, June 1978.
15. Savin, G.N., Stress Concentration Around Holes, Pergamon Press, p. 116 (1961).
16. Muskhelishvili, N.I., "Some Basic Problems of the Mathematical Theory of Elasticity", Wolters-Noordhoff Publishing, Groningen, p. 445 (1963).

APPENDIX

Cylinder stressed by a constant pressure P.

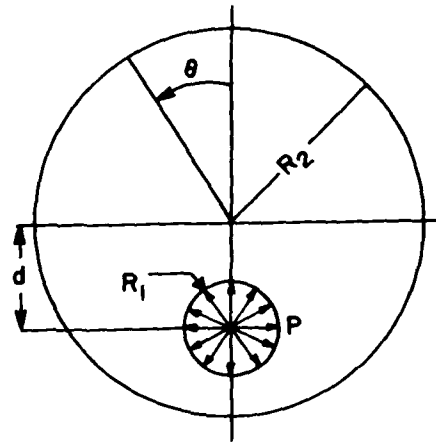


Figure 7.

In a cylinder of cross-section defined by two eccentric circles of radii R_1 and R_2 (Fig. 7), Savin¹⁵ has shown that the tangential stress component along the contour of the outside circle can be given by

$$\sigma_t = 2P \frac{R_1^2 [R_2^2 (R_2 - 2d \cos \theta)^2 - (R_1^2 - d^2)^2]}{(R_1^2 + R_2^2) [R_2^2 - (R_1 + d)^2] [R_2^2 - (R_1 - d)^2]} \quad (1)$$

In the case of stress generated by a rod shrunk fit into the inside circle, the pressure P may be calculated from¹⁶,

$$P = \frac{\mu R_1 (1 + \nu)}{R_2^2} \epsilon \quad (2)$$

where μ is the shear modulus ν is the Poisson's ratio, and ϵ is the difference between the diameters of the rod and the inside circle.

IBRASS HOLDER

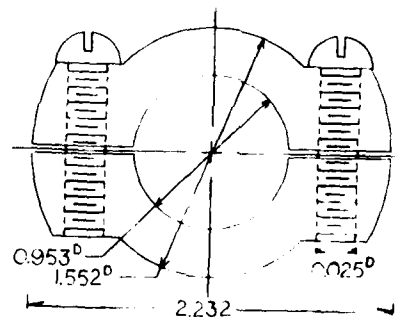


Fig. 1. Holder used to apply compressive stress to specimen.

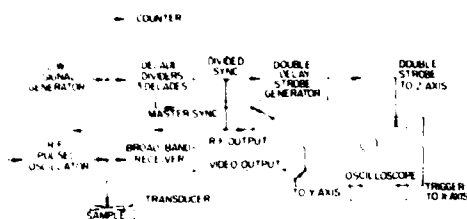


Fig. 2. Pulse-echo overlap system for measuring ultrasonic velocity.

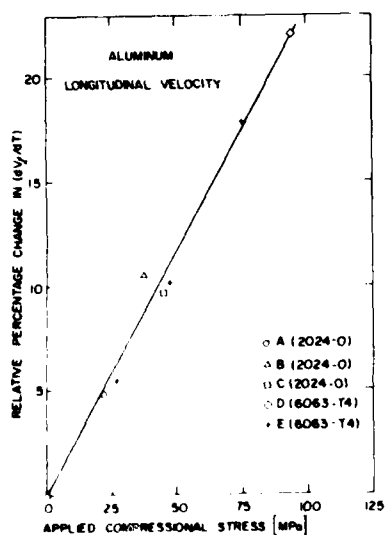


Fig. 4. Percentage of the relative change in the temperature dependence of ultrasonic longitudinal velocity as a function of applied stress in aluminum

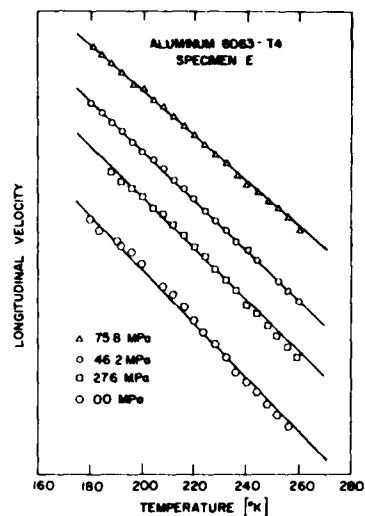
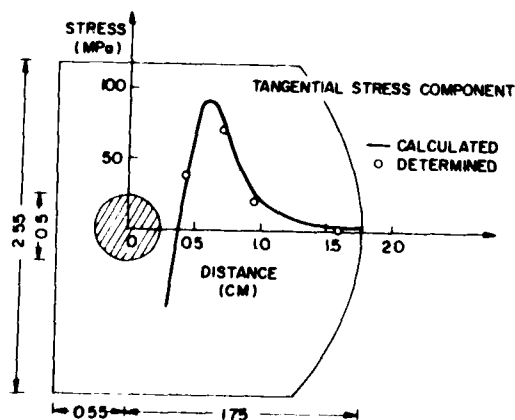


Fig. 3. Effect of applied compressive stress on the temperature dependence of ultrasonic longitudinal velocity in aluminum. Stress is applied in a plane perpendicular to the direction of propagation of the ultrasonic waves.

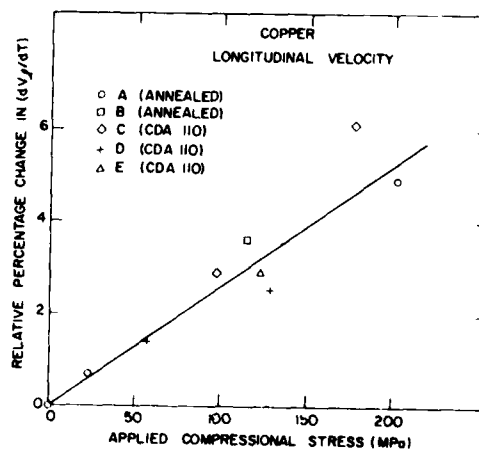


Fig. 5. Percentage of the relative change in the temperature dependence of ultrasonic longitudinal velocity as a function of applied stress in copper.

Fig. 6. Aluminum disc used for the determination of unknown stresses generated by shrink fit method.

TRIBOSTIMULATED EMISSION OF ELECTRONS AND NEUTRAL PARTICLES FROM ANODIZED ALUMINUM

J.T. Dickinson and P. Braunlich
Physics Department
Washington State University
Pullman, WA 99164

ABSTRACT

The physical and chemical properties of anodic oxide layers on metals such as Al play important roles in a number of applications such as adhesive bonding and corrosion resistance. An overall test of an oxide layer sensitive to a number of oxide properties is difficult to find. We have been studying the tribostimulated emission of charged particles, neutral particles, and photons during tensile deformation of anodically oxidized Al alloys. The characteristic emission curve (emission rate vs. strain of the Al substrate during constant strain rate) is found to depend strongly on the anodization parameters. A comparison of neutral particle emission with electron emission will be presented. Correlations between acoustic emission from oxide cracking and electron emission will also be discussed.

INTRODUCTION

Exoelectron emission is generally due to the release of highly localized energy at the surface of a solid in a relatively short time period. Many competing processes can dissipate this energy, particle emission being one of the least likely and phonon production being the most likely. The emission we observe in these experiments can be directly correlated with the propagation of cracks in the oxide coating. The manner in which an oxide coating responds to uniform straining of the aluminum substrate and the resulting emission of particles is strongly dependent on the mechanical and chemical nature of the oxide coating.

Experimental details of our experiments may be found in references 1-3. The electron emission is measured in 10^{-8} torr vacuum with a channeltron electron multiplier. A typical characteristic emission curve for a dense barrier-type oxide on Al 2024 clad is shown in Fig. 1. The shape of the large peak at 5% strain agrees well with optical microscopy measurements of rate of crack growth. The small peak at 14% strain coincides with the necking of the sample prior to rupture. Any phenomena which disrupts the oxide layer and initiates crack growth leads to the emission of electrons.

DEPENDENCE ON ANODIZATION PARAMETERS

Certain porous duplex oxides grown in H_3PO_4 are known to facilitate adhesive bonding of Al.⁴ The samples prepared by a laboratory "baseline" procedure provided by the Boeing Commercial Aircraft Co. are referred to as Boeing Baseline samples. Figures 2 and 3 show characteristic exoelectron emission curves (CECs) for a Boeing Baseline sample and two samples with oxides formed under slightly anodization conditions. One sees that the CECs change for these different conditions.

We have carried out a systematic variation of a number of anodization parameters around the Boeing Baseline procedures. One simple effect to show is the change in the total number of electrons counted as a function of this single parameter. Fig. 4 illustrates the manner in which total emission changes with oxide thickness (varied by varying the anodization voltage). The observed increase with film thickness is seen to be exponential above 2500 Å. Fig. 5 shows the effect of changing the electrolyte concentration and Fig. 6 is the total

emission as a function of electrolyte temperature. Qualitatively, the behavior observed in these last three figures can be explained on the basis of the assumption that the more bonds that are broken the greater the electron emission. Examination of the samples under the SEM shows variations in both thickness and porosity. Both these features will alter the number of bonds ruptured in the cracking process.

NEUTRAL PARTICLE EMISSION

We have also observed neutral particle emission during tensile deformation of anodized Al. It also takes on a characteristic shape and intensity which depends on the nature of the oxide. Fig. 7 shows the neutral emission observed during the elongation of a sample with a dense oxide (ammonium tartrate-3000 Å). For comparison, the electron emission curve for an identical sample is also shown. With a quadrupole mass spectrometer, the neutral species were determined to be O_2 and CO_2 for the dense oxide. For porous H_3PO_4 oxides, we only observed O_2 . We are fairly sure these molecules are associated with trapped impurities because they are the same species released when the samples are heated to a few hundred degrees C. One notices the much slower decay of the neutral emission relative to the electron emission in Fig. 7. This occurred on all samples studied. If one stops pulling the sample while it is emitting one finds that the neutral emission decays away with time constants of 6 sec for the CO_2 and 10 sec for O_2 . This implies a very slow process which we feel is the diffusion of atoms/molecules to the crack wall before desorption. The conduction of the cracks is much too large to account for these large time delays. We have modeled the release of neutral molecules following crack propagation and can fit the experimental data quite well. Fig. 8 shows the dependence of neutral emission on oxide thickness for dense oxide layers.

CORRELATION OF ELECTRON EMISSION WITH ACOUSTIC EMISSION

By attaching an acoustic emission (AE) transducer to the back of the sample, we can detect the bursts of acoustic energy associated with oxide cracking. Tests with no oxide present, various lengths of oxide on the sample gauge, and correlations with optical microscopy measurements show that

the acoustic emission observed is associated with oxide cracking. For this work we have been using Al 1350 (99.5% Al) annealed at 370 C which yields negligible substrate AE. The AE and exoelectron emission (EE) can be obtained simultaneously. With a 5 mm² patch of 5000 Å thick oxide (dense-ammonium tartrate) on the side of the sample facing the electron multiplier, healthy quantities of AE and EE are observed.

Fig. 9 shows AE and EE count rate vs. strain curves for the above oxide. The two curves are seen to be intimately related. We thus conclude that a necessary condition for tribostimulated EE is the occurrence of oxide cracking.

Fig. 10 shows AE and EE curves taken at a slower strain rate such that the absolute rates of detected emission were carefully determined throughout the experiment. This allows us to take an accurate ratio of EE to AE indicating what the probability of EE is relative to AE. The EE/AE ratio is seen to be near unity and depends on strain. The cracks that occur in the initial rise of the major peak (in the region of 0.8-0.9 % strain) appear to be significantly more "efficient" in producing electrons. These are the initial cracks formed in the oxide whereas the cracking occurring later is simply crack extension. In the major portion of the curve the ratio is one to one. Finally, the ratio climbs as the AE curve is seen to drop off faster than the EE curve. We believe this is due to chemi-emission as we will comment later.

Another basic question is the time relation between AE and EE. If one pulls the sample very slowly, the bursts of AE and EE can be displayed as single events by means of suitable pulse shaping and the use of two synchronized strip chart recorders (We refer to this as our two graduate student coincidence experiment). Manually, the observer can detect "coincidence" between the two emissions to perhaps within 0.1 sec. Fig. 11 shows the two sets of bursts over approximately 4 minute intervals: a) near the peak of exo-emission and b) out on the tail of exo-emission with the pulling stopped and the sample held at constant strain. The bursts labeled o are out of "coincidence" and those labeled i are in "coincidence". Near the peak one sees that nearly all of the electron bursts are in "coincidence" with an AE burst. Those EE bursts out of coincidence can easily be accounted for by background which is two to three counts per minute. This implies that EE occurs within 0.1 sec of the propagation of a crack in the oxide. Fig. 11-a also shows that a number of AE bursts occur without an accompanying electron burst. From our ratio determination in Fig. 10, this implies that many electron bursts consist of more than one electron.

In Fig. 11-b, one sees a few electron bursts in coincidence (those marked i) but a much larger number that are out of coincidence (o). It is this random component that we feel is due to chemi-emission⁴ due to the reaction of gaseous species with the freshly exposed Al upon cracking of the oxide. The source of the gas could be the oxide itself or it could be from the 10⁻⁶ torr background in which the experiments were performed. We are planning to repeat these experiments in UHV to determine the source of gas. With Al, O₂ is a likely candidate.

Finally, we have been attempting to measure more precisely the time interval distribution between the AE burst and the emitted electrons.

It is very difficult to determine the t=0 point of the AE burst. To within an uncertainty of about 20 usec, the two events appear simultaneous. Fig. 12 shows the distribution of time between AE and EE determined by a time-of-flight like experiment, where we mention again our t=0 mark is still uncertain. However, a very sharp distribution is observed, suggesting that the electrons are released very rapidly after the crack propagates and do not continue to emit for times on the order of a few microseconds. This is consistent with a mechanism wherein the energy available for emission is rapidly dissipated. We are nearly in the position to reduce the t=0 uncertainty by at least a factor of 10. We can then approach a model for EE with more confidence.

ACKNOWLEDGEMENTS

We gratefully acknowledge support for this work from the Air Force Office of Scientific Research, Grant No. 78-3650 and the Boeing Commercial Airplane Company. We also wish to thank E.E. Donaldson and D. Snyder for their contributions to this work.

REFERENCES

1. J.T. Dickinson, P.F. Braunlich, L.A. Larson and A. Marceau, *Appl. of Surf. Sci.* **1**, 515 (1978).
2. D.L. Doering, T. Oda, J.T. Dickinson, and P.F. Braunlich, *Appl. of Surf. Sci.* **3**, (1979).
3. L.A. Larson, J.T. Dickinson, P.F. Braunlich, and D.B. Snyder, *J. Vac. Sci. Technol.* **16**, 590 (1979).
4. N.K. Saadeh and J. Olmsted III., *J. Phys. Chem.* **79**, 1325 (1975).

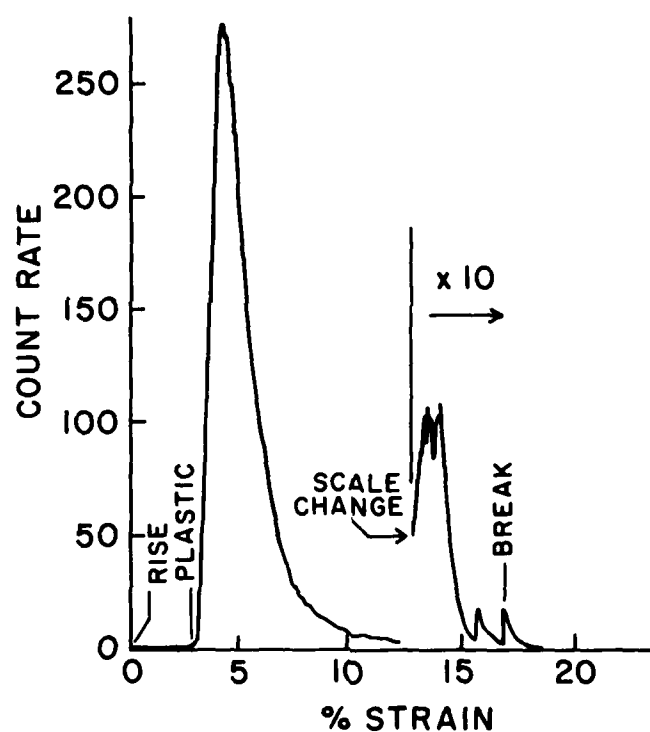
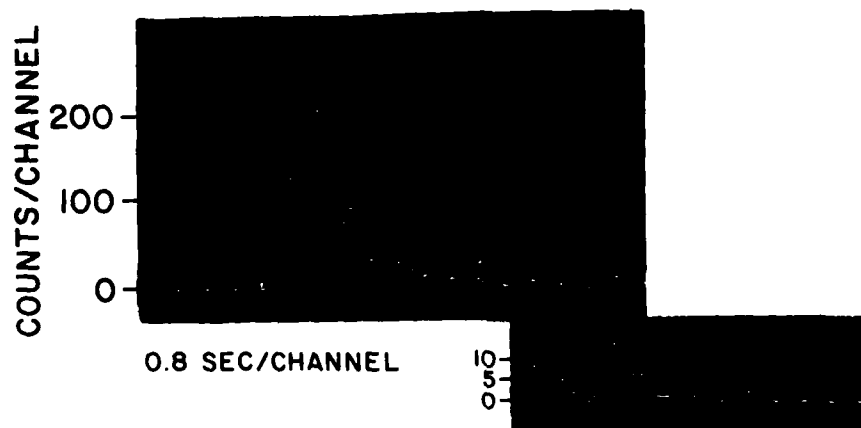


FIG. 1. Typical data obtained from a strong exoemitter (Al 2024 clad, covered with 3000 Å thick dense oxide grown in ammonium tartrate). The upper curve represents the recorded display of the multichannel analyzer. The lower curve is a strip chart recording of the rate-meter output obtained with a 5 second response time. The small peak preceding rupture occurs when the sample is necking down which severely disrupts the surface of the aluminum. This leads to additional oxide cracking and exoemission.

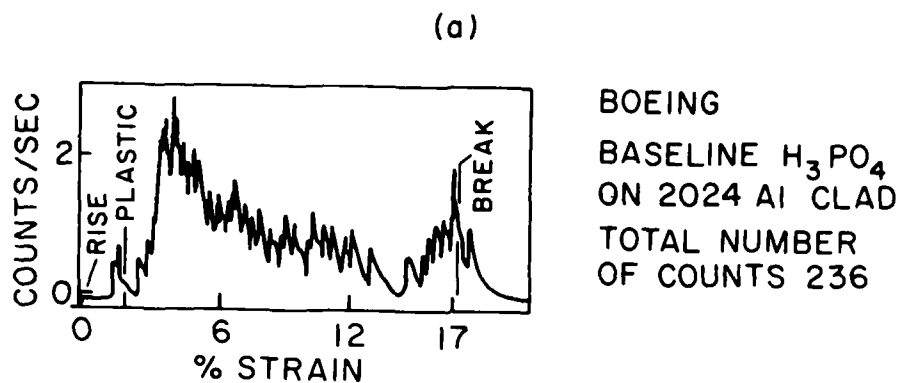


FIG. 2(a). The characteristic exoemission curve from a Boeing Baseline sample anodized in a 10% by weight H_3PO_4 solution. The substrate was Al2024 clad. Although the emission was weak, it was very reproducible from sample to sample.

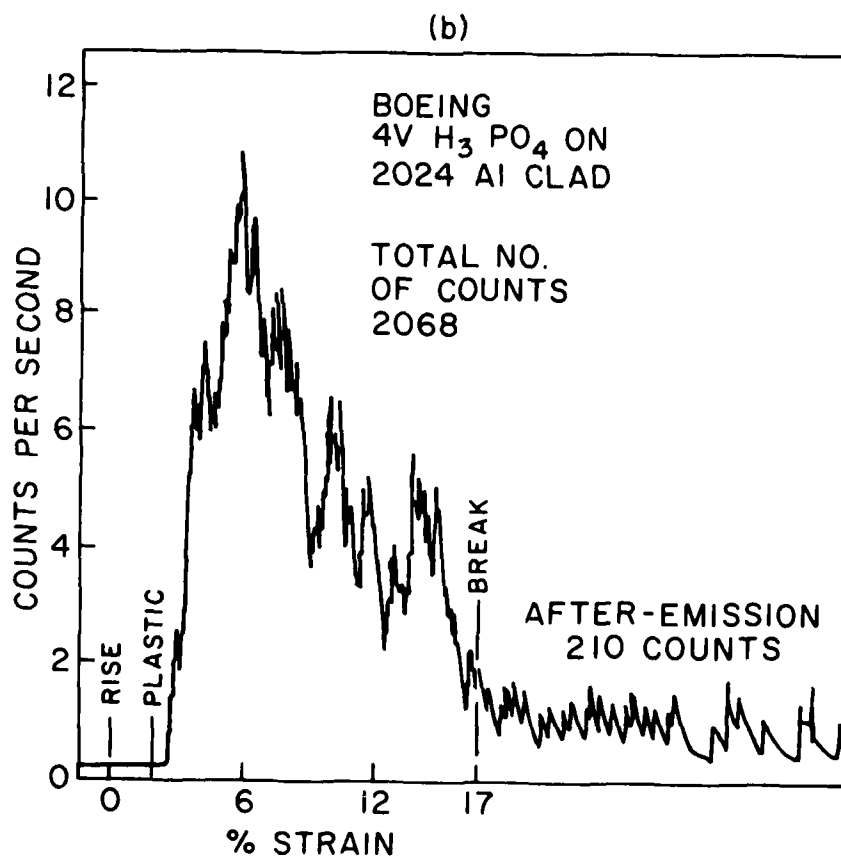


FIG. 2(b). Another CEC from a porous oxide with deviations from the Boeing Baseline procedure (a lower anodization voltage, lower anodization bath temperature and acid concentration). This produced a slightly thinner and smoother (less porous) oxide. Note the comparison with the Baseline CEC.

Figure 3. A third variation on the Boeing anodization procedure. A substantially higher anodization voltage, a slightly lower temperature, and a lower acid concentration were used for this sample. This produced a thicker oxide than the baseline sample. It is interesting that the CEC from thicker porous oxides resemble the CECs from dense oxides, suggesting similar cracking mechanisms.

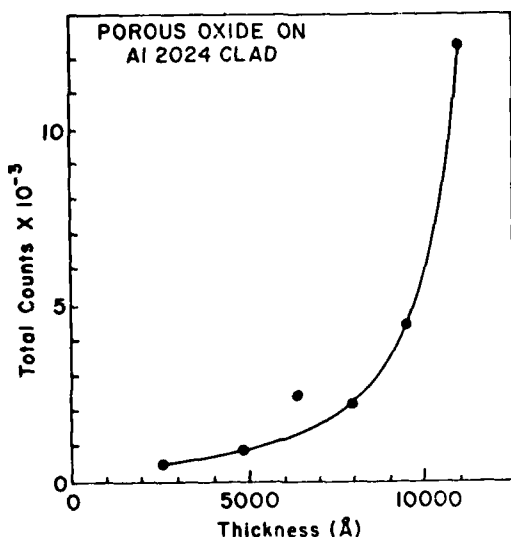
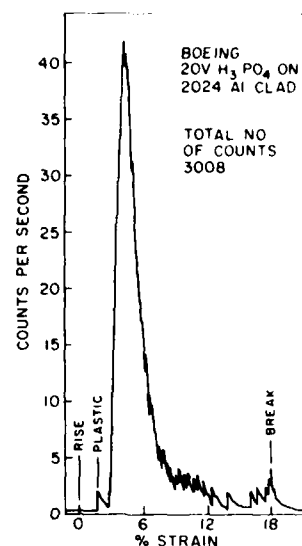


Figure 4. Total exoemission (total counts accumulated during the pull) vs. thickness for a voltage-varied porous oxide (H_3PO_4). All the anodization parameters other than voltage are the same as Boeing baseline.

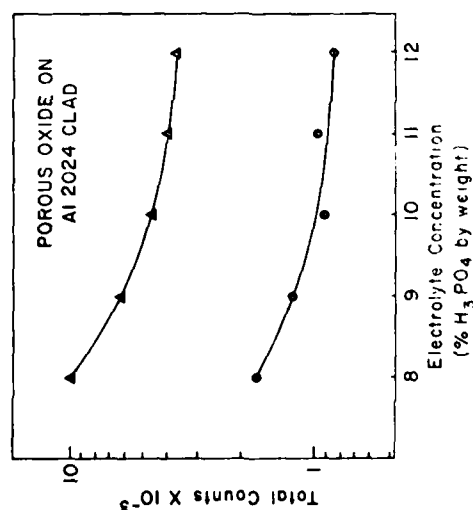


Figure 5. Total exoemission vs. electrolyte concentration for two porous oxides. The upper curve was grown at 30V, the lower curve at 10V. This results in a considerably thicker oxide for the 30V samples. The dominant effect in the concentration range studied here is an increase in the porosity of the oxide with concentration. This leads to less oxide material actually cracking and therefore a decrease in emission.

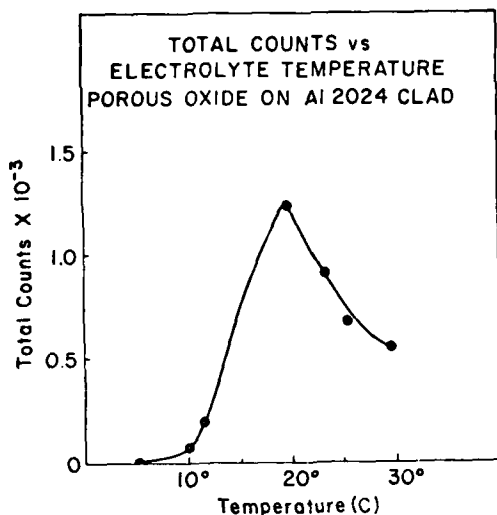


Figure 6. exoemission vs anodization temperature for a H_2PO_4 porous oxide. Both oxide thickness and porosity change with temperature.

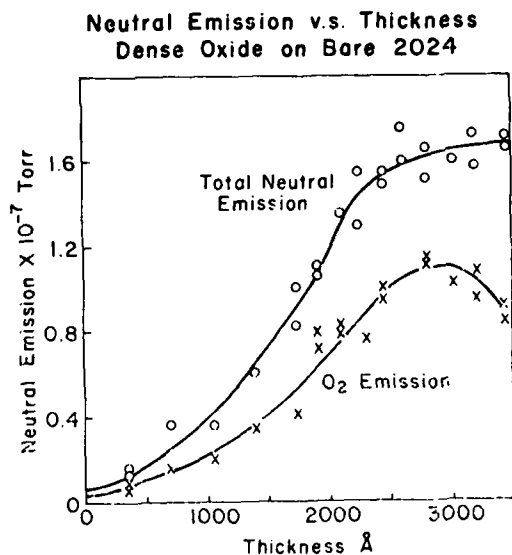


Figure 8. A summary of the total amount of neutral and O_2 emission from dense oxides on bare 2024 Al. This differs from exoemission in that in this thickness range, it grows exponentially. Note the the O_2 emission actually begins to decrease at higher thicknesses.

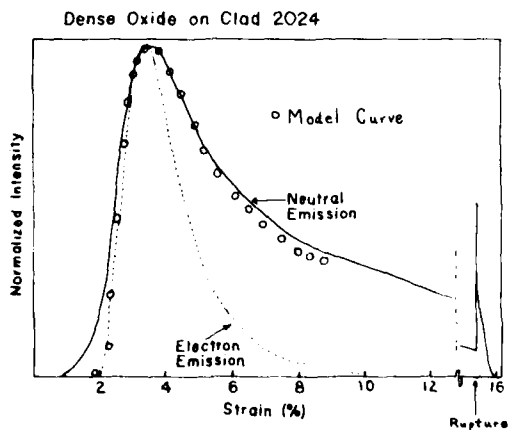


Figure 7. Total neutral emission as measured by a Bayart-Alpert gauge vs. strain for a dense ammonium tartrate oxide (3000 Å) on Al 2024 clad. Also shown is an electron emission curve for an identical sample. The circles are the calculated points for a model of neutral emission. The cracking of the oxide is clearly the initial step. Gases observed for the dense oxide were O_2 and CO_2 . Note the peak at rupture.

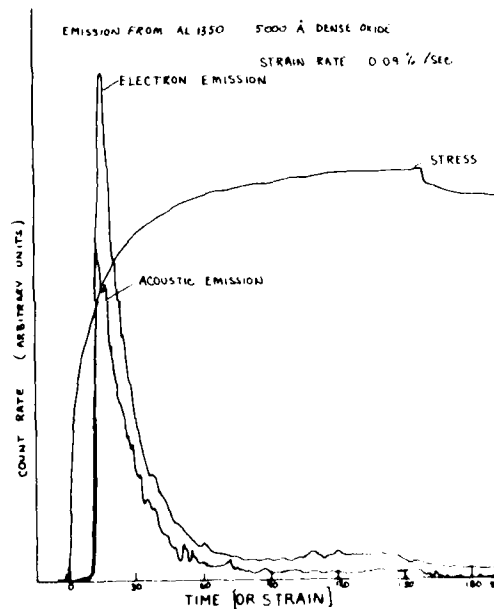


Figure 9. Correlation of acoustic emission from cracking oxide and exo-electron emission. The curves are very similar. This helps substantiate that the mechanism for electron emission is indeed the propagation of cracks in the oxide. Data is output of two count rate meters.

Figure 10. The AE and EE from anodized Al 1350. Care was taken to obtain the absolute intensities of the two emissions for the entire pull. This allows us to take the ratio of EE/AE, which is the dotted curve. "New" cracks emit electrons better. The rise in the ratio during the tails of the emission curves is believed to be due to chemi-emission.

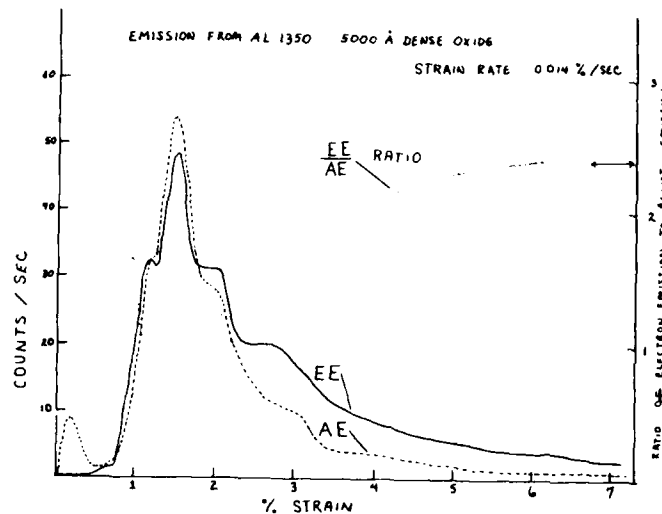


Figure 11. The correlation of EE and AE in time for relatively slow times. The spikes shown correspond to the occurrence of bursts of AE and EE.

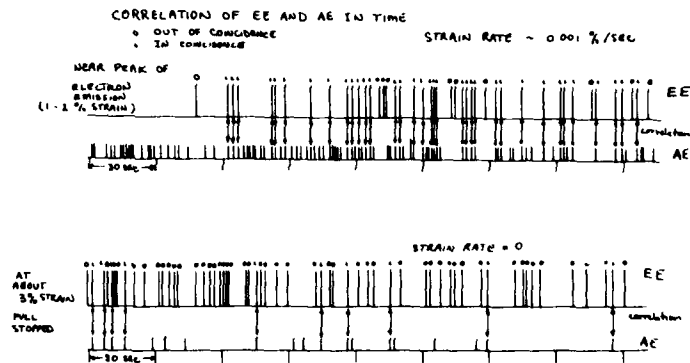
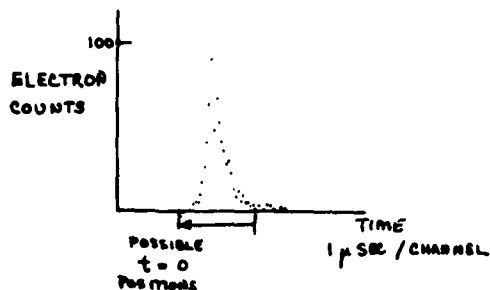


Figure 12. Distribution of time between occurrence of acoustic emission and electron emission.



The distribution of the time interval between the occurrence of AE and EE. A multichannel analyzer with a time-of-flight module was employed to detect electrons correlated in time with an acoustic burst. At the moment we can not say with certainty where $t=0$ is relative to this distribution. This is due to the nature of the AE burst. In spite of about a 20 usec uncertainty, we can say that within these few microseconds, all of the electron emission is over.

A REVIEW OF RECENT POSITRON ANNIHILATION NDE APPLICATIONS

S. Panchanadeeswaran, Po-We Kao, R. W. Ure, Jr., and J. G. Byrne
Department of Materials Science and Engineering
University of Utah
Salt Lake City, Utah 84112

ABSTRACT

This review will treat two recent applications of positron annihilation to metallurgical studies and will involve the measurement of the Doppler effect associated with the gamma rays emitted during positron annihilation. The applications will be: studies of the interactions of dislocations with pre-precipitates in aged Al-4 weight percent Cu single crystals and studies of the effect of hydrogen charging into polycrystalline nickel.

INTRODUCTION

Earlier¹ it was reported that a commercial aluminum base age hardening alloy, 7075, responded to Doppler broadening measurements by exhibiting higher values of the peak to wings shape parameter for harder conditions. Thus, the Doppler shape factor was behaving in much the same way in which it would respond to plastic deformation in a pure metal; that is, in a pure metal subjected to damage the Doppler peak shape becomes sharper because dislocations and vacancies provide locations for positron trapping which are lacking in ion cores. Hence, positrons attracted to and trapped in such regions will tend more to annihilate with lower energy conduction electrons. Such annihilations cause a smaller Doppler shift from the central energy value of 511 keV than would be caused were the positron to annihilate with a more energetic core electron. Thus, the curve representing the number of annihilations versus plus and minus deviations in annihilation gamma ray energy about a central value of 511 keV (the value if the electron-positron center of mass were stationary) sharpens with rising defect concentration and, conversely, the shape broadens with the annealing out of damage. The gamma rays emitted on annihilation enter a Ge(Li) spectrometer capable of measuring their energy.

RESULTS

To have a better chance of understanding the response of positrons to changes during age hardening², we set out to produce well documented aged states in a known alloy; that is, to look at G. P. zones, transition precipitates (θ'), and the equilibrium precipitate (θ) in both single and polycrystalline Al + 4 weight percent Cu alloy. The heat treatments used were: solution treated (S.T.) at 550°C for 1 hour + water quench (Q) for the supersaturated solid solution; S.T. + Q + 130°C for 48 hours for G.P. I zones; S.T. + Q + 190°C for 5 hours for G.P. II zones; S.T. + Q + 240°C for 24 hours for θ' ; and S.T. + Q + 400°C for 24 hours + 315°C for 48 hours for θ (the equilibrium precipitate).

When peak to wing (P/W) Doppler comparisons were made, both Na²² and Ge⁶⁸ were used as positron sources. The Na²² produces positrons with a maximum energy of 0.546 MeV and the Ge⁶⁸ produces positrons with a maximum energy of 1.9 MeV; thus, the former positrons will sample events closer to the

specimen surface than the latter positrons.

P/W data for an aged single crystal utilizing a Na²² positron source are shown in Fig. 1, plotted against the principal aging temperature. One sees a rise in P/W ratio from the solid solution level to the G.P. zone conditions and a later decline as θ' and θ are formed.

Figure 2 exhibits P/W data taken on the same samples, but with Ge⁶⁸ as the positron source. One sees a similar trend (except for the G. P. II point) in the data, all of which lie in a lower magnitude range. When these experiments were repeated with polycrystalline samples and the Ge⁶⁸ positron source, similar data trends to those of Fig. 2 resulted (with the exception of G. P. II).

A number of conclusions emerge at this point. For the "bulk" data obtained with Ge⁶⁸, the P/W values for the polycrystals were usually lower point for point than the corresponding values for the single crystal experiments. This would suggest that in the quenched condition fewer point defects are present in the polycrystal because of leakage to grain boundary sinks. In subsequent aging this would lead to a lower density of pre-precipitate nucleation sites in the polycrystal. This would account for the lower P/W ratios in a G. P. zone condition because the coherency strain or hardness of the region measured would be lower.

Again, the case of the G. P. II zone containing single crystal Ge⁶⁸ data violates this scheme. The same data point will later be seen to be at variance with the interpretation given to the θ' condition; that is, it can reasonably be regarded as a bad data point, but for reasons as yet unclear.

For θ' and θ data, the lower nucleation frequency again seems to explain the lower values of P/W ratio for the polycrystalline samples. However, the basis for the values themselves no longer can be ascribed to coherency strains, but rather may be reflective of positron trapping at the θ' and θ matrix-particle interface.

In every case, P/W values measured closer to the surface (Na²²) exceeded those measured at greater depths (Ge⁶⁸). This may be related to the higher quenching rates and point defect concentrations of the surface region which in turn would on aging produce a higher nucleation rate

of precipitation.

Independent of depth, the quenched solid solution was always lower in P/W ratio than either the G. P. zone or overaged conditions. This implies that the stain effect of G. P. zones is much more interactive with positrons than is the discrete point defect distribution created by quenching. The θ' and θ conditions are also more interactive with positrons than is the quenched state--again probably due to interfacial rather than strain field trapping reasons.

In comparing G. P. I and G. P. II zones, it seems (with the one exception previously noted) that the trapping of positrons is greater for the more highly stained G. P. II condition. As one then passes to the partially coherent (less strain) θ' situation, the positrons are less effectively trapped than by the coherent G. P. II particles. Finally, in comparing θ' and θ , it seems that the completely incoherent θ particles have a more effective positron trapping interface than do the θ' particles.

We now proceed to more recent single crystal experiments³ in which the interaction of various of the above aged states in single crystals respond to tensile deformation. It is known that for G. P. zone states dislocations must rigidly cut through the zones⁴, giving the crystal a high yield strength, but a modest rate of work hardening. For the θ' and θ situations, on the other hand, the dislocations bow out between the particles, wrap around, and pass on as in the Fisher-Hart-Pry⁵ or Orowan⁶ descriptions. The latter produces low initial strength, but a high rate of work hardening as multiple dislocation loops about the particles produce stress fields which resist the approach of new dislocations.

Figure 3 shows plots of I_v (the ratio of peak counts to total counts) and I_c (the ratio of wing counts to total counts) versus tensile strain for a G. P. I zone containing single crystals. The most important feature is that I_v does not change with tensile strain; that is, the cutting of G. P. I zones does not show up in Doppler broadening as would ordinary tensile strain. I_c changes appreciably only in the first 5 percent tensile strain. For G. P. II zone containing single crystals, I_v in Fig. 4 shows little but scatter once the initial 5 percent strain is completed.

For crystals containing the transition precipitate θ' and the equilibrium precipitate θ , the Doppler behavior is dramatically different from that for G. P. zones as might be expected from the very different deformation mechanisms involved. For example, for θ' containing crystals, both I_v and I_c respond quite rapidly to tensile strain as shown in Fig. 5. Again, for crystals containing the equilibrium precipitate θ , Fig. 6 shows a lesser magnitude, but an equally rapid response than for θ' .

The main distinguishing feature we seem to be seeing is that the cutting of G. P. zones does not appreciably change the positron response, but the operation of Fisher-Hart-Pry⁵ or Orowan⁶ work hardening mechanisms definitely does cause a positron response. The reason suggested is that positrons trap at the dislocations which wrap around the θ' and θ particles, but do not respond

very much to the cutting of G. P. zones by rigidly moving dislocations.

The second subject to be discussed is the hydrogen charging of metals⁷. Earlier work⁸ in this laboratory showed a hydrogen-positron relationship in steel which was appropriate for the non-destructive detection of hydrogen embrittlement. In the subsequent work⁸, nickel (after various amounts of cold work) was cathodically charged with hydrogen. The sharpness of the Doppler peak increased at first and to a greater extent the greater the amount of initial deformation. Following the initial sharpening, a broadening occurred. A mechanism which could explain this is one in which protons migrate to dislocations introduced by cold work and subsequently form gaseous hydrogen molecules which produce enough pressure to generate new dislocations at these locations. The broadening of the Doppler peak, following the initial narrowing, is attributed to protons reducing the attractive potential between positrons and dislocations. Figure 7 shows the undulating character of the positron-proton-dislocation relationship for two current densities for samples deformed 10.7 percent in tension.

A 70 percent cold rolled sample was cathodically charged for three hours and then measured as a function of time at 300°K. Figure 8 shows how P/W increased during this period. This is attributed in part to the diffusion of protons out of the sample. This would unscreeen some dislocations and thus raise P/W. Another cause may be that protons detrapped from dislocations or delivered by dislocation short-cut diffusion to inclusions or grain boundary locations may combine to form H_2 and generate new dislocations by exerting pressure.

Figure 9 shows a schematic diagram of microhardness measurement directions on special samples. The central impression was made with a 1 kg load and the two orthogonal directions enabled 25 gram microhardness measurements to be made as a function of distance from the large impression with and without hydrogen charging. Figure 10 shows on the upper curve (H_1) how the microhardness varies with distance from a high dislocation density after charging and after a one hour anneal at 365°K (curve H_2); that is, with no charging.

Cathodic charging produced no change in the P/W shape factor of annealed Ni; yet, the microhardness of annealed Ni increased with charging as is seen by the right end of curve H_1 (higher than right end of curve H_2). This suggests that the P/W ratio was seeing an exact balancing between defect generation and defect screening by protons during charging. Yet, the existence of the defects could be seen via microhardness.

ACKNOWLEDGEMENTS

The authors wish to acknowledge the financial support of the Air Force Office of Scientific Research which made this work reported in this review possible.

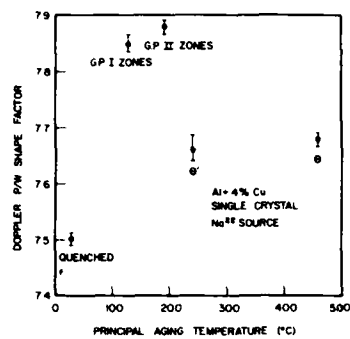


Fig. 1. Doppler P/W shape factors for an Al + 4 percent Cu single crystal in various aged states. Na^{22} positron source.

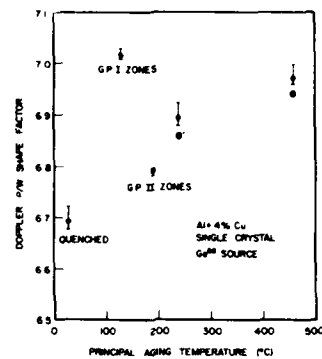


Fig. 2. Doppler P/W shape factors for an Al + 4 percent Cu single crystal in various aged states. Ge^{68} positron source.

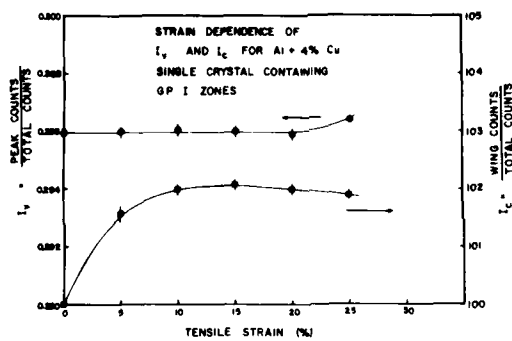


Fig. 3. Doppler peak to total (I_v) and wings to total (I_c) shape factors versus tensile strain for an Al + 4 percent Cu single crystal containing G. P. I zones.

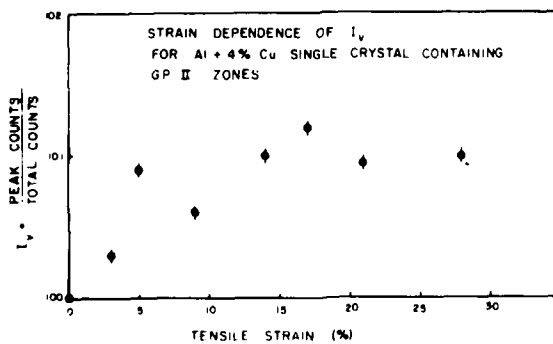


Fig. 4. Doppler peak to total (I_v) shape factor versus tensile strain for an Al + 4 percent Cu single crystal containing G. P. II zones.

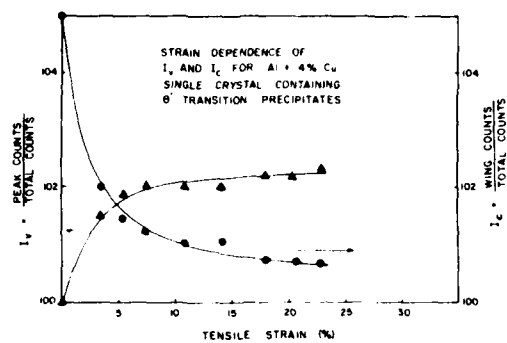


Fig. 5. Doppler peak to total (I_v) and wings to total (I_c) shape factors versus tensile strain for an Al + 4 percent Cu single crystal containing θ' transition precipitates.

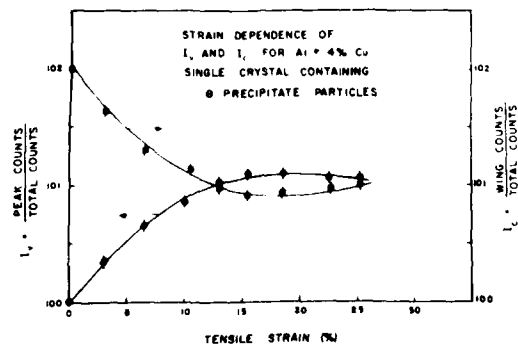


Fig. 6. Doppler peak to total (I_v) and wings to total (I_c) shape factors versus tensile strain for an Al + 4 percent Cu single crystal containing θ equilibrium precipitate particles.

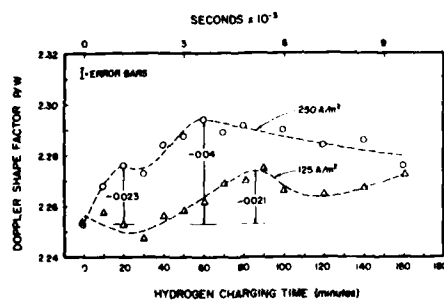


Fig. 7. Doppler peak to wings shape factor versus hydrogen charging time in polycrystalline nickel.

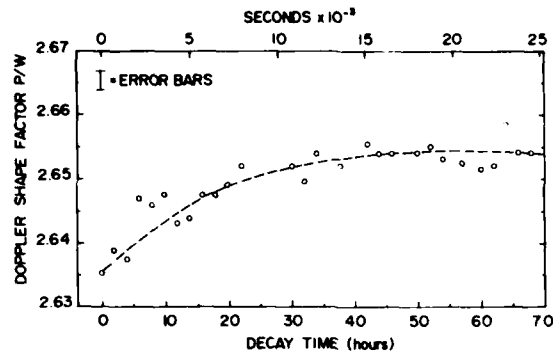


Fig. 8. Doppler peak to wings (P/W) shape factor versus decay time at ambient following cathodic charging of hydrogen into nickel.

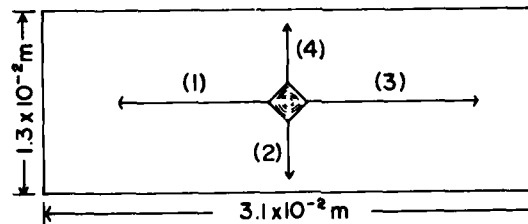


Fig. 9. Microhardness measurement directions and sample size for results shown in Fig. 10. Paths 1 and 2 could be used before and paths 3 and 4 after cathodic charging.

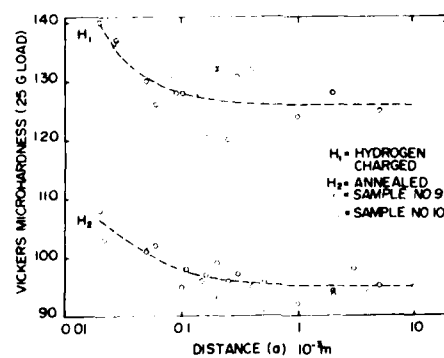


Fig. 10. Microhardness versus distance from a 1,000 gm impression before (curve H_2) and after (curve H_1) cathodic charging of hydrogen into nickel.

References

1. M. L. Johnson, S. Panchanadeeswaran, S. Saterlie, and J. G. Byrne, Phys. Stat. Sol. (a) 42, 175 (1977).
2. S. Panchanadeeswaran, R. W. Ure, Jr., and J. G. Byrne, Phys. Stat. Sol. (a) 48, 83 (1978).
3. S. Panchanadeeswaran, unpublished results (1979).
4. J. G. Byrne, M. E. Fine, and A. Kelly, Phil. Mag. 6, 1119 (1961).
5. J. C. Fisher, E. W. Hart, and R. H. Pry, Acta. Met., 1, 336 (1953).
6. E. Orowan, A Symposium on Internal Stresses (London: Inst. of Metals), 451 (1948).
7. Po-We Kao, R. W. Ure, Jr., and J. G. Byrne, Phil. Mag. (a) 39, 517 (1979).
8. F. Alex, Ph.D. thesis, University of Utah (1976).

ASSESSMENT OF POSITRON ANNIHILATION AS A POTENTIAL NON-DESTRUCTIVE EXAMINATION TECHNIQUE

W. B. Jones, J. A. Van Den Avyle, W. B. Bauster and W. R. Wampler
Sandia Laboratories
Albuquerque, NM 87185

ABSTRACT

The positron annihilation technique can provide a sensitive measure of defect density in metals. In this program the technique has been used to monitor defects generated during plastic deformation by cold work or fatigue cycling. The primary goals have been 1) to assess the degree of sensitivity of the technique, 2) to correlate positron annihilation readings with observed microstructural changes to better understand the physical basis for these readings, and 3) to determine correlations between positron annihilation measurements and number of fatigue cycles.

Examination of fatigued samples by transmission electron microscopy indicates some correlation between dislocation density and positron annihilation lineshape parameter (determined by the Doppler broadening technique). However, annealing studies of deformed samples indicate that positron annihilation response in 316 stainless steel is sensitive primarily to excess vacancies generated during the deformation and is less sensitive to dislocation density. Data on deformed nickel show sensitivity to both vacancies and dislocations. In general, lineshape parameter values tend to achieve a constant level at approximately 10 per cent of fatigue life.

INTRODUCTION

Elevated temperature design for advanced nuclear reactor components must incorporate creep and fatigue and their interaction. Current ASME Design Codes utilize the concept of damage accumulation to treat combined creep-fatigue loadings. This approach assumes that bulk changes occur during the service life that represent "damage". One question addressed by this study has been: Is there a measure of the bulk changes that occur during service that could be correlated to the accumulated "damage"? Flaw detection is not the purpose of such a technique.

Several candidate schemes have been surveyed with positron annihilation appearing to have more promise than the others (1,2). Positron annihilation has been shown (3) to be sensitive to vacancies, vacancy clusters and dislocations induced by irradiation or deformation of metals.

RESULTS AND DISCUSSION

Positrons injected into a metal annihilate with electrons emitting two gamma photons. The momentum of the annihilating electron causes a Doppler shift in the energy of the emitted photons. The sensitivity of positron annihilation to vacancy and dislocation concentrations in crystals arises from differences between electron momentum distributions in the perfect lattice and at defects. Figure 1 shows a schematic drawing of the apparatus used to measure the Doppler broadening of the annihilation line. Positrons are produced in the source by the β^+ decay of a naturally radioactive isotope. For this study, ^{22}Na was the isotope used. These positrons penetrate relatively short distances into the metal sample (Fig. 2) where they annihilate with electrons within about 100 psec. Test specimens examined in this study were sectioned normal to the stress axis so that the material sampled by the positrons was originally at the interior of the gauge section.

The result of the Doppler broadening measurement is a distribution of gamma energies around the 511 keV line. The parameter chosen to characterize this curve is the lineshape parameter, S . Details

concerning this characterization can be found in reference 1, however, it is important to note that the value of S depends on the density of dislocations and vacancies. The larger the value of S , the higher is the density of vacancies and dislocations.

To initiate this study, a number of fatigue tests on type 316 stainless steel were conducted at room temperature and the dislocation density monitored for comparison with lineshape data. The lineshape parameter, S , is plotted versus number of fatigue cycles in Fig. 3 together with transmission electron micrographs of representative dislocation substructures. For these test conditions the dislocation density and the lineshape parameter both increase with increasing number of fatigue cycles.

Figure 4 shows the results of fatigue tests conducted under several different conditions. For each set of conditions, the lineshape parameter followed the dislocation density changes; however, comparison of the values of S and the dislocation densities among the several conditions did not reflect a correlation (Fig. 5). In addition, the observed changes in S saturated at about 10% of life.

As pointed out earlier, the positron annihilation response is known to be sensitive to the presence of both dislocations and vacancies. In order to distinguish the relative magnitude of each contribution, isochronal annealing was conducted on samples of cold worked 316 stainless steel and pure nickel. Figure 6 shows the changes in lineshape parameter induced by cold work for both materials. In the present study, a pure Ni specimen was cold rolled to a 25% reduction in thickness and isochronally annealed (Fig. 7). Together with electron microscopy results, these data show that after annealing the Ni to 600 K to remove the excess vacancies, the lineshape parameter has noticeably decreased due to the loss of vacancies. However, about 60% of the total initial increase remains due to the dislocations. Figure 8 shows that after annealing 316 stainless steel at 873 K, the lineshape parameter has nearly completely recovered whereas electron microscopy and microhardness have shown that the dislocation structure has not

changed. From this we conclude that most of the initial response was due to the vacancies and only a very small fraction could be caused by the dislocations in the 316 stainless steel.

Figures 9 and 10 show the annealing response of 316 stainless steel cycled at room temperature and 866 K. As anticipated, the material fatigued at room temperature undergoes significant annealing of the lineshape parameter due to the large number of excess vacancies present after cycling. In contrast, cycling at 866 K results in a minimal accumulation of excess vacancies and, accordingly, the annealing treatment produced very little change in the lineshape parameter.

CONCLUSIONS

This study has shown that positron annihilation sensitivity to dislocation density must be established for each alloy. Even when such sensitivity is present, the response may be dominated by the presence of excess vacancies. Transmission electron microscopy has shown that the density and distribution of dislocations reaches a steady-state condition in the first 10% of the fatigue life so that, even with good dislocation sensitivity, the positron annihilation response would saturate at about 10% of total fatigue life.

ACKNOWLEDGEMENTS

Sandia Laboratories is a U. S. Department of Energy facility. This article was sponsored by the U. S. Nuclear Regulatory Commission under contract DE-AC04-DPO0789.

REFERENCES

1. W. B. Gauster, W. R. Wampler, W. B. Jones, and J. A. Van Den Avyle, Sandia Laboratories Report SAND-77-1570, May 1978.
2. J. A. Van Den Avyle, W. B. Jones, and J. H. Gieske, Sandia Laboratories Report SAND-77-1557, July 1978.
3. C. F. Coleman and A. E. Hughes, in Research Techniques in Nondestructive Testing, R. S. Sharpe, ed., (Academic Press, New York) Vol. 3, 1977.
4. G. Dlubek, O. Brummer, and E. Hensel, *Phys. Stat. Sol. (a)*, 34, 737 (1976).
5. W. Wysick and M. Feller-Kniepmeier, *J. of Nuc. Mat.*, 69 and 70, 616 (1978).

POSITRON ANNIHILATION DOPPLER BROADENING

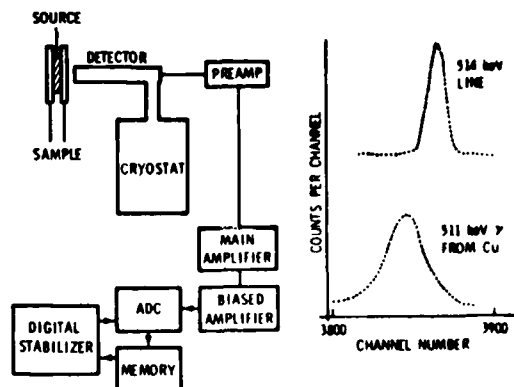


Figure ..

Depths of Penetration of Positrons in Copper
(Values for Steel will be ~10 to 20% Higher)

Source	e-folding distance*	maximum penetration
²² Na	23.1 μm ± 0.0009 in	0.31 mm ± 0.012 in
⁶⁸ Ge	165 μm ± 0.006 in	1.42 mm ± 0.056 in

* Depth in material at which positron flux is 1/e (37%) of its value at the surface.

Figure 2.

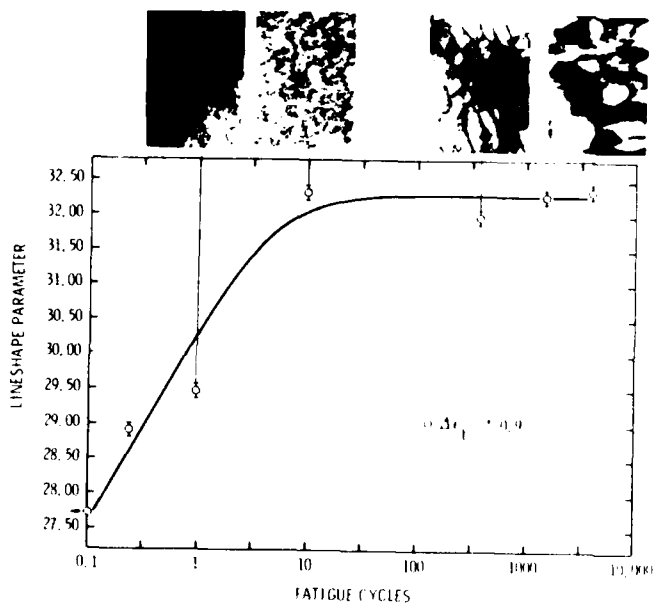


Figure 3.

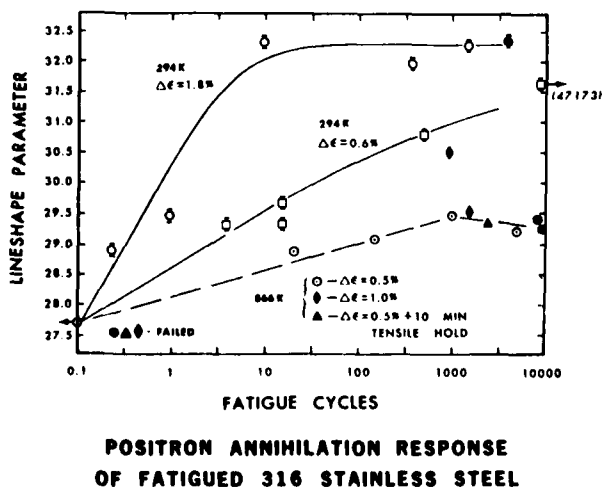


Figure 4.

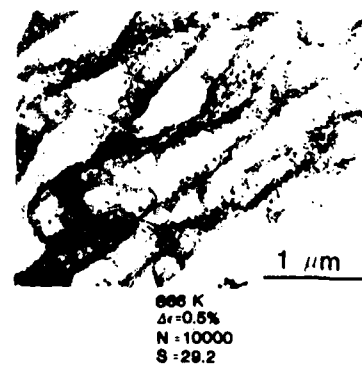
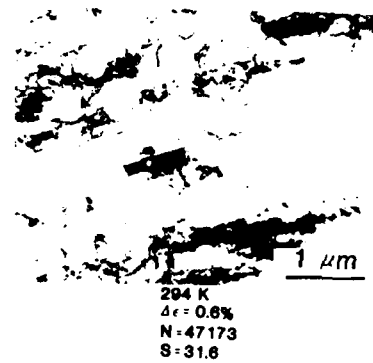
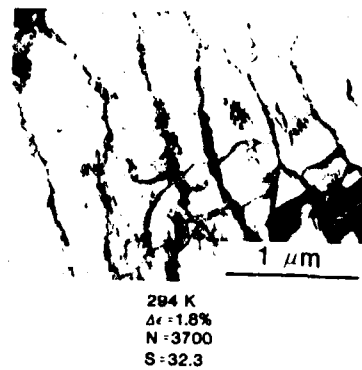


Figure 5.

POSITRON ANNIHILATION RESPONSE
OF COLD WORKED 316 STAINLESS STEEL AND NICKEL

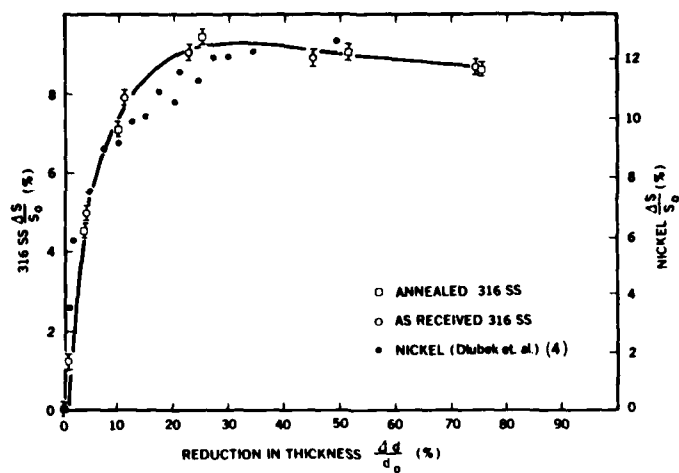


Figure 6.

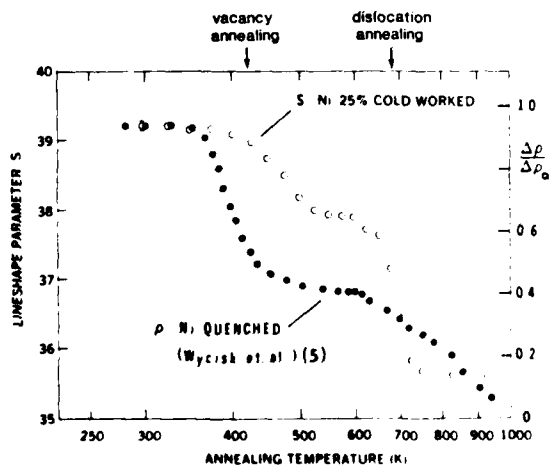


Figure 7.

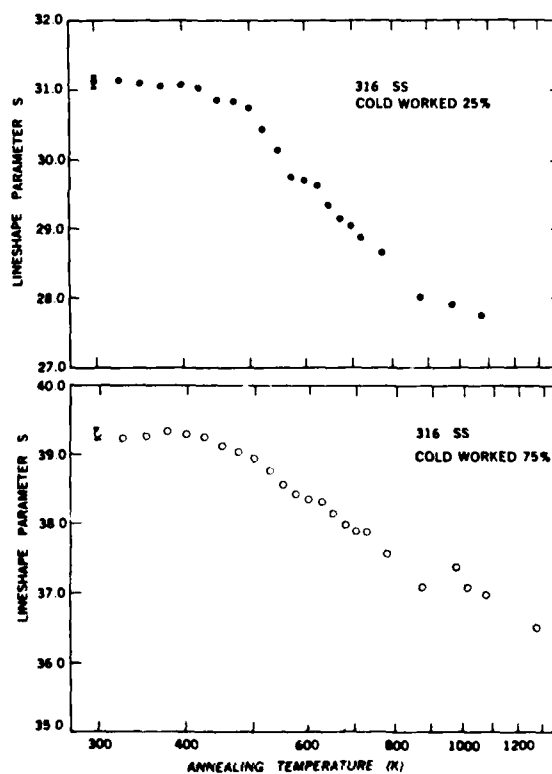


Figure 8.

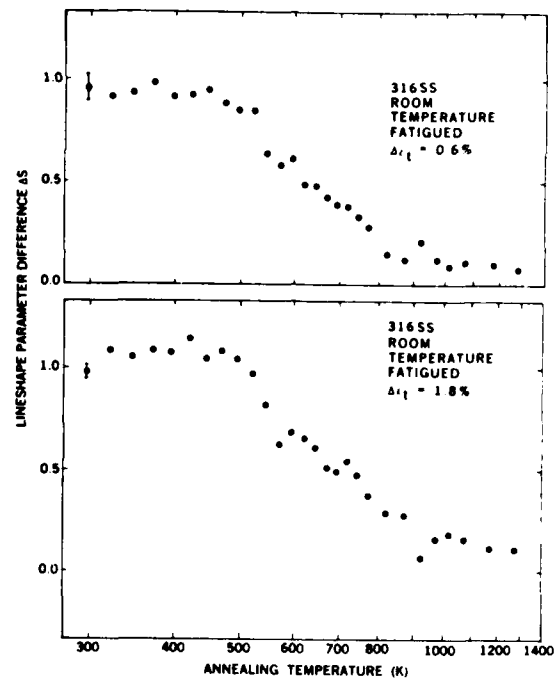


Figure 9.

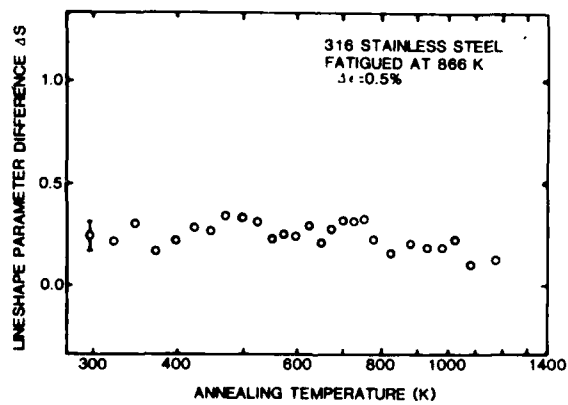


Figure 10.

DEVELOPMENT OF TRANSDUCERS FOR NDE

G. S. Kino, B. T. Khuri-Yakub, A. Selfridge, and H. Tuan
Stanford University
Stanford, California 94305

ABSTRACT

Several new types of transducers are described. These include 50 - 500 MHz transducers using thin film technology and indium techniques, transducer arrays for imaging, edge-bonded transducers, and uni-polar transducers.

INTRODUCTION

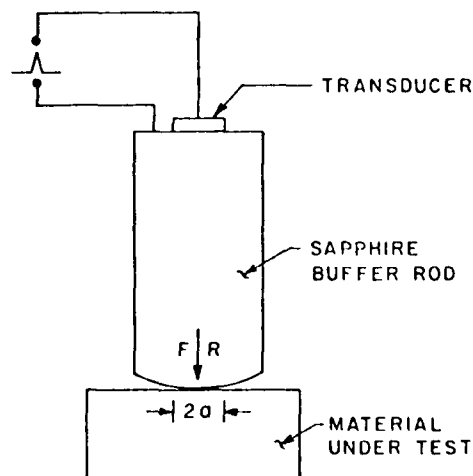
It has been necessary during the course of our research to develop several new types of transducers for nondestructive testing. The best commercial transducers available exhibit broad bandwidth but are usually highly inefficient. Good surface wave transducers are not easily available; transducer arrays for imaging were required, and extremely high frequency transducers for work on ceramics were needed. In addition, we have been interested in developing transducers which could produce a uni-polar pulse. It has therefore been necessary to develop design theory for transducers and to improve the technology for making them. This has involved a careful study of bonding techniques and the use of thin film technology which in the past has been widely employed for acoustic surface wave devices.

PISTON TRANSDUCERS

We have recently published a paper on the design of piston transducers for use in medical and NDE applications,¹ so we will not describe these transducers in much detail. The basic philosophy of design of our low frequency transducers intended for excitation of waves in water has been to improve the efficiency of excitation of waves from the high impedance piezoelectric transducer material to the low impedance water medium by using one or more quarter wavelength matching layers. This provides a broadband match with two way conversion efficiencies as low as 3.5 dB. This measurement was carried out using an electrical input, reflecting the emitted wave from a perfect reflector back to the transducer, then determining the electrical output into a 50 ohm load. At the same time, the transducers gave an excellent and compact impulse response. This basic philosophy has also been used in our transducer array designs.

When one is interested in transduction directly into solid materials which have an impedance close to that of the transducer material, quarter wavelength matching layers are not required. So at low frequencies, we have made transducers which are bonded to an aluminum buffer rod and demonstrated good broadband response and efficiency. We have carried this philosophy into the design of transducers operating in the 50 to 500 MHz frequency range, which is intended for examining ceramics. For very high frequencies, we employ a thin film technology, illustrated in Fig. 1. A gold film is laid down on a sapphire buffer rod on which a ZnO layer one quarter to one half wavelength thick is laid down by rf sputtering; the ZnO layer, in turn, has a small electrode, which defines the diameter of the beam, bonded

it on top of it. This forms a broadband transducer whose characteristics are shown in Fig. 2. The transducer is contacted to a ceramic work piece by arranging that the front surface of the sapphire buffer rod has a radius of the order of 20 cm. Under relatively small forces of the order of 50 pounds, this produces a Hertzian contact with a diameter of the order of 1 mm on the ceramic surface, which has a reflection coefficient of the order of .1. This is large enough to allow a well-defined high frequency cylindrical beam operating in the 100 to 300 MHz range to be passed through it. Such transducers give a return efficiency of the order of -20 dB.



$$\begin{aligned} R &= 20 \text{ cm} \\ 2a &= .1 \text{ cm} \\ F &= 172 \text{ N} \approx 39 \text{ Lbs.} \end{aligned}$$

Fig. 1. Illustration of a ZnO transducer on a buffer rod.

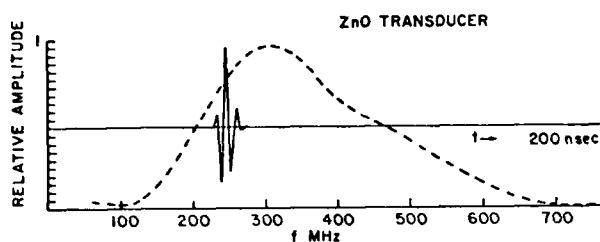


Fig. 2. The pulse and frequency response of a ZnO film transducer.

The ZnO technology is at its best for use with frequencies higher than 200 MHz. Otherwise because the thickness of the film must be chosen for either a quarter or half wave resonance, the films are required to be too thick ($> 8 \mu\text{m}$) to be conveniently deposited. So it is then necessary to use a different type of technology in which a layer of single crystal lithium niobate (LiNbO_3) or a piezoelectric ceramic is lapped down to the requisite thickness. We have made transducers of this kind for use in the frequency range from 10 to 300 MHz, but the technology is most convenient for 50 or 100 MHz transducers. One problem with this technology is that the bonding layer between the piezoelectric material and the buffer rod should be very thin, preferably having an acoustic impedance comparable to the materials to be bonded. We have employed an indium bonding technique for this purpose. This involves depositing gold layers approximately 1000 Å thick on the two surfaces to be joined. Then the two mating pieces are placed in a vacuum system, and indium layers of the order of 1000 Å are deposited on top of the gold layers. The two mating pieces are then pressed together, while still in the vacuum, and form a diffusion bond at room temperature. This diffusion bond has excellent impedance matching properties; in fact, the technique has been used up to 10 GHz by groups in several laboratories.

An illustration of the response of a 50 MHz transducer made this way is shown in Fig. 3. Typical losses of 50 MHz transducers and 200 MHz transducers are less than 10 dB from input to output with a perfect reflection from the end of the buffer rod. We have used buffer rods of sapphire and of silicon nitride ceramic. We employ LiNbO_3 for the higher frequency transducers because it is the ideal material for the purpose. But its dielectric constant is not large enough for a low enough impedance transducer at 50 MHz. In this case, the best material is potassium sodium niobate (PSN) ceramic which has a dielectric constant of 300 to 400, as compared to LiNbO_3 which has a dielectric constant of 39. We have made both shear wave and longitudinal wave transducers with these materials; we have also been able to make good longitudinal and shear wave contact through Hertzian contacts on the end of the buffer. This has been very convenient, because for NDE of ceramics up to 300 MHz, shear wave transducers cannot be made with a thin film technology. It has also been extremely convenient for low frequency experiments where we wish to make a transducer that can be moved from point to point easily under computer control. No grease is needed at the contact, and the forces required between the transducer and the

substrate of interest are relatively low.

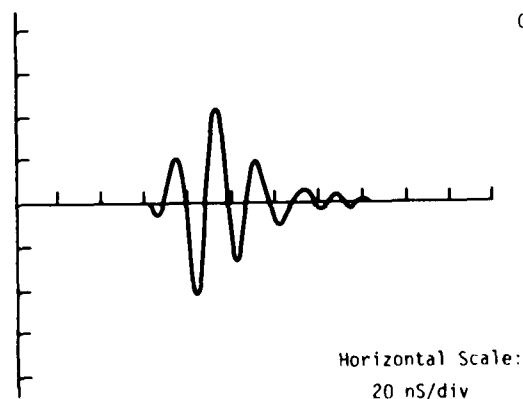
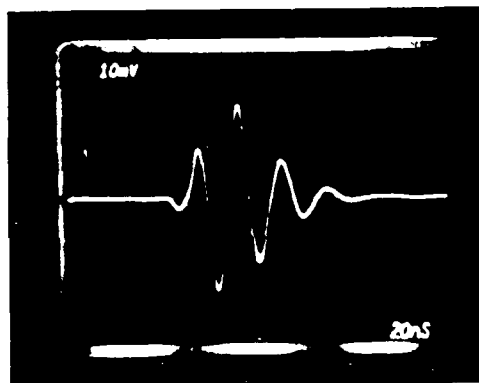
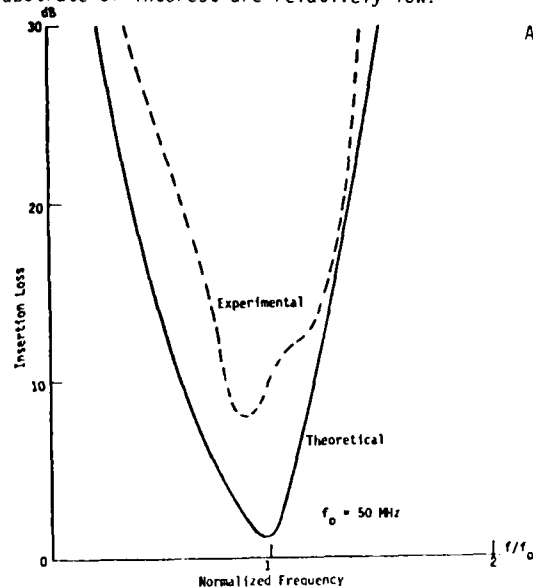


Fig. 3. (A) Insertion loss versus normalized frequency plot of a typical PSN/fused SiO_2 transducer (50 MHz center frequency); impulse response of a typical PSN/fused SiO_2 transducer (50 MHz center frequency) (B) experimental impulse response, and (C) theoretical impulse response.

TRANSDUCER ARRAYS

The design of transducer arrays for acoustic imaging systems is a more severe problem. The requirements are for broadband efficient operation, each element being able to excite a beam with an angle of acceptance which is possibly as large as $\pm 50^\circ$; furthermore, all the array elements must be identical in their frequency and amplitude response. Two types of arrays are required: one which can excite a wave in water, and the other which can excite either longitudinal, shear, Lamb, or Rayleigh waves directly on metal or ceramic substrates. So far, we have mainly concentrated on transducers which can excite waves in water and then used mode conversion for excitation of various types of waves in metals. More recently, we have constructed a different type of array, the edge-bonded transducer array, which is far easier to make than the first alternative, provides better efficiency, and, we believe, is the fore-runner of a large class of a range of new types of transducers.

An illustration of the basic form of the arrays used for exciting waves in water is shown in Fig. 4. The individual PZT ceramic elements operate at a center frequency of the order of 3 MHz with an octave bandwidth and are approximately .3 mm wide \times .5 mm high. In addition, they have one or two quarter wavelength matching layers, typically glass and epoxy, of the same width laid down upon them. The arrays are made by epoxy bonding the three layers together. The PZT ceramic element is bonded to a backing of tungsten epoxy or other filled epoxy. Individual elements are constructed by diamond sawing slots into the medium down to the backing. A thin layer of plastic such as mylar is bonded to the front surface to protect the elements from water. The array elements must be thin in order to give a large angle of acceptance and to avoid transverse resonances which can interfere with the broadband operation and reduce the efficiency.

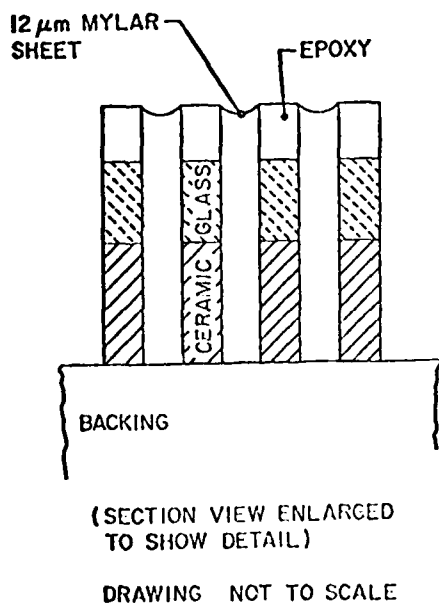


Fig. 4. Assembly drawing of longitudinal wave transducer array.

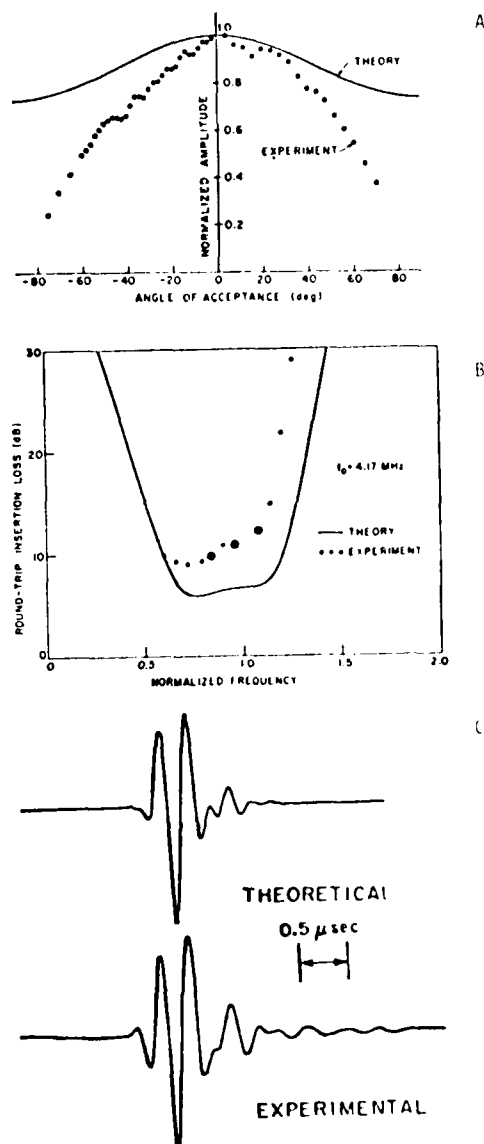


Fig. 5. (A) Comparison of theoretical and experimental angular acceptance of one element of test array. Element dimensions are $0.476 \text{ mm} \times 0.18 \text{ mm} \times 1.27 \text{ cm}$. Glass thickness is 0.305 mm . Epoxy thickness is 0.109 mm . Mylar face plate is 0.0127 mm thick; (B) Comparison of theoretical and experimental insertion loss of one element of the same test array as in (A); (C) Comparison of theoretical and experimental impulse response of element of the same test array as in (A).

Arrays of this type have proved to be extremely difficult to make reliably, basically because of the fragility of the elements and the many steps involved in their manufacture. Response characteristics of some of our better performing array elements of a double quarter wavelength matched system are shown

in Fig. 5. Systems of this type have been employed in our acoustic imaging device and are the ones used for demonstrating most of our imaging in water. We employ these kinds of arrays to excite waves in metals by exciting the waves at an angle to the metal surface as shown for Rayleigh waves in Fig. 6. This has enabled us to carry out imaging using Rayleigh waves and using shear waves in metals.

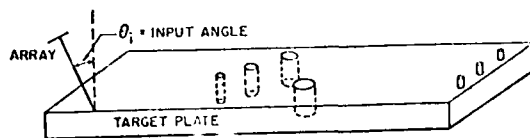


Fig. 6. A schematic of the setup used to excite Rayleigh waves in target plates from an array in water. For Rayleigh waves in aluminum, the angle $\theta_i \approx 28^\circ$.

The problems of mode conversion have become more severe as we have improved our imaging systems. The difficulty is that the mode conversion process introduces aberrations into the image because of the differences in velocity between the waves in water and the waves in the metal so that as the angle of attach of the array entering the metal is changed, the time and phase delays of the arrays change slightly. This makes the problem of the design of the imaging system very difficult. It was not a problem in our earlier systems; it has only become a problem now that the imaging systems have definitions of the order of .5 mm. Accordingly, we have designed a new type of imaging array, the edge-bonded array illustrated in Fig. 7, which we believe shows great promise. This array is used to excite surface waves on a metal substrate. A ceramic transducer is epoxy-bonded to an aluminum substrate as shown in Fig. 8. Thin film electrodes are deposited on the back of the ceramic, which is itself approximately a half Rayleigh wavelength thick. The electrodes are themselves approximately one wavelength long in the direction perpendicular to the top surface of the metal and ceramic. These electrodes, therefore, efficiently excite a Rayleigh wave whose penetration depth is of the order of one wavelength. The individual electrodes themselves are approximately one wavelength wide and are separated from each other by a gap of the order of a wavelength in which a grounding strip is deposited, to shield the individual array elements, one from the other. Because the impedance match between the ceramic and the metal is fairly close, a wave excited by a single electrode, which forms the array element, does not reflect back and forth in the ceramic, thus avoiding coupling the elements together. So the elements do not need to be slotted.

The response characteristic of this array is shown in Fig. 8 where it will be seen that the angle of acceptance is $\pm 35^\circ$, and the bandwidth of the array is of the order of an octave; the return echo efficiency is of the order of 10 dB. By using the array in the coupling configuration shown in Fig. 8 it is possible to transfer energy from the substrate in which the wave is excited to a neighboring identical substrate material. Two substrates are placed parallel to each other, with a thin layer of plastic between them, the layer of plastic being of the order of 5 mm to 1 cm long. Transfer efficiency from one substrate to the other has been measured to be approximately 2 dB. As will be seen, the

manufacturing process of this array is very simple; furthermore, by backing it with epoxy, one can damp out most of the unwanted resonances fairly easily, and the array response appears to be of good quality.

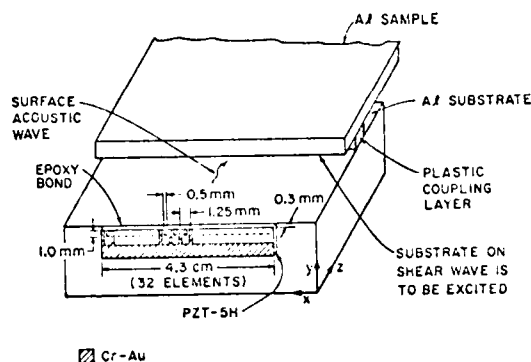


Fig. 7. The edge-bonded 32-element surface acoustic wave transducer array.

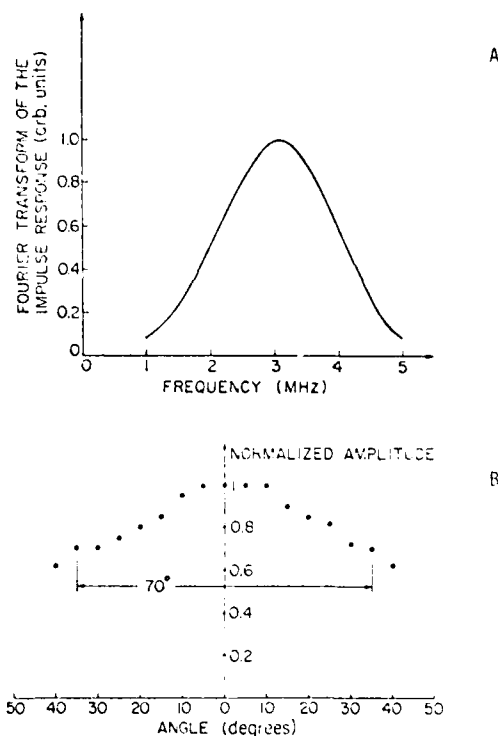


Fig. 8. (A) The impulse response and its Fourier transform of 22 elements of the array, excited in parallel, 0.5 $\mu\text{sec}/\text{Div}$ for the response; (B) the angular response of a single transducer element.

WEDGE TRANSDUCERS

The edge-bonded transducer is one example of the type of transducer that can be used for exciting surface waves. More generally, the classical tech-

nique is to use a wedge-type of transducer in which a bulk wave in a medium (the wedge) in which the wave velocity is less than that of the surface wave on the substrate of interest v_R is employed to excite a surface wave, as shown in Fig. 6. If the angle of incidence θ is chosen so that $v_w = v_R \sin \theta$, good coupling to the surface wave can be obtained. We have carried out a detailed design of such a wedge transducer, for a solid wedge rather than water, and optimized the choice of the wedge material for particular substrates. We have been employing such transducers normally for examining cracks in metals, ceramics, and glass and have been able to calibrate them accurately. These transducers typically exhibit a one-way efficiency of the order of 7 to 10 dB. There is some problem still with unwanted spurious responses in the wedge beyond the transmit main pulse. Typically this can be avoided by using two transducers, one a transmitter and one a receiver, placed at a slight angle to each other.

A technique has also been employed for exciting a surface wave one one substrate and transferring the wave over to a neighboring substrate. This is particularly convenient for high frequency work because it is then possible to design various types of surface wave transducers which are easy to construct at high frequencies. We have done this by making interdigital transducers on LiNbO_3 and placing the substrate at the correct angle to the substrate on which the wave is to be excited, using water as the transfer medium. This type of transducer has been used for examining ceramics with surface waves at frequencies of 64 MHz and 100 MHz.

THE UNIPOLAR TRANSDUCER

Finally, we have been developing unipolar transducers to excite a pulse which is basically of one sign. The reason for our interest in this type of transducer is because we wish to measure slight tapers of acoustic impedance of the material. It can be shown that if one excites a transducer with a pulse of the form $F(t)$, the return echo from a medium whose impedance varies with distance $Z(x)$ will be of the form

$$\begin{aligned} r(t) &\approx \frac{\alpha}{Z} \int \frac{dz}{dx} F(t - 2x/v) dx \\ &\approx \frac{2\alpha}{Zv} \int Z[\partial F(t - 2x/v)/\partial x] dx \end{aligned} \quad (1)$$

Our aim is to measure stress, which affects the acoustic impedance of the wave, by this technique. It is apparent from the form of the integrals that if the stress varied linearly through a material, as in a sample that was under bending stress, there would be no contribution from a bipolar pulse, but a unipolar pulse would give a good contribution to the return echo which would give a direct measure of the impedance gradient. Alternatively, a step function of applied stress transmitted from the transducer would measure the impedance directly.

We have been able to employ simple commercial transducers to produce unipolar pulses. The basic requirement is to have a well-matched backing and excite the transducer with a step function of voltage with a leading edge which need not rise extremely fast. To detect the unipolar pulse without differentiating it, we have shown that all that is

required is a receiving transducer of the same type connected to a very high impedance load of much higher electrical impedance than the transducer in the frequency range of interest. Two pictures of unipolar pulses obtained by this technique using identical transmitting and receiving transducers placed against each other are shown in Fig. 9. In Fig. 9a, the input pulse has a rise time comparable to the transit time of an acoustic wave through the transducer. In Fig. 9b the rise time is much longer than the transit time T . In this latter case, essentially a step function of stress is generated, which can be used directly for impedance measurements.

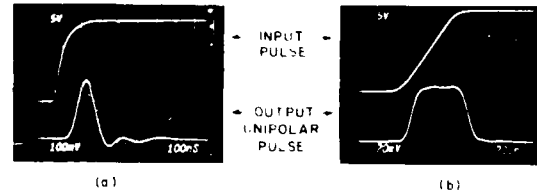


Fig. 9. The unipolar pulse generated by a commercial Panametrics 5 MHz transducer and received on an identical transducer with a high impedance electrical load. (A) Rise time of input pulse ≈ 100 ns (transit time in transducer); (B) Rise time of input pulse $\gg 100$ ns.

The configuration of using the two transducers is not necessarily the most convenient one because of the difficulty looking at reflected echoes this way. We have constructed a two layer transducer, one element being the receiver, one the transmitter. We had originally attempted to use a single transducer with appropriate electronics in which the receiver was of high impedance, but the transmitter was of low impedance; the problem here was to get rid of the transmitter pulse at the time the receiver was turned on. This proved to be too difficult, so it was better to make a two layer transducer. Initial results with a two layer transducer are encouraging, but further development is required. We will be using the indium bonding technique for this purpose which itself solves most of the problems of careful impedance matching required for these transducers.

CONCLUSION

We have described here a wide range of transducer designs required for nondestructive testing. Much remains to be done to limit spurious responses and to improve the ease of manufacture and design of transducer arrays.

ACKNOWLEDGMENTS

This work was supported by the Center for Advanced NDE operated by the Rockwell International Science Center for the Advanced Research Projects Agency and the Air Force Materials Laboratory under Contract RI 74-20773, EPRI Contract RP 609-1, the National Science Foundation under Grant ENG 77-28528, and by the Office of Naval Research Contract N00014-78-C-0283.

REFERENCES

1. C. S. DeSilets, A. R. Selfridge, and G. S. Kino, "Highly Efficient Transducer Arrays Useful in Nondestructive Testing Applications," 1978 Ultrasonics Symp. Proc., pp. 111-116.
2. P. D. Corl, P. M. Grant, and G. S. Kino, 1978 Ultrasonics Symp. Proc.
3. C. S. DeSilets, J. Fraser, and G. S. Kino, 1975 Ultrasonics Symp. Proc. pp. 148-152.
4. C. S. DeSilets, Ph.D. Dissertation, Stanford University, 1978.
5. C. S. DeSilets, J. D. Fraser, and G. S. Kino, IEEE Trans. Sonics and Ultrasonics SU-25, #3, May, 1978, pp. 115-125.

SUMMARY DISCUSSION
(Gordon Kino)

Harold Berger (Session Chairman--Nat. Bureau of Standards): Questions?

Wolfgang Sachse (Cornell University): Aren't the ideas of impedance-matching and bandwidths using quarter-wave layers inconsistent because the quarter-wave layer is going to be operative only at certain frequencies?

Gordon Kino: You could have several layers.

Wolfgang Sachse: Are these layers in series?

Gordon Kino: In series. With two layers from ceramics to water we have $3/4$ to 8 to 3 to 1.5.

Wolfgang Sachse: So, it's analogous to an acoustic horn, in other words?

Gordon Kino: Yes. Or to a microwave transmission line. There are lots of examples in the literature. It's like a tapered transmission line with a few steps, and you can design it to be maximumally flat and so on.

Harold Berger: Thank you.

Chris Fortunko (Science Center-ADL): Why do you need to have the receiving transducer to detect the unipolar pulse? I can see why you need the transmitting transducer.

Gordon Kino: Well, we are not going to measure a stress gradient. We will actually measure the differential of the stress gradient. In a uniform stress gradient, we will get an output which is virtually constant, say. If I differentiate that constant, which I will do if I use a low-impedance load which differentiates the output, I will get nothing. I may be able to integrate up again electrically, but noise-wise I think that's a bad way to go.

Chris Fortunko: To integrate is normally a fairly harmless procedure.

Gordon Kino: Granted. We may be using a sledge hammer to crack a nut maybe. You may be right. I was scared that eventually I would be losing my signal.

Harold Berger: Thank you again, Gordon.

#

NDE APPLICATIONS OF THIN FILM ULTRASONIC TRANSDUCER ARRAYS:
PROGRAMMABLE FILTER, SCANNED RECEIVER, AND POWER TRANSDUCER

K. Chuang, A. Lee, and R.M. White
Department of Electrical Engineering and Computer Sciences
University of California
Berkeley, California 94720

ABSTRACT

Piezoelectric zinc oxide films typically ten microns thick have been deposited in a planar magnetron rf sputtering system on a variety of substrates, including silicon and thin stainless steel, to make ultrasonic transducers for acoustic emission and NDE applications. Waveforms from a 10 MHz commercial NDE transducer and a transducer employing the zinc oxide on stainless steel sheet are shown for comparison. Designs for a coherent programmable receiving array and a transducer array responding to incident ultrasonic power are discussed.

INTRODUCTION

The ability to deposit thin films of piezoelectric insulators such as zinc oxide makes possible ultrasonic transducers having configurations which one cannot readily fabricate from bulk piezoelectric crystals. Examples have been given in previous reports on this project [1] where thin films of zinc oxide have been deposited by rf sputtering either in the gate region of a field-effect transistor (the PI-FET structure, as introduced by Muller and co-workers [2]) or adjacent to an FET to whose gate an electrode on the piezoelectric is connected. In both structures, the transistor provides electrical impedance transformation and possible amplification of the voltage from the piezoelectric. In addition, other electronic gating and mixing functions may be performed with the transistor, as reported earlier [1]. Further, if the zinc oxide is well isolated with thin silicon dioxide, one may observe response to static strain: in one test of 17.8 hours duration, no decay was observed in the decrease of source-drain current caused by the static flexure of a PI-FET in which the zinc oxide was so protected. The very high effective gauge factor observed in this test was about 6000 volts/unit strain.

In this paper we discuss two new developments in connection with transducers based on thin sputtered piezoelectric films of zinc oxide, and then consider the practical device consequences of these developments.

PLANAR MAGNETRON SPUTTERING

Recently we have modified our rf zinc oxide sputtering system by replacing the convention target (source) assembly with a planar magnetron assembly, as sketched in Fig. 1. In the modified sputtering system, because of the crossed electric and magnetic fields, there is reduced bombardment of the substrate on which the zinc oxide is depositing, and so there are consequently less heating of the substrate and lower interfacial stresses resulting from temperature excursions of the substrate and film which usually have different thermal expansion coefficients. Even more significant is the larger growth rate of the films which permits significant film thicknesses to be

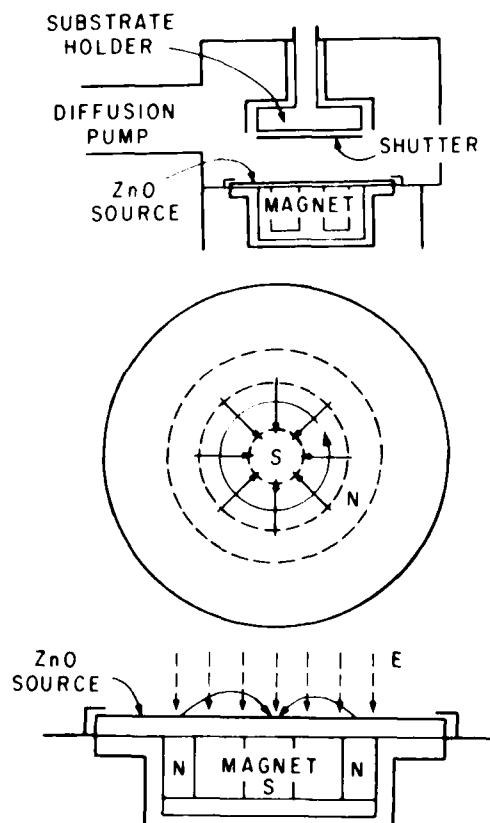


Fig. 1. Planar magnetron sputtering system shown schematically. Top sketch shows cross-section through vacuum chamber and target (source of zinc oxide) under which permanent magnets are located, and substrate holder (where one places material onto which sputtering occurs). Crossed electric and magnetic fields, indicated by dashed and solid lines respectively in middle and bottom sketches, cause electrons to bombard source and so increase rate of sputtering over values achieved with non-magnetron RF sputtering system.

achieved in shorter times than were previously possible; and, because of the more rapid deposition, the films suffer less contamination. Figure 2 shows a 10 μm thick film grown with this system at a rate of about 2 μm per hour; rates to 4 or 5 μm per hour are possible and are compatible with good growth and strong piezoelectricity as exhibited by the film of Fig. 2.

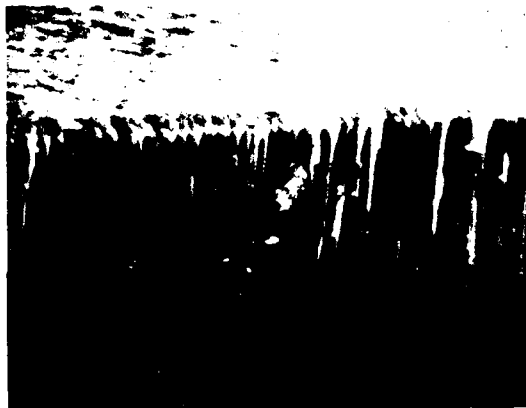


Fig. 2. Cross-section of zinc oxide film produced in planar magnetron sputtering system sketched in Fig. 1. In this scanning-electron microscope picture, the columnar structure of the ten-micron thick zinc oxide on a silicon substrate (dark region at bottom of photo) is indicative of highly-oriented piezoelectric zinc oxide growth. (Photo courtesy of Shu-Sheng Shiang, Materials Science and Engineering Department, U.C. Berkeley.)

PIEZOELECTRIC FILMS ON THIN METAL SHEETS

The second development is the ability to deposit piezoelectric zinc oxide films on thin metallic substrates to form transducers or arrays which are mechanically strong while being acoustically "thin". We have obtained 10 μm thick zinc oxide films exhibiting strong piezoelectric coupling by sputtering directly onto thin stainless steel stock only 0.002 inches thick. Because the supporting sheet is so thin, the resonances associated with the transducer substrates are pushed to frequencies much higher than those used in conventional NDE, and so the transducers should have smooth frequency responses. A transducer for bulk waves is shown in top view in Fig. 4. Figure 5 compares the output of a conventional NDT transducer (Fig. 5a) with the output from the transducer of Fig. 5 (in Fig. 5b) when tested in a water bath. Note the shorter duration of the response from the ZnO transducer suggesting less ringing.

With this technique it appears possible to make individual transducers in a wide variety of shapes and sizes, so as to fit well mechanically with the structures in which they are to be used. It is possible to include an electrically active element immediately adjacent to these transducing films, using either a hybrid approach and including the active semiconductor device within the

transducer package, or using packaged semiconductor devices outside the transducer. These transducers should be relatively inexpensive to make and they should be quite reproducible.

An analysis of the transducer response has been made and calibration tests for comparison with this predicted response are in progress.

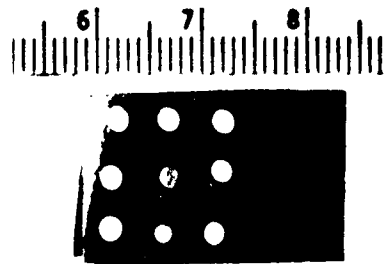


Fig. 3. Top view of stainless steel shim stock, 0.002 inches thick, onto which piezoelectric zinc oxide has been sputtered. The bright circles are evaporated aluminum top electrodes. Scale is in centimeters.



Fig. 4. Top view of a bulk wave transducer made using a portion of the zinc-oxide-coated stainless steel shim stock shown in Fig. 3. Coaxial cable lead has been connected to circular aluminum electrode by conventional thermocompression bonding. Scale is in centimeters.

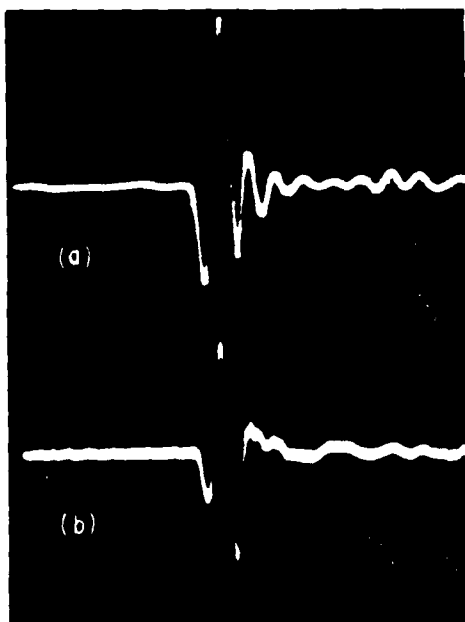


Fig. 5. Output of two ultrasonic transducers to signal produced in a water bath by a pulsed commercial NDT 10 MHz transducer. (a) Response of a commercial NDT transducer. (b) Response of zinc oxide transducer shown in Fig. 4. Horizontal scale: 0.2 μ s/division. Vertical scales are arbitrary owing to different electrical loading conditions in (a) and (b).

ARRAY APPLICATIONS OF THE TRANSDUCERS

Three different applications of arrays of the thin-film transducers have been considered: programmable filters, scanned coherent ultrasonic receiving arrays, and an incoherent array which responds to total incident ultrasonic power independent of the phases of the excitations of individual array elements. The first of these has been discussed previously [1] and is now being fabricated; it will not be considered further here. The latter two applications are described below.

Coherent Scanned Receiving Array - Figure 6 shows how a number of zinc oxide transducer stripes could be connected with dual-gate FETs to make a programmable coherent scanned ultrasonic receiving array. Both the amplitude and sign of the contribution of each element can be varied by application of the proper voltages to the second gates of the FETs associated with each element. The directivity of such an array would be the product of the array directivity factor with the directivity factor for each element of the array. If the elements have widths which are small compared with the ultrasonic wavelength, then this latter directivity factor will approach a cosine function of the angle of incidence of the incoming waves. An initial measurement of the directivity of a single zinc oxide elementary transducer on thin metal showed qualitatively the expected variation with angle of incidence. An entire array is now being fabricated for test.

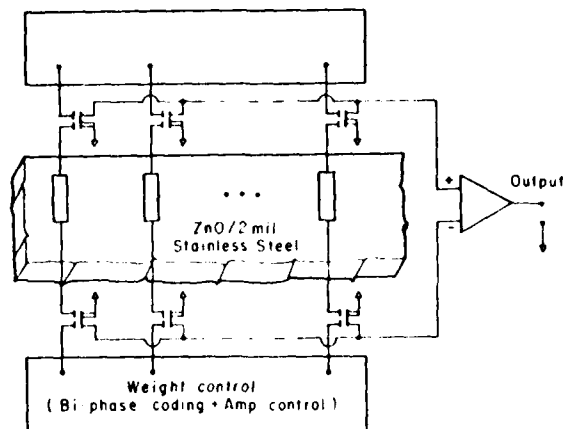


Fig. 6. Schematic diagram showing how an electronically programmable coherent ultrasonic scanning array could be constructed for use in a water bath or in contact with a solid.

Power Transducer - In applications where one wishes to have a large-area receiving transducer so as to achieve a large sensitivity, one may sum coherently the electrical outputs from all the array elements, but the transducer will then have a directivity pattern with an undesirably large number of extrema. If instead, the outputs of array elements are envelope detected and then added, the desired summation of output occurs without the highly complex directivity pattern being formed. If a nonlinear element is used at the output of each array element before the envelope detection and summation, an output proportional to total incident ultrasonic power can be obtained. We refer here to such a transducing array as a "power transducer".

The nonlinear properties of dual-gate FETs can be used in one realization of a power transducer. The nonlinearity to be employed appears in the input-output characteristics plotted in Fig. 7. Note that for this depletion-mode dual-gate FET, the drain current (output) is a strongly nonlinear function of the voltage on the first gate (the gate to which the signal is applied) for values of that voltage near zero. The degree of nonlinearity can be controlled over a fairly wide range by adjustment of the bias on gate no. 2, as Fig. 7 show. Thus, for a high degree of nonlinearity with this FET, one might use +2.0 volt bias on gate no. 2.

The circuit utilizing these FETs is shown in Fig. 8. Analysis shows that with +2.0 volt gate no. 2 bias, the output from each FET consists primarily of an amplified voltage at the fundamental frequency (the frequency of the incoming ultrasonic wave), and two terms connected with the second-order nonlinearity: one term is at twice the fundamental frequency and the other is a quasi-dc term which has frequency components associated with the envelope of the incident ultrasonic signal. (For example, if the incoming ultrasonic signal were an 8 MHz carrier which was amplitude modulated by a rectangular pulse of 1 μ s duration,

the quasi-dc term would have components around 1 MHz, while the fundamental and second-harmonic terms would be at 8 MHz and 16 MHz respectively.) The amplitudes of both the double-frequency and the quasi-dc term are approximately proportional to the square of the amplitude of the incident wave and hence to incident ultrasonic power. If the quasi-dc voltages are summed, the result is approximately proportional to total power incident, and the relative phasings of the waves at each transducing element do not affect the sum.

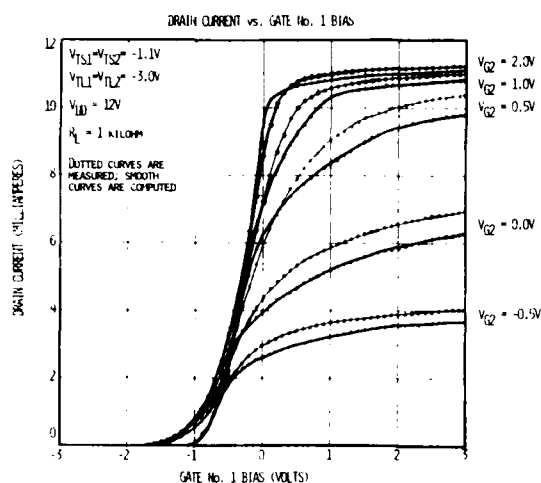


Fig. 7. Dependence of drain current on gate no. 1 bias for dual-gate FET. Bias of second FET gate is parameter.

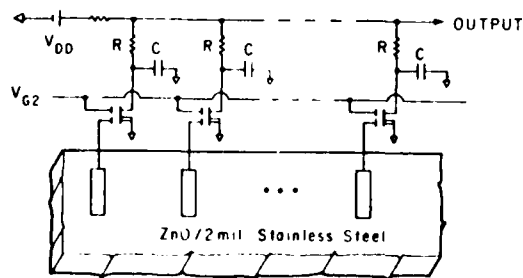


Fig. 8. Schematic diagram of an ultrasonic receiver array whose output ac voltage would be proportional to total acoustic power incident on the array elements of the array. Note lowpass RC filters at the outputs of the FETs.

An array to be used either in a water bath or on the surface of a solid is being built for evaluation. Meanwhile simulations of the summing and related calculations have been carried out. Figure 9 shows the square-root of the quasi-dc term plotted versus the amplitude of the electrical signal input to gate no. 1 of a dual-gate FET. This plot shows that, at low input signal levels, the amplitude of the quasi-dc output is indeed proportional to the square of the input, as expected. Finally, Fig. 10 shows test results for a simulation of two elements of such a power transducer array. The signal which occurs at the same time in each of the four waveforms was the source-drain current of a dual-gate FET responding to the output of an NDE transducer driven by a 10 MHz acoustical input wave train in a water bath. The other signal in each case is obtained by applying an electrical 10 MHz signal to the first gate of a dual-gate FET connected as indicated in Fig. 8. Lowpass RC filters were used at the outputs of the two FETs, and the filtered outputs were summed. One notes, as expected, that where the two pulses are coincident in time, they simply add without showing the sharp changes of level one would find if coherent waveforms at the fundamental frequency were summed.

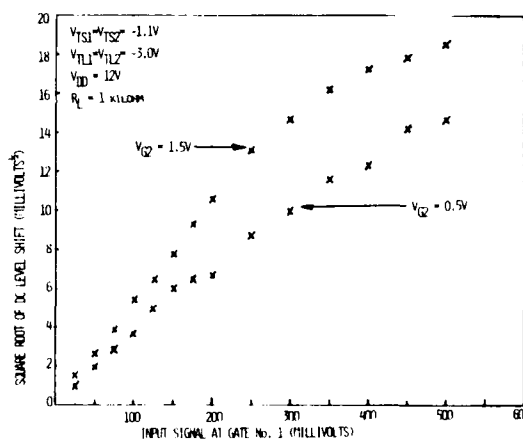


Fig. 9. Square root of shift in drain current versus amplitude of input signal at gate no. 1 of dual-gate FET for two different gate no. 2 biases. Note the linear dependences for small input amplitudes.

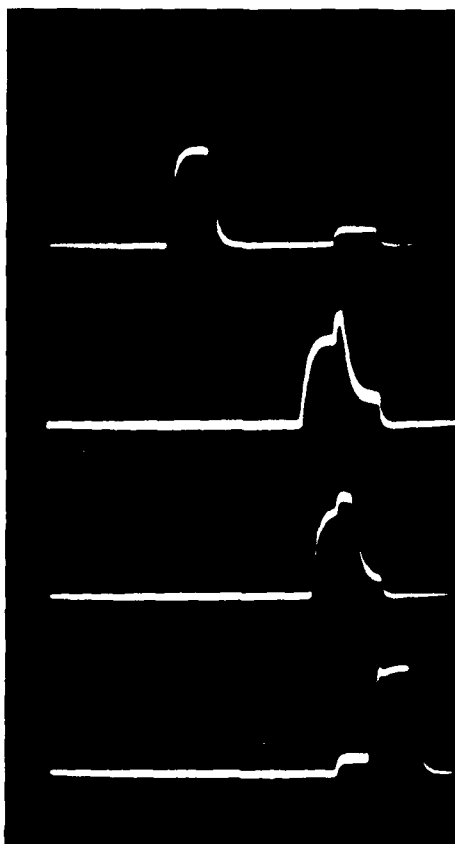


Fig. 10. Test results for simulation of power transducer array. Output of circuit simulating two elements of the array of Fig. 9 are shown, plotted versus time (20 μ s/division). See text for details.

REFERENCES

- [1] R.M. White, S.H. Kwan, K. Chuang, and R.S. Muller, "Integrated ultrasonic transducer", Proc. ARPA/AFML Review of Progress in Quantitative NDE, July 17-21, pp. 377-380, (1978).
- [2] K.W. Yeh, R.S. Muller, and S.H. Kwan, "Detection of acoustic waves with a PI-DMOST transducer", Proc. 8th Conference (1976 International) on Solid State Devices, Tokyo, 1976, Japan J. Appl. Phys. 16, Supplement, 16-1, pp. 527-531, (1977).

SUMMARY AND CONCLUSIONS

Transducers composed of thin piezoelectric zinc oxide films with associated transistors can be used as individual bulk-wave transducers or in arrays for acoustic emission and NDE applications. With the planar magnetron rf sputtering apparatus, films of zinc oxide tens of microns thick can be deposited. The deposition on thin sheets of stainless steel and the use of that structure as a bulk-wave transducer have been demonstrated.

ACKNOWLEDGEMENTS

Research sponsored by the Center for Advanced NDE operated by the Science Center Rockwell International, for the Advanced Research Projects Agency and the Air Force Materials Laboratory Contract F33615-74-C-5180

SUMMARY DISCUSSION
(Dick White)

Don Eitzen (Session Chairman): I think we have time for a couple questions. Please remember to identify yourself and your organization.

Wolfgang Sachse (Cornell University): The one picture that you showed with the ten megahertz excitation, comparing it to a piezoelectric transducer, is that typical of the bandwidth this thing is capable of, or what in fact governs the bandwidth of the response?

Dick White: I think it should be a very broad-band transducer because it's quite thin compared to the wavelength. We have used the thin film 167 at kilohertz and also at ten megohertz. We very much need to get a good calibration.

Gordon Kino (Stanford University): I have a couple of questions. First, how do you think this compares with PVF_2 , and second, if you are going to put zinc oxide down and connect it to FET's, why don't you use zinc oxide or silicon and be finished with it?

Dick White: When we put the zinc oxide on a reasonably thick substrate, such as a standard silicon wafer, we see a lot of ringing.

Gordon Kino: But you could thin the silicon down.

Dick White: We could do that, but I suspect the metal may have some practical advantages in terms of ruggedness and so forth. For example, I have worked, in fact, two millimeter thick silicon. You can bend it around at a 45-degree angle. But it also breaks. In terms of the PVT_2 , I think that one nice feature of the zinc oxide is that you deposit directly on a substrate. There is no problem of bonding. I'm not sure whether there is a bonding problem. Also, the zinc oxide can work over a much wider temperature range. I know that zinc oxide on one low-thermal expansion alloy has worked from minus 20 C to plus 80 C. I'm not sure what the limits are.

Tom Derkacs (TRW): You can deposit this in a shape other than a flat plane?

Dick White: The question is whether we could deposit it on other than a flat plane.

Tom Derkacs: A small band.

Dick White: I believe this could be done. You would have to put a shutter in the sputtering system, but certainly one can do that.

Don Eitzen: Thank you again, Dick.

#

ABSOLUTE ULTRASONIC MEASUREMENTS WITH PIEZOELECTRIC TRANSDUCERS

Wolfqang Sachse
Department of Theoretical and Applied Mechanics
Cornell University, Ithaca, New York - 14853

ABSTRACT

The absolute calibration of a piezoelectric transducer refers to the determination of the relationship between the electrical and acoustical quantities for a transducer coupled to a solid. It is shown how a well-characterized ultrasonic system, consisting of source, structure and receiver can be used to make such measurements for transducers operating as sources or receivers. Results are given, showing the effects of coupling between transducer and solid and the electrical characteristics of the associated source and receiver electronics.

This poster paper describes the principles and procedures for making absolute ultrasonic measurements with a piezoelectric transducer coupled to a solid. Publication of these results will be in the 1979 *Ultrasonics Symposium Proceedings* [1].

As described in a recent review article [2], the complete characterization of an ultrasonic transducer acting as source or receiver entails two parts. One part deals with the transduction process in which the relationship between electrical and mechanical quantities is established. The second deals with the characterization of the radiation field of the transducer. This paper concerns itself with measurements which characterize the transduction process of a piezoelectric transducer coupled to a solid.

INTRODUCTION

As elaborated in the review article by Sachse and Hsu [2], several assumptions need to be made in order to permit a ready characterization of the transduction process. As shown in Figure 1, a transducer operating as a source may involve processes which are not well understood or difficult to describe precisely. The excitation voltage and current imposed on a transducer result in a complicated distribution of time-dependent surface tractions and displacements (or velocities) each with longitudinal and shear components, acting over the transducer area on the specimen. Only when one makes the simplifying assumptions of mode uncoupling, field variable independency and linear system response does one find a simple matrix relationship between the electrical excitation parameters and the resulting mechanical excitation. Then, when restricted to a fixed specimen and electronics can a relationship between electrical excitation and produced mechanical force be written in terms of a linear transfer function equation in either the time- or frequency-domains,

$$F_0(t) = T_0(t) * V_0(t) \quad (1a)$$

or

$$F_0(\omega) = T_0(\omega) \cdot V_0(\omega) \quad (1b)$$

With similar assumptions, an analogous description is obtained for a transducer operating as a receiver,

$$V(t) = T(t) * U(t) \quad (2a)$$

or

$$V(\omega) = T(\omega) \cdot U(\omega) \quad (2b)$$

The above equations show that once the transfer function of a transducer is determined, the relationship between electrical and acoustical quantities

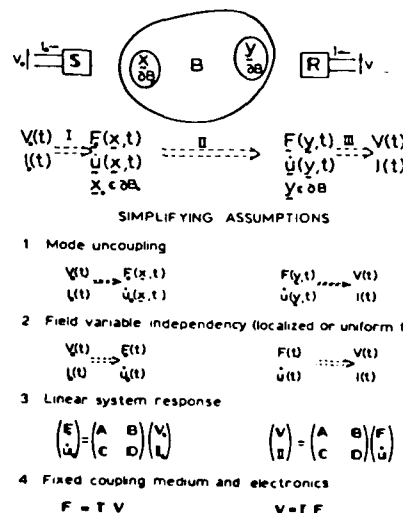


Figure 1 - Simplifying assumptions of the transduction process. (from Ref. 2)

ties across the transducer is established.

Recent experiments in which the deterministic aspects of acoustic emission have been studied have utilized a well-characterized ultrasonic system in which the characteristics of the source, structure and receiver can be independently measured or determined [3-5]. Here, the signals emitted by a known source (either electrical or mechanical) are propagated in a structure for which the impulse response is known. The signals are detected with a sensor whose transduction characteristics are also known. Such a system is over-determined, and thus it allows substitution of an unknown source or receiving transducer into the system and, provided that the

system is linear, the time- or frequency-characteristics of the transducer can be ascertained by linear signal deconvolution procedures.

METHOD

An ultrasonic system in which the various components comprising it are isolated is shown schematically in block form in Figure 2. When the

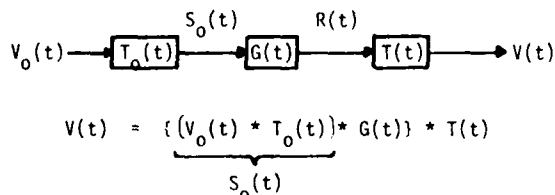


Figure 2 - A linear ultrasonic system.

excitation voltage, $V_0(t)$, is applied to the transducer whose transfer function is $T_0(t)$, the excitation force, $S_0(t)$, is produced in the specimen.

For cases in which the assumptions of mode uncoupling and field variable independency are valid, the impulse response of the structure $G(t)$, which depends on the type of source and receiving transducer, can readily be computed for any arbitrary locations of the transducers. The signal, $R(t)$, at any point is converted to a voltage, $V(t)$, by the receiving transducer whose transfer function is $T(t)$. Thus, for a linear, ultrasonic system, the received signal can be written as a convolution of the characteristics of each of the elements comprising the system, that is,

$$V(t) = V_0(t) * T_0(t) * G(t) * T(t) \quad (3)$$

Depending on the calibration to be done, the source used in the measurement may either be electrical (i.e. $V_0(t)$) or mechanical (i.e. $S_0(t)$) with the latter being used in place of the electrically produced excitation: $V_0(t) * T_0(t)$. In either case, a fast risetime excitation pulse works best. The propagating medium used, is a structure for which the theoretical impulse response is known. In the present experiments, a thick flat plate is used for which the impulse response has been computed by Pao, et al. [6]. An electrostatic, capacitive transducer or a special piezoelectric transducer was used as a displacement sensor having transfer characteristics $T(t) = A \delta(t)$ for some time interval.

Shown in Figure 3 is a comparison between the computed vertical displacements and the measured voltage of such a transducer when the excitation was a vertical step unloading directly under the receiver on the opposite side of the plate (i.e. plate epicenter). The agreement indicates how accurately the modelled source structure and receiver corresponds to the actual system.

MEASUREMENTS

Ultrasonic Force Function Determination - In order to determine the temporal characteristics of the force generated in a specimen by a source transducer, the signal $V(t)$ detected by a receiving transducer is measured and the transducer-generated force function is determined from

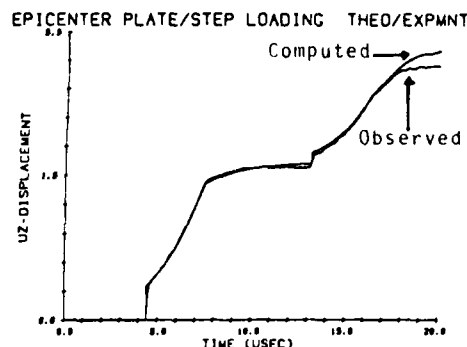


Figure 3 - Epicentral displacement: step unloading. Computed, observed.

$$S_0(t) = [G(t)]^{-1} * V(t) \quad (4)$$

To illustrate such a determination, ultrasonic signals were produced by a broadband longitudinal wave transducer which was shock excited with various electrical pulses produced by a pulser for which the output impedance could be adjusted between 5 and 250 Ω . The excitation voltage pulses ranged from -225 Volts/50 nsec to -325 Volts/100 nsec. The detected displacement signals were deconvolved according to Eq. (4) and the excitation forces, $S_0(t)$ determined. The results are shown below in Fig. 4.

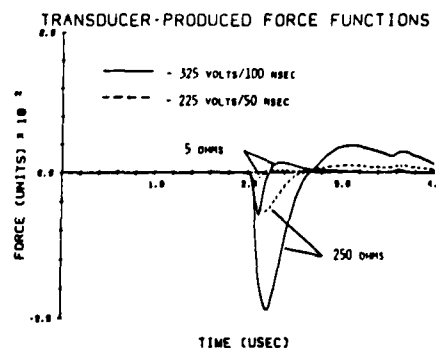
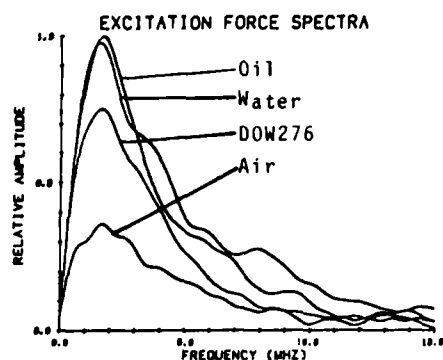
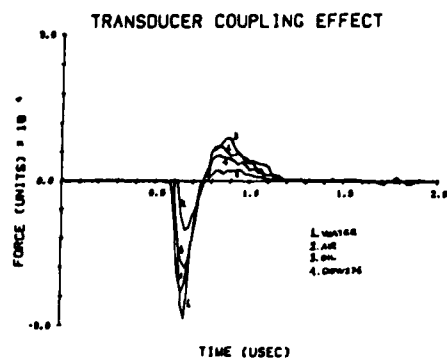


Figure 4 - Transducer-generated forces in a specimen of glass. Variable excitation voltage, damping.

To investigate the influence of transducer coupling on the generated ultrasonic excitation pulse, various couplants were used to attach a broadband longitudinal wave transducer to a glass plate. The couplants investigated were light-weight machine oil, water, DOW 276-V9, and air. The time-characteristics of the generated excitation forces produced in the glass specimen were determined again according to Eq. (4). These are shown in Figure 5(a). The force-time functions were transformed into the frequency domain to further investigate the transmission characteristics of these couplants. As shown in Fig. 5(b), the frequency characteristics of the generated ultrasonic forces appear to be quite similar for these couplant materials in this frequency range. These measurements suggest the possibility for systematically investigating the characteristics of various transducer



Figures 5(a) and 5(b) - Transducer Coupling Effect. couplant materials.

Source Transducer Transfer Function - As indicated previously, the transduction characteristics of a transducer coupled to a particular specimen and ultrasonic signal source can be specified in terms of its transfer function, $T_0(t)$. The transducer-produced ultrasonic force is given by

$$S_0(t) = V_0(t) * T_0(t) \quad (5)$$

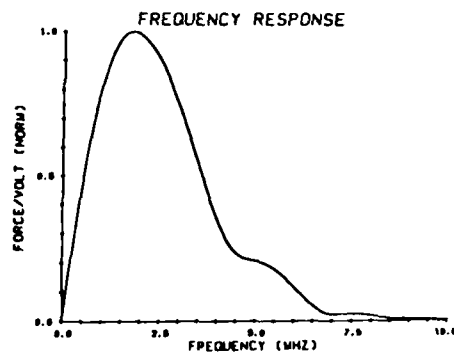
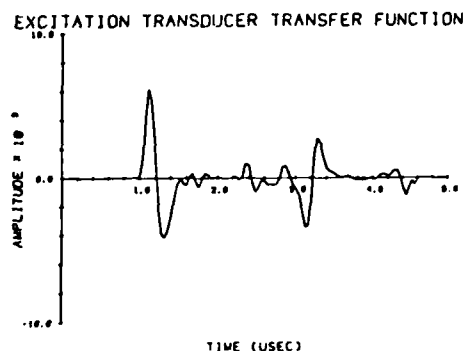
This force function can also be determined by using Eq. (4) to deconvolve the displacement signal detected at some point on the specimen. Thus, Eq. (4) and (5) can be combined to allow determination of the source transducer's transfer function, $T_0(t)$. This gives

$$T_0(t) = [V_0(t) * G(t)]^{-1} * V(t) \quad (6)$$

In applying Eq. (6), the inverse of the excitation voltage signal and the appropriate specimen impulse response are convolved with the signal detected by the receiving transducer which was again a displacement sensor. The device shown in Figure 6 incorporates the above ideas. It consists of a flat plate with a displacement sensor attached. It has been used in the transducer transfer function determination of several transducers. The transfer function determined for one broadband transducer is shown in Figure 7(a) and its corresponding frequency characteristics are in Figure 7(b). It is noted here that the vertical axes are in units of [Force/Volt].

To verify whether the transducer transfer function so obtained is correct, it was used to

Figure 6 - Transducer Calibrator device.



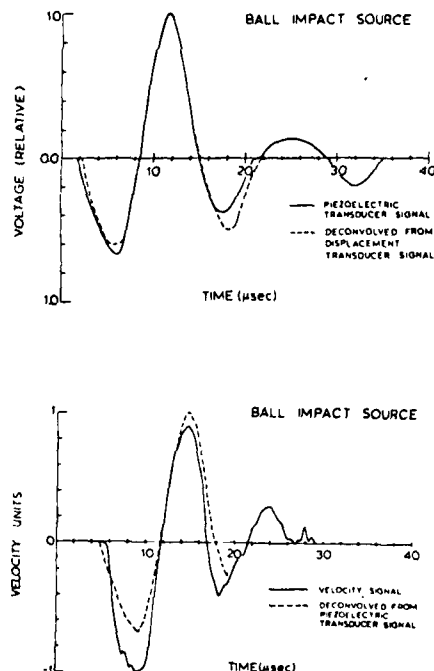
Figures 7(a) and 7(b) - Source Transducer Transfer function.

predict the displacement signal with Eq. (1) corresponding to other (arbitrary) excitation voltage signals applied to the source transducer. Figures 8(a) and 8(b) show the comparison between the predicted and the measured voltage (displacement) signals when the excitation was a 50 nsec shock pulse and a single cycle of a 2 MHz sine burst respectively. As an alternate check, a comparison was made between the ultrasonic source function, $S_0(t)$, computed by the convolution equation of excitation voltage and source transducer transfer function (Eq. (5)) and the source function obtained by deconvolution of the received displacement signals (Eq. (4)). Figures 9(a) and 9(b) show this comparison for a single-cycle and a four-cycle 2 MHz sine burst excitation respectively.

Receiving Transducer Transfer Function - The determination of the transfer function for a receiving

receiver.

As a check on the validity of the above procedure, another source was activated and the signals measured, in turn, by the displacement and piezoelectric sensor. By using the previously determined transfer function of the transducer (or its inverse) it is possible to convert one signal to another. Figures 11(a) and 11(b) show the results when this is done. In each case, a ball



Figures 11(a) and 11(b) - Piezoelectric transducer voltage signal measured by a displacement sensor, and actual voltage signal.

(b) Velocity signal measured by a piezoelectric transducer and actual velocity signal.

impact served as simulated source on an aluminum plate. Figure 11(a) shows the comparison between the detected piezoelectric transducer signal and the transfer function-converted displacement signal. The comparison between the measured velocity signal and the converted piezoelectric transducer signal into a velocity signal is shown in Figure 11(b).

CONCLUSIONS

It has been shown how a well-characterized ultrasonic system consisting of source, structure and receiver can be used to determine the ultrasonic pulse produced by a piezoelectric transducer operating under various excitation and coupling conditions. Based on the assumptions that the transduction characteristics of a transducer can be expressed as a transfer function, it has been shown how a well-characterized ultrasonic system can be used to experimentally determine the transfer function of a piezoelectric transducer operating either as source or receiver, thus establishing the rela-

tionship between electrical and acoustical quantities of the transduction process.

ACKNOWLEDGMENTS

This work was supported by the National Science Foundation through grants to the Materials Science Center and to the College of Engineering at Cornell University.

REFERENCES

1. W. Sachse and A. Ceranoğlu, in *1979 Ultrasonic Symposium Proceedings*, IEEE Cat. #79CH1482-9511. In press.
2. W. Sachse and N.N. Hsu, in *Physical Acoustics*, Vol. 14, W. P. Mason and R.N. Thurston, Eds., Academic Press, New York (1978), pp. 277-405.
3. N. N. Hsu, J. Simmons and S. C. Hardy, *Materials Evaluation*, 35, 100-106 (1977).
4. N. N. Hsu and S. C. Hardy, in *Elastic Wave and Non-Instructive Testing of Materials*, AMD-29, Y. H. Pao, Ed., ASME, New York (1973), pp. 85-106.
5. W. Sachse and A. Ceranoğlu, in *Ultrasonic International 1979, Conference Proceedings*, IPC Science and Technology Press, Guildford, England (1979). In press.
6. Y.H. Pao, R.R. Gajewski and A.N. Ceranoğlu, *J. Acoust. Soc. Am.*, 65(1), 96-105 (1979).
7. C. Fenq and R. Whittier, Technical Report DE79-1, Dunean-Endevco, San Juan Capistrano, CA (1979). To be published in *Proceedings of the International Conference on Acoustic Emission*, ASNT, Columbus, OH (1979).
8. N.N. Hsu and F.R. Breckenridge. To be published in *Proceedings of the International Conference on Acoustic Emission*, ASNT, Columbus, OH (1979).

SUMMARY DISCUSSION
(Wolfgang Sachse)

Dick Elsley (Science Center): You had a comparison of the received time domain signal with the computed time domain signal. How does that comparison look in the frequency domain, and are the differences long-term smooth ones or short-period ones?

Wolfgang Sachse: The comparison that we made was done in the time domain because there are some problems in finding the frequency spectrum of our signals. You notice that we were using displacement signals obtained by breaking a glass capillary on the surface of a specimen. The displacement found always increases in one direction. In order to take the signal into the frequency domain, we would have to window the signal. Since the signal is increasing monotonically, it would require a drastic truncation in the signal. It's conceivable we could take the signal, differentiate it, and then Fourier transform it. We have done that, but I don't think it's as sensitive as taking the original data, which is the displacement signal, which is okay as is. Furthermore, the displacement signal is what we compute from the theory. So, we generally don't deconvolve in the frequency domain.

Bob Harris (Pratt & Whitney): You did a deconvolution in the time domain with a nonunique function. How do you do that? You don't have an inverse, right?

Wolfgang Sachse: We do sometimes. You are right, there are cases in which we could not invert the function. And the cases that I have shown you obviously are the ones we could. We found out that if your function has a fast enough rise time and if it is a unipolar pulse, we were able to invert it easily. Whether that is true in general, I don't know. But it was true in the case of the mechanical signal. It's also true for the case of the electrical signal. For the transducer operating as a source, there we need to find the inverse function of the excitation voltage in order to find the transducer transfer function. That presented some problems at first, until we found out that we were able to invert a unipolar pulse which has a very fast rise time. By the way, I should say the theoretical solution of the structure, the Green's function, that can be inverted with no problem at all.

Don Eitzen: Thank you.

#

HALF-SPACE RADIATION BY EMAT's

William J. Pardee and R.B. Thompson
Rockwell International Science Center
1049 Camino Dos Rios
Thousand Oaks, CA 91360

ABSTRACT

A Green's function calculation of the far field radiation patterns of EMAT's is presented. The approach is based upon (a) closed form expressions for the eddy current and static magnetic field distributions, established by the EMAT, which react to produce the driving Lorentz forces and (b) a Green's function derived from the steepest descent approximation to the far field response of an arbitrary surface point force on a half space. Numerical results are presented, illustrating the radiation patterns of the three common EMAT designs. Included are vertically polarized shear waves as radiated by both meander coil and periodic magnet EMAT's and horizontally polarized shear waves as radiated by the latter.

INTRODUCTION

Electromagnetic acoustic transducers (EMAT's) have several features which are very useful in ultrasonic NDE. These features include non-contact operation, which permits high speed inspection and inspection of hot parts such as welded plates, the ability to produce beams of easily controlled polarization (including especially horizontally polarized shear waves), and the production of a beam which can be electronically scanned in angle. The increasing importance of these properties for both materials science studies (e.g., residual stress, micro-structure) and ultrasonic scattering NDE has made quantitative knowledge of their radiation patterns desirable.

Three dimensional calculations of these radiation patterns in the far field are presented on this paper for three types of EMAT's radiating into a half-space. Two of the EMAT's consist of periodically polarized magnets surrounded by solenoidal coils to produce, respectively, shear-horizontal (SH) and shear vertical (SV) bulk waves. The third consists of a uniformly polarized magnet and periodic meander coil which produces SV bulk waves. The computations differ from earlier treatments (1,2) of EMAT radiation patterns in several respects. All three components of the surface tractions are calculated directly from Maxwell's equations, based on the assumption that the transducer currents and magnetization are uniform. The very important effects of non-uniformity in the fields and eddy currents are thereby explicitly included, making it possible later to obtain a quantitative measure of the modal purity of the generated wave. Second, these calculations are done for rectangular (rather than cylindrical(2)) EMAT's. Third, the lateral (three dimensional) variation of the EMAT beam is obtained.

The paper is divided into three major parts; the solution of Maxwell's equations to obtain the eddy current and static fields for the three types of EMAT, the calculation of the far field response

to an arbitrary (three-dimensional) point force on the surface of a half-space, and the combination of these results to obtain the (non-point force) elastic wave radiation from the three types of EMAT. The point force response (Green's function) of the half-space is obtained analytically, as are the surface tractions, while the combination is evaluated numerically.

THE EMAT SURFACE TRACTION

The three types of EMAT considered here are illustrated in Fig. 1. In a convenient, although somewhat non-uniform terminology, the periodic magnet, longitudinal coil EMAT (upper left) will be referred to as SH (because it generates SH waves), the periodic magnet, transverse coil (upper right) as SV, and the single magnet, meander coil (which also generates SV waves) will be referred to as the MC EMAT. The current loops for the periodic permanent magnet EMAT's are schematically illustrated loosely wound, but are assumed to be a tightly wrapped (uniform sheet) coil in the calculations below. The coordinate system used throughout this paper will be right-handed, with the EMAT centered under the origin (the elastic waves are generated in a metal occupying the half-space $z > 0$), with the periodic variation (magnet or meander coil) along the x axis.

Calculation of Static Field

Consider first a single uniformly magnetized permanent magnet located at $-L/2 < x < L/2$, $-w/2 < y < w/2$, and $-(s+h) < z < -s$, as shown in Fig. 2. The magnetic field is readily obtained from classical magnetostatics. With uniform magnetization $\underline{M} = M_0 \underline{z}$, we have

$$\nabla \cdot \underline{H} = -\mu_0^{-1} \nabla \cdot \underline{M} = (M_0/\mu_0)[\delta(z+s) - \delta(z+s+h)] \quad (1)$$

Since the field is static, $\nabla \times \underline{H} = 0$, and we can find \underline{H} from a potential ϕ_M .

$$H = -\nabla\phi_M \quad (2)$$

which satisfies Poisson's equation,

$$\nabla^2\phi_M = \rho_M = \nabla \cdot M / \mu_0 \quad (3)$$

The result is

$$\phi_M(r) = -\int d^3r' \rho_M(r') / (4\pi R) \quad (4)$$

$$\text{or } H(r) = -\int d^3r' R \rho_M(r') / (4\pi R^3) \quad (5)$$

$$\text{where } R = r - r' \quad (6)$$

and $R = (R \cdot R)^{1/2}$. The integrals are two dimensional over the top and bottom surfaces of the magnet. The results for the top surface are conveniently written as double sums of two terms each, and with $B = \mu_0 H$,

$$B_x = M_0 / (4\pi) \sum_{m,n=1}^2 (-1)^{m+n} \log(y_n + R_{mn}) \quad (7)$$

$$B_y = M_0 / (4\pi) \sum_{m,n=1}^2 (-1)^{m+n} \log(x_m + R_{mn}) \quad (8)$$

and

$$B_z = M_0 / (4\pi) \sum_{m,n=1}^2 (-1)^n \tan^{-1}(x_m y_n / [s R_{mn}]) \quad (9)$$

with

$$x_m = -[x + (-1)^m L / 2] \quad (10)$$

$$y_n = -[y + (-1)^n W / 2] \quad (11)$$

and

$$R_{mn} = (x_m^2 + y_n^2 + s^2)^{1/2} \quad (12)$$

The contribution from the bottom surface is obtained from Eq. (7-9) by the substitutions $M_0 \rightarrow -M_0$, $s \rightarrow s + h$. These expressions will be used in predicting the performance of the MC EMAT.

For the SH and SV EMAT's the periodic magnet field can be obtained by summing contributions like those above with alternating sign, but it is preferable to take the magnet pair (Fig. 3) as the fundamental unit. The procedure is identical, though the integrals are somewhat longer. The results are, for the near surface,

$$B_x = M_0 / (4\pi) \sum_{m,n=1}^2 \text{sgn}(y_n) \log \left\{ (y_n - R_{2m-1,n}) / (y_n + R_{2,n}) \right\} \quad (13)$$

$$B_y = M_0 / (4\pi) \sum_{m=1}^3 (3 \bmod(m,2) - 2) \log [(x_m + R_{m,1}) / (x_m + R_{m,2})] \quad (14)$$

and

$$B_z = M_0 / (8\pi) \sum_{n=1}^2 \sum_{m=1}^3 (2 - 3 \bmod(m,2)) \tan^{-1} (y_n x_m / (s R_{mn})) \quad (15)$$

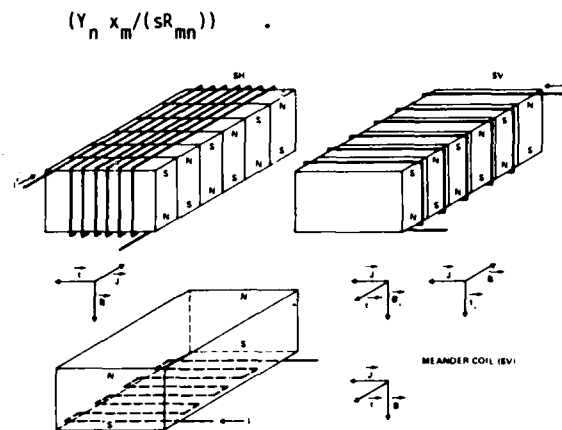


Fig. 1 The three EMAT configurations with the eddy currents, magnetic fields, and resulting forces schematically illustrated.

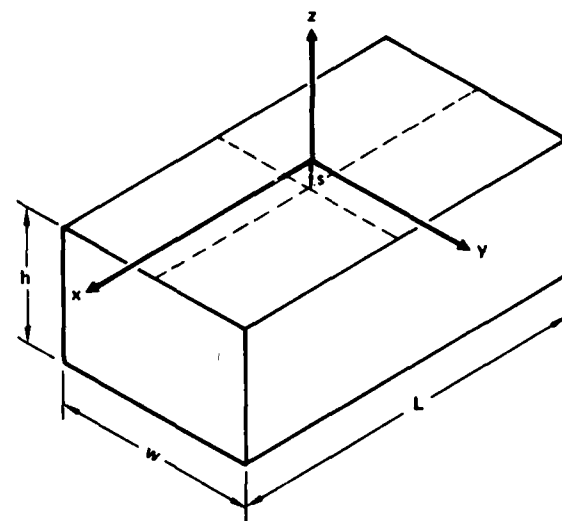


Fig. 2 Geometry for calculating the static field of a single permanent magnet such as used in the meander coil EMAT.

In the foregoing (Eq. 13-15) the expressions for y_n are given by Eq. (11) and

$$y_n = |y_n| \quad (15a)$$

but there are now three x values,

$$x_m = (m-1)D/2 - x, \quad m = 1, 2, 3 \quad (16)$$

and the factor $3 \bmod(m,2)-2$ is just the set of weights 1, -2, 1. With this convention, R_{mn} is still given by Eq. (12). The contribution from the lower (distant) surface can be obtained as before, but this is small, and is commonly made to vanish, in practice, by connecting the magnets with a soft iron shunt. One qualitative feature to be noted is the presence in the components of the static field parallel to the surface (B_x and B_y) of logarithmic singularities at each magnet boundary (Eqs. (13) and (14) evaluated for $s = 0$).

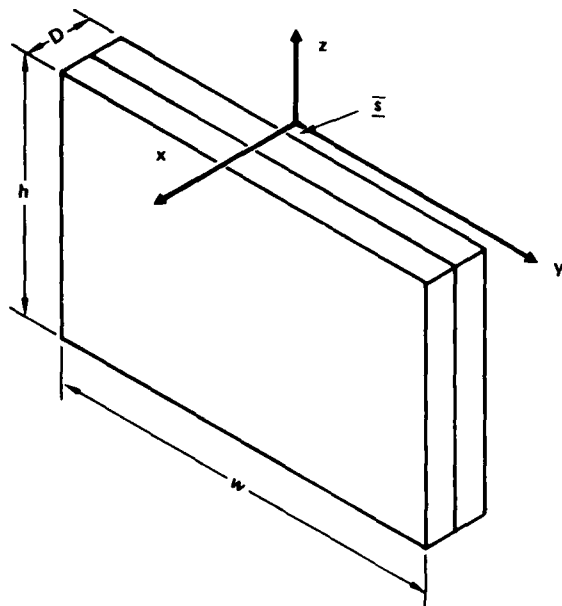


Fig. 3 Geometry for calculation of the static field of a single permanent magnet pair (quadrupole) which will be repeated periodically to form the SM and SV EMAT's.

Eddy Currents Induced by a Rectangular Current Loop

For the frequencies of interest (~1 MHz) and in highly conducting metals such as aluminum, the wavelength of the elastic waves is much greater than the skin depth, so the eddy currents can be treated as a surface current distribution (amps/meter).

$$\underline{K}(x,y) = \int_0^\infty dz \underline{J}(x,y,z) \quad (17)$$

By applying the Maxwell equations for $\nabla \times \underline{H}$ to a small planar closed path along a vector \underline{u} parallel to the metal surface, one obtains

$$\int \underline{H} \cdot d\underline{l} = \underline{H} \cdot \underline{u} = \underline{K} \cdot \hat{n} \times \underline{u} \quad (18)$$

where \hat{n} is normal to the surface. The most general vector \underline{u} parallel to the surface can be written in the form $\underline{u} = \underline{a} \times \hat{n}$ where \underline{a} is arbitrary. Inserting this in Eq. (18) yields the condition,

$$\underline{H} \cdot \underline{a} \times \hat{n} = \underline{K} \cdot \underline{a} \quad (19)$$

$$\text{or } \underline{K} = \underline{H} \times \hat{n} \quad (20)$$

and this enables one to obtain the surface current \underline{K} from the field \underline{H} . The field \underline{H} for the rectangle loop of the SH EMAT, shown in Fig. 4 is obtained from the Biot-Savart law.

$$d\underline{B} = \mu_0 d\underline{l} \times \underline{R} / (4\pi R^3) \quad (21)$$

where \underline{R} is as in Eq. (6), $d\underline{l} = I dy/b$, and $d\underline{l}$ is either $\hat{e}_1 dx$ or $\hat{e}_3 dz$. To satisfy the condition that the normal component of \underline{B} vanishes at the conductor surface, an image contribution must be included. The effect of the image is to double the parallel components. The results are

$$\begin{aligned} K_x = & -K_0 \sum_{i,j,k=1}^2 (-1)^{i+j+k} \left\{ \tan^{-1} [x_i y_j / (z_k R_{ijk})] \right. \\ & \left. + \tan^{-1} [y_j z_k / (x_i R_{ijk})] \right\} \quad (22) \end{aligned}$$

$$K_y = K_0 \sum_{i,j,k=1}^2 (-1)^{i+j+k} \log(z_k + R_{ijk}) \quad (23)$$

where

$$K_0 = NI / (2\pi b) \quad (24)$$

$$x_i = x + (-1)^{i+1} a/2 \quad (25)$$

$$y_i = y + (-1)^{j+1} b/2 \quad (26)$$

$$z_k = z + (2 - k)c \quad (27)$$

and

$$R_{ijk} = (x_i^2 + y_j^2 + z_k^2)^{1/2} \quad (28)$$

For the SV EMAT, the coil is rotated 90° about the z-axis and the same results hold after the appropriate rotation.

Eddy Currents Induced by a Meander Coil Segment

The meander coil primitive segment is shown in Fig. 5. The induced surface currents are calculated as for the rectangular loop of §2.2, but now require only one-dimensional integrals. The results are

$$\begin{aligned} K_x/K_0 = & \left(\frac{x_2}{R_{22}} - \frac{x_1}{R_{12}} \right) \frac{1}{y_2^2 + h^2} \\ & + \left[\left(\frac{x_3}{R_{31}} - \frac{x_2}{R_{21}} \right) \frac{1}{y_1^2 + h^2} \right] \quad (29) \end{aligned}$$

$$\begin{aligned} K_y/K_0 = & \left(\frac{y_2}{R_{12}} - \frac{y_1}{R_{11}} \right) \frac{1}{x_1^2 + h^2} \\ & + \left(\frac{y_1}{R_{21}} - \frac{y_2}{R_{22}} \right) \frac{1}{x_2^2 + h^2} \quad (30) \end{aligned}$$

where

$$K_0 = \mu_0 I h / (2\pi) \quad (31)$$

$$x_n = x + (3 - 2n)\alpha/2 \quad (32)$$

$$y_m = y - (-1)^m \beta/2 \quad (33)$$

and

$$R_{nm} = (x_n^2 + y_m^2 + h^2)^{1/2} \quad (34)$$

α and β define the coordinates of the coil as described in the caption to Fig. 5. The term in square brackets in Eq. (29) is the only contribution from the conductor at $\alpha/2 < x < 3\alpha/2$, $y = -\beta/2$, and this is to be omitted from the rightmost periodic repetition of the primitive meander coil segment.

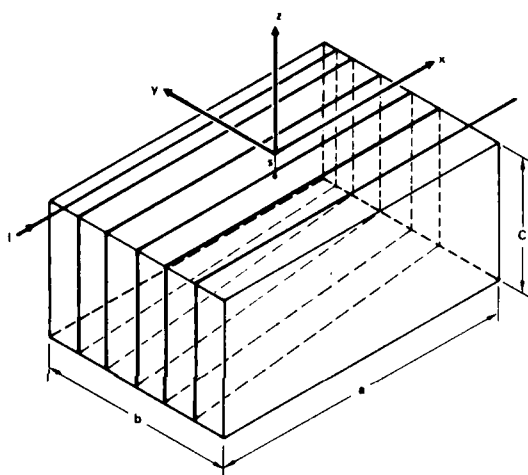


Fig. 4 Rectangular current loop of length a, width b, height c, located a distance s below the xy plane.

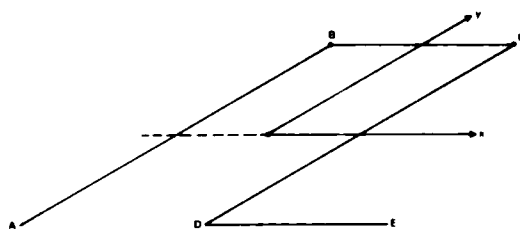


Fig. 5 One segment of a meander coil. Entire coil is built up by periodic repetition, with the last leg omitted from the last segment. The coordinates are A = 1/2 (- α , - β), B = 1/2 (- α , β), C = 1/2 (α , β), D = 1/2 (α , - β) and E = 1/2 (3 α , - β).

The Surface Traction

The Lorentz force per unit volume on the electrons, $\mathbf{f} = \mathbf{j} \times \mathbf{B}$, has been shown³⁻¹¹ to be transferred to the lattice. By integrating over z the surface traction (force per unit area) is obtained,

$$\mathbf{T} = \mathbf{K} \times \mathbf{B} \quad (35)$$

where it has been noted that the skin depth is small compared to both the variation in the static field, B, and the wavelength of the elastic waves. The symmetries of the currents, fields, and tractions are tabulated in Table 1. Note that the meander coil eddy currents have no symmetry in y. Three dimensional plots of the three components of surface traction for each of the three transducer types are shown in Figs. 6-14. The transducer parameters are given in Table 2. In interpreting the results, it is important to recall that the in-plane magnetic component perpendicular to a magnet boundary has a weak (logarithmic) singularity ($\sim \log s$) at that boundary, as can be seen from, e.g., Eq. (8) for B_y at $y = w/2$. The expression is singular for $-D/2 < x < D/2$, i.e., along the magnet boundary. Moreover, the derivative with respect to y, $\partial B_y / \partial y$, changes rapidly in magnitude and reverses sign at the boundary. This is evident, for example, in $t_3 = K_x B_y - K_y B_x$ for the SV EMAT, Fig. 11.

Table 1

	SH x y	SV x y	MC x y
K_x	+	-	+
K_y	-	+	-
H_x	+	+	+
H_y	-	-	-
H_z	-	+	+
t_x	+	-	-
t_y	-	+	+
t_z	-	+	+

Symmetries in x and y of the surface currents, static field and surface traction for the three varieties of EMAT shown in Fig. 1. K_x for the meander coil EMAT is neither symmetric or anti-symmetric.

Table 2

SH and SV	
Length, mm	38.1
Width, mm	7.87
Height, mm	4.0
Liftoff, mm	0.254
Magnet period, mm	6.35
# Magnet pairs	6
MC	
Length, mm	31.75
Width, mm	7.87
Liftoff, mm	0.254
Coil period, mm	6.35
Magnet height, mm	4.0
# m.c. loops	6

The SH EMAT tractions (Figs. 5-7) exhibit two desirable properties: the desired component (t_y , Fig. 6) is very smooth and periodic, and the undesired components (t_x, t_z , Figs. 5, 7) are much smaller. These undesired stress components are a result of fringing fields at the edges of the magnet and coil structure. The dominant currents and fields are K_y and B_z which combine to produce the t_y illustrated in Fig. 7. The major contributions to undesired components arise from terms in the cross product of Eq. (35) which contain one fringing field and one of the dominant fields. Thus the t_x distribution arises from the term $K_y B_x$ which, as shown in Fig. 6, is largest at the end of the magnet array where the current K_y is fringing as part of the closed paths in which it must flow. The undesired t_z distribution shown in Fig. 8 arises from two terms. $K_y B_z$ is again largest at the magnet array ends due to the same fringing of K_y , while $K_x B_y$ is largest at the edges. The latter has a sign change due to the change in sign of K_x , occurring because the direction of the fringing eddy currents is opposite to those under the coil. The t_x and t_z components are reduced by 13 dB below the t_y component for this transducer.

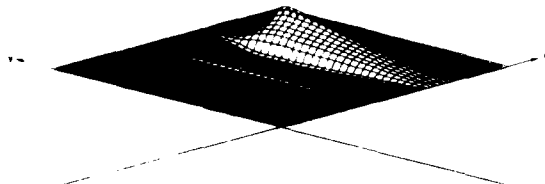


Fig. 6 Surface traction $t_x(x,y)$ in first quadrant ($x,y > 0$) for SH EMAT. Scale in y direction expanded by factor of 5.

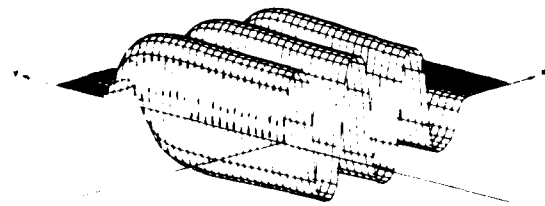


Fig. 7 Surface traction $t_y(x,y)$ in first quadrant ($x,y > 0$) for SH EMAT. All scales identical to those of Fig. 6.

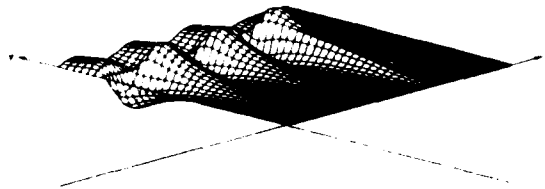


Fig. 8 Surface traction $t_z(x,y)$ in first quadrant, ($x,y > 0$) for SH EMAT. All scales identical to those of Fig. 6.

The SV EMAT generates elastic waves by a combination of t_x (Fig. 9) and t_z (Fig. 11) tractions; the undesired t_y (Fig. 10) component is much smaller. In this case, the periodic x and z

components are strongly modulated. This is a consequence of the solenoid-like coil which induces very large eddy currents near its ends but only weak currents near its center because the magnetic fields are nearly entirely contained by the coil. In this case, the K_y , B_x , and B_z fields are dominant. The undesired t_y stress component shown in Fig. 10 is produced by the term $K_z B_x$. For this coil geometry, the fringing current K_x is greatest at the magnet array ends (coil edge), and produces the indicated stress, which is about 10 dB from the desired components. The strong modulation in the desired stress components for the SV case, in contrast to the highly periodic behavior for the SH case, arises because of the different aspect ratios of the solenoidal coils when wound transversely or longitudinally around the magnet array.

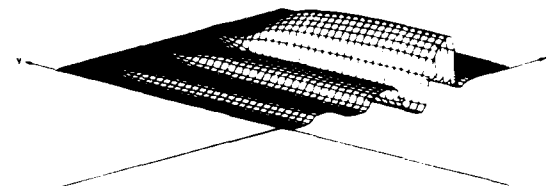


Fig. 9 t_x in first quadrant for SV EMAT. Transverse (y) scale expanded by a factor of 5.

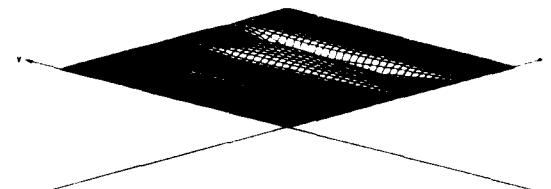


Fig. 10 t_y in first quadrant for SV EMAT. All scales as in Fig. 9.

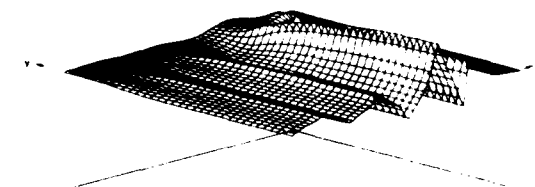


Fig. 11 t_z in first quadrant for SV EMAT. All scales as in Fig. 9.

The MC EMAT has singular behavior at both the wires and the magnet edges, as well as a lower amplitude traction (for given current and field) than the SV or SH magnets. It also lacks the symmetry (Table 1) of the other two EMAT types.

THE FAR-FIELD HALF-SPACE GREEN'S FUNCTION FOR A SURFACE SOURCE

The displacement field $u_m(t,r)$ satisfies

$$\rho \frac{\partial^2 u_m}{\partial t^2} = \frac{\partial \sigma_{mn}}{\partial r_n} \quad (36)$$

where

$$\sigma_{mn} = \lambda \frac{\partial u_j}{\partial r_j} \delta_{mn} + \mu \left(\frac{\partial u_m}{\partial r_n} + \frac{\partial u_n}{\partial r_m} \right) \quad (37)$$

with λ and μ the Lamé constants and summation over $j = 1, 2, 3$ implied. At the surface ($z = 0$), the stresses satisfy

$$\sigma_{m3}(t, x, y, 0) = T_m(t, x, y) \quad (38)$$

with T given by Eq. (35). This general solution is most conveniently obtained by superposition of solutions $G_{mn}(\omega, r)$ for the special case in which

$$T_n(t, x, y) = t_n \exp(j\omega t) \delta(x) \delta(y) \quad (39)$$

with t_n an arbitrary real number and δ the Dirac delta function. The solution for G_{mn} in the far-field is presented in Appendix B. The result is conveniently written in terms of longitudinal (L_{ij}) and transverse (T_{ij}) tensors as

$$4\pi\mu r G_{ij} = T_{ij} \exp(-j\omega r/c_T) + L_{ij} \exp(-j\omega r/c_L) \quad (40)$$

with c_L and c_T the longitudinal and transverse wave velocities.

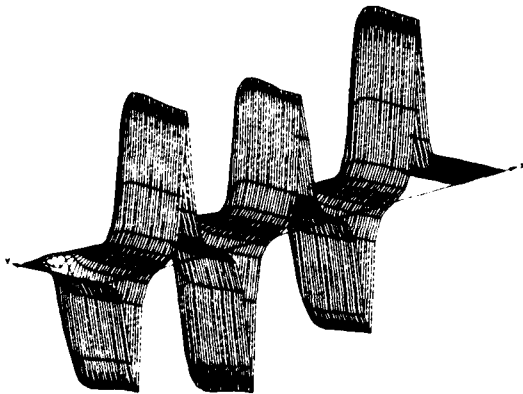


Fig. 12 $t_x(x, y)$ in first quadrant for meander coil EMAT. Transverse (y) scale expanded by a factor of 5.

Define

$$\kappa = c_L/c_T \quad (41)$$

and use spherical polar coordinates, $z = r \cos\theta$, etc., then, for both $i \neq 3$, and $j \neq 3$,

$$T_{ij} = \hat{r}_i \hat{r}_j [4 \cos\theta (\kappa^{-2} - \sin^2\theta)^{1/2} + 2 \sin^2\theta - 1] / d_T \quad (42)$$

with

$$d_T = (\cos 2\theta)^2 + 4 \sin^2\theta \cos\theta (\kappa^{-2} - \sin^2\theta)^{1/2} \quad (43)$$

and

$$L_{ij} = 2r_i r_j \cos\theta (\kappa^2 - \sin^2\theta)^{1/2} / d_L \quad (44)$$

with

$$d_L = (\kappa^2 - 2 \sin^2\theta)^2 + 4 \sin^2\theta \cos\theta (\kappa^2 - \sin^2\theta)^{1/2} \quad (45)$$

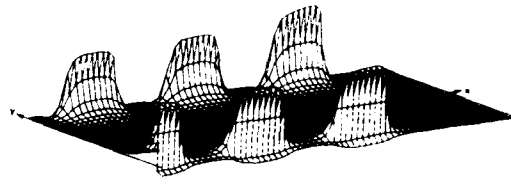


Fig. 13 t_y in right half plane ($x > 0$) for meander coil EMAT. Vertical scale as in Fig. 12.

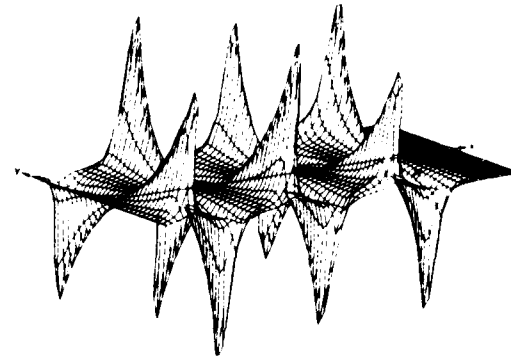


Fig. 14 t_z for meander coil EMAT. All scales as in Fig. 13.

The mixed subscript components (G_{3i} , G_{i3} , $i \neq 3$) are given by

$$T_{i3} = -2 \cos^2\theta r_i (\kappa^{-2} - \sin^2\theta)^{1/2} / d_T \quad (46)$$

$$L_{i3} = \cos\theta \hat{r}_i (\kappa^2 - 2 \sin^2\theta) / d_L \quad (47)$$

$$T_{3i} = \cos\theta \hat{r}_i (2 \sin^2\theta - 1) / d_T \quad (48)$$

and

$$L_{3i} = 2 \cos^2\theta \hat{r}_i (\kappa^2 - \sin^2\theta)^{1/2} / d_L \quad (49)$$

The remaining components of G are obtained from

$$T_{33} = 2 \sin^2\theta \cos\theta (\kappa^{-2} - \sin^2\theta)^{1/2} \quad (50)$$

$$L_{33} = \cos^2 \theta (\kappa^2 - 2\sin^2 \theta) / d_L \quad (51)$$

The square roots arise from the z component of a wave vector and become negative imaginary when their arguments are negative.

It is useful to identify the extent and nature of the polarization of the radiation. SH polarization is defined by a unit vector $\hat{e}^{(1)}$ perpendicular to both the propagation direction (\hat{r} , in the far field) and the normal (\hat{z}) to the surface. SV polarization is then defined to give a right handed triple by

$$\hat{e}^{(2)} = \hat{r} \times \hat{e}^{(1)} / r \quad (52)$$

The displacement of any transverse radiation can then be decomposed into components along these two directions

$$u = [u^{(1)}\hat{e}^{(1)} + u^{(2)}\hat{e}^{(2)}] \exp[j(\omega t - kr)]. \quad (53)$$

In general, $u^{(1)}$ and $u^{(2)}$ will be complex numbers and the polarization will be elliptical. The measurable displacement field will then be given by the real part of u . To describe the properties of the elliptical polarization more conveniently, we define

$$\tau = \omega t - kr \quad (54)$$

$$\alpha_i = \text{Re}(\hat{e}^{(i)} \cdot u) \equiv a_i \cos(\tau + \delta_i) \quad (55)$$

and

$$\delta = \delta_2 - \delta_1 \quad (56)$$

Here a_i and δ_i can be interpreted as the peak magnitude and phase of the displacements along the SH and axes. α_i is the instantaneous value along the axes. By elimination of τ one then obtains Eq. (12)

$$(a_1/a_2)^2 + (a_2/a_2)^2 - 2a_1a_2/(a_1a_2) \cos \delta = \sin^2 \delta \quad (57)$$

This quadratic form describes an ellipse, which has the simplified form

$$\sin^2 \delta = \lambda_1 \beta_1^2 + \lambda_2 \beta_2^2 \quad (58)$$

after a rotation of coordinates given by

$$\beta_1 = \alpha_1 \cos \psi + \alpha_2 \sin \psi \quad (59)$$

$$\beta_2 = \alpha_1 \sin \psi + \alpha_2 \cos \psi \quad (60)$$

Here ψ is the angle of the major axis of the elliptical motion, measured with respect to the SH polarization direction $\hat{e}^{(1)}$, and λ_1 and λ_2 are respectively the semi-major and semi-minor axes of the ellipse. The λ_i are the eigenvalues of the quadratic form and are given by

$$\lambda_i = \frac{1}{2} \left(\frac{1}{a_1^2} + \frac{1}{a_2^2} \right) + (-1)^i \left[\frac{1}{4} \left(\frac{1}{a_1^2} - \frac{1}{a_2^2} \right)^2 + \frac{\cos^2 \delta}{(a_1 a_2)^2} \right]^{1/2} \quad (61)$$

and satisfy

$$0 < \lambda_1 < \lambda_2 \quad (62)$$

$$\text{with } \tan \psi = (a_1^{-2} - \lambda_1) a_1 a_2 \sec \delta \quad (63)$$

β_1 and β_2 are the instantaneous displacements measured along the major and minor axes respectively. Note that $\delta = 0$ implies $\lambda_1 = 0$, and therefore the ellipse equation degenerates to $\beta_2 = 0$, a straight line. Circular polarization results from $\delta = (2n + 1)\pi/2$.

Let us consider the foregoing for the case of radiation from a surface point source oriented in the x direction, $\hat{f} = \hat{x}$. The amplitudes $a^{(i)}$ are obtained from $a^{(i)} = \hat{e}_m^{(i)} \cdot T_{mi}$, and are given by

$$a^{(1)} = \sin \phi \quad (64)$$

and

$$a^{(2)} = \cos 2\theta \cos \phi \cos \phi / [\cos^2 2\theta + 4\sin^2 \theta \cos \theta (\kappa^{-2} - \sin^2 \theta)^{1/2}] \quad (65)$$

For $0 < \sin^{-1}(\kappa)$ the $a^{(i)}$ are real; the radiation is plane polarized. At $0 = \sin^{-1}(\kappa) = \sin^{-1}(1/2)$, $\approx 30^\circ$ in the example to follow) the amplitude $a^{(2)}$ for SV radiation becomes complex and the radiation becomes, therefore, elliptically polarized. This transition can be appreciated physically by imagining the source to be infinitesimally inside the surface. For $0 < \sin^{-1}(\kappa)$ the beam contains SV waves propagating both directly from the source, and reflected from the surface, and to satisfy the boundary conditions on the surface a mode-converted longitudinal wave at $0' = \tan^{-1}[(1 - \kappa^2 \sin^2 \theta)^{-1/2}]$. At $0 = \sin^{-1}(\kappa)$ the mode-converted longitudinal wave becomes evanescent, and the coefficient $u^{(2)}$ concomitantly develops an imaginary part. The phase shift δ is negative; the polarization vector rotates from SH to SV (right-handed). At $0 = 45^\circ$ no SV beam can be radiated; the radiation is plane SH. For $0 > 45^\circ$ a small SV beam reappears with the opposite sign, and thus is left-handed elliptically polarized.

The angle ψ made by the plane of polarization (or of the major axis of the ellipse, depending upon whether $\delta \neq 0$) varies with ϕ as shown in Fig. 15. For small 0 (radiation directed upward) the radiation is plane polarized, varying smoothly

between pure SH at $\phi = 90^\circ$ and pure SV at $\phi = 0$. The discontinuity at $\phi = 0$ occurs because the SH amplitude disappears and reappears reversed symmetrically, as shown.

For θ just below and just above 45° the SV amplitude, because it disappears at 45° , is very small, so, except very close to the forward direction the radiation is nearly pure SH. Since the SV amplitude changes sign at $\theta = 45^\circ$, the angle ψ has a discontinuity of 180° at this point. This discontinuity is essentially one of phase, and obviously does not imply any discontinuity in the amplitudes themselves. The dependence of ψ upon θ for various planes at fixed ϕ ($x' = x \cos \phi + y \sin \phi$) is shown in Fig. 16.

The power radiated per unit area is most easily obtained from¹⁴

$$P_n = -v_m \sigma_{mn}^* \quad (66)$$

and is conveniently separated into SH, SV and L contributions. For the two transverse contributions

$$P(i) = |a(i)|^2 u_{\omega}^2 \hat{r} / c_T \quad (67)$$

and for the longitudinal power,

$$P^L = |a^L|^2 (\lambda + 2\mu) \omega^2 \hat{r} / c_L \quad (68)$$

with

$$a^L = \hat{r}_m u_m \quad (69)$$

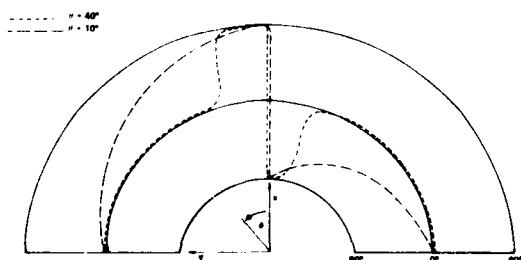


Fig. 15 Polar plot of the angle ψ between $q \times z$ [e(SH)] and the plane of the major axis of the possibly degenerate polarization ellipse vs ϕ for various θ .

The SH power radiated into the plane $\theta = 60^\circ$ by a point force along the x axis is shown in Fig. 17. Obviously, such a force produces no SH radiation in the forward ($\phi = 0$) direction. For fixed ϕ , the radiated SH power is independent of θ . Figure 18 shows the SV power radiated by the same force into planes at $\phi = 0, 40^\circ$, and 80° . For $\theta = 90^\circ$ the radiated power is pure SH. The cusp at $\theta = 30^\circ$ is due to the evanescent mode-converted longitudinal wave described earlier; the null at 45° arises because of reversal in sign of the SV amplitude as is evident from the vectors sketched on Fig. 18. For small θ ($\theta < 45^\circ$) the x directed force produces a relatively large SV

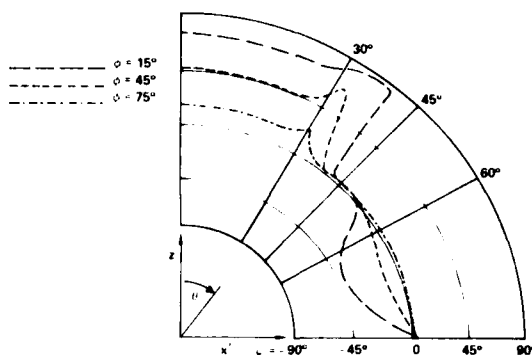


Fig. 16 Polar plot of the angle ψ between $q \times z$ [e(SH)] and the plane of the major axis of the polarization ellipse vs θ for various ϕ arising from a point force parallel to x axis.

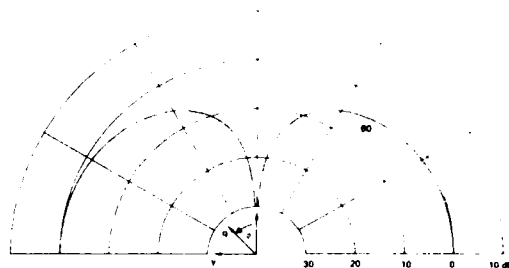


Fig. 17 SH power radiated at $\theta = 60^\circ$ by a point surface force in the x direction.

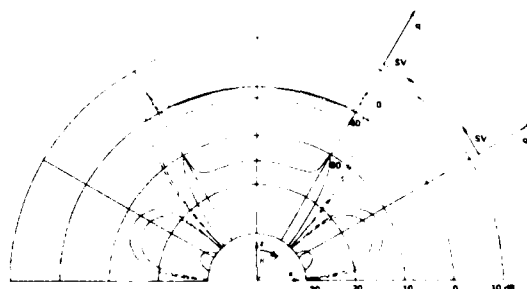


Fig. 18 SV power radiated into the zx' planes by a point force along x axis with $x' = x \cos \phi + y \sin \phi$ for $\phi = 0, 40^\circ$, and 80° . Change in sign of the SV amplitude at $\theta = 45^\circ$ is illustrated.

displacement roughly parallel to itself, but for $\theta > 45^\circ$ the SV displacement arises from the x force pushing up the material. This reverses the sign and produces a much lower SV efficiency. This is the origin of the reversal between right elliptically polarized and left elliptically polarized radiation at $\theta = 45^\circ$. The variation of the SV power as a function of ϕ , for $\theta = 30^\circ$ is shown in Fig. 19. The longitudinal power radiated by this x directed point force is shown in Fig. 20 as a function of θ for various ϕ . It is obvious from symmetry arguments that no longitudinal power will be radiated upward ($\theta = 0$) by this force, or to

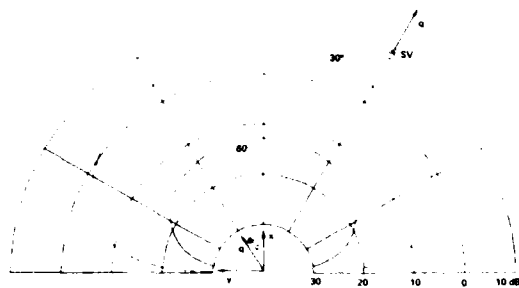


Fig. 19 Cross section of the SV power radiated into planes $\theta = 30^\circ, 60^\circ$ by a point surface force in x direction.

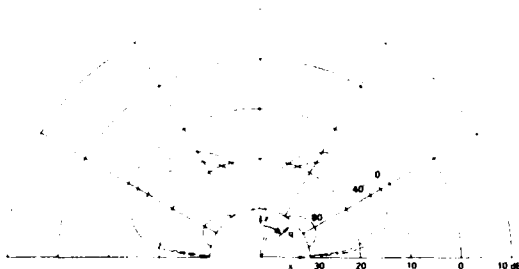


Fig. 20 Longitudinal power radiated into zx' planes ($x' = x \cos \phi + y \sin \phi$) by a point surface force along x axis for $\phi = 0, 40^\circ, \text{ and } 80^\circ$.

the side ($\phi = 90^\circ$). The less obvious fact that the power must vanish for $\theta = 90^\circ$ occurs because such a wave does not satisfy the stress free boundary conditions at the half space surface. Figure 21 exhibits the smooth cross section of this longitudinal radiation in the forward direction in the plane $\theta = 60^\circ$.

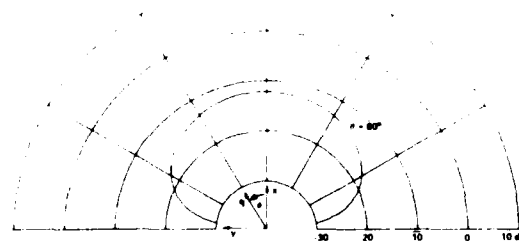


Fig. 21 Cross section in the plane $\theta = 60^\circ$ of the longitudinal power radiated by a point surface force in the x direction.

A point force along the y axis introduces differs from the above only by $\phi \rightarrow \phi - 90^\circ$. However, a point force along the z axis is fundamentally different. Note first that such a force produces no SH radiation, and its radiation is independent of ϕ (axially symmetric). The smooth, structureless longitudinal radiation cone is shown in Fig. 22. The SV radiation pattern is more interesting as shown in Fig. 23. Again by symmetry, no SV waves are radiated along the z axis. Furthermore, there is a second null where the direction of the SV radiation vector changes sign at $\theta = \sin^{-1}(k)$. This is again related to

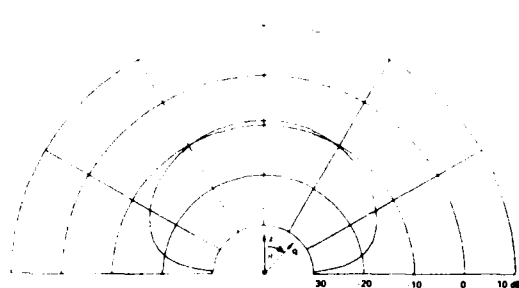


Fig. 22 Longitudinal power radiated by a point surface force along z axis. Pattern is independent of ϕ .

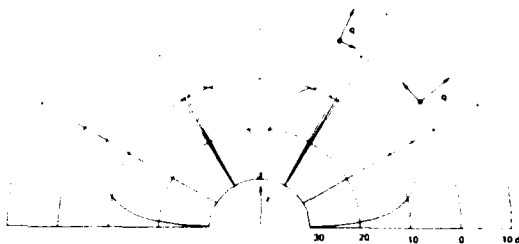


Fig. 23 SV power radiated by a point surface force along z axis. Pattern is axially symmetric.

the previously noted observation that, for a plane SV wave traveling at this angle, the phase matched longitudinal wave is evanescent.

It is interesting to note that numerical comparisons show that the radiation into the planes $\phi = 0$ and $\phi = 90^\circ$ for the force $\underline{f} = \hat{x}$ and into any plane for the force $\underline{f} = \hat{z}$ are equivalent to that for equivalently oriented line forces except for a scaling factor.

EMAT RADIATION PATTERNS

The far field radiation pattern of the EMAT can be obtained from the convolution of the surface tractions t_j with the asymptotic expression G_{ij} for the Green's function,

$$u_i(x, y, z) = \int d^2x' G_{ij}(x - x', y - y', z) t_j(x', y') \quad (70)$$

This convolution integral can be greatly simplified by working in the far field of the EMAT; i.e., at a distance large compared to the entire EMAT rather than compared to a single EMAT segment. This is only an entirely satisfactory approximation for quite large distances,¹⁴ but a great deal can be learned from it. The effect is to enable us to make replacements

$$|R - R'|^{-1} \exp(i\omega |R - R'|/c) \approx r^{-1} \exp(i\omega R/c) \exp(-iq \cdot R') \quad (71)$$

This produces the very compact expression

$$4\pi u R u_j(R) = T_{ij} t_j(q_T) \exp(-jq_T R) + L_{ij} t_j(q_L) \exp(-jq_L R) \quad (72)$$

where T_{ij} and L_{ij} depend only on θ and ϕ (Eq. 42-51), t_j is the two-dimensional Fourier transform of t_j , $q_T(q_L) = \omega/c_T(c_L)$, and summation on j is implied.

The two-dimensional Fourier transform of t_j needs to be computed only for a rectangular mesh, for which FFT techniques are convenient. The value of t_j is, of course, needed at non-mesh points, but this can be obtained by two-dimensional interpolation without further time consuming integration. An interpolation algorithm was chosen which used a sub-mesh of 16 points (x_n, y_m) surrounding the desired point (x, y) and first fits cubic polynomials to four sets of four points parallel to the x coordinate $[F(x_n, y_1), \text{etc.}]$ interpolates in x in each to obtain four new interpolated values $F(x, y_n)$ to which a cubic polynomial interpolation is applied to estimate $F(x, y)$. This was compared to linear (4 mesh points) and quintic (36 mesh points) with excellent results ($\sim 0.2\%$ change between cubic and quintic).

We turn to the individual consideration of the three specific transducers. The SH power radiated by the SH EMAT in the xz plane is shown in Fig. 24. At 1.8 MHz this EMAT produces main beams at $\theta = 15^\circ$ ($\phi = 0, 180^\circ$) and grating lobes at $\theta = 51^\circ$ ($\phi = 0, 180^\circ$). Note that the beams are very sharp ($\sim 3^\circ$), and that, without apodization, the side lobes are down the 13 db expected for a linear array of rectangular sources. The cross sections of these beams are shown in Fig. 25. The main beam is very broad ($\sim 30^\circ$, -3 db), and has two very small side lobes. The grating lobe is 15 db smaller and much narrower ($\sim 10^\circ$, -3 db). This fact could be used in data analysis to eliminate spurious signals from the grating lobe.

The contamination of the SH beam with SV and longitudinal power is shown quantitatively by the ϕ at which the radiation of that type is largest. The longitudinal power is very small (~ 28 db) and occurs at a much larger θ ($\theta = 31^\circ$), but the SV power occurs at the same angle (with a much different ϕ dependence) and is down only 13 db at peak. Since the generating tractions, t_x and t_z , for the SV radiation are antisymmetric (Table 1) the two lobes of the SV pattern represent amplitudes of opposite sign. It is possible that this antisymmetry could be used in signal processing to reduce the SV contamination further.

Figure 27 illustrates the θ dependence of the SV power radiated by the SV EMAT. The previously noted less-than-optimal aspect ratio of the particular transducer studied here contributes to the large side lobes. A cross section through the main beam at $\theta = 15^\circ$ is shown in Fig. 27.

Figure 29 exhibits the θ dependence of the longitudinal contamination of the predominantly SV

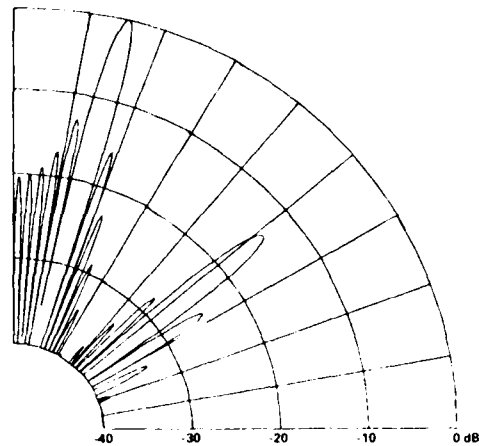


Fig. 24 SH power radiated into the xz plane by the SH EMAT.

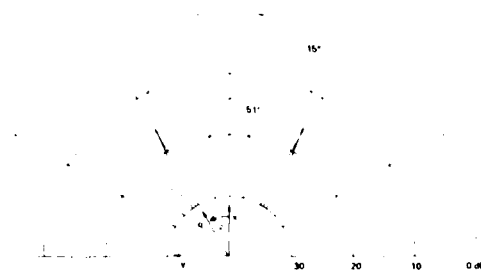


Fig. 25 Cross section of the main beam ($\theta = 15^\circ$) and grating lobe ($\theta = 51^\circ$, dashed curve) of the SH EMAT.



Fig. 26 Dependence upon ϕ of main (SH) and secondary (SV) shear beams at their maxima ($\theta = 15^\circ$) and of the longitudinal beam at its maximum ($\theta = 31^\circ$) from the SH EMAT.

beam. Cross sections in ϕ of the SH and longitudinal beams from this (SV) transducer are shown in Fig. 30. As with the SV contamination of the beam from the SH transducer, the SH lobes are of opposite sign.

The meander coil (MC) EMAT produces an SV radiation pattern which is narrower in θ , but with very rapid ($\sim 3^\circ$) variation with θ in the main beam, as shown in Fig. 31.

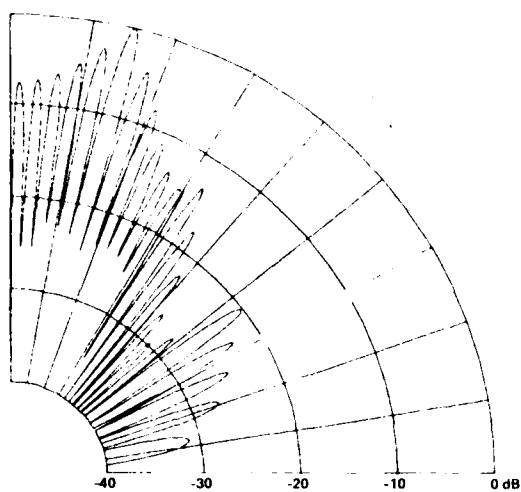


Fig. 27 SV power radiated into the xz plane by the SV EMAT.

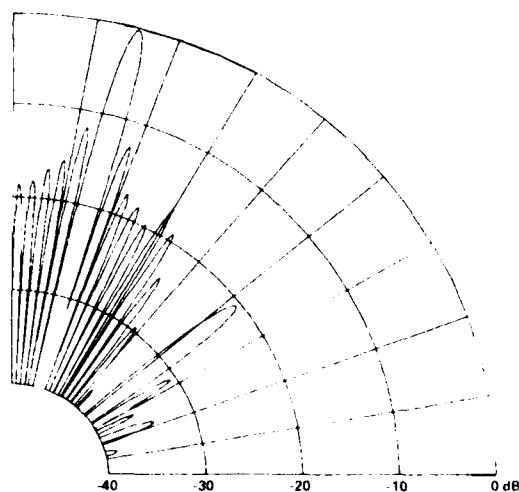


Fig. 31 SV power radiated into the xz plane ($\phi = 0$) by the meander coil EMAT.

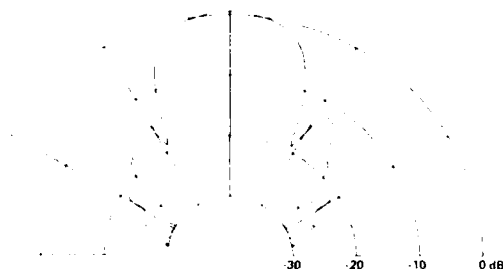


Fig. 28 Cross section of the SV beam radiated at $\theta = 15^\circ$ by the SV EMAT.

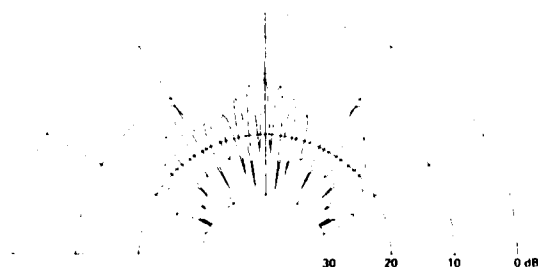


Fig. 29 Theta dependence ($\phi = 0$) of the longitudinal power radiated by the SV transducer into the xz plane.



Fig. 30 Cross section (ϕ variation) of SH (dash-dot) and L (solid curve) contamination of beam from SV EMAT.

The cross-section in ϕ of the main beam is shown in Fig. 32. The irregularities in the radiation pattern shown in Figs. 32, 33, and 34 are apparently due to the loss of numerical accuracy resulting from the coarser mesh required in the absence of symmetry. (Because of mini-computer memory limitations only 2145 elements were stored for each component; for symmetric problems all of these points were in the first quadrant). The (approximate) ϕ dependence of the SH beam from the MC transducer is illustrated in Fig. 33, and that of the longitudinal beam in Fig. 34.



Fig. 32 Cross section of the "main" ($\theta = 15^\circ$) SV beam radiated by the meander coil EMAT.



Fig. 33 Cross section of the SH contamination of the beam from the MC EMAT.

CONCLUSIONS

The major results of this paper, in order of decreasing rigor, are the expressions of Section 2 for the eddy currents and magnetic fields produced by various coils and magnets and their concomitant

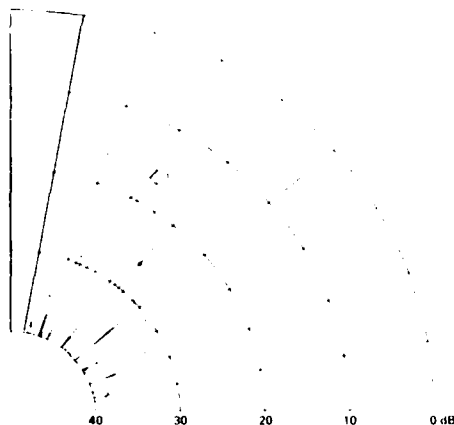


Fig. 34 Longitudinal power radiated into the xz plane by the MC EMAT ($\phi = 0$).

surface traction, the three-dimensional far-field half-space response to a point surface force presented in Section 3, and the radiation patterns of the three specific EMAT's in Section 4. The eddy current and magnetic field expressions can be used to generate the surface tractions for a very large set of EMAT's. Those tractions, when combined with suitable other Green's functions can provide, e.g., near or intermediate field radiation, or the radiation pattern in a plate. The simplest improvement would be to eliminate the approximation of Eq. (71), and work in the far field of the point source, which is not nearly as far as the far field for the EMAT. The increase in computational effort is large, however.

The most striking conclusion from the study of the EMAT radiation pattern is the remarkably good behavior of the SH EMAT. The beam is very sharp in ϕ , very smooth and broad in ϕ , and relatively free from other polarization components. In general, the most useful result of the study is the quantitative information about the lateral (ϕ) variation of the radiation pattern.

APPENDIX

The far field half space surface source Green's Function for the elastic wave equation can be constructed from solutions to the equation

$$[\rho\omega^2 + \mu\nabla^2 + (\lambda + \mu)\nabla\nabla]u(r) = 0 \quad (A1)$$

For any real vector Q with $Q_3 = 0$, there exist three independent solutions $u(r)$ of the form

$$u(r) = \hat{e}(r) \exp [j(\omega t - Q \cdot x - \kappa(r)z)] \quad (A2)$$

where $\kappa(r) = (\omega^2/c(r)^2 - Q^2)^{1/2}$ with $c(1) = c(2) = c_T$, $c(3) = c_L$. At $z = 0$ the surface stresses from an arbitrary linear combination U of these solutions can be calculated readily. If the combination U is written

$$U = \sum_{r=1}^3 a(r) u(r) \quad (A3)$$

the surface tractions are of the form

$$T_{m3} = \sum_{r=1}^3 a(r) T_{m3}(r) \quad (A4)$$

where $T_{m3}(r)$ are the stresses produced by the solution $u(r)$. For a spatially harmonic applied traction t_m , we require that

$$T_{m3}(x,y,0) = t_m \exp [j(\omega t - Q \cdot x)] \quad (A5)$$

By integrating the solutions $U(x,y,z;Q)$ over Q one obtains a solution $W(x,y,z)$.

$$W = \int \frac{d^2Q}{(2\pi)^2} U(x,y,z,Q) \quad (A6)$$

which has surface tractions

$$T_{m3}(x,y,0) = \int \frac{d^2Q}{(2\pi)^2} T_{m3}(x,y,0) = t_m e^{j\omega t} \delta^{(2)}(x) \quad (A7)$$

The $a(r)$ are obtained from combining (A7) with (A4).

$$T_{m3}(x,y,0) = \sum_{r=1}^3 a(r) (jT_{m3}(r)) = \sum_{r=1}^3 B_{mr} a(r) \quad (A8)$$

The oscillating exponential can be cancelled, and the matrix B in Eq. (A8) inverted to obtain $a(r)$.

$$a(r) = \sum_{m=1}^3 B^{-1}_{rm} t_m \quad (A9)$$

This leaves as the displacement field W whose surface tractions are given by Eq. (A7).

$$W_n = \int \frac{d^2Q}{(2\pi)^2} \sum_{m,r=1}^3 u(r) B^{-1}_{rm} t_m \quad (A10)$$

$$= \sum_{m=1}^3 G_{nm}(x,y,z) t_m \quad (A11)$$

The quantity G_{nm} is the displacement field Green's function.

The solutions $u(r)$ are conveniently chosen with polarization vectors $\hat{e}(r)$ given by

$$\hat{e}^{(1)} = (Q_2, -Q_1, 0) \quad (SH) \quad (A12)$$

$$\hat{e}^{(2)} = c_T/(\omega Q) (\kappa_T Q_1, \kappa_T Q_2, -Q^2) \quad (SV) \quad (A13)$$

and

$$\hat{e}^{(3)} = (Q_1, Q_2, c_L/\omega) \quad (L) \quad (A14)$$

where

$$\kappa_T = (\omega^2/c_T^2 - Q^2)^{1/2} \quad (A15)$$

and

$$\kappa_L = (\omega^2/c_L^2 - Q^2)^{1/2} \quad (A16)$$

The surface tractions associated with these modes are given by

$$\begin{aligned} t^{(1)} &= x_m T^{(1)}_{m3} = -\mu j \kappa_T (Q_2 - Q_1, 0)/Q \\ t^{(2)} &= -\mu j c_T / (\omega Q) [(\kappa_T^2 - Q^2) Q_1, \end{aligned} \quad (A16a)$$

$$(\kappa_T^2 - Q^2) Q_2, -2Q^2 \kappa_T] \quad (A17)$$

and

$$t^{(3)} = -2\mu j c_L / (\omega (\kappa_L Q_L \kappa_L Q_2 + \frac{1}{2} \omega^2/c_T^2 - Q^2)) \quad (A18)$$

These equations (A16-A18) define the 3×3 matrix B_{mr} whose inverse is easily obtained analytically.

No approximations have been made to this point, but now a considerable simplification can be obtained by going to the far field where the integral over Q can be evaluated approximately by the method of stationary phase. The integral needed is obtained from Eq. A10, A11, and A2.

$$G_{nm}(x, y, z) = j \int \frac{d^2 Q}{(2\pi)^2} \sum_{r=1}^3 \hat{e}_n^{(r)} \exp$$

$$j(\omega t - Q \cdot x - \kappa^{(r)} z) B_{rm}^{-1} \quad (A19)$$

We neglect the Q dependence of $\hat{e}_n^{(r)}$ and B_{rm}^{-1} and search for an extremum in the two variables Q_1, Q_2 of the phase ϕ .

$$\phi = \omega t - x Q_1 - y Q_2 - z (\omega^2/c^2 - Q_1^2 - Q_2^2)^{1/2} \quad (A20)$$

The resulting extremum Q^0 is given by

$$Q_1^0 = \omega x / (cR) \quad (A21)$$

and

$$Q_2^0 = \omega y / (cR) \quad (A22)$$

The corresponding value of κ, κ^0 , satisfies

$$\kappa^0 = (\omega^2/c^2 - Q_2^0)^{1/2} = \omega z / (cR) \quad (A23)$$

Then the phase ϕ is replaced by ϕ' .

$$\phi'(Q) = \phi(Q^0) + \frac{1}{2} (Q - Q^0)_i (Q - Q^0)_j \frac{\partial^2 \phi}{\partial Q_i \partial Q_j} \quad (A24)$$

with the second derivatives evaluated at Q^0 . The constant phase $\phi(Q^0) = \omega(t - R/c)$ can be removed from the integral. The remaining quadratic exponential can be integrated as a product of Fresnel integrals after a change of variables to eliminate the cross term, $Q_1 Q_2$. The results have the form

$$\begin{aligned} &\int \frac{d^2 Q}{(2\pi)^2} f(Q) \exp[j\phi(Q)] \sim j\omega \cos\theta f(Q^0) \\ &\exp[j\omega(t - R/c)] / (4\pi cR) \end{aligned} \quad (A25)$$

Note the integrals in (A19) include both values of $c^{(r)}$, and the integrands must be evaluated at $q^{(r)} = \omega x / c^{(r)}$, where $q = (Q_1, Q_2, \kappa)$. That is, the approximate Green's function is

$$\begin{aligned} G_{nm}(x, y, z) &= -\frac{\cos\theta}{4\pi R} e^{j\omega t} \sum_r \hat{e}_n^{(r)} e^{(r)} \\ &\exp(-j\omega R/c^{(r)}) B_{rm}^{-1} \end{aligned}$$

with $\hat{e}_n^{(r)}$ and B_{rm}^{-1} evaluated at $Q = (\omega/c^{(r)})(x, y, 0)/R$ where $R^2 = x^2 + y^2 + z^2$. Straightforward algebra produces the results given in Eq. (42-51).

ACKNOWLEDGEMENT

This research was sponsored in part by the Center for Advanced NDE operated by the Science Center, Rockwell International, for the Advanced Research Projects Agency and the Air Force Materials Laboratory under Contract F33615-74-C-5180.

REFERENCES

1. C.F. Vassile and R.C. Thompson, J. Appl. Phys. **50**, 2583 (1979).
2. K. Kawashima, J. Acoust. Soc. Am. **60**, 1089 (1976).
3. R.B. Thompson, IEEE Trans. Sonics Ultrasonics **SU-20**, 340 (1973).
4. T.J. Moran, M.J. Lin, F. Buchholtz, and R.L. Thomas, Rev. Sci. Instrum. **46**, 931 (1975).
5. L. Szabo and H.M. Frost, IEEE Trans. Sonics Ultrasonics **SU-23**, 323 (1976).
6. T.J. Moran and R.M. Panos, J. Appl. Phys. **47**, 2225 (1976).
7. W.D. Wallace, Int. J. Nondest. Test **2**, 309 (1971).
8. E.R. Dobbs, in Physical Acoustics, edited by W.M. Mason and R.N. Thurston (Academic, N.Y., 1975) **X**.
9. W. Mohr and P. Holler, IEEE Trans. Sonics Ultrasonics **SU-23**, 369 (1976).

10. Y.H. Pao and C.C. Mow, Diffraction of Elastic Waves and Dynamic Stress Concentrations (Rand Corp., N.Y., 1973) p. 116 ff.
11. M.R. Gaerttner, W.D. Wallace, and B.W. Maxfield, Phys. Rev. 184, 702 (1969).
12. M. Born and E. Wolf, Principles of Optics, Third edition, 24 (1965) Pergamon Press, N.Y.
13. B.A. Auld, IEEE Transactions on Microwave Theory and Techniques, MTT-17, 800 (1969).
14. A. Erhard, J. Kutzner, H. Wustenberg, "Radiation-Pattern of a Generalized Point-Source Near-To-Far-Field Transition," Proceedings of the International Symposium on New Methods of Non-Destructive Testing of Materials and Their Application, Especially in Nuclear Engineering, Saarbrücken, Germany, Sept. 17-19. (To be published by the Deutsche Gesellschaft für Zerstörungsfreie Prüfung e.V., Dortmund, W. Germany).

PVF₂ TRANSDUCERS FOR NDT

E. Carome, K. Fesler, H. J. Shaw, D. Weinstein, and L. T. Zitelli
Edward L. Ginzton Laboratory
Stanford University
Stanford, CA. 94305

ABSTRACT

We have investigated the spatial dependence of the longitudinal piezoelectric stress constant e_{zz} of PVF₂. Experiments were performed on a series of nominally identical brass-backed PVF₂ longitudinal wave transducers in water using commercial PVF₂ film. Computer programs were designed to predict the performance of the transducers as a function of $e_{zz}(Z)$, the thickness mode piezoelectric stress constant as a function of position Z through the thickness of the film. Our experiments indicate that the coupling coefficient is uniform across the film thickness. These computer programs were also used to model the insertion loss and bandwidth performance of the transducers. High voltage pulses were applied to PVF₂ transducers to determine the region of linearity and to find the maximum nondestructive voltage that can be used. Transducers of this type were also made using PVF₂ films fabricated in the Stanford Center for Materials Research using commercial resin, and found to perform as well as transducers using commercial film. Transducers of the above kind have also been used as bulk wave sources in wedge transducer assemblies for the production of surface acoustic waves on ceramic plates, and initial observations of reflections from surface cracks have been made.

It has been reported the PVF₂ film may have a spatially non-uniform piezoelectric coupling coefficient.¹ The claim is that the active piezoelectric region is concentrated near the positive side of the film, the positive side being the side that was charged positively during the poling process. The PVF₂ transducer, which consists of a piece of electroded PVF₂ bonded to a brass backing,² may have either the positive or negative side of the film exposed. The two possible configurations are shown below in Fig. 1. If the piezoelectric coupling constant is non-uniform across the thickness of the film, the insertion loss characteristics of a PVF₂ transducer should depend on the configuration of the transducer. This statement was verified using a computer matrix model that calculated the insertion loss of a single multi-layer PVF₂ transducer transmitting into water.³

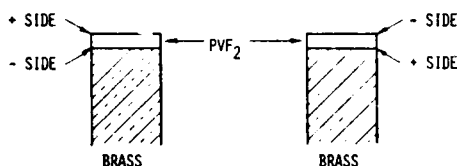


Fig. 1. Schematic of the PVF₂ brass-backed transducer configurations used.

Results obtained using this program are shown in Fig. 2. The PVF₂ was modeled as ten separate 3.1 μ thick layers, with e_{zz} values of (.1, .05, .025, .0125, .00625, .003125, 0, 0, 0, 0) in order across the 10 layers. The top curve is the predicted insertion loss when the layer with the maximum e_{zz} value is located next to the loading material (water). This configuration results in a resonance valley around $\omega = .6 \omega_0$ due to the layer of nonpiezoelectric PVF₂ trapped between the backing material (brass) and the active PVF₂. The bottom curve is the predicted insertion loss when the layer with $e_{zz} = .1$ is located next to the brass.

Figure 2 shows that large insertion loss dif-

ferences should be apparent if e_{zz} is strongly non-homogenous.

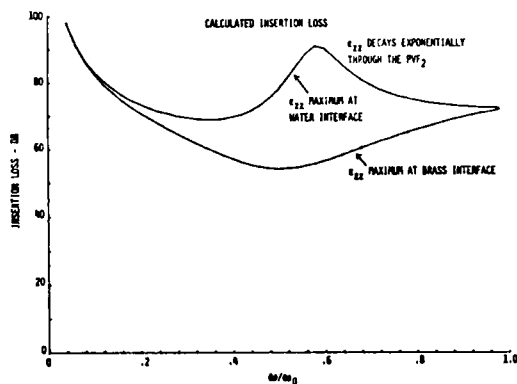


Fig. 2. Calculated insertion loss curves for PVF₂ with non-homogenous value of e_{zz} .

Six brass backed PVF₂ transducers were constructed using 25 μ thick film obtained from Kureha Corp. The aluminum electrodes originally on the PVF₂ were removed and replaced by a flash of chromium and a thin layer of gold (~1000 Å), deposited using an e-gun evaporation system. The polymer was then repoled with a voltage of 2500 volts ($\sim 10^6$ V/cm) placed across the PVF₂ for two hours. The positive electrode of the poling apparatus was connected to the side of the PVF₂ which had been poled positively by Kureha. The poling was performed in an air oven, at a temperature of 80°C.

Using this repoled material, the six transducers mentioned were constructed.³ Three of the transducers were bonded so that the side of PVF₂ which was charged positive during poling was exposed to the air. (These were labeled the +1, +2, and +3 transducers.) The other three transducers were bonded so that the positive side during poling was epoxied to the brass. (These were labeled the -1, -2, and -3 transducers.)

Two-way reflection mode insertion loss measurements were then performed on all transducers. Insertion loss is defined on the basis of a 50 Ω source generator driving the transmitting transducer and a 50 Ω load connected across the receiving transducer. The results of this experiment are shown in Fig. 3. The graph reveals no significant

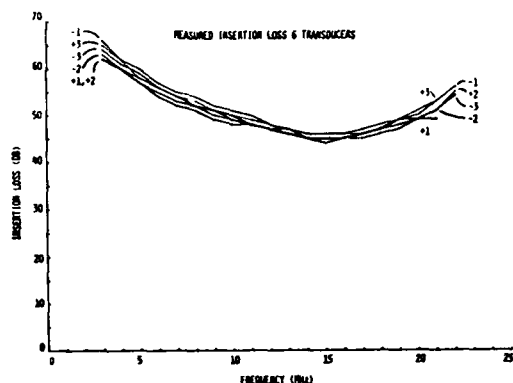


Fig. 3. Measured insertion loss curves for the six test transducers (-1, -2, -3, +1, +2, +3).

differences between the performance of the positive and negative devices. The high degree of similarity between the two sets of curves suggests that the piezoelectric activity of the PVF₂ used in this experiment is spatially symmetric and spatially uniform. Two-way insertion loss measurements were also performed using transducer -1 as the receiver and different transducers as the transmitter. These were consistent with the reflection mode measurements. We conclude that the PVF₂ used in our experiment did have a uniform value of e_{zz} across its thickness.

We next calculated the theoretical insertion loss curve of a transmitting PVF₂ brass-backed transducer using the matrix impedance model. The results were doubled to obtain the two-way insertion loss. The plot of this calculation, along with the average experimental results are shown in Fig. 4.

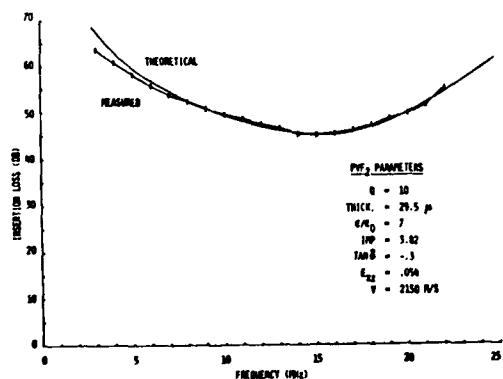


Fig. 4. Average insertion loss of the six test transducers of Fig. 3, and theoretical insertion loss curve adjusted for curve fitting.

By adjusting various parameters used in the calculation

we fitted the theoretical curve to the experimental results. Our choice of parameters was guided by previous measurements. A good fit was obtained without drastically changing the original parameter values. This implies that the material properties of PVF₂ are fairly well known and that the experimental and theoretical results are consistent.

The response of PVF₂ to high voltage pulses has also been investigated.² The idea behind these experiments was to investigate the maximum nondestructive voltage which can be applied to these transducers and also the linearity of the transducers with respect to voltage. As PVF₂ has relatively low piezoelectric strength compared to ceramic materials, it is of interest to see if this can be compensated by using high input voltages.

The transducers used in this experiment differed from earlier transducers used in that the electrode covering of the PVF₂ was etched back away from the edges of the polymer in order to prevent arcing.

An input voltage pulse was applied to such a transducer immersed in water. The input pulse was triangular in shape with a base width of ~ 200 ns. This pulse generated an essentially bipolar stress wave in the water which was then incident upon another PVF₂ transducer. Figure 5 is a plot of the amplitude of the input signal versus the peak-to-signal observed across the receiving transducer.

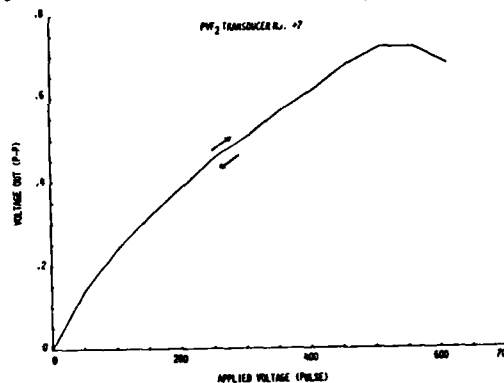


Fig. 5. Measured voltage across receiving transducer versus amplitude of voltage pulse applied to a PVF₂ transducer used as transmitter.

The output voltage is seen to increase in a roughly linear manner up to ~ 600 v(20v/μ). At this point the pulse generator could not supply a larger amplitude output pulse unless the width of the pulse was expanded significantly. This pulse widening resulted in a shift of the pulse energy from high to low frequencies, where the insertion loss is higher. The curve consequently leveled off at this point. Using the same transmitting transducer, the experiment was repeated and was found to yield repeatable results. This shows that PVF₂ transducers can withstand at least 20 v/μ without damage (in a pulse mode), while still operating well. Other experiments of this type suggest that PVF₂ transducers can withstand 45 v/μ without readily apparent damage. In that particular case, however, the transducer did appear to sustain some damage at voltage gradients above 50 v/μ. In either case the upper limit of

applied voltage is significantly larger than the maximum ac voltage which can be applied to most piezoelectric ceramics. For example, the ac depoling field for PZT-5A is ~ 0.7 V/ μ . The above results on linearity are consistent with earlier experiments carried out here. A high power cw rf generator was used to generate high rf voltage at the terminals of a transducer of the above type using 25 μ Kureha film, and the radiated acoustic field strength was monitored with a receiving transducer electrostatically shielded to suppress the direct electrical feedthrough signal. The radiated field strength was accurately linear with applied voltage up to a voltage gradient of 25 V/ μ , the highest gradient obtainable from the rf generator. It should be noted that PVF₂ transducers can be excited with high rf electric fields without requiring high terminal voltage by folding and bonding electroded film, producing a multilayer transducer in which voltages of the individual layers are in parallel while their acoustic fields are in series.⁴

The PVF₂ device programs are formally associated with an NSF supported materials program on piezoelectric polymers. Under this program, synthesis of PVF₂ from the monomer is carried out in the Chemical Engineering Department by C. Frank, S. Bowker and students, and PVF₂ film fabrication is carried out in the Center for Materials Research (CMR) by R. Feigelson, R. Route, R. DeMattei and students. Under the present device project we have tested PVF₂ films from this program, by using them to fabricate transducers of the type described above. Figure 6 shows measured two-way insertion

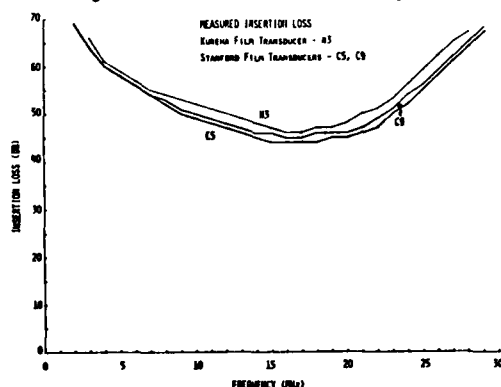


Fig. 6. Measured two-way insertion loss curves for transmitting transducers using Stanford and Kureha films.

loss results on two identical transducers (C5 and C9) made with film (thickness 25 μ) pressed at CMR from commercial polymer powder, compared with that of a transducer (N3) made using Kureha film (thickness 25 μ). In these measurements, the transducer under test was used as transmitter, and a fixed calibrated PVF₂ transducer was used as receiver.

PVF₂ surface wave transducers were used to generate and detect surface acoustic waves on ceramic substrates. Wideband acoustic impulses were easily generated with these assemblies with the dynamic range enhanced by the application of high level input pulses. These transducers were tested on unpolished Si₃N₄ plates containing half penny shaped cracks, to determine their potential for application to nondestructive evaluation. The performance of

the transducers was evaluated through measurement of direct and Fourier-transformed reflections from the cracks.⁵

The experimental system is outlined in block diagram form in Fig. 7. A single transducer is

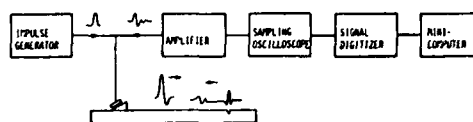


Fig. 7. Block diagram of system employed for surface flaw detection studies.

used as both source and detector. It consists of a 25 micron thick, 1.2 cm square element of uniaxially stretched PVF₂ obtained in sheet form from the Kureha Corporation, already stretched, aluminum coated and poled. The aluminum coatings were removed by etching and replaced with gold on chrome (~ 1000 Å) evaporated coatings, and the sheets then repoled. The transducer element was attached to a mirror finished brass backing plate with epoxy cement, taking care to obtain a very thin uniform bond. The opposite surface of the backing plate was angled to reduce reflections. It is pivot mounted in a brass holder, as indicated in Fig. 8, with a silicone rubber wedge (RTV 615) placed between the PVF₂ and the ceramic substrate. The orientation of the holder and the angle of the wedge were both adjustable so that the longitudinal-to-surface wave coupling could be optimized.⁶

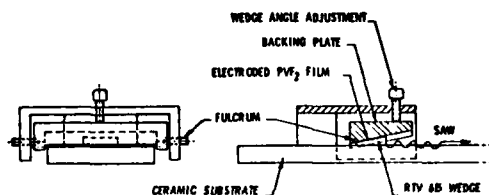


Fig. 8. Sketch of transducer assembly used for surface wave generation and detection.

The PVF₂ transducer was driven by a repetitive monopolar voltage impulse, approximately 300 volts peak amplitude and 50 nanoseconds full width at half amplitude, as indicated in the oscillogram shown in Fig. 9. This led to the launching of a surface wave impulse onto the top surface of the substrate. Surface wave impulses reflected back to this same transducer from the edges of the substrate and from surface flaws led to signals that were easily detected and processed.

As indicated in Fig. 7, the amplified received signal was fed to a sampling oscilloscope that effectively increases the time duration of the sub-microsecond received impulses, permitting them to be digitized using a relatively slow analog-to-digital converter. In addition, the sampling oscilloscope also served as a gated amplifier so that any desired temporal portion of the received signal could be selected for viewing and analysis. Hard copy graphs of the various received impulses and their Fourier spectra were obtained in approximately two minutes using a minicomputer and an x-y plotter.

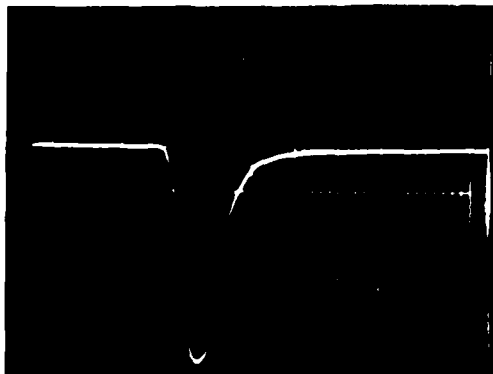


Fig. 9. Oscilloscope of voltage impulse employed to excite source transducer. Vertical - 50 V/div. Horizontal - 50 nsec/div.

To indicate the type of data that have been obtained with this system measurements were made using a substrate of 0.64 cm thick, 16 cm x 2.5 cm rectangular silicon nitride Si_3N_4 plate. The top and bottom flat surfaces of the plate were optically polished and the edges were finely ground perpendicular to these surfaces. Three surface flaws were produced adjacent to one end of the plate using the Knoop indentation technique.⁸ As indicated in the sketch shown in Fig. 10, two flaws designated "Type A," one on the top and the other on the bottom,

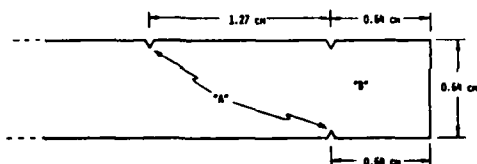


Fig. 10. Schematic diagram indicating flaw locations on ceramic test plate: "Type A" flaws generated with 750 Newton indent load, "Type B" flaw with 500 Newton load.

were produced by applying a 750 Newton force to a diamond indenter; the third "Type B" flaw was generated using a 500 Newton force. This technique yields "half penny" shaped flaws, and these were positioned along, and oriented transverse to, the center line of the flat surfaces, the "Type A" flaws are approximately 900 microns in diameter and the "Type B," 750 microns.

The transducer holder was positioned approximately 1 cm from the opposite end of the substrate and adjusted to maximize the reflection from the top edge. An oscilloscope of a portion of the amplified (40 dB) received signal, shown in Fig. 11, contains at succeeding later times echoes from the two top surface flaws (at 4.2 and 8.6 μsec), the top and bottom end edge echoes (at 10.8 and 13 μsec) and finally the echo from the bottom surface flaw (at 15.2 μsec). The echoes from the three flaws are well above the background noise level; it is to be expected, therefore, that substantially smaller flaws should be detectable even without

additional signal processing.

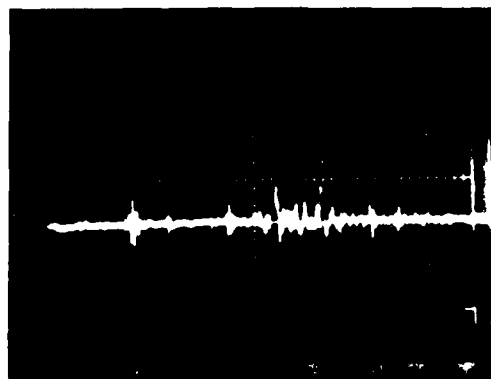


Fig. 11. Oscilloscope of amplified (40 dB) received signal indicating echoes from surface flaws at approximately 4.2 μsec , 8.6 μsec and 15.2 μsec , and the edge echoes at 10.8 and 13 μsec . Vertical: 0.5 V/div. Horizontal: 2 μsec /div.

Plots of the portion of the sampled and digitized received signal containing the reflected impulse from the top edge of the plate, and its Fourier spectrum, are shown in Figs. 12(a) and 12(b), respectively. Note that this impulse is tri-

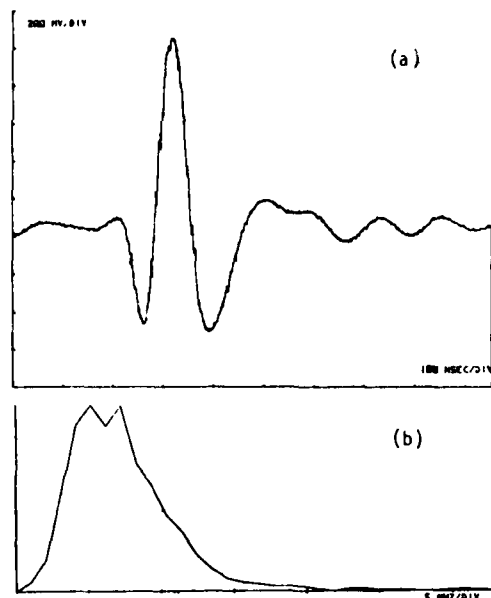


Fig. 12. (a) Plot of received echo from top edge of ceramic plate and (b) its Fourier spectrum.

polar and that it has substantial frequency components over the entire frequency range 0.5 to 10 MHz. This reflected impulse is expected to be reduced to amplitude by approximately 12 dB from the incident impulse.⁹ The received signals and corresponding Fourier spectra for the "Type A" and smaller "Type B"

flaw on the top surface of the plate and the "Type A" flaw on the bottom surface are shown in Figs. 13, 14, and 15, respectively. It may be seen that

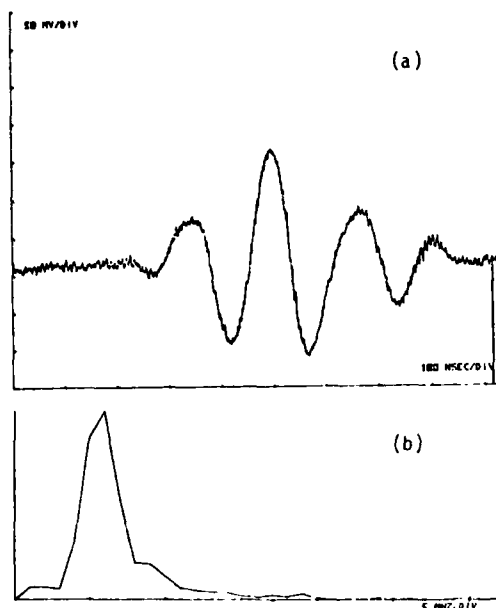


Fig. 13. (a) Plot of received echo from "Type A" flaw on top of plate and (b) its Fourier spectrum.

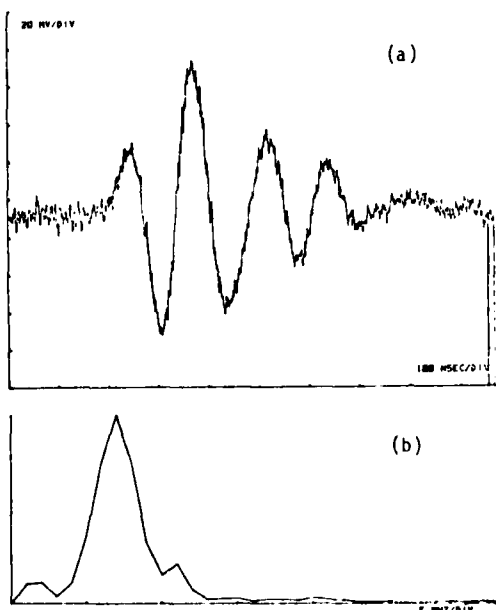


Fig. 14. (a) Plot of received echo from "Type B" flaw on top of plate and (b) its Fourier spectrum.

the peak-to-peak amplitudes for these three impulses

are approximately 270, 140 and 170 millivolts, respectively. The latter indicate that flaws on the reverse side of a substrate may be detected. The spectra of the signals from the flaws are substantially different from that of the edge reflection. As expected, both the lower and higher frequencies present in the incident pulse are attenuated in the scattered impulses. The spectrum of the top "Type A" flaw (Fig. 13(b)) peaks at approximately 6 MHz while that of the "Type B" flaw (Fig. 14(b)) peaks at 7 MHz. These correspond closely to the frequencies at which the acoustic wavelength is the same as the length of the flaw. Thus, as expected, the spectra of the scattered signals may yield useful information about the flaw size and other factors.

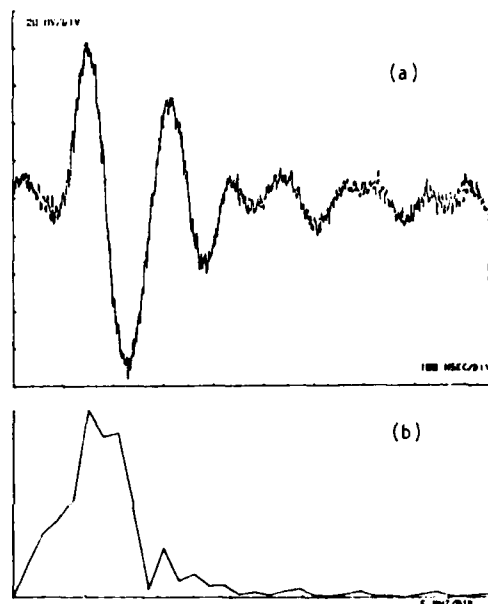


Fig. 15. (a) Plot of received echo from "Type A" flaw on bottom of plate and (b) its Fourier spectrum.

Measurements have also been made on Si_3N_4 plates with fine ground rather than polished surfaces. No substantial increase in the background noise was detected in the frequency range below 15 MHz. This appears to be the upper frequency limit for surface wave generation and detection with the transducer holding and mounting system currently being employed. Impulse propagation studies made in water using the same transducers as sources indicate that when they are driven by voltage impulses of the type shown in Fig. 14, they radiated impulses with spectra extending to 20 MHz and higher. This is illustrated in Fig. 16, where the received impulse and its Fourier spectra are shown for the case of two PVF₂ transducers, brass backed and mounted as described in this paper, one acting as source and the other as detector, used for longitudinal wave studies in water. The electronic and signal processing system is the same as that used in the present study. Note that the received signal spectrum is substantially broader than that shown in Fig. 12. With this result in mind, the design of the holder for the transducer and wedge is being improved in an effort to

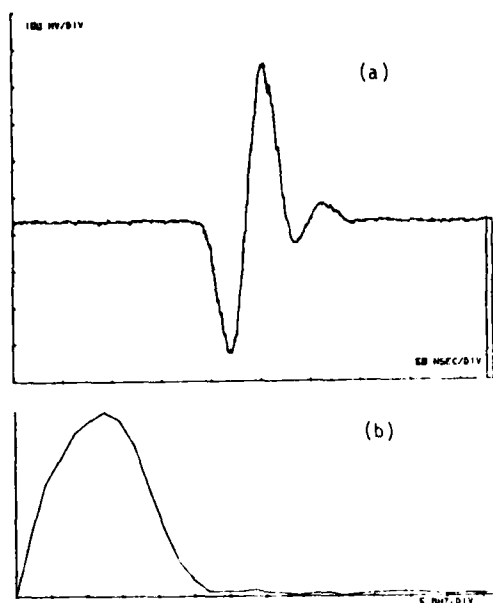


Fig. 16. (a) Plot of received impulse generated and detected in water using two PVF₂ transducers and (b) its Fourier spectrum.

increase the bandwidth and other capabilities of this technique. Further surface wave measurements are in progress on substrates with various smaller sized flaws; these are aimed at obtaining quantitative data on the relationship between flaw signal spectra and flaw length, orientation and depth, to further evaluate the applicability of PVF₂ transducers for such work.

ACKNOWLEDGMENTS

This work was supported by the Office of Naval Research under Contract N00014-77-C-0582, the Air Force Office of Scientific Research under Grant AFOSR-77-3386, and the NSF-MRL Program through the Center for Materials Research at Stanford University under Grant No. DMR77-24222.

REFERENCES

1. S. Hunklinger, H. Sussner, and H. Dransfeld, *Festkorperprobleme XVI*, p. 267 (1976).
2. L. Bui, H. J. Shaw, and L. T. Zitelli, *Electronics Letters* **12**, 16, 393 (5 August 1976).
3. E. Carome, H. J. Shaw, D. Weinstein, and L. T. Zitelli, "PVF₂ Transducers for NDT," 1979 Ultrasonics Symposium Proceedings.
4. W. H. Chen, H. J. Shaw, D. G. Weinstein, and L. T. Zitelli, "PVF₂ Transducers for NDE," 1978 Ultrasonics Symposium Proceedings, p. 780.
5. E. Carome, K. Fesler, H. J. Shaw, D. Weinstein, and L. T. Zitelli, "PVF₂ Surface Wave Transducers," 1979 Ultrasonics Symposium Proceedings.
6. J. Fraser, B. T. Khuri-Yakub and G. S. Kino, *Appl. Phys. Letters* **32**, 698 (1978).

7. B. T. Khuri-Yakub, private communication.
8. J. J. Petrovic and M. G. Mendiratta, *J. Am. Ceram. Soc.* **59**, 163 (1976).
9. F. Cuzzo, E. L. Cambiaggio, J. Damiano and E. Rivier, *IEEE Trans. Sonics and Ultrasonics* **SU-24**, 280 (1977).

UNDERSTANDING MATERIALS RELIABILITY - THE MECHANISMS OF FRACTURE

Robb M. Thomson
National Bureau of Standards
Washington, D.C. 20234

ABSTRACT

For the benefit of the NDE community, a personal view will be given of the current status of our understanding of materials fracture. The discussion will include a general description of the physical and chemical processes which occur when a solid under load possesses a crack. A physical picture is presented of the role of plasticity. The basic question of ductile vs brittle response of the solid is addressed and recent ideas and progress reviewed. Time dependence, and its manifestation in materials fatigue are briefly described. The implications for NDE are on two levels: (1) new insight generated by fundamental advances in the science of materials reliability will lead to new NDE tools; and (2) NDE techniques can and should be applied to further the fundamental understanding of reliability.

INTRODUCTION

The NDE community is closely attuned to the problem of finding and characterizing the geometry of flaws in a material, but is normally not involved in the questions which concern the mechanisms by which a material will actually fail. These mechanisms relate to how the stress is concentrated by a flaw, and to the response of the material to the stress and the environment in which the material is immersed. Since it is never a good practice to isolate one aspect of a total technical problem from another, this morning's session is designed to summarize the current status of these other aspects of materials failure.

A PHYSICAL OVERVIEW

Atomic processes are crucial to an adequate understanding of fracture. In this lecture I will address some problems associated with the physical and chemical events taking place at a crack tip where the atomic bonds rupture as the crack advances.

On this most fundamental atom mechanistic level, I know of few more complex sets of phenomena than those involved in fracture. To be specific, a crack is an opening surface interacting with various external and internal chemical environments presented to it. Our problem thus encompasses surface science in both its physical and chemical aspects. However, because a crack is difficult to get at, the powerful techniques which have recently been developed to study highly characterized surfaces are by and large not applicable to the study of fracture. We shall thus have to begin again in the development of more adequate tools to study fracture on a fundamental level.

Second, the atomic structure of the region surrounding the tip is important because the stress at the tip depends upon the positions of these atoms--that is to say whether they are in good material or on a grain boundary containing impurities or precipitates. Hence, fracture encompasses those aspects of solid state physics dealing with solid cohesion. Finally, deformation on a local level and microstructure in the material is crucial, because this determines whether the material is relatively brittle or relatively ductile. Hence, fracture contains most of materials science. Also, all these aspects interact intimately with one another.

In the face of this complexity, our first task is to sort out the basic elements of the problem and decide what are its fundamental aspects.

TABLE I
A Fracture Taxonomy

Prototypes	Material Factors	Fundamental Problems
Brittle Fracture	Plasticity	Ductile vs Brittle
Ductile Fracture	External & Internal Chemistry	Crack Kinetics
	Materials Structure	

Table I, I hope will be helpful as a kind of roadmap in thinking about the subject. There are two prototypes of fracture. The first is the classical brittle fracture in which bonds of the material are progressively broken at a crack tip. The second is fully ductile failure in which the material simply fails by ductile instability. As strain progresses locally, the cross-section of the specimen decreases, which increases the stress progressively until the last atom bond pops. On a localized basis, ductile instability leads to hole growth as depicted in the figures. Figures 1-8 show various aspects of ductile and brittle fracture.



Fig. 1

Brittle fracture of glass. This photo shows the smooth cleavage characteristic of brittle fracture in the lower portion of the photo. The upper half of the cleavage surface is termed "hackle" and is a feature of a fast moving brittle crack. The origin of the fracture was at the bottom of the rod.



Fig. 2

A truly brittle fracture in Al_2O_3 . In this thin film specimen viewed by transmission electron microscopy, a brittle crack has grown into the material from the lower left, across the field of view, and then receded to the middle of the picture. Misfit dislocations are visible in the upper portion where the crack has healed. The black bands at the bottom are interference fringes across the open crack. (Courtesy of B. Hockey)



Fig. 3

A partially brittle crack in Si. After the crack grew to the middle of the field of view in this thin film specimen, dislocations were formed around the crack tip as shown. (Courtesy of B. Hockey)

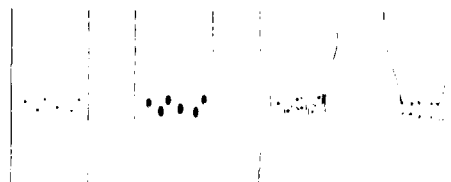


Fig. 4

Schematic view of a specimen in which fracture proceeds by hole growth. Holes are formed at precipitate particles, and under stress, grow until coalescence parts the material into two portions.



Fig. 5

Hole growth in a thin metal specimen. In this electron microscope picture, the thin specimen nucleates voids ahead of the advancing crack. The specimen fails by coalescence of the voids. (See Ref. 1)

Void Initiation in Ductile Fracture of Metals

891

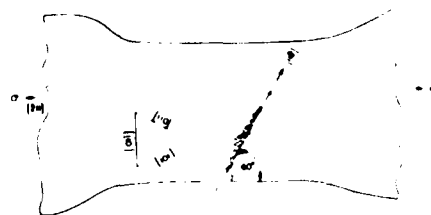


Fig. 6

Schematic view of Fig. 5. (See Ref. 1)

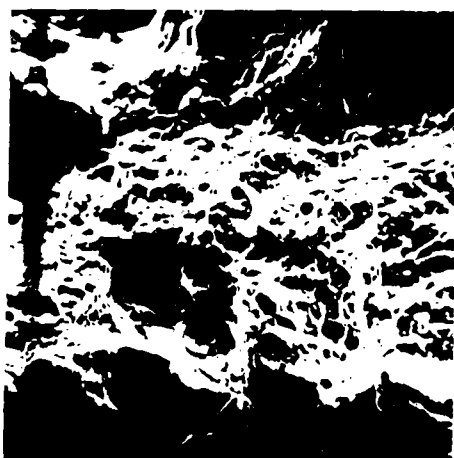


Fig. 7

Fractograph of steel fracture surface showing highly dimpled features characteristic of hole growth mode of fracture.



SEM fractograph

1800

Fig. 8

Fractograph of steel showing intergranular failure. In this case, a brittle crack progressed through the metal along its grain boundaries.

In the second column of Table I, I have listed the most important interactions with other phenomena both external to the material, and internal to it. For example, a brittle crack may emit a dislocation, and be blunted. A continuation of this process would turn a brittle crack into a hole and the brittle crack would disappear. Likewise, external chemical attack at the crack tip may assist the bond breaking process and cause fracture at lower stresses. The interaction of a crack with internal structure may be important as in the case of the grain boundary, where the stress for fracture is again lowered because of both chemical and structural lowering of the interfacial energy.

In the third column of Table I, I have grouped some major problem areas into "fundamental problems". The first is listed as the ductile vs brittle response of a material. In some ways, one can view this as the fundamental problem in fracture, because ductile failure with high toughness is always the most desired materials characteristic. The great surprises occur when the material becomes brittle because of external chemical attack. I imply that when this occurs the underlying fracture type changes from hole growth to brittle. This change of mechanism does not always coincide with the phenomenological transition from ductile to brittle behavior, but is most dramatic when it does--an extreme example is liquid metal embrittlement. I have also listed time dependent fracture effects as fundamental problems because they are kinetic effects, and are not governed by the type of thermodynamic considerations which basically dictate static phenomena.

Table I paints the field of fracture with a very broad brush. None of the topics listed there represents a highly developed and satisfactory body of fundamental knowledge. In the remainder of the lecture, I have time to delve only selectively into a few areas of special interest.

DUCTILE FRACTURE

Let us begin with a brief look at some aspects of the experimental situation in what is perhaps the most important material--steel. Steel is hardly a model material for sorting out the fundamental phenomena in fractures, but it is certainly the most intensively studied.^{2,3} In some very recent experiments, Hirth and co-workers^{2,3} have shown how a crack develops from a broad notch. See Figs. 9-12.

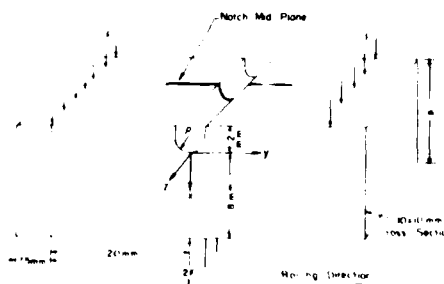


Fig. 9

Schematic of experimental arrangement. The specimen possesses a round notch from which the crack grows under bending stress. (See Refs. 2,3)

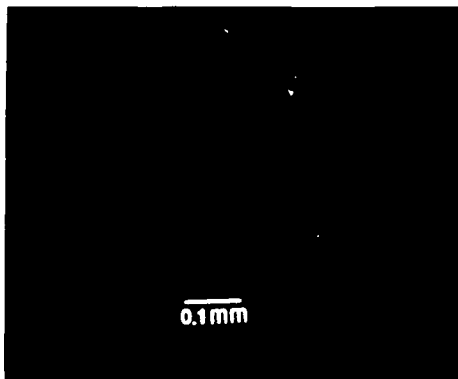


Fig. 10

Ductile fracture follows the curved lines of strain characteristics around the notch. (See Refs. 2,3)

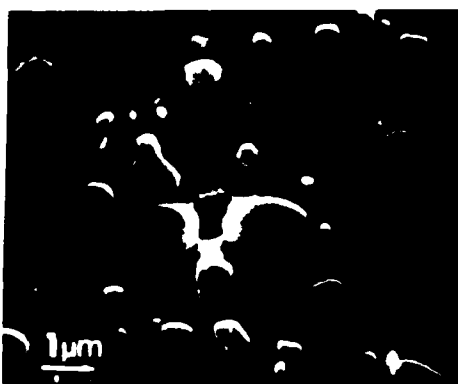


Fig. 11

Hole growth is observed to occur between closely spaced carbide particles in the matrix in the general vicinity of high shear stress. (See Refs. 2,3)



Fig. 12

Brittle fracture proceeds normal to notch surface in presence of hydrogen in high strength steel. (See Refs. 2,3)

A plastic zone develops around the notch, and then a shear instability sets in along the lines coincident with the plastic zone characteristics. In this region of very high localized strain, voids are formed at pairs of hard precipitates where strain incompatibilities are generated. The voids grow by plastic deformation and link up along the shear band, finally opening up into a crack. The effect of hydrogen has been studied, and in soft steels the same process takes place but at lower critical strain. When hydrogen is injected at the notch surface of a high strength steel, however, the whole process changes abruptly. Now a sharp brittle crack initiates at the surface, and grows in the classic fashion into the interior. The action of the hydrogen takes place either at the crack tip, or just inside, near the tip. These experiments illustrate in a beautiful fashion how the same material can exhibit both ductile and brittle fracture under different circumstances, and it illustrates in a straightforward way the important effects which external environments can play.

There are, however, additional chemical effects on fracture which are sufficiently general to be mentioned. Hydrogen not only affects the threshold for catastrophic fracture; it also causes cracks to grow slowly under a steady stress, and it enhances the fatigue failure of steel. Steady state slow crack growth and cyclic fatigue are particularly insidious from a practical point of view, because a part may perform adequately for a long period of time, and yet fail in service because of the undetected growth of cracks to the critical size for sudden failure.

Figure 13 shows the experimental results of Simmons, Wei, and their co-workers on hydrogen in steel. The observed stress dependence is characteristic of all chemically assisted fracture. Also,

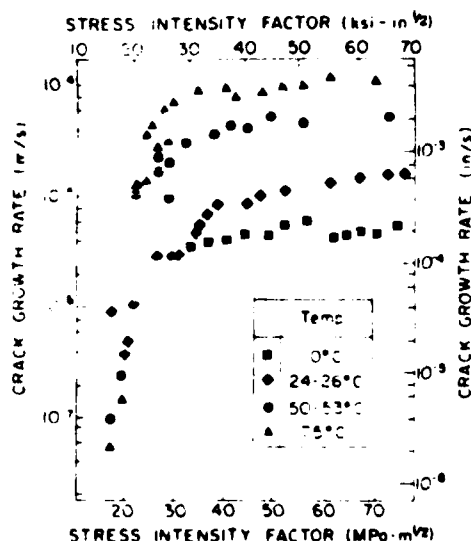


Fig. 13

Crack growth rate as a function of stress intensity factor. (See Ref. 4)

thermal fluctuations are important, and hydrogen shows an activation energy of about 0.15 eV for crack growth in Stage II. Since hydrogen is almost immediately adsorbed on clean iron surfaces, we can interpret the results as a direct interaction at the crack tip. Likewise, in dynamic fatigue shown in Fig. 14, hydrogen has an effect on fracture in

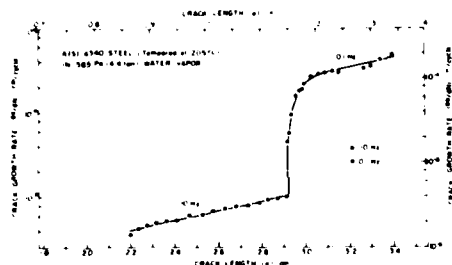


Fig. 14

Crack growth in fatigue is dependent upon frequency of stress cycle. (See Ref. 4)

high strength steel. Again, the crack growth depends upon both the magnitude of the stress and the temperature, although in this case the fundamental chemical effects at the crack tip are more obscure than for slow crack growth.

CHEMICALLY ASSISTED FRACTURE

With this sketchy experimental background, let us now turn to theory, and attempt to build some models which may help bring a measure of physical and chemical understanding to materials fracture. To begin, we focus on the problems of chemical kinetics at a crack tip, and for the moment I will ignore the role of plasticity. Consider the broadest possible picture of a crack which grows from one lattice position to the next by chemical adsorption. Figure 15 shows the configuration space of the entire system

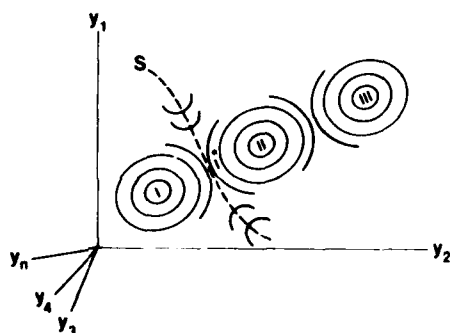


Fig. 15

Configuration space of a cracked material under stress and in presence of external environment. The successive local minima corresponds to crack growth by one atomic unit.

including the external chemical atmosphere. We shall assume that there are a series of local minima in this space corresponding to successive atomic positions of the crack. The rate, v , with which the system transverses a saddle point from one minimum to the next is given by a very simple expression,

$$v = \frac{kT}{h} \frac{Z(I^*)}{Z(I)} \quad (1)$$

where Z is the partition sum of the entire system including the external interacting chemical environment. If we assume that the external chemical environment is a gas of diatomic molecules, and that the material is a vibrating crystal lattice, these partition sums can be computed in principle. We shall assume that when the gas interacts with the crystal, it adsorbs on the surface, and that at the saddle position, one gas molecule interacts with the single breaking bond at the tip. With these assumptions, we can write a formal equation for the crack growth rate. However, I shall not burden you with it. Rather, from this approach we can get some interesting insight into the crack equilibrium condition. For a quiescent crack, we have equal forward and reverse reaction rates, and

$$v(\text{forward}) = v(\text{backward})$$

$$\frac{Z(I^*)}{Z(I)} = \frac{Z(I^*)}{Z(II)} \quad (2)$$

so the intermediate states in I^* cancel out. Since the partition sums are simply related to the free energies, F , of the system, we have at equilibrium

$$F(I) = F(II), \quad (3)$$

which is a thermodynamic statement one might almost have written down without going through the kinetics. We can carry through a transition to the macroscopic quantities one would measure in the laboratory, and when this is done, we have the familiar relation first derived by Griffith,

$$G = 2\gamma, \quad (4)$$

where G is the crack extension force, and γ is the surface energy.

The important interpretation of this result is that the equilibrium crack is governed by thermodynamics. We need to know nothing about the detailed force laws of the solid atoms or the external chemical environment to find the stable crack length. This crack length is governed solely by thermodynamic variables such as the surface tension of the solid, chemical potentials of the external gaseous molecules, and the crack extension force. This result was correctly stated by Griffith⁵, by Petch⁶, and more recently by Rice⁷, but is still not properly understood in the fracture community.

Chemical effects are universally thermally activated processes, and we next inquire about activated processes in fracture. You will not be surprised that I shall not get too realistic about such activation energies, but it is instructive to develop qualitative models. For this purpose, consider a two-dimensional array of atoms, Fig. 16.

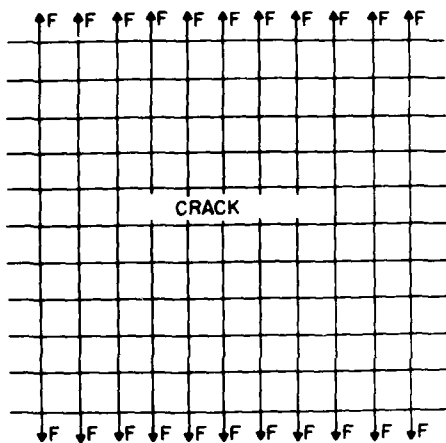


Fig. 16

Two-dimensional array of atoms stressed at outer boundaries and containing a crack.

Assume for the moment that the atoms are all connected with linear springs. Then the solution for a crack of length l is as shown in Fig. 17. When the crack is one atom spacing longer, $l+1$, the compliance is slightly lower, and the slope of the solution in Fig. 17 is likewise lower. For a given length, as

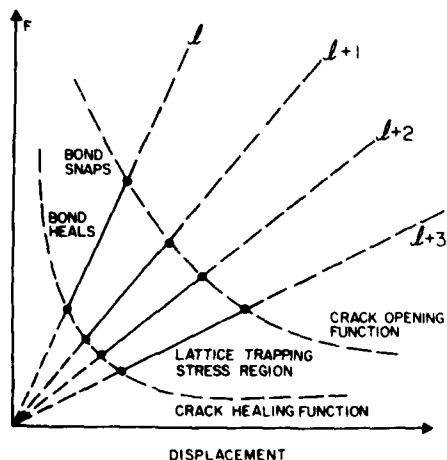


Fig. 17

Solution of two-dimensional array. Force is plotted as a function of displacement of central atom pair. Since forces are linear, solution is a set of straight lines, one for each length, l , of crack.

the stress is increased, the force on the bond at the tip increases until it can no longer hold. The bond breaks, and the solution snaps from one line to the next in Fig. 17. But we can also get from one line to the next by thermal fluctuations. Simple expressions can be derived for the activation energy for one dimensional models of cracks.

The chief conclusions from considerations such as these are: (1) the important chemical assistance to fracture comes from direct interaction at the crack tip; (2) activation energies appear to go as

$$\Delta E \propto (K - K_c)^n \quad (5)$$

where K is the stress intensity factor for the crack. n takes values from about 1.5 to 2; (3) chemical bridging reactions at the crack tip are possible and could have the effect of chemically strengthening a material; (4) molecule size factors can be important in chemically assisted fracture; (5) as in all surface chemistry reactions, chemical specificity will be important; and (6) chemically assisted fracture will have a different (although often analogous) chemistry from plane surface chemistry.

THE ROLE OF PLASTICITY

Recently, three investigators have addressed the effect of plasticity in brittle fracture in a fundamental way^{10,11}. They have all made the assumption that a brittle crack can coexist with a surrounding cloud of deformation without blunting. Figure 18 shows that if the plastic strain surrounding the crack tip is heterogeneous and limited, then

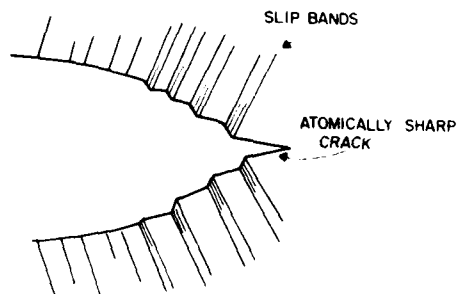


Fig. 18

Schematic drawing of a sharp crack in heterogeneous deformation field. The slip lines are visible on the crack surfaces.

a sharp crack will in fact not be blunted. One can then solve the stress problem, Fig. 19, assuming that the sharp brittle crack which we have just discussed sets the boundary condition for small distances.

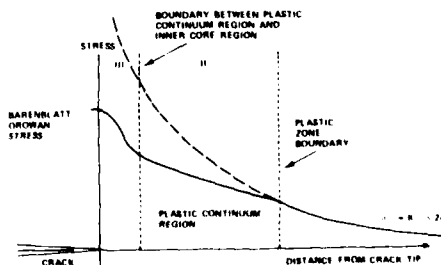


Fig. 19

Schematic view of the stress as a function of distance from a sharp crack embedded in a field of plastic deformation.

Some kind of continuum plastic region is formed in the intermediate region, and at large distances from the crack tip where the stress is below yield, an elastic solution is valid. One can then derive expressions in which the true surface energy of the core crack is a driving term for the whole stress distribution. One such expression predicts that the overall stress intensity factor, K , of the fracture is related to the intrinsic surface energy of the system by

$$K \propto K(\gamma, \sigma_y, \mu, n, \eta) \quad (6)$$

where n is the work hardening exponent, σ_y the yield stress, μ the modulus, and η the maximum density of dislocations at the crack tip. This theory appears to be consistent with the hydrogen embrittlement of high strength steels. The most important conclusion of the work of these three investigators is that a total theory of fracture is given which encompasses a fracture criterion, which is a missing ingredient in any continuum treatment. These theories indicate how the small effects--energywise--which go on at the crack tip of the brittle crack become magnified by the shielding effect of the plastic zone. In further work it will be necessary both to test the range of validity of these ideas, and to give them a more quantitative basis by means of the study of the response of small regions under inhomogeneous high stress. A fundamental understanding of how brittle fracture can become ductile is yet to be developed.

In summing up, from the fundamental physical and chemical point of view, we can begin to see how some of the basic fracture phenomena can be understood in a semi-quantitative way, but this field is characterized by much debate. A great deal of work remains to be done on model systems in order to sort out the elementary processes.

REFERENCES

1. R. Lyles and H. Wilsdorf, *Acta Met*, 25, 269 (1975).
2. T. Goldenberg, T. Lee, and J. Hirth, *Met Trans*, 9A, 1663 (1978).
3. T. Lee, T. Goldenberg, and J. Hirth, *Met Trans*, 10A, 439 (1979).
4. R. Wei and G. Simmons, *Tech Rpt 8*, Lehigh Univ. IF SM-79-94.
5. A. Griffith, *Phil Trans, Roy Soc London*, A221, 163 (1920).
6. N. Petch, *Phil Mag*, 1, 331 (1956).
7. J. Rice, MRLE 106, Brown Univ. report (1977).
8. For these results, see two forthcoming papers by R. Thomson and E. Fuller, *J Matls Sci*.
9. R. Thomson, *J Matls Sci*, 13, 128 (1978).
10. J. Weertman, *Acta Met*, 26, 1731.
11. E. Hart, *Int J Solids & Struct*, to be published.

SUMMARY DISCUSSION
(Robb Thomson)

George Herrmann (Stanford University): Just a point of information on relationship 3. How do you obtain it?

Robb Thomson: One carries through, through the program I just described. The problem is broken into three parts. The inner part consists of a brittle crack, perhaps even in a discrete lattice, there might also be chemistry affecting the crack tip. Then a cutoff radius is defined separating the inner region from the next, intermediate, region described by continuum plasticity. I really don't know how to do that, but results of experiments may eventually help. Of course, this difficulty brings up the whole question of whether the crack tip is blunted by the deformation or not. So, the intermediate region is easy, and the solution for it has been contained in the literature for some time. You can find it, for example, in Rice's article in the Fracture Treatise, Vol. II, even including work hardening. Finally, the third region is the linear region, that portion of the material where the stress is below the yield stress. When these three regions are pasted together, self-consistently, a fracture criterion can be derived.

George Herrmann: From which you derive this expression:

Robb Thomson: Yes. I must say, however, that several people have been deriving fracture criteria for quasi-ductile fracture from slightly different points of view. In addition to the one I have outlined, Wertman, Howard, and Hart have derived such expressions.

Don Thompson (Science Center): I was wondering, when you go through your models and discussion as you have, could you prioritize the properties that one could measure to give an early indication of impending crack growth?

Robb Thomson: You are bringing me down to earth. Well, that's actually going to be the subject of much of the latter part of the morning. It involves a study of the range of slow-crack growth. It involves a study of the threshold values for crack growth; all this is from the empirical point of view. And, of course, it involves a vast amount of study of the understanding of these things. The deeper understanding of fracture is what I have been talking about here. Although, I have tried to indicate where some progress in fundamentals is being made, this understanding has not reached a very complete stage yet in terms of the material factors that govern fracture threshold values and the crack growth values. And, as I indicated, there is a great deal of complexity that goes into the chemistry of the surface and the crack tip regions and the substructure at the crack tip. So, we are a long way from being able to have a very close relationship between the problems you want solved and fundamental understanding.

Unidentified Speaker: Simply a comment on your point 3 to which George Herrmann reacted. That point was made in 1963 by Bertram Grover, namely, the shielding of the plasticity onto the crack tip, and the fact that the intrinsic fracture energy may play a much more important role than has been believed so far. As a matter of fact, I think it was Orowan who suggested that plasticity and intrinsic fracture energy be additive quantities in the fracture process. It turns out in other dissipated materials, such as visco-elastic materials can show very clearly both analytically and experimentally that the two are not additive; they are multiplicative. So, if you make the intrinsic fracture energy zero, you have no strength, as it should be, and you cannot derive simply from plasticity strength. And what the dissipated characteristic does, it modifies the intrinsic fracture energy of the material. So, if you play around with the intrinsic fracture energy of the material, keeping the plasticity aspect, displacing it changes the strength of the material.

Robb Thomson: I couldn't have said it better.

Jim Rose (University of Michigan): What are the physical mechanisms that would lead to the shear crack tip?

Robb Thomson: Well, that's the question which I neither had time to discuss; nor does anybody know much about it. I view ductile fracture and brittle fracture as a competition between two completely different mechanisms. One is a completely plastic process. The other is true fracture, where atoms are pulled apart at a sharp crack tip. The factors which govern how one process overwhelms the other constitutes the fundamental problem which I listed in the beginning of my lecture.

#

SUBCRITICAL CRACK GROWTH AND ITS RELATION TO PREDICTIVE ANALYSIS

H. L. Marcus
The University of Texas at Austin
Austin, Texas 78712

ABSTRACT

This talk will discuss the relationships between subcritical crack growth and the nature of the loading, the environment under which the loading takes place and the type of material tested, and how this data is used in predictive analysis. Loading conditions will include sustained loading as well as constant and variable amplitude cyclic loading. The environments will include vacuum as a baseline environment and both gaseous and liquid aggressive environments. The comparison between crack growth behavior in brittle and ductile materials will also be made.

The data will be discussed from the viewpoint of reproducibility and reliability for use in predictive analysis.

INTRODUCTION

The question may be asked as to why should a talk on subcritical crack growth be included in a meeting on quantitative NDE. The answer may be best answered by an experience I have just had on my trip to this meeting. I found the battery in my minivan hanging out of the bottom of the vehicle. On closer inspection I found a nine-inch crack across one side of a nine-inch wide support plate and a combination of a three-inch and four-inch crack on the other side. Of course the nine-inch crack explained why the battery was hanging loose. But in regard to the topic of this talk, it was obvious that insufficient inspection, combined with the cyclically induced fatigue crack growth led to the premature failure. Even if the inspection was made initially to be able to decide when failure would occur, it requires a detailed understanding of how the crack would propagate in a specific material under the loading and environmental conditions to which it is exposed. This paper will try to give a general idea of what can be expected, including some of our recent efforts on load history effects. It is obvious that only a small segment of the topic can be discussed, so the reader is referred to some of the recent texts on the subject for details. (1-5)

SUBCRITICAL CRACK GROWTH

Subcritical crack growth can be separated into two types. The first is sustained loading where the load is applied to a material with a particular microstructure containing a flaw or crack exposed to a given environment. This is usually described as a stress corrosion crack growth phenomena. The second is where the flaw containing material of the given microstructure is exposed to an environment under a cyclic loading condition. This is usually referred to as corrosion fatigue crack growth. In general, a structure is exposed to both sustained and cyclic loading and both types of crack growth can be seen.

Stress Corrosion Crack Growth

Stress corrosion crack growth occurs for many materials under many environments. Examples are aluminum alloys in salt water, titanium alloys in salt water or methanolic solutions, and steels in aqueous solution or hydrogen on hydrogen sulfide gas. There are a great many combinations of microstructure of the material and the environment that can lead to stress corrosion cracking. An example of how the stress corrosion crack growth behavior is characterized is given in Figure 1 for a titanium alloy loaded in a methanolic solution. The experiment is to monitor crack growth as a function

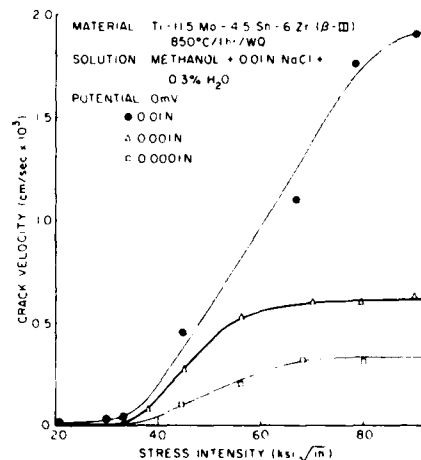


Fig. 1 Stress Corrosion Crack Velocity for Ti alloy in Methanolic Solution

of the applied stress intensity, $K = \sigma \sqrt{a}$, where σ is the remotely applied static stress, a is the geometric parameter and a the crack length. What is normally observed is a value of K defined as K_{ISCC} below which no crack growth occurs, a region where crack growth is virtually K -independent, and a region of fast crack growth when K approaches a critical value which is the fracture toughness of the material. This is shown schematically in Figure 2.

To account for the stress corrosion crack growth behavior in determining the life of a structure after an initial flaw size is determined by quantitative NDE, you just integrate the crack growth rate over the time of exposure in the sustained load and environment to establish when failure is expected. For example, if a structure

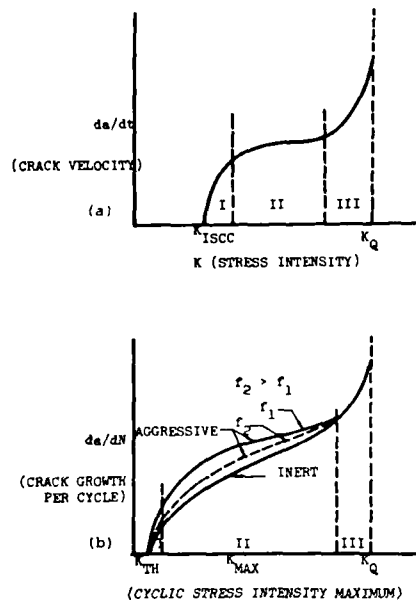


Fig. 2 (a) Schematic of stress-corrosion behavior
(b) Schematic of environmental influence on fatigue-crack growth for $R = 0$, $K_{max} = K$.

containing the titanium alloy was loaded at 40 Ksi \sqrt{in} for two days in 0.01 N NaCl, the crack would have grown about 50 cm. This is obviously a very intense material-load-environmental condition. The obvious problem in designing to stress corrosion cracking is that a large amount of data is required to make the predictive analysis. The particular material-load-environment of interest must be evaluated.

Fatigue Crack Growth

The second type of loading involves the application of cyclic loads. This type of behavior is characterized experimentally in two ways. The first involves not only the crack growth under cyclic loading, but the initiation of the propagating crack. This is shown in Figure 3, where a cyclic stress, S , is plotted against a number of cycles to failure. This plot could be considered to be separated into the two regions. The first is when a crack of NDE detectable size, a_0 , is established and the second, the fatigue crack growth region where the crack propagates to failure. This latter region, which is of most interest in this talk, is generally characterized by a plot of da/dN , which is the crack growth per

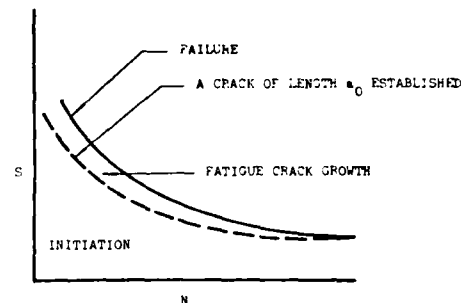


Fig. 3 S-N curve separated into crack-initiation and crack-propagation regimes.

cycle as a function of the cyclic stress intensity, ΔK , under constant amplitude loading. This is shown in Figure 2(b) for the case where $\Delta K = K_{max} - K_{min}$ and $K_{min} = 0$. Comparison of Figure 2(a) and Figure 2(b) shows some interesting effects. K_{ISCC} is at a stress intensity factor greater than the threshold stress intensity, K_{th} , the stress intensity below which no fatigue crack growth is observed. Although no sustained load crack growth effect of environment is seen below K_{ISCC} , there is an environmental effect under cyclic loading below that value. The environmental effect is also influenced by the cyclic frequency, another loading variable, as shown schematically for two loading frequencies, f_2 greater than f_1 . In general the higher the frequency the less the environmental effect after some minimum frequency. In many cases, such as in aluminum alloys, the failure mode will change such that it is intergranular in stress corrosion, with both da/dt and K_{ISCC} very microstructure-dependent and transgranular in corrosion fatigue crack growth with very limited microstructural dependence. In Figure 2(b) the inert environmental fatigue crack growth rate is determined in either vacuum or pure inert gases.

A modification of the environment can greatly change the fatigue crack growth rate. Figure 4 shows the influence of mixing gases with hydrogen on the fatigue crack growth rate of an A514B steel for fixed microstructure and loading conditions. Pure hydrogen has a factor of about ten greater growth than vacuum, and mixed gases have varying effects on the crack growth rate observed in pure hydrogen. Similar effects have been noticed on nickel base alloys. Here again, a fracture mode change can be observed. It is very common for intergranular failure to be associated with the hydrogen embrittlement, for both sustained and cyclic loading conditions. H_2S as a gas or in aqueous solution shows a much higher growth rate than pure hydrogen.

There is a great deal of scatter associated with both types of subcritical crack growth. Figure 5 shows an example of the scatter associated with a round-robin test where the steel used was identical. The laboratory-to-laboratory scatter was about a factor of three. Which line

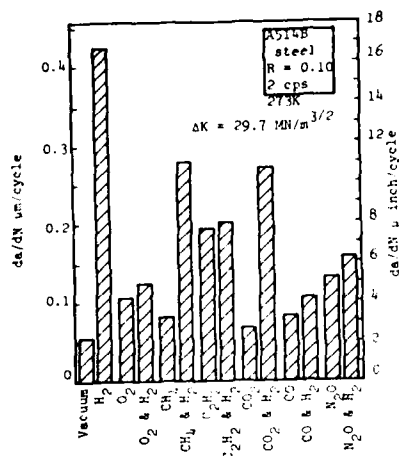


Fig. 4 The fatigue-crack propagation of ASTM A514B steel in various gaseous environments.

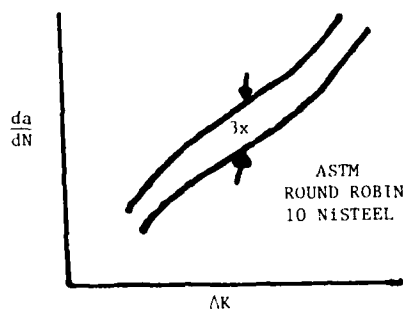


Fig. 5 Schematic of fatigue crack growth in 10 Ni steel showing scatter for round-robin testing.

to use in design is a constant problem in terms of how conservative to be.

Designing for a defined lifetime using fatigue crack growth data is similar to that discussed earlier for sustained load crack growth. The first approximation is a linear superposition of the constant amplitude da/dN data for each of the variable loads associated with a design loading spectrum. This is just the integration of the loading history combined with accounting for the continuing crack growth. The result is a crack length versus number of cycles or blocks of cycles as shown in Figure 6.

In general, the linear superposition model predicts a lifetime lower than that actually experimentally observed. This has been explained in terms of residual stresses at the tip or crack

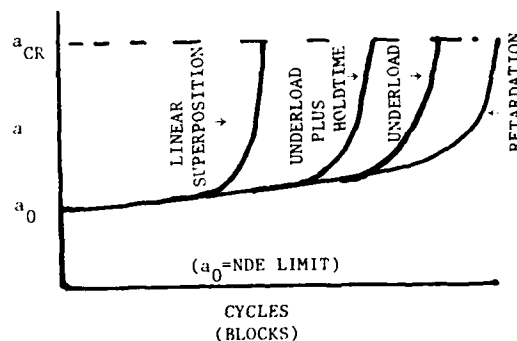


Fig. 6 Schematic of crack growth from the NDE limit a_0 to the critical value a_{CR} for several models of fatigue growth rate.

closure models. Both explanations rest on the fact that the prior non-uniform loading history must be taken into account. The crack closure model implies extra material is present on the surface of the crack which touches before the load is reduced to the minimum. This touching of the surfaces then eliminates the angularity at the crack tip and reduces the range in stress intensity, ΔK , to one that is an effective range in stress intensity, ΔK_{eff} , defined as $K_{max} - K_{closure}$. We have recently documented that at least part of the extra material on the surface is from the formation of an oxide.

The crack growth is then modeled based on one of the models and since the ΔK is reduced to ΔK_{eff} the predicted lifetime is extended. This is also shown in Figure 6.

Another factor in load history is shown on Figure 6. This is the influence of an underload on the predictive behavior. An underload will reduce the lifetime by lowering the crack closure load on the residual stress, which increases ΔK_{eff} . Another factor we have recently studied is the influence of hold time at an underload on the subsequent growth rate. What is observed in the 2000 and 7000 series aluminum alloys is that there is a relaxation process that further reduces the closure load, again increasing ΔK_{eff} and shortening the lifetime. This is also shown on Figure 6. The significant problem introduced by this result is how do you do laboratory tests in reasonable times and extrapolate them to the real time usage that a structure undergoes.

SUMMARY

In this paper I have tried to review the state of subcritical crack growth. Subcritical crack growth under either sustained or cyclic loading must be understood before the criticality of a quantitatively NDE determined flaw can be determined. It is the key link that merges the NDE crack length, a_0 , and the fracture mechanic critical crack length, a_{cr} .

ACKNOWLEDGEMENT

This research was supported by the Air Force Office of Scientific Research, NE contract number AFOSR 76-2955.

REFERENCES

1. Fatigue and Microstructure, 1978 ASM Materials Science Seminar, M. Mechii, Chairman, Published by The American Society for Metals (1979).
2. Stanley T. Rolfe and John M. Baisom, Fracture and Fatigue Control in Structures, Prentice-Hall (1977).
3. Richard W. Hertyberg, Deformation and Fracture Mechanics of Engineering Materials, John Wiley & Sons (1976).
4. M. R. Louthain, Jr., and R. P. McNitt, Environmental Degradation of Engineering Materials, VPI (1977).
5. Stress Corrosion Cracking - The Slow Strain Rate Technique, Ugiansky and Payer, eds., ASTM STP665 (1979).

SUMMARY DISCUSSION
(H. Marcus)

George Gruber (Southwest Research Institute): Davidson's laboratory received a fatigue crack specimen from the Electric Power Research Institute, and they closed it. I looked at it before closing and after closing ultrasonically. I have that specimen with me today, and I will bring it in tomorrow for my talk. I have been able to measure the fracture from the crack tip even when it was as closed as I could close it. The key to it is to get off normal and come at an oblique incidence of about 30 degrees, and there you see it. You made a statement I thought I should reply to that we can at times determine the crack tip, the length of the crack even if it has been already closed.

Harris Marcus: I'm sure there isn't a hundred percent transmission through the totally closed crack, and as you get better and better into the signal-to-noise, as you are doing, you will be able to bring it out.

George Gruber: You can monitor either growth or shrinkage of the crack, so to speak, even if it's very closed. You will get an ultrasonic signal if you get off the normal to the crack.

Harris Marcus: I'm not sure what you mean by shrinkage.

George Gruber: Closing.

Harris Marcus: You are monitoring the section that is closed.

Gordon Kino (Stanford University): Perhaps what we are saying is if you come at an angle to a crack, you can see the crack tip from time delay, but amplitude measurements are unreliable.

Harris Marcus: Good. That is what I think the whole name of the game is within this group, how to get at them when they are simple transmissional type of work that I have been using. The thing you have to recognize is that little signal is really the one you want if you want to measure the true crack, not the big one.

George Gruber: If you come on normal, the little signal gets swamped by reflective waves.

#

ELASTIC PLASTIC CRACK MECHANICS

J. R. Rice
Division of Engineering
Brown University
Providence, Rhode Island 02912

ABSTRACT

Recent developments in elastic plastic fracture mechanics are reviewed. These include the J-integral and its application, as well as recent work on predicting the crack surface opening profile and criterion for continuing quasi-stable crack growth for ductile solids.

#

SUMMARY DISCUSSION
(J. Rice)

Brian Defacio (Ames Laboratory): I would like to know if in your paper the theory is based upon (inaudible).

Jim Rice: The theory is based on this rate independent model. You can, in fact, do analogous things for strong idealizations of great dependent materials like, say, nonlinear viscous materials. But if you try to get very fancy about constitutive relations, you quickly lose any kind of path-dependent integrals. The thing is, no one really believes materials behave that way. As long as, in Eshelby's terms, if we don't call the material's bluff -- or I guess it's the opposite: if the material doesn't call our bluff, it's a simple approach which lets you attack very complex problems. So, why not use it.

Tom Collins (Air Force): When you start putting this "R" in there, you lost me. How does R vary from material to material? Can you relate that to some material characteristic?

Jim Rice: We think the R is simply an indication of the plastic zone size, so in fact it's something that you have calculated. It's a function of J. Complications come in only when you go to fully plastic geometries in cases where you have contained plasticity. We have at present a fair idea of how that parameter varies with J. Is that what you meant by R? Or did you mean the resistance curve itself?

Tom Collins: Why you related it. You have to be very careful on something like that. It's just an adjustable parameter. And so often in this game you begin to develop sight simulations, and the more you do it the more you believe it's the correct thing.

Jim Rice: I'm not sure we are making contact here. The R I introduced --

Tom Collins: This is capital R.

Jim Rice: Capital R is just part of the continuum mechanical solution. So, there is nothing in there. The thing to worry about is the crack growth criterion itself. Based on that requirement that in a certain sense the crack ought to look similar near the tip as it grows. Maybe there is no good reason for that. Especially if you consider cases where the plastic zone size at the start of the growth might be enormously different, very much smaller than that after a lot of growth.

#

MICROCRACK INITIATION AND GROWTH

W.L. Morris and M.R. James
Rockwell International Science Center
Thousand Oaks, California 91360

ABSTRACT

A Monte Carlo simulation technique to predict the mean and scatter in fatigue lifetime of certain 2000 and 7000 series aluminum alloys is described. The method is based upon models of surface microcrack nucleation and early growth, which comprise the initiation phase of the fatigue failure process. The experimental basis for the models is discussed, and examples of predicted numbers and lengths of microcracks developed during fatigue of Al 2219-T851 are compared with experiments. Scatter in lifetime and mean lifetime predictions are also discussed. These are obtained from repeated running of the fatigue simulation, for which scatter in lifetime results from the effect of local microscopic variations in alloy microstructure on the time of crack initiation. The association of the method with a "retirement for cause" philosophy is noted.

INTRODUCTION

For many structural applications, the fatigue lifetime of a metallic component is dominated by the crack initiation phase of the fatigue failure process. This is particularly true for components in "fail safe" usage, but applies to a significant number of "safe life" designs as well - for which the intent is to inspect components during service with sufficient frequency to remove damaged components before catastrophic failure. The large scatter in fatigue lifetime common to the crack initiation stage of fatigue failure presents a problem, both in the design and in the inspection of such components. In design, performance/cost considerations may dictate less conservative designs and a key design decision then hinges upon prediction of the effect of reduced design safety margin on early component failure. With respect to NDE, microcracking in the initiation stage is a challenge to detect, and the time of transition from initiation, to macroscopic cracking, to failure can be abrupt and sensitive to the statistics of the failure process. Conventional design practice is reasonably well equipped to specify component performance near the mean component lifetime. An approach is needed, however, to reliably predict the probability of infrequent early component failures.

Component fatigue lifetime may be sensitive to alloy surface condition, to residual stresses induced in manufacture and modified in use, and to alloy microstructure.¹⁻⁴ In principle, at least, surface condition and residual stresses introduce scatter in lifetime only if they are uncharacterized. In contrast, the effect of the statistics of the microscopic failure mechanisms on lifetime is inherently statistical in nature and must be dealt with in that vein. Reported here are the initial results of a technique to predict the scatter in lifetimes which arises from the statistical nature of the microscopic fatigue failure process of certain aluminum alloys. It is hoped that, in the future, the method may serve as a model for similar prediction procedures for other structural alloys. In the longer term, our concept is to integrate the lifetime prediction procedure with a contemporary computer aided design facility so that a designer can obtain "real time" predictions of the fatigue performance of a component during the design process.

Our general approach to lifetime prediction relies on a Monte Carlo simulation of microcrack initiation.⁵ To illustrate the nature of fatigue crack initiation in the alloys of interest, we refer to scanning electron micrographs of surface cracks in a polished, then fatigued, specimen of Al 2219-T851 (Fig. 1). The alloy surface is a preferred site for cracking due to a reduction of the

SC 79 4431



Fig. 1 Micrographs of Surface Microcracks in Al 2219-T851. Crack at arrow in (a) is 0.015 in. in length. Initiation phase occurs in crack size regime enclosed approximately by box (b), with crack lengths on the order of grain size and less. Nucleation is principally at intermetallic particles as in (c).

bulk constraint of deformation at the surface. The specimen is under a large tensile load to make the cracks more visible. The crack at the arrow in Fig. 1a is 0.015 in. in length. This is sufficiently long for subsequent propagation of the crack to be predicted using conventional fracture mechanics, were it not for the additional complexity of the prospect of multiple crack coalescence. The further magnified region in Fig. 1b contains several cracks

of approximately one grain size in length. It is the nucleation, early growth and coalescence of such cracks which comprise the initiation phase of fatigue failure. Nucleation in this alloy commonly occurs by fracture of intermetallic particles at or near the surface as the case illustrated in Fig. 1c. By definition, initiation ends with the formation of a macrocrack of sufficient size that its subsequent propagation rate can be estimated with conventional fracture mechanics. During initiation, rates of microcrack nucleation and growth are highly sensitive to the alloy microstructure in the region of a microcrack site. Scatter in the time of initiation reflects the statistics of nucleation and growth as determined by the possible distribution in microstructure which can occur in regions in a component vulnerable to crack initiation. Naturally, the initiation events illustrated in Fig. 1b have occurred much too late to have any appreciable effect on lifetime. It was similar events early in the formation of the 0.015 in. crack which were a principle factor in determining fatigue life.

Fatigue lifetime for the alloys of interest may be predicted using a Monte Carlo simulation of crack nucleation, early growth and coalescence. The computation scheme is illustrated in Fig. 2.

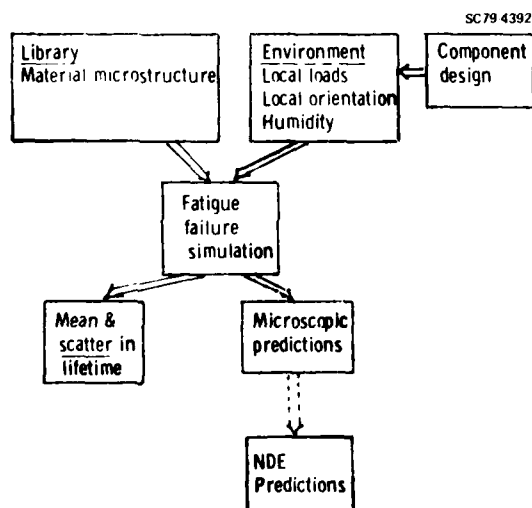


Fig. 2 Schematic illustration of steps in computer simulation of alloy fatigue failure.

A finite element analysis is used to identify regions in a tentative component design vulnerable to fatigue, and to calculate the distribution of surface stress in those areas. An additional input to the calculation is the material orientation and "average" microstructure in the vulnerable areas. Microstructure includes the distribution in grain and intermetallic particle sizes in the material, relative to the surface stress axis. The fatigue model combines a Monte Carlo simulation of initiation with a conventional fracture mechanics calculation of lifetime spent in propagation of a macrocrack to a critical size. By repeated running of the simulation, we obtain the scatter and mean in fatigue lifetime. At intermediate points in the lifetime of an individual specimen, a prediction of the numbers and lengths of the surface microcracks

can be obtained. This provides simulation data for a sensitive comparison between model and experiment. Such data also define the nature of cracking distributions which must be detected by NDE methods to determine the state of fatigue of a component at that point.

INITIATION MODELS AND MICROSCOPIC COMPARISONS OF SIMULATION TO EXPERIMENT

The models used to predict microscopic nucleation and early growth behavior are briefly described. Independent tests of the models are also shown, along with selected comparisons of microcracking parameters obtained experimentally and by simulation. With respect to crack coalescence, our simulation employs a rather simple view of the process. It considers only coalescence of cracks located initially, either in neighboring grains or separated by no more than one intervening grain. Our rationale is that coalescence of more widely spread cracks comes too late in the initiation process to have any substantial effect on lifetime. Additionally, we assume that the presence of one microcrack does not effect the propagation of another until their tips are in a common grain. There is some experimental evidence to support such a model, as is discussed below for propagation of isolated cracks. The key factor is that the plastic deformation at a microcrack tip is substantially confined inside the grain containing the microcrack for a wide range in grain sizes and crack lengths.

Nucleation. A dislocation based model has been proposed by Chang et al.⁶ which relates the rate of cracking of intermetallic particles during fatigue to the accumulated strain energy density at a potential nucleation site. A two step process is identified: 1) fracture of the intermetallic; 11) propagation of the crack into the matrix. Each process is described by its own rate equation. With reference to Fig. 3 for microscopic nomenclature, the earliest number of cycles N_I at which

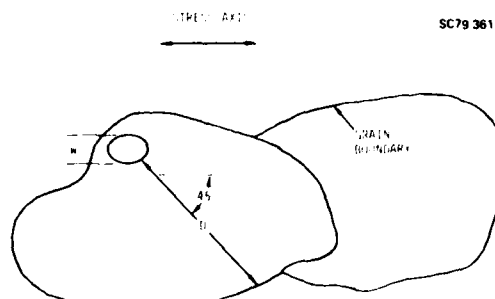


Fig. 3 Alloy surface section illustrating definition of intermetallic width (W) and slip distance (D) parameters.

cracking of an intermetallic can take place is given by,

$$N_I = C_0 / DW^3 (\tau_{eff} - \tau_0)^2 \quad (1)$$

Subsequent cracking into the matrix can occur no earlier than

$$N_{II} = C_0' / D'W (\tau_{eff} - \tau_0)^2 \quad (2)$$

σ_0, σ_0' and τ_0 are material constants. D is the maximum slip distance at 45° to the stress axis in the grain containing the intermetallic. W is the intermetallic width normal to the stress axis. τ_{eff} is an effective surface shear stress which is calculated from the grain's crystallographic orientation and external load, and accounts for the effect of grain orientation on the propensity for slip.

The predicted trend is, therefore, for nucleation to occur first in the largest grains (large D) at the largest intermetallics, and to proceed to smaller D, W with increasing fatigue. This behavior is modified, however, by the crystallographic orientation of the grains which can lead to instances of early nucleation at small D, W sites for favorable grain orientations.

To calculate an average nucleation rate, it is necessary to integrate over all possible D and W combinations which can occur as determined by the probability distribution of these quantities for the alloy microstructure. Results of such a calculation are shown in Fig. 4. Plotted are the number

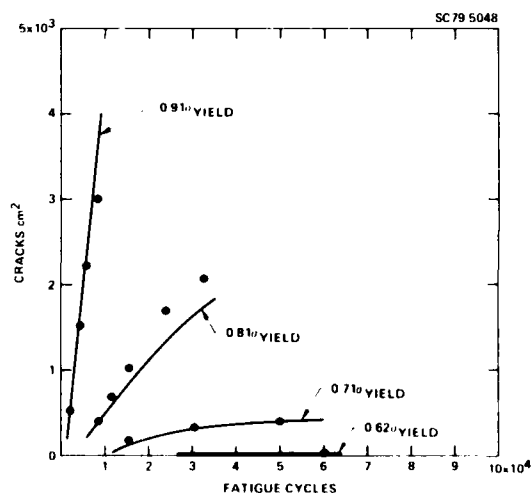


Fig. 4 Comparison of measured (dots) to predicted (lines) number/cm² of intermetallics fractured by fatigue of Al 2219-T851 for four maximum cyclic stress amplitudes (fractions of the yield strength, σ_{yield}) for fully reversed loading.

of broken intermetallics as a function of number of fatigue cycles. (Thus, the figure describes the step I nucleation process.) Data are shown for four cyclic stress amplitudes for a Al 2219-T851 alloy. Fatigue was terminated when the largest microcrack reached approximately 400 μm . The solid curves are from the computer simulation, the dots are experimental points. Several features should be noticed. Cyclic amplitude effects crack density by several orders of magnitude. Nucleation begins early in the specimen lifetime even for the smallest stress amplitude. The decreasing rate of nucleation with fatigue for the small stress amplitudes is attributed to a cyclic hardening of the surface. This is strictly a near surface effect which disappears in dry air.

The derivative of the curves in Fig. 4 give, naturally, the corresponding average rates at which intermetallics fracture with fatigue. By random selection, these are used to choose the cycles N_1 of each nucleation event. D and W values are then selected, consistent with constraints of the rate equation, and N_{II} is calculated. Figure 5 shows a comparison between measured values of D vs. W , and

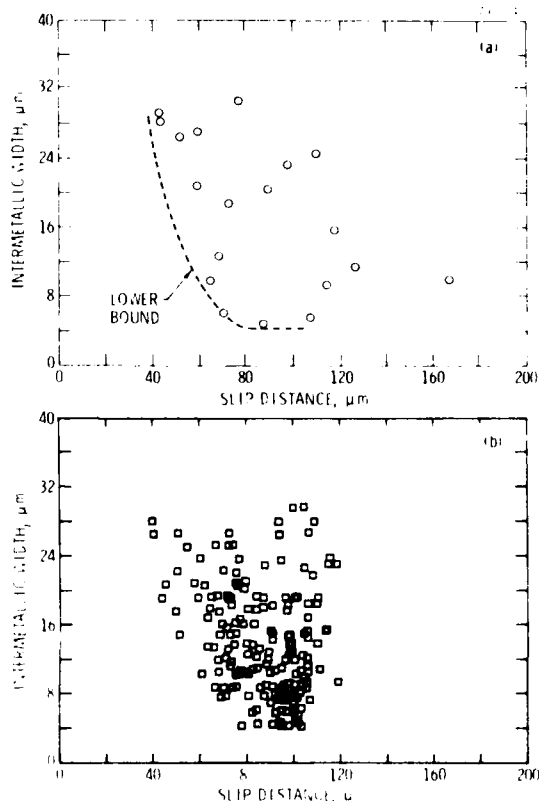


Fig. 5 Comparison of measured to simulated values of D, W producing cracking into the matrix for Al 2219-T851 for 500 fatigue cycles with maximum stress amplitude of 90% of the yield strength. Dashed lower bound of experimental data (Top) is obtained from the simulation (Bottom).

values obtained from simulation for the step II nucleation process for a selected set of fatigue cycles and cyclic stress amplitude. Each datum for both cases corresponds to an individual nucleation event. The dashed lower bound to D vs. W on the experimental data is obtained from the simulation. Scatter behind the lower bound in the simulation, and by inference in the experiment, results from the distribution in crystallographic orientations of the grains.

Early Propagation. Microcrack closure stress is the dominate factor in controlling the rate of microcrack growth in the aluminum alloys of interest.⁷⁻⁹ In the presence of crack tip closure, strain at the crack tip induced on a tensile loading cycle is not completely reversed on unloading and the resulting rate of propagation can be described by

$$\frac{dc}{dN} = A(\Delta K_{eff})^m \quad (3)$$

$$\Delta K_{eff} = \sigma_{max} - \sigma_{cc}$$

A and m are material constants. The effective stress intensity range, ΔK_{eff} , includes only that portion of the fatigue cycle for which the crack is open to the tip (i.e., for the maximum cyclic stress, σ_{max} , minus the crack closure stress, σ_{cc}).¹⁰ The crack closure stress is found to be highly sensitive to the location of the crack tip relative to the grain boundaries. The plastic zone size at a surface microcrack tip is not determined by continuum constraints, but is instead principally determined by the distance of the crack tip to the next grain boundary. The majority of plastic slip is not continuous across a grain boundary and hence, most deformation accumulates from within the grain itself. If the slip distance within the grain is large, the residual tensile strain developed at the crack tip is also large, and the crack closure stress is correspondingly large. An empirical expression which relates distance of a crack tip to grain boundary to σ_{cc} allows one to estimate σ_{cc} from the instantaneous location of a microcrack relative to the alloy microstructure.¹¹ Thus,

$$\sigma_{cc}/\sigma_{max} = \alpha Z_0/2c \quad (4)$$

α is a material constant which is a function of relative humidity, but is approximately unity. With reference to Fig. 6, Z_0 is the distance of a crack tip to the grain boundary and $2c$ is crack length. Of course, if $\sigma_{cc}/\sigma_{max} > 1$, no propagation of tensile opening (Mode I) cracks can occur. With the initial condition $2c = W$, it therefore results that only cracks located so that, at least for one tip, $Z_0 < 2c$ will propagation occur. Consequently, most fractured intermetallics never lead to propagation into the matrix as σ_{max}/σ_{cc} exceeds unity at both surface tips. The rare exceptions which result in propagation are intermetallics located near grain boundaries with a succession of small grains beyond. Propagation begins and continues in the direction of maximum constraint of the plastic zone size (i.e., small Z_0). An alternate mode of propagation occasionally observed in the alloys of interest is for propagation from an intermetallic to proceed by a shear mode, which is unaffected by tensile closure. Ultimately, this process must also be modeled. Currently, it is deemed sufficiently rare to be handled in an empirical way by assigning smaller α values to a fraction of the microcrack on a random basis.

To illustrate the success of the closure modeling of growth of cracks of approximately the grain size, we compare measured microcrack propagation rates to ΔK_{eff} for Al 2219-T851. In Fig. 7, the ΔK_{eff} values have been determined experimentally by measuring σ_{cc} directly at the surface crack tips. The data are taken near the threshold of propagation for ΔK and, hence, no correlation between dc/dN and ΔK is found. Conversely, the ΔK_{eff} model provides a good description of microcrack growth rate.

The distribution of lengths of surface microcracks at any point in the fatigue life is also obtained by Monte Carlo methods. The nucleation and early growth of each crack is simulated, and the sizes of the grains in the region of each crack



Fig. 6 Surface microcrack showing definition of nomenclature for crack length ($2c$) and distance to next grain boundary Z_0 .

is chosen at random from the measured grain size distribution for the alloy. An example comparison between simulated and measured lengths of microcracks with sizes less than $200\mu m$ is shown in Fig. 8. Agreement between experiment and simulation is relatively good.

PREDICTION OF FATIGUE LIFETIME

The nature of the scatter in lifetime of a component is sensitive to both to the cyclic stress amplitude and to the surface area at that amplitude. If the total number of cracks developed over the course of a typical lifetime are small, then the statistics of crack nucleation can be expected to dominate lifetime scatter. As crack numbers increase, with increased stress or increased area, the statistics of the early crack growth phase becomes relatively more important. For very large numbers of cracks, crack coalescence becomes an additional statistical factor. If one were to prepare two smooth bar specimens of the same diameter, but with different lengths, the shorter bar (with

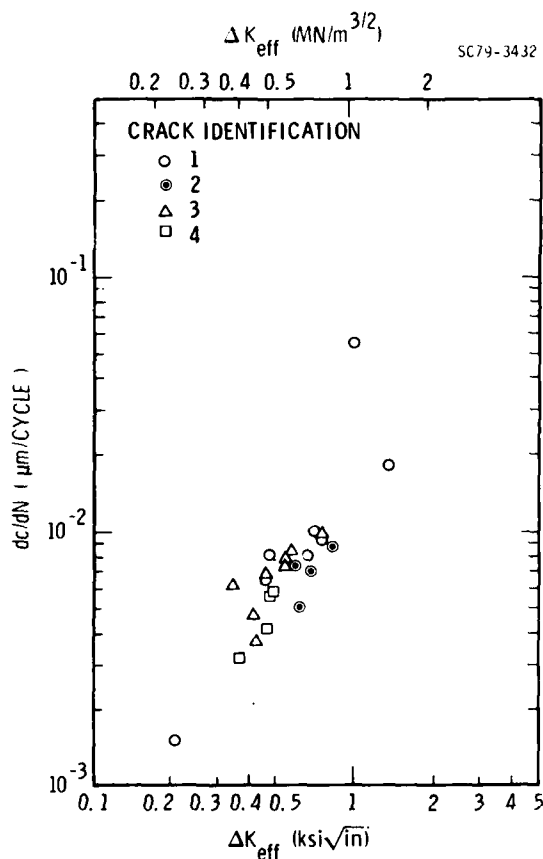


Fig. 7 Relationship of microcrack propagation rate to ΔK_{eff} .

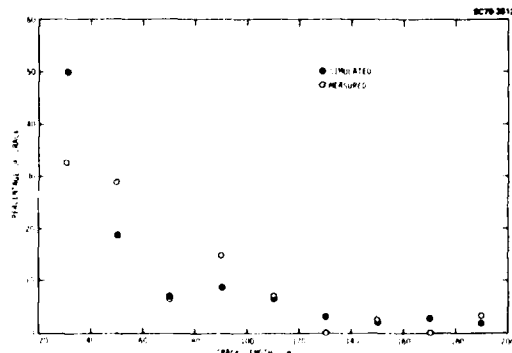


Fig. 8 Comparison between predicted and measured microcrack lengths for Al 2219-T851 with maximum crack lengths approximately 200μm.

smaller surface area) would have a longer fatigue lifetime on the average. A computer simulation illustrates this effect (Fig. 9). Plotted against fatigue cycles is the probability density of

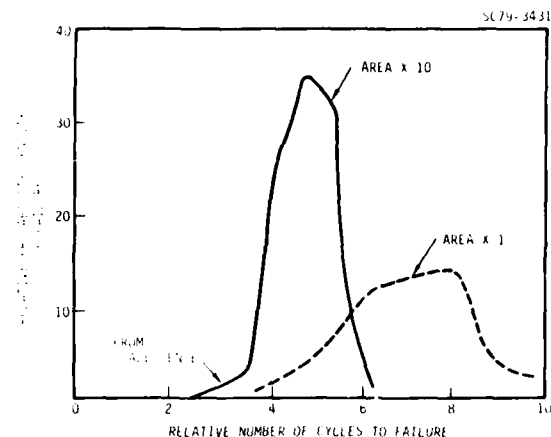


Fig. 9 Probability density of failure for two smooth bars of different surface areas obtained by simulation.

failure for the two bar geometries. The total area under each curve is 100% failure. The cyclic stress amplitude has been chosen so that lifetime for the short bar is determined principally by nucleation statistics. For the longer bar, operating at the same cyclic stress amplitude, the resulting lifetime is dominated by crack growth statistics. The early dropout tail at short lifetimes for the long bar is the result of crack coalescence.

Mean lifetime is directly obtainable from such plots. Figure 10 illustrates a comparison between measured¹² and predicted mean fatigue lifetime for

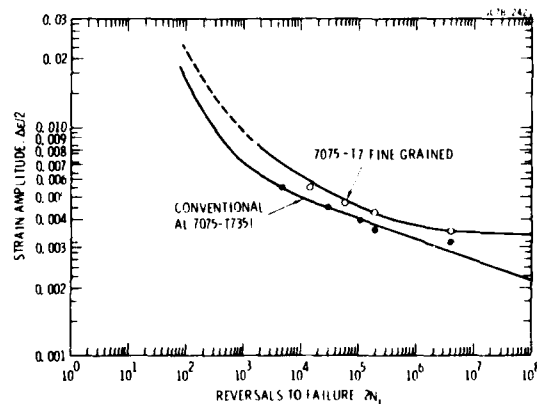


Fig. 10 Predicted vs. measured fatigue lifetimes for Al 7075 alloys having different mean grain sizes (75μm vs. 25μm).

a large grain as compared to a fine grain¹³ Al 7075 alloy. Mean grain size differs by approximately a factor of 3 for the two materials. The improved lifetime in the simulation results from an increased time to first crack nucleation in the fine grain material.

SUMMARY

A Monte Carlo simulation of the initiation stage of fatigue failure of certain 2000 and 7000 series aluminum alloys has been described. The technique allows one to predict the scatter in lifetime of a material which results from the statistics of the microscopic failure processes, which are determined by the alloy microstructure. An ultimate application of the method may be to predict the probability density of early fatigue failure of components. It is unlikely that such predictions can be made with confidence with any other approach as the low probability events, which the procedure addresses, are extremely expensive to define experimentally. Furthermore, the technique, in principle, allows one to predict the effect of a change in alloy heat (microstructure) on the early failure statistics with a minimum of additional experimental characterization. Computer simulations which accurately reflect the microscopic nature of crack initiation may also be useful in defining inspection schedules in the event that NDE techniques are developed which can characterize the small cracks present during the initiation process.

ACKNOWLEDGEMENTS

This research was supported by Rockwell IR&D funds. The scatter in lifetime predictions were made using a one-dimensional computer simulation of the nucleation process developed under an Office of Naval Research Contract No. N00014-76-C-0952.

REFERENCES

1. N.E. Frost, K.J. March and L.P. Pook: Metal Fatigue, Clarendon Press, Oxford, England, pp. 332-337.
2. G.R. Leverant, B.S. Langer, A. Yuen and S.W. Hopkins: Met. Trans., 1979, Vol. 10A, pp. 251-258.
3. W.L. Morris, O. Buck and H.L. Marcus: Met. Trans., 1976, Vol. 7A, pp. 1161-65.
4. B. Syren, H. Wohlfahrt and E. Macherauch: Harterei-Tech. Mitt., Vol. 31, pp. 90-94.
5. W.L. Morris, M.R. James and O. Buck: "Computer Simulation of Fatigue Crack Initiation," to be published in Eng. Fract. Mech.
6. R. Chang, W.L. Morris and O. Buck: Scripta Met., 1979, Vol. 13, pp. 191-194.
7. W.L. Morris and O. Buck: Met. Trans., 1977, Vol. 8A, pp. 597-601.
8. W.L. Morris: Met. Trans., 1977, Vol. 8A, pp. 1087-1093.
9. W.L. Morris: Met. Trans., 1979, Vol. 10A, pp. 5-11.
10. W. Elber: STP 486, pp. 230, Am. Soc. Test. and Mat., Philadelphia, 1971.
11. W.L. Morris: "The Non-Continuum Deformation Behaviors of Surface Microcracks," submitted to Met. Trans.
12. M.R. Mitchell, J. Wert and N.E. Paton, Rockwell International Science Center, to be published.
13. N.E. Paton and C.H. Hamilton: "Method of Imparting a Fine Grain Structure to Aluminum Alloys having Precipitating Constituents," United States Patent #4,092,181, May 30, 1978.

SUMMARY DISCUSSION
(Fred Morris)

Michael Resch (Stanford University): I would like to know what experimental techniques you use to measure your crack growth rates at the very low K effective for the small surface cracks.

Fred Morris: All the measurements were done with a scanning electron microscope. The specimens were fatigued in air and then transferred to the microscope at 500 cycle increments. Crack length measurements were done with the specimen under load so we could see the cracks. It's tedious, but that's the only way I know to do it with any degree of accuracy.

Michael Resch: What size were the cracks?

Fred Morris: The crack lengths were in the range of five microns to 150 microns.

Phil Hodges (Rockwell, Los Angeles Division): It looks to me like you have very excellent data base for using acoustic emission for low cracking density to verify the number of fractures. Have you thought of that?

Fred Morris: Yes. Acoustic emission is, of course, one way to observe the brittle fracture of the individual intermetallic particles. Lloyd Graham, at the Science Center, has done some of that research several years ago. The other nice thing about being able to predict crack densities is that there is now available a surface technique using harmonic waves to count cracks. Otto Buck is going to be talking about that tomorrow.

Mark Weinberg (U.S. Army RADCOM): I'm kind of an outsider in this R&D community. I'm more concerned with applications. I would like a clarification of what you mean by crack closure. I can understand forces tending to keep cracks closed or from propagating. Do you mean by crack closure that there is a tendency to actually heal the material?

Fred Morris: I'm using the same definition used by Harris Marcus this morning. What happens with a crack that's very near the surface, that's in a plain stress condition, is that as you load it up to a maximum external surface stress, excess material is drawn into the region of the plastic zone near the crack tip. As you release the external stress the crack tip starts to close down on itself before the external stress reaches zero. The stress at which the first closure begins, we call the closure stress. The effect of having a positive closure stress is to reduce the plastic deformation per cycle during fatigue, and the altered crack propagation rate can be calculated. It's only an approximate technique because the crack closure stress and the crack opening stress are not exactly the same. But it's the best we can presently do.

Robb Thomson: Thank you very much.

#

AD-A094 826

ROCKWELL INTERNATIONAL THOUSAND OAKS CA SCIENCE CENTER F/8 11/2
PROCEEDINGS OF THE DARPA/AFML REVIEW OF PROGRESS IN QUANTITATIVE—ETC(U)
JUL 80 D O THOMPSON; R B THOMPSON F33615-74-C-5180
SC595.70AR

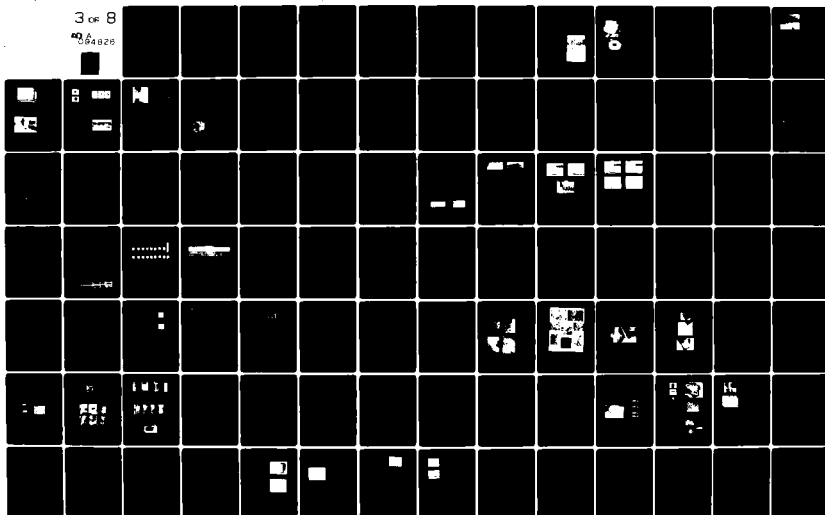
UNCLASSIFIED

AFWAL-TR-80-4076

NL

3 OF 8

04820



J-INTEGRAL ELASTIC-PLASTIC FRACTURE MECHANICS
TECHNOLOGY IN THE U. S. NAVY

J. P. Gudas
David W. Taylor Naval Ship R&D Center

J. A. Joyce
United States Navy Academy

H. H. Vanderveldt
Naval Sea Systems Command

ABSTRACT

The United States Navy has historically been interested in the development of fracture safe materials for ship construction, and in developing fracture mechanics criteria for design considerations. Recently, a substantial research effort has been directed to the development of J-Integral technology. The purpose of this presentation is to review recent Navy advances in this area. The main points will include a discussion of the applicability of the J-Integral to fracture in ductile materials, the development of test procedures for J_{IC} , recent results in the areas of J-controlled crack growth, dynamic J-Integral properties, and instability criteria based on the J_I versus crack growth resistance curve.

#

TURBINE DISK RETIREMENT-FOR-CAUSE: MEASUREMENT OF INSPECTION
UNCERTAINTY FOR DISK EDDY CURRENT INSPECTIONS

C. A. Rau, Jr., S. W. Hopkins, J. W. Eischen and D. E. Allison
Failure Analysis Associates
Palo Alto, California 94304

ABSTRACT

Major cost savings are possible through life extension of high-cost jet engine components until damage develops. Retirement-for-cause (RFC) decisions will be based upon both non-destructive inspection (NDI) to detect and size defects, and engineering analysis to assess defect severity under future usage. Failure Analysis Associates is performing a three-year program for ARPA/AFML to define and verify an optimum RFC strategy for jet engine disks. In depth, quantitative characterization of NDI performance is a major part of this project. This presentation summarizes the quantitative evaluation of inspection (NDI) uncertainty for four independent inspections - two state-of-the-art eddy current inspections of disk bolt holes, one with conventional hardware but improved signal processing, and one higher resolution eddy current inspection system assembled for this project.

Separate inspections of the same 490 bolt holes in 49, 3rd stage disks retired from service in TF33 engines were performed with each of the four NDI techniques. Inspection results were compared with each other and with the actual cracks measured by surface plastic replicas and selected destructive metallography. The variation of detection probability and sizing errors with flaw size and indication level is defined in a form suitable for the probabilistic reliability analysis and RFC strategy formulation. Progress in the other project tasks, especially the stress and fracture mechanics analysis to define the conditional failure probability if a flaw of specified size were present will also be summarized.

#

SUMMARY DISCUSSION
(C. Rau)

Robb Harris (Pratt & Whitney): When you showed that the inspection probability deteriorated for finding positions accurately, would one possibly infer from that that the things you found weren't really cracks - you found something else, and it happened to correlate with the one you found in the same hole?

Charles Rau: I think that's part of the problem. I don't know that that's all of the problem. In our destructive sectioning, which is under way now, we're going to be answering just that kind of question. I think we have to infer that, because some of the misses are way off, they found a defect up at the top of the hole and it spiraled down and 25 turns later you receive a signal. That's obviously not the same defect. If anything, they found a defect that somebody else missed. But the inspection reliability for that defect is not in fact as high as we think it is.

Al Morton (Los Alamos Scientific Lab): Are these new or used disks?

Charles Rau: These disks are used disks. They were actually removed from service in C-140's, C-141's and they had a various number of cycles on them. They were rejected by the field depot inspections. Of course, they had been rejected for one bolt hole. We were inspecting all the bolt holes. We were characterizing not just the biggest cracks, but the whole range of cracks--much smaller than with which they were concerned. But they were used. I'd like to amplify this point. An advantage of this program is that we're producing a demonstration program of the retirement-for-cause strategy on actual, used hardware which has been exposed to actual engineering environments, realistic statistical variations and duty cycles, and all the other problems that go along with the real world as opposed to the laboratory. Further, we will be verifying the strategies we developed through a laboratory testing program where we actually make bolt hole specimens and fly them in the laboratory where the inspectors won't know what the duty cycle is, and we will basically inspect many accept-reject decisions and continue running them to see what breaks. Appropriate economic factors will be ascribed onto relative to the consequences of breakage or nonbreakage, and the entire procedure that produces a total payoff will be verified.

Bill Sturrock (Northrop): Did you repeat any of the eddy current inspections after electropolish?

Charles Rau: No. We wanted to simulate the real world inspection. Sure, we were likely to see different results. We saw some of the cracks weren't surface-connected. We noticed that on these high-frequency probes we obviously interrogated a very local region. I'm sure we could have improved the resolution by opening up some of the defects at the surface, but that wasn't what we were really looking for.

Bob Addison (Science Center): I was curious about the micrographs that you showed. Were those micrographs of the plastic piece, or were they actual photos of the hole?

Charles Rau: Bob, they were both there. There were replicas which were, in fact, the surface of the bolt holes. We scanned the surface first to detect the surface length. Then we took others at cross sections through the bolt holes. You also saw those planes. We used those to determine the crack depth at various positions along the surface level. So, both were involved there. I'm sorry I was running through them pretty quick and didn't tell you which was which.

Mike Buckley (ARFA): Is your optimism for a retirement-for-cause strategy on these disks based on the fact that the crack growth rate is very slow and, therefore, you can tolerate a fairly large crack?

Charles Rau: My optimism is not based on the fact that the crack propagation is slow, although obviously it has to be slow enough to have some margin. The optimism is based on the fact that, first of all, there is a lot of money being thrown away. Secondly, we can establish inspection intervals so that we can miss a crack one time and still catch it at another interval. We can improve our total reliability by redundant inspections without the probability of failure being very high. Further, we have ten bolt holes in a disk. The fact that we're going

(continued)

Charles Rau (discussion continued)

to reject a disk for any one of them adds additional conservatism to the whole R.F.C. strategy. You put all of these things together probabilistically, and your probabilities of failure come out to be quite low. And you multiply those by cost of failure, and it's still a small number compared to the cost of throwing away the whole fleet of disks.

Warren Berger (RADCOM): We have recognized the three elements in a probability of failure, although not in as formal a manner as you have presented today. Our problems are significantly different, I think, in that we have one-shot devices. We have to screen the entire production to try to isolate, quantify, and reject those elements that will be failures in functioning. Our biggest problem currently is getting a handle on the reliability of our inspection in terms of removing from stockpile or preventing from getting into stockpile those metal parts that contain critical cracks, whatever that might be.

Charles Rau: Just a comment. We have looked at the problem, also, of nonsubcritical crack growth. I think you can handle it by many of the same procedures, and I think it's amenable to the same kind of calculation. I think you are right: the inspection reliability is one of the key inputs. But the preinspection, the probabilities of flaws being there, is equally important. The probability of failure, instead of involving fatigue or subcritical growth, is just a probabilistic overlap of the strength distribution and the stress distribution, but methodologically it's very similar except for that difference.

Robb Thomson: Any other questions?

John Duke (Virginia Tech): You indicated you have some very complex crack shapes, and I tend to agree, after looking at those pictures. I was wondering if you feel that your classification by means of length is sufficient to indicate the significance of what you're monitoring with your eddy current? Do you think that using a different classification scheme based more on the performance that results from that particular type of a crack would be a better means of characterizing your inspection?

Charles Rau: There is no question about that--particularly with these complex geometries. I hope when we get done with our destructive work we will be able to identify additional parameters. For example, the opening of the crack at the surface or the integrated opening over the crack depth may turn out to be a lot more important than the length of the crack. But at this point in time we are already three or four orders of magnitude more sophisticated in our comparisons than most people have been able to do with theirs.

#

SESSION V. MISCELLANEOUS DISCUSSION

Robb Thomson (Session Chairman): In the few minutes we have left before adjourning this session, I'd like to review briefly various points that have been made this morning. The development of a failure predictive technology evidently involves a proper combination of several ingredients. These include a quantitative measurement capability, a proper description of the mechanisms of failure, a way to combine these elements into a probabilistic failure predictor that takes account of the variance in both the above quantities, a way to include a priori data that may exist which will help to sharpen the prediction, and finally, a way so that management choices (which govern the cost-risk tradeoffs) can be injected into the predictions. This morning we have heard a number of talks relating to one of the above items, i.e., the mechanisms of failure in metallic materials with an emphasis upon fatigue processes including fatigue initiation, crack growth mechanisms, and complications that are introduced by consideration of the fully plastic problem.

In order to help focus our discussion, I would like to suggest that we consider three elements that must be considered in our development of a realistic, failure-predictive set of procedures for metallic materials. These might be labeled deterministic, probabilistic, and a category called surprises. In the deterministic category, we might include fatigue crack initiation, coalescence, crack growth and topics related to plastic treatments; in the probabilistic category we have such things as materials variability, statistical variances in essentially all the deterministic properties, and non-programmed effects of environment and loads; in the surprise category, we might expect unexpected complications in all the above and we might find some "lucky" alternate paths that would enable solutions to be found more easily. With these categories in mind, let us get into discussion.

Don Thompson (Science Center): I would like to address the deterministic category and to try to relate it to the probabilistic requirements. In particular, how accurate and comprehensive does a deterministic model of failure have to be in order to yield a good probabilistic model?

Charles Rau (Failure Analysis Associates): One of the things in the combined analysis approach which we have been using minimizes the sensitivity to getting the correct deterministic model. Of course, you want to have as good a model as you can get because your overall predictive system will be better. For example, we have done a Monte Carlo simulation of a flaw population where we assumed the analyst got the cracking mechanism altogether wrong. He thought it was fatigue, and it was stress corrosion. So, he had a crack exponent of three, where it should have been six. I mean, he really botched the engineering model altogether. However, the retirement-for-cause analysis still worked very well with the binned analysis. It didn't work as well as it would have with the right model; he saved a factor of three in total cycle costs whereas he could have saved a factor of five if he had the right model. I don't mean to downplay it, but I would like to indicate that even in those circumstances where we can't get at the determination of the uncertainties, and by paying attention to the field data and retirement-for-cause strategy, you can get by with a lot of uncertainty.

Robb Thomson (Nat. Bureau of Standards): Could you come a little closer to this in the case of the fatigue problem in high-strength steel. Where do you need better data? Would better understanding give you better, refined statistical results?

Charles Rau: The key thing, I think, in most of these predictive models is to get the stress-dependence (or whatever parameters are driving the crack) right. In other words, if you worry about the fatigue of high-strength steels, it's important to know whether the environment changes the K dependence or stress dependence from three to four to six or whether your stress corrosion rate becomes almost K independent. If you think your stress dependence is six and the threshold is really in a flat range where it's almost independent of stress, your model is going to be really way off and then you can really get into trouble. I think the key thing is to identify the functional relationship between the key engineering parameters and not necessarily to get the absolute scale factor right.

Robb Thomson: Any other comments along that line?

(continued)

SESSION V. - Miscellaneous Discussion (continued)

Jim Carson (AFOSR): Let me pose another question and make some comments along related lines, primarily to the fracture mechanics people. Let's assume that you can measure the length of a crack and the depth and its orientation and any other characteristic you would like. My question is: how much do you need in order to make some kind of reasonable prediction? Or more specifically, what do you need in order to feel comfortable in making that prediction. In looking at the kinds of cracks that Charlie Rau pictured, which were fairly nasty-looking things, we don't even necessarily know they were fatigue cracks. They could have been cracks that were produced during the manufacturing of the part, and may have been in an orientation which was not in fact critical. That's a possibility. I see a head shaking. In any case, I think that's a question that needs to be addressed too. There are certainly some cracks which were not fatigue cracks which will be detected, and then you need to determine whether they are important or not.

Mike Buckley (ARPA): If I could just make a comment on the surprises you had down there. One way of reducing the uncertainty is, in the case of the engine disk question, to monitor the engine itself in service - its temperature, its RPM's - so that we have a much better measure of a load cycle fatigue that is accumulated. We can reduce the surprises quite a bit by looking at the engine as a system, for example, and by expanding our horizons past just that component.

Robb Thomson: I'm glad you focused on that, Mike. I also feel this is certainly one of the major directions you want to be able to go. Of course, it poses a whole set of new problems itself in cost and what parts you want to monitor, and there are a number of probabilistic aspects there, too, e.g. how often you read the meters, how often do you get the red light, and so forth.

Mike Buckley: I'll just make a comment. I think that we will have an agreement with the Australians to instrument TF-30's in Australia and also to look at retirement-for-cause strategy on F-111's. The nice part is they are a very small organization and we probably can get very good data.

Robb Thomson: Mike, can I ask you a question? What is your sense of the breakdown between the periodic inspection that Charlie Rau spoke of versus the actual real time inspection of the sort that you're mentioning. Another aspect of that question is: there is a testing problem. Is there anything besides acoustic emission that looks like it's a possible practical tool in real time?

Mike Buckley: I was primarily referring to monitoring the engine conditions, which is state-of-the-art and which you can do. If you had a system for maintaining the engine which was flexible, then you could have a self-optimizing maintenance approach to the whole problem.

Robb Thomson: This is actually a third one.

Mike Buckley: That's right. But that takes a very flexible organization which can manage their engines and air frames. It's very complicated. Besides acoustic emission we do have a system flying in Australia, which you probably heard about. Sometime we can talk about why we do business with the Australians. An adaptive maintenance thing, a maintenance-for-cause philosophy, can be extremely cost-effective, it seems to me. The hardest problem is probably the actual logistics of it, how you implement it. I think it would fit. Charlie has modeled it very nicely.

Charles Rau: First I would like to answer the question because I think it gives me a chance to make a point that is important. You asked basically what parameters we really need to measure to make a cost-effective decision. I think maybe that's obvious if you stare at these equations, but the key point is that you have to measure more than just the minimum size defect you can find some of the time. Obviously, you can identify the critical areas which is done by stress analysis and the fracture mechanics predictions of defects in those areas. There is no reason to inspect everything. At least not in the same detail. That's obvious. But assuming you have identified the critical areas, it's also important to specify and to quantify the inspection reliability of whatever NDE technique you're using as well as its resolution capabilities. And people I think in your industry-- I guess it's kind of mine now, too--don't do as much of that, I think, as we ought to. And I also think we need to know those numbers not only under the ideal laboratory conditions but under the realistic conditions on the wing or in the

(continued)

SESSION V. - Miscellaneous Discussion (continued)

shop, wherever the inspection process is going to be defined. I think the people who are designing new systems, new probes, have to be consciously thinking about the specific application it may eventually be applied to if in fact we are really going to get the inspection reliability to a level which makes it useful.

Fred Morris (Science Center): Let me make a small commercial for probabilistic initiation models. We have to remember at least in design terms that design problems can be divided into two classes--safe-life and fail-safe designs. In fail-safe, where you plan never to do an inspection, of course, it's crucial to understand the initiation behavior, and that's particularly where initiation-based probabilistic models shine. But in safe-life designs there are several areas where the potential power of probabilistic failure models manifests itself, aside from models that can be developed from periodic inspections of critical components. These include loading conditions in structures where the failure probabilities are determined by very low probability events. Another point of concern is the discontinuous nature of multiple crack coalescence in which you can go from 100 micron cracks to 1,000 micron cracks - an incredible jump in size over a very few cycles. The statistics at which that occurs, of course, are of enormous interest. It may be a rare phenomenon, but it's a rare phenomenon that brings a plane down under certain conditions. Probabilistic models can also provide guidance with respect to materials variability. If you have been making everything out of sheet 1 and sheet 2 comes in the door, there may be enormous effects of microstructure on the failure process. Probabilistic failure models that relate the microstructure of the material to performance characteristics are particularly important. A somewhat related problem is that of predicting the effects of a fleet duty cycle. Again, appropriate failure models may be able to make a prediction as to what that change in duty cycle will do to the statistics of the failure, and that's something very often you won't have time to get an insight into by only an inspection technique.

Robb Thomson: We're just about to run down. I would like to make one plug, however. It's a little orthogonal to most of what the Air Force and Defense Department are generally worried about, which is high-strength relatively brittle materials, where the plasticity is well-contained in the part. That's the classic fracture mechanics situation. It's the one that most of us are most comfortable and familiar with, but let me simply remind you there is another failure problem when you're dealing with a softer, possibly tougher material, or even the case of a thin structure material wherein a crack goes through. For example, a pipe with a crack in the girth is such a situation. There the plastic zone goes clear through the part to the opposite side, and ordinary fracture mechanics doesn't help you there at all. These are tremendously important in many applications. In this case we are not in very good shape from the fracture mechanics point of view. I would urge the NDE community to keep its eye on this problem because it's an important one. And as we begin to get insights from the fracture mechanics point of view about what are the important parameters that can be identified and which you need to measure, that will then be a challenge to the NDE community.

#

ULTRASONIC INSPECTION OF RUBBER SONAR DOME WINDOWS

G. A. Alers and C. M. Fortunko
Albuquerque Development Laboratory
Rockwell International
2340 Alamo, SE
Albuquerque, New Mexico 87106

ABSTRACT

By using a rubber window acoustically matched to sea water, the Sonar system on a destroyer can be made considerably more sensitive. However, if the layered construction of the window develops delaminations while in service, the hydrodynamic characteristics of the structure may become modified and acoustic noise can be generated during high-speed operations. In order to inspect for these delaminations while the ship is tied up to its dock, a pulse-echo ultrasonic scan performed by a diver using a sea-water coupled transducer would appear to be ideal. However, the choice of acoustic parameters suitable for inspecting rubber were unknown. Laboratory studies showed that by utilizing very short time duration pulses whose center frequencies lie between 0.5 and 1.0 Mhz, it was possible to detect water-filled pockets within 0.2 inches of the outer surface of the window. A prototype instrument suitable for shipboard and dry dock operation has now been constructed. This instrument features optimized pulse excitation of low-frequency broad band transducers when attached to 50 to 100 feet of coaxial cable. A signal light is also incorporated to provide the diver with information on the condition of the rubber window under his transducer.

INTRODUCTION

When Sonar systems were first added to the Navy's surface fleet, the acoustic energy was usually coupled to the sea water through the steel hull of the vessel. For anti-submarine warfare from a destroyer, this procedure proved to be sufficiently lossy that a submarine could escape detection. To alleviate this situation, a region of the steel hull is now replaced by a rubber window in which the rubber has been chosen to be a good acoustic impedance match to sea water to make the structure as transparent to sound waves as possible. Figure 1 shows a photograph of a modern destroyer in dry dock and the bulbous Sonar Dome structure under the bow of the ship can be easily seen. Although not clearly delineated in the photograph, this bulb is nearly surrounded by a rubber strip approximately 8 feet high and 80 feet in circumference. It is constructed in a manner similar to an automobile tire with steel reinforcing wires embedded in it.

THE PROBLEM

The outer layer of the rubber window is approximately $\frac{1}{4}$ inch thick and has a somewhat different chemical composition than the rest of the window structure so that it will repel barnacles. Since it lies on the surface of the dome, any defects such as a disbond under the layer could interact with the hydrodynamic flow past the window and cause turbulence or cavitation which, in turn, could act as a source of unwanted noise in the Sonar receivers. In order to have an instrument for detecting disbonds or other discontinuities near the outer surface of the window, the Science Center was asked to investigate the possibility of using ultrasonic pulse-echo techniques. Laboratory studies showed that special electronic circuits coupled to conventional, broad-band piezoelectric transducers would detect near-surface flaws if the frequency were between 0.5 and 1.0 Mhz and the total pulse durations were less than 6 usec.



Figure 1. Photograph of a destroyer in dry dock. The round bulb below the bow contains the Sonar "antenna" and the Sonar window is a rubber strip around this bulb.

THE INSTRUMENT

Once the electronic and acoustic specifications had been defined, the Albuquerque Develop-

ment Laboratory was asked to construct a complete instrument package suitable for operation by Navy personnel at dockside or in dry-dock. Figure 2 shows a photograph of the completed instrument as well as the transducer holder. It can be operated either from a self-contained battery pack or from 110 volt, 60 cycle AC sources. The CRT displays the RF



Figure 2. Photograph of the battery operated, portable instrument for inspection of rubber Sonar Windows.

signal reflected by the Sonar Dome on an expanded time base so that an echo from an inhomogeneity near the Dome surface can be time resolved from the echo from the front surface itself. A gating circuit is available to separate out those signals that arrive after the front surface echo and to activate an alarm if they exceed a preset level. This alarm consists of three parts: (1) a speaker that generates an audible noise signal; (2) the region of time comprising the gate duration appears on the CRT display as an intermittent square wave superimposed on the signal; and (3) a red light on the transducer package that is held on the Sonar Dome becomes activated. The latter alarm is of particular utility, because it alerts the diver scanning the transducer over the dome that he is in the region of a suspected defect. In the usual mode of operation, the person scanning

the transducer over the rubber window area will be a professional diver while the person viewing the CRT display will be one who is trained in ultrasonic inspection techniques and will be stationed on a dock or surface vessel some distance away from the Sonar Dome itself. Once a suspect area is located, the diver and the inspector can communicate over a separate audio communication link to make detailed comparisons of the conditions of the signal that activated the light on the transducer package and to establish the location of the transducer on the dome.

Because the CRT display is expected to be at least 100 feet away from the transducer, special transmitter and receiver circuits had to be developed to insure that there would be no degradation of the signal between the transducer and the display. To meet this requirement, very compact transmitter and preamplifier circuits were designed to fit into the small container housing the transducer. Thus the long, water-proof cable connecting the instrument with the diver held probe need only transmit DC power supply voltages and the preamplified RF signals detected by the transducer. The remote transmitter-circuit consists of a carefully chosen transistor switch designed to discharge a capacitor into the transducer with a time constant tailored to the desired center frequency of operation. The preamplifier consists of high gain, low noise amplifier stages designed to recover quickly from the transmitted burst, as well as to present an optimum impedance to the transducer at the input and to the long cable at the output.

OPERATION

Delivery of the final instrument and acceptance tests on the Sonar Window of a destroyer are scheduled for October of 1979, so only laboratory simulations of the actual operation of the instrument are available at this time. Figure 3(a) shows the RF signal

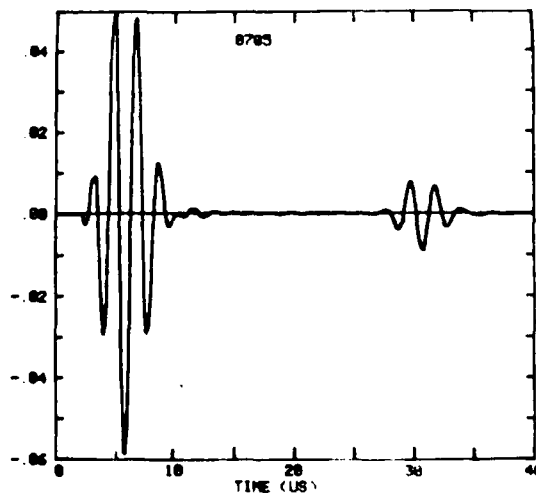


Figure 3(a). Example of the RF signal observed on the Sonar Window of a good Sonar Dome.

display for the case of a defect free test sample of the rubber window structure. The large signal on the left is the reflection from the front surface of the sample. That is, the reflection from the sea water to rubber window interface. The small signal on the right of the trace is from a layer of steel reinforcing wires buried in the test rubber sample, approximately $\frac{1}{2}$ inch below the surface. Its amplitude is reduced because of attenuation of the sound in the rubber. Figure 3(b) shows the signal observed when the acoustic path between the rubber surface and the steel reinforcing wires is interrupted by a water-filled dishond. Clearly the thin layer of water in the dishond causes a reflection of ultrasonic energy which can be detected by the ultrasonic pulse-echo technique. By adjusting the signal gate to coincide in time with this dishond echo and setting the alarm trigger level to be activated by a signal of that amplitude, the instrument alarm system could be initiated whenever the transducer was scanned over the dishonded region of the sample.

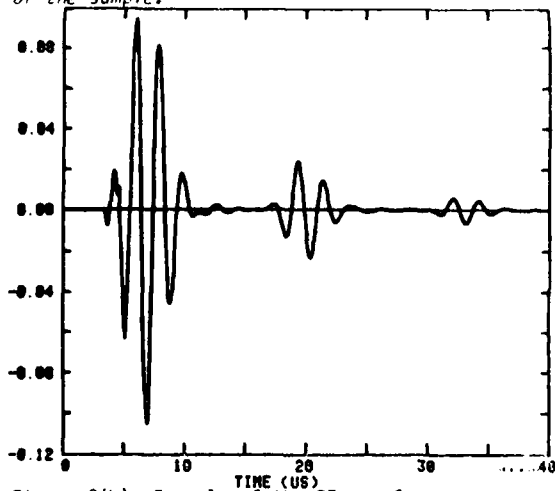


Figure 3(b). Example of the RF waveform observed on the CRT in the region of a dishond.

ACKNOWLEDGMENTS

The instrument being developed here is supported by contract N00140-78-C-8824 from the Naval Underwater Systems Center, New London, Ct. Mr. Andy Loesch deserves very special thanks for his ingenuity at building the special circuits within the small space available in the transducer head as well as for his utilization of the power supplies and display circuits of a Krautkramer-Branson Sonoray 303 flaw detector which served as the initial instrument.

The authors would also like to acknowledge the technical assistance of Mr. Philip Walker, presently with Smith-Kline Instruments.

APPLICATION OF NONDESTRUCTIVE EVALUATION (NDE) IN ASSESSING THE STATE-OF-HEALTH OF PHOTOVOLTAIC SOLAR ARRAYS

C. D. Coulbert and J. C. Arnett
Jet Propulsion Laboratory
California Institute of Technology
Pasadena, CA 91103

ABSTRACT

The U.S. Department of Energy's program to develop photovoltaic solar arrays by 1986, that have a useful life of twenty years with a selling price of fifty cents per watt, has resulted in a new rapidly advancing photovoltaic industry and technology. Current projections based on current solar module hardware experience indicate that the 1986 electrical performance and cost goals can be met. However, field exposure experience with newly formulated solar cell configurations and encapsulation material systems is very limited, and the long-term, life-limiting failure modes and degradation rates have yet to be determined.

To develop a data base for life prediction and performance degradation rate measurement a number of new and state-of-the-art NDE methods are being evaluated for laboratory and field use in detecting flaws, failures and subtle material changes in experimental solar modules. In addition to the normal visual, photographic, and electrical performance measurements being made, several new techniques show promise of practical application.

INTRODUCTION

Photovoltaic solar arrays for the direct conversion of sunlight to direct current electrical power may consist of large numbers of individual flat plate solar modules generating about ten watts (peak power) per square foot of solar cell surface area. A 25 kilowatt solar array at the University of Nebraska Agricultural Experiment Station shown in Fig. 1 indicates the type of hardware for which NDE techniques are sought.

The objectives of these NDE measurements (Fig. 2) are to determine or identify by cost-effective techniques (1) the changes in array performance, (2) the failure modes and their causes, (3) quantitative degradation rates, and (4) incipient failures in operational solar modules.

Figure 4 shows the current standard laboratory performance measurement technique which is a large area pulsed solar simulator (LAPSS) manufactured by Spectrolab Inc. A pulsed xenon arc lamp provides one sun of uniform illumination of short duration without solar cell heating. The output terminals are swept by an electronic load during the pulse and the data stored. The module current-voltage (I-V) curve corrected for temperature and illumination is plotted automatically. Analysis of these curves identifies changes in the internal characteristics of the photovoltaic circuit.

OTHER NDE APPROACHES EVALUATED

Infrared Camera - With large numbers of solar cells connected in series, the degradation of one cell can cause localized overheating and subsequent module failure. The infrared camera may be used in the field and laboratory to detect and locate overheating and identify its cause as in Fig. 5.

Laser Scanner - Figure 6 outlines the operation of a solar cell laser scanner. A focused laser beam is deflected in a raster pattern over the cell surface, generating a photocurrent which varies from point to point due to localized defects in the cell structure. The amplified current is used to produce

a module image on a cathode ray tube where cracked and inoperative cells are revealed.

Partial Corona Discharge - Figure 7 shows the test equipment and typical output data used to detect partial corona discharge in a photovoltaic module due to incipient voltage breakdown between the solar cell circuit and the grounded supporting frame. Although single solar cell voltage output is only 0.5 volt, solar cells may be series connected to produce solar array output voltages of 1000 Vdc in utility power generation applications.

FTIR - A direct measurement of chemical degradation changes occurring in the exposed solar module encapsulant materials (polymers) is possible by taking small specimens of polymer from the layer of encapsulant surrounding an operational cell and conducting a Fourier Transform Infrared (FTIR) spectroscopic analysis (Fig. 8) to measure the time-related production and loss of chemical species. A subsequent step would be to relate these chemical changes to physical and electrical degradation.

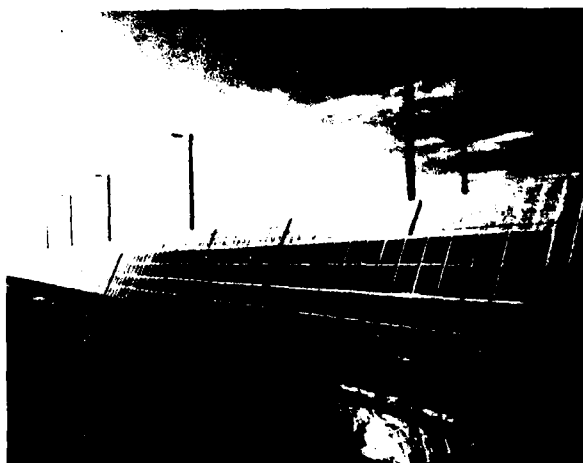
Ultrasonics and Ellipsometry - Figures 9 and 10 show the detection and imaging capabilities of ultrasonic and ellipsometric techniques applied to solar modules. The focused ultrasonic probe readily identifies the encapsulant/cell interface and the differences between bonded and disbonded conditions. At this time, however, the technique does not reveal the quality of the bond itself. Ellipsometric surface analysis reveals first surface conditions and surface contamination but does not provide an effective assessment of interface phenomena.

CONCLUSIONS

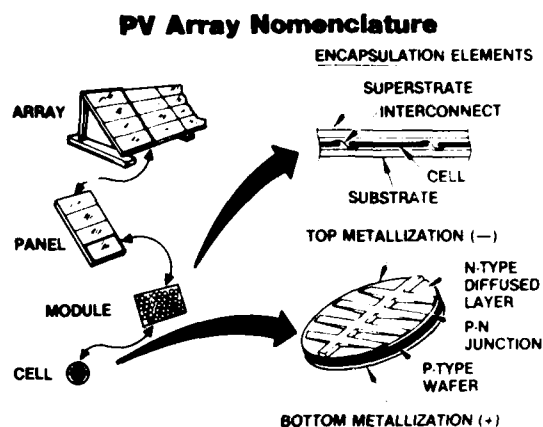
Performance measurement and failure detection techniques are furthest developed. Still needed are degradation rate techniques for field tracking and life prediction.

ACKNOWLEDGMENTS

The research described in this paper was carried out at the Jet Propulsion Laboratory, California Institute of Technology, and was sponsored by the Department of Energy through an agreement with NASA.



25 KILOWATT SOLAR ARRAY AT UNIVERSITY OF NEBRASKA. MEAD AGRICULTURAL EXP. STATION - IRRIGATION AND CROP DRYING APPLICATION



ELEMENTS OF A PHOTOVOLTAIC SYSTEM - NDE TECHNIQUES HAVE HIGH POTENTIAL FOR APPLICATION AT MODULE AND ENCAPSULATED CELL LEVEL.

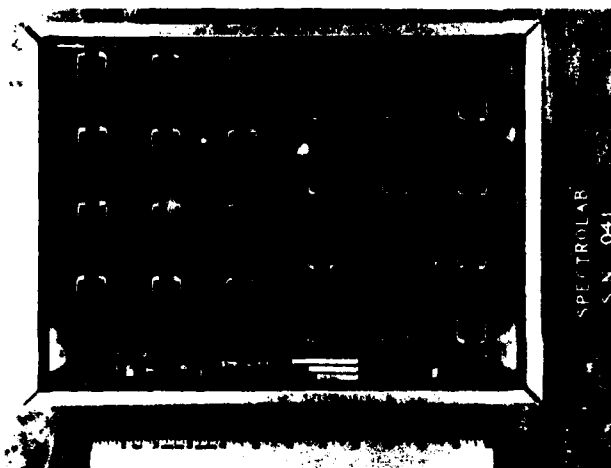
Fig. 1. Photovoltaic Arrays - Energy From the Sun

Objective —

Apply NDE Methods to Solar Arrays in Order to:

- QUANTIFY CHANGES IN PERFORMANCE
- IDENTIFY FAILURE MODES/CAUSES
- ESTABLISH DEGRADATION RATES
- IDENTIFY INCIPIENT FAILURES

Fig. 2. Objective



MFG. - SPECTROLAB INC.
SUN VALLEY, CA.

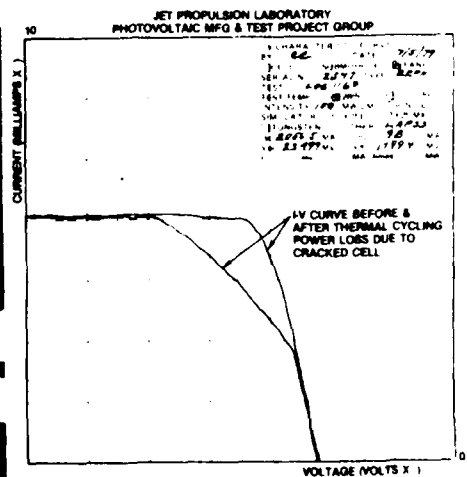
OUTPUT - 5 WATTS @
6 VOLTS DC

ENCAPSULATION -
• GLASS SUPERSTRATE
• POLYVINYL BUTYRAL
• MYLAR MOISTURE BARRIER
• ALUMINUM SUPPORT FRAME

Fig. 3. Photovoltaic Module - 2nd Generation



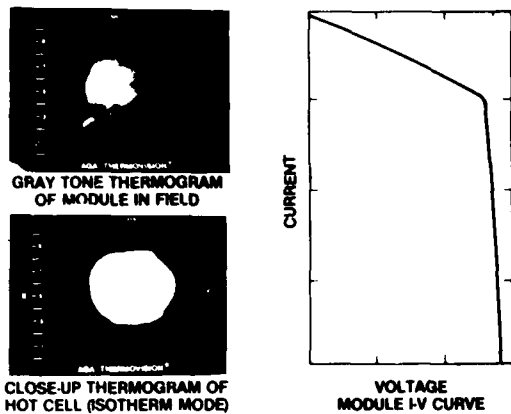
LARGE AREA PULSED SOLAR SIMULATOR (LAPSS)
MANUFACTURED BY SPECTROLAB. PULSED XENON
ARC FOR UNIFORM ILLUMINATION WITHOUT CELL
HEATING. MODULE OUTPUT SWEEP BY ELECTRONIC
LOAD & DATA STORED.



POWER I-V CURVE CORRECTED AND PLOTTED
AUTOMATICALLY. ANALYSIS OF CURVES
IDENTIFIES TRANSMISSION LOSSES & CHANGES
IN INTERNAL RESISTANCE.

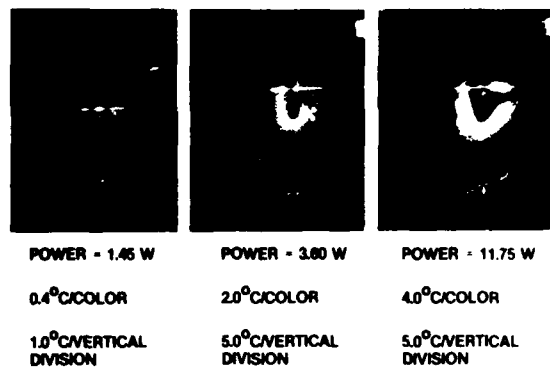
Fig. 4. Solar Module Power Output

IR Failure Detection of Field Modules



PORTABLE IR CAMERA USED TO LOCATE MODULE IN FIELD OPERATING WITH DEGRADED PERFORMANCE DUE TO CRACKED CELL - SUBSEQUENT I-V CURVE (RT.) CONFIRMED REDUCED ELECTRICAL PERFORMANCE

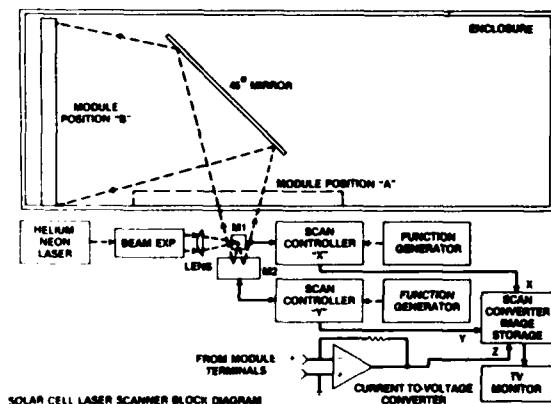
Thermograms of Back Biased Solar Cell



NON-UNIFORM HEATING OF A SOLAR CELL DUE TO MODULE SHADOWING INDUCED BACK-BIASED OPERATION. THERMAL MAPPING PIN-POINTED INCIPENT CELL JUNCTION FAILURE LOCATION

Fig. 5. Infrared Camera

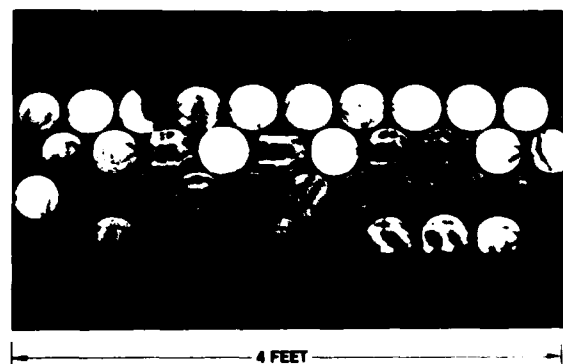
Solar Cell Laser Scanner Block Diagram



JPL LASER SCANNING SYSTEM AMPLIFIES OUTPUT OF ILLUMINATED SPOT ON CELL TO PRODUCE POSITION KEYED VIDEO IMAGE. ONLY FUNCTIONAL PORTIONS OF SOLAR CELLS RESPOND TO INCIDENT SWEEP LASER BEAM

4 INCH SOLAR CELLS

CRACKED CELLS



SOLAR CELL MODULE LASER SCAN CONFIRMED THAT REDUCED ELECTRICAL PERFORMANCE WAS CAUSED BY 2 CRACKED CELLS NOT DETECTED BY X10 POWER VISUAL INSPECTION

Fig. 6. Laser Scanning For Solar Cell Evaluation

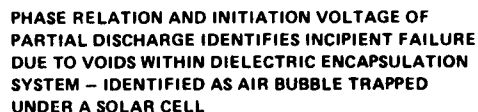
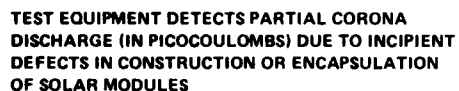
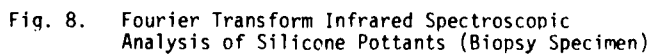
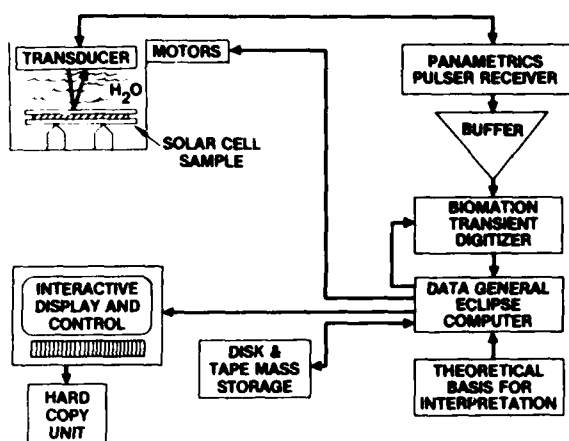
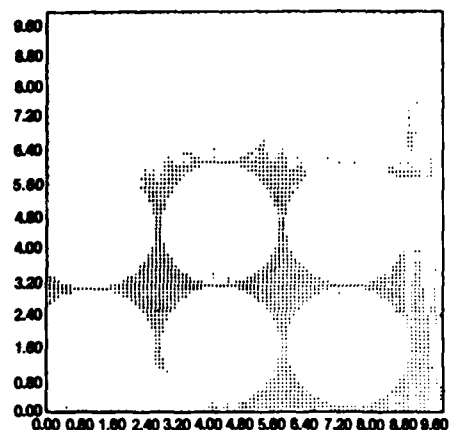


Fig. 7. Partial Discharge (Corona)



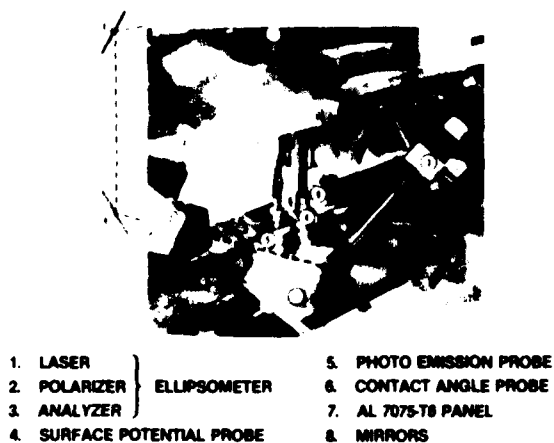


BLOCK DIAGRAM OF COMPUTERIZED ULTRASONIC SYSTEM FOR TESTS OF SOLAR CELL MODULES IN STUDY OF DEBOND DETECTION

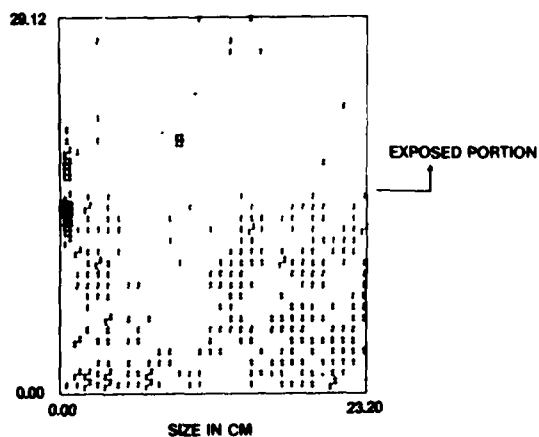


ULTRASONIC MAP OF NULLED REFLECTION FROM THE ENCAPSULANT TO SILICON SOLAR CELL INTERFACE

Fig. 9. Ultrasonics



ELLIPSOEMETER MULTIPROBE FACILITY AT ROCKWELL SCIENCE CENTER USED FOR INTERFACE ANALYSES



DIFFERENCE OFF NULL ELLIPSOEMETER MAP OF SOLAR MODULE PARTIALLY EXPOSED TO ULTRAVIOLET & MOISTURE

Fig. 10. Ellipsometer

POLYMER COMPOSITE RELIABILITY REQUIREMENTS FOR LARGE SPACE STRUCTURES

Jovan Moacanin
Jet Propulsion Laboratory
California Institute of Technology
Pasadena, California 91103

ABSTRACT

Long-life (10-30 years) large space structures are considered by NASA for a number of future earth-orbiting missions. The use of very thin graphite-fiber composites have been considered as structural materials for the fabrication of these structures. A combination of analytical and experimental approaches will be needed to provide a reliable data base on engineering properties of these materials to be used in the design and fabrication of these structures, which will be able to withstand the space environment.

Studies of planned NASA missions indicate that multiuser, multipurpose science and application platforms can achieve cost efficiencies and enhanced reliability through shared support systems, shared operations, and on-orbit serving using the operational Space Shuttle. These multiuser platforms will evolve in succeeding years into highly complex platforms for communications of scientific observations capable of greatly increasing spacecraft efficiency and utilization (Fig. 1). Technical considerations and economics require these structures to be designed for space operational loads and for long life (10 to 30 years).

The technological issues for these new structures may be exemplified by current activities on the development of precision deployable antennas (Ref. 1) for applications such as large earth viewing radiometers. This concept is intended for antennas from 30 to several hundred meters in diameter and for operation at 100 GHz and above. The deployable reflector structure requires high surface precision (Fig. 2). Pulsed laser ranging systems (Fig. 3) are being evaluated for measuring and controlling the surface curvature (Ref. 2).

In order to meet the requirements for lightweight and adequate strength, very thin (1.0 mm or less) graphite fiber composites are being considered as primary structural materials. Both epoxy and polyimide based composites are being investigated. The possibility of using polysulfone (a thermoplastic) based composites is being considered for its potential for fabrication in space using techniques such as pulltrusion. For large structures, technology applications long-term dimensional integrity along with minimal tendency for thermal distortion are essential.

One of the major uncertainties in the use of composites is the effect of space radiation on mechanical and physical properties. The effects of high energy electrons and protons (and to a lesser extent other high energy particles) must be considered. Although their penetration depth is rather low, the effects will be significant considering the thinness of the composites to be used. The nature and the extent of degradation will depend on the radiation profile in a particular orbit (e.g., geosynchronous) and on the chemical nature of the composites (e.g., epoxy or polyimide/graphite).

The complexity of the long-term effects of the space environment and the lack of an applicable data base dictate the development of a combined analytical and accelerated experimental program to realistically predict temporal energy degradation profiles in materials of interest. Analyses of the relative complexities and costs of the various test program options show that for a cost and time effective approach one cannot simulate the space environment in detail, but that one must reproduce material degradation profiles by a judicious combination (some simultaneous and some sequential) of radiation/temperature/time (Ref. 3).

Experimental techniques which are being developed at JPL rely to a large extent on transient measurements in order to identify primary effects of radiation on materials. For an assessment of UV induced degradation mechanisms flash photolysis is being used (Fig. 4). Similarly, pulsed e-beam sources are being used to study high energy electron mechanisms (Ref. 4). These experimental data are used then along with other conventional measurements for determining radiation effects to develop analytical models for predicting long-term effects in space.

Material defects which ultimately may compromise the performance of a structure may have their origin beginning with the selection of materials prior to fabrication and all the way to the final operational environment (Fig. 5). The previously proposed reliability concepts (Ref. 5) are applicable provided that preventive NDE is used extensively to assure that components such as prepregs and adhesively bonded structures are cured to final states which were qualified by extensive tests and analyses of the long-term effects of space radiation. For the duration of a mission NDE will be required for inspection and for repair/replace decisions.

Acknowledgement This paper represents one phase of work performed at the Jet Propulsion Laboratory, California Institute of Technology, sponsored by the National Aeronautics and Space Administration under Contract NAS7-100.

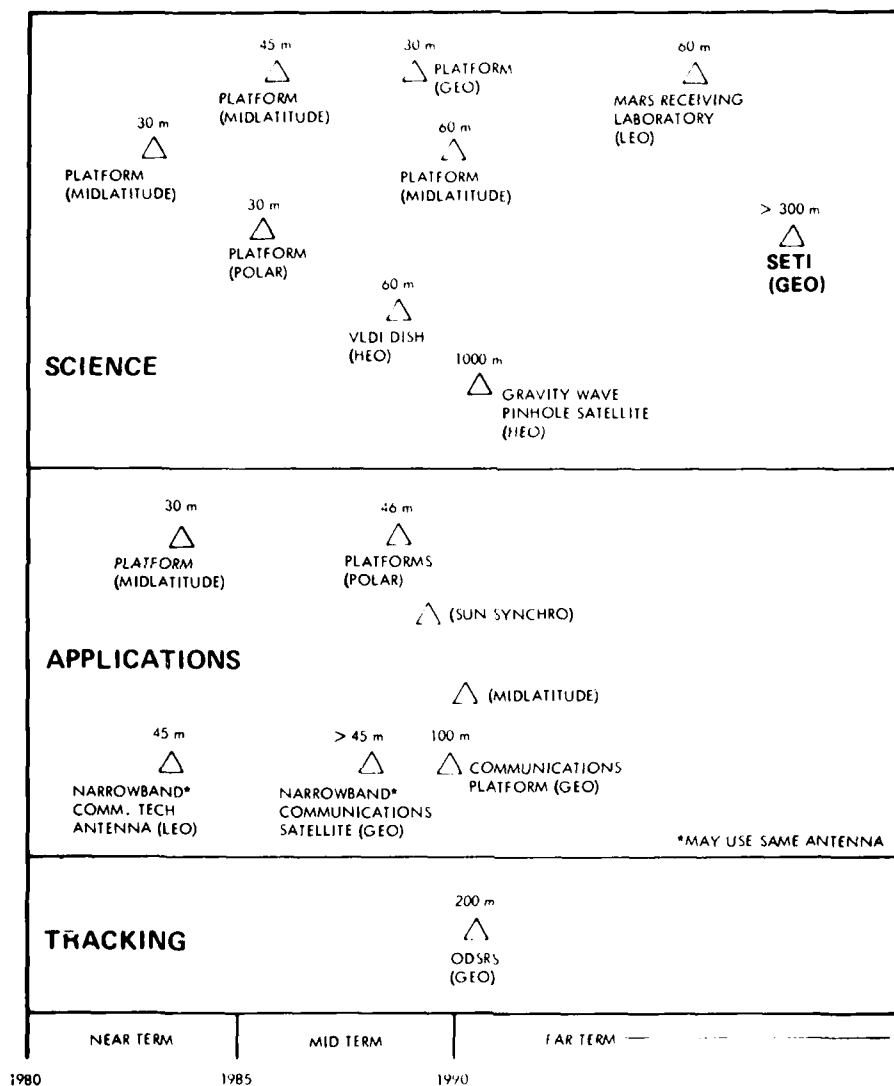


Fig. 1. NASA OAST Missions Involving Large Space Systems (Ref. 1).

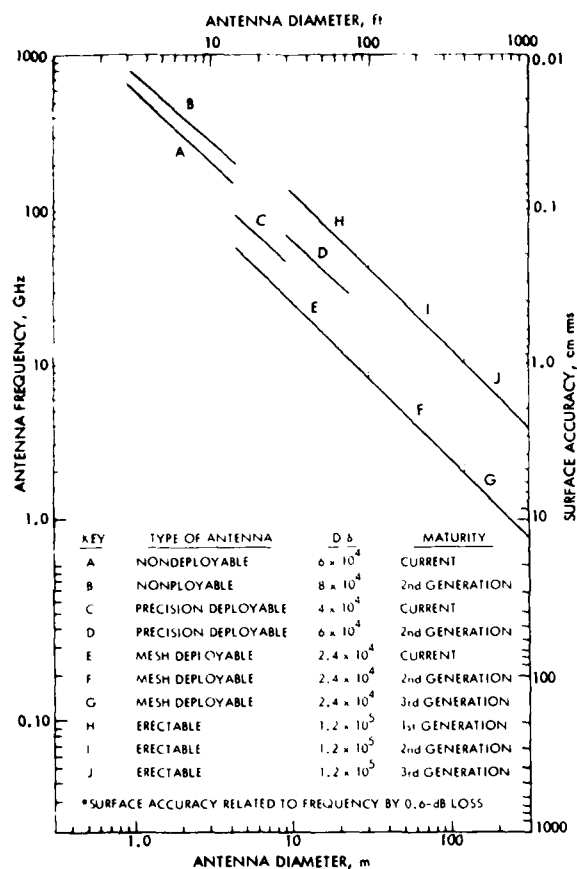


Fig. 2. Surface Precision Requirements for Deployable Antennas.

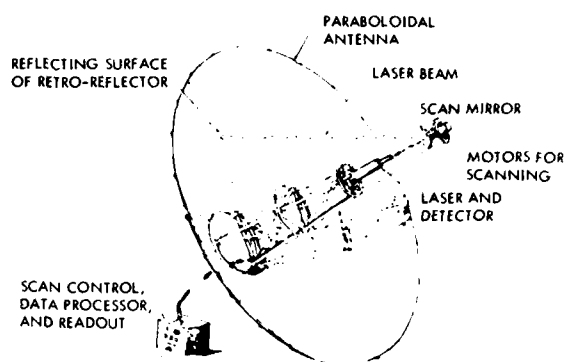


Fig. 3. Antenna Surface Measuring System (Ref. 2)

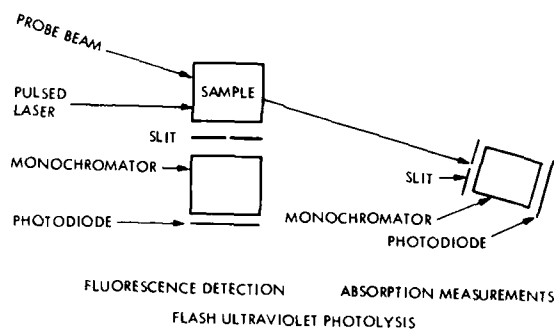


Fig. 4. Flash Photokinetic Spectroscopy Utilizing A Pulsed Laser in the Ultraviolet; Time Resolution of Such Systems Can Be 1 ns.

A. CHEMICAL STRUCTURE DEFECTS	B. MANUFACTURING DEFECTS	C. MACROSCOPIC FATIGUE DEFECTS
<ul style="list-style-type: none"> • 10 - 200 Å IN SIZE • CONTROL CRITICAL DESIGN PROPERTIES (T_g, MOISTURE ABSORPTION, DIMENSIONAL STABILITY) • CONTROLLED BY <ul style="list-style-type: none"> • CHEMICAL ANALYSIS • SELECTION OF MATERIAL 	<ul style="list-style-type: none"> • 10 μm IN SIZE (INCLUSIONS, VOIDS, DEBONDS) • RESULTS FROM NON OPTIMUM PROCESS AND QUALITY CONTROL • DETECTED BY <ul style="list-style-type: none"> • ULTRASONICS • OPTICAL SCANNING • TECHNIQUES SENSITIVE TO INTERFACIAL IMPERFECTIONS 	<ul style="list-style-type: none"> • RESULTS FROM THE INTERACTION OF (A) AND (B) WITH MECHANICAL AND ENVIRONMENTAL STRESSES • NETWORK OF MICROCRACKS • SINGULAR MICROSCOPIC CRACK GROWTH • DETECTED BY <ul style="list-style-type: none"> • ULTRASONIC EMISSION • MOISTURE DIFFUSION ANALYSIS • OPTICAL INSPECTION

Fig. 5. Origins of Material Defects

REFERENCES

1. Freeland, R. E. and Campbell, T. G., "Deployable Antenna Technology Development for the Large Systems Technology Program," Paper No. 79-0932, Proceeding of AIAA/NASA Conference on Adv. Technology for Future Space Systems, held at Langley Research Center, Hampton, Virginia, March 1979.
2. Bergdahl, M., "A Self-Pulsed Laser Ranging System Under Development at JPL," Paper No. 79-0934, Proceeding of AIAA/NASA Conference on Adv. Technology for Future Space Systems held at Langley Research Center, Hampton, Virginia, March 1979.
3. Gupta, A., Carroll, W. F. and Moacanin, J., "Effects of Space Environment on Composites: An Analytical Study of Critical Experimental Parameters," JPL Publication 79-47, National Aeronautics and Space Administration, July, 1979.
4. Moacanin, J., Gupta, A. and Carroll, W. F., "An Analytical Approach to Evaluation of Space Radiation Effects on Materials for Long-Life Missions," Proceedings of Symposium on Spacecraft Materials in Space Environment held at European Space Agency, Noordwijk, The Netherlands, October 1979.
5. Kaelble, D. H., "Polymer Composite Reliability," Proceedings of the ARPA/AFML Review of Progress in Quantitative Nondestructive Evaluation, held at La Jolla, California, July, 1978, Report No. AFML-TR-78-205, p. 193.

NONDESTRUCTIVE MONITORING OF FLAW GROWTH
IN GRAPHITE/EPOXY LAMINATES UNDER SPECTRUM
FATIGUE LOADING

I.M. Daniel and S.W. Schramm
IIT Research Institute
Chicago, Illinois 60616
and
T. Liber
Travenol Laboratories
Round Lake, Illinois 60073

ABSTRACT

Ultrasonic and acoustic emission techniques were used to monitor flaw growth in graphite/epoxy laminates containing four types of initial flaws and subjected to fully reversed spectrum fatigue loading, including temperature and moisture variations. In general, it was found that flaw growth was much more pronounced in the specimens exposed to environmental fluctuations in addition to the load spectrum, than in those tested in an ambient environment. Flaw growth was also greater in specimens of [(0/+45/90)_s]₂ layup than in those of [0₂/+45]_{2s} layup. No significant reduction in residual tensile strength (in general less than ten percent) was observed for any of these groups of specimens.

EXPERIMENTAL PROCEDURE

Specimens - The specimens were graphite/epoxy (AS3501-5A) coupons of [(0/+45/90)_s]₂ and [0₂/+45]_{2s} layups. The initial flaws investigated were: (1) circular hole, (2) embedded film patch, (3) internal ply gap and (4) surface scratches (Fig. 1). The specimen gage section was 5.08 cm (2 in.) long and 3.81 cm (1.5 in.) wide.

Loading - The specimens, three of each flaw type and layup, were preconditioned by exposing them to 21 days of 347 degK (165°F) temperature at a relative humidity of 98 percent in an environmental chamber, during which time they absorbed 1.29 ± 0.05 percent by weight moisture. The load spectrum consisted of 127,500 cycles of tension-compression at various levels of peak stress per lifetime. At a cycling frequency of 3 Hz this was accomplished in approximately 12 hours. Two series of tests were conducted, one with the load spectrum above at an ambient environment and the other with the same load spectrum but including environmental fluctuations of 219 degK (-65°F) to 406 degK (270°F) in temperature and up to 95 percent in relative humidity. Each lifetime was segmented into various combinations of load peaks and temperature and humidity levels.

Stress cycling was applied to a chain of five specimens at a time by means of an electrohydraulic closed loop system. The maximum cyclic stress was 161 MPa (23 ksi) for the [(0/+45/90)_s]₂ graphite/epoxy specimens and 223 MPa (32 ksi) for the [0₂/+45]_{2s} specimens.

Nondestructive Monitoring - A number of acoustic emission transducers were mounted on the specimens in the fatigue loading chain and cumulative counts and count rate

were selectively monitored and recorded. This continuous acoustic emission monitoring was done to complement the ultrasonic monitoring which was done only at specified intervals. At intervals corresponding to each half lifetime of loading the specimens were removed from the fatigue machine and inspected ultrasonically. Immersion ultrasonic techniques were used using a 5 MHz broad band focused transducer. The specimens were tested up to a maximum of four lifetimes. The various C-scans obtained for each specimen were combined into maps illustrating the progressive flaw growth.

Residual Strength - Following the fatigue loading above and the ultrasonic monitoring, the specimens were tested statically in tension to failure to determine their residual strength and thus assess the criticality of the various flaws.

RESULTS

Flaw growth maps obtained for specimens with the four types of initial flaws discussed before for two layups and two environmental spectra are shown in Figs. 2-5. In general, it was found that flaw growth was much more pronounced in the specimens exposed to environmental fluctuations in addition to the load spectrum, than in those tested in an ambient environment. More extensive flaw growth was observed at one to two lifetimes in the former group than at four lifetimes in the group tested at ambient environment. In general, flaw growth was greater in specimens of [(0/+45/90)_s]₂ layup than in those of [0₂/+45]_{2s} layup with some exceptions in the environmentally cycled specimens. In the case of specimens with circular holes delaminations grow around

the hole boundary in the early stages of load cycling (one to two lifetimes) but no further growth is seen thereafter, with two exceptions in the environmentally cycled specimens which showed early extensive delaminations throughout the specimen. In the specimens with embedded patches initial delaminations were present throughout. These grew with the number of load cycles and additional ones developed throughout the specimens. Specimens with internal ply gaps, especially those of $[0_2/+45]_{2s}$ layup showed the least amount of flaw growth. Specimens with surface scratches developed the most extensive delaminations, but mostly localized on the surface or near surface plies.

Acoustic emission count rates follow the same trends as the loading spectrum with an overall trend for higher average count rates with increasing time (lifetimes) of fatigue loading (Fig. 6). In this respect there seems to be some correlation between acoustic emission count rate and flaw size as detected by ultrasonic scanning.

No significant reduction in residual tensile strength (in general less than ten percent) was observed for any of these groups of specimens. This may be due to the relatively low fatigue loads and to the fact that the resulting delaminations are not critical under the subsequent static tensile loading.

CONCLUSIONS

1. Flaw growth is greater in specimens of $[(0/+45/90)_s]_2$ layup than in those of $[0_2/+45]_{2s}$ layup.
2. Flaw growth is more pronounced in specimens exposed to environmental fluctuations than those tested in an ambient environment.
3. Delaminations around holes occur mostly in the initial stages (one to two lifetimes) with no further growth thereafter.
4. Delaminations in specimens with embedded patches extend throughout the specimen.
5. Specimens with internal ply gaps, especially those of $[0_2/+45]_{2s}$ layup, show the least amount of flaw growth.
6. Specimens with surface scratches develop the most extensive delaminations, but mostly localized on the surface or near surface plies.
7. No significant reduction in residual strength was observed for any group of specimens.

ACKNOWLEDGEMENTS

The work described herein was sponsored by the Air Force Materials Laboratory and the Air Force Flight Dynamics Laboratory, Wright-Patterson Air Force Base, Ohio, through a subcontract from Rockwell International Corporation, Los Angeles, California. The authors would like to thank Dr. George Alers and Mr. Lloyd J. Graham of the Rockwell International Science Center for their assistance and advice on ultrasonics and acoustic emission and Messrs. K.E. Hofer and G. Waring for the fatigue task of the program.

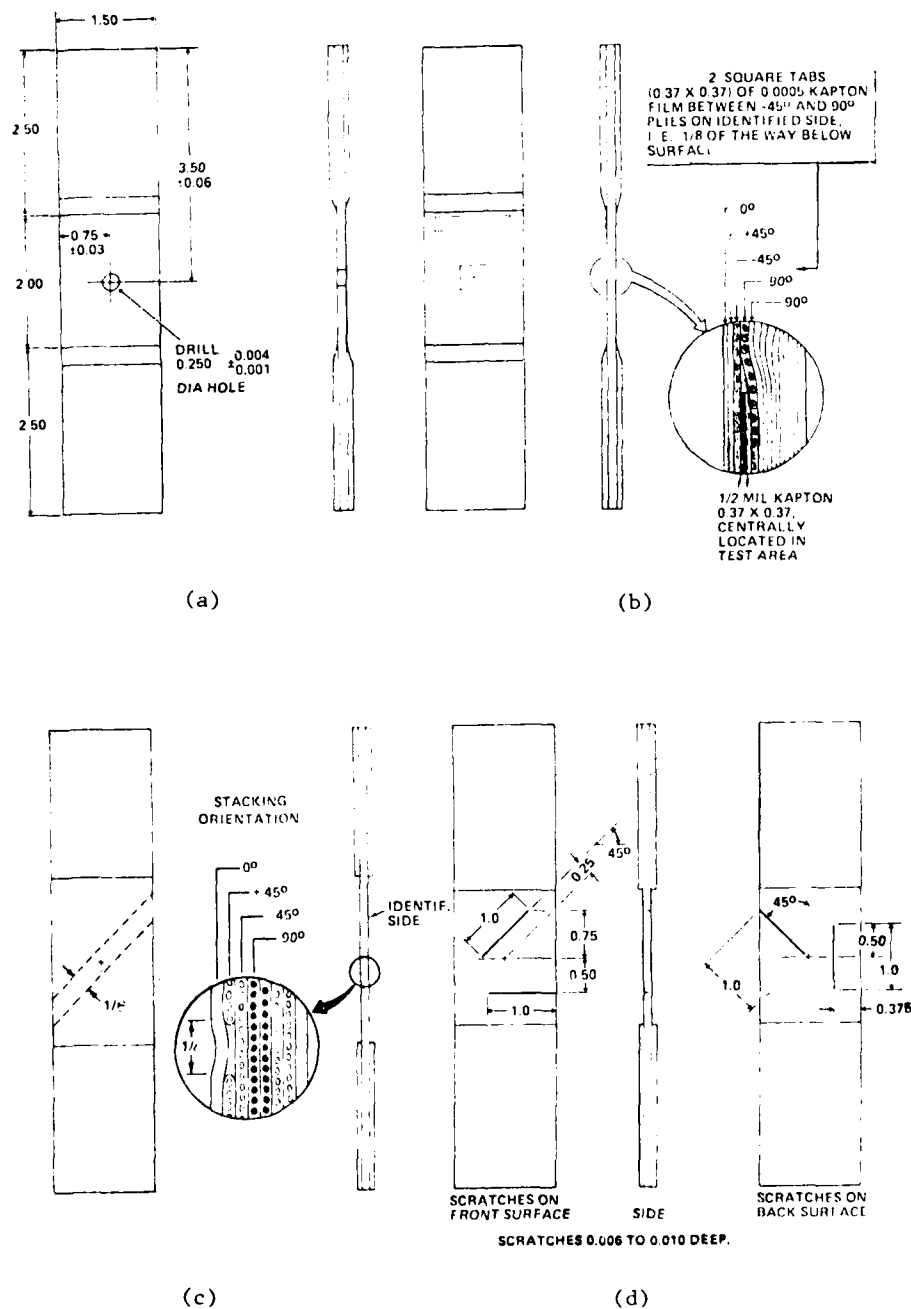


Fig. 1 Graphite/Epoxy Coupons with Four Types of Initial Flaws: (a) Circular Hole, (b) Embedded Film Patch, (c) Internal Ply Gap and (d) Surface Scratches.

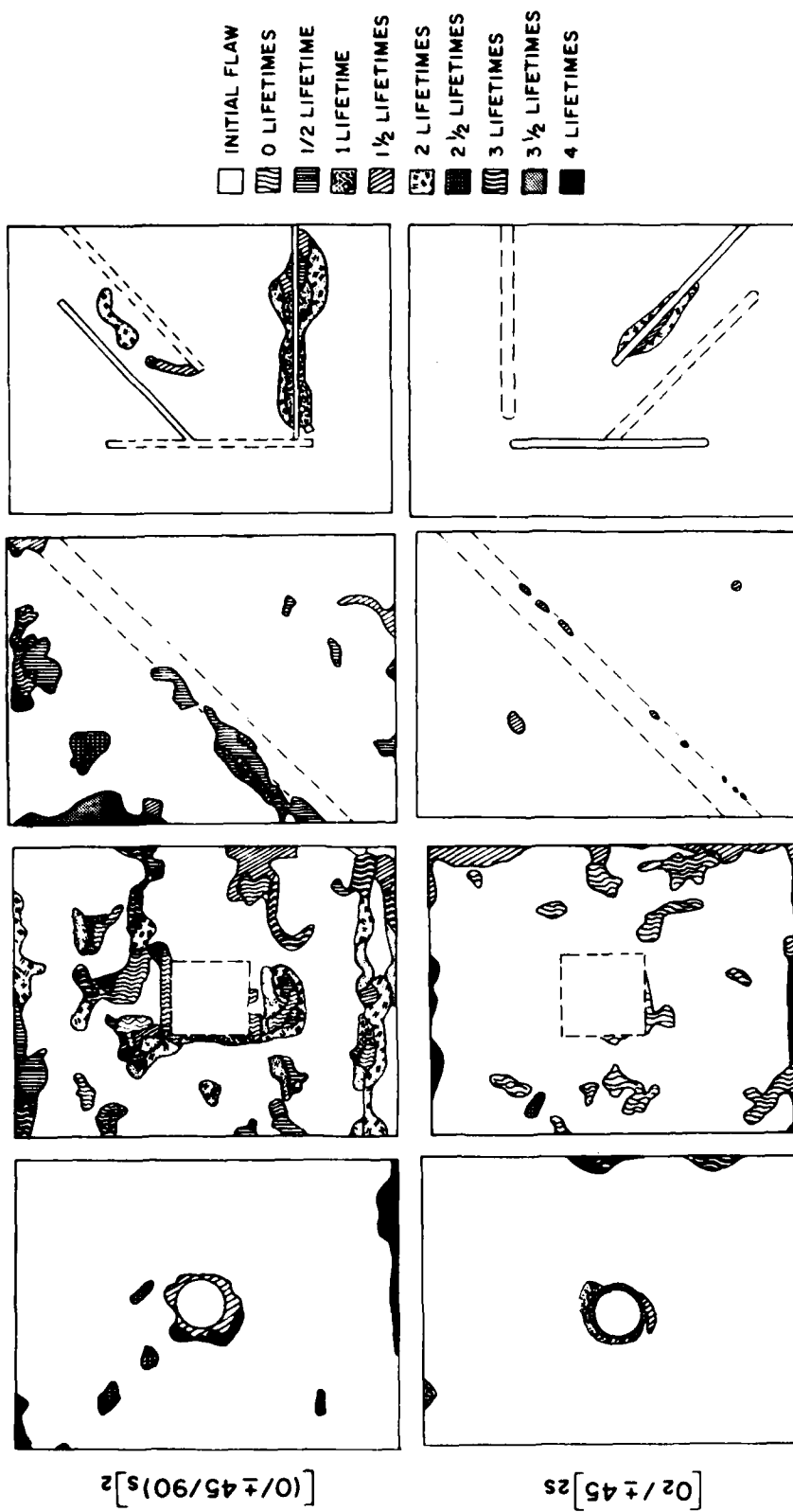


Fig. 2 Flaw Growth Under Spectrum Fatigue Loading In [(0/±45/90)_s]² and [0₂/±45]_{2s} Graphite/Epoxy Specimens with Four Types of Initial Flaws. (Ambient Environment)

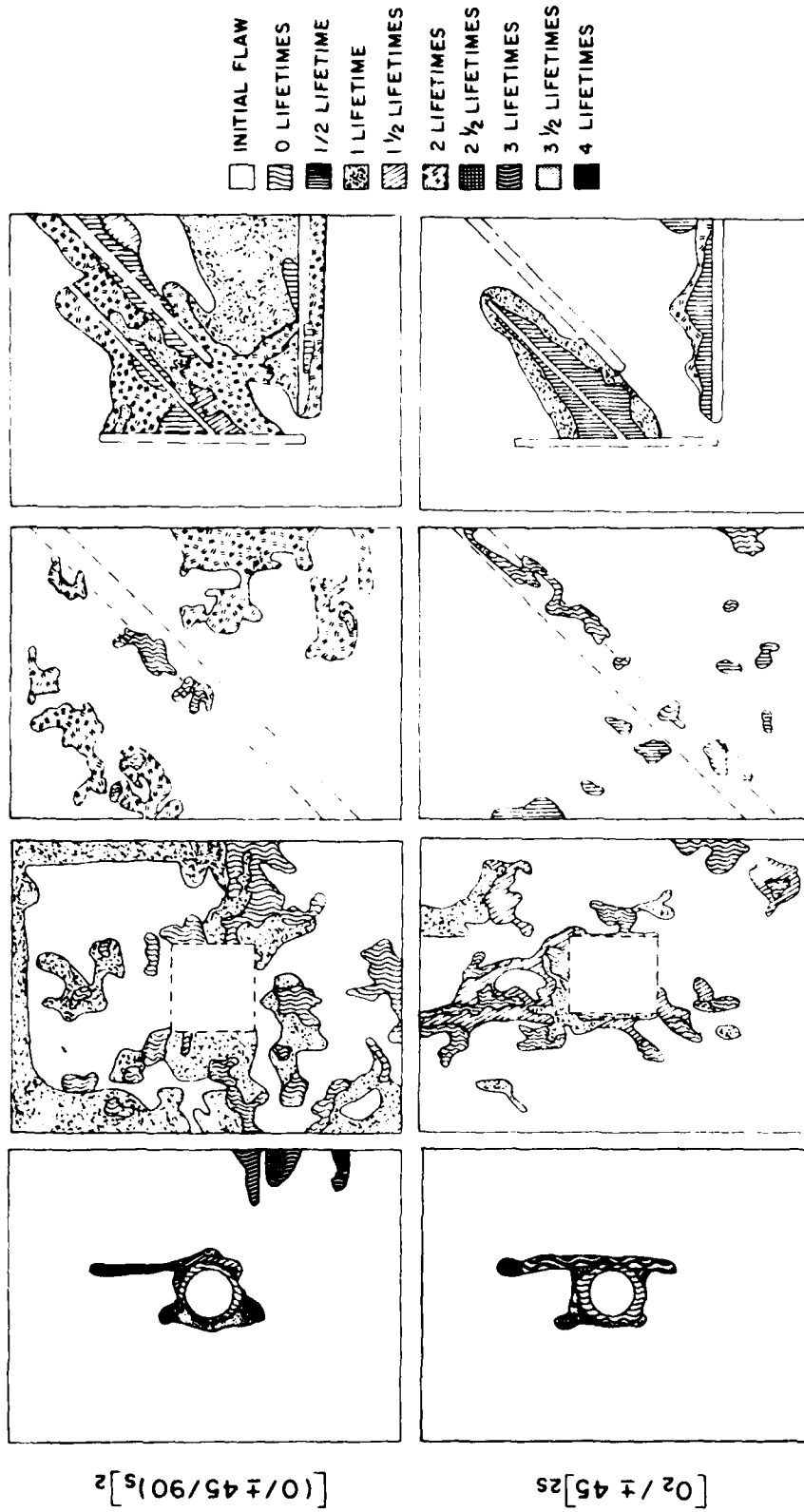


Fig. 3 Flaw Growth Under Spectrum Fatigue Loading in $[0_2/\pm 45]_2$ s and $[(0/\pm 45/90)_s]_2$ s Graphite/Epoxy Specimens with Four Types of Initial Flaws. (Temperature and Humidity Variations)

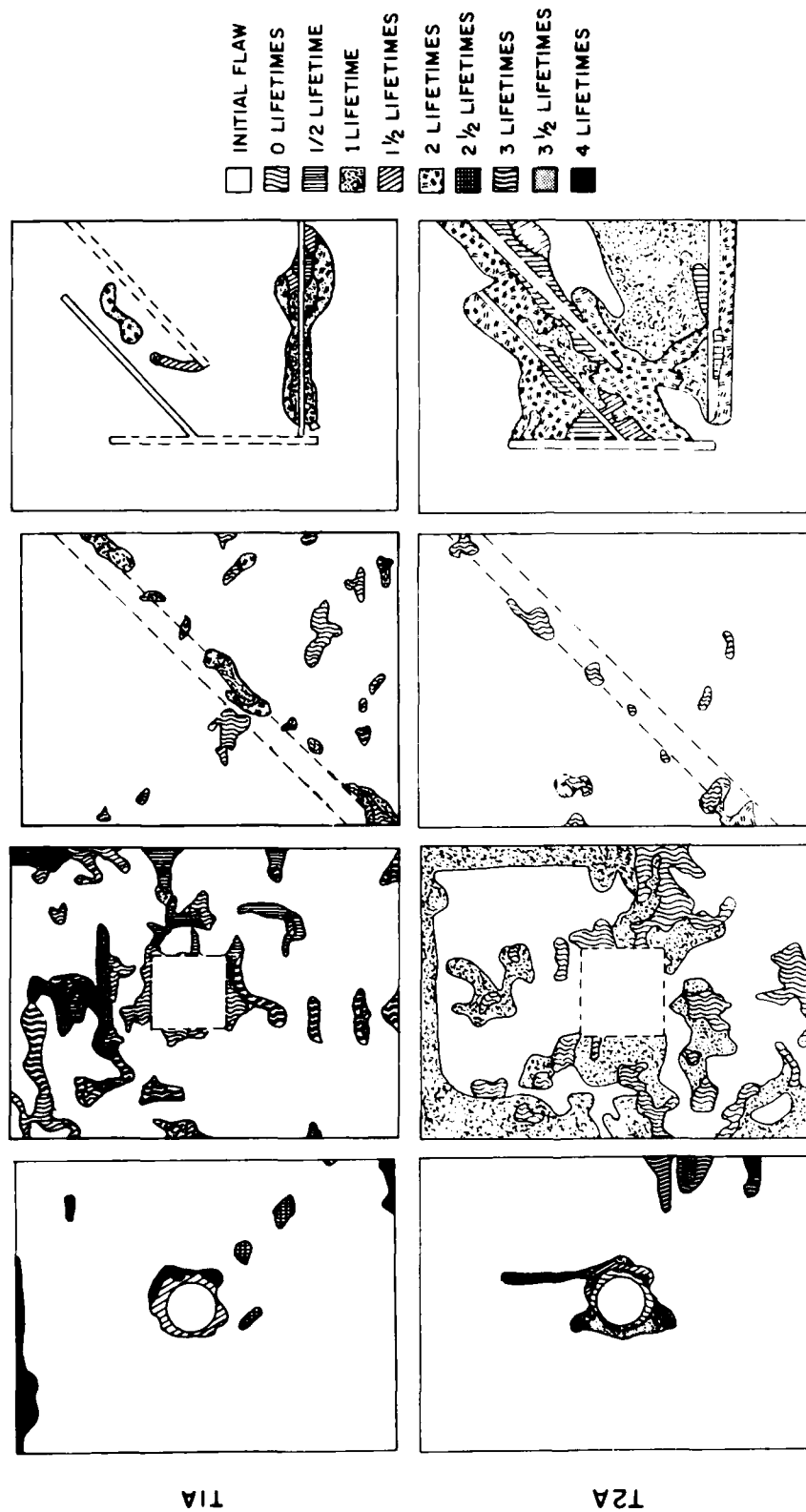


Fig. 4 Flaw Growth Under Spectrum Fatigue Loading in [(0/+45/90)_s]2 Graphite/Epoxy Specimens with Four Types of Initial Flaws (T1A: Specimens Tested in Ambient Environment; T2A: Specimens Exposed to Environmental Cycling).

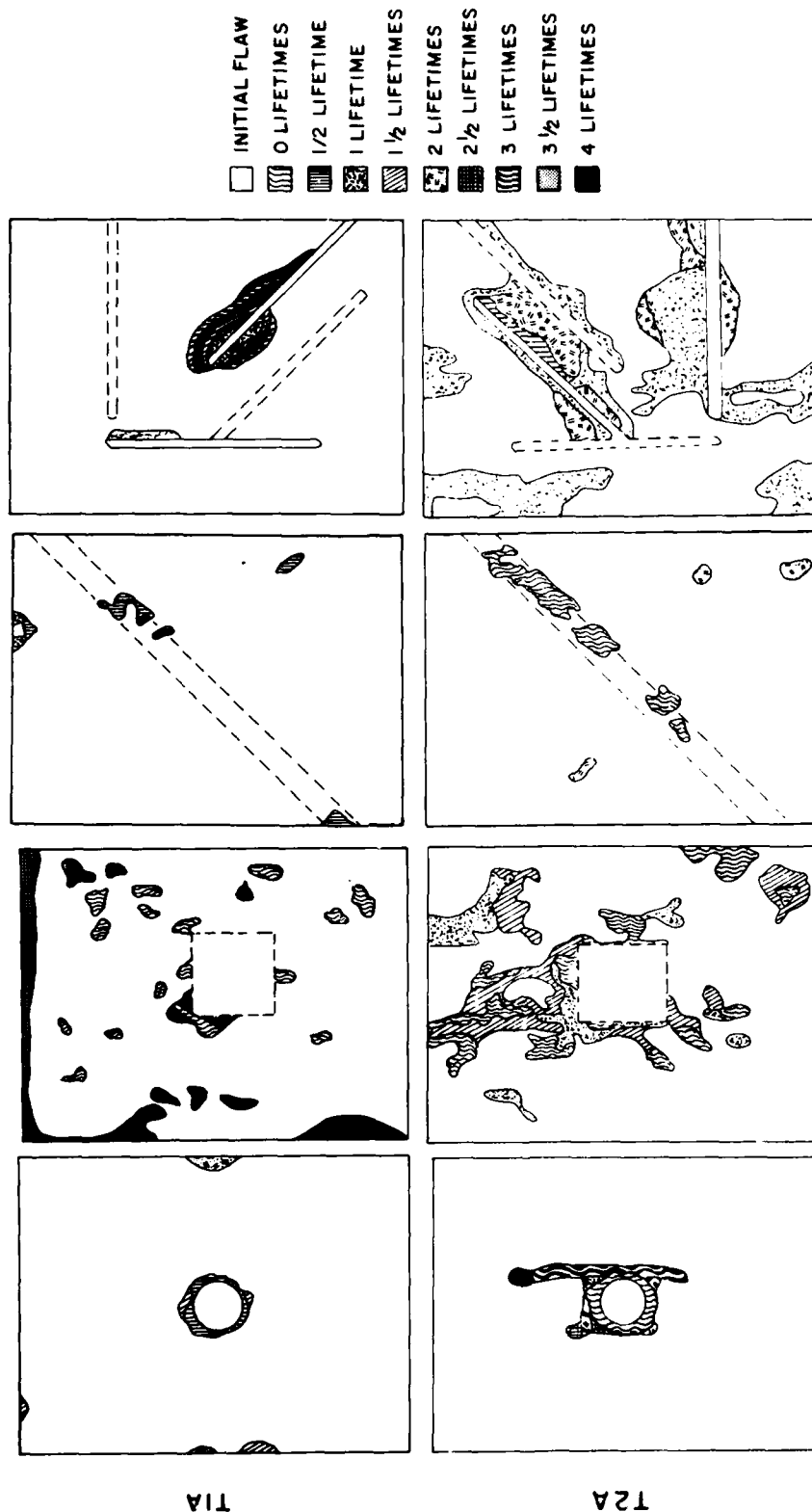
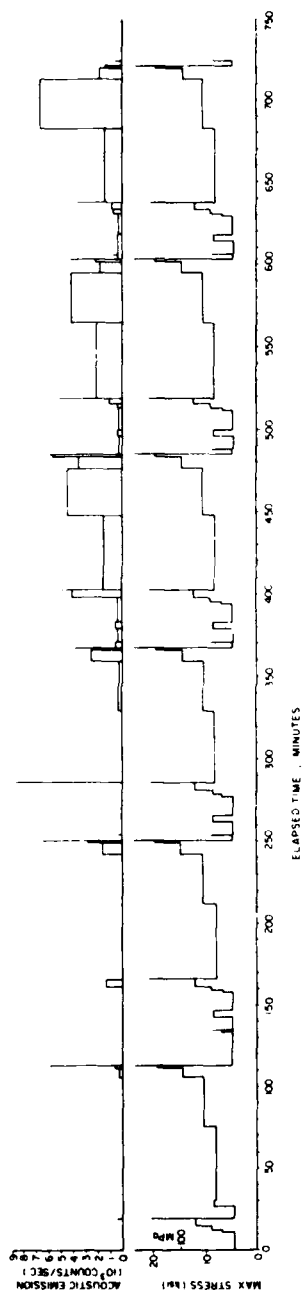
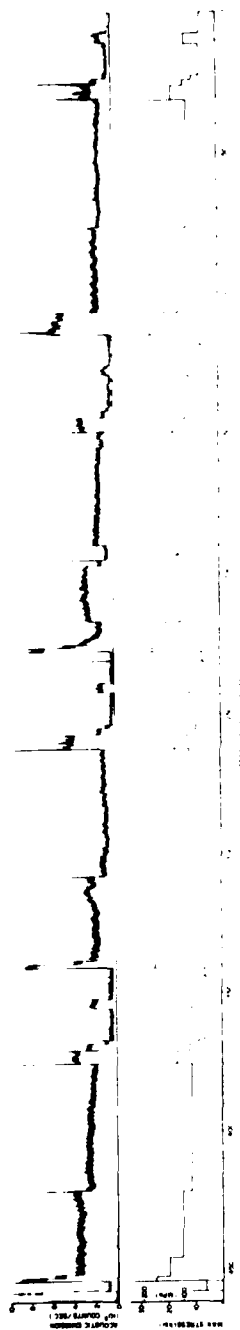


Fig. 5 Flaw Growth Under Spectrum Fatigue Loading in [02/+45]_{2s} Graphite/Epoxy Specimens with Four Types of Initial Flaws (T1A: Specimens Tested in Ambient Environment; T2A: Specimens Exposed to Environmental Cycling)



(a)



(b)

Fig. 6 Acoustic Emission and Corresponding Load Spectrum as a Function of Elapsed Time for Graphite/Epoxy Specimens with Holes. (a) [(0/+45/90)_s]₂ Specimen, (b) [0₂/+45]_{2s} Specimen (time increases from right to left).

IMPLEMENTATION OF AN ULTRASONIC, ADHESIVE BOND TEST BED: SAMPLE PROBLEMS:
ALUMINUM TO ALUMINUM AND HONEYCOMB STRUCTURES

E. Segal, G. Thomas and J. Rose
Drexel University
Philadelphia, PA 19104

ABSTRACT

The complex problems of predicting adhesive bond strength for both adhesive and cohesive defects have been studied using an ultrasonic, experimental test bed system. This experimental test bed incorporates the ultrasonic and computer equipment necessary to acquire and process data from various types of adhesively bonded test specimens. The computer hardware and software have been developed to allow the design of reliable pattern recognition algorithms for the prediction of adhesive bond strength. Two different types of adhesive bonded structures were studied. First, the problem of inspecting the adhesive bond joint in an aluminum to aluminum step-lap specimen to predict the bond strength that could be affected by adhesive or cohesive defects was studied. A set of 164 bond specimens was used to design an algorithm that is 91% reliable for separating the specimens into a good class or a weak class. A Fisher Linear Discriminant function was selected by the test bed system as the optimal pattern recognition routine for the classification problem. The second structure studied is the honeycomb configuration. Specimens were acquired that contained many of the typical adhesive defects common to honeycomb structures. A feasibility study was conducted to determine the test bed's potential for solving honeycomb inspection problems.

INTRODUCTION

Adhesive bonding is rapidly becoming an important part of joint technology because of its inherent nature to provide more uniform stress transfer, increased fatigue life, and a reduction in structural weight. These characteristics are particularly important in high performance structures utilizing aluminum to aluminum and aluminum to composite joints as those found in aircraft. Adhesives are often suitable for solving many joining problems compared to the more common techniques of welding, riveting, and the use of other mechanical fasteners. One of the major limitations on the use of adhesives as a structural element, however, is associated with the difficulty encountered in making an accurate determination of bond quality or potential performance after the joint has been completely assembled. An important part of using adhesives is to develop a nondestructive evaluation technique that makes use of a single ultrasonic measurement for predicting the potential bond performance level.

Recently many investigators have studied this difficult problem of ultrasonic inspection of adhesive joints. The more successful techniques for determining bond strength where gross flaws are not present have been with the aid of computerized, sophisticated signal processing and feature extraction [1-8]. Though a tremendous advance in the state of the art of ultrasonic adhesive bond inspection has been made, there still exists much work to be done in the area of producing a complete bond flaw prediction algorithm which includes all bonding defects. The solution to this problem is the goal of this study. The problem of developing a complete bond flaw prediction algorithm has been attacked by assembling an ultrasonic design tool and experimental test bed for the prediction of adhesive bond defects. This system includes ultrasonic equipment, computer hardware, and software for the design of adhesive bond defect prediction algorithms which could account for a variety of bonding

flaws. Two sample adhesive bond problems have been studied using this test bed system. Some of this work will be presented at the Ninth World Conference on Nondestructive Testing [9].

The first sample problem which called for the classification of bonding defects in an aluminum to aluminum structure, was quite successful. A computerized algorithm was developed that provided an overall reliability of 91% for classifying adhesive bond defects. The second sample problem which involved the classification of bond defects in honeycomb structures is in its preliminary stages. Data acquired to date clearly indicates a strong potential for successful classification.

TEST BED CONCEPT

The test bed idea was conceptualized out of need for a means to study new ultrasonic inspection problems that could not be solved using traditional techniques. These inspection problems required advanced, state of the art, methods for solutions. A test bed is a self-contained assemblage of equipment, controlled by a computer, to acquire data, process the data and design classification schemes for new ultrasonic inspection problems.

The test bed system provides a systematic approach to a new problem in ultrasonic nondestructive evaluation. Once a new inspection problem has been defined, the ultrasonic test bed can be implemented. For example, in the case of an adhesive bond problem, the first step is to perform a parametric study using Brekovskik's layered media program [1, 11] to model the bond structure. This study will provide a resource base for selecting pertinent features, plus determine a transducer selection criteria. The test bed equipment is used then to acquire data using the appropriate transducer from a set of training specimens. This data can next be reduced by signal processing to provide the desired features' values. After the training set's feature vectors have been determined, a collection of computer augmented pattern recognition algorithms that are included in a package called "Generalized Approach to New Problems in Ultrasonic Inspections" (GANPUI) [12] can be instituted to find the optimal classification technique. Then a different set of specimens, a test set, are inspected by the test bed system and classified by the newly designed bond defect prediction algorithm to determine the algorithm's reliability. If the reliability is not adequate, the process is started from the beginning using new data acquisition techniques, selecting different features, and instituting other pattern recognition algorithms.

TEST SPECIMEN DESCRIPTION- ALUMINUM TO ALUMINUM, STEP-LAP JOINT

Two series of test specimens have been fabricated for the aluminum to aluminum sample study. The first series of bond specimens was used as a training set to design the bond defect prediction algorithm. This first series included good specimens, adhesively defective specimens, and cohesively defective specimens. The second series was used to test the algorithm and it included good specimens, adhesively defective specimens, cohesively defective specimens, and combined adhesive and cohesive defects. The specimen geometry is

that of a typical step-lap joint as shown in figure 1. An industrial adhesive, FM-73, from American Cyanamid Co., was used in this study. Manufacturing techniques for the adhesive system are described in [1].

Several types of bonding defects were manufactured into the bond specimens so that a bond defect prediction algorithm could be developed that considered adhesive and cohesive defects. First, properly prepared and cured specimens were made to provide data from good bonds. Then weak bonds were manufactured by either contaminating the adherent surfaces to cause an adhesive defect, under-curing the specimen to cause a cohesive failure, or varying the bond line thickness to provide weak bonds. Specimens were also manufactured that included combinations of the previous defects such as various thickness, undercured bonds.

TEST SPECIMEN DESCRIPTION - HONEYCOMB

Two specimens were used in order to investigate the feasibility of this test bed to identify flaws in Honeycomb Structures.

The specimens are described in Fig. 2. Specimen A has two kinds of programmed defects, unbonds and damaged honeycomb. The unbonds were simulated by thin pieces of teflon. Specimen B contains two kinds of unbonds. Skin Unbond (SU) - where the teflon was placed between the facing and the adhesive, and Core Unbond (CU) - where the teflon was placed between the adhesive and the Honeycomb core.

TEST BED SYSTEM

Ultrasonic Test Equipment

An ultrasonic pulse echo immersion system was used for the data acquisition procedures required in this experimental test bed. A block diagram of the ultrasonic equipment is shown in figure 3. The system consists of an Aerotech UTA 2 Pulser/Receiver driving the ultrasonic inspection probe. This pulser/receiver also amplifies the returning ultrasonic RF signal and has a gate circuit to separate and output any specific part of the ultrasonic waveform. The gate signal was used in this test bed as a means to trigger the analog to digital converter.

A Tektronix 7704 oscilloscope is used to display the ultrasonic RF waveform along with the gate signal. A computer controlled x-y scanner is incorporated into this test bed system as a tool to acquire automatically and accurately, ultrasonic data for a variety of bond specimen configurations.

Transducer Parameters for Adhesive Bond Inspection

The selection of the ultrasonic probe to be used for the inspection of the adhesive bond structure is a critical phase in the assembly of the ultrasonic equipment. The main concern when selecting the inspecting transducer is to provide the proper frequency content for accurate feature value selection. A theoretical modelling approach to the adhesive bond system was conducted on a computer to determine the significant features of the ultrasonic signal which was reflected by the bond layer. Once the features are selected, a transducer acceptance criteria is established to insure visibility of the features chosen. For example, if discrimi-

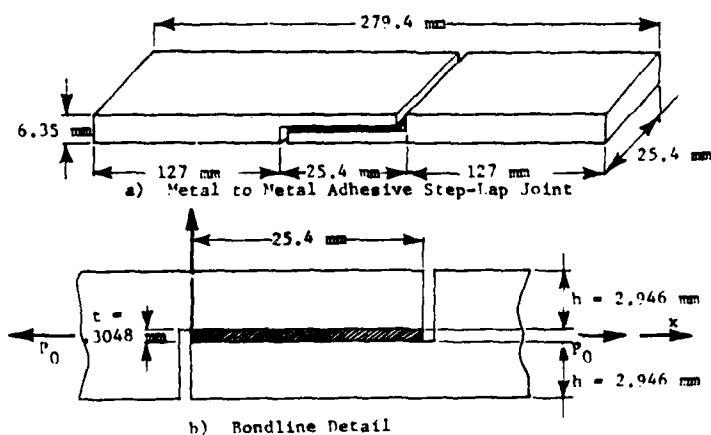
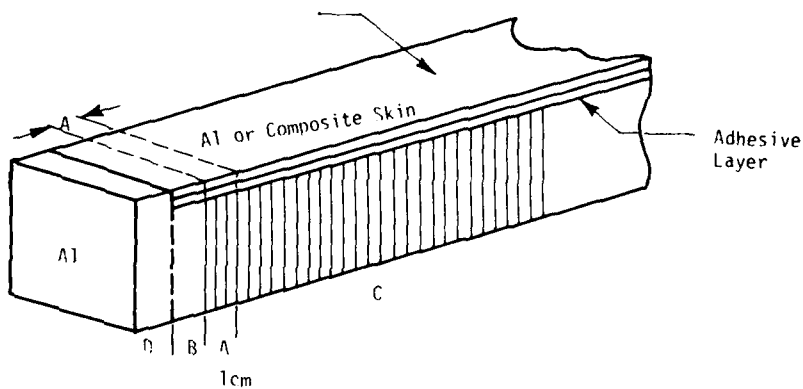
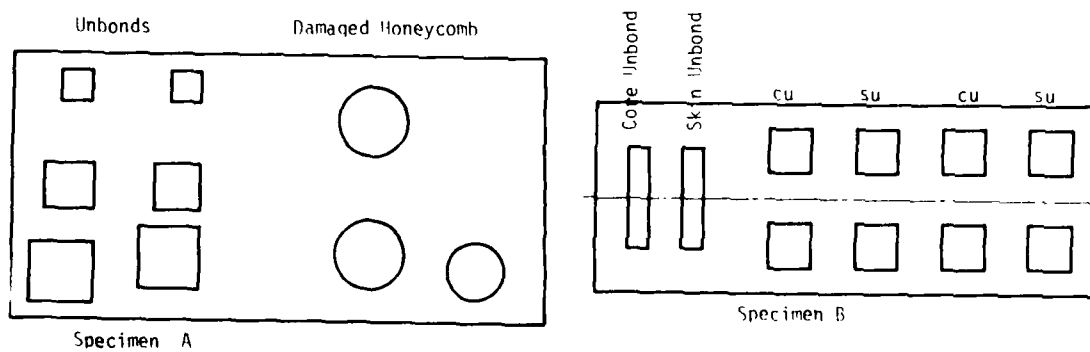


Figure 1. Step-Lap Joint Test Specimen (SI conversion: 25.4 mm = 1 in.)



a. Honeycomb to Aluminum Joint Configuration



b. Test specimen A and B

Figure 2. An Aluminum Core - Aluminum Facing Honeycomb Structures Containing Programed Defects

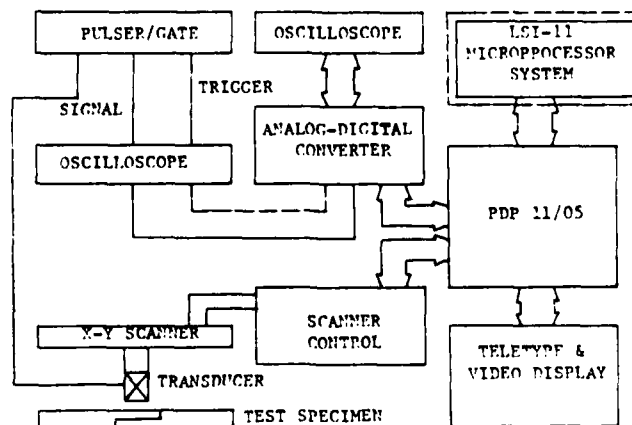


Figure 3. Block Diagram of the Fast Ultrasonic Data Acquisition and Analysis System

nating features are determined to occur at five and twelve megahertz, then the search probe must have a frequency bandwidth which includes these frequency modes to be acceptable.

Computer Hardware

The automatic data acquisition system for adhesive bond inspection is developed around a Digital Equipment Corporation PDP 11/05 minicomputer with various peripherals including a RK05 disk drive, a RX01 floppy disk drive, dual cassette drives, a Decwriter teletype and line printer, a Tektronix 4014 video terminal and a 4631 hard copy unit.

Analog to Digital Converter

The analog to digital converter used in this test bed is a Biomation 8100 unit capable of sampling intervals to .01 μ sec. Digitizing ultrasonic RF waveforms at this rate will yield approximately ten points per cycle on a ten megahertz pulse. The converter is an eight bit machine and thus digitizes to an accuracy of one part in 256, and can store 2,048 amplitude-time points in its memory at one time.

TEST BED PROTOCOL

Data Acquisition Details

The data acquisition procedure used for ultrasonically inspecting the test specimens is as follows. The transducer was automatically located over each of six inspection points on the bonded specimen, and these signals were spatially weighted and averaged to account for the shear stress distribution in the step-lap joint [13]. A one and a quarter inch water path separated the transducer from the specimen. At each location, five amplitude-time signals, which included a reference reflection from the top of the aluminum-water interface, and an echo from the adhesive bond layer, which was composed of the superposition of both adherent-adhesive interfaces, were gathered by the analog to digital converter. These signals were averaged to eliminate some of the random noise generated by the system. The result of the averaging is a single

reference and bond line echo which is stored in the computer's memory. A program is then called which calculated the Fourier transforms of the reference and the bond line echoes. The reference spectrum is divided, point by point, into the bond layer's echo spectrum using a complex division algorithm. This division results in the transfer function for the bond layer [10]. The transfer function is then used to determine various feature values because the transfer function is a function solely of the bond layer and is independent of the transducer. The features from the amplitude-time signals and the transfer functions are stored and later used in the pattern recognition algorithm. The pattern recognition algorithm function which accepts the feature values from each bond layer and classifies the bond specimen according to the presence or absence of defects. The data acquisition for the honeycomb specimens was similar to that used in the aluminum to aluminum adhesive bond work.

Signal Processing

An important phase in the development or implementation of an adhesive bond prediction algorithm is signal processing and data reduction. This is done before the feature values are determined to provide better, more accurate values. There are several noise influences in this experimental test bed system. One source is noise picked up by the transducer from the specimen and its surroundings. Another source of noise is from the measurement equipment. And finally, the quantization noise caused by the finite quantization levels of the A/D converter. Random noise can be significantly reduced by averaging the ultrasonic RF waveform many times as it is passed to the computer. A moving average is beneficial in reducing high frequency noise in the ultrasonic signal. And low frequency noise can be accounted for in the frequency domain or by a DC offset setting in the A/D converter.

The major data reduction technique used in this test bed is Fourier Transforming the ultrasonic RF signals. The Fourier Transform changes amplitude-time information into the amplitude-frequency domain. The Fourier Transform is a good data reduction technique because, for example, a 512 point amplitude-time signal can easily be represented by

a 50 point Fourier transform spectrum. Thus a significantly reduced feature vector is able to represent the signal in the frequency domain. Furthermore, the ultrasonic signal might be described by only a few characteristic features such as peak frequency, 6 dB down bandwidth, and a number of significant depressions. These features can then be used in a pattern recognition algorithm to classify the ultrasonic signal's origin.

Feature Selection

One of the more critical steps in the implementation of any pattern recognition techniques is the selection of the best features to distinguish the different classes being studied. To aid in feature selection, a theoretical, computer generated model, based on Brekhovskikh's layered media theory [12] was developed to provide a large set of idealized ultrasonic transfer function data for a variety of adhesive bonding situations. These transfer functions provided a means to select the distinguishing features. These features were then compared with the same features from the actual bond specimens to determine their usefulness. Features found promising by other authors [2, 3, 4, 5, 6, 14, 15] were also considered and either incorporated into the algorithm or rejected. The features used were primarily extracted from the transfer function as shown in figure 4, and are described in more detail in reference [16].

Algorithm Development

After the entire set of bond specimens have been ultrasonically inspected and the data stored in the computer, the bond defect prediction algorithm may be developed. A fairly large set of specimens must be used to produce an accurate bond defect prediction scheme. The data set which in this study included 154 bonds was Fourier transformed and the transfer functions were calculated. The data set of features were then separated into two random groups, the training set and the test set. The first set of 64 specimens was used in the Fisher Linear Discriminant [8] function to calculate the optimal coefficients for the linear discriminant function. The same data set is then substituted into the Fisher Linear Discriminant function's equation and the scalar result for each bond specimen is calculated. These scalar results are then correlated with their respective failure loads and a threshold for the good bond-bad bond boundary is derived. The final task is to test the second set of 90 unknown bond specimens with the linear discriminant function so as to determine the bond defect prediction algorithm's reliability. If the reliability is not acceptable, the process must be restarted using improved data acquisition, better signal processing and possibly different features.

RESULTS - ALUMINUM TO ALUMINUM STUDY

Two sources of feature values were considered for this sample problem of adhesive bond defect prediction. First, a more classical technique of selecting features from the Fourier transform frequency spectrum was considered, but this method is dependent on one transducer as described by Rose and Thomas [8]. Their method used Fourier spectrum features in a Fisher Linear Discriminant function to classify adhesively defective bond specimens and was 91% reliable for the design transducer. See figure 5. Any other transducer produced poorer

results. Figure 5 also presents the results from an earlier study conducted by Rose and Thomas [8] to predict "adhesive defects" in aluminum to aluminum, step-lap specimens. This study differed from the present study because the present study includes cohesive defects as well as adhesive defects. A second more desirable technique of directly selecting most of the features from the transfer function of the bond system was considered because of its inherent transducer independence. Both methods of selecting features used the same training set and test set of specimens. Both methods considered a two class problem, good or bad bonds. The bad bonds in this study were either adhesive defects or cohesive defects. The adhesive defects were caused by surface contamination as in the earlier study [8], and the cohesive defects were manufactured by undercuring the adhesive. Features from the earlier study [8] were used to find adhesive problems and new features, determined by a theoretical study, were added to find the cohesive problems.

The first method of selecting features from the Fourier transform provided rather reliable results, but again these results are only good for a single transducer. The training set of specimen's defect was predicted with 97% reliability by the Fourier transform alone. Then the test set reliability dropped to 74% when using only the Fourier transforms for feature value determination (figure 5). In this case, as in the second case, a Fisher Linear Discriminant function was designed to predict the adhesive bond defects.

The second method, using the transfer function provided a 91% reliability for the same 64 bond specimens used in the previous training set. The algorithm was designed to produce an optimal loss function reliability, which in this case was 97%. The loss function analysis concept allows for the incorrect prediction of good bonds, but does not tolerate incorrect prediction of weak bonds. Sometimes adjusting the pattern recognition algorithm to produce best function results decreases the total reliability of the algorithm. A test set of 90 bond specimens was inspected and the transfer function based algorithm provided an 84% reliability, which was better than the Fourier transform based algorithm for the same specimens (see figure 5). Also, the loss function results for this test set using the function approach was 91% reliable.

Preliminary Results for Honeycomb Study

The preliminary results for the Honeycomb specimens are summarized in Fig. 6. Fig. 6 also compares these data with other NDT methods, i.e. Neutron Radiation (NRT), Optical Holography (OH), Ultrasonic: Resonance - Fokker Bond Tester (FBT), Pulse Echo (PE) and Through Transmission (TT). All defects have been detected and differentiated by the combined effort of the NDT methods presented in Fig. 6.

Neutron Radiography Fig. 6a can detect clearly core Unbonds but not Skin Unbonds. Honeycomb defects are detected by NRT but not as clearly as by x rays (RT). 17, 18

Optical Holography can detect clearly all three types of defects presented in Fig. 6b - i.e. Damaged Honeycomb, Skin Unbonds, Core Unbonds and differentiate them clearly from the situation of

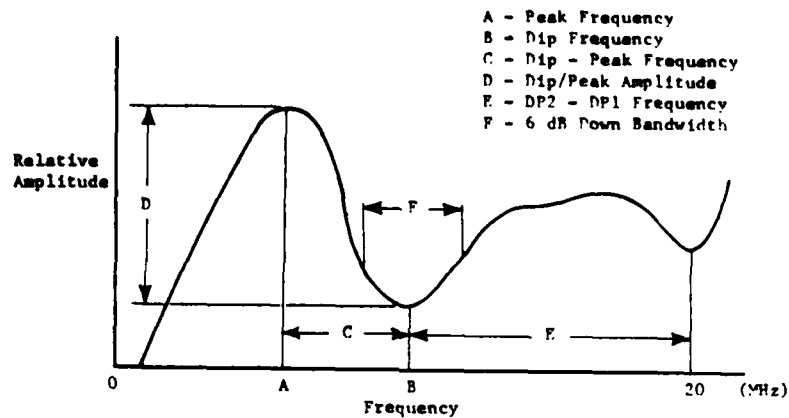


Figure 4. Features Selected from Transfer Function

	Training Set		Test Set	
	Reliability	Loss Function	Reliability	Loss Function
Rose and Thomas Fisher Algorithm (adhesive defect only)	96%	100%	88%	100%
Fisher Algorithm Using Fourier Spectrum Features	97%	100%	74%	87%
Fisher Algorithm Using Transfer Function Features	91%	97%	84%	91%

Figure 5. Sample Problem Results Compared with Results of Previous Adhesive Bond Study

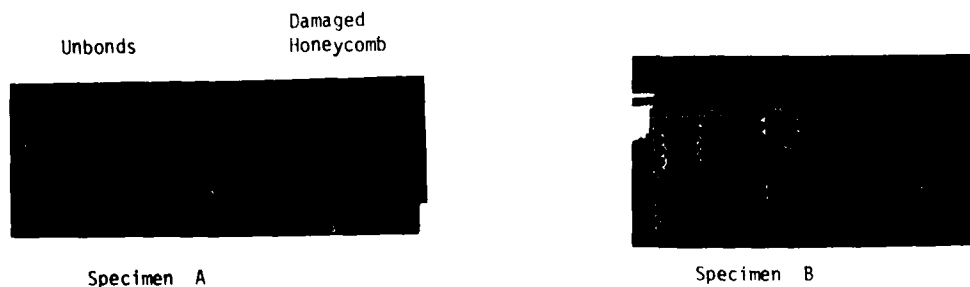


Figure 6a. Neutron Radiographs of Specimens A & B of Fig. 2b.

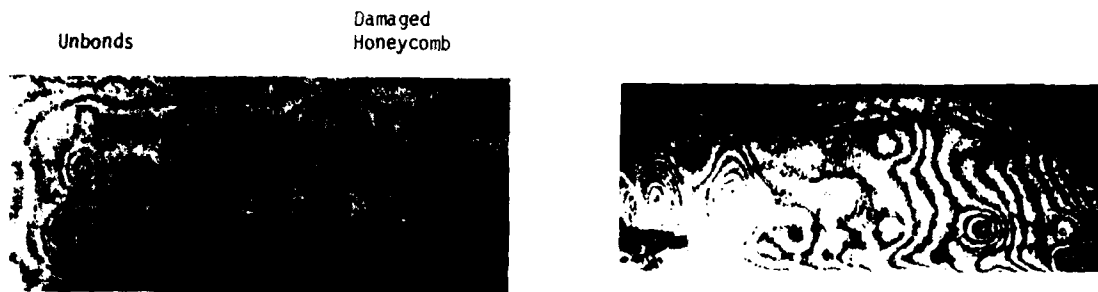
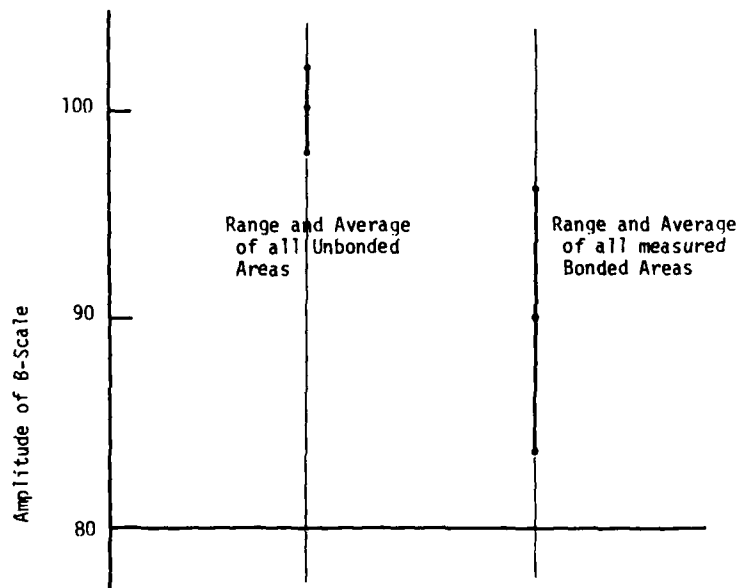


Figure 6b. Optical Holography NDT Results for Specimens A & B of Fig. 2b.



Note: Flaws with less than 0.5 inch diameter were not detected

Figure 6c. Fokker Bond Tester Results of Test Specimen A & B of Fig. 2b Prof. # 1214: Adhesive FM-123-5

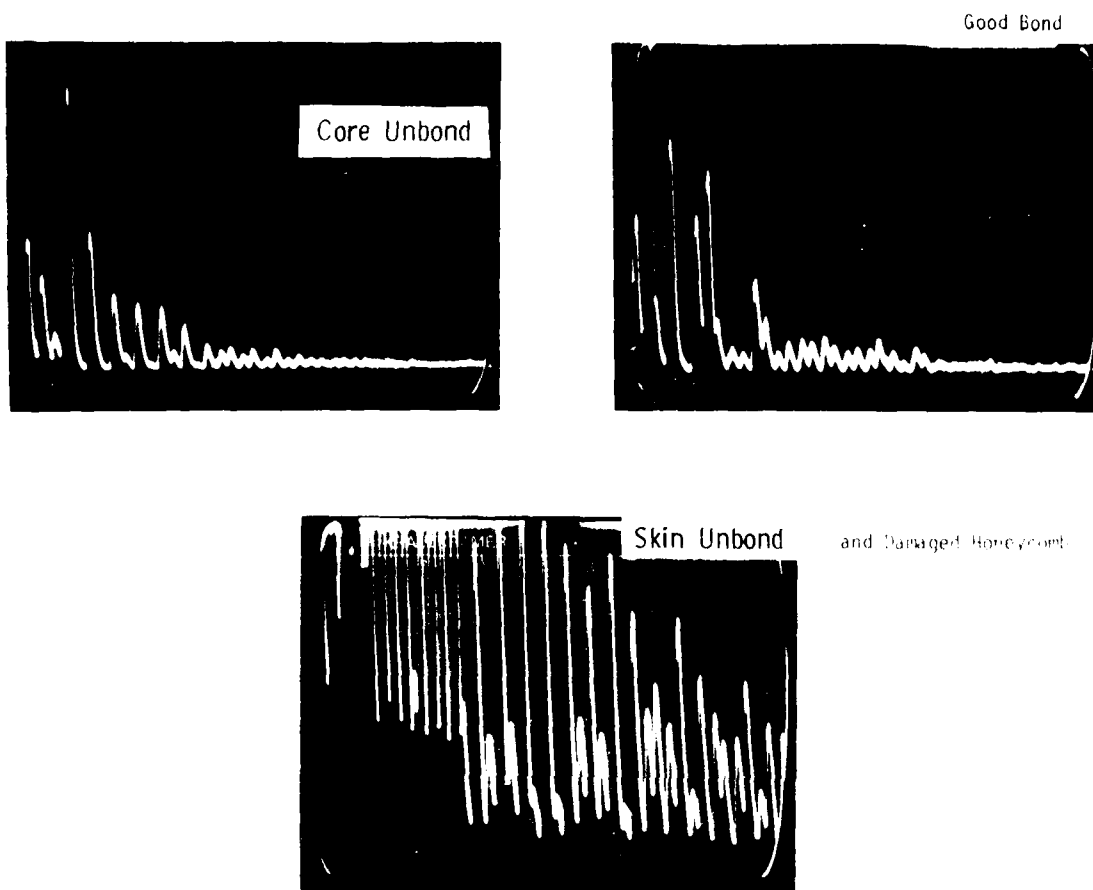


Fig. 6d. Ultrasonic Pulse Echo NDT Results for Specimens A & B of Fig. 2b.

the Good Bond (Fig. 6b). The optical Holography method can not differentiate between the three types of defects.

The specimens of Fig. 2b were bonded with the FM123-5 adhesive. It seems that for this adhesive the Fokker Bond Tester is quite limited as the B-Scale Amplitude for different bonded areas is dispersed and it can hardly differentiate between a situation of Unbond or a Void and a situation of Bonded areas, Fig. 6c.

The UTPE and UTFT together can differentiate between the four situations (good bond, SU, CU, damaged honeycomb). The PE technique can differentiate clearly between the damaged honeycomb and skin unbond on the one hand and Good Bond and Core Unbond on the other hand. But it does not differentiate clearly between good bond and CU or between damaged honeycomb and SU (Fig. 6d). The Through Transmission can differentiate clearly between damaged honeycomb and Skin Unbond and between good bond and Core Unbond. But it does not differentiate clearly between SU and CU, (Fig. 6e).

We see that the Ultrasonic test method has the full potential to detect and differentiate between the different types of defects. A detailed study of the different parameters of the Ultrasonic signal may detect and classify the defects in an honeycomb structure by a single measurement. Commercial interests prefer the PE technique as this technique needs access to only one surface and is more economical than the through transmission technique. The new sophisticated technique may in the future predict a sub-standard bond strength in a honeycomb structure.

CONCLUSIONS

A major concern of the adhesive bonding industry has been the nondestructive evaluation of the bond layer in an assembled structure. This study has produced a computer augmented, ultrasonic test bed system which is designed to attack and solve problems in classifying adhesive bonding defects. The types of problems considered are not the gross flaws such as delaminations or debonds by the more subtle defects such as improper surface preparation and adhesive under-cure. State of the art ultras-

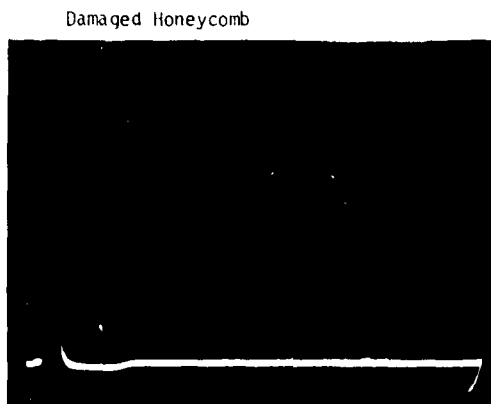
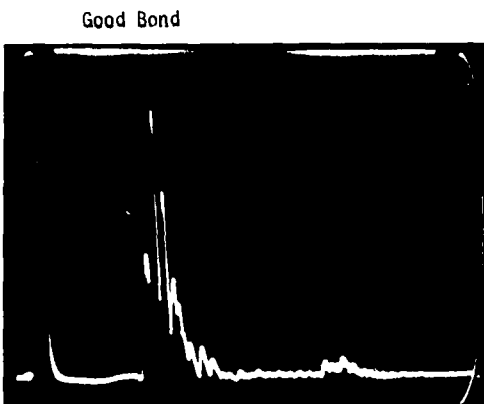
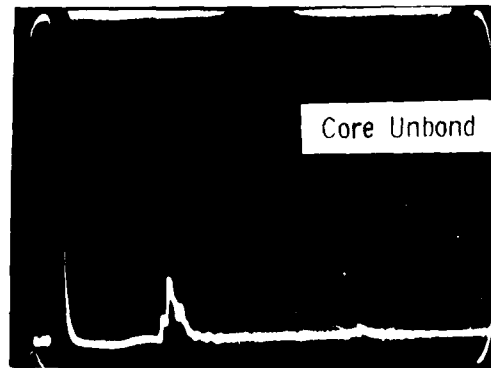
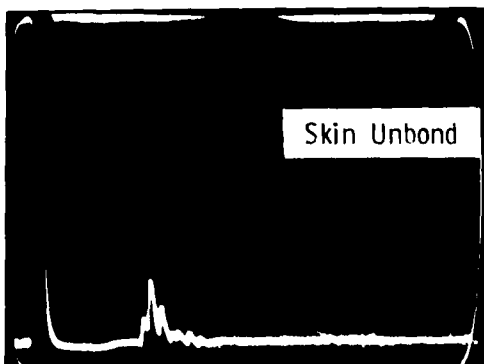


Figure 6e. Ultrasonic Through Transmission NDT Results for Specimens A & B of Fig. 2b.

sonic data acquisition procedures, sophisticated signal processing and feature extraction methods, and advanced pattern recognition techniques are incorporated in the test bed system.

A sample problem of identifying improper surface preparation or adhesive under-cure in aluminum to aluminum step-lap joints has been solved using the ultrasonic test bed system. An overall reliability of 91% has been achieved for this classification problem. The success of this sample problem clearly indicates the potential of the ultrasonic test bed to solve many of the adhesive bonding inspection problems plaguing the industry today.

REFERENCES

- [1] Raisch, J.W. and Rose, J.L., "Computer Controlled Ultrasonic Adhesive Bond Evaluation," (presented at the Fall meeting of ASNT, Detroit, October 6, 1977), Materials Evaluation, pp. 55-64, May 1979.
- [2] Flynn, Paul L., "Cohesive Strength Prediction of Adhesive Joints," General Dynamics/Fort Worth, Project II, Unit I, Task 3.
- [3] Chang, F.H., Kline, R.A., and Bell, J.R., "Ultrasonic Evaluation of Adhesive Bond Strength Using Spectroscopic Techniques," presented at ARPA/AFML Conference in La Jolla, California, July 1978.
- [4] Couchman, J.C., Yee, B.G.W., and Chang, F.H., "Adhesive Bond Strength Classifier," Materials Evaluation, pp. 48-50, April 1979.
- [5] Alers, G.A., Elsley, R.K., Richardson, J.M., and Fertig, K., "Ultrasonic Measurement of Interfacial Properties In Completed Adhesive Bonds," presented at the ARPA/AFML Conference in La Jolla, California, July 1978.
- [6] Alers, G.A., and Elsley, R.K., "Ultrasonic Measurement of Adhesive Bond Strength," Rockwell Science Center Report No. SC595. 32SA, Project III, Unit A, Task I.
- [7] Mucciardi, A.N., and Elsley, R.K., "Characterization of Defects in Adhesive Bonds by Adaptive Learning Networks," presented at the ARPA/AFML Conference in La Jolla, California, July 1978.

- [8] Rose, J.L., and Thomas, G.H., "The Fisher Linear Discriminant Function for Adhesive Bond Strength Prediction," to be published in the British Journal of Nondestructive Testing, 1979.
- [9] Thomas, G.H., and Rose, J.L., "A Generalized Adhesive Bond Strength Prediction Algorithm Based on Ultrasonic Signal Analysis," Ninth World Conference on Nondestructive Testing, November, 1979, Australia.
- [10] Rose, J.L., and Avioli, M.J., "Transducer Compensation Concepts of Value in Flaw Classification," presented at the Spring ASNT Conference, New Orleans, 1978, and to be published in a reliability supplement to Materials Engineering.
- [11] Brekhovskikh, L.M., Waves in Layered Media, Academic Press, New York, 1960.
- [12] Rose, J.L., and Avioli, M.J., "Generalized Approach to New Problems in Ultrasonic Inspection," Naval Air Engineering Center report February 12, 1979.
- [13] Erdogen, F. and Ratwani, M., "Stress Distribution in Bonded Joints," Journal of Composite Materials, Vol. 5, July 1971, p. 378.
- [14] Chang, F.H., Flynn, P.L., Gordon, D.E., and Bell, J.R., "Principles and Applications of Ultrasonic Spectroscopy in NDE of Adhesive Bonds," IEEE Transactions on Sonics and Ultrasonics, Vol. SU-23, No. 5, September 1976.
- [15] Flynn, P.L., and Henslee, S.P., "Cohesive Bond Strength Prediction," Rockwell Science Center Report No. SC595.32SA, Project III, Unit A, Task 3.
- [16] Anderson, G.P., Bennett, S.J., and Devries, K.L., Analysis and Testing of Adhesive Bonds, Academic Press, New York, 1977.
- [17] Segal, E., and Rose, J.L., NDT Techniques of Adhesive Bonded Joints, to be published in Research Techniques in NDT, Vol. IV, R.S. Sharpe Ed. Academic Press.
- [18] Segal, E., Thomas, G., and Rose, J.L., 12th Symposium on NDE San Antonio, Texas, April 24-26, 1979.

NONDESTRUCTIVE EVALUATION OF FLAW CRITICALITY
IN GRAPHITE-EPOXY LAMINATES

S.N. Chatterjee and Z. Hashin
Materials Sciences Corporation, Blue Bell, PA 19422

R.B. Pipes
University of Delaware, Newark, DE 19711

ABSTRACT

An analytical and experimental study is conducted to determine criticality of inter-laminar disbonds by NDE methods. Criticality of such flaws in a shear environment (action of shear near support) is defined in terms of crack propagation and is analyzed by principles and methods of fracture mechanics. Growth of disbonds under cyclic loading is also being studied. Failure under compressive loading in presence of a disbond is defined in terms of buckling and an elastic stability analysis is utilized for assessing criticality. Analytical predictions are compared with experimental results in both cases.

INTRODUCTION

Various kinds of defects can cause relevant strength and stiffness degradation in composite laminates, namely, (i) inter-laminar disbonds, (ii) through-the-thickness defects, (iii) defects in bolted and bonded joints, (iv) impact damage, (v) fatigue damage. Different NDI techniques (active and passive), which are usually used for studying effects of such defects, are listed below:

- (i) Ultrasonics (modulus degradation measurement and damage detection)
- (ii) Acoustic emission (sequential recording of the damage growth process)
- (iii) X-ray and thermography (visual and real-time detection of defect growth)
- (iv) Structural vibrations (stiffness degradation measurement)
- (v) Penetrants
- (vi) Holography

This work is mainly directed towards use of ultrasonics for detection and following growth of interlaminar disbonds. Attempts are also being made to use measurements from wave propagation studies for estimating possible modulus degradation due to damages induced by fatigue and moisture conditioning. Analytical studies are aimed at:

- (i) definition of required NDI observations,
 - (ii) model physically realistic damage modes
 - (iii) assess property, degradation, and flaw criticality, and
 - (iv) translation of results from test systems to real world composite structures.
- Mechanical testings are conducted to relate observed state of magnitude and geometry of damage and/or degradation to estimate residual performance capability. Correlations of data from NDI, mechanical tests and analyses are carried out to demonstrate feasibility of using fundamental approach at laminate level for development of quantitative NDE of flaw severity in composites.

CRACK PROPAGATION IN SHEAR ENVIRONMENT

Analytical methodology for stress analysis of a laminated beam containing two symmetrically located disbonds as shown in Figure 1 has been developed. The mixed boundary value problem of anisotropic elasticity has been reduced to the solution of a coupled pair of singular integral equations. This method of reduction has been computerized. For numerical solutions these equations are converted to a discretized system. Evaluation of the unknown functions appearing in these equations yields the stress intensity factors and strain energy release rates. Methods of analysis are based on principles and mathematical techniques commonly used in crack problems of linear elastic homogeneous media. Details of the methods are omitted here for brevity, but can be found in [1].

BUCKLING FAILURE UNDER COMPRESSION

Buckling failures under compression near disbonds can be expected in different types of structural configurations. One example is a sandwich construction under flexure with a disbond in the compression flange (Figure 2a). For stability analysis the delaminated compression flange is modeled as a system of four interconnected beams (Figure 2b). Beams 3 and 4 are considered as semi-infinite beams. Beams 2, 3 and 4 are supported on an elastic foundation which can carry extensional and shear loads. The foundation elastic moduli (spring constants) are calculated from the properties of the sandwich construction. All beams are analyzed with laminated beam theory including the effects of shear deformations and prestresses.

A stiffness formulation is employed and the critical value of prestress needed to cause buckling (instability in beam 1 is usually critical) is calculated by solving the resulting eigenvalue problem by a trial and error procedure.

THICK LAMINATE BEAMS WITH IMPLANTED DEFECTS

Graphite-epoxy thick beam laminates with implanted defects of various geometries were fabricated using AS3501-6 prepreg material. The fiber orientation of the 10" long beams was $[(0/90)_6]_2$ and the defect geometries were of square, diamond and "hourglass" shapes. The square defects were fabricated by welding .001" thick teflon film into a tube. The seam in the tube was put in the center of the defect so that the edges of the defect have the same radius of curvature. The diamond and "hourglass" shaped defects were fabricated by shearing two layers of teflon film against an abrasive surface in a manner which causes the two layers of teflon to remain together after shearing. The defects were implanted between the center plies of the laminate at the quarter-span position of the beams.

Ultrasonic C-scans were made of all laminates before and after machining. All beams are precracked prior to testing in order to obtain a sharp crack front. The method used to precrack the beams is to subject the beams to three point bending with clamps placed at the boundaries of the defects. The clamps are used only during the precracking operation to prohibit the defects from propagating completely through the beam. Attempts to precrack the 0.6" rectangular defects and the "hourglass" defects resulted in laminate flexure failure. Attempts to precrack the 1.0" rectangular defects were partially successful. C-scans of these specimens after precracking are shown in Figure 3. Beam No. 12 is the only specimen which exhibited the desired degree of precracking. Figure 4 shows the results of precracking the diamond defect beams. Precracking of these beams occurs at a load of approximately 400 kg as compared with 600 kg for the 1" rectangular defect beams. The results of precracking the diamond defect beams are the most satisfactory. After precracking, three beams with diamond defects and three beams with 1.0" rectangular defects were loaded to failure which occurred due to catastrophic growth of disbands. Figure 5 shows a magnified view of the interlaminar defects. Figure 6 depicts the growth pattern of such flaws under cyclic loading [2].

COMPOSITE SANDWICH BEAM WITH IMPLANTED DEFECTS

Test specimens are sandwich beam construction consisting of graphite-epoxy laminate adhesively bonded to an aluminum honeycomb core. The graphite epoxy system is AS-3501-6 CF. Two 23" panels were fabricated in the following configurations, where D denotes the disbond.

$[0/+45/\pm 45/0/D/0/\mp 45/\mp 45/0];$
 $[0/+45/+45/0/0/\mp 45/D/\mp 45/0]$

Disbands were fabricated from 0.001 inch teflon film. The disbond lengths (L) were 0.5", 1.0", 1.5". Disbond strips were implanted in the laminates on the longitudinal mid-plane at the aforementioned

locations in the laminate. The laminates were cured and subjected to ultrasonic C-scan to locate the exact position of the disbands. Next the laminates were bonded to a 24 lb/ft³ aluminum honeycomb (Hexel Corp.). American Cyanamid's FM-300/BR 127 sheet adhesive system was the bonding agent. The laminate with the near surface disbands was oriented so that the disbands were farthest from the laminate-honeycomb interface. The laminate-adhesive-honeycomb system was cured together in an autoclave. Specimens of 1.0" width and 22.0" length were cut using a rotary diamond saw (figure 7). The beams were instrumented with two strain gages (one on each laminate surface) located at midspan parallel to the beam longitudinal axis. The specimens were tested in a tension-compression load frame employing a four point bending fixture with spans of four and 20" (see Figure 8). A strain rate of .05/ins/in/min was applied to the beams.

The strain from the compressive face of the beam was plotted on the X-axis and tensile strain on the Y-axis using an X-Y recorder. Load levels at which variations from linearity occurred were noted. (Table 1)

The laminates with 0.5" disbands may have exhibited a catastrophic buckling instability. The tensile and compressive strain increased linearly until failure occurred. The 1.0" specimens with disbands at the laminate mid-plane exhibited the same type of behavior except the buckling of the laminate occurred in a stable manner which was shown by the abrupt change from linear to nonlinear behavior. The specimens with 1.5" mid-plane disbands exhibited the same gradual nonlinear response from the onset of loading followed by a quasi linear response. The initial compressive strain of the tensile face laminate was due to the initial out of plane deformation due to residual thermal stresses. The 1.5" near surface disbands were prebuckled to such an extent that the initial tensile strain on the compressive face continued to increase throughout the test. The buckling failure mode is illustrated in a photograph (Figure 9).

CORRELATION STUDIES

Correlation of experimental results for growth of delaminations in precracked $[(0/90)_6]_2$ laminated beams with defects located in mid-plane under static loading is given in table 2. Results from past studies on a different laminate (not precracked) reported in [2] are also shown in this table. The critical values of strain energy release rate from two sets of data reported in table 2 are of the same order and show the same amount of scatter. It appears, therefore, that precracking does not have any significant influence on crack propagation.

Experimental results from honeycomb sandwich beam tests, reported in table 1, are compared in figure 10 with the analytical predictions. The results agree well with one another over a wide range of

disbond length.

MODULUS DEGRADATION DUE TO MOISTURE AND FATIGUE DAMAGE

Wave propagation studies on neat resin and $(+45)_2s$ coupons are being conducted to measure effects of conditioning on storage and loss moduli. The objective is to determine the possibility of using ultrasonic techniques for assessing magnitude and criticality of damages caused by such conditioning.

Sample No.	Defect Size (In.)	Location in Laminate	Buckling Load (Lb.)
1T	1/2	Center	1345
10B	1/2	"	1477
3T	1	"	522
7B	1	"	661
12T	1	"	584
8B	1	"	661
6T	1.5	"	295
5T	1.5	"	309
11T	1.5	"	293
9B	1.5	"	364
3B	1	Near Surface	22
12B	1	"	22
7T	1	"	49
8T	1	"	29

ACKNOWLEDGEMENTS

This work is being performed under NADC contract N62269-78-C-0111-Dr. William Scott, Contract Monitor.

REFERENCES

- Chatterjee, S.N., "On Interlaminar Defects in Laminated Composites," to be presented at the Winter Annual Meeting of ASME to be held December 2-7, 1979 New York.
- Ramkumar, R.L., Kulkarni, S.V. and Pipes, R.B., "Definition and Modelling of Critical Flaws in Graphite Fiber Reinforced Composites," NADC-76228-30, January 1978.

Laminate	Specimen	G_c (lb/in)
$[(0/+45_2/$	1-1	5.63
	1-2	6.34
	1-3	2.94
	1-4	3.74
	Avg.	4.66
$0_{12}]_s$	1-1	4.37
	1-3	6.53
	1-6	5.02
	D-2	5.23
	D-5	4.14
	D-3	2.93
	Avg.	4.70

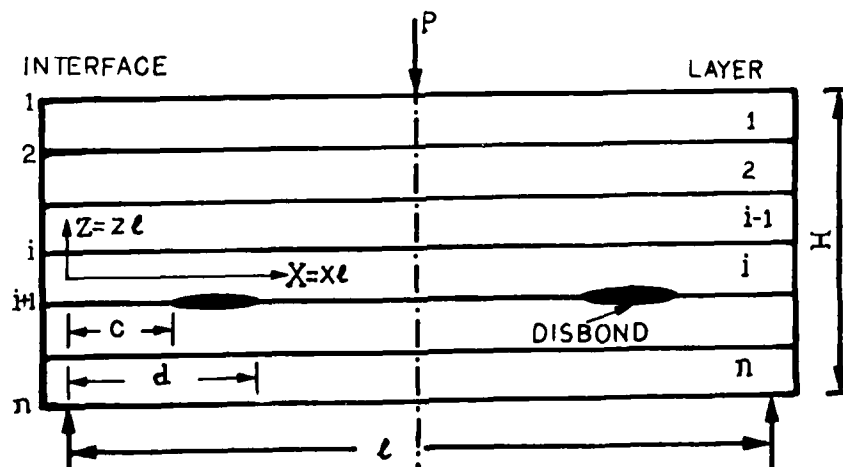


FIG. 1. LAMINATED BEAM CONTAINING DISBONDS

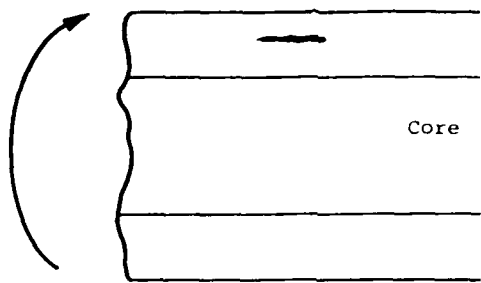


FIG. 2A. SANDWICH BEAM

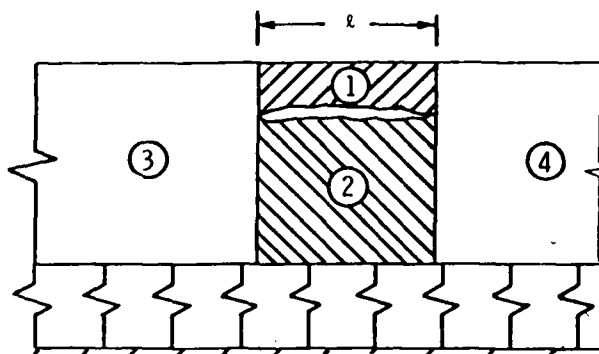


FIG. 2B. INTERCONNECTED BEAM SYSTEM

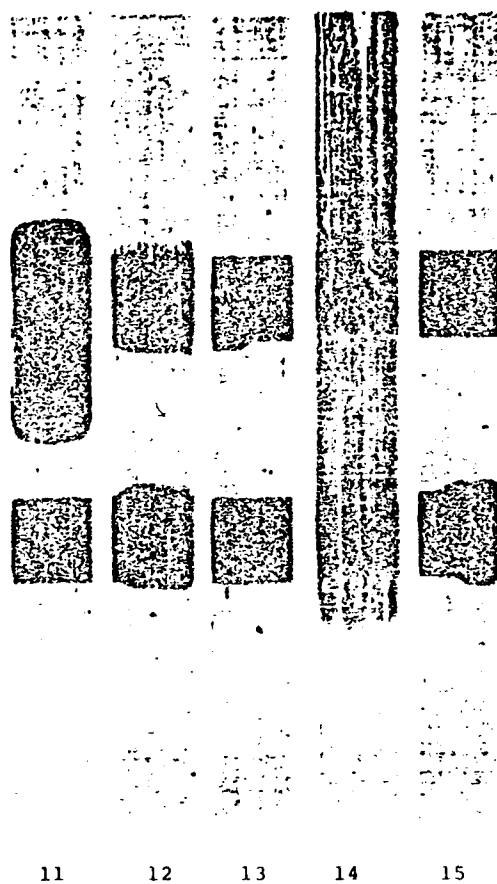


FIG. 3. PRECRACKING SQUARE DEFECTS

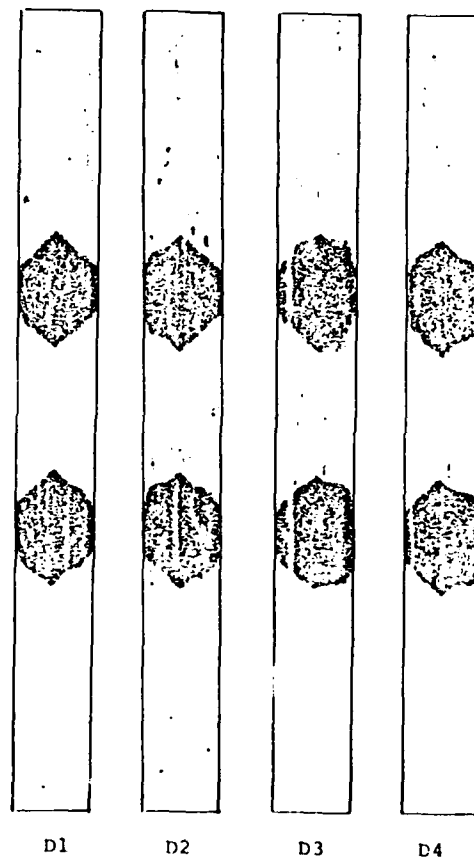


FIG. 4. C SCAN OF DIAMOND DEFECTS



FIG. 5. MAGNIFIED VIEW OF INTERLAMINAR DEFECTS

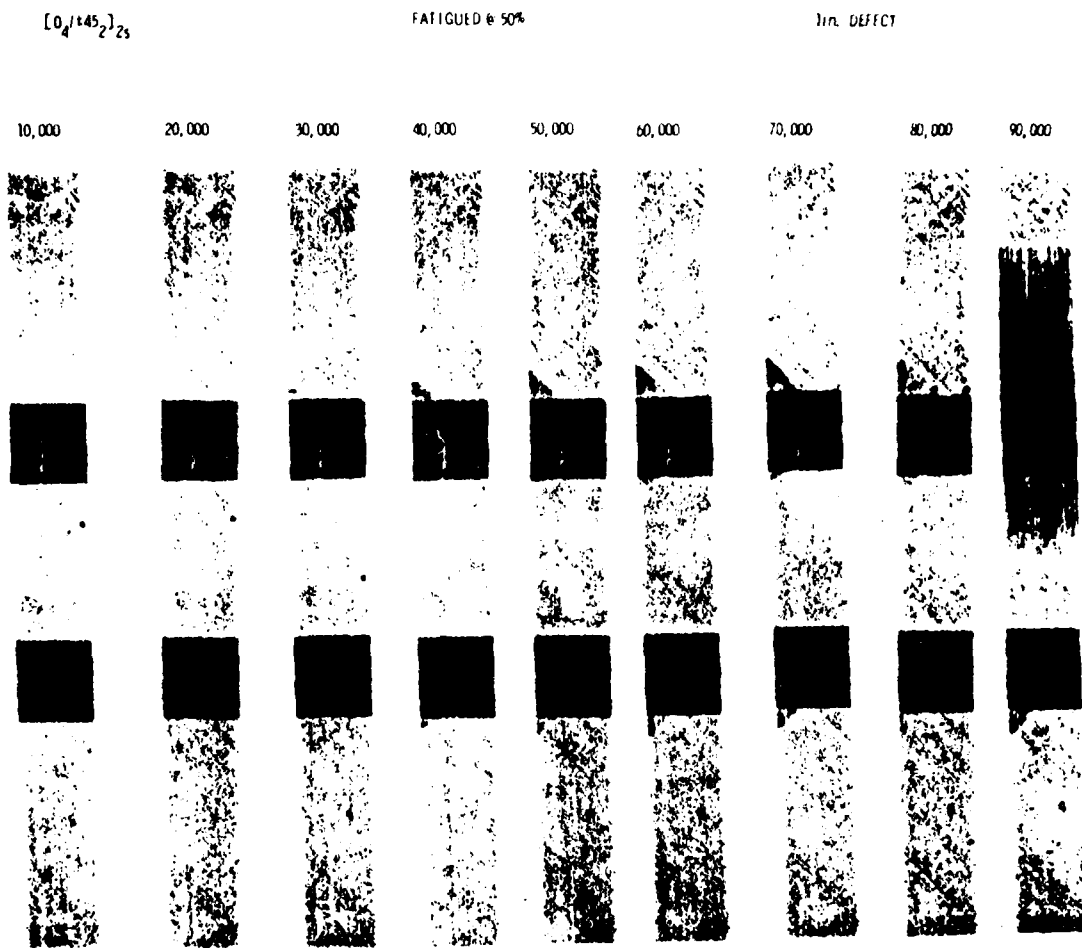


FIG. 6. GROWTH OF DELAMINATION WITH FATIGUE CYCLING

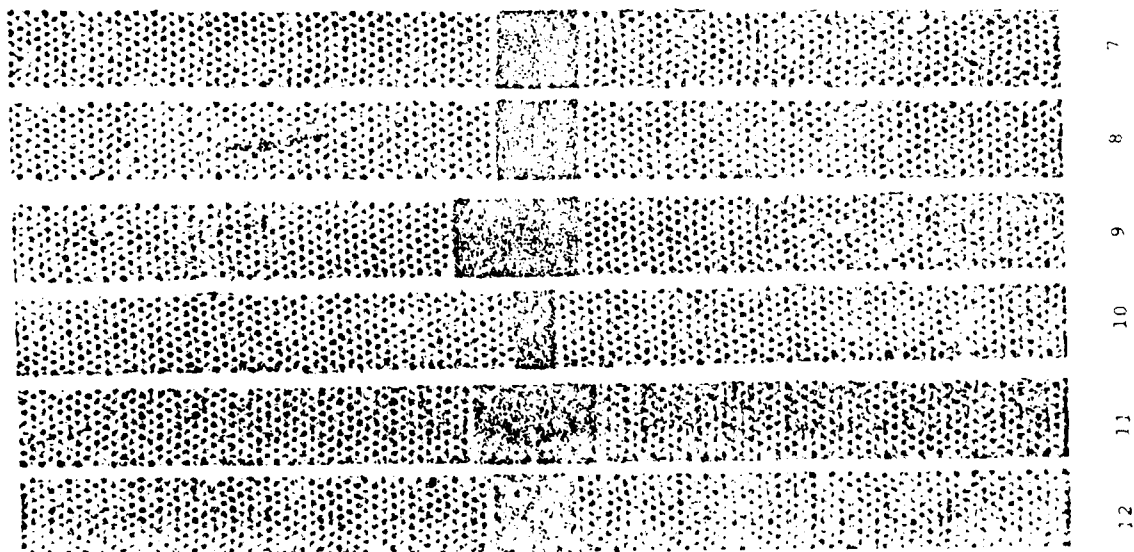


FIG. 7. C SCAN OF SANDWICH BEAM SPECIMENS

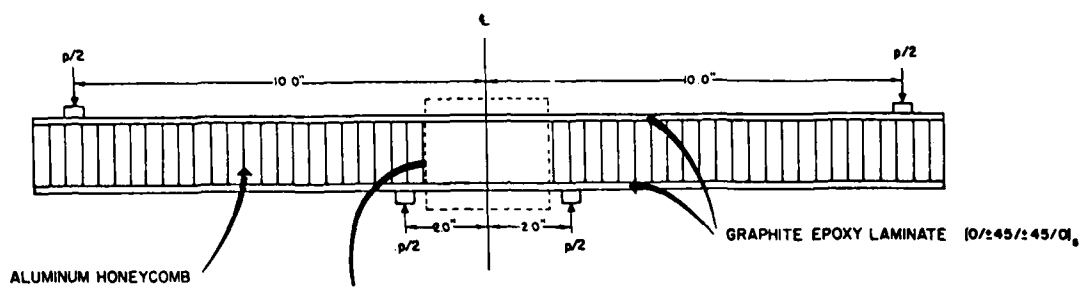


FIG. 8. TEST ON SANDWICH BEAM WITH DISBOND

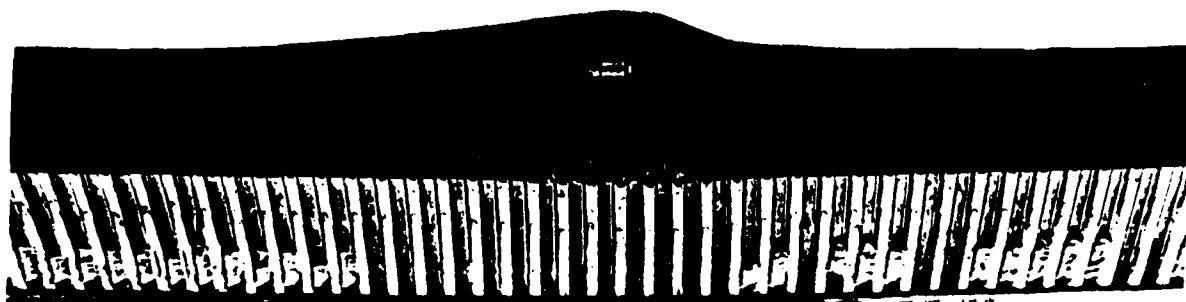


FIG. 9. FAILURE OF COMPRESSION SKIN

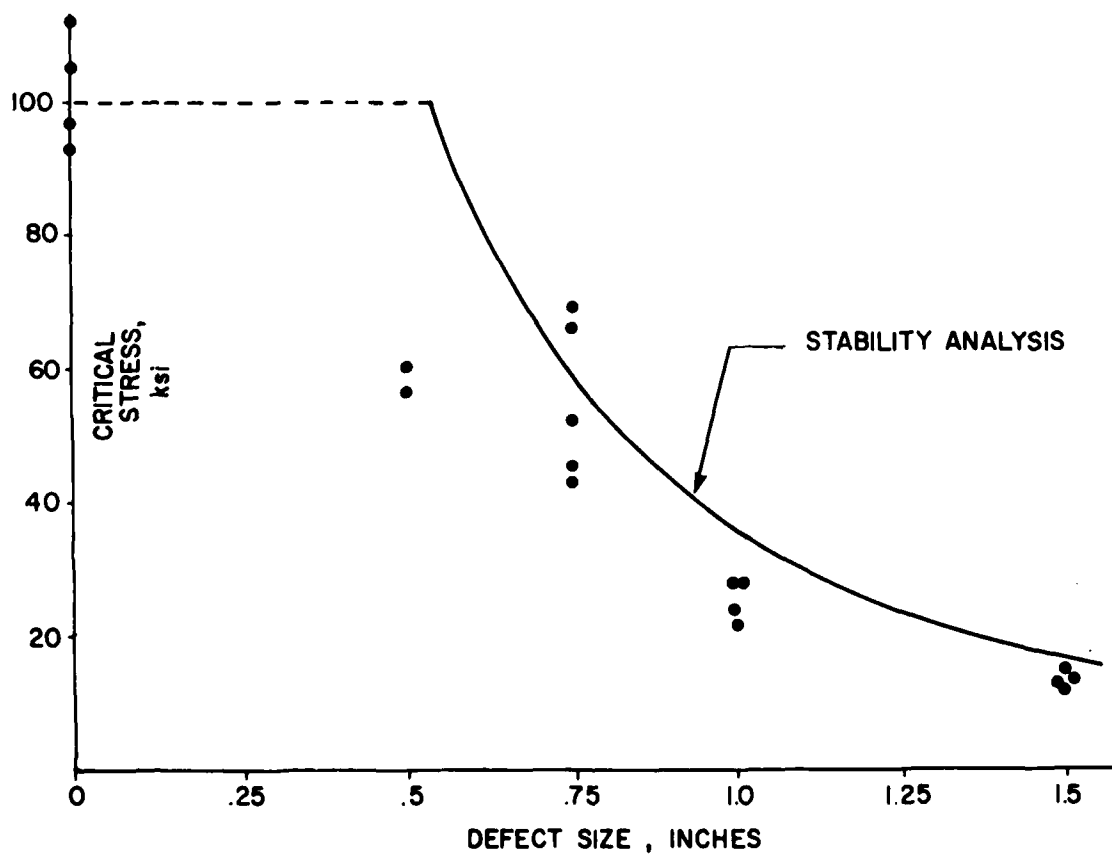


FIG. 10. CRITICAL STRESS VS. DEFECT SIZE

X-RAY STRESS MEASUREMENT IN GRAPHITE/EPOXY COMPOSITES

P. Predecki and C. S. Barrett
University of Denver Research Institute
Denver, CO 80208

ABSTRACT

Small amounts ($< 2 \text{ mg/cm}^2$) of Al and Nb filler powders were incorporated between the first and second plies of 6-ply unidirectional graphite/epoxy laminates. Cu $K\alpha_1$ X-rays were diffracted from specific crystallographic planes in these fillers: 333 + 511 for Al and 411 + 330 for Nb, giving peaks in the back reflection region. The peak positions shifted linearly with stress applied to the laminates in the fiber direction and had stress sensitivities of 8.52 and $3.92 \times 10^{-4} \text{ deg } 2\theta/\text{MPa}$ for Al and Nb respectively. Elastic strains in the filler particles measured by X-rays were found to be proportional to the corresponding composite strains measured by strain gages, in agreement with the model of H. T. Bawn. Residual strains and stresses in filler particles were also measured.

INTRODUCTION

It has recently been shown that information about residual and applied stresses in non-crystalline polymeric materials including polymer matrix composites can be obtained by X-ray diffraction from small amounts of crystalline fillers incorporated into the polymer.⁽¹⁻³⁾ The method has the advantage that the filler particles can be placed at varying depths below the sample surface and can be chosen so as to give sharp, well-resolved diffraction peaks at large diffraction angles. The disadvantage is that relations must be established between the principal elastic strains measured in the filler particles and the stresses in the composite. Thus far these relations have been found to be linear with several fillers at stresses below the yield point of the filler particles. We present here experimental evidence for such linear behavior using two metallic fillers; Al and Nb having promising properties for technological applications.

EXPERIMENTAL PROCEDURE

Al and Nb metal powders of -325 mesh were spread in a thin layer ($< 2 \text{ mg/cm}^2$) between the first and second plies of uncured 6 ply unidirectional graphite/epoxy laminates (Fiberite T-300/934, Fiberite Corp., Winona, Minn.). The Nb powder (Fansteel Corp., No. Chicago, Ill.) was vacuum annealed 1 hr at 1300°C to sharpen the X-ray peaks prior to use. Spreading of the powders was done as uniformly as possible by rubbing the powders onto the surface of one prepreg ply and shaking off particles which did not adhere. The laminates were laid up in $7.62 \times 30.48 \text{ cm}$ stacks and cured using the recommended procedures for this prepreg. SEM and energy dispersive X-ray analysis of cross-sections of cured laminates showed that transverse migration of filler particles into adjacent plies during curing was negligible.

Longitudinal tensile samples $15.25 \times 1.905 \times .089 \text{ cm}$ thick were cut from the cured laminates, tapered aluminum (2014-T6) end-tabs were applied and a strain gage (2 element, 90° stacked) attached near the center of the gage area of each sample. Samples were held in clevis grips in a small tensile frame mounted on a Siemens diffractometer as described elsewhere.⁽²⁾

The principle of the method is shown in Fig. 1. X-radiation is incident on the laminate sample near

the strain gage. Cu $K\alpha_1$ X-rays diffracted by specific crystallographic planes in the filler particles (333 + 511 for Al and 411 + 330 for Nb) pass through a monochromator into a detector. Strain in the particles appears as a shift in the diffracted peak positions as required by the Bragg law.

Diffracted peak positions were determined using a standard procedure.⁽⁴⁾ The upper $1/3-1/4$ of each peak was step-scanned and a parabola fitted to the points by least squares. The apex of the parabola was taken as the peak position. The direction of strain measurement in the diffraction method is defined by the angles ϕ and ψ relative to the laminate axes 1, 2, 3 (Fig. 1). The three principal filler particle strains, assumed parallel to the laminate axes, are readily obtained from peak position measurements using 3 different incident beam directions and the peak position for an unstressed powder sample of the filler. Equations for calculating the filler strains were presented elsewhere.⁽⁵⁾ For the present applied stress experiments, only two directions of strain measurement were needed: $\phi=\psi=0$ and $\phi=0, \psi=45^\circ$. For residual stresses, the direction $\phi = 90^\circ, \psi = 45^\circ$ was added.

RESULTS AND DISCUSSION

Applied Stresses - The shift in the diffraction angle, 2θ at $\phi=\psi=0$ with applied tensile stress σ_1^* in the fiber direction is shown in Figs. 2 and 3 for laminates containing Al and Nb respectively. The breaks in these curves at 150 and 650 MPa respectively on the first loading are thought to be due to yielding in the filler particles. If the samples are loaded above these filler yield points, then on release of the load the 2θ values are lower than before the first loading (Figs. 2 and 3) indicating that a compressive strain contribution remains after unloading. Possible reasons for this contribution are that the surrounding matrix is compressing the yielded particles in the fiber direction on unloading or that pseudo macrostresses are present in the particles themselves, resulting from the plastic deformation.⁽⁶⁾ The slopes of the lines below the yield point in Figs. 2 and 3 are termed the stress sensitivities, S , of the filler and are listed in Table I.

The mean filler strains in the fiber direction ϵ_{ff} and normal to the laminate ϵ_{nf} were calculated from the X-ray peak shifts below the yield point for the second loading. The results are shown in Figs.

TABLE I
Stress Sensitivities and Hahn Factors of Fillers

Filler and Loading Cycle	$(d\epsilon_{1f}/d\sigma_1^*)/(d\epsilon_1^*/d\sigma_1^*)$ (MPa) ⁻¹	η_1	E_f (10 ⁵ MPa)	ν_f	E_{11}^* (10 ⁵ MPa)	$S(10^{-4} \text{ deg } 2\theta/\text{MPa})$	
						Experiment	Theory (Eq. 3)
Al							
1st loading	---	---	.7034	.347	1.06	8.39	---
2nd loading	.267	.184	.7034	.347	1.06	8.65	6.54
Nb							
1st loading	---	---	1.035	.38	1.20	4.12	---
2nd loading	.154	.22	1.035	.38	1.20	3.72	3.50

E_f and ν_f data for Al from ref. (4), for Nb from ASM Metals Handbook, 8th ed., 1961, Vol. 1, p. 1202.

4 and 5 for Al and Nb respectively. Longitudinal and transverse strain gage strains ϵ_1^* and ϵ_2^* divided by ten are shown for comparison. The data fall on straight lines within experimental error. The ratios of the slopes; $(d\epsilon_{1f}/d\sigma_1^*)/(d\epsilon_1^*/d\sigma_1^*)$ in these figures are given in Table I.

It has been proposed by Hahn⁽⁷⁾ that in a particulate composite the mean matrix stress, $\bar{\sigma}_{im}$ is simply proportional to the mean filler stress σ_{1f} with a proportionality constant. For the isotropic case,

$$\bar{\sigma}_{im} = \eta_1 \sigma_{1f}, \quad \eta_1 = 1-6 \quad (1)$$

For a unidirectional composite, if $\bar{\sigma}_{im}$ and σ_{1f} are the only non-zero stress components; it has been shown⁽⁸⁾ that at small volume fractions of filler, the Hahn factor

$$\eta_1 = \frac{\epsilon_1^*}{\epsilon_{1f}^*} \frac{E_m}{E_f} \quad (2)$$

where E_m is the Young's modulus of the matrix, taken as 3.45×10^3 MPa (0.5×10^6 psi) and E_f is the Young's modulus of the filler. Values of η_1 calculated from eq. (2) using the ratio of slopes in Table I are given in Table I. Knowing η_1 and assuming that σ_1^* is the only non-zero stress, an expression for the stress sensitivity, S , can be derived.⁽²⁾

$$S = \frac{[2\theta]_{\phi=\psi=0}}{\epsilon_1^*} = \frac{2}{E_f} \frac{\nu_f}{\eta_1} \frac{E_m}{E_{11}^*} \cdot \tan[\theta]_{\phi=\psi=0} \text{ (rad/MPa)} \quad (3)$$

Values of S calculated from eq. (3) and obtained from the data in Figs. 2 and 3 are compared in Table I. The agreement is reasonable in view of the assumptions required for eq. (3). Equation (3) also predicts approximately a constant slope for the lines in Figs. 2 and 3 below the yield point, as observed. Desirable filler properties for high stress sensitivity are obviously a diffusion peak at large θ and a small filler modulus and Hahn factor. Al and Nb possess the highest S values of candidate fillers tested to date with $\text{CuK}\alpha_1$ radiation.

Residual Stresses - The principal residual strains

in the filler particles in cured laminates after 1/2 yr storage under ambient conditions are listed in Table II. The principal stresses in the fillers calculated from the strains assuming isotropic filler properties are also shown. The standard deviations in residual filler stresses obtained from duplicate measurements were ± 5.7 MPa for Al and ± 4.7 MPa for Nb. The larger standard deviation with the Nb filler is due to the larger particle size and fewer particles of the Nb powder used which resulted in a more non-uniform distribution of diffracting particles in the irradiated area and a greater standard deviation in 2θ measurements than with Al.

TABLE II

Residual Strains and Stresses in Filler Particles in Unidirectional Laminates

Filler	Microstrains			Stresses (MPa)		
	ϵ_1	ϵ_2	ϵ_3	σ_1	σ_2	σ_3
Al	439	-56	-218	27	3.5	-4.2
Nb	573	-307	-286	40.6	-25.4	-23.8

The values in Table II require experiments with fillers in neat resin before their significance can be fully assessed; however, they all show the same trend. The stresses and strains in the fiber direction are algebraically the largest, indicating a residual tensile stress in the resin in this direction. The remaining two stresses are significantly smaller and not greatly different from zero. They result from differences in Poisson contraction and thermal expansion coefficient between the resin and the filler.

S^2

ACKNOWLEDGEMENTS

The samples were kindly fabricated for us at the Martin-Marietta Co. Denver Division by J. Lager, B. Burke and R. Campbell. The research was supported by the Air Force Office of Scientific Research grant # 77-3284.

REFERENCES

1. Charles S. Barrett and Paul Predecki. Polymer Eng. and Sci. 16, 602 (1976).
2. Paul Predecki and Charles S. Barrett. J. Composite Matls. 13, 61 (1979).
3. Charles S. Barrett and Paul Predecki. Submitted to Polymer Eng. and Sci.
4. Soc. Automotive Engineers Information Report SAW J784a (1971).
5. C. S. Barrett and P. K. Predecki in "Advances in X-Ray Analysis," Vol. 21, p. 305, Plenum Publ. Corp. N.Y. (1978).
6. B. D. Cullity, "Advances in X-Ray Analysis," Vol. 20, p. 259, Plenum Publishing Co. N.Y. (1977).
7. H. T. Hahn in "Composite Materials Workbook," AFML -TR-78-33 p. 65, March 1978.

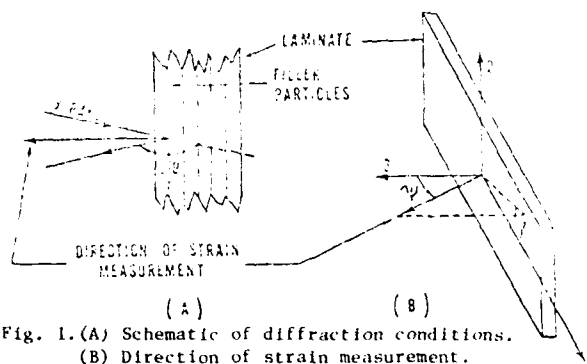


Fig. 1. (A) Schematic of diffraction conditions. (B) Direction of strain measurement.

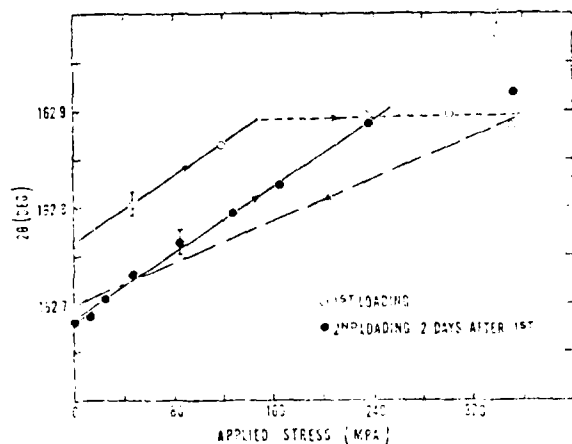


Fig. 2. Linear increase in 333+511 X-ray peak position with tensile stress applied in fiber direction of a 0° laminate containing Al particles. ($\phi = \psi = 0$, $\text{CuK}\alpha_1$ radiation). Error bars in this and subsequent figures are \pm one standard deviation.

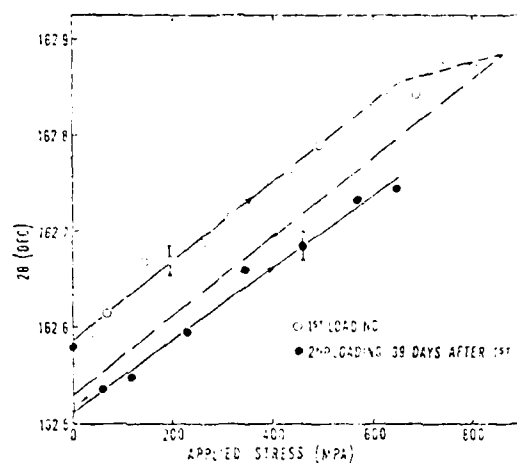


Fig. 3. Linear increase in 411+330 X-ray peak position with applied tensile stress in a 0° laminate containing Nb particles. Conditions are similar to Fig. 2.

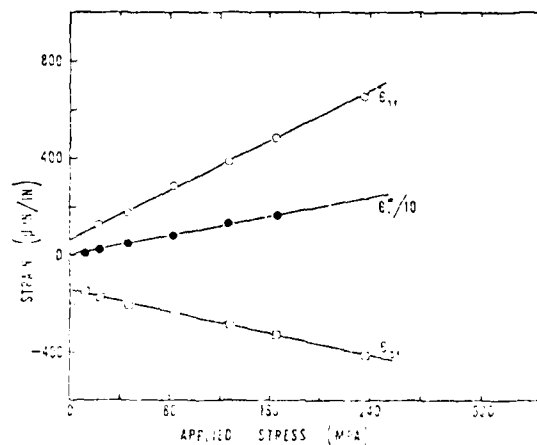


Fig. 4. Linear change in X-ray strains, ϵ_{11} and ϵ_{33} with applied stress in the Al containing laminate (2nd loading). Strain gage strain is also shown.

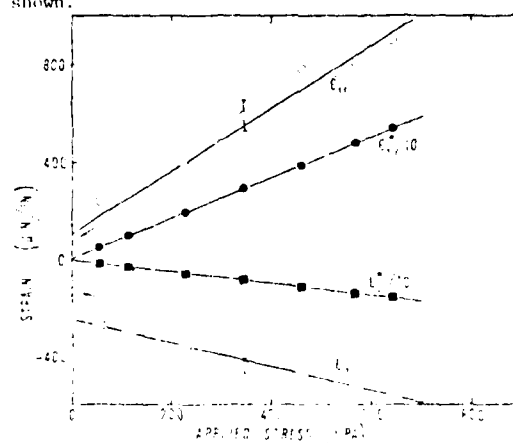


Fig. 5. Linear change in X-ray strains, ϵ_{11} and ϵ_{33} with applied stress in the Nb containing laminate (2nd loading). Strain gage strain is also shown.

STATISTICAL EVALUATION OF SOURCES OF ACOUSTIC EMISSION IN COMPOSITES

L. J. Graham
Rockwell International Science Center
Thousand Oaks, CA 91360

ABSTRACT

Acoustic emission (AE) signals that are generated by different microscopic processes during flaw growth in graphite-epoxy specimens have measurably different characteristics. In particular, the amplitudes of the emissions and a parameter that describes their frequency spectral content seem to give the most information about the processes. These parameters have a range of values for a given process which can be described by certain types of analytical distribution functions. When several processes occur simultaneously during flaw growth, such as epoxy crazing, fiber fracture, fiber-matrix disbond and inter-laminar cleavage, the distributions in the values of the AE parameters generally overlap so that identification of an individual AE signal as being caused by a particular process is not possible. However, statistical evaluation of the data for a few hundred events in terms of the analytical distributions, once the shape and modal value of these distributions are defined for each process, should provide a quantitative measure of the relative amounts of the various processes which occurred. Analyses of many data sets are required to develop confidence in the decomposed distributions as being descriptive of the individual processes. The ultimate purpose for this determination is to provide a description of the stage of flaw growth from the quantitative knowledge of the types and the amounts of the microscopic processes which occurred.

INTRODUCTION

The purpose of this study is to determine the current mechanical state of a composite by acoustic emission (AE) signature analysis and from that knowledge predict its remaining lifetime. Several laboratory specimen configurations were used in interpreting the signatures of the AE from the different fracture mechanisms, i.e. matrix fracture, fiber fracture, fiber-matrix disbond, fiber pullout, delamination. The data presented here are all from specimens with the triangular reduced cross-section shown in Poster 1.

EXPERIMENTAL RESULTS

Specimens with the triangular reduced cross-section were loaded in four-point bending so that the high stress region at the apex of the triangle was either in tension or compression. Some specimens had never been exposed to water and, others were fully saturated by soaking in 98°C water for several days. The relative amounts of the several possible fracture mechanisms were different under these four test conditions of otherwise identical specimens which permitted identification of the acoustic signature of those mechanisms. Posters 2 and 3 show some aspects of the acoustic signatures that can be obtained from among the 23 parameters collected for each AE event by the Acoustic Emission Multi-Parameter Analyzer (AEMPA) system. The most useful information in the acoustic signature was in the amplitudes and frequency spectra of the AE. For example in Poster 3 the trends in the frequency spectral amplitude ratio (the four scatter diagrams at the bottom) are quite different for the tension and compression tests. Here, the ratio of the peak amplitude at 56kHz to that at 560kHz for each AE event is plotted as a point at the time that the AE event occurred. For the tensile specimen this spectral amplitude ratio shows definite trends from about -5dB to -30dB to +20dB as different fracture mechanisms occurred during the loading history. The data for compressive failure, which is dominated by a single mechanism, do not show

these trends. The amplitudes of the AE (the center scatter diagrams) also show that some of the mechanisms in tension are more energetic than those operating in compression.

ANALYSIS OF RESULTS

The scatter diagrams of Posters 2 and 3 are useful in showing trends in the acoustic signatures but cannot provide quantitative information about the amounts of the different fracture processes which occurred. This information can be obtained from the data by forming number distributions (cumulative or differential) of the events based on the values of one of the parameters of those events for various time periods throughout the tests. These distributions are then decomposed into their component distributions due to the various mechanisms which occurred during each time period.

Decomposition of Amplitude Distributions - Poster 4 shows the method and results of decomposing amplitude distributions for the four specimen conditions. It is realized that any such decomposition is not necessarily unique and that evidence for the reasonableness of the decomposition must be established. In modeling the shape of the amplitude distributions for the individual mechanisms it was realized that the power-law distribution function traditionally used to describe AE amplitude data was not appropriate, particularly when more than one mechanism occurs within the analysis time period. The power-law distribution function, $N=N_0(V/V_0)^{-b}$, implies an unbounded range of possible amplitudes for a given mechanism with an infinite number of events approaching zero amplitude.

The extreme value distribution function which was used in the present analysis, Poster 4, is identical to the power-law distribution for large amplitude values but includes the condition that if an increment of fracture occurs by a given mechanism, the amount of energy released has a minimum value related to the parameter V_0 . Thus V_0 takes on a significance that it did not have in the

power-law description of the amplitude distribution, the modal value for the mechanism, while N_0 and b are still the number of events due to that mechanism and the spread in the amplitudes (or energies) of those events.

The example on Poster 4 for the first 500 AE events detected from a wet tension specimen (Specimen #LSW-83) shows decomposition of the experimental amplitude distribution into cumulative distributions due to four mechanisms, each with their own values of b and V_0 . These values should not change unless the material properties change, e.g. wet vs. dry, but the number N_0 for each mechanism may change with time or loading conditions, and may be zero under some conditions.

Inspection of the table of decomposed distributions in Poster 4 shows this to be the case, particularly for the wet compression specimen (Specimen #LSW-82). At times during the test, the amplitude distribution shows that only one mechanism was operating and at other times either two or three. In each case these distributions have the same values of b and V_0 that were found for identical specimens tested with the fibers at the apex of the triangle in tension although the values of N_0 are quite different. Decomposition of the amplitude distributions for specimens from the dry material result in somewhat different values of b and V_0 as expected but are also less consistent. Part of the inconsistency may be due to a shallow layer of moisture absorbed during specimen fabrication although this can not explain all of it.

Decomposition of Spectral Type Distributions -

Unlike the amplitude distributions, there has been no prior history of spectral type distribution analysis and no theoretical development of the functional form of these distributions. While the modal value can reasonably be expected to be related to the specific type of mechanism from past studies, the shape of the distribution is thought to be related to details of the localized surroundings of the source and perhaps the orientation and size of the source. For example, the AE due to the tensile fracture of graphite fibers are expected to have similar frequency spectra modified slightly by the distribution and spacing of nearby unbroken fibers, the radial distribution in the thickness of the surrounding epoxy, the local interfacial bond strength between the fiber and the epoxy, the local stress distribution, the occurrence of a single fiber fracture or an avalanche of fractures, or a number of other localized differences. Analysis of these effects on the shape of the spectral parameter distribution was not attempted at this time. Decomposition of the experimental distributions was strictly empirical.

The first attempts to decompose the experimental spectral type distributions, such as the ones shown on Poster 5, were made with the arbitrary restriction that the shapes of the differential distribution peaks be symmetric about their modal values. It was found that in addition to the symmetrically shaped distributions centered at -16 dB, -4.5 dB and 5.5 dB, which are apparent (and are indicated) on the figure of Poster 5, curve fitting required distributions centered at -12 dB, -8.5 dB, -1.5 dB and occasionally a small peak at -23 dB. With these six (or seven) distributions, curve fitting to the experimental distributions, as in Poster 5, could be done with extremely small least squares residuals by just changing the number of events in each individual distribution for the different time periods of the test.

A very convincing conclusion about the validity of the decomposition of the spectral distributions would be if the number of decomposed distributions and the number of events in each of these distributions were in agreement with the decomposed amplitude distributions for the same time periods. This would indeed strongly indicate that separate mechanisms had been identified, each with its distinctive distribution of AE amplitude and frequency spectral characteristics. This correspondence has not yet been found, however, which leaves nagging questions about restricting the analysis to symmetric distributions and about overfitting the experimental data. More analysis is required to answer these questions but the results so far are encouraging that this analysis will be fruitful.

CONCLUDING REMARKS

If AE signature analysis is successful in quantitatively assessing the amounts of the various source mechanisms which occurred during a small load increment, then, in those cases where the flaw grows by a well defined sequence of mechanistic steps, a description of the current state of the flaw can be made. Combining this information with stress analysis and fracture mechanics, as outlined on Poster 6, leads to the possibility for life prediction for a composite structure.

ACKNOWLEDGMENTS

This research was sponsored by the Center for Advanced NDE operated by the Science Center, Rockwell International, for the Advanced Research Projects Agency and the Air Force Materials Laboratory under Contract No. F3361-74-C-5180. The efforts of R. Govan in specimen fabrication and testing and Dr. R. K. Elsley and G. Lindberg in computer software development are gratefully acknowledged.

PURPOSES:

- DETERMINE THE CURRENT MECHANICAL STATE OF A COMPOSITE.
- PREDICT ITS REMAINING LIFETIME.

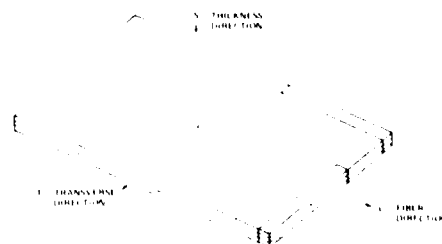
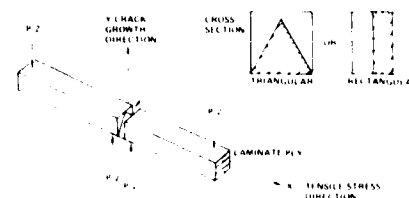
APPROACH:

- IDENTIFY CHARACTERISTIC ACOUSTIC EMISSION SIGNATURES USING MULTI-PARAMETER ANALYSIS.
- RELATE AE SIGNATURES TO SPECIFIC FLAW GROWTH MECHANISMS.
- COMBINE THIS INFORMATION WITH FRACTURE MECHANICS ANALYSIS TO PREDICT REMAINING LIFETIME.

EXPERIMENTAL METHOD:

- UNIDIRECTIONAL GRAPHITE EPOXY COMPOSITE (AS/3501.5) TESTED DRY AND HYDROTHERMALLY AGED.
- FOUR-POINT BEND SPECIMENS WITH VARIOUS ORIENTATIONS AND GEOMETRIES TO ENHANCE SPECIFIC FRACTURE MECHANISMS.
- USE MULTI-PARAMETER ANALYZER AND MINICOMPUTER TO COLLECT AND ANALYSE ACOUSTIC EMISSION DATA.
- OBTAIN LOAD CURVES, VISUAL OBSERVATIONS AND SEM PHOTOGRAPHS TO IDENTIFY FRACTURE MECHANISMS.

TEST SPECIMENS



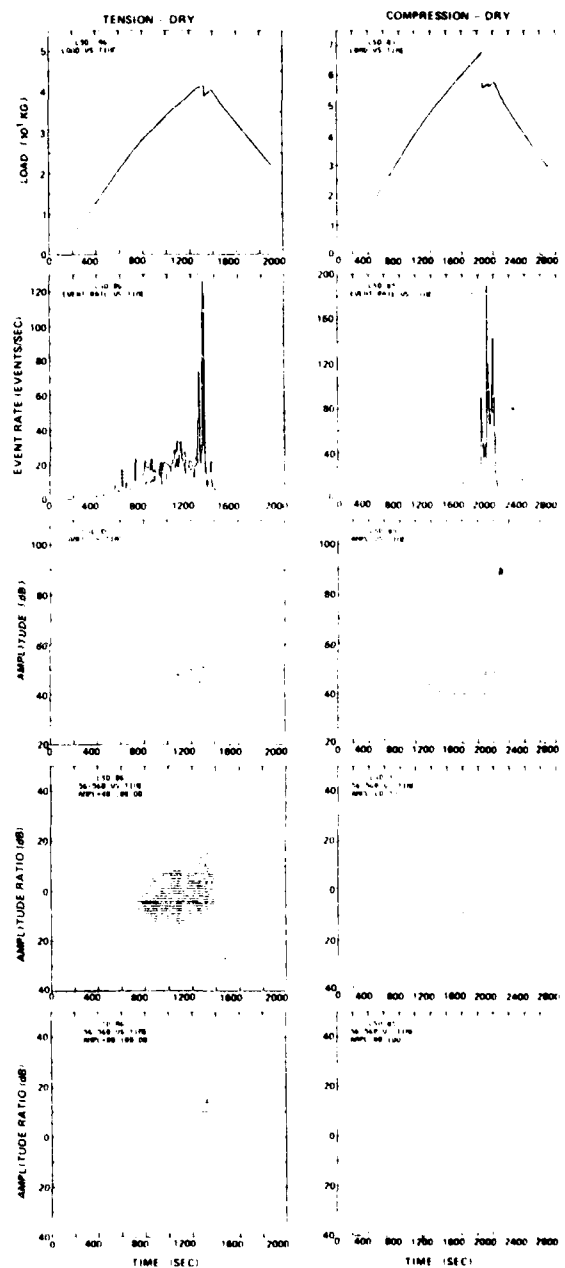
SPECIMEN DESIGNATIONS, XY:

- LS - FIBERS IN TENSION, CRACK GROWTH THRU THICKNESS
- LS - FIBERS IN COMPRESSION, CRACK GROWTH THRU THICKNESS
- LT - FIBERS IN TENSION, CRACK GROWTH TRANSVERSE
- LT - FIBERS IN COMPRESSION, CRACK GROWTH TRANSVERSE
- TS - TENSION NORMAL TO FIBERS, CRACK GROWTH THRU THICKNESS
- TL - TENSION NORMAL TO FIBERS, CRACK GROWTH ALONG FIBERS

Poster 1

AE SIGNATURES

- **LOAD** – WHEN DRY, COMPRESSIVE STRENGTH IS GREATER.
- **AE EVENT RATE** – QUITE VARIABLE WITH TIME AND FROM SPECIMEN TO SPECIMEN. INDICATES DAMAGE RATE.
- **AMPLITUDE** – LARGER AMPLITUDE EMISSIONS DUE TO TENSILE FRACTURE OF FIBERS AND INTERPLY DELAMINATION WHEN TESTED IN TENSION.
- **RATIO OF AMPLITUDE IN TWO FREQUENCY BANDS** – THIS DEFINITION OF FREQUENCY SPECTRAL TYPE SUGGESTS:
 1. FIBER FRACTURE IS HIGHER FREQUENCY.
 2. DELAMINATION IS LOWER FREQUENCY.
 3. FIBER-MATRIX DEBONDING AND MATRIX FRACTURE ARE INTERMEDIATE FREQUENCY.
 4. DELAMINATION TENDS TO CREATE LARGER AMPLITUDE.
 5. MATRIX FRACTURE TENDS TO LOWER AMPLITUDE.
 6. FIBER FRACTURE IN COMPRESSION TENDS TO LOWER AMPLITUDE.



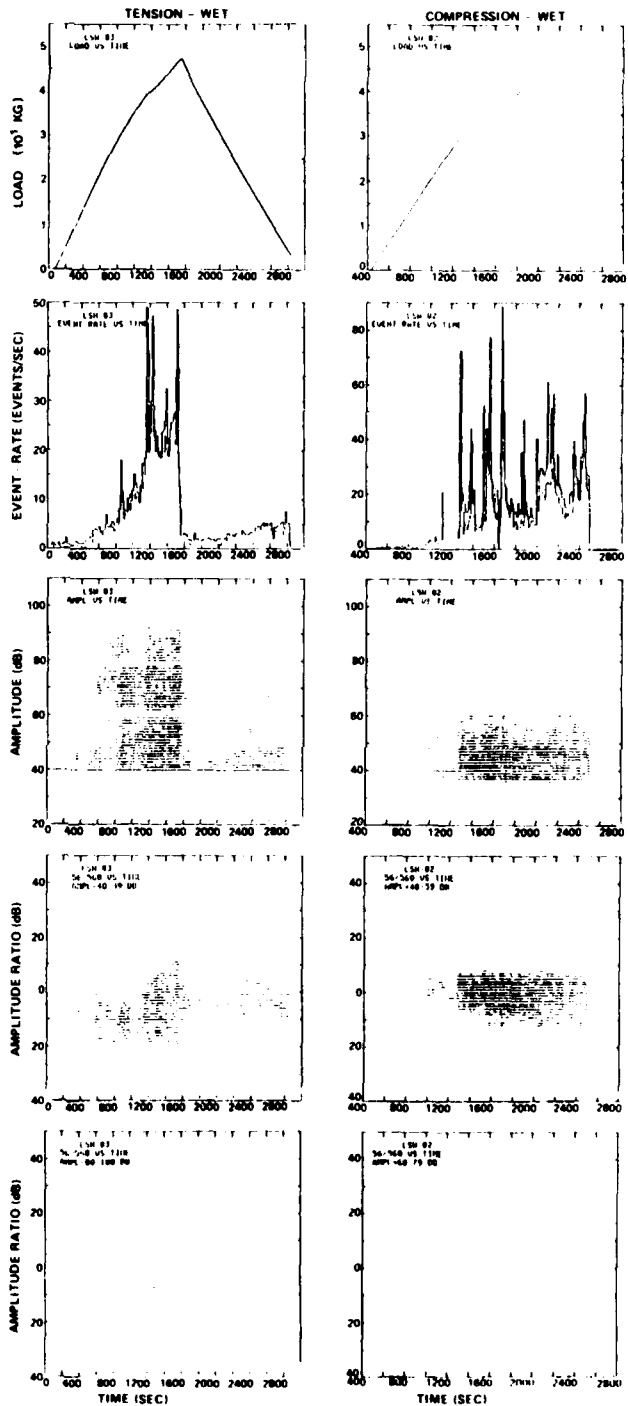
AE SIGNATURES

- LOAD WHEN WET – TENSILE STRENGTH IS GREATER.

- AE EVENT RATE – VARIABLE.

- AMPLITUDE – TENDS TO LOWER AMPLITUDES WHEN WET AND WHEN TESTED IN COMPRESSION.

- RATIO OF AMPLITUDE IN TWO FREQUENCY BANDS – SIMILAR OBSERVATIONS WET OR DRY

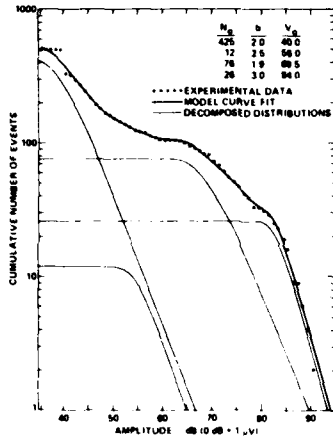


DECOMPOSITION OF AMPLITUDE DISTRIBUTIONS BY CURVE FITTING

THE AMPLITUDE DISTRIBUTION FOR EACH ACOUSTIC EMISSION MECHANISM (MATRIX FRACTURE, FIBER FRACTURE, FIBER MATRIX DISBOND, ETC.) WAS ASSUMED TO HAVE THE FORM OF AN EXTREME VALUE FUNCTION

$$N = N_0 \left[1 - e^{-\left(\frac{V}{V_0}\right)^b} \right]$$

WHERE N = CUMULATIVE DISTRIBUTION
V = PEAK VOLTAGE AMPLITUDE OF THE AE
N₀ = NUMBER OF AE EVENTS IN THE SAMPLE
V₀ = MODAL AMPLITUDE VALUE OF THE DISTRIBUTION
b = SHAPE OF THE DISTRIBUTION



A CHECK ON THE REASONABLENESS OF THE DECOMPOSED DISTRIBUTIONS IS THAT THEIR SHAPE AND MODAL VALUES REMAIN CONSTANT THROUGHOUT A TEST OR CHANGE IN A RATIONAL WAY. THE NUMBER OF EVENTS IN EACH DISTRIBUTION WILL CHANGE DURING A TEST AND WILL REVEAL THE MIX OF THE TYPES OF PROCESSES OCCURRING

CHANGING MATERIAL PROPERTIES, E.G. BY EXPOSURE OF THE COMPOSITE TO WATER, MAY CHANGE THE MODAL VALUES AND SHAPES OF THE DISTRIBUTIONS.

SUMMARY OF DECOMPOSED DISTRIBUTIONS

EVENT NO	MECHANISM #1			MECHANISM #2			MECHANISM #3			MECHANISM #4		
	N ₀	b	V ₀	N ₀	b	V ₀	N ₀	b	V ₀	N ₀	b	V ₀
COMPRESSION - WET (LSB 82)												
1 500	530	2.0	40.0	80	2.5	64.0	51	1.9	66.5	0		
501 1000	525	2.0	40.0	38	2.5	64.0	18	1.9	66.5	0		
1001 1500	800	2.0	40.0	0			0			1	3.0	64.0
1501 2000	820	2.0	40.0	16	2.5	64.0	0			0		
2001 2500	875	2.0	40.0	0			0			0		
2501 3000	905	2.0	40.0	33	2.5	64.0	0			0		
TENSION - WET (LSB 83)												
1 500	475	2.0	40.0	12	2.5	64.0	76	1.9	66.5	26	3.0	64.0
501 1000	280	2.0	40.0	67	2.5	64.0	710	1.9	66.5	20	3.0	64.0
1001 1500	200	2.0	40.0	61	2.5	64.0	230	1.9	66.5	64	3.0	64.0
1501 2000	215	2.0	40.0	52	2.5	64.0	206	1.9	66.5	56	3.0	64.0
14 001 14 500	308	2.0	40.0	80	2.5	64.0	173	1.9	66.5	27	3.0	64.0
14 501 15 000	293	2.0	40.0	130	2.5	64.0	169	1.9	66.5	25	3.0	64.0
15 001 15 500	273	2.0	40.0	170	2.5	64.0	139	1.9	66.5	18	3.0	64.0
COMPRESSION - DRY (LSB 85)												
1 500	470	2.0	40.0	47	2.5	64.0	17	3.0	66.5	2	3.0	64.0
501 1000	248	2.0	40.0	50	2.5	64.0	46	3.0	66.5	0		
1001 1500	275	2.0	40.0	41	2.5	64.0	68	3.0	67.5	0		
1501 2000	315	2.0	40.0	38	2.5	64.0	62	3.0	66.5	0		
2001 2500	320	2.0	40.0	40	2.5	64.0	70	3.0	67.5	0		
8001 8000	290	2.0	40.0	80	2.5	64.0	58	3.0	67.5	2	3.0	64.0
8501 9000	336	2.0	40.0	80	2.5	64.0	61	3.0	67.5	3	3.0	64.0
7001 7500	336	2.0	40.0	80	2.5	64.0	17	2.4	67.5	0	3.0	64.0
7501 8000	335	2.0	40.0	28	2.5	64.0	27	3.0	67.5	2	3.0	64.0
TENSION - DRY (LSB 86)												
1 500	145	2.0	40.0	85	2.5	64.0	153	2.0	66.5	34	3.0	64.0
501 1000	170	2.0	40.0	80	2.5	64.0	180	2.0	66.5	55	3.0	64.0
1001 1500	150	2.0	40.0	70	2.5	64.0	190	2.0	66.5	50	3.0	64.0
1501 2000	130	2.0	40.0	50	2.5	64.0	202	2.0	66.5	56	3.0	64.0
8001 8500	155	2.0	40.0	66	2.5	64.0	186	2.0	66.5	34	2.5	67.0
8601 10 000	136	2.0	40.0	75	2.5	64.0	190	2.0	66.5	48	3.0	64.0
10 001 10 500	110	2.0	40.0	60	2.5	64.0	210	2.0	66.5	66	2.5	64.0

Poster 4

DECOMPOSITION OF SPECTRAL TYPE DISTRIBUTIONS BY CURVE FITTING

SPECTRAL TYPE IS DEFINED AS THE RATIO OF THE AMPLITUDE OF AN AE AT LOW FREQUENCY TO THE AMPLITUDE AT HIGH FREQUENCY.

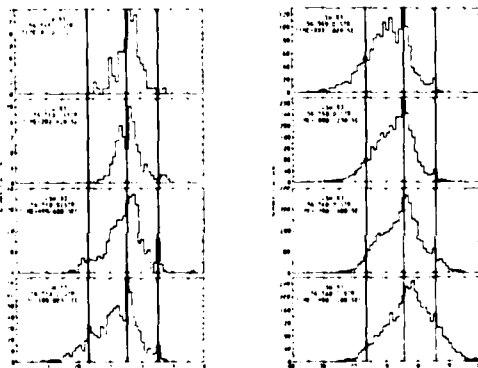
NUMBER DISTRIBUTIONS OF AE EVENTS BASED UPON THIS SPECTRAL TYPE PARAMETER VARY SYSTEMATICALLY DURING A SPECIMEN TEST AS NEW FRACTURE MECHANISMS OCCUR.

CAN THESE DISTRIBUTIONS BE DECOMPOSED INTO COMPONENT PARTS WHICH CAN BE ASSOCIATED WITH SPECIFIC MECHANISMS?

THE FIRST ATTEMPTS WERE ENCOURAGING

WILL THE COMPONENT AMPLITUDE AND SPECTRAL TYPE DISTRIBUTIONS AGREE IN ASSESSING THE AMOUNTS OF THE VARIOUS AE SOURCES?

THIS REMAINS TO BE ANSWERED



IF AE SIGNATURE ANALYSIS IS SUCCESSFUL IN QUANTITATIVELY ASSESSING THE AMOUNTS OF THE VARIOUS SOURCE MECHANISMS WHICH OCCURRED DURING A SMALL LOAD INCREMENT

THEN, IN THOSE CASES WHERE THE FLAW GROWS BY A WELL DEFINED SEQUENCE OF MECHANISTIC STEPS, A DESCRIPTION OF THE CURRENT STATE OF THE FLAW CAN BE MADE

COMBINING THIS INFORMATION WITH STRESS ANALYSIS AND FRACTURE MECHANICS LEADS TO THE POSSIBILITY FOR LIFE PREDICTION FOR A COMPOSITE STRUCTURE

Poster 5

LIFE PREDICTION USING AE SIGNATURE ANALYSIS

PROCEDURE	STEPS	RESULTS
APPLY A REALISTIC PROOF LOAD TO A COMPONENT AND MONITOR ACOUSTIC EMISSION ACTIVITY.	DETERMINE SERVICE LOAD SPECTRUM. LOCATE ACTIVE REGIONS IF MORE THAN ONE. MINIMIZE FURTHER DAMAGE DUE TO PROOF LOAD.	PREVIOUS MAXIMUM SERVICE LOAD OR EXTENT OF PREVIOUS DAMAGE THROUGH KAISER EFFECT.
COLLECT A SAMPLE OF ACOUSTIC EMISSION EVENTS USING MULTI-PARAMETER ANALYZER.	LOCALIZE DATA SET TO ONE ACTIVE REGION. OBTAIN SAMPLE FOR EACH ACTIVE REGION. ACCOUNT FOR GEOMETRICAL EFFECTS IN SIGNAL.	RELATIVE AMOUNT OF VARIOUS FRACTURE MECHANISMS WHICH OCCURRED THROUGH AMPLITUDE AND SPECTRAL TYPE DISTRIBUTIONS. LOAD LEVEL AT WHICH THEY OCCURRED.
CALCULATE STRESS DISTRIBUTION FOR EACH ACTIVE REGION AT PROOF LOAD.	ACCOUNT FOR COMPLEX STRUCTURE. ACCOUNT FOR PLY ORIENTATION. DETERMINE THROUGH THICKNESS DISTRIBUTION OF TENSILE, COMPRESSIVE AND SHEAR STRESSES.	MAGNITUDE AND THROUGH THICKNESS LOCATION OF MOST PROBABLE CRITICAL STRESS COMPONENT.
APPLY FRACTURE MECHANICS ANALYSIS.	ACCOUNT FOR MATERIALS PROPERTIES. ACCOUNT FOR PLY LAY-UP AND INTERACTIONS. DETERMINE FRACTURE CRITERION.	SEQUENCE OF MECHANISTIC STEPS IN THE GROWTH OF A FLAW TO CRITICALITY
PREDICT FUTURE SERVICE CONDITIONS.	ESTIMATE LOAD SPECTRUM. ESTIMATE ENVIRONMENTAL EFFECTS.	FUTURE FLAW GROWTH RATE.
CONCLUSIONS:	*PRESENT MAXIMUM FLAW SIZE AND TYPE AT EACH ACTIVE LOCATION AS A FUNCTION OF ITS ASSUMED LOCATION THROUGH THE THICKNESS.	
	*PREDICTED SERVICE LIFE BASED ON PRESENT FLAW DESCRIPTION, SEQUENCE OF MECHANISTIC STEPS, AND FUTURE GROWTH RATE.	

Poster 6

DIGITAL DISPLAY OF ACOUSTIC HOLOGRAPHIC IMAGES

J. W. Brophy, A. E. Holt, J. H. Flora
Nondestructive Methods & Instruments Section
Babcock & Wilcox Company
Lynchburg, Virginia 24505

ABSTRACT

Acoustic holography is an elegant and accurate technique for characterizing defects by forming visual images of them. Traditionally, optical reconstruction methods have been used to display the images but due to constraints of the optical systems, digital reconstruction techniques are now being employed.

INTRODUCTION

Optical reconstruction of scanned acoustic holographic information on a transparency is accurate and relatively flexible but it suffers from various constraints due to the magnification factor that must be applied to the reconstructed defect images. These constraints limit the ease in interpreting defect images for the purpose of characterization.

The major influences on the magnification factor for the optical image are the dependence on the depth of the defect in the material and the frequency of the interrogating sound beam. Reconstructions of a test block with flat bottom holes in the shape of a "Y" pattern at different inspection frequencies shows the effect directly.

Computer reconstruction of acoustic holograms eliminates most of the display problems associated with optical images because the image size is no longer directly dependent on frequency or defect depth. The only limitations are from the particular display device being used. Eliminating the magnification factor variables make it possible to create images that are composites of several images as functions of depth, frequency, or just displacement on the inspection surface. Display and fitting together of images taken at different inspection angles can be used to create three-dimensional views of defects also.

To make composite images meaningful, all the images must be made relative. The method we use is to form binary images and then threshold the noise portion out of the image before forming any composites. A means of systematically determining the "best" threshold for each image has been developed and is being expanded in use.

ULTRASONIC HOLOGRAM FORMATION BY A SCANNED TIME GATED PULSE-ECHO SYSTEM

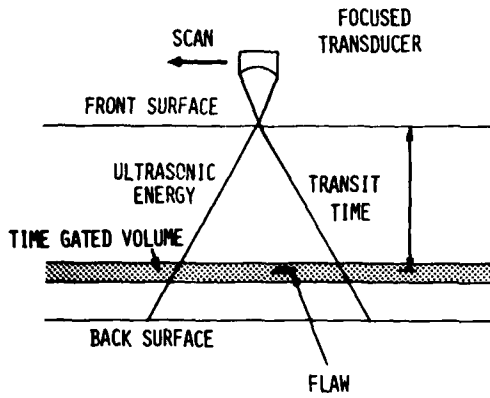


FIGURE 1: SCANNING TRANSDUCER GEOMETRY

FIGURE 2: ELECTRONIC PROCESSOR SCHEMATIC

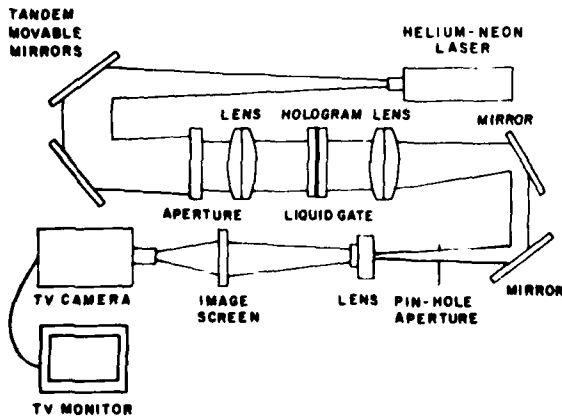
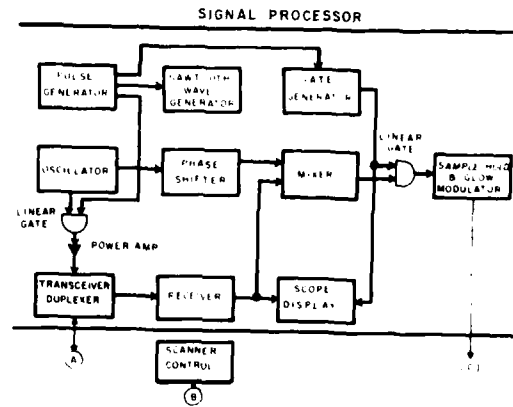


FIGURE 3: OPTICAL IMAGE RECONSTRUCTION

THE IMAGE MAGNIFICATION FACTOR IS GIVEN BY:

$$M = (\alpha * F) / (v_m * R_1)$$

WHERE

α = constant

F = ultrasonic frequency

v_m = sound velocity in the material

R_1 = sound travel path to defect

OPTICAL RECONSTRUCTION OF TEST BLOCK IMAGES

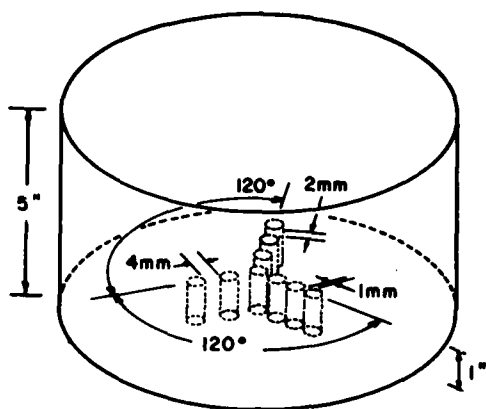


FIGURE 4: ALUMINUM TEST BLOCK SCHEMATIC



FIGURE 5: 3 MHz OPTICAL IMAGE



FIGURE 6: 5 MHz OPTICAL IMAGE

TABLE 1: DISADVANTAGES OF OPTICAL IMAGE RECONSTRUCTION

- A) FINAL IMAGE SIZE IS DEPENDENT ON DEFECT DEPTH, INSPECTION FREQUENCY AND MATERIAL VELOCITY.
- B) DEFECT SIZING IS DEPENDENT ON OPERATOR JUDGEMENT AS TO "BEST" IMAGE.
- C) COMPOSITE IMAGES FROM DIFFERENT DEPTHS AND/OR FREQUENCIES ARE VERY DIFFICULT TO CREATE.
- D) OPTICAL BENCH SET-UP AND ADJUSTMENT REQUIRE A SKILLED OPERATOR.

TABLE 2: ADVANTAGES OF DIGITAL IMAGE RECONSTRUCTION.

- A) ELIMINATION OF IMAGE SIZE ON DEFECT DEPTH, FREQUENCY AND MATERIAL VELOCITY.
- B) COMPOSITE IMAGE FORMATION FROM DIFFERENT DEFECT DEPTHS AND/OR INSPECTION FREQUENCIES.
- C) IMAGE ENHANCEMENT USING DIGITAL TECHNIQUES.
- D) DEVELOPMENT OF "INTELLEAGENT" IMAGING HARDWARE.
- E) EVENTUALLY WILL BE ABLE TO DO NEAR REAL-TIME IMAGING.

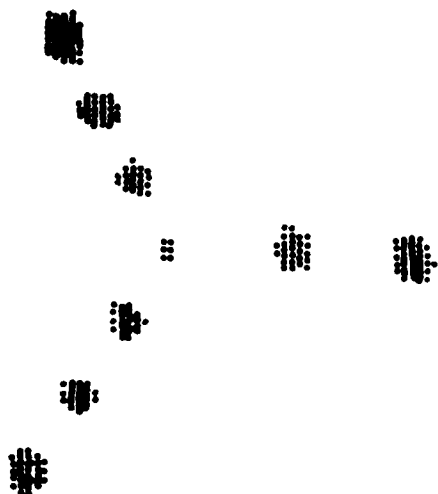


FIGURE 7: DIGITAL TEST BLOCK IMAGE
FIVE TIMES ACTUAL SIZE

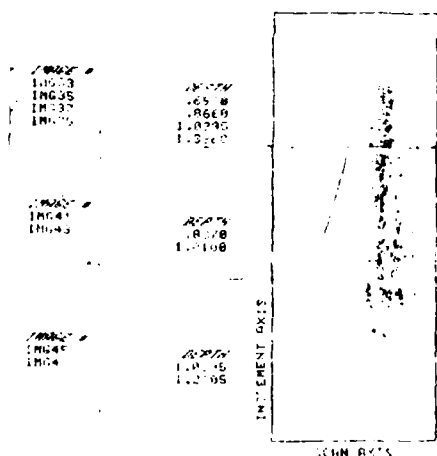


FIGURE 10: DEPTH AND LOCATION COMPOSITE OF
AN ACTUAL DEFECT THAT WAS LARGER
THAN THE SCANNER APERTURE.
TOTAL LENGTH = 9.4 INCHES
TOTAL WIDTH = 1.45 INCHES



FIGURE 8: DIGITAL TEST BLOCK IMAGE
TWICE ACTUAL SIZE

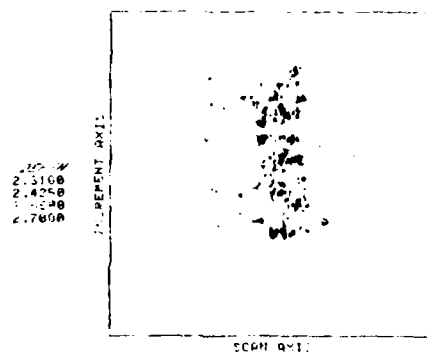


FIGURE 9: DEPTH COMPOSITE OF ACTUAL DEFECT
AFTER DIGITAL IMAGE RECONSTRUCTION

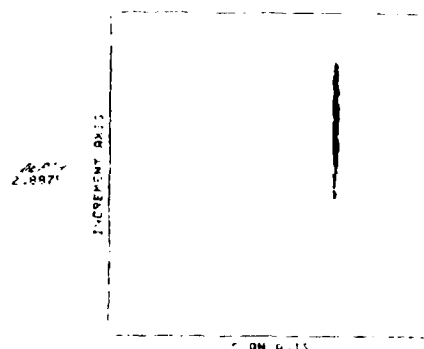


FIGURE 11: RECONSTRUCTED IMAGE OF A SIDE-
DRILLED HOLE: LENGTH AND WIDTH
ARE DIRECTLY MEASURABLE FROM
THE IMAGE.
LENGTH = 2.55"
WIDTH = 0.13"

BINARY IMAGES THRESHOLD EFFECT ON IMAGE SIZE

IMAGE	THRESHOLD	SIZE
IMAGEA	.5000	2.4250
IMAGEB	.5400	2.4250
IMAGEC	.4000	2.4250

CLAD FLAW IMAGES 1MHZ INSPECTION FREQUENCY

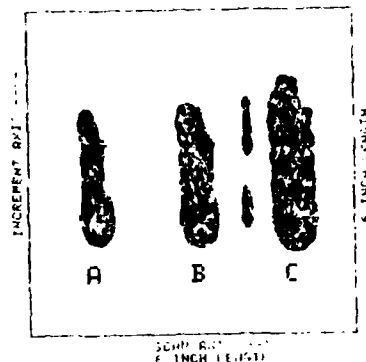


FIGURE 12: THRESHOLD EFFECT, FOR NATURAL DEFECTS. ONE PRESSING PROBLEM IS IMAGE QUALITY CRITERIA. WHAT IS THE "BEST" IMAGE DISPLAY THAT CORRECTLY SIZES THE DEFECT.

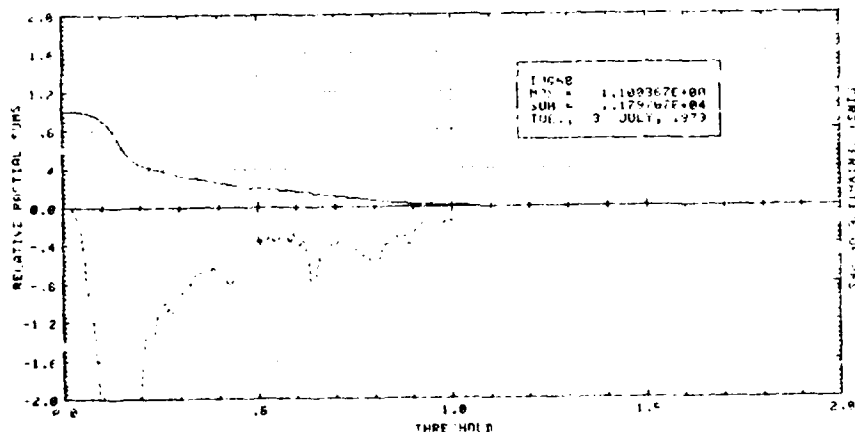


FIGURE 13: RELATIVE PARTIAL SUMS (RPS) PLOT TO DETERMINE "BEST" IMAGE DISPLAY

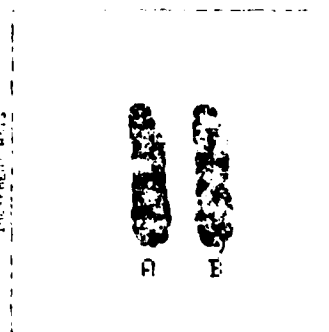
DEFINE S = GRAND SUM OF THE ENTIRE IMAGE ARRAY
M = MAXIMUM VALUE OF A POINT IN THE ARRAY
 T_i = THRESHOLD VALUE

THE RELATIVE PARTIAL SUMS ARE THE SUMS OF THE ARRAY ABOVE THRESHOLDS T_i AND NORMALIZED WITH RESPECT TO THE GRAND SUM.

1MHZ IMAGES

IMAGE 1 2 3
 15000 15000 15000
 15000 15000 15000

INCIDENT 0-12



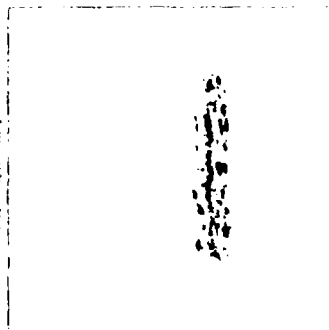
A B

1 MHZ

3 MHZ

IMAGE 1 2 3
 15000 15000 15000
 15000 15000 15000

INCIDENT 0-12

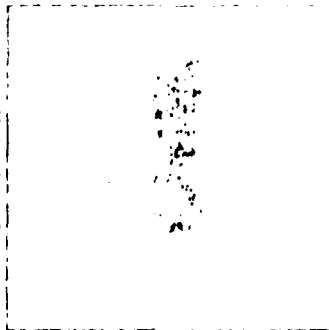


3 MHZ

5 MHZ

IMAGE 1 2 3
 15000 15000 15000
 15000 15000 15000

INCIDENT 0-12



5 MHZ

FIGURES 14, 15, 16: IMAGE CHANGE DUE TO INSPECTION
 FREQUENCY FOR A NATURALLY
 OCCURRING ROUGH SURFACE DEFECT

ACOUSTIC MICROSCOPY VIA SCANNING

A. Atalar and C. F. Quate
Edward L. Ginzton Laboratory
Stanford University, Stanford, California 94305

ABSTRACT

We offer via posters some of the latest images recorded with the scanning acoustic microscope operating near 2.5 GHz.

Our report at the 1978 Review included a description of the scanning instrument which had been scaled up in frequency to 3 GHz. This was accomplished in large part by fabricating acoustic lens with smaller radii and by heating the liquid to reduce the absorption. In our report for this year, we will present the results of our material studies as carried out with the new instruments operating near 2.5 GHz. We will include results on four different materials - steel, Cobalt-Titanium, brass and alumina ceramic. Each of these have distinctive characteristics in the acoustic micrographs and each of these have information which is distinct from their optical counterparts.

The sketch of Fig. 1 outlines the essential features of the instrument. The lens itself is a spherical cavity in a sapphire block. When this cavity is filled with water it serves as an ideal lens which will converge the acoustic energy to a narrow waist at the focal point. The waist diameter is less than the acoustic wavelength and it is this feature that determines the resolving power of the instrument. The overall view of the sapphire crystal with the acoustic film transducer is shown in the upper right. The sample surface is scanned across the focused beam and it is the reflected signal from this surface that we monitor and display. The mechanical set-up for implementing the mechanical scanning is shown in Fig. 2.

The first illustration of this type of reflection microscopy is shown in Fig. 3. There we see the optical and acoustic comparisons of the steel surface before and after the preferential etching. It is a low-alloy steel used for auto bodies. One has to use chemical etching in order to bring out the grain boundaries in the optical images. On the other hand, the acoustic image shows these boundaries before the etching process. Also the different grains appear here with different contrast. It is this texture that we find in the acoustic micrograph that is important. We attribute this to different orientation of the grains. We have determined from previous studies that the reflected signal is sensitive to the elastic properties of the surface under examination. In turn, the various orientations show up since the individual grains are anisotropic and they present different elastic properties as their orientation is altered.

In Fig. 4 we present the optical and acoustic comparison of a surface of the alloy Cobalt-Titanium. This material has condensed in different phases - each with a different ratio of cobalt to titanium and each with different elastic constants.

The central points of interest in this material are the various regions of high reflectivity (bright regions) in the acoustic images. The corresponding points in the optical images reveal nothing. But as the sample is etched the bright points in the acoustic field turn out to have a much higher etch rate and they form small surface cavities in these regions. We are unclear about the origins of these pits. They might be attributable to different material compositions or perhaps subsurface cavities. It is a clear demonstration of the power of acoustic microscopy to delineate various inhomogeneities in material surfaces.

In Fig. 5 we show the polished surface of a brass sample. Again, the boundaries between grains and the twin boundaries stand out with high contrast. The contrast in the optical image is much less.

In the final images of Fig. 6 we present the comparative images of the surface of alumina ceramic which is partially coated with gold. The SEM images and the optical images exhibit much less contrast than does the acoustic images. Also, we see imperfections in the gold film that are uninteresting in the image taken with the SEM.

The acoustic microscope can now be used to record image surface and subsurface detail of various materials with a resolution similar to the optical microscope. The content of the acoustic image is often greater than the optical images. The two forms of microscopy taken together reveal much more information on material structures and formations.

ACKNOWLEDGEMENT

This work was supported by the Advanced Research Projects Agency of the Department of Defense and monitored by the Air Force Office of Scientific Research under Contract No. F49620-78-C-0098.

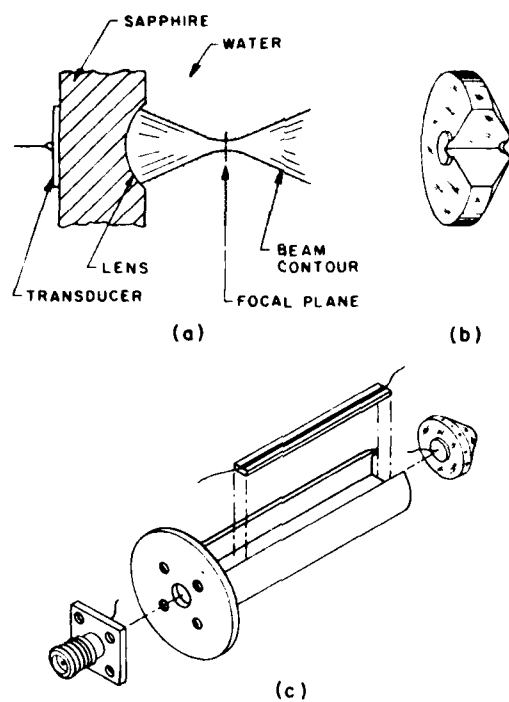


Fig. 1 (a) Piezoelectric transducer and acoustic lens as used in the acoustic microscope.
 (b) Sapphire rod which carries the transducer and the lens.
 (c) Lens holder with a matching network for the transducer.

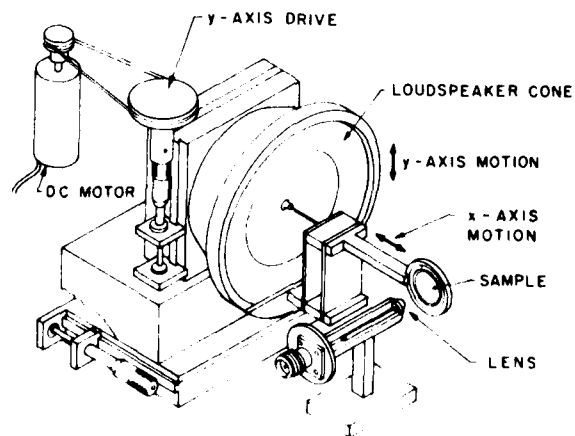
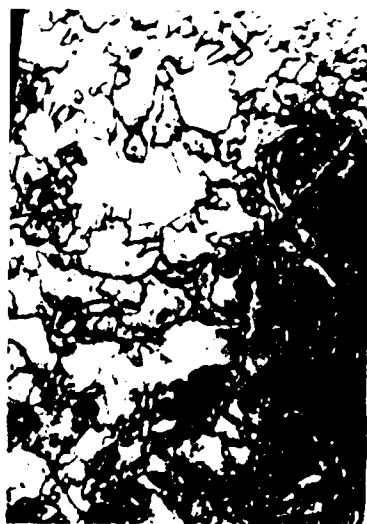


Fig. 2 The components used for the mechanical scanning.



B



D



A



C

Fig. 3 Optical and acoustic comparisons of steel surface

- A. Optical before etching
- B. Optical after etching
- C. Acoustic before etching
- D. Acoustic after etching.

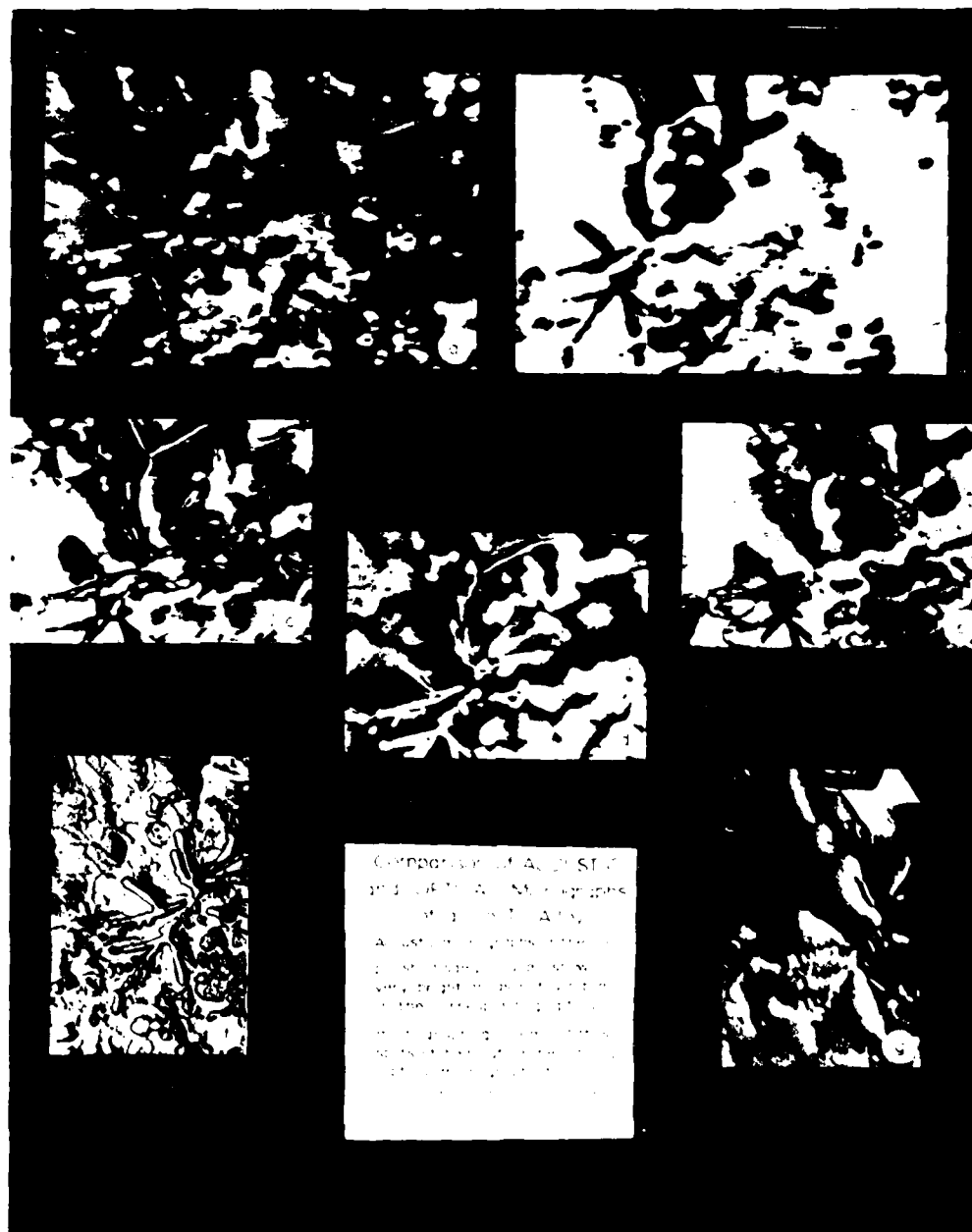
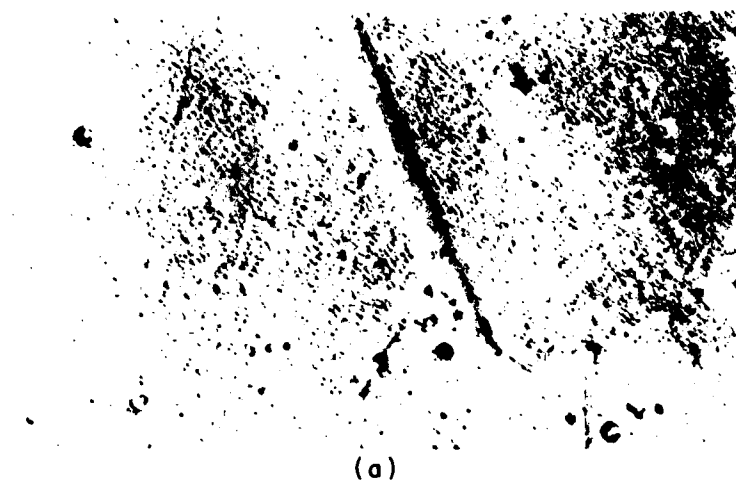


Fig. 4 Comparison of acoustic and optical micrographs of a Co-Ti alloy.



(a)



(b)

Fig. 5 Optical (a) and acoustic (b) comparison of polished brass surface.
Field of view is 55 X 90 μm .

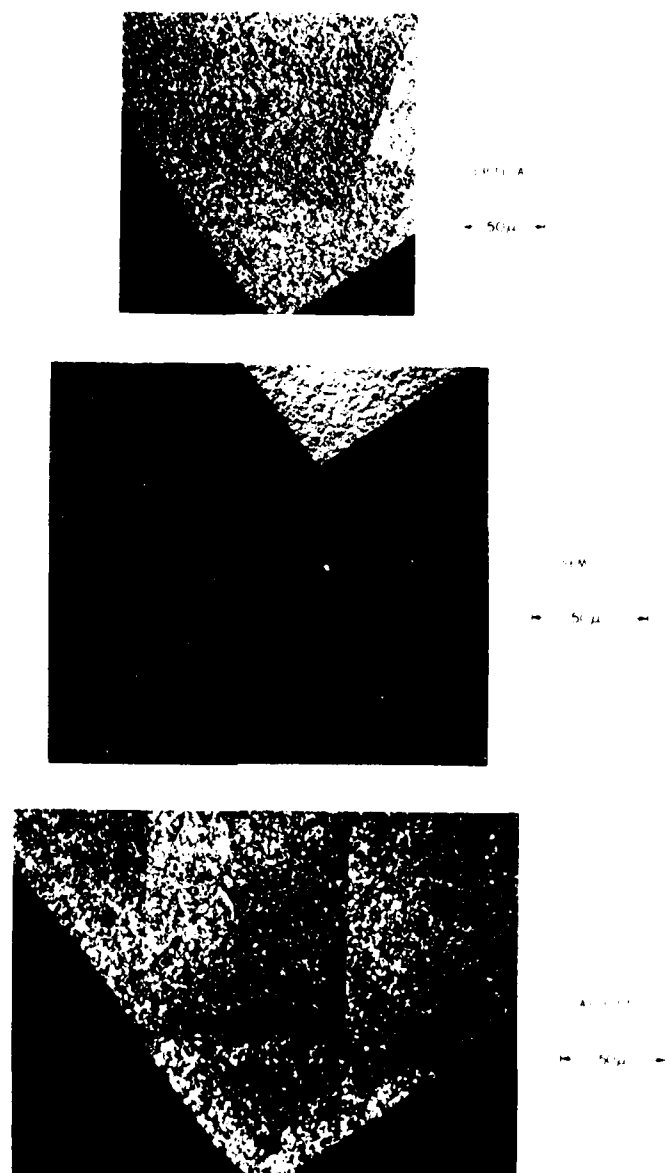


Fig. 6 Comparison of optical, SEM and acoustic micrographs of a gold layer on alumina substrate.

FURTHER PROGRESS ON NONDESTRUCTIVE DIAGNOSIS OF HYBRID MICROELECTRONIC
COMPONENTS USING TRANSMISSION ACOUSTIC MICROSCOPY

J. K. Wang, C. C. Lee, and C. S. Tsai
Center for the Joining of Materials
and
Department of Electrical Engineering
Carnegie-Mellon University
Pittsburgh, PA 15213

ABSTRACT

Recent progress on diagnosis and characterization of defects in hybrid microelectronic components using a transmission scanning acoustic microscope (SAM) operating at 150 MHz is summarized. A simple method has been established to locate (in three dimensions) and classify the defects. The study also shows that two optically identical thick-film resistors having a ratio of 5×10^3 in resistance value exhibit a 43 db contrast in acoustic amplitude.

INTRODUCTION

The characteristics of microelectronic components are greatly affected by the elastic faults or defects such as inclusions, voids, delaminations, and nonuniform particle distribution. Due to impedance mismatch, scattering and absorption associated with a defect, significant attenuation is expected in the transmitted acoustic signal. Therefore, the degree of darkness at an image area is a measure of the acoustic opacity, and thus the irregularity or defect at a corresponding area in the specimen. We had earlier employed a transmission-type scanning acoustic microscope⁽¹⁾ (see Fig. 1), operating at 150 MHz, to image the internal structures of some hybrid microelectronic components.^(2,3)

It is highly desirable to distinguish between a VOID-type defect and an INCLUSION-type defect through quantitative measurement. We have recently found that a definitive distinction can be made by translating the specimen along the lens axis at small increments and recording the corresponding amplitudes and phases of the transmitted signal through the particular defect. The amplitude and phase data obtained indicate not only the depth, size, but also the type of the defect. Phase information is important because the variation in the local acoustic phase is a measure of the acoustic velocity of an isolated defect and also of the interface profile of a mechanical or metallurgical bond.⁽⁴⁾

CAPABILITIES OF THE SCANNING ACOUSTIC MICROSCOPE

The modes of operation and the key parameters of the scanning acoustic microscope (SAM) employed in this study are listed as follows:

Modes of operation:

	Amplitude
Transmission Mode	Phase
	Confocal
	Nonconfocal

Acoustic lenses: $f/4$ (focal length in water = 4 mm)
Spatial resolution: 30 μm in water at 150 MHz
(confocal)

Field of view for the sample: $3 \times 4 \text{ (mm}^2\text{)}$

Magnification of acoustic images = 35

Total electrical throughput loss (without specimen):
55 db

Dynamic range: 50 to 70 db at 20 dbm input electrical power, depending on the specimen.

DIAGNOSIS AND CHARACTERIZATION OF HYBRID
MICROELECTRONIC COMPONENTS

The findings on three types of hybrid microelectronic components are now discussed:

Thin-Film Circuits - Defects which result from contaminants and blisters introduced during the fabrication process greatly affect the resistance, adhesion, and solderability of the thin-film circuits. Figures 2(a), (c) show the acoustic micrograph and the amplitude profile of a thin-film resistor (Fig. 2(b) for its cross-sectional view). The defects and the nonuniformity of the multilayer structure are clearly seen. Figure 2(c) shows a differential amplitude variation as large as 30 db.

Thick-Film Circuits - The dark and gray areas in the optical micrographs (Fig. 3(b)) correspond, respectively, to the three individual resistors (100 Ω , 1.3 k Ω , and 500 k Ω) and the conductors of a production-line thick-film circuit (Fig. 3(a)). The acoustic micrographs (Fig. 3(c)) show a high degree of contrast as a function of resistance values. Specifically, a differential attenuation of 43 db is observed between the 100 Ω and the 500 k Ω resistors. Some defects in the form of inclusions are also observable in the resistor and circuit-free regions.

Multilayer Chip Capacitors - The defects referred to in the Introduction are potential causes for a leaky capacitor, and end metallization of poor quality is often a sufficient cause for open-circuit failure.⁽⁵⁾ Figure 4(a) is an example of a faulty end metallization (dark stripes designated as L) in a production-line ceramic chip capacitor (Fig. 4(b)). Figure 5(a) is another capacitor which shows two areas of delamination together with some voids (see Fig. 5(b) for its optical image).

A definitive identification of the above defects was facilitated by comparing the detected signal levels with the noise level. Since the detected signals were buried in noise, the defects should be of the "void"-type. For an "inclusion"-type defect, however, the detected signal level was found to be substantially above the noise level.

The last example, also involving a production-line chip capacitor, serves to demonstrate that the SAM is capable of determining not only defect location (in three dimension) but also defect type. Figures 6(a) to 6(c) show a series of acoustic micrographs obtained for the capacitor shown in Figure 7. Figure 8(a) indicates that area (2.2) is defect-free. However, for area (1.1), there is an "inclusion"-type defect at the depth designated by P since the minimum detected signal (-54 dbm) is well above the noise level. Figure 8(b) shows two "void"-type defects located at different depths A and B since the detected signals are at the same level as noise.

CONCLUSION

We conclude that the transmission SAM operating at several hundred megahertz range is a highly useful technique for nondestructive diagnosis and characterization of thick hybrid microelectronic components.

ACKNOWLEDGEMENTS

Support from the Materials Research Laboratory Section, Division of Materials Research, National Science Foundation under Grant No. DMR72-03297-A03 is gratefully acknowledged.

REFERENCES

1. R. A. Lemons and C. F. Quate, "Acoustic Microscope - Scanning Version," Appl. Phys. Lett., 24, 163 (February 1974).
2. C. S. Tsai, J. K. Wang and C. C. Lee, "Imaging and Characterization of Thick Production-Line Microelectronic Components Using Transmission Acoustic Microscopy," Proceedings of the ARPA/AFML Review of Progress in Quantitative NDE, Report AFML-TR-78-205, Jan. 1979, pp. 257-262.
3. J. K. Wang, C. C. Lee, and C. S. Tsai, "Non-destructive Diagnosis of Thick Production-Line Microelectronic Components Using Transmission Acoustic Microscope," 1978 International Electron Devices Meeting, Technical Digest, pp. 449-451, IEEE Cat. No. 78CH1324-3ED.
4. S. K. Wang, C. C. Lee and C. S. Tsai, "Non-destructive Visualization and Characterization of Material Joints Using a Scanning Acoustic Microscope," 1977 Ultrasonic Symposium Proceedings, pp. 171-175, IEEE Cat. No. 77CH1264-TSU; C. C. Lee, J. K. Wang, S. K. Wang, P. Hower and C. S. Tsai, "Detection and Characterization of Alloy Spikes in Power Transistors Using Transmission Acoustic Microscopy," to appear in the Proceedings of First International Symposium on Ultrasonic Materials Characterization, National Bureau of Standards, Maryland, June 7-9, 1978.

5. T. F. Brennan, "Ceramic Capacitor Insulation Resistance Failures Accelerated by Low Voltage," IEEE Trans. on Electron Devices, ED-26, pp. 102-108, January 1979.

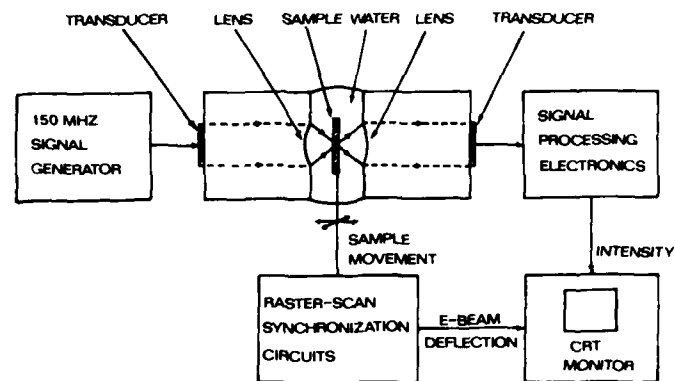


FIG.1
BLOCK DIAGRAM OF A TRANSMISSION SCANNING ACOUSTIC MICROSCOPE

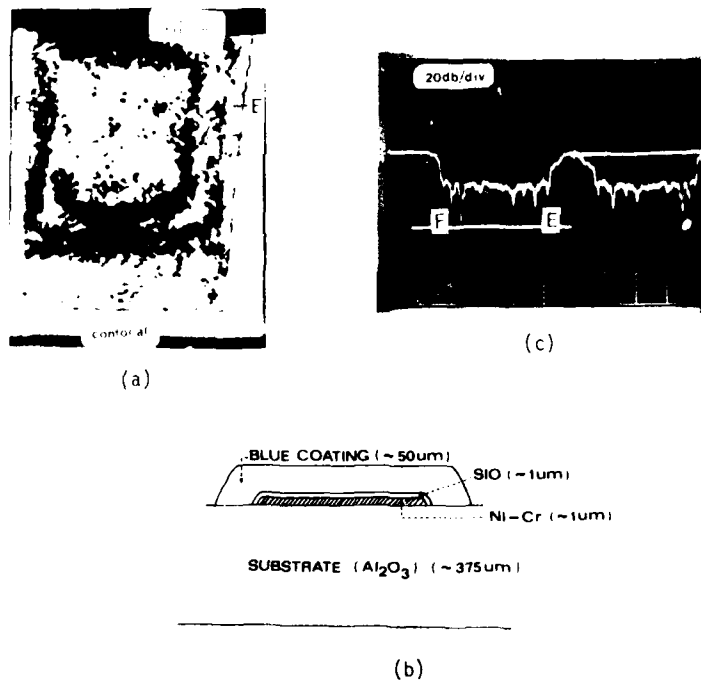


Fig. 2 Imaging of a Thin-Film Chip Resistor
(a) Acoustic Micrograph
(b) Cross-Sectional Sketch of the Multilayer Structure
(c) Acoustic Amplitude Variation Along Line EF

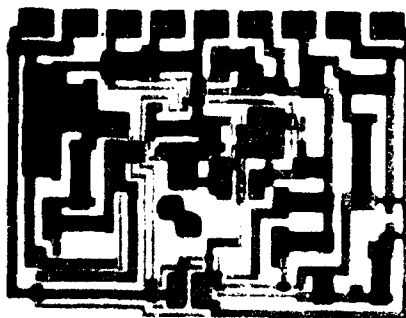


Fig. 3(a) Optical Micrograph of the Production-Line Thick Film Circuit (Thickness: 30 mils) (3.2 X)

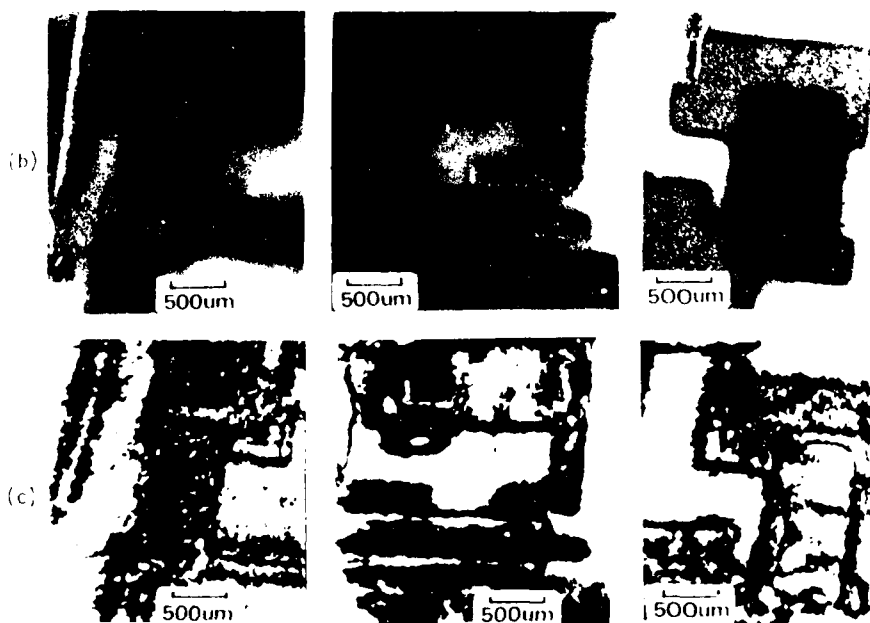


Fig.3(b) Optical Micrographs for Three Resistors (100 Ω , 1.3 K Ω , and 500 K Ω : From Left to Right)

3(c) The Corresponding Acoustic Micrographs Depicting High Degree of Contrast



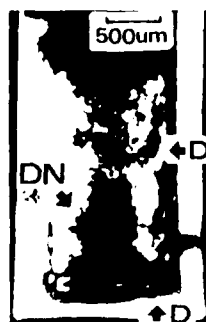
(a)



(b)

Fig. 4(a) Acoustic Micrograph of a Chip Capacitor Showing the Faulty End Metalizations in the Form of Stripes Designated by L

4(b) Optical Micrograph



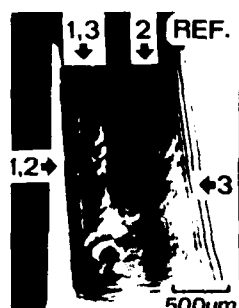
(a)



(b)

Fig. 5(a) Acoustic Micrograph of Part of a Chip Capacitor Showing One of the Areas of Delamination Designated by DN, and Voids by D

5(b) Optical Micrograph Showing the Particular Cross Section Where Two Areas of Delamination are Located (Local Brighter Areas)



(a)



(b)



(c)



(d)

Fig. 6 Acoustic Micrographs of a Production-Line Chip Capacitor (Thickness: 27 mils)

(b) and (c) Obtained by Displacing the Capacitor Along the Lens Axis by 20 and 40 mils, Respectively, From the Capacitor Position of (a)

(d) Obtained After the Capacitor was Heated at 100°C for 80 Minutes

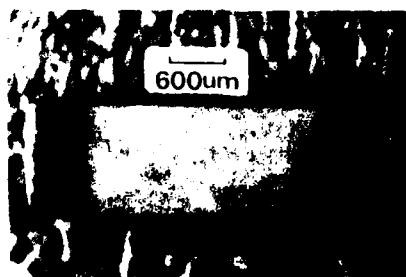


Fig. 7 Photograph of a Production-Line Chip Capacitor (Thickness: 27 mils)

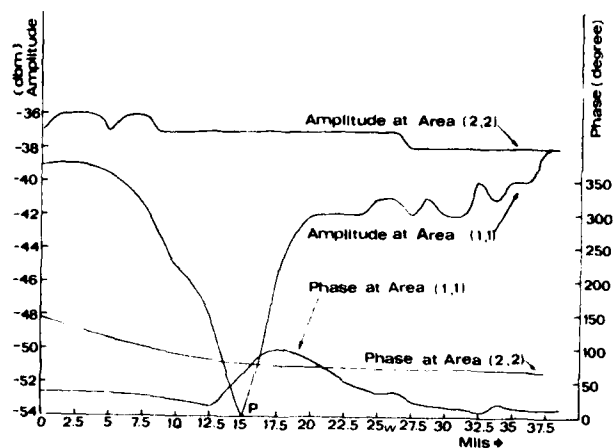


Fig. 8(a) Measured Amplitude and Phase of Transmitted Acoustic Signals as the Chip Capacitor was Translated Along the Lens Axis - An "Inclusion" is Shown to Exist in Area (1,1) at Depth P

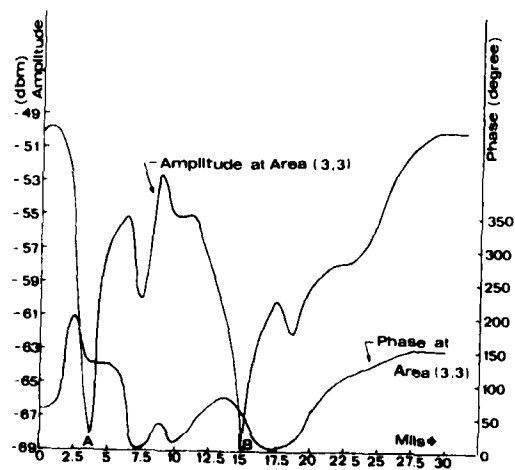


Fig. 8(b) Amplitude and Phase of Transmitted Acoustic Signal (Measured at a Fixed Position of the Chip Capacitor) as the Capacitor was Translated Along the Lens Axis - "Voids" are Shown to Exist at Depths A and B

NONDESTRUCTIVE SUBSURFACE IMAGING WITH THE
REFLECTION ACOUSTIC MICROSCOPE

R. D. Weglein
Hughes Research Laboratories
Malibu, California 90265

and

D. A. Bergren
Hughes Aircraft Company
Culver City, California 90230

ABSTRACT

The Reflection Acoustic Microscope, operating at a microwave frequency near 400 MHz, has been used to image and examine subsurface detail in a multilayer ceramic chip capacitor (MCCC). Bulk examination of the 0.9 mm thick MCCC is at present not possible with this high resolution acoustic microscope because of the short depth of focus of the particular lens designed for the system and because of the short wavelength ($\lambda = 4 \text{ m}$).

However, the interdigitally layered structure of the ceramic-metal capacitor permits the subsurface examination of either a metallic or ceramic layer, once the surface coating has been physically removed. Acoustic micrographs, obtained in the scanning mode of the acoustic microscope under these conditions, were analyzed for subsurface defects in the acoustically exposed layers. Comparison was made with optical images of the same area after removal of an optically opaque 15 μm thick layer by planar surface grinding.

Finally, the Acoustic Material Signature (AMS)⁽¹⁾ mode was used to interpret the observed contrast reversals in these images. Periodic image contrast reversal occurred as the specimen was translated axially from the focal plane toward the acoustic lens. The period of this transducer output voltage variation has been shown to be proportional to the square of the Rayleigh velocity in the region near the surface.⁽¹⁾ Thus, this measurement may be used to obtain information of the elastic properties in this surface region. The small surface area required for this measurement permits the surface to be characterized elastically with good lateral resolution.

1. R. D. Weglein, "A Model for Predicting Acoustic Material Signature." Appl. Phys. Letters, Vol. 34, No. 3, 1 Feb. 1979, pp. 179-181.

A COMPARISON OF ACOUSTIC MICROSCOPY, IMAGING, HOLOGRAPHIC AND TOMOGRAPHIC PROCEDURES

C. F. Quate
Edward L. Ginzton Laboratory
Stanford University, Stanford, California 94305

ABSTRACT

In this paper we offer our view on the various systems that are used or should be used in the field of NDE. We conclude that imaging systems evolve around a given form of radiation and that a given imaging system is not easily adapted to an alternate form.

INTRODUCTION

Imaging can be defined as a system for making the invisible visible. Optical waves are magnificent and optical imaging is the cornerstone. However, these cannot be used for the entire spectrum of applications - other forms of radiation must be employed.

The theme that we will follow in this paper starts with the premise that each form of radiation has characteristics which are unique. Each provides us with a form of imaging that allows us to examine selected properties with great clarity. In optics it is phase contrast, or differential interference contrast, that depends upon and exploits the two degrees of polarization. It is holography which exploits the non-linear properties and speed of photographic film and that has now been simplified with Speckle Interferometry. With the Scanning Electron Microscope it is the large depth of focus that gives us the three-dimensional images. With radio waves it is the side-looking radar and with X-rays it is tomography. With acoustic waves it is total internal reflection.

Our continuing theme relates to the great amount of effort that has been spent on the problem of transferring one technique for imaging to another form of radiation. Holography was invented for electron wave imaging and it tried out with X-rays but there was little progress until Leith and Upatnieks¹ realized that the proper radiation for holography was coherent optical waves. The results with ultrasonic holography are not commensurate with the work that has been done in that field. Side-looking radar was invented to exploit the path of a moving airplane.² There is nothing quite like that with other forms of radiation. Tomography is a powerful system for imaging with X-rays.³ That system was invented for the purpose of using waves that travel in straight lines without refraction. It will be futile to try to adapt this to radiation that undergoes strong refraction. Similarly imaging through total internal reflection is unique to acoustic waves⁴ - it will be unprofitable to try to adapt the system to optical waves.

In summary - holography with coherent optical waves works because of the speed and non-linear character of film. Detectors for acoustic energy are linear and much slower. Differential interference contrast in optical microscopes is based on the two modes of polarization with electromagnetic waves.⁵ There is nothing equivalent for acoustic waves in liquids. Tomography is based on the

constant velocity of X-rays and the absence of refraction. The refraction effects for other forms of radiation can be large and the simplicity of tomography is lost. Imaging through total internal reflection works for acoustic waves since the media carrying the energy has a velocity that is much less than the velocity of sound in the object. With optical waves the opposite is true. This unique property of ultrasonic imaging systems has not been fully recognized. Rollins at the Midwest Institute,⁶ Breazeale at Tennessee,⁷ and Andrews and Keightley⁸ at the British Steel Corporation have carried out important work with this system. Hildebrand and Becker⁹ at Battelle have exploited this phenomena in a direct imaging system.

IMAGING AND THE NEED FOR FOCUSING

In this section we will write down some simple, but fundamental, properties of imaging systems in order to establish a few points that we will need in later discussions. The most common and the most often used system for ultrasonic imaging is a simple probe that is moved mechanically to "paint" the image. We can represent this by the schematic of Fig. 1 where we display the diffraction pattern from a plane wave source. With a transducer of diameter D we eventually have a wave diverging with a half-angle θ ($= 1.22\lambda/D$). The beam extends for a distance $L \approx D/2\theta \approx \frac{D^2}{2.44\lambda}$. If we wanted to use this system to probe to a depth of 25 cm (L) with a sound wavelength of 1 millimeter we would require $D \sim 25\lambda$. This determines the resolving power of this imaging system. We see that it is 50 times larger than a perfect system where the resolution can approach $\lambda/2$.

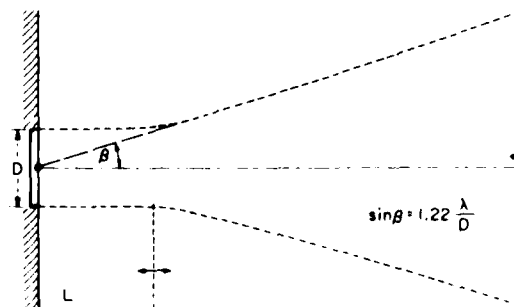


Fig. 1 Beam Contour with a Flat Transducer of Diameter D .

The higher resolution requires that we focus the energy with some kind of lens. The fundamental relations sketched in Fig. 2 where we show a single lens with images two sources spaced apart by a distance d . The minimum value of d is determined by the diffraction patterns of these two point sources in the image plane. The Rayleigh criteria for resolution establishes the minimum angle for the separated points as $1.22\lambda/D$. It is the same angle as the angle of divergence for the plane wave source of Fig. 1. The minimum distance, d , is now given by

$$\frac{1.22\lambda}{D} L$$

But we can see that $D/2L = \sin \theta$ where θ is the maximum angle of acceptance for this lens. It is known as the numerical aperture, N.A. In these terms the resolution as defined by the minimum separation between two resolvable points is given by

$$\frac{0.61\lambda}{\text{N.A.}}$$

This resolving power requires an ideal lens (without aberrations) and a large numerical aperture.

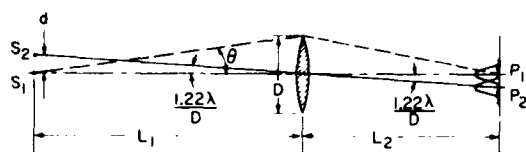
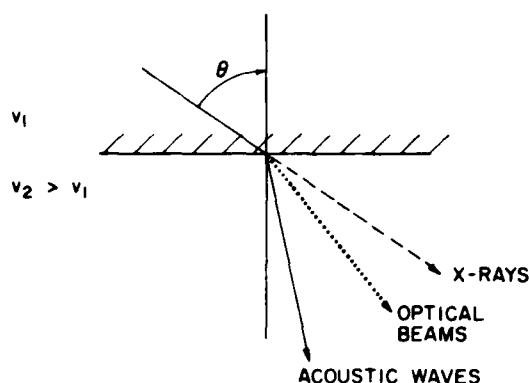
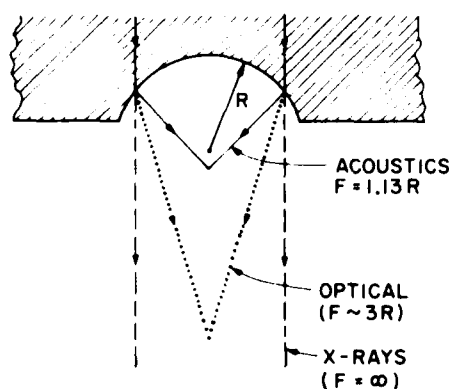


Fig. 2 Minimum spacing, d , is determined by overlap of diffraction patterns P_1 and P_2 . The spacing d must be greater than $\frac{1.22\lambda}{2 \sin \theta} = \frac{0.61\lambda}{\text{N.A.}}$.

In turn, it depends on the refraction of waves at the lens interface. Let us look at that phenomena for three systems of waves, acoustic, optical and X-rays. The refraction angle as determined by Snell's law is determined by the velocity difference at the interface. For acoustic waves at a solid-liquid interface can be as high as 10 to 1. For optical waves a velocity ratio of 2 to 1 is possible but it is more usual to find a ratio of 1.5 to 1. With X-rays there is no velocity difference. All of this is sketched in Fig. 3(a). In Fig. 3(b) we see how this translates into the action of a lens. For acoustic waves the large angle of refraction brings the waves into focus near the center of curvature. For optical waves the focal distance is 3 or 4 times the radius of the lens surface. For X-rays the focal length is infinity (i.e. no focussing). This means that we do not have a lens for X-rays and most X-ray images are mere "shadowgraphs". It is the basic reason that tomography works so well. Optical lens formed with a single spherical surface suffer from a large degree of spherical aberrations and these are overcome with multiple surfaces in compound lens. A small acoustic lens with a single surface is free from aberrations and this is the basic reason that the scanning acoustic microscope works so well. At low frequencies where we need a longer reach for the beam the lens must necessarily be large. This increases the aberrations and



(a)



(b)

Fig. 3 Refraction and focusing for three forms of radiation.

makes it difficult to put in motion. The preferable solution is electronically scanned arrays. There are two points that I would like to raise in connection with scanned arrays and acoustic imaging. The arrays that I am familiar with control the phase of the electrical signal feeding each element - often with a continuous variation of phase. It is not necessary to use a continuous variation - discrete steps of 22.5° will do the job. For this we only need four elements in series (1) $\Delta\phi_1 = 22.5^\circ$, (2) $\Delta\phi_2 = 45^\circ$, (3) $\Delta\phi_3 = 90^\circ$ and (4) $\Delta\phi_4 = 180^\circ$. This simplifies the problem in microwave systems. If we think about it there may be a way to use this to simplify the phase shifting networks for acoustic arrays. We should also give consideration to a phase shift in the acoustic element rather than the electrical side. My intuition tells me that this may give us a cleaner system. Finally, I would suggest that we move away from the flat ends on the array elements and use domed rods. The advantage of the spherical dome is that it would generate a spherically diverging wave at the position of the array and ensure a wide coverage angle from each element. In summary, an array where the phase shift is introduced into the acoustic path consisting of a series of rods placed on a hexagonal grid and with spherical domes at the liquid interface

should be investigated. The sketch of Fig. 4 outlines the overall system.

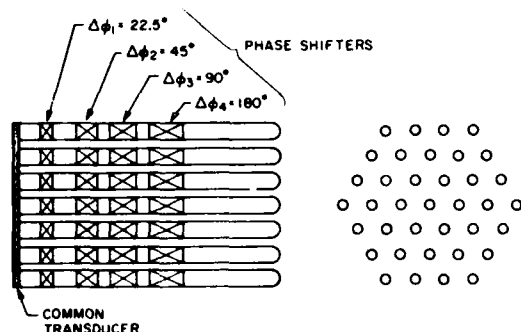


Fig. 4 Proposal for domed hexagonal array with discrete acoustic phase shifters and a common transducer.

TOMOGRAPHY

Tomography is a method for reconstructing the image from a series of linear scans. It has been used successfully by Bracewell^{12,13} using microwave radiation traveling through outer space and by Hounsfield using X-ray beams in the human body.³ In both cases the radiation travels in straight lines with refraction. It is used in these two cases to map a single parameter - the emission of microwaves from the region of the sun and the density of material in the human body. In neither case is it possible to focus the radiation and measure these parameters point-by-point. The principle is quite simple and we use a two-dimensional rectangular array to illustrate the process. In Fig. 5 we illustrate a 3 X 3 grid of discrete points with differing densities. The X-ray beam is in the form of a pencil. When it is positioned along the first row it will suffer a change in intensity, ΔR_1 , which is proportional to the sum of $\rho_{11} + \rho_{12} + \rho_{13}$. The beam traveling along the second row will undergo a change

$$\Delta R_2 = \rho_{21} + \rho_{22} + \rho_{23}$$

and along the third row

$$\Delta R_3 = \rho_{31} + \rho_{32} + \rho_{33}$$

We next rotate the beam and let it travel along the column to obtain

$$\Delta C_1 = \rho_{11} + \rho_{21} + \rho_{31}$$

$$\Delta C_2 = \rho_{12} + \rho_{22} + \rho_{32}$$

$$\Delta C_3 = \rho_{13} + \rho_{23} + \rho_{33}$$

For a 45° degree rotation it travels along the diagonal with a change

$$\Delta D_1 = \rho_{11} + \rho_{22} + \rho_{33}$$

Other rotations will give other sums. It is easy to convince oneself that the separate values of ρ_{11} through ρ_{33} can be unraveled from all these.

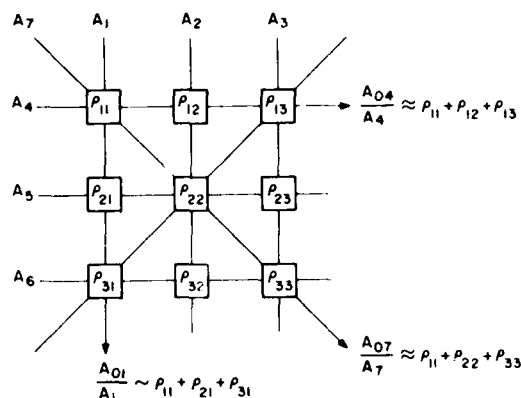


Fig. 5 Sketch of a simple system for tomography. By measuring the A_{01} through A_{0n} one can find the individual values of ρ_{nm} .

The problem becomes complex for a real imaging problem such as a cross-section of the human head. We don't have nine values of ρ but more like 10,000 or 100,000. For that we need the computer. Hence the name Computer Aided Tomography (CAT). It is a very striking system and it has made an enormous impact on the medical profession.¹⁴ Will it have a similar impact with systems based on other forms of radiation such as ultrasound? My answer is "No, it will not."

The reasoning is not complicated - tomography serves a grand purpose when the effects of diffraction are absent. Furthermore, X-rays can be collimated and they will travel for a great distance without spreading. For example, with a beam 1 mm in diameter the path length before appreciable spreading takes place, as worked out previously, is D^2/λ . For a 1 mm diameter and a 10 nm wavelength this distance turns out to be

$$10^{-6}/10^{-9} = 10^3 \text{ mtrs} = 1 \text{ Km.}$$

Bracewell¹² worked with diameter D equal to 1000λ and a wavelength of 10 cm. His beam maintained its pencil shape for 100 Km. On the other hand, acoustic beams with a 1 mm wavelength would begin to spread immediately from a source 1 mm in diameter. From a source 1 cm in diameter the acoustic beam would travel only 10 cm before spreading. It is even worse since most objects - such as the human head, or complex materials - have large changes in the acoustic velocity. The media is inhomogeneous for sound waves. There the conceptual simplicity of tomography is lost. I doubt that we will ever see an ultrasonic system based on tomography. On the other hand, I would expect a more widespread use for X-ray tomography in NDE. The virtues there will be pointed out by Morris, Kruger and Wecksung at this session.

HOLOGRAPHY AND SPECKLE INTERFEROMETRY

Holography both optical and ultrasonic - preserving as it does both the phase and amplitude of the scattered waves - is so well known that it is not necessary to describe that system here. In any event, it has been done in a recent article by Campbell and McLachlan.¹⁵ Speckle interferometry

is important to NDE in that it may find more widespread use than holography. "The speckle pattern, caused by the random interference of light scattered from various depths on the object surface (assumed to be rough) acts as a grid naturally printed on the object surface" (Hung, p. 51).¹⁶ In a sense it thus serves the same purpose as the pattern used in the moire technique. "Speckle photography offers a comparatively easy method of separating the various displacements from a complex distorting structure, simplifying the process as compared with the fringe information of holographic interferometry" (Gregory, p. 184).¹⁷ Interferometers based on speckle are primarily used to monitor vibrations and map nodal lines where the nulls in the vibration modes exist. As such these instruments have been used for crack detection, pressure vessel inspection and composite material inspection. The system holds some advantages over holographic techniques. It does not appear to have found application in ultrasonic systems. Again I suspect that it will turn out to be uniquely suited for coherent optical beams. The working space for such beams can be extended and this permits the inspection of large structures. Further the wavelength near 0.5 micrometers compares favorably with the surface roughness on many objects. Ultrasonic waves with 1 mm wavelength would not enjoy this advantage.

ULTRASONIC MICROSCOPY

We come now to the subject of microscopy. In one sense it can be viewed as a scaled version of imaging as discussed previously. But, there are two characteristics that distinguish it from the imaging at low frequencies and qualify it for inclusion as a separate section. First, the ideal lens consisting of a spherical cavity produces a diffracted limited beam with a beam diameter that is less than one wavelength. The manner in which this can be exploited to form an image with mechanical scanning has been illustrated with the mounts in the poster session. The second, and equally important, is the fact that in reflection imaging with spherically converging waves we encounter the phenomena of total internal reflection (TIR). This is quite unique to acoustic systems. I would hope that it could be used over a much wider front in acoustic systems.

We can begin with some early work of Rollins.⁶ He studied the reflection of acoustic waves from a plane surface of copper as a function of the angle of incidence. As the angle increased he encountered the usual critical angles as first the longitudinal wave in the solid moved parallel to the interface. Beyond this he encountered the critical angle for shear waves and near there he found that the excitation of Rayleigh waves along the interface would strongly influence the reflected signal (Fig. 6). Rollins pointed out that the critical angle for Rayleigh waves was sensitive to the parameters of the two materials forming the interface. He also showed that changes in these parameters by whatever means could be monitored by studying the variation in the critical angle as determined by the variations in the reflected signal (Fig. 7). Breazeale⁷ in a subsequent article analyzed the reflection of a Gaussian beam incident at the critical angle for Rayleigh waves. He observed that the shape of the reflected beam was dependent upon the nature solid material at the interface - that reflection from a water steel

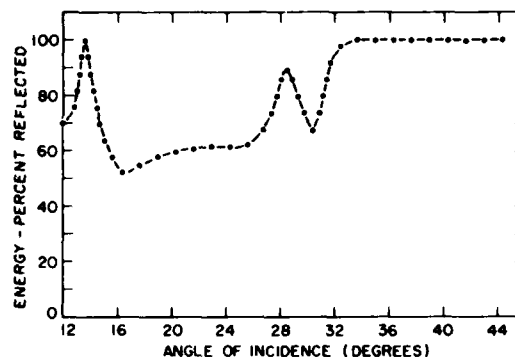


Fig. 6 The reflection versus incident angle from a water-aluminum interface. (Rollins⁶)

interface generated a reflected beam with a cross-section that differed from that of a beam reflected from a water-brass interface. Breazeale was primarily interested in the phenomena of "Schoch" displacement where the reflected beam was actually displaced or translated from the point of contact for the incident beam. The effect is named after Arnold Schoch who first observed it.¹⁸

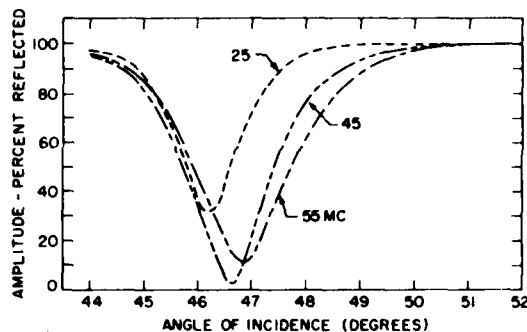


Fig. 7(a) The reflection near the critical angle for electrolytic copper. (Rollins⁶)

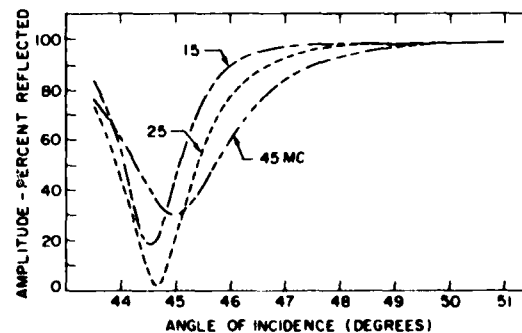


Fig. 7(b) Reflection near the critical angle for the copper of Fig. 7(a) after heat treating (600°F) and quenching in water.

The people at the British Steel Corporation have used this technique to good advantage with a real instrument. Andrews and Keightley⁸ have built

the apparatus sketched in Fig. 8. It has a source for the incident acoustic beam and a receiver for the reflected beam. The device is made such that the angle of the receiving transducer as measured from the normal is equal to the angle of the incident beam. The transducers are moved in a way that maintains this equal relationship between the two elements as the angle of incidence is varied to accommodate variations in the critical angle for the Rayleigh wave. This variation can arise from either of two causes - a change in the material parameters or a change in the level of stress. The curves of Fig. 9 and Fig. 10 show the quantitative relationship as presented in their paper. They used the technique to monitor levels of stress in sheet steel but there radiography with X-ray appears to be a faster technique. They have found it to be an important instrument for measuring compositional changes and case hardening. In my opinion this system is worthy of a great deal of study.

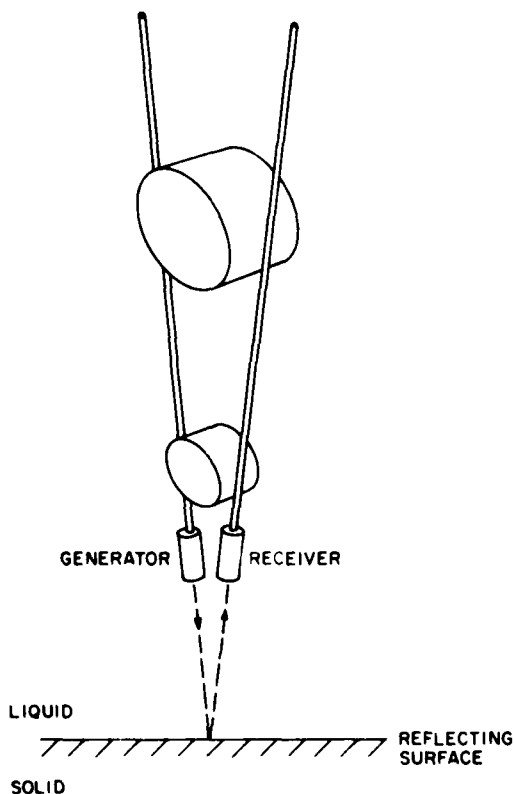


Fig. 8 Critical angle goniometer. (Andrews and Keightley⁸)

With this background, I believe the next logical step is to replace the mechanical scanning goniometer with electronic scanners. The most obvious comes not from arrays, but from Shaw's¹⁹ idea of converting surface waves to traveling bulk waves. The beauty of this system is that the angle can be precisely controlled with the frequency. The elegance, the simplicity of this system, all argue that it will one day come into use as an instrument in NDE. The basic proposal for adapting the Grating Acoustic Scanner for TIR is sketched in Fig. 11. I suspect that EMATS could be designed to

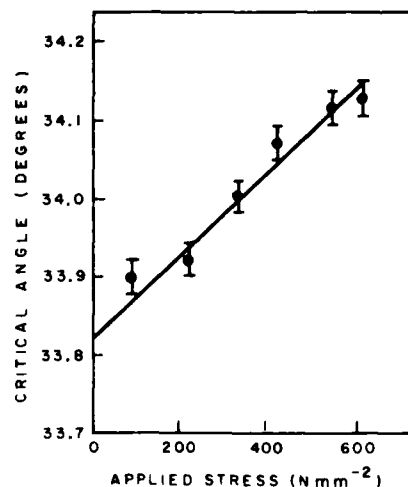


Fig. 9 Variation in critical angle with stress in steel. (Andrews and Keightley⁸)

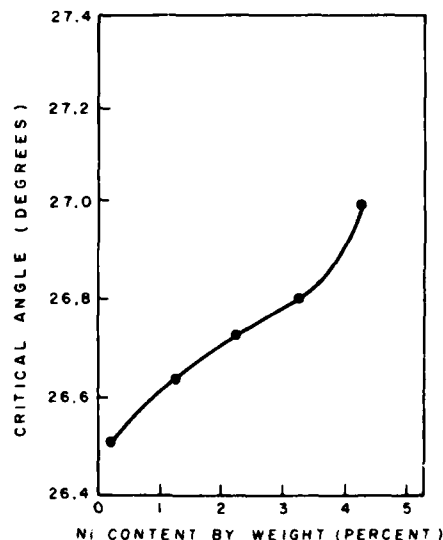


Fig. 10 Variation in critical angle with composition of steel. (Andrews and Keightley⁸)

operate in a mode that is quite analogous to this. In any event, it is important to study the phase shifts of the reflected wave when the waves in the solid are changed from propagating waves to evanescent waves.

Total internal reflection is important since it is unique to acoustic radiation. It does not occur in optical systems. The reason is straightforward. In many optical systems the region between the lens and the object is a fast medium and the object itself is a slower medium. The optical ray is refracted toward the normal as it enters the object. The system (with total internal reflection) has been used by McCutchen²⁰ in a modified optical microscope where the light traveled through oil and a cover slip is common before reaching the object but its use has been limited. We can also simulate the

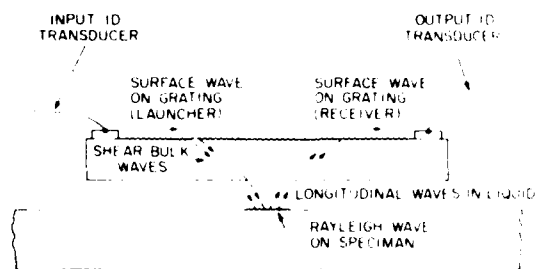


Fig. 11. Proposal for a critical angle acoustic scanner for examining surfaces. It is modelled from the Grating Acoustic Scanner. (Shaw¹⁹)

effect with guided optical waves and Tien has done just that.²¹ He used optical beams that were confined to a surface. The surface was coated with a dielectric film of differing thickness such that the wave velocity in one guide is slower than it is in the other. With the input beam incident at the proper angle the translation along the interface is larger than the beam diameter. The reflected beam is well separated from the incident beam as seen in Fig. 12.



Fig. 12. The remarkable reflection properties of a guided optical beam at the boundary between two dielectric waveguides. (Tien²¹)

In acoustic systems we need not resort to these artificial constructions. This phenomenon is naturally occurring at a liquid-solid interface when the wave is incident from the liquid. In that situation the wave is bent toward the interface as it enters the solid. The refraction is so strong that the angle between the tilt and the normal for total internal reflection is easily met. The critical beam used in a mirror is perpendicular to the surface. This means that a large part of the beam undergoes total internal reflection. Important as all of this is, the phase shift between that part of the beam inside the critical angle and that part outside of the critical angle. The relative phase shift promises to become important near the critical angle for whatever reason we care to choose. The details of the details of how this work are part of the interesting field of work we are going to explore.

The "phase" character of this system of images may not be evident in the images themselves as recorded by scanning the object through the transverse coordinates. But it is clear when we study the variation in the reflected signal when the object is moved axially along the beam axis toward the lens. A display of this type is shown in Fig. 13 for three different materials - YAG, Si, and Ag. The periodicity of this curve which appears when the object is moved in from the focal point yields information on the elastic coefficients. A plot of this periodicity for various materials has been published by Weglein²⁴ and analyzed by Atiles²⁵ with the results of Fig. 14. Another form of this display is shown in Fig. 15 which is a simple object consisting of a chrome strip on glass. Some of you may recognize this as the central component of a mask for integrated circuit technology. The curve of reflectance versus lens-object separation is here displayed in a two-dimensional plot where the change in periodicity with the addition of the chrome layer is clearly revealed.

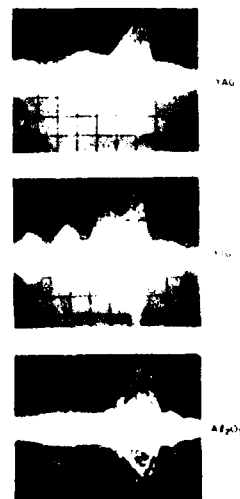


Fig. 13. Lens exposures of the dependence of the returning phase on the distance between the sample and lens in various. Envelope shows envelope for different materials. (Weglein²⁴)

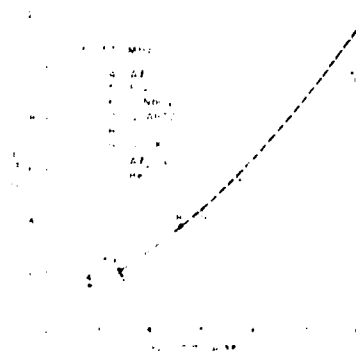


Fig. 14. The periodicity of the returning phase as a function of the distance between the sample and lens in various. (Weglein²⁴)



Fig. 15 Acoustic images of a chrome strip on glass. (a) and (b) are images in the x-y plane for two focal positions. Central image is a single scan line (horizontal) as a function of the lens sample spacing.

The type of periodicity, or interference if you will, can be explained by the phase shift that takes place across the critical angle. But there are interference lines of a much finer structure in some of these displays. This comes from a separate source - the energy that moves back and forth between the transducer and the lens. It is a result of residual reflection at the lens surface and its phase does not vary as the object spacing is varied. Although it is small it can be equal to the signal from the object. With this strong interference fringes can be recorded. The optical and acoustic images of Fig. 16 and Fig. 17 clearly show this. The optical image was taken with an interference reflection microscope. Again, this is to be distinguished from the phase shifts associated with the critical angle. Those permit us to record twin boundaries and grain boundaries in the acoustic images - boundaries that are not evident optically. In the illustration of Fig. 18 this effect can be seen in a surface of polished copper.

SUMMARY

Imaging with acoustic waves is unique in many ways. We should concentrate more effort in these areas where it is unique. The EMT transducers is a clear example.²⁵ The scanned arrays and the conversion to surface waves at a liquid-solid boundary is another.¹⁹ The photoacoustic scanning of surfaces is a third.²⁶ We should focus more effort on complex shapes - the turbine blades - the holes that are covered with rivet heads. There I think we can progress. In more simple geometry such as the inspection of flat steel plates we will probably lose out to radiography with X-rays as in the example cited with the British Steel Corporation. Tomography with X-rays should be exploited on a

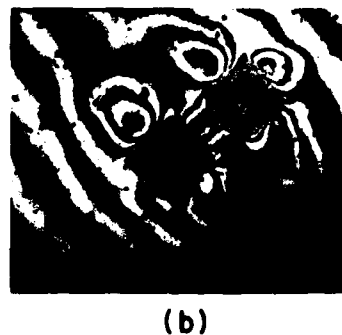
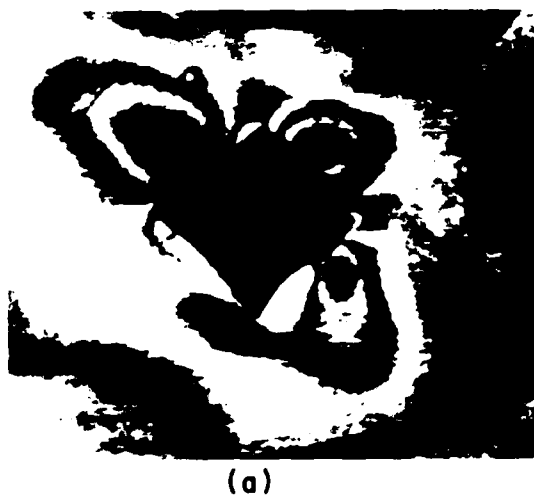


Fig. 16 Acoustic (a) and optical (b) interference patterns for a sample of brass. This is a result of surface contour near the diamond indent.



Fig. 17 Acoustic (a) and (b) and optical (c) interference patterns for a sample of brass. It is similar to Fig. 16.

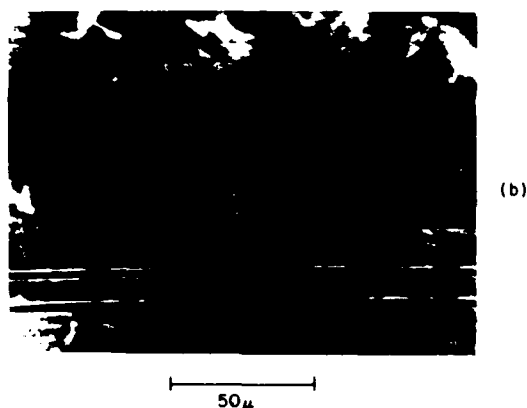
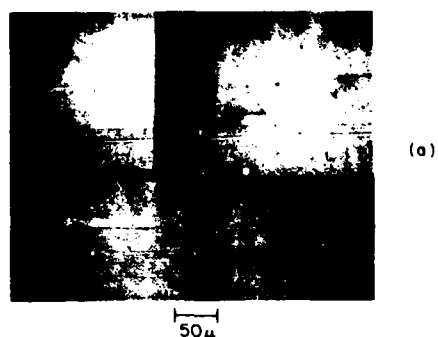


Fig. 18 (a) Optical and (b) acoustic (1100 MHz) images of a copper surface.

much wider base. It is uniquely suited to X-radiation which travels without refraction and is sensitive to one and only one parameter - mass density. We should not try to adapt this system to ultrasound. There are much more profitable areas to study. Holography is ideal for optical waves - it is fast - large areas can be explored - stop-action images can be easily recorded. This permits us to study minute changes that take place between successive shots.¹⁵ Holography is not a mode well suited for ultrasound. We should carefully limit our work there. Primarily because there are important areas that need more and still more effort. Surface wave effects, total internal reflection with evanescent waves, and the combination found in photoacoustics are areas where acoustic radiation is superior.

ACKNOWLEDGEMENT

This work was supported by the Advanced Research Projects Agency of the Department of Defense and monitored by the Air Force Office of Scientific Research under Contract No. F49620-78-C-0098.

REFERENCES

1. E. N. Leith and J. Upatnieks, "Wavefront Reconstruction with Continuous-Tone Objects", *J. Opt. Soc. Am.* **53**, 1377-1381 (December 1963).
2. H. Jensen, L. C. Graham, L. J. Porcello and E. N. Leith, "Side-Looking Airborne Radar", *Sci. Am.* **237**, 84-95 (October 1977).
3. G. N. Hounsfield, "Computerized Transverse Axial Scanning (Tomography): Part 1. Description of System", *Brit. J. Radiol.* **46**, 1016-1022 (November 1973).
4. A. Atalar, C. F. Quate and H. K. Wickramasinghe, "Phase Imaging in Reflection with the Acoustic Microscope", *Appl. Phys. Lett.* **31**, 791-793 (15 December 1977).
5. J. Padawer, "The Nomarski Interference Contrast Microscope", *Royal Microscopical Soc.* **88**, 305-316 (June 1968).
6. F. R. Rollins, Jr., "Ultrasonic Reflectivity at a Liquid-Solid Interface near the Angle of Incidence for Total Reflection", *Appl. Phys. Lett.* **7**, 212-214 (15 October 1965).
7. M. A. Breazeale, L. Adler and G. W. Scott, "Interaction of Ultrasonic Waves Incident at the Rayleigh Angle onto a Liquid-Solid Interface", *J. Appl. Phys.* **48**, 530-537 (February 1977).
8. K. W. Andrews and R. L. Keightley, "An Ultrasonic Goniometer for Surface Stress Measurements", *Ultrasonics*, **16**, 205-209 (September 1978).
9. B. P. Hildebrand and F. L. Becker, "Ultrasonic Holography at the Critical Angle", *J. Acoust. Soc. Am.* **56**, 459-462 (August 1974).
10. D. O. Reudink and Y. S. Yeh, "A Scanning Spot-Beam Satellite System", *Bell Sys. Tech. J.* **56**, 1549-1560 (October 1977), also, B. Glance, "A Fast Low-Loss Microstrip p-i-n Phase Shifter", *IEEE Trans. Microwave Theory Tech.* **MTT-27**, 14-16 (January 1979).
11. R. M. Mersereau, "The Processing of Hexagonally Sampled Two-Dimensional Signals", *Proc. IEEE*, **67**, 930-949 (June 1979).
12. R. N. Bracewell and A. C. Riddle, "Inversion of Fan-Beam Scans in Radio Astronomy", *Astrophys. J.* **150**, 427-434 (November 1967).
13. R. N. Bracewell, "Strip Integration in Radioastronomy", *Aust. J. Phys.* **9**, 198-217 (1956).
14. R. Gordon, G. T. Herman and S. A. Johnson, "Image Reconstruction from Projections", *Sci. Am.* **233**, 56-68 (October 1975).
15. J. M. Campbell and E. H. McLachlan, "Holographic Non-Destructive Testing", *Brit. J. Non-Destructive Testing*, **21**, 71-75 (March 1979).
16. Y. Y. Hung, *Speckle Metrology*, R. K. Erf, Editor, Academic Press, New York (1978), Chap. 4.
17. D. A. Gregory, *Speckle Metrology*, R. K. Erf, Editor, Academic Press, New York (1978), Chap. 8.

18. L. M. Brekhovskikh, Waves in Layered Media, R. T. Beyer, Editor, Academic Press, New York (1960), p. 107.
19. A. Ronnekleiv, H. J. Shaw and J. Souquet, "Grating Acoustic Scanners", Appl. Phys. Lett. 28, 361-362 (1 April 1976).
20. C. W. McCutchen, "Optical Systems for Observing Surface Topography by Frustrated Total Internal Reflection and by Interference", Rev. Sci. Instr. 35, 1340-1345 (October 1964).
21. P. K. Tien, "Integrated Optics and New Wave Phenomena in Optical Waveguides", Rev. Mod. Phys. 49, 361-420 (April 1977).
22. V. Jipson and C. F. Quate, "Acoustic Microscopy at Optical Wavelengths", Appl. Phys. Lett. 32, 789-791 (15 June 1978).
23. A. Atalar, "An Angular-Spectrum Approach to Contrast in Reflection Acoustic Microscopy", J. Appl. Phys. 49, 5130-5139 (October 1978).
24. R. D. Weglein, "A Model for Predicting Acoustic Material Signatures", Appl. Phys. Lett. 34, 179-181 (1 February 1979).
25. R. B. Thompson, "A Model for the Electromagnetic Generation of Ultrasonic Guided Waves in Ferromagnetic Metal Polycrystals", IEEE Trans. Sonics and Ultrasonics SU-25, 7-15 (January 1978).
26. H. K. Wickramasinghe, R. C. Bray, V. Jipson, C. F. Quate and J. R. Salcedo, "Photoacoustics on a Microscopic Scale", Appl. Phys. Lett. 33, 923-925 (1 December 1978).

SUMMARY DISCUSSION
(C. Quate)

- Bob Addison (Rockwell Science Center): You indicated you could say something about the adhesion of the chrome by that technique. Can you say any more about that?
- C. Quate: We have been given chrome that has four enduring layers, and this periodicity changes, the contrast will change as the adhesion changes. So, the reflection, the critical angle depends very much on how you adhere the film to the substrate. It's very easy to measure, correlate your search.
- B. Hildebrand (Spectron): I would like to remark that the paper Larry Becker and I did was in 1972. We did exactly that kind of imaging using the 180-phase clip, and we measured differences in hardness, and we drilled a hole up through within one radio wavelength of the surface, and it worked real well.
- C. Quate: That's beautiful. Where is it? Why hasn't it gone on?
- B. Hildebrand: It's in the Journal of Acoustical Society of America. Not much interest was shown.
- C. Quate: Why not?
- B. Hildebrand: I don't know.
- C. Quate: Do you still think it's important?
- B. Hildebrand: Yes, I do.
- C. Quate: I do too. I apologize for missing that reference.

#

DIGITAL SYNTHETIC-APERTURE ACOUSTIC IMAGING SYSTEM

D. Corl, G. S. Kino, D. Behar, H. Olaisen, and P. Titchener
Stanford University
Stanford, California 94305

ABSTRACT

A real-time 32-element synthetic aperture acoustic imaging system has been developed. We can test new ideas for the system by using an acoustic array and carrying out image reconstruction on a computer. Contour plots of simple images are shown to illustrate the resolution (0.4 - 0.5 mm in range and transverse resolution) and sidelobe levels obtained with this synthetic-aperture technique. Rayleigh wave images of surface cracks and holes in metal samples have been obtained and a new type of monolithic edge-bonded acoustic transducer array has been developed for use in Rayleigh wave imaging. A number of techniques for reducing the sidelobe levels and improving the resolution have been investigated. The results obtained with a new 32-tap digital delay line for deconvolving the pulse response of a transducer in real time are described.

INTRODUCTION

This project has as its aim the development of a real-time synthetic-aperture acoustic imaging system for use in nondestructive evaluation. Last year we described a hardware implementation of such a system which makes use of digital electronics in order to obtain real-time images using an 8-element acoustic transducer array and we also described the results obtained with computer reconstruction of images using a 32-element array. Since that time, we have made a number of significant advances which we will describe in this paper.

Our work during the past year has had four main thrusts:

(1) The construction of a second generation synthetic aperture acoustic imaging system. This new system incorporates a number of improvements over our previous system and it is designed to produce real-time images using a 32-element transducer array. This system is currently in the debugging stage, and based on past experience, we expect to obtain our first experimental results in the very near future;

(2) The use of computer processing techniques for displaying quantitative image information. We have recently investigated the use of contour plotting for the display of quantitative image information. This contour plotting technique has been employed to study in detail the point spread function of our imaging system, and in the future, we intend to use this method, as well as other techniques such as pseudo-color images, in order to display quantitative information about actual flaws;

(3) The development of new types of transducers for acoustic imaging. This work is described in greater detail in a companion paper. The technology for constructing reliable high-efficiency broadband transducer arrays for the excitation of bulk waves in water has made considerable progress and we believe that most of the construction difficulties have been overcome. A major breakthrough has been achieved in the design of a new type of transducer array for the excitation of Rayleigh waves in solids, the edge-bonded transducer. Using this edge-bonded transducer array, Rayleigh wave images of both real and simulated flaws in

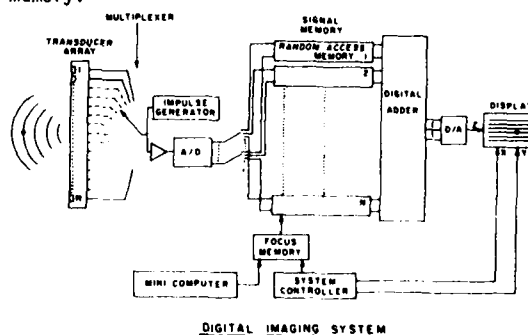
aluminum samples have been obtained;

(4) The demonstration of a real-time programmable filter. We have constructed a 32-tap real-time programmable filter which makes use of a novel digital-analog technique in order to achieve a wide bandwidth (DC to 5 MHz) from a reliable low-cost design. There are a number of potential uses for this filter in acoustic imaging and other signal processing applications, a few of which will be illustrated in this paper.

REAL-TIME IMAGING SYSTEM

Last year we reported the results obtained with our first generation 8-element transducer array hardware system. This year we have constructed a new synthetic aperture acoustic imaging system which is designed to utilize a 32-element transducer array in order to produce real-time images. The theory of synthetic-aperture imaging has been described in detail in our previous paper.¹ Here we will briefly review the basic principles of operation of this system.

A block diagram of the actual hardware system is shown in Fig. 1. This new system incorporates a number of design improvements over our previous hardware system and it contains 80 kilo-bytes of high-speed (50 nsec cycle time) memory as well as all of the electronics required for computer interfacing, display control, and array multiplexing. The memory is partitioned as thirty-two 1 kilo-byte blocks of signal memory and 48 kilo-bytes of focus memory.



The construction of this system has been hampered by delays in the delivery of a number of key components. The system is now completed and we are currently in the process of debugging the circuitry. Based on past experience with our first generation hardware system and our computer reconstruction techniques, we are confident that this new system will perform as expected, and we anticipate obtaining real-time images from this system within the next month.

The operation of this system consists of two phases: the signal acquisition phase and the image reconstruction phase. During the signal acquisition phase, an analog multiplexer selects a single element of the transducer array. This element is excited with an impulse from the impulse generator and an acoustic signal propagates out into the medium. The return echoes are received by that same transducer element, and after passing through the multiplexer and input amplifier, the signal is digitized by a high-speed analog-to-digital converter and stored in a digital memory. This process is repeated for successive elements of the transducer array, with each of the signals being stored in a corresponding memory. During the image reconstruction phase, the focus memory controls the addressing of the signal memories. The outputs of the signal memories are summed together in the digital adder and converted to an analog voltage which modulates the intensity of a raster scanned display in order to produce a two-dimensional image. This entire process is accomplished in approximately 30 msec, with about 10 msec for signal acquisition and 20 msec for image reconstruction, resulting in a frame rate of approximately 30 Hz, well above the rate required for real-time imaging.

COMPUTER PROCESSING

Last year, using our real-time hardware system as well as computer processing techniques, images of wires in a water tank were produced and it was demonstrated that low sidelobe levels could be obtained. As this work has progressed, we have realized that there are serious limitations to the use of intensity display of images obtained from a high-quality imaging system. One problem is the limited grey scale range of an intensity image which makes it difficult to observe a weak reflector in the vicinity of a strong reflector. This method of display also makes it hard to obtain quantitative information about the image, and we expect that as the NDE field progresses, more quantitative information will be required from our images in order to make a better determination of the shape, size and nature of a flaw.

There are a number of simple examples which can be used to illustrate how quantitative measurements can help us interpret the image obtained from a flaw. First, consider a point defect which gives rise to a scattered field that falls off inversely as the distance from the flaw. If the defect has a higher impedance than the surrounding medium, the reflected signal will have the same sign as the incident signal. In the case of a low-impedance defect, such as a void, the reflected signal will be opposite in sign to the incident signal. Now, consider the case of a wave scattered from a crack which is aligned at an angle to the wave so that the specular reflection cannot return to the transducer array. In this case, only the two ends of the

crack are observed and they appear in the image as two isolated points.^{2,3} However, the fields associated with these two radiating points fall off inversely as the square root of the distance from the end of the crack, and furthermore, the scattered signals from the two ends of the crack are of opposite sign. It can be seen that there is quantitative information available from this imaging technique which, if adequately displayed, could be utilized to aid in the interpretation of the images produced.

Accordingly, we have written a contour plotting program which at the present time gives us magnitude plots of an image, but which at a later time might give us plots of both amplitude and phase. This contour plotting technique has proven to be extremely useful in making quantitative measurements of our imaging system performance.

In order to measure the point-spread function of our imaging system, a small (.25 mm diameter) wire was placed in a water tank at a range of 3.2 cm from a 32-element transducer array having a 1.6 cm aperture and a 3.3 MHz center frequency. By using computer reconstruction techniques, images of this wire were produced from both real data and from artificially constructed theoretical data. From these images, a set of contour plots were obtained which show lines of constant amplitude around the wire. Due to space limitations, only two of these plots will be shown. It suffices to say that there were no great differences between the experimental and theoretical plots, which, of course, is very encouraging. The results shown in Fig. 2 were obtained using 32 transducer elements with linear processing, and we see here a 3 dB resolution of .5 mm in the transverse direction, and .4 mm in the range direction. These results are essentially in agreement with the theoretical predictions of about .5 mm resolution in both the range and transverse directions. This contour plot shows the sharp fall-off from the main lobe down to a background sidelobe level of about -24 dB. It is important to note the smooth contours around the main lobe; others have predicted that there might be higher sidelobe levels at a 45° angle to the axis of the array,⁴ but it is apparent from our results that there is no such problem with this system. Figure 3 shows a similar contour plot obtained using the nonlinear processing technique which has been discussed in the past.¹ As described last year, this technique, using square root gain compression, is expected to give a significant reduction in the sidelobe levels. This can be seen quite clearly in the contour plot, with the background sidelobe level reduced to about -36 dB. Again, there is a sharp fall-off from the main lobe and with this nonlinear processing technique, the resolution in both the range and transverse directions is actually somewhat improved over that obtained with linear processing. Knowing that there are no anomalous directions where the sidelobe levels are particularly high, it is convenient to describe the resolution of this system by showing a pair of slices through the point spread function, one in the range direction and one in the transverse direction, as shown in Fig. 4.

With this contour plotting technique, we have been able to obtain accurate measurements of the performance of our imaging system. The sidelobe levels and resolution obtained with this synthetic

aperture technique are far better than those obtained with any comparable imaging system we have worked with in the past, or seen in the literature.

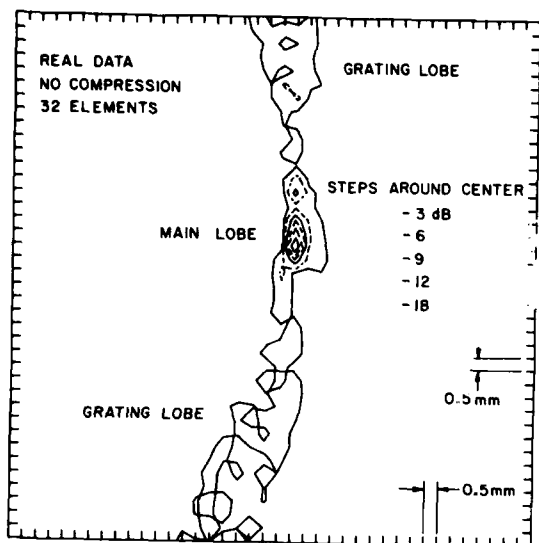


Fig. 2. Contour plot of the image of a small wire obtained with linear processing.

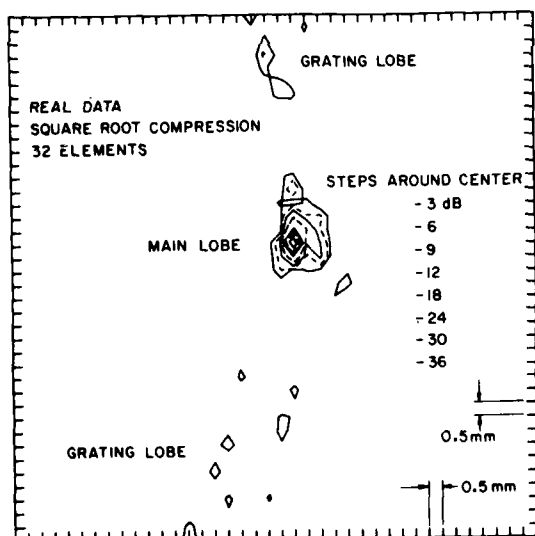


Fig. 3. Contour plot of the image of a small wire obtained with nonlinear processing.

RAYLEIGH WAVE IMAGING

Because of our interest in NDE, we have recently investigated a number of techniques for the excitation of Rayleigh waves (surface waves) in solids. Looking at wires in a water tank, as we have done in the past, is very convenient during the early stages of development of an imaging system, but for NDE applications, we are more likely to be interested in using bulk (longitudinal

and shear) waves in solids or Rayleigh waves, as well as other types of Lamb waves. We have recently developed a new type of array, the edge bonded transducer array, which is a major breakthrough for the excitation of Rayleigh waves and several computer reconstructed images obtained using this array will be shown.

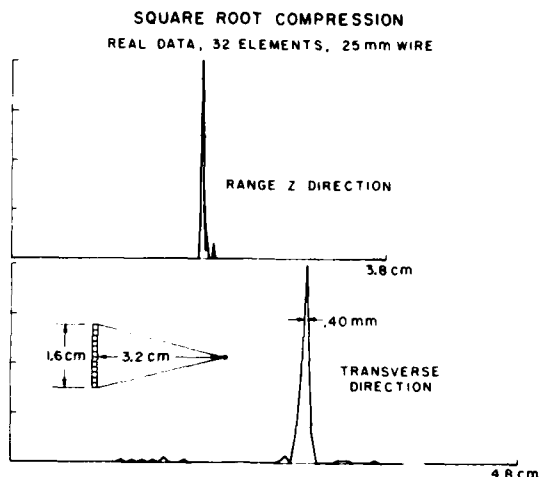


Fig. 4. Range and transverse resolution with nonlinear processing.

Several years ago, Kino and his colleagues developed an acoustic imaging system based on a 2.5 phased array technique which used chirp-focusing. With this system, it was demonstrated that various types of waves, including shear, Lamé, and Rayleigh waves could be excited using mode conversion from a longitudinal wave array and that imaging could be performed using these types of acoustic waves. All of these techniques are applicable to our synthetic aperture imaging system and the wedge coupling technique has been used with our system in order to obtain Rayleigh wave images of both real and simulated flaws in aluminum samples.⁶ One drawback to this technique is that it introduces aberrations due to the compound angles involved, which in turn lead to a degradation in the performance of our imaging system. In the past, this degradation was not noticeable, but as the performance of our imaging systems has improved from a resolution of 2 mm to a resolution of better than 0.5 mm, this effect has become significant.

Therefore, a new type of array, the edge-bonded transducer (EBT) array has been developed to eliminate these problems. This transducer has a number of important advantages over other techniques used for the excitation of Rayleigh waves. First of all, the array is very simple to construct and it gives both high efficiency and broad bandwidth. Secondly, because it is used in a configuration where a Rayleigh wave on a solid substrate excites a Rayleigh wave on a test object of the same material, the EBT array is free from the aberrations introduced by the wedge coupler formerly employed. This is because there is no difference in the acoustic velocity of the two substrates. The array is shown schematically in Fig. 5, and it is described

in detail in a companion paper.⁷ The array is constructed by epoxy-bonding a slab of piezoelectric ceramic onto an aluminum substrate. Thin film electrodes are deposited on the back of the ceramic which is one-half of a Rayleigh wavelength in thickness. The electrodes are approximately one wavelength long in the direction perpendicular to the surface of the substrate; therefore they efficiently excite a Rayleigh wave whose penetration depth is on the order of a wavelength. Each element is approximately one wavelength wide and the individual elements are shielded from one another by ground strips. Our first edge-bonded transducer array has exhibited high-efficiency (7 dB round trip insertion loss), broad bandwidth (about an octave) and wide angle of acceptance ($\pm 35^\circ$). The spurious modes excited by this first array are quite high, but we have already developed a number of techniques for reducing these spurious signals to negligible levels in our future arrays.

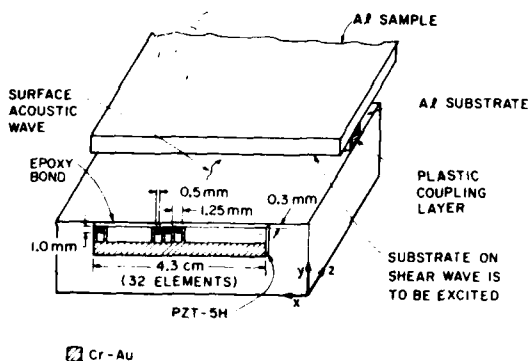


Fig. 5. Edge bonded transducer array.

The edge-bonded transducer array can be used to excite Rayleigh waves in a test sample by placing the test sample on top of the array substrate with a thin strip of coupling material (typically plastic or rubber) placed between them as shown in Fig. 5. The loss in going from one substrate to the other has been measured to be approximately 2 dB, which adds another 4 dB to the round trip insertion loss. Computer reconstructed images of several test objects were obtained using this EBT array. Figure 6 shows an image of four center-punch marks and one drilled hole on the surface of the array substrate. This image was obtained using square root gain compression to reduce the sidelobes from the end of the block. Three of the defects show up quite clearly, while the last two defects are difficult to see amidst the clutter from the end of the substrate. Figures 7 and 8 show images obtained using the EBT array to look at an electron discharge machined (EDM) slot in a separate test sample. In Fig. 7, the slot was placed parallel to the transducer array and it shows up quite clearly over its entire length. In Fig. 8, the slot was placed at a 25° angle to the array and once again the slot shows up quite clearly over its entire length, since the array was able to receive the specular reflection from the slot. This illustrates the width of the aperture and large angle of acceptance which can be used with this imaging system. In the future, we intend to place the slot at an even steeper angle to

the array so that only the ends of the slot will be observed. The clutter in this image is due mainly to the spurious modes which are excited by the EBT array, which will be eliminated in a later version of the array.

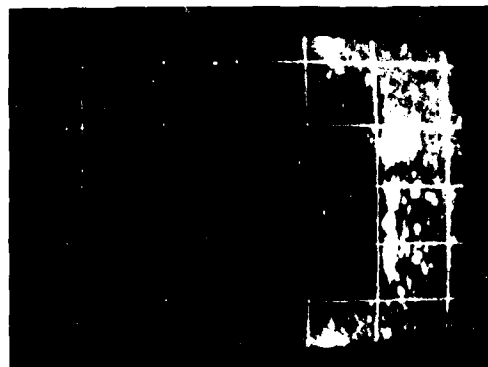


Fig. 6. Rayleigh wave image of center-punch marks in aluminum substrate (1 cm squares).

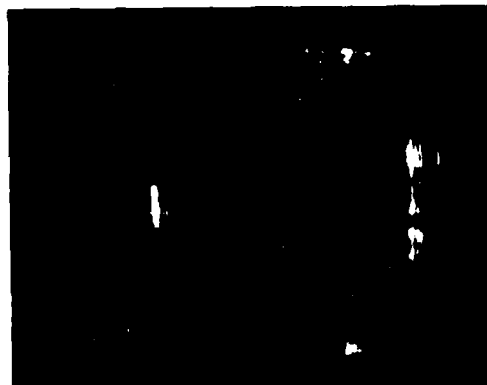


Fig. 7. Rayleigh wave image of an EDM slot placed parallel to the transducer array (1 cm squares).

In the near future we plan to look at these images in detail using our contour plotting program to see if any of the predicted features in these images, namely the $1/\sqrt{R}$ fall-off from the end of the crack can be observed. Because of the success of our Rayleigh wave imaging experiments, we intend to continue the development of the EBT array and to use this array in most of our future imaging experiments. The limited number of images so far obtained illustrates one of the disadvantages of computer reconstruction: it is very slow (up to 1 hour). The real time system eliminates this difficulty and makes adjustments to obtain the optimum images relatively simply.

REAL-TIME PROGRAMMABLE FILTER

We have developed a real-time programmable filter for use with our synthetic aperture acoustic imaging system. This programmable filter

is an extremely flexible signal processing element which can be employed for inverse filtering, real time deconvolution, matched filtering or any number of other applications. The basic idea here is to use the filter to compensate for deficiencies in the transducer so as to obtain as compact an impulse response as possible within the bandwidth limitations of the system. Another potential application of great importance in imaging systems is to remove distortion which is introduced by propagation through an inhomogeneous medium, or poor contact between the transducer array and substrate.



Fig. 8. Rayleigh wave image of an EDM slot placed at 25° to the transducer array (1 cm squares).

It has been demonstrated earlier by White that a surface acoustic wave (SAW)⁸ filter could be designed for this type of application, and we have demonstrated a programmable charge-coupled device filter.⁹ There are a number of limitations to these techniques: the SAW filter is not programmable; rather it must be tailored to a specific application, while the CCD filter has a limited bandwidth, much less than 1 MHz. In order to overcome these limitations, we have developed a new type of programmable filter which makes use of a hybrid digital-analog approach in order to achieve a 5 MHz bandwidth from a reliable low-cost design.

A block diagram of the actual hardware is shown in Fig. 9. The filter makes use of a high-speed analog-to-digital converter which samples the input signal and converts it into 8-bit digital words which are sequentially loaded into an 8-bit wide digital shift register. This shift register acts as a tapped delay line and at each stage of the shift register, a multiplying digital-to-analog converter (MDAC) is used to multiply the digital word by an analog tap weight reference voltage to produce an analog current output. The outputs of all the MDAC's are tied together on a common output bus where all the currents are summed to produce the filter output. The tap weight reference voltages are established by a set of latching digital-to-analog converters which are programmed by the computer.

In operation, the digital signal at the input to the filter is inserted into a computer. By using Fourier transform techniques or an iterative technique, such as the LMS algorithm, the computer calculates the time response of the filter required to transform the input signal into the desired

output. We currently favor the use of the Fourier transform technique to calculate the Wiener filter solution because of its high speed (a few seconds) and the fact that it gives us a picture of how the filter is performing in both the frequency domain and the time domain. Suppose the spectra of the input signal and the desired output signal are $X(\omega)$ and $D(\omega)$ respectively. The frequency response of the filter which gives the least mean-squared fit to the desired output signal in the presence of noise is given by the Wiener solution

$$H(\omega) = \frac{D(\omega)X^*(\omega)}{X(\omega)X^*(\omega) + N^2(\omega)} \quad (1)$$

Here, $X^*(\omega)$ is the complex conjugate of $X(\omega)$ and $N^2(\omega)$ is the noise power. If the noise level is low, optimum use of the available bandwidth can be made in order to sharpen a transducer impulse response or to remove distortion from an acoustic signal. Once the required filter response has been calculated, by whatever means, the filter is programmed and it then operates in real time with a 5 MHz bandwidth and a 40 dB dynamic range.

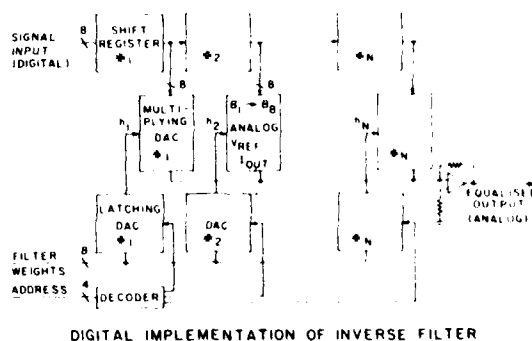
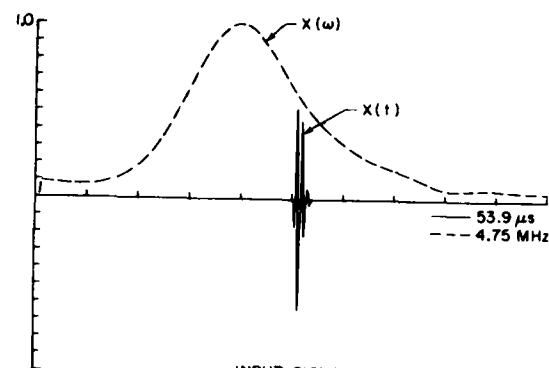


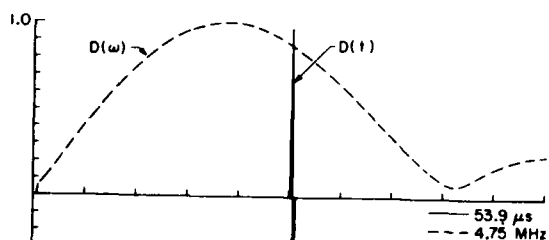
Fig. 9. Hardware implementation of a real-time programmable filter.

A number of experiments have been performed to illustrate potential applications of this filter, two of which will be shown here. One application of this filter is to improve the impulse response of an acoustic transducer. Theoretical calculations have been done which indicate that the optimum tradeoff between range resolution and transverse resolution is obtained with approximately a single sinusoid transducer impulse response. Figure 10(a) shows an actual impulse response of a commercial 2.25 MHz transducer in both the time and frequency domains, while Fig. 10(b) shows the desired signal, a single sinusoid. Fourier transform techniques are employed to calculate the frequency response, Fig. 10(c) and time response, Fig. 10(d), of the filter required to transform the input signal into the desired output. Figure 10(e) shows the results obtained with our real-time hardware. The top trace shows the actual transducer impulse response at the input to the filter, while the bottom trace shows the filter output, a good approximation of a single sinusoid.



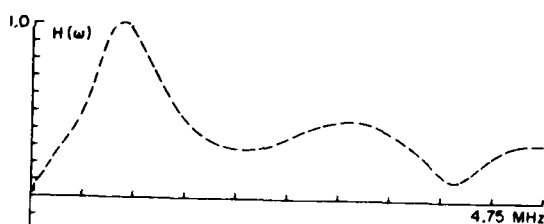
INPUT SIGNAL

(a)



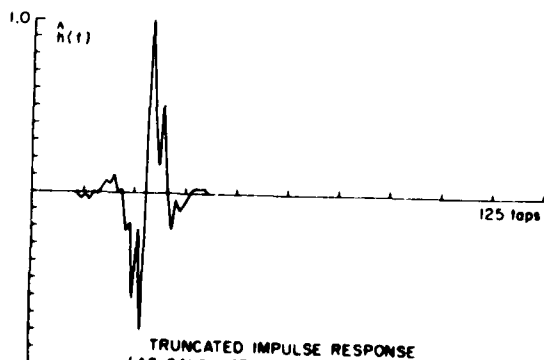
DESIRED SIGNAL

(b)



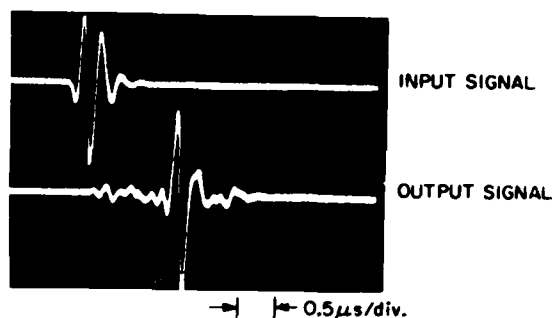
FREQUENCY RESPONSE OF WIENER FILTER

(c)



TRUNCATED IMPULSE RESPONSE
(AS CALCULATED BY THE COMPUTER)

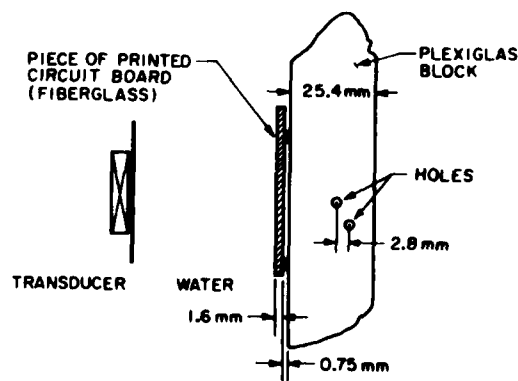
(d)



(e)

Fig. 10. Shaping of the transducer impulse response using a real-time programmable filter.

Another application for this filter is to remove distortion introduced by propagation through an inhomogeneous medium. Figure 11 is a schematic of the experimental set-up. While looking at the echoes from two small holes in a plastic block, a sheet of fiberglass printed circuit board was placed in front of the plastic block, causing reverberations which distorted the echoes, as would a poor contact between a transducer and a substrate. Figure 12(a) shows the undistorted signal. Here, the echoes from the two holes and from the back-face of the plastic block can be picked out quite clearly. At the top of Fig. 12(b), the distorted echoes can be seen; the individual echoes from the two holes are now difficult to distinguish from one another. The object of this experiment was to use the back-face echo to train the filter to remove the distortion. If the distortion can be removed from the back-face echo, then presumably, the same filter will remove the distortion from the other echoes as well. In the bottom trace of Fig. 12(b), it can be seen that the filter has been quite successful in removing the distortion, and it is once again possible to distinguish the individual echoes from the two holes.



EXPERIMENTAL SET-UP FOR DISTORTION DECONVOLUTION

Fig. 11.

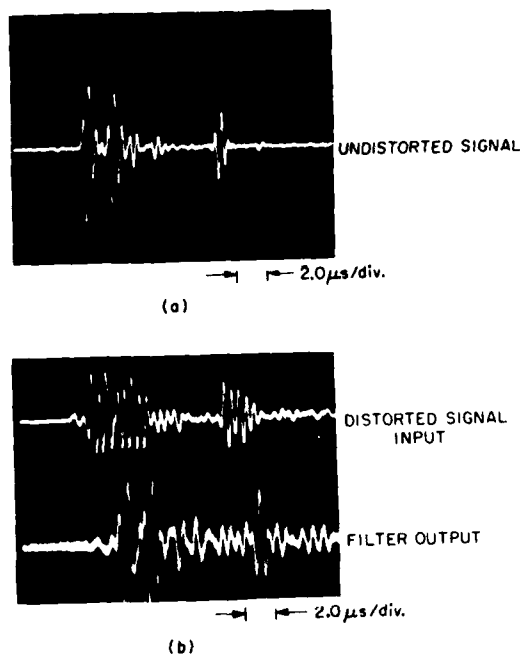


Fig. 12. Experimental results of distortion deconvolution.

CONCLUSIONS

We have continued to make advances in a number of areas related to our work with digital synthetic-aperture acoustic imaging. Our second generation hardware system is currently under test and preliminary experimental results are expected in the near future. Computer processing techniques for the display of quantitative image information are being investigated and a contour plotting program has already been used to help characterize the performance of our imaging system.

A significant breakthrough has been achieved in the design of a new type of transducer array for the excitation of Rayleigh waves (the edge-bonded transducer array) and this new array has been used to obtain Rayleigh wave images of surface defects in aluminum samples. A new real-time programmable filter has been developed which shows a great deal of promise for use in imaging as well as other signal processing applications.

ACKNOWLEDGMENTS

This work was sponsored by the Center for Advanced NDE operated by the Science Center, Rockwell International for the Advanced Research Projects Agency and the Air Force Materials Laboratory under Contract RI 74-20773.

REFERENCES

1. G. S. Kino, P. M. Grant, P. D. Corl, C. S. DeSilets, "Digital Synthetic Aperture Acoustic Imaging for NDE," Proceedings ARPA/AFML Review of Progress in Quantitative NDE, La Jolla, Ca., July, 1978.
2. G. S. Kino, "Acoustic Imaging for Non-destructive Evaluation," Proc. IEEE, **67**, 510-25 (1979).
3. J. D. Achenbach, A. K. Gantesen, H. C. McMaken, "Diffraction of Elastic Waves by Cracks - Analytic Results," Elastic Waves and Nondestructive Testing of Materials, AMD-Vol. 29, Edited by Y. H. Pao, ASME (1978).
4. A. Macovski, "Ultrasonic Imaging Using Arrays," Proc. IEEE, **67**, 484-95 (1979).
5. T. M. Waugh, G. S. Kino, "Real Time Imaging with Shear Waves and Surface Waves," Acoustical Holography, Vol. 7, Plenum Press, 103-115 (1977).
6. G. S. Kino, "Ultrasonic Imaging and Signal Processing," Progress Report, RISC Contract 74-20773, March, 1979.
7. G. S. Kino, B. T. Khuri-Yakub, A. Selfridge, H. Tuan, "Development of Transducers for NDE," To be published in Proc. ARPA/AFML Review of Progress in Quantitative NDE, La Jolla, Ca., July, 1979.
8. R. M. White, "Signal Processing Research in Connection with Ultrasonics in Nondestructive Testing," ARPA/AFML Interdisciplinary Program for Quantitative Flaw Detection, Contract F33615-74-C-5180, 3rd Year Report, 43-58, Sept, 1977.
9. D. Corl, "ACTD Adaptive Inverse Filter," Electronics Letters, **14** (3), 60-62 (1978).

SUMMARY DISCUSSION
(Doug Corl)

Jerry Posakony (Session Chairman - Battelle Northwest): Is there a question? We can handle one right now.

Vicki Panhuise (General Electric): I am used to looking at graphic systems, and I realize you studied your images and especially your punched holes. Have you tried taking an unknown sample where you had no idea what the indication was in trying to pick it out of your displays?

Doug Corl: No, we haven't done that. If you punched a hole similar to the ones that I have in an aluminum block and gave me that sample, I could easily find the location of it. But if I didn't know it was a punched hole--for example, if it was a scratch or something like that--it would be difficult to pick it out. A single isolated flaw in a clean surface I can find, and then I can see the general shape of it or something like that, get some more information. But if the flaw is in a complicated object, it would be difficult to get a good image of it.

Vicki Panhuise: Is that your ultimate goal?

Doug Corl: The problem with the complicated object is the sidelobes from one object might appear--you don't really know whether they are another object or just sidelobes. Using more transducer elements, for example, to reduce the sidelobe level, makes it easier to distinguish an actual object from a sidelobe. If you can get the sidelobe level down to minus 36 db, it's much easier to distinguish a sidelobe from an actual signal than in the case where you have a minus 12 db sidelobe.

Jerry Posakony: One more question.

Paul Holler (Inst. fur Zerstörungsfreie Prüfverfahren): I wonder if you have a special reason not to excite the Rayleigh wave by just putting the array on the specimen and matching the wave by your array control. Is there any reason not to do it that way? You know what I mean? Just put the plane array on your specimen, no edge or nothing, and simulate a wedge by the array control. I think that's the normal way to use for things like that.

Doug Corl: I understand the question. You're suggesting using a linear phase across the array to excite a Rayleigh wave.

Gordon Kino (Stanford University): Now you're really asking for two-dimensional array.

Paul Holler: It's a one-dimensional array.

Gordon Kino: One dimension to simulate the wedge and another to do the focusing that's across the wave.

Paul Holler: It's because you want to do focusing.

#

WAVEFRONT RECONSTRUCTION ACOUSTIC IMAGING USING TWO-DIMENSIONAL ARRAYS

K. M. Lakin, W. R. Sheppard and K. Tam
University of Southern California
Los Angeles, California 90007

ABSTRACT

This report describes an imaging system employing the digital reconstruction of the near fields of an object using the amplitude and phase of the scattered fields measured on a remote plane in the Fresnel zone. This imaging technique is shown to be significantly different from holographic and phased array systems and basically computationally implements a classical lens system having the reconstruction plane parallel or perpendicular to the measurement plane. The theory of the imaging approach is detailed and the method of obtaining a real-time implementation is described. Test data for the first 64x64 element array using PVDF elements and electronic scanning is presented.

I Introduction

In this report we describe the theory and experimental results for a technique of acoustic imaging using wavefront reconstruction to obtain the source or scatter near-in fields from a measurement of the scattered fields in the Fresnel zone of the object or source. The reconstruction technique has its roots in physical optics wherein the operation of lens are described by mathematical operations and visa versa [1]. Thus the procedure is to perform the image formation through a series of mathematical operations rather than via a set of physical objects such as lens. The burden of the image quality is thus placed upon the initial data collection and finally the precision of the mathematical transformation process. There is of course considerable flexibility offered by this approach because, as will be shown, one set of two dimensional data can yield an infinity of reconstruction planes, whereas variable focal length acoustic lens are much more difficult to implement and still require field measurements in their focal planes.

This paper discusses the formalism of the imaging technique, progress obtained on the implementation of the imaging system using two dimensional acoustic arrays, and a brief comparison with holographic [2] and phased array systems.

II Theoretical Basis of the Imaging Approach

The basis of the imaging system, Figure 1, starts from Huygens theory describing the superposition of a radiation field from many point sources of the source or scattered field, [1]

$$U(u,v) = \frac{2\pi}{ik} \int \int U(x,y) \frac{e^{ikr}}{r} dx dy \quad (1)$$

where $U(u,v)$ is the measured field in the u,v plane located a distance R from an

assumed scattering plane, k is the wavenumber, $U(x,y)$, the source or scattered field and r is the distance between a scattering element and field position,

$$r = R \left[1 + \frac{1}{R^2} ((x-u)^2 + (y-v)^2) \right]^{1/2} \quad (2)$$

Using the small angle approximation we essentially restrict the transverse dimensions of the scattering region and measurement plane such that they are much less than R the distance between planes. In practice this para-axial approximation restricts the maximum angle between r and R to approximately 30 degrees. However, for the usual cases of water-solid interfaces this represents a more than adequate angle of incidence due to longitudinal wave cutoff conditions.

Using the paraxial ray approximation, the distance r is approximated by

$$r \approx R + \frac{1}{2R} [(x-u)^2 + (y-v)^2] \quad (3)$$

and (1) becomes $U(u,v) = 2\pi \frac{e^{ikR}}{ikR} \int \int U(x,y)$

$$\cdot \exp i \left(\frac{k}{2R} \right) [(x-u)^2 + (y-v)^2] dx dy \quad (4)$$

The quadratic phase factor may now be expanded and a normalized relationship is obtained

$$\bar{U}(u',v') = C \int \int \bar{U}(x',y') \exp [-ik' (u'^2 + v'^2)] dx' dy' \quad (5)$$

where

$$\bar{U}(u',v') = U(u,v) \exp -ik' (u'^2 + v'^2) / 2 \quad (6)$$

$$U(x',y') = \bar{U}(x',y') \exp -ik' (x'^2 + y'^2) / 2 \quad (7)$$

$$C = 2\pi a^2 \frac{e^{ikR}}{ikR}, \quad x' = x/a$$

$$y' = y/a, \quad u' = u/a, \quad v' = v/a$$

$$k' = \frac{k a^2}{R} = \frac{\pi a}{\Delta z}$$

or where $\Delta s = \lambda R/2a$ maximum sampling interval allowed without considerable information loss. At the widest angle of operation, R/a would have a minimum value of $\sqrt{3}$ and the maximum allowed sampling interval would be $\Delta s = (\sqrt{3}/2)\lambda$.

The image is formed by a sequence of mathematical operations. First, the actual field at the measurement plane must be obtained by taking the measured data and multiplying by a correction factor that accounts for variations within the measurement system. Next the data is columniated by multiplication by a parabolic phase factor, an operation equivalent to lens L1 in Fig. 2. Next the data is corrected by a smoothing function in order to reduce ringing in the final image due to the finite spatial sampling that is necessarily employed in the measurement process. Clearly, small defects or sharp edges of defects, such as crack tips, scatter widely, and a truncation of the fields due to finite spatial sampling causes a smoothing in the image. The weighting function is used to eliminate the Gibb's ringing created by this artificial truncation.

By taking the inverse transform of (5) we obtain

$$\bar{U}(x', y') = C' \iint U(u', v') \exp + ik' (u'x', v'y') du'dv' \quad (9)$$

which is the normalized image field. If phase information is desired then the parabolic phase unnormalization is carried out, (7). The Fourier transform has the same effect as lens L2 in Fig. 2. Note that the plane of reconstruction is determined by the parabolic phase normalization and that many images may be formed from one set of measured data. However, only one image would be in focus. The operation is like that of an optical microscope wherein the operator adjust the focus for the desired image except that here the focus is obtained electronically. If the distortion caused by the detector or array element spatial response requires correction, then the final image is divided by the known transform of the detector field pattern.

Since the imaging technique has its roots in conventional optics, many processing techniques employed there may be usefully employed with the added advantage of having phase and amplitude as variables and not just intensity.

The imaging process may now be summarized: 1) measure the amplitude and phase U_m in the measurement plane, 2) weight the fields and correct for known measurement errors such as array non-uniformities, 3) choose a reconstruction plane and phase normalize the measured fields, 4) do a two dimensional Fourier transform to obtain the

normalized scattered fields, 5) and phase un-normalize to obtain the complete fields. This data is now ready for display and possible enhancement.

III Side Looking Imaging

In NDE applications there are situations where the parallel plane reconstruction technique, currently employed in our work, is not suited to the physical test configuration. Such a case might be the inspection of vertical weld joints where the top surface is generally non-planar due to the crown of the weld. In other cases it might be of interest to have the depth information available in real time rather than in near-real time through successive parallel plane transformations.

The fundamental requirement of the parallel plane reconstruction algorithm is the small angle approximation. It is this approximation that allows the problem to be cast into the Fourier transform format. Once in the Fourier transform format the inversion is accomplished by the inverse Fourier transform. Finally, an unnormalization of the fields gives the desired result. With that procedure in mind the reconstruction algorithm can be derived for the case of side looking perpendicular plane imaging similar to that described above for parallel plane imaging.

The geometry of the side looking imaging problem is shown in Figure 3. Here the (x, y) plane is taken as the source plane or origin of scattered fields and (u, v) the measurement plane just as for the previous case. The scattering region is centered a distance S to the side and a distance D in depth from the measurement plane. The planes are taken to be perpendicular. Here r is given exactly by

$$R = [(x-u)^2 + (s+v)^2 + (D+y)^2]^{1/2} \quad (10)$$

and may be factored to obtain,

$$r = R_0 \left[1 + \frac{2}{R_0^2} (vs + yD) + \frac{v^2 + u^2 + x^2 + y^2 - 2xu}{R_0^2} \right]^{1/2} \quad (11)$$

$$\text{where } R_0 = (S^2 + D^2)^{1/2} \quad (12)$$

is the distance between the centers of the two regions of interest. If the x, y and u, v regions are of limited extent and much smaller than the total distance r then,

$$R \approx R_0 \left[1 + \frac{1}{R_0^2} (vs + yD) + \frac{1}{2R_0^2} (v^2 + u^2 + x^2 + y^2 - 2xu) \right. \\ \left. + \frac{1}{2R_0^2} (vs + yD)^2 + \dots \right] \quad (13)$$

This may now be written in the form

$$R = R_0 + R_s(x, y) + R_m(u, v) + R_{sm}(x, u, y, v,) \quad (14)$$

where

$$R_x(x, y) = [x^2 + y^2(1 - D^2/R_0^2) + 2yD]/2R_0 \quad (15)$$

$$R_m(u, v) = [u^2 + v^2(1 - S^2/R_0^2) + 2vS]/2R_0 \quad (16)$$

$$\text{and } R_{sm}(x, u, y, v) = -(xu + yvSD/R_0^2)R_0 \quad (17)$$

This factoring of r is most essential to the formulation because it allows the field quantities to be normalized by phase terms and then cast into the Fourier transform format. The $1/r$ dependence in (1) may be removed from the integral under the small angle approximation which essentially assumes all sources are equally distant from the measurement plane for the purposes of amplitude determination. Using (14) for R , the field expression (1) becomes

$$U'_m(u, v) = C \iint U'_s(x, y) e^{ikR_{sm}} dx dy \quad (18)$$

$$\text{where } C = e^{ikR_0/R_0} \quad (19)$$

$$U'_s(x, y) = U_s(x, y) e^{ikR_s(x, y)} \quad (20)$$

normalized source field

$$U'_m(u, v) = U_m(u, v) e^{-ikR_m(u, v)} \quad (21)$$

normalized measured field.

In (18) the normalized fields are clearly in the Fourier transform format through the definition of r in (17). Taking the inverse transform of (18) yields.

$$U'_s(x, y) = C' \iint U'_m(u, v) e^{ikR_{sm}} du dv \quad (22)$$

which completes the major part of the field inversion process.

There is a distortion in the relationship between the y and v coordinates due to the scale factor, SD/R , in (17). The effect of this is most apparent when (22) is cast in the form of a discrete Fourier transform, DFT. In transition to the DFT formulation the coordinates are given by

$$x = Idx \quad (23a)$$

$$u = Jdu \quad (23b)$$

$$y = Kdy \quad (23c)$$

$$v = Ldv \quad (23d)$$

$$\text{where } I, J, K, L, = 1, 2, \dots, N. \quad (23e)$$

The phase factor in (22) is now written as

$$e^{-ikR_{sm}} = e^{i\theta(x, u)} e^{i\theta(y, v)} \quad (24)$$

$$\text{where } \theta(x, u) = 2\pi \frac{xu}{\lambda R} \quad (25a)$$

$$\text{and } \theta(y, v) = 2\pi \frac{yvSD}{\lambda R_0^3} \quad (25b)$$

Using (23) the phase factors become,

$$\theta(x, u) \rightarrow \theta_{IJ} = 2\pi \frac{IJ}{N} \frac{Ndxdu}{\lambda R_0} \quad (26a)$$

$$\text{and } \theta(y, v) \rightarrow \theta_{KL} = 2\pi \frac{KL}{N} \frac{NdydvSD}{\lambda R_0^3} \quad (26b)$$

$$\text{where } \frac{NdxduSD}{\lambda R_0^3} = 1 \quad (27a)$$

$$\text{and } \frac{NdydvSD}{\lambda R_0^3} = 1 \quad (27b)$$

These relations are necessary to make θ_{IJ} and θ_{KL} cyclic of period 2π as required by the FFT algorithms. Thus from (27) we find

$$dX = \frac{\lambda R_0}{Ndu} \quad (28a)$$

$$\text{or } dX' = \frac{R'_0}{Ndu'} \quad (28b)$$

$$\text{and } dy = \frac{\lambda R_0^3}{NdvSD} \quad (28c)$$

$$\text{or } dy' = \frac{R'_0}{Ndv'S'D'} \quad (28d)$$

In (28) the primed quantities are the coordinates normalized in terms of the wavelength. For parallel plane imaging both x and y are related to u and v by the same reduction factor, in the perpendicular plane case the reduction factor may be different. In practice this linear distortion would cause no problems because there is always the option of compensating the distortion in the display device. Also, note that if $S = D$ there is no distortion.

IV Two Dimensional Acoustic Arrays

From the standpoint of this particular imaging technique there is no real size limitation on the array other than the small angle requirement suggesting some bounds on the ratio of array area to object distance from the array. Thus a small array could be located close to the scattering fields and a large array farther away assuming both had the same number of array elements. The number of array elements is largely determined by the resolution and number of pixels desired. Our previous work on transducer

characterization suggested that an array of size 64 x 64 is satisfactory from the reconstruction standpoint and that 32 x 32 would give somewhat less favorable images for these confined fields. The rate of sampling is determined by the characteristics of the image and how the scattered fields interfere at the remote sampling plane. The mathematical requirements on the number of sampling points is determined by sampling theory. If the image were known to have a simple symmetry then a two dimensional array would not be required or at most a simple array would give all the necessary information required.

In a two dimensional array one major technological problem is that of accessing the elements of the array. In the imaging system described above, the actual image is formed by computation using a matrix of data. Accordingly there is some flexibility in the manner in which the data is gathered and sequential acquisition seems most appropriate. In addition, the array may be operated in either the send only, send and receive, or receive only mode.

There are acoustical constraints placed on the array as well in terms of transducer element bandwidth, efficiency, and radiation pattern.

Below is discussed the electronic and acoustic problems in more detail.

Electronic Scanning

In an array of size 64 x 64 there are 4096 transducer elements that must be sequentially or randomly accessed. Such a large number of elements implies that the cost per element must be small if the overall array is to be practical. A further constraint was the decision to use 254 microns (100 mil) spacing of the array elements. This was a reasonable choice based upon the finite amount of piezoelectric available and the desire to keep the overall array and associated electronics of finite size. Thus with elements on a 254 micron (100 mil) grid the available cross-sectional area for the electronic switching is somewhat limited whereas the depth may be anything reasonable.

The electronic switching is accomplished using CMOS 8-1 multiplexer hybrid integrated circuits. These eight channel switches are enclosed in a standard sixteen pin DIP ceramic package. A group of eight such switches form a 64 element cell, Figure . Here eight MUX chips are stacked side by side and share common power and row address lines. The eight analog I/O lines are further multiplexed to produce a single I/O line and resultant column address lines. This 8 x 8 cell was used for prototype array designs before going to the full sized array. Accordingly various combinations of such cells can be

used to form a larger array although any subset of the 8 x 8 cell would work as well. In a 64 x 64 array, 64 such cells are combined in a manner indicated schematically in Figure 5. Here representative signal paths are shown in order to illustrate the decoding technique and to facilitate the computation of the signal attenuation and spurious feedthru within the array. Also shown schematically is a 64 x 64 array composed of 64 8 x 8 cells having one cell (shaded) with one chip active (solid line) and within that chip one channel is active. The dashed line denotes the selected 8 x 8 cell and within that cell the active chip. The inhibited chip, denoted by INH, represents the remaining seven inactive chips within that cell. The two chips below the active cell represent the remaining seven 8 x 8 inactive cells in the selected row of cells common to the active cell. The bottom most chips represent all those other cells which are inactive because they occupy unselected rows of cells. Such a picture is necessary for computing the attenuation because the attenuation through a chip is greater for the unselected state than for the selected state. In an active chip the adjacent channel isolation is from 25 dB to 35 dB and all other channels within the chip show approximately 40 dB isolation. An inactive chip shows a much larger attenuation of 45 to 50 dB. If we let A represent the fractional isolation of unselected channels within an active chip, and A_1 the fractional isolation in an inactive chip, then, assuming unit amplitude at all 4096 channels, and no attenuation through the ON switches, the output signal is given by,

$$A_{out} = 1 + 7A[1 + 8A_1 + (8A_1)^2 + (8A_1)^3]$$

and results in a worst case condition. Clearly the $7A$ term dominates and indicates that the given switch isolation are adequate.

For the 64 x 64 array, there are 512 MUX chips at the first level nearest the array which are in turn multiplexed by 64 MUX chips which in turn are multiplexed by 8 chips and finally one chip. The result is 585 analog MUX chips and some low power TTL decoder chips. The output wires from the immediate vicinity of the array consist of 12 address lines 6 for row and 6 for column, two power supply lines, one analog I/O line and ground for a total of only 16 wires. The digital lines plug into an IEEE 488 interface which provides sequential scanning via external or computer trigger or complete random access of the array elements.

Transduction Elements

In the large two dimensional array it is necessary to have 4096 transduction elements. Because of the number of elements involved the construction of an individual element must be simple if the overall array fabrication is to be practical. The physical constraints

imposed upon the individual elements by the imaging process are somewhat flexible. First of all, the bandwidth of the transducers need only be sufficient to pass a 5 MHz tone burst of duration greater than approximately 5 microseconds since the imaging system employs coherent waves. The lower limit of the pulse duration is determined by the physical extent of the object since all of the object must be illuminated. The upper limit is set by stray echo considerations since a modest amount of pulse delay discrimination is very desirable.

The beam angle of the array element must be large enough to sample the object area. A practical upper bound is set by the small angle requirement of the imaging process and is approximately 30 degrees for the half angle. It is only necessary that the element transducer sample the entire image area preferably without any nulls, since the detector response can always be compensated for in the final image. It is more important to have uniformity in the beam pattern from one element to the next than to have a wider pattern but with greater variance between elements.

The transduction efficiency of the element should be as high as possible as in any acoustic array. However, in this case the element may be optimized for either send or receive. For the 64 x 64 array actually constructed, we chose PVDF for the piezoelectric elements because it is readily available in 10 x 20 cm sheets.

The configuration of the elements is shown in Figure 6. Here two possible configurations are shown, the left one uses a spherical surface radiator and shows the PVDF film pressed over the electrode posts. The posts are in turn connected to the MUX IC through a socket, left, or directly as shown on the right. The posts are made of brass and act as high impedance acoustic backings for the low impedance PVDF films. Although several such configurations were evaluated as 8 x 8 cells, the final 64 x 64 array was constructed using flat posts and IC sockets in order to simplify the PVDF bonding and to allow the IC's to be moved to other arrays. The 64 x 64 array was constructed using four blocks of 32 x 32 since 32 x 32 was the largest physical size that could be fabricated using available PVDF sheet and hydraulic press areas. The final array is shown in Figures 7, 8.

V Comparison to Other Imaging Systems

The image reconstruction system described above has some similarity to acoustic holography [2] in that the fields are measured in a two dimensional plane. However, in this case the phase information acquired in the data collection is used directly in the reconstruction process. This system does not require an acoustic reference beam during the measuring process and consequently the high spatial frequency

introduced by the reference beam is absent. Thus the data may be collected with more widely spaced transducers significantly aiding the physical implementation. In optical holography the high spatial frequency caused by the interference of the angled reference beam with the scattered waves does not cause any difficulty because the recording media, high resolution film, has a spatial resolution much greater than the spatial frequency of the interference pattern. In implementing an acoustical holographic system, the high spatial frequency must be sampled by a mechanically spaced transducer or finely spaced transducer array whose implementation is much more difficult except at very low frequencies (long wavelengths). In addition, the number of sampling points is determined by the extent of the scattered field divided by the sampling interval. Thus a holographic system requires a significantly larger number of sampling points due to the smaller sampling interval required by the high spatial frequencies created by the reference beam.

In phased array systems a number of array elements are excited in such a manner that signals arrive at a common focal point. In order to have only one focal point the array elements are closely spaced (of order $\lambda/2$) in order to eliminate grating lobes caused by the finite element spacing. In such systems spatial resolution is obtained by the use of short pulses and also by the size of the focal spot as determined by the number of array elements. In the reconstruction system described here the object is illuminated with a tone burst of sufficient duration to encompass the entire object but not so long as to introduce stray reflections from regions that are not of interest. The spacing of the transducer is determined by the spatial frequency of the scattered fields created by the interference of waves coming from different regions of the object. Since in our case the image is formed by a Fourier transform process the nature of the reconstruction is only dependent upon the sampling interval and number of sampling points chosen just as in any other Fourier transform operation. Since the sampling is discrete, the transforms become periodic and therefore the image is periodic and unless the sampling is done carefully the images will run together creating the well known aliasing effect. Thus sampling more closely in the measurement plane causes the periodicity of the image to decrease and increasing the number of sampling points better defines the image.

VI Experimental Results

A two dimensional array was fabricated using the switching and transduction system described above. Measured data for the array are shown in Figs. 9-11. In Fig. 9 the amplitude data for each element is shown in a grey scale display in order to test the element fallout pattern. Here each element was mechanically positioned

ROCKWELL INTERNATIONAL THOUSAND OAKS CA SCIENCE CENTER F/B 11/2
PROCEEDINGS OF THE DARPA/AFML REVIEW OF PROGRESS IN QUANTITATV-ETC(U)
JUL 80 D O THOMPSON; R B THOMPSON F33615-74-C-5180
SC595.70AR AFWL-TR-80-4078 NL

UNCLASSIFIED

5C595.70AR

AFVAL-TR-80-4078

NL

4 of 8

104

0000
0000
0000

over a 0.5 inch diameter 5 MHz transducer located 18 inches away. The system was operated in the pulsed CW mode, the signal envelope digitized by an A/D converter and then sent to the display memory. In the display, the black regions represent zero signal conditions which are due to faulty MUX chips or wiring errors. The 1x8 drop-out regions are due to errors within the 8x8 cells and the 8x8 drop-outs are due to errors in wiring at the next higher (64 chip) decoding level. Since the chips are replaceable, the 1x8 and 8x8 drop-out regions may be repaired. The 1x1 or single element regions are either due to short-circuited transducer elements or bent pins where the IC's plug into the transducer socket. Single element drop-outs occurring in a random manner do not degrade image quality because of the nature of the Fourier transform process.

In Figs. 10 and 11 are shown the measured radiation pattern of the source transducer. Clearly visible is the side lobe structure in the linear amplitude plots. No correction was made for variations in element transfer functions although this would be required in as eventual imaging system.

VII Conclusions

An acoustic imaging system has been detailed and the means to implement the system using two dimensional arrays has been described. The two dimensional array has been constructed using PVDF piezoelectric films and CMOS analog switches for sequential accessing. The experimental results obtained to date on the 64x64 array clearly demonstrate the feasibility of the imaging implementation using two dimensional arrays. The imaging technique was previously demonstrated in relation to transducer characterization using a single mechanically scanned transducer rather than an array.

VIII Acknowledgements

The authors wish to acknowledge the technical assistance of F. Lum, Y. Rubin, F. Baroudi, and M. Skidmore. This research was sponsored by the Center for Advanced NDE operated by the Science Center, Rockwell International, for the Advanced Research Projects Agency and the Air Force Materials Laboratory under contract F33615-74-C-5180.

IX References

1. K. Lakin and A. Fedotowsky, IEEE Transactions Sonics and Ultrasonics, SU-23, 317 (1976)
2. J. W. Goodman, Introduction to Fourier Optics, McGraw-Hill, New York, 1968
3. B.P. Hildebrand and B.B. Brendon, Introduction to Acoustic Holography, Plenum Press, New York, 1972.

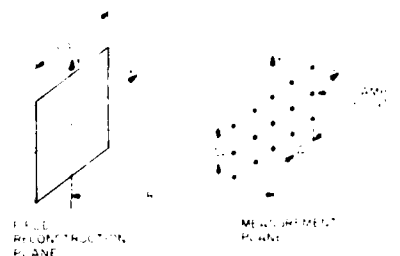


Fig. 1. Relationship between field reconstruction or source region and measurement plane.

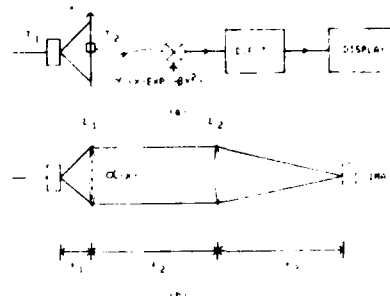


Fig. 2. Schematic of imaging system, a) compared to classical optics and lens system b)

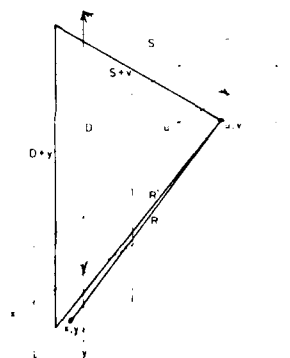


Fig. 3. Configuration for side looking imaging reconstruction system.

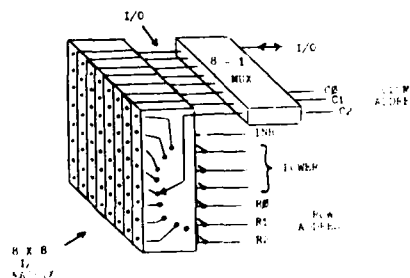


Fig. 4. Schematic of basic 8 x 8 multiplexing cell composed of 8 chips connected to the transducer elements, left side, and electronic interface, right side.

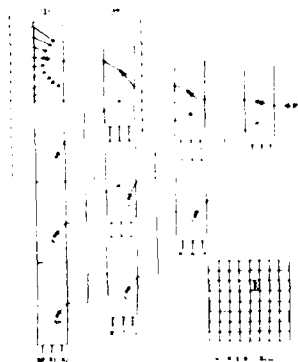


Fig. 5. Schematic of overall multiplexing system. Dashed lines outline the 8 x 8 cell, next lower row of chips, the bottom 8 x 64 row, and finally the bottom row represents all other inactive chips.

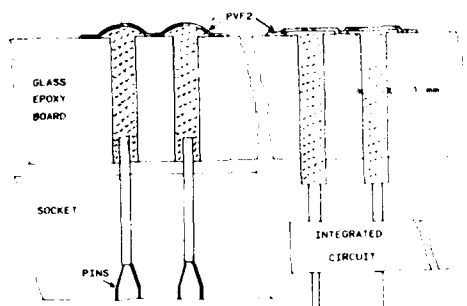


Fig. 6. Array element construction showing high impedance electrode posts connected to IC socket or the IC directly as possible choices.



Fig. 7. View of array on acoustic side showing 64 x 64 elements in groups of 32 x 32. Imperfections are only in the regions between the electrode posts.

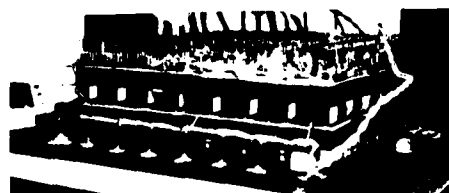


Fig. 8. Electronics side of the array showing the MUX integrated circuits.



Fig. 9. Fallout pattern of array, grey scale amplitude display. Black represents zero signal level.



Fig. 10. Radiation pattern of 0.5" dia. transducer; grey scale display.

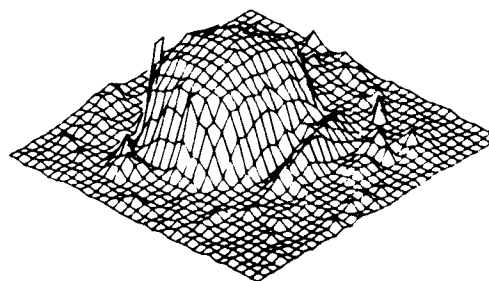


Fig. 11. Plotted data of 32 x 32 region of radiation pattern of Fig. 10.

SUMMARY DISCUSSION
(Ken Lakin)

Jerry Posakony (Session Chairman-Battelle Northwest): We have time for a couple of questions.

Gordon Kino (Stanford University): This is basically a holographic reconstruction system, as I understand it.

Ken Lakin: I don't use that terminology because it gets confused with holographic systems where you use an optical wave. I prefer to speak of it as a digital lens by implementing the acoustic lens mathematically.

Gordon Kino: The question I'm asking: doesn't it have the same problems in that you're using a single frequency. You're going to have the speckle problems, aren't you? You're going to have, essentially, range definition problems, too.

Ken Lakin: It has no more problems than a lens. It is a lens.

Gordon Kino: Fair enough.

Ken Lakin: What you get in the way of aliasing depends on how you do the reconstruction. I have been a little hesitant to charge off on the array processor because my current feeling is I don't want to do a 64 by 64, two-dimensional transforms. Instead, I want to take my 64 by 64 data and mesh it in a 128 square matrix. That helps reduce the alias problem.

Dale Collins (Holosonics, Inc.): I think what we have seen is the longitudinal resolution problem due to using coherent sound. When you use a lot of range and use coherent sound, your range resolution is very poor in a coherent system. I'm just saying, like Kino says, it's very difficult for range resolution in a coherent system.

Ken Lakin: Range resolution is dependent on how much angle you get in the lens, and right now I feel that the reconstruction algorithm is good for plus or minus 30 degrees.

Dale Collins: But you do compute your image in a certain plane?

Ken Lakin: Yes, we just take slices --

Dale Collins: If you had your range resolution (inaudible) you could make your algorithm.

Ken Lakin: The question of range resolution is one of the reasons I looked at the side looking imaging approach. There I could make out a vertical slice because I could get transverse interference patterns.

Jerry Posakony: One last question up here, please.

Paul Gammell (Jet Propulsion Lab): Do I understand what you're bringing out on the range resolution was the fact that the length of the burst which you're using to get the azimuthal resolution is sacrificing your time of flight information?

Dale Collins: That's true usually in the pulse echo system. We use a broadband system to obtain range resolution.

Paul Gammell: You can get a data trade-off -- there's mathematical limitations still. If you were to use something where there is some time coding. I'm thinking of specifically phase coded or pseudo-random techniques.

Dale Collins: Such coding will bring back broadband situations.

Ken Lakin: The spatial resolution here comes from the interference phenomenon and therefore I do not want the shortest possible pulse. If you have two objects, one behind each other, then you can see that if you're going to measure any sort of reasonable interference from that configuration, you have to be sufficiently off to the side in order to get a large enough angle to see where the interference starts. If the objects are side-by-side there is no problem and you get nice transverse resolution. That's why I was looking at an algorithm for side-looking imaging. Because, if you get off to the side, then you can see objects behind one another, and the interference pattern from those two sources can be easily measured off to the side.

#

PROGRESS REPORT ON VARIAN ULTRASOUND IMAGING SYSTEM FOR NDE

George Jahn and Steve Gehlbach
Varian Associates, Inc.
Palo Alto, CA 94303

ABSTRACT

This report describes an effort to develop a portable ultrasonic imaging system for NDE use. Results of a short applications study undertaken to identify important NDE problems which would benefit from such a system are presented. The overall system design goals and methods to accomplish them are described.

INTRODUCTION

In late 1977 the Systems & Techniques Laboratory within the Corporate Research Division of Varian contacted Mike Buckley regarding development of an ultrasound imaging system for use in nondestructive evaluation based on previous work in medical ultrasound imaging. A contract was subsequently awarded in late 1978 which has two parts: an applications study and a development program. The applications study was intended to identify important NDE problems whose solution might be assisted by high-speed ultrasonic imaging. Also, an appropriate instrument configuration was to be described. The instrument development phase called for development of a portable ultrasonic imaging system for nondestructive evaluation. Features were to include phased-array steering techniques with transducer frequencies between 5 and 10 MHz, real-time contact scanning, and a display and simple operator interface. Development of appropriate multi-element transducers whose beams could be steered were also specified in the work statement.

A list of the Varian professional staff involved in this project is shown in Fig. 1.

Robert Alvarez
Weston Anderson
Doug Clark
Ron Daigle
Ted Davids
Steve Gehlbach
George Jahn
Wendell Lehr
William Painter
Joseph Sharp
Peter Stonestrom
Dennis Wantzelius
Alice Wehlay

Fig. 1
Participants in Varian NDE Development Project

APPLICATIONS STUDY

Earlier this year Wendell Lehr and I went to a number of military and commercial facilities to learn about NDE problems. The list includes United Airlines in South San Francisco, Mare Island Naval Station in Vallejo, California, Kelly Air Force Base, Tinker AFB, McClellan AFB, Wright Patterson AFB, Naval Research Laboratories, and AMMRC in Watertown, Massachusetts. We asked the NDE users to describe the kinds of problems they

had, the types of flaws, the size, the material, the seriousness of the problem, and current methods of detecting and characterizing the flaw, and how the detection and evaluation process could be improved, hopefully with an imaging system. In the course of the study we had hoped to learn the economic severity of various NDE problems. Unfortunately this information was not discernible in the interviews.

Figure 2 shows a table of the kinds of defects about which we learned. Figure 2 was reorganized into Fig. 3 according to types of flaws including cracks, disbonds, honeycomb core damage, voids, and corrosion damage. The minimum critical dimensions are shown along with the different types of material involved. In looking over Fig. 3 we attempted to determine which problems could be helped by high-speed imaging. We came to the conclusion that examining high-quality bearing-grade steel billets to provide a cleanliness index would be a good first application. Among other things, the geometry is simple to understand and there is a good opportunity to make good acoustic contact with the specimen. Imaging of welds also seems to be an extremely important NDE problem. While examination of fastener holes for cracks is an important subject, techniques for detecting the flaws already seem to exist. Also, the detection of flaws in the second and third layers is difficult, if not possible, using ultrasound. Core damage due to corrosion appears to be important; however, there also seem to be suitable techniques for determining the core damage and disbonds. We felt that the problems with contact and geometry of engine discs would not be appropriate for our contact scanner. The conclusion of the study is that we would design our instrument to inspect high-quality steel billets and welds using an imaging technique.

INSTRUMENT DESIGN

Figure 4 shows a block diagram of the proposed instrument. The transducer is a multi-element piezoelectric design; the initial prototypes have been built by Pierre Khuri-Yakub of Stanford University. The transmitter shock excites a single element of the transducer. The ultrasonic echoes resulting from a single transmit pulse are received by the transducer array and preamplified by each channel prior to frequency conversion. All elements of the transducer except the transmitter element are connected to wide band rf amplifiers which are low noise and have a dynamic range of approximately 70 dB. The output from each

TYPE OF FLAW, STRUCTURE	MAT'L	LOCATION	BRANCH	INSTR. SITU.	FLAW SIZE	PRESENT METHOD
CRACKS, FASTENER HOLES	AL	SURFACE OF 2nd, 3rd LAR	UAL	DEPOT		1
CRACKS, BOLT HOLES, LANDING GEAR	AL	SURFACE	UAL	DEPOT		2
CRACKS, WHEELS (STRESS)	ST, ALL	SURFACE	UAL	DEPOT		3
CRACKS, TURBINE BLADES	TI	SURFACE	UAL	DEPOT		4
CRACKS, ENGINE DISK	NI, ALL	SURFACE	UAL	DEPOT		5
DISBOND, AIR SEAL	NI	AT BOND	UAL	DEPOT	1/4" x 1/8"	6
DISBOND, SKIN TO CORE	GE/AL	AT BOND	N'ROP	HFR, QA	1/8"	7
CORE DAMAGE	AL	AT BOND	N'ROP	HFR, QA	1/8"	8
DISBOND, TANK TRACKS	R/ST	AT BOND	ARMY	FIELD	1"	9
VOIDS, TANK WHEELS, TREADS	R	INSIDE	ARMY	HFR, QA		10
VOIDS, STEEL BILLET	ST	INSIDE	ARMY	HFR, QA	04"	11
DISBOND, SKIN TO CORE	AL	AT BOND	ARMY	FIELD	LARGE	12
CRACKS IN HELDS	ST	SURF INSIDE	ARMY	HFR, QA		13
CRACKS, ARTILLERY SHELLS	ST	SURFACE	ARMY	HFR, QA	025"	14
DISBOND, ARTILLERY SHELLS	BR/ST	AT BOND	ARMY	HFR, QA		15
CRACKS IN HELDS-MULLS	ST, NC	SURFACE	ARMY	DEPOT		16
CRACKS, BASE OF WING	AL	SURFACE	AF	DEPOT	05"	17
CRACKS, FASTENER HOLES	AL	SURFACE	AF	DEPOT	010"	18
DISBOND, SKIN TO CORE	AL	AT BOND	AF	DEPOT	010"	19
CRACKS, ENGINE DISK	NI, ALL	SURFACE	AF	DEPOT	015"	20
CONDITION DAMAGE, STARTER	AL	SURFACE	AF	DEPOT		21
DISBOND, SKIN TO CORE	AL	AT BOND	AF	DEPOT	01" x 5"	22
METHODS						
① Ultrasonic						
② Penetrants						
③ Tapping						
④ SEAL IS "FELT METAL" BONDED TO NICKEL						
⑤ GRAPHITE EPOXY, AL HONEYCOMB						

Fig. 2
Flaw Data

Type of Flaw and Location	Dimension, Inches	Material	Contact Numbers
CRACKS			
Fastener Hole (Airfoils, etc)	Unknown	Aluminum	1, 18
Bolt Holes (Landing Gear, Wheels)	-	-	2, 3
Wheels (Tire Wall)	-	-	3
Turbine Blades	.015	Titanium	4
Engine Disks	Unknown	Nickel Alloy	5, 20, 21
Welds (Tanks, Mulls)	025	Steel	13, 16, 24
Artillery Shells	05	Steel	14
Base of Wing	05	Aluminum	17
DISBONDS			
Air Seal (Jet Engine)	1/4 x 1/8	Felt Metal to nickel	6
Skin to Core	1/8	(Graphite Epoxy or Aluminum skin over)	7, 12, 19
Tank Pads to Tread (Tanks)	1	Aluminum honeycomb	9
Artillery Shells (Rot Bands)	Unknown	Rubber on Steel	15
CORE DAMAGE			
	1/8	Aluminum Honeycomb	8
VOIDS			
Tank Pads, Tanks	Unknown	Rubber	10
Steel Steel Artillery	14	Steel	11
VOIDS IN DAMAGE			
Mulls, Landing Gear	Unknown	Steel	2
Various Landing Gear	-	Steel	24, 25
Starters	-	Aluminum	22

Fig. 3
Summary of Flaw Data

receiver channel is frequency converted to base band. The down converted signals are processed using nonlinear square root circuits to compress the 70 dB dynamic range into approximately 35 dB. The multiple channel outputs are A/D converted using high-speed TRW 6-bit converters clocked at approximately 10 MHz. The multiple outputs are written into high-speed static memory. Approximately 100 microseconds worth of data are captured for each transmit pulse. Each point in the field of view of the transducer corresponds to a point on the display. Signals at various memory locations are summed to reconstruct a specific point in the field of view. The reconstructor generates a picture 30 times per second. Control hardware,

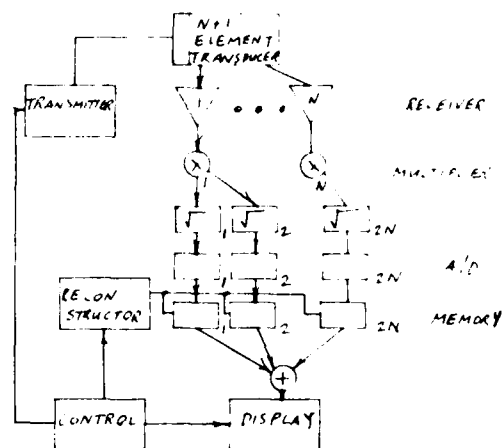


Fig. 4
Block Diagram of Proposed Instrument

keyboard, and display are included in the instrument.

Figure 5 shows a block diagram of the frequency conversion process. We decided to down convert because the A/D converters can sample the bandwidth adequately but not the carrier. The data storage memory is also reduced. The frequency translation operation is performed in quadrature by using multipliers and local oscillators with 90° phase difference. The difference frequency is selected by the low pass filter and then the signal is A/D converted and stored in the random access memory. The data rate for the A/D converter is consistent with the Nyquist rate for the half bandwidth of the bandpass signal since two channels are used. All of the information contained in the input signal is retained by this method so that signal reconstruction and beam forming can be performed.

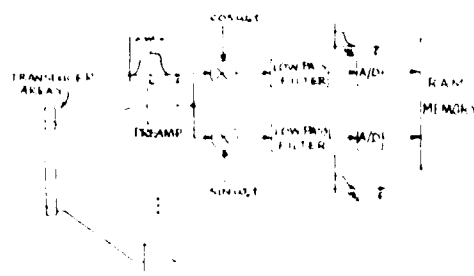


Fig. 5
Block Diagram of Frequency Conversion Process

Figure 6 shows some of the specifications of the instrument. Our initial transducers will have 16 elements but we may go to a wider aperture 32-element design. The digital approach allows

Transducer Frequency	5-10 MHz
Bandwidth	2-4 MHz
Number of Receiver Elements	16-32
Field of View	$\pm 45^\circ$
Depth	30 cm
Flaw Detected	1 mm
Frame Rate	30/sec.
Physical	Portable
Display	CRT, Polaroid
Focus	Dynamic
Delay	Digital
Aperture	Up to 3 cm
Transmitter	300 V 15 ns Falltime
Receiver Dynamic Range	70 dB

Fig. 6
Specifications

expanding the size of the array easily. A receiving time period of 100 microseconds after the transmit pulse corresponds to a depth of approximately 30 cm in steel. One of the components which makes this digital delay approach now possible is the TRW LSI A/D converter. We have found that the circuits work well and are relatively easy to use. It was a pleasant surprise recently to learn that they have been reduced in price by 50% so now they are less than \$100 each in quantity.

A simple mock-up of the system has been constructed. The mock-up multiplexes the outputs from 16 channels into one A/D converter channel, then into a minicomputer system. Computer reconstruction of the images will provide information on the exact reconstruction algorithms to be implemented and hardware. Preliminary pictures are not yet available. The design work on the project should be finished by the end of August at which time the construction will begin.

ACKNOWLEDGEMENTS

This work is funded by ARPA under Contract No. MDA903-79-C-0147.

MAPPING OF MATERIALS STRESS WITH ULTRASONIC TOMOGRAPHY

B. P. Hildebrand
Spectron Development Laboratories, Inc.
Costa Mesa, CA 92626

and

T. P. Harrington
Battelle, Pacific Northwest Laboratories
Richland, WA 99352

ABSTRACT

It is known that internal stress concentrations can give rise to microcracks which then grow when the structure is subjected to external forces. It has also been found that the velocity of sound is altered as it propagates through a region of stress. In this paper we discuss a technique called Computer-Assisted Tomography (CAT) and describe an application that provides pictures of stress fields. We report the results of both simulated and experimental models used to evaluate the technique. We conclude that the CAT approach has great potential for locating and mapping residual stress in metals.

INTRODUCTION

One of the outstanding problems of non-destructive testing is the location and measurement of areas of residual stress. In the manufacture of large structures, such as pressure vessels, a number of very large welds are required. The heat-affected zone surrounding the welds will contain residual stresses due to uneven cooling rates. In practice, these stresses are relieved by heating the entire vessel to some appropriate temperature and then carefully controlling the cooling rate. This standard procedure has not always been successful in relieving the residual stress that is induced by the welding process (Ref. 1). Structural designers realize this, and try to compensate for the possibility of stress concentrations by overdesigning. This leads to penalties in terms of both added weight and cost. Consequently, there is high motivation for finding and delineating such concentrations.

Currently there is no satisfactory test for measuring the success of stress-relief procedures. Thus, it may happen that high residual-stress regions exist in the pressure vessel. If these regions occur in critical areas (such as nozzle-to-vessel joints), cracks may develop, which would require subsequent plant shut-downs and expensive repair. If it were possible to detect and map residual stress, local stress relief could be applied, and future problems could be avoided.

Standard Nondestructive Testing (NDT) examinations consist of radiology and ultrasonic pulse-echo. Neither of these techniques can reveal the presence of residual stress; the former because it shows only density variations, and the latter because stress regions are not sharply defined; hence, they do not reflect much sound. It is known, however, that the velocity of sound in a solid is affected by stress. This phenomenon is a third order effect, and has been used primarily to determine the Lamé and Murnaghan elastic constants for various materials.

A number of studies have shown that it is possible to measure velocities with sufficient accuracy to detect and calculate residual stress (Ref. 2-4). Typically, for steel, the stress-

acoustic constant is approximately 0.197 nsec/cm/6895 kPa. This constant means that a 6895-kPa increment in stress produces a 0.5 nsec change in travel time through a 2.54 cm thick specimen. Since it is relatively easy to measure time-of-flight changes to this accuracy, the sensitivity of the proposed method should be approximately 6895 kPa.

At the present time, a number of researchers have made velocity measurements for the computation of stress. This data, however, has been obtained in the form of spot measurements or profiles. No one has yet attempted to take a number of profiles at different angles in order to reconstruct a cross-section of the residual stress. The purpose of this paper is to discuss our efforts to develop a method for mapping stress anomalies utilizing velocity information and an image reconstruction technique known as Tomography.

A Tomogram could be described as a picture of a slice. Over the past several years, CAT scanners have revolutionized the field of diagnostic medicine. This technique uses x-rays to obtain visible, thin slices through any section of the human body. We are applying the same reconstruction algorithms used in medical applications, (except for the substitution of ultrasound for the x-rays), to generate velocity maps of cross-sections of thick metal sections.

In the following section, we briefly discuss the principles of Tomography, and describe the Algebraic Reconstruction Technique (ART) we are using to construct the velocity profile. The third section describes several computer simulations for testing the ART algorithm. In the third section, we also discuss the effect of varying several parameters and describe the effect they have on the quality of the reconstruction. In the fourth section, we describe an experimental apparatus, which we have developed in our laboratory, for obtaining time-of-flight measurements. It also includes a discussion of reconstructions generated from these experimental data, and a description of the calibration procedure we are using in order to relate the velocity of sound to stress. In our conclusion,

we comment on the validity of this method for mapping residual stress and also describe a prototype instrument that we are building to test this technique.

PRINCIPLES OF IMAGE RECONSTRUCTION IN COMPUTED TOMOGRAPHY

As we noted in the introduction, Tomography has had its greatest impact to date in the field of diagnostic medicine. A good source of references on medical Tomography can be found in a paper by Brooks and Dechiro (Ref. 5). The principles of image reconstruction using Tomography have also been applied in a number of other disciplines: Electron Microscopy, Radio Astronomy, and Nondestructive Testing (Ref. 6-11).

To clarify the discussion that follows, a brief digression into the principles and terminology of Tomography will be necessary. Consider Figure 1a, which is a particular cross-section of a general three-dimensional object. Define the velocity distribution of the object as $v(x,y,z)$. Assume an ultrasound pulse, transmitted from location t , traverses the object along path ℓ to a point r where it is received. The time-of-flight along path ℓ is a function of the velocity distribution along the path, and is given as the line integral

$$t_O(\rho) = \int_{\ell} \frac{ds}{v} \quad (1)$$

where ρ and ℓ define the path ℓ from t to r . If the variable ρ is allowed to vary continuously over the object at a constant angle, a one-dimensional projection of the velocity distribution will be obtained.

The reconstruction problem is to estimate the velocity of the cross-section $v(x,y,z)$ from the projection values. Clearly, this can only be done if the projection values are available for a large number of angles ϕ_j . Also, in actual practice the projection values are available only at a discrete number of the ϕ_j for each angle ϕ_j . Thus, the reconstruction is an approximation to the actual velocity field, with resolution being a function of the spacing between rays $\Delta\phi_j$ and the degrees between angles $\Delta\phi_j$.

In theory, the velocity field can be reconstructed quite easily from the projection information. To see this, visualize a square grid superimposed over the object of Figure 1a as shown in Figure 1b. If we assume that the velocity within each square (pixel) is constant, then the total travel time through the grid becomes the sum of the travel times in each of the pixels. Each ray that passes through the velocity field will intersect various pixels.

The length of the ray segment in each pixel can be determined quite easily by using geometry. If a ray of length l_k lies in a cell with velocity v_k , the travel time through the cell is l_k/v_k . Thus, the total time-of-flight can be expressed as a linear equation whose unknowns are the velocities v_k . By using a number of independent rays that is equal to the number of grid cells, a linear system of algebraic equations can be generated and solved for the unknown velocities.

The difficulty with solving for the unknown velocities by inverting a system of algebraic equations is that, even for small grid systems, the size of the resulting matrix is prohibitive. For example, consider a grid system of 20 by 20 pixels.

This means that there are 400 unknown velocities to solve for. If we take 20 independent views with 20 rays per view, the result is 400 equations in 400 unknowns, or a 400 by 400 matrix to invert. Furthermore, the matrix will be sparse, since each ray will usually intersect less than 30 pixels.

Other reconstruction algorithms are available that overcome the limitations imposed by the matrix inversion method, some of these alternatives are:

- (1) Convolution, which is based on the work of Johann Radon (who first solved the equations governing image reconstruction in 1917)(Ref. 12-13).
- (2) Fourier Transform, which is the spatial frequency version of convolution (Ref. 14).
- (3) Back Projection, which was used in the first attempts to produce Tomograms of living patients.
- (4) Iterative Techniques, which are probably the most widely used reconstruction methods.

ITERATIVE RECONSTRUCTION ALGORITHMS

All the iterative algorithms start with an "initial guess" as to what the image looks like. Typically, the average value of the projections is divided among all the pixels that make up the image. The algorithms then adjust the pixel values to bring them into better agreement with the measured projections. These algorithms are iterative in that they continually sequence through the set of projection data, updating the pixel values until a stopping criteria is met. An example of a stopping criteria would be a measurement of the change that has been made to the image during an iteration. If the change is less than some prespecified minimum, the iteration is stopped.

The three most popular iterative reconstruction algorithms currently in use are: the Iterative Least Square Technique (ILST) of Goitein (Ref. 15), the Simultaneous Iterative Reconstruction Technique (SIRT) introduced by Gilbert (Ref. 16), and the Algebraic Reconstruction Technique (ART) discovered by Gordon, et al (Ref. 7, 17). Our preliminary investigation of both ART and SIRT indicates that ART produces better reconstructions than SIRT, given the amount and nature of the data that is available.

You will remember from the discussion earlier in this section that the time-of-flight for a given projection can be approximated as a sum of the time-of-flights in individual pixels. Briefly, the ART algorithm works as follows: for each ray in the data set, ART compares the experimentally obtained time-of-flight with the time-of-flight calculated using the current pixel values. If they are different, ART updates the velocity in each of the pixels as a function of the length of the ray path in the pixel. After the pixels along the ray have been modified, the time-of-flight calculated from the pixel values matches that obtained experimentally. ART then cycles through the remainder of the rays in the data set, repeating the process described above. However, as each new ray is processed, the value of previously updated pixels will be changed. This is the reason for the need to iterate. It has been shown, however, that the image improves after each iteration and converges to the best solution in a least squares sense (Ref. 17).

The majority of medical CAT scanners in use today employ one of two geometries for obtaining profiles. These two geometries are usually referred to as fan beam and parallel beam. Fig. 2 points out the differences between these two approaches. In the parallel beam method, a set of measurements are obtained by scanning the source and detector linearly past the patient. The entire scanner assembly is then rotated by a fixed amount and the scan is repeated. In the fan beam approach, the source rays are formed into a fan of narrow beams that encompass the patient. The rays are received simultaneously by an array of detectors. For this geometry, the source and detector array are also rotated about the patient. Since the fan beam method does not require a linear translation of the source and detector, it is capable of much superior performance.

SIMULATED DATA

To test the feasibility of using time-of-flight information along with the ART algorithm to reconstruct velocity fields, we have simulated several different images on the computer. As mentioned in the previous section, the time-of-flight for a particular ray crossing a velocity field is given by the line integral

$$t_0(\rho) = \int_L \frac{ds}{v} \quad (2)$$

To obtain simulated time-of-flights on the computer, this integral can be discretized to:

$$t_{0i,p_j} = \sum_{k \in l} \ell_{kij} / v_k \quad (3)$$

where ℓ_{kij} is the path length of the ray defined by θ_i and ρ_j through the cell k . And K is the set of all cells which intersect the line l .

To visually compare the reconstructions with the simulated velocity fields that were used to generate the data, we construct both isometric views and black-and-white gray scale images of the reconstruction. We will use both of these techniques to display results in this paper. To obtain a more qualitative idea of how the reconstructions compare with the original image, we calculate several error parameters at each iteration of the ART algorithm. The discrepancy is defined as:

$$\delta^q = \left(\frac{\sum_k (v_k^q - v_k)^2}{\sum_k (v_k - \bar{v})^2} \right)^{1/2} \quad (4)$$

This is a normalized Euclidian norm where v_k is the velocity value of the k^{th} pixel of the test image, \bar{v} is the average velocity of the test image, and v is the velocity of the k^{th} pixel after the q^{th} iteration. This equation shows that the discrepancy is the ratio of the root-mean-square error to the standard deviation of the test picture. This measure was suggested by Gilbert (16), and has since been used by Herman, et al (17) and Colsher (Ref. 16, 17, 8).

The second error parameter we calculate is the mean relative (or average) error which is defined as:

$$E_{av}^q = \frac{\sum_k |v_k^q - v_k|}{\sum_k v_k} \quad (5)$$

This has also been used by Sweeney and Colsher (Ref. 18, 8). The final error function that we calculate is the residual, which is defined by:

$$R^q = \left\{ \sum_i \sum_j \left| p(\theta_i, \rho_j) - p^q(\theta_i, \rho_j) \right|^2 \right\}^{1/2} \quad (6)$$

where $P(\theta_i, \rho_j)$ is the actual measured time-of-flight for the ray path defined by θ_i and ρ_j and $p^q(\theta_i, \rho_j)$ is the computed time-of-flight for the same path using the pixel values after the q^{th} iteration. This measure indicates the degree to which the reconstructed image satisfies the measured time-of-flight data. Notice also that this is the only error measure of the three that is valid for experimentally obtained data. This criterion has been employed by Colsher (Ref. 8).

An obvious deficiency of the first two error criteria is that the test image must be discretized. Several of the velocity fields that we used to generate our simulated data are circular and thus difficult to discretize. This problem tends to negate the usefulness of these two criteria.

All of our reconstructions were performed on a PDP 11/70 minicomputer. It is not valid to discuss execution time, since this computer operates in a multi-user environment. On the average, however, each iteration of the ART algorithm required approximately 30 sec of wall clock time and 5 sec of computer time. All of the isometric and gray scale images presented in this report were post-processed after the ART reconstruction program was completed.

In our initial investigation of the ART algorithm, we simulated parallel beam geometry, as described in the previous section. Fig. 3a represents a velocity field having two islands of 2% velocity increase in a uniform region. Fig. 3b shows the reconstruction when time-of-flight profiles are taken over a full 180° field of view. Notice that the tops of the two islands in this reconstruction are fairly flat and the steep sides approximate the test image very well. In Fig. 3c, a 90° field of view was available to the reconstruction algorithm. In this image, the tops of the islands are somewhat irregular and the sides have less slope than the 180° field of view reconstructions. The 90° data base, however, still provides an adequate reconstruction of the test image. Fig. 3d shows the result of using a 45° data base. In this reconstruction, the two islands have been smeared into the uniform velocity region. The tops of the islands are rough, and the height does not represent a 2% velocity difference. The walls of the islands in this reconstruction also have a very shallow slope. The reason for the poor reconstruction with a 45° field of view is that the majority of the rays pass through one of the two islands. As discussed in the last section, the velocity differences are divided among all the pixels in the path of the ray. Since there are few rays which pass completely outside the two velocity islands, the smearing effect is not counteracted.

A major goal of our present work is to develop procedures for mapping residual stress in thick metal sections (typically 10 to 20 cm). In many practical situations, it may not be feasible to obtain

time-of-flight profiles by either of the geometries discussed in the previous section. For instance, it may be physically impossible to position a detector inside a pressure vessel.

To overcome this difficulty, we have been investigating the feasibility of locating both the transmitter and the receiver on the same side of the metal section. Figs. 4a and 4b illustrate the differences between this geometry and those discussed in the last section. Fig. 4a illustrates the case in which both sides are accessible. The only way in which different angular profiles can be taken is to launch the waves at different angles by tilting the source. Theoretically, it is possible to launch waves over a $\pm 90^\circ$ field. However, note that the receiver would need to be moved farther away with increasing angle. Hence, a practically obtainable field of view with this method is $\pm 45^\circ$.

Fig. 4 illustrates the dilemma produced by the requirement for single surface inspection, and the solution. The back surface of the section is used as a reflector, with the receiver placed to receive the reflected signal. Note, however, that the reconstruction will now include a mirror image as well as the object itself. Also note that in both cases, the total geometric path length changes as a function of angle of view. Both of these peculiarities must be taken into account by the reconstruction algorithm.

EXPERIMENTAL DATA

Parallel Beam - To demonstrate the ultrasonic tomography technique for mapping velocity fields, we developed a model which allows us to obtain time-of-flight profiles in the vicinity of a known stress concentration. This experimental model, diagrammed in Fig. 5, consists of an aluminum specimen measuring 25 mm x 50 mm x 380 mm. At the center of the 50 mm x 380 mm plane, we caused a 6.35 mm diameter, 3.17 mm deep, flat bottom depression by applying a 6,350 kg force. We then obtained three sets of time-of-flight profiles at Positions A, B, and C as shown in Fig. 5, Position A being 3.17 mm below the bottom of the depression and B and C being 9.52 mm and 15.87 mm below, respectively.

The time-of-flight measurements were made using the parallel beam method. The source and receiver were adjusted to obtain 27 views from -52° to $+52^\circ$ in steps of 4° .

Figure 6 shows the time-of-flight profiles obtained for the B scan: 6a shows the profiles from 0° to 52° , while 6b shows profiles from the angles -4° to -52° . In this representation, the profiles are all scaled by the same factor but they have been repositioned along the vertical axis so that each set could be displayed on a single plot. One important point to notice in Fig. 6 is that as the angle increases, the resulting profiles deteriorate (contain points which appear to be inconsistent); however, we have found that if a small number of time-of-flights obtained are in error, the resulting reconstruction is not drastically affected.

Figures 7a, 7b, and 7c show gray scale images of the reconstructions from Positions A, B, and C respectively. In generating these images, we have applied the same maximum and minimum velocities to scale each of the reconstructions. Doing this shows how the velocity falls off with distance from the stress region. For these images, we have also positioned the levels of gray so that the middle shade (Level 5, counting from the darkest level of gray) corresponds to the average velocity measured in the aluminum sample. This average velocity was

determined by making a series of pulse-echo measurements as far as possible from the induced stress region. Levels lighter than 5 indicate velocity increases and those darker than 5 indicate velocity decreases. Each level represents a 0.3% velocity change. The physical dimensions of the reconstructed region are 38 mm x 38 mm.

Notice that by scaling all three images to the same maximum and minimum velocities, no detail can be observed for the C scan. This is because the velocity change assigned to each shade of gray exceeds the total change in the C scan. The calculated maximum velocity variation was 2.6%, 1.8%, and 0.4% for Scans A, B, and C respectively.

In Figs. 3a, 8b, and 8c, we show the same reconstructions, but here we have scaled each image by its own maximum and minimum. That is, for 8a, the levels represent 0.3% velocity change; for 8b, 0.2%; and for 8c, 0.04%. As in Fig. 7, the middle gray level corresponds to the average velocity in the aluminum section away from the stress region. By using this scheme for displaying reconstructions, we can see detail in the C scan which was hidden in Fig. 7c. However, there is now no convenient way to compare Figs. 8a and 8c.

Reflected Beam - We have performed several experiments to test the reflected beam techniques. As a model of a region of velocity change in an otherwise uniform metal volume, we chose a rubber glove filled with a water-alcohol mixture surrounded by a large volume of water. The ratio of water to alcohol in the glove was intended to provide a 3% increase in the velocity of sound over the surrounding water bath.

To simulated reflection from a back surface, we placed a transmitter-receiver pair on the same side of the rubber glove, and a mirror on the opposite side of the glove centered between the two transducers. A single profile was obtained by scanning the transmitter-receiver combination linearly past the glove. Additional profiles were obtained by changing the distance between the transmitter and receiver and repeating the linear scan.

In one experiment, we used a data set consisting of 23 profiles taken at angles from 10° to 120° in steps of 5° . Each profile consisted of 31 time-of-flight measurements taken at intervals of 7.37 mm. Fig. 9 shows the reconstruction of a cross-section of a single finger of the rubber glove obtained from this data set. The reconstruction indicates a sharp velocity change in the region of the finger. The maximum velocity change calculated for this reconstruction was 2.7%, which is close to our measurement of the actual velocity change within the glove.

Calibration - In order to relate velocity measurements to stress, we have initiated a calibration experiment. The purpose of this experiment is to obtain velocity measurements as a function of stress, both tensile and compression. To accomplish this, we fabricated tensile and compression specimens from 6.45 cm, A516-74A, grade 70, pressure vessel steel plate. These were placed in an MTS 810 material-test-system machine located in our laboratory.

Time-of-flight measurements were made with a system consisting of a Metrotek MP 215 High-energy Pulser (driving a wide-band transducer), and a Metrotek MR 101 Receiver and Metrotek MG 703 Interval Gate (driving an HP 5345A Time Interval Counter). The transducer was coupled directly to

one side of the specimen and stress was applied. The MG 703 was set to gate out the first and second echos from the back surface of the specimen. This eliminates any possible error due to the coupling thickness. We have found this measurement to be repeatable to 0.1 nsec. Transverse strain was measured with a Lion Precision Corporation Metri-Gap 300-3 Capacitive Micrometer to a precision of 25 μm . A thermocouple was also attached to the specimen to keep track of the temperature as the specimen was stressed.

The results of these tests are summarized in Figs. 10 and 11. Curves 1, 2, and 3 of Fig. 10 are derived from one tensile specimen and curve 4 is derived from another. Curve 1 represents a test run well below the yield point, curve 2 is a test run of the same specimen taken past the yield limit, and curve 3 is a final run taken to failure. This set of curves is extremely interesting since it seems to indicate that the specimen retains a memory of its last test if taken beyond yield. Curves 1 and 2 follow the expected path of a linear velocity increase with stress. However, after stressing the specimen into yield, as was done in curve 2, the behavior of the velocity (curve 3) is that of a specimen under compressive load. It appears as though a net residual compressive stress is present in the sample. The tension introduced by the machine must first overcome the residual compressive stress before the velocity again increases. This residual stress appears to be about 2.07×10^5 kPa. Note also, that the yield strength of the material increases from about 3.10×10^5 kPa to 4.55×10^5 kPa due to work hardening (as is well known). Curve 4 is the result of a test on a second identical specimen, performed to corroborate the stress acoustic constant derived from the first specimen. This factor, which is the slope of the curve, is $7.33 \times 10^{-4} \text{ } \%/6.9 \times 10^5 \text{ kPa}/2.54 \text{ cm}$.

In Fig. 10, the curves are drawn only for the stress region before yield is reached. This is because the readings become erratic past this point. For this material, the velocity change appears to flatten out. However, this may be due to the well known behavior of materials in tension such as dislocation and slip fractures in the material. In compression, a much smoother behavior is revealed, as shown in Fig. 11. In this case, linear velocity decrease (with about the same stress acoustic constant) occurs up to the yield point. After the material begins to yield, the velocity decreases in a highly non-linear manner with the slope increasing precipitately. This, too, is expected from theory.

CONCLUSION

We have discussed an application of Computer-Assisted Tomography (CAT) for locating and mapping regions of residual stress. The simulations and experiments described have demonstrated that velocity anomalies of 2% can be quite easily resolved. In work not reported here, we have also experimentally mapped velocity anomalies as low as 0.2% and feel that 0.05% is technically feasible. These velocities translate to a sensitivity of 6895 kPa in a 2.54 cm-thick region.

We feel that the reflected beam geometry represents an important advance in the development of methods for inspecting structures which do not physically lend themselves to either the parallel beam or the fan beam geometries. Thus, the reflected beam geometry could have important applications in the area of in-service inspection.

We are currently testing a prototype instrument for measuring stress in an online production environment. The instrument consists of an array of transducers placed in contact with the metal surface. Two elements of the array are selected to form a pitchcatch arrangement. One is used to transmit a pulse and the other to receive it. The choice of elements defines the angle of the ray to be measured. After a time-of-flight measurement has been made, the selected set of two elements are electronically moved over by one element and a second measurement made. In this way, a whole profile can be made very quickly.

After one profile is made, the separation between the two elements is changed by selecting two different transducers and the process is repeated, giving another profile at a different angle. All of the necessary data can thus be taken in a few seconds or less, depending upon the accuracy desired.

The time-of-flight measurements are fed directly into the memory of a microprocessor. When a complete set of data is available, the computer executes the ART algorithm and displays the resulting reconstruction on a CRT display.

An additional problem also needs to be discussed at this time. When sound waves travel through media with different velocities, they are refracted. In the work discussed in this report, we have assumed that the sound travels in a straight line between the source and receiver. The difficulty in trying to include the effect of refraction in our analysis is that we need to know the velocity field to calculate the refraction. However, the velocity field is exactly what we are attempting to determine.

Several solutions to this problem have been suggested. The most accurate method would be to include the refraction equations in a simultaneous solution for the velocities. However, as we discussed earlier, a simultaneous solution to the problem is impossible because of the large number of equations and unknowns involved. A more practical solution would be to first compute the velocity field as we have described. Once we have an estimate of the velocities, we could iterate several additional times using a modified version of the ART algorithm which would take into account the ray path bending.

To date, we have not investigated the problems caused by refraction because the velocity changes which we are interested in are small and will cause only slight bending. However, in the near future we apply this technique to examine regions containing large velocity variations, we will have to modify our reconstruction method to account for the refraction.

This research is sponsored by the Electric Power Research Institute under Contract RP504-2.

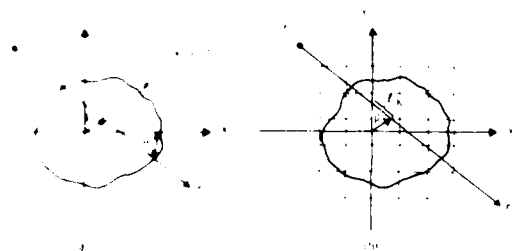


Fig. 1. Geometry for (a) computation of the time-of-flight profile and (b) the reconstruction of the object from the profiles.

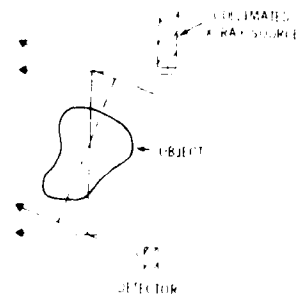


Fig. 2. Two Reconstruction Geometries.

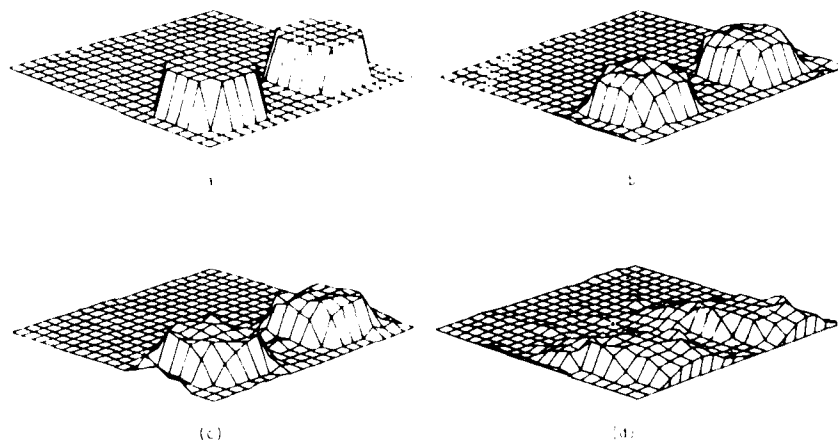
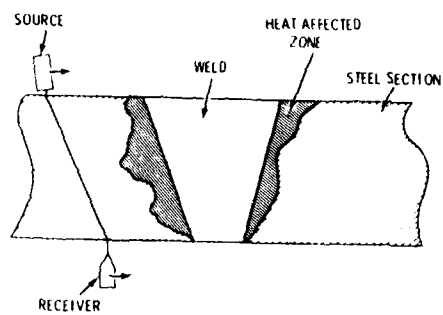
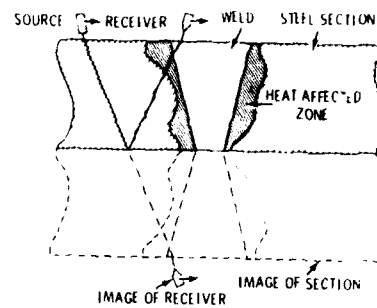


Fig. 3. (a) Test Image. Reconstructions: (b) 180° Field of View (c) 90° Field of View (d) 45° Field of View.



(a) Scanning Thick Sections by Transmission



(b) Scanning Thick Sections by Reflection

Fig. 4. Scanning Thick Sections by Transmission and Reflection.

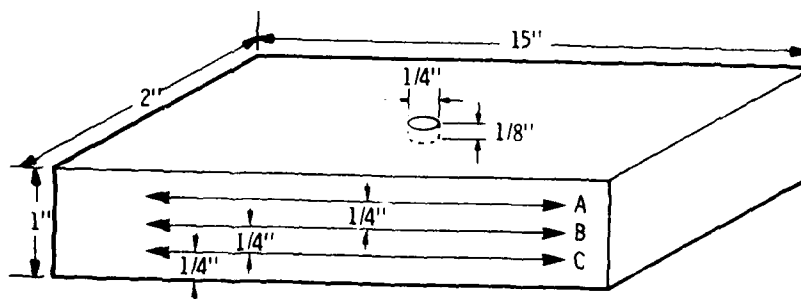


Fig. 5. Sketch of Aluminum Stress Sample Showing Scans at Levels A, B, and C.

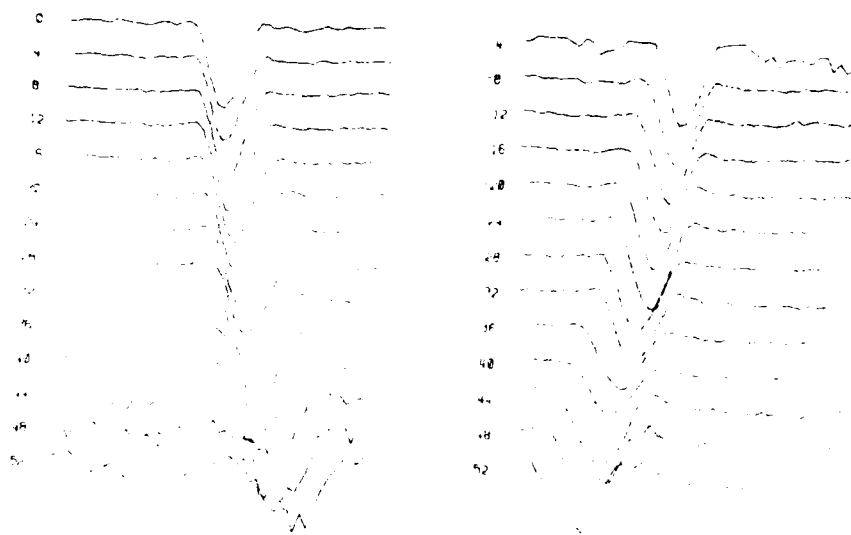


Fig. 6. Time-of-Flight Profiles for Aluminum Sample at Level B.



Fig. 7. Reconstructions at (a) Level A, (b) Level B, and (c) Level C in the aluminum block described in Fig. 5. The gray scale for all three is normalized to Level A.



Fig. 8. Fig. 7 repeated with gray scale normalized to each individual scan.



Fig. 9. Reconstruction of Rubber Glove Model Using Reflected Beam Tomography.

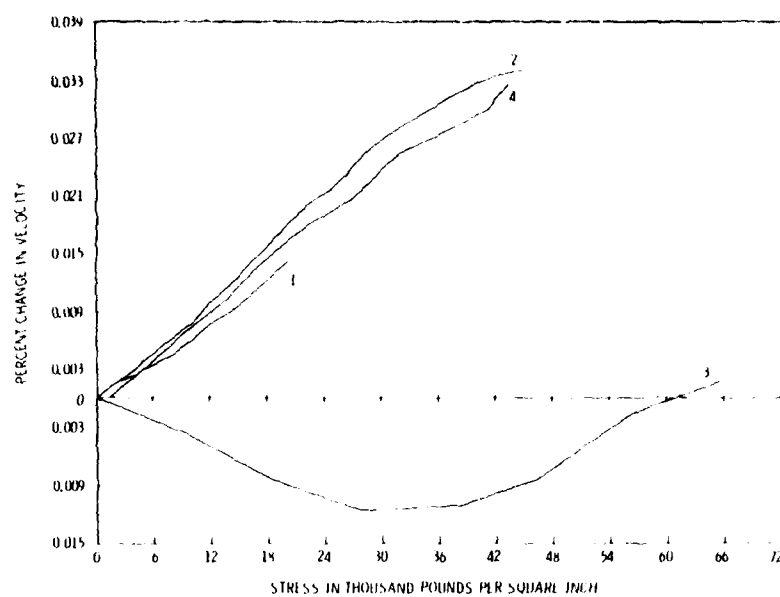


Fig. 10. Velocity Change as a Function of Tensile Stress.

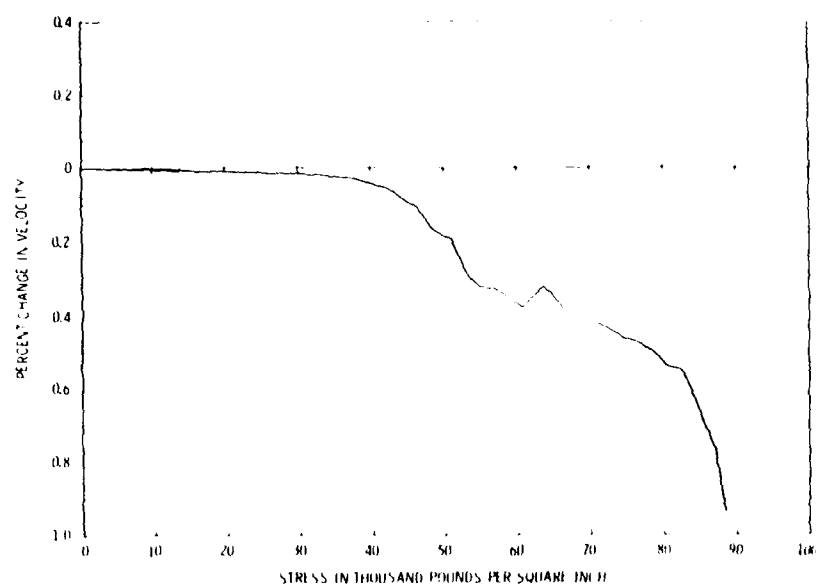


Fig. 11. Velocity Change as a Function of Compressive Stress.

REFERENCES

1. Gott, K. E., "Residual Stresses in a Weldment of Pressure Vessel Steel", AB Atomenergi Report, Nykoping, Sweden (1978).
2. Hsu, N. H., "Acoustical Birefringence and the Use of Ultrasonic Waves for Experimental Stress Analysis", Experimental Mechanics, May 1974.
3. Smith, R. T., "Stress-Induced Anisotropy in Solids--The Acousto-Elastic Effect", Ultrasonics, July-September 1963.
4. Noronha, P. J. and Wert, J. J., "An Ultrasonic Technique for the Measurement of Residual Stress", J. of Testing and Evaluation, March 1975, Vol. 3.
5. Brooks, R. A. and DiChiro, G., "Theory of Image Reconstruction in Computed Tomography", Radiology, December 1975, Vol. 117, pp. 561-572.
6. DeRosier, D. J. and Klug, A., "Reconstruction of Three-Dimensional Structures from Electron Micrographs", Nature (London), January 1968, No. 217, pp. 130-134, 13.
7. Gordon, R., Bender, R. and Herman, G. T., "Algebraic Reconstruction Techniques (ART) for Three-Dimensional Electron Microscopy and X-Ray Photography", J. Theoretical Biology, December 1970, Vol. 29, pp. 471-481.
8. Colsher, J. G., "Iterative Three-Dimensional Image Reconstruction from Projections: Applications in Electron Microscopy", Ph.D. Thesis, University of California-Livermore, UCRL-52179, December 1976.
9. Bracewell, R. N. and Riddle, A. C., "Inversion of Fan-Beam Scans in Radio Astronomy", The Astrophysics J., November 1967, Vol. 150, pp. 427-434.
10. Kruger, R. P. and Cannon, T. M., "The Application of Computed Tomography, Boundary Detection, and Shaded Graphics Reconstruction to Industrial Inspection", Materials Evaluation, April 1978, Vol. 36, No. 5.
11. Falconer, D. G. and Gates, D. C., "Reactor-Component Inspection with Computed Tomography", EPRI NP-213, Project 610-1, July 1976.
12. Radon, J., "Über die Bestimmung von Funktionen durch ihre Integralwerte langs gewisser Mannigfaltigkeiten", Ber. Akad. Wiss. (Leipzig), Math. Phys. Klasse, Vol. 69, pp. 262-277, 1917.
13. Rammachandran, G. N. and Lakshminarayanan, A. V., "Three-Dimensional Reconstruction from Radiographs and Electron Micrographs: Applications of Convolutions Instead of Fourier Transforms", Proceedings of National Academy of Science U.S.A., September 1971, Vol. 68, pp. 2236-2240.
14. Mersereau, R. M. and Oppenheim, A. V., "Digital Reconstruction of Multidimensional Signals from their Projections", Proceedings of the IEEE, October 1974, Vol. 62, No. 10, pp. 1319-1338.
15. Goitein, M., "Three-Dimensional Density from a Series of Two-Dimensional Projections", Nucl. Instr. Meth., June 1972, Vol. 101, pp. 509-518.
16. Gilbert, P., "Iterative Methods for the Three-Dimensional Reconstruction of an Object from Projections", J. Theoretical Biology, July 1972, Vol. 36, pp. 105-117.
17. Herman, G. T., Lent, A. and Rowland, S. W., "ART: Mathematics and Applications; A Report on the Mathematical Foundations and the Applicability to Real Data of the Algebraic Reconstruction Techniques", J. Theoretical Biology, 1973, Vol. 42, pp. 1-32.
18. Sweeney, D. W., "Interferometric Measurement of Three-Dimensional Temperature Fields", Ph.D. Thesis, University of Michigan-Ann Arbor, 1972.

SUMMARY DISCUSSION
(B. Hildebrand)

Jeffrey Eberhard (General Electric): Can you tell me how accurately you measured the time of flight and, secondly, what's that smallest size stress distribution you can see?

B. Hildebrand: We are using commercial time of flight, time interval counters, and have been measuring time of flight to around .3 nanoseconds. This is using an average of 100 measurements to 1000 measurements, a thousand pulses, for example. Now, the minimum stress measurement, that's a very good question. We have estimated that we should be able to measure in the neighborhood of 5,000 psi in steel over a one-inch length.

Don Thompson (Science Center): As background experience, we found when you load a sample, that you can find contributions of velocity changes from dislocation density changes that are as large or larger in some cases than the contributions from third-order constants. Do you have any way to know whether the total change in velocity is seen or is due to stresses, or is there a part due to changes in dislocation constant due to the loading and the working of the material?

B. Hildebrand: We really have no way of determining that. We were simply measuring velocity change and, unfortunately, velocity change can come about due to other things besides stress.

Don Thompson: I don't know if the third-order constants are known independently according to this material, but did you say plug those values in and calculate what expected velocity changes you would get from simply the stress component?

B. Hildebrand: No, we haven't done that.

Richard King (Stanford University): In answer to the last question, what we do is a uniaxial tension test, and you can calibrate the material because we know the stress change, so we just do a curve. I think in the curve you showed a velocity change. We do one of those by checking the relative velocity change in the last region. We cannot get the third-order constant separately, but the full expression in their combination adds up, so that's how you can determine that for different material. And it varies quite widely. For different types of aluminum, for instance, it can be as much as 30 percent change in the constant. The other comment I wanted to point out: if all you're using is longitudinal waves, what you're measuring is just the sum of the principal stresses, not really the separate stress components.

B. Hildebrand: That's right.

Richard King: Have you made any attempt to separate them out?

B. Hildebrand: No we haven't. On the grounds that any information about stress distribution will be useful. Currently, no knowledge of stress is nondestructively obtainable, so if we can show them anything, it's great.

Unidentified Speaker: It seems to me if you have a stress gradient in the material as you do have when you punch it on the top, you should worry about the assumption that you have straight-line motion just as you do if you have inclusions, but the effect would show up differently. There would be an analogy to see the change in position or the flattening, the distortion of the sun when it's setting or, in the case of a hot day, seeing mirages and double images and that kind of thing. Are you worried about these effects?

B. Hildebrand: We haven't worried about them. I have shoved those worries into the background on the grounds that let's do one thing first.

Unidentified Speaker: But if you have a transmitter and a receiver, you're going to have to worry about the geodesic paths of sound.

(continued)

B. Hildebrand (discussion continued)

B. Hildebrand: When you really get down to it, you're eventually going to have to do something like that.

Gordon Kino (Stanford University): I think you have to remember these effects are very weak effects. All you can do to measure them is the transit time, and you're only talking a half-percent.

Unidentified Speaker: It's much more than the change of the velocity of sound in the atmosphere when you see two images, mirages, an image of the sun.

Gordon Kino: You're talking about thousands and thousands of wavelengths. Here you are not. These are relatively short paths.

#

APPLICATIONS OF TOMOGRAPHY TO THE NUCLEAR INDUSTRY

R. A. Morris, R. P. Kruger and G. W. Wecksung
Los Alamos Scientific Laboratory
Los Alamos, New Mexico 87545

ABSTRACT

While tomographic methods of reconstructing three-dimensional x-ray images are becoming more common in the medical field, their application to industrial problems has only started. Some of the features that differentiate industrial tomography from medical tomography are

- 1) x-ray energies may vary from < 10 keV to > 22 MeV,
- 2) radiation dose to the object is not a constraint,
- 3) inspection times (within economic constraints) are not as important,
- 4) the anomalies to be detected offer sharp, high contrast boundaries to the inspection system,
- 5) high spatial resolution rather than high contrast sensitivity is the primary design goal, and
- 6) the number of views may be limited by other (mechanical) constraints.

This paper will describe the effort the Los Alamos Scientific Laboratory (LASL) is making to define the design parameters that affect the constraints listed above. A tomographic test bed in which various design features may be evaluated will be described. The computational facilities at LASL, which include a versatile modeling code that can simulate tomographic systems with various types of radiation, geometrics, and detector types, will also be discussed.

Finally some applications of tomography to the nuclear industry will be described. These range from detection, identification, and quantitative mass estimates of fissile material within a container to the detection and measurement of stress corrosion cracks in reactor cooling systems.

Tomographic techniques have recently captured the public interest, particularly in the medical field, although some of the early work was done in disciplines far removed from medicine.^{1, 2, 3} The interest now seems to be shifting somewhat back to nonmedical areas and in particular to industrial applications. This paper will describe some of the work being done at the Los Alamos Scientific Laboratory (LASL) and some of our applications of tomography to the nuclear industry.

The basic principles involved are illustrated in Fig. 1. Details of the theory of tomographic reconstruction will not be discussed as they are covered more than adequately in the literature.⁴

First, the constraints imposed upon medical and industrial tomography will be compared.

Medical tomography is primarily interested in one subject, the human body. Granted, different parts of the body are looked at, but compared to the diverse objects inspected in industry, the medical problem is somewhat limited. Within the human body,

medical tomography is trying to detect subtle changes in object density or composition using a relatively narrow range of x-ray energies (50 kV to 150 kV). Spatial resolution, while important, is not the primary parameter of interest. In contrast, industrial tomography is interested in reconstructing a cross section from objects that range from a nuclear reactor core (to detect broken or ruptured fuel elements) to the microbeads used as targets in laser fusion research (to measure wall thickness and asymmetries). With these examples of tomographic applications, the x-ray energies needed to penetrate the object will vary from > 25 MeV to 5 keV. With this diversity of objects, the parameter of interest has changed from object density to spatial resolution. Object density is still of interest, but typical features detected in a reconstruction will have air-to-metal interfaces and therefore should be easy to detect. However, the features that are desired to be detected can be small as a crack less than 0.1 mm wide.

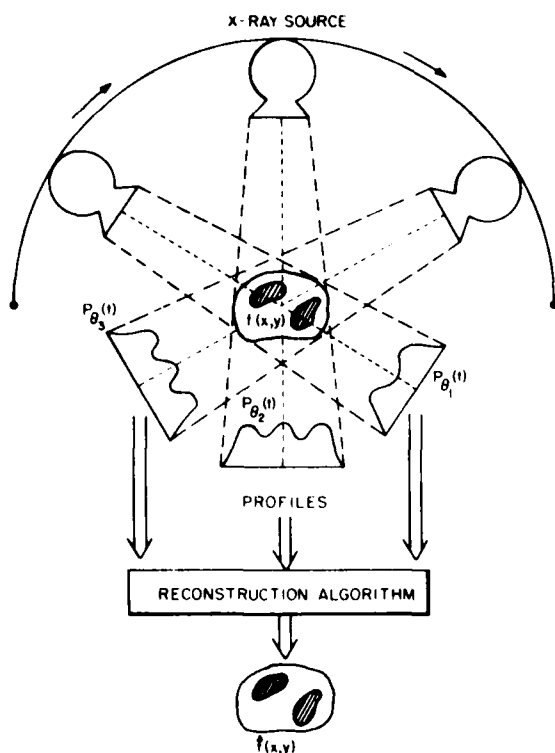


Fig. 1. Typical Tomographic Configuration.

There are other, more obvious differences between medical and industrial tomography. The radiation dose absorbed by the object is unimportant to the industrial user. Time, except as an economic constraint, is relatively unimportant. In many cases, the tomographic equipment may have to go to the object instead of the other way around. And finally, the projection data collected may be less than optimum in terms of number of views, signal-to-noise ratio and spatial resolution for a number of reasons unique to the object being inspected. Because of these differences, medical tomographic equipment and techniques cannot be adapted to industrial use except in a few special cases.

At the Los Alamos Scientific Laboratory, we are developing a modular tomographic system that will enable us to explore the effect of changing parameters (spatial resolution, number of views, etc.) on image quality as well as demonstrate feasibility of performing tomography on particular objects. Figure 2 illustrates the scanner that is being used and Fig. 3, the schematic of the complete system. It must be emphasized that this is a start-up system utilizing as much equipment that is on

hand as possible. The data acquisition and scanner motion is controlled by a PDP-11/40 minicomputer. While the PDP-11/40 can perform the reconstruction, it does not have a suitable display device for presenting the results to the operator. For this (and other) reasons, the projection data is stored on a nine-track magnetic tape which is then transported to a CDC-7600 computer for reconstruction and display.

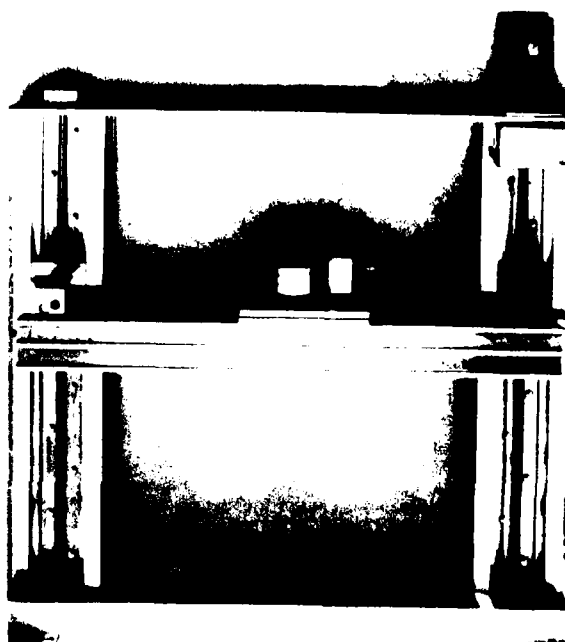


Fig. 2. Tomographic Scanner.

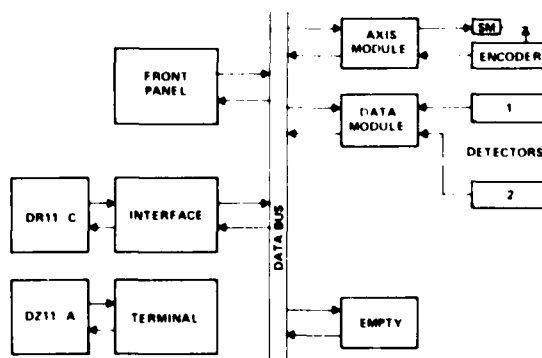


Fig. 3. Tomographic System Schematic.

The first application of tomography conducted by LASL was to detect and locate simulated air bubbles in reactor cooling water piping.⁵ Figure 4 illustrates one of the radiographs from which the reconstruction in Fig. 5 was made. In this particular case, the projection data was obtained by scanning 36 radiographs (one every 5 degrees) with a 0.8-mm aperture. The tube wall thickness in this case was 0.35 mm.



Fig. 4. Radiograph of Simulated Air Bubble

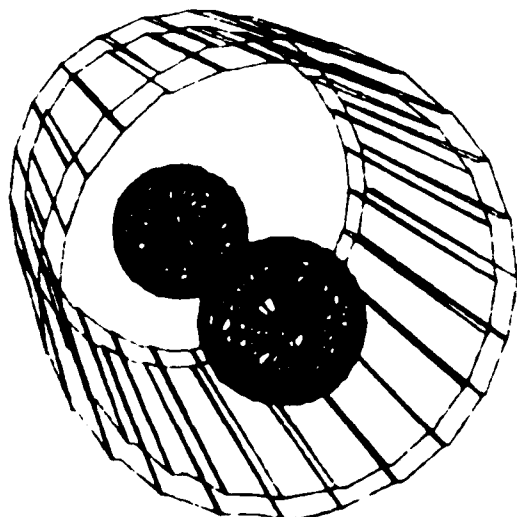


Fig. 5. Line Graphic of 3-D Tomographic Reconstruction

The significance of this simulation is that conventional film techniques, tomographic algorithms, image enhancement algorithms, and line graphic techniques can be combined to produce a useful result.

The next application of tomographic techniques does not involve any data collection. It is a pure simulation to demonstrate the feasibility of performing multi-energy tomography to not only locate objects but also to identify their elemental components.⁶

The object being inspected is a steel can containing pellets of fissile material (U233, U235, PU238). The intent is to generate three tomographic reconstructions of the object using a thermal neutron beam with three fission chambers. One each of the fission chambers would be made from each of the fissile materials. The hope is that the response of each detector will be sufficiently different from the others that an unambiguous determination of the Z number can be made. Figure 6 illustrates the results and Table I tabulates the amplitudes of each material as a function of detector type.

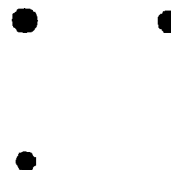


Fig. 6. Tomographic Reconstruction of Fissile Materials.

TABLE I
VARIOUS RESPONSE PEAKS

Detector Type	^{233}U	Peak Response ^{235}U	^{239}Pu
^{233}U	.312	.240	.193
^{235}U	.264	.264	.201
^{239}Pu	.288	.264	.265

The simulated results show that the responses are independent and in principle are sufficiently different to resolve the different materials.

The last application of tomography to be discussed is the detection of small stress corrosion cracks in reactor cooling pipe.⁷ The intent is to develop a technique to detect and measure cracks originating on the outside of 22-mm diam, 1.2-mm wall pipe. The results would be used to calibrate the eddy current equipment used in the actual inspection of the pipe.

Again radiographic film was used as the detector. Radiographs were taken every degree for 200 degrees and the projections digitized with an aperture size of 0.1 mm. Figure 7 illustrates the results with some of the obvious tomographic indications correlated with the visual surface indications.

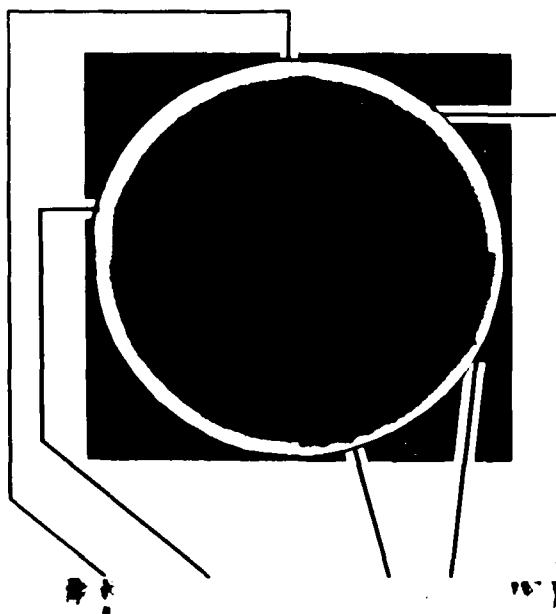


Fig. 7. Tomographic Reconstruction of Cracked Cooling Pipe.

The detection of some of the stress corrosion cracks in the pipe is significant in itself but much work remains to be done.

- 1) Determine the lower limit of detectability.
- 2) How well does the shape of the tomographic indication reflect the actual shape?
- 3) Can we use larger pixel sizes (to increase the signal-to-noise ratio) but overlap the pixels and deconvolute to get back the spatial resolution?

The examples described in this paper just scratch the surface of the work that remains to be done in industrial tomography. For instance the field of tomographic simulation needs a good radiation transport code (Monte Carlo?) that can be adapted to calculate the projection data. With such a simulation package, the feasibility of performing a tomographic reconstruction on a unique object can be determined at a fraction of the cost of actually building the equipment. Experimentally, the trade offs between results and experimental constraints must be measured and parameterized.

REFERENCES

1. D. E. Kuhl and R. Q. Edwards, "Reorganizing Data from Transverse Section Scans of the Brain Using Digital Processing," *Radiology* 91 (1966) 975-983.
2. R. N. Bracewell and A. C. Riddle, "Inversion of Fan Beams in Radio Astronomy," *The Astrophys. J.* 15 (1967) 427-438.
3. R. A. Crowther, D. D. DeRosier, and A. Klug, "The Reconstruction of a Three-Dimensional Structure from Projections and Its Application to Electron Microscopy," *Proc. Roy. Soc. London* A317 (1970) 319-340.
4. R. A. Brooks and G. deChiro, "Principles of Computer Assisted Tomography (CAT) in Radiographic and Radioisotopic Imaging," *Phys. Med. Biol.* Vol. 21, No. 5 (1976) 689-732.
5. R. P. Kruger and J. M. Cannon, "The Application of Computed Tomography, Boundary Detection, and Shaded Graphics Reconstruction to Industrial Inspection," *Mat. Eval.* Vol. 36, No. 5 (1978)
6. R. P. Kruger and R. A. Morris, "Simulated Neutron Tomography for Nondestructive Array," *Proceedings of the SPIE, Technical Symposium East and Instrument Display*, April 1979, Washington, DC.
7. R. A. Morris, R. P. Kruger, and G. W. Wecksung, "Tomographic Visualization of Stress Corrosion Cracks in Tubing," *Los Alamos Scientific Laboratory Report LA-7891MS* (June 1979).

SUMMARY DISCUSSION
(R. A. Morris)

Jerry Losakony (Session Chairman--Battelle Northwest): I might say this last program that Dr. Morris was talking about was part of our eddy current program to try to characterize flaws in nuclear reactor steam generator tubing which is about three quarters of an inch in diameter, and it is the only way that we have been able to define the nature of the crack and then try to correlate the eddy current signals with that and come up with some sort of response of what the eddy current signals look like for true intragranular stress curves and patterns. All the rest of the work we have done in machine notches and things of that kind. This is the first time we have been able to nondestructively characterize real flaws. It's very, very encouraging kind of work.

Dr. Bush (Battelle Northwest): Can you angle your beam on a case such as the last one so that you can see if you go through an intensity maximum it will then establish the angle of crack with respect to the surface?

R. Morris: The geometry we are using here is a fan-beam geometry, so it's already angled, so to speak. I really don't know if I understand your question.

Dr. Bush: If you section a tube, if you have a crack that is essentially along the radius, then as you pass through you would expect a maximum intensity. Unfortunately, stress corrosion cracks don't obey those laws. They go at an angle. They might be at 30 degrees or 70 degrees away from the radius. And to see what the angle is, if you turn and angle the beam and go through an intensity maximum--

R. Morris: In principle, the algorithm doesn't care what angle or what orientation the defect or feature that is reconstructing is at. In practice, of course, there are sensitivity problems. If this thing is such an angle where you have to go through thicker material, I guess my answer would be we can detect -- we are not limited to radial cracks. We can detect cracks that go off at any angle, in principle. In practice there might be a sensitivity limit beyond which we can't see it, if it's too large an angle.

Dov Rosenfeld (S.I.I. Intl.): It's a comment. That is, it's my feeling that the greatest application of computer tomography in nonmedical is not going to be taking the medical and applying it, but there are big differences in the non-medical. For example, in most of the work you were showing here you really have a binary problem. It's off-on; crack-no crack.

R. Morris: I think that's characteristic of a lot of industrial problems.

Dov Rosenfeld: You also have a nongeometry. For example, you're talking about pipes. It's conceivable to me that one could look for hairline cracks by scanning every two millimeters of a pipe in all orientations, but then each pipe would then take five weeks. Pipes are circular and if you can detect a crack visually after obtaining a tomograph, you can detect a crack in the projections themselves. That is, several people have shown that result. Mathematically, you must have detectability projections before you can have detectability in your final, so two projections, for example, for a circular object will do it all for you, including locating where it is.

R. Morris: That's right. If you can invoke symmetry or any a priori knowledge.

Dov Rosenfeld: That's what I think the future will go for inspection.

R. Morris: That's correct. We feel that in contrast to the medical field, industrial tomography, like you say, is binary. You're normally not looking for subtle density changes, although there are exceptions. I think the primary requirement or constraint is that there is a requirement on industrial tomography in resolution. And that's another reason. Not only the fact that our scanner wasn't working, but that's another reason we went to X-radiographic film as a detector. We felt in the case of the Battelle pipe we needed the extra resolution. And film has very, very good spatial resolution compared to a collimated detector. It would be very, very difficult to get the kind of resolution we got.

(continued)

R. A. Morris (discussion continued)

Dov Rosenfeld: You can have resolution as good as you want. It just makes a smaller hole.

R. Morris: As a practical problem, in film you have the resolution directly on the film. Incidentally, the aperture size on scanning the pipe was 100 microns along in the direction of the scan

#

OVERVIEW OF ULTRASONIC DEVELOPMENTS

R. B. Thompson
Rockwell International Science Center
Thousand Oaks, CA 91360

ABSTRACT

An overview of the ultrasonic developments which have occurred in the DARPA/AFML Interdisciplinary Program for Quantitative NDE is presented. The paper is introduced by a discussion of the philosophy of the program and a review of the progress made during the last five years towards the development of quantitative techniques and criteria for accepting or rejecting parts. This is followed by a summary of the relevant papers presented at this meeting and of the role which they play in the evolution of this new technology. The paper concludes with a discussion of the use of these technical building blocks in establishing on-line systems and stand alone spin-offs for DoD application.

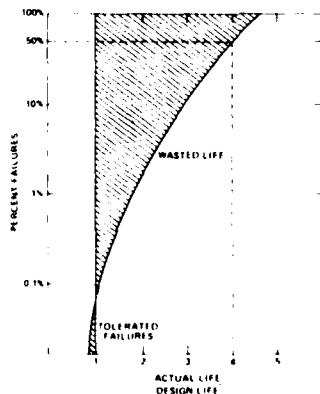
This paper will present a slightly broader perspective than an overview of the papers in this session. It will cover those papers, but it will also delineate the relationship between them and a number of papers presented in other sessions. In this way, a picture of the thrust and philosophy of the DARPA/AFML Interdisciplinary Program for Quantitative Flaw Definition can be presented.

The first figure is a summary of results obtained by Rau.¹ It provides us with a very good description of the motivation for the development

of quantitative NDE techniques. The left hand part of the figure uses the example of turbine disks to illustrate the wastes that occur when part service lives are based on average fatigue behavior rather than the condition of individual parts. Since the distribution of failure times is broad, one must select a design life that is quite conservative for most parts in order to avoid the premature failure of more than a few. As shown for this example, if one requires that only one part in a thousand will fail during the design life, one finds that 50 percent of the parts would

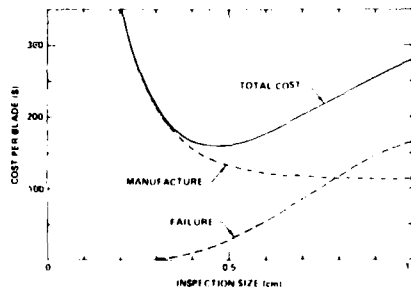
PROBLEM

STATISTICAL NATURE OF FAILURE CAUSES MUCH WASTAGE FOR A SPECIFIED RELIABILITY.



STRATEGY

NONDESTRUCTIVE EVALUATION TO ALLOW LIFE EXTENSION OF INDIVIDUAL COMPONENTS UNTIL DAMAGE DEVELOPS. INSTRUMENT ADJUSTED TO MINIMIZE COSTS.



CRITICAL ELEMENTS

- NONDESTRUCTIVE METHOD OF MEASURING FLAW SIZE
 - QUANTITATIVE
 - RELIABLE
- QUANTITATIVE METHOD TO SELECT ACCEPT/REJECT CONDITION
 - FAILURE MODELS
 - ECONOMIC ANALYSIS

TOTAL COSTS

	\$100K FAILURE	\$1M FAILURE
MANUFACTURE	\$100	\$100
NO INSPECTION	\$328	\$2,000
HISTORICAL INSPECTION	\$215	\$1,115
OPTIMUM INSPECTION	\$150	\$234

Fig. 1 Economic benefits of quantitative NDE.

have lasted more than four times the design life. This excess life is wasted. To overcome this problem, one must, in some way assess the condition of individual parts by the use of NDE techniques or other approaches. One is then no longer governed by the statistical distribution, but can retire specific parts as needed: Retirement-for-Cause.

The center of the figure presents economic data illustrating how, when using NDE, the system costs can be minimized by the proper selection of the accept-reject criteria. Improving the ability of the NDE technique to quantitatively separate good and bad parts increases the depth of the cost minima and further reduces costs. The objective of the papers that you will hear today, and in several other sessions, is to ultimately make such savings possible.

Figure 2 presents some further background on the role of NDE in lifetime prediction, as also noted by Thomson² and Marcus.³ One of the models commonly used to predict part lifetimes or failure is fracture mechanics, coupled with crack growth rate models. To use these models, one needs three inputs. One needs environmental inputs, including both loading and any gaseous or aqueous environmental conditions that might influence crack growth rates. These inputs can be determined during design or by monitoring of the part during its service. The second inputs one needs are material properties, such as resistance to crack growth. Thirdly, one needs to know flaw sizes and orientations. Material properties have been studied extensively and can be found in handbooks and other sources. However, no satisfactory techniques are available on line for determining flaw size and orientations. The present program is addressing this deficiency.

Figure 3 indicates the philosophy that has been utilized in developing a quantitative NDE

capability. In order to predict a part lifetime, three types of information must be combined: a failure model, measurement results which have been processed by an inversion technique to give estimates of flaw parameters, and if possible, independent information, or a priori information about what types of flaws might be expected in the part under study.

The a priori information is needed since, under many conditions found in practice, it is not possible to experimentally make enough measurements to uniquely determine the state of the flaw. Examples of these conditions include high ultrasonic attenuation, which limits the use of high frequencies, or complex geometries, which restrict the range of angles that can be used in a measurement. Under such conditions, the measurements can rule out many possible flaw types, but they can not uniquely define the flaw. Independent information about the flaws likely to be present for the particular processing and service history of the part may eliminate other possibilities and improve the flaw estimate.

Once a lifetime prediction has been made based on these inputs, an accept-reject criteria must be applied to determine whether or not the part should be removed from service. This criteria must be based on a risk-benefit analysis for the part in question.

Before proceeding with this overview, it should be emphasized that only work performed as a part of the DARPA/AFML Interdisciplinary Program for Quantitative NDE will be addressed. Many other papers are included in this meeting which were supported by other agencies. They also form important parts of the same technology but will not be explicitly discussed.

Referring again to Fig. 3, it should be noted that a major emphasis of the DARPA/AFML Program

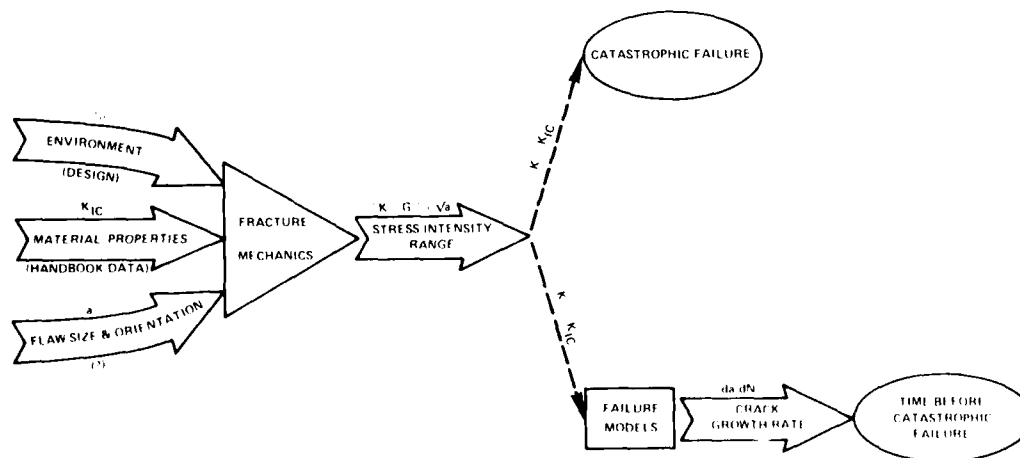


Fig. 2 Lifetime prediction showing role on NDE inputs.

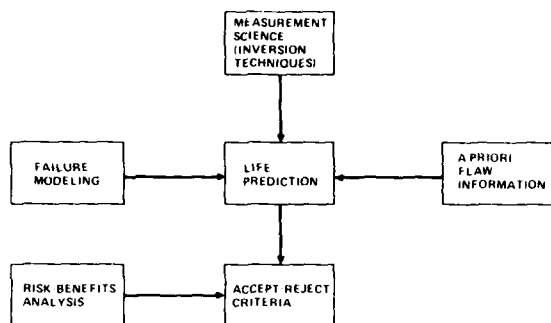


Fig. 3 Elements of development of quantitative accept/reject criteria.

has been the improvement of measurement sciences (including inversion techniques). This has been treated generically, with the objective of developing basic techniques which could be applied to many different material systems. Additional efforts have been directed towards applying these techniques to specific material systems, ceramics and metals.

In order to discuss the technique development, it is useful to review briefly what has been done during the previous years of this program and what appears to lie on the horizon. Figure 4 illustrates just a few of the highlights of the past years. Also included is a schematic flow diagram that presents the steps needed to develop inversion techniques. One must first solve the forward problem of the interaction of energy with a known flaw. In this session, ultrasonic energy is being considered but the same concepts apply to the electromagnetic techniques that were discussed in a previous session. Solution of the forward problem involves an interaction between theory and experiment. Once that is in hand, one must concentrate on the inverse problem, which ultimately will lead to a predictor that can be used in life prediction. Of course, at the same time, one must continue to study the forward problem because extensions to more difficult situations are needed to enable these inverse techniques to become more widely applicable.

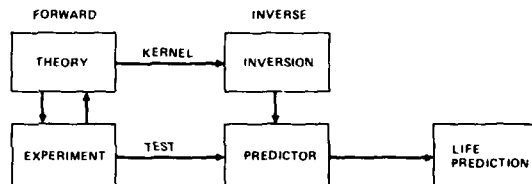
In 1975, the DARPA/AFML Interdisciplinary Program for Quantitative NDE was initiated, and an interdisciplinary team was gathered which established active communications between a group of scientists and set the stage for major contributions from the different disciplines. Also during the year, some basic elements of scattering theory and experiment were developed. The next year a set of several different experimentally verified scattering models were completed, particularly for the case of bulk inclusions.

In 1977, the annual conference was held at Cornell. One of the high points of that meeting was the first demonstration of quantitative inversion of experimental data. In that case, the adaptive learning technique had been trained on

theoretical solutions and then used to predict flaw parameters from experimental data. In addition, work was initiated on the problem of characterizing surface cracks.

By 1978, last year, a family of inversion algorithms had been developed. Techniques for shape reconstruction, adaptive learning, and long wavelength techniques for parameter estimation were included. There was further extensions for the case of surface cracks. In ceramics, a framework for life prediction was developed, and strategies were defined for incorporating failure modeling and risk analyses to quantify the determination of the accept/reject criteria.

In this meeting, the work to be presented will include refinement of inversion techniques, extension of the scattering models to the case of irregular flaw shapes and multiple flaws, a more detailed demonstration of the life prediction strategy for ceramics, and an initial demonstration of the life prediction strategies for the case of metal fatigue. Also included will be a discussion of an ultrasonic test bed which will play a key role in reducing some of these techniques to practice.



- 1975: ESTABLISH INTERDISCIPLINARY TEAM AND BASIC ELEMENTS OF SCATTERING THEORY AND EXPERIMENT
- 1976: DEVELOP SET OF EXPERIMENTALLY VERIFIED SCATTERING MODELS FOR BULK INCLUSIONS
- 1977: DEMONSTRATE FIRST QUANTITATIVE INVERSION (ADAPTIVE LEARNING TECHNIQUE) BEGIN DEVELOPMENT OF MODELS FOR BULK CRACKS
- 1978: DEMONSTRATE FAMILY OF INVERSION ALGORITHMS (RECONSTRUCTION, ALN, LONG WAVELENGTH) BEGIN DEVELOPMENT OF MODELS FOR SURFACE CRACKS DEVELOPMENT OF FRAMEWORK FOR LIFE PREDICTION STRATEGY FOR CERAMICS
- 1979: REFINEMENT OF INVERSION TECHNIQUES BEGIN EXTENSION OF SCATTERING MODELS TO CASES OF IRREGULAR FLAWS, MULTIPLE FLAWS, ROUGH FLAWS DEMONSTRATION OF LIFE PREDICTION STRATEGY FOR CERAMICS DEMONSTRATION OF LIFE PREDICTION STRATEGY FOR METAL FATIGUE ASSEMBLY OF ULTRASONIC TEST BED

Fig. 4 Progress in quantitative ultrasonics.

Figure 5 illustrates one of the future directions of the program. One question that must be addressed is, "How good are the models that have been developed for inversion of data from ellipsoidal flaws when the models are applied to more realistic shapes such as irregular or multiple

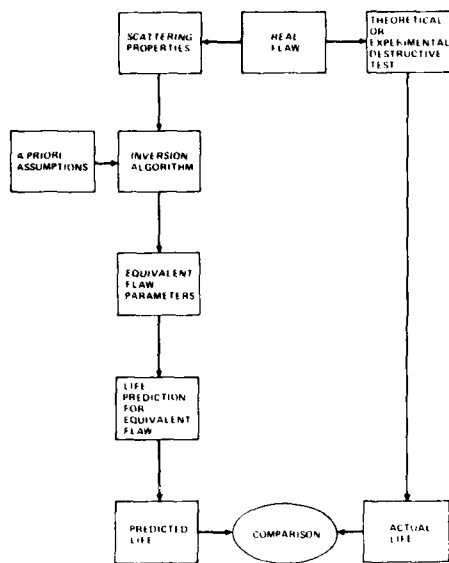


Fig. 5 Proposed test of robustness of inversion algorithms.

flaws?" A program that will answer this is schematically indicated. Measurements, or theoretical predictions, of scattering from irregular and multiple flaws will be obtained and used as inputs to the existing inversion algorithms (which were optimized for ellipsoidal shapes). The algorithms will then give, as outputs, a set of equivalent flaw parameters. These flaw parameters will then be used to make a prediction of the lifetime of that equivalent flaw. Finally, this lifetime will be compared with the actual life of the flaw. The degree of agreement is actually the bottom line in evaluating the performance of any inversion technique. It's not really important whether the technique tells exactly what the flaw shape is. It is important whether it predicts the lifetime of that flaw with sufficient accuracy.

In order to perform this test, it is necessary to have a theoretical and experimental understanding of the behavior of flaws that do not have simple geometries. A number of the papers that are presented in this session provide the foundation for this understanding.

Figure 6 summarizes the papers to be presented in this session. The Distorted Wave Born Approximation will be presented by Domany. In this integral equation approach to ultrasonic scattering, a general flaw shape is viewed as a perturbation of a spherical shape. For flaws with irregular surfaces, but generally spherical shapes, this can be expected to give quite accurate results. Gubernatis will then discuss the use of PADE Approximates to improve the accuracy of scattering calculations at higher frequencies. The PADE Approximates are functions in a series expansion of the ultrasonic scattering. They can be derived from various classical expansions of the scattered fields, but often have much better

COMPLEX, ROUGH, AND MULTIPLE FLAWS

- DISTORTED WAVE BORN APPROXIMATION - DOMANY
(VIEW GENERAL SHAPE AS PERTURBATION OF SPHERE)
- PADE APPROXIMANTS - GUBERNATIS
(EXTRAPOLATION OF TRUNCATED SERIES TO CONVERGENT RESULTS)
- T MATRIX APPROACH - VARADAN
(EXTENDED BOUNDARY CONDITION)
- EXPERIMENTAL RESULTS - TITTMANN
(NEW DIFFUSION BONDED SAMPLES)

CRACKS

- CRACK OPENING DISPLACEMENT - REPRESENTATION THEOREM - ACHENBACH
(REFORMULATION OF ELASTODYNAMIC RAY THEORY TO AVOID DIFFICULTIES AT SHADOW BOUNDARIES AND CAUSTIC SURFACES)
- EXPERIMENTAL RESULTS - ADLER
(MEASUREMENTS THROUGH WATER - SOLID INTERFACE)

Fig. 6 Summary of ultrasonic fundamentals session.

convergent properties and therefore a finite number of terms give useful results at higher K_a values. The T-matrix approach will be treated by the Varadans. Through the use of a technique known as the extended boundary condition, with somewhat greater computational effort than is needed in the other techniques presented, they are able to obtain very precise scattering predictions. Again, the results are useful for rough and multiple flaws. Tittmann will discuss experimental investigations of the predictions of these theories. The measurements were made on a new set of diffusion bonded samples containing irregular and multiple flaws.

Papers will be presented on the scattering from cracks as well as volumetric flaws. The Crack-Opening Displacement Representation Theorem approach, which is a reformulation of elastodynamic theory to avoid some of the difficulties that occur at caustic points and shadow boundaries, will be discussed by Achenbach. Adler will present experimental tests of this theory.

Figure 7 illustrates some of the fundamental information that will be included in these talks. This is a result obtained by the Varadans in the study of the effects of surface roughness on scattering. The dependence of the scattering at 45 degrees is shown, as a function of K_a , for three flaws. These are characterized by a parameter σ , which is a ratio of roughness to size, and N , which gives number of roughness periods around the circumference. The solid line shows

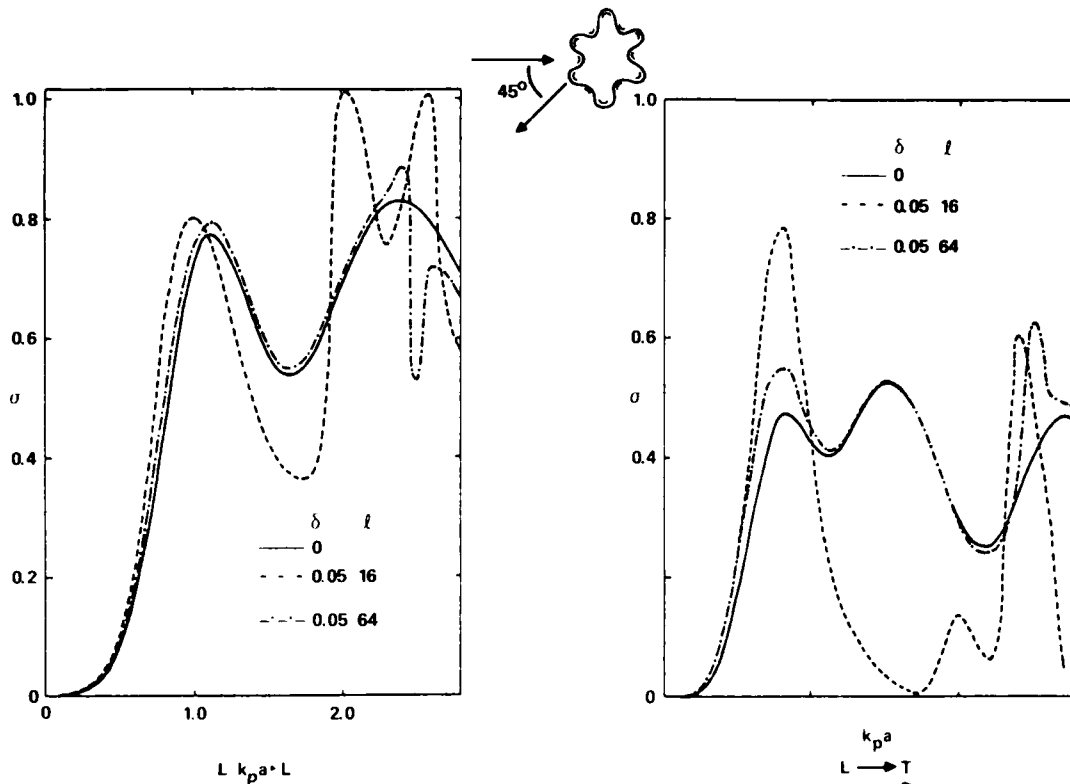


Fig. 7 Effect of roughness on scattering.

the results for a smooth flaw, $\sigma = 0$. The dashed line gives the results for a roughness of 0.05 for the case of 16 periods around the periphery. The dash-dotted curve presents the results for the same roughness parameter but with 64 roughness periods, i.e. a finer scale roughness. It can be concluded from results such as these that the flaw characterization techniques based on ideal ellipsoidal shapes should still work fairly well when surface roughness is present, as long as that roughness is fine with respect to the ultrasonic wavelength.

Once the forward scattering problem has been solved, attention must focus on the inversion problem. Figure 8 summarizes some of the approaches presented in this area. The inversion techniques are classified into two categories. Reconstruction techniques can be used when Ka is greater than two or three. Then there is enough information to draw a picture of the flaw. The papers presented in the imaging session fall in this category. In particular, Kino's work on electronically focused and scanned imaging systems, and Lakin's work on wave front reconstruction imaging were a part of the DARPA/AFML program. Two other techniques, which can be categorized as reconstruction techniques, will be presented today. The work of Bleistein and Cohen on Physical Optics Farfield Inverse Scattering (POFFIS) and the work of Rose on the Inverse Born Procedure.

Each of these reconstruction techniques has been optimized on the basis of slightly different physical assumptions about the flaw, as is indicated by the table in the figure. For example, in the classical imaging approaches of Kino and Lakin, the basic processing algorithm is optimal when the flaw itself has diffusely reflecting surfaces. On the other hand, the POFFIS algorithm is probably optimal when the surfaces are smooth and specular. That is, there is not an intrinsic roughness built into that algorithm. The Inverse Born Approximation is based intrinsically on an elastic wave model. Approaches of that type promise to be able to treat some of the more complex phenomenon associated with elastic wave propagation, internal reverberations, and mode conversion. This is shown as a broken check in the table of Fig. 8 because the simplicity of the Born Approximation precludes all of those effects from being included in detail. Nevertheless, they are implicitly included.

On the other hand, if sufficiently high frequency information is not available to reconstruct flaw shapes, another family of techniques are available. These are techniques which require some independent information or assumptions about the flaw state. For example, if one knows that the flaw is an elliptical crack, then its axes and orientation can be determined. Examples of this are the adaptive learning technique of Mucciardi, the long wavelength technique that will be dis-

cussed by Richardson, and also some unified algorithms which contain elements of several techniques which will be discussed by Fertig.

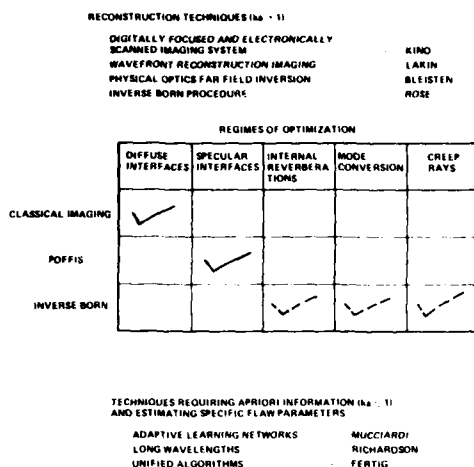


Fig. 8 Summary of ultrasonic inversion session.

Figure 9 presents an example of a reconstruction result. Here the POFFIS algorithm has been used to reconstruct a picture of the shape of an elliptical flaw.

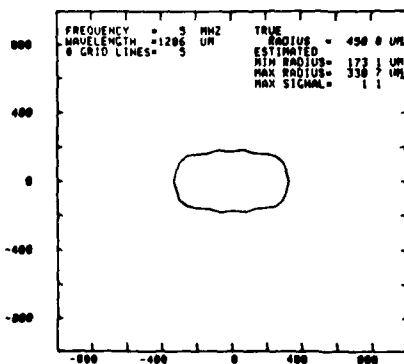


Fig. 9 Reconstruction of oblate spheroid using POFFIS algorithm.

Figure 10 presents a flow diagram of a technique applicable at lower frequencies. Here, Fertig has integrated two independent flaw characterization techniques, and some a priori information, to develop a unified prediction. In the left hand sketch is shown the case of a long wavelength scattering measurement. From the initial curvature of the scattered amplitude versus frequency plot, one derives a parameter known as A_2 . This is combined with a second piece of information, illustrated in the right hand sketch,

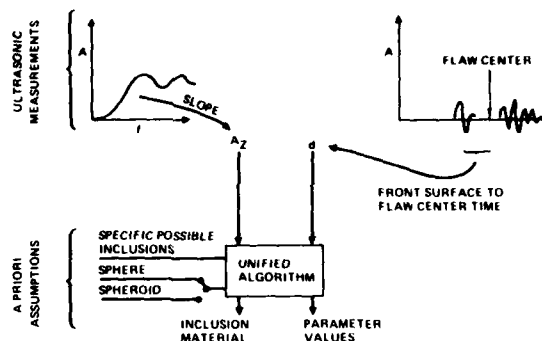


Fig. 10 Unified inversion algorithm.

which provides a measure of the distance from the front surface of the flaw to the center of the flaw. These two pieces of information are combined in an algorithm which incorporates the a priori assumption that only inclusions of a few specific materials can be expected. For ceramics, this assumption is based on known processing conditions. In addition, the flaw can be assumed to have either a spherical, or spheroidal shape. The output of the algorithm is the material of the inclusion and its dimensions. This, then, is an example of the application of the technique where a priori information is explicitly used to allow us to determine key flaw parameters.

Thus far, the measurement science part of the DARPA/AFML Program has been discussed. These general results have been applied to two distinct material systems: metals failing under fatigue and ceramics failing under brittle fracture.

As shown in Fig. 11, three papers will be presented on the fatigue problem: one on fatigue life prediction in the microcrack regime by Buck, one on fatigue life prediction in the macrocrack regime by Tittmann, and one on the theory of the surface wave scattering from macrocracks by Auld.

FATIGUE LIFE PREDICTION IN MICROCRACK REGIME	BUCK
FATIGUE LIFE PREDICTION IN MACROCRACK REGIME	TITTMANN
THEORY OF SURFACE WAVE SCATTERING	AULD

Fig. 11 Summary of ultrasonic surface wave session.

The relationship between these three talks is illustrated in Fig. 12. As discussed in previous papers by Marcus and by Morris, metal fatigue can be broken down into two regimes. The fatigue starts with an initiation process, in which microcracks are nucleated at a material discontinuity, for example, intrametallc particles. These microcracks gradually grow and coalesce to the point of the formation of a macrocrack, which ultimately then grows to failure in accordance with the rules of fracture mechanics.

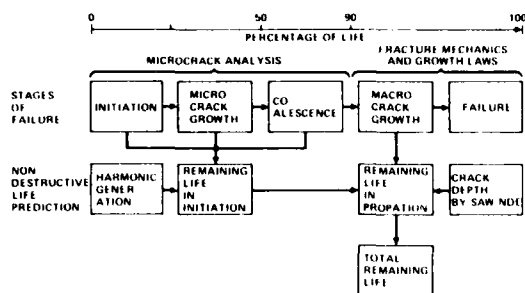


Fig. 12 Strategy for nondestructive prediction of metal fatigue life.

The relationship of the experimental results is as follows. In the microcrack regime, Buck has studied the use of ultrasonic harmonic generation to predict a remaining fatigue life in initiation. From that remaining life in initiation, combined with the crack size at the end of initiation, one can use the results of the fracture mechanics and growth laws to predict remaining life in propagation. The total remaining life is the sum of the two.

If one of these microcracks has already become a macrocrack, one can directly measure its depth by surface acoustic wave NDE, as will be discussed by Tittmann, based on some of Auld's models. Here one can predict a remaining life in the propagation regime, now equal to the total life. The three papers comprise an integrated approach to the detection of metal fatigue. This is a very limited demonstration because the work is just beginning. However it provides an example of a methodology which has the potential of finding widespread application in fatigue life detection.

Figure 13 summarizes the application of the general measurement techniques to the prediction of ceramic strength. An overview of the strategy will be presented by Evans. Experimental results obtained using a number of specific ultrasonic measurement techniques will then be presented: high-frequency bulk wave scattering by Chou, surface wave scattering by Khuri-Yakub, long wavelength bulk wave scattering by Graham and Allberg, and acoustic microscopy by Kessler and Yuhas. Finally, the decision theory which is necessary to derive conditional probabilities of failure and to optimize accept/reject criteria from these inputs will be discussed by Richardson.

ACCEPT-REJECT STRATEGY

DECISIONS BASED ON ULTRASONIC MEASUREMENTS - EVANS

MEASUREMENT TECHNIQUES

HIGH FREQUENCY BULK WAVES	- CHOU
SURFACE WAVES	- KHURI YAKUB
LONG WAVELENGTH BULK WAVES	- GRAHAM
ACOUSTIC MICROSCOPY	- KESSLER

DECISION THEORY

CONDITIONAL PROBABILITY OF FAILURE - RICHARDSON AND ACCEPT/REJECT CRITERIA

Fig. 13 Summary of ceramics session.

To put all these in context, Fig. 14 illustrates the thrust of the ceramics program. One starts with a sample, on which ultrasonic measurements are made. The resultant data is utilized as inputs to the unified inversion algorithm, illustrated in Fig. 10. The estimates of this algorithm will be combined with failure modeling to yield life predictions, which will be checked against destructive tests.

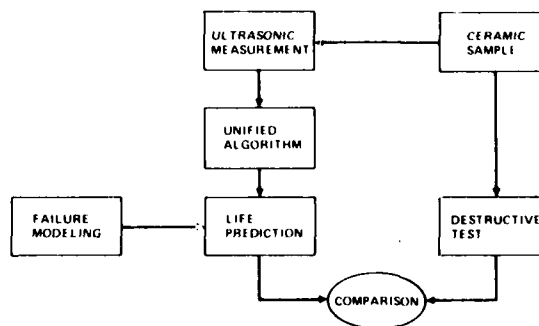


Fig. 14 Flow diagram of ceramics program.

Figure 15 illustrates the final element of the program, the ultrasonic test bed program to be discussed by Addison. The objective of this program is to develop a hardware system which incorporates the many newly developed quantitative NDE techniques and enable them to be evaluated on realistic parts. This is an important step in transferring the technology from a set of research reports into working hardware that can be used on the production or maintenance lines. The system consists of a water bath, mechanical manipulators with six degrees of freedom that are controlled by a microcomputer system, a dedicated mini-computer for the signal processing and general control of the system, and a color graphics display for use in presenting the information. This is a very important step in transferring the research results discussed in this meeting into the field

applications which is, of course, the ultimate objective of DARPA/AFML NDE effort.

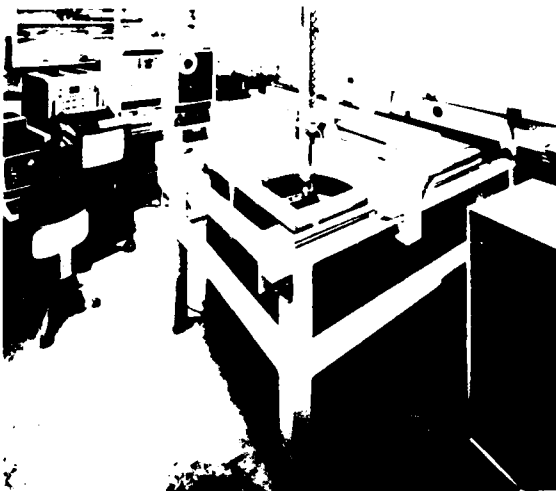


Fig. 15 Photograph of ultrasonic testbed.

Figure 16 summarizes the evolution of the quantitative ultrasonics capability, which is based on the building blocks of scattering theory and experiments, inversion theories and experiments, and engineering developments. From each of the building blocks, long-term capabilities are developed. The scattering work improves our understanding of the flaw-ultrasound interaction, and it has some specific applications in the areas of standards and calibration techniques. Inversion theories lead to flaw characterization techniques, which are being used in the ceramics and metal fatigue work, and which are finding application in slightly different form in a program to detect cracks under fasteners. Engineering development is transferring these techniques into advanced NDE prototype systems, including imaging

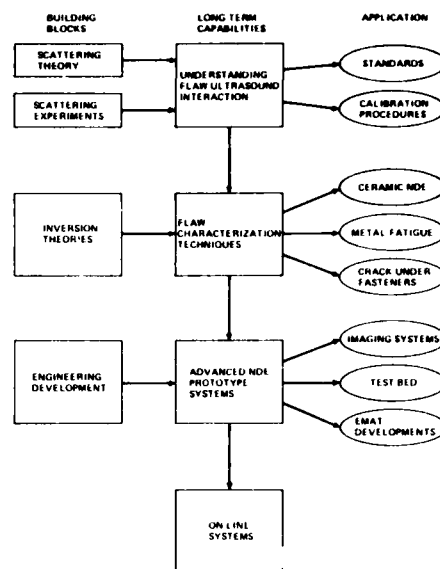


Fig. 16 Evolution of quantitative ultrasonics capability.

systems and test beds. Also in this category are EMAT transducers, which were part of earlier DARPA/AFML engineering developments and which are now finding a number of applications.

The final use of all of this technology is in on line systems for the DoD mission agencies.

REFERENCES

1. C. Rau, "The Impact of Inspection and Analysis Uncertainty on Reliability Prediction and Life Extension Strategy," Proceedings of the ARPA/AFML Review of Progress in Quantitative NDE, AFML-TR-78-205 (Air Force Materials Laboratory, Dayton Ohio, 1979), p. 150.
2. R. Thomson, "Understanding Materials Reliability - The Scientific Challenge," Proceedings of the ARPA/AF Review of Progress in Quantitative NDE (this Proceedings).
3. H. Marcus, "Subcritical Crack Growth and Its Relation to Predictive Analysis," *ibid*.
4. W. L. Morris, "Microcrack Initiation and Growth," *ibid*.

SESSION VII. MISCELLANEOUS DISCUSSION

Gerald Fosakony (Session Chairman): We have a few minutes before adjournment. Are there any other questions?

Mark Weinberg (RADCOM): I have a question for Dr. Lakin. It's on your multiple 64 by 64 eight-element unit, isn't that essentially -- can we draw a parallel between that and a radar antenna? If you're handling the data somewhat differently in that you're scanning across there and reconstructing it.

Ken Lakin (Univ. of Southern Calif.): I think not. I'm not that familiar with the radar, but I suspect the pulse-echo systems are more analogous to radar. For example, I don't think in radar they bother to try to focus. They are usually too far away.

Mark Weinberg: One can scan it, of course, by control of phasing on the elements.

Ken Lakin: That sort of thing is really more analogous to pulse-echo imaging arrays where you program a time delay, whereas they program a phase shift through radar and you send a pulse through the system. In their case, the pulse is coherent not by design but by physical constraints. It might be more similar to the synthetic aperture where they take data for long, long distances and they try to correlate it. In that case it would be a huge angle on the target.

Paul Gammell (Jet Propulsion Lab): I would like also to ask Dr. Lakin a question. It looks like the basic principles are very similar to Dr. Jahn's description where the only difference is that yours uses the same transducer. So it looks like a true synthetic aperture they're moving along at angles.

Ken Lakin: I'm talking about the USC system, synthetic aperture, several transducers.

Paul Gammell: The main question I have is: you have one constant transmitter sitting up here; is that correct? How does the mathematics compare when you transmit and receive?

Ken Lakin: You don't get the double phase shift as you would on others. You get a change in phase from the object, from the object to the receiver element. You have a constant transducer and the transducer to the scatterer.

Unidentified Speaker: Does it make your reconstruction easier or more difficult?

Ken Lakin: It pulls it.

#

FINITE DIFFERENCE METHODS APPLIED TO ULTRASONIC NON-DESTRUCTIVE TESTING PROBLEMS

L. J. Bond
Department of Physics
The City University
London EC1V 0HB
England.

ABSTRACT

The scattering and reflection of ultrasonic pulses is the basis for ultrasonic non-destructive testing techniques. However problems are encountered in the interpretation of experimental results in many systems especially those which have target dimensions of the order of a wavelength, where there are no analytical solutions. It is shown that the lack of an adequate analytical theory can be overcome by the use of numerical models based on finite difference approximations of the basic elastic equations of motion. Finite difference methods, which have previously had a successful history in seismology, are introduced to study non-destructive testing problems and provide a complete description of the interactions of elastic waves, including mode-conversion as an intrinsic part of the formulations. A review is given of the types of problem, that are of interest to non-destructive testers and which finite difference methods are best suited to solve. Specific examples of the technique are shown applied to pulsed Rayleigh, compressional and shear wave scattering by such features as open slots. The descriptions given by the numerical models are confirmed by laboratory experiments on both aluminium and steel blocks. The prediction of a new family of mode-conversion techniques for crack detection and sizing, suggested by the numerical models, is confirmed by experimental results.

INTRODUCTION

Ultrasonic methods of non-destructive testing have been developed considerably in recent years, both in terms of the range of systems that are examined and the importance placed on the results that are obtained. The importance of pre-service and in-service inspection is going to increase in the future as the consequences of the failure of a system, such as a nuclear plant or an aircraft, increase in magnitude. However although considerable progress has been made in improving ultrasonic testing techniques, many problems remain, especially in the interpretation of experimental results. These problems are in part due to the lack of adequate theories for the elastic wave propagation and scattering processes involved.

If ultrasonic non-destructive testing methods are to become increasingly reliable and quantitative it is necessary to develop a well-founded theory for such problems as the interaction of pulsed waves with small targets, particularly those with dimensions of the order of a wavelength.[1] The lack of adequate analytical theories for such problems has caused the attention of some workers to turn to consider numerical methods. It is found that numerical methods, which give full-wave descriptions of the interaction of elastic waves with structures that are of relevance to engineers, can be found in the seismological literature.[2]

The activities within the research group at The City University fall into three related areas. Firstly there is the development of practical ultrasonic non-destructive testing techniques, in particular using short pulses and spectroscopy. Secondly, there is the development of instrumenta-

tion required for broad-band and spectroscopic studies, together with a transducer development programme which includes using visualisation techniques. Thirdly, there are the studies of wave propagation and scattering using numerical models supported by experimental measurements.

This paper is based on the work in the third area of study and considers finite difference methods and the application of such techniques to problems which form the basis for ultrasonic non-destructive testing.

BASIC EQUATIONS AND BOUNDARY CONDITIONS

The basic elastic equations for wave propagation and scattering have been presented by many authors, including Graff [3], so only a brief summary is included in this paper.

For a general heterogeneous, linear, isotropic, perfectly elastic medium, an elastic wave can be described by the equation[4]

$$\rho \frac{\partial^2 \bar{u}}{\partial t^2} = (\lambda + \mu) \nabla(\nabla \cdot \bar{u}) + \mu \nabla^2 \bar{u} + \nabla \times (\nabla \times \bar{u}) \quad (1)$$

where \bar{u} is the displacement,
 ρ is the density,
 t is the time and
 λ and μ are the Lamé parameters of the medium.

With a restriction to two spatial dimensions and homogeneity, the basic equations which describe the displacements in the system are

$$\begin{aligned}\frac{\partial^2 u_1}{\partial t^2} &= V_C^2 \frac{\partial^2 u_1}{\partial x_1^2} + V_S^2 \frac{\partial^2 u_1}{\partial x_3^2} + (V_C^2 - V_S^2) \frac{\partial^2 u_2}{\partial x_1 \partial x_3} \\ \frac{\partial^2 u_2}{\partial t^2} &= V_C^2 \frac{\partial^2 u_2}{\partial x_3^2} + V_S^2 \frac{\partial^2 u_2}{\partial x_1^2} + (V_C^2 - V_S^2) \frac{\partial^2 u_1}{\partial x_1 \partial x_3}\end{aligned}\quad (2)$$

where u_1 and u_2 are displacements parallel to the x_1 and x_3 axes respectively.

V_C is the compressional wave velocity,

V_S is the shear wave velocity.

The velocities are related to the Lamé parameters of a medium by the relations

$$V_C = \sqrt{\frac{\lambda + 2\mu}{\rho}}; \quad V_S = \sqrt{\frac{\mu}{\rho}} \quad (3)$$

The boundary conditions for free surfaces and interfaces can be defined in terms of components of Cartesian stress tensor τ .

$$\tau = \begin{bmatrix} T_{11} \\ T_{13} \\ T_{33} \end{bmatrix} \quad (4)$$

and

$$\begin{aligned}T_{11} &= V_C^2 \frac{\partial u_3}{\partial x_1} + (V_C^2 - 2V_S^2) \frac{\partial u_1}{\partial x_3} \\ T_{13} &= T_{31} = V_S^2 \left(\frac{\partial u_3}{\partial x_3} + \frac{\partial u_1}{\partial x_1} \right) \\ T_{33} &= V_C^2 \frac{\partial u_1}{\partial x_3} + (V_C^2 - 2V_S^2) \frac{\partial u_3}{\partial x_1}\end{aligned}\quad (5)$$

where for the cases of: (in two spatial dimensions) no bodily rotation, $T_{13} = T_{31}$

stress free horizontal surface, $T_{31} = T_{33} = 0$

and at the horizontal interface, u_1 , u_2 , T_{31} and T_{33} are all continuous.

FINITE DIFFERENCE METHODS

Finite difference methods replace the basic elastic equations which describe the system under study with an incremental approximation. Although the detailed difference forms used can vary, they give both the time development of the system and the full wave solution, in the spatial dimensions considered, as intrinsic parts of the formulation. They allow free surface and interface boundary conditions to be handled. They can also handle transients and pulses and from the view of a potential user, who is not a mathematician, they have a good history of successful applications to a range of hyperbolic problems. All these advantages have been demonstrated, in the late 1960's, by the work of the mathematical seismology group of the late Professor Alterman [5].

Two different approaches have been used for constructing finite-difference representations for the elastic equations. The most common approach is to treat the elastic medium as a collection of homogeneous regions, each characterized by constant values of density and elastic parameters. Motion in each region is described by a finite difference approximation to the elastic wave equation for a homogeneous region (equation 2) and the boundary conditions across all interfaces are satisfied explicitly [2].

An alternative approach, based on finite difference representations for the more general elastic equation 1, incorporates boundary conditions implicitly. This idea has been applied to a scalar wave propagation problem by Boore[6], by the association of different values of density and the elastic parameters with every grid point. Such a formulation permits the treatment of complex subsurface geometries. For this reason it has been used for a number of seismological problems.[7] If the density is assumed constant, equation 1 in rectangular coordinates has the same form as for the homogeneous case given as equation 2.

In the work, reported in this paper, by the author and his coworkers it is the former technique which has been used.[8,9]

A model using finite difference methods consists of four parts, which are the finite difference nodal formulations, the initial impulse, the artificial internal boundaries and the material data. Each of these parts of the problem is now considered in turn.

FINITE DIFFERENCE FORMULATIONS

The incremental forms of the basic elastic equations consist of combinations of displacements at two time levels and these are used to give the new displacements at a future time. The detailed mathematical technique used in this study has been described in detail elsewhere.[2,10] Here only the main features of the techniques are indicated.

Body nodes: The basic body node formulation, for two spatial dimensions, is obtained by the application of centred-difference forms to equation 2. The basic coordinate scheme used is shown in fig. 1.

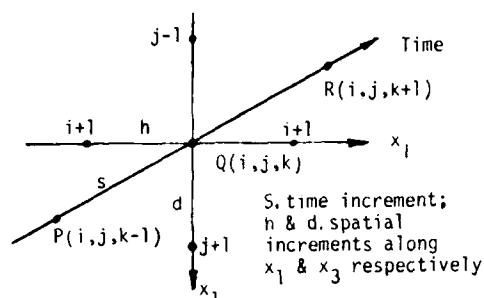


Fig. 1. Basic coordinate scheme for finite difference formulations.

The resulting nodal formulation obtained is:

$$u(i, j, k+1) = 2u(i, j, k) - (u(i, j, k-1) + S^2(F(u))) \quad (6)$$

where $F(u)$ is an explicit function of displacements and velocities, [11]. However this formulation applies only to the body of the medium, so that at boundaries and interfaces special forms are required.

Boundary nodes: The boundary nodal forms can be either of first or second order type: The first order schemes use the concept of pseudo-nodes, a line of imaginary or fictitious nodes introduced outside the boundary of the materials as shown in fig.2.

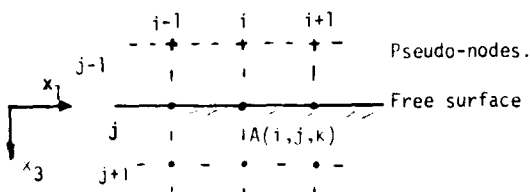


Fig. 2. Nodes for free-surface pseudo-node formulations.

The fictitious nodes allow the boundary conditions to be satisfied and the equations used for the horizontal free surface are obtained from the stress tensor components, equation 4. When centered-difference forms are used the resulting equation is

$$u(i, j-1, k) = u(i, j+1, k) + C(u(i+1, j, k) - u(i-1, j, k)) \quad (7)$$

where C is a constant, which for the vertical component of displacement has the form;

$$(V_C^2 - 2V_S^2) / V_C^2$$

The use of equation 7 to give the displacements at the pseudo-nodes enables the application of the body-node formulation, equation 6, to the node $A(i, j, k)$, to give the time development of the node.

The second-order schemes have the time development as an intrinsic part of the formulation. These are obtained by direct solution of the basic equations subject to the relevant boundary conditions and use only nodes within the body of the medium or on the surface. The equation for a horizontal free surface has the form:

$$u(i, j, k+1) = 2Au(i, j+1, k) - u(i, j, k-1) + S^2[B(u)] \quad (8)$$

where A is a constant and $B(u)$ is a function of displacements at time level k and velocities. B can take various forms, the original derivation of which was performed by Ilan, Ungar and Alterman [12].

ACCURACY AND STABILITY OF FINITE DIFFERENCE SCHEMES

The limits of accuracy and a stability for a finite difference scheme are of considerable importance, and they are found not only to be affected by the nodal formulation but also by the form of input pulse used and the material data.

For the body node formulation, equation 6, the limit to the size of the time increments is set by the von Neumann criterion [11].

$$S \leq h / \sqrt{V_C^2 + V_S^2} \quad (9)$$

where h is the spatial increment for a uniform grid.

The limit set by equation 9 is found for many schemes to be insufficient. The limits of stability for four sets of boundary node formulations have been investigated for the half and quarter spaces respectively by Ilan and Loewenthal [13] and Ilan [14]. The schemes have limits in the Poisson's Ratio (σ) value up to which they are stable, and for most schemes this is about $\sigma = 0.4$.

One parameter which is found to be of considerable importance is the number of nodes per wavelength. This is especially so when impulses or short pulses are used. Various workers [6,15] have shown that there is a lower limit of 7 nodes per wavelength at the shortest wavelength present and it has been found that a compressional wave impulse must be spread over 18 grid units if aliasing errors and numerical dispersion are not to affect the results.

The problems of scheme stability and accuracy have now been considered by a number of workers, and, although further work is required, working guide lines have been established. [10,15,16]

INPUT PULSES

The initial conditions for a model require the specification of the displacements at all grid points, for two time levels, separated by the time increment, as set by stability considerations.

Two techniques have been used to obtain pulses. The first, which was used for a pulse of Rayleigh waves is after Boore[6] and Munasinghe[16], and the sets of displacements are obtained by applying a fast Fourier transform to an analytically obtained wave number spectrum for each time level[8,10]. The basic type of pulse obtained is shown in fig.3.

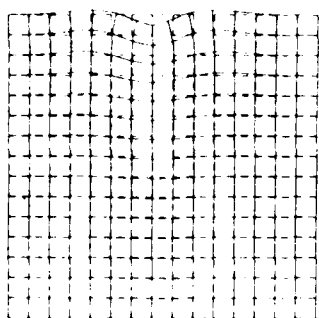


Fig. 3. Short pulse of Rayleigh waves.

The second technique, which has been used for body wave impulses is obtained by a procedure adapted from Boore[6], and this computes a set of displacements from a Dirac delta function which is integrated five times (G_1 to G_5) and then five consecutive central finite differences of G_5 are taken over an arbitrary interval Δ . The function is then normalized to unity at $t = 0$. This gives a smoothed δ -function.

$$\begin{aligned} \delta(t) = & [G_5(t + 5\Delta) - 5G_5(t + 3\Delta) + 10G_5(t + \Delta) \\ & - 10G_5(t - \Delta) + 5G_5(t - 3\Delta) \\ & - G_5(t - 5\Delta)] / (230.4\Delta^4) \end{aligned} \quad (10)$$

which has the shape shown in fig.4.[9].

The basic impulse, shown in fig. 4 has been used to give line compressional[9] and shear impulses, impulses of limited extent and as a cylindrical source.

AMPLITUDE

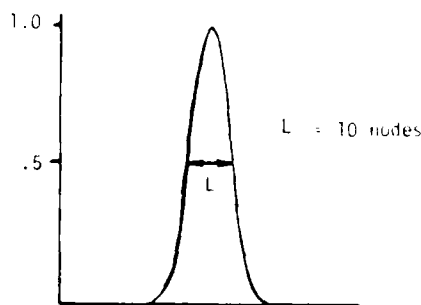


Fig.4. Shape of basic impulse.

ARTIFICIAL GRID BOUNDARIES

In almost all models, irrespective of the size of computer available, as it is not possible to model a semi-infinite medium, artificial internal boundaries must be set at some distance from the region of special interest in the calculations. These boundaries can be considered in one of several ways. These include producing an absorbing nodal formulation, as is done in the finite element model by Lysmer and Drake[17]; keeping a larger iteration space[2]; by specifying that the internal boundaries have zero displacement; or by using symmetry considerations and/or an analytical solution to follow the development of the input pulse at the boundaries as is done by Ilan, Bond and Spivack[9].

There is no universally applicable procedure for the artificial boundary nodes. In the studies performed at The City University, all the procedures, except absorbing nodes, have been applied in various studies. In all studies it is necessary to be sure that the grid used is large enough to provide results that are not contaminated by artificial reflections, up to the times of interest.

For example when an impulsive line source is used on a semi-infinite half-space containing a slot[9] the artificial boundary nodal displacements were calculated using equations for the analytical solution on a half-space[18]. This solution is accurate until the first scattered pulse reaches a boundary node.

MATERIAL DATA

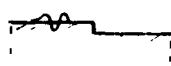
The requirements for the basic material data are that enough data should be given to enable the calculation of a consistent set of parameters, such as elastic moduli. In the studies at The City University the material data which are used are the shear wave velocity, the compressional wave velocity and the density. All other necessary parameters are calculated using relationships between elastic moduli and velocities[10].

TYPES OF WAVE PROBLEM SUITABLE FOR SOLUTION USING FINITE DIFFERENCE METHODS.

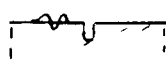
Finite difference methods have proved themselves as a technique for solving specific types of wave-propagation problems in seismology and geophysics. It is important to understand what these are when applying them to problems of ultrasonic wave propagation and scattering for non-destructive testing. Problems which can be solved are restricted to the following types:

- (a) Problems that can be reduced to two spatial dimensions and time.
- (b) Pulsed-wave and transient-impulse problems in both solids and fluids for which basic equations of motion can be formulated.
- (c) Problems for which a wave source can be completely specified at two times.
- (d) Problems that can fit into grids, the size limits for which are set by the computer available, using about 10 nodes per wavelength, (practically, about 300 x 100 nodes for the system at The City University).
- (e) Problems for which a basic data set of compressional wave velocity (v_p), shear wave velocity (v_s) and density (ρ) or equivalent elastic constants can be specified for all media involved.
- (f) Problems for which the geometry can be reduced to smooth curves, or straight lines and their intersections, for the free surfaces and the material interfaces.

Rayleigh wave pulses on:-

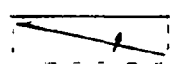


down step

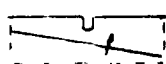


open slot

Compressional impulses on:-

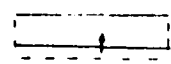


half-space

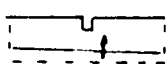


open slot

Shear impulse on:-

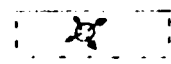


half space



open slot

Cylindrical line source on:-



half-space



plate

Fig.5. Examples of basic models considered at The City University.

The six constraints above may appear to be very restrictive: They are so in some senses, but the method can be applied to many problems of importance.

Constraint (a) provides for the reduction to systems with two spatial dimensions. This reduction results in two families of problems, one including the horizontal shear (SH) wave and the other the vertical shear (SV) wave. To solve systems requiring both SH and SV waves or mode conversion between the two families requires the full 3-D system which is only possible if a very large computing system is available. The studies at The City University have only considered the two dimensional problems involving shear (vertical), compressional and Rayleigh waves, and some examples of the basic configurations considered are shown in fig.5.

Other material properties such as internal friction[19] and piezoelectricity[20] have been added by some workers and some models have also been constructed using cylindrical and spherical coordinate systems, with restriction to reduce problems to two dimensions[2].

MODEL STUDIES

The basic finite difference model formulations are combined, subject to the basic model initial conditions, to give a computer program for a basic configuration, with a particular type of input wave pulse.

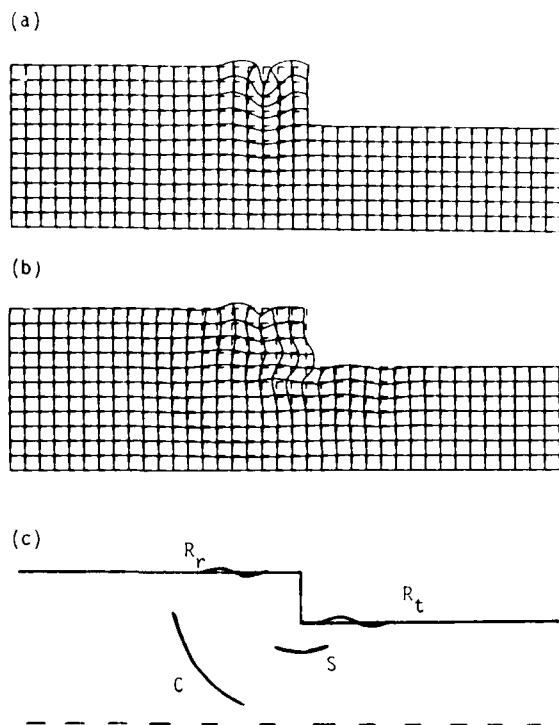
Each computer program is written in Fortran and run on the University of London Computer Centre's CDC 7600 computer. The models require in excess of 32K of core and have run times between 20 and about 200 seconds. The exact requirements vary considerably, depending mainly on the size of the basic grids of nodes, the velocities of the main wave or waves of interest, the graphics output produced and the peripheral calculations performed. Models in which either the shear or the Rayleigh wave is under investigation require computer program run times about twice those required for the same configuration and grid size when studying compressional waves. The limits on the size of system which can be modelled are set only by the size of the computing facilities available.

Two types of system have been studied; these are firstly the near field systems and secondly the far field systems. Examples of the models which have been produced at The City University are now presented.

RAYLEIGH WAVE MODELS

The original finite difference models developed at The City University were used to study pulsed Rayleigh wave propagation and scattering. This work provided an opportunity for the collection and development of sets of boundary node formulations and an investigation of basic model accuracy and stability[10].

The problem of scattering by open slots was approached by first considering individual corners and their combinations into steps with depths of the order of a wavelength. This work is illustrated by a pulse at a down step shown in fig.6.



Rayleigh pulse at a half wavelength deep down step, using aluminium data and 35 nodes per wavelength. System after, (a) 20, and (b) 200 iterations, (c) Main pulse identification:

C Compressional wave, S shear wave
 R_r Reflected and R_t Transmitted Rayleigh waves.

Fig. 6.

The energy in the various pulses generated is found to vary considerably as the depth of the step changes. The reflection coefficients were measured and this was compared with experimental results and is shown in fig.13.

LINE BODY WAVE SOURCES

The analytical solutions for the problems of line impulses of compressional and shear (SV) waves on semi-infinite half spaces are well known.[18]. These solutions provide a means of testing the accuracy of the finite difference solutions to the same problems. It is found that finite difference models can be produced which give solutions that are indistinguishable from the analytical cases.

The example of a line compressional impulse on a half space of material with Poissons ratio of 0.25 is shown in fig.7. The angle of reflection for the mode converted shear wave given by the theory is $65^\circ 54'$ and that given by the finite difference model is 66° , and the energies are also in good agreement.

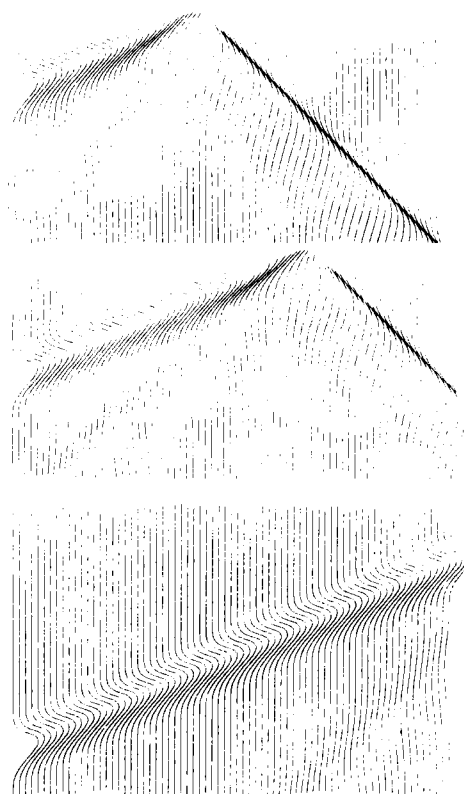


Fig.7. Line Compressional wave impulse incident on a half-space incident angle 45° .

The scattering of the impulse shown in fig.4, in both compressional and shear form, by open slots was studied for slots with a range of widths and depths and with a range of angles of incidence (fig.8). The case of a compressional impulse at 45° angle of incidence is shown in fig.9. The amplitude and direction of individual nodal displacements is clearly shown by the vector-visualisation which is after Harumi.[21].

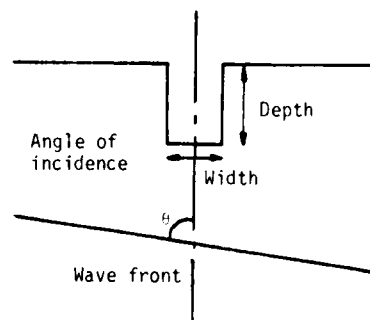


Fig.8. Basic model for body wave scattering by open slots.

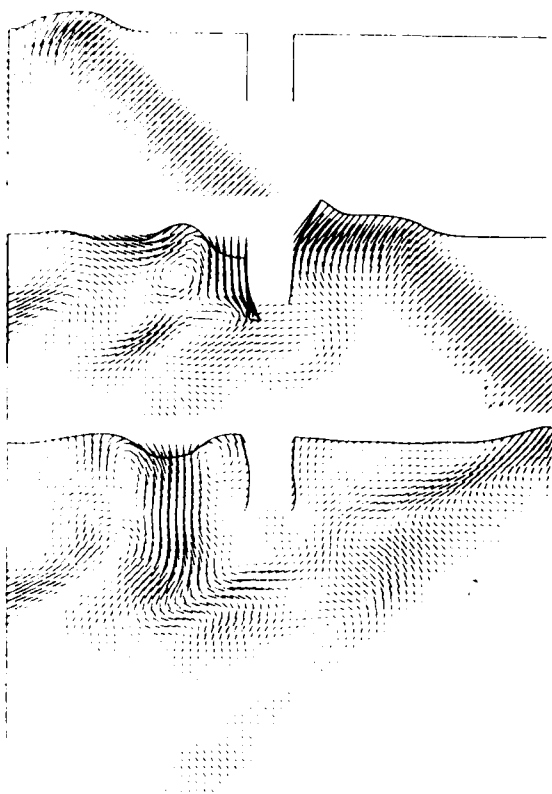


Fig.9. A line compressional impulse incident on an open slot, for the case of 45° angle of incidence.

For compressional wave scattering it is found that complex patterns of scattered and mode converted pulses are generated, the energy is each mode being dependent on slot dimensions and material properties. For all angles of incidence between 0° and 90° , strong pulses of Rayleigh waves are seen to be generated, the wavelength of which appears to be related to the slot dimensions.[9]

The interaction of a line shear impulse with 80° angle of incidence and an open slot is shown in fig.10. As for a compressional pulse it is found that a complex pattern of scattered and mode-converted pulses is generated.

In addition to the presentation of results in various forms of visualisation, synthetic time domain signals are generated. These provide results which can be directly compared to the time domain signals from transducers. Examples of this type of results for surface points is the model shown as fig.10 and are shown as fig.11.

A cylindrical line source of compressional waves based on the smoothed δ -function shown in fig.4 is shown on a half-space by both numerical and vector visualisations in fig.12. Both the vectors and grid show only every fourth node in the scheme.

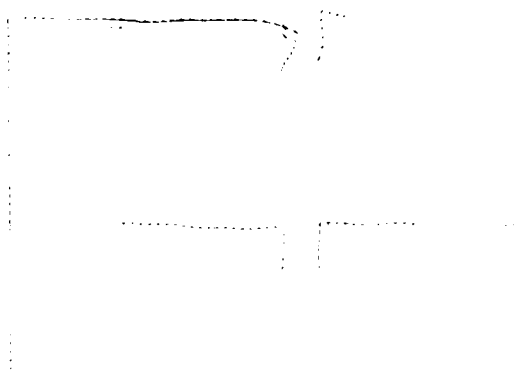
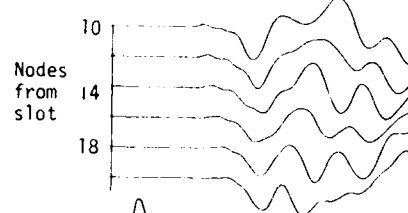


Fig.10. Line shear impulse on a slot in a half-space, with 80° angle of incidence.

VERTICAL DISPLACEMENT
 $Q = 80.$



HORIZONTAL DISPLACEMENT
 $Q = 80.$



Fig.11. Synthetic time domain signals for the shear wave system shown in fig.10.

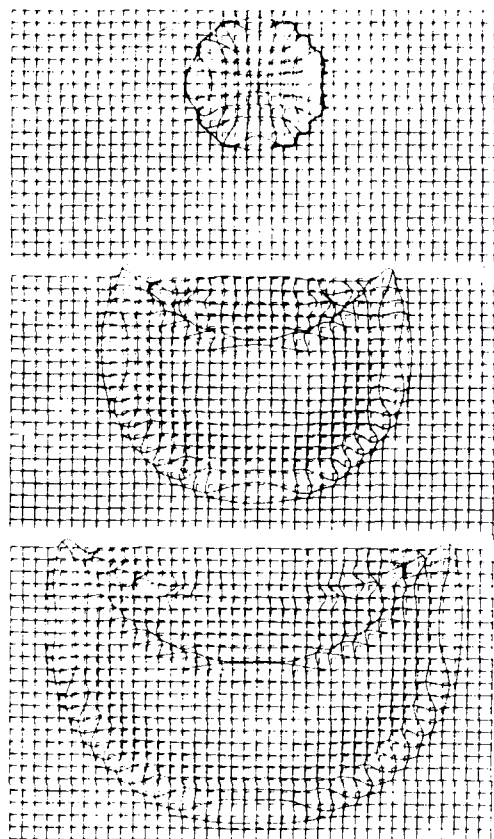


Fig. 12. Expanding line cylindrical compressional wave source on a half-space.

COMPARISON BETWEEN NUMERICAL MODEL AND EXPERIMENT

In parallel with the production of the computer models a series of experimental measurements have been made to test the model results on simple configurations.

The experimental equipment used is the Central Ultrasonics Test Equipment (CUTE) of The City University Ultrasonics Group which includes a spectrum analyser[22], and is on line to a PDP 11/34 computer. In outline, the experiments consist of using broadband pulses (0.5 - 6 MHz) generated by piezoelectric transducers on both aluminium and steel blocks and looking at the reflected, transmitted and mode converted pulses resulting from interactions with corners, steps and slots.

The reflection coefficients from both models and experiments for a set of measurements made at down step are shown in fig.13, together with experimental results obtained by Frost et al [23]. The curve plotted for the model using data for media with Poisson's ratio = 0.24 is identical with that given by Munasinghe[16], who used a finite difference model to obtain his results.

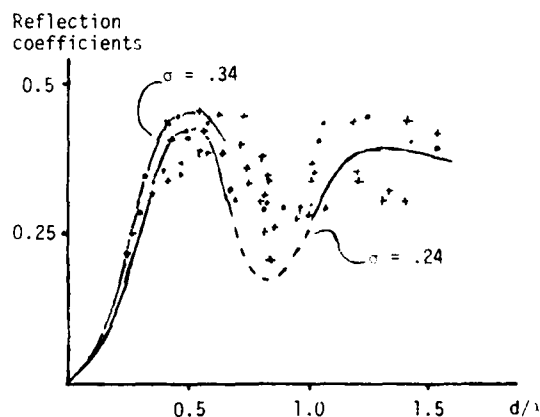


Fig.13. Transmission & reflection coefficients at down steps with depth (d) measured in wavelengths (λ).

Numerical and experimental results for the case of compressional impulses normally incident on an open slot[9], are shown in fig. 14.

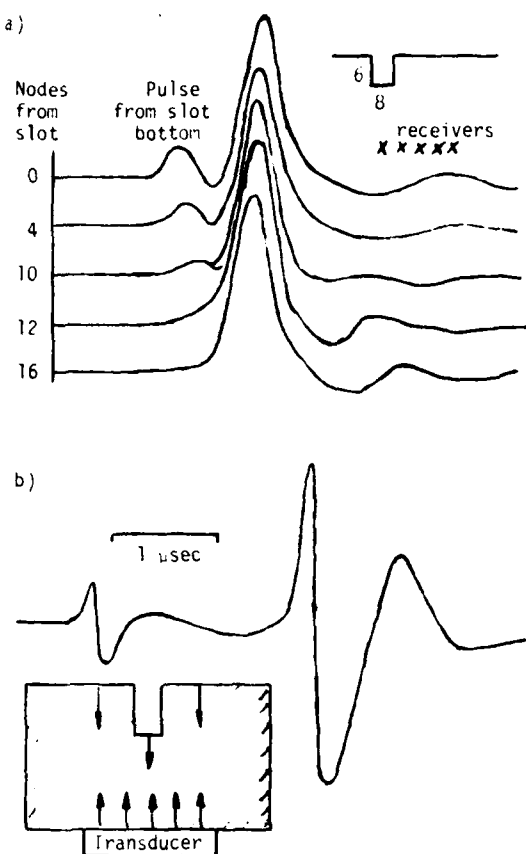


Fig. 14 Compressional impulse normal to a slot. Vertical displacements below a slot given by: (a) the numerical model (b) experiments.

All the experimental measurements performed have provided results which are in good agreement with those given by the numerical models, subject only to limitations set by transducer coupling, surface roughness and pulse width (normal to direction of propagation).

NEW MODE-CONVERSION TECHNIQUES FOR NDT

The numerical model predicts that, when compressional waves are incident on a surface-breaking defect, they cause it to oscillate and generate Rayleigh waves. This is clearly visible in figs. 9 and 15 and is strikingly shown in the computer-generated 16 mm film [25]. This type of mode conversion has been previously used for bulk-surface wave mode conversion in Acoustic Surface Wave devices [24], the fundamentals of which are shown in fig. 15, together with comparisons between numerical-model and experimental results. The energy found in the mode-converted pulses measured by this technique is large, typically about 20 dB above noise levels when using normal commercial transducers on undamped blocks, this being increased to between 30 and 40 dB above noise levels when damping material is added around the test block and the maximum pulse used to excite the transducer.

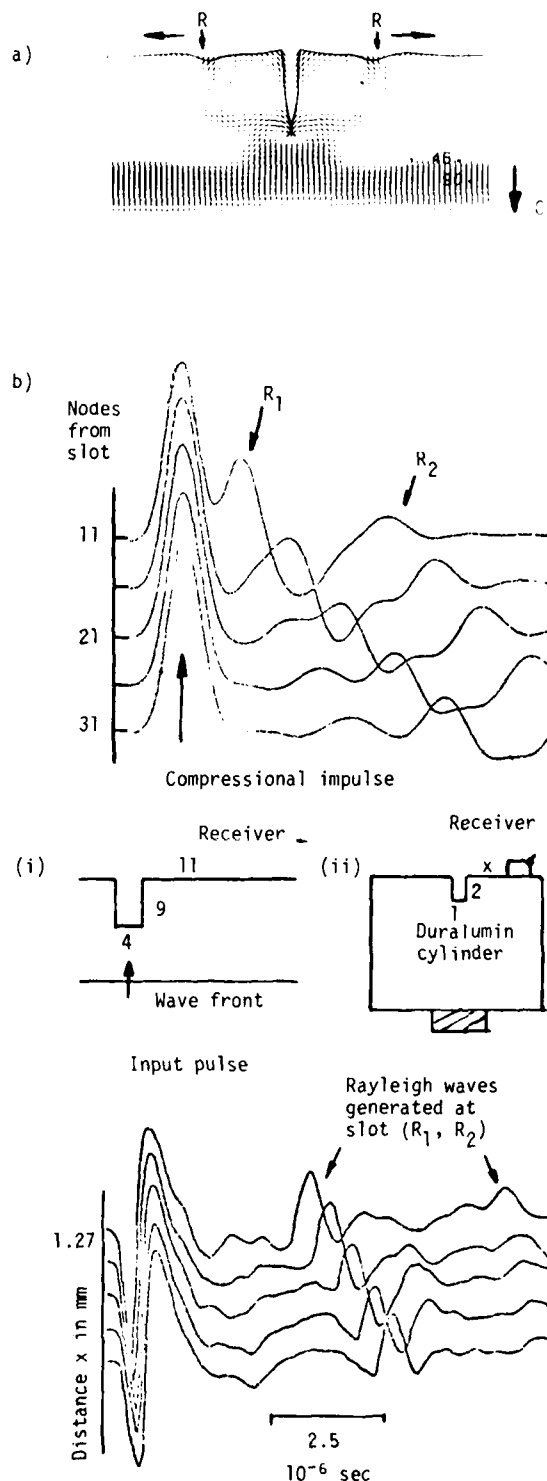


Fig. 15. Compressional-Rayleigh wave mode conversion at a slot. (a) Visualisation of system. (b) Vertical components of displacement on the free surface of block with slot as given by (i) numerical model; (ii) experiment on duralumin block.

The potential of the new technique was investigated by a set of time domain and spectral measurements performed on pulses scattered by slots 0.3 (± 0.02) mm wide and with a range of depths. An example of a time domain signal and its spectrum are shown in fig. 16a. For each slot studied the peak frequency in the mode converted Rayleigh wave was measured and it is shown plotted against slot depth as in fig. 16b.

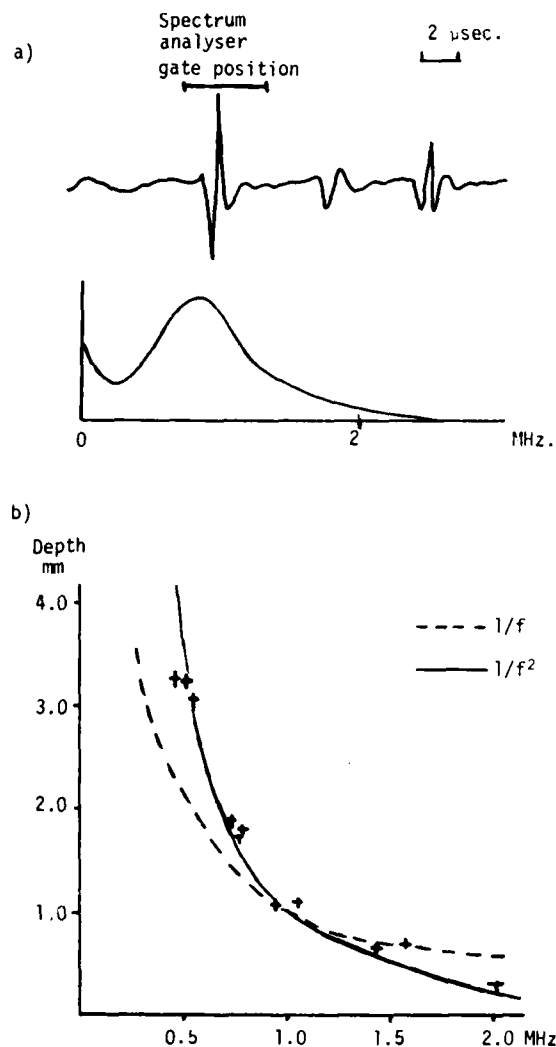


Fig. 16 Mode-converted Rayleigh waves at open slots. (a) Time domain signals and spectra for slot 1.11 mm deep, 0.33 mm wide. (b) Plots of frequency against depth for range of slots.

Both $1/f$ and $1/f^2$ curves were plotted; these are also shown in fig. 16b, and it would appear that the depth of the slot is related to the Rayleigh wave pulse peak frequency by a relationship of the form:

$$\text{Slot Depth} \propto 1/f^2$$

(11)

where f is the peak frequency in the spectrum of the slot generated Rayleigh wave. It would therefore appear to offer a new method for crack sizing, in addition to just detection. [28].

In general the observation of mode-converted pulses generated at defects would appear to form the basis for a new range of non-destructive testing techniques. The use of the crack-tip-generated shear wave has previously been investigated by Silk [27] and there are indications from the present studies that several of the different types of mode-converted pulses can be used for crack detection. It also appears that for the mode-converted pulses both pulse spectral content and their relative energy can be related to crack size.

CONCLUSIONS

The finite difference method provides a means of studying systems which have no analytical solutions. When used to follow ultrasonic wave propagation and scattering, it has given models which include mode conversions as an intrinsic part of the formulation, which have specific elastic properties, and which are free of coupling and other practical problems of laboratory models. These numerical models give both numerical and visual results which provide material for direct comparison with laboratory results.

In addition to providing insight into many scattering problems, a new family of crack detection methods have been discovered and it is shown that using compressional/Rayleigh mode conversion, slots can be sized by taking the spectrum of the slot-generated Rayleigh wave pulse generated by the slot.

ACKNOWLEDGEMENTS

This work forms part of a programme of research which seeks to provide an adequate theory for the understanding of ultrasonic non-destructive testing problems. It has been carried out with the support of the Procurement Executive, Ministry of Defence (U.K.), the Natural Environment Research Council, The Science Research Council, and the British Gas Corporation.

Thanks are due to all the members of the group who have been involved in this work, especially Dr. Almog Ilan (formerly of Tel-Aviv University), for her contribution as a colleague during her 15 month stay at The City University and also by correspondence.

REFERENCES

1. Morgan, L.L.: Crack size evaluation using ultrasonic surface wave spectroscopy. Acustica 30 (4) 222-228 (1974).
2. Alterman, Z., Loewenthal, D.: Computer generated seismograms. Methods in Computational Physics 12 35-164. Academic Press (New York, London) (1972).
3. Graff, K.F.: Wave Motion in Elastic Solids. Clarendon Press (Oxford) (1975).
4. Karal, F., Keller, J.: Elastic wave propagation in homogeneous and inhomogeneous media. Journal Acoustical Soc. America 31 694-705 (1959).
5. Bolt, B.A., Loewenthal, D.: Memorial Biography - Z.S. Alterman. Journal of Computational Physics 29 313-317 (1978).
6. Boore, D.M.: Finite difference methods for seismic wave propagation in heterogeneous materials. Methods in Computational Physics 11 Academic Press, (New York) (1972).
7. Kelly, K., Alford, R., Iretal, S., Ward, R.: Application of finite difference methods to exploration seismology. Royal Irish Academy Conference on Numerical Analysis, (1974) (preprint).
8. Bond, L.J.: A computer model of the interactions of surface acoustic waves with discontinuities. Ultrasonics 17 (2) 71-77, (1979).
9. Ilan, A., Bond, L.J., Spivack, M.: Interaction of a compressional impulse with a slot normal to the surface of an elastic half-space. Geophysical Journal of the Royal Astronomical Society 57 463-477 (1979).
10. Bond, L.J.: Surface cracks in metals and their characterisation using Rayleigh waves. Ph.D. Thesis The City University (1978).
11. Alterman, Z. and Loewenthal, D.: Seismic waves in a quarter and three quarter plane. Geophysical Journal of the Royal Astronomical Society 20 101-126 (1970).
12. Ilan, A., Ungar, A., Alterman, Z.S.: An improved representation of boundary conditions in finite difference schemes for seismological problems. Geophysical Journal of the Royal Astronomical Society 43 727-742 (1975).
13. Ilan, A., and Loewenthal, D.: Instability of finite difference schemes due to boundary conditions in elastic media. Geophysical Prospecting 24 431-453 (1976).
14. Ilan, A.: Stability of finite difference schemes for the problem of elastic wave propagation in a quarter plane. Journal of Computational Physics. The Z. Alterman Memorial Volume, 73 389-403 (1978).
15. Alford, R., Kelly, K., Iretal, S.: Accuracy of finite-difference modelling of the acoustic wave equation. Geophysics 49 16, 834-842, 1974.
16. Murumori, M.: Numerical solutions for acoustic Rayleigh wave scattering in discontinuous media. Ph.D. Thesis McGill University (Canada) (1977).
17. Ogden, J., Drake, J.: A finite element method in seismology. Methods in Computational Physics 11 161-186 Academic Press (New York) (1972).
18. Ewing, W., Jardetzky, W., Press, J.: Elastic Waves in Layered Media. McGraw Hill (New York) (1957).
19. Alterman, Z., Aboudi, J.: Impulsive sound propagation in a fluid sphere of variable internal friction. Israel Journal of Technology 2 135-147 (1964).
20. Cambiaggio, L., Guozzo, F., River, L.: Piezoelectric surface wave scattering on a semi-infinite short-circuited surface. Applied Physics Letters 28 (2) 71-73 (1976).
21. Harumi, K.: Numerical calculation of the near field of elastic wave in the solid half space. In: Seventh International Conference on Non-destructive Testing, Warsaw 1973 Proceedings. Warsaw: Polish Society of Mechanical Engineers. (1975). Paper C-48.
22. Brown, A.F., Weight, J.P.: Generation and reception of wideband ultrasound Ultrasonics 12 161-167 (1974).
23. Frost, H., Sethares, J., Szabo, T.: Applications for new electromagnetic SAW transducer. Proceedings Ultrasonics Symposium 604-607, IEEE. (1975).
24. Humphries, R., Ash, E.: Acoustic bulk-surface wave transducers. Electronics Letters 5 (9) 175-176 (1969).
25. Ilan, A.: Compressional plane impulse at a half-space. Film produced by The City University, Department of Physics (1978).
26. Bond, L.J., Ilan, A.: Ultrasonic pulse scattering by other slots. Proceedings Ultrasonics International '79. Graz, Austria, 15-17 May (1979). (In Press).
27. Silk, M.G.: The determination of crack penetration using ultrasonic surface waves. NDT International 9 (6) 290-297 (1976).
28. Bond, L.J.: Methods of Ultrasonic non-destructive Testing. (Patent application 1979)

SUMMARY DISCUSSION
(Leonard Bond)

James Krumhansl (Session Chairman--Cornell University): I would like to start off the questioning. The frequency F in your Quad S versus one over F squared, is that the center?

Leonard Bond: That's the center frequency.

Wolfgang Sachse (Cornell University): Have you made a comparison between this model or calculations to the exact solution, say the lambda problems or the epicenter knock-off problem?

Leonard Bond: The cylindrical epicenter on half space, yes, we have been comparing that. And where we have got a lambda solution, we do compare them. The results are in good agreement. So, the case of line sources on a half space, which is in fact how we solve the artificial boundaries for all the slots once they're in excellent agreement, the angles are the same and amplitudes are very close.

Gordon Kino (Stanford University): Do you have any feel from these solutions as to what the sharpness of the corners are? We, for instance, in experiments look at a corner and we look at Cornell's theory, which is an early forerunner of this, I think, and the results, therefore, are agreed, sometimes they do, sometimes they don't with the kinds of theories that people have already done, and we have always (inaudible) to that corner. Do you have any feel for this?

Leonard Bond: With the Rayleigh wave work, yes, we did start looking at the corners because we found on the 90-degree corner, if the radius of the corner was greater than twice the wavelength, the wave just didn't see it. And as you came in, there was a critical point where it became much sharper, and suddenly got to a deflection coefficient. For the 270 corner we had one set of steps that were cut, and we were getting very funny results. The pulse was just going around them. And so, yes, the corner sharpness does have a considerable effect. And that does come into the model because if you change the modes for wavelength and take it down too far, you start getting (inaudible).

Gordon Kino: Can the model really reproduce the corner well? Because it's a numerical procedure, this finite difference. What do you do about these sharp edges?

Leonard Bond: If you keep the nodes for the wavelength above 10 nodes per wavelength, it's okay because we have compared it with experiments, and we use both. We use mechanical modeling and lab experiments, the two working together.

James Krumhansl: May I supplement that question? Is there a technique in which you use a different grid, different mesh size in the vicinity of some artifact which you know to be critical, so you could use a much finer mesh size and map it onto the--I'm asking a question about--

Leonard Bond: You can change your grid size. It increases the complexity of the programming, and there's a group that has been using different grid sizes. We tended to stick with a very fast algorithm for uniform grid, the problem is every time you change grid size, unless you're very careful, you can introduce an artificial impulse at this artificial grid change.

J. D. Achenbach (Northwestern University): I'm sure every time you give these talks somebody brings up the finite element matter, and it would seem that in this connection the finite element might have some advantage in the sense you could construct a special element that would take into account singularities that appear at corners and at crack tips. Is that true, or?

Leonard Bond: Basically, you can do static problems either with finite elements and finite differences and your grid special elements are very useful. When it comes to this type of pulse problem, hyperbolic problem, some people have had some success with finite elements. As yet they really have got to prove themselves for general hyperbolic problems. You end up with a problem where you have to invert, albeit band spars matrices, and you got size limitations on the grid. In principle, you can probably get it out eventually using finite elements, but the algorithms are much more complicated.

(continued)

Leonard Bond (discussion continued)

George Herrmann (Stanford University): Have you been interested in problems where you have a physical boundary relatively far away from your (inaudible) and you're interested in the reflected wave? There is a problem there, obviously, that you cannot model the whole body because the computer capability is insufficient, and you have to try to match analytically a solution in the interested region, and it turns out it's rather difficult to do that because of artificial wave reflections at the interfaces.

Leonard Bond: It is difficult indeed to match the two together.

George Herrmann: Do you have any experience in that?

Leonard Bond: We tended to do it on (inaudible) where we have been comparing experiments, and we mainly use the finite difference for looking at local interactions. If you want to follow propagations in the body of the material, we follow the array theory besides the seismological ones.

#

APPLICATION OF MOOT TO SCATTERING OF ELASTIC WAVES FROM INCLUSIONS AND CRACKS

W. M. Visscher
Los Alamos Scientific Laboratory
Los Alamos, NM 87545

ABSTRACT

The method of optimal truncation (MOOT), a convergent T-matrix scheme, has been applied to the computation of scattering of elastic waves from axially symmetric fluid and elastic inclusions imbedded in an isotropic homogeneous medium. Cones, pillboxes, and spheroids have been considered; an example of frequency and angular dependence of scattering from an oblate spheroid is given. Cracks may be considered as special cases of inclusions wherein the included material is identical to the host. A circular crack, for example, may be simulated by imposing free boundary conditions on the top surface of a pillbox and requiring continuity of displacements and surface tractions elsewhere. Alternatively, it may be feigned by an equatorially cloven spherical inclusion, wherein free boundary conditions are imposed on the bisecting plane and the spherical surfaces are welded.

INTRODUCTION

The problem we wish to solve is illustrated in Fig. 1. A flaw, which is a uniform inclusion in a homogeneous isotropic elastic medium, scatters an incident elastic wave \vec{S}_{inc} . The shape, orientation, density, and elastic constants of the inclusion are assumed to be known, and we want to calculate the scattered wave.

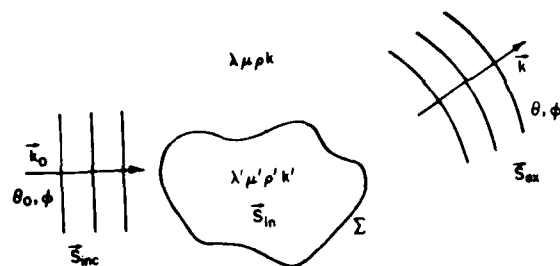


Fig. 1. A flaw, which is an inclusion with different parameters λ, μ, ρ, k' is imbedded in the host medium. An elastic plane wave \vec{S}_{inc} is incident with polar angles θ, ϕ ; the problem is to compute the scattered wave in a direction θ, ϕ . The vector displacement is called \vec{S} ; the suffixes inc, in, and ex abbreviate incident, internal, and external respectively. Σ is the surface which separates the inside from the outside of the flaw; the boundary conditions imposed here determine the scattering.

The method⁽¹⁾ whereby we proceed can be briefly explained as follows. We expand the displacements in a series of partial waves;

$$\vec{S}_{ex} = \vec{S}_{inc} + \sum_{p, \ell, m} a_{p\ell m} \vec{S}_{p\ell m}^{(+)} \quad (1)$$

$$\vec{S}_{in} = \sum_{p, \ell, m} b_{p\ell m} \vec{S}_{p\ell m} \quad (2)$$

where each of the \vec{S} 's solves the elastic wave equation in the appropriate domain.

$$\nabla^2 \vec{S}_{p\ell m} = -\omega^2 \vec{S}_{p\ell m} = (\lambda + 2\mu) \nabla \nabla \cdot \vec{S}_{p\ell m} - \mu \nabla \nabla \times \nabla \times \vec{S}_{p\ell m} \quad (3)$$

We have assumed a steady-state situation wherein $\vec{S} = \partial \vec{S} / \partial t = -i\omega \vec{S}$.

The eigenfunctions $\vec{S}_{p\ell m}$ are specified by the three integer indices p, ℓ, m , which arise naturally when Eq.(3) is written in spherical coordinates. Details, including explicit expressions for the basis functions, can be found elsewhere.⁽²⁾ The elastic wave polarization is specified by p , which takes on 3 values corresponding to one longitudinal and 2 transverse polarizations. ℓ and m are the usual radial and azimuthal eigenvalue indices; $\ell = 0, 1, 2, \dots$ and $m = -\ell, -\ell+1, \dots, \ell$.

$\vec{S}_{p\ell m}^{(+)}$, a solution of Eq.(3), behaves for $r \rightarrow \infty$ like $\exp(ikr)/r$; it is a linear combination of the spherical Hankel function $h_\ell^{(2)}(kr) = j_\ell + i y_\ell$ and its first derivative. $\vec{S}_{p\ell m}$ is a solution of Eq.(3) which is regular at the origin (always inside Σ); it is obtained from $\vec{S}_{p\ell m}^{(+)}$ by replacing $h_\ell^{(2)}$ with j_ℓ , the spherical Bessel function of the first kind. The incident wave in Eq.(1) is expanded in the exterior regular functions \vec{S} ; it is

$$\vec{S}_{inc} = \sum_{p, \ell, m} \vec{S}_{p\ell m} = 4\pi \sum_{\ell, m} i^\ell Y_{\ell m}^*(\theta, \phi) \vec{S}_{p\ell m} \quad (4)$$

for a plane wave with polarization p incident from (θ, ϕ) . The wavenumber k depends on the polarization p ; its magnitude is $k_l^2 = \omega^2/(\lambda + 2\mu)$ and $k_t^2 = \omega^2/\mu$ for longitudinal and transverse polarizations respectively. An incident longitudinal wave scatters into both polarizations; this is called mode conversion. $\vec{S}_{p\ell m}$ is a regular solution of (3) inside the flaw; it is the same as $\vec{S}_{p\ell m}$ except for the wavenumber, which is k' rather than k .

Hooke's law for the elastic solid is embodied in the expression for the stress tensor σ_{ij}

$$\sigma_{ij} = \frac{1}{2} \sum_{k, \ell} C_{ijkl} (S_{k, \ell, i} + S_{k, \ell, j}) \quad (5)$$

in cartesian coordinates. The index following the

comma signifies differentiation. For the isotropic case Eq.(5) simplifies to

$$\sigma_{ij} = \mu(S_{i,j} + S_{j,i}) + \lambda \delta_{ij} \text{div } \xi \quad (6)$$

in terms of the Lamé elastic moduli λ and μ . If \hat{n} denotes the unit normal to Σ (see Fig. 2), the surface traction may be written as the contraction of σ_{ij} with it;

$$t_i = \sum_j \sigma_{ij} \hat{n}_j. \quad (7)$$

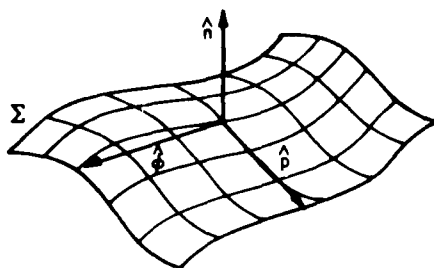


Fig. 2. Surface coordinate system with basis $(\hat{n}, \hat{p}, \hat{q})$. A cartesian system; \hat{n} is the unit normal, \hat{p} and \hat{q} are in the surface.

In the cartesian coordinate system shown in Fig. (2), this equation reduces to

$$\begin{aligned} t_n &= 2\mu S_{n,n} + \lambda \text{div } \xi \\ t_p &= \mu(S_{n,p} + S_{p,n}) \\ t_q &= \mu(S_{n,q} + S_{q,n}), \end{aligned} \quad (8)$$

which are convenient expressions because the boundary conditions which determine the displacements and stresses are most easily expressed in terms of normal and parallel components at the surface.

MINIMUM PRINCIPLE

If the $a_{p\ell m}$'s of Eq.(1) are found, then it is easy to get the various observables like cross-sections and phases from them. They are determined by the boundary conditions on Σ and may be found in the following way. For the present, for illustrative purposes we consider the simplest flaws: fixed rigid obstacles or voids. For these cases the boundary conditions are

$$\xi_{ex} = 0 \quad \text{on } \Sigma \quad (\text{rigid obstacle}) \quad (9)$$

$$\xi_{ex} = 0 \quad \text{on } \Sigma \quad (\text{void}). \quad (10)$$

If (9) or (10) hold, then surely the surface integrals

$$I = \int_{\Sigma} d\ell \xi_{ex}^2 \quad (11)$$

and

$$J = \int_{\Sigma} d\ell \xi_{ex}^2 \quad (12)$$

must vanish if ξ is an exact solution. But our

computers are finite, and the sum over ℓ in (1) must be truncated, say at $\ell = \ell_{\max}$. We take the best choice of $\{a_{p\ell m}\}$ $\ell = 0, 1, \dots, \ell_{\max}$ to be that which minimizes I or J . Thus the equations from which the amplitudes may be determined are

$$\frac{\partial I}{\partial a_{p\ell m}} = 0 \quad (\text{obstacle}) \quad (13)$$

$$\frac{\partial J}{\partial a_{p\ell m}} = 0 \quad (\text{void}). \quad (14)$$

It is easy to show that the sequence

$$\dots I_{\ell_{\max}} > I_{\ell_{\max} + 1} > \dots \quad (15)$$

converges to $I_{\infty} = 0$ if an exact solution exists which satisfies appropriate smoothness conditions.

MATRIX EQUATIONS

The fixed rigid obstacle provides a simple example for the derivation of the matrix equation from which the $a_{p\ell m}$'s may be determined. Now I is, explicitly

$$I = \left| \sum_{\ell} \sum_{p\ell m} d_{p\ell m} \xi_{p\ell m}^* + \sum_{p\ell m} a_{p\ell m} \xi_{p\ell m}^* \right|^2 \quad (16)$$

The derivatives of this equation are

$$\frac{\partial I}{\partial a_{p\ell m}} = \sum_{p'\ell'm'} (Q_{p\ell m, p'\ell'm'} \xi_{p'\ell'm'}^* + \tilde{Q}_{p\ell m, p'\ell'm'} d_{p'\ell'm'}) = 0 \quad (17)$$

where

$$Q_{p\ell m, p'\ell'm'} = \int_{\Sigma} d\ell \xi_{p\ell m}^* \cdot \xi_{p'\ell'm'}, \quad (18)$$

$$\text{and } \tilde{Q}_{p\ell m, p'\ell'm'} = \int_{\Sigma} d\ell \xi_{p\ell m}^* \cdot \xi_{p'\ell'm'}. \quad (19)$$

Equation (17) can be abbreviated

$$Qa + \tilde{Q}d = 0, \quad (20)$$

or

$$a = -Q^{-1}\tilde{Q}d = Td. \quad (21)$$

This defines the T -matrix, which is independent of the direction and polarization of the incident wave; this information is contained in $d_{p\ell m}$.

As a practical matter it should be noted that the Q and T -matrices are diagonal in m if the flaw has axial symmetry. They can therefore be written in block-diagonal form⁽¹⁾, which usually reduces the amount of computation required by orders of magnitude. For this reason the shapes we calculate are always axially symmetric.

T -matrices which in the limit of $\ell_{\max} \rightarrow \infty$ become identical to that defined in (21) can be defined in an infinite number of ways^(1,3). This one is unique and optimal in the sense that it is generated by a convergent sequence of surface integrals.

BOUNDARY CONDITIONS

In Table I we bring together the boundary conditions for various kinds of defects, and show the integral functionals of the surface fields which must be minimized in MOOT.

Table I

<p style="text-align: center;"><u>Void</u></p> <p>$\vec{s}_{ex} = \text{unrestricted}; \vec{t}_{ex} = 0$ $J = \int \vec{t}_{ex} ^2 d\sigma$</p>
<p style="text-align: center;"><u>Fixed Rigid Obstacle</u></p> <p>$\vec{s}_{ex} = 0; \vec{t}_{ex} = \text{unrestricted}$ $I = \int \vec{s}_{ex} ^2 d\sigma$</p>
<p style="text-align: center;"><u>Elastic Inclusion (welded)</u></p> <p>$\vec{s}_{ex} = \vec{s}_{in}; \vec{t}_{ex} = \vec{t}_{in}$ $I = \int \vec{s}_{ex} - \vec{s}_{in} ^2 d\sigma; J = \int \vec{t}_{ex} - \vec{t}_{in} ^2 d\sigma$</p>
<p style="text-align: center;"><u>Elastic Inclusion (slippery)</u></p> <p>$s_{exn} = s_{inn}; \vec{s}_{ex } = \vec{s}_{in } = \text{unrestricted}$ $t_{exn} = t_{inn}; \vec{t}_{ex } = \vec{t}_{in } = 0$ $I = \int s_{exn} - s_{inn} ^2 d\sigma; J = \int t_{exn} - t_{inn} ^2 d\sigma;$ $K = \int (\vec{t}_{in } ^2 + \vec{t}_{ex } ^2) d\sigma$</p>
<p style="text-align: center;"><u>Fluid Inclusion</u></p> <p>Same as slippery elastic, with $\mu = 0$ (i.e. $\vec{t}_{in } = 0$ automatically)</p>
<p style="text-align: center;"><u>Elastic Inclusion (unglued)</u></p> <p>$\vec{s}_{ex} = \vec{s}_{in} = \text{unrestricted}; \vec{t}_{ex} = \vec{t}_{in} = 0$ $J = \int (\vec{t}_{in} ^2 + \vec{t}_{ex} ^2) d\sigma$</p>

Table I. Boundary conditions to be imposed on Σ for various types of flaws. Conditions on displacements and surface tractions are given, as are the surface integral functionals of the amplitudes which are to be minimized in several cases. Where more than one functional (I, J, and K) of the surface fields is to be minimized, we will minimize a positive linear combination of them, as discussed in the text. The Elastic Inclusion (unglued) can be made the basis for a treatment of a crack, as is also discussed in the text.

As an example of how the expressions given in Table I can be used to derive linear equations for the amplitudes we consider the case of the welded elastic inclusion. Here we need to worry about the internal displacements and stresses \vec{s}_{in} and \vec{t}_{in} ; thus after forming a positive linear combination of I and J

$$K = \alpha I + \beta J \quad (22)$$

and using (1), (2), (4), and (8) we can write, sup-

pressing subscripts,

$$\frac{\partial K}{\partial a^*} = 0 = Qa - \hat{Q}b + \tilde{Q}d \quad (23)$$

$$\frac{\partial K}{\partial b^*} = 0 = -\hat{Q}^+a + \hat{Q}b - \hat{Q}d. \quad (24)$$

In these equations the matrix \hat{Q} is given by

$$\hat{Q}_{p\ell m, p'\ell' m'} = \alpha \int \vec{s}_{p\ell m}^{(+)\dagger} \cdot \vec{s}_{p'\ell' m'} d\sigma + \beta \int \vec{t}_{p\ell m}^{(+)\dagger} \cdot \vec{t}_{p'\ell' m'} d\sigma. \quad (25)$$

The involved reader can easily deduce what the meanings of Q with the various other decorations are. In particular, the multiplicity of carets is equal to the number of inside functions occupying each integral.

The linear system (23), (24) can be solved for the T-matrix of Eq.(21);

$$T = -(Q - \hat{Q}\hat{Q}^{-1}\hat{Q}^+)^{-1}(Q - \hat{Q}\hat{Q}^{-1}\tilde{Q}). \quad (26)$$

The effects of vibrations of the medium inside the flaw, including possible resonances, is contained in the second term within each set of parentheses.

The positive parameters α and β occurring in (22) require some discussion. Clearly in the limit $\ell_{\max} \rightarrow \infty$ their choice has no effect on the answers, but for small ℓ they (actually only their ratio is significant)^{mgk} should be chosen carefully. From the expression (8) for the tractions it is clear that dimensionally

$$\alpha / \beta \approx \mu^2 k^2, \quad (27)$$

and it is easy to invent plausible arguments for promoting this into an equality. Not the least of these arguments is that (27) works well in practice, giving results which agree quite well with reciprocity and the optical theorem for small ℓ_{\max} . We note in passing that arbitrariness, illustrated explicitly by (27), is also implicit in all the surface integrals. The integration measure $d\sigma$ is taken to be the surface area, but it could be taken to be any positive measure whatever without affecting the results in the limit $\ell_{\max} \rightarrow \infty$.

RESULTS

To demonstrate the application of this method to the computation of scattering from an inclusion, we show in Fig. 3 the backscattering as a function of ka from an oblate spheroidal magnesium inclusion in stainless steel.

CRACKS

There are several ways this method and related methods can be applied to scattering from cracks with axial symmetry. One might, for example, take a circular crack to be the limit of an oblate spheroid as its aspect ratio $\rightarrow 0$. Or one might imagine that the crack is the top surface of a pillbox-shaped identical inclusion (λ', μ', ν') , welded in place except for the top surface, which is free (unglued). Alternatively, a circular crack might be

viewed as an identical bisected spherical inclusion. These 3 crack simulations are pictured in Fig. 4.

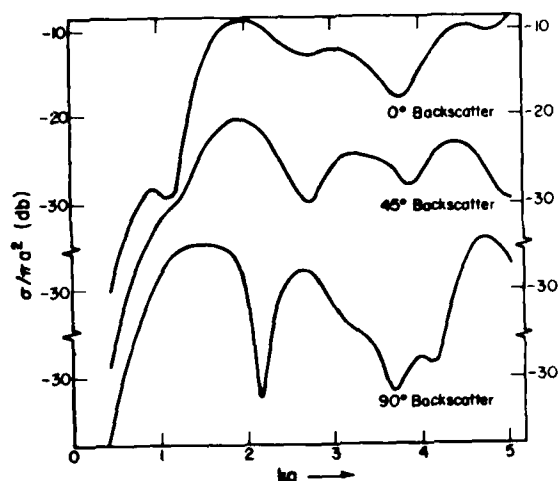


Fig. 3. Backscattering of an incident longitudinal elastic wave from an oblate (aspect ratio = 2) spheroidal inclusion of magnesium in stainless steel ($\nu/\nu' = \lambda/\lambda' = \rho/\rho' = 4$; $\lambda/\mu = 2$). The axis of the spheroid is at $\theta = 0$; the curves for successively larger angles of backscatter are displaced downward 10 db. $\ell_{\max} = 8$ was used for these calculations, which were done for 50 values of $ka = 0.1(0.1)5.0$. About 10 min. were consumed on a CDC 6600 to generate the scattered amplitudes which produced these data. Thirty Gauss-Legendre quadrature points were used in the numerical integrations which produced the matrix elements.

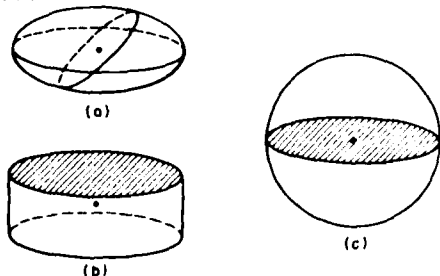


Fig. 4. Three ways to simulate a circular crack with MOOT. (a) is an oblate spheroidal void, with aspect ratio $\rightarrow 0$. (b) is an identical inclusion, pillbox-shaped (or with any other rotationally symmetric shape) welded everywhere except over a free circular surface, where free boundary conditions are imposed. (c) comprises a pair of identical opposed hemispherical welded inclusions, each with its plane circular surface free.

Figure 4(a) depicts the ingenuous representation of a crack as the limit (aspect ratio $\rightarrow 0$) of an oblate spheroidal void. Problems arise here in the evaluation of the surface integrals because the integrands often become singular when the surface approaches the origin (the dots in Fig. (4)). These difficulties can be partly mitigated in different formulations of T-matrix theory⁽⁴⁾, but we have not found a way to overcome them in MOOT. The schemes

illustrated in Fig. (4b & 4c) avoid singular integrands by keeping the origin away from the region of space where the fields are expanded in regular functions. Fig. (4c) has the apparent disadvantage that it requires an additional eigenfunction expansion; that is, space is divided into an external region and two internal regions. Because of the up-down symmetry when the crack is plane circular, though, this drawback can be circumvented, and for this case Fig. (4c) is the formulation of preference. The very asymmetry responsible for the inferiority of Fig. (4b) for the plane crack, though, makes it the preferable picture when the crack is not planar, e.g. a spherical cap or a Frisbee shape.

A difficulty common to all 3 crack simulations shown in Fig. (4) is caused by the fact that the displacements and stresses near a crack edge are singular; the displacement behaving like $\rho^{1/2}$, the stress like $\rho^{-1/2}$, where ρ is the distance to the edge. These singularities cannot be well represented by a partial wave expansion (1) and (2) with a reasonable number of terms, and an accurate description of the singularities appears to be critically important to a scattering calculation⁽⁵⁾.

The form of the singular displacements can be easily calculated asymptotically close to the crack edge in terms of just 3 independent amplitudes⁽⁶⁾. This fact can be exploited to solve the problem of the edge singularities in a number of ways. One way is to actually surround the crack edge with a torus and expand the displacement in the torus in terms of the amplitudes of the 3 singular modes. Then one has additional surface integrals over the torus and 3 additional amplitudes to determine for each m . Another way is to require, in a least-squares sense, that the fields satisfy crack conditions at the quadrature points of the surface integrals nearest the crack edge. This is the simplest alternative and is presently being pursued.

REFERENCES

1. William M. Visscher, Los Alamos Report LA-UR-78-3008. (To be published in J. Appl. Phys.)
2. William M. Visscher, Los Alamos Report LA-UR-79-399. (To be published in J. Appl. Phys.)
3. William M. Visscher, Proceedings of the ARPA/AFML Review of Progress in Quantitative NDE (1978) p. 424 (AFML-TR-78-205).
4. V. V. and V. K. Varadan, Elastic Wave Scattering by Rough Flaws and Cracks (these proceedings).
5. B. Budiansky and J. R. Rice, J. Appl. Mech. 45, 453 (1978).
6. S. N. Karp and F. C. Karal, Jr. Comm. Pure and Appl. Math. 15, 413 (1962).

SUMMARY DISCUSSION
(William Visscher)

Don Yuhas (Sonoscan): You listed two types of elastic inclusions, one slippery and one with welded boundary conditions. Could you give a physical example of each?

William Visscher: Well, not really. The real reason that I listed the slippery inclusion is that it's a stepping stone from the welded inclusion to the fluid inclusion.

Don Yuhas: I'm just trying to get some idea so that if somebody goes into a lab should they measure in order to confirm what you're calculating.

William Visscher: I haven't calculated anything for the fluid inclusion yet, but the physically realistic ones are the welded inclusion and the fluid inclusion. Slippery elastic is sort of halfway between.

James Rice (Brown University): It's a very small point, but you said it was obvious that for the rigid inclusion, the displacements have to vanish from the surface, and I thought it was obvious that the displacements have to be those of a rigid body, which can move.

William Visscher: I should have said rigid immovable inclusion.

George Gruber (Southwest Research): I'm very dubious about extrapolating from an inclusion-like defect to a crack-like defect because I basically believe that inclusion-like defects behave like scatterers having smooth boundaries, and a crack-like defect has sharp boundaries and basically behaves like a diffracter. And, mathematically you might be able to come over, but physically the interaction mechanisms of the ultrasound with the defect types of these two basic types seem to be widely different and seem to come from a different direction.

James Krumhansl (Session Chairman): I guess that comment is an interesting comment. It has a variety of applications to discuss. Maybe you want to comment, Bill, but we will call it at that.

William Visscher: It was worries like that which motivated me to have a different expansion in the neighborhood of the crack edge. That is, you can put in exact forms for the displacement and stress in the immediate neighborhood of the crack edge and use separate expansions there.

James Krumhansl: So my comment isn't entirely opaque: certainly the crack properties, for example, by Rice and Budiansky have been mapped on the very long wavelength region where there is no diffraction.

#

MATRIX THEORY OF ELASTIC WAVE SCATTERING: APPLICATION TO SCATTERING OF TRANSVERSE WAVES

Jon L. Opsal
Lawrence Livermore Laboratory
Livermore, California 94550

ABSTRACT

New calculations of elastic wave scattering using Visscher's matrix theory have been made for transverse waves incident on axially symmetric defects. Longitudinal incident waves have also been considered with the results in agreement with those obtained previously by Visscher. A number of interesting features for incident transverse waves will be presented as well as some of the practical aspects of the calculation (e.g. convergence, accuracy, and computer time).

INTRODUCTION

The transition matrix (T-matrix) approach to solving elastic wave scattering problems has received considerable attention with essentially three methods having recently been developed.¹⁻⁵ Of these, the only method for which convergence has been demonstrated is the method of optimal truncation (MOOT) by Visscher, which he has proven converges uniformly to the exact solution. Some aspects of the rate of that convergence, however, have not yet been appreciated and will be discussed in the first part of this talk.

An attractive feature of any transition matrix theory is that the T-matrix is independent of the incident wave. Taking advantage of this, I have written a program based on MOOT which calculates scattering of both longitudinal and transverse waves incident on a defect from any number of prescribed angles. I should point out at this time that my results for the longitudinal case agree with Visscher's, suggesting that the method has been implemented correctly by both of us. Some examples for scattering from cylindrical voids will be shown in the latter portion of this presentation.

DISCUSSION

In any T-matrix theory, the incident and scattered waves are expanded in some finite subset of a complete set of functions, with the particular theory based on the method used to relate the unknown scattered wave coefficients to the known expansion coefficients of the incident wave. Using a finite number of terms in the expansion results in an error in satisfying the boundary conditions. MOOT optimizes the solution by a least squares minimization of that error which guarantees uniform convergence to the exact solution. A very interesting and significant point regarding the convergence of MOOT is perhaps best made with the following simple example.

Consider a system of two equations in two unknowns,

$$\begin{pmatrix} A_{11} & A_{12} \\ A_{21} & A_{22} \end{pmatrix} \begin{pmatrix} X_1 \\ X_2 \end{pmatrix} = \begin{pmatrix} Y_1 \\ Y_2 \end{pmatrix} \quad (1)$$

where A and Y depend on a parameter ka as

$A_{ij} = a_{ij}(i/ka)^{i+1}(j/ka)^{j+1}$, $Y_i = y_i(i/ka)^{i+1}$, with a and y independent of ka. This behavior is analogous to that encountered when implementing MOOT for terms in the spherical wave expansion corresponding to $i \gg ka$, where i is the order of the spherical Bessel, Neumann, or Hankel function, k the wave vector, and a the "size" of the defect (e.g., for a spherical defect, a equals the radius of the sphere). In this limit, the spherical Neumann function becomes very large, increasing approximately as $(2/ka)^{i+1}$. Inverting Eq.(1) one obtains for X,

$$\begin{pmatrix} X_1 \\ X_2 \end{pmatrix} = \frac{1}{d} \begin{pmatrix} (a_{22}y_1 - a_{21}y_2)(ka/i)^{i+1} \\ (a_{12}y_2 - a_{11}y_1)(ka/i)^{i+1} \end{pmatrix} \quad (2)$$

where $d = a_{11}a_{22} - a_{12}a_{21}$.

The X_i in this example correspond to the scattered wave expansion coefficients and illustrate that once i exceeds ka by some significant amount, the series has converged. However, Eq.(2) also shows that if the off-diagonal elements of a are comparable to either of the diagonal elements of a, the full matrix needs to be inverted for an accurate determination of X. This would be the case even when X_1 is found to be insignificant compared to X_2 . Another way of saying this in terms of the scattering problem is, that while it is wavelength relative to some characteristic size parameter that determines the number of terms required for the partial wave series to converge, the accurate solution for those expansion coefficients requires a matrix whose rank depends to a large extent on the shape of the scatterer (i.e., its degree of departure from sphericity).

RESULTS

There are several checks that one can make to test the convergence and accuracy of the calculations. In particular, the total cross-section, SIGMA, can be calculated at some order, N, (where N is the highest order spherical Bessel function in the expansion) and then at successively higher orders until no significant change in SIGMA is noted. The accuracy of the calculation is also reflected in the extent to

which the optical theorem is satisfied. This theorem states that the imaginary part of the forward scattering amplitude, IMF, is equal to the total cross-section and depends on having calculated the phase of the scattered wave correctly. A different kind of test, which to my knowledge hasn't been done before, is to calculate the scattering from a sphere displaced from the origin of the coordinate system in which the spherical wave functions are defined. In this displaced geometry, the wave functions are no longer orthogonal, consequently, a relatively larger matrix than in the undisplaced geometry will have to be inverted. Since the cross-sections are invariant, comparing these results with the known exact solution provides an additional test.

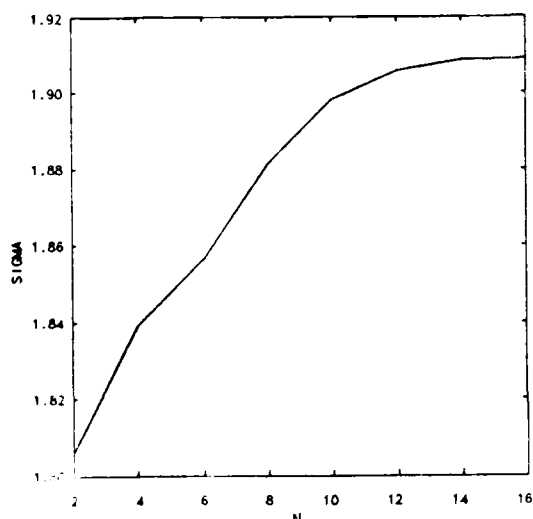


Fig. 1 Longitudinal waves incident on sphere.

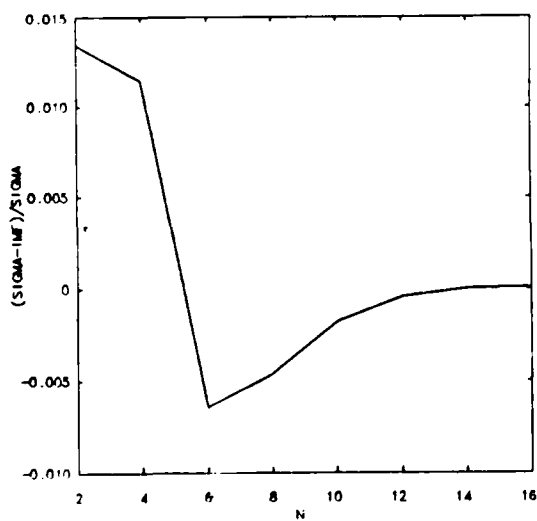


Fig. 2 Longitudinal waves incident on sphere.

In Figs. 1-4, the total cross-section and optical theorem are shown to converge for longitudinal and shear waves incident on a spherical void which has been displaced by an amount equal to one-half its radius. The values for SIGMA at convergence are exactly those obtained in the undisplaced configuration. Although only terms of order up to and including $N=4$ were needed in the resulting partial wave series, the calculation didn't converge until $N=14$, as indicated in the figures.

In these figures and in all remaining figures, THETA is the polar angle in the coordinate system whose polar axis is defined by the incident wave vector, and THETA0 is the angle of incidence measured from the symmetry axis of the scatterer.

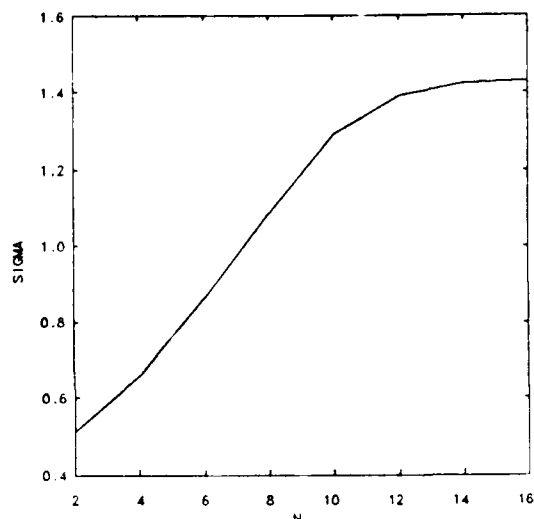


Fig. 3 Shear waves incident on sphere.

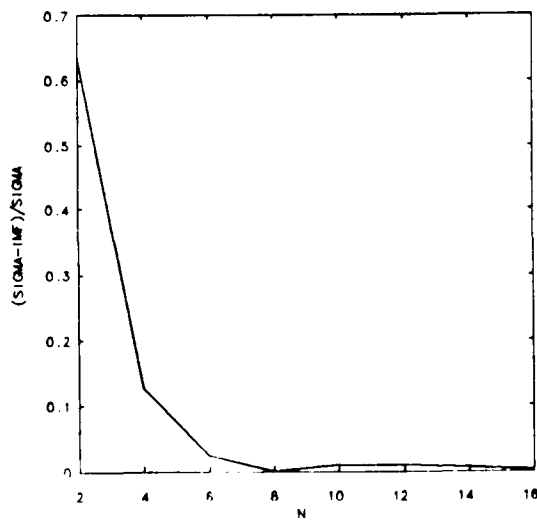


Fig. 4 Shear waves incident on sphere.

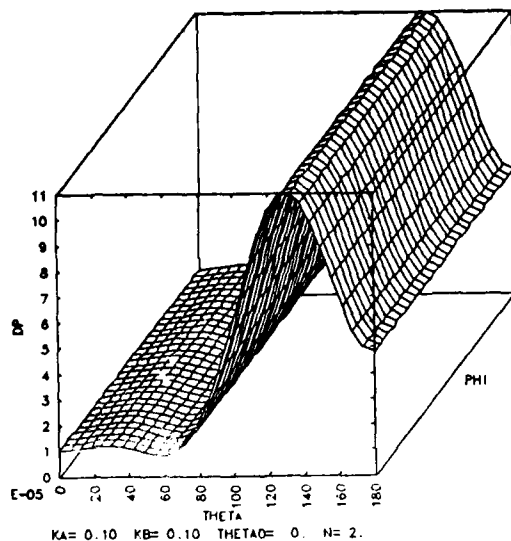


Fig. 5 Longitudinal waves incident on sphere.

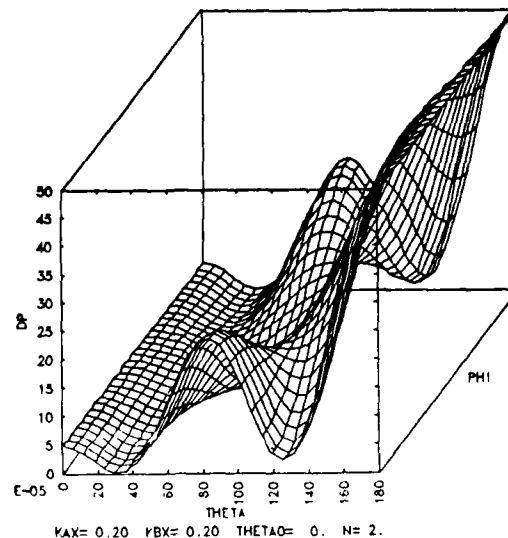


Fig. 7 Shear waves incident on sphere.

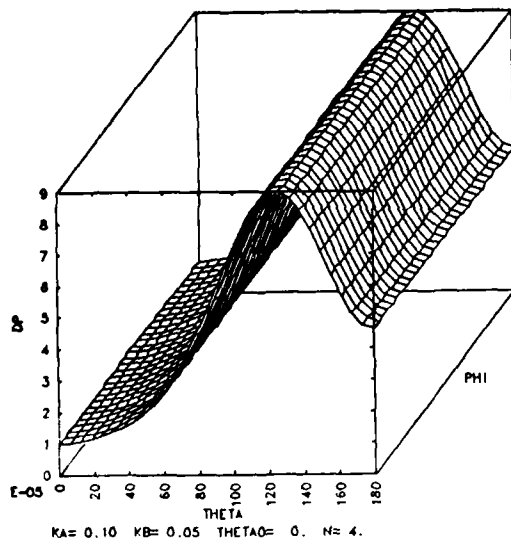
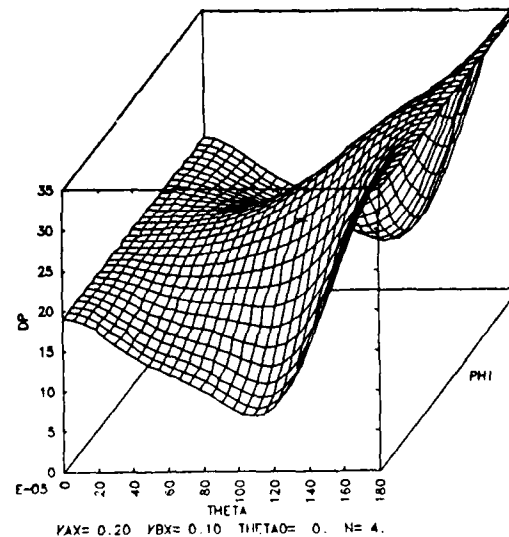


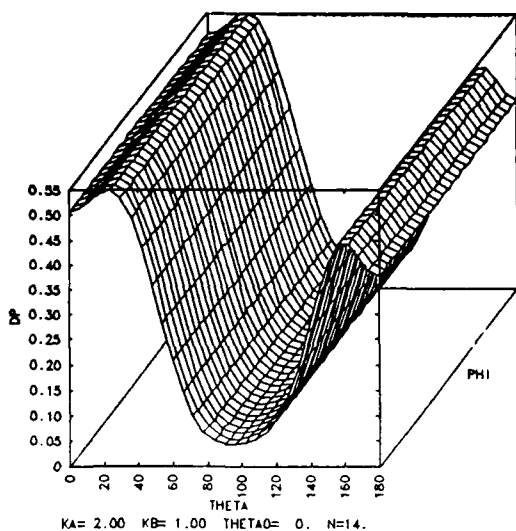
Fig. 6 Longitudinal waves incident on sphere(displaced)



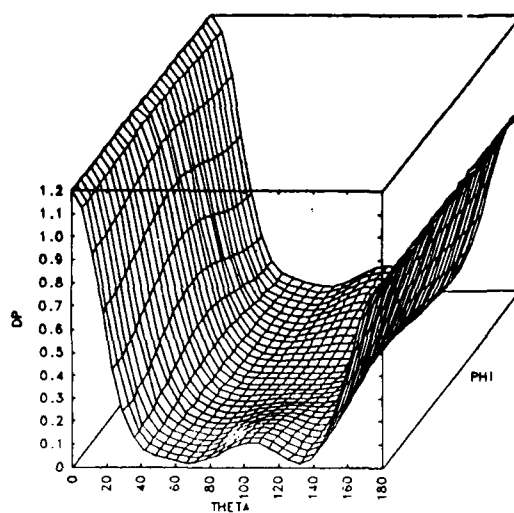
In Figs. 5-8 are shown differential cross-sections, D_p , for scattering from a spherical void in the long-wavelength limit. For these calculations, and for all the calculations discussed in this talk, the cross-sections have been normalized to the geometrical cross-section (which for the sphere is πa^2). The azimuthal angle ϕ , ranges from 0 to 180 degrees and is measured from the x-axis which in the case of incident shear waves lies along the shear wave polarization vector. For convenience, the shear wave velocity has been set equal to one-half the longitudinal velocity in all calculations. In the long-wavelength limit, $N=2$ is sufficient for convergence when the sphere is centered about the origin, the results for this case shown in Figs. 5 and 7. Figures 6 and 8 show calculations for the displaced sphere to order $N=4$ which clearly have not converged. For this case, $N=12$ is required for the

results to agree with those shown in Figs. 5 and 7.

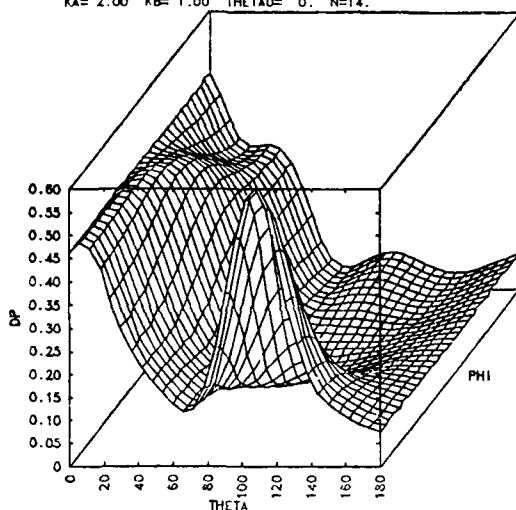
The results shown in Figs. 9-10 are for waves incident at 0° , 45° , and 90° on a cylindrical void having aspect ratio of $1/2$. Evidence can be found in these figures that one is approaching the short wavelength limit, especially at the 45° incidence. For longitudinal incident waves, the peak centered about 110° is where one would expect a mode-converted specularly reflected shear wave. All of that peak is in fact due to the mode converted scattered wave. Strong backscattering at normal incidence and weak backscattering at 90° is also the expected behavior as one goes to short wavelengths. I should point out that for shear waves incident, mode conversion contributes about an order of magnitude less to the cross-section than in the case of incident longitudinal waves. All that one sees in Fig. 10 is the direct scattered wave.



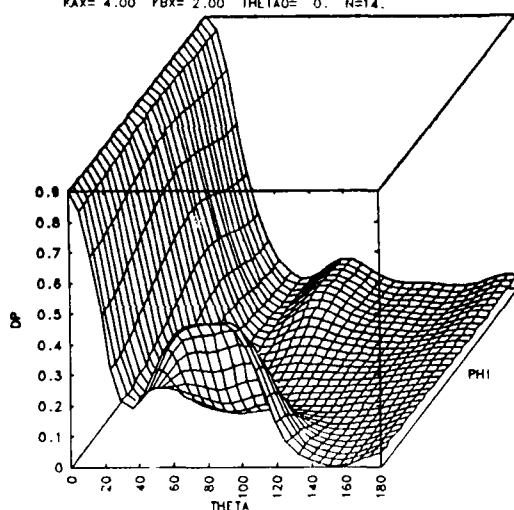
$KA=2.00$ $KB=1.00$ $\theta_0=0$ $N=14$



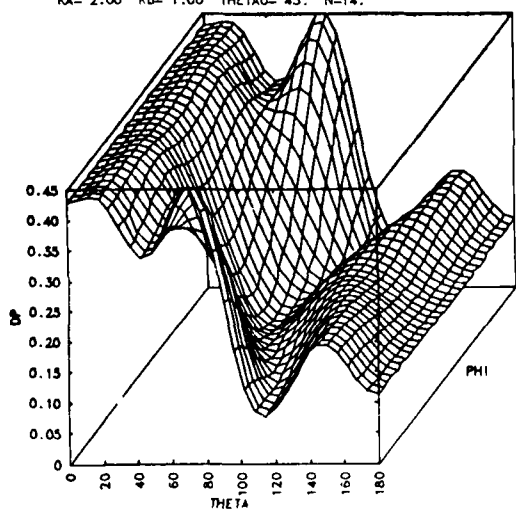
$KAX=4.00$ $YBX=2.00$ $\theta_0=0$ $N=14$



$KA=2.00$ $KB=1.00$ $\theta_0=45$ $N=14$

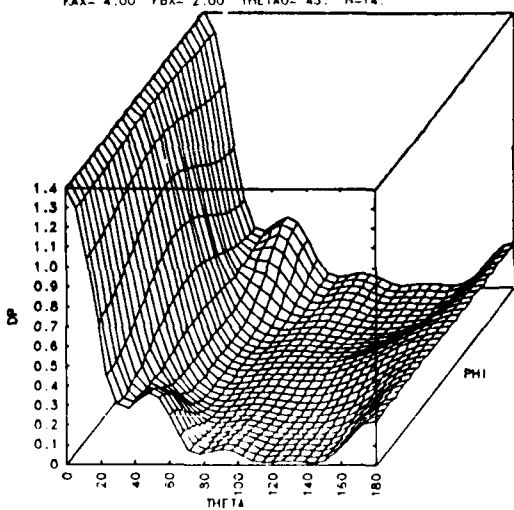


$KAX=4.00$ $YBX=2.00$ $\theta_0=45$ $N=14$



$KA=2.00$ $YB=1.00$ $\theta_0=90$ $N=14$

Fig. 9 Longitudinal waves incident on cylinder.



$KAX=4.00$ $YBX=2.00$ $\theta_0=90$ $N=14$

Fig. 10 Shear waves incident on cylinder.

In conclusion, I would like to express my opinion that the method of optimal truncation has advanced the theory of elastic wave scattering to the extent that it should be seriously considered as a standard with which to test the validity of other more approximate schemes. It is my intention to make such comparisons with other methods and place some quantitative limits on their range of usefulness.

ACKNOWLEDGMENT

This work performed under the auspices of the U. S. Department of Energy by the Lawrence Livermore Laboratory under contract number W-7405-ENG-48.

REFERENCES

1. P. C. Waterman, J. Acoust. Soc. Am. 60, 567 (1976).
2. V. Varatharajulu, Y.-H. Pao, J. Acoust. Soc. Am. 60, 556 (1976).
3. W. M. Visscher, Proceedings of the ARPA/AFML Review of Progress in Quantitative NDE, ed. D. O. Thompson, AFML-TR-78-205, p.425 (1978).
4. W. M. Visscher, J. Appl. Phys. , in press.
5. W. M. Visscher, these proceedings.

SUMMARY DISCUSSION
(Jon Opsal)

Norman Bleistein (Denver Applied Analytics): I would like to address myself to this question of spherical harmonics. It would seem the difficulty is that you try to use spherical harmonics to do a problem where the coordinates are not the most desirable coordinates. Have you tried to use ellipsoidal harmonics?

Jon Opsal: In these kinds of problems it's only the spherical coordinates that you can actually separate the waves into longitudinal and transverse.

Norman Bleistein: Okay. So, the elasticity constrains against the mathematical.

Jon Opsal: You expect in the far fields spherical waves coming out, so it seems like a good choice. It's a matter of properly determining the coefficient.

#

AN APPLICATION OF PADÉ APPROXIMANTS TO ELASTIC WAVE SCATTERING

J. E. Gubernatis
Theoretical Division
Los Alamos Scientific Laboratory
Los Alamos, NM 87545

ABSTRACT

Several Padé methods were used to try to accelerate the convergence of partial wave sums for scattering amplitudes. A specific test problem of longitudinal-to-longitudinal scattering from a spherical void was studied in detail. Results for this test case and the behavior of partial wave amplitudes for general cases are presented and discussed.

INTRODUCTION

Recently, numerical procedures,¹⁻⁴ based on the method of eigenfunctions expansions, were devised to calculate the scattering of an elastic wave from a flaw. If the shape of the flaw is axially symmetric, then these procedures are efficient, accurate and easily implemented. Their implementation requires only a computer of modest memory; their coding, standard numerical techniques; and the execution of the code, small amounts of computer time. However, if the flaw is generally shaped, practical concerns impede their implementation. The principal impediment is the need to compute and store more information. In general, the computing time and storage requirements are at least an order of magnitude greater. Simply using a bigger, faster computer is generally inadequate; a computer system with "virtual" memory (or very fast discs) and more sophisticated coding techniques are needed. Furthermore, the calculation becomes expensive.

The present investigation sought a method to permit the use of the eigenfunction expansion techniques for generally-shaped flaws without the need of bigger, faster computers and more sophisticated coding techniques and still permit an inexpensive calculation. Simply stated, a method was sought that would take whatever information the eigenfunction expansion techniques could practically yield and then extrapolate this information into an accurate scattering result.

In detail, one wants to calculate a scattering amplitude. The exact scattering amplitude A is a complex number which in terms of a partial-wave eigenfunction expansion is

$$A(\cdot, \cdot) = \sum_{l=0}^{\infty} \sum_{m=-l}^l a_{lm} Y_{lm}(\cdot, \cdot) \quad (1)$$

where the a_{lm} are partial wave scattering amplitudes, Y_{lm} are spherical harmonics, and \cdot and \cdot are scattering angles. The eigenfunction expansion techniques give the a_{lm} , and the object of these techniques is to compute enough a_{lm} so the sequence of partial sums for $A(\cdot, \cdot)$, i.e.,

$$A_L = \sum_{l=0}^L \sum_{m=-l}^l a_{lm} Y_{lm}(\cdot, \cdot) \quad (2)$$

converges to some required accuracy, e.g.,

$$|A_L - A_{L-1}| \leq \epsilon |A_{L-1}| \quad (3)$$

where ϵ is a relative error criterion. The object of present investigation is to take unconverged information and mathematically extrapolate it to approximate $A(\cdot, \cdot)$ to required accuracy. To do this, various approximations theories, classified as Padé Approximants, were studied and used on a specific test problem. This problem was the calculation of longitudinal-to-longitudinal scattering of a plane wave from a spherical cavity. For this problem the exact scattering amplitude⁵ has a simple partial wave expansion,

$$A(\cdot) = \sum_{l=0}^{\infty} a_l P_l(\cos \cdot) \quad (4)$$

where the $P_l(\cos \cdot)$ are Legendre polynomials and the partial wave amplitudes a_l are known in terms of simple, analytic expressions. The partial sums

$$A_L = \sum_{l=0}^L a_l P_l(\cos \cdot) \quad (5)$$

were easily computed to a relative error of $\epsilon = 10^{-12}$.

The initial Padé Approximants studied were ones recently developed in nuclear physics.⁶⁻¹² They are very successful for accelerating the convergence partial sums (4) for the scattering from large classes of long and short-ranged potentials. These techniques are generalizable to two variable partial wave sums, i.e. (2).

PADÉ APPROXIMANTS

The Padé Approximant.¹³ The $[M/N]$ Padé Approximant to a function $F(x)$ is

$$F^{[M/N]}(x) = P_M(x)/Q_N(x) \quad (6)$$

where $P_M(x)$ is a polynomial of degree at most M and $Q_N(x)$ is a polynomial of degree at most N . If $F(x)$ has the formal power series expansion

$$F(x) = \sum_{\ell=0}^{\infty} f_{\ell} x^{\ell} \quad (7)$$

and $P_M(x)$ and $Q_N(x)$ are

$$P_M(x) = p_0 + p_1 x + \dots + p_M x^M \quad (8a)$$

$$Q_N(x) = 1 + q_1 x + \dots + q_N x^N \quad (8b)$$

Then the equation

$$Q_N(x)F(x) - P_M(x) = O(x^{M+N+1}) \quad (9)$$

completely and uniquely determines the $M+1$ coefficients of $P_M(x)$ and N coefficients of $Q_N(x)$ in terms of the first $M+N+1$ coefficients of the power series expansion of $F(x)$. Specifically, one carries out the implied power series multiplications in (9), equates terms of like powers of x , and then solves an $M+N+1$ set of linear algebraic equations for the p 's and q 's in terms of the f 's.

Padés have numerous uses, but their use in summing series is of immediate interest. In this use, one takes the first $M+N+1$ coefficients in a partial sum to

$$F_{M+N} = \sum_{\ell=0}^{M+N} f_{\ell} x^{\ell} \quad (10)$$

computes various sequences of Padés, and examines their convergence. For certain classes of functions the Padés must converge to the correct answer. For many other classes of functions for which convergence proofs are absent experience shows that if the Padés converge, they converge to the correct answer.

It is helpful to be mindful that in the construction of (6) only the coefficients of a partial sum of the infinite series in (7) is used. However, (6) has the formal power series expansion

$$F^{[M/N]}(x) = \sum_{\ell=0}^{\infty} f_{\ell}^{[M/N]} x^{\ell} \quad (11)$$

and it is easy to show the first $M+N+1$ coefficients of this series equal the first $M+N+1$ coefficients of (7). The higher order coefficients in (11) approximate the higher order coefficients in (7). With respect to (7) these higher order coefficients were not used to construct (6). This is useful if the higher order terms are unknown, slowly convergent, or too expensive to calculate. The idea is to get the Padé to approximate them for us.

Generalized Padé Approximants.¹³ The generalized Padé Approximant (or Baker-Gammel Approximants) apply to functions $G(x)$ which have the representation

$$G(x) = \sum_{\ell=0}^{\infty} g_{\ell} k_{\ell}(x) \quad (12)$$

where

$$k_{\ell}(x) = \frac{1}{\ell!} \left[\left(\frac{\partial}{\partial u} \right)^{\ell} K(x, u) \right]_{u=0} \quad (13)$$

with the generating function $K(x, u)$ to be specified. For example, if $K(x, u) = (1 - 2xu + u^2)^{-1/2}$

$$G(x) = \sum_{\ell=0}^{\infty} g_{\ell} P_{\ell}(x) \quad (14)$$

where $P_{\ell}(x)$ is the Legendre polynomial. The $[M+J/M]$ generalized Padé Approximant to $G(x)$ is

$$G^{[M+J/M]}(x) = \sum_{j=0}^J \beta_j k_j(x) + \sum_{j=1}^M \alpha_j K(x, u_j) \quad (15)$$

with the j -summation absent if $J = -1$. The β_j , α_j and u_j are to be specified. When the generating function for Legendre polynomials is used for $K(x, u)$, the generalized approximants are called Legendre-Padé Approximants.⁶

One way to specify the β_j , α_j , and u_j is with the g_{ℓ} in (12) to create the formal series

$$F(x) = \sum_{\ell=0}^{\infty} g_{\ell} x^{\ell}$$

and then construct $F^{[M+J/M]}(x)$. It then can be shown that

$$g_{\ell} = \beta_{\ell} + \sum_{j=1}^M \alpha_j u_j^{\ell}, \quad \ell = 0, 1, \dots, J \quad (16a)$$

and

$$g_{\ell} = \sum_{j=1}^M \alpha_j u_j^{\ell}, \quad \ell = J+1, J+2, \dots, 2M+J \quad (16b)$$

That is, the β_j , α_j and u_j are unknowns in a non-linear system of equations with the known constants g_{ℓ} . More conveniently, it can also be shown that u_j^{-1} and α_j/u_j are the poles and residues of $F^{[M/N]}(x)$, and β_j the coefficients in the series expansion of $F^{[M+J/M]}(x)$ as $x \rightarrow \infty$. All these quantities (the poles, residues, etc.) are easily obtained by simple numerical analysis. The generalized approximant (15) has the property that

$$G^{[M+J/M]}(x) = \sum_{\ell=0}^{\infty} g_{\ell}^{[M+J/M]} k_{\ell}(x) \quad (17)$$

with the first $2M+J+1$ terms identical to the first such terms in (12). Again, the Padé Approximant has taken the coefficients in a partial sum and returned them plus an approximation for the remaining coefficients of the actual infinite sum.

n-Point Padé Approximants.¹³ If a function $F(x)$ has the values F_1, F_2, \dots, F_n at x_1, x_2, \dots, x_n then the n -Point $[M/N]$ Padé Approximant (or the Lagrange interpolation polynomials) is the ratio of two polynomials of degree at most M and N

$$F^{[M/N]}(x) = P_M(x)/Q_N(x) \quad (18)$$

so that

$$F^{[M/N]}(x_i) = F_i, \quad i = 1, 2, \dots, n \quad (19)$$

(P_M and Q_N are defined as in (8).)

Of immediate interest is the 1-Point (or Punctual¹⁰) Padé Approximant. This approximation applies to the sum

$$B = \sum_{\ell=0}^{\infty} b_{\ell} \quad (20)$$

and its partial sums.

$$B_L = \sum_{\ell=0}^L b_{\ell} \quad (21)$$

Now if one considers the formal power series

$$F(x) = \sum_{\ell=0}^{\infty} b_{\ell} x^{\ell} \quad (22)$$

then $B = F(1)$. The 1-Point $[M/N]$ Padé Approximant to (20), i.e. $B^{[M/N]}$, is constructed by forming $F^{[M/N]}(x)$ for (21) (i.e. find the p 's and q 's) and equating

$$B^{[M/N]} = F^{[M/N]}(1) = \frac{\sum_{m=0}^M p_m}{1 + \sum_{n=1}^N q_n} \quad (23)$$

The approximants $B^{[M/N]}$ are equivalent to Shanks's¹⁴ formal generalization of Aicken's extrapolation formula. This approximation is applied to partial wave sums by defining

$$b_{\ell} = a_{\ell} P_{\ell}(\cos \theta) \quad (24)$$

RESULTS

To achieve the same degree of accuracy, the various Padé methods used were found to need at least as many partial wave coefficients as the partial sums. The Padé methods investigated afford no computational advantage over directly summing the series.

In Fig. 1 the magnitudes of the partial sum (5) are plotted as a function of L . As a reminder, the test problem is the longitudinal-to-longitudinal scattering of a plane wave from a spherical cavity; $A(\theta)$ is the scattered amplitude; a is the radius of the sphere; and k is the incident and scattered wavenumber. (For the partial sum A_L , $L+1$ coefficients are needed.) Figure 1 shows that for different values of ka the partial sums behave similarly. Each sequence rises monotonically to a plateau. For each ka , there is a particular L which marks the beginning of the plateau ($L=2, 5, 10$). For these L 's the partial sum has a

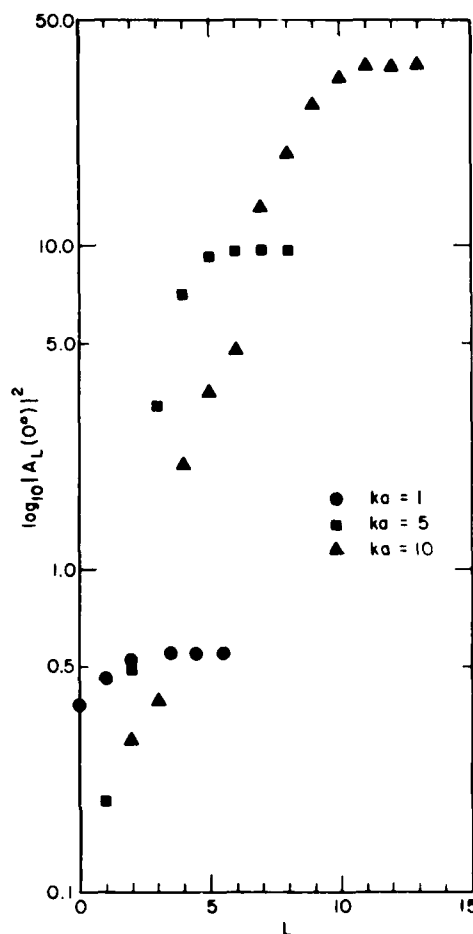


Fig. 1. The convergence of the forward scattering differential cross-section as a function of L .

relative error $\epsilon = 10^{-2}$. For smaller L values the partial sums are bad approximations to the exact answer; for larger L values the partial sum converges rapidly. The sums achieve a $\epsilon = 10^{-12}$ for $L=8, 17$ and 25 when $ka = 1, 5$ and 10 .

The Padé methods behave similarly: Convergence starts abruptly and then proceeds rapidly. This behavior is listed in Tables I, II and III for $ka = 1, 5$ and 10 . (The $[M/N]$ need $M+N+1$ coefficients.) Except for $[M-1/M]$ all sequences $[N/M]$ for $N \leq M$ and a given method behave as those listed.

Table I. The longitudinal differential cross-section at $\theta = 0^\circ$ and $ka = 1$ for three diagonal sequences of the 1-Point, Legendre and Asymptotic Legendre Padé Approximants.

M	1-POINT				LEGENDRE		ASYMPTOTIC LEGENDRE		
	$[M-1/M]$	$[M/M]$	$[M+1/M]$	$[M-1/M]$	$[M/M]$	$[M+1/M]$	$[M-1/M]$	$[M/M]$	$[M+1/M]$
1	0.3814	0.5021	0.5705	0.3814	0.5021	0.5705	0.4448	0.5198	0.5570
2	0.5492	0.5517	0.5533	0.5492	0.5517	0.5533	0.5560	0.5533	0.5530
3	0.5536	0.5533	0.5533	0.5536	0.5533	0.5533	0.5533	0.5533	0.5533
4	0.5533	0.5533	0.5533	0.5533	0.5533	0.5533	0.5533	0.5533	0.5533

Table II. The longitudinal differential cross-section at $\theta = 0^\circ$ and $ka = 5$ for three diagonal sequences of the 1-Point, Legendre and Asymptotic Legendre Padé Approximants.

M	1-POINT			LEGENDRE		ASYMPTOTIC LEGENDRE			
	[M-1/M]	[M/M]	[M+1/M]	[M-1/M]	[M/M]	[M+1/M]	[M-1/M]	[M/M]	[M+1/M]
1	0.0077	0.1447	0.4000	0.0077	0.1447	0.3648	0.1850	0.4060	7.4391
2	0.0283	0.6722	8.7317	0.0104	0.1084	8.7317	5.8718	9.0476	12.5913
3	0.6091	2.4488	9.6990	0.1889	1.7738	9.6990	9.8046	9.3165	9.5915
4	14.1791	9.6471	9.6179	14.1791	9.6471	9.6179	9.5810	9.6143	9.6179
5	9.5925	9.6209	9.6179	9.5925	9.6209	9.6179	9.6178	9.6179	9.6179
6	9.6195	9.6179	9.6179	9.6195	9.6179	9.6179	9.6179	9.6179	9.6179
7	9.6179	9.6179	9.6179	9.6179	9.6179	9.6179	9.6179	9.6179	9.6179

furthermore, the behavior is essentially independent of scattering angle. We note that for $ka = 10$ the 1-Point and Legendre Padé methods need more coefficients than the partial sum to achieve $\epsilon = 10^{-12}$.

In all cases the partial sums converge when $L > ka$. To try to understand the behavior of these sums, the behavior of the coefficients a_n were studied. In particular, their behavior for $n \gg ka$ was found.⁵ For a spherical void and inclusion

$$a_n = \frac{i^n (ka)^{2n-2}}{[(2n+1)!!]} - c_n (ka)^{2n-2} \quad (25)$$

If one lets

$$d_n = a_n / c_n \quad (26)$$

then

$$\frac{1}{(ka)^2} \left(\frac{d_n}{d_{n-1}} \right) \rightarrow 1 \quad (27)$$

The left-hand side of the above is plotted in Fig. 2 as a function of n . From this figure one sees that for $n = 8$ and 17 (for $ka = 1$ and 5), the ratio has approached its asymptotic limit. (Actually the limits are still several percent away.) For $ka = 10$ the limit is not yet attained. For these n values the ϵ for the partial sums is 10^{-12} .

Figures 1 and 2 and (25) suggest the following: Although the partial wave coefficients eventually fall off very rapidly, this rapid fall-off (or asymptotic behavior) occurs after the rapid convergence of the partial sum. The behavior of the

partial wave coefficients needed in a converged partial sum is quite different than the asymptotic behavior. The Padé methods might be ineffective because of this. What was devised is a new Padé method, the Asymptotic Legendre-Padé Approximant,¹⁵ which utilizes the asymptotic behavior of the partial wave coefficients. The Padé coefficients are forced to anticipate the correct asymptotic behavior so hopefully the convergence of predicted partial wave summation is accelerated.

The Asymptotic Legendre-Padé can be constructed in the following way: For the Legendre series

$$A(x) = \sum_{n=0}^M a_n P_n(\cos \theta)$$

instead of constructing the $[M+J/M]$ Legendre Padé from

$$F(x) = \sum_{n=0}^M a_n x^n$$

construct it from

$$F(x) = \sum_{n=0}^M d_n x^n$$

that is with the asymptotic behavior divided out. (d_n is given by (25) and (26).)

After constructing the $[M+J/M]$ Padé, one has

$$F^{[M+J/M]}(x) = \sum_{n=0}^M d_n^{[M+J/M]} x^n \quad (28)$$

Then,

Table III. The longitudinal differential cross-section at $\theta = 0^\circ$ and $ka = 10$ for three diagonal sequences of the 1-Point, Legendre and Asymptotic Legendre Padé Approximants.

M	1-POINT			LEGENDRE		ASYMPTOTIC LEGENDRE			
	[M-1/M]	[M/M]	[M+1/M]	[M-1/M]	[M/M]	[M+1/M]	[M-1/M]	[M/M]	[M+1/M]
1	0.0003	0.0291	0.2877	0.0003	0.0291	0.2877	0.0382	0.2756	0.3434
2	0.0224	0.0942	0.4015	0.0081	0.0210	0.0541	0.3732	0.3488	0.3617
3	0.0733	0.6031	1.5343	0.0335	0.1820	0.4131	3.6576	10.5304	25.9763
4	1.4516	1.3077	2.4237	0.3678	0.4141	0.6907	25.9288	31.8504	53.5930
5	3.5562	4.3865	2.6270	3.9362	1.0873	0.7402	53.1786	41.1073	48.3262
6	0.0879	2.2731	1.7432	0.0385	0.7730	0.4011	49.3442	36.5396	36.0059
7	0.9116	2.3716	76.5076	0.4305	1.2012	76.5076	36.0028	35.8575	35.8543
8	0.1463	24.1197	35.8899	0.0597	24.1183	35.8899	35.8543	35.8518	35.8518
9	48.5999	35.871	35.8515	48.5999	35.8766	35.8515	35.8518	35.8518	35.8518
10	35.8242	35.8517	35.8518	35.8242	35.8517	35.8518	35.8518	35.8518	35.8518
11	35.8518	35.8518	35.8518	35.8518	35.8518	35.8518	35.8518	35.8518	35.8518
12	35.8518	35.8516	35.8518	35.8518	35.8518	35.8514	35.8518	35.8518	35.8518

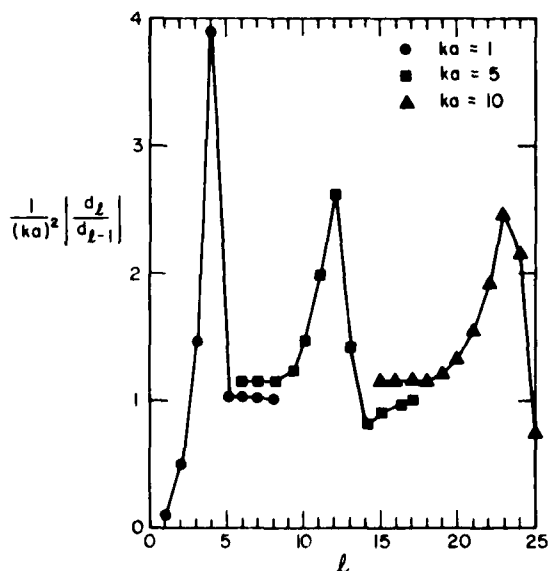


Fig. 2. The convergence of the partial wave amplitudes to their asymptotic value as a function of L . (See (27) in text.)

$$A_{[M+J/M]} = \sum_{l=0}^{\infty} a_{[M+J/M]}^{(l)} P_l(\cos \theta) \quad (29)$$

where

$$a_{[M+J/M]}^{(l)} = d_{[M+J/M]}^{(l)} c_l \quad (30)$$

(The analysis can be made more formal by specifying a $V(x, u)$.)

The results of the application of the new method are also listed in Tables I, II and III. For $ka = 10$ (Table III) this new method converges faster than the 1-Point and Legendre-Padé; however, the convergence is still no faster than the partial sum.

DISCUSSION

Clearly, not all possible summation techniques were studied and those studied were applied to a specific flaw shape. However, the 1-Point and Legendre-Padé Approximants are "state-of-the-art" for nuclear physics scattering problems. The Asymptotic Legendre-Padé Approximant, developed for this investigation, will probably advance the state-of-the-art.

Why do the techniques work for nuclear scattering and not for elastic wave scattering? There is an important difference between the scattering problems studied in nuclear physics and the problem studied here. For the problem under discussion the flaw (or scatterer) is modeled as a finite, homogeneous region of space. The corresponding scatterer in nuclear physics is the square-well potential. This is a short-ranged potential; however, the short-ranged potentials to which the Padé methods are being successfully applied are families of the Yukawa potential. For the pure Yukawa potential, the asymptotic behavior of its partial wave amplitudes

is¹⁶

$$a_l \sim \frac{(2l+1)!}{[(2l+1)!!]^2} (ka)^{2l+1} \quad (31)$$

which does not fall off as rapidly as (25). For the square-well potential¹⁶

$$a_l \sim \frac{(ka)^{2l+1}}{[(2l+1)!!]^2 (2l+3)} \quad (32)$$

which is quite similar to (25). The partial sums for square-well-type potential apparently converges too fast for the Padé methods to be advantageous over the partial sums.

The asymptotic behavior in (25) is apparently not limited to spherical flaws. For generally-shaped flaws, the Born approximation provides a useful estimate of the asymptotic behavior of the partial wave coefficients.¹⁶ One has

$$A(\cdot, \cdot) \sim \int_{\text{flaw}} dV e^{i(k-k_0) \cdot r} \quad (33)$$

where k and k_0 are the scattered and incident wave vectors. Since

$$e^{ik \cdot r} = 4\pi \sum_{l=0}^{\infty} \sum_{m=-l}^l i^l j_l(kr) Y_{lm}^*(\hat{r}) Y_{lm}(\hat{r}) \quad (34)$$

then

$$A(\cdot, \cdot) = \sum_{l=0}^{\infty} \sum_{m=-l}^l a_{lm} Y_{lm}(\cdot, \cdot) \quad (35)$$

where

$$a_{lm} \sim \int_{\text{flaw}} dV j_l^2(kr) = V j_l^2(kR) \quad (36)$$

with V being the volume of the flaw and R some characteristic length of the flaw. For $k \gg kR$

$$j_l(kR) \sim \frac{(kR)^l}{[(2l+1)!!]} \quad (37)$$

Hence as $l \rightarrow \infty$

$$a_{lm} \sim \frac{(kR)^{2l}}{[(2l+1)!!]^2} \quad (38)$$

which is very similar to (25). Again the above estimate and (25) is independent of the flaw being a void or inclusion. One can easily convince oneself that the finite volume of the flaw, not its homogeneity, is the significant factor for the rapid fall-off.

Equation (38) implies that the partial wave expansion, even for generally shaped objects, is quite rapidly convergent. However, question is not whether the sum converges, but how many terms are needed? The goal was to produce an accurate sum with no more than ten terms.

Just because the Padé techniques afford no computational advantage when the flaw is spherical does not prove that the techniques will be as ineffective for non-spherical flaws. What is

needed is a clearer picture how the partial wave sums behave for non-spherical flaws. There are few studies of the convergence properties of the eigenfunction expansion method. There is some indication that for a spheroidal flaw the partial sums behave at least differently; furthermore, different implementations of the eigenfunction expansion method may converge differently.²

ACKNOWLEDGEMENTS

It is my pleasure to acknowledge helpful discussions with George A. Baker, Jr.

REFERENCES

1. W. M. Visscher, Los Alamos Scientific Laboratory Report 78-3008 (1978); J. Appl. Phys. (in press).
2. W.M. Visscher, Los Alamos Scientific Laboratory Report 79-0399 (1979); J. Appl. Phys. (in press).
3. P.C. Waterman, J. Acoust. Soc. Am. 60 567 (1976).
4. V. Varatharajulu and Y.-H. Pao, J. Acoust. Soc. Am. 60 556 (1976).
5. C.F. Ying and R. Truell, J. Appl. Phys. 27, 1086 (1956).
6. A.K. Common and T. Stacey, J. Phys. A 11, 259 (1978).
7. A.K. Common and T. Stacey, "The Convergence of Legendre-Padé Approximants to Coulomb and Other Scattering Amplitudes," unpublished.
8. A.K. Common, "Calculation of Yukawa Scattering and Impact Parameter Amplitudes using Legendre-Padé Approximants," unpublished.
9. C.R. Garibotti and F.F. Grinstein, J. Math Phys. 19, 2405 (1978).
10. C.R. Garibotti and F.F. Grinstein, J. Math Phys. 19, 821 (1978).
11. C.R. Garibotti and F.F. Grinstein, "Summation of Partial Wave Expansions in the Scattering by Long Range Potentials: II. Numerical Applications," unpublished.
12. F.F. Grinstein, "Summation of Partial Wave Expansions in the Scattering by Short Range Potentials," unpublished.
13. George A. Baker, Jr. Essentials of Padé Approximants, (Academic Press, New York, 1975).
14. D. Shanks, J. Phys. and Math. (Mass.) 34, 1 (1955).
15. G.A. Baker, Jr. and J.E. Gubernatis, unpublished.
16. K. Gottfried, Quantum Mechanics, Vol. 1, (W.A. Benjamin, Inc., New York, 1966), Chap. III.

SUMMARY DISCUSSION
(James Gubernatis)

Jim Krumhansl (Cornell University): Let me see if I understand. In other words, this was an exploration of certain theoretical methods to find out how efficient they might be in the elastic wave calculations using partial wave expansions?

Jim Gubernatis: Yes, but it was just a test problem, and I can't infer too much more beyond the test problem.

#

ELASTIC WAVE SCATTERING BY GENERAL SHAPED DEFECTS: THE DISTORTED WAVE BORN APPROXIMATION

E. Domany,^a K.E. Newman and S. Teitel^b
Department of Physics, University of Washington
Seattle, Washington 98195

ABSTRACT

An approximate theory for scattering of elastic wave by general shaped defects has been developed. A defect of arbitrary shape can be represented by a sphere S and a remainder volume R . Using the exact solution for a sphere and treating R as a perturbation, the solution corresponding to the Distorted Wave Born Approximation is obtained. This solution contains non-trivial frequency dependence and phase information. Preliminary comparisons with experiments will be presented.

INTRODUCTION

Development of reliable approximation methods to elastic wave scattering by defects is an important part of NDE research. We have recently introduced the Distorted Wave Born Approximation,¹ to study scattering by defects of quite general shape. This method is expected to yield nontrivial phase information and frequency dependence of the scattered fields. Such information is of importance for development of inversion procedures, and for selecting an optimal set of measurements needed to characterize the defect.

The relative advantages of the DWBA were presented in a previous communication,¹ where the basic definitions and formulae were also given. In what follows we present a brief summary of the formalism and proceed to the new, final results.

THE DISTORTED WAVE BORN APPROXIMATION-- REVIEW OF FORMALISM

The DWBA starts by representing a general shaped defect R as a spherical region S and a remainder R (see Fig. 1). The exact solution of the scattering equation satisfies the integral equation¹

$$u_i(r) = u_i^S(r) + \delta\rho\omega^2 \int_R dr' g_{im}^S(r, r') u_m(r') - \delta C_{jklm} \int_R dr' g_{ij,k}^S(r, r') u_{l,m}(r') \quad (1)$$

$$R = S + \bar{R}$$

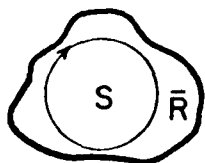


Fig. 1. The defect R is represented as a sphere S and a "remainder" volume R .

where u_i^S is the solution to the scattering problem by the sphere S , and $g_{ij}^S(r, r')$ is the associated Green's function, that describes the i component of the response at r to a point-source force in the j direction at point r' , in the presence of the sphere S . $\delta C(\delta\rho)$ are the difference between the elastic tensors (densities) of the defect and the medium in which it is embedded.

The DWBA consists of replacing in the integrals of (1) the exact solution u_i by the spherical solution u_i^S , i.e.,

$$u_i^{DWBA}(r) = u_i^S(r) + \delta\rho\omega^2 \int_R dr' g_{im}^S(r, r') u_m^S(r') - \delta C_{jklm} \int_R dr' g_{ij,k}^S(r, r') u_{l,m}^S(r') \quad (2)$$

The solution u^S is known² and can be evaluated numerically. However the Green's function g^S is not known; only one component has been explicitly evaluated, and the resulting expressions are rather complex.³ Therefore last year we studied an intermediate approximation, obtained by replacing g^S in (2) by the infinite Green's function. This approximation is one of a hierarchy of approximations that are discussed below. The main problem in obtaining the DWBA is twofold: to evaluate g^S and to set up the numerical procedure to calculate the integrals.

THE SPHERICAL GREEN'S FUNCTION

To evaluate $g_{ij}(r, r')$ we use the principles of superposition and reciprocity.⁴ Our method yields the function for $r \rightarrow \infty$, which is precisely the one needed in (2), since the point of observation, r , is assumed to be at infinity for calculation of scattering amplitudes and cross sections.

First note that if the infinite medium Green's function $g^0(r', r)$ can be expanded in terms of plane waves,

$$g_{ij}^0(r', r) = \int d\mathbf{k} A_j(r, \mathbf{k}, \lambda) u_i^0(r', \mathbf{k}, \lambda) \quad (3)$$

where $u_i^0(r', \mathbf{k}, \lambda)$ are plane wave solutions of the (homogeneous medium) wave equation, the spherical Green's function will be given by

(a) Address, after September 1979: Department of Electronics, Weizmann Institute of Science, Rehovot, Israel
(b) Permanent address: Department of Physics, Cornell University, Ithaca, New York

$$g_{ij}^S(r', r) = \int dk A_j(r, k, \lambda) u_i^S(r', k, \lambda) \quad (4)$$

where $u_i^S(r', k, \lambda)$ is the solution of the scattering problem by a sphere, of the incident plane wave $u_i^0(r', k, \lambda)$. (The index λ stands for the various possible polarizations.) Therefore, once the expansion coefficients $A_j(r, k, \lambda)$ are known, the spherical Green's function can be constructed, in principle, by superposition of solutions for the incident plane wave scattering problem. In general it is not trivial to find the $A_j(r, k, \lambda)$ needed to expand $g_{ij}^0(r', r)$; however, when the "source" position $r \rightarrow \infty$, the expansion for the A_j is simple. To see this, note

$$4\pi\rho\omega^2 g_{ij}^0(r', r) = \frac{\delta_{ij} B^2 e^{i\alpha R}}{R} - \partial_i \partial_j \left(\frac{e^{i\alpha R}}{R} - \frac{e^{i\alpha R}}{R} \right) \quad (5)$$

with $R = |r - r'|$, $\partial_i = \partial/\partial r_i$, and $\alpha^2 = \rho\omega^2/(\lambda + 2\mu)$, $\mu^2 = \rho\omega^2/\mu$. In the limit $r \rightarrow \infty$, this expression becomes

$$4\pi\rho\omega^2 g_{ij}^0(r', r) = R^2 \frac{e^{i\alpha R}}{r} e^{-i\alpha \hat{r} \cdot \hat{r}'} (\delta_{ij} - \hat{r}_i \hat{r}_j) + \alpha^2 \frac{e^{i\alpha R}}{r} e^{-i\alpha \hat{r} \cdot \hat{r}'} \hat{r}_i \cdot \hat{r}_j \quad (6)$$

Introducing now three unit vectors $\hat{e}^1, \hat{e}^2, \hat{e}^3$, $\hat{e}^1 = \hat{r}$, $\hat{e}^2 = \hat{\theta}$, $\hat{e}^3 = \hat{\phi}$, this reads

$$4\pi\rho\omega^2 g_{ij}^0(r', r \rightarrow \infty) = R^2 \frac{e^{i\alpha R}}{r} e^{-i\alpha \hat{r} \cdot \hat{r}'} (\hat{e}_j^2 \hat{e}_i^2 + \hat{e}_j^3 \hat{e}_i^3) + \alpha^2 \frac{e^{i\alpha R}}{r} e^{-i\alpha \hat{r} \cdot \hat{r}'} \hat{e}_j^1 \hat{e}_i^1 \quad (7)$$

This expression has the form (3), with only three incident plane waves,

$$u^0(r', k, \lambda) = \hat{e}^\lambda e^{-i\gamma(\lambda) \hat{r} \cdot \hat{r}'} \quad (8)$$

needed to expand g^0 . The coefficients A_j can be read off as given by

$$A_j(r, k, \lambda) = \frac{1}{4\pi\rho\omega^2} \hat{e}_j^\lambda e^{i\alpha R} k^2 \delta[k + \gamma(\lambda) \hat{r}] \quad (9)$$

where

$$\gamma(1) = \alpha, \quad \gamma(2) = \gamma(3) = \beta \quad (10)$$

Finally, in this limit, the spherical Green's function reads

$$4\pi\rho\omega^2 g_{ij}^0(r', r \rightarrow \infty) = \int \hat{e}_j^\lambda \frac{e^{i\gamma(\lambda)r}}{r} \gamma(\lambda)^2 u_i^S(r', -\gamma(\lambda) \hat{r}, \lambda) \quad (11)$$

where $u_i^S(r', -\gamma(\lambda) \hat{r}, \lambda)$ is the solution for scattering by a sphere of a plane wave with polarization λ , wavevector $\gamma(\lambda)$, incident in the $-\hat{r}$ direction, evaluated at point r' .

Inspecting Eq. (2) we note that in order to evaluate $u_{DWBA}^S(r)$ in the far field, i.e., $r \rightarrow \infty$, we need g^S with the point of observation at ∞ . To obtain this function, we use reciprocity, e.g.,

$$g_{ij}(a, b) = g_{ji}(b, a) \quad (12)$$

to get

$$g_{ji}^S(r \rightarrow \infty, r') = \frac{1}{4\pi\rho\omega^2} \sum_{\lambda} \hat{e}_j^\lambda \frac{e^{i\gamma(\lambda)r}}{r} \gamma(\lambda)^2 \cdot u_i^S(r', -\gamma(\lambda) \hat{r}, \lambda) \quad (13)$$

THE DISTORTED WAVE BORN APPROXIMATION-- FAR FIELD AMPLITUDES

In the far field limit, the scattered wave has the form

$$u_{DWBA}^S = \sum_{\lambda} \hat{e}^\lambda A(\lambda) e^{i\gamma(\lambda)r/r} \quad (14)$$

The solution of the scattering problem by a sphere, u^S , has this asymptotic form, and by inspection of Eq. (13), so does the spherical Green's function, and therefore, u_{DWBA}^S .

To obtain closed form expressions for u_{DWBA}^S , we substitute (13) in Eq. (2). To make the notation uniform, we denote the scattered solution that corresponds to the physical incident wave as $u^S(r, -\gamma(\mu) \hat{r}_0, \lambda_0)$ where $-\hat{r}_0$ is the direction of incidence, and λ_0 the polarization of the incident wave. Substitution of (13) in (2) yields, for $r \rightarrow \infty$,

$$u_{DWBA}^S(r, -\gamma(\lambda_0) \hat{r}_0, \lambda_0) = u^S(r, -\gamma(\lambda_0) \hat{r}_0, \lambda_0) + \sum_{\lambda} \hat{e}^\lambda \gamma(\lambda)^2 \frac{e^{i\gamma(\lambda)r}}{r} [D_1 + D_2 + D_3] \quad (15)$$

where

$$D_1 = \frac{\delta\rho}{4\pi\rho} \int_R dr' u_m^S(r', -\gamma(\lambda) \hat{r}, \lambda) u_m^S(r', -\gamma(\lambda_0) \hat{r}_0, \lambda_0) \\ D_2 = -\frac{\delta\lambda}{4\pi\rho\omega^2} \int_R dr' u_{m,m'}^S(r', -\gamma(\lambda) \hat{r}, \lambda) u_{1,1}^S(r', -\gamma(\lambda_0) \hat{r}_0, \lambda_0) \\ D_3 = \frac{-2\delta\mu}{4\pi\rho\omega^2} \int_R dr' u_{jk}^S(r', -\gamma(\lambda) \hat{r}, \lambda) u_{jk}^S(r', -\gamma(\lambda_0) \hat{r}_0, \lambda_0) \quad (16)$$

with

$$u_{i,j} = u_{i,j}/r_j$$

and

$$u_{jk} = \frac{1}{2} [u_{j,k} + u_{k,j}]$$

Note that the constants D depend on the incident and scattered directions \hat{r}_0 and \hat{r} , as well as on the polarizations of the incident and scattered fields, λ_0 and λ .

We have numerically evaluated the longitudinal scattered fields for incident longitudinal waves. For this problem only the $r = e'$ component enters, and therefore, only the spherical solutions for an incident longitudinal wave are needed.

The results are given below.

RESULTS

We first performed various checks on our procedure. In particular, we used g^S in the exact integral equation (1). For the case where the defect R is a sphere of radius a_2 , represented as a sphere of radius $a_1 < a_2$ and a remainder volume, the exact solution inside R can be calculated, inserted in (1), and the result is compared with the far field solution for R. We obtained agreement, with accuracy that characterizes our numerical integration procedure ($\sim 1\%$). Next, we turned to study the accuracy of the DWBA, by calculating the scattered field from a sphere R using (15)-(16). This was done for Al spheres in Ti and for cavities in Ti; the ratios of the radii of the actual sphere R and the inner sphere S was $a_2/a_1 = 1.2$ and $a_2/a_1 = 2$. Note that in the former case the volume "perturbation" is $R/S \approx 70\%$, while for $a_2/a_1 = 2$ it is $R/S = 700\%$.

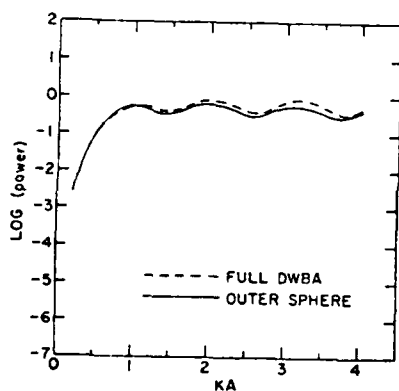


Fig. 2. Spherical cavity in Ti: Longitudinal back-scattered wave, log (power) versus ka for a ratio of radii of 6/5.

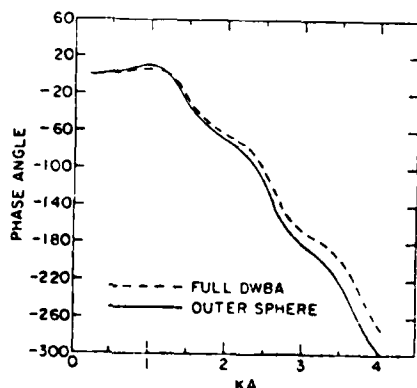


Fig. 3. Spherical cavity in Ti: Longitudinal back-scattered wave, phase angle versus ka for a ratio of radii of 6/5.

For the sake of comparison, we also show the results of the intermediate approximation (i.e., g^S replaced by g^0 in Eq. (2)).

The results of these checks are shown in Figs. (2) - (8). In general, the DWBA reproduces fairly well the exact results for the frequency and angular dependence of both power and phase. For the large perturbation $a_2/a_1 = 2$, the DWBA breaks down, for Al in Ti, at around $ka > 3.5$. However, for $a_2/a_1 = 1.2$ the DWBA is good, even for a strong scatterer like a cavity, for a wide range of ka .

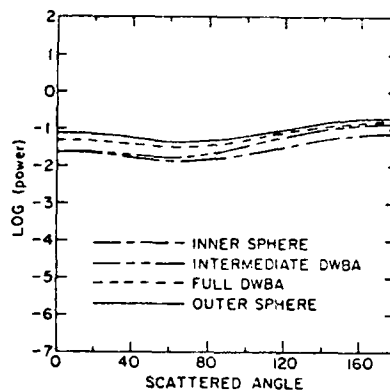


Fig. 4. Spherical cavity in Ti: Longitudinal wave, log (power) versus θ for $ka = .6$ and ratio of radii of 6/5.

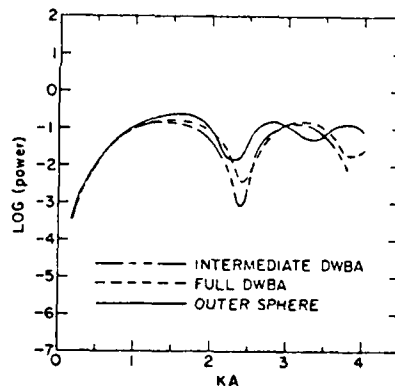


Fig. 5. Al sphere in Ti: Longitudinal backscattered wave, log (power) versus ka for a ratio of radii of 2.

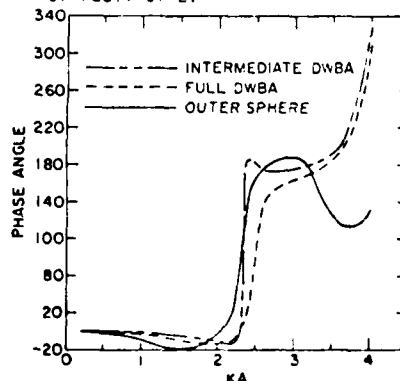


Fig. 6. Al sphere in Ti: Longitudinal backscattered wave, phase angle versus ka for a ratio of radii of 2.

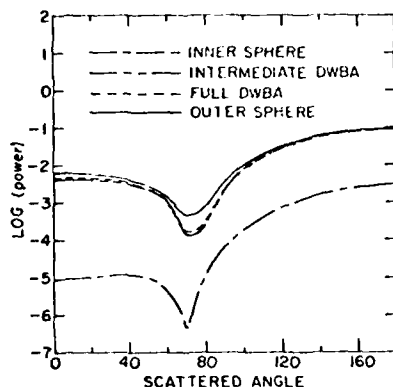


Fig. 7. Al sphere in Ti: Longitudinal wave, log (power) versus θ for $ka = 1$ and ratio of radii of 2.

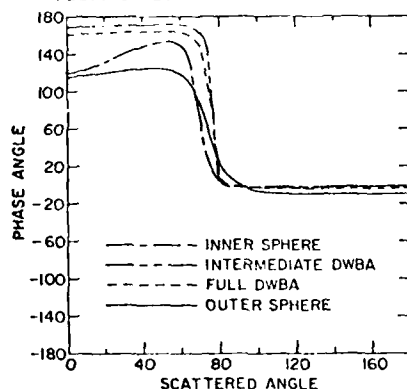


Fig. 8. Al sphere in Ti: Longitudinal wave, phase angle versus θ for $ka = 1$ and ratio of radii of 2.

Next, we turn to study a nonspherical defect, shown in Fig. (9). The defect is a spherical cavity of diameter 800μ , to which a hemisphere cavity of diameter 400μ has been added. We will refer to the hemisphere as the "bubble"; it represents a deviation of size b from a simple shaped smooth cavity of characteristic size a . The questions we addressed are the following:

- (1) At what frequencies (e.g., values of kb) is the bubble observable?
- (2) At what angles of incidence and scattering is its effect most pronounced?

To answer these questions, we present, first, Figs. (10) - (12), which show the backscattered power vs. ka for three incident directions. These figures compare the scattering by the large sphere to that of the nonspherical defect. We find that experimentally observable differences (i.e., $\sim 3\text{db}$) show up when $ka \approx 1.5$ (i.e., $kb \approx .75$). We also note that the largest deviation is obtained for $\theta_0 = 180^\circ$ (see Fig. 12), i.e., when the bubble is directly illuminated.

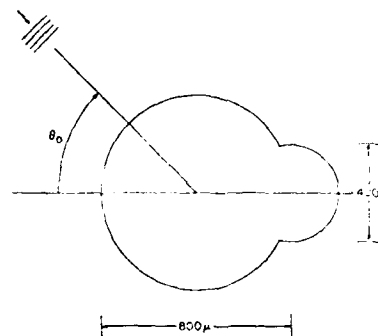


Fig. 9. Bubble defect: Direction of incidence is denoted by θ_0 .

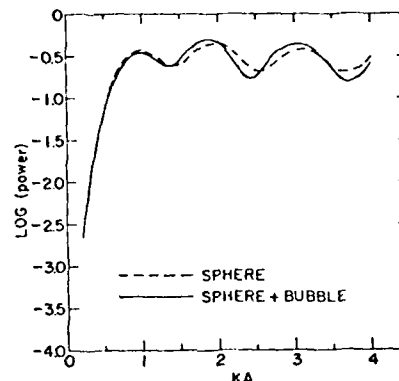


Fig. 10. Bubble defect in Ti: Longitudinal back-scattered power, log (power) versus ka for shadowed incidence, $\theta_0 = 0$.

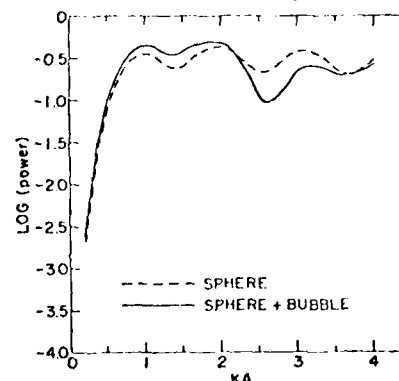


Fig. 11. Bubble defect in Ti: Longitudinal back-scattered wave, log (power) versus ka for incidence direction $\theta_0 = 90$.

The frequency spectrum is modulated with about the same periodicity as that of a sphere, but a modulation with longer periodicity (in k) is superimposed. While for the sphere the first three peaks are of approximately equal amplitude, with the bubble present the amplitudes decrease in magnitude (for the first three peaks).

Turning now to angular distribution of power the sequence of Figs. 13-15 shows polar plots of power vs. scattering angle for three directions of incidence and ka values of 1 and 2.

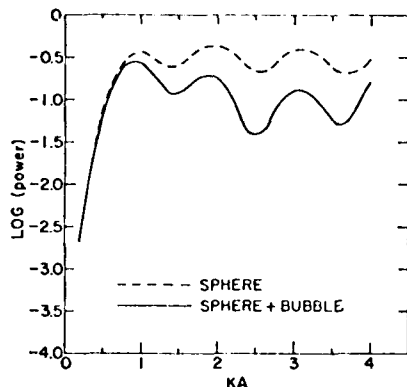


Fig. 12. Bubble defect in Ti: Longitudinal back-scattered wave, log (power) versus ka for direct incidence, $\theta_0 = 180$.

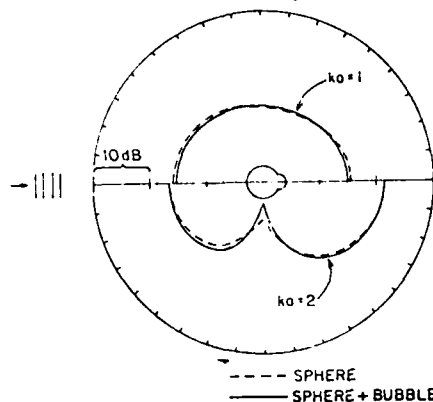


Fig. 13. Bubble defect in Ti: Longitudinal wave, log (power) versus θ for shadowed incidence, $ka = 1, 2$.

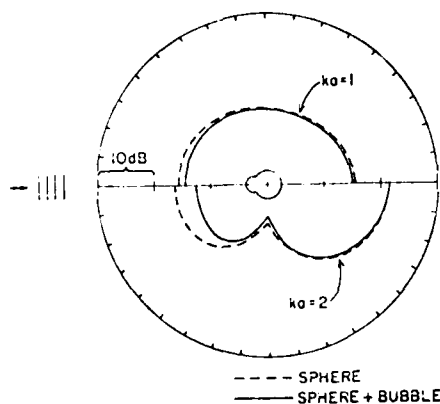


Fig. 14. Bubble defect in Ti: Longitudinal wave, log (power) versus θ for direct incidence, $ka = 1, 2$.

Again we note that the effect of the bubble is observable at $ka = 2$, and not at $ka = 1$. Also, the largest effect is obtained for $\theta_0 = 180$ (i.e., direct illumination), and even then the best results are obtained for backscattering.

It is of interest to observe the loss of symmetry of the scattered power, caused by the presence

of the bubble. Figs. 15 and 16 show this effect: in particular, the results of Fig. 16, with incidence at $\theta_0 = 90$ and scattering at $\theta = 135^\circ$ have been verified experimentally.⁵

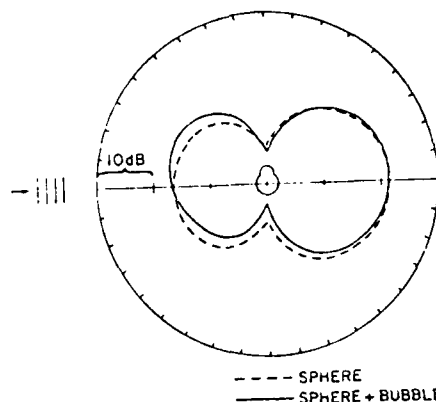


Fig. 15. Bubble defect in Ti: Longitudinal wave, log (power) versus scattering angle θ for incident direction $\theta_0 = 90$, $ka = 2$; the scattered direction is in the plane defined by the incident direction and the symmetry axis of the scatterer.

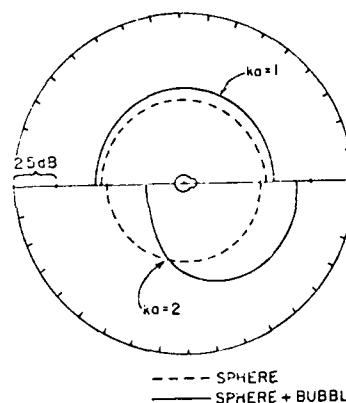


Fig. 16. Bubble defect in Ti: Longitudinal wave, log (power) versus azimuthal angle ϕ for incidence direction $\theta_0 = 90$, scattering angle $\theta = 135$, and $ka = 1, 2$.

SUMMARY

The DWBA gives analytically simple forms for the scattering of elastic waves by defects of quite general shape. Our numerical studies indicate that the approximation yields reliable frequency dependence and phase information. Initial comparisons with experiment were most encouraging.

We plan to extend this work to obtain the scattered shear waves, and to use the procedure to test inversion procedures⁶ and the concept of defect representation by effective ellipsoids.

ACKNOWLEDGMENTS

This research was sponsored by the Center for Advanced NDE, operated by the Science Center, Rockwell International, for the Advanced Research Projects Agency and the Air Force Materials Laboratory under contract F33615-74-C-5180. We thank C. Kirschbaum and B. Yanoff for programming assistance.

REFERENCES

1. K.E. Newman and E. Domany, Proceedings of the ARPA/AFML Review of Progress in Quantitative NDE, ed. D.O. Thompson, AFML-TR-78-205, p. 404 (1978).
2. C.F. Ying and R. Truell, J. Appl. Phys. 27, 1086 (1956); G. Johnson and R. Truell, J. Appl. Phys. 36, 3466 (1965).
3. K.E. Newman, C.K. Lam and E. Domany; The Elastodynamics Green's Function for a Spherical Defect, submitted for publication.
4. J. E. Gubernatis, unpublished.
5. B. R. Tittmann, these proceedings.
6. J. H. Rose, these proceedings.
7. A. N. Mucciardi, these proceedings.

SUMMARY DISCUSSION
(Eytan Domany)

John Richardson (Science Center): When you talk about deviation from a sphere, is it the original sphere you have drawn or slightly larger sphere that has the same volume or something like that, the perturbed --

Eytan Domany: I just meant from the original sphere from which the sensor is attached. That's what we compare.

Jim Krumhansl (Cornell University): If I were to intuitively extrapolate what you say to the issue of whether some kind of join which was just bad glue and had fluctuations on a scale, you know, like a tenth of the radius, I would really have to go to the K equal 10 or something like that to find that.

Eytan Domany: If you characterize the deviation from the structure you want to look at, which in this case would be the small ripples, as having the characteristic length of B , then KB should be about one. That's the right measure. I think the thing that should be done is to extend the comparison experiment to see whether the phase angle you can get out of this is borne out by the approximate theory.

Jim Rose (University of Michigan): Your perturbation seems to be δDOD , or a change in volume. Does that mean for small changes in volume you can do sharp corners or that kind of thing?

Eytan Domany: That's a good question. The question is what do you mean by "can do"? You can do anything with born approximations. I can fully transform this microphone. The question is when you do that whether it makes any sense. So, in the same way here, one has to integrate a deviation from the sphere, so you have to have sharp corners just to integrate, or a volume that has sharp corners. Now, the physics of sharp corners is mainly, as I understand it, singularities in the ray of physical sphere near those sharp corners. Those will not be picked up by this method. What you will pick up is that you take some smooth field and you integrate it over an object that has sharp corners. As far as that effect goes, it will be in there. But the real physics of physical displacement and stray field, which is singular as a result of having those sharp corners, that's not going to be in there. And I sort of feel if it's not going to be in any of the approximations that have been discussed, I think that's moot. You're not having either, because they're also, unless you view the singularity effect that Bill was talking about. Did I answer your question?

Jim Rose: You answered the question.

#

ELASTIC WAVE SCATTERING BY ROUGH FLAWS AND CRACKS

V. V. and V. K. Varadan
Department of Engineering Mechanics
Ohio State University
Columbus, OH 43210

ABSTRACT

The scattering of elastic waves by three dimensional rough flaws and cracks is analyzed using the T-matrix approach. The scattering cross section is obtained for spheroidal cavities with a periodically corrugated surface which may be used as a model for flaws with a rough surface. The dependence of the scattering cross section on the wavelength of the corrugations is studied as a function of the incident wavelength. Cracks are modelled as degenerate oblate spheroids and the scattering cross section is obtained for incident P-waves. Multiple scattering analysis of two cavities is also discussed with some numerical results.

SCATTERING FROM ROUGH SPHEROIDAL CAVITIES

The Scattering from rough oblate spheroidal cavities is very important since they may be used to serve as models for flaws found in structural applications. Theoretical data obtained in such analysis are very helpful in experimental verification as well as in the inverse problem of scattering. In this respect the T-matrix approach is ideal since it is an efficient computational scheme to obtain the frequency spectrum of the scattered energy which is the quantity measured in experiments. Any symmetry in the shape of the scatterer can be used to optimize computer time. The computer program can also be written in a very general manner so that the number of input parameters are minimal and any variations in the shape of the flaw can be easily incorporated into the program. Thus one could obtain scattering cross sections for spheroidal cavities with a periodically corrugated surface.

Plane monochromatic waves of frequency ω are incident on a spheroidal cavity. The axis of revolution of the cavity is taken as the z-axis and a Cartesian coordinate system is defined in the usual way. The dimensions of the spheroid are taken to be '2b' along the z-axis and '2a' in the x-y plane (see Fig. 1). In spherical polar coordinates r, θ, ϕ , the equation to the surface of the spheroid is given by

$$r(\theta, \phi) = \left(\frac{\cos^2 \theta}{b^2} + \frac{\sin^2 \theta}{a^2} \right)^{-1/2} \quad (1)$$

A detailed description of T-matrix calculations for a spheroidal cavity is given in Ref. 1. Detailed results have also been presented in the 1978 ARPA/ARML Review on QNDE². For a comprehensive report of the T-matrix approach, we refer to the book edited by the investigators.

We now perturb the surface of the spheroidal cavity by a periodic corrugation in the x-z plane, so that the equation to the surface is now given by

$$r(\theta, \phi) = \left(\frac{\cos^2 \theta}{b^2} + \frac{\sin^2 \theta}{a^2} \right)^{-1/2} + \epsilon \cos \phi \quad (2)$$

The parameters ϵ and λ describe the degree of roughness of the spheroidal cavity. Equation (2) has the same symmetry properties as the spheroidal cavity if λ is chosen properly, say, $\lambda = 4n$, $n = 0, 1, 2, \dots$. If this is so done, then the Q-matrix and hence the T-matrix has the same symmetry properties as well. This symmetry could be destroyed by multiplying the second term in Eq. (2) by a function of ϕ . This will significantly complicate the numerical computations since an additional numerical integration on ϕ will have to be performed to generate the Q-matrix elements. In this problem, two parameters of interest are ϵ/a which is the ratio of the amplitude of roughness to size of the spheroidal cavity and the ratio of λr , see Fig. 1, to the wavelength of the incident wave. λr is, of course, inversely proportional to λ .

Using Eq. (2), scattering cross sections were obtained for compressional waves incident along the axis of revolution for several different angles of observation. Sample results are presented below as a function of the non-dimensional wave number $k_p a$. For purposes of comparison the scattering cross section of a smooth spheroidal cavity is also included. The ratio of wave speeds in the host material is taken as 2.0. Two sets of parameters (ϵ, λ) are presented in the graphs, although many other values were also tried.

In Figs. 2-6, θ is the angle of observation in the x-z plane, the differential scattering cross section is plotted as a function of $k_p a$. The notation P-P is used for scattering of incident compressional waves to compressional waves and P-S denotes mode converted scattering. In the plots for rough cavities ϵ/a is taken to be 0.05. This parameter describes the relative heights of the corrugations with respect to the axis of the smooth spheroid. The aspect ratio of the spheroid is taken to be $b/a = 0.8$, so that it is oblate. The second parameter that we can vary is the integer ' λ ' that gives the number of lobes. The graphs show the scattering cross section for two values of λ ; $\lambda = 16$ and $\lambda = 64$ in the range of $0 \leq \theta \leq \pi/2$.

From the present calculation we conclude the following. (1) if $\epsilon/a < 0.05$, then the scattering

cross section is not too different from that for a smooth cavity for $0 < k_{pa} < 3.0$ at higher wave numbers, it may be possible to observe significant differences. (2) For $\delta/a < 0.05$, the scattering cross section changes dramatically as we vary the parameter ϵ for a given δ/a . If the number of lobes is very large, for example, $\epsilon = 64$, the scattering cross section for smooth and rough cavities agree more or less. But if ϵ decreases as δ/a is increased, then the scattering cross section is markedly different, as can be seen from the plots for $\epsilon = 16$.

We conclude that if ϵ is large, on the average the scattered waves are not too affected by the roughness. Numerical results become quite unstable, however, if $\delta/a > 0.05$ and ϵ is decreased. So that the conclusions for large δ/a and small ϵ can be qualitative. If $\delta/a < 0.05$, $\lambda r/\lambda_{\text{wave}} < 0.1$ and for the range of $k_{pa} = 0.1$ to 3.0 , then we find that there is no significant difference between scattering from smooth and rough spheroids. The range we have considered corresponds to experiments in the MHz range with flaw size of the order of 300μ . At these frequencies, we expect to have no resonance effects associated with the periodicity of the roughness. However, for higher wave numbers, it may be possible to observe some significant difference. The accuracy of the calculation was checked at each stage by verifying the symmetry and unitary properties of the scattering matrix. The results presented here should be checked by experiments. To obtain more noticeable effects, i.e., for longer values of the roughness parameters, other alternative methods such as finite elements may be tried. The investigators are pursuing along these lines as well.

SCATTERING OF ELASTIC WAVES BY CRACKS

Last year we began to investigate whether the T-matrix method is suitable for calculating the scattering cross section of cracks in two dimensions. Cracks are modelled as degenerate ellipses in two dimensions and three dimensional penny shaped cracks are realized by collapsing oblate spheroids into circular discs. Last year we derived systematic closed form expansions of the T-matrix in powers of the non-dimensional wave number 'ka' for arbitrary aspect ratio b/a . The expressions obtained for the far field scattered amplitude agree with exact analytical results.⁴ On taking the limit of zero aspect ratio ($b/a \rightarrow 0$), exact agreement was obtained for both strips and circular discs with published results. With existing computer programs for elliptic cylinders of finite aspect ratio, calculations for P- and SV- wave scattering for $b/a = 0.08 - 0.1$ show close agreement with numerical results obtained by Tan⁵ for special scattering geometries.

The penny shaped crack is considered as the limiting case of an oblate spheroid and we are interested in obtaining results for $k_{pa} < 3.0$ to complement the work of Achenbach, et al.⁶ who are using Geometrical Theory of Diffraction (GTD). We derived systematic closed form expansions of the T-matrix in powers of the non-dimensional wave number k_{pa} for arbitrary aspect ratio b/a . On taking the limit of zero aspect ratio, exact agreement was obtained for penny-shaped cracks with the results published in the literature.⁷

Two different approaches were tried to adapt the T-matrix method to study penny-shaped cracks in elastic materials: (1) using the regular T-matrix program for a spheroidal cavity for very small values of $b/a = 0.05$ testing symmetry, unitary properties at all values of k_{pa} to check for numerical stability (2) using special representations for the unknown displacement field on the surface of the crack that incorporates the condition of zero crack opening displacement at the crack edge (see, for example, Achenbach⁶). A sample calculation is shown in this report for SH-waves for comparing this approach with that of (1). A similar approach for 3-D problems was done and for the reasons described below we do not see any additional advantage over the procedure presented in step 1. The representation should be such that it renders the Q-matrix symmetric so that the matrix is well conditioned for inversion. This version is tested for small values of b/a . The results agree with those obtained by step 1. For an actual crack, one takes $b/a \rightarrow 0$ before numerical computations are performed. We find that the result of steps 1 and 2 are not different, hence we prefer to use the technique that is more efficient, convenient and economical. The highest advantage of using the regular computer programs for the oblate spheroidal cavity taking an aspect ratio $b/a = 0.05$ is that we can use a well tested program and there is no need to develop any new algorithms.

The essential differences between the formulation for ellipses of finite aspect ratio and strips that have aspect ratio identically zero is the way in which we expand the unknown anti-plane displacement field W^+ on the surface of the flaw on which stresses are prescribed to be zero. For cracks there is an additional requirement that the displacement vanishes as $\sqrt{1-x^2}/a^2$ at the crack tip where the x-axis is parallel to the crack and $2a$ is the width of the crack. This is not necessary for the ellipse of finite aspect ratio.

We choose cylindrical basis functions to expand the incident (W^0) and scattered (W^S) and surface (W^+) fields. W^0 and W^S are expanded in the usual way.

$$W^0(r, \theta) = \sum_{n=0}^{\infty} \sum_{\alpha=1}^2 a_n^{\alpha} \text{Re} \phi_n^{\alpha}(r, \theta) \quad (3)$$

$$W^S(r, \theta) = \sum_{n=0}^{\infty} \sum_{\alpha=1}^2 f_n^{\alpha} \phi_n^{\alpha}(r, \theta) \quad (4)$$

where

$$\begin{cases} \phi_n^1(r, \theta) \\ \text{Re } \phi_n^2(r, \theta) \end{cases} = \sqrt{\frac{2}{n}} \begin{cases} H_n(kr) \\ J_n(kr) \end{cases} \begin{cases} \cos n\theta; & n = 1 \\ \sin n\theta; & n = 2 \end{cases} \quad (5)$$

In Eq. 5, H_n and J_n are cylindrical Hankel and Bessel functions and ν_n is the Neumann factor. For a plane monochromatic wave frequency ω (wave number $k = \omega/c$ incident at an angle θ_0 to the x-axis,

$$W^0(r, \theta) = \exp [ikr \cos(\theta - \theta_0)] \quad (6)$$

and hence

$$a_n^1 = \sqrt{\epsilon_n} i^n \cos n\theta_0 \quad (7)$$

$$a_n^2 = \sqrt{\epsilon_n} i^n \sin n\theta_0 \quad (8)$$

For an ellipse of major and minor axes $2a$ and $2b$, the equation to surface is given by

$$r(u) = \left(\frac{\cos^2 u}{a^2} + \frac{\sin^2 u}{b^2} \right)^{-1/2} \quad (9)$$

In the usual formulation of the T-matrix, we obtain the following relations between a_n^1 and f_n^1

$$f_n^1 = -T_{mn}^1 a_n^1 \quad (10)$$

$$T = \text{Re } Q(Q^{-1}) \quad (11)$$

The elements of matrix Q in Eq. 11 are given by integrals on the surface of the cavity. The integrand of Q_{mn} involves H_m and J_n . It is seen that if $m \neq n$, the integrand will involve negative powers of $r(u)$ which do not cause any difficulty for the ellipse of finite aspect ratio. However, for the crack $r(u) = |x|$ and the integration on x is from 0 to $2a$. Thus terms involving inverse powers of x are apparently singular if the limit $b/a \rightarrow 0$ is taken before integrating. The singularity is only apparent since we can show that these apparent singularities are not present if the integration is performed first and then the limit taken. Thus it is advisable to construct a Q -matrix that is perfectly symmetric for ellipses of arbitrary aspect ratio b/a , so that if $b/a = 0$, we need evaluate numerically only matrix elements above the diagonal.

In addition to make $W^+ \rightarrow 0$ at the crack tip, we choose

$$W^+ = \sqrt{1 + \left[\frac{(r/r_0)^2}{k^2 r} \right]} n \cdot \nu_n b_n^1 \text{Re} a_n^1 \quad (12)$$

We note that

$$\lim_{b/a \rightarrow 0} \frac{(r/r_0)}{r} = \frac{1}{b} \sqrt{1-x^2/a^2} \quad (13)$$

In addition Eq. 12 renders the Q -matrix perfectly symmetric and for cracks

$$Q_{mn}^1 = \frac{mn}{b} \int_{-a}^a \frac{\sqrt{1-x^2/a^2}}{k^2 x^2} H_m(k|x|) J_n(k|x|) dx \quad (14)$$

and

$$Q_{nn}^{11} = Q_{nn}^{12} = Q_{nn}^{21} = 0 \quad (15)$$

The only troublesome integral in Eq. 14 occurs in the diagonal elements. The integration in Eq. 14 is performed by expanding H_m and J_n in powers of $k|x|$ which reduces the integrals to standard form and the result can be written as an infinite sum truncated at a suitable value. However, when $m = n$, the leading term in $H_m J_n$ is $(kx)^0$ which results in the following singular integral

$$\int_{-a}^a \frac{\sqrt{1-x^2/a^2}}{x^2} dx \quad (16)$$

The corresponding integral for the ellipse of finite aspect ratio is of the form

$$\int_0^{2\pi} \left[\frac{r(u)}{r(u)} \right]^2 \frac{1}{r^2(u)} \cos^2 m u \, du \quad (17)$$

On evaluating the integral in Eq. 17 exactly and then taking the limit of $b/a \rightarrow 0$, we find

$$\int_{-a}^a \frac{\sqrt{1-x^2/a^2}}{x^2} dx = -\frac{\pi}{2} \delta_{mn} \quad (18)$$

Using this value of the integral when $m = n$, the Q - and T -matrix for the crack can be calculated in the usual manner.

Graphs of the scattering cross section are presented as a function of ka for $\theta_0 = 45^\circ, 90^\circ$. For $\theta_0 = 0$, there is no scattering since the incident wave does not feel the presence of the crack. The results plotted in Figs. 7-9 are in excellent agreement with existing results obtained using Mathieu functions (11). These results were also checked with calculations for $b/a = 0.05$ and for the wavelengths considered, there is no difference between the results for $b/a = 0.05$ and $b/a = 0$.

In Figs. 10-15, the results for a penny shaped crack are shown. Figures 10 and 11 are polar plots of the scattered far field amplitude for P-waves incident along the symmetry axis. The plots compare very well with those obtained by Mal (7). The symbol P-S denotes the scattered S-wave amplitude for incident P-waves. In Figs. 12-15, the scattering cross section is presented as a function of $k_p a$ for P-waves incident along the symmetry axis for various angles of observation denoted by θ . For the range of wavelengths considered, for a crack of radius 'a', $0 \leq k a \leq 2.0$, only one maximum can be observed in the cross section. It is hoped that these results will complement those obtained by Achenbach and coworkers using GTD at higher values of $k_p a$.

T-MATRIX FORMULATION FOR TWO SCATTERERS

Consider two scatterers described by the surfaces S_1 and S_2 with outward drawn normals \hat{n}_1 and \hat{n}_2 (See Fig. 16). O_1 and O_2 are the origins of the coordinate systems centered in S_1 and S_2 , respectively, and O is the origin of the coordinate system exterior to S_1 and S_2 . Let \vec{d}_1 and \vec{d}_2 be the vectors drawn from O to O_1 and O to O_2 , respectively. At any point \vec{r} with respect to O , the total field \vec{u} is given by

$$\vec{u}(\vec{r}) = \vec{u}^0(\vec{r}) + \vec{u}^s(\vec{r}) \quad (19)$$

where \vec{u}^s is the total scattered field at \vec{r} and \vec{u}^0 is the incident field. The scattered field \vec{u}^s can be represented as

$$\vec{u}^s(\vec{r}) = \vec{u}_1^s(\vec{r}_1 + \vec{d}_1) + \vec{u}_2^s(\vec{r}_2 + \vec{d}_2) \quad (20)$$

where \vec{r}_1 and \vec{r}_2 are the vectors drawn from O_1 to O_2 to the point under consideration and \vec{u}_1^s and \vec{u}_2^s are the fields scattered from S_1 and S_2 , respectively.

All the fields can be expanded in vector spherical functions with respect to the various coordinate systems. The vector functions and coefficients defined with respect to O_1 and O_2 are distinguished by superscripts 1 and 2, respectively. We use the following abbreviation for the vector spherical functions

$$\vec{\psi}_{\tau n m}(\vec{r}) = \vec{\psi}_{\tau n}(\vec{r}) \quad (21)$$

where $\tau = 1, 2, 3$ are same as the \vec{L} , \vec{M} and \vec{N} functions defined by Morese and Feshbach (9). If a qualifier Re is used with the wavefunction, we use spherical Bessel functions instead of spherical Hankel functions.

Translation theorems have been given by Cruzan (10) to translate the wavefunctions from one coordinate system to another. Thus,

$$\text{Re} \vec{\psi}_{\tau n}(\vec{r}_1 + \vec{d}_1) = \sum_{\tau' n'} R_{\tau n, \tau' n'}(\vec{d}_1) \text{Re} \vec{\psi}_{\tau' n'}(\vec{r}_1) \quad (22)$$

$$\vec{\psi}_{\tau n}(\vec{r}_1 + \vec{d}_1) = \sum_{\tau' n'} T_{\tau n, \tau' n'}(\vec{d}_1) \vec{\psi}_{\tau' n'}(\vec{r}_1);$$

$$|\vec{d}_1| > |\vec{r}_1| \quad |\vec{d}_1| > |\vec{r}_1| \quad (23)$$

$$\vec{\psi}_{\tau n}(\vec{r}_1 + \vec{d}_1) = \sum_{\tau' n'} R_{\tau n, \tau' n'}(\vec{d}_1) \vec{\psi}_{\tau' n'}(\vec{r}_1);$$

$$|\vec{d}_1| < |\vec{r}_1| \quad |\vec{d}_1| < |\vec{r}_1| \quad (24)$$

The translation matrices have the following properties

$$R(\vec{d}) = \text{Re}(d) \quad (25)$$

$$R^t(\vec{d}) = R(-\vec{d}) \quad (26)$$

Explicit expressions for R and T may be found in a convenient form in a report by Böstrom (11). The matrix elements are given in terms of the spherical Bessel and Hankel functions, the associated Legendre polynomials and the Wigner 3-j symbols.

The scattered fields are expanded as follows

$$\vec{u}_1^s(\vec{r}) = \sum_{\tau n} f_{\tau n}^1 \vec{\psi}_{\tau n}^1(\vec{r}_1) \quad (27)$$

$$\vec{u}_2^s(\vec{r}) = \sum_{\tau n} f_{\tau n}^2 \vec{\psi}_{\tau n}^2(\vec{r}_2) \quad (28)$$

where the field scattered by each obstacle is assumed to be outgoing with respect to the center of that obstacle.

The exciting field or the field incident on a particular scatterer is the incident field \vec{u}^0 plus the field scattered by the remaining scatterer. Thus

$$\vec{u}_1^e(\vec{r}) = \vec{u}^0(\vec{r}) + \vec{u}_2^s(\vec{r}_2); \quad 0 < |\vec{r}| \leq 2a_1 \quad (29)$$

$$\vec{u}_2^e(\vec{r}) = \vec{u}^0(\vec{r}) + \vec{u}_1^s(\vec{r}_1); \quad 0 < |\vec{r}| \leq 2a_2 \quad (30)$$

where a_1 and a_2 are the radii of the spheres circumscribing the two scatterers. The exciting fields are expanded in terms of coefficients that are unknown since \vec{u}_1^s and \vec{u}_2^s are undetermined as yet.

$$\vec{u}_1^e(\vec{r}) = \sum_{\tau n} a_{\tau n}^1 \text{Re} \vec{\psi}_{\tau n}^1(\vec{r}_1) \quad (31)$$

$$\vec{u}_2^e(\vec{r}) = \sum_{\tau n} a_{\tau n}^2 \text{Re} \vec{\psi}_{\tau n}^2(\vec{r}_2) \quad (32)$$

Similarly, the incident field \vec{u}^0 in the vicinity of each scatterer can be expanded as

$$\vec{u}^0(\vec{r}) = \sum_{\tau} a_{\tau n}^{01} \text{Re} \vec{\psi}_{\tau n}^1(\vec{r}_1) = \sum_{\tau} a_{\tau n}^{02} \text{Re} \vec{\psi}_{\tau n}^2(\vec{r}_2) \quad (33)$$

From Eqs. (27) - (32), we obtain the following relation between the expansion coefficients

$$\sum_{\tau n} a_{\tau n}^1 \text{Re} \vec{\psi}_{\tau n}^1(\vec{r}_1) = \sum_{\tau n} a_{\tau n}^{01} \text{Re} \vec{\psi}_{\tau n}^1(\vec{r}_1) + \sum_{\tau n} f_{\tau n}^2 \vec{\psi}_{\tau n}^2(\vec{r}_1 + \vec{d}_1 - \vec{d}_2); \quad (34)$$

$$\sum_{\tau n} a_{\tau n}^2 \text{Re} \vec{\psi}_{\tau n}^2(\vec{r}_2) = \sum_{\tau n} a_{\tau n}^{02} \text{Re} \vec{\psi}_{\tau n}^2(\vec{r}_2) + \sum_{\tau n} f_{\tau n}^1 \vec{\psi}_{\tau n}^1(\vec{r}_2 + \vec{d}_2 - \vec{d}_1) \quad (35)$$

Further, from the definition of the T-matrix for each scatterer

$$f_{\tau n}^1 = \sum_{\tau' n'} T_{\tau n, \tau' n'}^1 a_{\tau' n'}^1 \quad (36)$$

$$f_{\tau n}^2 = \sum_{\tau' n'} T_{\tau n, \tau' n'}^2 a_{\tau' n'}^2 \quad (37)$$

Using the translation theorems and imposing the restriction that $|\vec{d}_1 - \vec{d}_2| < |\vec{r}_1|$ in Eq. (34) and $|\vec{d}_1 - \vec{d}_2| < |\vec{r}_2|$ in Eq. (35), we obtain from Eqs. (33)-(37) in matrix notation

$$f^1 = T^1 [a^0 + o(\vec{d}_2 - \vec{d}_1) f^2] \quad (38)$$

$$f^2 = T^2 [a^0 + o(d_1 - d_2) f^1] \quad (39)$$

Similarly, the incident field \vec{u}^0 and total scattered field \vec{u}^s can be expanded with respect to the origin at 0 and again using translation theorems, we obtain

$$f = R(\vec{d}_1) f^1 + R(\vec{d}_2) f^2 \quad (40)$$

$$a^0 = R(-\vec{d}_1) a^0 \quad (41)$$

$$a^0 = R(-\vec{d}_2) a^0 \quad (42)$$

From Eqs. (38), (39), (41), and (42), we obtain

$$f^1 = T^1 \left\{ 1 - o(\vec{d}_2 - \vec{d}_1) T^2 o(\vec{d}_1 - \vec{d}_2) T^1 \right\}^{-1} \left\{ R(-\vec{d}_1) - o(\vec{d}_2 - \vec{d}_1) T^2 R(-\vec{d}_2) \right\} a^0 \quad (43)$$

and

$$f^2 = T^2 \left\{ 1 - o(d_1 - d_2) T^1 o(d_2 - d_1) T^2 \right\}^{-1} \left\{ R(-\vec{d}_2) - o(d_1 - d_2) T^1 R(-\vec{d}_1) \right\} a^0 \quad (44)$$

The T-matrix of the two scatterer configuration is the matrix that relates f to a^0 in the form

$$f = T^{12} a^0 \quad (45)$$

where T^{12} is the combined T-matrix. Substituting for f^1 and f^2 in Eq. (40), we see that

$$T^{12} = R(\vec{d}_1) T^1 \left\{ 1 - o(\vec{d}_2 - \vec{d}_1) T^2 o(d_1 - d_2) T^1 \right\}^{-1} \left\{ R(-\vec{d}_1) - o(\vec{d}_2 - \vec{d}_1) T^2 R(-\vec{d}_2) \right\} + \dots \quad (46)$$

where the second term in T^{12} is obtained by interchanging superscripts and subscripts 1 and 2.

The formalism given here is different from the one given by Peterson and Strom (12) for electromagnetic scattering and is similar to the multiple scattering formalism for an ensemble of scatterers proposed by the authors (13, 14). We further note that the nature of the scatterer is yet unrestricted except for weak restrictions on the geometry of the configurations. The scatterers could be cavities, solid inclusions, fluid inclusions or any combination.

ACKNOWLEDGEMENTS

This research was sponsored by the Center for Advanced NDE operated by the Science Center, Rockwell International, for the Advanced Research Projects Agency and the Air Force Materials Laboratory under Contract F33615-74-C-5180.

The authors wish to thank Dr. Bo Peterson for computations on the scattering from two spheroidal cavities.

REFERENCES

1. V. V. Varadan and V. K. Varadan, "Scattering Matrix for Elastic Waves: III. Application to Spheroids," *J. Acoust. Soc. Am.* **65**, 896 (1979).
2. V. V. Varadan and V. K. Varadan, "T-matrix Calculations for Spheroidal Cavities and Inclusions and Crack-like Flaws," Interdisciplinary program for Quantitative Flaw Definition, Special Report fourth year effort, prepared for ARPA/AFML by D.O. Thompson, Center for Advanced NDE, Rockwell International, Thousand Oaks, CA 91360 (1978).
3. "Recent Developments in Classical Wave Scattering: Focus on the T-matrix Approach," edited by V.K. Varadan and V.V. Varadan, Pergamon Press, New York (in press).
4. V.V. Varadan and V.K. Varadan, "Low Frequency Expansions for Acoustic Wave Scattering using Waterman's T-matrix approach," *J. Acoust. Soc. Am.* **66**, 586 (1979).
5. T.H. Tan, "Diffraction Theory for Time Harmonic Elastic Waves," Ph.D. Thesis, Delft Institute of Technology, Delft, The Netherlands (1975).
6. J.D. Achenbach, A. Gautesen, and H.M. McMaken, "Application of Ray Theory to Elastic Wave Scattering by Cracks," Recent Developments in Classical Wave Scattering: Focus on the T-matrix Approach, V.K. Varadan and V.V. Varadan (Editors), Pergamon Press, New York (in press).
7. A.K. Mal, "Interaction of Elastic Waves with a Penny-Shaped Crack," *Int. J. Engng. Sci.* **8**, 381 (1970).
8. J.D. Achenbach, "Direct and Inverse Method for Scattering by Cracks at High Frequencies," These proceedings.
9. P.M. Morse and H. Feshbach, "Methods of Mathematical Physics," McGraw-Hill, New York, 1953, p. 1408, Volume 11.
10. O.R. Cruzan, "Translational Addition Theorems for Spherical Vector Wave Equations," *Q. Appl. Math.* **20**, 33 (1962).
11. A. Boström, "Multiple Scattering of Elastic Waves by Bounded Obstacles," Report No. 79-4, Institute of Theoretical Physics, S-41296 Göteborg, Sweden.
12. P. Peterson and S. Strom, "T-matrix for Electromagnetic Scattering from an Arbitrary Number of Scatterers and Representations of $E(3)$," *Phys. Rev. D* **8**, 3661 (1973).

13. V.K. Varadan and V.V. Varadan, Frequency Dependence of Elastic (SH-) Wave Velocity and Attenuation in Anisotropic Two Phase Media," *Int. J. Wave Motion*, 1, 53 (1979).
14. V.K. Varadan, V.N. Brongi and V.V. Varadan, "Coherent Electromagnetic Wave Propagation through Randomly Distributed Dielectric Scatterers," *Phys. Rev. D*, 19, 2480 (1979).

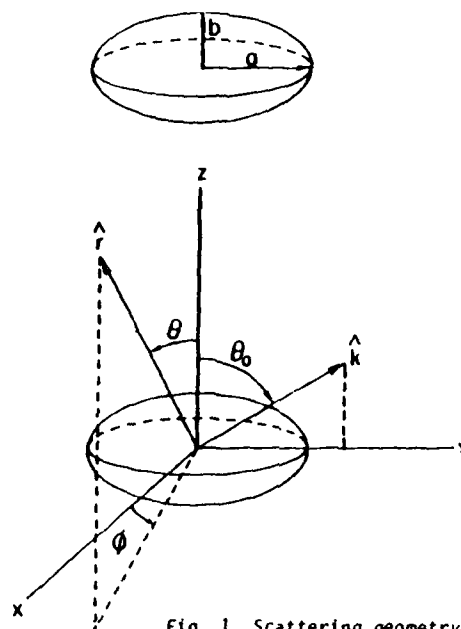
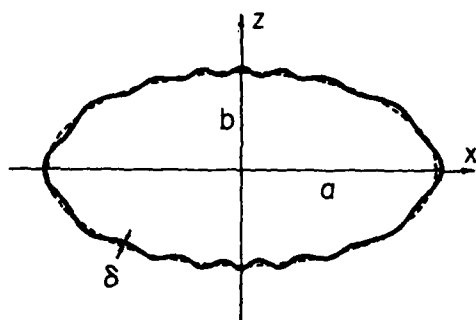


Fig. 1 Scattering geometry

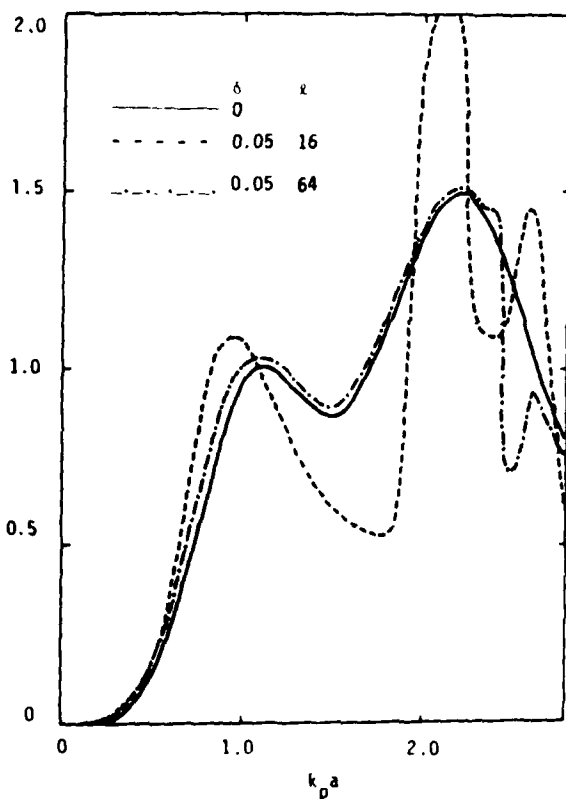


Fig. 2. Back scattering cross section for incidence along z-axis; P-P scattering.

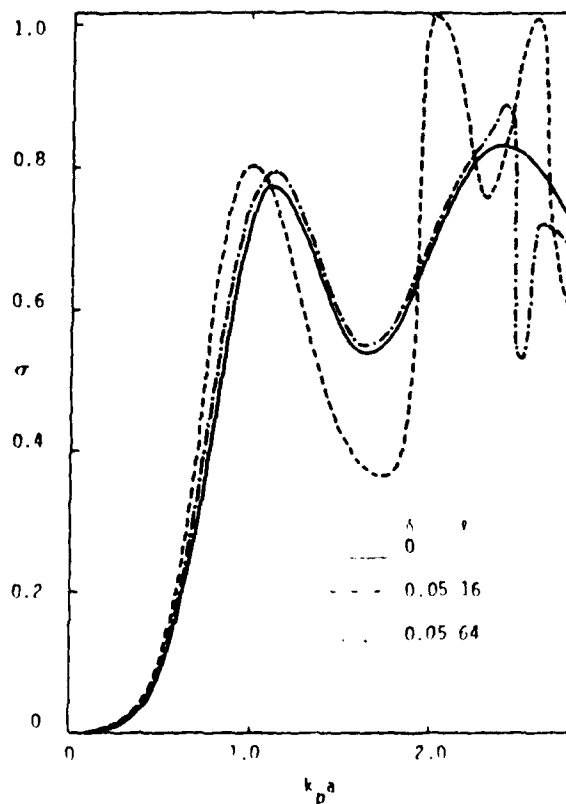


Fig. 3 Differential scattering cross section at $\alpha = 135^\circ$ for incidence along z-axis; P-P scattering.

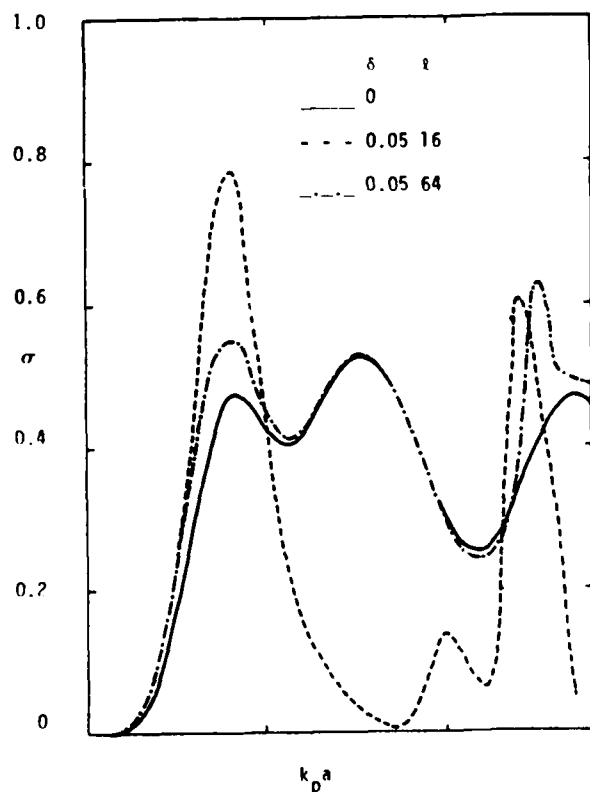


Fig. 4 Differential scattering cross section at $\theta = 135^\circ$ for incidence along z-axis; P-S scattering.

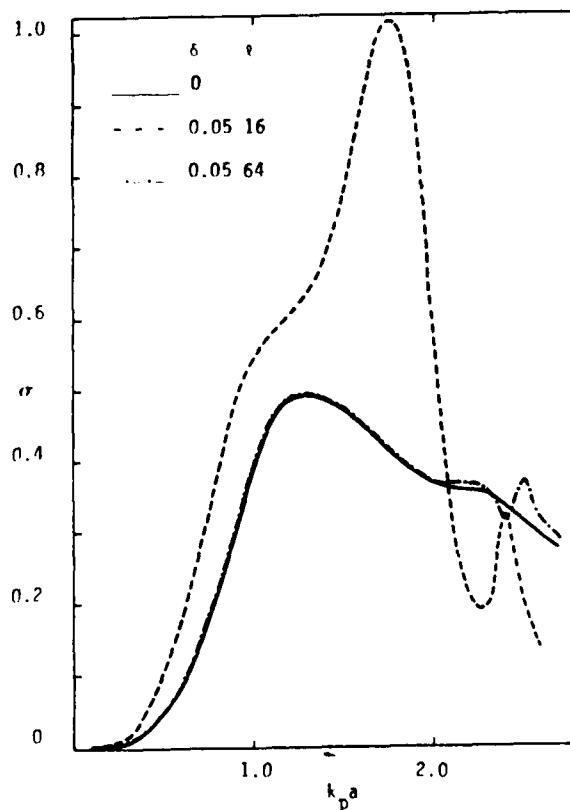


Fig. 6 Differential scattering cross section at $\theta = 90^\circ$ for incidence along z-axis; P-S scattering.

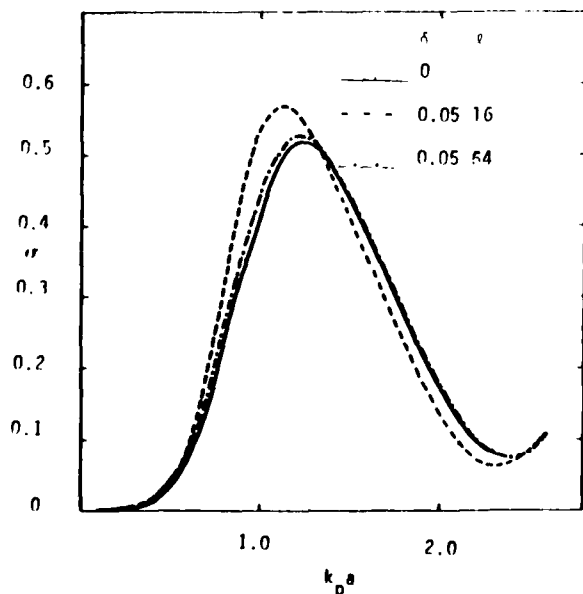


Fig. 5 Differential scattering cross section at $\theta = 90^\circ$ for incidence along z-axis; P-P scattering.

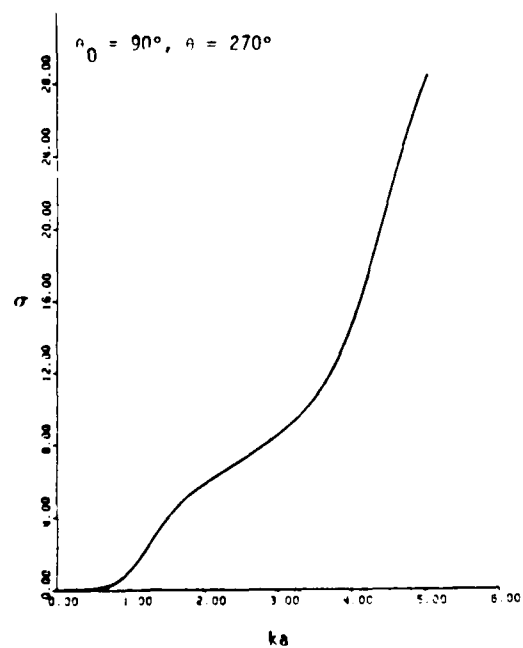


Fig. 7 Back scattering cross section for a crack.

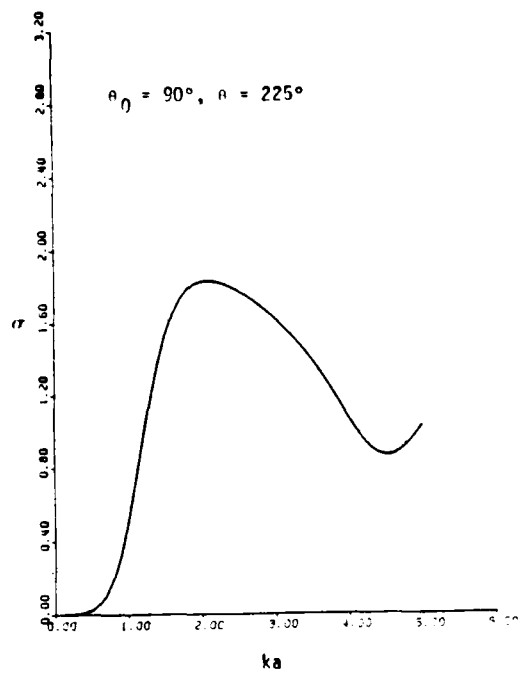


Fig. 8 Differential scattering cross section from a crack.

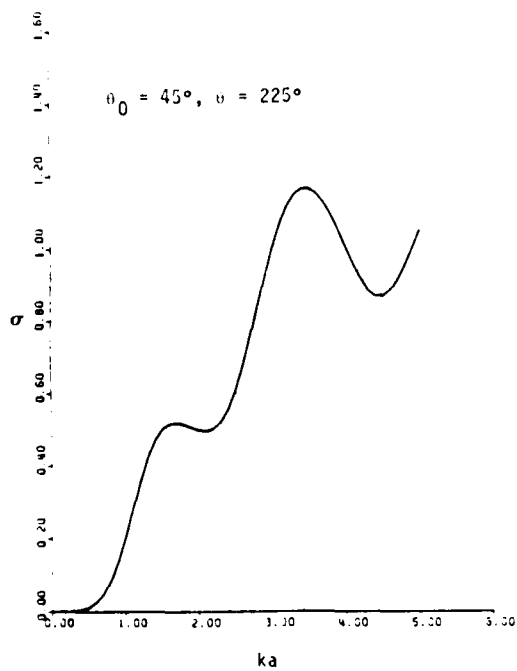
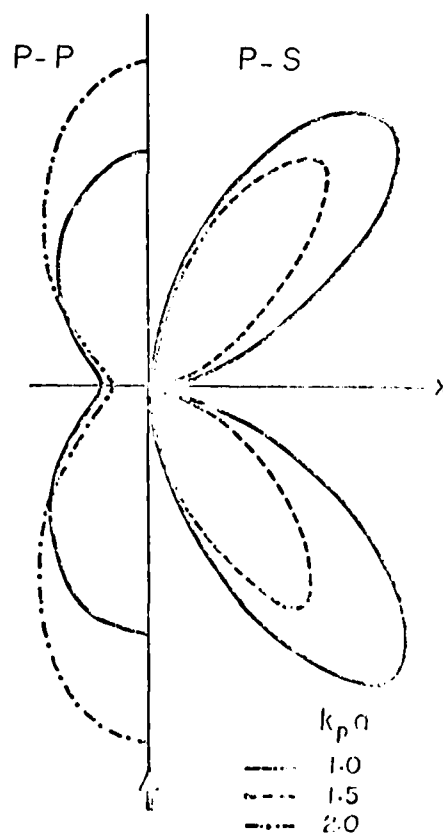
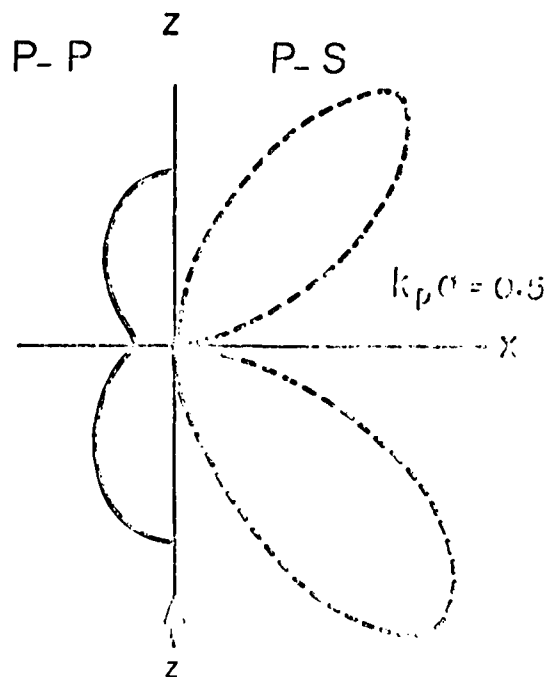
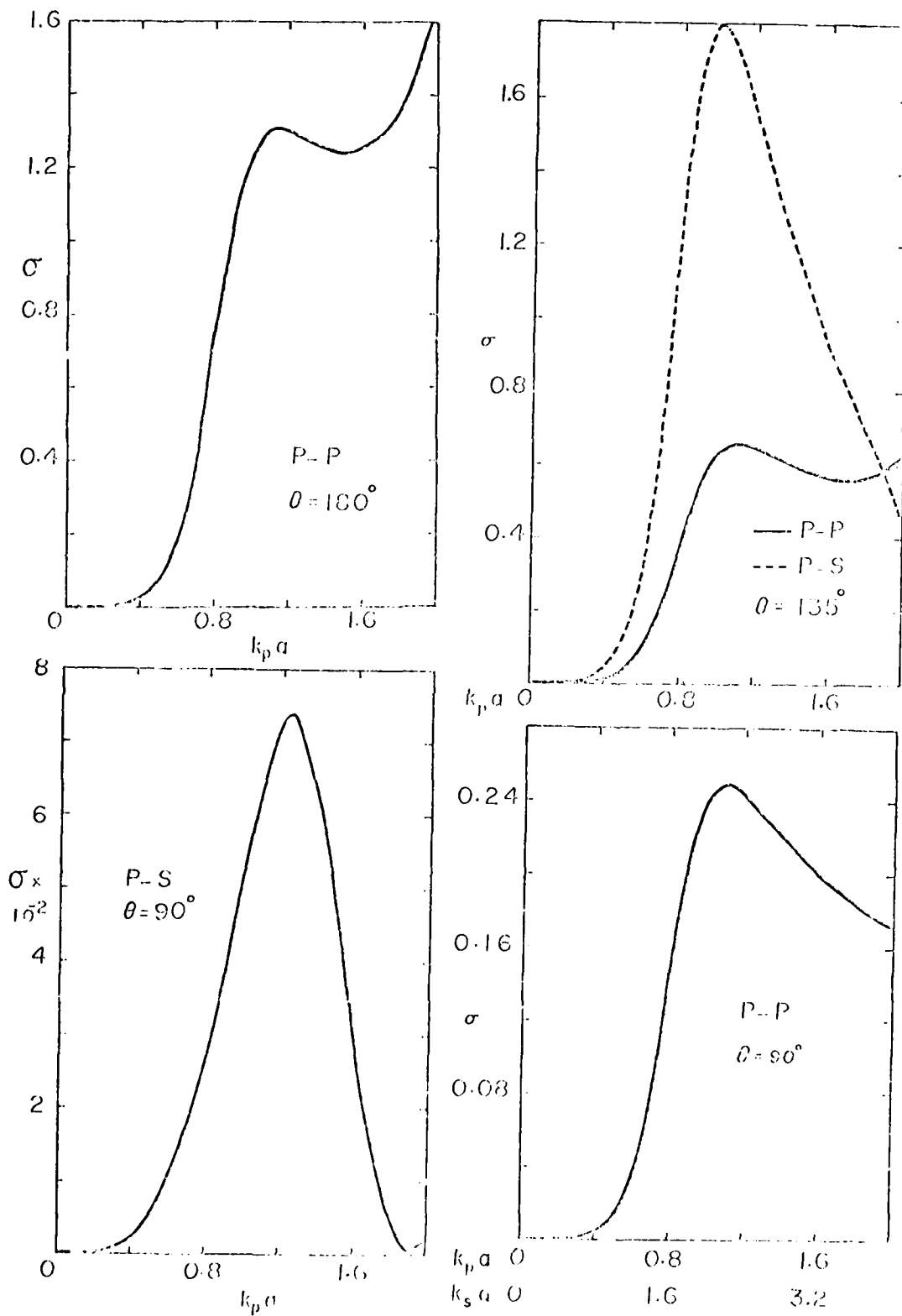


Fig. 9 Back scattering cross section from a crack.



Figs. 10 and 11 Polar plots of the far field amplitude scattered by a penny shaped crack.



Figs. 12, 13, 14 and 15 Scattering cross-section as a function of frequency ($k_p a = \omega a / c_p$) for P-waves incident along the symmetry axis of a penny shaped crack.

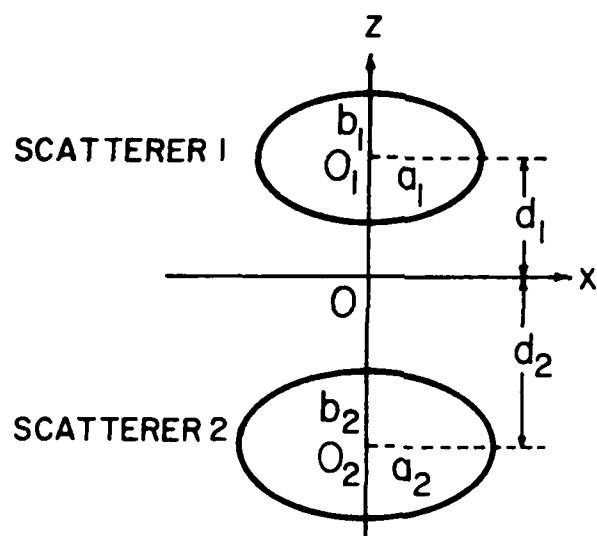


Fig. 16 Scattering geometry for two spheroidal cavities

SUMMARY DISCUSSION
(V. V. Varadan)

Laszlo Adler (University of Tennessee): For the spherical cases where you looked at surface roughness, did you work out the problem for the P2S scattering also?

V. Varadan: P2S? Yes. I didn't show that --

Laszlo Adler: A bigger variation?

V. Varadan: Yes, there is a variation. I can show you one thing. For example, if I plot the cross section as a function of the number of nodes, for example. In that case, if I go 16 lobes from zero to π over 2, in this case, from here to there, 16 lobes, and go more than that, I don't see any variation at all in the crack cross section because of roughness. But where P2S is a little higher than that, there is no resonance associated with that, you take just the number of lobes. For example, if you take the number of lobes below 16, and using a ferrometer solution, probably you may be able to get some information which we are talking on. So, at this moment I can't tell you about what would happen with P2S scattering where the lobes are less than 16. But when the lobes are more than 16 there is no difference in the smooth and the rough surface.

#

MEASUREMENTS OF ULTRASONIC SCATTERING FROM BULK FLAWS OF COMPLEX SHAPE

B.R. Tittmann, R. Elsley, N. Paton
Rockwell International Science Center
Thousand Oaks, CA 91360

ABSTRACT

The report summarizes the design and early results of scattering experiments on flaws of complex shape. In close collaboration with the various theoretical groups representing different inversion algorithms, a unique set of diffusion bonded samples have been designed. These samples contain a variety of irregular and multiple flaws whose scattering characteristics will be obtained in order to guide and evaluate developments of theoretical approaches and test specific theoretical predictions. The majority of these samples have been received and the measurements have begun. Results on selected samples are presented and compared with scattering from ellipsoidal voids. The measurements will include angular, frequency and time domain variations of the scattered signals made possible with a new ultrasonic data acquisition system.

INTRODUCTION

The objective of this task is to predict the fatigue life of a metallic component containing a defect in its interior, by ultrasonic nondestructive evaluation. We report on progress on data acquisition for testing inversion algorithms, the preparations of new diffusion bonded samples, and the characteristics of spherical voids with small perturbations.

DESIGN AND PREPARATION OF NEW TRAILER-HITCH SAMPLES

Earlier phases of this program were concerned with the development of methods for producing flaws of known size, shape and location for use as ultrasonic reference standards. A range of defect sizes and shapes for which theoretical solutions for the scattering of incident ultrasonic energy is available have been produced. In addition, a number of defect geometries such as fatigue cracks¹ and crack-like defects in diffusion bonded samples were also prepared. Previous work has emphasized rather simple internal voids and inclusions such as spherical defects and prolate or oblate spheroids. The new effort places more emphasis on modifications of these basic defect types and on rather more realistic flaws such as actual fatigue cracks, multiple defects and regular defects such as prolate spheroids, but with controlled surface roughness such as might be found in a realistic flaw.

New samples produced during the current year's program are listed in the Sample Inventory in Table 1. Only those samples produced under the current program have been listed in Table 1. Samples No. 69 and 70 are described in previous reports of this program. Drawings for samples No. 69 and 70 are contained in Figs. 1-9. The following section gives only a general description of the defect type, and a precise description is obtained from the appropriate drawings. Figures 1-9 show three views, a

SAMPLE No. 69

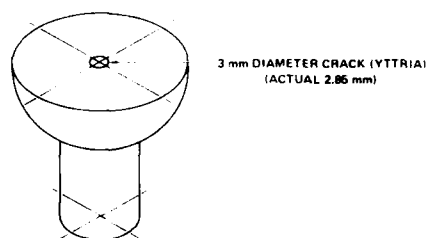


Fig. 1 Sample No. 69.

three-dimensional view of the lower half of the trailer hitch, a more detailed view of the defect with design dimensions, and a micrograph of the actual defect after machining, but before bonding. Sample No. 69 is a simple circular 3 mm-diameter crack-like defect produced by inserting a thin layer of yttria in the bonding plane before the bonding operation. This sample and all other samples through Serial No. 74 are machined to a spherical shape as was done previously in order to permit acoustic scattering experiments over a wide range of angles in three dimensions. Sample No. 70 contains two overlapping spheres, the purpose

SAMPLE No. 70

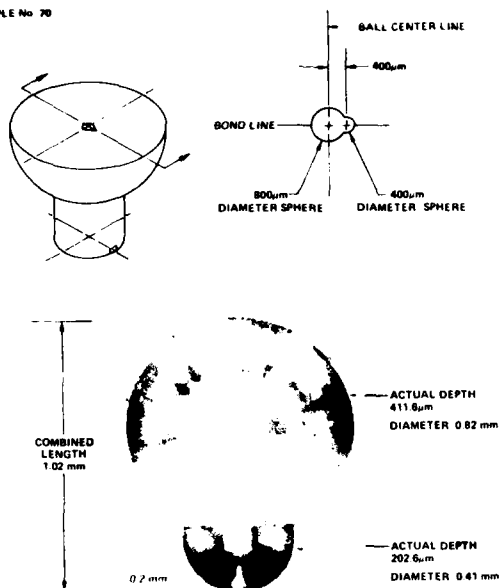


Fig. 2 Sample No. 70.

SAMPLE No. 72

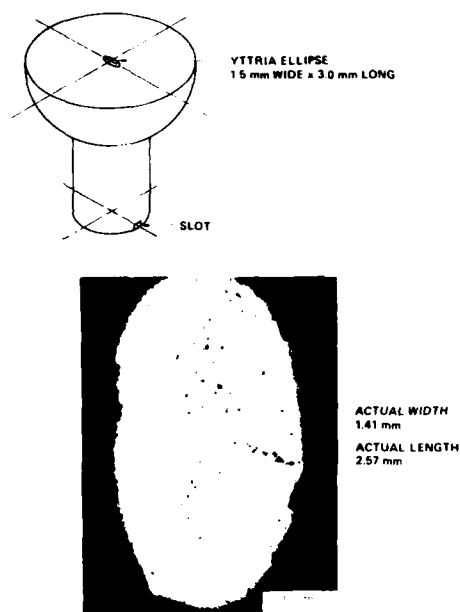


Fig. 4 Sample No. 72.

SAMPLE No. 71

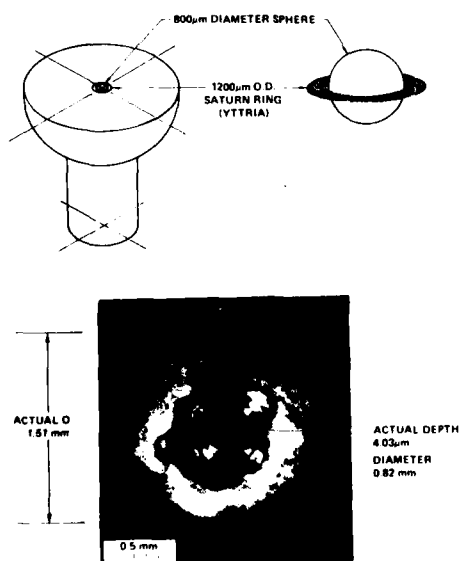


Fig. 3 Sample No. 71.

SAMPLE No. 73

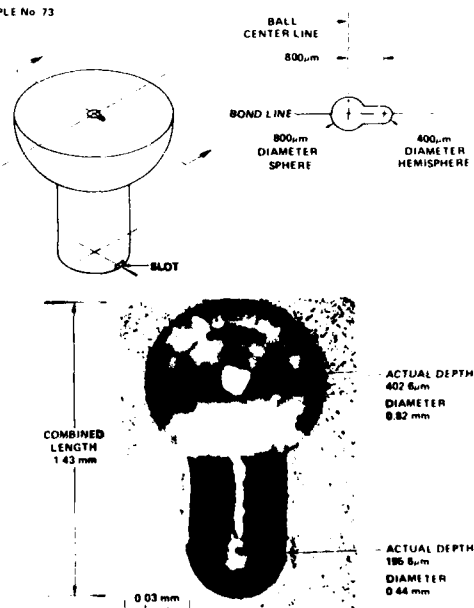


Fig. 5 Sample No. 73.

of this geometry being to test the applicability of summation procedures in the theoretical work. Sample No. 71 contains a single 400µ radius void surrounded by a 200µ wide simulated yttria crack in the form of a "Saturn" ring. This geometry simulates a crack initiating out of an internal void and is probably as close to a realistic defect causing a crack in an actual material as can be produced by the sample preparation procedures used in this study. Sample No. 72 is a simulated elliptical crack in the interior of a

spherical sample, while sample No. 73 contains an overlapping sphere and a modified prolate spheroid of the form shown in the drawing. Sample No. 74 contains a rough oblate spheroid to simulate a void with a realistic internal roughness to study the interaction of this rough surface with a ultrasound of various frequencies. The surface of the oblate spheroid was roughened mechanically prior to the bonding operation. Samples 75-87

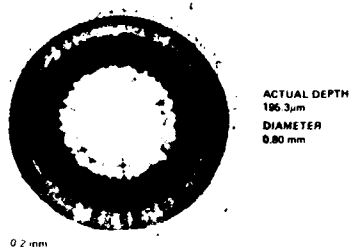
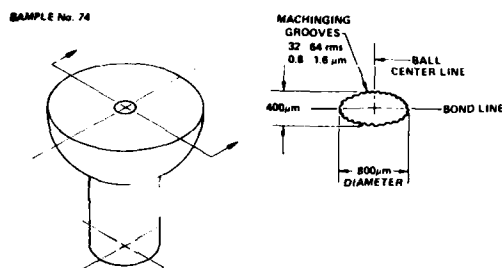


Fig. 6 Sample No. 74.

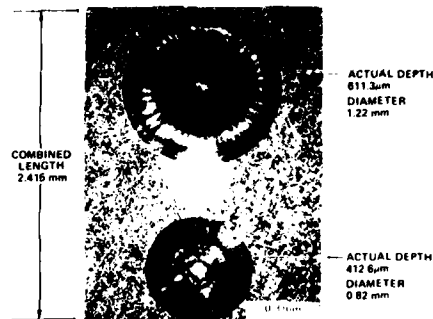
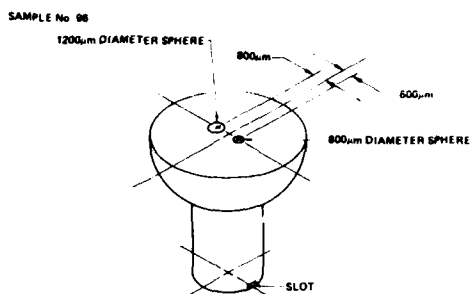


Fig. 8 Sample No. 96.

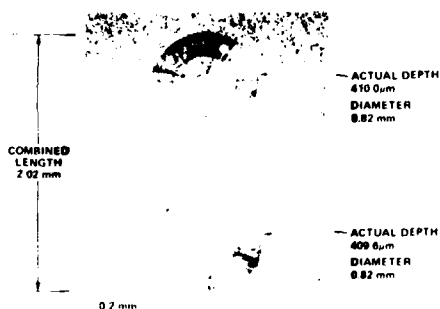
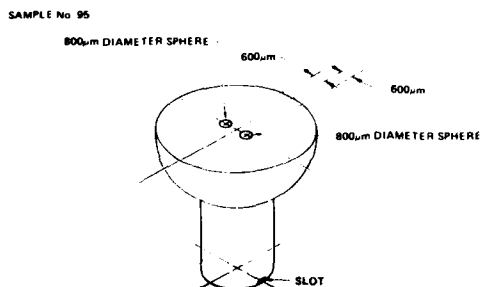


Fig. 7 Sample No. 95.

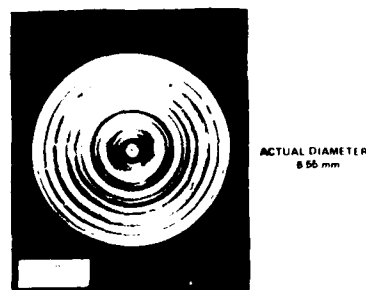
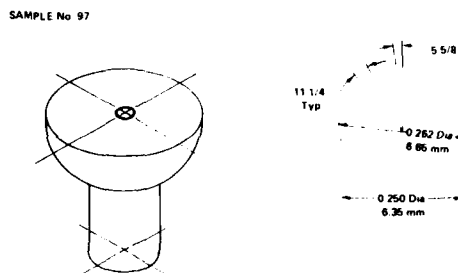


Fig. 9 Sample No. 97.

have been described in a previous report and are basically 2 1/4-inch diameter, 1/2-inch high experimental samples for studying various means of producing internal defects in diffusion bonded samples. Samples 88-94 are 4-inch diameter blanks used to produce the ultrasonic test standards for the test-bed program, and are described more fully elsewhere in this report.²

Sample No. 95 is a 2 1/4-inch diameter, 3 11/16-inch high sample, again with spherical external geometry, and contains two separated

spheres, both with 400μ with 1200μ between centers. Sample No. 96 also contains two spheres, on a 400μ radius, the other a 600μ radius with a center-to-center separation of 1400μ. Sample No. 97 contains a 6.35 mm sphere with pronounced machining grooves, sample No. 99 is a spare, while sample No. 98 is a 4-inch diameter, 1-inch high specimen with a simulated fatigue crack 3 mm diameter produced internally by a spark erosion method. The manner in which this simulated fatigue crack surface was produced is worth describing in detail since it is somewhat complex. A

fatigue fracture surface produced by a fatigue crack growth at high ΔK in a pure titanium specimen was used as a model fatigue crack surface. A 3 mm diameter disc was then cut from the Ti specimen and placed into a suitably cut recess in one of the specimen halves. The opposite face was left smooth and the two specimens bonded together to form an internal fatigue crack-like surface.

The last sample produced in the current series is illustrated in Fig. 10 and consists of a specimen bonded together such that an internal defect introduced at its center line was used to initiate a fatigue crack laterally out from the diffusion bond. By producing specimens in this manner, the bond line was not in a fatigue crack plane and therefore would not interrupt or perturb the crack propagation process. This sample is to be used in some experiments to simultaneously study fatigue crack growth while examining the crack using ultrasonic methods of various kinds from the exposed specimen surface. The grips used to load the specimen enable access to both top and bottom faces of the specimen, thus allowing the study of both transmitted and reflected waves during fatigue cycling of the sample. The design of this sample is described in detail in a later section.

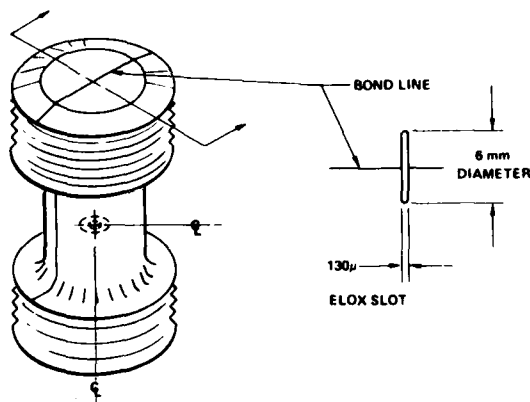


Fig. 10. Sample No. 98.

In summary, as a necessary part of calibrating and evaluating new NDE procedures and test equipment, standard samples containing defects of known size, shape and location, some of which simulate real defects found in service, have been designed and fabricated under this portion of the program. Rather than using the conventional flat-bottom hole, internal defects of accurately controlled geometry have been produced by a diffusion bonding method, since in general, scattering from internal defects is more completely understood than scattering from surface defects. In the current year, an attempt has been made to produce realistic defects of the type that might appear in service, and fatigue cracks growing from internal voids is a good example of this type of defect. Most of the samples have been produced from Ti-6Al-4V by

methods which have been described in detail in previous reports.³

Table 1
Sample Inventory

Serial No.	Code	Height (in)	Diameter (in)	Date	Heat Treatment (Heat No.)
69	5-30-64	3-11/16	2-1/4		DB900C (DG18)
70	2-2-64	3-11/16	2-1/4		DB900C (DG18)
71	2-4-64	3-11/16	2-1/4		
72	5-15E-64	3-11/16	2-1/4		
73	2-4-64	3-11/16	2-1/4		
74	3-4-64	3-11/16	2-1/4		
88			4		
89			4		
90			4		
91			4		
92			4		
93			4		
94			4		
95	2-4-64	3-11/16	2-1/4		DB900C (DG18)
96	2-4-64	3-11/16	2-1/4		DB900C (DG18)
97	2-635-64	3-11/16	2-1/4		
98	6-30-64	1	4		DB900C (D-47058)
99	*	1	4		(D-47058)
100	6-63-64	5	3		

*Blank

DESIGN OF A CENTRAL CRACK FATIGUE SPECIMEN

We have designed a dumbbell shaped specimen which will be used to monitor ultrasonically the growth of a central fatigue crack. Two Ti-6-4 plates, each with a 1/8 inch radius thumbnail EDM notch have been diffusion bonded together such that the two semicircular notches will form a circular starter notch (1/4 inch diameter). With suitable grips, the specimen can be installed into a 200,000 lbs electrohydraulic fatigue frame. The grips have been designed in such a way that the two end faces are accessible for placement of transducers. Growth of the central crack under fatigue conditions will be monitored in the pulse-echo mode. It is also intended to perform tests in which the signal scattered in the plane of the crack will be interrogated. For this purpose, a receiver transducer will be mounted to the cylindrical surface of the specimen.

In the tension-tension fatigue loading the cyclic stress intensity range for this specimen is given by (1)

$$\Delta K = 1.95 \Delta \sigma \sqrt{\frac{a}{Q}} \quad (1)$$

where $\Delta \sigma = \sigma_{\max} - \sigma_{\min}$, a is the instantaneous radius of the central crack and $Q = 0.5$ for an aspect ratio of 0.5 (circular crack). For Ti-6-4 the yield strength, σ_y , of the material is $\sigma_y = 130$ Ksi. Using full load capacity of the fatigue frame the specimen can be cycled at $\sigma_{\max} = 200,000$ lbs/3.14 (inches)² = $0.5 \sigma_y$. A load ratio

$R\sigma_{min}/\sigma_{max} = 0.08$ will yield $\Delta\sigma = 26.5 \text{ Ksi}/\sqrt{\text{in}}$ will be achieved. For this stress intensity range a fatigue crack growth rate da/dN of about 20μ inches/cycle is deduced from published data. The growth of a fatigue crack will be continuously monitored in the pulse-echo mode. For verification of the growth, "marker cycles" will be applied periodically. For $\Delta K > 20 \text{ Ksi}/\sqrt{\text{in}}$ the growth should occur according to the Paris equation (5)

$$\frac{da}{dN} = A(\Delta K)^m \quad (2)$$

with $A = 7.2 \times 10^{-4}$ and $m = 3.15$. Combining Eqs. (1) and (2) and integration over the total growth regime yields the remaining cycles to failure

$$\Delta N = \frac{2}{(m-2)A(1.95Q)^{-1/2}\Delta\sigma)^m} \left[\frac{1}{a^{(m-2)/2}} - \left(\frac{1.95\sigma_{max}}{Q^{1/2}K_c} \right)^{m-2} \right] \quad (3)$$

where K_c is the fracture toughness of the material ($K_c = 45-50 \text{ Ksi}/\sqrt{\text{in}}$). Since the K_c is not that accurately known, we will actually determine K_c from the critical flaw size

$$a_c = \left(\frac{Q^{1/2}K_c}{1.95\sigma_{max}} \right)^2 \quad (4)$$

for our particular material and geometry. Equation (4) is a consequence of Eq. (3) for $\Delta B = 0$.

DATA ACQUISITION TECHNIQUES FOR TESTING INVERSION ALGORITHMS

Data has been collected on two samples, one containing an 800μ diameter spherical void and another containing $800\mu \times 400\mu$ oblate spheroid (void) in accordance with the requirements for the POFFIS algorithm used by N. Bleistein and J. Cohen of Denver Applied Analytics. The data set includes explicit timing information defining the velocity in the trailer-hitch for several different angles and the absolute arrival times of the flaw echos for the determination of absolute flaw position. Data has also been collected and sent to J. Rose of the University of Michigan, comprising waveforms along the longitude and equator of trailer hitches containing a thin elliptic disk and an oblate spheroid. New requirements on transducer placement have been received from A. Mucciardi of Adaptronics so that both pitch-catch and pulse-echo waveforms may be collected in a new window format to be used for inversion. The data were collected on a trailer-hitch with an oblate spheroid and sent to Adaptronics. Data obtained in the recent past on a variety of trailer-hitch defects have been transmitted to J. Gubernatis at Los Alamos.

In order to provide scattering data for use with the POFFIS algorithm, it is necessary to record pulse echo waveforms of the flaw as viewed from a variety of angles including the absolute position of the flaw echo in each waveform. Given a knowledge of the velocity of the sound in the host material, absolute position can be determined

from absolute arrival times of the flaw echos. In conventional ultrasonic NDE, arrival time is used as an approximate measure of flaw location. In that case it is not necessary to know the arrival time (position) more accurately than about one diameter of the flaw. However, in the POFFIS algorithm, the position information directly affects the reconstructed shape and size of the flaw. It is therefore necessary to know arrival time (position) to a small fraction of the diameter of the flaw.

In order to obtain absolute position information for echos from the flaws in the spherical ("trailer hitch") specimens, the following data were collected:

1. The known shape of the surface of the specimen (in this case a sphere).
2. The velocity of sound in the measurement directions in the specimen.
3. The arrival time of the flaw waveform with respect to the instant when the peak of the incident sound pulse passed from the transducer into the specimen. For normal incidence immersion measurements, this instant can be measured directly from the received waveform, but for angle beam or (as in our case) contact measurements, it must be separately determined.

The procedures used to obtain the absolute arrival time and sound velocity measurements are described below:

Arrival Time - Received ultrasonic waveforms are usually timed with respect to a trigger pulse which is approximately coincident with the generation of the transmitted sound pulse. In our apparatus, which consists of a Parametrics 5052PR Pulser/Receiver and a Biomation 8100 Transient Recorder, time is measured with respect to an instant, 50 sample intervals before the trigger pulse from the Parametrics crosses the trigger threshold of the Biomation. In order to be able to time the ultrasonic echos precisely, it is necessary to determine when the peak (or some other feature) of the ultrasonic pulse emerges from the face of the transducer. The peak is used because it is the time at which most of the frequency components of the pulse are in phase and is therefore a high signal-to-noise feature which can be identified in either the time or frequency domains.

Because the transducer cannot be used as a receiver while it is transmitting, the pulse peak time is measured by placing the transducer in contact with a 1 inch thick layer of aluminum and measuring the first round trip time. Then the pulse peak time is calculated using the thickness and velocity of sound of the aluminum block. The velocity of sound is in turn determined by separating the transducer from the block by a water buffer and measuring the front surface and first round trip times and the thickness of the block.

The resulting pulse peak time is then used as the reference of time for flaw waveform measurements. It will vary if any of the components of the apparatus (transducer, pulser, transient recorder) are changed or even readjusted (for example, pulser damping or Biomation trigger

level). It is found in practice that the Bio-mation triggers about 1/8 cycle after the beginning of the pulse and therefore about 5/8 cycle before the pulse peak for each of the two 5 MHz broadband transducers.

Sound Velocity - In order to convert the absolute arrival times measured above into absolute positions, it is necessary to know the sound velocity of the specimen. For anisotropic materials, such as Ti-6Al-4V, this requires measurements in several directions. We have made sound velocity measurements in the trailer hitch specimens by through transmission measurements along various diameters of the hitches. The technique used is to divide the thickness of the hitch (including end caps) by the time when the peak of the pulse reaches the receiving transducer minus the time when the peak emerges from the transmitting transducer. This requires a 2-transducer reference measurement analogous to the single transducer reference measurement described above, consisting of measuring and transmission arrival time through the 1 inch aluminum reference block and subtracting the known propagation time through the block.

The results of the sound velocity measurements (for those angles where physical access allowed a through transmission measurement to be made) are given below. They show a consistent anisotropy as well as a systematic variation between the two samples.

SOUND VELOCITY

Angle from Symmetry Axis (degree)	Sample 37 (mm/ μ s)	Sample 39 (mm/ μ s)
55-1/2	6.193	6.175
73-1/2	6.219	6.203
90	6.232	6.215

ELASTIC WAVE SCATTERING BY BUBBLE DEFECT

Next, we turn to study a non-spherical defect shown in Fig. 2. The defect is a spherical cavity of diameter 800 μ , to which a hemisphere cavity of diameter 400 μ has been added. The hemisphere will be referred to as the "bubble"; it represents a deviation of size b from a simple shaped smooth cavity of characteristic size a . The questions addressed were the following:

- (1) At what frequencies (e.g., values of kb) is the bubble observable?
- (2) At what angles of incidence and scattering is its effects most pronounced?

To answer these questions preliminary experiments were first carried out to compare the backscattering by the large sphere to that of the non-spherical defect. Figures (11a, b, c) show the backscattered amplitude vs frequency for (a) an 800 μ sphere without the bubble defect (b) a side view of the defect normal to the axis-of-symmetry, and (c) a frontal view of the bubble defect. The differences appear above about 4 MHz

($ka = 1.5$, $kb = 0.75$). The largest deviation is obtained for the case of Fig. 11c, i.e., when the bubble is directly illuminated.

The frequency spectra were experimentally obtained by Fourier analyzing and normalizing the observed backscatter waveforms. The spectra of Figs. 11b and 11c are modulated with about the same periodicity as that obtained for a sphere, Fig. 11a, but a modulation with longer periodicity (in k) is superimposed. While for the sphere the first three peaks are of approximately equal amplitude, with the bubble present, the amplitudes decrease in magnitude. These observations agree qualitatively well with the findings of Domany et al (6).

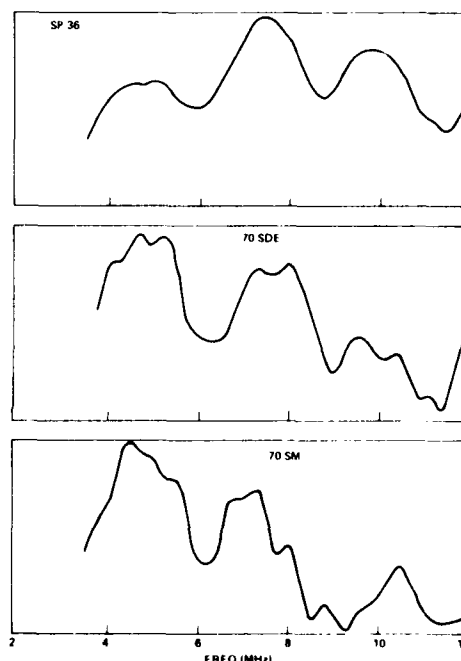


Fig. 11 Frequency spectra of pulse echo signals from (a) a sphere, and (b) and (c) a bubble defect.

Turning now to the angular distribution of power, Fig. 12 shows the polar plot of power versus scattering angle for an incident direction along the normal to the axis of symmetry (side view) and a scattering angle of $\theta = 135^\circ$ from the forward scattering direction. This work is for $ka = 2$ and shows that the presence of the bubble has caused noticeable loss of the symmetry associated with a "true" spherical cavity. Also shown in the plot are results of calculations by Domany et al (6) and Opsol (7) in qualitative agreement with the experiment. Domany's calculations are based on the use of the Distorted Wave Born Approximation, while Opsol's results are based on the use of Vissher's matrix theory (8).

We plan to extend this work to the other defects described earlier and attempt to achieve a quantitative comparison.

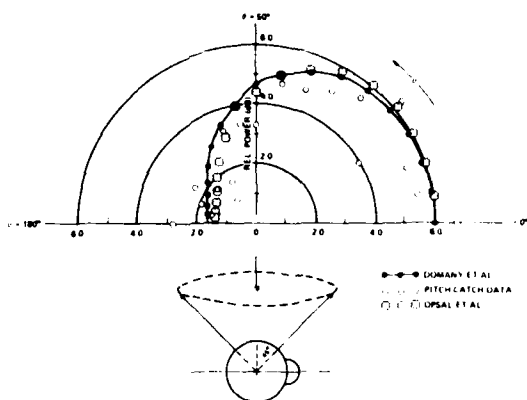


Fig. 12 Polar plot of power scattered (dB) as a function of scattering angle in a pitch-catch experiment.

ACKNOWLEDGEMENT

This research was sponsored by the Center for Advanced NDE operated by the Science Center, Rockwell International, for the Advanced Research Projects Agency and the Air Force Materials Laboratory under Contract No. F3315-74-C-5180.

REFERENCES

1. N. Paton, "Sample Preparation," Interdisciplinary Program for Quantitative Flaw Definition, Contract No. F33615-74-C-5180, covering period July 1, 1974 - June 30, 1975, D.O. Thompson, Program Manager.
2. R. Addison, this volume.

3. N. Paton, "Sample Preparation," Interdisciplinary Program for Quantitative Flaw Definition, Contract No. F33615-74-C-5180, covering period July 1, 1976 - June 30, 1977, D.O. Thompson, Program Manager.
4. G.R. Irwin, J. Appl. Mechanics 29, 651 (1962).
5. P.C. Paris and F. Erdogan, J. Basic Eng. 85, 528 (1963).
6. E. Dormany, K.E. Newman and S. Teitel, this volume.
7. J.L. Opsal, this volume.
8. W.M. Visscher, Proc. of the ARPA/AFML Review of Progress in Quantitative NDE, ed. D.O. Thompson AFML-TR-78-205, p. 425 (1978).

MEASUREMENTS OF ULTRASONIC SCATTERING FROM BULK FLAWS OF COMPLEX SHAPE

B. Tittmann

DISCUSSION

JIM ROSE: Jim Rose, University of Michigan.

I notice that in your experiments that you just showed, you have the deeper split. Is that possibly true for --

MR. TITTMANN: That's fine structure that I think we can get rid of by being a little more precise in our normalization.

MR. ROSE: You don't think it's physical?

MR. TITTMANN: I don't think so.

MR. HÖLLER: When you showed your experiments with the sphere and the bubble, I didn't understand the designations on the axes.

MR. TITTMANN: This was a polar plot with the bubble oriented towards $\theta = 0$. The radial axis is calibrated in dB of relative power.

SUMMARY DISCUSSION
(B. Tittmann)

Jim Rose (University of Michigan): I notice that in your experiments you just showed, you have the deeper split. Is that possibly true for --

Bernie Tittmann: That's fine structure that I think we can get rid of by being a little more precise in our normalization.

Jim Rose: You don't think it's physical?

Bernie Tittmann: I don't think so.

Paul Holler (Inst. fur Zerst. Pruf.): When you showed your experiments with the sphere and the bubble, where the abscissa is, the ordinate with decibels, I didn't understand what you were -- must be an angle.

Bernie Tittmann: This was a polar plot. If we wanted to assign a reference, make the bubble direction zero degrees and this is 90 and that's 180; and so looking into that direction, then, you're looking away from the bubble and the amplitudes are in terms of DB.

#

DIRECT AND INVERSE METHODS FOR SCATTERING BY CRACKS AT HIGH FREQUENCIES

J. D. Achenbach
The Technological Institute
Northwestern University
Evanston, IL 60201

ABSTRACT

Further results are presented for the direct problem of scattering of high-frequency waves by cracks in elastic solids. Results for a penny-shaped crack, obtained on the basis of geometrical diffraction theory, are compared with experimental data. For simple crack geometries a hybrid method, whereby the crack-opening displacement is computed by ray theory, and the scattered field is subsequently obtained by the use of a representation theorem, is tested by comparison with exact results. The simple form of the far-field high-frequency solutions to the direct scattering problem suggests the application of Fourier-type integrals to solve the inverse problem. Two different inversion integrals are discussed. The inversion method is checked by applying it to the scattered field of a flat elliptical crack, for which an analytical expression is derived. Some computational technicalities are discussed, and numerical results are presented.

INTRODUCTION

Several recent publications have been concerned with solutions to the direct problem of high-frequency scattering of time-harmonic waves by cracks in elastic solids. From the phenomenological point of view the high-frequency approach is appealing in that the probing wavelengths are of the same order of magnitude as the length-dimensions of the crack. This gives rise to interesting and detectable characteristic interference phenomena. The high-frequency approach is also very attractive from the mathematical point of view, because the intuitively straightforward methods of elastodynamic ray theory can be applied to yield accurate solutions.

For flat cracks with a smoothly curved edge in the interior of a homogeneous, isotropic, linearly elastic body, the direct scattering problem in the high-frequency domain can now be solved accurately, provided that ka is sufficiently larger than unity, where k is the wavenumber and a is a characteristic radius of curvature of the crack edge. Results, which have been obtained on the basis of either geometrical diffraction theory (GTD), or a hybrid method, whereby the crack-opening-displacement (COD) is computed on the basis of GTD, and the scattered field is subsequently obtained by the use of a representation theorem, have been reported by Achenbach et al.^{1,2}

In the present paper a very brief summary of GTD is given, and some recent comparisons with experimental results are reviewed. For simple crack geometries, the hybrid method is tested by comparisons of both COD computations and scattered-field computations with exact results which have been obtained by numerical solution of a governing singular integral equation.

A major part of the present paper is devoted to the inverse problem. It is known that at high frequencies the far-field generated by a volume scatterer in an acoustic medium is proportional to the Fourier transform of the characteristic function associated with the scatterer. The

characteristic function is defined so that it has unit value for every point inside the scatterer and vanishes elsewhere. The Fourier transform parameter which enters in this relation is a function of the wave-number and the angle of observation. A number of studies have recently been devoted to examine the extent to which the far-field data can be used to numerically invert this Fourier transform relation and recover the size, shape and the location of the scatterer. In these studies the possible limitation on the bandwidths of the observed scattered signals has been taken into account, as well as the restricted range of the aperture covered by the angles of observation. For details, the reader is referred to the recent work of Cohen and Bleistein^{3,4}.

In the present paper the inversion of far-field crack-scattering data in the high-frequency range by a method which does not involve a three dimensional Fourier inversion but only a single integration in the wave-number domain is discussed. The method was introduced by Achenbach et al.⁵, and it is further explored in the present paper.

ELASTODYNAMIC RAY THEORY

Ray theory provides a method to trace the amplitude of a high-frequency disturbance as it propagates along a ray. In a homogeneous, isotropic, linearly elastic solid the rays are straight lines, which are normal to the wave-fronts. An unbounded solid can support rays of longitudinal and transverse wave motion. These rays are denoted as L-rays and T-rays, respectively.

In analogy with geometrical optics, the simplest theory for diffraction of elastic waves by cracks may be called geometrical elastodynamics (GE). In GE a crack acts as a screen which creates a shadow zone of no motion, and zones of reflected waves. The geometrical theory of diffraction (GTD) provides a first correction to GE, in that terms arising from edge diffraction are

taken into account.

For plane longitudinal and transverse waves, which are under arbitrary angles of incidence with a traction-free semi-infinite crack, the fields on the diffracted rays can be obtained by asymptotic considerations, as shown by Achenbach et al^{6,7}. The results can be expressed in terms of diffraction coefficients which relate the diffracted fields to the incident fields. Geometrical diffraction theory provides modifications to the semi-infinite crack results, to account for curvature of incident wave-fronts and curvature of crack edges, and finite dimensions of the crack. In the usual terminology the results for diffraction of plane waves by a semi-infinite crack are the canonical solutions. For incident waves with curved wavefronts and for curved diffracting edges, the cones of diffracted rays have envelopes, at which the rays coalesce and the fields become singular. The envelopes are called caustics, and GTD breaks down at caustics.

A more complete discussion of GTD can be found in the papers by Achenbach et al^{1,2}.

Experiment. Experimental results in the high-frequency range that are suitable for comparison with theoretical results have been reported by Adler et al^{8,9}. The sample was a circular disk (2.5 x 10 cm) of titanium alloy which contained a penny-shaped crack of radius 2500 μ parallel to the flat faces, and located at the center of the disk. The disk was immersed in water. A transmitter launched a longitudinal wave to the water-titanium interface under normal incidence. This wave was transmitted into the solid, diffracted by the crack, and the diffracted waves were transmitted back into the fluid, where they were received by a second transducer. The experimental set-up and the processing of the data are discussed in some detail elsewhere⁹.

In the experimental work the nature of the diffracted signals is determined by their arrival times. Since the first arriving signals are related to longitudinal waves in the solid, it is possible to gate out and separate the purely longitudinal diffracted signals from subsequent signals. By appropriate processing of the experimental data, as discussed in Ref. 9, the amplitude-spectrum is obtained for the longitudinal diffracted waves only. Thus for the present comparison of analytical and experimental results we need to consider only the primary diffracted body-wave rays in our analytical work.

The interference patterns for the first arriving longitudinal waves in the fluid are generated by phase differences and amplitude differences on the direct rays from the two crack tips, see Fig. 1. Adding the primary diffracted longitudinal fields from the points O_1 and O_2 we obtain in the far-field

$$u_L = F(\dots) \exp[i(S/c_L + \pi/4)] u_{0L}^i \quad (1)$$

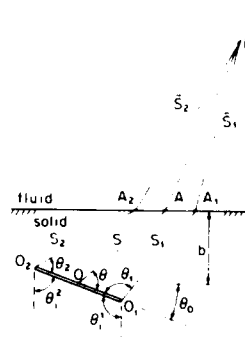


Fig. 1: Geometry in the plane of symmetry of a penny-shaped crack.

$$F(\theta, \theta_0) = H_1 \exp[-i(\omega a/c_L)(\cos\theta - \sin\theta_0)] + H_2 \exp[i(\omega a/c_L)(\cos\theta - \sin\theta_0)] \quad (2)$$

$$H_j = \frac{\text{sgn}(\cos\theta_j) T(\theta_j^i) |D_L^L(\theta_j; \theta_0^i)|}{(\omega S_j/c_L)^{1/2} (1+S_j/C)^{1/2} (1+\bar{S}_j/E)^{1/2} (1+\bar{S}_j/\bar{C})^{1/2}} \quad j = 1, 2 \quad (3)$$

Here ω is the circular frequency, a is the crack radius, $S = AB$, u_0 represents the incident wave at point O , and c_L and c_F are the velocities of longitudinal waves in solid and fluid respectively. The geometrical quantities are indicated in Fig. 1. In Eq.(3) $T(\cdot)$ is the transmission coefficient at the solid-fluid interface, and $D_L^L(\cdot; \cdot)$ is the diffraction coefficient. For details of the derivation of Eqs.(1) - (3) we refer to Ref. 9. It should be noted that one of the terms H_j is imaginary, since the ray has crossed a caustic. Of particular interest is the absolute magnitude of F ,

$$|F| = (|H_1|^2 + |H_2|^2 + 2|H_1||H_2|\sin 2(\omega a/c_L)(\cos\theta - \sin\theta_0))^{1/2} \quad (4)$$

Here we have taken into account that either H_1 or H_2 is imaginary.



Fig. 2: Comparison of Eq.(4) with experimental results in Ref. 9.

Comparisons with Experimental Data. Theoretical results obtained from Eq.(4) have been plotted together with experimental data in Fig. 2. The frequency varies from 2 MHz to about 14 MHz. The angle in the solid is $\theta'(\pi/2 - \theta) = 35^\circ$ respectively. The amplitudes of the first few cycles agree well. At higher frequencies (above 6 MHz) the experimental results are lower than predicted by theory. One possible explanation is the effect of attenuation which is not accounted for in the theory. In all cases the positions of maxima and minima of the spectra agree well. The locations of the maxima are significant for the inversion process. Additional comparisons with experimental data have been reported in Ref. 9.

A HYBRID METHOD

In this method the crack-opening-displacement (COD) is computed on the basis of elastodynamic ray theory, and the diffracted field is subsequently obtained by the use of a representation theorem. The advantage of this approach is that the trouble with ray theory at shadow boundaries and boundaries of zones of specular reflection is eliminated, and caustics only need to be dealt with on the faces of the crack.

Elastodynamic representation theorem. The field generated by scattering of incident waves by an obstacle with surface S can be expressed in terms of a representation integral over S. For a stress-free crack with plane faces A^+ and A^- the representation integral can be simplified. If the total field is written as $u^t = u^{in} + u^{sc}$, where u^{in} is the incident field and u^{sc} is the scattered field, then at an arbitrary field point x the latter can be expressed in the form

$$u_m^{sc}(x) = \int_{A^+} \tau_{ij;m}^{(x-X)} \Delta u_i^{sc}(X) n_j dA(X) \quad (5)$$

Here x represents any point outside of the crack, and n is the outward normal (pointing from the A^+ to the A^- face). Also $\Delta u_i^{sc}(X)$ is the crack-opening displacement defined by

$$\Delta u_i^{sc}(X) = (u_i^{sc})^{A^+} - (u_i^{sc})^{A^-} \quad (6)$$

and

$$\tau_{ij;m}^{(x-X)} = \text{tensor of rank three,} \quad (7)$$

which represents the stress-components at X

due to a unit load in the x_m direction at the

point defined by X . Provided that the crack-opening-displacement can be adequately approximated, Eq.(5) may be expected to give a good approximation to the scattered field. In this section we employ GTD to compute an approximation to the COD.

Crack-opening displacement. Four principal difficulties must be overcome, in the hybrid method presented here. First, GTD predicts unbounded COD's at the crack edge. It is however, seen below by

comparison with exact numerical results that this effect is negligible. Secondly, caustics remain, although they are reduced by one dimension. In GTD caustic surfaces occur. To compute the COD, only caustic curves which are confined to the crack faces are encountered. Thirdly, Eq.(5) must be numerically integrated which becomes progressively more difficult with decreasing wave lengths. Finally, the computation of the COD becomes more complicated if "boundary-waves" are included to achieve the desired accuracy.

We now give a brief description of the terms included in the COD, with emphasis on the boundary-wave terms. The COD can be represented by

$$\Delta u_j = \Delta u_j^{GE} + \Delta u_j^S + \Delta u_j^{TH} + \Delta u_j^{BL} + \Delta u_j^{BT} \quad (8)$$

The first term is the geometrical elastodynamics (GE) contribution to the COD. On the illuminated crack face it consists of the incident wave and the specular reflections. The GE contribution vanishes on the crack face at the shadow side. The second term consists of the diffracted and reflected surface waves which have been described in the previous section. This term is of order one in wavelength with respect to the incident wave. The third term is the contribution to the COD from the diffracted body waves. It includes only horizontally polarized transverse rays, and it is of order the square root in wavelength with respect to the incident wave. We note that the longitudinal diffraction coefficients and those parts of the transverse diffraction coefficients which give rise to vertically polarized waves vanish on the crack faces. The last two terms are the boundary-wave contributions to the COD. In principle they are of order three halves power in wavelength with respect to the incident wave. However, at moderate wave numbers, their amplitude can be large.

Boundary-waves occur because the diffracted body waves do not satisfy the boundary conditions of vanishing traction on the crack faces. The transverse boundary-wave (which is generally known as the "head-wave") and the diffracted longitudinal body-wave combine to satisfy the boundary condition of vanishing tangential tractions on the crack faces. The longitudinal boundary-wave and the diffracted transverse body-wave combine to satisfy the boundary condition of vanishing normal tractions on the crack faces. More details can be found in a paper by Gautesen [10]. From the mathematical point of view, boundary-waves represent branch-point contributions to the inverse Fourier transforms of the displacement fields. The amplitude of the longitudinal boundary-wave is large at moderate wave numbers due to the proximity of the Rayleigh pole to the branch point. The amplitude of the transverse boundary-wave is large at moderate wave numbers because the branch point is close to the extraneous roots of the rationalized Rayleigh function.

SOME RESULTS

In this section we present comparisons between the scattered fields computed by GTD, by the hybrid method and by exact theory, for a penny-shaped crack and for a slit.

For the penny-shaped crack we consider normal incidence of a longitudinal wave. The radius of the crack is a , and the origin of an (r, θ) -coordinate system is placed at the center of the crack, where r and θ vary in a plane normal to the plane of the crack. Thus $\theta = 0$ in the plane of the crack, and $\theta = \pi/2$ along a line through the center of the crack normal to the crack-plane.

A dimensionless crack-opening displacement computed by the method discussed in the previous section is shown in Fig. 3. It is noted that the agreement between the exact COD (solid line) and the approximate COD (dashed line) is excellent. The approximate COD, which is relatively easy to obtain can be substituted in Eq.(5) to obtain the scattered field.

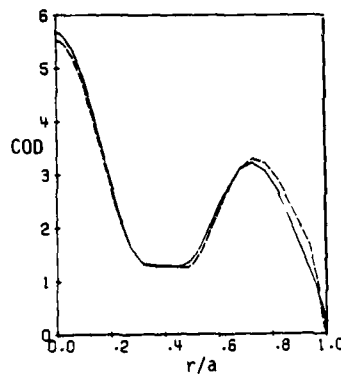


Fig. 3 Dimensionless crack-opening displacement for normal incidence of a longitudinal wave on a penny-shaped crack; $\nu = 0.25$, $k_L a = 5$; — exact theory, - - - approximate COD.

Comparisons of the scattered displacements as functions of the angle θ , for $r/a = 10$ and $k_L a = 5$ are shown in Figs. 4 and 5. The GTD results have been corrected at the shadow boundary and at the line through the center of the crack normal to the crack-plane (which is a caustic). For the scattered displacement in the x_2 -direction (normal to the crack) there are, however, still deviations near the shadow boundary.



Fig. 4 Scattered longitudinal x_1 -displacement for normal incidence of a longitudinal wave; $r/a = 10$, $k_L a = 5$; — GTD, Δ hybrid theory, \circ exact results.

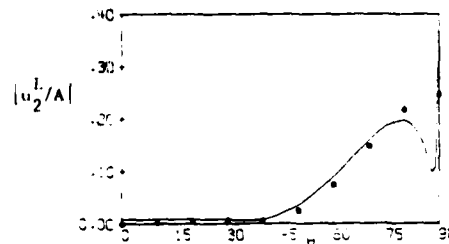


Fig. 5 Scattered longitudinal x_2 -displacement for normal incidence of a longitudinal wave; $r/a = 10$, $k_L a = 5$; — GTD, Δ hybrid theory, \circ exact results.

Figure 6 shows the geometry of a slit with oblique incidence of a longitudinal wave. Comparisons of the displacements are shown in Fig. 7. The agreement is generally better for the scattered longitudinal-wave displacements than for the scattered transverse-wave displacements.

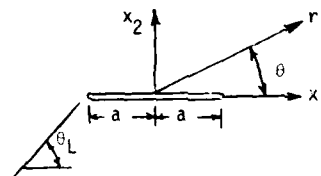


Fig. 6 2-D Geometry for a slit

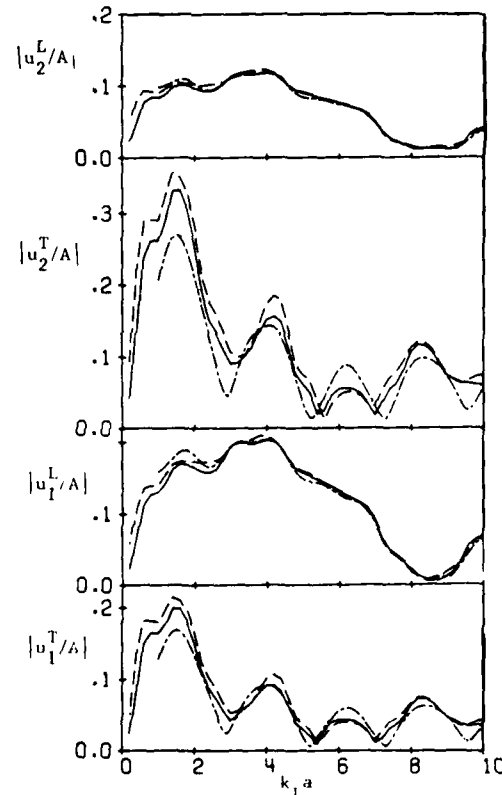


Fig. 7 Displacements due to scattered waves versus $k_L a$; $r/a = 10$, $\nu = 0.25$, angle of incidence $\theta_i = 60^\circ$; — exact, - - - hybrid method, - . - GTD, \circ 30° .

The far-field longitudinal solution. Let us assume that the origin O of the coordinate system is close to the crack while the source S of the incident field and the observation point Q are far away, see Fig. 8

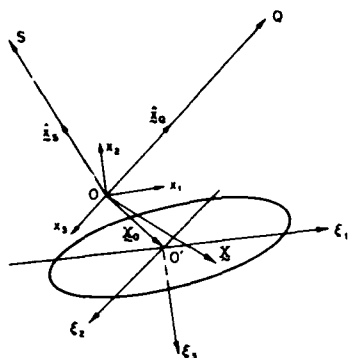


Fig. 8 Flat crack, with source point S and point of observation Q .

Thus, if \underline{x}_S , \underline{x}_Q , and \underline{x} denote the position vectors of S , Q and any point on the crack, and $x_S = |\underline{x}_S|$, $x_Q = |\underline{x}_Q|$ and $X = |\underline{x}|$, then $x_S, x_Q \gg X$. Defining the unit vector $\hat{\underline{x}}_Q = \underline{x}_Q/x_Q$, we can write

$$|\underline{x}_Q - \underline{x}| \approx x_Q - (\hat{\underline{x}}_Q \cdot \underline{x}), \quad x_Q \gg X \quad (9)$$

The expression for $\tau_{ij;m}^G$ then simplifies considerably. Substituting this simplified result in Eq. (5), we find for the longitudinal field

$$\{u_m^{sc}(\underline{x}_Q)\}^L = -ik_L b_{ij;m}^{G;L}(\hat{\underline{x}}_1) G_L(x_Q) n_j I_1^L(\hat{\underline{x}}_Q) \quad (10)$$

where

$$b_{ij;m}^{G;L} = (\lambda + 2\mu)^{-1} (2\mu \hat{x}_i \hat{x}_j + \lambda \delta_{ij}) \hat{x}_m \quad (11)$$

$$G_L(x) = \frac{1}{4\pi x} \exp(ik_L x) \quad (12)$$

$$k_L = \omega/c_L; \quad c_L^2 = (\lambda + 2\mu)/\rho \quad (13)$$

and

$$I_1^L(\hat{\underline{x}}_Q) = \int_{A^+} \exp(-ik_L \hat{\underline{x}}_Q \cdot \underline{X}) \Delta u_1^{sc}(\underline{X}) dA(\underline{X}) \quad (14)$$

In Eq. (10) the summation convention applies, and in (11)-(13) λ and μ are Lamé's elastic constants, and ρ is the mass density.

PHYSICAL ELASTODYNAMICS

The physical elastodynamics approximation is obtained if only the leading contributions arising from the incident field and the specularly reflected body waves from the illuminated face are included

in Δu , i.e.,

$$\Delta u^{sc} \approx \Delta u^{GE} = -(\underline{u}^{in} + \underline{u}^{re}) A^- \quad (15)$$

For the incident field we assume a longitudinal wave from S given by

$$\underline{u}^{in} = -A \hat{\underline{x}}_S G_L(x_S) \exp(-ik_L \hat{\underline{x}}_S \cdot \underline{X}), \quad x_S \gg X \quad (16)$$

The reflected field \underline{u}^{re} from A^- can be found from the standard results on reflection of plane waves, as

$$\Delta u^{sc} \approx A \hat{\underline{x}}_S G_L(x_S) \exp(-ik_L \hat{\underline{x}}_S \cdot \underline{X}) \quad (17)$$

An expression for $\hat{\underline{x}}_S$ can be found elsewhere.⁵ Substitution of (17) into (14) yields the scattered longitudinal far-field as

$$\frac{\{u_m^{sc}(\underline{x}_Q)\}^L}{G_L(x_S) G_L(x_Q)} = -A \alpha_i(\hat{\underline{x}}_S) b_{ij;m}^{G;L}(\hat{\underline{x}}_Q) n_j I(k_L) \quad (18)$$

where

$$I(k_L) = ik_L \int_{A^+} \exp(-ik_L \hat{\underline{q}} \cdot \underline{X}) dA(\underline{X}) \quad (19)$$

and

$$\hat{\underline{q}} = (\hat{\underline{x}}_S + \hat{\underline{x}}_Q) \quad (20)$$

is a vector in the bisector-direction of \overline{OS} and \overline{OQ} . The far-field dependence on the crack occurs only through the function $I(k_L)$, which depends on the wave-number k_L and the bisector-vector $\hat{\underline{q}}$.

Various alternate expressions can be written for the integral $I(k_L)$. After introducing the ξ_1 and ξ_2 coordinates in the plane of the crack, see Fig. 8, $I(k_L)$ can be reduced to

$$I(k_L) = -\frac{\exp(-ik_L \hat{\underline{q}} \cdot \underline{X})}{q_1^2 + q_2^2} \int_C \underline{v} \cdot \hat{\underline{q}} \exp(-ik_L \hat{\underline{q}} \cdot \underline{\xi}) ds \quad (21)$$

where \underline{v} is the outward unit normal to the crack edge, and s is arc length measured along the crack edge C . By means of Eq. (21) the scattered longitudinal field is expressed as radiation generated by a superposition of sources over the edge of the crack. This kind of representation seems to be analogous to the method of equivalent currents, which has been explored by several authors in electromagnetic scattering theory.

It is convenient to consider still another system defined by (see Fig. 9)

$$\bar{\xi}_1 = q_1 \xi_1 + q_2 \xi_2; \quad \bar{\xi}_2 = -q_2 \xi_1 + q_1 \xi_2;$$

$$\bar{\xi}_3 = \xi_3 \quad (22)$$

Note that the $\bar{\xi}_1$ -axis is parallel to the projection

of q on the crack-plane. The q_1 used here are defined in the ξ -system. Then Eq. (18) can be reduced to the simple form⁵

$$I(k_L) = -\frac{\exp(-ik_L q \cdot X_0)}{q_1^2 + q_2^2} \int_C \exp(-ik_L \bar{\xi}_1) d\bar{\xi}_2 \quad (23)$$

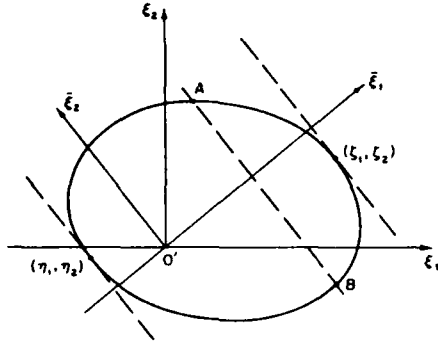


Fig. 9 Coordinates in the plane of the crack

Another useful approximation results by introducing local coordinates near the points E and F on C where the tangents are parallel to the ξ_2 -axis, (see Fig. 9). For instance, near $E(\zeta_1, \zeta_2, 0)$, the points on C can be represented by

$$\bar{\xi}_1 = \zeta_1 + \frac{1}{2!} s^2 \beta_0 + \frac{1}{3!} s^3 \beta_1 \quad (24)$$

$$\bar{\xi}_2 = \zeta_2 + s - \frac{1}{2!} s^3 \beta_0^2 \quad (25)$$

where s is measured from $E(\zeta_1, \zeta_2, 0)$ and β_0 and β_1 are the curvature of C and the value of $d\beta_0/ds$ at this point. We next substitute (24) and (25) into Eq. (23) and apply the stationary-phase approximation. The contribution from $E(\zeta_1, \zeta_2, 0)$ then becomes

$$I(k_L) \sim -\frac{(2\pi)^{1/2} e^{-i\pi/4}}{(q_1^2 + q_2^2)^{1/2}} k_L^{-1/2} \exp(-ik_L(\zeta_1 + q \cdot X_0)) \quad (26)$$

where

$$\zeta_1 = (a^2 q_1^2 + b^2 q_2^2)^{1/2} \quad (27)$$

A similar contribution arises also from $F(\eta_1, \eta_2, 0)$. Details of the derivation of Eqs. (21), (23) and (26) can be found in Ref. 5.

It is of interest to note that for a crack of elliptical shape defined by

$$\xi_1^2/a^2 + \xi_2^2/b^2 = 1; \quad \xi_3 = 0 \quad (28)$$

Eq. (21) can be evaluated analytically to give

$$I(k_L) = -2\pi i \frac{ab}{\rho} J_1(k_L \zeta_1) \exp(-ik_L q \cdot X_0) \quad (29)$$

where $J_1(\cdot)$ is the cylindrical Bessel function, and ζ_1 is defined by Eq. (27). The simple result given by (29) in conjunction with (18) has been shown to give quite good agreement with experimental results.¹¹ It has also proven to be very useful in practical inversion procedures based on the application of adaptive learning networks.¹²

An asymptotic expression for the Bessel function $J_1(k_L \zeta_1)$ for $k_L \zeta_1 \gg 1$ may be written as

$$J_1(k_L \zeta_1) \sim -\frac{1}{2} \left(\frac{2}{\pi k_L \zeta_1} \right)^{1/2} \{ \exp[-i(k_L \zeta_1 - 3\pi/4)] + \exp[i(k_L \zeta_1 - 3\pi/4)] \} \quad (30)$$

and it may be checked that the first term in (30) corresponds to the contribution from E stated by (26), while the second term corresponds to the contribution from F.

INVERSION INTEGRALS

The different forms of $I(k_L)$ in Eqs. (21), (23) and (26) suggest simple Fourier-type inversion integrals to recover the size, shape and orientation of a crack from the far-field data. The following inversion integrals have been investigated in some detail in Ref. 5.

$$1. \quad f_1^*(\lambda) = \int_{-\infty}^{\infty} \exp(ik_L q \cdot \lambda) f(k_L) dk_L \quad (31)$$

$$2. \quad f_2^*(\lambda) = \int_{-\infty}^{\infty} k_L^2 \exp(ik_L q \cdot \lambda) f(k_L) dk_L \quad (32)$$

where λ defines any test-point in the medium.

Application of the operator of Eq. (31) to the expression for $I(k_L)$ in Eq. (23) gives

$$I_1^*(\lambda) = -\frac{1}{(q_1^2 + q_2^2)^{1/2}} \int_C \delta[q \cdot (\lambda - X_0) - \bar{\xi}_1] \frac{d\bar{\xi}_2}{d\bar{\xi}_1} d\bar{\xi}_1 \quad (33)$$

where we have used the relation

$$\int_{-\infty}^{\infty} e^{ik_L \rho} dk_L = 2\pi \delta(\rho) \quad (34)$$

Evaluating the integral in Eq. (33) by the sifting property of the δ -function we obtain

$$I_1^*(\lambda) = \begin{cases} \frac{-1}{(q_1^2 + q_2^2)^{1/2}} \left[\left(\frac{d\bar{\xi}_2}{d\bar{\xi}_1} \right)^A + \left(\frac{d\bar{\xi}_2}{d\bar{\xi}_1} \right)^B \right]_{\bar{\xi}_1 = \kappa}; & (\eta_1 < \kappa < \zeta_1) \\ 0, & (\kappa < \eta_1; \kappa > \zeta_1) \end{cases} \quad (35)$$

$$\quad (36)$$

where

$$\kappa = q \cdot (\lambda - X_0) \quad (37)$$

Here the range of variation of $\bar{\xi}_1$ on C is given by $\eta_1 < \bar{\xi}_1 < \zeta_1$, where η_1 and ζ_1 were defined earlier

AD-A094 826 ROCKWELL INTERNATIONAL THOUSAND OAKS CA SCIENCE CENTER F/O 11/2
PROCEEDINGS OF THE DARPA/AFML REVIEW OF PROGRESS IN QUANTITATIV--ETC(U)
JUL 80 D O THOMPSON, R B THOMPSON F33615-74-C-5180
UNCLASSIFIED SC595.70AR AFMIL-TR-80-4078 NL

5 of 8

000020



in the context of the local coordinate system. In Eq. (35) A and B are the points at which the plane $\xi_1 = \kappa$ intersects the crack edge C when $\eta_1 < \kappa < \zeta_1$. At the extreme positions $\kappa = \zeta_1$ the gradient terms in Eq. (35) become infinite, usually, in the inverse square-root sense, as will later be illustrated by the example of an elliptical crack.

In practice, we can choose λ along the q -direction from 0 and determine the finite layer normal to q which contains the crack. The singular behavior of the gradient terms will be the principal test for identification of the end-planes of the layers.

The inverse operator of Eq. (31) when applied to Eq. (29) gives

$$I_1^*(\lambda) = \begin{cases} \frac{2\pi ab}{\zeta_1^2} \frac{\kappa}{(\zeta_1^2 - \kappa^2)^{1/2}}; & |\kappa| < \zeta_1 \\ 0; & |\kappa| > \zeta_1 \end{cases} \quad (38)$$

which clearly exhibits the inverse square root singularity at $\kappa = \pm \zeta_1$, where κ is defined in Eq. (37). Conversely it is not difficult to verify that the planes

$$\kappa = \pm \zeta_1 \quad (40)$$

touch the ellipse at the following points in the ξ -system:

$$\left(\pm \frac{q_1 a^2}{\zeta_1}, \pm \frac{q_2 b^2}{\zeta_1}, 0 \right) \quad (41)$$

These results verify that the application of the inversion integral of Eq. (31) to the expression for the scattered field of longitudinal motion given by Eq. (29), yields two planes which touch the edge of the crack.

It is often desirable to identify the end planes of the layer by a singularity of the Dirac delta function type. To this end we apply the inverse operator defined by Eq. (32) to the stationary phase approximation of $I(k_L)$ given by Eq. (26). This gives

$$I_2^*(\lambda) \sim - \frac{(2\pi)^{3/2} e^{-i\pi/4}}{(q_1^2 + q_2^2)(\beta_0)^{1/2}} \delta(\kappa - \zeta_1) - \frac{(2\pi)^{3/2} e^{i\pi/4}}{(q_1^2 + q_2^2)(\beta_0)^{1/2}} \delta(\kappa - \eta_1) \quad (42)$$

These expressions have the desired δ -function behavior across the planes $\kappa = \zeta_1$ and $\kappa = \eta_1$.

NUMERICAL EXAMPLES

Source and receiver in a plane of symmetry of the crack. The inversion procedure simplifies tremendously if it can be assumed a-priori that both the source and the receiver are located in a plane of symmetry of the crack. The inversion procedure then becomes essentially two-dimensional. Numerical

examples have been discussed in Refs. [5] and [13]. An iteration procedure which improves the accuracy was discussed in some detail in Ref. [5]. Reference [5] also includes an application of the inversion method to the experimental data of Ref. [9].

The 3-D crack. As a 3-D example we consider an elliptical crack of semi-major and semi-minor axes a and b respectively. Relative to a coordinate system at the center of the crack, the ellipse is defined by Eq. (28). The diffracted far-field will be assumed in the form discussed earlier, with $I(k_L)$ given by Eq. (29), in terms of a Bessel function. For any given pair of source and observation points, the inverse operator of Eq. (31) will then lead to a pair of end-planes touching the crack edge as given by Eq. (40). The plane of the crack and segments of the crack-edge will now be constructed by using the far-field diffraction data from two source locations S_k , $k = 1, 2$ and a set of observation points Q_n , $n = 1, \dots, 20$. For our numerical example the spherical coordinates of S_k ($k = 1, 2$) are taken as $(25, \pi/6, \pi/2)$ and $(25, \pi/6, 2\pi/3)$.

The points Q_n are taken at $\xi^{(n)}$ where

$$\xi_1^{(n)} = 10 + (n-5) \sin(\pi/3) \cos(3\pi/4)$$

$$\xi_2^{(n)} = 10 + (n-5) \sin(\pi/3) \sin(3\pi/4)$$

$$\xi_3^{(n)} = (n-5) \cos(\pi/3), \quad n = 1, \dots, 20$$

A tentative origin 0 in the neighborhood of the crack is taken at $(0.2, 0.3, 0.15)$. The inversion integral then leads to a number of layers for given source and observation points as described earlier. For a source at S_k and an observation point at Q_n the pair of layer-end-planes $\Omega(k, n; p)$, $p = 1, 2$ obtained from Eq. (40) are defined by

$$q_1(k, n) \xi_1 + q_2(k, n) \xi_2 = \pm \{a^2 q_1^2(k, n) + b^2 q_2^2(k, n)\}^{1/2} \quad (43)$$

where \pm signs correspond to $p = 1, 2$, respectively. The bisector vector $q(k, n)$ is associated with OS_k and OQ_n .

For large n , each set of planes $\Omega(k, n; p)$ defined by Eq. (43) for a given k , forms a prismatic surface, which will touch the crack-edge C at a set of points. These points span a polygon, which approximates a segment $C(k; p)$ of the edge C. The intersection of the two prismatic surfaces for the same p but $k = 1$ and $k = 2$, respectively, will lead to points on C common to $C(1; p)$ and $C(2; p)$. We can use these points to generate the crack-plane. The above points are obtained as follows. The prismatic surface formed by the first-set of planes $\Omega(1, n; p)$ will be intersected by the various individual planes of the set $\Omega(2, n; p)$ along a set of polygons $\Gamma(2, n; p)$, which we initially determine. The points where the polygons of this set intersect in 3-D space constitute points for an approximate determination of the crack-plane. These points are easily found by testing where any polygon $\Gamma(2, n; p)$ with a given n is intersected by the remaining planes of $\Omega(2, n; p)$. The plane of the crack can thus be determined, and once this has been achieved the

intersection of this plane with the set of planes $\Omega(k,n;p)$ gives the desired tangent lines enveloping the crack edge. For $a = 1$ and $b = 0.5$, Table 1 gives the vertices of the polygon formed by the tangent-lines corresponding to $\Omega(1,n;1)$ which envelopes the arc $C(1;p)$ with $p = 1$. These points evidently lie very close to the crack-plane $\xi_3 = 0$. The last column of Table 1 shows that these points lie very close to the elliptical boundary as well. A similar set of points corresponding to the arc $C(1;p)$ with $p = 2$ is also generated by the above calculations, since they define an opposite quadrant of the crack-edge referred to the origin at the center of the crack.

The extent of the crack-edge recovered will depend on the relative locations of S_k and Q_n with respect to the crack-plane. A proper choice can usually be made once the crack-plane is determined from an initial configuration.

ξ_1	ξ_2	ξ_3	$\xi_1^2/a^2 + \xi_2^2/b^2 - 1$
.85076	.26265	.00041	-.26033E-03
.82938	.27927	.00036	-.16001E-03
.80476	.29679	.00031	-.40334E-04
.77657	.31505	.00026	.10016E-03
.74455	.33388	.00020	.26192E-03
.70851	.35301	.00014	.44407E-03
.66841	.37211	.00007	.64425E-03
.62437	.39084	.00000	.85866E-03
.57670	.40881	-.00007	.10824E-02
.52589	.42566	-.00014	.13099E-02
.47260	.44107	-.00022	.15359E-02
.41760	.45480	-.00029	.17556E-02
.36175	.46667	-.00036	.19654E-02
.30585	.47661	-.00043	.21628E-02
.25070	.48464	-.00049	.23466E-02
.19695	.49085	-.00055	.25162E-02
.14513	.49538	-.00061	.26719E-02
.09565	.49841	-.00066	.28143E-02
.04877	.50014	-.00071	.29440E-02

Table 1: Computed coordinates of vertices of polygon enveloping the crack edge, for $a = 1$ and $b = 0.5$. Coordinates relative to origin at center of elliptical crack.

ACKNOWLEDGEMENT

This paper was sponsored by the Center for Advanced NDE operated by the Science Center, Rockwell International, for the Advanced Research Projects Agency and the Air Force Materials Laboratory under Contract F33615-74-C-5180. The assistance of A. K. Gautesen and H. McMaken (direct problem) and K. Viswanathan and A. Norris (inverse problem) is gratefully acknowledged.

REFERENCES

1. Achenbach, J. D., Gautesen, A. K., and McMaken, H., "Application of Geometrical Diffraction Theory to QNDE Analysis," in Proceedings of the ARPA/AFML Review of Progress in Quantitative NDE, 1978 (edited by D. O. Thompson), Science Center, Rockwell International, Thousand Oaks, Cal., January 1979, pp. 321-330.
2. Achenbach, J. D., Gautesen, A. K., and McMaken, H., "Diffraction of Elastic Waves by Cracks - Analytical Results," in Elastic Waves and Non-Destructive Testing of Materials (edited by Y. H. Pao), American Society of Mechanical Engineers, AMD-29, 1978, pp. 33-52.
3. Cohen, J. K., Bleistein, N. and Elsley, R. K., "Nondestructive Detection of Voids by High-Frequency Inversion Technique," in Proceedings of the ARPA-AFML Review of Progress in Quantitative NDE, 1978 (edited by D. O. Thompson), Science Center, Rockwell International, Thousand Oaks, Cal., January 1979, pp. 454-458.
4. Cohen, J. K. and Bleistein, N., "The Singular Function of a Surface and Physical Optics Inverse Scattering," WAVE MOTION 1, 1979, pp. 153-162.
5. Achenbach, J. D., Viswanathan, K. and Norris, A., "An Inversion Integral for Crack-Scattering Data," WAVE MOTION 1, 1979, in press.
6. Achenbach, J. D., and Gautesen, A. K., "Geometrical Theory of Diffraction for Three-D Elastodynamics," J. Acoust. Soc. Amer., 61, 1977, pp. 413-421.
7. Gautesen, A. K., Achenbach, J. D., and McMaken, H., "Surface-Wave Rays in Elastodynamic Diffraction by Cracks," J. Acoust. Soc. Amer., 63, 1978, pp. 1824-1831.
8. Adler, L. and Lewis, K., "Frequency Dependence of Ultrasonic Wave Scattering from Cracks," in Proceedings of the ARPA/AFML Review of Progress in Quantitative NDE, 1978, (edited by D. O. Thompson), Science Center, Rockwell International, Thousand Oaks, Cal., January 1979, pp. 393-399.
9. Achenbach, J. D., Adler, L., Lewis, D. Kent, and McMaken, H., "Diffraction of Ultrasonic Waves by Penny-Shaped Cracks in Metals: Theory and Experiment," J. Acoust. Soc. Amer., in press.
10. Gautesen, A. K., "On Matched Asymptotic Expansion for Two-Dimensional Elastodynamic Diffraction by Cracks," WAVE MOTION 1, 1979, pp. 127-140.
11. Adler, L. and Lewis, D. K., "Diffraction of Ultrasonic Waves by Elliptical Cracks in Metals," this volume.
12. Whalen, M. F., O'Brien, L. J., Mucciardi, A. N., "Application of Adaptive Learning Networks to Determine Size and Orientation of Two-Dimensional Flaws in Solids," this volume.
13. Achenbach, J. D., Norris, A., and Viswanathan, K., "Inversion of Crack Scattering Data in the High-Frequency Domain," Recent Developments in Classical Wave Scattering: Focus on the T-Matrix Approach, Pergamon Press, 1980.

SUMMARY DISCUSSION
(J. D. Achenbach)

- Unidentified Speaker: I wasn't quite sure on that one plot that you put on and took off, where there were experimental points. Is that the same thing as Bernie talked about last year? Is Bernie here? Is that the same kind of plot you showed last year? Is that the comparison between your theory and Laszlo's experiments?
- J. Achenbach: Okay. I will show you that one. Laszlo will talk about similar things, but here is plotted the relative amplitude versus the frequency. At three, four locations. The angle of observation is at 35, 45 degrees, 55 degrees, 60 degrees. It compares theoretical results which were obtained on the basis of these ray theory considerations which I pointed out, and then the dots are the points that Laszlo measured. So he has gone up to 14 megahertz. The point I was trying to make with this plot is that it is important for the inverse method to know something about the spacing of the peaks because the peaks come about because of the interference of rays. The interference of the rays is related to the dimension of the crack. So, if I can get this spacing of the peaks reasonably accurately, I am in relatively good shape. I can't get the magnitude right for two reasons. The specimen is immersed in a water bath. The transition from the solid to the water we only approximately describe. There is a certain damping effect there. And the titanium has a certain amount of damping. Perhaps the water also. So, it's natural that at a higher frequency the agreement becomes worse because of damping.
- Unidentified Speaker: The other question was: in your equation for the C.O.D., how do you devise change in the C.O.D.? Do you make C.O.D. measurements?
- J. Achenbach: No. These are computed.
- Unidentified Speaker: Laszlo will talk --
- J. Achenbach: Laszlo is not involved in this work. This is a different theory. What we did was, we said we can either use ray theory all the way out in the field away from the crack and then we get conceivably into trouble at shadow boundaries. And that is just because of the asymptotic nature of the theory. An alternative would be just to use ray theory to compute the crack opening displacement. In other words, the fields on the crack faces. And then stick that result into this elastodynamic representation theorem, and then things integrate nicely out, and you get the field everywhere bounded. You get it bounded at shadow boundaries, you get it bounded at caustics - and that's the idea of introducing the crack opening displacement.
- Jim Krumhansl (Cornell University): Could I just add: the point about this, of course, is that in a certain sense the method exhibits some of the properties that one could have gotten from acoustics, simply a scaled approximation, but now you can pick out a particular type of incident wave and you can compare the features of the longitudinal to the transverse wave, and elastodynamics allows you to get some semi-quantitative, fairly quantitative, measure of the magnitude of the relative features in those different polarizations.
- J. Achenbach: That's right. Of course, the elastodynamics appears when the coupling between longitudinal and shear waves is built in, because it's built in, in the way the signals distribute over those two cones. If I had pure acoustics, I would only have one cone. If I had treated this problem as a pure acoustic problem, the longitudinal wave diffracted by an edge would produce just a diffracted longitudinal wave. Here it produces both. However, we never use those transverse waves because, I guess, in experiments you only work with the first arrival anyway. As soon as you can measure transverse signals, then we will stick in these other transverse signals, and you get the whole field.
- Jim Rice (Brown University): Just for clarification, the inversion procedure is based on extremely high frequencies in that limited crack face is motion taken into account?
- J. Achenbach: If you can follow my hands here from the two crack tips, at low frequency you would have an ellipse. At high frequency you have waves on the crack faces; at still higher frequencies you have more waves. We ignore the wiggles due to secondary surface motions.

(continued)

J. Achenbach (discussion continued)

Jim Rice: When you compare your inversion procedure with experiments, how small must the wavelength in fact be compared to crack size for this kind of an approximation?

J. Achenbach: Okay. We have to let Laszlo discuss this; he will show that in the next talk because we used physical elastodynamics for an elliptical crack. You can actually work out analytically the results, and you get a Bessel function and compare it with experiments. The comparison was good for a wavelength range which he will show.

#

DIFFRACTION OF ULTRASONIC WAVES BY ELLIPTICAL CRACKS IN METALS

L. Adler and D. K. Lewis
Department of Physics
The University of Tennessee
Knoxville, Tenn. 37916

ABSTRACT

Ultrasonic spectrum analysis is used to study the frequency and angular behavior of diffracted longitudinal waves from elliptical cracks with arbitrary orientation in diffusion bonded titanium alloy. The aspect ratio of the cracks (ratio of major to minor axis) ranged from 1 to 8 and the bandwidth of the input signal was such that the scattering diameter was $ka \geq 1$. The experimental data are analyzed based on a recently developed elastodynamic diffraction theory (by Achenbach et al.). Some of the key parameters of the scattering data are identified to address the inverse problem.

INTRODUCTION

It has been recognized for some time that quantitative ultrasonic flaw characterization requires the understanding of interaction of ultrasonic waves with discontinuities in solids. The physical phenomenon describing this interaction is generally referred to as scattering, but in the region of $ka > 1$ (where k is the wave number and a is some dimension of the discontinuity) we speak of this interaction as diffraction. For the diffraction of ultrasonic waves by planar cracks Adler and Lewis¹ used Keller's² geometrical diffraction theory to analyze their experimental results. Achenbach, Gautesen and McMaken³ extended geometrical theory to the three-dimensional diffraction by cracks in solids where wave motions are governed by a scalar and a vector wave equation. This analysis for diffraction of elastic waves from circular cracks has been evaluated and compared to experimentally obtained results by Achenbach, Adler, Lewis and McMaken.⁴ In the same paper they obtained a simple formula for the inverse problem. Part of their results will be presented here. In addition, the diffraction of elastic waves by elliptical cracks of various eccentricities will be addressed.

THEORY

Elliptical Crack - Let's consider an elliptical crack in a linear elastic isotropic solid with major axis b and minor axis a . The orientation of the crack is described by angles α and β . β is measured from the major axis of the ellipse and α is the measure from the plane of the crack to the z axis; e.g., if $\alpha = 90$ the plane of the crack is in the xy plane. The longitudinal wave is incident to the crack from point (R_1, θ_1, ϕ_1) and with displacement amplitude u_i . The diffracted L wave with amplitude u^d is observed in space at a point which describes (R, θ, ϕ) . The problem is then to relate the angular and frequency dependence of u^d and u_i to the α , β , a and b . McMaken, Achenbach and Gautesen⁵ has obtained a closed form solution of the diffracted L waves from elliptical cracks in the far field. The diffracted field amplitude u^d is represented by the integral over a crack surface S :

$$u^d = \iint_S \tau_{3j,k} \Delta u_j d\sigma \quad (1)$$

where $\tau_{3j,k}$ is the part of the Green's function corresponding to waves of longitudinal motion and u_j is the crack opening displacement. Evaluating (1)

for the geometry described in Fig. 1, one obtains

$$u^d = i \exp \left\{ \left[\left(\frac{C_L}{C_T} \right)^2 - 2(P_1^2 + P_2^2) \right] \left[\left(\frac{C_L}{C_T} \right)^2 - 2(\hat{x}_1^2 + \hat{x}_2^2) \right] + 4\hat{x}_3 \left[\left(\frac{C_L}{C_T} \right)^2 - P_1^2 - P_2^2 \right]^{1/2} [P_1 \hat{x}_1 + P_2 \hat{x}_2] \right\} \frac{b P_3 J_1(h_L a r)}{r R |\hat{\chi}|} \quad (2)$$

where

$$k_L = \frac{\omega}{C_L}$$

$\hat{\lambda} = (P_1, P_2, P_3)$ defines the direction of propagation of incident wave,

$\hat{\chi} = |\hat{\chi}| (\hat{x}_1, \hat{x}_2, \hat{x}_3)$ defines the point of observation,

$C_L, (C_T)$ is the velocity of longitudinal (transverse) waves in the solid,

b is the length of the major axis,

a is the length of the minor axis,

$J_1(x)$ is the Bessel function of order one,

$$r = \left[\left(\frac{b}{a} (x_1 - P_1) \right)^2 + (x_2 - P_2)^2 \right]^{1/2},$$

$$R = \left[\left(\frac{C_L}{C_T} \right)^2 - 2(P_1^2 + P_2^2) \right]^2 + 4(P_1^2 + P_2^2) P_3^2 \left[\left(\frac{C_L}{C_T} \right)^2 - P_1^2 - P_2^2 \right]^{1/2}.$$

Equation (2) is programmed for various crack geometries to obtain some representative configurations of the diffracted field to choose the experimental parameters. For an ellipse with major axis 2500μ and minor axis 612μ and for a normally incident L wave, the amplitude (frequency ranges from 2 to 14 MHz) spectra is calculated for three different polar angles— $\theta = 30^\circ, 52^\circ$, and 60° . The observation point moves gradually from major to minor axis (Fig. 2). There are at least three conclusions which can be drawn from the 3D plots shown on Fig. 2: (a) along a fixed axis the periodicity in the frequency will decrease with increased θ ; (b) for a given θ the periodicity will increase going from major to minor axis; and (c) the scattered amplitude will increase as the observation point is approaching the minor axis from the major

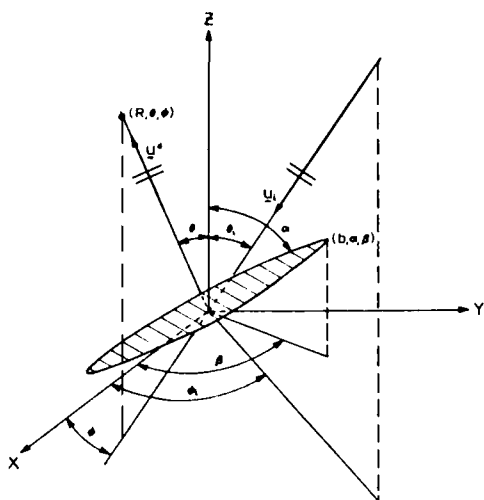


Fig. 1. Geometry of Ultrasonic Wave Diffraction from an Elliptical Crack in Solid.

axis. The effect of different aspect ratio (ratio of major to minor axis) of the elliptical crack on the diffracted field is shown on Fig. 3. For $b/a = 1, 2, 4, 8$ the amplitude vs. frequency and azimuthal angle (changing from along the major to minor axis) for a fixed polar angle of 60° is given. Since the b , the major axis, for all four cases was 2500μ , the amplitude spectra is the same along the major axis. The periodicity (separation between consecutive frequency maxima) will increase along the minor axis and it is largest for the elliptical crack with the largest aspect ratio. The energy of the scattered energy along the major axis is always less than along the minor axis and the difference of the energy scattered along these axes will increase with aspect ratio. The elliptical crack with aspect ratio of 8 shows very little energy scattered along the major axis. The special case is the elliptical crack with aspect ratio of 1 is the circular crack. In a different formalism by using geometrical theory of diffraction⁴ analytical expressions for the diffraction of longitudinal waves from penny-shaped cracks has been obtained. This analysis accounts for the liquid-solid interface which is in line with our experimental technique. It also leads to a simple inversion procedure, therefore the results will be repeated here briefly.

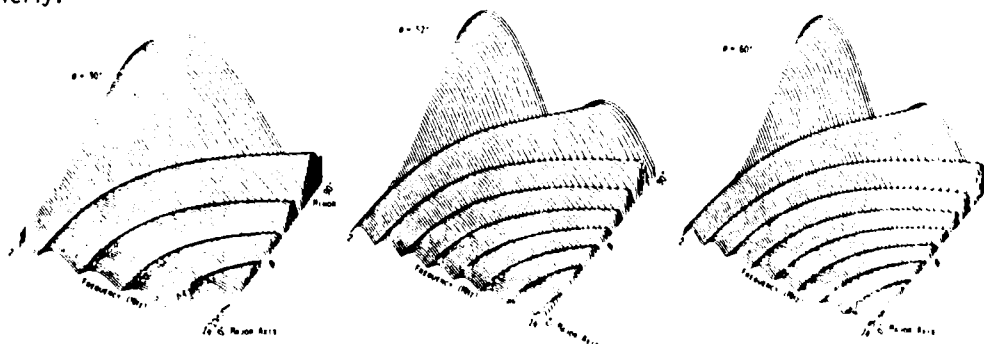


Fig. 2. Theoretical Amplitude Spectra of Normal Incidence L Wave Scattered from $2500\mu \times 625\mu$ Elliptical Cracks in Titanium.

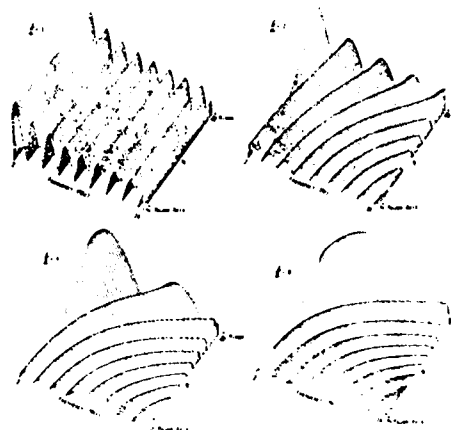


Fig. 3. Theoretical Amplitude Spectra of Normal Incidence L Waves Scattered from Elliptical Cracks. Polar Angle is 60° .

Penny-Shaped Cracks. An incident L wave diffracted from a penny-shaped crack produces diffracted rays at the two extreme edges of the crack (see Fig. 4). The diffracted rays are refracted at the solid-liquid interface and combined at point B. The diffracted field u_L at that point is given as

$$u_L \sim F(\theta, \theta_0) \exp[i\omega(S/c_L + \bar{S}/c_L + \bar{S}/c_F) + i\pi/4] U_0 \lambda_F$$

$$F(\theta, \theta_0) = H_1 \exp[-i(\omega a/c_L)(\cos\theta - \sin\theta_0)] + H_2 \exp[i(\omega a/c_L)(\cos\theta - \sin\theta_0)]. \quad (3)$$

Comments on the Inverse Problem. In the previous sections expressions were obtained for the diffracted field of ultrasonic waves from cracks when the size, shape, and orientation of the crack are known. This is the so-called direct problem. The aim of the ultrasonic scattering studies by flaws is to characterize them from the measured scattered field which is the inverse problem. The fact that the frequency distribution of the diffracted field leads to simple inversion procedure has been recognized for special cases earlier⁴ and can be shown from the theoretical analysis. From Eq. (3) the absolute magnitude (modulus) in the far field can be written as

$$|F| = \left\{ |H_1|^2 + |H_2|^2 + 2|H_1||H_2|\sin[2(\omega a/c_L)] \right. \\ \left. (\cos\theta - \sin\theta_0) \right\}^{1/2}. \quad (4)$$

This result implies that the amplitude of the diffracted field is modulated with respect to ω/c with period

$$P = \pi/a |\cos\theta - \sin\theta_0| \quad (5)$$

where θ is the scattering angle in the solid, a is the radius of the crack, and θ_0 is the orientation of the crack. For two different scattering angles the amplitude spectra can be used to evaluate the size and orientation of the penny-shaped crack by using Eq. (5). In the first approximation the diffracted field can be inverted also by expanding the Bessel function in Eq. (2). Along the major and minor axes the diffracted field is modulated in the same fashion as obtained in Eq. (5).

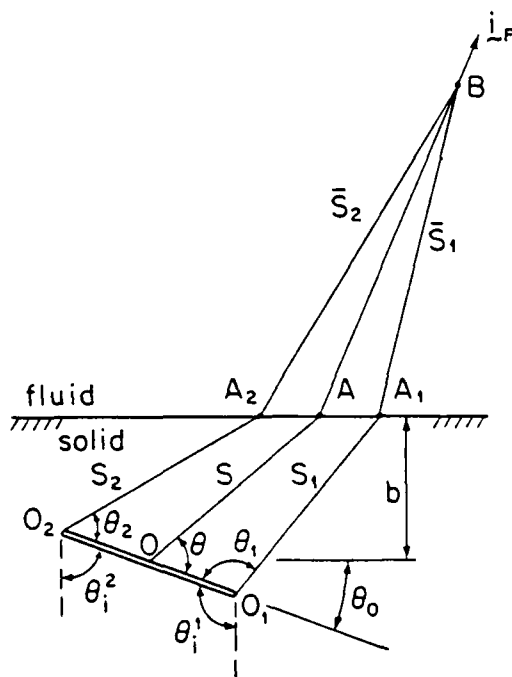


Fig. 4. Geometry in the Plane of Symmetry of a Penny-Shaped Crack.

EXPERIMENT

Experimental System. The present configuration of the ultrasonic data acquisition and processing system is illustrated in Fig. 5. The SCR pulser produces a fast rise-time high voltage (162 volts) negative spike with an exponential return to zero. This wide band electrical pulse excites an untuned, highly damped ceramic transducer with center frequency of 10 MHz. The ultrasonic pulse (pulse length ~ 1 μ sec) which is produced contains a broad band of frequencies. Ultrasound scattered by the target is received by either (1) the transmitting transducer (pulse-echo) or (2) a receiving (identical) transducer (pitch-catch). The electrical pulse produced by this receiving transducer is amplified by a wide bandwidth gain stage. A stepless gate is used to select a portion of the received signal for

further analysis. Signals falling outside the gated regions are highly attenuated. An oscilloscope displays both the entire receiver output and the section of waveform passed by the gate.

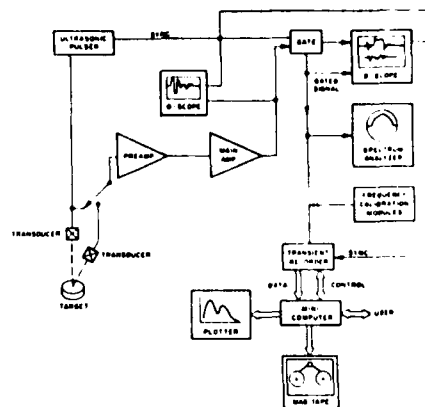


Fig. 5. Experimental System.

The frequency content of the gated waveform is presented on an analog spectrum analyzer. The gated pulse may also be captured and stored through use of the digital acquisition system. A transient recorder samples the ultrasonic signal at 100 MHz, and stores the amplitude at discrete times in its digital memory. The minicomputer controls the acquisition of the ultrasonic pulse and then transfers the digitally represented signal from the recorder to the minicomputer memory. The signal may also be permanently stored by writing it onto magnetic tape. Processing of the ultrasonic signal (Fast Fourier Transform, correlation and deconvolution) is performed on the minicomputer. An electrostatic plotter provides a visual display of pertinent information. For the Fourier Transform both amplitude and phase spectra can be calculated. In this experiment the amplitude spectra are used only. The digital amplitude spectra is monitored by the analog spectra (i.e., the spectrum offered by the spectrum analyzer).

Experimental Technique and Procedure. The technique used is shown in Fig. 6. The sample, which is a disk (2.5 x 10 cm) titanium alloy with a flat surface, is immersed in water. The transmitter launches a longitudinal wave to the liquid-solid interface at some angle. For nonnormal incidence both L and T waves are produced in the metal. The cavity can be insonified either by the L wave or by the T wave with incident angle α . At the cavity the waves are scattered and mode converted. The scattered waves are received and analyzed separately due to their separation in time. The various types of waves present are illustrated schematically on Fig. 7 by the so-called time mapping. The interface corresponds to $t = 0$ where t is the time in μ sec. A is the incident pulse whose position is shown 3.5 μ sec before it hits the interface. B and D are the T and L waves at $t = 1.5$ μ sec after they entered the sample. With the illustrated configuration only the L wave will interact with the cavity. At a later time, at $t = 4.5$ μ secs F and G are the scattered T and L waves and are clearly separated due to their differing velocities. C and E are the positions of T and L waves at $t = 4.5$ μ secs not interacting with the defect.

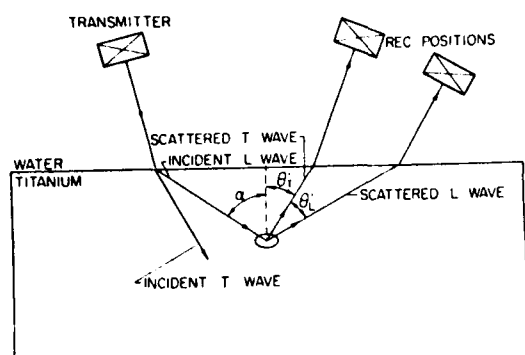


Fig. 6. Experimental Technique

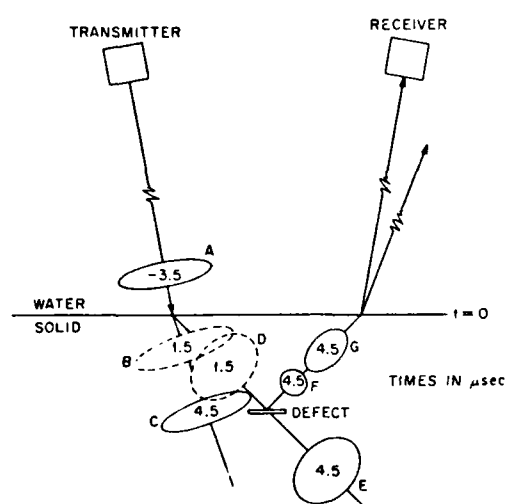


Fig. 7. Time Mapping of Transverse and Longitudinal Waves before and after Interaction with Defect. (A) Incident Wave in Water; (B) and (C) Transverse Waves; (D) and (E) Longitudinal Waves; (F) Scattered Transverse; (G) Scattered Longitudinal.

A specially designed goniometer is used (Fig. 8) to mount the transmitter and the receiver. The position of both transmitter and receiver in polar angle can be changed separately. A special feature of the goniometer is its flexibility of keeping the polar angle fixed and varying the azimuthal angle. This latter feature is especially important for elliptical cracks because of the asymmetry in the scattered field along the different axes of the ellipse (see Figs. 2 and 3).

The selection of the polar and azimuthal angles were so that the data could also be used by Adaptronics's data base for inversion (see their results in this report).

Data Correction. In order to analyze the experimental results based on the analytical prediction the effect of the transducers and the crack had to be separated. In a linear time invariant system this is done in the frequency domain by dividing the frequency response from a system by the so-called transfer function. In this problem the spectra of the transmitted signal through the material (without

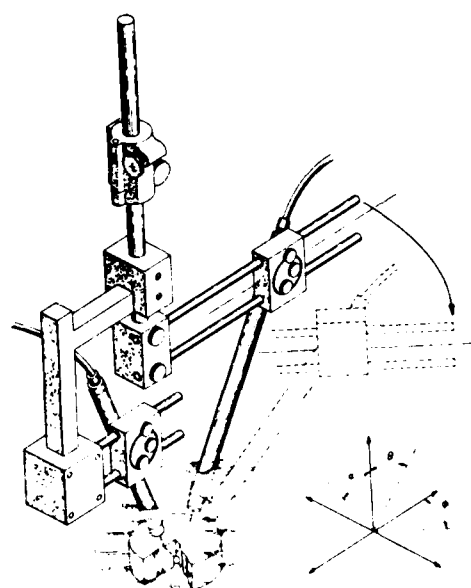


Fig. 8. Multiplane Ultrasonic Goniometer.

the crack) is considered the transfer function. Figure 9A shows the RF signal transmitted (normally) through a 2.5 cm thick parallel flat smooth titanium (flawless) disk immersed in water. There is usable energy through the frequency range from 2 to 15 MHz. The amplitude spectrum shown on Fig. 9B is the transfer function of the system. The spectrum of the scattered wave is then divided by this transfer function.

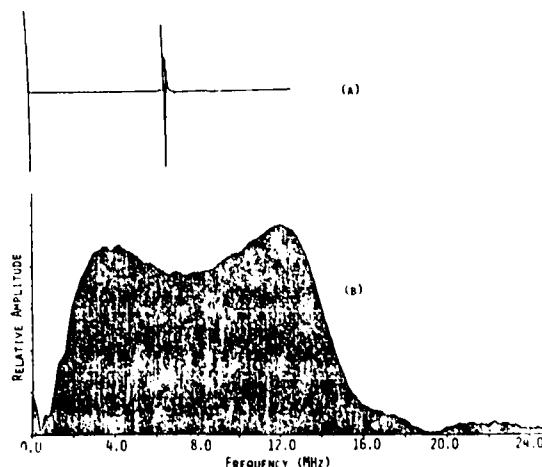


Fig. 9. Transfer Function. (A) RF Signal; (B) Amplitude Spectrum.

RESULTS

3-Dimensional Display of the Experimental Data. The diffracted waveforms have been processed, stored, and collected from different points in space and displayed in a 3D fashion to obtain an overall view of the diffracted field due to different cracks. Typical displays are shown on Fig. 10 where the diffracted amplitude vs. frequency and azimuthal angle by 15° intervals from major to minor axes is

shown. The ellipse is $2500\mu \times 1250\mu$ and the incident wave is normal to the crack. The polar angles were 52° and 60° . The amplitude of the scattered wave is higher toward the major axis as was predicted by the theory (Figs. 3 and 4). Another feature of the diffracted field is shown on Fig. 11. The amplitude is plotted vs. frequency and polar angle for three cases when the receiver is placed along the minor axis along 45° and along the major axis. The polar angles change from 30° to 60° in 5° intervals. The elliptical crack's dimensions are $2500\mu \times 612\mu$. Although these 3D plots are very useful to obtain qualitative features of the diffracted field, the comparison between experiment and theory was carried out in 2-dimensional displays.

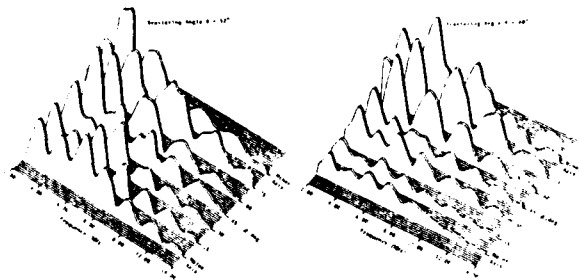


Fig. 10. Experimental Amplitude Spectra of Normal Incidence L Wave Scattered from a $2500\mu \times 1250\mu$ Elliptical Crack in Titanium.

Comparison between Theory and Experiment. The experimental data have been normalized (divided by the transfer function, Fig. 9B) and the diffracted amplitude is shown vs. frequency for the penny-shaped crack of 2500μ radii. Two different polar angles, 45° and 55° , are shown on Figs. 12 and 13. The solid curve is calculated from Eq. (3) and the dots are experimental points. The agreement is good for the lower frequencies. For higher frequencies the attenuation is significant in water and theory does not include attenuation.

On Fig. 14 the experimental data is compared to theory for the $2500\mu \times 1250\mu$ elliptical crack. The data are displayed when the receiver is along the minor and along the major axis. The receiver's position is such that the polar angle is 30° . The agreement with theory is very good for the periodicity but the measured amplitudes are lower at

high frequencies than predicted by theory. Similar results are shown for the case of the 60° polar angles (Fig. 15).

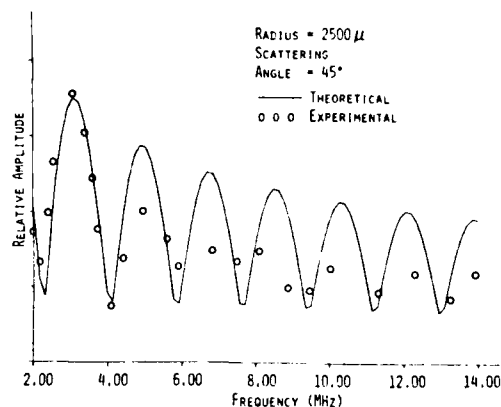


Fig. 12. Amplitude Spectrum of 45° Scattered Longitudinal Wave.

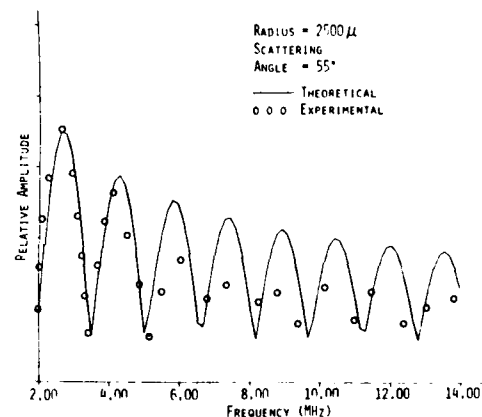


Fig. 13. Amplitude Spectrum of 55° Scattered Longitudinal Wave.

Determination of Crack Size. The periodicity of the amplitude spectra gives very good agreement between experiment and theory which is the basis for inversion. On Table 1 the result of inversion is shown for the penny-shaped crack for different

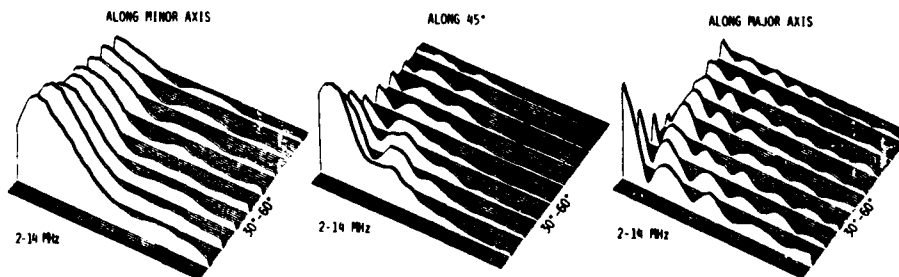


Fig. 11. Experimental Data for L-L Scattering from a $2500\mu \times 625\mu$ Elliptical Crack.

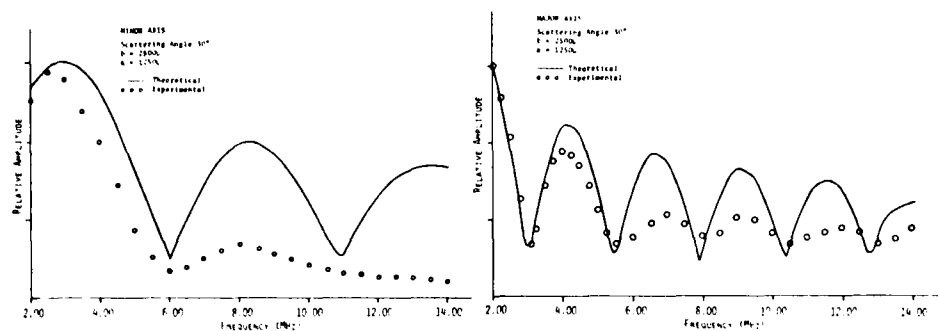


Fig. 14. L-L Scattering from an Elliptical Crack.

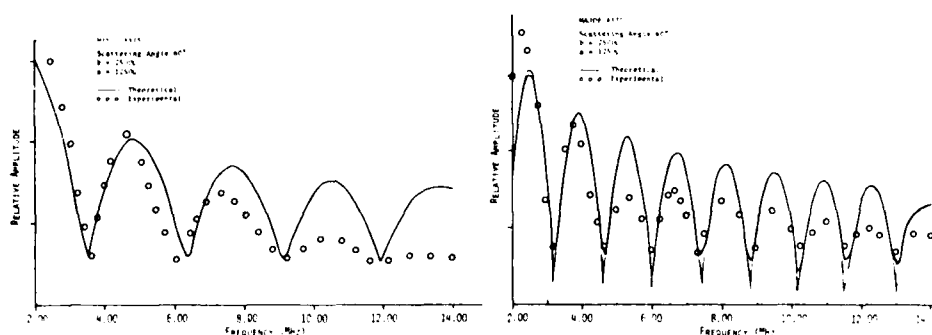


Fig. 15. L-L Scattering from an Elliptical Crack.

Table 1

Result of Size Determination from the Spectral Components of the Diffracted Wave

Scattering θ_L Angle	Δf_{\max}	Measured Radius of the Crack in μ
35	2.18	2530
40	1.87	2630
45	1.83	2450
50	1.68	2460
55	1.60	2410
60	1.47	2500
65	1.39	2510

polar angles. The largest deviation is less than 5% between measured and actual values of the 2500 μ circular crack. The result of the inversion for the elliptical crack is given in Table 2. From several angular measurements the averages were taken. The major and minor axes are calculated from Eq. (4) and compared to the actual values. The agreement is good except for the case of the major axis of the 8 to 1 aspect ratio ellipse. The signal along the major axis is too noisy to be meaningfully analyzed in the frequency domain. Additional data for nonnormal cases have also been taken and sent to Adaptronics for their data base (see details in this report).

Correction for Attenuation. The agreement between theory and experiment for the periodicity in the amplitude spectra is very good. The theoretical prediction of the amplitude values for the higher frequencies are consistently larger than is observed experimentally. It appears that one of the reasons

is the attenuation in water. At a water column of 15 cm (the distance between the sample surface and the receiving transducer) the attenuation is .033 f^2 dB, where f is in MHz. Because of the square dependence in frequency the effect of attenuation is more dominating at higher frequencies. We have corrected the theoretical curve with attenuation as shown on Fig. 16. The solid line is the theoretical curve without attenuation. The theoretical curve with attenuation correction (dashed line) agrees much better with experimental data points. The effect of the attenuation in the titanium is less significant but it appears that the complete report should include the effect of attenuation in both the solid and in water to calculate the diffracted field due to cracks.

Table 2

Determination of Major (B) and Minor Axis (A) of Elliptical Cracks in Titanium from Scattered Amplitude Spectra

(B) In Microns		(A) In Microns	
Actual	Measured	Actual	Measured
2500	2498	2500	2498
2500	2587	1250	1291
2500	2358	625	830
2500	--	312	285

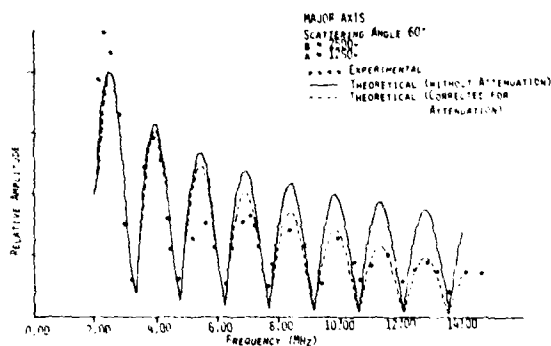


Fig. 16. L-L Scattering from an Elliptical Crack with Attenuation Correction.

SUMMARY

Experimental studies of the diffraction of elastic waves from elliptical cracks have been carried out. The diffracted amplitudes were measured in a broad range of frequencies as a function of polar and azimuthal angles for cracks with various eccentricities. Key parameters were identified such as periodicity in amplitude spectra, total scattered power to aid the inversion process. From the experimental data the major and minor axes were determined with good accuracy by using simple expressions obtained from diffraction theory. The diffraction theory calculations accurately predicting the periodicity of the amplitude spectra were observed in the experiment. The amplitude values at higher frequencies are predicted too high. This can be corrected by the attenuation of the diffracted waves in the water column.

ACKNOWLEDGMENT

This research was sponsored by the Center for Advanced NOE operated by the Science Center, Rockwell International, for the Advanced Research Projects Agency and the Air Force Materials Laboratory under Contract F32615-74-C-5180.

REFERENCES

1. Laszlo Adler and D. K. Lewis, J. Acoust. Soc. Am. 57a, Supp. No. 1 (1975).
2. J. B. Keller, J. Appl. Phys. 28, 426 (1957).
3. A. K. Gautesen, J. D. Achenbach, and H. McMaken, J. Acoust. Soc. Am. 63, 1824-1831 (1978).
4. Jan D. Achenbach, Laszlo Adler, D. Kent Lewis, and Harry McMaken, accepted for publication in J. Acoust. Soc. Am.

LASER DETECTION AND IMAGING TECHNIQUES FOR SURFACE EXAMINATION

S. Ameri, E. A. Ash, U. Htoo, D. Murray and H. K. Wickramasinghe
University College, London
Torrington Place, London, WC1E 7JE

ABSTRACT

A coherent laser probe provides the basis for the recording of complex SAW distributions. Using three or more scans, the surface wave velocity can be deduced with an accuracy of a few parts in 10^4 . Such measurements are sufficiently sensitive to detect small changes in surface characteristics; as an example, results will be presented on the effect of doping a Si surface. It is also possible to improve the accuracy of the basic elastic constants of the material by reference to the velocity characteristic. Of particular importance is the fact that this technique provides evidence on the effective value of these constants close to a surface; it is, therefore potentially useful for surface layer characterisation.

Surface defects can be detected by means of scattered waves in both the forward as the reverse directions. In principle, either can be used to "image" the defect. Using both these components, the defect size and location can be determined with improved accuracy.

1.

INTRODUCTION

The detection of defects using surface acoustic waves is normally based on the observation of scattered waves, using either the transmitting transducer in a receiving mode, or an additional transducer dedicated to the reception role. In most cases, there is a concentration on the amplitude of received pulse signals. It is usually difficult to explore many different locations with the transducer(s). To some extent, the limitations of fixed locations can be overcome by resorting to frequency variation - which provides a change in the normalised distances. These effects may, however, be overlaid by the frequency dependence of the scattering function of the defect itself.

An alternative approach is based on the use of cw or pseudo-cw illumination, coupled with the measurement of the complex field distribution along one or a number of scan lines. At low frequencies, particularly below about 2MHz, one can hope to obtain a faithful record of such a field distribution using a stylus sensor. However, even at these frequencies, there are great benefits to be derived from the use of a laser probe, acting as a "non-contacting" sensor. Moreover, laser probing techniques can be extended to very high frequencies - our own experiments have reached 150 MHz and stopped there for lack of immediate application, rather than any formidable technical problems. In this paper, we will present some of the techniques of surface characterisation which can be implemented using such a laser probe.

It would be particularly attractive if it were possible to devise a non-contacting source, to complete the inspection system. It is, of course, well known that a high power pulsed electron or laser beam can generate intense acoustic waves; a number of groups are seeking to exploit this phenomenon. The idea has been given further credence recently by the emergence of photoacoustic microscopy (1), which

demonstrated the generation of significant acoustic powers in the 0.8 GHz frequency range. The generation of these waves is being studied using a numerical technique for determining temperature and, hence, stress distributions (2). In the remainder of the paper, we will confine ourselves to a discussion of the laser as a receiving sensor.

An immediate application of the laser probe is to the evaluation of the velocity characteristic of a surface. The basis of the method will be briefly described in section 2, and some recent results are presented in section 3. It turns out that the technique is capable of achieving a very high accuracy - of the order of a few parts in 10^4 . This is an improvement by about two orders of magnitude on the precision which can be achieved by computation based on the best available data of materials constants. It suggests that, perhaps, one might be able to improve our knowledge of these constants by working from SAW velocity data back to the constants. This process has been applied to LiNbO_3 , and the conclusions will also be presented in section 3.

The detection of defects using laser probing techniques involves the evaluation of scattered waves from the defect. One can use these to "image" the defect, if this is sufficiently large. One can, alternatively, as in usual scattering experiments, deduce a great deal of information about the defect without attempting the reconstruction of an image. The basic approach is outlined in section 4, together with some very preliminary results obtained with some simple deliberate "defects".

The potential role for laser probing techniques in NDE is briefly discussed in a final section.

2. LASER PROBE VELOCITY MEASUREMENT TECHNIQUES

The laser probe has evolved over a number of years (3), (4). The basic optical and electronic

systems are shown in Figs. 1 and 2.

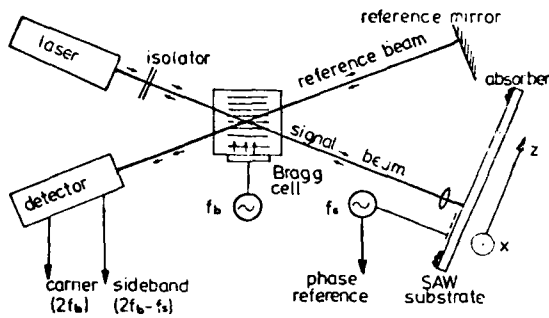


Fig. 1 Schematic of phase sensitive laser probe.

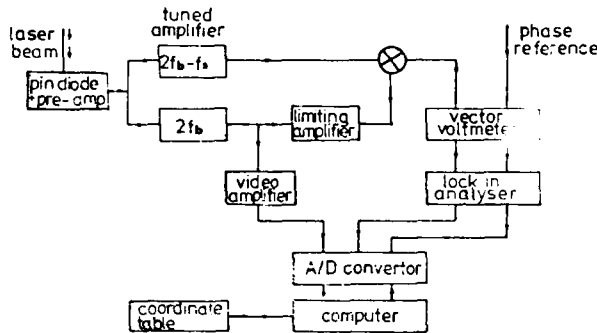


Fig. 2 Block diagram of electronics for recording amplitude and phase of SAW distribution.

The probe is driven by computer controlled stepping motors. It can be positioned with an accuracy of about 1μ , and can measure the phase of the surface wave displacement with an accuracy of about 3° .

The technique of velocity measurement is based on a comparison of the complex distributions measured along two scan lines, $U_0(x)$ and $U_1(x)$. If the wave vector in a direction making an angle θ to the z axis is $k(\theta)$, we can define the spatial frequency spectrum $f_0(\alpha)$ by

$$f_0(\alpha) = \int U_0(x) e^{j\alpha x} dx$$

$$\alpha \equiv k(\theta) \cos \theta$$

The function $f_1(\alpha)$ relating to the distribution $U_1(x)$ is similarly defined. In the absence of any defects between the scan lines, the amplitude of the spectra differ only by an attenuation constant. However, the phase difference depends on $k(\theta)$; given $f_0(\alpha)$ and $f_1(\alpha)$, the variation $k(\theta)$ can be derived - given only a single value, such as $k(0)$. In this form, the method is, therefore, relative. It can be made absolute by resorting to three rather than two scan lines (4).

The accuracy which can be obtained by this technique may be limited by the performance of the laser probe, or, by the maximum available size of sample. Under optimum conditions, we have achieved a repeatability accuracy of about 2:10. With this precision, one encounters a number of variations in materials which, under normal circumstances, one would regard as beyond reproach. There is, for example, now some evidence that there are variations in the velocity of both quartz and LiNbO₃ which are of potential concern to SAW device manufacturers.

The measurement technique works equally well on piezo electric as on non-piezo electric materials. In the latter case, one encounters the problem of transduction. We have solved this in some cases by butt-jointing of a piezo electric material, but, more frequently, by resorting to the liquid coupling technique (5); indeed, this technique is so simple to use that we now tend to employ it even for piezo electric materials - thereby saving the need for the photolithographic definition of a transducer pattern.

3. VELOCITY MEASUREMENT RESULTS

We have carried out a large number of measurements on LiNbO₃ in view of its importance to SAW devices. A particular concern has been the precise curvature in the Z -direction for Y -cut material, as this controls the diffraction rate. Fig. 3 shows a particularly precise result obtained over a range of angles very close to the Z axis.

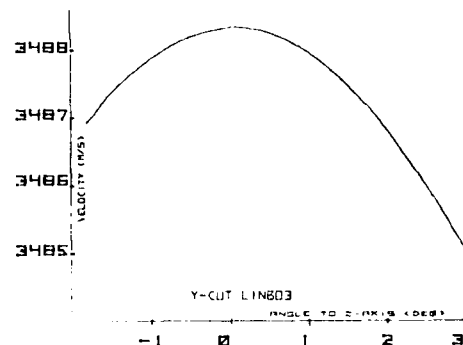


Fig. 3 High resolution velocity measurement for YZ Lithium Niobate.

Fig. 4 shows a result obtained with the liquid coupler on a sample of (111) Si. The experimental result is compared with a computed curve based on book-values of the elastic constants. The maximum deviations here are of the order of $2 \cdot 10^{-2}$ and attributable to the limited accuracy of the elastic constants.

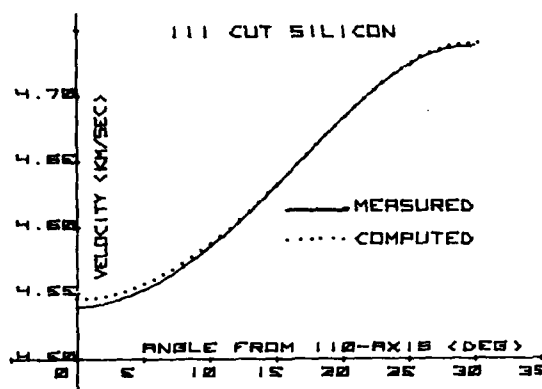


Fig. 4 Measured and theoretical velocity characteristics for (111) silicon

Of greater interest to application is the variation in velocity arising from variations in doping density. Fig. 5 shows the effect of N-type doping on a relatively high resistivity sample of (100) Si. The figure also shows the effect of an oxide layer 0.3 μ in thickness. We are embarking on a program to establish the value of this technique for characterising the surface preparation as well as doping levels for Si wafers.

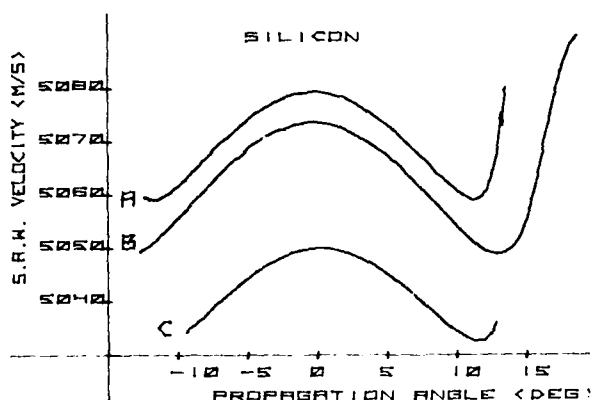


Fig. 5 Effects of surface perturbations on the velocity characteristics of (100) silicon:

- a) P type 3 ohm-cm
- b) N type 0.01 ohm-cm
- c) P type, 3 ohm-cm with 0.3 micron oxide layer

3.1. Deduction of Elastic Constants

The very precise velocity data encourages their use for improving the knowledge of the elastic constants. It is important to appreciate that this technique - if it can be successfully applied - establishes the value of these constants in a thin surface layer. It is, therefore, a technique for measuring the elastic constants of thin films - which it would be almost impossible to establish by the classical techniques.

In attempting to deduce the elastic constants from SAW velocity data, one technique is to obtain a measure of the deviation between the experimental and the calculated curve - for example, by calculating a mean square deviation integral. One can then resort to an optimization method, thereby perturbing the elastic elements until the error integral is minimised. The computation which would be involved in applying this technique directly would be prohibitive. The program we are using - originally devised by Slobodnik, and subsequently modified by P. LaGasse - is efficient but still requires minutes rather than seconds on a large computer for a single curve. We have, therefore, found the gradients of the velocity characteristic with respect to all of the relevant elastic elements by numerical differentiation. We can then use these gradient functions to linearize the optimisation method. This procedure works very satisfactorily. However, there is a more fundamental problem in the fact that the problem appears to be rather unstable in the face of the inevitably finite accuracy of the data and the subsequent computations. We have, therefore, found it necessary to be very selective in the elastic elements which we are seeking to improve. This selection is based on establishing the "strength" of an element - effectively the magnitude of the gradient functions; further, we define its "effectiveness", being a measure of its potency in reducing the discrepancy between the computed and the experimental data. If we confine our attention to those elements which are both strong and effective, we are able to deduce revised values for the constants which stand up to independent checks. These considerations have led to the following proposed changes:

	SLOBODNIK	% CHANGE
C_{11}	$20.3 \times 10^{10} \text{ N/m}^2$	- 2.3
C_{12}	5.3×10^{10}	- 2.4
C_{14}	0.9×10^{10}	-19.0

The effect of using the revised values are indicated in Fig. 6. The result is encouraging - but one is left with an uneasy feeling that, given three parameters to adjust, the mere fact of a fit is, perhaps, less than conclusive. To sharpen the criterion, we then measured the velocity for Y-cut LiNbO₃ near the X direction and used the revised elastic elements as tabled above - which have been derived purely on the basis of experimental results near the Z direction.

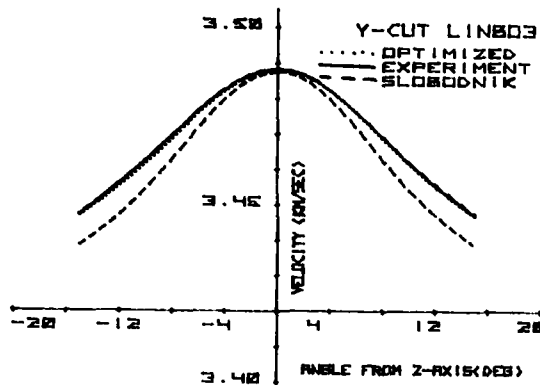


Fig. 6 Experimental, theoretical and optimised velocity curves for Y cut Lithium Niobate over the range $\pm 15^\circ$ about Z.

It is seen in Fig. 7 that the improvement in the computed curve is very convincing. We believe, therefore, that the values indicated do represent a distinct improvement on the previously known values.

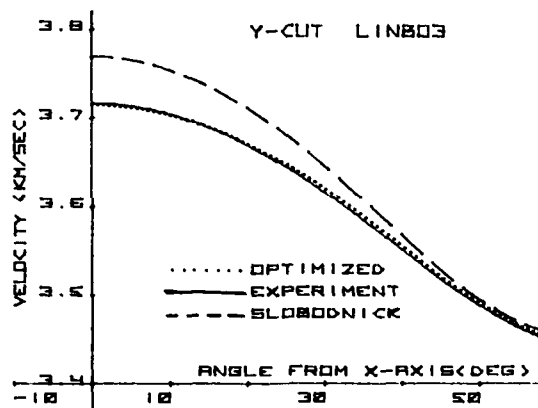


Fig. 7 Comparison between the experimental velocity curve and the computed curve obtained using the revised elastic constants for YX Lithium Niobate.

4. DETECTION AND SIZING OF SURFACE DEFECTS

We can illuminate a surface with a wide beam, and then examine the complex field distribution along a scan line, such as AA', Fig. 8. Given a sufficiently accurate knowledge of the surface wave characteristic, we can then reconstruct the field distribution at smaller values of z. If there is a defect at z_d , a reconstruction at that position will reveal a pattern with much sharper gradients than could arise from the source alone. In principle, this system can, therefore, serve to locate defects, and, if sufficiently large, provide some information on their size. It is worth emphasising that a single scan near the far end of the sample contains all the information required, provided that the signal to noise ratio is sufficiently large, and provided that the density of defects is sufficiently low. Moreover, the search for defects can, to a large extent, be

automated; the procedure would be to calculate the field distribution in successive planes, in each looking for amplitude or phase gradients exceeding a prescribed threshold.

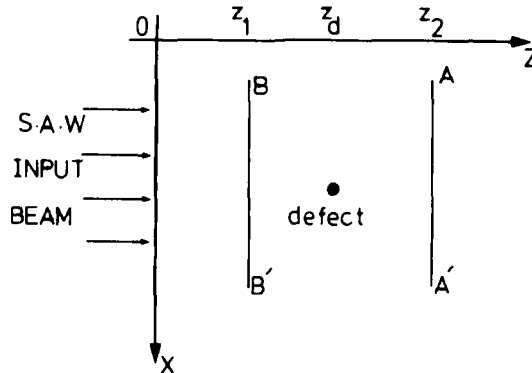


Fig. 8 Recording configuration for defect characterisation.

If, in the first instance, one is content merely to establish whether or not there are any defects, one can avoid the need for the back-propagation altogether. It suffices to record two scans, one at AA', the other at BB'. In the absence of any defects, the spectral density of the two scans would be identical. The probability of a defect between the two scan lines would then be assessed by forming:

$$P = \frac{\int \{f_A(\alpha)f_A^*(\alpha) - f_B(\alpha)f_B^*(\alpha)\}d\alpha}{\int f_A(\alpha)f_A^*(\alpha)d\alpha}$$

The limitation of all these techniques - the smallest detectable defect - lies in the attainable signal to noise ratio as also in the signal to spurious ratio. The former is capable of indefinite improvement, if only by increasing integration times. The latter is more fundamental; for example, reflections from the side of the sample, and the incidence of bulk waves are major sources of difficulty. This suggests that one might be able to effect an improvement in the detection ability if one could, in some way, make a comparison between samples which differ only in the incidence of defects. We have shown, (6) that in principle, this approach can lead to a much greater detection sensitivity. The experiment we conducted was designed to detect a "defect" consisting of a gold dot, 30μ in diameter, and 4000\AA in thickness. Fig. 9 shows the distribution along the scan line AA' and 9(b) its backward reconstruction in the plane of the defect - which is clearly not resolved. The comparison with a defect-free sample was effected very simply by removing the gold dot. The complex distribution now measured along AA' was subtracted from the first scan, and the difference reconstructed in the plane of the defect, Fig. 9(c). The defect is now clearly resolved.

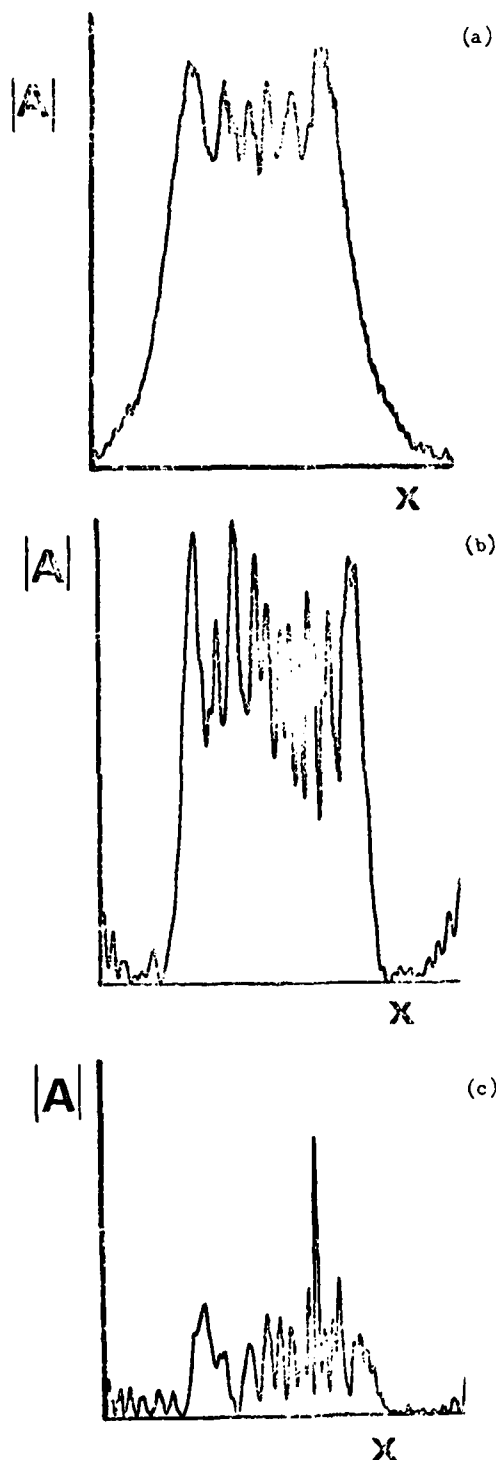


Fig. 9 Reconstruction of defect
(a) Hologram with defect
(b) Reconstruction of (a)
(c) Reconstruction after background subtraction

The experiment as described is somewhat artificial. However, it is possible that with some modifications the basic technique could be used to search for defects in components, given one component known to be defect free. The approach is reminiscent of ultrasonic spectroscopy (7), where the vibration spectra of components are compared with that of a standard. However, it would obviously be advantageous if it were possible, in some way, to derive the comparison standard from the component under test. These considerations have led us to a somewhat different approach, in which we record *three* scans instead of one which, as we have seen, under idealised circumstances should suffice.

The basic approach is as shown in Fig. 8. The defect is illuminated by an incident wave having a spectrum $I(\alpha)$. In principle, it would be possible to measure this directly by recording the field at $z=0$, if we could devise an attenuating section starting just above $z=0$, and which could wholly absorb the surface wave before it reaches the defect at $z=z_d$. In fact, it is, in practice, not difficult to do this. However, we can avoid the necessity for such a manoeuvre by recording the field at $z=z_1, z_2$ where $z_1 < z_d < z_2$. If the defect extends over a sufficiently small range of z , it will give rise to a perturbation of the incident wave field, which can be rigorously described in terms of a scattered wave spectrum $s(\alpha)$ in the region $z > z_d$, and a reflected wave spectrum $R(\alpha)$ in the region $z < z_d$. If the spectra recorded at $z=0, z_1, z_2$ are $f_{0,1,2}(\alpha)$ we can then write:

$$f_0(\alpha) = I(\alpha) + R(\alpha)$$

$$f_1(\alpha) = I(\alpha)e^{-j\beta(\alpha)z_1} + R(\alpha)e^{j\beta(\alpha)z_1}$$

$$f_2(\alpha) = I(\alpha)e^{-j\beta(\alpha)z_2} + S(\alpha)$$

where we have chosen to define $R(\alpha)$ at $z=0$ and $S(\alpha)$ at $z=z_2$. We can then readily solve the equations for the three spectra. Suppressing the α -dependence

$$I = f_0 - \frac{j(f_0 e^{-j\theta_1} - f_1)}{2 \sin \theta_1}$$

$$R = \frac{j f_0 e^{-j\theta_1} - f_1}{2 \sin \theta_1}$$

$$S = f_2 - f_0 e^{-j\theta_2} + \frac{j(f_0 e^{-j(\theta_1+\theta_2)} - f_1 e^{-j\theta_2})}{2 \sin \theta_1}$$

$$\theta_{1,2} = \beta(\alpha)z_{1,2}$$

It is at once clear that we must avoid values of z_1 that will make $\sin \theta_1 = 0$. The optimum choice of z_1 depends on the precision of the measurement of distance, the accuracy with which we know $R(\alpha)$ and also the range of $\beta(\alpha)$ with which we are concerned. A simple error analysis indicates that the optimum choice is given by $\theta_1 = (n+\frac{1}{2})\pi$ with $n=0$ or 1 in most cases. In some circumstances, it may be advantageous to utilize an additional scan line to reduce the errors when unfavourable values of θ_1 are encountered.

In principle, one would like to make z_2 as large as possible - if only to effect a search for defects over the largest possible region. In practice, one will be limited, as always, by signal to noise considerations but also by the limited accuracy of our knowledge of $B(u)$. If we require a phase accuracy of $\delta\phi$ for the scattered spectrum S, we require $\delta B \cdot (z_2 - z_1) < \delta\phi$. This implies that $(z_2 - z_1)$ expressed in the number of wavelengths N , should be limited so that

$$N \leq \left(\frac{\delta\phi}{2\pi} \right) \frac{\beta}{\delta B}$$

If the velocity error is only $3:10^5$, if $\delta\phi = 0.1$, the maximum value of N is around 500. We see that a very accurate knowledge of the velocity is a prerequisite to the use of these techniques.

As has been pointed out by a number of authors (8), a knowledge of the scattered spatial spectrum can give a good deal of information about the shape and size of the defect. Varying the frequency over a substantial bandwidth (9), can provide further information on the depth of a defect. In addition, we must, of course, also establish its location. In principle, one can readily back-propagate the S wave or forward-propagate the R wave. The reconstruction of the field in this way remains valid only up to the defect in each case. If, however, one uses some simple criterion, such as the position of maximum amplitude, it should be possible to estimate the location of the defect.

In the case of a defect which is thin in the Z-direction, both the S and the R reconstruction will provide an image of the defect which, in principle, is as perfect as the limited spatial bandwidth allows. The two reconstructions should be identical at the defect. If, therefore, one were to carry out a correlation between the back-propagated S wave and the forward-propagated R wave, at various positions in z , the correlation should peak at the location of the defect. For such defects as give rise to sensibly similar signal levels in the S and the R waves, this correlation criterion can be expected to provide substantially greater accuracy in the location of z_d .

There is a further technique for locating z_d which we intend to explore. If we measure the spectrum of S at $z = z_2$ at a particular frequency, and then remeasure it at a slightly different frequency, in addition to the large global phase shifts which will be imposed on the spectrum as a whole, there will be a differential phase shift between various angular components of $S(u)$. This differential phase shift is directly indicative of the distance of the source i.e. of the defect. From such a measurement, one can deduce the location of z_d unambiguously in the case of a point defect. In the more general case, the deduction is necessarily less precise - but can be expected to give results with an accuracy comparable to the size of the defect.

4.1. Experimental results

We have carried out a series of experiments on fused quartz substrates, at a frequency of 60 MHz. The waves were launched using the liquid coupler technique. In most of the experiments we made

$z_1 = 45\mu$, (i.e. 0.8λ), and $z_2 = 700\mu$ (i.e. 12.7λ). We obtained additional control on the angular spectrum of the illuminating wave by restricting the aperture on the substrate using a wax barrier.

In order to obtain some measure of the available dynamic range, we carried out one test without any defect. Fig. 10 shows the result for I, S and R. It is seen that the average level of the spectral density for R and S is about 30 dB below that of I; we should be able to detect scattered waves which exceed this level.

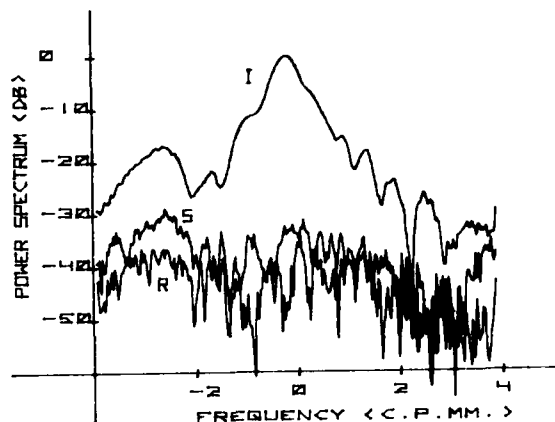
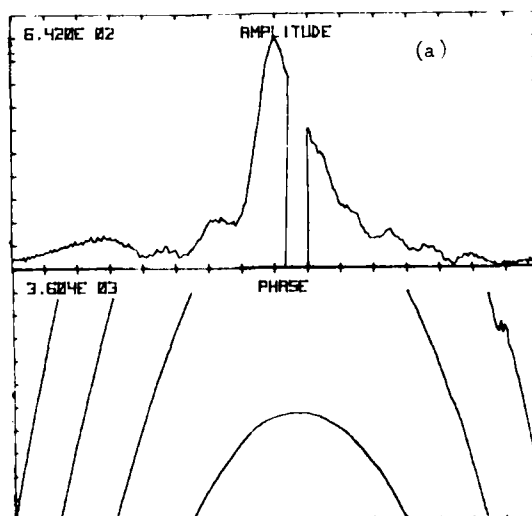


Fig. 10 Determination of I, S and R for a surface with no defect.

As a further test on the method, we took the experimental data which led to Fig. 10 and modified the spatial distribution measured at $z = z_2$ by reducing the amplitude to zero over a distance of 512μ , Fig. 11a. This essentially stimulates a totally absorptive defect located at $z = z_2$. The calculated scattered wave is shown in Fig. 11b. The location of the first zeros accords with expectation for a "defect" of this width.



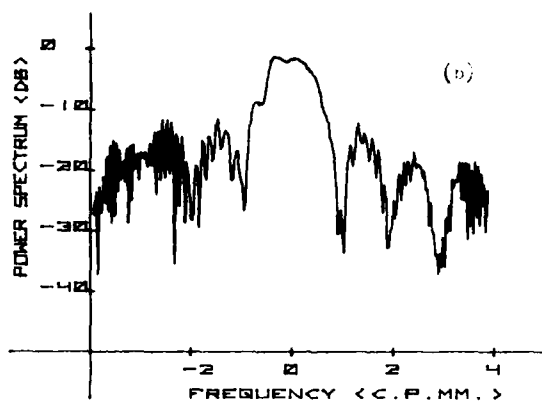


Fig. 11 Sizing of simulated defect
(a) spatial distribution of field just behind defect
(b) the calculated scattered spectrum.

The first physical defect which we have explored consisted of a hole 125μ in depth and 600μ in diameter. The S and R spectra are shown in Fig. 12. Again, the location of the zeros in S are roughly in accord with expectation for a defect of this size.

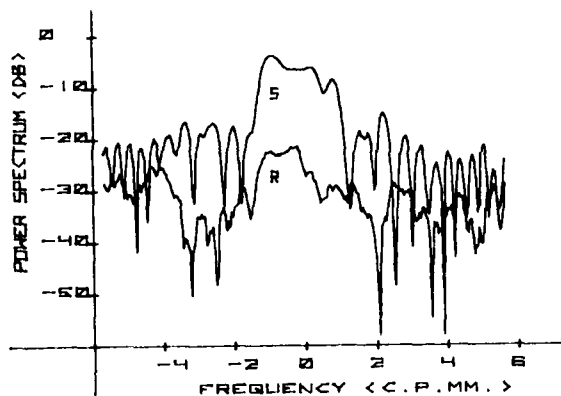


Fig. 12 Sizing of a circular shaped defect.

Finally, we have carried out experiments on a rectangular slot defect ($0.5\text{mm} \times 0.35\text{mm}$) in both broadside and end-on orientations. The results are shown in Figs. 13 and 14 respectively. In general, the spatial frequency bandwidth corresponding to the main lobes in S and R must equal twice the inverse width of the defect. This predicts the length of the defect in Fig. 13 and the width in 14.

The reflected spectrum in Fig. 13, however, did not provide useful information, as it was within the noise level of our system.

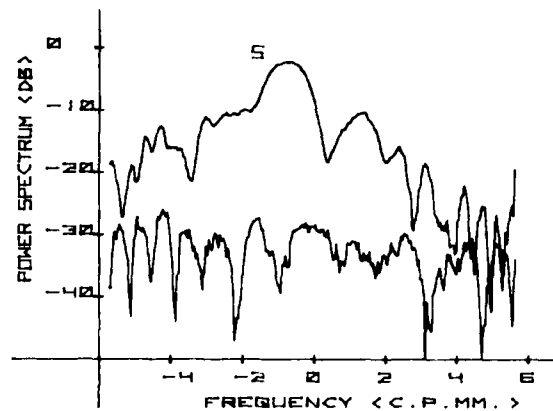


Fig. 13 Length determination of a rectangular slot defect.

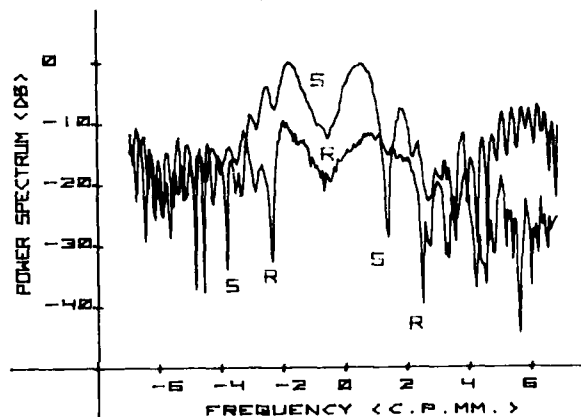


Fig. 14 Width determination of a rectangular slot defect.

CONCLUSIONS

The use of laser probing techniques for precision velocity determination is well established. The accuracy achieved is such that it encourages an extension of the range of applications in three distinct directions. The first is towards surface characterization for both piezo and non-piezo electric materials. Secondly, it leads to an improvement in the determination of elastic constants of materials - a technique which is of unique relevance to the determination of the elastic constants in thin films. Finally, it permits the detection, sizing and location of surface defects.

The examination of this third application is only just beginning but looks very promising. It is immediately clear that the method is effective on highly polished planar samples where high frequency probing is relevant. We believe, however, that the method is also capable of extension to lower frequencies and less idealised surfaces.

ACKNOWLEDGEMENTS

The authors are most grateful to Mr. G. Nicholls who has contributed greatly to the electronic design of the probe and to Mr. M. Gillette for assistance in the mechanical construction.

REFERENCES

- (1) H.K. Wickramasinghe, R.C. Bray, V. Jipson C.F. Quate and J.R. Salcedo, "Photoacoustics on a Microscopic Scale", Appl. Phys. Lett 33 (11), 1 December, 1978, pp. 923-925
- (2) C.R. Petts, unpublished work.
- (3) H.K. Wickramasinghe and E.A. Ash, "Optical Probing of Acoustic Surface Waves - Application to Device Diagnostics and to Non-destructive Testing", Proc. of MRI Symp. on Optical and Acoustical Micro-Electronics, Polytechnic Inst. of New York, April 1974, pp 413-431.
- (4) D.K. Murray and E.A. Ash, "Precision Measurements of SAW Velocities", Proc. 1977 Ultrasonics Symposium, pp. 823-826.
- (5) B.T. Khuri-Yakub and G.S. Kino, "A New Technique for Excitation of Surface and Sheer Acoustic Waves on Non-piezo electric Materials", Appl. Phys. Lett., 32(9), 1 May 1978, pp. 513-514.
- (6) E.A. Ash and H.K. Wickramasinghe, "Background Subtraction in Surface-Wave Holography", Elect. Letts., Vol. 11, No. 22, 30th Oct, 1975, pp. 526-527.
- (7) O.R. Gericke, "Ultrasonic Spectroscopy, Research Techniques in NDT", Academic P., 1970, pp. 31-61
- (8) B.R. Tittman, O. Buck, L. Ahlberg, M. de Billy, F. Cohen-Tenoudji, A. Jungman and G. Quentin, "Surface Scattering from Elliptical Cracks for Failure Prediction", Proc ARPA Conf. on Review of Progress in Quantitative NDE, July 1978, pp. 132-141
- S. Ayter and B.A. Auld, "Characterization of Surface Wave Scattering by Surface Breaking Cracks", *ibid* pp. 126-131
- B.T. Khuri-Yakub, G.S. Kino, J.C. Shyne, M.T. Resch and V. Domarkes, "Surface Crack Characterisation: Geometry and Stress Intensity Factor Measurements". *ibid*.
- G.S. Kino, "The Application of Reciprocity Theory to Scattering of Acoustic Waves by Flaws", J Appl. Phys., 49 (6), June 1978, pp 3190-3199.
- (9) V. Domarkes, B.T. Khuri-Yakub and G.S. Kino, "Length and Depth Resonances of Surface Cracks and their Use for Crack Size Estimation", Appl. Phys. Lett. 33(7), 1 Oct 1978, pp 557-559

SUMMARY DISCUSSION

(Eric Ash)

Gordon Kino (Stanford University): Maybe I missed it, but it's impressive that the forward wave scattering - the effect is much larger than the reflection. And it's always very difficult with a straight transducer to make that. What do you attribute the big effect to?

Eric Ash: We have used rather crude defects. If you imagine a defect as essentially just absorbing everything that hits it and you create a gaping hole in what would have been the forward-going wave, and in our imitation you simply represent this by the negative of the missing amplitude, which would be a larger phase where as if the wave is essentially absorbed and converted into bulk waves. Obviously, a lot of the conversion will be to bulk waves. We don't see that in the reflected wave.

Gordon Kino: But basically you seem to be receiving converging waves?

Eric Ash: Yes. It is quite possible, of course, to calculate the bulk wave loss from the point of entry.

Donald Thompson (Science Center): Do you have a special requirement on the reflectivity on the surface in order to get good pickup?

Eric Ash: The more reflective it is, the better. But just to give you an example, we have done experiments on ordinary smooth, ground stainless steel. We certainly have no problem in doing it on lithium niobate without any metallization, but it's a signal-to-noise issue.

Donald Thompson: I was wondering in particular how bad could the surface be and still have a reasonable signal-to-noise ratio?

Eric Ash: We really haven't tried any experiments with very bad surfaces, but it is a signal-to-noise ratio issue, and we have a great deal of signal-to-noise ratio to spare. There are--I won't go into details--things that we could do to increase the signal-to-noise ratio. If it's too rough, of course, eventually you will start to get

Don Yuhas (Sonoscan, Inc.): What sort of variation do you see in, say, the typical silicon wafers, or silicon? I don't know if it's wafers or not. You described the ten meter per second variation as being due to doping. Did you pick up a handful? What sort of variations?

Eric Ash: I'm afraid we just simply haven't picked up a handful. That's one of the things we wanted to do. We have just done a very small number of experiments so far.

Ed Kraut (Science Center): Eric, I would like to ask you: when you started out your talk, you spoke about lithium niobate and the surface wave loss in lithium niobate. You mentioned the matter of C.I.J.'s, the elastic constants. You didn't say anything about the question of the piezoelectric constants or dielectric constants in lithium niobate which also enter into the surface wave velocity determination. Did you also consider possibilities of errors, small errors, in the piezoelectric constants as well?

Eric Ash: We have tried this. We have looked at the gradients with respect to the piezoelectric constants, and we are convinced they haven't seriously come into what we have done so far. We would like to find them. And we propose to do this by doing essentially $\Delta V/V$ tests which will isolate them specifically. As far as the dielectric constants are concerned, I don't know whether we have ever calculated that. I think we were rather hoping they were good enough.

Ed Kraut: One other question. The laser technique for velocity measurement on surface waves was used a number of years ago, also, for example, by Eric Lean in studies of harmonic generation on lithium niobate. Could you contrast the -- I don't know what accuracies they were dealing with there, but I would like to ask you what the relative accuracy might have been?

(continued)

Eric Ash (discussion continued)

Eric Ash: The kind of probe that Eric Lean was using was different in principle because it's a diffraction probe; it has to have a spot size which extends over a number of wavelengths, and I think I'm right in saying that he has used it exclusively for amplitude measurements. But, I mean, you can make the thing phase-sensitive. In contrast, our probe here, we focused to something in the experiments we have been describing as probably less than a tenth of a wavelength. I think it would be very difficult to get the phase accuracy, which is really the fundamental measurement we're making here, using a diffraction probe.

Don Yuhas: There's a detection scheme that's used in acoustic microscopes that works essentially the same way, although the optical detection scheme is quite different. But you can get the same phase accuracy.

Eric Ash: I'm not sure you're going to get the same phase accuracy. You certainly can get the same determination.

Don Yuhas: The spot is focused down to the same size.

George Herrmann (Stanford University): I was wondering whether you used your technique to determine applied stresses quantitatively or whether you think it might be suitable.

Eric Ash: I was intrigued to hear this stuff from yesterday. If one gets the effect of the order of ten to minus four, we should never see them.

#

ON THE RESONANCES OF SURFACE BREAKING CRACKS

S. Ayter and B. A. Auld
Edward L. Ginzton Laboratory
Stanford University, Stanford, California 94305

ABSTRACT

The resonance phenomenon observed in Rayleigh wave scattering from surface-breaking cracks has been investigated using Freund's results on reflection of Rayleigh waves from an infinite crack edge. To model the crack as a section of acoustic waveguide, resonances are treated as standing waves in the length and depth directions. The model takes both faces of the crack into consideration, and this makes it possible to explain the observations of all order resonances in the length direction for excitation by a Rayleigh wave beam at normal incidence. Calculations are made for rectangular and half-penny shaped cracks and differences between the two cases are discussed.

INTRODUCTION

One of the sources of data for the estimation of dimensions of surface breaking cracks is their frequency response. Experimental results have shown that crack response shows resonance-like variations in the short wavelength regime.^{1,2} Some of those variations were found to be associated with the length and depth of the cracks,² however previous interpretations fail to explain the observation of all order length resonances for a symmetric excitation in length dimension. Such interpretations take only the illuminated face of the crack into account, neglecting the effect of its back face.^{1,2,3} Freund has demonstrated in Reference 4 that the crack edge couples the fields between the front and back faces and the coupling parameters have been calculated. Using those parameters, he also showed that an infinite slit structure can guide waves if the edge separation is wide enough and he derived dispersion relations for the modes of this structure.⁵ In this study, these calculations are reviewed and a model is proposed for surface crack resonances, using the waveguide modes obtained from the calculations.

RAYLEIGH WAVE PROPAGATION IN TWO DIMENSIONS

A surface wave, traveling on the plane defined by x and y axes and decaying in z direction can be expressed in terms of its component along the decay direction (z -axis) only.⁶ The particle velocity component along the decay direction then can be written as

$$V_z(x, y, z) = f(z) \bar{V}_z(x, y) e^{i\omega t} \quad (1)$$

where $\bar{V}_z(x, y)$ satisfies the two-dimensional reduced wave equation

$$\left[\nabla^2 + (\omega/V_R)^2 \right] \bar{V}_z(x, y) = 0 \quad (2)$$

and $f(z)$ is a known function describing the decay along the depth of the plate. The other components of particle velocity can easily be found once $V_z(x, y)$ is known.⁶

REFLECTION OF RAYLEIGH WAVES FROM AN INFINITE CRACK EDGE

Consider a semi-infinite crack with its edge along the y axis and faces in the $x-y$ plane for $x > 0$. The faces are assumed to lie on either

side of the $z = 0$ plane. They are denoted as the z^+ and z^- faces. Let a Rayleigh wave on the z^+ face be incident obliquely on the edge, its propagation vector lying at an angle θ with the crack edge (y -axis). The incident wave will yield two scattered surface waves, one on each face of the crack. Bulk waves will also be radiated into the medium outside the crack when the angle of incidence θ is large enough. Of the two scattered surface waves, the one on z^+ face will be called the reflected wave (with reflection coefficient $R(\theta)$) and the one on z^- face will be identified as the transmitted wave (with transmission coefficient $T(\theta)$). The reflection and transmission coefficients are defined in terms of the component of particle displacement in the z direction.

Using the three-dimensional representation theorem due to deHoop, Freund solved this scattering problem and calculated the parameters $R(\theta)$ and $T(\theta)$.⁴ When the angle of incidence $\theta < \theta_{CR,S} = \cos^{-1}(V_R/V_S)$, (V_R - Rayleigh wave velocity; V_S - shear wave velocity), the incident wave cannot excite propagating bulk waves and all the power is scattered into surface waves on the z^+ and z^- faces. That is

$$|R(\theta)|^2 + |T(\theta)|^2 = 1 \quad \text{for } \theta < \theta_{CR,S} \quad (3)$$

In the same angular region, the phases of the reflection and transmission coefficients satisfy the following relation,

$$A(\theta) = \arg T(\theta) - \arg R(\theta) = \frac{\pi}{2} \quad \text{for } \theta < \theta_{CR,S} \quad (4)$$

For $\theta > \theta_{CR,S}$ the incident wave is able to excite radiating shear waves which can carry energy away from the crack edge; and, for $\theta > \theta_{CR,L} = \cos^{-1}(V_R/V_L)$, (V_L - longitudinal wave velocity) $R(\theta)$ and $T(\theta)$ approach small purely imaginary quantities with magnitudes in the order of 0.1. Under this condition $|T(\theta)| \approx |R(\theta)|$.

Crack Modeling. We first solve the guidance problem for the infinite crack geometry, using the transverse resonance technique, then impose the finite length of the crack in order to find its resonances. For the partial waves to be used in transverse resonance analysis, we will use solutions of Eq. (2) in an appropriate coordinate system.

(a) **Rectangular crack:** Rectangular crack geometry is shown in Fig. 1(a). The solutions of Eq. (2) are ordinary plane waves propagating in x-y plane. Since the power is confined to surface waves only for $\theta < \theta_{CR,S}$, only the partial waves with incidence angle satisfying that relation will be considered. Otherwise the waveguide modes will be very lossy and will not produce good resonances.

Slit waveguide modes. The slit waveguide geometry is shown in Fig. 1(b). On each face of the crack we assume two partial waves propagating in opposite x directions with the same angle of incidence at $x = \pm L/2$, L being the width of the slit. We will assume that each partial wave reflects from an edge as if the other edge were absent. The validity of this assumption depends on the relative magnitude of the slit width L with respect to the Rayleigh wavelength λ_R , and for the frequency range of interest to us, where $2\pi(L/\lambda_R) > 1$, this assumption is verified by Freund.⁵ Considering the configuration in Fig. 1(b), the partial waves $P_i, i=1,2,3,4$ can be expressed as follows:

- $P_1: A_1 \exp(-ik_x x - \beta_G y)$ with decay in +z direction
 $P_2: A_2 \exp(-ik_x x - \beta_G y)$ with decay in -z direction
 $P_3: A_3 \exp(ik_x x - \beta_G y)$ with decay in +z direction
 $P_4: A_4 \exp(ik_x x - \beta_G y)$ with decay in -z direction

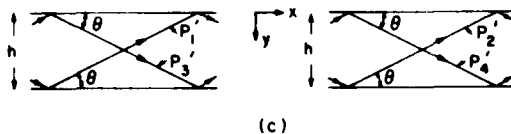
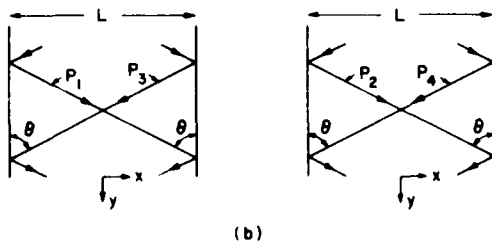
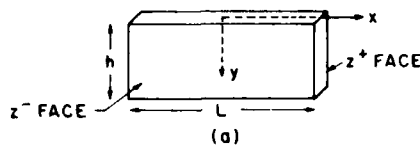


FIG. 1. (a) Rectangular crack geometry;
 (b) Partial waves for slit waveguide;
 (c) Partial waves for crack waveguide.

Writing the boundary conditions at $x = \pm L/2$ and keeping in mind that R and T are defined in terms of +z components of the partial waves,

one obtains the following eigenvalue expression:

$$e^{ik_x L} \begin{pmatrix} A_1 \\ A_2 \\ A_3 \\ A_4 \end{pmatrix} = \begin{pmatrix} 0 & 0 & R & -T \\ 0 & 0 & -T & R \\ R & -T & 0 & 0 \\ -T & R & 0 & 0 \end{pmatrix} \begin{pmatrix} A_1 \\ A_2 \\ A_3 \\ A_4 \end{pmatrix} \quad (6)$$

Each solution of Eq. (6) defines a modal field distribution. The solutions are tabulated in Table 1. Mode identifications are made considering Fig. 1(b), where E and O stands for even (symmetric) and odd (antisymmetric) variations along the direction defined by the subscripts x and z. The modes are consistent with the symmetry of the structure.

Table 1. Slit waveguide modes

A_1	A_2	A_3	A_4	$e^{ik_x L}$	Mode Identification
1	1	1	1	R - T	$E_x E_z$
1	-1	1	-1	R + T	$E_x O_z$
1	1	-1	-1	-(R - T)	$O_x E_z$
1	-1	-1	1	-(R + T)	$O_x O_z$

Dispersion relations can be obtained in the following manner. From the fifth column, one can write

$$k_x L = \arg(R + T) + 2m\pi \quad (7a)$$

and plot the RHS as a function of θ . Considering Fig. 1(b), the following relation can readily be shown to be required

$$k_x L = \beta_G L \tan \theta \quad (7b)$$

Taking $\beta_G L$ as a parameter, $k_x L$ vs θ can also be plotted. Intersection of two curves for $\theta < \theta_{CR,S}$ determines k_x (and β_G) for the propagating modes. This is illustrated in Fig. 2 where dashed lines correspond to Eq. (7b) and solid lines correspond to Eq. (7a). This figure is for a Poisson ratio of 0.25, for which $\theta_{CR,S} = 23.2^\circ$. The following points are worth considering:

- 1) For the lowest order propagating mode, $\beta_G L \approx 2$, $k_x L \approx \pi/4$, $k_R L \approx 2.2$. Therefore the analysis is valid only for cracks with $L > 0.4 \lambda_R$.
- 2) Since $\theta < \theta_{CR,S} = 23.2^\circ$, the guided wave velocity $V_G = V_R / \cos \theta$ is very near to the Rayleigh wave velocity.

Crack waveguide modes. Consider the crack waveguide shown in Fig. 1(c). Through a similar analysis, one can analyze the waveguide modes supported by this structure, if scattering coefficient of Rayleigh wave at the upper edge of a crack face is known. To our knowledge this problem has not been solved for other than normal incidence.⁷ We will denote the relevant reflection coefficient by $R(\theta)$ and either approximate it or treat it as an adjustable parameter to be fitted to experimental results. Scattering at the bottom of the crack is treated as in the previous subsections, by the Freund theory. Although the crack waveguide has no symmetry in the plane of the crack, it is symmetrical with respect to the z direction. The analysis shows that

modes of even and odd symmetry with respect to the z direction have the properties listed in Table 2.

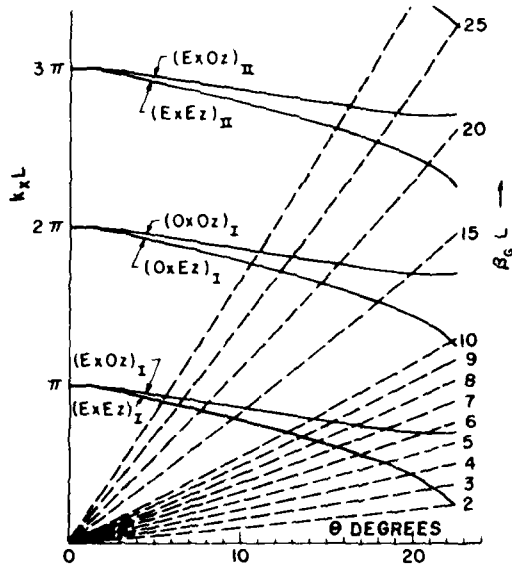


FIG. 2. Graphical solution of dispersion equation for slit waveguide modes.

Table 2. Crack waveguide modes

A_1	A_2	A_3	A_4	$e^{i2k_y h}$	Mode Identification
1	1	\bar{R}	\bar{R}	$\bar{R}(R-T)$	E_z
1	-1	\bar{R}	$-\bar{R}$	$\bar{R}(R+T)$	O_z

For the crack waveguide modes to be non-leaky, the dispersion relations must be satisfied for real $k_y h$ (or real B_0) since for small angles of incidence $|R \pm T| = 1$, $|\bar{R}| = 1$ is necessary for non-leaky modes to exist. As before, we impose this condition in order to obtain strong resonances. Dispersion curves can be obtained in the manner described in the previous section. If we assume that $\bar{R}(\theta) \approx 1$ (which corresponds to $\partial U_z / \partial y = 0$ at $y = 0$), the curves in Fig. 2 can be used with the following substitutions: $k_x L \rightarrow 2k_y h$, $B_0 L \rightarrow 2B_0 h$. The O_x modes should be ignored. This shows that for the lowest order mode to propagate $B_0 h \sim 1$ and $h > 0.2 \lambda_R$, provided that $\bar{R} \approx 1$ is a good approximation for $\theta < \theta_{CR,S}$. We will comment further on the existence of crack waveguide modes when we discuss half-penny shaped cracks.

Resonances of rectangular surface cracks. Following the approach used in References 1 and 2 we treat resonance effects as due to standing wave resonances along the depth or the length of the crack. However, we do not use simply Rayleigh waves, but rather the guided waves of the crack in which the vibrations of the front and back faces are coupled at the edges. We restrict ourselves to non-leaky waveguide modes only, on the grounds that leaky standing waves will not have sufficient high Q 's to be strongly excited and to give useful NDE

signatures. Our analysis therefore treats only depth standing wave resonances of the trapped slit waveguide modes and length standing wave resonances of trapped crack waveguide modes (Fig. 3).

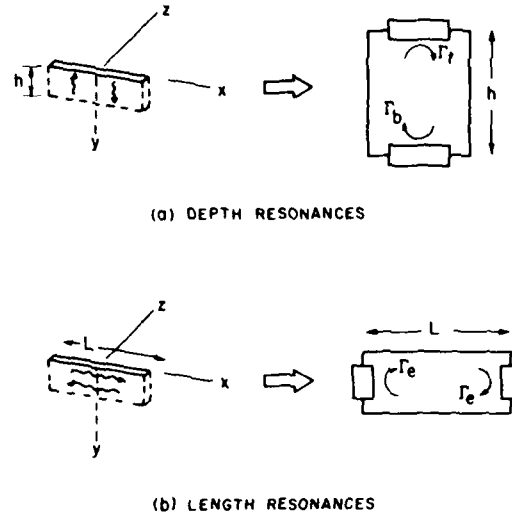


FIG. 3. Waveguide standing wave model for (a) depth resonances, and (b) length resonances of the crack.

To continue this approach we must evaluate the modal reflection coefficients at the top and bottom of the crack for the depth resonances and the analogous reflection coefficients at the edges of the crack for the length resonances. With the present model, we are able to introduce more realistic boundary conditions than the rigid boundary conditions assumed previously by others. These boundary conditions are evaluated by considering the behavior of each partial wave in Fig. 1 at an edge boundary normal to the guided wave propagation direction.

For reflection from crack edges and the crack bottom, the results given by Freund apply, and we have the reflection coefficients listed in Table 3 for the various types of modes treated previously. Note that R and T should now be evaluated near 90° since partial waves grazing the guiding edges hit the terminating boundaries normally. There is no coupling at the crack edges between modal families or between modes of the same family. In the case of reflection from a crack top, there is no coupling between the z^+ and z^- faces of the crack, and each partial wave reflects with the reflection coefficient \bar{R} , for which the results given by Cuozzo, et al,⁷ can be used as an approximation. In this way we obtain the reflection coefficients Γ_t , Γ_b and Γ_e defined in Fig. 3.

Table 3. Reflection coefficients at a crack edge for slit and crack waveguide modes

Mode	Reflection Coefficient
$E_z, E_x E_z, O_x E_z$	$(R - T)$
$O_z, E_x O_z, O_x O_z$	$(R + T)$

To investigate the depth resonances, we model the crack as a slit waveguide terminated by a crack edge at one end and a crack top at the other. The resonance condition of the transmission line model as shown in Fig. 3(a) is

$$\Gamma_t \Gamma_b e^{-i2\beta_G h} = 1 \quad (8)$$

where $\Gamma_t = \rho_t e^{i\alpha_t}$ and $\Gamma_b = \rho_b e^{i\alpha_b}$ are the reflection coefficients for the mode of concern at the top and bottom of the crack respectively, and β_G is the propagation constant for that particular mode. Due to the fact that terminations are lossy, one should allow for a complex resonant frequency, i.e.,

$$\beta_G = \frac{\omega(1+i/2Q)}{V_G} \quad (9)$$

The resonant frequency and quality factor are found to be

$$f = \frac{V_G}{2h} \left[\frac{\alpha_t + \alpha_b}{2\pi} + N \right] \quad (10)$$

and

$$Q = \frac{0.5(\alpha_t + \alpha_b) + N\pi}{-\log_e(\rho_t \rho_b)} \quad (11)$$

For $\sigma = 0.25$, $\Gamma_t \approx 0.25$, $\Gamma_b(O_z \text{ modes}) = 0.3e^{i(\pi/2)}$, $\Gamma_b(E_z \text{ modes}) = 0.1e^{-i(\pi/2)}$. The analysis predicts a quality factor in the order of unity, although experimental quality factors are reported to be somewhat higher than this.

For length resonances, the same kind of procedure gives

$$\Gamma_e^2 e^{-i2\beta_G L} = 1 \quad (12)$$

writing $\Gamma_e = \rho_e e^{i\alpha_e}$, one obtains the resonance frequency and quality factor as

$$f = \frac{V_G}{2L} \left(M + \frac{\alpha_e}{\pi} \right) \quad (13)$$

and

$$Q = \frac{\alpha_e + M\pi}{-2 \log_e(\rho_e)} \quad (14)$$

where $\Gamma_e(O_z \text{ mode}) = 0.3e^{i(\pi/2)}$, $\Gamma_e(E_z \text{ mode}) = 0.1e^{-i(\pi/2)}$ and $V_G \sim V_R$ for trapped modes.

It is interesting to note that the edge reflection coefficients Γ_e for the O_z and the E_z modes are π radians out of phase. This indicates that standing wave pattern of an E_z mode and standing wave pattern of the same order O_z mode have a shift of $\lambda/4$ with respect to each other. In other words, if the E_z mode for a specific resonance frequency is even, the corresponding O_z mode is odd or vice versa. Keeping in mind that $V_G \sim V_R$ for both modes we see that, at each

resonance frequency predicted by Eq. (13), there is always an even and an odd standing wave pattern that can be supported by the crack structure. In experimental observations of crack resonances excited by normally incident Rayleigh waves, length resonances of all orders have been noted. This poses a difficulty for the single surface model used previously. In this model the resonances are alternately x-symmetric and x-antisymmetric, while the excitation of normal incidence is x-symmetric only. One therefore predicts excitation of alternate modes only. We see that the two surface model used here resolves the dilemma since it predicts an x-symmetric vibration for every order of resonance, alternating from an E_z type mode to an O_z type mode as the order increases.

(b) Half-penny shaped crack: Here, the solutions of Eq. (2) are $H_\nu^\pm(k_R r) e^{\pm i\nu\phi}$, where r and ϕ are polar coordinate variables and $H_\nu^\pm(k_R r)$ are Hankel functions of the first and second kind of order ν . We do not restrict ourselves to integer values of ν since the structure is not periodic in ϕ ($-\pi/2 \leq \phi \leq \pi/2$). It is appropriate in this problem to express the Hankel functions in the following form:

$$H_\nu^\pm(x) = M_\nu(x) e^{\mp i\psi_\nu(x)} \quad (15)$$

where $M_\nu(x)$ is the magnitude and $\psi_\nu(x)$ is the phase of the Hankel functions, i.e.,

$$M_\nu(x) = \left[J_\nu^2(x) + Y_\nu^2(x) \right] \quad (16)$$

and

$$\psi_\nu(x) = \tan^{-1} \frac{Y_\nu(x)}{J_\nu(x)} \quad (17)$$

In our notation, the $-$ and $+$ signs in Eq. (15) correspond to radially outgoing and incoming waves, respectively.

To get a feeling about the behavior of these circular partial waves, let us examine them more closely. Any of the partial waves shown in Fig. 4 can be expressed in the form

$$P_i = M_\nu(k_R r) \exp[\pm i(\psi_\nu(k_R r) \pm \nu\phi)] \quad (18)$$

The propagation vector at any point (r, ϕ) can then be found by taking the negative gradient of the phase function:

$$\vec{k} = -\nabla[\pm \psi_\nu(k_R r) \pm \nu\phi] = \mp k_R \frac{d\psi_\nu(k_R r)}{dk_R r} \hat{r} \mp \frac{\nu}{r} \hat{\phi} \quad (19)$$

where \hat{r} and $\hat{\phi}$ are unit vectors in polar coordinates. If we make an analogy between the circular and rectangular cases, $k_R \psi_\nu$ corresponds to k_y and ν/r corresponds to k_x . Therefore one can form the analogous cases of slit and crack waveguides, as shown in Fig. 4. It is seen that the analogous case of slit waveguide is such that the modes are guided by the crack top — that is, the waves are radial. For the case of crack waveguide, the guidance is assumed via the crack edge and the waves are angular. In both cases, the partial waves should graze the guiding boundaries for non-leaky propagation. We will assume that Freund's

results are also applicable for the curved crack boundaries.

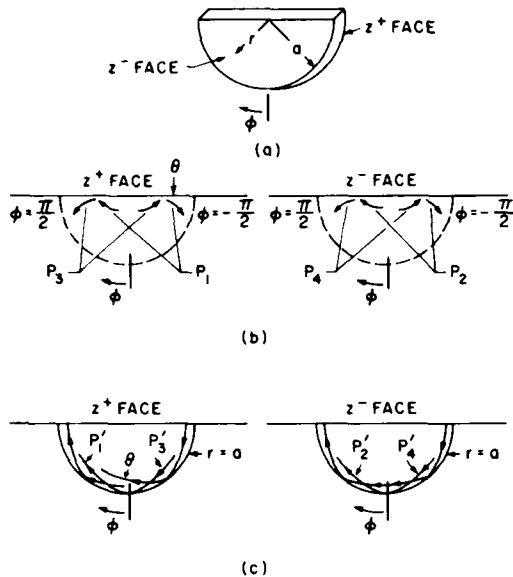


FIG. 4. (a) Half-penny shaped crack geometry; (b) Partial waves for radial waveguide modes (cf Fig. 1(b)); (c) Partial waves for angular waveguide modes (cf Fig. 1(c)).

The radial waveguide modes can now be investigated. The partial waves are:

$$\begin{aligned} P_{1,2} &= A_{1,2} M_\nu(k_R r) e^{-i\psi_\nu(k_R r)} e^{-i\nu\phi} \\ P_{3,4} &= A_{3,4} M_\nu(k_R r) e^{-i\psi_\nu(k_R r)} e^{+i\nu\phi} \end{aligned} \quad (20)$$

Writing the boundary conditions at $\phi = \pm \pi/2$, one obtains

$$e^{i\nu\pi} \begin{pmatrix} A_1 \\ A_2 \\ A_3 \\ A_4 \end{pmatrix} = \begin{pmatrix} 0 & 0 & \bar{R} & 0 \\ 0 & 0 & 0 & \bar{R} \\ \bar{R} & 0 & 0 & 0 \\ 0 & R & 0 & 0 \end{pmatrix} \begin{pmatrix} A_1 \\ A_2 \\ A_3 \\ A_4 \end{pmatrix} \quad (21)$$

for which the solutions can be obtained as

A_1	A_2	A_3	A_4	$e^{i\nu\pi}$	Mode Identification
1	1	1	1	\bar{R}	$E_\phi E_z$
1	-1	1	-1	\bar{R}	$E_\phi O_z$
1	1	-1	-1	$-\bar{R}$	$O_\phi E_z$
1	-1	-1	1	$-\bar{R}$	$O_\phi O_z$

If we again assume a boundary condition of $(\partial U_z / \partial n) = 0$ at $\phi = \pm \pi/2$, (i.e., $\bar{R} = 1$), we

obtain the restriction

$$\nu = \begin{cases} 0, 2, 4, \dots & \text{for } E_\phi \text{ modes} \\ 1, 3, 5, \dots & \text{for } O_\phi \text{ modes} \end{cases} \quad (22)$$

The resonance condition for the modes can be written in a similar manner, and one obtains

$$e^{i2\psi_\nu(k_R a)} = \begin{cases} (R-T) \cong 0.1e^{-i(\pi/2)} & \text{for } E_z \text{ modes} \\ (R+T) \cong 0.3e^{i(\pi/2)} & \text{for } O_z \text{ modes} \end{cases} \quad (23)$$

Again equating the phases, one can graphically obtain the depth resonances as shown in Fig. 5. The resonances corresponding to $\nu > 0$ must be eliminated since "the incidence angles of partial waves", $\theta \cong \tan^{-1}(\nu/kr)$ do not allow "grazing incidence" at $\phi = \pm(\pi/2)$, especially around $r=0$. For $\nu=0$, we approximate the angle of the Hankel function by its asymptotic expansion,

$$\psi_0(k_R a) \approx k_R a - \frac{\pi}{4} \quad (24)$$

The accuracy of the approximation can be seen from Fig. 5. We then obtain the resonance frequency and quality factor

$$f = \frac{V_R}{2a} \cdot N \quad (25)$$

$$Q = \frac{N\pi}{-\log_e(\rho_e')} \quad (26)$$

where (ρ_e') is the magnitude of $(R \pm T)$ given in Eq. (23).

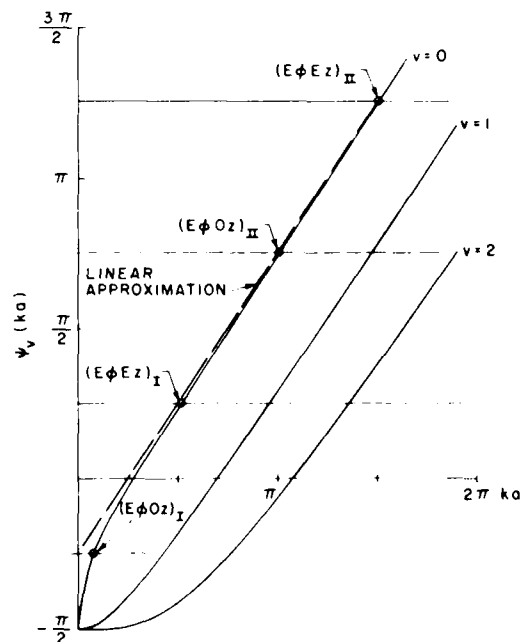


FIG. 5. Graphical evaluation of radial (i.e. depth) resonance frequencies for a half circular crack.

Comparing Eqs. (25) and (26) with Eqs. (10) and (11) we see that depth resonance frequencies are almost the same, and that the circular crack yields a higher quality factor.

For length resonances, the same kind of analysis yields the following equation

$$e^{i2\psi_v(k_R a)} = \begin{cases} (R-T) & E_z \text{ mode} \\ (R+T) & O_z \text{ mode} \end{cases} \quad (27)$$

provided that the incidence angle of partial waves at $r = a$ is small. That angle can be expressed as

$$\theta = \tan^{-1} \left[k_R r \frac{d\psi_v(k_R r)/d(k_R r)}{v} \right]_{r=a} \quad (28)$$

Taking v as a parameter and eliminating $k_R a$, one can plot $\psi_v(ka)$ vs θ . From Freund's boundary conditions $\frac{1}{2} \arg(R \pm T)$ vs θ can also be plotted. As in the rectangular crack case, the intersection of two curves should give the guide parameters. We have plotted these curves in Fig. 6 and one readily observes that there is no solution for the "angular waveguide" modes. In other words, the guide proposed in Fig. 4(c) does not act as a non-leaky waveguide.

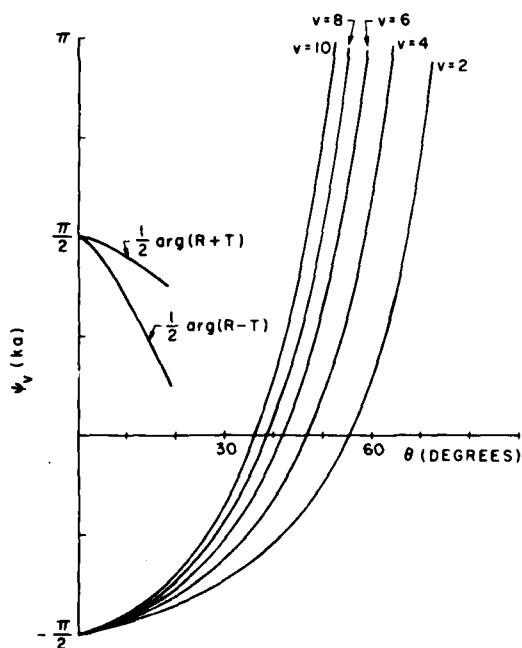


FIG. 6. Graphical solution of dispersion equation of angular waveguide modes.

Experimentally, length resonances have been found to not depend significantly on the shape of the crack, and they are found to exist even in circular cracks. The basic analytical difference between rectangular and circular cracks is that in the rectangular case, guidance is achieved via the bottom of the crack. The "mode switching" between E_z and O_z modes noted in the previous section as the explanation for observations of resonances in all orders is caused by edge coupling between the front and back faces of the crack. However in the circular crack, the analysis shows that there are no corresponding non-leaky resonances in the angular direction. Furthermore scattering at the top of the crack does not introduce the coupling between the back and front faces required for "mode switching". An explanation of the length resonance behavior observed in circular cracks must therefore be sought elsewhere.

One possible explanation for length resonances could be through the concept of edge waves introduced by Bondarenko and Dubovitskii,⁸ Wagers,⁹ and Sharon.¹⁰ These waves can propagate along the top edge of the crack, decaying in two other directions. Using the concepts introduced by crack waveguide two such waves, one on each top edge, can be postulated. As in the crack waveguide, these waves are coupled at the crack corners and the reflection coefficients at the corners must behave differently for even and odd field distributions relative to the z direction, resulting in a similar "mode switching" to that noted above. The drawback of this hypothesis is that the edge waves travel slower than Rayleigh waves (for $\sigma = 0.25$, $V_{\text{edge}} \sim 0.87 V_R$), which results in lower resonance frequencies. Assuming that boundary conditions are the same as those of the crack waveguide, the length resonances with edge waves can be found to occur at

$$f = \frac{V_{\text{edge}}}{2L} \left(M + \frac{1}{2} \right) \quad (29)$$

COMPARISON WITH EXPERIMENTAL DATA

We have compared our analytical results with the data given in References 2 and 11. Our results (Tables 4 and 5) agree fairly well with the length resonances of Reference 2, and good agreement is obtained for both resonances of Reference 11. For each resonances, we can assign the mode indices M and N (see Eqs. 10, 13, 25, 29) with reasonable accuracy. The formulas used in calculations are repeated below.

$$\text{Length resonances: } f_L = \frac{V_R}{2L} \left(M + \frac{1}{2} \right) \quad (30)$$

$$\text{Depth resonances: } f_D = \frac{V_R}{2h} N \quad (31)$$

TABLE 4. Comparison of Theoretical Calculations with the Data of Reference 2

Crack #	f_L (MHz) (Experimental)	f_L Eq. (30)	M	f_D (MHz) (Experimental)	f_D Eq. (31)	N
1	3.48	3.55	5	5.8	6.62	1
	4.02	4.20	6			
	4.58	4.84	7			
	5.20	5.49	8			
2	3.60	3.62	2	5.68	5.94	1
	5.18	5.08	3			
3	3.86	3.56	1	5.6	5.94	1
	*	5.94	2			
4	3.18	3.43	1	5.1	4.58	1
	5.72	5.72	2			
5	3.00	3.43	1	4.0	3.3	1
	5.80	5.72	2			
6	3.00	3.43	1	3.6	2.57	1
	5.80	5.72	2			

The cracks tested were EDM notches on a steel sample, with their aspect ratios varying between 0.097 and 0.89. The asterisk for the second resonance of the third crack means that the resonance also corresponds to a depth resonance.

TABLE 5. Comparison of Theoretical Calculations with the Data of Reference 11

f_L (MHz) (Experimental)	f_L Eq. (30)	M	f_D (MHz) (Experimental)	f_D Eq. (31)	N
0.83	0.84	1	3.41	3.74	1
1.24	1.40	2	7.93	7.47	2
1.79	1.96	3			
2.27	2.52	4			
2.90	3.07	5			
*	3.63	6			
4.00	4.20	7			
4.48	4.75	8			
5.24	5.31	9			
6.13	5.87	10			
6.41	6.43	11			
7.03	6.99	12			

The crack is a (2.54 mm × 0.38 mm) EDM notch on the aluminum sample.

In the length resonance calculations above, we used Rayleigh wave velocities instead of edge wave velocities. A complete analysis of the edge waves can be found in Reference 12, where the equations of motion are solved by expanding each displacement component in a double series of Laguerre functions. The analysis shows that there are two symmetry modes that can be supported by the edge, and for $\sigma = 0.25$ the corresponding edge wave velocities are $V_{\text{edge}}/V_R \sim 0.98$ and 1.002, which are very close to the Rayleigh wave velocity.

There have been other approaches for the solution of edge wave modes and velocities.^{3,9} In Reference 8 the solutions are approximated such that the boundary conditions are not fully satisfied on the two free surfaces of the edge. For $\sigma = 0.25$, this approach yields a numerical value of $V_{\text{edge}}/V_R = 0.86$. In Reference 9 a variational approach is utilized and their result gives $V_{\text{edge}}/V_R \sim 0.7$ for $\sigma = 0.34$. This result is in

agreement with what can be obtained from Reference 8. One reason for this agreement is that the trial functions used in the variational approach are of the same nature as the functions resulting from the analysis of Reference 8.

In conclusion, considering the results given by Maradudin, et al.,¹² the use of Rayleigh wave velocities instead of edge wave velocities does not ignore the role of edge waves for length resonances. The open question is the verification of the hypothesis of π radians phase shift between the even symmetric and odd symmetric edge wave modes in the z direction.

ACKNOWLEDGEMENT

This research has been sponsored by the Center for Advanced NDE operated by the Science Center, Rockwell International for the Advanced Research Projects Agency and the Air Force Materials Laboratory under Contract No. F33615-74-C-5180.

REFERENCES

1. B. R. Tittmann, M. de Billy, F. Cohen-Tenoudji, A. Jungman, and G. Quentin, "Measurements of Angular and Frequency Dependence of Acoustic Surface Wave Scattering from Surface Cracks," IEEE Ultrasonics Symposium Proceedings, 78CH 1344-1SU, pp. 379-383 (1978).
2. V. Domarkas, B. T. Khuri-Yakub, and G. S. Kino, "Length and Depth Resonance of Surface Cracks and Their Use for Crack Size Estimation," Appl. Phys. Lett. 33, 7, 557-559 (October 1978).
3. B. A. Auld, S. Ayter, and M. Tan, "Theory of Scattering of Rayleigh Waves by Surface Breaking Cracks," IEEE Ultrasonics Symposium Proceedings, 78CH 1233-1 SU, pp. 384-390 (1978).
4. L. B. Freund, "The Oblique Reflection of a Rayleigh Wave from a Crack Tip," International Journal of Solids and Structures 7, 1199-1210 (1971).
5. L. B. Freund, "Surface Waves Guided by a Slit in an Elastic Solid," J. Appl. Mechanics, 1027-1032 (December 1972).
6. J. K. Knowles, "A Note on Elastic Surface Waves," J. Geophysical Research, 71, 22, 5480-5481 (November 1966).
7. F. C. Cuozzo, E. L. Cambiaggio, J-P Damiano, and E. Rivier, "Influence of Elastic Properties on Rayleigh Wave Scattering by Normal Discontinuities," IEEE Trans. Sonics Ultrason. SU-24, 4, 280-289 (July 1977).
8. V. S. Bondarenko and V. F. Dubovitskii, "Acoustic Edge Waves in Isotropic Solids," Sov. Phys. Acoust. 22, 2, 159-160 (March-April 1976).
9. R. S. Wagers, "Variational Analysis of Acoustic Waveguides," IEEE Ultrasonics Symposium Proceedings, 121-125 (1973).
10. T. M. Sharon, "Edge Modes for Piezoelectric Wedges of Arbitrary Interior Angles," IEEE Ultrasonics Symposium Proceedings, 126-130 (1973).
11. B. R. Tittmann, private communication.
12. A. A. Maradudin, R. F. Wallis, D. L. Mills, and R. L. Ballard, "Vibrational Edge Modes in Finite Crystals," Phys. Rev. B. 6, 4, 1106-1111 (August 1972).

SUMMARY DISCUSSION
(S. Ayter and B. Auld)

Ed Kraut (Session Chairman--Science Center): Questions on this talk?

Unidentified Speaker: Let me see if I get this straight. Talking about the rectangular crack, you excite the Rayleigh wave along the ZED plus or minus face, and the waves travel down in the Y direction and up again on the other side and back again, or is this --

S. Ayter: You don't excite simple Rayleigh waves. You excite the wave guide modes which are combinations of Rayleigh waves, and those waves go down and come up, but they go down on both faces and come up on both faces.

Unidentified Speaker: How do you excite the wave? What is the excitation scheme?

S. Ayter: We have calculated the coupling quotient, but we don't have the results here. The way to excite is you have a crack here, and you illuminate it normally with the Rayleigh wave, and these Rayleigh waves excite the waveguide modes going down.

Unidentified Speaker: There is no wave going down there. It's only on the two surfaces, and the two surfaces are separated by distance between ZED plus and ZED minus. How does it go from one side to the other? It has to go down one crack and up the other side.

S. Ayter: On each face, each face is a traction-free surface. So, each face separately can support Rayleigh waves. And, a combination of those Rayleigh waves can guide waves that are going down.

B. Auld: Could I make a comment, in response here? The fact is, the two faces are coupled at the edges. These Rayleigh waves that are propagating on the faces at an angle are coupled at the edges all the way down, and it's that edge coupling that gives rise to the guided waves which exist on both surfaces.

#

LIFE PREDICTION FOR AL IN THE MICROCRACK REGIME USING SAW NDE

O. Buch, W. L. Morris, F. R. Jones and R. J. Richards
Rockwell International Science Center
Thousand Oaks, California 91360

ABSTRACT

Harmonic generation of surface acoustic waves (SAW) is a useful tool for studying surface microcrack initiation during fatigue of high strength aluminum alloys. We have developed a model which relates the length and density of such microcracks, initiated during fatigue, with SAW harmonic generation signals. It was found that the resulting quantitative relationship between the acoustic data and the remaining fatigue life is accurate to within 5% over the last 50% of the fatigue life, spent in the microcrack initiation phase. Extensive tests are now underway to study the general applicability of these concepts to a wide range of high-strength Al alloys. Furthermore, we have started to separate the various contributions to harmonic generation from microcracks that are smaller than the average grain diameter, from those that have been able to grow out of the grain of their origin. These considerations are important in that they (1) provide detailed insight into the process of fatigue damage and (2) may improve our remaining life prediction capability, particularly during the first 90% of the total fatigue life. This concept seems to have applicability to the "Retirement for Cause" program of the Air Force.

INTRODUCTION

The objective of the present work is to establish a procedure for the prediction of the remaining life of an originally smooth, unflawed metallic component. Extensive scanning electron microscopy (SEM) studies on certain aluminum alloys have shown¹⁻⁶ that the presence of intrinsic defects in the material such as brittle intermetallic inclusions, will lead to the nucleation of microcracks during fatigue of these alloys. After nucleation the microcracks grow into the matrix, interact with the grain boundaries, and eventually coalesce with other microcracks to form a macrocrack whose subsequent growth will finally terminate the life of the specimen, as discussed extensively by Morris and Jones in this volume. Furthermore, it has already been shown that simple analytical models of crack nucleation, early crack growth and coalescence in aluminum alloys are able to describe the fatigue failure process, yielding mean and scatter of the life even as the grain diameter of the alloy is changed.⁷⁻⁹ These models, which are the basis for a Monte Carlo simulation, relate the probability of nucleation and rate of early crack propagation to the alloy microstructure in the vicinity of an initiation site. Further studies are underway to improve these models.

Such knowledge of the development of fatigue damage is one necessary input for a successful life prediction, prior to the formation of the macrocrack. The monitoring of this damage, using a nondestructive testing method, forms the other input. Present day, standard nondestructive testing methods are, in general, not sensitive enough to detect such microscopic damage before the ultimate macrocrack is formed. Therefore, and in parallel to the above investigations on the microscopic events leading to ultimate failure, evaluations on new nondestructive testing methods capable of monitoring these microscopic events have been performed.¹⁰ One of these methods, the

generation of harmonics in surface acoustic waves, has been extensively studied and was found to be sensitive to microcracks developed during fatigue.¹⁰⁻¹² In the following a tentative relation between the harmonic generation and microcracking parameters is suggested and tested, leading to a semi-quantitative prediction of the remaining life for a high-strength aluminum alloy. At the present time it is believed that the remaining life prediction is accurate to within 5% over the last 50% of the total fatigue life, starting with a smooth bar specimen. This is certainly an improvement over present day fatigue life prediction capabilities, which can only be applied after the formation of the macrocrack. Since the critical flaw sizes in metals may be quite small (low fracture toughness materials) the present results suggest that harmonic generation may be a useful tool for early crack detection and that the suggested procedures may be applicable to programs such as the "Retirement for Cause" program of the Air Force.

PARTICIPLES

The generation of second harmonics by surface acoustic waves during fatigue of a high strength aluminum alloy has recently been reported.¹⁰⁻¹² The enhanced generation of a second harmonic with fatigue is attributed to an increased anelasticity of the surface due to development of surface microcracks. Considering a surface crack as an unbonded interface, a possible mechanism for this generation is the distortion that the fundamental surface wave experiences as it propagates across the unbonded interface. The effect was predicted by Richardson¹⁰ who calculated the harmonic amplitude generated by the opening and closing of an unbonded interface between two semi-infinite solid materials for the particular case of an incident plane, longitudinal bulk wave. These calculations indicate that the harmonic generation efficiency is extremely low on the

external applied stress, and that under optimum conditions (close to zero applied stress) the second harmonic amplitude is larger than 17% of the fundamental, exceeding by far all generation from other nonlinear sources, such as lattice anharmonicity¹⁴ or dislocation.¹⁵ It is believed at the present time, that similar considerations are applicable to the harmonic generation of surface waves, as will be discussed in the following.

The experimental set-up to determine harmonic generation in surface waves as a function of fatigue was extensively discussed in Ref. 12. Briefly, a fundamental SAW (5 MHz) was transmitted across the gauge section of cantilever beam specimens (Al 7075-T6) that were fatigued in flexure. The tapered geometry generates a uniform surface stress and thus a fairly homogeneous density of microcracks (however note that the through-the-thickness stress distribution is non-uniform).

The amplitude of the second harmonic (10 MHz) was measured at several increments of fatigue. This second harmonic signal is at a maximum close to zero surface stress (the specimen being under static load during the measurement) and this maximum increases with expended fatigue life, consistent with the formation of microcracks during fatigue. A summary of these results¹² is shown in Fig. 1.

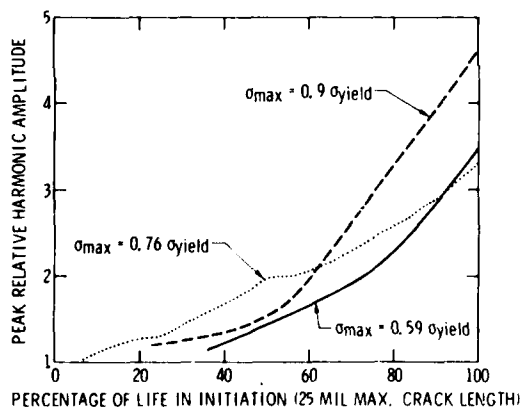


Fig. 1. Harmonic generation as a function of percentage of life in initiation for three different cyclic stress amplitudes (Ref. 12).

in which the change of the peak value of the second harmonic is given as a function of the fraction of expended life in the initiation phase of fatigue, which is here defined as that part of the total life necessary to produce the first large microcrack having a length of approximately 500 μm . Actual total numbers of fatigue cycles applied to each specimen are given in Table I. The curves presented are basically "raw" data since a portion of the second harmonic generation is obscured by the changes in attenuation the SAW experiences due to scattering at the microcracks. In order to unfold these competing effects, a simple analysis has been made taking attenuation

TABLE I

Total number of fatigue cycles applied to produce a longest microcrack of 500 μm .

Stress Level	Fatigue Cycles
0.59 σ_{yield}	22,000
0.76 σ_{yield}	8,000
0.9 σ_{yield}	2,500

effects into account.¹⁶ Assume that the fundamental is attenuated according to

$$A_1(x) = A_1(0)e^{-\alpha_1 x} \quad (1)$$

where $A_1(0)$ is the (constant) fundamental amplitude generated by the transmitter, α_1 is the attenuation coefficient of the fundamental and x the propagation distance away from the transmitter. Between x and $x + \Delta x$ the incremental second harmonic generation would be¹⁷

$$\Delta A_2(x) = \beta [A_1(x)]^n e^{-\alpha_2 x} \Delta x \quad (2)$$

with β being a coefficient of second harmonic generation efficiency, α_2 the attenuation of the second harmonic and n the power relationship between the second harmonic and the fundamental amplitude. Integration over the total path-length, ℓ , yields the received second harmonic amplitude

$$A_2(\ell) = \frac{\beta [A_1(0)]^n e^{-\alpha_2 \ell}}{(\alpha_1 - \alpha_2)} [1 - e^{-(\alpha_1 - \alpha_2)\ell}] + \text{const}, \quad (3)$$

in which the integration constant is determined by the second harmonic contributions from the lattice anharmonicity and dislocation harmonic generation. In previous work¹⁸ it was observed that the effects of attenuation are appreciable only if the interrogated surface of specimen is under tension or, in other words, if the cracks are fully open. The present work is concerned only with the development of the maximum in harmonic generation, which occurs close to zero surface stress (see Fig. 1). Therefore both α_1 and α_2 will be neglected in the following discussion. Furthermore the harmonic generation data will be normalized to the value obtained prior to fatigue, so that the integration constant in Eqn. (3) is equal to 1. Under these simplified conditions

$$A_2(\ell) - 1 = B \ell [A_1(\sigma)]^n \quad (4)$$

The second harmonic generation coefficient B is the quantity that is related to the microcracking parameters, important to a successful fatigue life prediction.

Such microcracking parameters have been obtained from each of the specimens interrogated, using SH and in some cases, using optical microscopy. Since most of the cracks are partially closed, it was necessary to load the specimen in tension for easy observation of the cracks. Histograms of the cracking density Λ (cracks/cm²) as a function of crack length

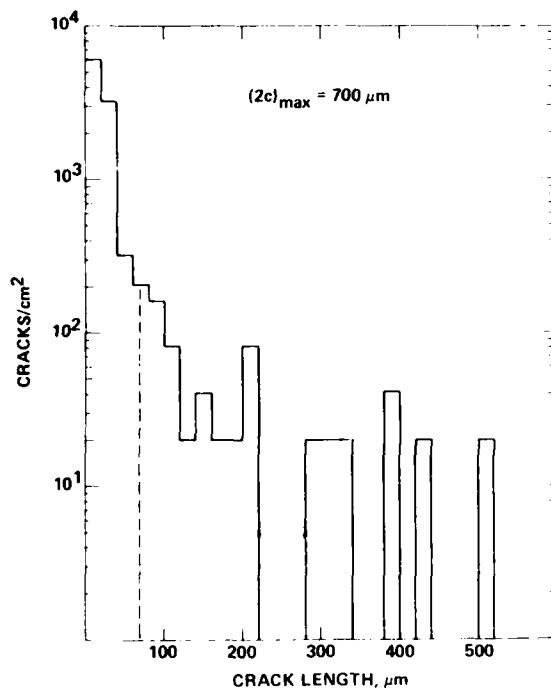


Fig. 2 Histogram of the cracking density as a function of crack length.

($2c$) were then obtained, an example of which is shown in Fig. 2. Such histograms as a function of fatigue should contain all information necessary to determine the harmonic generation coefficient B . In the work reported here, detailed histograms have been taken only after termination of the harmonic generation experiments (100% of the fatigue life expended in the initiation phase). Histograms of the intermediate states have been obtained using a Monte Carlo simulation of microcrack development for the particular microstructure of the aluminum alloy used. In all cases, the calculated histograms matched the experimental ones quite well. Since the Monte Carlo simulation is based upon actual crack nucleation and early growth data on aluminum alloys, there is every reason to believe that this interpolation method

reflects the actual microcrack development with sufficient accuracy, and, in the few cases studied so far, this speculation has been confirmed.

RESULTS

A. Life Time Prediction in Initiation - In the following, an attempt is made to relate the second harmonic generation data to microcracking parameters, a step necessary to arrive at a successful fatigue life prediction during the initiation phase of fatigue. To arrive at such a relation the assumption was made that harmonic generation occurs where the fracture surfaces contact each other gently. This area of contact is schematically shown in Fig. 3 as a dark

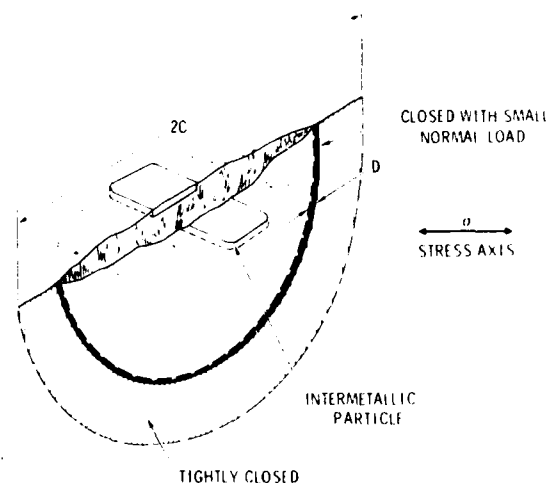


Fig. 3 Representation of a partially closed crack.

band. It is this region of low contact stress in which Richardson's analysis would be qualitatively applicable. As an external tension or compression stress is applied, the crack will start to open or close. If the stress is high enough, harmonic generation will cease to occur for both tension and compression. Semi-quantitatively, the second harmonic amplitude generated per microcrack should then be proportional to the crack length ($2c$). For any length element in the path of the SAW of width $d\ell$ the microcrack density of Λ cracks per cm² will make an infinitesimal contribution to the harmonic generation given by

$$\Delta A_2 = \frac{dA_2}{d\ell} \ell(2c) \quad (5)$$

In Eqn (5), $\ell(2c)$ is the total crack length interrogated by the SAW and $d\ell$ (ℓ = total path length). In the following the quantity $1/\ell \ell(2c)$ will be simply defined as $(2c\Lambda)$, where Λ can be interpreted as the cracking density. Therefore

$$\Delta A_2 \approx d(2cA) \Delta x. \quad (6)$$

Integration over the total path length (assuming that the attenuation is negligible) and combining Eqns. (4) and (6), yields

$$B \approx \frac{d(2cA)}{[A_1(c)]^n} \quad (7)$$

so that the relative change in harmonic generation (due to microcracks) is given by

$$A_2(l)-1 = kF(2cA), \quad (8)$$

where k is a proportionality constant. The quantity $F(2cA)$ may be interpreted as the total crack length, seen by the SAW, which can be obtained either by direct experimental observation or from the Monte Carlo simulation (which is based on experimental data as pointed out before). First results, obtained by a comparison of the harmonic generation data taken at $\sigma_{max} = 0.9\sigma_{yield}$ (see Fig. 1), with the total crack length, as obtained from a Monte Carlo simulation, verify the prediction of Eqn. (8) satisfactorily, as shown in Fig. 4.

In addition, the Monte Carlo simulation yields information about the relation of the quantity $(2cA)_t$ and the fraction of life spent in fatigue, N_i . The result, for the same specimen as previously discussed, is shown in Fig. 5 which can be expressed by the empirical relation

$$(2cA) = (2cA)_t N_i^2, \quad (9)$$

at least above about $N_i = 0.5$. In Eqn. (9) the quantity $(2cA)_t$ is primarily related to the total crack length at the point where 100% of the fatigue life in the initiation phase has been spent. Combining Eqns. (8) and (9) yields the remaining fatigue life

$$\Delta N_i = 1 - N_i \quad (10)$$

to be

$$\Delta N_i = 1 - \sqrt{\frac{A_2(l)-1}{kF(2cA)_t}} \quad (11)$$

From the Monte Carlo simulation a value $F(2cA)_t = 14.3$ mm is obtained for the experimental conditions under discussion and from Fig. 4, $k = 0.245$ mm⁻¹. Using the second harmonic data (at $\sigma_{max} = 0.9\sigma_{yield}$) from Fig. 1, this yields a measured fraction of remaining fatigue life, $\Delta N_{measured}$, which can be compared with the actual fraction of remaining life in initiation, ΔN_{actual} . As shown in Fig. 6, ΔN_{actual} and $\Delta N_{measured}$ (using Eqn. 11) basically follow a one-to-one relationship to within 5% above about 50% of expended fatigue life. Below 50% of expended fatigue life, deviations seem to be mainly caused by the statistics of nucleation

and early growth within the first grain. The above analysis appears to be applicable, however, as soon as the longest cracks overcome the first grain boundaries. Indications for this transition at 50% life expended become quite apparent by splitting the quantity $(2cA)$ into a part that contains all cracks smaller than D , the mean grain diameter, and a part that contains all cracks larger than D :

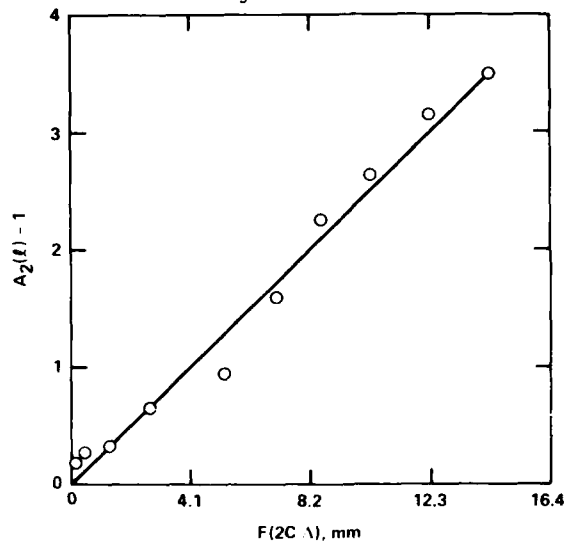


Fig. 4. Harmonic generation data as a function of total crack length $F(2cA)$.

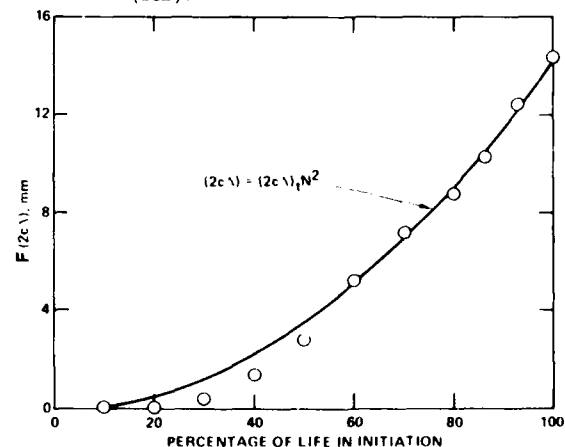


Fig. 5. The quantity $F(2cA)$ as a function of life in initiation at $\sigma_{max} = 0.9\sigma_{yield}$.

$$(2cA) = (2cA)_{<D} + (2cA)_{>D} \quad (12)$$

The result is shown in Fig. 7. After an initial growth, the quantity $(2cA)_{<D}$ stays about constant above 50% of life expended. At the same time $(2cA)_{>D}$ starts to grow rapidly. Based upon this separation it is possible to express the quantity $(2cA)_t$ in Eqn. (11) in the following way (without going into the

details). For a material of mean grain size diameter $D = 70 \mu m$ (as investigated in the present work) the longest crack after 100% of life have been expended in initiation, has a size

$$(2cA)_t \approx 3.1 D \Sigma_t \quad (13)$$

(where Σ_t is the cracking density of all cracks that are larger than D), and since, in the present case,

$$(2c)_t \approx 8L \quad (14)$$

we obtain

$$(2cA)_t \approx 1/3 (2c)_t \Sigma_t \quad (15)$$

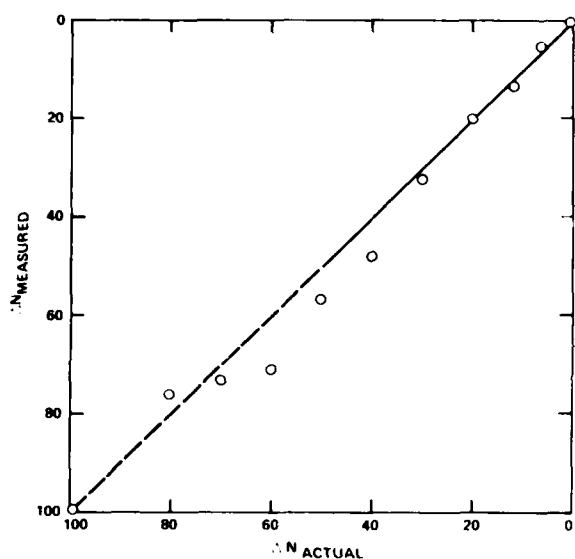


Fig. 6 Comparison of remaining fatigue life, $\Delta N_{\text{measured}}$, determined from harmonic generation data, versus ΔN_{actual} .

These quantities in Eqn. (15), as obtained from actual SEM and optical microscopy, are given in Table II for the three stress levels at which harmonic generation data have been obtained. These data show that Eqn. (15) holds reasonably well at the lower stress levels. Some deviation at $\sigma_{\text{max}} = 0.9 \sigma_{\text{yield}}$ is caused by the fact that the largest cracks on this specimen started to grow predominantly at the specimen edges outside the region of microscopy. Indications are, however, that the quantity $(2cA)_t$, which is related to the total crack length (thus including all cracks, even the ones that are unimportant to failure) may be replaced by the product of length and density of the cracks, important to failure.

Even of more interest may be the last column in Table II. On all specimens, subjected to a wide range of fatigue stress levels, we find that the quantity $(2cA)_t$ is basically independent of σ_{max} . Since it is to be expected

that the values for L and F in Eqn. (11) are also independent of σ_{max} , the harmonic generation should be independent of σ_{max} , a result which is basically observed, as evidenced by Fig. 1.

B. Life Time in the Propagation Phase - In order to confirm the previous statement, that for smooth bar specimens the major part of the total fatigue life is spent in initiation,

Table II
Cracking Parameters as a Function of Maximum Fatigue Stress Level

σ_{max}	$(2c)_t$ mm	Σ_t cm ⁻¹	$(2cA)_t$ mm cm ⁻¹
0.59 σ_{yield}	0.75	341	25.7
0.70 σ_{yield}	0.56	492	23.7
0.9 σ_{yield}	0.40	175	20.1

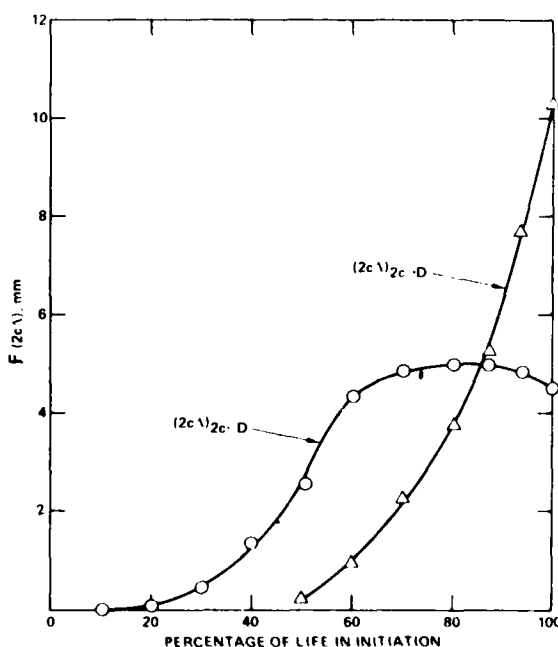


Fig. 7 The separation of the quantity $F(2c\Delta)$ into a part for which all cracks are smaller than D and a part for which all cracks are larger than D .

specimens that had been pre-fatigued in flexure were exposed subsequently to unidirectional tension - tension fatigue (thus avoiding the non-uniform through-the-thickness stress distribution experienced in flexure). After pre-fatigue, the tapered geometry of the specimen was changed to one of uniform cross section, to give the longest crack, which may be anywhere along the tapered section, a chance for further growth, leading to failure of the specimen.

Three specimens were prepared, as indicated in Table III. A first one was not exposed to pre-fatigue at all, a second one was pre-fatigued to $N_1 = 0.65$ (1800 cycles) and a third one to $N_1 = 1$ (2700 cycles) at $\sigma_{max} = 0.9 \sigma_{yield}$. As expected the second specimen contained cracks, the longest one having a size of the mean grain diameter. The longest crack of the third specimen had grown to a surprisingly large size (1400 μm).

For a lifetime prediction it is important to know the crack depth a . Certainly, the aspect ratio is smaller than the usual value of 0.5, which is the equilibrium value in a uniform stress field over the total cross section, since in flexure the stress goes to zero at the needed axis. We estimated, therefore, that the cracks grown in pre-fatigue may have an aspect ratio in the vicinity of 0.3, yielding the crack depth estimates given in Table III. Failure is assumed to occur as soon as the longest crack, achieved during pre-fatigue, reaches the backface of the specimen, thus yielding

$$\Delta N_{res} = \frac{2}{(n-2)A(f\Delta\sigma)^{1/n}}$$

$$\left\{ \frac{1}{a^{(n-2)/n}} - \frac{1}{d^{(n-2)/n}} \right\} \quad (16)$$

where $f = 2.8$, $A = 1.6 \times 10^{-8}$, f a geometrical factor (chosen for a part-through crack), $\Delta\sigma = 350 \text{ MNm}^{-2}$, a the initial crack depth and d the specimen thickness (1.5 mm). As may be seen from Table III, the calculated ΔN_{res} for the third specimen is somewhat too high (by about a factor of 2.5). This overestimate is to be expected, since we used a (straight line) "Paris Equation" which does not account for the sigmoidal shape of the actual da/dN versus Δh curve. Furthermore possible coalescence of the longest crack with other microcracks has not been taken into account. From this point of view, we have to consider the agreement between the calculated and observed ΔN_{res} as reasonable. Most important, however, is the observation that the remaining life of the third specimen, $\Delta N_{res, observed} = 333$ cycles, is indeed short with respect to the life in initiation. Comparing the data for the

specimen fatigued at $\sigma_{max} = 0.70 \sigma_{yield}$ (see Table I) with the ones above indicates that for fatigue at a comparable stress level only about 5% of the total life is spent in the propagation phase.

Table III also shows that the discrepancy between the calculated and observed Δh becomes worse, the smaller the longest crack, and it is quite clear, that the simple minded fatigue life prediction becomes more and more inadequate. It is satisfying, however, that the observed Δh becomes larger, the smaller the longest crack.

CONCLUSIONS

The presented work is an initial attempt to develop a life prediction methodology in the initiation phase of metal fatigue. This methodology is based upon the relation between microcrack development and the outputs of a nondestructive testing method, in the present case harmonic generation. It is clear that improvements are necessary, particularly in describing the functional relations of microcrack density and length of the longest crack on one hand and the remaining life in initiation on the other hand in a more appropriate statistical form, rather than in an empirical one. However, even in the present form, it seems possible, to take the microstructural parameters of the alloy investigated into full consideration. Further work is also needed to pinpoint the exact mechanism of harmonic generation at fatigue cracks, presently thought to be due to the opening and closing of the cracks.

However, we believe we have shown, that fatigue life prediction in metals is possible over the last 50% of the life spent in initiation, which is a vast improvement over present day technology. It is thus believed, that the developed methodology may be applicable to programs such as "Retirement for Cause" in which early fatigue crack detection is necessary.

ACKNOWLEDGMENT

This research has been sponsored by the Center for the Advanced NDI operated by the Science Center, Rockwell International, for the Advanced Research Project Agency and the Air Force Materials Laboratory, under contract number F33615-74-C-5180.

TABLE III.

Calculated and observed remaining life in tension-tension fatigue of pre-fatigued specimens.

Tension-Tension conditions: $\Delta\sigma = 350 \text{ MNm}^{-2}$, $\sigma_{yield} = 500 \text{ MNm}^{-2}$, $\frac{da}{dN} = 1.6 \times 10^{-8} (\Delta h)^{2.8}$

Specimen	$2c$ (μm) (Typically)	a (μm) (Estimate)	ΔN_{Start} ($HN^{-3/2}$)	Δh (Observed)	Δh (Calculated)
No Prefatigue ($N_1 = 1$)	0	0	0	6420	-
1800 cycles ($N_1 = 0.65$)	70	20	1.3	3560	5.0×10^4
2700 cycles ($N_1 = 1$)	1400	400	11	330	100

REFERENCES

1. W. L. Morris, O. Buck, and H. L. Marcus: Met Trans. 7A, 1161 (1976).
2. W. L. Morris: Met. Trans. 8A, 589 (1977).
3. W. L. Morris and O. Buck: Met. Trans. 8A, 597 (1977).
4. W. L. Morris: Met Trans. 8A, 1079 (1977).
5. W. L. Morris: Met Trans. 8A, 1097 (1977).
6. W. L. Morris: Met Trans. 10A, 5 (1979).
7. W. L. Morris and M. R. James in this volume.
8. W. L. Morris, M. R. James and O. Buck, Eng. Fracture Mechanics (accepted for publication).
9. O. Buck and G. A. Alers, in Fatigue and Microstructure, Am. Soc. for Metals (on press).
10. O. Buck, W. L. Morris, and R. V. Inman: in Proceedings of the ARPA/AFML Review of Progress in Quantitative NDE, Technical Report AFML-TR-78-55, May 1978.
11. O. Buck, W. L. Morris and J. M. Richardson: Appl. Phys. Letters 33 371 (1978).
12. W. L. Morris, O. Buck, and R. V. Inman: J. Appl. Phys. (accepted for publication).
13. J. M. Richardson: Int. J. Eng. Sci. 17, 83 (1979).
14. M. A. Freazcale and D. O. Thomson: Appl. Phys. Letters 3, 77 (1963).
15. A. Hikata, P. Chiel, and G. Elbaum: J. Appl. Phys. 36, 229 (1965).

SUMMARY DISCUSSION
(Otto Buck)

Gordon Kino (Stanford University): Can you tell me why there is an N squared relation for the life prediction curve?

Otto Buck: You mean, why does $(2c\Delta)$ increase with N squared? No, I cannot at the present time.

Gordon Kino: It's empirical?

Otto Buck: Yes. It's empirical.

Alastair Morton (NSRDC): Did you look at any other methods of fatigue life prediction other than this one before you started? For example, any dislocation density measurements? Is there something in the literature that relates to degree of hardening due to dislocation density changes in the surface layers with the life?

Otto Buck: What we are looking at right now are residual stresses in the surface and the change of those with fatigue and you can see these effects using X-ray or acoustic techniques. In direct answer to your question, we have looked at dislocations in pure aluminum and there are indications that the acoustic harmonic generation changes due to a shakedown of the dislocation structure during fatigue, but I don't think that these are, at least in the high-strength aluminum alloys, overriding effects because of dislocation repinning. There are certain materials, high purity aluminum, e.g., where you can see slight effects on the attenuation, but these are very small. The major attenuation effect in the present case stems from generation of the microcracks. In general, I believe that in materials where immediate dislocation repinning is possible, you should be able to see dislocation rearrangements (fatigue hardening or softening). The only method that I know of, that is not hampered by this problem, is positron annihilation, because it does not require dislocation mobility. In addition, and if you are lucky, you may be able to use an eddy current method, but that may require low temperatures to see effects due to dislocation resistivity.

#

FATIGUE LIFETIME PREDICTION WITH THE AID OF SAW NDE*

B.R. Tittmann and O. Buck
Rockwell International Science Center
Thousand Oaks, CA 91360

ABSTRACT

The scattered radiation of elastic waves from fatigue cracks in metals is interpreted for their detection and characterizations. The studies concentrated on predicting the remaining fatigue life for single fatigue cracks above the "threshold" value for macrocrack propagation. Acoustic surface waves were used to interrogate the crack during cyclic fatigue. The inversion of the scattering data provided crack depth and crack length as a function of fatigue. Auxiliary experiments were conducted to study effects of crack closure. Since the closure load depends strongly upon crack depth, especially in the near-threshold regime, improved life prediction is the expected result.

INTRODUCTION

The increasing use of failure prediction techniques has motivated the rapid evolution of methods to measure the length and depth of part-through (surface breaking) cracks. In a recent review Doyle and Scala¹ presented a progress report on both bulk acoustic and surface acoustic wave (SAW) methods of the measurement of the depth of part-through cracks. Since this review, there have been several reports on new techniques and approaches using surface waves which show considerable promise.

Khuri-Yakub and Kino² have developed a new technique for exciting high-frequency (100 MHz range) surface and shear acoustic waves on non-piezoelectric materials. Fraser, Khuri-Yakub and Kino³ have produced a design for an efficient broad-band wedge transducer. Resch et al⁴ have carried out measurements with a surface wave probe and predicted fracture stresses in good agreement with those measured. The calculations of the fracture stress were based, in part, on theoretical developments by Kino.⁵ Domarkas et al⁶ have observed structure in the frequency dependence of the acoustic surface reflection coefficient associated with a rectangular slot which they have interpreted in terms of resonances across the length and depth of the slot. Ayter, Auld and Tan⁷ have developed two theoretical approaches based on real reciprocity relations for the scattering of Rayleigh surface waves by part-through cracks. Tittmann et al^{8,9} have reported experimental data and a simple model on the estimation of the size of small part-through cracks.

None of these techniques make use of a concept, developed a long time ago by Cook at the British Railways Board.¹⁰ This concept is illustrated in Fig. 1, taken from the work of Hudgell, Morgan, and Lumb,¹¹ and makes use of monitoring transit times of ultrasonic echoes associated with the crack and specimen geometry. They consider that portion of the generated Rayleigh wave which is not reflected at A. It splits into three components - one travels down the crack face as a Rayleigh wave,

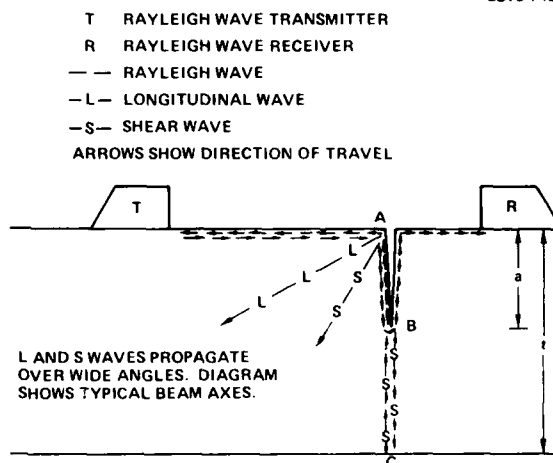


Fig. 1 Behavior of ultrasonic Rayleigh wave impinging on surface-breaking crack.
(Courtesy of Hudgell, Morgan and Lumb.)

whilst the other two mode convert into shear and longitudinal mode bulk waves propagating into the plate at approximately the angles shown.¹² When the Rayleigh wave travelling down the crack face reaches the crack tip, further modification occurs. Part of the energy propagates around the crack and up the other face as a Rayleigh wave. The remaining energy converts to a shear wave and possibly some longitudinal waves also. The shear component at the tip of the crack travels to and reflects from the back wall of the plate, impinging on the crack face at grazing incidence, thereby undergoing re-conversion back to a Rayleigh wave. Lumb, Hudgell and Winship¹³ have proposed to utilize this change in mode at the crack tip to estimate crack depth in parallel sided components. Hudgell, Morgan and Lumb¹¹ have employed this concept for depth measurements of fatigue cracks induced in gas pipe line material. This approach has recently been criticized by A. Brown¹⁴ on the

*This research was sponsored in part by the Center for Advanced NDE operated by the Science Center, Rockwell International, for the Advanced Research Projects Agency and the Air Force Materials Laboratory under Contract No. F33615-74-C-5180.

basis that this model, in principle, should be valid only in the limit where the Rayleigh wavelength is very much smaller than the crack depth, a condition not accessible in most practical applications. Typically, the wavelengths are more nearly of the order of the crack depth so that the Rayleigh wave sees the entire crack at the same time.

The work described in this report attempted to test and evaluate the technique on an aerospace material undergoing fatigue cracking. The prediction of the crack depth was compared with those obtained from fracture mechanics during and after specimen failure. The technique was tested under various static loads ranging from tension to compression loading. Finally the limitations of the technique were explored in terms of sources of errors, the influence of specimen geometry, the effect of crack orientation, and the role of Rayleigh wavelength vis-a-vis the crack depth.

CRACK LENGTH

Experimental Technique - The material chosen for the measurements was Ti-15A, which is an unalloyed, relatively clean titanium, often used for tubing material in corrosive environments. The specimens were prepared as plates (10 cm x 30 cm x 1 cm) with a spark eroded starter notch. The plates were first subjected to fatigue cycling in a four-point bending apparatus. After a true fatigue crack had been initiated, the plates were ground and polished to remove the starter notch, leaving a nearly closed part-through fatigue crack in the remaining material. These cracks were typically 2-3 mm in length and about 1 mm deep. With the specimen plates prepared in this way, the first phase of measurements of crack depth and length was carried out. Figure 2 shows a micrograph of one of the cracks during the phase I measurements.

To study the growth of these true fatigue cracks under well specified conditions, the plates were machined into dog-bone type specimens and subjected to cyclic tension-tension fatigue. This part-through crack geometry (PTC) specimen had the following dimensions: 0.45 cm thick, 3.8 cm wide and a 6 cm gauge length. The specimens were cyclically loaded in an MTS electrohydraulic system in laboratory air under the following loading conditions:

$$\sigma_{\min} = 1 \text{ ksi}, \sigma_{\max} = 39 \text{ ksi}$$

with the external gross section stress being of the form

$$\sigma = \frac{\sigma_{\max} + \sigma_{\min}}{2} + \frac{\sigma_{\max} - \sigma_{\min}}{2} \sin \omega t.$$

The specimens were cycled at a rate $(\omega/2\pi) = 1 \text{ sec}^{-1}$

In the SAW experiments, commercial broadband longitudinal wave transducers were used with water wedges to provide both the transmitter and receiver, as described previously. A Parametrics Pulser-Receiver was used with an external attenuator to generate and receive the signals. A Biomation 8100-D was employed to digitize the signals received and to provide an interface with a Data General S/200 Eclipse computer. This minicomputer was used to obtain the Fourier transform of the signal, which was typically divided by the transducer transfer functions in order to calculate and display the normalized magnitude of the resulting Fourier transform. The transducer transfer function was obtained in a separate experiment in which the surface waves were back-scattered from a reference scatterer, typically a sharp edge of quasi-infinite extent.

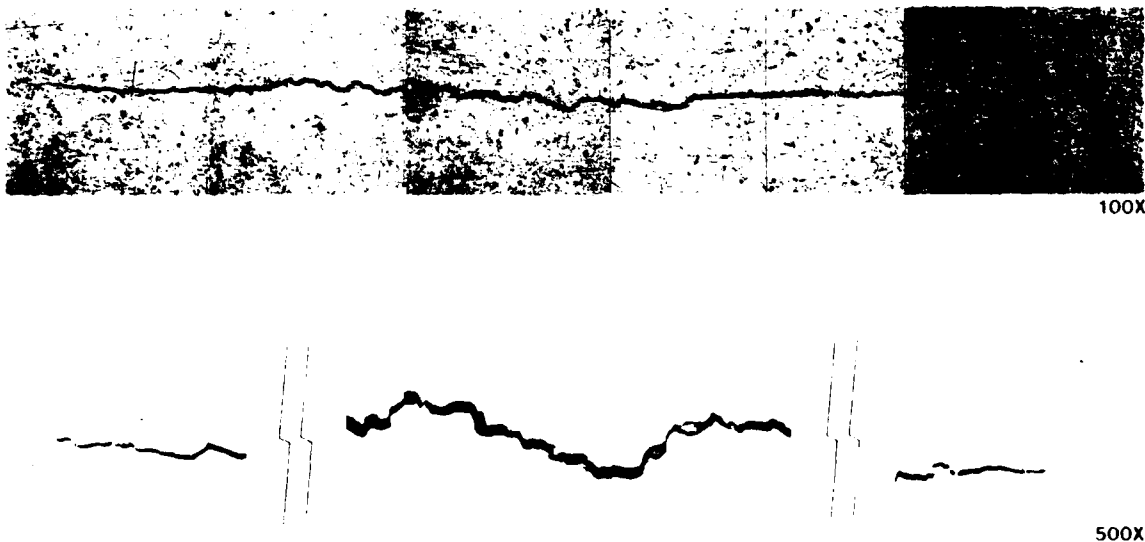


Fig. 2 Micrograph of fatigue crack

Results - The fatigue cracks discussed above were studied in both the time and frequency domain to determine the length of the cracks. For sufficiently short pulses, the signals from the extremities of the cracks can be resolved such that an analysis in the time domain is possible. This procedure is demonstrated in Fig. 3 which shows rf waveforms for pitch-catch, in which one transducer sends its beam normal to the crack face, while the other transducer receives the scattered radiation in the direction parallel to the crack plane. Two closely spaced signals are observed, which are thought to be associated with two point-sources each corresponding to the crack tip near the surface. The radiation corresponds effectively to a dipole source producing rf waveforms in phase opposition as is apparent in the figure. The separation of the two signals corresponds to the time-delay calculated on the basis of a Rayleigh wave traveling along the length of the crack. The calculated crack length of 2.85 mm is in good agreement with the 2.80 mm measured under an optical microscope.

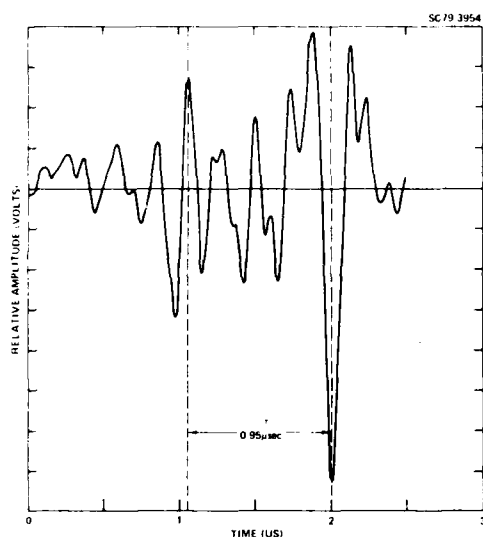


Fig. 3 Length determination for fatigue crack in commercial Ti from side-scatter time-domain signals.

Figure 4 shows the normalized Fourier transforms of the time domain waveforms shown in Fig. 3. It is easy to see that the existence of two somewhat separated pulses in the time domain is equivalent to interference in the frequency domain. With the use of algorithms developed in previous papers^{2,3} it is relatively straightforward to estimate the length of the fatigue crack by noting the spacing between the nulls and peaks. The calculated values for the length (3 mm) are in good agreement with those obtained in the time domain. Note that the observations of multiple nulls (peaks) allows, in turn, a multiple set of estimates and the obtainment of a statistical average. An additional advantage of the frequency domain analysis is that careful signal processing would still allow estimates to be made in the situation where the two corresponding waveforms are overlapping and cannot be resolved.

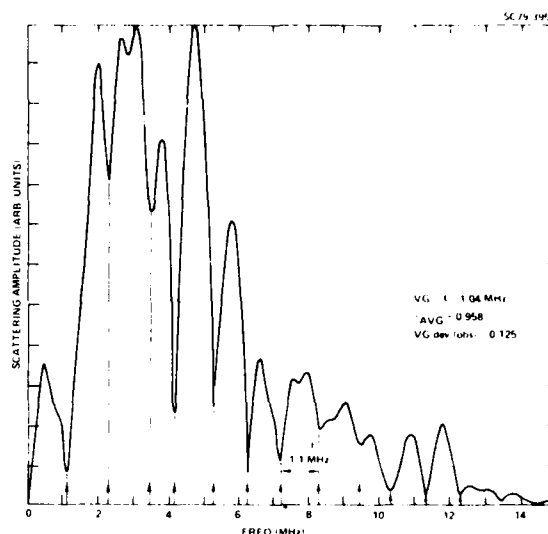


Fig. 4 Length determination of fatigue crack in commercial Ti from side-scatter frequency domain studies.

CRACK DEPTH

Experimental Procedure - From Fig. 1 it can be readily deduced that the transit time between the echo at A and the echo from the back wall¹ is

$$\Delta T = \frac{2a}{V_R} + \frac{2(t-a)}{V_S} \quad (1)$$

where V_R and V_S are the velocities of the Rayleigh and shear mode waves respectively, a is the crack depth, and t is the plate thickness. From this expression, a can be determined by precision measurements of ΔT , t and a knowledge of V_R and V_S .

Figure 5(a) presents a photograph displaying the two echoes as observed on the cathode ray oscilloscope. The signals were obtained on a reference specimen into which a slot had been cut by spark erosion. The slot was cut such that it was possible to inject alcohol into its interior without wetting the exterior specimen surface. The result of the alcohol injection is presented in Fig. 5(b) which shows the second echo attenuated and spread out in time. This result demonstrates that the second echo, indeed, has spent some of its travel time as a surface wave propagating on one of the surfaces of the slot. Figure 6(a) shows the same two echoes for a crack in one of the Ti-15A plates. The instrument used here was a Tektronix 475 DM44 Digital Time Interval Oscilloscope which allows display of two traces of the same signal with an accurate (to 1 nanosec) time delay count between the two traces. In Fig. 6(a) the top trace shows the same two echoes (echo A and the back wall echo C) as the bottom trace except attenuated such that echo A in the top trace is the same amplitude as the echo C in the bottom trace. This comparison reveals the similarity between the two echoes and demonstrates the ease by which the two can be superimposed, so as to align the detailed structures of the two waveforms. Once this matching is accomplished ΔT is simply read on the digital time

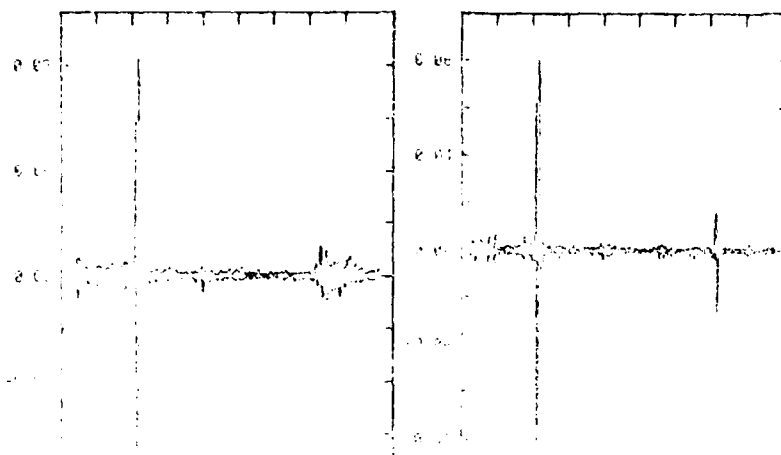


Fig. 5 Cathode-ray oscilloscope photo of crack echoes (a) empty crack (b) crack filled with alcohol.

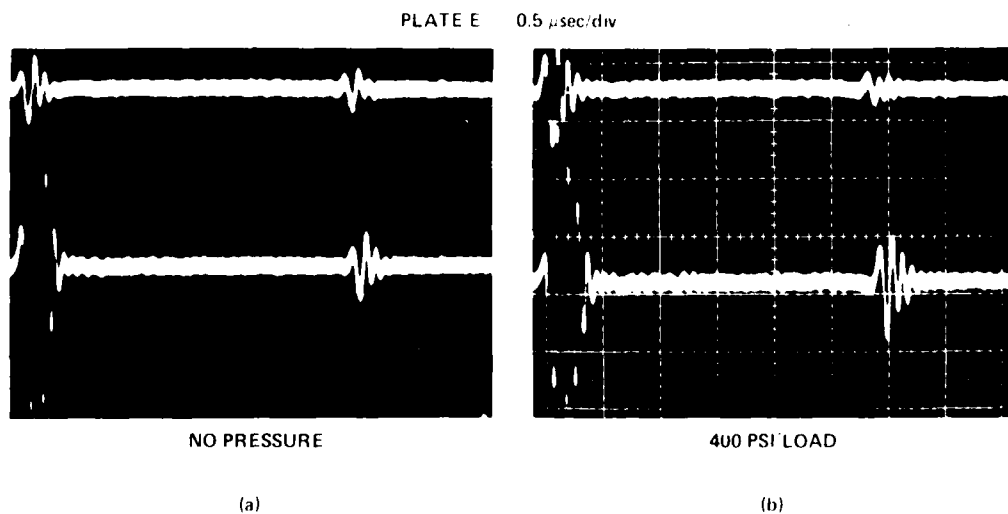


Fig. 6 Cathode-ray oscilloscope photo crack echoes (a) without crack closure stress (b) with 400 psi crack closure load.

interval counter. Repeatability for the ΔT determination was within 1 nanosec. Figure 6(b) shows a similar photo for a tensile (crack opening) load of 400 psi. This load was achieved again by subjecting the specimen plate to a static four-point bending load in a commercial vertical loading rig. A comparison of Fig. 6(a) and (b) shows a noticeable increase in the amplitude of echo C when the crack is pulled apart. This and other features were investigated more fully under systematic variations of the loading condition both under tension and compression stress. One example of these studies is shown in Fig. 7, which plots in the bottom graph the amplitude of echo A, in the middle graph ΔT ,

the time interval between echo A and C and in the top graph the amplitude of echo C. The three graphs show the same basic trends, namely that as the crack is forced to close, the crack edge echo A and crack tip (back wall) echo C develop lower amplitudes and ΔT becomes smaller. The total change in ΔT is only about 2%, which is reasonable for this case of fully stabilized cracks in which the plastic zone had time to relax to an equilibrium situation. As will be discussed later, for fresh cracks, examined during the second phase of the experiments, i.e., during the fatigue cycling to failure, the total changes in ΔT are much larger since the plastic zone had had no time to relax.

Thus, the nature and amount of stress, as well as time after crack propagation, clearly play a role in the determination of the crack depth.

As shown in Eq. (1) the determination of the crack depth a is based on a knowledge of v_R and v_S , the Rayleigh and shear wave velocity, respectively. Rewriting Eq. (1) as

$$a = \frac{v_R(\Delta T v_S - 2t)}{2(v_S - v_R)} \quad (2)$$

shows that d is determined from differences of nearly equal numbers and is therefore sensitive to errors in the values of v_S and v_R . Handbook values are not sufficiently accurate so that additional measurements are necessary.

For the v_S measurements in the plates of Ti-15A, it soon became apparent that variations due to texture were too severe to be ignored. For example, $v_S = 3.254$ km/sec and $v_S = 3.147$ km/sec for polarization parallel and perpendicular to the plane of the crack face. The mounting of a shear wave transducer on the back wall opposite the crack tip established that the conversion produces a shear wave polarized perpendicular to the crack face. Use of this shear wave transducer alternately as receiver and transmitter with a Rayleigh wave transducer on the opposite wall near the crack opening demonstrated the reciprocity of the crack tip mode conversion process.

The Rayleigh wave velocity was determined to be 2.920 km/sec by allowing the waves to reflect from the top and bottom of one of the specimen plate edges oriented parallel to crack plane. One may infer from the model of Hudgell, Morgan and Lumb,¹¹ that the velocity of the surface wave traveling along the face of the crack is identical to the Rayleigh wave velocity for propagation on a stress-free surface of an infinite half-space. If this interpretation is correct, then the measurement described above should yield the value for v_R needed in Eq. (2) within the assumptions that the specimen plate is homogeneous and that roughness on the crack face does not appreciably affect the actual v_R . Another possible source of error¹⁵ is the presence of a residual stress at and in the vicinity of the crack tip. This effect is more likely to influence the value of v_S ; Herrmann and Kino¹⁶ have observed small changes in velocity in the region around a stressed crack tip.

Results -During the second phase of the investigation the plate was machined into a tensile specimen, as described before, and examined at periodic intervals during the fatigue cycling. Because of the tensile specimen shape, the crack length determination could not be carried out and only the crack depth measurements were performed. Since the influence of static stress was shown to play an important role in the crack depth determination before, as seen in Fig. 7, these types of experiments were also carried out here. Figure 8 summarizes those data by showing the crack echo delay time ΔT as a function of tension and compression load for four stages: 0, 4000, 9000, and 11,000 cycles. The bottom curve represents the stable, relaxed crack (several months after precracking) and shows a very weak dependence of ΔT on load. The fresh cracks,

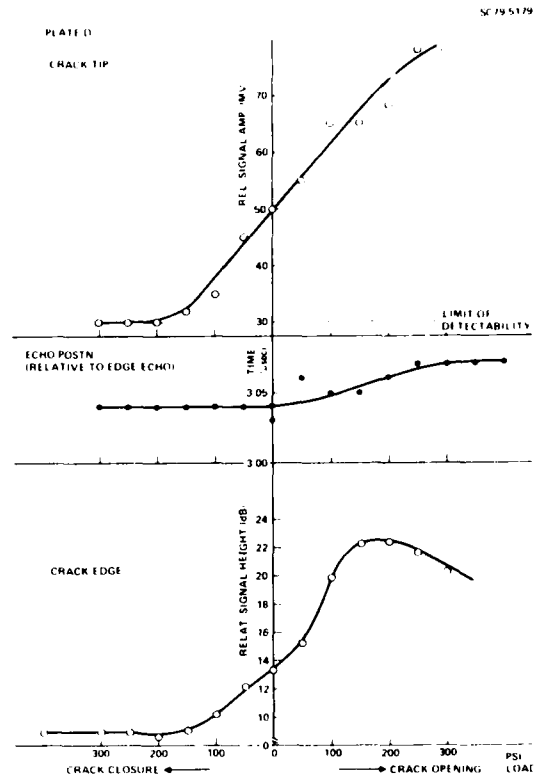


Fig. 7 Effects of crack closure/crack tension stresses on amplitude of echo A (bottom) on time delay ΔT between echoes A and C (middle) and amplitude of echo C (top).

by contrast, show a much stronger dependence on load, as identified by a pronounced knee in the graphs. We interpret the knee to be due to crack opening and crack closure. Note that, as the crack was allowed to grow further, the knee is seen to move to the left from tensile to compressive stresses which is a tendency in Ti-alloys we have observed before. It is clear, that an arbitrarily chosen stress, say zero load, for calculation of the crack depth could lead to a meaningless comparison between the crack growth phases. It was therefore decided that the ΔT values corresponding to the high tension loads would be used for the crack depth determination since the crack is fully open. These measurements were augmented by optical measurements of the crack length after polishing away the surface fatigue damage. The results are presented in Table I by tabulating the delay time ΔT and the optical length of each phase of the fatigue cycle experiment. With Eq. (2) and a knowledge of v_S and v_R , the crack depths can now be calculated. Before the presentation of the crack depth value is made, it is important to discuss an independent check and develop an alternate approach to the crack depth determinations. This was accomplished with the aid of fracture mechanics whose application is discussed in the next section.

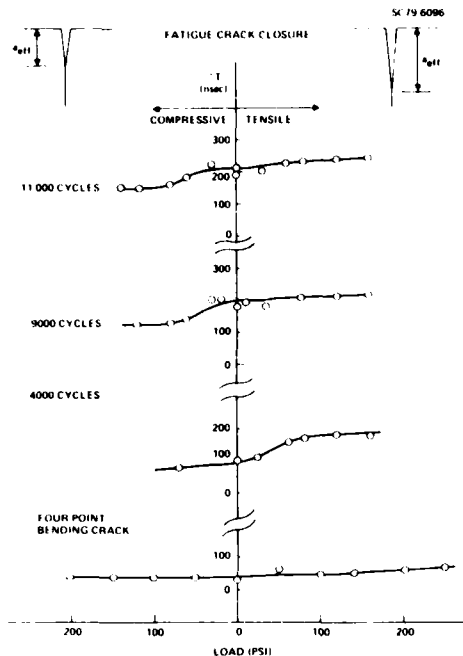


Fig. 8 Crack closure studies during fatigue cycling experiment.

Table I
Measured Crack Parameters

Number of Cycles	Delay Time ΔT (nsec)	Optical Length (mm)
0	3040	3.30
1,000	3170	--
4,000	3180	3.30
9,000	3220	4.42
11,000	3240	5.10
12,700	3290	6.17

Since the crack growth takes place over a relatively long time it is important to speak in terms of a stress intensity range and a remaining life in terms of the number of cycles for failure. After Irwin¹ the stress intensity range (in mode I), ΔK_I , is

$$\Delta K_I = C \Delta \sigma \sqrt{a/Q} \quad (3)$$

where

$$C = 1.95$$

$$Q = \phi^2 - 0.212 \left(\frac{\sigma_{\max}}{\sigma_{\text{yield}}} \right)^2$$

$$\phi = \int_0^{\pi/2} [\sin^2 \psi + (a/c)^2 \cos^2 \psi]^{1/2} d\psi$$

and where $\Delta \sigma$ is the stress range, a is the true crack depth, $2c$ is the crack length, σ_{yield} is the yield stress, σ_{\max} is the maximum applied stress and ψ is the angle in the crack plane with respect to the crack length. For a given applied cyclic stress the stress intensity range ΔK_I may be calculated from a knowledge of the mechanical properties of the part (i.e., σ_{yield}), the crack depth a and the depth-to-length ratio.

Assuming the crack is in the Paris regime of validity, the crack-depth-increase-per-unit fatigue cycle da/dN is¹⁸

$$da/dN = A(\Delta K_I)^m \quad (4)$$

where A and m are material constants. The remaining life or number of cycles to failure is then

$$\Delta N = \frac{2}{(m-2)A(CQ^{-1/2} \Delta \sigma)^m} \left[\frac{1}{a^{(m-2)/2}} - \left(\frac{CQ^{-1/2} \sigma_{\max}}{K_{IC}} \right)^{m-2} \right]$$

where K_{IC} is the fracture toughness in mode I failure. Failure is imminent, i.e., $\Delta N = 0$, when

$$a_c = \left[\frac{K_{IC}}{CQ^{-1/2} \sigma_{\max}} \right]^2 \quad (5)$$

Figure 9 presents data obtained by Chesnutt¹⁹ for da/dN versus ΔK_I . These data allowed determination of $A = 3.5 \times 10^{-9}$, $m = 3$ and $\sigma_{\text{yield}} = 40$ ksi for the Ti-15A material. This information plus the externally imposed stress range $\Delta \sigma = 38$ ksi allowed the calculation of the remaining number of cycles ΔN .

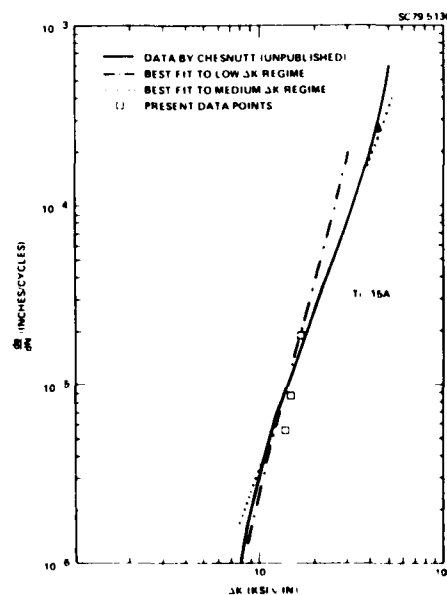


Fig. 9 Crack growth data for Ti-15A.

From previous studies it is well known²⁰ that soon after crack initiation, further fatigue crack growth is marked by the appearance of a semi-circular crack shape. This means that a careful

optical microscopy can give not only the crack length, $2c$, but also the crack depth, a , since $c = a$. Figure 10 shows data points based on this assumption in reasonable agreement with the actually observed remaining number of cycles. The point at the origin, i.e., at the beginning of the cycling experiment is shown with large error bars to indicate the possible uncertainty in the shape of the crack and therefore its depth from the simple optical observation in this early stage of crack growth. These results provide a useful way to check on the crack depth determination from the use of the acoustic waves.

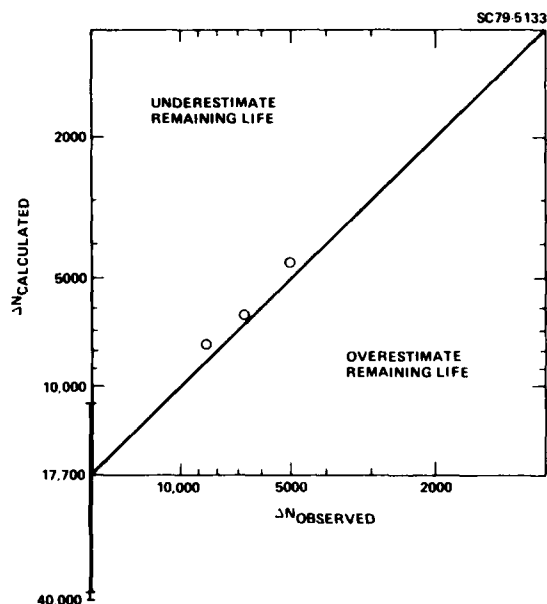


Fig. 10 Fatigue life from optical and fracture mechanics measurements.

Figure 11 summarizes the results by plotting the crack depth observed (estimated from acoustic waves) versus the actual crack depth inferred from fracture mechanics. Two graphs are displayed: open squares on a dashed line obtained from Table I in the way already described, and, round dots on a solid line in good agreement with the calculation (triangular) from the optical observations. The open circles are based on a fit of the crack depths from Table I with v_p as variable parameter. A choice of $v_p' = 0.96 v_R = 2.80$ km/sec gave good agreement with the crack depths inferred from fracture mechanics. Figure 12 shows the quality of fit of the calculations for ΔN based on this new value for the velocity of the surface waves traveling on the crack face. Figure 11 shows the sensitivity of the crack depth determination to the value of v_p : a change of 4% in v_p is seen to cause a change in a of 50%. Since the precision of determining v_p is much better than 4%, the results suggest an inaccuracy in the model. One can speculate that the surface waves traveling on the crack face are guided waves which are in fact dispersive having a phase velocity higher than, and a group velocity lower than the Rayleigh wave velocity. Recent theoretical

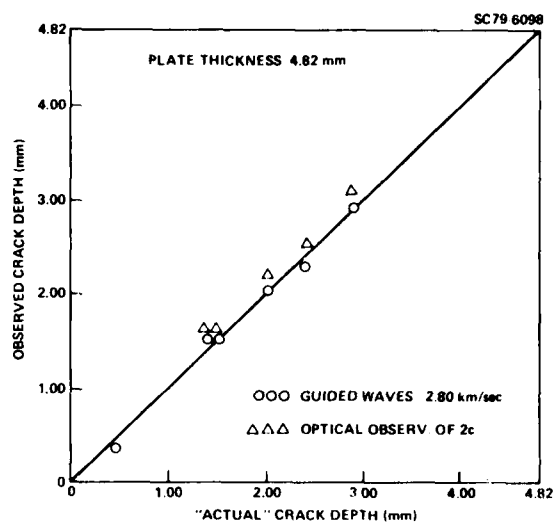


Fig. 11 Crack depths from SAW NDE.

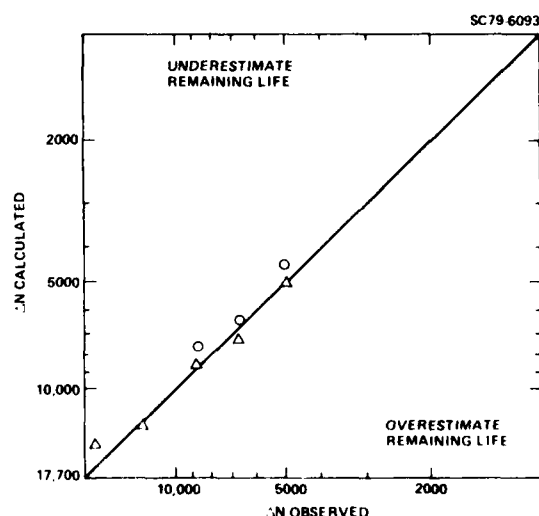


Fig. 12 Fatigue life estimates from SAW NDE.

work carried out by Ayter and Auld²¹ demonstrates the complexity of the situation by proposing the presence of circumferential waves which become leaky in certain situations depending on the crack geometry and crack size-to-wavelength ratio. A good understanding of what goes on is clearly an important factor in employing this technique for quantitative failure prediction.

CONCLUSION

In this report, techniques for determining crack depths and lengths have been applied to fatigue cracks in plates of Ti-15A. The main emphasis was placed on evaluating an echo timing technique for determining the crack depth. The results of the technique were used in a failure

predictive mode such that well-established methods from fracture mechanics could be used to check the technique. The results of the evaluation may be summarized by listing its weakness and strengths.

One of the chief advantages of the technique is that it employs well-defined signals with high signal-to-noise ratios. These signals originate as surface waves which are easily identified by standard techniques. Advanced timing techniques now commercially available make the time delay measurements a straight-forward endeavor with excellent precision.

These factors should be weighed against some important disadvantages among which must be listed the restrictions on specimen geometry for the proximity of a suitable backwall, the sensitivity of the calculations on errors in the shear and Rayleigh wave velocity, and the apparent need of refinements in the model describing the interaction between the surface waves and the crack. A much more fundamental limitation of the technique is its inability to provide information for cracks inclined to the surface. Especially, for cracks with curved contours the technique would provide deceptively longer crack depth values than required for quantitative life time prediction.

Within the scope of these limitations, the technique has shown to be a powerful tool for predicting the remaining number of cycles for a specimen with a fatigue crack. It has also shown to be a new technique to study crack closure which is an effect of importance in explaining the driving force for fatigue crack propagation, in particular, under spectrum loading, and at the least, under mildly aggressive environmental conditions.

REFERENCES

1. P.A. Doyle and C.M. Scala, *Ultrasonics* **16**, 164 (1978).
2. B.T. Khuri-Yakub and G.S. Kino, *Appl. Phys. Lett.*, **32**, 513 (1978).
3. J.D. Fraser, B.T. Khuri-Yakub, and G.S. Kino, *App. Phys. Lett.*, **32**, 508 (1978).
4. M.T. Resh, B.T. Khuri-Yakub, G.S. Kino and J.C. Shyne, *Proceedings of the First International Symposium of Ultrasonic Material Characterization at Gathersburg, Md., June 1978* (in press).
5. G.S. Kino, *J. Appl. Phys.* **49**, 3190 (1978).
6. V. Domarkas, B.T. Khuri Yakub, G.S. Kino, *Appl. Phys. Lett.* **33**, 557 (1978).
7. B.A. Auld, S. Ayter and M. Tan, 1978 *Ultrasonics Symposium Proceedings*, IEEE Cat. No. 78, Ch. 1344-1SU.
8. B.R. Tittmann, F. Cohen-Tenoudji, M. De Billy, A. Jungman and G. Quentin, *App. Lett.* **33**, 6 (1978), see also 1978 *Ultrasonic Symposium Proceedings IEEE, Cat. No. 78, Ch. 1344-1SU*, p. 379.
9. B.R. Tittmann, O. Buck, L. Ahlberg, M. De Billy, F. Cohen-Tenoudji, A. Jungman, and G. Quentin, *J. Appl. Phys.*, in press.
10. D. Cook, "Crack depth measurement with surface waves." *Proc. British Acoustical Soc. Spring Meeting, Loughborough Paper 72U19* (1972).
11. R.J. Hudgell, L.L. Morgan, R.F. Lumb, *Brit. Jn. of NDT*, Sept. issue, 144 (1974).
12. H.W. Reinhardt and J.W. Dally, "Some characteristics of Rayleigh wave interaction with surface flaws." *Materials Evaluation* Oct. pp. 213-220 (1970).
13. R.F. Lumb, R.J. Hudgell and P. Winship, "Monitoring slow crack growth by ultrasonic methods." *Proc. 7th Int. Conference on NDT, Warsaw 1973, Paper H-01*.
14. A. Brown, private communication.
15. J. Heyman, private communication.
16. G. Herrmann and G.S. Kino, "Ultrasonic measurements of inhomogeneous stress fields," in *Proc. of ARPA/AFML Rev. of Progr. in Quant. NDE, La Jolla, Calif., Air Force Rep. AFML-TR-78-205*, p. 447 (1978).
17. G.R. Irwin, *J. Appl. Mechanics* **29**, 651 (1962).
18. P.C. Paris and F. Erdogan, *J. Basic Eng.* **85**, 528 (1963).
19. J. Chesnutt, private communication.
20. O. Buck, J.D. Frandsen, and H.L. Marcus in *Fatigue Crack Growth Under Spectrum Loads*, ASTM STP 595, Am. Soc. Testing and Materials, p 101 (1976).
21. S. Ayter and B. Auld, private communication.

FATIGUE LIFE PREDICTION WITH THE AID OF SAW NDE

B. Tittmann
Discussion

Mr. Kraut: Questions on this paper?

George Herrmann: George Herrmann from Stanford University

Sort of a general question by a person who does not work in fatigue himself at all. Is it possible that the rate of cycling is important? And did you consider this as a parameter? Particularly because the cycling rate in the laboratory will certainly be quite different, I presume, than the cycling rate of a natural structure in the field.

Mr. Tittmann: I think that would be important. Is Otto here? Can he answer that as a fracture mechanics person?

Otto Buck: This work was all done under constant amplitude cycling. Certainly, performing

random spectrum loading, life would be different. With respect to your first question, I would not expect a large effect of cyclic frequency on the results. We did the experiments at about one cycle per second. I think one can go up or down a few orders of magnitude, and you would not see too much effect on the results.

Does that answer your question?

Professor Herrmann: Yes, it does.

Gordon Kino: Bernie, why was the choice of titanium? It's a very esoteric sort of material.

Mr. Tittmann: People know a lot about it. For example, the da/dN data were immediately available.

Mr. Buck: We want to change over to aluminum alloys now because we do not see markers and therefore we can not really pinpoint the crack front at any instant in life of the titanium 15-A. I don't know why that is. In aluminum you can clearly see markers on the fracture surface so that one can perform a clear identification of the aspect ratio as the crack grows.

Ralph Weglein: Bernie, how did you measure the shear wave velocity?

Mr. Tittmann: We measured the velocity of a shear wave traveling through the thickness of the plate.

Mr. Weglein: I have another question. How did the shear wave velocity you measured compare with the value in the handbook?

Mr. Tittmann: Before I made that measurement, I predicted Poisson's ratio based on book values, and then compared the values and found them very close.

Mr. Weglein: Another comment: The Rayleigh waves and the shear waves themselves are essentially nondispersive but the guided wave isn't. So when you take measurements as a function of fre-

quency, you might get some additional information on the nature of the guided wave.

Mr. Tittmann: Yes. We plan to really look into that fairly carefully and look at the dispersive nature of the waves. I have some preliminary evidence that as the crack length changes, the guide wave velocity changes. And I plan to look into that fairly carefully.

Mr. Kraut: Eric

Eric Ash: Eric Ash, University College

With regard to your model, I couldn't quite understand how the shear waves reflected from the bottom of the part were reconverted to Rayleigh waves. Is there any focusing of the shear waves?

Mr. Tittmann: This is an interesting question and concerns the details of the conversion process at the crack tip, which we do not understand yet.

Alastair Morton: Morton, N.S.R.D.C.

These measurements of crack depth were single crack specimens; is that right?

Mr. Tittmann: Yes, that's right.

Mr. Morton: How confident or how optimistic can we all be about making the crack depth measurements this way when you have, say, several, maybe two or three cracks, in the specimen and then moving on, say, eight to ten or perhaps many? Do you think you will be able to distinguish which is which?

Mr. Tittmann: That's our next step in the work. We have to first of all distinguish a single crack from surface damage or machine grinding marks. In other words, surface roughness. Then we intend to investigate to multiple cracks and learn to distinguish the deeper cracks from the shallow cracks. That's a tough job.

Mr. Kraut: All right, thank you, Bernie.

SUMMARY DISCUSSION
(B. Tittmann)

George Hermann (Stanford University): Sort of a general question by a person who does not work in fatigue himself at all. Is it possible that the rate of cycling is important? And did you consider this as a parameter? Particularly because the cycling rate in the laboratory will certainly be quite different, I presume, than the cycling rate of a natural structure in the field.

Bernie Tittmann: I think that would be important. Is Otto (Buck) here? Can he answer that as a fracture mechanics person?

Otto Buck (Science Center): That was all done in the constant amplitude cycling. Certainly, if you would do random spectrum loading, life would be different. I guess respecting the first question, I would not expect a large effect of cycling frequency on those results. At least we did it at about two cycles per second. I think it can go up or down a couple two orders of magnitude, and you would not see too much effect on that. Are any titanium people in the audience that would contradict that statement?

Gordon Kino (Stanford University): Bernie, why was the choice of titanium? It's a very esoteric sort of material.

Bernie Tittmann: People know a lot about it. For example, the D.A.D.M. data was immediately available.

Otto Buck: As Bernie said, we want to go over to aluminum alloys now because we did not see striations where we can really pinpoint the crack blunt at any instant in life on the titanium 15-A. I don't know why that is. Again, I'm not a titanium specialist, but in the aluminum you can clearly see striations so you can do later on clear identification of aspect ratio as the crack grows. We start off here in that particular case I believe the (inaudible) ratio of .2, which is quite low. That is how we started the fatigue crack in the first place, and then it would (inaudible) and shoot over to (inaudible) 45. And from then on go stable. But with that aspect ratio staying constant you could clearly see that in aluminum. So, our next choice will be aluminum or something else where we see the striations.

Ross Weglein (Hughes Research Lab): Bernie, how did you measure the sheer wave velocity? (Cylindrical Rayleigh Wave velocity)

Bernie Tittmann: We measured the velocity of a plane sheer wave traveling through the plane. The comment about the cylindrical sheer wave, that follows simply because you have a long line; and if it's going to be a bulk wave, it has to be cylindrical.

Ross Weglein: I have another question. From that sheer wave, now a surface wave, you can calculate a relationship. How does that compare with (inaudible)?

Bernie Tittmann: Very close. I predicted Poisson's ratio first before I made that measurement based on book values, and then checked it. And it was very close.

Ross Weglein: Another comment. The Rayleigh waves and the sheer waves themselves are essentially nondispersive but the guided wave isn't. So when you take measurements on frequency, you might get some additional information on a guided wave.

Bernie Tittmann: Yes. We plan to really look into that fairly carefully and look at the dispersive nature. I have some preliminary evidence that as the crack length changes, the guide wave velocity changes. And I plan to look into that fairly carefully.

Eric Ash (University College, London): With regard to your model, I couldn't quite understand why the reflected sheet waves from the bottom were reconverted to a Rayleigh wave because it's coming out more or less cylindrically and will continue to expand cylindrically and focus back.

Bernie Tittmann: No, I didn't make any statements about focusing, although I could. There is a plastic zone around the crack tip which has a slightly different velocity, as Gordon will tell you, and there might be some focusing present. You don't think so? Okay, I'll withdraw my statement.

(continued)

Bernie Tittmann (discussion continued)

Eric Ash: I was referring to the reflected wave from the bottom of the sample. I don't see why that ever finds the crack again unless the bottom of the crack is very close to it. It should have expanded enormously.

Bernie Tittmann: Oh, these are plates, and the crack is not that far away from the bottom.

Alastair Morton (N.S.R.D.C.): These measurements of crack depth were single crack specimens; is that right?

Bernie Tittmann: Yes, that's right.

Alastair Morton: How confident or how optimistic can we all be about making the crack depth measurements this way when you have, say, several, maybe two or three cracks in the specimen and then moving on to, say, eight to ten or perhaps many? Do you think you will be able to distinguish which is which?

Bernie Tittmann: That's our next step in the process. We have to first of all distinguish a crack from the cuts or machine grinding marks. In other words, roughness. And then go to multiple cracks and be able to pick out perhaps the deeper cracks from the lesser cracks. And that's a tough job. I don't want to offer you a panacea. We have to look into that to be able to answer that. It's clearly the next step.

#

THE USE OF ACOUSTOELASTIC MEASUREMENTS TO CHARACTERIZE THE STRESS STATES IN CRACKED SOLIDS

J. Hunter, R. King, G. Kino, D. M. Barnett, G. Herrmann, and D. Ilić
Stanford University
Stanford, CA. 94305

ABSTRACT

The theory of acoustoelasticity predicts that a plane longitudinal acoustic wave passing through a solid which is already in a deformed state will propagate with a velocity (v) which is different from the (v_0) of the same wave propagating through the undeformed medium. It may be shown that $\Delta v/v_0 = (v - v_0)/v_0 = B(\sigma_1 + \sigma_2)$ where σ_1 and σ_2 are the principal stress in the plane normal to the wave propagation direction and B is the acoustoelastic constant. Wave transit time measurements allow the relative velocity change $\Delta v/v_0$ to be determined, so that contours of constant principal stress sum ($\sigma_1 + \sigma_2$) may be mapped by acoustically scanning a stressed solid.

We have used the technique described above to characterize the states of stress in cracked and notched aluminum panels. A method for extracting crack stress intensity factors from the acoustic data is proposed and illustrated for center-cracked panel specimens. The results indicate that the technique may offer a promising method for nondestructive testing and evaluation.

Scanning experiments involving both shear and longitudinal acoustic wave probes may, in principle, be used to nondestructively determine the complete state of plane deformation in a stressed solid. We shall point out how one may use such acoustic information to determine the J integral and the M integral associated with cracked specimens. The integrands of these elastostatic conservation integrals contain terms involving elastic rotations which are not directly obtainable from the acoustic data, but it is possible to use forward integration of the compatibility equations to obtain the requisite information. An illustration example in which J and M are determined using this technique will be presented. This technique may find practical applications in the continuous nondestructive monitoring of critical structural elements.

INTRODUCTION

In recent years research has been conducted on development of acoustoelastic measurement techniques, in conjunction with the theory of acoustoelasticity, into a nondestructive experimental stress analysis tool.¹⁻⁴ This paper discusses the application of ultrasonic stress measurements to fracture mechanics. With knowledge of fracture mechanics quantities such as the stress intensity factor and the J integral, and making use of appropriate fracture criteria, an assessment can be made of how dangerous flaws might be which exist in structural elements. Attempts which have been made to use ultrasonics to nondestructively evaluate these quantities are summarized here. The first part of the paper describes measurement of the stress intensity factor while the J and M integrals are discussed in the second.

MEASUREMENT OF K_I FROM FAR FIELD ULTRASONIC DATA

Investigation has been made into the use of longitudinal wave ultrasonic stress measurements to nondestructively determine the stress intensity factor in specimens containing cracks. This work is part of the recently completed doctoral thesis of John Hunter.⁵ Discussion will be limited to mode I, or opening mode deformation, although the technique to be described is applicable to mixed mode cases.

The use of ultrasonics to measure stress is based on the theory of acoustoelasticity, which predicts that the velocity of an acoustic wave propagating through a solid depends on the state of deformation and hence the state of stress in the solid. For a plane longitudinal wave at normal

incidence to a body in a state of plane stress, with wave speed (v_0) and (v) in an undeformed and deformed medium, respectively, acoustoelasticity predicts

$$\Delta v/v_0 = (v - v_0)/v_0 = B(\sigma_1 + \sigma_2) \quad (1)$$

where (σ_1) and (σ_2) are the in-plane principal stress components, and B is a material constant which depends on the elastic constants (E , ν , and the third order Murnaghan constants) of the material. For a given material B can be determined directly using a uniaxial tension calibration test. It is important to calibrate the material under study because B varies widely among different materials. The relative velocity change, ($\Delta v/v_0$) is measured with longitudinal ultrasonic waves using a technique described in detail in Ref. 1. It should be emphasized that longitudinal wave measurements permit the determination of the principal stress sum only. The separate principal stress components and the principal directions cannot be evaluated with longitudinal waves only. The laboratory apparatus used to make ultrasonic measurements is shown in Fig. 1. With the aid of a laboratory minicomputer, this testing machine is capable of making measurements throughout a two-dimensional grid. Using our capability of determining the sum of the principal stresses point by point in plane specimens, an attempt has been made to evaluate stress intensity factors. In Fig. 2, an infinite plate containing a crack and subjected to remote uniaxial tension is shown. The elasticity solution for this case has been recently discussed by Eftis et al.⁶ and is given in terms of a complex potential function:

$$\sigma_{xx} = 2\text{Re}\phi' - 2y\text{Im}\phi'' - \sigma_0/z$$

$$\sigma_{yy} = 2\text{Re}\phi' + 2y\text{Im}\phi''$$

$$\sigma_{xy} = -2y\text{Re}\phi'' \quad (2)$$

where $\phi(z) = (\sigma_0/2)\sqrt{z^2 - a^2} - (\sigma_0/4)z$. (Primes denote differentiation of a function with respect to its argument.) Expanding this solution for small values of r , the radius measured from the crack tip, and introducing the mode I stress intensity factor for an infinite plate

$$K_I = \sigma_0\sqrt{\pi a} \quad (3)$$

leads to

$$\sigma_{xx} = \frac{K_I}{\sqrt{2\pi r}} \cos(\theta/2)[1 - \sin \theta/2 \sin 3\theta/2] - \sigma_0 + O(r^{1/2})$$

$$\sigma_{yy} = \frac{K_I}{\sqrt{2\pi r}} \cos(\theta/2)[1 + \sin \theta/2 \sin 3\theta/2] + O(r^{1/2})$$

$$\sigma_{xy} = \frac{K_I}{\sqrt{2\pi r}} \sin \theta/2 \cos \theta/2 \cos 3\theta/2 \quad (4)$$

In fracture mechanics the assumption is made that regardless of the geometry and loading on a body containing a crack, the stresses in the near tip region have the same geometric dependence as that shown in Eqs. (4) for the infinite plate, and the boundary conditions only affect the value of the single parameter K_I . Summing the first of Eqs. (3), one obtains

$$\sigma_{xx} + \sigma_{yy} = \frac{2K_I}{\sqrt{2\pi r}} \cos \theta/2 - \sigma_0 + O(r^{1/2}) \quad (5)$$

and for plane specimens

$$\sigma_1 + \sigma_2 = \sigma_{xx} + \sigma_{yy} \quad (6)$$

Making use of the assumption discussed above, if ultrasonic measurements were available in the near field, the stress intensity factor could be evaluated easily. A method which makes use of several data points is shown in Fig. 3. Referring to the coefficient of K_I in (5) as the "geometric factor" measured values of the principal stress sum could be plotted versus the value of the geometric factor at those points. A straight line fit through the data would give an estimate of K_I as its slope. Unfortunately near tip data are difficult to obtain and there are nonlinear effects occurring in this region which are not accounted for by the theory underlying the stress measurement. (This is true of other experimental techniques as well as ultrasonics.) Consequently it is desirable to be able to measure the stress intensity factor from data further away from the crack tip, a region in which the neglected terms in Eq. (5) become important. To do so, it is necessary to extend the concepts discussed thus far. Returning to the expressions for stresses in the infinite plate solution, and summing the first two leads to

$$\sigma_{xx} + \sigma_{yy} = \sigma_0 \text{Re}\{2Z/(Z^2 - a^2)^{1/2}\} - \sigma_0 \quad (7)$$

Again introducing the same stress intensity factor, Eq. (3), used earlier,

$$\sigma_{xx} + \sigma_{yy} = \frac{2K_I}{\sqrt{\pi a}} \text{Re}\{2Z/(Z^2 - a^2)^{1/2}\} - \sigma_0 \quad (8)$$

In Eq. (8) the stress intensity factor is multiplied by a new geometric factor which will be valid anywhere in the infinite plate. Now, in attempting to measure K_I for a specimen, an assumption is made similar to that made previously: in the region in which data is being taken, it is assumed that the principal stress sum for the specimen under test has the same geometric dependence exhibited by the infinite plate solution in Eq. (8), the boundary conditions only affecting the value of K_I . If this assumption is valid, and a straight line is fit through a plot of measured $(\sigma_{xx} + \sigma_{yy})$ at various points versus the value of the geometric factor at those points, the stress intensity factor would be given by the slope of that line (Fig. 4).

An attempt was made to apply the procedure described above on a center-cracked panel (Fig. 5). It was proposed to take ultrasonic data in a 20 mm square grid in front of the crack. Before the experiment was conducted, the validity of the assumption discussed above was investigated using a numerical (boundary collocation) solution for stresses in a center-cracked panel.⁸ The numerical solution was scaled so that the principal stress sum matched the infinite plate solution at one point, and the contours for the stress sum for the numerical solution were plotted on top of those for the infinite plate. These contours matched quite well in the 20 mm square region of interest, indicating the assumption was valid in this case. Ultrasonic measurements were then made in this region using the experimental apparatus described previously at 400 data points (1 mm point spacing). Since the acoustoelastic B (Eq. (1)) was known from a calibration test on the material (aluminum 6061-T6), the principal stress sum could be determined from the ultrasonic data. Plots of measured values of principal stress sum versus geometric factor are shown in Fig. 6. For two values of applied load, the straight lines that fit through the data points give an estimate for K_I within 20% of the handbook value for this geometry.⁹

From these preliminary results we are encouraged that this technique can be developed into a useful tool for determining the stress intensity factor in practical situations.

DETERMINATION OF THE J AND M INTEGRALS USING ULTRASONIC DATA

Another area of application of ultrasonic stress measurement capabilities to fracture mechanics is experimental evaluation of the J and M integrals. The definition and physical interpretation of these quantities is discussed in Ref. 10 and will be summarized here. The J integral is a contour integral around the tip of a flaw in a solid and is defined as

$$J = \int_C (Wn_x - T_k U_{k,x}) ds \quad (9)$$

where W is the strain energy density, T_K is the traction, and U_K is the displacement along the contour. J represents the mechanical energy release rate with respect to translation of the tip of the flaw in the x direction. M is defined as

$$M = \oint_C (W n_i x_i - T_K U_{K,i} x_i) ds \quad (10)$$

where C is a contour completely enclosing a flaw. M represents the energy release rate with respect to self-similar expansion of the flaw. The practical significance of these quantities is similar to that of the stress intensity factor. For elastic deformation J is the same as the crack extension force G_I , thus

$$J = G_I = K_I^2 \quad (11)$$

and knowledge of J enables determination of K_I . J is more generally useful than K_I , however, because while K versus K_{IC} as a fracture criterion is restricted to cases of small scale yielding, J vs J_{IC} is valid for general yielding so long as no unloading occurs. The M integral is useful because, using path independence arguments, J can be determined from M (and M gives useful results for closed contours, which are sometimes more convenient, while J gives zero). For instance, it is easily shown for an interior crack that

$$M = 2aJ \quad (12)$$

where a is the half crack length. Applications of the M integral in determining stress intensity factors have been discussed by Freund.¹¹

Nondestructive measurement of the J and M integrals involves evaluation of the integrand at several points along a contour and then numerically integrating to determine J or M . By expanding the J integral in Eq. (9) it becomes clear what this entails for in plane stress:

$$J = 1/E \int_C \left[\frac{1}{2} (\sigma_{yy}^2 - \sigma_{xx}^2) dy + \sigma_{xy} (\sigma_{xx} + \sigma_{yy}) dx + \int_C \sigma_{xy} (\sigma_{xy} dy - \sigma_{yy} dx) \right] \quad (13)$$

Thus determination of J requires knowledge of the entire stress tensor along the contour as well as the rotation component ω_{xy} . The same holds true for M . While in some geometries the integrand simplifies considerably and knowledge of the principal stress sum is sufficient to evaluate the integrand¹², in general this is not true. However, shear wave measurements are capable of determining the full state of stress point by point in a plane specimen.⁴ Unfortunately it is difficult to take shear wave data at many points due to the problem of coupling the wave to the specimen.^{2,3} A shear wave scanning apparatus similar in principle to that shown in Fig. 1 but using direct mechanical coupling of the transducer to the specimen has been constructed at Stanford University. Preliminary testing is underway, and it is hoped this device will enable the use of shear waves to determine the stress state in plane stress specimens in the near future. Of the terms in the integrand in Eq. (13), it would then remain to determine ω_{xy} . It is not clear how to directly measure this quantity at many points

nondestructively by any experimental technique. The importance of the rotation term was investigated for both the J and M for two analytical cases, and it was found to contribute from 50% - 75% of the results; thus it is certainly not negligible.

A method for determining ω_{xy} from stress data by making use of compatibility relations is proposed. Using the definitions of stress and rotation,

$$\begin{aligned} \epsilon_{ij} &= 1/2(u_{i,j} + u_{j,i}) \\ \omega_{ij} &= 1/2(u_{i,j} - u_{j,i}) \end{aligned} \quad (14)$$

the gradients of rotation can be expressed in terms of strain gradients by

$$\begin{aligned} \omega_{xy,x} &= \epsilon_{xx,y} - \epsilon_{xy,x} \\ \omega_{xy,y} &= \epsilon_{xy,y} - \epsilon_{yy,x} \end{aligned} \quad (15)$$

Noting

$$d\omega_{xy} = \omega_{xy,x} dx + \omega_{xy,y} dy \quad (16)$$

and using Hooke's law, in plane stress one obtains

$$d\omega_{xy} = 1/E \left[(\sigma_{xx,y} - \sigma_{yy,y} - (1+\nu)\sigma_{xy,x}) dx + [(1+\nu)\sigma_{xy,y} - \sigma_{yy,x} + \nu\sigma_{xx,y}] dy \right] \quad (17)$$

The rotation at any point can now be determined by integrating forward from a point at which rotation is known:

$$\omega_{xy}(x,y) = \omega_{xy}(x_0,y_0) + \int_{x_0,y_0}^{x,y} d\omega_{xy} \quad (18)$$

The stress gradients in Eq. (17) are determined numerically using a central difference formula. It now appears that shear wave measurements will permit determination of all quantities in the integrand of J and M for plane specimens. This technique was tested on the infinite plate solution. The stress values from this solution were stored in a two-dimensional grid in the first quadrant (Fig. 7), taking advantage of symmetry. The rotation was determined using Eq. (18), and the J and M integrals were determined by integrating numerically. The results for the rotations are shown in Table I. There is an apparent smoothing effect in numerically integrating the data resulting in more accurate determination of the J and M integrals than for the rotations themselves (Table II). In an effort to simulate experimental data, random noise was introduced into the experimental data. The technique appeared quite capable of handling this as shown in Table III. Consequently it is hoped that when shear wave measurements are available it will be possible to use this method to evaluate the J and M integral for practical plane specimens.

CONCLUSIONS

Application of ultrasonic stress measurements to the nondestructive evaluation of fracture mechanics quantities has been presented. It is expected

that these techniques can be developed into a useful tool for assessing the status of flaws in practical situations.

ACKNOWLEDGMENTS

This work was supported by the Air Force Office of Scientific Research under Grant AF 78-3726, EPRI Contract RP609-1, and the NSF-MRL Program through the Center for Materials Research at Stanford University under Contract DMK-76-00726.

REFERENCES

1. G. S. Kino, J. B. Hunter, G. C. Johnson, A. R. Selfridge, D. M. Barnett, and C. R. Steele, "Acoustoelastic Imaging of Stress Fields," *J. of Appl. Phys.*, vol. 50, no. 4, pp. 2607-2613, April 1979.
2. D. I. Crecraft, "The Measurement of Applied and Residual Stresses in Metals Using Ultrasonic Waves," *J. of Sound & Vibrations*, vol. 5, no. 1, pp. 173-192, 1967.
3. N. Hsu, "Acoustoelastic Birefringence and the Use of Ultrasonic Waves for Experimental Stress Analysis," *Experimental Mech.*, vol. 14, no. 5, pp. 169-176, 1974.
4. G. C. Johnson, "Acoustoelasticity: Stress Measurements Using Ultrasonics," Ph.D. dissertation, Stanford University, April 1979.
5. J. B. Hunter, "Acoustoelastic Analysis of Center Cracked Panels," Ph.D. dissertation, Stanford University, June 1979.
6. J. Eftis, N. Subramonian, and H. Liebowitz, "Crack Border Stress and Displacement Equations Revisited," *Fracture Mech.*, vol. 9, pp. 189-210, 1977.
7. P. S. Theocaris and E. E. Gdoutos, "A Photoelastic Determination of K_I Stress Intensity Factors," *Eng. Fract. Mech.*, vol. 7, pp. 331, 1975.
8. A. S. Kobayashi, R. D. Cherepy, and W. C. Kinsel, "A Numerical Procedure for Estimating the Stress Intensity Factor of a Crack in a Finite Plate," *J. of Basic, Eng., Trans. ASME*, December 1964.
9. H. Tada, *The Stress Analysis of Cracks Handbook*. Del Research Corporation, 1973.
10. B. Budiansky and J. R. Rice, "Conservation Laws and Energy Release Rates," *J. of Appl. Mech.*, vol. 40, pp. 201-203, 1973.
11. L. B. Freund, "Stress Intensity Factor Calculations Based on a Conservation Integral," *Internat'l J. of Solids and Struc.*, vol. 14, pp. 241-250, 1978.
12. G. Herrmann, and G. S. Kino, "Ultrasonic Measurements of Inhomogeneous Stress Fields," *Proc. of ARPA-AFML Conf. on NDT*, July 1978.

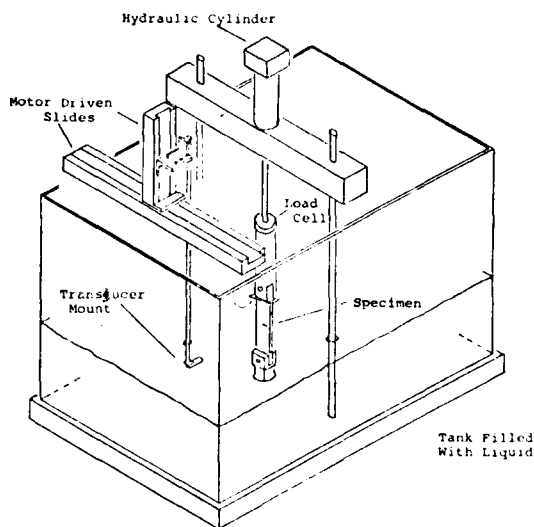


Fig. 1. Diagram of testing machine for acousto-elastic measurements.

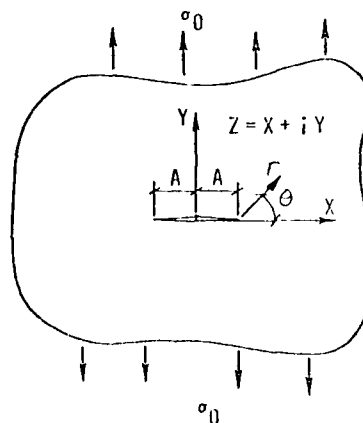


Fig. 2. Stress field in an infinite cracked panel under remote uniaxial tension.

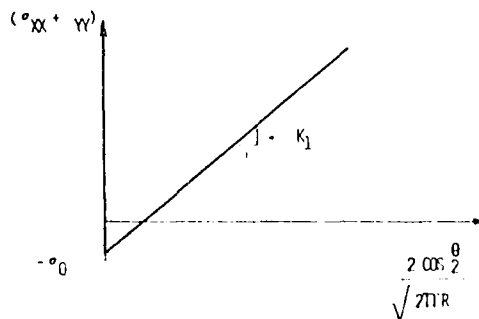


Fig. 3. Calculation of K_I for a mode I crack using near field data.

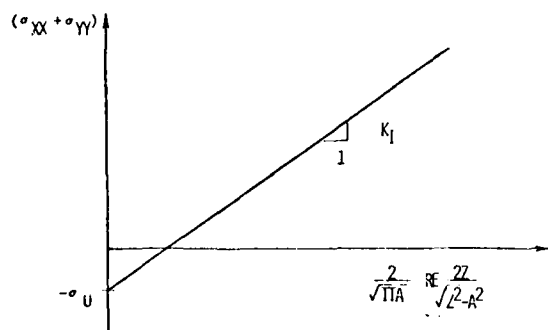


Fig. 4. Calculation of K_I for a mode I crack using extended field solution.

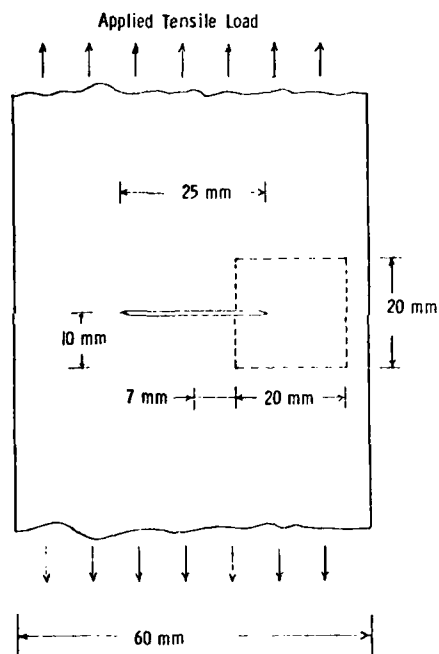


Fig. 5. Center cracked panel showing scanned area.

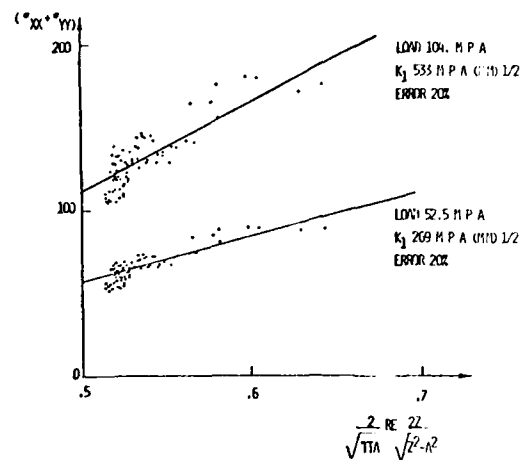


Fig. 6. Calculation of K_I for a center cracked panel for two values of applied load.

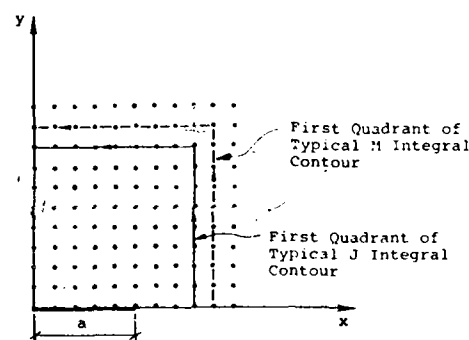


Fig. 7. Contours used for evaluating J and M using the infinite plate solution.

COMPARISON OF ROTATIONS

X	Y	EXACT	APPROX	% ERROR
8.00	0.00	0.000000	0.000000	0
8.00	1.00	0.000241	0.000217	-9.95
8.00	2.00	0.000384	0.000329	-1.04
8.00	3.00	0.000427	0.000438	+2.58
8.00	4.00	0.000414	0.000423	+2.17
8.00	5.00	0.000375	0.000379	+1.10
8.00	6.00	0.000350	0.000328	- .61
8.00	7.00	0.000285	0.000281	-1.40
8.00	8.00	0.000245	0.000233	-2.86
7.00	8.00	0.000262	0.000250	-4.58
6.00	8.00	0.000270	0.000255	-5.56
5.00	8.00	0.000264	0.000247	-6.44
4.00	8.00	0.000401	0.000273	-7.47
3.00	8.00	0.000701	0.000183	-8.96
2.00	8.00	0.001144	0.000128	-11.1
1.00	8.00	0.001575	0.000051	-18.67
0.00	8.00	0.000000	0.000014	-----

AVE. ERROR: 5.632

Table I. Comparison of rotations determined numerically versus theoretical values.

J. INTEGRAL:		
APPROX	EXACT	ERROR
2.005	2.014	.44
M. INTEGRAL:		
APPROX	EXACT	ERROR
19.94	20.14	0.99

Table II. Results for the J and M integrals evaluated using theoretical data.

EFFECT OF NOISE

NOISE LEVEL ($\pm 2\%$)	J INTEGRAL (EXACT J = 2.014)	% ERROR	M INTEGRAL (EXACT M = 20.14)	% ERROR
0	2.005	.44	19.94	.99
10	2.013	.05	20.04	.50
20	2.033	.94	20.26	.60
30	2.065	2.50	20.53	2.20

Table III. Results for the J and M integrals using simulated experimental data.

SUMMARY DISCUSSION
(R. King)

Unidentified Speaker: What was the sensitivity of these measurements?

R. King (Stanford University): We usually do measurements on aluminum because we feel our system will do a better job on that. It depends on the value of the P constant I showed, the proportionality constant. For aluminum that constant is high, which means there is a high relative velocity change with stress. I'm not sure percentage-wise how accurately we can measure stress. I would say probably plus or minus ten-percent. With steel, the effect is smaller, and although we can make stress measurements in steel, it is somewhat more difficult. The trick we have used is to first attempt to make stress measurements on a certain specimen configuration on aluminum, and then go back and try it on steel.

Unidentified Speaker: I wanted to congratulate you. That was really beautiful work. But I wanted to ask you - you did K measurements, as a function of crack depth. Now, was it a real, true fatigue crack, or did you guys give a saw cut and change the depth of the saw cut?

R. King: Actually, this one was a fatigue crack. I didn't mention it was grown by a colleague, Mike Resch, who helped us make a laser burn on the specimen to create a small cavity. We fatigued the specimen and grew a crack outwards from this cavity. We have also made measurements on "phoney" cracks made by saw cuts.

P. Holler (Inst. fur Zerstorungsfreie Prufverfahren): You can do it on C.O.D. specimens. Do you have any idea how to get the proper radiation in the normal case? You need an angle of incidence parallel to the crack face, and also to the crack growth, or is it mainly a thought for C.O.D. experiments and things like that?

R. King: We need an angle of incidence normal to the plane of the specimen. Everything I have done is restricted to that. We are looking into methods of three-dimensional stress determination. It's more complicated. We're going to lick the two-D case first.

P. Holler: Thank you very much again.

#

ACOUSTIC MEASUREMENT OF MICROSTRUCTURES IN STEELS

N. Grayeli, D. B. Ilıc, F. Stanke, G. S. Kino, and J. C. Shyne
Stanford University
Stanford, California 94305

ABSTRACT

The measurement of acoustic properties can be used for the nondestructive characterization of the microstructure of materials. We have measured the changes in longitudinal acoustic wave velocity and acoustic attenuation in steel specimens whose microstructure and properties differ widely because of differing compositions and heat treatment. The spatial variation of the relative acoustic velocity in standard Jominy end-quench hardenability test specimens was found to correlate very well with Rockwell C hardness scans, indicating a potentially practical method for measuring the hardening response of heat treated steel. Absolute velocity measurements on steel specimens were found to be subject to random scatter related to minor compositional variations; this limits the utility of absolute velocity measurements for microstructural NDE. Attenuation measurements have also been performed on steel samples with different microstructures. The measurement utilized broadband acoustic pulses corrected for transducer response, liquid buffer/solid specimen reflection, and diffraction effects. Attenuation coefficients were seen to be proportional to frequency squared for martensite and to the fourth power of frequency for pearlite. Higher attenuation was observed for pearlitic than for martensitic microstructures.

Acoustic methods can be applied to the nondestructive characterization of the microstructure of materials. This paper reports the initial efforts of our interdisciplinary program to explore microstructural acoustic NDE. The experimental materials were steels.

The properties of materials, especially mechanical properties such as tensile strength, hardness, and impact toughness, are strongly dependent on microstructural features like grain size and shape, the proportions and spatial distribution of the phases present, and macroscale heterogeneities in microstructure resulting from local compositional or thermal-mechanical processing variations. This is true of both metallic and ceramic materials. The microstructural character of materials and their related properties are usually assessed by microscopic examination or by direct measurement of properties; such procedures are often costly, and are necessarily destructive, requiring sacrificial example specimens.

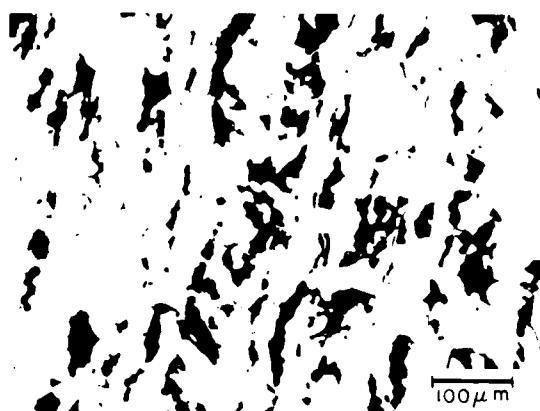
Steels are basically alloys of iron and carbon modified by minor additions of other elements. Steels exhibit remarkable variability of mechanical properties. These useful properties are dependent upon the rather complex microstructure of steel which can be closely controlled by proper selection of composition and heat treatment.

The dependence of steel microstructure on composition and heat treatment is illustrated in Fig. 1. Figures 1(a) and 1(b) compare the microscopic appearance of polished and etched steel specimens containing 0.2 and 0.6 wt. pct. carbon respectively; after annealing at 900°C and slow cooling in air to room temperature both steels consist of ferrite, the white grains, and pearlite, the darker constituent. Ferrite is essentially pure iron, pearlite is a mixture of two different crystalline phases (too finely dispersed to be resolved at the magnification shown), iron carbide (Fe_3C) and ferrite. Since virtually all the carbon resides in the pearlite, the proportion of pearlite is greater in the higher carbon steel. Figure 1(c) shows a steel with 0.4 wt pct carbon with a martensitic microstructure

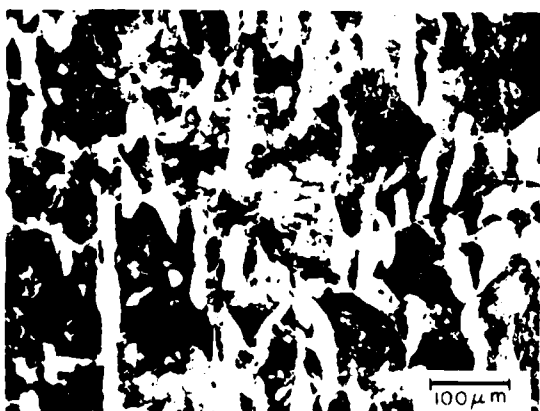
rather than pearlite and ferrite. This steel has been cooled rapidly in water after annealing at 900°C; the fast cooling causes the formation of martensite, a supersaturated solid solution of carbon in iron. Mechanical properties are strongly affected by the proportions of ferrite and pearlite and by the existence of martensite rather than pearlite and ferrite. Changes in microstructure such as these, enable steels to be heat treated to obtain optimum combinations of properties.

ACOUSTIC VELOCITY MEASUREMENT

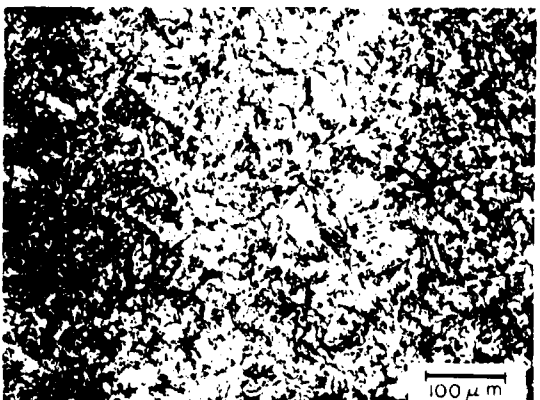
Our measurements of longitudinal acoustic wave velocity in metallic samples were made with a computer-controlled system developed for measuring acoustic velocity fields in solid samples immersed in a liquid buffer. The measurements use a two pulse-echo technique that cancels out the effects of the liquid buffer. The measuring method is illustrated in Fig. 2. Two sets of tone bursts several rf cycles long are transmitted, and their reflections from the specimen are received by a mechanically scanning commercial transducer. The delay between the two pulses is adjusted to overlap the back-face echo of the first pulse with the front-face echo of the second pulse, and this sum is gated out and detected. The product term is then used as an error signal in a phase-lock loop, which adjusts the frequency to keep the phase difference between the two echoes constant. Effectively, the measurement of phase change introduced by propagation through the specimen is converted to that of frequency, which can be performed with great precision. All of the above operations, including the mechanical scanning of the transducer, data collection, reduction, and display are controlled by a PDP 11-34 minicomputer. The resulting system precision is about 1 part in 10^6 of the measured longitudinal acoustic velocity. The accuracy of the absolute velocity measurement is 2 parts in 10^4 , as dictated by the accuracy in measuring the acoustic path length, the specimen thickness.



(a)



(b)



(c)

FIG. 1. Different steel microstructures resulting from difference in composition and heat treatment. 1(a): pearlite and ferrite in normalized 0.2 wt pct C steel; 1(b): pearlite and ferrite in normalized 0.6 wt pct C steel; 1(c): martensite in water quenched 0.4 wt pct C steel.

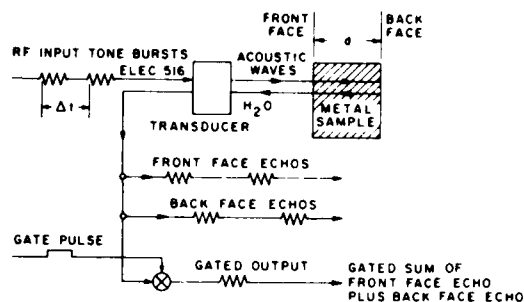


FIG. 2. Schematic of the precision acoustic velocity measuring system.

ABSOLUTE VELOCITY MEASUREMENTS

Specimens of 5 plain carbon steels were prepared by machining 1 cm thick flat plates oriented both longitudinally and transversely relative to the steel bar stock. Since the acoustic wave propagation direction was through the 1 cm plate thickness, acoustic velocity could be measured both parallel to and transverse to the rolling direction for each steel composition to detect the influence of any preferred orientation or crystal texturing. The compositions of the steels are shown in Table I. All specimens were given identical heat treatment; they were heated to 900°C and air cooled (normalized). This resulted in pearlite/ferrite microstructures, the pearlite varying from 12 to 100 volume pct over the range of carbon contents. After machining, the flat specimens were lapped to assure that their flat surfaces were parallel to within 2.5 μm.

TABLE I

Composition of Plain Carbon Steels used for Acoustic Velocity Measurements

Steel Type (AISI)	C	Mn	Si	P	S
1010	0.10	0.45	0.03	0.007	0.032
1020	0.20	0.52	0.21	0.009	0.028
1035	0.33	0.72	0.17	0.018	0.025
1060	0.55	0.80	0.19	0.012	0.023
1095	0.93	0.50	0.22	0.009	0.030

The resulting velocity measurements exhibited random scatter that totally obscured the variation in velocity anticipated from the variation in microstructure, Fig. 3. One can easily calculate an expected acoustic velocity from the known densities of pure iron ferrite¹ and Fe₃C,² and known elastic constant data for ferrite/Fe₃C mixtures.³ Increasing carbon should cause a decrease in the longitudinal acoustic velocity linearly proportional to carbon content; velocity should decrease

0.85 pct per wt. pct carbon in the steel, all other factors being identical. The scatter observed in the measured velocity was not caused by variations in preferred orientation; had there been any significant degree of preferred orientation, the longitudinal and transverse velocities would differ much more than the slight variations, which can be attributed to sample thickness variations, seen in Fig. 3. We believe that the random variations in such elements as manganese, silicon, sulfur and others always present in at least trace amounts, cause variations in density and elastic modulus and thus introduce random variations in acoustic velocity equal to or greater than the systematic effect of carbon in changing the microstructure. For example, we have calculated that the range of manganese contents in our specimens (see Table I) causes density variations large enough to obscure all the above change attributable to variations in microstructure. Therefore we conclude that absolute velocity measurements are not practical means for characterizing steel microstructure, because random compositional variations will confuse any attempt to calibrate absolute acoustic velocity with microstructure.

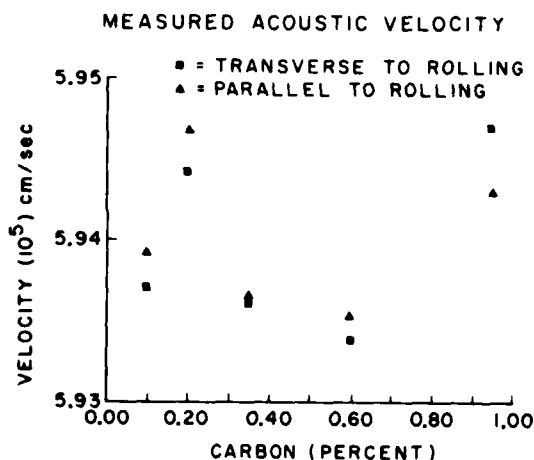


FIG. 3. Measured acoustic velocity in plain carbon steels of varying carbon content. The random scatter caused by minor fluctuations in alloying elements obscures the systematic variation in velocity related to the microstructure.

RELATIVE VELOCITY MEASUREMENTS

By relative velocity measurements we mean measurements of acoustic velocity at different locations within a given object. If the material composition is uniform within the object (as is usually the case), variations in acoustic velocity can be unequivocally related to microstructural variations from one location to another. There are many situations where microstructure is not uniform and the pattern of microstructural variation is important, e.g., in an induction hardened steel shaft heat treated to be martensitic on the outer surface but pearlitic in its interior. Velocity variation within a given object, i.e., relative velocity, could be

used to map out the microstructural pattern. Jominy end-quench test bars provide another example of steel objects containing microstructural gradients. We successfully used relative velocity measurements to survey quantitatively the microstructure of end quench test bars of several different alloy steel compositions.

The Jominy Test or End-Quench Test is the standard metallurgical quality control procedure for measuring the hardening response of heat treatable steels. The end-quench test specimen is a one-inch diameter round bar, four inches long. The bar is heated to about 850°C. It is then placed in a fixture and cooled by a jet of cold water impinged upon one end as shown in Fig. 4. This results in uniaxial heat flow toward the water-quenched end, and reproducible cooling rates that decrease with increasing distance away from the rapidly-cooled quenched end. The fast cooling rate at the quenched end causes the formation of hard, strong martensite; the slower cooled end transforms to softer, weaker pearlite or a pearlite and ferrite mixture, depending on composition. At intermediate locations mixed martensite/pearlite microstructures result from the intermediate cooling rates. The position of the transition from martensite to pearlite is a measure of the hardening response. The usual way of assessing the microstructural gradient along the length of an end-quench bar is to survey the Rockwell C hardness measured on flats ground along the side of the end quench test bar. This is possible because there is a pronounced hardness gradient caused by the microstructural gradient. Although surveying hardness is a great deal easier and less time consuming than directly observing the microstructure under a microscope, the hardness surveys are tedious because up to 60 individual manual hardness measurements may be required to survey a single test bar, a procedure taking about one hour.

DIAGRAM OF A JOMINY TEST IN ACTION

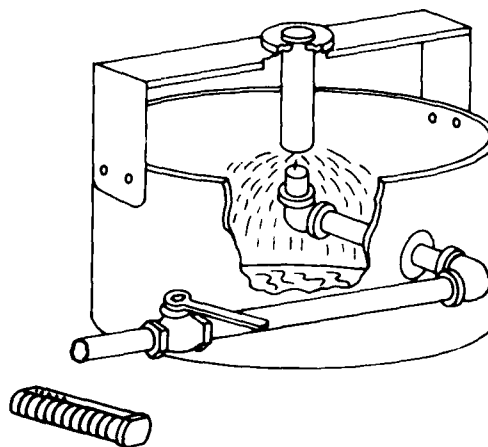


FIG. 4. End-quench test.

Figure 5 compares a conventional hardness survey with a longitudinal velocity scan of an end-quench test bar of AISI type 4140, a common, low alloy, heat-treatable steel. The longitudinal acoustic wave velocity was measured by the method described above

and illustrated in Fig. 2. The acoustic path was transverse to the axis of the test bar. Parallel flats were ground on opposite sides the full length of the test bar; the acoustic path was thus along bar diameters through the thickness of the bar between the ground flats. The relative acoustic velocity is plotted as $\Delta V/V_0$, the fractional change in velocity at any point relative to V_0 the velocity at the slower cooled, pearlitic end of the test bar. As seen in the plot the velocity decreased by about 0.7 pct at the martensitic, quenched end. The accuracy of the relative acoustic velocity measurement is limited by the uniformity of the thickness and the deviation from perfect parallelism of the ground flats. This is estimated to be 1 or 2 parts in 10^4 which is about 2% of the actual range of velocities measured. Thus the sensitivity and discrimination of the velocity measurement is equal to or better than that of the hardness measurements.

Figure 6 is a cross plot showing the relative velocity change $\Delta V/V_0$, versus the hardness. The correlation is virtually linear except for the extreme values. However, it is the intermediate values that are most important, because these occur at the region of transition from martensite to pearlite, the location critical to the measurement of hardening response.

The computer controlled automatic acoustic velocity scan requires only 4 minutes from start to finish with the data automatically plotted as $\Delta V/V_0$ vs position in the bar. This contrasts favorably with the hour or so required for a manual hardness survey. To our knowledge, this is the first time an end-quench test has been performed using a velocity scan rather than a hardness scan.

In addition to the 4140 steel end-quench test we have also performed similar acoustic velocity scans on end-quench test bars of types 52100, 4615, 8640, and 1095 steels with similarly encouraging results. We find these results persuasive that acoustic velocity measurements can be used to map out microstructural variations within steel objects.

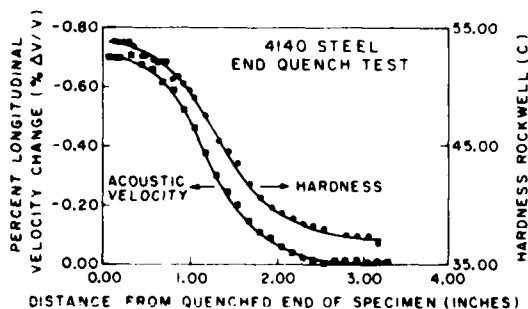


FIG. 5. End-quench test results measured in type 4140 steel. The two curves compare the microstructure gradient as surveyed acoustically and by conventional hardness measurements.

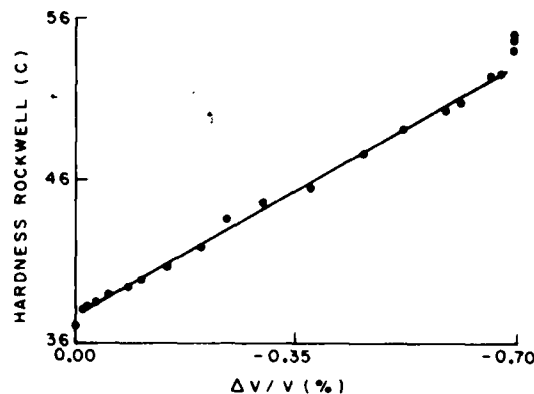


FIG. 6. Relative acoustic velocity vs hardness Rockwell C correlated for the data shown in Fig. 5.

ACOUSTIC ATTENUATION

In principle, attenuation measurements are more attractive than velocity measurements as the basis for acoustic NDE microstructural characterization. Where velocity is weakly a function of microstructure, acoustic attenuation is strongly affected by microstructure because of scattering at grain boundaries, second phase particles and other microstructural features.⁴ Moreover, the strong frequency dependence of the acoustic attenuation coefficient can provide additional information related to microstructure.

This paper reports only our earliest, preliminary efforts to characterize microstructure by means of acoustic attenuation measurements.

A computer interfaced system has been developed for quickly and easily measuring the attenuation of acoustic waves traveling through metal samples. The same samples used for the velocity measurements can be used for attenuation measurement. A commercial ultrasonic transducer launches longitudinal waves through a water bath at normal incidence to the sample and then receives the echoes. Normal incidence is attained by swiveling the transducer to maximize the amplitude of the front face echo. A narrowband pulse (i.e., a tone burst with at least 10 rf cycles) must be used for this alignment because the various components of a broadband pulse are not equally affected by non-normal incidence and therefore the maximum is difficult to determine. Computer controlled digital stepping motors can also be used to move the transducer for spatial scanning.

The three-echo method is used to determine the attenuation, as described by Papadakis.⁴ This method uses the measured amplitudes of three echoes to solve the equations for these echoes for any of the three unknowns in the system. In our experiment, these unknowns are the pulse-echo frequency response of the system, the reflection coefficient at the sample-water interface, and the attenuation through the sample. Broadband pulses are used to obtain

information over the frequency range of an octave or more. The front face echo and first two back face echoes are digitized and then stored in a computer. Since the dynamic range of these echoes can be 40 dB or more, many samples of each echo are averaged to improve the signal-to-noise ratio. The echoes are gated and separated in the computer, and the moduli of their Fourier transforms are computed by an FFT program. Figure 7 shows three gated, averaged pulses with their frequency spectra superimposed for a typical sample. The spectral components of the three echoes at each frequency are compared in the three-echo method to calculate the attenuation through the sample, correcting for transducer response and also for reflection and diffraction losses. Figure 8 illustrates the importance of including the diffraction correction for the echoes shown in Fig. 7. The scales are logarithmic, log dB/cm versus log f , so that the slopes of the linear plots give the powers of the frequency dependence. These curves are plotted by a computer and an analog plotter by simply connecting 128 attenuation data points within the passband. No curve fitting techniques have been used. One measurement produces a large amount of attenuation information about the sample.

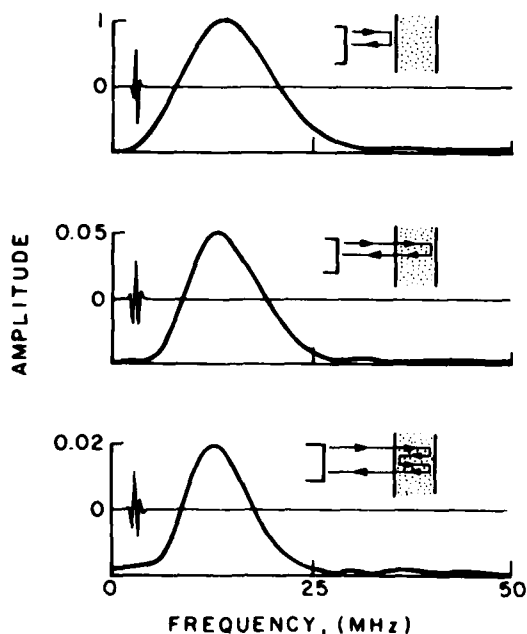


FIG. 7. Three echoes of the same broadband pulse (plotted in both the time and frequency domains) used to obtain the attenuation coefficient in the specimen for the range of frequencies in the pulse.

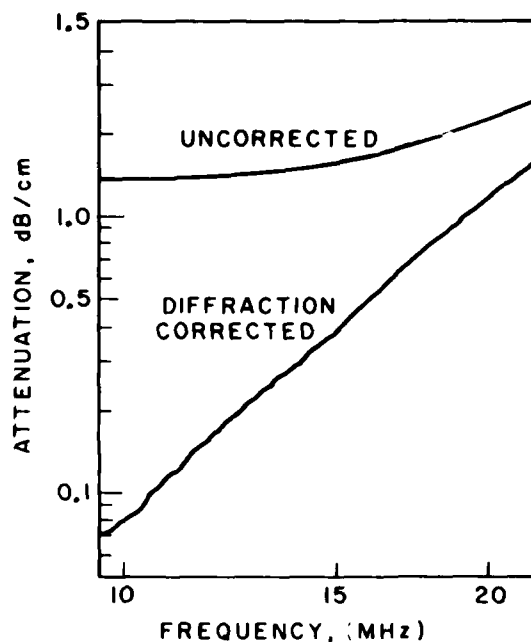


FIG. 8. Attenuation vs frequency for a steel sample illustrating the importance of corrections for diffraction.

Figure 9 shows the attenuation in two different steel samples with identical composition but

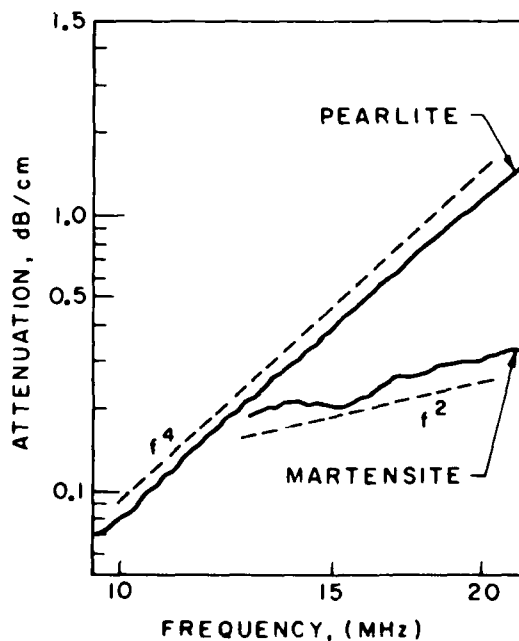


FIG. 9. Attenuation vs frequency for two specimens of the same steel heat treated differently to have martensite in one but pearlite in the other.

different microstructure. The curve for pearlite shows a frequency dependence very close to f^4 indicating that Rayleigh scattering is the dominant mechanism for attenuation. The curve for martensite exhibits lower values of attenuation, with a frequency dependence nearer to f^2 , indicating a different mechanism for attenuation from that in martensite. These results are comparable to previous results by Papadakis.⁵

CONCLUSIONS

1. Absolute acoustic velocity measurements are subject to random variations that limit their utility for microstructural NDE.
2. Relative velocity change measurements can be used to map microstructure with precision in a given piece of steel.
3. Acoustic attenuation measurements are very sensitive to microstructure, and they have good potential for practical, microstructural NDE.

ACKNOWLEDGEMENTS

This work was sponsored by the Air Force Office of Scientific Research under Grant AFOSR78-3726. The experimental steels were provided by the U.S. Steel Corporation.

REFERENCES

1. G. S. Barnett and T. B. Massalski, Structure of Metals, McGraw-Hill, 1966, p. 628.
2. W. Hume-Rothery, The Structures of Alloys of Iron, Pergamon Press, 1966, p. 140.
3. L. A. Glikman, A. M. Kartashov, Z. M. Ru-ashkina, and A. F. Lobov, Met. Sci. Heat Treat., **17**, 5-6 (May-June 1975), pp. 398-399.
4. E. P. Papadakis, K. A. Fowler, and L. C. Lynnworth, J. Acoust. Soc. Am., **53** (1973), p. 1336.
5. E. P. Papadakis, J. Appl. Phys. **35** (1964), p. 1474.

SUMMARY DISCUSSION
(N. Grayeli)

John Schuldies (Airesearch): Was the jominy test bar sectioned up into disks, essentially, and the velocity measurement made on the disk?

N. Grayeli: No

John Schuldies: Was it a radial measurement, then?

N. Grayeli: Two parallel surfaces are made on the jominy bar, and acoustic wave is sent into the sample, perpendicular to the bar axis, and we scan along the sample.

John Schuldies: So, it is a radial velocity measurement time of flight through diameter of the bars?

N. Grayeli: I really don't understand what you mean.

Gordon Kino (Stanford University): It's a flat bar. You scan along the length of the bar through its thickness.

N. Grayeli: Sure.

Unidentified Speaker: You are measuring across that bar.

Gordon Kino: It's a standard kind of thing.

Don Yuhas (Sanoscan): Did I read that attenuation curve right on pearlite and martensite? The number I got was something like one db per centimeter at 20 megahertz.

N. Grayeli: Maybe I can ask my colleague.

Gordon Kino: We have increased the frequency to 50 megahertz because of this and we were quite surprised. As you look back at Papadakis' work, indeed he saw these low attenuations.

Unidentified Speaker: The structure with 100 percent of pearlite is very good two-phase material. Did you measure anything of the frequency-dependent velocity at any higher frequency? 15 and 20 megahertz?

N. Grayeli: No, we didn't.

Unidentified Speaker: It's to be expected?

N. Grayeli: We don't know.

John Duke (Virginia Tech): You know, if you measure -- I was interested in -- the gentleman didn't follow up on his question. In the jominy bar, in quenching it in that particular fashion it's unlikely that you probably have uniformity of hardness throughout the diameter perpendicular to the faces that you ground. The measurement that you're making I think is probably characterizing the character of the material better than in fact the hardness test is because it's a bulk measurement. The hardness test, of course, is a surface measurement, and you, of course, would expect if you were to plate something with aluminum, and the hardness of the aluminum would be independent, necessarily, of the material which is deposited. So, I think, you know, you could make a lot more out of this than comparing it to hardness measurements.

N. Grayeli: Yes, it is a good comment in general, but in the case of a jominy bar, the structure is uniform throughout the diameter perpendicular to the faces on which we ground.

J. White (Westinghouse): Did you look at grain size in terms of the relationship on frequency dependence of attenuation?

N. Grayeli: That's our next step.

J. White: It's quite a strong relationship.

N. Grayeli: I think so.

(continued)

N. Grayeli (continued discussion)

Albert Birks (Battelle Northwest): In that respect there's a rather definitive Japanese study looking at grain size. And if you don't look at the substructure within the grains, the correlation is not very good.

N. Grayeli: Yes, it is true, but the effect of substructure is not very much, and I think to get a better correlation we have to consider that part which comes from substructure inside the grain.

F. Holler: One question. How do you calculate the influence of manganese on the velocity?

N. Grayeli: We use the data from the Barrett and Massalski (structure of metals) to calculate the velocity change by addition of Mn and other alloying elements. The change in lattice constant, caused by Mn will change the density and the density change, will change the velocity in the materials.

#

FAST SIGNAL-AVERAGING UNIT FOR ULTRASONIC TESTING.
CHARACTERIZATION OF MATERIALS PROPERTIES AND SNR-IMPROVEMENT FOR COARSE GRAINED MATERIALS

K. Goebbels, S. Kraus, R. Neumann
Fraunhofer-Institut für zerstörungsfreie Prüfverfahren
D-6600 Saarbrücken 11, Germany

ABSTRACT

The scattering of ultrasonic waves depends on the relation scatterer diameter to wavelength. Coarse grained materials and high frequency ultrasonic waves therefore are exciting high scattering amplitudes. During pulse-echo testing a backscattering signal is the result of superimposing all the single scattering processes in the sound beam for a given time of flight. Rectifying, digitizing and adding up several A-scans from several different probe positions, angles of incidence or frequencies equalizes interference maxima and minima. The resulting backscattering curve can be evaluated qualitatively and quantitatively for the materials structure characterization. Additionally, an improvement of the signal-to-noise ratio (SNR) is achieved for a defect surrounded by a coarse grained structure. The application in practice depends among other things on the time in which a sufficient number of digitized A-scans is averaged and on the dimensions and operating conditions of the equipment. With these limits a prototype instrument was developed. Up to 1024 digitized A-scans (each 400 μ s long, digitizing rate 20 MHz) are averaged in 0.4 sec. The result is recorded on a CRT-display and the whole unit is microcomputer-controlled. The equipment consists of an ultrasonic instrument (USIP 11) and the averager unit (averager/ADC/display, 1 P). Examples are given of applications to the characterization of materials structure (detection of heterogeneities in steel, grain size determination) and to the ultrasonic testing of coarse grained materials (austenitic welds, castings, fibre reinforced plastics).

INTRODUCTION

The qualitative characterization of materials structure with ultrasonic waves is a well known procedure. The attenuation coefficient α , measured for example by a backwall echo sequence (Fig. 1) allows to describe the anelastic structure behaviour. But some boundary conditions have to be regarded:

- The measured attenuation is only an integral value over the sample thickness.
- Planparallel surfaces of appropriate quality are the condition sine qua non.
- For quantitative measurements the coupling of the probe (reflection coefficient) and the beam divergence have to be corrected. Otherwise for low attenuating materials their influence can be many times greater than the true attenuation by absorption and scattering.

On the other hand backscattering measurements as described below avoid these difficulties:

- the measured signal is a continuous one. Therefore it is possible to differentiate the structure behaviour along the sound path.
- Only one surface is needed to transmit and to receive the scattering signals.
- The coupling of the probe is of qualitative influence but does not influence quantitatively the backscattering curve parameters. At last beam spreading is not a problem of backscattering measurements because the scattered signals are propagating back the same way as propagating forward.

The boundary conditions of backscattering measurements are others:

- The signal amplitudes usually ly some ten dB below e.g. backwall echoes (Fig. 2 for 10 MHz

longitudinal waves and an austenitic base material with grain size ASTM 4). Therefore an extremely high dynamic range is necessary to evaluate quantitatively these scattering signals.

- The backscattering signal is at first a high frequency amplitude modulated signal. Phase and amplitude for a given time of flight are resulting from the superposition of the single scattering signals excited at the grain boundaries inside the sound beam and integrated over the pulse length $1/f$. To get a smooth curve appropriate to evaluate, one has to change e.g. the probe position by a small amount (about one wavelength or one grain diameter) resulting in a new backscattering signal. Rectifying and adding several of such generated signals as shown in Fig. 3 leads to the final backscattering curve (it seems to be possible to omit the averaging procedure using a phase insensitive transducer as receiver [2]).

From a different point of view this scattering behaviour is of importance for the detection of defects in coarse grained materials like austenitic castings and welds [3]. For a single A-scan the amplitudes of scattering signals can be equal to or higher than the amplitudes of defect signals. Additionally, the scattering signals are coherent to the reflector signals. Therefore, with sophisticated methods regarding the frequency spectrum it is not possible to distinguish between defect and structure indication.

But the same procedure as described above (the small variation of the probe position) changes drastically the scattering signal but leaves unchanged - at least in a first approximation - the reflector signal. Again adding several of these signals results in either vanishing of the scattering signals (averaging of high frequency signals) or reducing the scatter indication to

the smooth curve shown in Fig. 3 (averaging of rectified signals). In each case the signal-to-noise ratio (SNR) is improved. This spatial averaging procedure can be replaced by or combined with the directional averaging (variation of the angle of incidence) and the frequency averaging (variation of the frequency exciting the probe in a burst manner).

The only condition for this signal-enhancement is, that the grain size in the material under test is not greater than the reflector to be detected. Otherwise the variation of e.g. the probe position would change the defect signal too, especially in its amplitude.

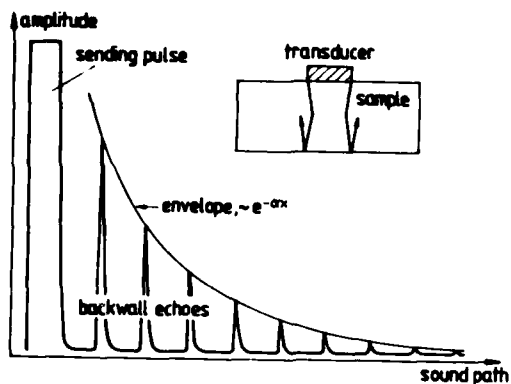


Fig. 1 Attenuation measurement

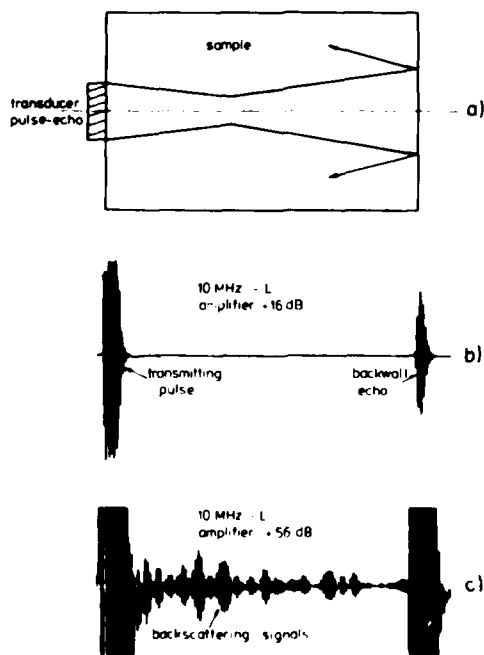


Fig. 2 HF-backwall echo and HF-backscattering signal

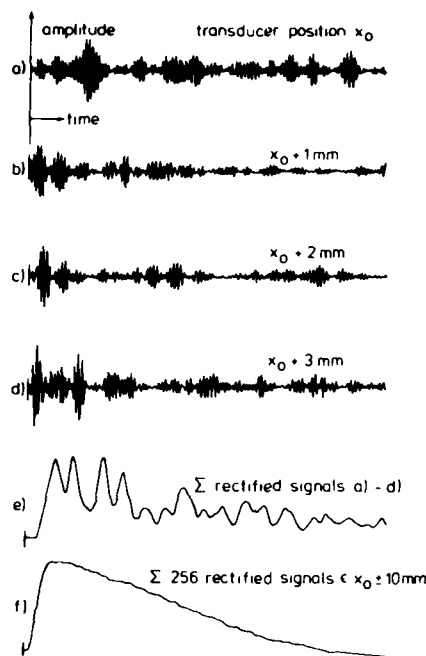


Fig. 3 Spatial averaging procedure

GRAIN SIZE

The attenuation of ultrasonic waves (attenuation coefficient α) is the sum of absorption (absorption coefficient α_A) and scattering (scattering coefficient α_S). Absorption is the result of many physical interaction effects between ultrasound and materials structure (e.g. with dislocations, thermoelastic and magnetoelastic losses /4/). Scattering on the other hand depends only on two parameters: elastic anisotropy (efficient at grain boundaries and phase boundaries) and the ratio d/λ (d = scatterer diameter, λ = wavelength). For multiphase materials (e.g. cast iron with graphite segregations or pearlitic structures) the concentration of the different phases is an additional parameter. α_S is well known for polycrystalline quasi-monophase materials in the Rayleigh region ($d \ll \lambda$), e.g. for shear waves /4/:

$$\alpha_S (\text{mm}^{-1}) = \frac{6\pi^3}{375} \cdot \left(\frac{A}{2} \right)^2 d^3 f^4 \frac{1}{v_T} \left(3 + 2 \left(\frac{v_L}{v_T} \right)^5 \right) (1)$$

$$= S_T d^3 f^4$$

where $A = c_{11} - c_{12} - 2c_{44}$ = elastic anisotropy (for cubic materials),
 c_{11}, c_{12}, c_{44} = second order elastic constants,
 ρ_0 = density, f = frequency,
 v_L, v_T = velocity of longitudinal and shear waves, respectively.

Backscattering curves $A_S(x)$, where x is the sound path, are containing α_A and α_S , e.g. for a homogeneous structure /1/:

$$A_S(x) = A_0(\alpha_S \Delta x)^{1/2} \exp(-(\alpha_A + \alpha_S) x) \quad (2)$$

where A_0 = amplitude at the surface,
 Δx = pulse length.

Figure 4 shows backscattering amplitudes from one sample of given grain size measured with two different frequencies and from two samples of different grain sizes measured with the same frequency. Under the assumption that the frequency dependence of α_A is known (e.g. $\alpha_A = a \cdot f$, with $a = \text{const}$) two measurements with two different frequencies allow to separate α_A and α_S and to evaluate α_S for the grain size determination:

$$\alpha_1^T = a f_1 + S_T d^3 f_1^4 \quad (3a)$$

$$\alpha_2^T = a f_2 + S_T d^3 f_2^4 \quad (3b)$$

$$d = (|\alpha_2 - \alpha_1| f_2 / f_1 |1 / S_T f_2 (f_2^3 - f_1^3)|)^{1/3} \quad (3c)$$

The attenuation coefficients α_i ($i = 1, 2$) are measured by evaluating the half-logarithmic plot of equation (2):

$$\ln A_S(x) = \ln (A_0 \alpha_S^{1/2} \Delta x^{1/2}) - \alpha x \quad (4)$$

Figure 5 shows the comparison between the grain size of steel samples determined by this two-frequencies method (and two further methods /5,6/) and the usual metallographic analysis. The agreement is so good that at the moment an ultrasonic equipment is under development which makes this nondestructive grain size determination automatically and in field.

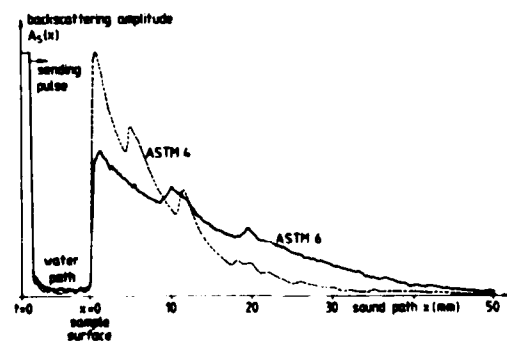
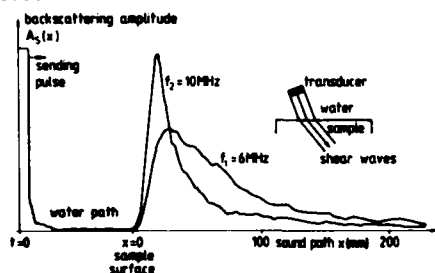


Fig. 4 Backscattering curves obtained with different frequencies and different grain sizes

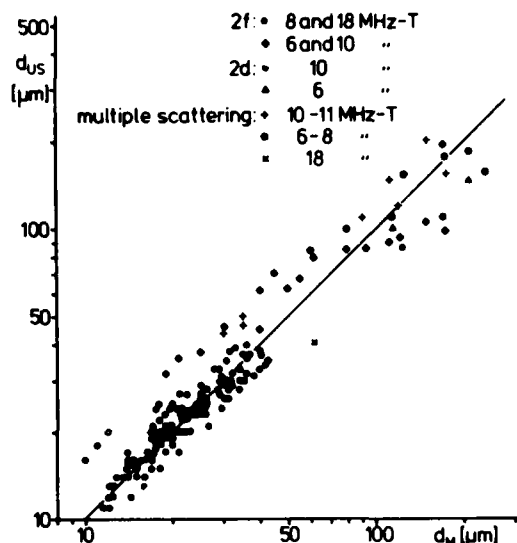


Fig. 5 Comparison between grain size determination by backscattering measurements and by metallography.

INHOMOGENEITIES

One of the advantages of backscattering measurements is the continuous signal between the surface backscattering amplitude

$$(A_S(0) = A_0 (\alpha_S \Delta x)^{1/2})$$

according to Equ. (2) and the electronic noise level. Variations in the attenuating behaviour along the sound path and especially in the scattering behaviour can be clearly identified. Equation (2) has the general form, valid for inhomogeneous materials, too. ($\alpha = \alpha(x)$), of /7/:

$$A_S(x) = A_0 (\alpha_S \frac{x}{2} \Delta x)^{1/2} \exp(-2 \int_0^{x/2} \alpha(z) dz) \quad (5)$$

This is shown schematically but with realistic values for α , α_A and α_S in Fig. 6: If the scattering coefficient changes between 75 mm and 100 mm depth by a factor of 4 compared with depths below 75 mm and above 100 mm then this will change the backscattering curve between 150 mm and 200 mm sound path. According to the kind of inhomogeneities (fields of microcracks, segregates, non-metallic inclusions), their volume contents and the general behaviour of the structure anomalies totally different curves $A_S(x)$ will occur. Two examples from the same specimen are shown in Fig. 7. At the moment it is not possible to identify the kind of heterogeneities (increased knowledge is necessary about the scattering of two-phase, polycrystalline materials), but the region where they are and a qualitative measure how strong the basic structure is changed are simply to obtain.

Another kind of inhomogeneity is the anisotropic structure especially of thin components. In different directions (e.g. parallel and perpendicular to the rolling direction) different types of $A_S(x)$ with different $A_S(0)$ and attenuation coefficients according to Equ. (3) will be measured: each direction has its own value of A (cf. Equ.(1), where A is given for a random distribution of the grain orientations).

Thirdly, weldments can be regarded as structure heterogeneities, too, and in Figs. 8 and 9 some examples are given of 450 shear wave backscattering measurements through welded thick components: the base material inhomogeneity in one case (Fig. 9) as well as the fusion line and single defects in definite weld positions are clearly superimposed to the usual curve $A_S(x)$. Therefore, it is one interesting point to identify fusion lines along weldments with high-frequency backscattering measurements where they are completely transparent for usual frequency ranges at about 1 MHz. Inside the weld itself it is difficult to characterize e.g. the grain size by backscattering signals, but depending on the direction of the sound beam in relation to the weld direction the overlay structure of the passes can easily be analysed (Fig. 8).

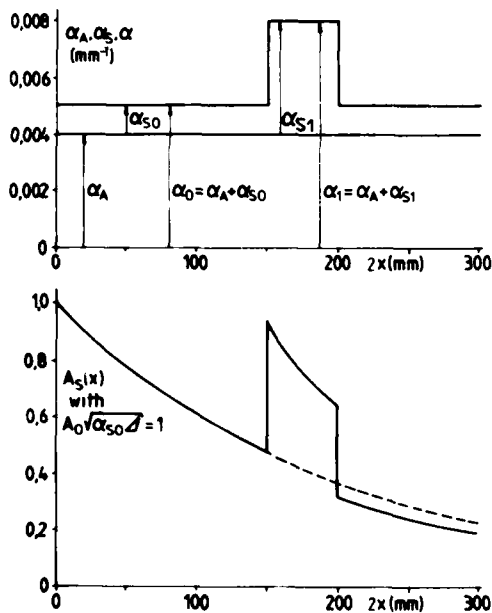


Fig. 6 Characterization of regions of heterogeneities by backscattering curves - schematically.

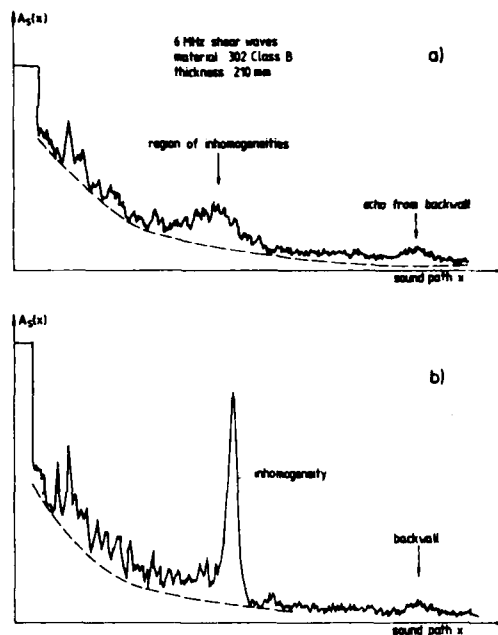


Fig. 7 Examples of inhomogeneous materials structures

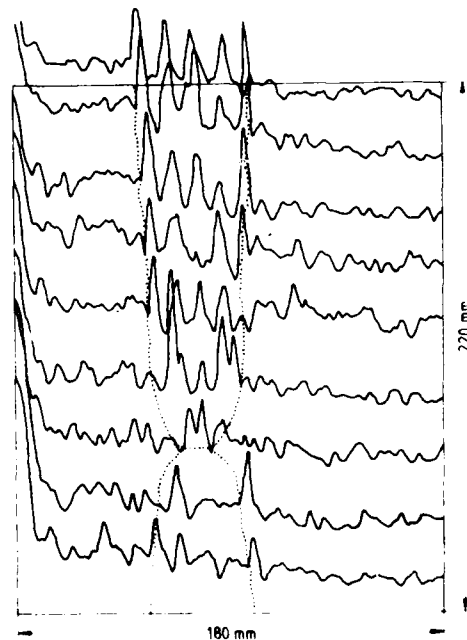


Fig. 8 Backscattering curves through weld regions

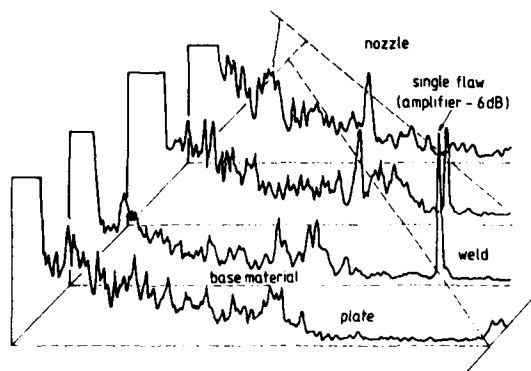


Fig. 9 Backscattering curves through weld regions

SIGNAL-TO-NOISE RATIO

In coarse grained materials the coherent noise amplitudes ("grass") are many times higher than the electrical noise and this makes it difficult to detect signals. Restricting us to the analysis of rectified signals, the averaging processes as described in the introduction reduce the grass-level to a curve corresponding to Equ. (2). On the other hand reflector signals correspond to

$$A_R(x) = A_0 \exp(-\alpha x), \quad (6)$$

disregarding beam diffraction and distance laws of the different types of reflectors (e.g. sphere, disc). The optimal value for the SNR therefore is

$$SNR = A_R(x) / A_S(x) = (\alpha_S \Delta x)^{-1/2} \quad (7)$$

Figure 10 exemplifies for backwall echoes the efficiency of averaging processes. Above 8 A-scans are plotted from 8 different positions. The backwall echo is unaffected but the scattering amplitudes change drastically from A-scan to A-scan (the variation of the probe position between each A-scan is about 0.3 mm, corresponding to one grain diameter). Below 2, 4, 64 and 1024 averaging processes are shown and until 4 backwall echoes can be resolved.

The difficulty to detect defects with spatial averaging is given by the echo dynamic curve of the reflector. The variation of the probe position should be limited to an echo decrease of less than 6 dB. But for a 3 mm flat bottom hole in about 100 mm depth this is + 10 mm, therefore enough to get many different A-scans with different noise signals. The Figs. 11 and 12 compare A-scans and averaging results from different types of defects.

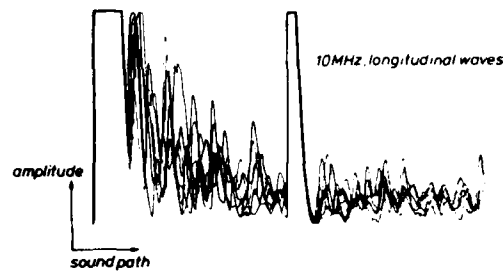


Fig. 10 Signal enhancement by spatial averaging

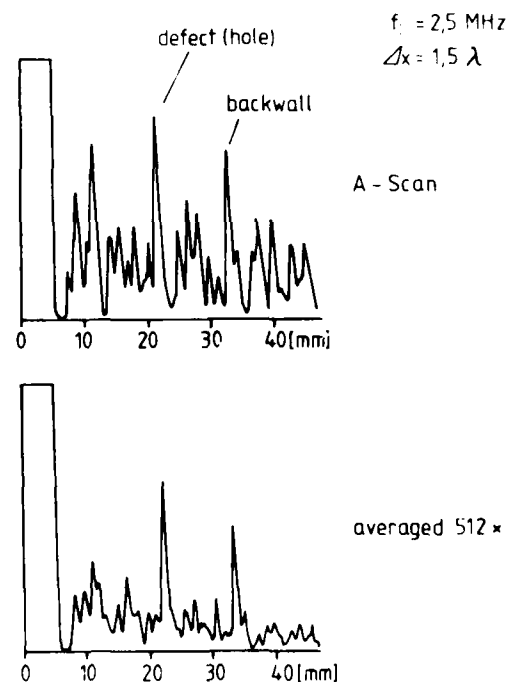


Fig. 11 Improvement of the SNR for a natural defect in austenitic casting

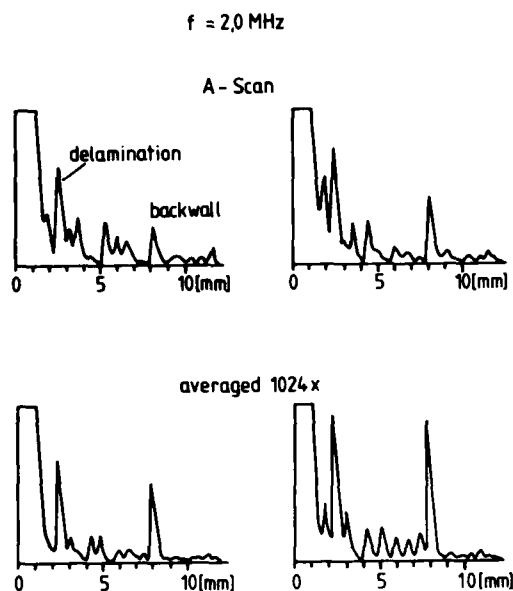


Fig. 12 Improvement of the SNR for a delamination in GFRP.

EQUIPMENT

The applicability in practice of equipment for backscattering measurements and averaging techniques depends among other things upon the velocity with which the processes will be performed, the size of the equipment and the operating procedures.

The apparatus developed consists of an usual UT-equipment with an output for the rectified signals. They will be digitized by an 8 bit/20 MHz ADC into 400 μs long signals (8 K/8 bit). Microcomputer-controlled they come to 8 parallel working averager modules (each containing 1 K memory and 18 bit resolution). From 1 to 1024 averaging processes can be selected in steps of powers of 2. The result of the averaging process is displayed on a CRT, selectable between "averaging and hold" and "continuous averaging". 1024 averaging processes are made in 0.4 sec resulting in a quasi-on-line averaging. Additionally an output is installed to plot the result on an X-Y recorder. A photograph of the UT-equipment and the averager is shown in Fig. 13.

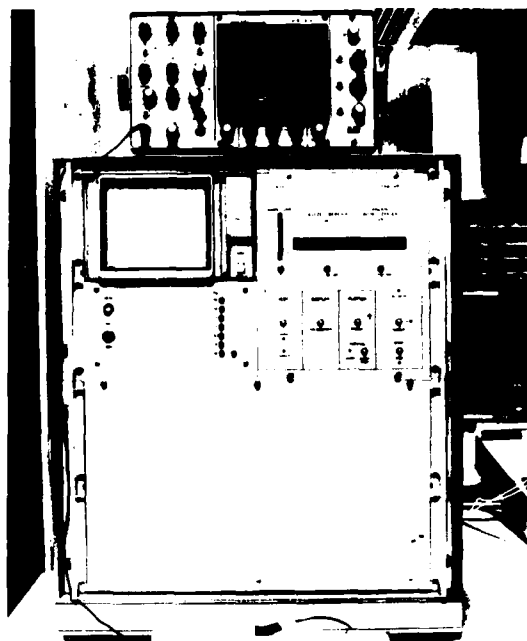


Fig. 13 Photograph of UT-equipment and averaging unit

ACKNOWLEDGEMENT

This work was supported by the Bundesministerium für Forschung und Technologie and the European Community for Carbon and Steel.

REFERENCES

- /1/ B. Fay: *Acustica* **28** (1973) 354-357
- /2/ J.S. Heyman, J.H. Cantrell, J.D. Whitcomb: *Proceedings of the 1st Intern. Symp. Ultras. Mater. Characteriz.*, Gaithersburg, June 1978
- /3/ S. Kraus, K. Goebbels: *ibid.*
- /4/ A.B. Bhatia: "Ultrasonic Absorption". Clarendon Press, Oxford 1967
- /5/ K. Goebbels: *Materialprüfung* **17** (1975) 231-33
- /6/ K. Goebbels: *ibid.* **18** (1976) 86-88
- /7/ K. Goebbels, P. Höller: *Proceedings of the 1st Intern. Symp. Ultras. Mater. Characteriz.*, Gaithersburg, June 1978

SUMMARY DISCUSSION
(K. Goebbels)

P. Holler (Session Chairman): Any questions?

Bruce Thompson (Science Center): I have two questions: One, over what sort of area do you typically move the transducer in performing the averaging? And, I'm aware of some of the limitations in using attenuation measurements to try to measure grain size. What are the corresponding limitations for the backscattering technique, having to do with the presence of porosity or grain aspect ratio and so forth?

K. Goebbels: The first question is easy to answer because you need only to change the probe position by one grain diameter to get a change in your backscattering high-frequency signal. Therefore, moving some millimeters, e.g. plus or minus five millimeters, or in a ring of ten millimeters diameter, you make very good backscattering measurements. It is not necessary to go over several centimeters to make this measurement. This is the reason you can use it for signal-to-noise improvement, too, because there's a small amount of change of probes position which does not influence (first approximation) the amplitude of defect signal. But there you can see is one limit of the averaging in this kind of technique: if the grain size in very coarse-grained materials comes to the size of the defect you want to see, you have to move farther. And the second question: In the Rayleigh region, it seems from the grain alignment or the form of the grains there is no limit on the grain size determination. Another point is grain sizes smaller than ten microns: we cannot characterize them nondestructively, because then the frequencies needed are too high. And on the opposite side of this, more than 500 microns, or one millimeter, then you have too low a number of grains inside the sound beam, and the statistic value is not so good. And there are some restrictions for steel. Porosity is not a problem. The problems are multi-phase structures like free-machining steel with mus-inclusions.

Paul Gammel (Jet Propulsion Lab): I would like to know the effect of the size of the transducer beam. I assume this is of influence on the averaging process. Obviously, if you have a very large beam, you have already done a lot of averaging by beam size, and I would just like to know what effect it has on the statistics going from quarter-inch to half-inch transducers.

K. Goebbels: We could not find any effect of the size of the transducer, if you are making backscattering measurements to measure the slope and decay because when we have homogeneous material, inside the sound beam every time it's the same mean grain size. If the material is inhomogeneous, then you can get some changes in this. And for the improvement of the signal-to-noise ratio with the averaging process, that depends on the reflector diameter you want to see, what type of probe you're using. But we don't have any characteristic differences from probe to probe and from diameter to diameter for the backscattering signal.

Paul Gammel: Does this mean that if you went to, let's say, an inch and a half transducer, two inch transducer -- it would seem intuitively you would have done the averaging.

K. Goebbels: No. I can have done it if I am using a phase-insensitive transducer. Then it must go. But the usual transducer -- and every time you have interference processes from the different grain centers into the sound beam for a given time of flight, and this is resulting in this high-frequency signal. And if you are going from such a transducer to such a transducer, it is every time a high frequency signal.

Gordon Kino (Stanford University): I'm a little unclear on the kind of averaging process. We have tried the same thing on ceramics, and for the same reasons. But it seems to me that if the diameter of the beam, say, is one centimeter and you move the beam one millimeter, which is much larger than the grain size, there is very little change because the same grain is exciting the same transducer, and it's basically a parallel beam coming out. So, there is no phase change, and it's only the extra one millimeter you have moved it across that brings new grains into the beam and it gives you some averaging.

K. Goebbels: It seems not to be the influence that there are other grains inside the beam. It seems to be that the sound field itself is not so homogeneous. This makes the changing of your structure interference. For example, if you are using

(continued)

K. Goebbels (continued discussion)

for one position the transducer and only going around and no changing of the transducer position and every time the same grains are in the beam, but this is enough to make an averaging measurement.

P. Holler: It may be completely different for ceramics.

Gordon Kino: Yes, unfortunately. I wish it were the same in ceramics.

John Duke (Virginia Tech): Wouldn't in fact the range over which you move your center in effect limit the size of the certain defects that you could see? In effect, wouldn't moving it in a sense average out that?

K. Goebbels: Yes. One example: If I have a three-millimeter-flat-bottom hole in one-hundred millimeter depths; and if I have a transducer of seven millimeter diameter, I can go six millimeters forward and six millimeters backward or in a ring and just change the amplitude not more than six db.

John Duke: It seems you could almost use this in a way to sort in a certain sense the flaw size by, you know, variations in the actual amount of movement you do with your transducer.

K. Goebbels: I did not understand.

John Duke: In other words, if you can effectively make a flaw seem like it disappears, you can in a sense determine the size.

K. Goebbels: Yes.

P. Holler: One more question.

John Shyne (Stanford University): When you made your scattering coefficient measurement to get the grain size, you separated out the grain size effect by taking it as frequency to the fourth from the absorption by taking it as a frequency to the one. What were the relative magnitudes of the two parts of the attenuation coefficient?

K. Goebbels: Well, we have the measurement of more than 200 samples of steel, and there are samples where with low frequencies the scattering makes only three to five percent of the whole attenuation coefficient and other samples where it makes 85 to 90 percent of the whole attenuation coefficient. It depends on the D over λ and the absorption.

John Shyne: If you're at frequencies, say, like ten megahertz --

K. Goebbels: It depends on the microstructure, and then for small grained material the scattering is of lower influence on the attenuation than for coarse grained material.

#

DEFECT IDENTIFICATION AND SIZING BY THE ULTRASONIC SATELLITE-PULSE TECHNIQUE

G. J. Gruber
Southwest Research Institute
San Antonio, Texas 78284

ABSTRACT

Type and size are the most important defect characteristics that need to be determined for reliable prediction of the remaining service lifetime of a defective structure or part. The analytical and supporting experimental results presented in this paper concern a universal ultrasonic defect-identification-and-subsequent-sizing method. The conceived satellite-pulse technique (SPT) is based on the interpretation, in terms of defect types and dimensions, of the separation in time-of-arrival between the specularly-reflected pulse and its tip-diffracted or tangentially-scattered "satellite" contained in the composite defect signal. Several alternate calibration procedures were also developed, any one of which enables the ultrasonic examiner to make the time scale of the oscilloscope read directly in terms of equivalent crack depth or void diameter as appropriate.

Introduction

The current trend toward a defect-tolerant-design philosophy places increased importance on accurate ultrasonic defect-sizing techniques, because it requires the technique to estimate the size of a detected and identified defect with a specified probability and degree of confidence. The difficulties of present ultrasonic techniques in meeting the needs of fracture mechanics lifetime-prediction models can be attributed to several causes, all stemming principally from the poorly-established relationships between the peak amplitude of the reflected pulse and defect characteristics. A crack oriented perpendicular to the examination surface may produce a relatively weak reflected wave. A large compressive stress may close the crack and thereby diminish the reflected pulse amplitude. Other sizing difficulties are encountered when the defect is located in the "dead zone" of the ultrasonic probe.

The four materials evaluation tasks for the determination of structural integrity are listed in Table 1. The important ultrasonic issue that we are now faced with is what type and severity of defect are present. The next frontier for

Task	Objective
I. Defect Detection	"where?"
II. Defect Identification	"what type?" (void or crack like?)
III. Defect Characterization	"how big?" ("what size?") "what shape?" "what orientation?"
IV. Lifetime Prediction	"how severe is the problem?" "prognosis?"

Table 1. Materials evaluation tasks and their objectives.

ultrasonics is thus to provide quantitative information needed to distinguish between those small, nonpropagating, void-like defects that are "benign" with respect to failure and those significant, propagating, crack-like defects that are "malignant" or critical with respect to failure.

Ultrasonic Defect-Sizing Methods

Ultrasonic-signature-analysis methods currently available or under development for estimating the size of crack-like or void-like defects are listed in Table 2. It is convenient to group these techniques in three broad categories according to the kind of analysis performed on the received defect signal. Useful quantitative information about the characteristics of the defect with implications for structural performance and safety may be obtained by arrival-time analysis or frequency-content analysis of the defect signal distorted or otherwise modified in relation to a replica of the transmitted pulse. Analysis of the peak amplitude of the principal component of the composite defect signal is most useful for defect detection (Task I in Table 1).

Analysis	Technique
Peak AMPLITUDE	Artificial Defect Echo Comparison Backwall Echo Comparison Decibel Drop
FREQUENCY Content	Deconvolution Frequency Response
Arrival TIME	Impulse Response Delay Time Satellite Pulse (SPT)

Table 2. Ultrasonic defect-sizing methods.

Signal distortion may register in the time domain as "satellite-pulse" formation and in the frequency domain as amplitude modulation¹ (see Figure 3). Selection of a particular method of defect sizing and its accuracy are dependent on exploiting established relationships between defect type, shape, orientation, size, composition, tightness, and surface roughness and certain extractable ultrasonic signal parameters. The size of defects which are large compared to the wavelength of the employed ultrasound can be determined with adequate accuracy by conventional peak-amplitude-comparison techniques. However, small defects in areas of high mechanical or thermal stress may affect the service strength of the

structure or part sufficiently to warrant its rejection, and measurement of the peak amplitude of the principal component of the defect signal ("echo height") for sizing small defects is unreliable. Differences in the capabilities and limitations of the ultrasonic defect-sizing techniques listed in Table 2, with the exception of the last method, are reviewed elsewhere.² The ultrasonic satellite-pulse technique (SPT)* for defect indication and subsequent sizing is the subject of this paper.

Defect IDENTIFICATION by the Ultrasonic Satellite-Pulse Technique

The extension of delay-time analysis for sizing crack-like defects to identifying and sizing defects of all types has led us to the satellite-pulse technique. An infinite variety of shaped defects is possible; but it seems reasonable initially to consider only two types: planar, crack-like defects, and volumetric, void-like defects.** From these, most other defect shapes of interest could be constructed.

The physical principles and feasibility demonstration of the SPT for identifying void-like and crack-like defects are presented, respectively, in the following two sections.

Identification of Void-Like Defects

Whenever an ultrasonic wave reaches a distinct boundary, mode conversion, refraction, reflection, scattering, or diffraction occurs. The Rayleigh-type surface waves generated by an incident ultrasonic beam upon encountering a spherical or cylindrical void in a metal may be described in terms of the simple concepts of acoustic ray theory. Geometrical theories of scattering from relatively smooth, generally convex targets imbedded in homogeneous, isotropic, linear elastic media provide good results at relatively low frequencies.³⁻¹³ The models developed to describe the scattering of ultrasonic plane waves by volumetric defects do not account for materials attenuation effects which make the received specularly-reflected and tangentially-scattered pulse components of the defect signal inexact replicas of the transmitted pulse. Nor do these models predict the speed and attenuation of the signal components as they propagate along the various ray paths. An oversimplified model of scattering by a void in metal assumes that the speed of the "creeping wave" along the void's periphery is identical to that of the incident longitudinal bulk wave, c_p , rather than that of a Rayleigh surface wave.^{8,10-12} These authors derived a linear expression for the separation in time-of-arrival of the specularly-reflected and first pair of scattered pulses, Δ_0 , in terms of the void's diameter, d_0 , as shown below:

$$\Delta_0 = \frac{2.57d_0}{c_p} \quad (1)$$

*The SPT research and development program was sponsored by Southwest Research Institute. The concepts are covered in appropriate patent applications.

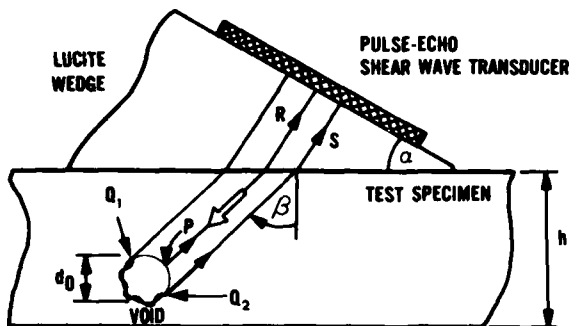
**Such broad defect classifications make a good deal of intuitive sense, and are supported by research findings.

Freedman^{4,5} assumed the backscattered signal for simple bodies of arbitrary convex shape to be composed of several discrete pulses, each identical to the transmitted pulse ("composite echo theory"). The first pulse is produced by the specular reflection of the incident wave at the point on the surface of the scattering defect nearest to the source of ultrasound. This follows from Fermat's principle of least action and geometrical acoustics considerations. Additional echoes are formed wherever there is a discontinuity in solid angle subtended at the pulse-echo probe by parts of the inclusion within range r or in its k th derivative with respect to range, $dJ(r)/dr^k$. Separate scattered pulses are received only from certain discrete ranges of a volumetric defect. The magnitude of each scattered pulse is proportional to the magnitude of its generating discontinuity in the defect's shape function, $J(r)$, or its k th derivative, and it decreases with increasing frequency and defect diameter. Usually only the first one or two orders of derivative ($k = 0$ or 1) in which discontinuities occur need to be considered. The pulses are separated in time-of-arrival by the difference in times taken to travel to and return from the defect's "extremities" marked by the discontinuities in the k th derivative of its shape function. There are inherent difficulties in defining the discontinuities which contribute significantly to the composite echo structure of scatterers of arbitrary shape.

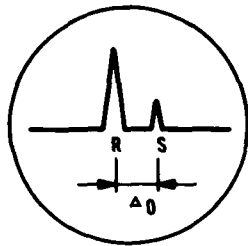
Rudgers⁷ developed a model for describing the scattering process by volumetric defects of simple shape based on the creeping-wave formalism. Rudgers' geometrical theory of scattering provides a simple explanation of the type-and-size-information-carrying pulse, S , in the ultrasonic signature of a hole drilled into the side of a test specimen (see Fig. 1). In the defect-characterization position, the incident ultrasonic beam is aimed at the center of the void of diameter d_0 so as to maximize the amplitude of the first pair of creeping waves which arrive at the pulse-echo shear wave transducer simultaneously after having traveled ("crept") once around the back surface of the void in opposite directions. For clarity, only the counterclockwise creeping wave is shown by the wiggly line from Q_1 to Q_2 in Fig. 1(a). When the ultrasound encounters the front surface of the void at point P , a specularly-reflected wave ("R-wave") is sent back to the transducer (front reflection). A pair of Rayleigh-type surface waves is also produced by the incident wave at points Q_1 and Q_2 . These Rayleigh waves circumvent the void a number of times until they disappear into the noise since their energy is continuously depleted by tangential radiation. Each time the counterclockwise creeping wave reaches point Q_2 , tangential reradiation, in the form of a tangentially-scattered wave ("S-wave") from the void during its circumvention, is launched at the desired detection angle to be received by the pulse-echo transducer (back scattering). The delay time between the R pulse and its first scattered satellite, Δ_0 , is a linear function of the void diameter, d_0 , as expressed by the relationship

$$\Delta_0 = \left(\frac{n}{2v} + \frac{1}{c} \right) d_0 \quad (2)$$

where c is the shear wave velocity and v is the Rayleigh wave velocity of the test specimen. This equation differs from Equation (1) in one respect:



- a. Splitting of the incident wave (hollow arrow) into a specularly-reflected component, R, and a circumferentially-scattered component, S, by a void of diameter, d_0 .



- b. Reflected and scattered pulses separated by delay time Δ_0 on the oscilloscope screen.

Fig. 1. The interaction of an ultrasonic shear wave with a void-like defect resulting in a reflected pulse and a lagging scattered satellite pulse.

the creeping wave travels along the defect's periphery with the Rayleigh velocity (rather than the bulk velocity).

The ratio of the Rayleigh and shear wave velocities, termed as the surface velocity ratio, m , is given by the Bergmann approximation,

$$m = \frac{v}{c} = \frac{0.87 + 1.12\sigma}{1 + \sigma}, \quad (3)$$

where σ is the Poisson ratio. In terms of the ratio of the longitudinal and shear wave velocities, termed as the bulk velocity ratio, n , Poisson's ratio is given by

$$\sigma = \frac{1 - 2n^2}{2 + 2n^2}. \quad (4)$$

For carbon steel 1020, Equation (2) becomes

$$c\lambda_0 = 2.71d_0. \quad (5)$$

The constant of this equation differs from that of Equation (1) (i.e., 2.57), and its validity was borne out by experimental results.

Void-like defects may, therefore, be distinguished from other reflector types (corners, notches, cracks, etc.) by their lagging satellite pulses.

Identification of Crack-Like Defects

For an axially-sited spherical cap target, Freedman's composite echo theory⁴ predicts two pulse components; the first is a reflected pulse that is the same as for a sphere, and the second pulse is formed by diffraction of the incident wave at the cap rim.⁴ The discontinuities in the first derivative of the spherical cap's shape function as a function of range, $J(r)$, are located at its nearest and farthest points relative to the source of ultrasound. Similarly, for an axially-sited right circular cone, there is a discontinuity in the second derivative of $J(r)$ at the cone apex or tip and another one in the first derivative of $J(r)$ at the cone base. At aspect angles other than axial or normal, there are three pulse components; one is associated with the apex and the other two originate from the nearest and farthest points on the base rim directly receiving ultrasonic energy. The sequence in which these tip- and edge-diffracted pulses arrive at the probe is a function of the aspect angle.

With the direction of the ultrasonic beam other than parallel to a disc's axis, an infinite number of discontinuities occur in the second derivative of $J(r)$ at the near and far ranges of the disc. Edge-diffracted pulses are thus expected to arise at these defect "limiting ranges." The diffracting "extremities" of the internal crack shown in Fig. 2 are at points Q_a and Q_b . A single

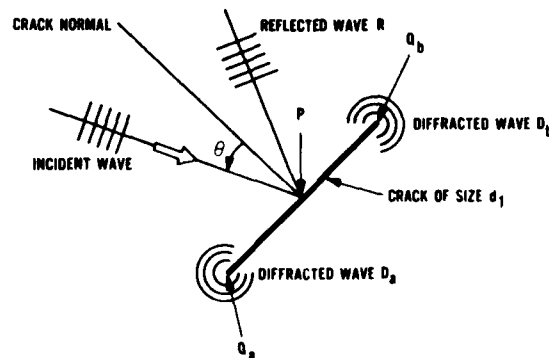


Fig. 2. The interaction of an ultrasonic shear wave with an internal crack resulting in a specularly-reflected wave and two tip-diffracted waves (adapted from Reference 1b).

incident pulse splits into three parts; a specularly-reflected wave, R, which will not be received by the pulse-echo transducer, and two cylindrically-spreading, edge-diffracted waves, D_a and D_b . These waves are produced respectively at points P, Q_a and Q_b on the defect's surface. The separation in time-of-arrival of the edge-diffracted pulses is given by the delay time

$$\Delta_1 = \frac{2d_1}{c} \sin^2 \theta, \quad (6)$$

where d_1 is the distance between the defect's extremities (i.e., crack depth) and θ is the angle the incident beam makes with the line perpendicular to the crack. The defect signal may be represented by the sum of two identical pulses:

$$s(t) = u(t + \Delta_1/2) + u(t - \Delta_1/2), \quad (7)$$

where $u(\cdot)$ denotes the form of the transmitted pulse. This composite waveform Fourier transforms into

$$S(f) = (2 \cos \pi f \Delta_1/2) [U(f)] \quad (8)$$

The defect energy density spectrum is thus the same as that obtained for a specularly-reflected pulse, $|U(f)|^2$, modulated by the low-frequency cosine term involving the separation in time-of-arrival of the edge-diffracted pulses. The periodicity of the modulated spectrum is given by

$$p_1 = 1/\Delta_1 \quad (9)$$

Thus, defect size and orientation information in the time domain (i.e., Δ_1) carries over to the frequency domain (i.e., p_1) in a reciprocal manner. The feasibility of using waveform-distortion or spectrum-modulation information for estimating the size and orientation of crack-like defects is illustrated in Fig. 3. The ultrasonic responses of narrow slits of various depth ($d_1 = 100$ mils and 200 mils) and orientation ($\theta = 25^\circ$ and 32°) were determined to aid in the interpretation of the composite signal received from a turbine rotor fatigue crack. For purposes of comparison, the unmodulated reference spectra are also shown in envelope form in Fig. 3 along with the modulated signal spectra.

The temporal representations on the left side of Fig. 3 indicate two distinct echoes that originate from the secondary source points located at the bases and tips of the surface-breaking slits. The tip-diffracted pulses, D, arrive ahead of the larger base-reflected pulses, R. The spectral representations on the right side of Fig. 3 contain

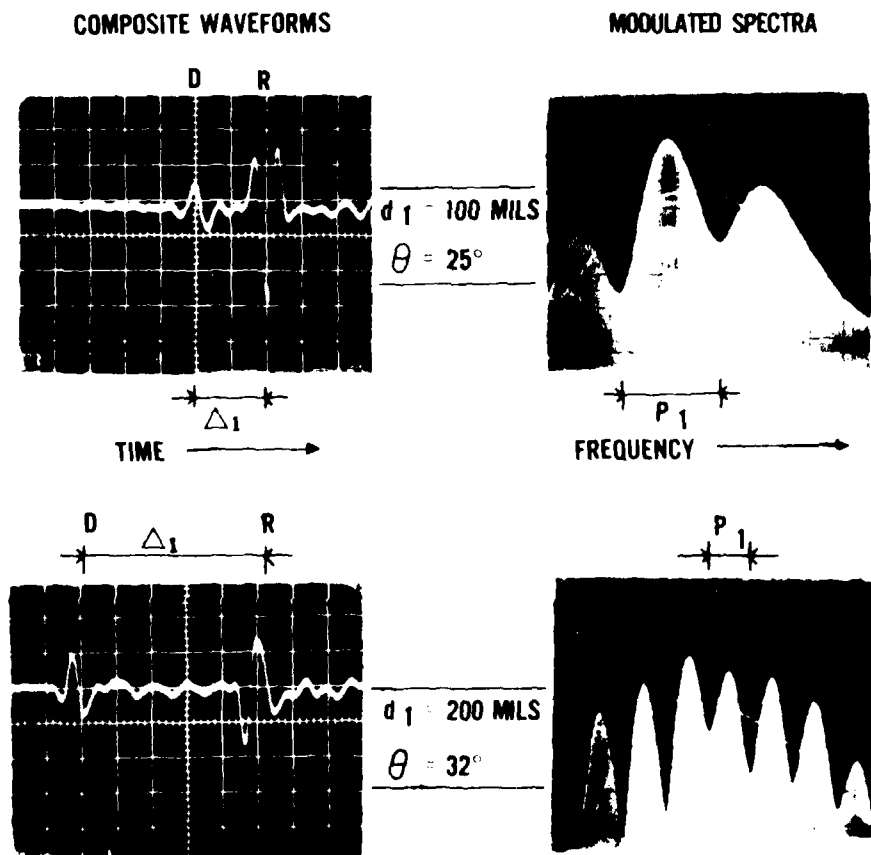
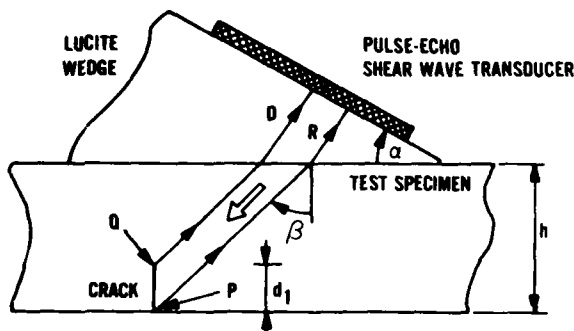


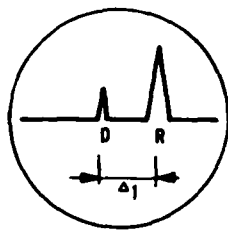
Fig. 3. Illustrating the inverse relationship between delay time, Δ_1 , and spectrum periodicity, p_1 , obtained for slits simulating surface-breaking fatigue cracks.

equivalent information.* Although the spectral approach has considerable potential for revealing details about important defect characteristics, the expertise and sophistication needed to acquire, process, and interpret the pertinent data limit its use to specialized applications. The field applications of frequency-content analysis for defect sizing thus have experimental difficulties. Arrival-time analysis yields advantages over spectral analysis not only in data acquisition but also in data processing and interpretation.

There are other mathematical models which have been developed to account for the ultrasonic diffraction process by planar defects. At high frequencies, Keller's geometrical theory of diffraction provides a simple explanation of the type-and-size-information-carrying extra pulse, D , in the ultrasonic signature of a surface-breaking crack^{17,18} [see Fig. 4(b)]. The geometrical theory of diffraction assumes that when the obliquely-incident ultrasonic beam encounters a surface-breaking crack such as that shown in Fig. 4(a), in addition



- a. Splitting of the incident wave (hollow arrow) into a corner-reflected component, R , and a tip-diffracted component, D , by a crack of depth d_1 .



- b. Reflected and diffracted pulses separated by delay time Δ_1 on the oscilloscope screen.

Fig. 4. The interaction of an ultrasonic shear wave with a crack-like defect resulting in a reflected pulse and a leading diffracted satellite pulse.

*The spectral representations of the defect's response actually provide less information since no phase information is present at the output of the spectrum analyzer.¹⁶

to the generally observed reflected wave, R , a diffracted wave, D , is produced when the beam encounters the tip of the crack at point Q . In the defect-characterization position, the incident ultrasonic beam is aimed at point Q so as to maximize the amplitude of the tip-diffracted wave. Upon the incident beam's encountering the base of the crack at point P , a corner-reflected wave is sent back to the transducer which arrives after the diffracted pulse [see Fig. 4(b)]. The delay time between the R -pulse and its diffracted satellite, Δ_1 , is a linear function of the crack depth, d_1 , as expressed by the relationship

$$\Delta_1 = \frac{2d_1}{c} \cos \beta, \quad (10)$$

where β is the angle the incident beam makes with the line perpendicular to the upper surface of the test specimen. For a refraction angle of 45 degrees, we obtain

$$c\Delta_1 = 1.41d_1. \quad (11)$$

Crack-like defects, may, therefore, be distinguished from other reflector types (corners, inclusions, voids, etc.) by their leading satellite pulses.

Defect SIZING by the Ultrasonic Satellite-Pulse Technique

The first two reflections from the test specimen's end, or from the end of a plain piece of similar material, may be used to eliminate the influence of the generally unknown shear wave velocity on the derived linear relationship between d_1 and Δ_1 in Equation (11) and on that between d_0 and Δ_0 in Equation (5). Figure 5 illustrates the simple calibration procedure that may be performed right on the specimen (i.e., without having notches and/or side-drilled holes available in a separate calibration block). The calibration delay time between the first two corner-reflected pulses from the end of a plate or pipe specimen of thickness h is given by

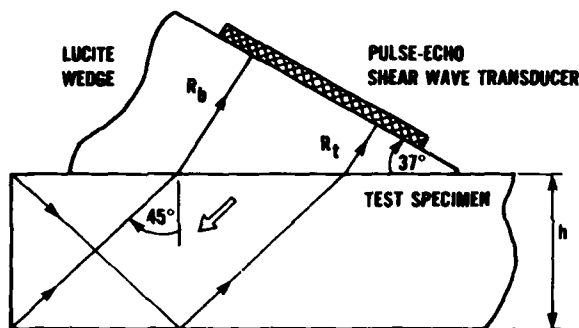
$$c\Delta_h = 1.41h. \quad (12)$$

Sizing of Crack-Like Defects

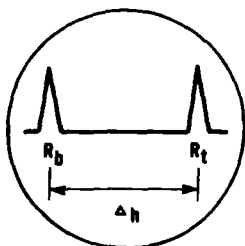
Division of Equation (12) by Equation (11) for $\Delta_1 = d_1$ yields the calibration equation for sizing crack-like defects:

$$\left\{ \begin{array}{l} \Delta_h = h \end{array} \right\} \text{ for } \beta = 45^\circ. \quad (13)$$

This means that if we adjust the time scale of the oscilloscope to read h units between the first two reflections obtained with a 45-degree beam from the test specimen's end, or from the end of a plain piece of similar material, the depth of the crack-like defect can be read directly in mils or millimeters on the oscilloscope screen, provided that the examination is carried out with a 45-degree shear wave.



- a. Splitting of a 45-degree incident wave (hollow arrow) into a bottom-reflected wave, R_b , and a top-reflected wave, R_t , by the end of a steel specimen.



- b. Bottom and top-reflected pulses separated by the calibration delay time, Δh , on the oscilloscope screen.

Fig. 5. The interaction of a 45-degree ultrasonic shear wave with the test specimen's end resulting in two reflected waves.

For a refraction angle of 60 degrees, the calibration equation becomes:

$$\Delta h = 1.41h \quad \text{for } \beta = 60^\circ. \quad (14)$$

This means that if we adjust the time scale of the oscilloscope to read 1.41h units between the first two reflections obtained with a 45-degree beam from the test specimen's end, or from the end of a plain piece of similar material, the depth of the crack-like defect can be read directly in mils or millimeters on the oscilloscope screen, provided that the examination is carried out with a 60-degree shear wave.

Notches and steps were used in proof-of-principle measurements since their depth could be determined visually without breaking open the test specimens. The results shown in Fig. 6 are of particular interest since they provided an early confirmation of the potential of the direct-sizing SPT. The experiments were carried out using 45- and 60-degree shear-wave probes and a range of frequencies (2 to 4 MHz) and defect locations (0.05 to 2 inches) in six different steel specimens with otherwise unspecified properties. The ultrasonic estimates of slit depth compare very favorably with the visual measurements of slit depth.

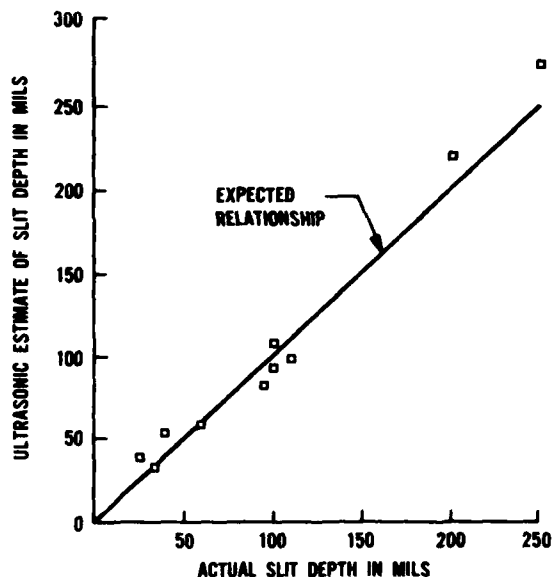


Fig. 6. Illustrating the one-to-one correspondence between the ultrasonically estimated and visually determined slit depths.

The SPT has now been used to size a number of laboratory and inservice-produced fatigue and intergranular stress corrosion cracks in steel specimens. The results of SPT measurements for a fatigue crack in a turbine rotor specimen are shown in Figs. 7 and 8. Both methods of "attack" and operating frequencies yielded depth estimates for the fatigue crack at its deepest mid-length point of 115 mils.

Sizing of Void-Like Defects

Division of Equation (12) by Equation (5) for $\Delta_0 = d_0$ yields the calibration equation for sizing void-like defects:

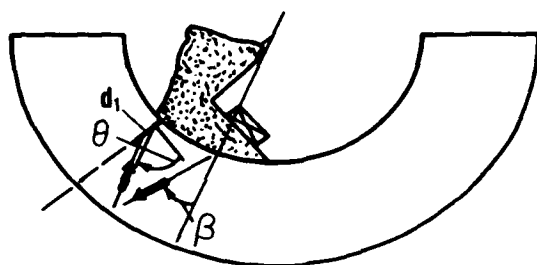
$$\Delta h = 0.52h \quad \text{for any } \beta. \quad (15)$$

This means that if we adjust the time scale of the oscilloscope to read 0.52h units between the first two reflections obtained with a 45-degree beam from the test specimen's end, or from the end of a plain piece of similar material, the diameter of the void-like defect can be read directly in mils or millimeters on the oscilloscope screen, regardless of the refraction angle of the ultrasonic beam.

Figure 9 reveals that the experimental results are in keeping with the main predictions of the satellite-pulse model derived for void-like defects in metals. The data were obtained over a range of frequencies (2 to 4 MHz) and defect locations (0.05 to 1.3 inches) in four different steel plates with otherwise unspecified properties. The time scale of the oscilloscope was recalibrated each time the hole was in a different plate. The agreement between the ultrasonically and visually determined hole diameters is seen to be excellent.

Conclusions

The results obtained so far are very encouraging. In view of the improved defect discrimina-

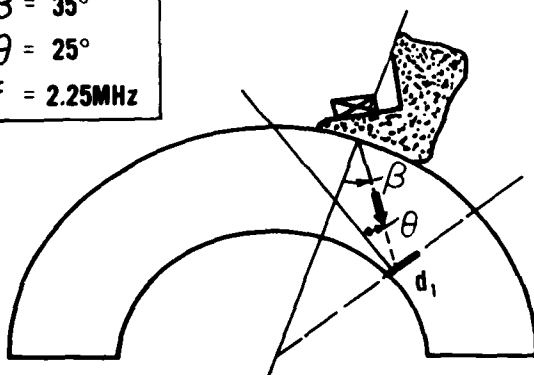


$$\begin{aligned}\beta &= 35^\circ \\ \theta &= 65^\circ \\ f &= 4\text{MHz}\end{aligned}$$

- a. Probe position for sizing crack-like defects breaking the accessible surface.

Fig. 7. SPT-sizing of a laboratory-produced fatigue crack in a turbine rotor specimen breaking the accessible surface.

$$\begin{aligned}\beta &= 35^\circ \\ \theta &= 25^\circ \\ f &= 2.25\text{MHz}\end{aligned}$$



- a. Probe position for sizing a fatigue crack breaking the inaccessible surface.

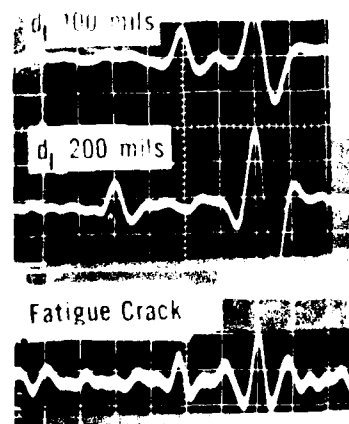
Fig. 8. SPT-sizing of a laboratory-produced fatigue crack in a turbine rotor specimen breaking the inaccessible surface.

tion and sizing capability offered by the SPT, it would be preferable to replace the sole use of the peak amplitude of the reflected pulse component in the characterization of an already detected defect by less ambiguous signal parameters. The most suitable signal parameter for this purpose appears to be the separation in times-of-arrival between the resolved pulse components of the defect signal (i.e., Δ). The usually smaller extra pulses (i.e., the satellites) have been shown to originate from the sharp diffracting edge boundaries of a crack-like defect and from the smooth scattering shadow boundaries of a void-like defect.

The ultrasonic SPT for defect identification and sizing is especially attractive in terms of reliability and simplicity of operation. Unique

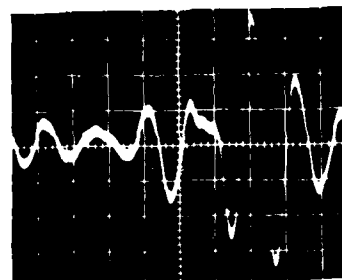
features and other advantages of the developed technique include:

- its general applicability;
- independence of signal parameter (i.e., Δ) from the peak amplitudes of the associated echoes;
- independence of signal parameter from defect location;
- independence of signal parameter from operating frequency;
- linear relationship of signal parameter to defect size;



- b. Tip-diffracted pulses preceding corner-reflected pulses in the composite ultrasonic signature of narrow slits (upper and middle traces) and the fatigue crack (lower trace).

Scale: \longleftrightarrow 50 mils



- b. Ultrasonic signature of a fatigue crack of unknown depth.

Scale: \longleftrightarrow 50 mils

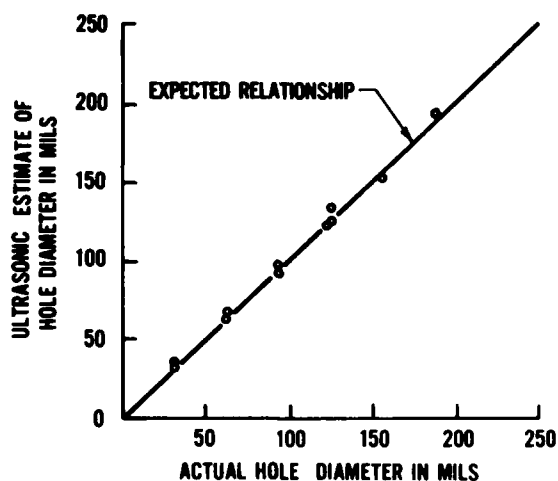


Fig. 9. Illustrating the one-to-one correspondence between the ultrasonically estimated and visually determined side-drilled-hole diameters.

- ease of calibratability of ultrasonic apparatus;
- direct readability of defect size on the oscilloscope screen;
- use of single probe; and
- use of standard equipment and probes.

The SPT is immune to variations in reflected, diffracted, and scattered pulse amplitudes which occur with variations in material properties, defect location, ultrasonic coupling efficiency, operating frequency, etc. The ultrasonic data required for defect identification and sizing may be acquired by a single pulse-echo shear wave transducer with equipment currently used in ultrasonic testing and evaluation of materials. The ultrasonically determined defect sizes were within 10 percent of the actual values over a 2-inch defect location range. A simple calibration procedure for making the time scale of the oscilloscope of the ultrasonic apparatus read directly in terms of equivalent crack depth or void diameter, as appropriate, was also developed which bypasses the need for notches and side-drilled holes in separate calibration blocks.

References

1. P. Höller, "Identification of Crack-like Flaws and Determination of Crack Parameters in Ultrasonic Nondestructive Evaluation," Fraunhofer-Institut für Zerstörungsfreie Prüfverfahren, Saarbrücken, West Germany, 1979 (in press *Materialprüfung*).
2. G. J. Gruber, "Development of Relationships between Defect Characteristics and Signal Parameters," Final Report 17-9210, Southwest Research Institute, San Antonio, Texas, 1979.
3. B. T. Khuri-Yakub, G. S. Kino and Y. Murakami, "Ultrasonic Wave Scattering for Defect Characterization Applied to Ceramic Materials," paper presented at 38th American Society for Nondestructive Testing Conference, Denver, Colorado, October 1978.
4. A. Freedman, "The High Frequency Echo Structure of Some Simple Body Shapes," *Acustica*, 12, 61-70, February 1962.
5. A. Freedman, "A Mechanism of Acoustic Echo Formation," *Acustica*, 12, 10-21, January 1962.
6. D. M. Johnson, "Model for Predicting the Reflection of Ultrasonic Pulses from a Body of Known Shape," *J. Acoustical Soc. Am.*, 59, 1319-1323, June 1976.
7. A. J. Rudgers, "Acoustic Pulses Scattered by a Rigid Sphere Immersed in a Fluid," *J. Acoustical Soc. Am.*, 45, 900-910, April 1969.
8. W. Sachse, "The Scattering of Elastic Pulses and the Nondestructive Evaluation of Materials," *Materials Evaluation*, 35, 83-106, October 1977.
9. Y. H. Pao and Y. Varadan, "Spectral Analysis of Elastic Waves Scattered by Objects with Smooth Surfaces," in *Proceedings of the 1977 ARPA/AFML Review of Progress in Quantitative Nondestructive Evaluation*, Report No. AFML-TR-78-55, 92-98, May 1978.
10. Y. H. Pao and W. J. Sachse, "Interpretation of Time Records and Power Spectra of Scattered Ultrasonic Pulses in Solids," *J. Acoustical Soc. Am.*, 56, 1478-1486, November 1974.
11. F. Bifulco and W. Sachse, "Ultrasonic Pulse Spectroscopy of a Solid Inclusion in an Elastic Solid," *Ultrasonics*, 13, 113-116, May 1975.
12. W. Sachse and C. T. Chian, "Determination of the Size and Mechanical Properties of a Cylindrical Fluid Inclusion in an Elastic Solid," *Materials Evaluation*, 33, 81-88, April 1975.
13. R. E. Beissner and G. L. Burkhardt, "The Quantitative Characterization of Flaws by Ultrasonic Scattering," Final Technical Report 15-9150, Southwest Research Institute, San Antonio, Texas, April 1976.
14. R. C. McMaster, Editor, *Nondestructive Testing Handbook*, The Ronald Press Company, 1963.
15. R. S. Sharpe, Editor, *Research Techniques in Nondestructive Testing*, Chapters 1 and 2, Academic Press, 1977.
16. J. Seydel, "Computerized Enhancement of Ultrasonic Nondestructive Testing Data," doctoral dissertation, University of Michigan at Ann Arbor, 1973.
17. J. B. Keller, "Geometrical Theory of Diffraction," *J. Optical Soc. Am.*, 52, 116-130, February 1962.
18. J. D. Achenback, A. K. Gautesen and H. McMaken, "Application of Geometrical Diffraction Theory to Scattering by Cracks," in *Proceedings of the 1977 ARPA/AFML Review of Progress in Quantitative Nondestructive Evaluation*, Report No. AFML-TR-78-55, 102-107, May 1978.

SUMMARY DISCUSSION
(G. J. Gruber)

J. K. White (Westinghouse Research): It seems to me there is an effect, a modulation effect, both of depth and of angle and of flaw size. Presumably you separate out the depth effect by gating only a certain portion of the signal. How do you separate out the angle? By making sure you're perpendicular to the reflection?

George Gruber: I have to make more measurements. We never did get to the crack sizing situation. The relationship between delay time, Δt , D-1, which is the depth and sound speed, and it's also the orientation angle that's involved. So, what I have is three unknowns, four unknowns. Δt I can measure okay; C I eliminated by the calibration technique. Same sort of things that went for the pulse. I have to make two measurements, at least, because I got two unknowns, the size and the orientation. What I'll do is know my theta that I'm sending in, make two measurements, and I have eliminated two unknowns. So I can make one more measurement. If I don't know the orientation, if it's cracked, if it's a hole like, if it's axially symmetric, then I just make one measurement. Then I can only expect to get from the tip. But if it's curving on me, it's not perfectly in a plane, then of course I can only give you equivalent depths, which sometimes is important.

N. K. Batra (Systems Research Lab): In addition to the size, your beam must cover both the tips; is that right?

George Gruber: Yes. A round focus transducer. And it looks relatively big compared to the thicknesses of the place that I'm looking for. Actually, it works down to one tenth of an inch below the surface. It picks up and gives you the same information, independent frequency, the location, a lot of niceties that this has. I must admit one of the disadvantages--and it ties in nicely with the previous speaker's topic--is to lift it out from the microstructure nodes, that could be the problem. As you will see, those signals from the crack tip are not big.

N. K. Batra: I have a question then. If the crack is very large, say larger than your beam spread, then what do you do? You can't scan because you want to see both --

George Gruber: You use a transducer this big (indicating). I would think there are other methods of doing it better ways. This is aimed at sizing very small defects, and I'm going down and down right now, and the resolution is about half a milliliter in about 20 mills, and I'm going up in frequency trying to eliminate the noise. All kinds of improvements are needed here, but this is right now in a very unoptimized state, but still now I have it down to a half a millimeter.

Paul Holler (Inst. fur Zerst. Pruf.): That's better than your other method.

George Gruber: The amplitude method works good, but the oscillation disappears.

Paul Holler: I would like to commend that the goal of this paper is to classify whether it is a crack or not. In the philosophy or strategy in our country, it is very important because we have--also in this country--the experience that only a few percent of the indications we have are worthwhile to be handled later. So, I just want to give this headline -- or this remark because in the explanation of strategies, also in your paper, I was missing this point. In our country it's one of the very basic things, to find out whether a defect makes a stress concentration or not. And this is one of the goals -- one of the ways to solve it. But there are several others, and one not mentioned work is published on this using the derivative, but I do not want to start a new discussion.

#

Bill D. Cook
 Department of Mechanical Engineering
 University of Houston
 Houston, Texas 77004

ABSTRACT

From some low frequency scattering investigations in radar, it is suggested that interrogating the target with "ramp" function has distinct advantages. This "ramp" function is a ramp in amplitude, not frequency. The returning echo is predicted to exhibit directly in the time domain, information of the cross-sectional area of a target as the ramp passes the target. From this information, one can infer size, volume, and orientation of the target.

The theory for this interpretation is based on the physical optics approximation. This approximation is commonly used in acoustic and elastic wave scattering when the boundary conditions are approximate. The concepts can be "verified" by exact scattering theories for back-scatter from hard spheres (acoustic) and spherical voids (elastic). Our calculation for these two cases do show that their returning could show cross-sectional information.

A proposed system to launch and receive ramp pulses will be discussed. The generation mechanism uses the demodulation properties of absorptive, nonlinear media on a large amplitude pulse train. The detection mechanism utilizes fiber optics.

INTRODUCTION

Current field operating NDE ultrasonic devices are based on interpretation of signals in the time domain. Presence, location and sizing of flaw is usually found from an oscilloscope display of a processed signal of a returning echo. However, many research investigators in NDE are now advocating frequency domain for size determination partially because the amplitude of the returning echo depends on many factors other than flaw size. With the knowledge that amplitude techniques now exist and the belief that they can be made better, I am proposing an alternative time domain technique from which size, shape, and some orientation can be implied, in principle, from an oscilloscope display. Moreover, this pattern can be converted by computer to yield a first approximation image of the flaw from one view of the flaw.

The chief feature of this technique is that the ultrasonic pulse launched toward the flaw is preprocessed to have a "ramp" waveshape. This is a ramp in amplitude, versus time, not frequency, and the ramp designation is defined to mean an abrupt change of the first time derivative of the shape of the pulse.

The conceptual theory for this technique was developed by Kennagh and Moffett [1] for electromagnetic scattering, i.e. radar. Their theory based on physical optics suggest that the backscattered echo $s(t)$ of a ramp pulse provides a mapping of the cross-sectional area $A(z)$ of the target as a function of distance z through the target, i.e.

$$s(t) \propto A(z)$$

with $t = z/2c$

where c is the velocity of the radiation in the host medium. This concept is illustrated in Fig. 1, where the incoming ramp function is shown separated from the backscattered for display convenience. The difference of the heights and lengths of the upper and middle returns show how orientation can be inferred. The areas under the backscattered curves yields the volume of the scatters while the height indicates the greatest cross-sectional area and the length in time corresponds to the length of the target.

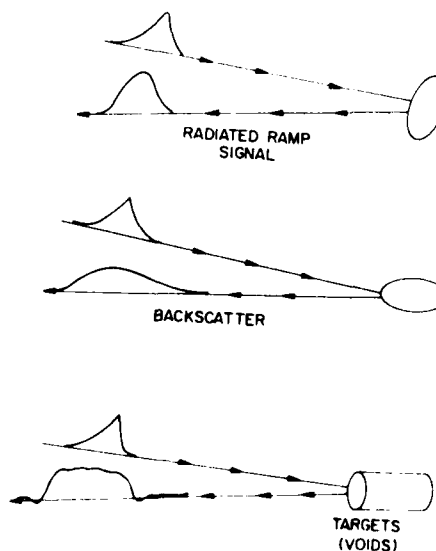


Figure 1. Concept of ramp pulse scattering.

It must be emphasized that Fig. 1 is only conceptual and somewhat an exaggeration in as much as the theory allows only the region illuminated by the radiation to be mapped and not the shadowed region. Also this theory is based on the assumptions of physical optics which are almost entirely invalid for the frequency range of operation.

PHYSICAL OPTICS CONCEPTS

The physical optics approximation is a common theory used in radar, acoustic, and elastic scattering. Among its many assumptions are the target is convex and smooth, larger than a wavelength, and has large radii of curvature. However, the ramp function concept has been shown experimentally for radar by Young [2] but it utilizes the frequency dependence of scattering outside the domain associated with the physical optics approximation. Namely, it works in the Rayleigh and lower resonance regions as shown in Fig. 2. In this figure, the general form of frequency dependence of the backscattered signal from a class of simple targets is shown. It applies in principle, to electromagnetic scattering from voids. The following regions are designated for discussion. The high frequency region is generally known as geometrical optics; whereas the low signal is quadratically dependent on frequency (or ka) is known as the Rayleigh region. The resonance region becomes by arbitrary definition the physical optics region which in turns becomes the geometrical optics region without precise definition. It is generally believed that imaging of objects requires information from the higher physical and geometrical optics frequencies.

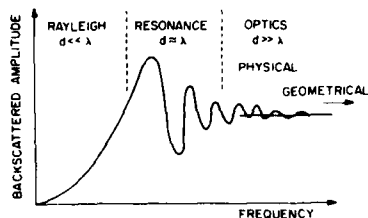


Figure 2. Typical frequency dependence of backscatter illustrating regions of nomenclature.

ELECTROMAGNETIC RESULTS

In Young's experimental studies with electromagnetic waves, a true ramp function is not generated but a synthesized ramp backscatter is formed from individual harmonics, as low as ten in number. Success in construction is illustrated in Fig. 3 which shows a computer generated image composed of information nose-on and 30° from nose-on viewing angles. It is to be noted that the sharp edges of the cone violates assumptions of the physical optics approximation. The wavelength of the fundamental frequency of the synthesized ramp is approximately three times the diameter of the cone.

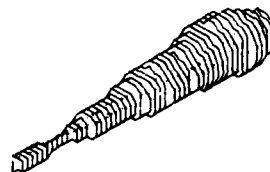


Figure 3. Results of Young for electromagnetic waves. The image of the cone is constructed from measured profile function of 0° and 30° incident angles. Size of cone in inches.

ACOUSTIC AND ELASTIC RESULTS

To test the applicability of the ramp concept to acoustic and elastic scattering, ramp responses have been computed using the exact scattering theory for hard spheres in acoustic scattering and spherical voids in elastic scattering. Figures 4 and 5 show typical results, respectively for acoustic and elastic scattering. These figures have been normalized by range and area of the scatterer. The fact that the curves are approximately the same height is an indication that the backscattered echo is proportional to area of scattering sphere. Similarly, the increasing width of the theoretical return with increasing size of the scatterer agrees with the concept.

These figures were generated with ramp waves synthesized from harmonic functions; thus, the Ka label on each of the curves corresponds to the Ka for the lowest frequency in the synthesized ramp function.

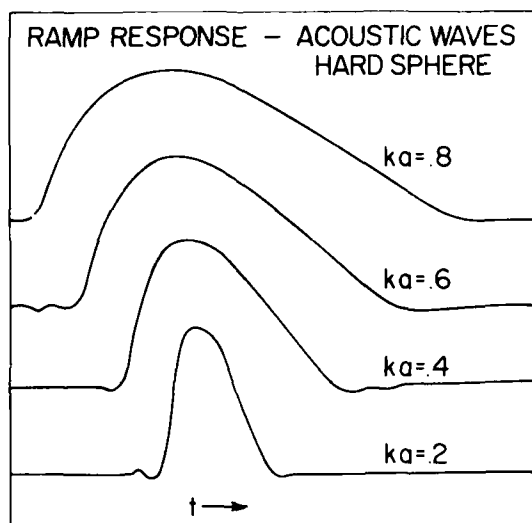


Figure 4. Theoretical calculations of ramp back-scattered acoustic pulses from hard spheres.

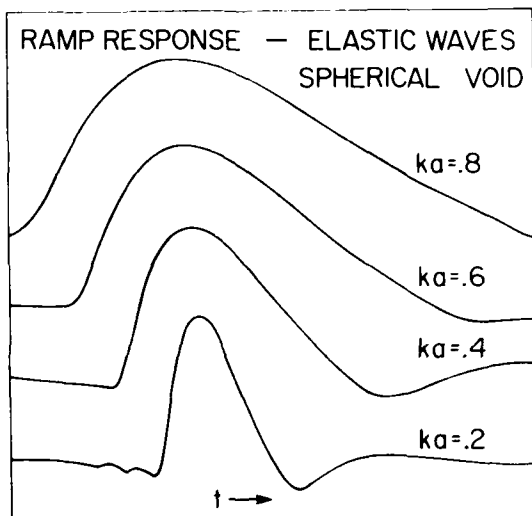


Figure 5. Theoretical calculation of ramp back-scattered elastic pulses from spherical voids.

GENERATION AND DETECTION OF RAMP RESPONSE

The above results seem encouraging enough to explore methods of generating ramp functions. One technique is generate unipolar function as suggested by Selfridge, et al. At this meeting. However, I would like to suggest novel system to launch and receive ramp or other pulses.

The generation mechanism is based on a nonlinear phenomena of acoustic wave propagation known as self-demodulation. Experiments by M.B. Moffett [3] in which as intense, modulated pulse was propagated through CCl_4 (as shown in Fig. 6) illustrates the principle. The receiving transducer detects a changing waveform as the pulse waveform undergoes distortion and absorption as seen in Fig. 7. The end results is a pulse containing lower frequencies and whose shape is related to the second derivative of the square of the modulation of the ultrasound leaving the transducer. By controlling the modulation of pulse to the sending transducer, one has some control of the resultant pulse. An additional benefit is the beam pattern generated by nonlinear effect is extremely narrow and in some cases have virtually no side lobes.

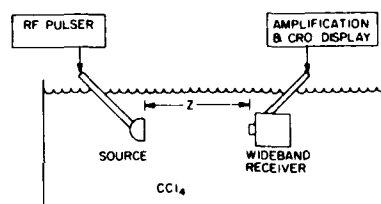


Figure 6. Experimental apparatus used in detection of nonlinear phenomena

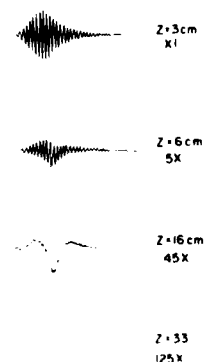


Figure 7. Illustration of changing pulse waveform undergoing self-demodulation

The concept can be incorporated into a transducer housing, in which the nonlinear processes occur and the pulse transmitted to a material under test would be the desired ramp pulse. In Fig. 8, such a transducer configuration is shown.

In order to receive the sound, another transducer would have to be included. In the illustration I have included a possible broadband system. It has a fiber optic sensor which responds to the backscattered wave. Figure 9 shows a proposed system for the fiber optics detection in which optical phase modulation is detected by a heterodyne technique. Fiber optics hydrophones have been built for lower frequencies and have sensitivities approximating piezoelectric hydrophones.

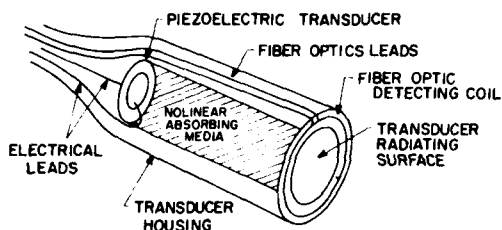


Figure 8. Proposed ultrasonic transducer configuration incorporating nonlinear generation and fiber optic detection.

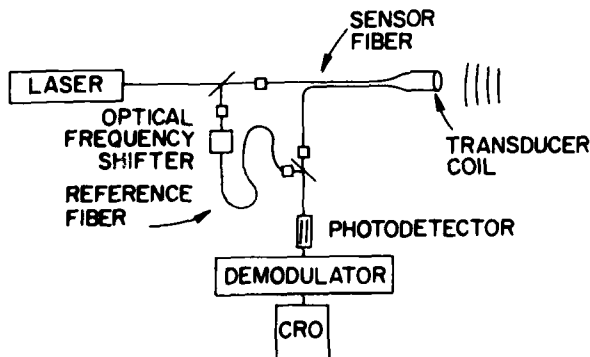


Figure 9. Detection system for fiber optic sensor of ultrasonic waves.

REFERENCES

1. E.M. Kennagh and D.L. Molfat, "Transient and Impulse Response Approximations", Proc. IEEE, Vol. 53, p 893-901 (1957).
2. J.D. Young, et al "Basic Research in Three-dimensional Imaging From Transient Radar Scattering Signatures" Annual Status report to Ballistic Missile Defense Systems Command by the Electroscience Laboratory, The Ohio State University, Columbus, Ohio, (July 1978). Also see J.D. Young, "Radar Imaging from Ramp Response" IEEE Trans. on Antennas and Propagation, Vol. AP-24, pp 276-282 (1976)
3. M.B. Moffett, "Large Amplitude Pulse Propagation, a Transient Effect", Proceedings of the ARL 1969 Symposium on Nonlinear Acoustics, Austin, Texas.

SUMMARY DISCUSSION
(B. D. Cook)

Bruce Thompson (Rockwell Science Center): In your last slide you showed utilizing the nonlinear absorbing medium to take up all the high frequency contents, what was the efficiency of that?

Bill Cook: It was very efficient. You list the reasons it's not efficient. But the key feature is that the signal that you get is related to the modulation envelope, and it is given by the second derivative of the modulation to the square. So, if you can control the modulation at a high frequency, you can get a bandwidth that you need.

Faul Holler: Any other question?

George Gruber (Southwest Research Institute): You and I never have seen each other's technique, right?

Bill Cook: Right.

George Gruber: But they are similar somewhat because you're trying to get size information from the time function. And you would like to have high Q transducer, ten to one --

Bill Cook: Low Q.

George Gruber: I take it back.

Bill Cook: Some of the people from Ohio State think the argument is just backwards, you're trying to use the satellite pulses for example, and what they're trying to use is time discriminated and throw that all away because all the rest of that information in the high frequency range is noise to them; essentially, by using just a regular region they can throw the other out.

#

MATHEMATICAL PRINCIPLES OF DATA INVERSION

D. A. Lee
Air Force Institute of Technology
Wright-Patterson Air Force Base, OH 45433

ABSTRACT

Inverse elastic-wave scattering problems are shown to be ill-posed in general. Standard simplifying assumptions--the first Born approximation, the physical optics approximation, and the stopping power approximation of tomography--are shown to reduce to the same ill-posed mathematical problem, that of inverting a Fourier transform. Practical implications of this fact are illustrated with examples.

INTRODUCTION

This paper points out general features of the mathematical problems to which one is led in recovering information about materials' defects, from scattered elastic waves. These problems typically present two complications: non-linearity and ill-posedness. The non-linearity appears because the same defects which serve as sources of scattered elastic waves also affect the waves' propagation. The ill-posedness reflects the fact that significant but sharply localized flaws may cause only insignificant scattering. These two complicating features, which are common to many inverse scattering problems, must be borne in mind when making rational inferences from scattered elastic waves.

Standard simplifying assumptions bring one to linear approximate versions of inverse scattering problems. The ill-posed character of the original problem remains. Data inversion for each of three cases considered here--the first Born approximation, the physical optics approximation, and the stopping-power approximation of tomography--all reduce to the same mathematical problem, that of evaluating the inverse Fourier transform of a function determined from experimental data. Examples are given of an approach for treating this standard regularizable ill-posed problem, and its treatment in general is discussed.

A GENERAL INVERSION PROBLEM

Many cases are covered by the following general problem:

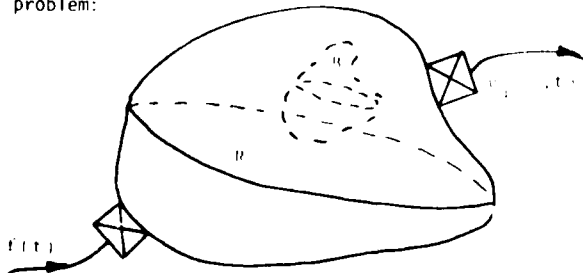


Figure 1.

Elastic waves are excited in a piece R of a linear elastic material by an input $f(t)$ to a transducer of known characteristics, located on a part of the surface ∂R of R. Responses $g_i(\xi, t)$ are observed, possibly by a second transducer, located near points ξ of a subset A of ∂R . (Observations are limited to

∂R because, if the interior of R were accessible for observations, there would perhaps be no need for any nondestructive evaluation.) The responses g_i might be the three displacement components at points of parts of ∂R not constrained in the test or the g_i might be traction components at parts of ∂R whose displacements are constrained by the test. The piece R includes a region B, in which elastic properties may differ from standards. The flawed region B might be a crack, a void, or an inclusion; it might be a region of anomalous elastic constants. The nonstandard elastic properties of the material in B are associated with nonstandard values of some set Q of characteristics of the performance of the piece R in service; Q might include fatigue life or yield stress.

It being impossible or inconvenient to observe Q directly in a nondestructive way, the objective of the test is to estimate the actual value of Q for a given sample part R, from knowledge of the input $f(t)$ and a set of observed responses $g_i(g, t)$, for g in A and t in some interval. It is important to note that the solution of the general inversion problem is a set of estimated values of performance factors, and not necessarily the shape of the defective region B.

In the next section, we'll discuss the ideas of ill-posed and well-posed problems. After that, we'll show by an example that inverse elastic wave scattering problems are in general ill-posed.

WELL-POSED AND ILL-POSED PROBLEMS

A well-posed problem, as defined by Hadamard about 1904, is a problem that has a unique solution, which depends continuously on the problem's data. For example, consider the problem of finding the deflection $Y(x)$ of a string fixed at both ends and subjected to a distributed load $W(x)$ reduces, for an appropriate system of units, to finding $Y(x)$ such that

$$Y''(x) = -W(x) \quad (1)$$

$$Y(0) = 0 = Y(1) \quad (2)$$

The solution of this problem is

$$Y(x) = \int_0^1 r(x, t) W(t) dt, \quad (3)$$

where

$$r(x, t) = \begin{cases} t(1-x) & 0 \leq t \leq x \\ x(1-t) & x \leq t \leq 1 \end{cases} \quad (4)$$

Clearly the problem defined by (1) and (2) has a unique solution $Y(x)$, for any continuous $W(x)$. Moreover, if $W(x)$ changes by an amount δW , then Y changes by δY , with

$$\delta Y(x) = \int_0^1 K(x,t) \delta W(t) dt \quad (5)$$

since

$$|K(x,t)| \leq \frac{1}{4} \quad (6)$$

for all x and t of interest,

$$|\delta Y| \leq \frac{1}{4} \max |\delta W| \quad (7)$$

Thus, changes in the solution are commensurate with changes in the data, and this is the essence of continuous dependence of the solution on the data.

On the other hand, consider the problem of finding an unknown load W , given the displacement Y which it produces. The solution of this problem is obvious from (1): to find W given Y , differentiate Y twice and multiply by (-1) . There is, thus, a unique solution of the present problem, at least for each twice continuously differentiable Y . However, this problem is ill-posed, because there are functions Y_0 and Y_1 which differ arbitrarily little, whose second derivatives differ arbitrarily greatly. Specifically, let

$$Y_0 = x(1-x); Y_1 = x(1-x) + \epsilon \sin n\pi x, n=1,2,\dots \quad (8)$$

Both Y_0 and Y_1 satisfy boundary conditions (2), and

$$|Y_1 - Y_0| = |\epsilon \sin n\pi x| \leq |\epsilon| \quad (9)$$

However,

$$W_0 = -Y_0'' = 2 \quad (10)$$

while

$$W_1 = -Y_1'' = 2 + n^2 \pi^2 \epsilon \sin n\pi x \quad (11)$$

so that

$$W_1 - W_0 = n^2 \pi^2 \epsilon \sin n\pi x \quad (12)$$

Now, by choosing ϵ sufficiently small, Y_1 and Y_0 can be made to differ as little as one pleases; given any ϵ , n can be chosen sufficiently large so that, at some points, W_1 and W_0 differ by as much as one pleases.

This ill-posedness due to lack of continuous dependence on the data greatly hampers the solution of the last problem in practice, since all experiments—even numerical ones—involve some error. As we'll see in the following section, the general elastic wave inverse scattering problem also exhibits discontinuous dependence of solution on data.

ILL-POSED NATURE OF INVERSE ELASTIC-WAVE SCATTERING

The case of a slab with varying elastic properties is one of the few inverse elastic wave scattering problems to be solved in great detail (1). The material of this section shows that this problem is ill-posed.

The geometry of the problem is shown in Fig. 2. Elastic waves are launched from surface s_1 of a slab whose elastic properties are functions only of x . The objective of the experiment is to determine the variation of elastic-wave impedance with travel time. (Reference (1) shows that this is, in fact, all that one can infer from inverse scattering for this

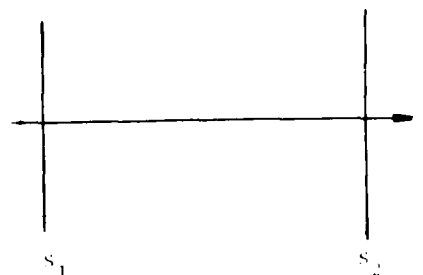


Figure 2.

case) by analyzing elastic waves scattered back to surface s_1 , and transmitted to surface s_2 .

We can focus on the essential aspects of the problem by regarding the slab as very thick, and considering elastic wave reflection and transmission at interior points. If the material is "perfect", i.e., has constant elastic-wave impedance, then no elastic waves will be scattered, and an incident elastic wave train will propagate through the slab without attenuation.

Now, consider the following particular case of varying elastic wave impedance: the slab is of constant impedance, save for a segment of length $2l$ (Fig. 3). Let us consider for the moment time-harmonic waves, with frequency ω and wave numbers

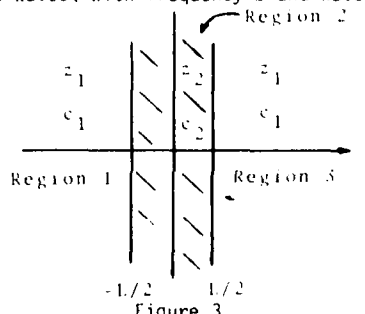


Figure 3.

$k_1 = \omega/c_1$. One finds by elementary methods that a right-moving incident wave $U_0 e^{ik_1 x}$ in region 1, causes a left-moving reflected wave $g e^{-ik_1 x}$ in region 1, and a right-moving transmitted wave $h e^{ik_1 x}$ in region 3, with

$$g = U_0 R(\omega); h = U_0 T(\omega) \quad (13)$$

If

$$\frac{\omega l}{2c_1} \ll \frac{\pi}{4} \quad (14)$$

then

$$R(\omega) = \frac{i}{2} \left(\frac{L}{c_2} \right)^2 \frac{z_2^2 - z_1^2}{z_1 z_2} + O \left(\frac{L}{c_2} \right)^2 \quad (15)$$

and

$$T(\omega) = 1 + O \left(\frac{L}{c_2} \right)^2 \quad (16)$$

Clearly, for any given ω and any given z_1, z_2, c_1, c_2 , one could make $R(\omega)$ as close to zero as he pleased—and, simultaneously, make $T(\omega)$ as close to 1 as he pleased—by taking l sufficiently small.

From this, and from the fact that $R(\omega)$ and $T(\omega)$ are uniformly bounded for all ω , it follows that if the actual incident wave is any given band-limited signal, then there exist two impedance profiles--the constant, and the constant with an inclusion like that of Fig. 3--for which both reflected and transmitted signals are as nearly the same as one wishes, while the profiles differ, locally, by as much as one wishes.

Thus we see that a particular inverse elastic wave scattering problem is ill-posed. This pathology is shown to be quite general, in Reference (2). In the following sections we will see that three widely used approximate treatments of inverse elastic-wave scattering problems all lead to the same ill-posed mathematical problem.

THE FIRST BORN APPROXIMATION

Reference (2) gives the details of a demonstration that the Fourier transform $U_i^S(x; \omega)$ of the displacement field of the elastic wave scattered by a defect in a finite region B of an otherwise unbounded homogeneous isotropic elastic material satisfies the integral equation

$$U_i^S(x; \omega) = -\frac{1}{4\pi\rho_0\omega^2} \iiint_B g_{ijk}(y-x) \delta c_{lmnp}(y) U_{n,p}^S(y) dv_y + \frac{1}{4\pi\rho_0} \iiint_B g_{ijk}(y-x) \delta\rho(y) U_j^S(y) dv_y + G_i(x; \omega) \quad (17)$$

where

$$G_i(x; \omega) = \frac{1}{4\pi\rho_0\omega^2} \iiint_B g_{ijk}(y-x) [(\delta c_{lmnp} U_{n,p}^0)_{,m} + \omega^2 \delta\rho U_j^0](y) dv_y \quad (18)$$

In (17) and (18), $\delta c_{ijk\ell}(x)$ is the variation of the stiffness tensor from the values $\lambda_0 \delta_{ij} \delta_{k\ell} + \mu_0 (\delta_{ik} \delta_{jl} + \delta_{il} \delta_{jk})$ found in the unbounded medium, and $\delta\rho(x)$ is the variation in density from the value ρ_0 found in the unbounded medium. The $U_j^0(x; \omega)$ are the Fourier transforms of the displacement field incident wave, and $g_{ijk}(x; \omega)$ is the free-space elastic Green's tensor

$$g_{ijk}(x; \omega) = k_b^2 \frac{e^{ik_b x}}{x} \delta_{jk} - \left[\frac{ik_a x}{x} - \frac{ik_b x}{x} \right]_{,jk} \quad (19)$$

This formulation deals explicitly with the scattered field, which we will find convenient.

The first Born approximation (3) here means the solution of the approximation to (17) obtained by assuming that $\delta c_{ijk\ell}$ and $\delta\rho$ are "small", and that the scattered fields and their derivatives are also "small", so that the integrals in (17), which involve products of "small" terms, are negligible in comparison with $G_i(x; \omega)$. This approximation gives $U_i^S(x; \omega)$ immediately in terms of the $U_j^0(x; \omega)$. If the incident wave $u(x, t)$ is a plane dilatation pulse, i.e., if

$$u = U\phi\left(t - \frac{e \cdot x + r}{a_0}\right) \quad (20)$$

with

$$\phi(t) = 0, \quad t \notin (0, T) \quad (21)$$

and

$$\phi(t) \in C^{(4)}, \quad \forall t \quad (22)$$

then $U_i^S(x; \omega)$ is given (2) by

$$U_i^S(x; \omega) = \frac{-g(\omega)}{4\pi\rho_0\omega^2 a_0} \iiint_B g_{ijk}(y-x) [ik_a \delta c_{lmnp, m} e_n e_p - k_a^2 \delta c_{lmnp} e_m e_n e_p + \omega^2 \delta\rho e_l] e^{ika\psi} dv_y \quad (23)$$

where

$$g(\omega) = \frac{1}{\sqrt{2\pi}} \int_0^T \phi(u) e^{i\omega u} du$$

and

$$\psi(x) = x \cdot e + R \quad (24)$$

In the far field, i.e., when

$$\frac{|y|}{|x|} \ll 1, \quad k_b |y| \ll \frac{\pi}{4} + y \cdot B U \cdot B \quad (25)$$

the free-space Green's tensor g_{ijk} is given approximately by

$$g_{ijk}(y-x) \approx k_a^2 x_i x_j \frac{e^{ik_a x}}{x} e^{-ik_a \hat{x} \cdot y} + k_b^2 (\delta_{ij} - \hat{x}_i \hat{x}_j) \frac{e^{ik_b x}}{x} e^{-ik_b \hat{x} \cdot y} \quad (26)$$

where \hat{x} is a unit vector in the direction of x . In the back-scatter direction, where $x = -x$ and

$x = -e$, it can be shown (2) that

$$U_i^S = \left\{ \begin{aligned} & \left[\frac{-g(\omega) e^{ik_a R}}{4\pi\rho_0 a_0} k_b^2 \frac{e^{ik_b x}}{x} (\delta_{il} - e_i e_l) \right] x \\ & \iiint_B \delta c_{lmnp} e_m e_n e_p e^{i(k_a + k_b) e \cdot y} dv_y \end{aligned} \right\} + \left\{ \begin{aligned} & \left[\frac{g(\omega) e^{ik_a R}}{4\pi\rho_0 a_0} k_a^2 \frac{e^{ik_a x}}{x} e_i \right] x \\ & \iiint_B \left[\frac{\delta c_{lmnp} e_m e_n e_p}{a_0^2} + \delta\rho \right] e^{2ik_a e \cdot y} dv_y \end{aligned} \right\} \quad (27)$$

The two terms in large brackets appearing in the right side of (27) have straightforward physical interpretations. The first term is polarized transversely, since

$$(\delta_{ii} - e_i e_i) e_j = 0$$

This term represents a train of scattered shear waves. The second, polarized longitudinally, represents a train of scattered longitudinal waves. Time-gating will make it possible to separate these two trains, when the parameter T of (21) is sufficiently small and x is sufficiently large. Analysis of first arrival times of scattered dilatation waves, as e varies over all directions, makes possible the estimation of the location of a point in B , so that x may be regarded as known, as the source/observation point moves over ∂B . Thus it is possible, in principle, to recover

$$D(\omega) \equiv \iiint \left[\frac{1}{a_0^2} \delta c_{\ell m n p}(\underline{y}) e_{\ell} e_m e_n e_p + \delta \rho(\underline{y}) \right] e^{2ik_a \underline{e} \cdot \underline{y}} dv_y \quad (28)$$

and

$$S_i(\omega) \equiv (\delta_{i\ell} - e_i e_{\ell}) \iiint \delta c_{\ell m n p}(\underline{y}) e_m e_n e_p e^{i(k_a + k_b) \underline{e} \cdot \underline{y}} dv_y \quad (29)$$

by observing back-scattered dilatation waves in the far field.

$D(\omega)$ and $S_i(\omega)$ are equivalent to spatial Fourier transforms of quantities related to the stiffness and density perturbations. For example,

$$D(\omega) = \frac{1}{(2k_a)^4} \iiint_B \left[\frac{1}{a_0^2} (2k_a)^4 \delta c_{\ell m n p}(\underline{y}) e_{\ell} e_m e_n e_p + (2k_a)^4 \delta \rho(\underline{y}) \right] e^{2ik_a \underline{e} \cdot \underline{y}} dv_y$$

Defining

$$\underline{p} \equiv -2k_a \underline{e},$$

we see that

$$D(\omega) = \frac{1}{(2k_a)^4} \iiint_B \left[\frac{1}{a_0^2} \delta c_{\ell m n p} p_{\ell} p_m p_n p_r + p^4 \delta \rho \right] e^{-\underline{p} \cdot \underline{y}} dv_y$$

By repeated applications of Gauss' divergence theorem, under the assumption that $\delta c_{\ell m n r}$ and have fourth derivatives which are piecewise smooth, we find

$$\tilde{D}(\omega) \equiv \frac{1}{(2k_a)^4} D(\omega) = \iiint_B \left[\frac{1}{a_0^2} \delta c_{\ell m n r, \ell m n r} + \delta \rho_{, \ell \ell m m} \right] e^{-\underline{p} \cdot \underline{y}} dv_y \quad (30)$$

Thus observations of scattered dilatation waves from a plane dilatation pulse, over all incidence directions and all frequencies would, under the assumptions of this section, yield the Fourier transform of

$$g(\underline{x}) \equiv \frac{1}{a_0^2} \delta c_{\ell m n r, \ell m n r} + \delta \rho_{, \ell \ell m m}$$

In principle, $g(\underline{x})$ could be recovered from those observations. Reconstruction of a function from partial, corrupted values of its Fourier transform is an ill-posed problem (2). This ill-posedness is not, of course, unexpected: the non-linearity of

the inverse scattering problem was eliminated by the assumptions of the first Born approximation, but the ill-posedness might have been expected to remain--and it does.

THE PHYSICAL OPTICS APPROXIMATION

By the "physical optics approximation" we mean the approximation obtained for the elastic waves scattered from a void or from a rigid inclusion, when, at each point of the surface of the scattering body, the traction and displacement components of the scattered wave are taken to have the values they would take on if the incident wave were scattered from a plane boundary, coincident with the tangent plane to the surface at the point in question. Reference (2) provides a proof that the dilatation wave component of the far-field back scattered elastic wave due to a plane dilatation wave incident on a void, in the physical optics approximation, is given by

$$\tilde{U}_j^s = \frac{ik_a U}{2\pi} e^{\frac{ik_a x}{x}} e_j \iint_{\partial B_1(\underline{e})} (n \cdot \underline{e}) e^{2ik_a \underline{e} \cdot \underline{y}} d\omega(\underline{y}) \quad (31)$$

where \underline{n} is the outward unit normal to the void, \underline{e} a unit vector in the direction of the incident wave, $k_a = \omega/a$, where a is the dilatation wave speed, and $\partial B_1(\underline{e})$ denotes the insonified portion of the surface of the void.

Thus, in principle one can recover, by observing the far-field back-scattered dilatation waves the quantity

$$\Phi(\underline{p}) \equiv \frac{i}{4\pi} \iint_{\partial B_1(\underline{e})} (n \cdot \underline{p}) e^{-i\underline{p} \cdot \underline{y}} d\omega(\underline{y}) \quad (32)$$

where

$$\underline{p} \equiv -2k_a \underline{e} \quad (33)$$

If B is convex, then $\partial B_1(\underline{e})$ consists of those parts of B for which $(n \cdot \underline{p}) > 0$. Thus for convex B ,

$$\Phi(\underline{p}) = \frac{i}{4\pi} \iint_{n \cdot \underline{p} > 0} (n \cdot \underline{p}) e^{-i\underline{p} \cdot \underline{y}} d\omega(\underline{y}) \quad (34)$$

We will use (34) in general, recognizing that an approximation is thereby introduced, if B is not convex. Equations (32) and (33) are, apart from a constant in the definition of $\Phi(\underline{p})$, the same as Equations (5) and (6) of Reference (3), which considered electromagnetic scattering. As in (3), straightforward manipulations show that

$$\begin{aligned} \Phi(\underline{p}) &= \frac{1}{2} \left[\Phi(\underline{p}) + \Phi(-\underline{p}) \right] \frac{1}{2\pi} \iint_B e^{i\underline{p} \cdot \underline{y}} dv \\ &= \frac{1}{2\pi} \iint_B \gamma(\underline{y}) e^{-i\underline{p} \cdot \underline{y}} dv \quad (35) \end{aligned}$$

where $\gamma(\underline{y})$, the characteristic function of B , is defined by

$$\gamma(\underline{y}) = \begin{cases} 1, & \underline{y} \in B \\ 0, & \text{otherwise} \end{cases}$$

Then, by the Fourier integral theorem,

$$\gamma(\underline{y}) = \frac{1}{(2\pi)^2} \iiint_{\underline{p}} \gamma(\underline{p}) e^{i\underline{y} \cdot \underline{p}} d\underline{p} \quad (36)$$

Thus we see that in the short-wavelength limit, as in the first Born approximation, observations lead to the Fourier transform of a quantity of interest. Equation (35) is the Bojarski-Lewis identity (3), which can now be seen to apply to elastic wave scattering as well as to electromagnetic wave scattering.

ELASTIC WAVE TOMOGRAPHY

If elastic waves are assumed to propagate through a body B without refraction, but with attenuation according to

$$\frac{dI}{ds} = -S(r(s))I, \quad (37)$$

where s is arc length along the ray $\underline{x} = \underline{r}(s)$ and the function $S(\underline{x})$, the "elastic wave stopping power", characterizes flaws in the body, then it can be shown (2) that a function $h(\underline{p}; \underline{e})$ which can be determined from intensity observations made on the surface of B, has the property

$$h(\underline{p}, \underline{e}) = \iiint_B e^{-i\underline{p} \cdot \underline{x}} S(\underline{x}) d\underline{x}. \quad (38)$$

Here \underline{e} is a unit vector in the direction of a plane elastic wave in B. The function $h(\underline{p}, \underline{e})$ can be determined for any \underline{p} perpendicular to \underline{e} . Thus, the spatial Fourier transform of $S(\underline{x})$ can be determined, for certain spatial wave vectors \underline{p} .

The geometry of the part may allow one to find a family--or families--of propagation vectors \underline{e} , whose normal planes fill all of three-dimensional wave-space. This is the case, for example, if the part is any figure of revolution. In such a case, the Fourier transform of $S(\underline{x})$ can in principle be evaluated, and $S(\underline{x})$ re-constructed, by techniques such as the one considered in the following section. In other cases, the Fourier transform of S can be evaluated on parts of wave-number space, and this partial information may give useful insights into the nature of the flaws characterized by $S(\underline{x})$.

INVERSION OF FOURIER TRANSFORMS WITH NOISY DATA

Section 5.10 of reference (2) gives a proof by example that the problem of inverting a Fourier transform is ill-posed, in the sense that there are transforms which differ arbitrarily little on all of wave-number space, but whose inverse transforms differ arbitrarily greatly at some points. Thus, while the simplifying assumptions of the first Born approximation, physical optics and tomography each eliminate the non-linear character of the general inversion problem, leaving us with the linear problem of inverting a Fourier transform, the ill-posed character of the original problem is still very much to be reckoned with. The fact that arbitrarily small deviations in transforms can lead to arbitrarily large deviations in inverse transforms, coupled with the fact that all experiments involve errors of observation, certainly warns one not to treat the inversion problem lightly. However, we'll see now that approximate inversion methods can be constructed, whose errors may be estimated. In the process we'll see how observation errors set limits on our ability to resolve details of disturbances in elastic properties.

For a first approach to this task, we may note

that, according to (30), (35), and (38) observations may yield values of Fourier transforms of quantities of interest at discrete points of wave-number space. Now, suppose we know that there is some cube, of edge $2L$, inside which the defect region B must lie. Then the quantity $g(\underline{x})$ which characterizes the imperfections, e.g.,

$$g(\underline{x}) = \frac{1}{a_0} \delta c_{lmnq, lmnq} + \nabla^4 \delta \rho$$

for the first Born approximation or

$$g(\underline{x}) = \gamma(\underline{x})$$

for the physical optics approximation will, if sufficiently smooth, be given by the sum of a Fourier series. That is, there will be coefficients c_{lmn} such that

$$g(\underline{x}) = \sum_{l,m,n} c_{lmn} e^{i\frac{\pi}{L}(\ell x_1 + m x_2 + n x_3)} \quad (39)$$

The connection between the c_{lmn} and $g(\underline{x})$ is

$$c_{lmn} = \frac{1}{8L^3} \iiint_{-L}^L e^{-i\frac{\pi}{L}(\ell x_1 + m x_2 + n x_3)} g(\underline{x}) d\underline{x} \quad (40)$$

Now, Equations (30), (35), and (38) show that values of integrals of precisely the form of (40) are directly observable, when the appropriate approximations hold. This suggests a testing program--one should observe those waves which generate the integrals of (40)--as well as a data reduction scheme given experimental values c_{lmn} for some of the c_{lmn} . one produces

$$g_N(\underline{x}) = \sum_{l,m,n}^N c_{lmn} e^{i\frac{\pi}{L}(\ell x_1 + m x_2 + n x_3)} \quad (41)$$

as an approximate solution to the inverse scattering problem. The family of approximate solutions (41) is an example of a regularizer for the ill-posed inversion problem (17, 20). Now let us explore the connection between the approximation $g_N(\underline{x})$ and the actual $g(\underline{x})$. If

$$c_{lmn} = c_{lmn} + \delta c_{lmn}$$

where δc_{lmn} includes both observation and modeling errors, then

$$\begin{aligned} g_N(\underline{x}) - g(\underline{x}) &= \sum_{l,m,n}^N \delta c_{lmn} e^{i\frac{\pi}{L}(\ell x_1 + m x_2 + n x_3)} \\ &= 2\text{Re} \sum_{N+1}^{\infty} [A_{lmn} + A_{-l,m,n} + A_{l,-m,n} + A_{l,m,-n}] \\ &= 2\text{Re} \sum_{N+1}^{\infty} [A_{00k} + A_{0k0} + A_{k00}] \\ &= 2\text{Re} \sum_{N+1}^{\infty} [A_{0jk} + A_{0-j,k} + A_{j0k} + A_{j0-k} + A_{j,k,0} + A_{-j,k,0}] \end{aligned} \quad (42)$$

where

$$A_{lmn} = c_{lmn} e^{i\frac{\pi}{L}(\ell x_1 + m x_2 + n x_3)} \quad (43)$$

In writing the second error term, we have used the fact that $c_{-l-m-n} = c_{lmn}^*$. A study of the behavior of the two error terms,

$$E_1 \equiv \sum_{-N}^N \sum_{-N}^N \delta c_{lmn} e^{i\frac{\pi}{L}(lx_1 + mx_2 + nx_3)} \quad (44)$$

and

$$E_2 \equiv 2\text{Re} \sum_{N+1}^{\infty} (a_{00k} + a_{0k0} + a_{k00}) + 2\text{Re} \sum_{N+1}^{\infty} (a_{0jk} + a_{0-jk} + a_{j0k} + a_{j0-k} + a_{jko} + a_{-jko}) + 2\text{Re} \sum_{N+1}^{\infty} [a_{lmn} + a_{-lmn} + a_{l-mn} + a_{l-m-n}] \quad (45)$$

is instructive. Because the series of (39) converges, E_2 must tend to zero as N increases.

Working with very large values of N is not, however, the way to ensure small errors in \hat{g}_N , because E_1 generally increases rapidly with increasing N . Indeed, if we know only that $|\delta c_{lmn}| < \epsilon$, then we may say

$$|E_1| \leq \epsilon(2N+1)^3 \quad (46)$$

Unfortunately, the estimate is "sharp", in that there are choices of δc_{lmn} , all with magnitude not exceeding ϵ , for which the equality sign holds in (46) at some x . Consequently, if N is taken too large, E_1 may be large. On the other hand, if N is taken too small, E_2 will be large. It follows that, in fact, there is an optimum number N^* of terms to take, for which $E_1 + E_2$ is a minimum. This optimum number may be estimated, if one knows enough about $g(x)$ to be able to characterize the truncation error E_2 , and if he has some knowledge of the errors δc_{lmn} . Calculations of this kind are to be found in References (4), (5), and (6). Reference (2) shows that, if $\nabla^4 g(x)$ is continuous and $|\nabla^4 g(x)| \leq c_1$, and also $|\delta c_{lmn}| \leq \epsilon$, then

$$|g_N(x) - g(x)| \leq \epsilon(2N+1)^3 + B/N \quad (47)$$

where B is a constant proportional to $L^4 c_1$. The right side of (47) attains its minimum at

$$N = N^* = \frac{1}{2} + \sqrt{\frac{1}{4} + \frac{B}{6\epsilon}} \quad (48)$$

While (48) is only an estimate of the optimum N , it is nevertheless so, that taking many fewer than N^* terms in (41) results in large values of E_2 , and

"wastes" information, while taking many more than N^* terms results in large values of E_1 , in which observation and modeling errors are unduly amplified.

The regularizer (41), like many other regularizers, may also be viewed as providing an approximation to a convolution of $g(x)$ with a member of a class of "aperture" functions, and this interpretation may be helpful in practice. Reference (7) shows that

$$g_N(x) = \int_{-L}^L \int_{-L}^L \int_{-L}^L G_N(x-u) g(u) du + \sum_{-N}^N \sum_{-N}^N \delta c_{lmn} e^{i\frac{\pi}{L}(lx_1 + mx_2 + nx_3)} \quad (49)$$

where

$$G_N(v) = \frac{1}{8L^3} \sum_{-N}^N \sum_{-N}^N \sum_{-N}^N e^{i\frac{\pi}{L}(lv_1 + mv_2 + nv_3)} \quad (50)$$

That is, the approximation $\hat{g}_N(x)$ is equal to the convolution of $g(x)$ with the aperture function $G_N(x)$, plus the error E_1 . Some examples of the behavior of $G_N(v)$ for various values of N are shown in Figs. 4a and 4b. These figures show how the width of the principal lobe of $G_N(v)$ decreases with increasing N . This width is, of course, a measure of the resolution attained by the approximation (49). The presence of the error term E_1 in (42) limits the value of N which can be used effectively. It is in this way that the presence of errors sets resolution limits for the regularizer of (41). In general, errors limit the amount of fine-scale detail which can be recovered in solving regularizable ill-posed problems. Figures 5a and 5b show the results of applying (41) to perfect (approximately 15-place) data, and Figs. 6a and 6b show the results of applying (41) to noisy data with values of N which are about equal to, and greater than the optimal value N^* .

While the "best possible" estimate of the function $g(x)$ obtained from a given regularizer applied to experiments with given error processes may be discouraging, it will often be the case, as pointed out above that this function is not itself the solution to the inversion problem under consideration, but only an intermediate step. It may be, that an error analysis of the actual solution presents a brighter picture. Reference (2) shows that, generally speaking, low-order integral moments of $g(x)$ may be estimated with much more confidence than can $g(x)$ itself. If one knows in advance the form of $g(x)$, if, for example one knows a priori that B is a sphere with a given center so that only one parameter need be estimated to determine $g(x)$ the picture presented by the error analysis may be brighter still. This is borne out by the work of Richardson (7), and suggests that use of long-wavelength limit data to evaluate moments of quantities associated with defects, as discussed by Kohn and Rice (8), may be a good approach to practice.

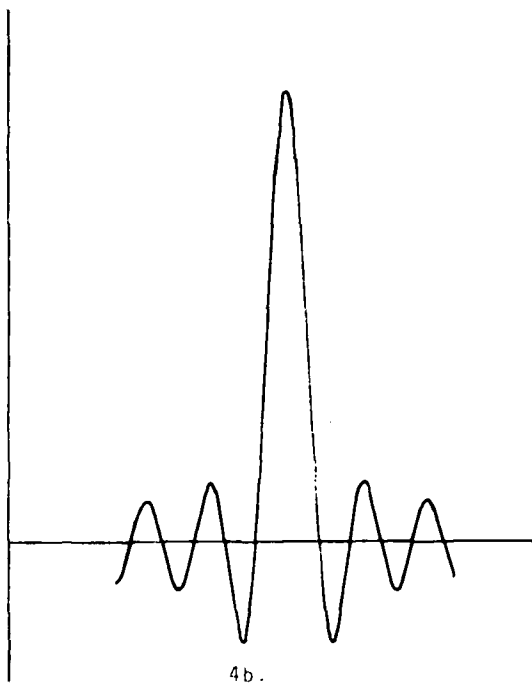
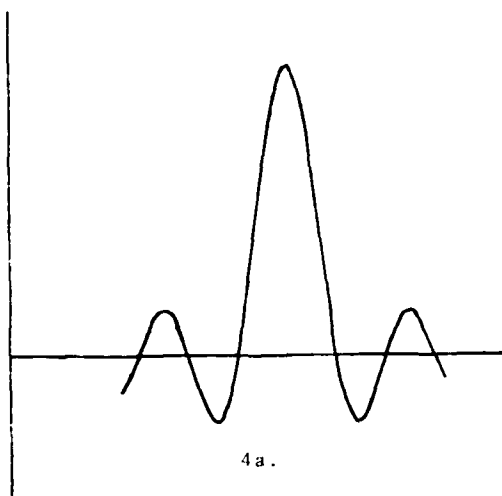


Figure 4.

Values of $G_N(v)$ vs. $|v|$ for $N = 3$ (Fig. 4a), and $N = 5$ (Fig. 4b). The same arbitrary scale is used for the abscissas of both figures, but the ordinate scale varies from figure to figure.

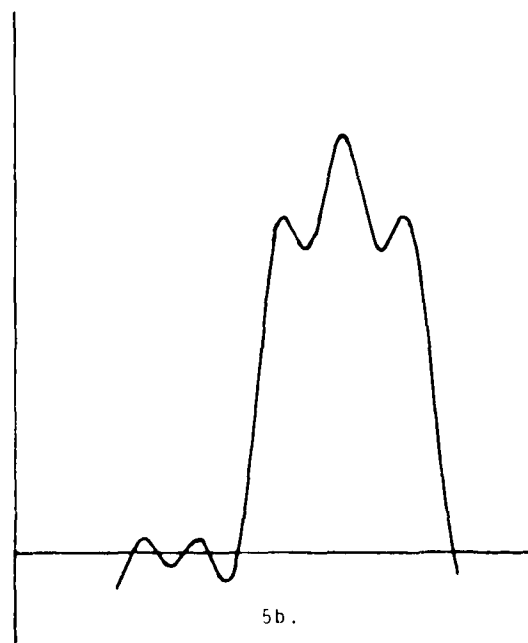
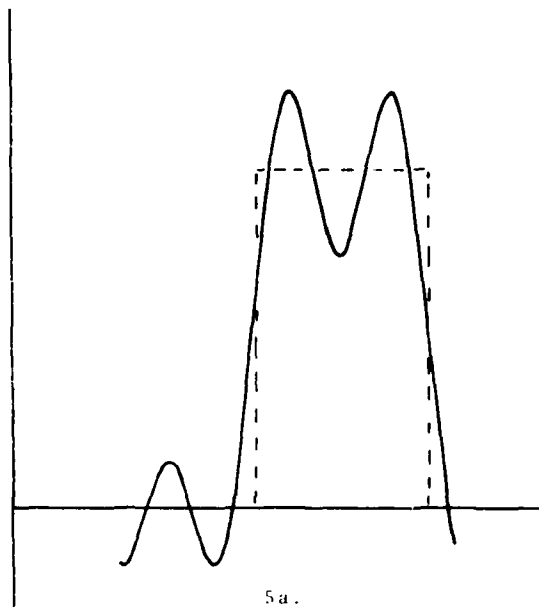


Figure 5.

Partial sums of the Fourier series of a function of three variables as its argument varies along a straight line. The function is the characteristic function of a sphere, whose center is off-set from the center of the cube within which the series is determined. Values of the function itself are shown on the dashed curve of Fig. 5a for reference. Figure 5a corresponds to $N = 3$ in Equation (4) while Fig. 5b corresponds to $N = 5$. The same arbitrary scale is used for both figures.

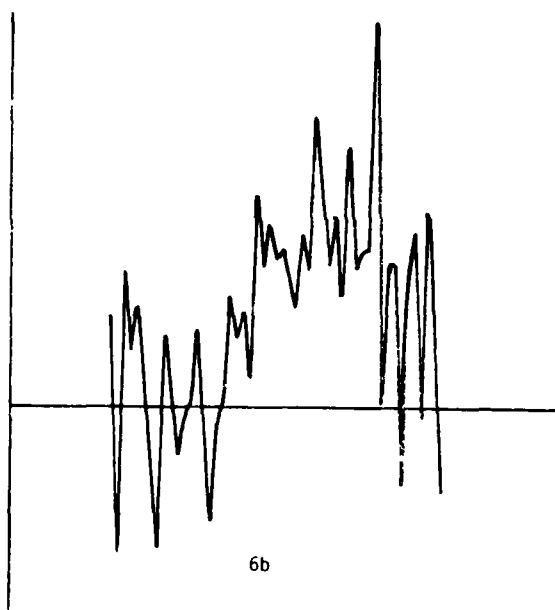
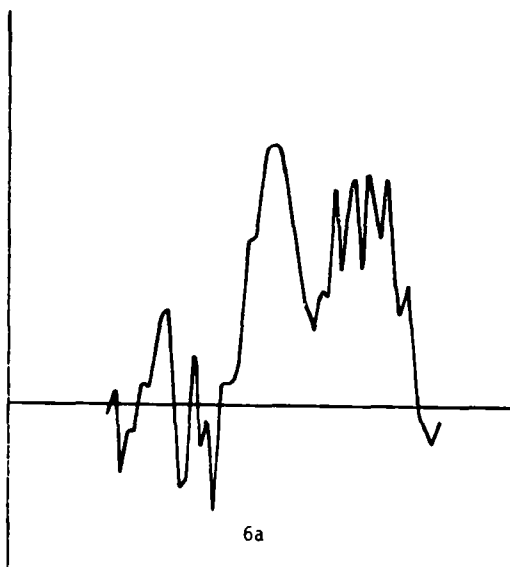


Figure 6.

The same partial sums, respectively, as in Fig. 5, with noisy values of the c_{ijk} . The same arbitrary scale is used for both figures.

REFERENCES

1. R. J. Krueger, Q. App. Math 34.
2. D. A. Lee, Mathematical Principles of Data Inversion, Chapter 5 of Non-Destructive Evaluation, Buckley and Thompson, Editors, Springer-Verlag, New York-Heidelberg, in press.
3. R. M. Lewis IEEE Trans. Antennas and Propagation AP-17, 308 (1969).
4. A. N. Tikhonov and V. Y. Arsenin, Solutions of Ill-Posed Problems, Winston, Washington (1977).
5. D. A. Lee, J. Polymer, Sci. A-28, 1039 (1970).
6. D. A. Lee, R. M. Potter, W. Perry, W. Schmaedeke Some Practical Aspects of the Treatment of Regularizable Ill-Posed Problems by Regularization, U. S. Air Force Aerospace Research Laboratories TR75-0022 (1975).
7. J. M. Richardson, Proc. ARPA/AFML Review of Progress in Quantitative NDE, U. S. Air Force Materials Laboratory Report, AFML-TR-78-205, 1978.
8. W. Kohn and J. R. Rice, J. Appl. Phys. 50, 3346 (1979).

SUMMARY DISCUSSION
(D. A. Lee)

Jack Cohen (Denver Applied Analytics): I have seen the pictures of Kino and pictures of Quate, and we realize there must be something wrong here because they're certainly getting images. I think what's wrong is that the Fourier transform in particular and the (inaudible) to the fact well-conditioned, not ill-conditioned. The particular Fourier transform (inaudible) a unitary matrix. What more could you want?

David Lee: For most of the inverse problems we are talking about, I can exhibit data which differ by as little as you please, which correspond exactly to solutions which differ by as much as you please.

Jack Cohen: After you discretize unwisely. If you discretize wisely, you have unitary measurements.

David Lee: I'm not making any approximate solutions at all. I'm simply talking about a property of the problems themselves. I claim I can exhibit data which differ by as little as you please, which correspond exactly to arbitrarily greatly differing solutions. There is no approximate solution involved. Now, I certainly do think you can find wise approximate solution procedures which minimize these effects, but the effects are there. My claim is that one should be aware of them.

Jack Cohen: I really disagree (inaudible).

John Richardson (Rockwell Science Center): I would like to make a comment which may clarify the previous discussion, namely, that indeed if you have a set of spatial frequencies from your actual scattering data that are completely congruent to the set of spatial frequencies you're trying to determine in your image, then there is no ill-posedness at all.

David Lee: That's true.

John Richardson: Now, there are two kinds of ill-posedness that may enter, and one is when you have a set of spatial frequencies available in the scattering data which are (inaudible) the set of spatial frequencies of using to represent their function to be determined, and that's where the particular difficulties come into discussion. But there is also the super resolution type of problem where you're trying to determine something which is of higher resolution than your data justified, and there is another kind of proposedness which can only be handled by a priori information.

David Lee: I agree with that. In fact, the thing I'm advocating is when you're doing business with inverse scattering problems, it is very important that you are aware of the ill-posed character of the problem and that you do just what I understand you have been saying: you think about the errors that you have in your data and you ask yourself what frequencies will allow you to infer rationally; if in fact they allow you to infer, with acceptable error, those frequencies which you need to do the reconstruction you want to do. Then everything is fine. The time you get into trouble is just as you said, when you try to infer things about frequencies which the data won't allow you to do.

#

APPLICATIONS OF IMAGE RECONSTRUCTION IN NDE

R.V. Denton and S. Maitra
Systems Control, Inc.
Palo Alto, CA 94304

ABSTRACT

The nondestructive evaluation (NDE) of materials often involves the solution of an inverse problem. It is shown that image reconstruction techniques lead to the direct solution of the 3-D inverse problem when radiographic measurements are made. In particular, it is suggested that the convolve-and-backproject solution to the 3-D divergent ray geometry problem should be useful for NDE. There is also a discussion of the accept-reject criteria appropriate for various classes of defects.

INTRODUCTION

There has been a strong emphasis on defect characterization through ultrasonic scattering measurements in the previous ARPA/AFML Progress Reviews [1]. Here the ultimate goal is to invert the scattering data, i.e., to solve the inverse problem, in order to arrive at quantitative estimates of the three-dimensional size, the shape, and the orientation of defects. This problem can be solved for the case of fairly simple defects that are situated in structures of uncomplicated geometries. However, this inverse problem becomes extremely difficult to solve for complex structures, due to the many possible internal reflections which can occur. In an industrial setting, it is the many internal reflections, together with refraction and diffraction phenomena, which lead to ambiguities in identifying defects when using ultrasonic measurements.

It is for this reason that radiographic measurements, whenever applicable, will always play an important role in nondestructive evaluation (NDE). The geometric optics limit is applicable in radiographic techniques; the wavelength of the X-rays or of the emitted radiation from radioisotopes is much smaller than the size of the scatterers. The rays travel in straight-line paths between scattering events, and a typical transmission measurement simply determines the net scattering out of the beam direction.

Radiographic transmission measurements, often called shadowgraphs, have been an integral part of industrial NDE for decades. Their disadvantage is that depth information is lost; a three-dimensional (3-D) object is projected onto two-dimensions, i.e., onto a plane. Associated with this, a small defect can be difficult to resolve in standard radiography, since it contributes to the transmission measurement in the ratio of its linear dimension to the depth of the material along the transmission direction. It should, therefore, be of considerable economic interest to develop techniques which combine the transmission measurements from different viewing angles to obtain a three-dimensional, well resolved image of the object being evaluated.

The purpose of this paper is to describe two image reconstruction algorithms which are applicable to this general problem of reconstructing a 3-D object from a set of radiographic measurements. Image reconstruction techniques have been discussed extensively in the literature, and yet there has

been relatively minor treatment of the case that the measurements are made in a truly three-dimensional arrangement around the object being evaluated. Rather, the measurements are typically made in sets of separate planes intersecting a 3-D object. The object is then reconstructed by obtaining the reconstruction of each plane separately, after which the planes are stacked together to obtain the 3-D result.* The main reason for the interest in a true 3-D measurement arrangement is that it should be possible to develop an efficient real-time system for the determination of defects.

After carrying out the image reconstruction, the problem still remains of identifying the defects which may be in the object. A defect must be classified, and there will usually be a set of accept-reject criteria which depends on the type of defect, taking into account the specific application of the object under evaluation. The accept-reject criteria must be analyzed from a statistical standpoint, and methods of statistical hypothesis testing are appropriate. Some of the main ideas in this approach are indicated in the last section of the paper.

IMAGE RECONSTRUCTION

As pointed out in the introduction, the bulk of the work in image reconstruction has involved measurements which are line integrals (designated projections) through a 2-D density $f(x,y)$.

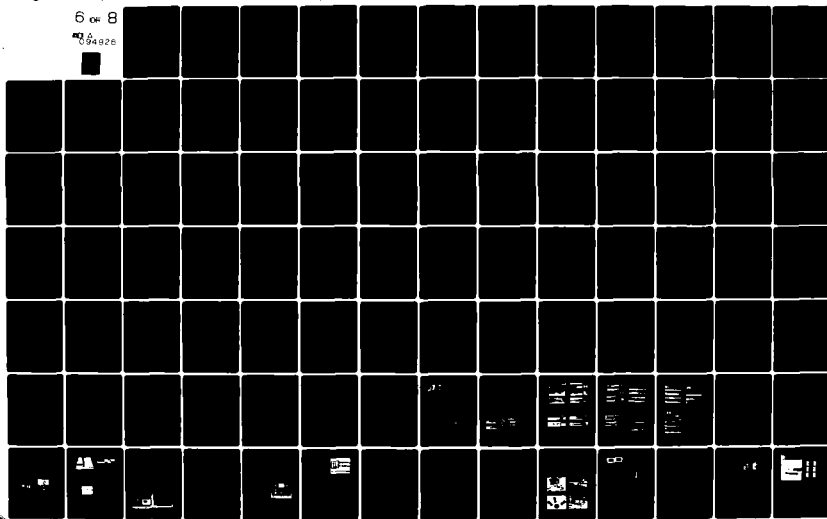
The orientation of the line integral paths can be described in two geometries. In the early work sets of parallel ray projections through the density were utilized; projections in a given set are parallel to one another, but displaced in angle with respect to projections in the other sets. One such set of parallel ray projections is shown in Fig. 1(a). Reviews of a variety of reconstruction algorithms for the parallel ray geometry can be found in Refs. [4-7]. In some of the more recent work the sensors are arranged at fixed positions around the density to be reconstructed. A set of ray projections diverging from each source position is then utilized; this arrangement is shown in Fig. 1(b). Descriptions of the divergent ray (sometimes designated fan beam) reconstruction algorithms can be found in Refs. [8-10].

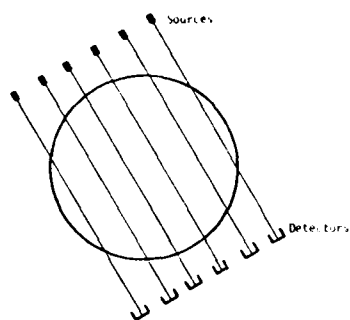
*This approach has also been used in using image reconstruction to determine stresses from ultrasonic measurements [2,3].

AD-A094 826 ROCKWELL INTERNATIONAL THOUSAND OAKS CA SCIENCE CENTER F/6 11/2
PROCEEDINGS OF THE DARPA/AFML REVIEW OF PROGRESS IN QUANTITATIV--ETC(U)
JUL 80 D O THOMPSON, R B THOMPSON F33615-74-C-5180
UNCLASSIFIED SC595.70AR AFWAL-TR-80-4078 NL

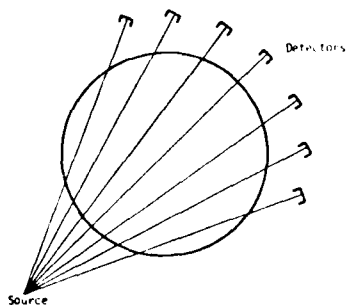
6 OF 8

064026





(a) Parallel Ray Geometry. One set of projections is shown; other sets cut through the density region at different angles.



(b) Divergent Ray Geometry. One set of projections is shown; other sets emanate from other source locations around the density region.

Fig. 1 Measurement Geometries for Two-Dimensional Image Reconstruction

There are two principal methods which have been used to carry out the image reconstruction. The algebraic reconstruction techniques (ART) involve the inversion of a large matrix. They have the advantage that general density fields, even including spreading losses in the propagation of the signal to the detector, can be reconstructed. The convolution methods [11], on the other hand, are somewhat more restrictive but are usually an order of magnitude faster in computing time. This can be a significant difference if one is interested in developing real-time systems. It is the convolution approach which will be treated in this paper.

Both the 2-D parallel ray and the divergent ray reconstruction geometries of Fig. 1 have generalizations to three dimensions. The convolution solutions to the 3-D problem will be described next.

Reconstruction in 3-D From Parallel Rays - The basic equations for direct reconstruction from 3-D parallel ray projections were developed by Vainshtein and Orlov [12-14]. Their parameterization of the projections is convenient and, with minor modifications, is applicable to the divergent ray geometry also. With reference to Fig. 2, a ray is parameterized by the unit vector $\hat{\tau}$, as specified by the spherical coordinate angles (θ, ϕ) , and a vector $\vec{\ell}$ lying in the plane perpendicular to $\hat{\tau}$ (denoted hereafter as the

τ -plane).^{*} The length $|\vec{\ell}|$ is the distance in the τ -plane from the ray to the origin. A convenient pair of orthogonal axes for decomposing $\vec{\ell}$ is given by

$$\hat{\ell}_{xy} \triangleq (\hat{\tau} \times \hat{k}) / (|\hat{\tau} \times \hat{k}|), \quad (1)$$

$$\hat{\ell}_z \triangleq (\hat{\ell}_{xy} \times \hat{\tau}) / (|\hat{\ell}_{xy} \times \hat{\tau}|),$$

where \hat{k} is the unit vector along the positive z axis. The ray is defined as the locus of points $\vec{\ell} + \tau\hat{\tau}$ as τ varies over $[-\infty, \infty]$. The parallel ray projections are thus given by

$$p(\vec{\ell}, \hat{\tau}) = \int_{-\infty}^{\infty} f(\vec{\ell} + \tau\hat{\tau}) d\tau, \quad (2)$$

where $f(\vec{x}) = f(x, y, z)$ is the density to be reconstructed. As seen in Fig. 2, the vector $\vec{\ell}$ is the projection of the sensor location onto the τ -plane. In a realistic arrangement it is assumed that the sensor is outside the region being measured; the actual sensor distance above the τ -plane (i.e., along the line $\vec{\ell} + \tau\hat{\tau}$) is not important due to Eq. (2). The reconstruction problem consists of determining $f(\vec{x})$ in Eq. (2), given all projections $p(\vec{\ell}, \hat{\tau})$. The solution to this problem, as derived by Orlov [14], is

$$f(\vec{x}) = \frac{1}{4\pi^3} \int_0^\pi \sin \theta d\theta \int_0^\pi d\phi \iint_{-\infty}^{\infty} d\vec{\ell} p(\vec{\ell}, \hat{\tau}) \psi(\vec{x}_\tau - \vec{\ell}) \quad (3)$$

where $\vec{x}_\tau = \vec{x} - (\vec{x} \cdot \hat{\tau})\hat{\tau}$

and $\psi(\vec{x}_\tau - \vec{\ell}) = - \frac{1}{|\vec{x}_\tau - \vec{\ell}|^3} \quad \vec{x}_\tau \neq \vec{\ell}.$

Here the point to be reconstructed, \vec{x} , is projected onto the τ -plane (the latter defined by the angles θ and ϕ); the point \vec{x}_τ then enters in the argument of a convolving function ψ . The $\vec{\ell}$ -integration is the 2-D convolution of the projections $p(\vec{\ell}, \hat{\tau})$ for each τ -plane with $\psi(\vec{x}_\tau - \vec{\ell})$. After carrying out this convolution separately for each τ -plane, the contribution of each τ -plane is summed according to the angle integrations over θ and ϕ . The latter integrations are usually known as back-projections. It should be noted that in the solution form given in Eq. (3) we have neglected a contribution due to the singularity at $\vec{x}_\tau = \vec{\ell}$ which must be taken into account in a practical implementation. This contribution will be discussed later in the paper.

That Eq. (3) is actually a solution to the 3-D parallel ray reconstruction problem can be established by taking as the object density a 3-D Dirac delta function, and by verifying that Eq. (3) results in an output image which is, in fact, a delta function [14].

^{*}Vectors will be denoted by an arrow, while the caret symbol designates a unit vector. The vector dot and cross product are denoted by "." and "x" respectively.

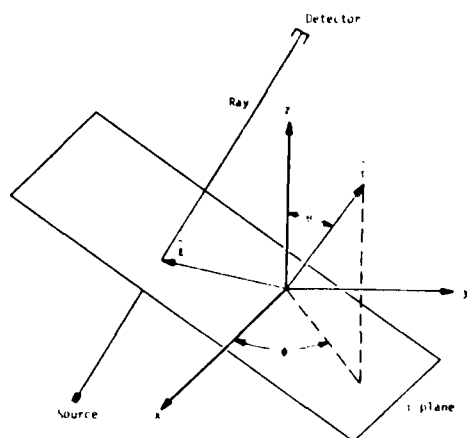


Fig. 2 Three-Dimensional Parallel Ray Geometry

Due to the structure of the solution in Eq. (3), a computer implementation is straightforward; in particular, an array processor can lead to extremely rapid computing times. In carrying out the implementation, a discrete form of the convolving function ψ must be obtained. This involves a careful treatment of the singularity at $\hat{x}_T = \hat{x}$, as already indicated.

Reconstruction in 3-D From Divergent Rays - The measurement apparatus required for the above 3-D parallel ray reconstruction algorithm leads to some of the same difficulties that pertain in the 2-D case. For each set of parallel ray measurements, a series of translations of the source-detector combination is necessary. Following this, the entire apparatus must be rotated, after which the next set of parallel ray measurements is obtained, etc. This is difficult to achieve mechanically, especially if one is interested in a real-time imaging system. It is for this reason that the divergent ray reconstruction algorithm has found widespread application in the 2-D case, and similarly, the divergent ray geometry should be significant for the 3-D reconstruction problem. This problem, and its solution, will be discussed next.

The 3-D parallel ray parameterization shown in Fig. 2 can be modified for the case of the divergent ray projections. For this geometry, the sources are taken to lie on a sphere of radius D , with source coverage over the full solid angle. Referring to Fig. 3, \hat{x} still lies in the i -plane, but τ now specifies the location of the source at $-D\hat{\tau}$. Varying \hat{x} values now correspond to projections which scan the field in the angular variables.

The projections are given by

$$p(\hat{x}, \hat{i}) = \int f(\hat{x} + \hat{i}\hat{\tau}) d\hat{\tau} \quad (4)$$

where the direction of the ray is given by

$$\hat{\tau} = \frac{D + \hat{x} \cdot \hat{i}}{\sqrt{D^2 + |\hat{i}|^2}} \quad (5)$$

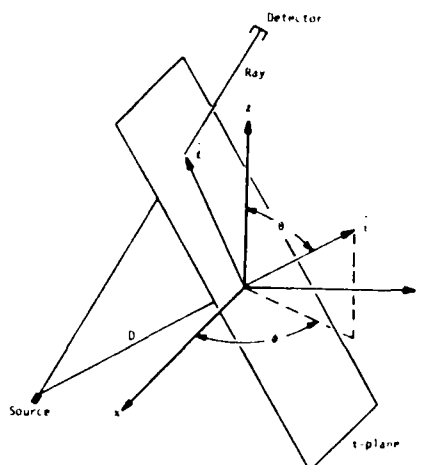


Fig. 3 Three-Dimensional Divergent Ray Geometry

The reconstruction problem is again to determine $f(\hat{x})$, given the projections $p(\hat{x}, \hat{i})$. The solution to this inverse problem can be obtained by a direct transformation of the 3-D parallel ray solution in Eq. (3). The details are rather lengthy [15] and will be omitted here. The result is

$$f(\hat{x}) = \frac{1}{8\pi} \int_0^\pi d\theta \sin\theta \int_0^{2\pi} d\phi \frac{D^3}{(D + \hat{x} \cdot \hat{i})^3} \iint_{i\text{-plane}} d^2x_y d^2x_z \cdot \frac{Dp(\hat{x}, \hat{\tau})}{\sqrt{D^2 + |\hat{i}|^2}} \psi(\hat{x}_T, \hat{i}) \quad (6)$$

$$\text{where } \hat{x}_T \hat{=} \frac{D}{D + \hat{x} \cdot \hat{i}} [\hat{x} - (\hat{x} \cdot \hat{\tau}) \hat{\tau}] ,$$

$$\text{and } \psi(\hat{x}_T, \hat{\tau}) = -|\hat{x}_T - \hat{\tau} - \hat{\tau} \times \hat{x}_T / D|^{-3} ,$$

$$\text{with } \hat{x}_T \neq \hat{x} .$$

The reconstruction algorithm, Eq. (6) is similar to a convolve-and-backproject solution. However, because of the extra term $\hat{\tau} \cdot \hat{x}_T / D$, the inner integral over $\hat{\tau}$ is not a convolution integral. Thus, an exact implementation of Eq. (6) requires that the integrals be evaluated for each point \hat{x}_T in the i -plane. This would require a somewhat heavier computational burden than a true convolve-and-backproject solution.

In many experimental arrangements the cross product term can be neglected. To motivate this approximation, we note that the extra term $\hat{\tau} \cdot \hat{x}_T / D$ is relatively small if the source distance D is large compared to the distances $|\hat{x}_T|$ or $|\hat{\tau}|$. In a practical arrangement the sources would be outside of the volume to be reconstructed, so the values $|\hat{\tau}|$ and $|\hat{x}_T|$ would be smaller than D . The contribution of the cross product to the function ψ is only of order $|\hat{\tau}| |\hat{x}_T| / D^2$ with respect to the contribution due to the vector $\hat{x}_T - \hat{\tau}$; this follows from noting that the cross product is orthogonal to \hat{x}_T and $\hat{\tau}$, which allows ψ for this case to be written as

$$\varphi = - \left\{ |\vec{x}_T - \vec{\ell}|^2 + |\vec{\ell} \times \vec{x}_T|^2 / D^2 \right\}^{-3/2}$$

This function is singular at $\vec{\ell} = \vec{x}_T$, as suggested by looking at only the first term above; the added cross product term does not alter the position of the singularity. When the cross product term is neglected as an approximation, then the φ for this 3-D divergent ray solution becomes identical to that of the 3-D parallel ray case; it can then be implemented fairly easily.

Discrete Versions of the 3-D Solutions - The previous discussion applies when there is a continuum of sensors located around the region to be reconstructed, and when there is only a finite number of sensors and measurements per sensor. Assume that there are N sensors with location as given by the unit vector $\tau_i = (\theta_i, \phi_i)$, where the N angle pairs have some arbitrary distribution over the solid angle sphere. A discrete form of the backproject integral, the (θ, ϕ) integrations, is straight-forward to develop; it involves an appropriate weighted sum over the N sensor contributions.

On the other hand the discretized version of the convolving function φ appearing in the inner integrals requires more careful treatment, due to the singularity. To derive the result, we note that the exact convolving function is the result of a limiting process. It can be shown [15] that the convolving function, φ_ϵ , is given by

$$\varphi_\epsilon = \begin{cases} \frac{2}{\epsilon^3} & , \quad |\vec{x}_T - \vec{\ell}| < \epsilon \\ -\frac{1}{|\vec{x}_T - \vec{\ell}|^3} & , \quad |\vec{x}_T - \vec{\ell}| \geq \epsilon \end{cases} \quad (7)$$

where φ_ϵ satisfies the equation

$$\iint d\vec{\ell} \varphi_\epsilon(\vec{x}_T - \vec{\ell}) = 0, \text{ for all } \vec{x}_T. \quad (8)$$

In numerical approximations to φ , the components of $\vec{\ell}$ take on a set of discrete values. On a cartesian grid φ has the form, for example,

$$\varphi(m\Delta\ell_{xy}, n\Delta\ell_z) = \frac{-w(m,n)}{[m^2\Delta\ell_{xy}^2 + n^2\Delta\ell_z^2]^{3/2}}, \text{ for } |m| + |n| \neq 0, \quad (9)$$

$$\varphi(0,0) = - \sum_{m,n} \varphi(m\Delta\ell_{xy}, n\Delta\ell_z) \\ |m| + |n| \neq 0.$$

The coefficient $\varphi(0,0)$ is determined in accordance with Eq. (8).

The coefficients $w(m,n)$ are typically of order 1 and were discussed in connection with the analogous 2-D problem in [16]. To each choice of coefficients $w(m,n)$ corresponds a particular numerical integration procedure for the integral representation of $f(\vec{x})$.

One obvious choice for $w(m,n)$ is simply unity for all m and n . In this case the convolving function in Eq. (9) is

$$\varphi(m,n) = - \frac{1}{\Delta^3} \frac{1}{[m^2 + n^2]^{3/2}}, \quad (10a)$$

for $|m| + |n| \neq 0$

where for simplicity both quantization lengths $\Delta\ell_{xy}$ and $\Delta\ell_z$ have been assumed identical:

$$\Delta \triangleq \Delta\ell_{xy} = \Delta\ell_z.$$

The exact value of $\varphi(0,0)$ must be determined numerically, using Eq. (9); it can be shown through use of the Euler-Maclaurin summation formula to be approximately given by

$$\varphi(0,0) \approx \left[\frac{2\pi^2}{3} + 2\zeta(3) \right] / \Delta^3, \quad (10b)$$

with $\zeta(\cdot)$ being the Riemann-Zeta function.

The above convolving function is only one of several possible ones that could be developed. Any discrete, well-behaved convolving function for this problem has the property that it involves a band-limiting approximation. In other words, a reconstruction according to Eq. (3) or Eq. (6), using the convolving function Eq. (10), is only accurate out to spatial frequencies of order $\omega \approx 1/\Delta$.

DEFECT DETERMINATION

Whether by solving the 3-D inverse problem using image reconstruction or by any other method, the result is a 3-D matrix of values corresponding to the observable being reconstructed, the density in the present case. In searching for defects, all the density values must be tested for deviations away from "normality." There is, of course, not a sharp division between normality and abnormality; the division depends upon the level of statistical error that can be tolerated in searching for the defects.

The simplest scheme for detecting the defects is to test each cell, or value of the 3-D matrix, in isolation from the other cells. Each cell can be examined in a binary hypothesis testing framework where the measured density is tested for belonging to one of two classes H_0 : normal and H_1 : abnormal. A simple Bayesian, Minimax [17] threshold may be set which distinguishes between the two classes.

The meaning of this test for the case of a defect consisting of a void in the material is sketched in Fig. 4. Here any density value greater than the indicated threshold T is declared normal, while any cell with density less than T is presumed to correspond to a void in the material; the cell is then declared abnormal. The density values for each hypothesis have a range as described by probability distributions. It is important to note that the two probability distributions invariably overlap in a practical system. Given the threshold setting, there is then a probability of detection P_D corresponding to hypothesis H_1 : defect present, and a probability of false alarm P_{FA} corresponding to

the hypothesis H_0 : cell normal, but with a defect nevertheless declared.

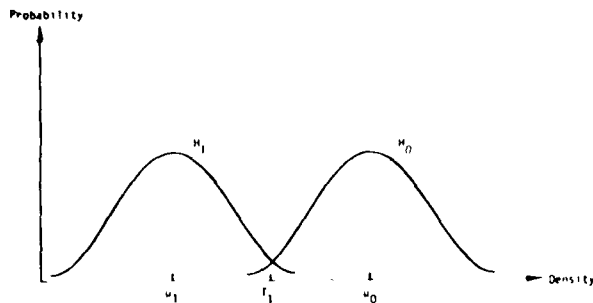


Fig. 4 Density Distributions for the two Hypotheses H_0 : normal and H_1 : abnormal

Depending on the resolution of the 3-D image that is actually achieved, the effect of a defect on the density will be somewhat reduced by an average over the cell volume. It will often be the case that the above test for an isolated cell does not then quite result in a threshold crossing for the outright classification as abnormal. Such cells must be evaluated in the context of the neighboring cell values. A number of classification procedures can be developed to treat this situation, to provide a more general and robust test than the simple binary hypothesis test. Several possible procedures will be described below.

To flag a cell that is marginal, a second threshold must be introduced. The second threshold can be set using the same Bayesian or Minimax criterion, but with a higher probability of false alarm. All marginal cells flagged in this manner constitute the input to the next stage of the detection process. Prior to the declaration of any region containing one of these cells as a flaw, an associative test procedure must be followed. One such associative measure is the volume of the connected region declared marginal. The connectedness can be tested using a minimal-spanning-tree algorithm [18] with a threshold on the maximum length between nodes. There are other measures for connectedness using clustering algorithms that have been used extensively in the literature [18].

The volume of the suspected region is a simple measure of the severity of the defect; the larger the volume, the more severe the defect. However, since the severity of any cell's variation is not taken into account, the measure lacks robustness. To improve on this, the volume can be weighted by the deviations of the questionable cell densities from the surrounding mean. If the region being tested has a mean μ , then the weighted volume V of the connected marginal cells with density values f_i and volumes v_i can be defined to be

$$V = \sum_i v_i |f_i - \mu|$$

The weighted volume measure V can then be used in a binary hypothesis test. The measure V has the properties of being translation and rotation invariant, as well as contrast independent.

However, this one-dimensional volume (weighted or unweighted) measure may not be enough, for some applications, to fully categorize the acceptability of the material. There are other multidimensional measures that take into account not only the size, but also the shape and distribution of the intensities. These measures are also invariant under rotation, translation and change in contrast [19]. These n -measures can then be tested [20] under the same H_0 , H_1 hypotheses with the exception that the decision surface is then multidimensional. The number of dimensions that can be analyzed depends on how many statistical samples can be gathered prior to testing. The advantages to be gained from a multidimensional hypothesis testing is that, in the limit, one can use all the information embodied in the reconstructed image intensities.

CONCLUSION

The main purpose of this paper was to describe two direct 3-D image reconstruction algorithms involving a convolve-and-backproject approach. One of these, the 3-D divergent ray reconstruction algorithm, could be useful in radiographic NDE, in that it is amenable to a real-time implementation.

In addition, the statistical aspects of acceptance-rejection criteria were described. Several possible tests for defects were presented.

REFERENCES

1. See, for example, "Proceedings of the ARPA/AFML Review of Progress in Quantitative Nondestructive Evaluation," Third Annual Report, AFML-TR-78-55, under Contract F33615-74-C-5180, May 1978.
2. B.P. Hildebrand and D.E. Hufferd, "Mapping Residual Stress Fields by Ultrasonic Tomography," *ibid.*, pp. 131-136.
3. J.D. Young and F.L. Lederman, "Quantitative Ultrasonic Tomographic Imaging," *ibid.*, pp. 137-140.
4. Special Issue on Physical and Computational Aspects of 3-Dimensional Image Reconstruction, *IEEE Trans. on Nucl. Sci.*, Vol. NS-21, No. 3, June 1974.
5. R.A. Brooks and G. DiChiro, "Principles of Computer Assisted Tomography (CAT) in Radiographic and Radioisotopic Imaging," *Phys. Med. Biol.*, Vol. 21, No. 5, pp. 689-732, September 1976.
6. R.M. Mersereau and A.V. Oppenheim, "Digital Reconstruction of Multi-Dimensional Signals from Their Projections," *Proc. IEEE*, Vol. 62, No. 10, pp. 1319-1338, October 1974.
7. R. Gordon and G.T. Herman, "Three-Dimensional Reconstruction from Projections: A Review of Algorithms," *Int. Rev. Cytol.*, Vol. 38, pp. 111-151, 1974.
8. G.T. Herman, A.V. Lakshminarayanan and A. Naparstek, "Convolution Reconstruction Techniques for Divergent Beams," *Comput. Bio. Med.*, Vol. 6, pp. 259-271, 1976.

9. J.W. Beattie, "Tomographic Reconstruction from Fan Beam Geometry Using Radon's Integration Method," IEEE Trans. on Nucl. Sci., Vol. NS-22, pp. 359-363, 1975.
10. Z.H. Cho and J.K. Chan, "A Comparative Study of 3-D Image Reconstruction Algorithms with Reference to Number of Projections and Noise Filtering," IEEE Trans. on Nucl. Sci., Vol. NS-22, pp. 344-358, 1975.
11. G.N. Ramachandran and A.V. Lakshminarayanan, "Three-Dimensional Reconstruction from Radiographs and Electron Micrographs: Application of Convolution Instead of Fourier Transforms," Proc. Nat. Acad. Sci. U.S., Vol. 68, pp. 2236-2240, 1971.
12. B.K. Vainshtein and S.S. Orlov, "Theory of the Recovery of Functions from Their Projections," Soviet Physics-Crystallography, Vol. 17, No. 2, pp. 213-216, September-October 1972.
13. S.S. Orlov, "Theory of Three-Dimensional Reconstruction: I, Conditions for a Complete Set of Projections," Sov. Physics-Crystallography, Vol. 20, No. 3, pp. 312-314, May-June 1975.
14. S.S. Orlov, "Theory of Three-Dimensional Reconstruction: II, The Recovery Operator," Sov. Physics-Crystallography, Vol. 20, No. 4, pp. 701-709, July-August 1975.
15. R.V. Denton, B. Friedlander, and A.J. Rockmore, "Direct Three-Dimensional Image Reconstruction from Divergent Rays, to be published in IEEE Trans. on Nuc. Sci.
16. B.K.P. Horn, "Density Reconstruction Using Arbitrary Ray-Sampling Schemes," Proc. IEEE, Vol. 66, No. 5, pp. 551-562, May 1978.
17. S. Zacks, The Theory of Statistical Inference, John Wiley, 1971.
18. R.O. Duda and P.E. Hart, Pattern Classification and Scene Analysis, John Wiley, 1973.
19. Sidhartha Maitra, "Moment Invariants," Proc. IEEE, Vol. 67, No. 4, pp. 697-699, April 1979.
20. A.K. Jain and W.G. Waller, "On the Optimal Number of Features in the Classification of Multivariate Gaussian Data," Pattern Recognition, Vol. 10, No. 5/6, 1978.

SUMMARY DISCUSSION
(R. V. Denton)

Norman Bleistein (Denver Applied Analytics): I would like to make a suggestion as to why that cross product doesn't matter that much. If you look back in Fourier space, you're merely using high-frequency data. The point is, for high-frequency data the stationary phase contribution is the region where X and L are parallel. But that part vanishes due to the cross product.

R. Denton: I tend to agree with that.

#

PROGRESS ON A MATHEMATICAL INVERSION TECHNIQUE FOR NON-DESTRUCTIVE EVALUATION

H. Bleistein and J. K. Cohen
Denver Applied Analytics
Denver, Colorado 80222

ABSTRACT

Last year, computer output was presented for synthetic pulse-echo data which was processed according to a mathematical imaging technique. This technique was based on the physical optics farfield inverse scattering (acronym, POFFIS) formalism for scattering by volume defects. This year, a number of theoretical advances have been made in the POFFIS formalism, with attendant revisions in the computer algorithm.

Firstly, a revised POFFIS formalism was developed in which the surface of the scatterer is directly related to the scattering data. In this formalism, aperture limited scattering data yields an image of a corresponding aperture of the scattering surface of the defect. Secondly, this formalism will also yield an image of the scattering surface of a crack. Thirdly, for true amplitude data, the impedance or reflection coefficient may be read directly from the computer output. Related to this last result was the elimination of an "image fading" phenomenon at certain critical angles. Fourthly, the computer algorithm, which was originally designed to process data for a spherically symmetric "trailer hitch", was modified (and tested) to process data when the range to the center of the coordinate system was different at each observation angle. Fifthly, the algorithm was modified (and tested) to process data when the average propagation speed varied with angle.

Implementation on a real data set is discussed.

INTRODUCTION

A major objective of our present research in this program is to develop a technique for generating images of flaws inside the titanium "trailer hitch" samples described by Tittmann, et al. [1] from pulse-echo or backscatter data. The mathematical basis of the method used for generating these images is called the Physical Optics Far Field Inverse Scattering identity - to be referred to below by the acronym POFFIS.

As is implied by the term "physical optics", this is a high frequency method with "high" in practice meaning that the product (ka) of a typical wave number (k) and typical radius of the flaw (a) ranges between 3 and 7, however in the application below, the range was 1.2 to 7.

The term "far field" means that for this implementation the size of the flaw to be imaged is "small" compared to the distance from the flaw to the outer surface of the test object.

Parenthetically, it should be noted that the authors have developed mathematical inversions for the case of non-far-field data [2] and for non-far-field and wide band data [3] in two and three dimensions. The latter does not lend itself to implementation with state of the art computers but, for high frequency data, a computer algorithm based on this inversion technique has been successfully implemented for both synthetic and real seismic data. The ka range was 3 to 7, slightly better for a high frequency theory than the above cited range used in the NDE problem.

THE POFFIS IDENTITY

The POFFIS formalism used here is based on an acoustic model of scattering of "probe" signals by the flaw. However, it can be shown that, for back-

scatter, this does yield the dominant contribution in the case of elastic wave scattering, as well. The scattered signals in the host (titanium) medium are represented by a Kirchhoff integral over the surface of the flaw of the values of the scattered field and its normal derivative. In the high frequency limit, these surface values are approximately proportional to the values of the incident (probe) field and its normal derivative, the constant of proportionality being (plus or minus) the reflection coefficient. These physical optics approximations are often credited to Kirchhoff. (Recent extensions of the physical optics or Kirchhoff approximations to the elastodynamic case by Achenbach, et al. [4] make the extension of the entire theory to the elastic case quite imminent).

The fundamental POFFIS identity was developed by Bojarski [5] and was subsequently refined by the present authors and others [6, 7, 8, 9, 10, 11, 12, 13, 14, 15]. This identity relates the Fourier transform of the characteristic function of the scattering domain to the phase and range normalized backscattered field. The characteristic function of the scattering domain is equal to unity in that domain and zero outside. Thus knowledge of this function is sufficient to create an image of the flaw. The phase and range normalizations account for geometric spreading and delay time of propagation to and from the probe.

Fourier inversion would require the use of full band width data, however, there are both practical and theoretical problems associated with the use of low frequency data in the POFFIS identity. Firstly, the low frequency data is often not available. Secondly, even when it is available, its use in a formula derived on the assumption of high frequency data, is suspect. Until recently, the problem of inversion without the use of low frequency data was overcome by a technique whose mathematical justification was developed in a ser-

ies of papers [13, 14, 15]. The basis of the technique was to apply Fourier inversion to yield a directional derivative of the characteristic function itself. The directional derivative is the product of a direction cosine and a Dirac delta function which peaks on the boundary of the scattering domain. In the above cited references it was shown that in two and three dimensions, the delta function behaves asymptotically (for high frequency) just like its one dimensional analog, namely, like a difference of "sinc" functions which peak at the peak of the delta function.

A computer program implementing these ideas was developed last year [16] and tested extensively on synthetic data. However, two disadvantages of this method remained to be overcome. Firstly, the direction cosine mentioned above is zero when the directional derivative is tangent to the (unknown) scattering surface. This leads to "image fading" in certain directions. Secondly, even when this is not the case, one must correct for this direction cosine in a post-processing step in order to estimate the impedance coefficient across the surface of the flaw. In practice, this step proved to be the least accurate of the implementation.

Motivated largely by these shortcomings, a computer algorithm was developed during this past year with an entirely new theoretical basis. In this revised formulation, the phase and range normalized far field scattering amplitude is shown to be proportional to the Fourier transform of the singular function of the scattering surface. The singular function is defined to be a Dirac delta function which peaks on the scattering surface. Thus, knowledge of this function provides a means of imaging the scattering surface, with no "image fading". Furthermore, as we shall show below, the impedance coefficient can be estimated in a straightforward manner from the output of the computer program.

Another major advance of this new result is that the scattering surface need no longer be the closed boundary of an inclusion, but could be an open surface, i.e., a crack.

Mathematically, the singular function may be defined in one of the following ways. Firstly, given a surface, S , let us introduce surface coordinates u, v on S and a third coordinate s normal to S , as shown in Fig. 1. Then we denote positions in three-space by $x = (x_1, x_2, x_3)$ and we denote

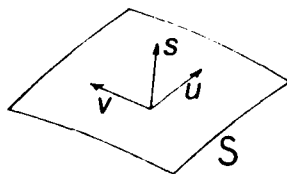


Fig. 1

the singular function by γ , this function is defined by

$$\gamma(x(s, u, v)) = \delta(s) \quad (1)$$

where δ denotes the Dirac delta function. Alternatively, if the surface is described by $z(x) = 0$, then

$$\gamma(x) = \delta(z(x)) \quad (2)$$

These two definitions can be shown to be equivalent. In particular, the gradient factor in the second definition assures that the line integral of the singular function through the surface is equal to unity.

The Fourier transform of γ is defined as

$$\gamma(k) = \int d^3x \gamma(x) \exp(-i k \cdot x) \quad (3)$$

By exploiting the singular nature of γ , this integral can be rewritten as a surface integral

$$\gamma(k) = \int_S dS \exp(-i k \cdot x) \quad (4)$$

In practice, γ can only be observed in some band limited range of the values of the magnitude k of the vector k . Thus, the following function is introduced:

$$\gamma_B(k) = \begin{cases} \gamma(k) & k_- \leq k \leq k_+ \\ 0 & \text{otherwise} \end{cases} \quad (5)$$

with k_{\pm} the handlimits of interest.

The POFFIS identity for the singular function of the scattering surface is as follows:

$$R \gamma_B(k) = 8\pi i r \omega^{-1} u_S(r, \omega) \exp(-2i \omega r/c) \quad (6)$$

$k_- \leq k \leq k_+$

The quantities in this expression are described in the following list:

- R reflection coefficient.
- r range to the region of the scattering surface.
- ω frequency in radians/second.
- u_S backscattered impulse response.
- c speed of propagation in the host medium (in this case, the titanium ball).

The value of k is given by

$$k = 2\pi/\lambda/c \quad (7)$$

while the direction, k , is given by

$$k = r \sin \theta \quad (8)$$

Here r is the direction of the source-receiver, $r = r \hat{r}$. This result is derived in [2] by the authors.

When observations of the backscatter are made in all directions r , then Fourier inversion in (6)

produces a three dimensional "sinc" function, i.e., the band limited singular function. This function peaks on the scattering surface. When observations are made over some limited range of aspect angles, then Fourier inversion of (6) produces the band limited singular function in the region where the normal to the surface S is in the range of back-scatter directions of observation. Outside of this range of directions, the inversion produces a tangential continuation of the aspect-angle-limited surface. If the scattering surface has an edge and the normal to the edge is within the range of observation directions, then the Fourier inversion will reproduce the edge "sharply". Both theoretical support and computer demonstration of these results can be found in the above cited references or in [17].

In particular, we state the following result from [2] on the asymptotic inversion of (6).

$$R_{\gamma_r}(x) \begin{cases} R(1-v_1\kappa_1s)^{-1/2}(1-v_2\kappa_2s)^{-1/2} \frac{\sin k_+s}{\pi s} & k_+ > k_- \\ R(k_+ - k_-)/\pi & s = 0 \end{cases} \quad (9)$$

Here, s is the coordinate shown in Fig. 1; κ_1 and κ_2 are the principle curvatures at the point on S back along the normal to S from x ; v_1 and v_2 are equal to ± 1 according to whether $(+1)$ or not (-1) x is on the same side of S as the center of curvature associated with $\kappa_{1,2}$.

One can verify from (9) that asymptotically $R_{\gamma_r}(x)$ peaks at $s = 0$, i.e., on the scattering surface. Furthermore, multiplication of the peak value by π and division by the bandwidth provides an estimate of the reflection coefficient and, hence, a means of classifying the material inside the flaw (with void a special case of inclusion).

COMPUTER IMPLEMENTATION

Our original computer implementation was based on the assumption of a homogeneous, spherical "trailer hitch" test object. Precision experiments carried out by experimentalists at Rockwell (B. Tittmann, J. Martin and R.K. Elsley) made it apparent that these were unreasonable assumptions. The asphericity of the test objects proved to be on the order of 200 microns. The velocity variations are on the order of 100 m/s. Each of these leads to ranging variations on the order of 400 microns. Since we are seeking to image flaws with radial values ranging from 100-600 microns, these are clearly unacceptable errors.

To overcome these difficulties, two extensions of the basic computer algorithm were required, namely, that both r and c in (6) were allowed to be functions of r . The assumption $r = r(r)$ is implicit in (6) and thus this extension required only a revision of the computer algorithm. Accommodation of $c = c(r)$ is somewhat more ad hoc in that (i) this is not, in fact, a true model of the inhomogeneous host medium and (ii) in a rigorous theory, this would change the dispersion relation (7) and make the identity (6) invalid. Nonetheless, the assumption $c = c(r)$ was also incorporated into the algorithm with (7) assumed valid under this assumption. Synthetic tests were performed and showed errors of less than 5% in the location

of the scattering surface and of less than 10% in the estimation of the reflection coefficient. For these tests, $3 < ka < 7$.

This extension should be viewed as a temporary measure to allow us to process the experimental data to be described below. The present experimental procedure requires a separate set of "control" experiments to estimate $c(r)$ and $r(r)$. In cooperation with the experimentalists at Rockwell, two alternative procedures have been proposed. In both procedures, wider band (including low frequency) experiments will be performed at each observation angle. In each procedure, the gain of performing a single wideband experiment in each direction of observation is counterbalanced by a loss of precision (on the order of 200-600 microns) in the absolute location of the flaw. This is viewed as a small loss and hence a worthwhile tradeoff. Since both of these procedures are conjectural and tentative and it is unclear which (if either) will ultimately be implemented, they will not be described at this time.

APPLICATION TO REAL DATA

We turn now to a description of the computer implementation of the Fourier inversion of (6) as applied to a real data set on a trailer hitch sample. The computer algorithm performs the three dimensional inversion in polar coordinates, integrating in $k = |k|$ and over the angles of observation k . The algorithm is designed to discretize the unit sphere over L latitudes and $2L$ longitudes, for $2L$ data points in all. In the experiments performed, $L = 7$, so that there are 98 directions over the entire sphere or about 12 observations required per octant. In fact, data was gathered in only 30 directions, 5 latitudes and 6 longitudes.

The algorithm requires, at present, an accurate recording of "zero time" for each experiment. This is defined to be the time when the peak of the pulse enters the trailer hitch from the transducer. It was assumed that for each of the 30 backscattered records, the zero time preceded the turn-on time of the record by the same amount.

To find this zero time (once and for all for this transducer) a separate experiment was performed on a cylindrical sample. The first two reflections off the flat surface to a transducer on the opposite flat surface were recorded. Observing the time between peaks and measuring back from the first peak an equal time provided our estimate of zero time.

A second trailer hitch with a known spherical void was used to estimate the speed variations $c(r)$. In fact, the speed was assumed to be a function of latitude alone and only five experiments were performed. Implicit in this means of finding speeds is the assumption that this lateral-only variation is similar from one trailer hitch to another. Furthermore, it was assumed that the trailer hitches were in fact spherical and the spherical void of the control object was indeed a well-centered sphere. Thus, all the burden of angular variations of the variables in (6) as well as all the possible inaccuracies of the control were imposed on the five values of the speed c . The values calculated are given in Table I, as a function of polar angle.

Table I

θ	c
31.0	6032.9
55.15	6086.2
73.40	6133.6
90.0	6147.3
106.60	6106.4

One further experiment was performed in which the signal from the transducer was introduced into a hemispherical sample. The reflection from the flat surface was used as a reference source for the purpose of deconvolution of the experimental records to provide the equivalent impulse response.

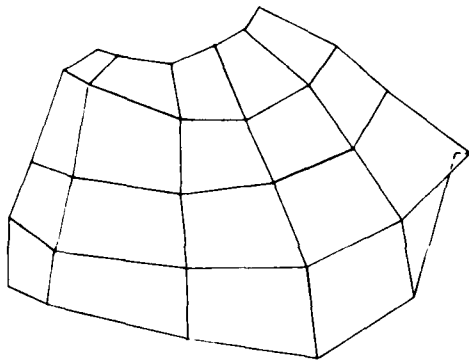


Fig. 2

The result of processing the data is shown in the perspective plot, Fig. 2. The output depicts slightly more than an octant of a flaw which is oblate and not symmetric with respect to the vertical axis. In fact, the flaw is known to be an oblate spheroid with diameters 400 μm by 800 μm . For such a body, tabulation in polar angle of r as a function of θ may be carried out. In particular, the value of r at 31° is 223 μm . The output of the experiment was 210 μm at the first three azimuthal angles and 240 μm at the next three. At the equator, the values were 270, 300, 300, 345, 360, 390 μm with varying azimuth. While the latter values are extremely good the first three are somewhat less satisfactory. It should be noted, however, that near the equator, $1.2 < ka < 3.6$, with a the radius of curvature at the equator. Thus, in addition to all of the uncertainties described above, the theory itself is only marginally valid here and certainly less so than at $\theta = 31^\circ$ where both the bounds on ka are double of the above cited values. Therefore, these values are considered to be more than satisfactory.

PHYSICAL OPTICS INVERSION NOT IN FAR FIELD

When it is not assumed that the scattering surface(s) is in the far field, the following integral equation may be derived for the singular function.

$$u_s(r, \omega) = -\frac{i\omega R}{8\pi^2 c} \int \frac{\gamma(x) \exp(2i\omega|x-r|/c)}{|x-r|^2} dv. \quad (10)$$

Remarkably, this integral equation has an analytical inversion, namely,

$$R \tilde{\gamma}_B(k) = -2\pi i c^2 k_3 \omega^{-1} \frac{\partial \tilde{u}_S(k_1, k_2, \omega)}{\partial \omega}. \quad (11)$$

Here (\tilde{u}_S) denotes a transverse spatial transform of the observed data and the dispersion relation is

$$k_3 = \text{sgn } \omega \sqrt{\omega^2 - k_1^2 - k_2^2}. \quad (12)$$

This result was derived in the context of the seismic inversion problem under the assumption that the backscattered data is observed on a flat ($r_3 = \text{const.}$) surface. It is clearly equally applicable to the non-destructive testing problem with similar geometry in the case where the far field approximation is invalid.

While (10) is a Fredholm integral equation of the first kind, the integral operator is non-compact and the inversion of the integral equation is well conditioned. The asymptotic solution (11) shows a division by ω ; the exact solution contains only one other term with a division by ω^2 . However, in three dimensions these factors are counterbalanced by a factor of $\omega^2 = c^2(k_1^2 + k_2^2 + k_3^2)$ in the volume element of the Fourier inversion. Thus, perturbations of the data near $\omega = 0$ cause no excessive perturbations of the solution. Furthermore, the differentiation $\partial/\partial\omega$ is equivalent to the Fourier transform of the data multiplied by t . Thus, for an appropriate class of data (e.g., experiments which are turned off after a finite time) this differentiation causes no ill-conditioning. Finally, in real world problems, there is always an upperbound on the frequency range of the observations. In this case, perturbations of the data which are too small (e.g., on the order of a half-wave-length or less at maximum frequency) will produce too small (e.g., zero) a perturbation in the solution. This is not ill-conditioning, in which small changes in the data produce unacceptably large changes in the solution, but is merely a demonstration of the uncertainty principle. Thus, for all practical purposes, the inversion (11, 12) or (10) is well-conditioned. It is our experience that this is generally true of this class of linearized inverse problems.

ACKNOWLEDGEMENTS

The authors wish to express their gratitude to Willene Grady for her fine programming, to J. Martin, B. Tittmann and R.K. Elsley of Rockwell International for their efforts in obtaining experimental data and to Corinne Ruokangas of Rockwell International for her supportive programming efforts.

This research was sponsored by the Center for

Advanced NDE operated by the Science Center, Rockwell International, for the Advanced Research Projects Agency and the Air Force Materials Laboratory under contract F33615-74-C-5180.

REFERENCES

- [1] Tittmann, B.R., Elsley, R.K., Nadler, H. and Cohen, E.R., "Experimental Measurements And Interpretation of Ultrasonic Scattering By Flaws", Interdisciplinary Program for Quantitative Flaw Definition - Special Report Third Year Effort, prepared by Rockwell International Science Center for ARPA, AFML, D.O. Thompson, Program Manager.
- [2] Cohen, J.K., and Bleistein, N., "The Singular Function Of A Surface And Physical Optics Inverse Scattering", Wave Motion, 1, 153-61, (1979)
- [3] _____, "Velocity Inversion Procedure For Acoustic Waves, Geophysics, 44, 6, June 1979, pp. 1077-1087.
- [4] Achenbach, J., Viswanathan, K., Norris, A., "An Inversion Integral For Crack Scattering Data", Wave Motion, to appear.
- [5] Bojarski, N.N., "Three Dimensional Electromagnetic Short Pulse Inverse Scattering", Syracuse New York, NTIS, # AD-845 126 (1967).
- [6] Lewis, R.M., "Physical Optics Inverse Diffraction", IEEE Transactions on Antennas and Propagation, AP-17, 3, 308-314 (1969).
- [7] Bojarski, N.N., Inverse Scattering, Company Report #N00019-73-C-0312/F, prepared for Naval Air Systems Command, AD-775 235/5 (1974).
- [8] Perry, W.L., "On The Bojarski-Lewis Inverse Scattering Method", IEEE Transactions on Antennas and Propagation, AP-22, 6, 832-839 (1974).
- [9] Tabarra, W., "On An Inverse Scattering Method", IEEE Transactions on Antennas and Propagation, AP-21, 245-247 (1973).
- [10] _____, "On The Feasibility Of An Inverse Scattering Method", IEEE Transactions on Antennas and Propagation, AP-23, 446-448 (1975).
- [11] Rosenbush-Raz, S., "On Scatterer Reconstruction From Far Field Data", IEEE Transactions on Antennas and Propagation, AP-24, 66-70 (1976).
- [12] Bleistein, N., "Direct Image Reconstruction Of Anomalies In A Plane Via Physical Optics Far Field Inverse Scattering", J. Acoustical Soc. Amer., 59, 2, 1259-1264 (1976).
- [13] _____, "Physical Optics Far Field Inverse Scattering In The Time Domain", J. Acoustical Soc. Amer., 60, 6, 1249-1255 (1976).
- [14] Mager, R.D., and Bleistein, N., "An Examination Of The Limited Aperture Problem Of Physical Optics Inverse Scattering", IEEE Transactions on Antennas and Propagation, AP-25, 5, 695-699 (1978).
- [15] Armstrong, J.A., and Bleistein, N., "An Analysis Of The Aperture Limited Fourier Inversion Of Characteristic Functions, University of Denver Mathematics Department Report #MS-R-7812 (1978).
- [16] Cohen, J.K., Bleistein, N., and Elsley, R.K., "Nondestructive Detection Of Voids By A High Frequency Inversion Technique", Proceedings of the ARPA/AFML Review of Progress in Quantitative NDE, Science Center, Rockwell International, D.O. Thompson, Program Manager.
- [17] Cohen, J.K., and Bleistein, N., "The Role Of The Kirchhoff Approximation In Velocity Inversion", preprint.

SUMMARY DISCUSSION
(N. Bleistein)

Unidentified Speaker: Just a quick question. You made a comment in your talk having to do with the amount of calculations you can do and the amount of number-matching, arithmetic, you can do. You said that the more number-matching you do, the worse the result gets.

Norm Bleistein: What I was saying is that if I have to correct to the cosine factor after the fact -- you know, it's like post-processing arithmetic where I got to use three pieces of data to know where the normal to the surface is, but I got to take -- I have to correct for directional derivatives with the normal. It's not a nice kind of calculation to do, and I would prefer not to do it. It turns out that now, because of the extra (inaudible) I don't have to do it at all. That cosine factor is no longer in the problem. It's just eliminating a post-processing problem. It has nothing to do with the direct number punching. The method you quoted is really a Fourier type integration, extremely stable. There was noise in this data. The line along the equator, every set of data points along the equator was noisy because that's where these pieces of fusion bonded, and you could see both in the time record and in the Fourier transform record. The Fourier transform of the signal along the equator, 10, 15 percent noisier. Really jumped. In fact, that showed up in one of Bernie's pictures yesterday or well (inaudible) did not mess up the method at all, and it's really what we expect because we're doing integration. We never do differentiations; we never do divisions.

Unidentified Speaker: For the sake of the trailer hitch, what kind of accuracy did you require on your velocity data?

Norm Bleistein: I will give you some numbers for that. Every seven meters per second makes an error of 30 microns. All right? But now what I'm saying is: by using low-frequency measurements, we can make that be an error in absolute location rather than an error in the size of the flaw. That's what I really expect we're going to have. That's also what our preliminary analysis shows. And Dick reminded me of that yesterday, and Jim mentioned it the other day, and I'm dense, and it finally got through. So, that's the point. In other words, how you want to set errors in the velocity. And you will likely make errors on the order of 200 microns of the absolute locality of the flaw, but the errors on the order of 30 microns in the size of the flaw. All the processing for all those 30 lines, ten seconds on a CDC 6600, less than ten seconds on a cyber 76 to do that processing.

David Lee (Applied Mechanical Res. Lab-WIAFB): You seem to be coming perilously close in this last point to saying something which I'm sure you're not saying, i.e., that Fourier inversion is a boundary operation.

Norm Bleistein: If I look at Fourier integrals (inaudible) Fourier integral units, plus or minus (inaudible) therefore, that's not an ill-posed problem doing Fourier inversion. Fourier discretization gives you all the eigen values on the same circle, all right? I do not use a stiff matrix. If you discretize the Fourier transform, the one integral inverse problems are not exact operators with integrals bounded away from zero. If you discretize incorrectly, you make a whole column of zeroes in the matrices' discretization, and that's what people regularly do. If you discretize properly, you can bound the integrals away from zero to discrete problems, which is only just because a continuous problem has no values. When you do that the dumbest kind of inversion works.

David Lee: That seems very strange because I think it exhibits functions everywhere different wherever you please.

Norm Bleistein: That's because what you're doing, you can always do that when you take the perturbation of the function, integral perturbation, to be less one over delta K where within the scale --

David Lee: Oh, sure.

Norm Bleistein: I can't do it.

David Lee: Okay, fine.

Norm Bleistein: If you ask me to do that.

(continued)

N. Bleistein (continued discussion)

David Lee: The last contradicts what you're saying and what the facts are.

Gordon Kino (Stanford University): I think you can't get super resolution unless you --

Norm Bleistein: That's right. ΔK times ΔX is a half or something like that.

Gordon Kino: If you try to overdo it, you're in trouble.

Norm Bleistein: We all agree on that.

#

APPLICATION OF ADAPTIVE LEARNING NETWORKS FOR THE CHARACTERIZATION OF TWO-DIMENSIONAL AND THREE-DIMENSIONAL DEFECTS IN SOLIDS

M. F. Whalen
L. J. O'Brien
A. N. Mucciardi

Adaptronics, Inc.
McLean, Virginia 22102

ABSTRACT

The objective of the work was to develop an ultrasonic inversion procedure which (1) discriminates, (2) sizes, and (3) determines the orientation of two-dimensional (crack-like) and three-dimensional (void-like) defects in materials. Adaptive learning networks (ALN's) were used to estimate directly the defect size and orientation parameters from the spectrum of the echo transient. A 19-element hexagonal synthetic array measured the scattered field within a 60-degree solid angle aperture. The ALN's were trained on theoretically generated spectral data where the crack forward scattering model was based on the Geometrical Diffraction Theory and the void model was based on the exact Scattering Matrix Theory. The theoretically trained models were evaluated on both theoretical and experimental data. Excellent results were obtained, and the errors for size and orientation estimates were, in general, less than 10%.

The significance of this work is that: (1) the ALN approach to defect characteristics provides a systematic procedure for discovering relationships in the data which could otherwise be overlooked, and (2) significant economic benefits can be gained by simulating difficult-to-produce defect reflector scenarios. Furthermore, a result of this work has been the development of an algorithm which can ultimately be applied in field and industrial use.

SUMMARY OF RESULTS, CONCLUSIONS, AND RECOMMENDATIONS

Table 1 presents the relative errors for the nine ALN models developed in this study and evaluated on both theoretical and experimental data. Models 1 through 4 were trained to estimate the four parameters of the 3-dimensional spheroid models; 5 through 8 were trained to estimate the four parameters of the 2-dimensional crack; Model 9 was trained to discriminate between the spheroid and crack and, thus, to act as a selector for the appropriate size model.

Table 1. ALN Model Results Summary

Model No.	Model Type	Parameter	Theoretical Relative Error (%)	Experimental Relative Error (%)
1	Spheroid	A	9	23
2	Spheroid	B	8	6
3	Spheroid	α	5	7
4	Spheroid	β	1	4
5	Crack	A'	15	10
6	Crack	B'	14	5
7	Crack	α'	4	3
8	Crack	β'	2	0
9	Spheroid/Crack		0	11

The symbols A, B, α , and β are the size and orientation parameters for oblate spheroid defects, and A', B', α' , and β' are the size and orientation parameters for elliptical cracks. A separate ALN model was trained for each parameter. Model 9 was the network trained to discriminate crack-type defects from spheroidal defects.

The parameter easiest to estimate for both spheroids and cracks was the azimuthal orientation angle (respectively, β and β'). Both theoretical and experimental errors were less than 5%. The final ALN's were dependent mainly on the total power distribution in the array.

The polar defect angle (α and α') also depended mainly on the distribution of power for both defect types. The theoretical errors of 5% for spheroids and 4% for cracks is excellent when one considers that the array elements were 30° apart. The experimental errors for these networks were also very low as indicated in Table 1.

The size parameters for spheroids depended mainly on shifts in the low-frequency energy. The first spectral moment and the relative energy in the low-frequency band (1-2 MHz) were selected for both A and B. Features of the characteristic function $|Y(r)|$, also selected for A, are sensitive to low frequency spectral shifts. The size parameters for cracks were mainly dependent on ripple period type features.

The larger size parameter (B and B') was estimated with theoretical errors of 8% for spheroids and 14% for cracks. For both defect types, the smaller defect dimension (A and A') yielded the largest error when evaluated on experimental data. However, note in Table 1 that the theoretical error for spheroids is only 9%. This means that the variation in the experimental spheroid data was the probable cause of the high error. In the case of cracks, the error in the minor axis was due to the poor resolution of the ripple period for small cracks. This resolution could be increased by using a maximum entropy technique for measuring the ripple period.

The variation inherent in the experimental data is shown in Fig. 1. These waveforms were recorded in the pulse-echo model at eight different azimuthal locations from a 200 μm by 400 μm oblate spheroid defect, but the polar angle between transducer and defect axis remained constant at 60° . Hence, all waveforms should be identical. Note, however, that differences in peak amplitudes vary up to 4.7 dB. Also, the waveforms taken at $\psi = 0, 45$ and 90° have quite different shapes compared to the others. These variations could be caused by: (1) anisotropies in the host metal; (2) undesirable reflections from the diffusion bond plane; (3) uneven coupling; or (4) beam-steering due to polarized grains. Undoubtedly, these contributed to the error in the ALN size and orientation estimates, such as the 23% error for A in Table 1. This experimental variation leads to an "irreducible error" source because it provides a lower bound to the modeling error. This lower bound is not known at present but, as seen in Fig. 1, it is certainly not zero.

The ALN trained to discriminate cracks from spheroids yielded 100% discrimination accuracy when evaluated on theoretical data. The experimental error was 11% when evaluated on the nine spheroid experiments. Unfortunately, no experimental pulse-echo crack data were available to process through this network.

CONCLUSIONS

- Adaptive learning network models provide an accurate and practical means for inverting scattered data from defect reflectors when the ALN's are trained on theoretical data and evaluated on experimental data. This approach allows spectral features to be combined in an optimum fashion.
- The defect orientation for both cracks and spheroids can be determined primarily from the distribution of total power in the 19-element hexagonal array.
- A significant factor in estimating the size of spheroidal defects is the percentage of energy in the low-frequency (long wavelength) region. The size parameters for cracks can best be found from the spectral ripple period.
- The SMM (T-Matrix) Theory for spheroids provides a reasonably good match to experimental data, especially in the long wavelength regime and in the total power distribution.
- The Geometrical Diffraction Theory provided very good agreement with experimental data for ka less than 10. Above this range, the

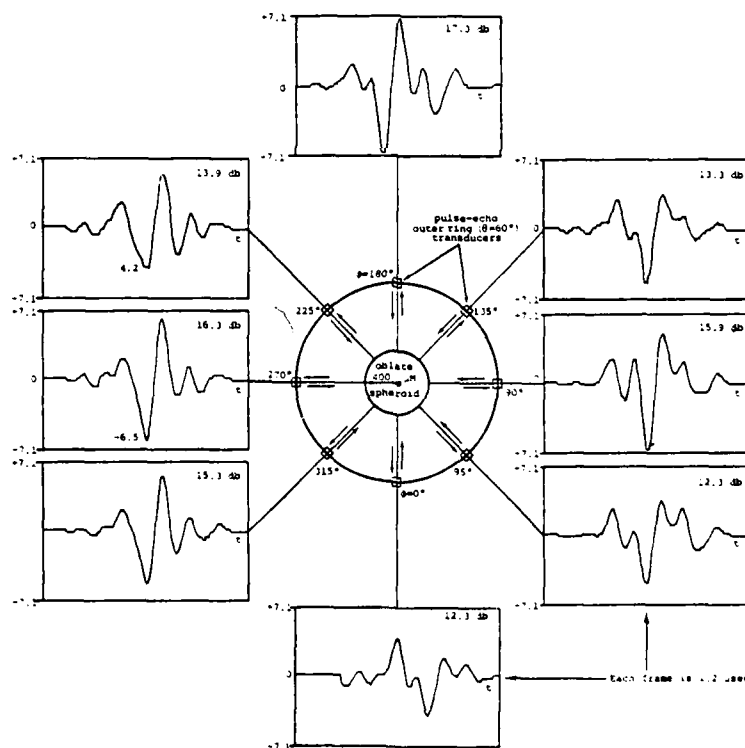


Fig. 1 Experimental pulse-echo responses from a 200 by 400 micron oblate spheroid showing the variance in the data. All experimental waveforms should be identical. The defect axis of symmetry is normal to the page. The transducers are located on the outer ring ($\psi=60^\circ$). (db values are derived from mean peak-to-peak levels.)

spectral ripple period still provided a good match, but the spectral amplitude underwent considerable attenuation for the experimental data, not observed in the theory. In this report, a method was devised for correcting the experimental data for this attenuation.

- Deconvolution, which is inherently an unstable numerical process at the band limits, can be stabilized considerably by adding a complex quantity called the "epsilon factor" to the reference signal before performing the deconvolution.

RECOMMENDATIONS

The following recommendations are suggested for future work:

- Investigate prolate spheroids in a manner similar to the work performed for oblate spheroids. This should include a comparison of theory and experiment, development of an inversion procedure, and development of a discrimination logic between oblate and prolate spheroids.
- Formulation of inversion procedure for semi-elliptical cracks growing from a free surface. This analysis could be directly applied to many practical and timely problems. Examples of free-surface cracks are intergranular stress corrosion cracks in stainless steel pipe welds, thermal fatigue cracks in nozzle forgings, and fatigue cracks under fasteners.
- Retrain the crack inversion model, including the third orientation angle, γ . This angle was assumed to be 90° in the present work. γ is the spin around the major axis.
- Process data from irregular-shaped compound void samples through the existing ALN inversion logic. This would serve as a further evaluation of the present algorithm.

INTRODUCTION

Adaptronics became a contributor to the Interdisciplinary Program for Quantitative Flaw Definition in 1976 after the Second Year Effort. During the first two years, adaptive learning networks were successfully applied to the inversion of spheroidal defects. The network models were trained directly from theoretical spectral features and evaluated in a blind test on experimentally recorded defect samples. This past year's effort has been devoted to classifying and characterizing both three-dimensional (void-like) and two-dimensional (crack-like) defects as shown in Fig. 2. A discrimination network first determines if the unknown defect is crack-like or void-like in nature based on power spectral measurements computed from the spatial array. The appropriate branch is then taken to estimate the defect size and orientation parameters. In general, a different set of spectral features is needed to estimate each parameter.

As in the previous two-year effort, the ALN models were trained on theoretical data and evaluated on experimental data. The advantage of training the ALN models with theoretical data is

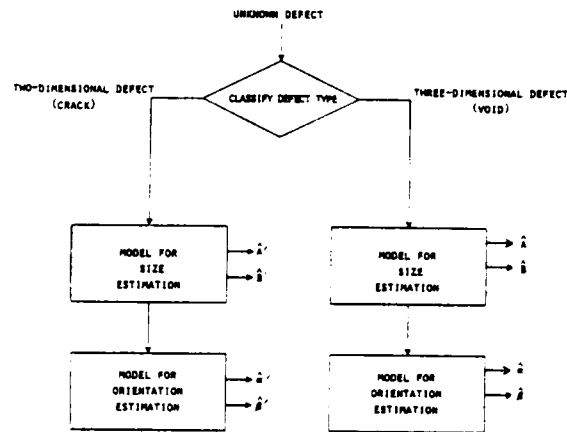


Fig. 2 Decision logic for characterization of two- and three-dimensional defects.

that the scattered field from many defect geometries can be produced quickly and at a fraction of the cost of what is required to fabricate physical defect calibration specimens. The theoretical data have the added advantage of being noise-free. Ultimately, as the theories become more sophisticated, mimicking complicated defect shapes, surface roughness, and defects in the vicinity of geometrical reflectors, data bases for field and industrial use can be generated entirely in a computer. This data base can always be augmented with experimental data as they become available.

A number of investigators have contributed in the development and evaluation of the ALN inversion models, as illustrated in Fig. 3. The forward scattering theory for spheroidal defects was provided by V. Varadan; the elliptical crack theory was developed by J. Achenbach; P. Tittmann and P. Elsley collected the experimental void data; and L. Adler provided the experimental crack data. Technical advice was also offered by J. Rose, E. Domany, and H. McMaken.

THREE-DIMENSIONAL DEFECT CHARACTERIZATION DEFECT GEOMETRY

Fig. 4 shows the characteristic size parameters (A and B) and characteristic orientation parameters (μ and ψ) for the oblate spheroid. The objective is to estimate these four parameters from the scattered energy field. The following definitions apply:

- A - minor axis (along one dimension),
- B - major axis (along two dimensions),
- μ - polar orientation: angle between positive Z -axis and symmetry axis; and
- ψ - azimuthal orientation: angle between positive X -axis and projection of the symmetry axis on the X - Y plane.

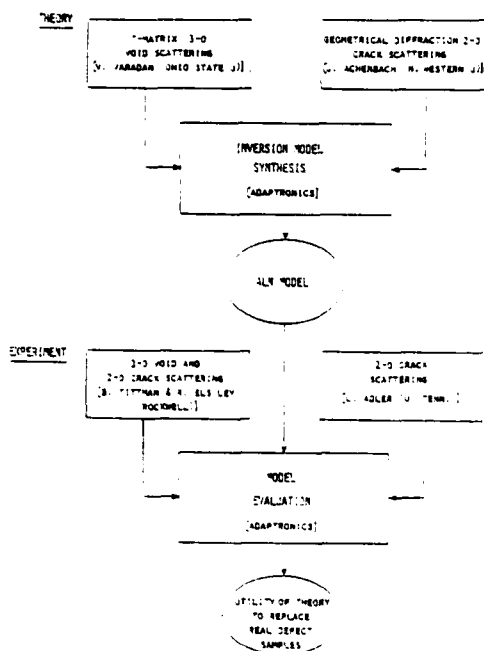


Fig. 3 Project overview.

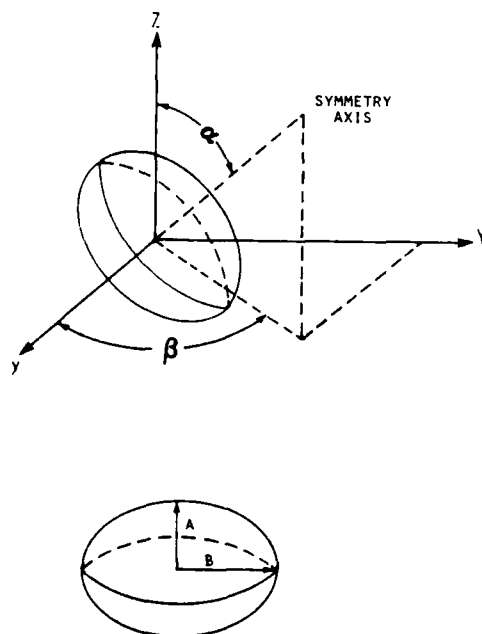


Fig. 4 Oblate spheroid coordinate geometry.

The choice for using oblate spheroids for the three-dimensional defect model was motivated by two factors:

- (1) many naturally occurring material defects can be approximated by oblate spheroids; and,
- (2) the forward scattering theory for this configuration was readily available.

THEORETICAL SPHEROID DATA BASE

A total of 240 theoretical oblate spheroid experiments were generated with the Scattering Matrix Method (SMM) forward-scattering model.¹¹ The SMM theory, developed by V. Varadan, produced the complex scattered field for both longitudinal and transverse waves given the defect geometry, host material elastic constants, transducer location, and frequency of the incident wave. Comparison of SMM generated power spectra with experimentally obtained oblate spheroid spectra has shown favorable similarity between the two (see below, "Comparison of Theoretical and Experimental Waveforms").

Each hypothetical experiment consisted of generating the complex power spectrum at 19 pulse-echo spatial positions covering a 60° solid angle aperture. The 19 transducer positions are defined below. The frequency range of the theoretically generated spectrum was 1.0-8.8 MHz in increments of 0.39 MHz which corresponds to a ka range of approximately 0.30 to 4.4.* So, information in the long and medium wavelength regimes was represented.

The elastic constants of the host material were:

$$\begin{aligned}\lambda &= .965 \times 10^{12} \text{ dynes/cm}^2 \\ \mu &= .406 \times 10^{12} \text{ dynes/cm}^2 \\ \rho &= 4.42 \text{ gm/cm}^3\end{aligned}$$

where λ and μ are the Lamé parameters and ρ is the material density. These parameters convert to longitudinal and transverse wave velocities of

$$\begin{aligned}V_L &= 6.34 \times 10^5 \text{ cm/sec} \\ V_T &= 3.03 \times 10^5 \text{ cm/sec}\end{aligned}$$

which represent the velocities in the Ti-6Al-4V experimental titanium alloy samples.

Six defect sizes, each at 40 orientations ($6 \times 40 = 240$ experiments) were represented in the theoretical data base. The smallest size was 50 μm by 300 μm , and the largest was 300 μm by 500 μm . Ten polar orientations and four azimuthal orientations were generated. Table 2 shows the theoretical data base sizes and orientations along with the specific ka ranges of each defect.

Only L-L scattering was considered in the present work.

TRANSDUCER ARRAY GEOMETRY

A 19-element hexagonal array was used to measure the scattered field. This array is illus-

*"ka" is the product of the wave number ($\frac{2\pi}{\lambda}$ = wavelength) and the defect radius (a).

Table 2. Spheroidal Defect Sizes And Orientations Represented By The Theoretically-Generated Power Spectra

Scattering Data at 40 Orientations Were Produced for Each Defect Size

SIZE NUMBER	DEFECT SIZE		KA RANGE	
	A (MICRONS)	B (MICRONS)	MINIMUM	MAXIMUM
1	50	300	0.297	2.516
2	150	300	0.297	2.516
3	100	400	0.396	3.488
4	200	400	0.396	3.488
5	100	500	0.496	4.361
6	300	500	0.496	4.361

ORIENTATION NUMBER	DEFECT ORIENTATION	
	α (DEGREES)	β (DEGREES)
1	1	65
2	10	
3	20	
4	30	
5	40	
6	50	
7	60	
8	70	
9	80	
10	89	65
11	1	150
12	10	
13	20	150
14	30	150
15	40	150
16	50	150
17	60	150
18	70	150
19	80	150
20	89	150

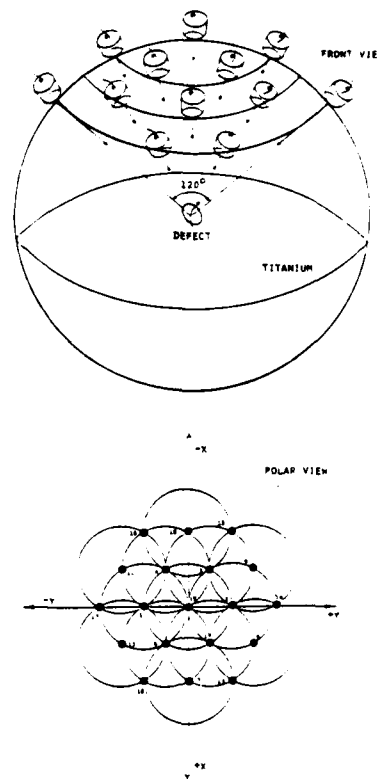


Fig. 5 19-Element hexagonal transducer array.

trated in Fig. 5. The transducer angular positions are defined in Table 3. This array is advantageous since all elements are equi-spaced. Thus, the scattered field is equally represented at all points in the aperture. Also, the hexagonal structure provides a maximum amount of coverage for a minimum number of transducers.

Table 3. Location Of Transducer Elements

TRANSDUCER NUMBER	POLAR ANGLE (DEGREES)	AZIMUTHAL ANGLE (DEGREES)
1	30	30
2	30	90
3	30	150
4	30	210
5	30	270
6	30	330
7	52	0
8	52	60
9	52	120
10	52	180
11	52	240
12	52	300
13	60	30
14	60	90
15	60	150
16	60	210
17	60	270
18	60	330
19	0	0

The 19-element array was used both for spheroidal and elliptical crack data generation. However, for generating theoretical spheroid data, the transducers operated in the pulse-echo mode; a pitch-multiple-catch mode was employed for the cracks.

EXPERIMENTAL SPHEROID DATA BASE

The experimental spheroid data were collected by the Pockwell International Science Center (RISC). This data set consisted of nine experiments recorded on two "trailer-hitch" diffusion bonded test samples with radii of

100 μ m by 400 μ m; and
200 μ m by 400 μ m.

A full description of the fabrication procedure and the sample geometry can be found in Ref. (2).

Table 4 shows the sizes and defect orientation of the nine experiments. The spherical shape of the trailer-hitch samples allowed pulse-echo data to be collected from a variety of orientations without changing the metal distance between defect and transducer.

Table 4. Sizes And Orientations Of The Nine Physically Recorded Spheroidal Defect Specimens

EXPERIMENT NUMBER	DEFECT SIZE		DEFECT ORIENTATION	
	A (MICRONS)	B (MICRONS)	α (DEGREES)	β (DEGREES)
1	200	400	0	0
2	200	400	30	225
3	100	400	90	160
4	100	400	0	0
5	200	400	90	160
6	100	400	30	180
7	200	400	30	180
8	100	400	30	225
9	200	400	15	180

Experiments 1 through 8 were conducted in May 1978 using a 5 MHz center-frequency transducer where the pulse-echo positions were those of the 17-element array employed in last year's work. Experiment 9 was conducted in May 1979 using a 7 MHz center-frequency transducer, and the 19-element hexagonal array described above. Fig. 6 shows the frequency responses of the two transducers. Note the higher frequency response of the transducer used in Experiment 9.

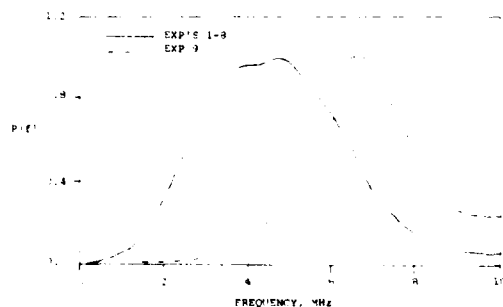


Fig. 6 Frequency responses of the two transducers used to collect experimental spheroid data.

DECONVOLUTION

Deconvolution of ultrasonic waveforms is necessary to remove the transducer response from the signal. Simple division of the defect power spectrum by the reference spectrum frequently leads to instabilities at both ends of the transducer's bandwidth.

The complex deconvolved spectrum of $Y(f)$ is given by:

$$Y(f) = \frac{X(f)}{R(f) + \epsilon(f)} \quad (1)$$

where $X(f)$ is the complex spectrum of the defect, $R(f)$ is the complex spectrum of the reference, and

$\epsilon(f)$ is a complex function having constant magnitude but whose phase is identical to that of $R(f)$. Selection of the magnitude of ϵ depends on the signal-to-noise ratio of the input $X(f)$. Typical values can range from five to twenty percent of the peak value of $|R(f)|$. The phase of ϵ was made identical to that of the reference so as not to change the phase of $R(f)$. Since all quantities in Eq. (1) are complex, the result is also complex. This allows the deconvolved spectrum to be transformed back to the time domain if the defect impulse response is desired.

Figure 7 demonstrates the effect of adding the epsilon factor. Figure 7(a) shows the pulse-echo response 32° off axis from a 200 μm by 400 μm oblate spheroid. (This is one of the receiver responses from Experiment 9.) Figure 7(b) shows the same waveform after deconvolving the reference waveform when an epsilon of zero ($|\epsilon| = 0$) was used. Note the instability at the low-frequency end of the spectrum. This instability has completely vanished in Fig. 7(c) where an epsilon of 0.1 ($|\epsilon| = 0.1$) was used. In all nine experiments, an epsilon of 0.1 was used.

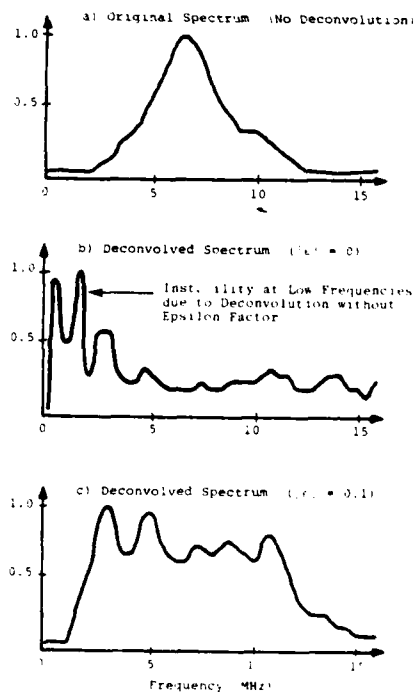


Fig. 7 Pulse-echo response from a 200 μm by 400 μm spheroid demonstrating the effect of the epsilon factor (ϵ) in stabilizing the deconvolution process.

The deconvolution reference, $R(f)$, for Experiments 1 through 8 was obtained by pulsing a transducer on one side of the trailer hitch and recording the pulse with a similar transducer on the opposite side. $R(f)$ for Experiment 9 was obtained by recording the pulse-echo transient from an 800 μm spherical void, then dividing the exper-

imental void spectrum by the theoretical void spectrum. B. Tittmann of RISC has found this latter method to be superior in determining the reference waveform.¹²

COMPARISON OF THEORETICAL AND EXPERIMENTAL WAVEFORMS

A comparison between the theoretical scattering data (SSM theory) and the physically recorded data (Experiments 1-9) has been made. Examples were found where theory and experiment matched very closely. On the other hand, there were many cases where no similarities existed between the two data types. In general, there was much variation in the experimental measurements (particularly in Experiments 1 through 8). These variations could have been caused by (a) poor transducer coupling; (b) inhomogeneities in the test sample; (c) reflections from the diffusion bond plane; and (d) electronic drift, to name a few.

The quality of the data in Experiment 9 was superior to that in the other eight. Also, the power spectra in Experiment 9 matched the theory quite well, as will be shown below. Several improvements in data collection and processing have been made in the last year which contributed to this better quality data. These include (a) use of a higher frequency transducer; (b) use of a better quality transducer shoe; and (c) determina-

tion of a better deconvolution reference using the 800 μm sphere.

Some of the better examples of power spectra, phase spectra, and characteristic functions $r(r)$, have been selected from Experiments 1 through 9 and are plotted in Figs. 8, 9 and 10 along with the functions generated from the SSM theory.

Note in Fig. 8 that the power spectra, especially at 30° incidence, match the theory very well. Excellent examples of the phase spectra (Fig. 9) have also been found. However, there were many more cases of phase spectra which did not resemble the theory (not shown).

The characteristic function shown in Fig. 10 is a function of distance (r). It has been shown that for spherical defects the inflection point of the curve is a good approximation to the sphere radius. The results shown in Fig. 10 indicate the characteristic function provides size and orientation information relative to the defect. Note in the figures how the inflection point shifts to the right as the defect orientation is increased or the size is increased.

Eighteen of the nineteen power spectra from Experiment 9 are shown in Fig. 11. Some cases matched the theory very well. Just about all cases matched the theory in the long wavelength regime.

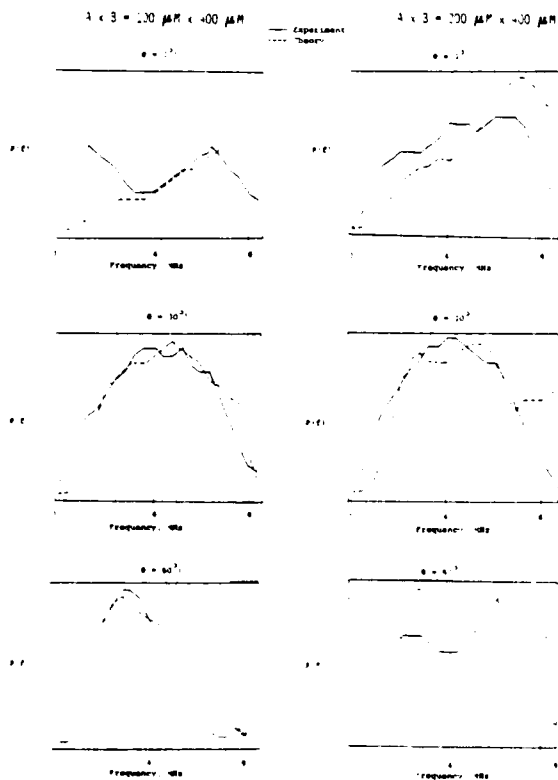


Fig. 8 Power spectra scattering responses from a 100 μm \times 400 μm and a 200 μm \times 400 μm oblate spheroid void at various pulse-echo receiver orientations. Comparison of theory (T-matrix scattering) to experiment.

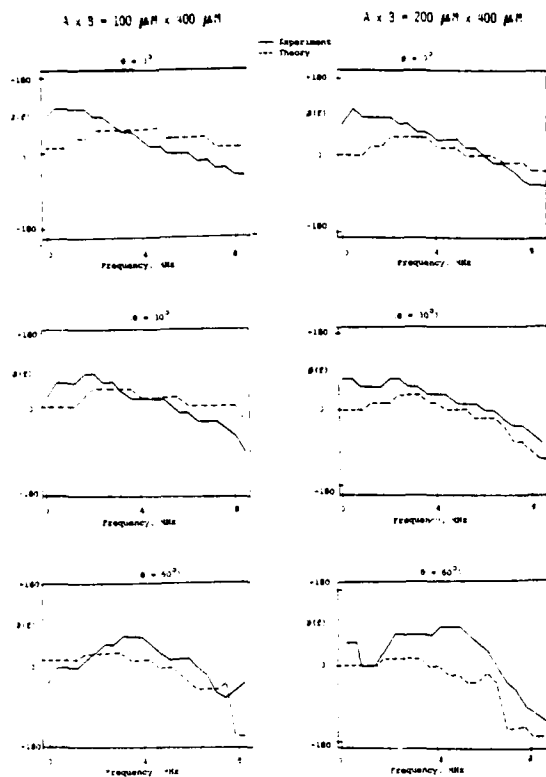
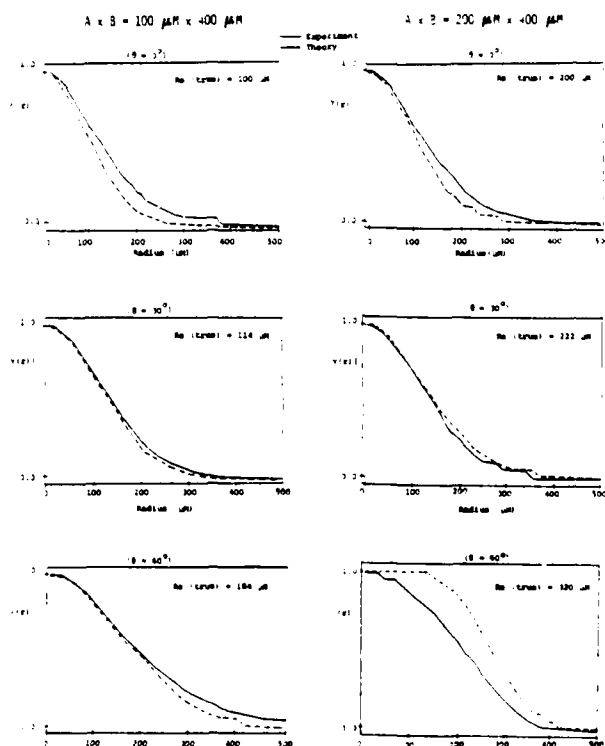


Fig. 9 Phase spectra scattering responses from 100 $\mu\text{m} \times 400 \mu\text{m}$ and a 200 $\mu\text{m} \times 400 \mu\text{m}$ oblate spheroid void at various pulse-echo receiver orientations. Comparison of theory (T-matrix scattering) to experiment.

Fig. 10 $\gamma(r)$ -Transform scattering responses from a 100 $\mu\text{m} \times 400 \mu\text{m}$ and a 200 $\mu\text{m} \times 400 \mu\text{m}$ oblate spheroid void at various pulse-echo receiver orientations. Comparison of theory to experiment.



$$\gamma(r) = \int_0^{\infty} A(s) \frac{\sin(2\pi s r)}{2\pi s} ds$$

where $A(s)$ = complex magnitude spectrum

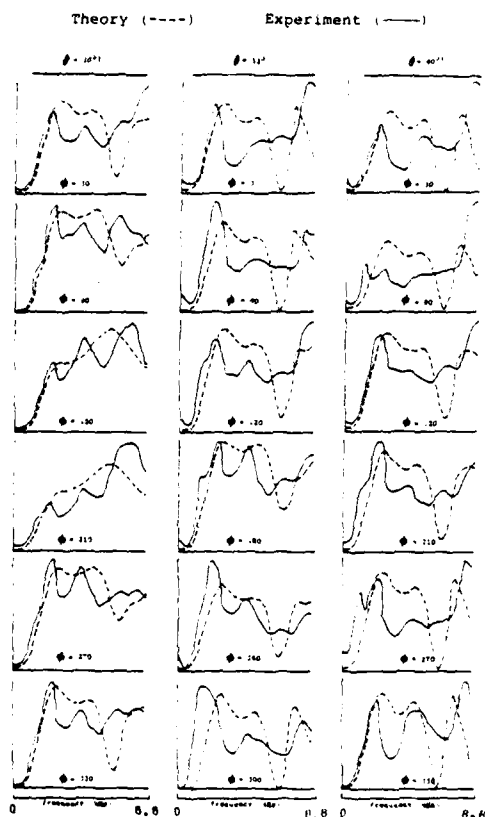


Fig. 11 Comparison of theoretical and pulse-echo experimental power spectra from Experiment 9. (200 μm \times 400 μm oblate spheroid, $\alpha = 15^\circ$, $\beta = 180^\circ$). Theory is SSM method (V. Varadan). Experimental data were recorded by B. Tittmann, May 1979.

FEATURE EXTRACTION

The features used as ALN inputs were computed in two steps: first, a set of representative spectral features were derived from each pulse-echo power spectrum and its associated transforms, and secondly, a set of spatial features was computed over the 19 receiver positions to describe the surface formed by each of the spectral features. A description of both feature types appears below.

A total of 79 spectral features (not listed) were computed originally from the following waveforms at each receiver position:

1. Power Spectrum $P(f)$
2. Log-Power Spectrum $L(f)$
3. Log-Log Power Spectrum $M(f)$
4. Characteristic Function $\gamma(r)$
5. Auto-Correlation Function $R(r)$
6. Phase Spectrum $\phi(f)$

A statistical analysis was performed to determine which of the 79 features yielded good agreement between theory and experiment. It was necessary to eliminate features in poor agreement so the ALN synthesis procedure could select features informative and stable on both theoretical and experimental data. Six spectral features were selected for further processing. These are shown in Table 5.

Table 5. The Six Candidate Spectral Features Selected For ALN Training

Symbol	Description	Computation
$U_1: P(f)$	First Moment of the Power Spectrum	$\int_0^f f P(f) df$
$B_1: P(f)$	Relative Energy, Band 1 of Power Spectrum	$\frac{\int_{f_1}^{f_2} P(f) df}{\int_0^f P(f) df}$
$P_T: P(f)$	Total Power in Power Spectrum	$\int_0^f P(f) df$
$B_2: M(f)$	Relative Energy, band 2 of Log-Log-Power Spectrum	$\frac{\int_{f_1}^{f_2} M(f) df}{\int_0^f M(f) df}$
$u_1: \gamma(r)$	First Moment of the Characteristic Function	$\int_0^r r \gamma(r) dr$
$u_2: \gamma(r)$	Second Moment of the Characteristic Function	$\int_0^r r^2 \gamma(r) dr$

The characteristic function, $\gamma(r)$, was suggested as a useful inversion function for spheroids by Dr. Jim Rose (U. Michigan). It is defined as

$$\gamma(r) = \int_0^{K_{\max}} \frac{\sin(2Kr)}{2Kr} dK \quad (2)$$

where $A(K)$ is the complex Fourier spectrum of which the phase has been minimized by subtracting out the linear trend.

The Log-Log Power Spectrum was computed by taking the log of the power spectral amplitude, then resampling the frequency axis at logarithmically spaced intervals. The formula for determining the frequency intervals is

$$f_i = f_{\min} (f_{\max}/f_{\min})^{\exp[(i-1)/(N-1)]}; \quad i = 1, 22 \quad (3)$$

where f_i is the sampling interval, f_{\min} and f_{\max} are the band limits of the power spectrum, and N is the original number of points in the spectrum ($N=22$).

The total power spectral feature, P_T , was normalized by the average power in the 19-element array. Hence, this feature measured the relative distribution of power in the array.

The following 13 spatial features were computed from each of the six spectral features mentioned above. The total number of candidate features input to the ALN training process was therefore 78.

Feature Number	Symbol	Description
1	w_1	Surface coefficient on x^2
2	w_2	Surface coefficient on y^2
3	w_3	Surface coefficient on z^2
4	w_4	Surface coefficient on xy
5	w_5	Surface coefficient on xz
6	w_6	Surface coefficient on yz
7	\bar{c}_x	x-component of centroid
8	\bar{c}_y	y-component of centroid
9	\bar{c}_z	z-component of centroid
10	ATAN1	$\tan^{-1} (\bar{c}_y / \bar{c}_x)$
11	ATAN2	$\tan^{-1} (x_2 / x_1)$
12	ATAN3	$\tan^{-1} (\sqrt{w_1^2 + w_2^2} / w_3)$
13	ATAN4	$\tan^{-1} (\sqrt{\bar{c}_x^2 + \bar{c}_y^2} / \bar{c}_z)$

Features 1 through 6 (w_1 - w_6) are the least squares coefficients on the quadric surface:

$$w_1 x^2 + w_2 y^2 + w_3 z^2 + w_4 xy +$$

$$w_5 xz + w_6 yz = 1 \quad (4)$$

It is assumed that the 19 feature values are sampled points on a continuous surface in (x, y, z)-space. If the surface is limited to an ellipsoid, hyperbola, conic, or sphere, it can be completely represented by Eq. (4). The x, y, and z spatial values for the features can be computed since the receiver positions are known. A matrix inversion is required to solve for the w's. A hypothetical surface is shown in Fig. 12 along with the matrix equation which is solved to find the six coefficients.

The features, \bar{c}_x , \bar{c}_y , and \bar{c}_z , are the x, y, and z components of the centroid of each spectral feature group. They are computed by finding the average feature in each direction:

$$\bar{c}_x = \frac{1}{19} \sum_{i=1}^{19} P_i \cos \phi_i \sin \theta_i \quad (5)$$

$$\bar{c}_y = \frac{1}{19} \sum_{i=1}^{19} P_i \sin \phi_i \sin \theta_i \quad (6)$$

$$\bar{c}_z = \frac{1}{19} \sum_{i=1}^{19} P_i \cos \theta_i \quad (7)$$

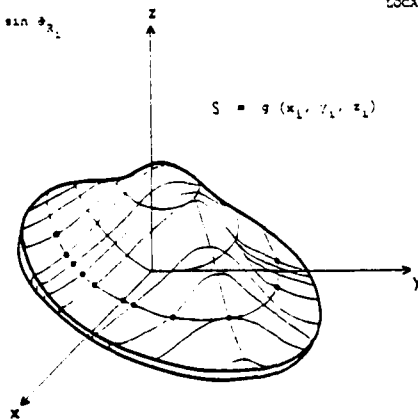
$$x_i = P_i \cos \beta_{i1} \sin \theta_{i1}$$

$$y_i = P_i \sin \beta_{i1} \sin \theta_{i1}$$

$$z_i = P_i \cos \theta_{i1}$$

P_i = WAVEFORM FEATURE
COMPUTED AT EACH RECEIVER
LOCATION

$$S = g(x_1, y_1, z_1)$$



$$S = w_1 x_1^2 + w_2 y_1^2 + w_3 z_1^2 + w_4 x_1 y_1 + w_5 x_1 z_1 + w_6 y_1 z_1 = 1$$

$$\begin{bmatrix} x_1^2 & y_1^2 & z_1^2 & x_1 y_1 & x_1 z_1 & y_1 z_1 \\ x_2^2 & y_2^2 & z_2^2 & x_2 y_2 & x_2 z_2 & y_2 z_2 \\ \vdots & \vdots & \vdots & \vdots & \vdots & \vdots \\ x_n^2 & y_n^2 & z_n^2 & x_n y_n & x_n z_n & y_n z_n \end{bmatrix} \begin{bmatrix} w_1 \\ w_2 \\ w_3 \\ w_4 \\ w_5 \\ w_6 \end{bmatrix} = \begin{bmatrix} 1 \\ 1 \\ \vdots \\ 1 \end{bmatrix}$$

Fig. 12 Idealized surface representation of extracted array measurements.

where P_i is one group of 19 spectral features and the angles (ψ_i, θ_i) specify the receiver orientations.

The arctangent features are angular measurements which have been included since the ALN models estimate directly the defect orientation angles α and β .

The spatial features listed above have the advantage of being computable even when a few of the receiver positions cannot be accessed. This situation may arise during the inspections of non-spherical test pieces.

ALN MODEL SYNTHESIS

Individual ALN models were trained on theoretical (SMM) scattering data to estimate the four defect parameters A , B , α , and β . The network structures, selected features, and weighting coefficients appear below.

Figure 13 shows the resultant network structures to estimate the spheroid's minor axis, A . The ALN selected six input features, most of which measured shifts in the low-frequency position of the power spectrum. Each element in the network is comprised of a six-term quadratic multinomial of two inputs where the weights have been optimized to produce a minimum error at the output. The average absolute error computed from theoretical evaluation data was 10.4 microns. The average absolute percent error was 9%. The centroid-type features were frequently selected for both A and B size parameters.

The ALN to estimate the major spheroid axis, B , is shown in Fig. 14. The two features selected were both centroids, and both measured shifts in the power spectrum. The average absolute error for this network was 33.5 microns, or 8% error.

Figure 15 shows the network structure for the spheroid's polar orientation angle, α . This network selected three features, all of which were arctangent functions of the total power. The error for this network model was quite small when evaluated on theoretical data. An average absolute error of 4.7° was observed. This corresponds to an error of 5%.

The network structure for the azimuthal orientation angle, β , is shown in Fig. 16. The features selected were arctangent types of the first moment of $|r(r)|$ and total power. The observed error on theoretical data was very small, 1.1°, which corresponds to a 1% average absolute error. This parameter was the easiest to estimate.

EXPERIMENTAL RESULTS

Features were computed from the nine experiments described in the section titled "Experimental Data Base" and were processed through the theoretically trained ALN networks. Estimates for A , B , α , and β for the nine experiments appear in Table 6. Values for β in Experiments 1 and 4 are not shown since β is undefined when α is zero. An error summary appears at the bottom of Table 6. The relative error shown is the percent average absolute error computed over the nine experi-

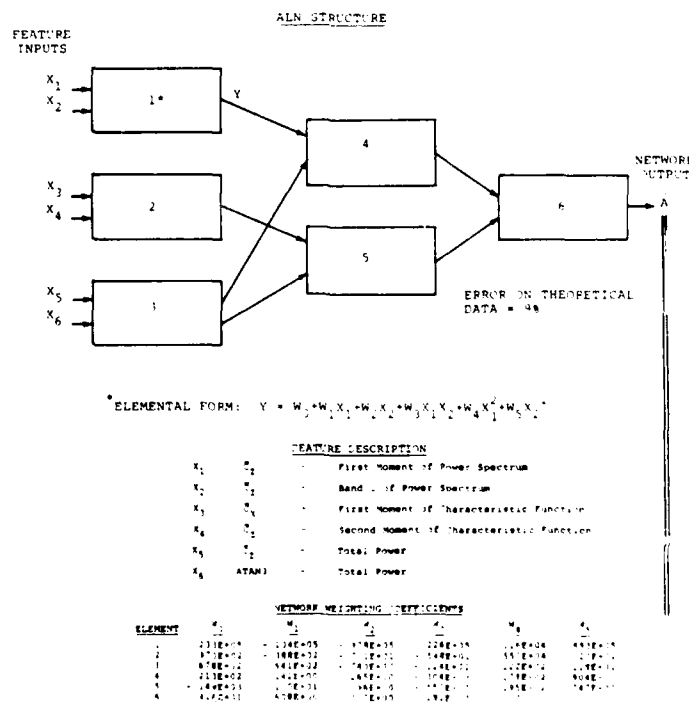


Fig. 13 Adaptive learning network to estimate size parameter A for spheroidal defects.

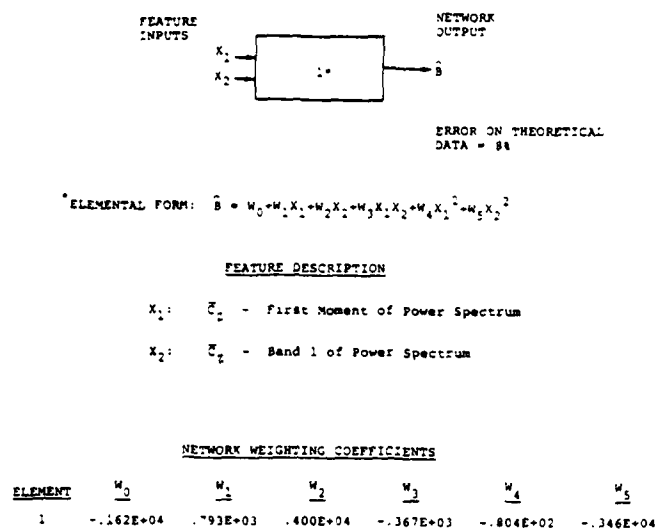


Fig. 14 Adaptive learning network to estimate size parameter \hat{B} for spheroidal defects.

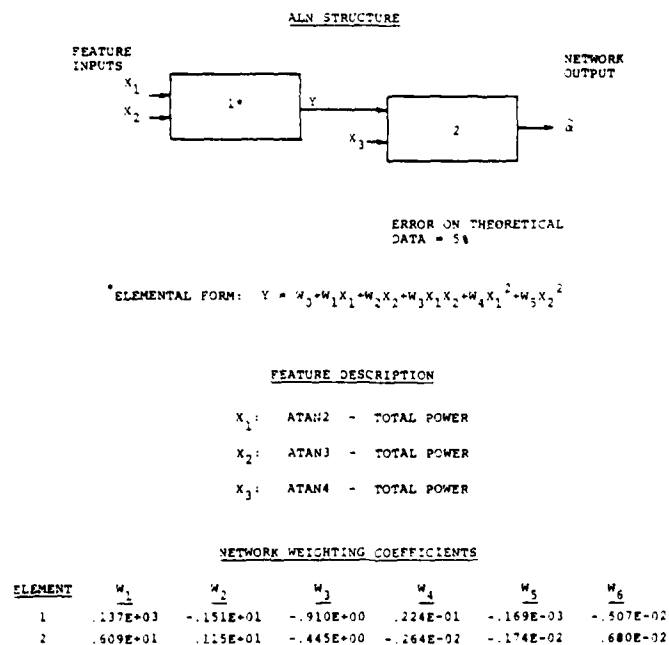


Fig. 15 Adaptive learning network to estimate orientation parameter \hat{a} for spheroidal defects.

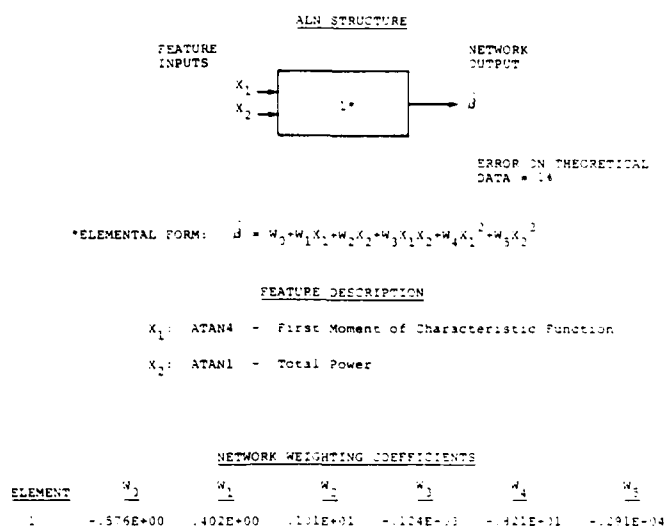


Fig. 16 Adaptive learning network to estimate orientation parameter ψ for spheroidal defects.

ments. ALN estimates for the orientation angles α and ψ were excellent, with errors of 7% and 4%, respectively. Estimates for the larger size parameter B were also excellent with a relative error of 6%. The results for the minor axis A were generally small for the 200 micron cases, except for Experiment 9 which used the higher 7 MHz center-frequency transducer. The poorer estimates for the minor axis may be attributed to the limiting resolution of the system bandwidth. The ka value along the minor axis was 0.5, which implies the A -dimension is less than 1/12 of the longitudinal wavelength. This small defect size in relation to the wavelength has a very small effect on the incident waveform. This effect could possibly be less than the inherent experimental error.

It is interesting to note that the ALN models were able to produce very good defect estimates for all nine experiments despite the fact that Experiments 1 through 8 were collected under different conditions, with a different transducer, and with a different array configuration than was Experiment 9. This insensitivity to variation of experimental conditions is a good indication that the ALN inversion procedure could be easily adapted to practical use.

CHARACTERIZATION OF TWO-DIMENSIONAL DEFECTS

INTRODUCTION

In many respects, the procedures employed in the analysis of the two dimensional crack problem are analogous to those described for the three-dimensional case presented in the previous section. The objectives sought for each of the two geometrical configurations are identical, namely the characterization of the defect both in terms of its size and its orientation. The specific approach selected for the two-dimensional defect

problem was to (1) obtain theoretical amplitude spectra from a geometrical diffraction model, (2) extract diagnostic features from these spectral estimates for use in training Adaptive Learning Networks (ALN) and (3) assess the predictive capability of the resulting networks using experimental data collected from specimens of known size and orientation.

The subsections which follow contain detailed discussions of the crack geometry, the composition of both the theoretical and experimental data bases, the features selected for analysis purposes, the configurations of the resulting ALN models and results obtained from the comparisons of the theoretical and experimental data inversion processes.

DEFECT GEOMETRY

The geometrical representation of the two-dimensional elliptical crack problem is illustrated in Fig. 17. For the purposes of this study, we assumed the defect was described in terms of four distinct parameters:

- A' - the radius of the minor axis,
- B' - the radius of the major axis,
- α' - the polar angle (measured from the positive Z -axis to the major axis),
- ψ' - the azimuthal angle (measured from the positive X -axis to the projection of the major axis on the XY -plane).

It should be noted that one additional measurement, representing the rotation of the defect about the major axis, would be required to describe the most general case, however, the theoretical approach used in the generation of the amplitude spectra assumed this angle to be 90° and

Table 6. Size And Orientation Estimates For Nine Experimental Spheroid Defect Samples Determined From Theoretically Trained ALN Models

Exp. No.	A (μm)		B (μm)		α (degs)		β (degs)	
	True	Estimated	True	Estimated	True	Estimated	True	Estimated
1	200	123	400	413	0	4	-	-
2	200	180	400	381	30	23	225	222
3	100	105	400	415	80	79	160	167
4	100	72	400	372	0	12	-	-
5	200	127	400	341	80	89	160	174
6	100	94	400	406	30	29	180	190
7	200	121	400	370	30	46	180	189
8	100	97	400	393	30	36	225	227
9	200	216	400	453	15	14	180	184

Error Summary

Parameter	Relative Error
A (μm)	23%
B (μm)	6%
α (degs)	7%
β (degs)	4%

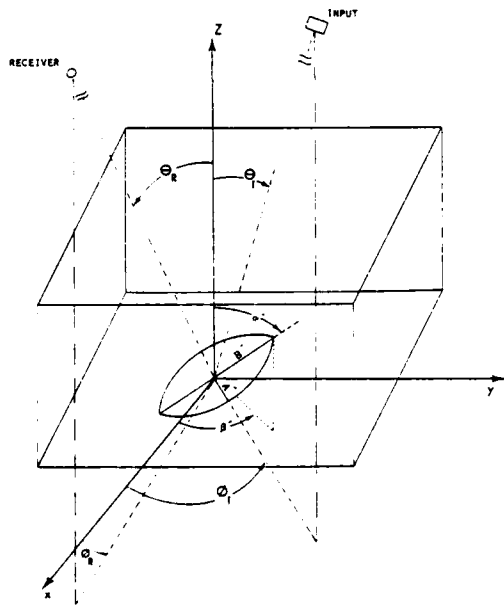


Fig. 17 Two-dimensional elliptical crack coordinate geometry.

was therefore the only case considered in this study. Modifications to the geometrical diffraction theory which enable variations in this angle to be evaluated have been recently completed and

will be incorporated into future analyses.⁵ Throughout the remainder of this section, the defect will be represented in terms of the four measurements described above.

The locations of the input signal and received signal are also shown in Fig. 17 and are defined in terms of their polar angles (θ_i , θ_p) and azimuthal angles (ϕ_i , ϕ_p) with respect to the same reference coordinate system used in the crack representation.

ARRAY CONFIGURATION

The 19-element hexagonal array discussed in an earlier section was also used in the two-dimensional crack analysis. The locations of these individual receivers are presented graphically in Fig. 5. Both the theoretical and experimental amplitude spectra were generated in terms of this array configuration.

The mode of collection selected for evaluation of the theoretical and experimental data was the pitch-catch type in contrast to the pulse-echo type. In the pitch-catch mode, the signal is input at one of the elements in the array and the diffracted signal is recorded at the input location as well as at the other 18 different locations within the hexagonal array. For the purposes of this study, the input signal was always assigned to the center element (0,0, 0,0) of the array.

THEORETICAL DATA BASE

A computer code representing a far-field approximation to the geometrical theory of diffraction

tion was developed at Northwestern University for use by Adaptronics in calculating estimates of the amplitude spectrum recorded at a particular location when an input ultrasonic signal is diffracted from a defect of specified geometry. The derivation of this model has been extensively discussed and has been shown to be in favorable agreement with experimental results.^{6,7,8}

Theoretical amplitude spectra corresponding to longitudinal-longitudinal mode scattering were generated at each receiver point in the 19-element array using the pitch-catch operating characteristic with the transmitter located at the center of the array. A total of 1890 different defect geometries were considered and are identified in Table 7. Synthetic spectra were obtained for 14 different defect sizes (A' and B'), 9 polar angles (α') and 15 azimuthal angles (β'). The frequency band of interest used in the calculation of these spectra ranged from 2 to 14 MHz with a frequency resolution of approximately 0.1 MHz. The corresponding ka range of the theoretical data was from 0.62 to 34.69 which encompasses a wide range of wavelengths.

Table 7. Theoretical Data Base

ELLIPTICAL CRACK SIZES — 14 CASES

A (MICRONS)	B (MICRONS)	A' (MICRONS)	B' (MICRONS)
312	312	625	2500
312	625	1250	1250
312	1250	1250	1875
312	2500	1250	2500
625	625	1875	1875
625	1250	1875	2500
625	1875	2500	2500

POLAR ANGLE ORIENTATION — 9 CASES

$\alpha = 10^\circ, 20^\circ, 30^\circ, 40^\circ, 50^\circ, 60^\circ, 70^\circ, 80^\circ, 90^\circ$

AZIMUTHAL ANGLE ORIENTATION — 15 CASES

$\beta = 30^\circ, 25^\circ, 50^\circ, 75^\circ, 100^\circ, 125^\circ, 150^\circ, 175^\circ, 200^\circ, 225^\circ, 250^\circ, 275^\circ, 300^\circ, 325^\circ, 350^\circ$

RECEIVER LOCATIONS — 19 CASES

$\theta_1 = 30^\circ, \theta_2 = 30^\circ, 90^\circ, 150^\circ, 210^\circ, 270^\circ, 330^\circ$
 $\theta_1 = 52^\circ, \theta_2 = 70^\circ, 60^\circ, 120^\circ, 180^\circ, 240^\circ, 300^\circ$
 $\theta_1 = 60^\circ, \theta_2 = 10^\circ, 90^\circ, 150^\circ, 210^\circ, 270^\circ, 330^\circ$
 $\theta_1 = 70^\circ, \theta_2 = 70^\circ$

EXPERIMENTAL DATA BASE

The experimental data used in this study were collected at the University of Tennessee from a set of known defect specimens. The basic characteristics of the collection process and the electronic configurations of the recording devices are summarized by Adler, et al.⁸ Basically, a broadband transducer emits an L wave which passes through a 15 cm water column, enters a 10 cm by

2.5 cm titanium disk and is diffracted by a crack within the disk. The diffracted signal then leaves the disk, enters the water, and is recorded at a specified location, displayed and subsequently digitized. A total of three experiments were evaluated by Adaptronics in the course of this investigation. The size and orientation of the defects are presented in Table 8.

Table 8. Summary Of Experiments Analyzed

EXPERIMENT NUMBER	MINOR AXIS (MICRONS)	MAJOR AXIS (MICRONS)	POLAR ANGLE (DEGREES)	AZIMUTHAL ANGLE (DEGREES)
1	2500	2500	90	0
2	1250	2500	90	0
3	625	2500	90	0

COMPARISON OF THEORETICAL AND
EXPERIMENTAL SPECTRAL DATA

Since one of the main objectives of this study involves using models trained on a theoretical data set to evaluate experimental conditions, the final results depend ultimately on how well the experimental and theoretical spectra agree. A direct comparison of theory and observation cannot be performed until an assessment of the differences in the two different approaches is evaluated. Several complex processes, which are not accounted for in the theory, are involved in collecting the experimental data. Some of the more pronounced incompatibilities are identified in Fig. 18. The differences shown in this illustration can be divided into two main categories -- those related to the electronic features of the recording system and those pertaining to the properties of the metal specimen. A more detailed discussion of each of these problem areas and of the procedures employed in compensating for their influence on the recorded signal will be presented in the following paragraphs.

The theoretical model used in calculating the diffracted spectra is characterized by a noise-free environment and by a receiver which responds uniformly to diffracted energy over a wide range of frequencies. Both of these ideal situations are not present when real data are collected. Background and ambient noise is always introduced in the recordings as well as that associated with the electronic devices comprising the hardware system. In the experiments analyzed in this study, the noise levels related to these different sources can be minimized, but not totally removed, by proper selection of attenuator and amplifier gains in the recording devices. Since the geometrical properties of the defect are known prior to the collection effort, the operator can selectively monitor the resulting signal-to-noise ratio and thus obtain recordings of very high quality.

The other experimental system feature which deviates from the theoretical case is the frequency response of the transducer. The reference spectrum shown in Fig. 19 was obtained from an analysis of the signal recorded after the input

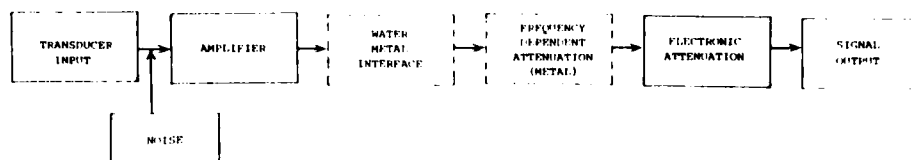


Fig. 18 Simplified view of the processes influencing the recorded signal.

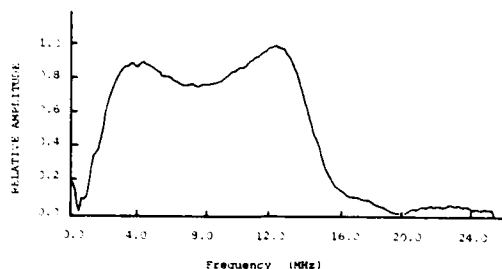


Fig. 19 Normalized amplitude spectrum representing the transducer reference spectrum.

energy had passed through a 2.5 cm thick titanium sample containing no defect. Over the frequency range of interest in this study (2 to 14 MHz), the transfer function depicted here shows that the response does depend on the frequency under analysis. To compensate for this nonuniform response, a deconvolution algorithm was applied to the recorded data to guarantee a flat amplitude response over the range between 2 and 14 MHz. The exact form of this deconvolution process was presented in an earlier section.

In summary, any discrepancies between the theory and experiment related to characteristics of the recording system can be accounted for by established procedures and should not affect any comparison studies.

A direct comparison of the theoretical predictions and experimental amplitude spectra corresponding to a 2.5 mm disk defect for receivers at polar angles between 30° and 65° is shown in Fig. 20. The experimental results have been deconvolved to reflect the reference transducer spectrum. Some very interesting inferences can be drawn from this illustration. The most obvious agreement between these two sets concerns the ripple period structure. Measurements made from each spectrum are in very good agreement, with each indicating a slight decrease in the ripple period as the polar angle of the receiver increases. The relative amplitude levels agree reasonably well at the low-frequency end of the spectra (2-6 MHz) but deviate at the intermediate and high-frequency portions of the spectra. This observation appears to suggest that frequency dependent effects related to the titanium specimen may be influencing the experimental results.

Further comparisons of the theoretical and experimental data are shown in Figs. 21 and 22. Fig. 21 represents the data recorded at various orientations along the major and minor axes of a 1.25 by 2.5 mm ellipse. Figure 22 presents the

diffracted spectra obtained from a 0.625 by 2.5 mm elliptical crack. The ripple periods obtained from these two defect sizes agree very favorably with those predicted from the theory. The agreement between the relative amplitude levels is excellent for the low frequencies but deteriorates as the frequency becomes larger. The consistent deviations in the normalized amplitude values noticed in these two comparisons, when added to the previous case (Fig. 20), appear to indicate that a certain amount of frequency dependent attenuation related to the specimen is being introduced in the experimental data.

Two potential problem areas can be identified where the theoretical model differs from the experimental collection with regard to properties of the titanium sample. The first relates to the incorporation of a water bath in collecting the diffracted spectra. This introduces a transmission coefficient into the recorded data because of the water/metal interface. Using properties of the titanium sample and water, this transmission coefficient was calculated according to a well-known formula given in Ref. 9 for various polar angles and is shown in Fig. 23. Over the angular range of 0° to 90°, this coefficient varies from approximately 0.1 to 0.04. The analysis presented here indicates that the water/metal interface characteristics can influence the amplitude level observed at a particular receiver location. This coefficient is independent of frequency and would not be of much assistance in explaining the deviations noted above. However, since the transmission coefficient is a function of polar receiver angle, it, therefore, must be applied to preserve the relative energy distribution in the array. The second area in which the theoretical and experimental spectra differ relates to the attenuation of the diffracted energy in the titanium specimen. No attenuation of energy was considered in developing the model, but it is evident that incorporation of its effect on the diffracted spectra could improve the spectral comparisons presented thus far, especially at the higher frequency components. Recalling the comparisons presented earlier, it was observed that the ripple periods measured from the two spectra were in good agreement. If we assume that the theory and experiment should be in good agreement when considering the relative amplitude levels, then the differences we have observed can be partially related to attenuation features.

Perhaps the simplest method which could be used to obtain an estimate of the attenuation effects would be to calculate a ratio of the two spectra. However, a more detailed examination of the two spectral curves illustrates that the locations of the peaks and nulls occur at slightly different frequency values. This slight

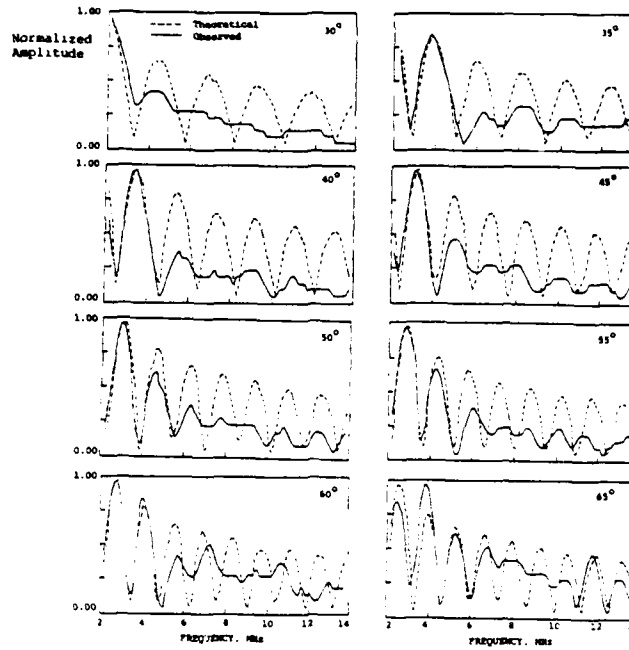


Fig. 20 Comparison of theoretical and experimental amplitude spectra for a 2.5 millimeter disc-shaped defect in Ti at various pitch-catch scattering angles. (The experimental data have been deconvolved.)

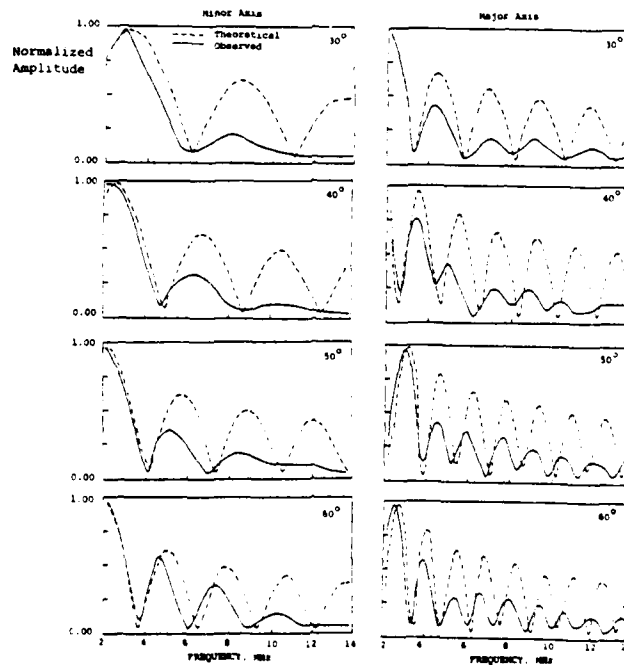


Fig. 21 Comparison of theoretical and experimental amplitude spectra for a 1.25 by 2.50 millimeter elliptical crack in Ti at various pitch-catch scattering angles. (The experimental data have been deconvolved.)

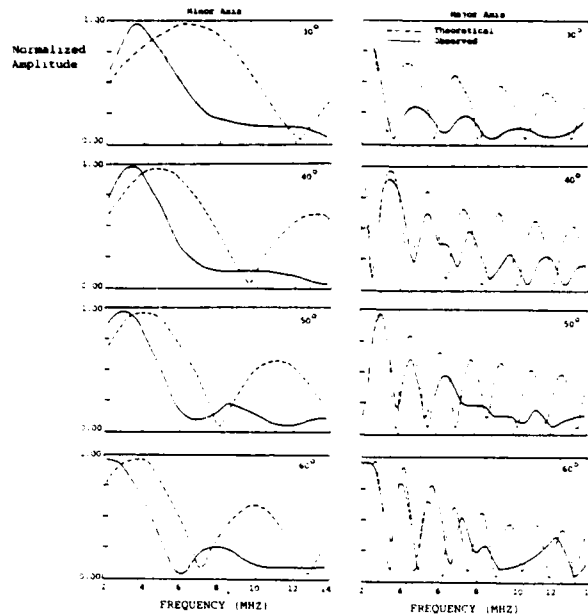


Fig. 22 Comparison of theoretical and experimental amplitude spectra for a -.625 by 1.50 millimeter elliptical crack in Ti at various pitch-catch scattering angles. (The experimental data have been deconvolved.)

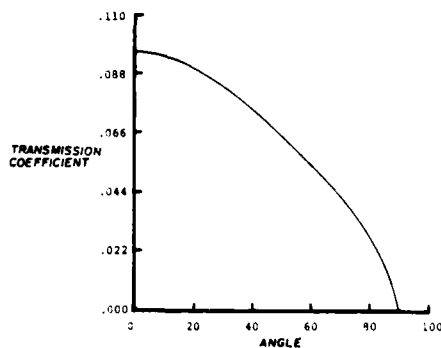


Fig. 23 Transmission coefficient as a function of polar angle for the titanium sample.

difference introduces several spurious peaks in the ratio and complicates the attenuation measurement as well as its interpretation.

To circumvent this problem area, a series of peak values were determined for both curves and plotted at their true frequency value. A typical example illustrating this procedure is shown in Fig. 24 which shows the results obtained for the 2.5 mm disk at a polar angle of 30°. The curved line connecting these measurements represents the decay of energy with frequency for both the theoretical data and experimental data. The dif-

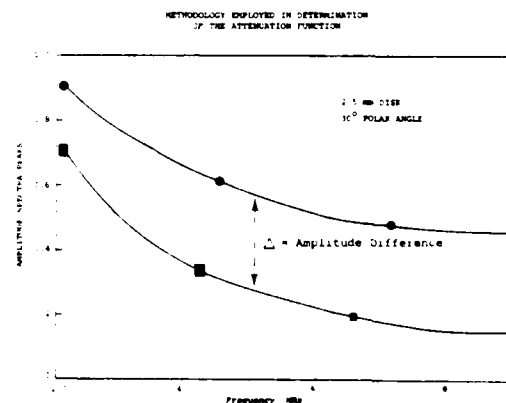


Fig. 24 Decay of normalized amplitudes as a function of frequency determined from the theoretical (circles) and experimental (squares) normalized amplitude spectra.

ference (Δ) between these two curves at a given frequency tends to increase linearly with increasing frequency. The logarithm of this difference, measured at various frequencies, is plotted as a function of frequency in Fig. 25. It is obvious that the data points represented in

this illustration are well described by the linear functional relationship of the form

$$\log \Delta(\omega) = -k\omega \quad (8)$$

or

$$\Delta(\omega) = e^{-k\omega} \quad (9)$$

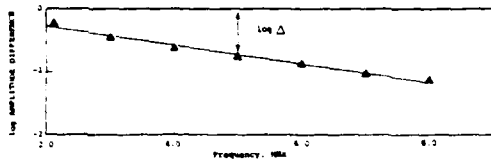


Fig. 25. Logarithm of the difference in amplitude between the theoretical and experimental spectra as a function of frequency.

This empirically determined relationship is quite compatible with theoretical attenuation models described in Ref. 10 which can be expressed as

$$A(\omega) = e^{-\omega X/2CQ} \quad (10)$$

where X is the distance of propagation, C is the wave velocity and Q is the specific dissipation function. Equating k in Eq. (9) to $X/2CQ$ results in an empirically determined estimate of Q in the range from 3000 to 3500.

The experimentally determined attenuation functions were applied to the recorded data and resulted in a much better comparison with the diffraction model predictions. Examples of the resulting spectra are illustrated in Figs. 26 and 27 over the frequency range from 2.0 to 8.0 MHz. Spectral data for frequencies higher than 8 MHz appeared to be bordering on very low signal-to-noise ratios and were not used in the analysis. The comparisons shown in these figures indicate that the relative amplitude values are in much better agreement, especially around the spectral peaks, when attenuation effects are considered. The ripple period structure shows no appreciable change when these effects are incorporated into the analysis.

The comparison study presented in this section appears to confirm that theoretical and experimental diffracted spectra can be shown to be in reasonable agreement over the frequency range from 2 to 8 MHz when modifications to the assumptions made in the development of the theory are taken into account. The experimental results obtained during this analysis will require more detailed examination to verify the conclusions made in this preliminary evaluation. The agreement achieved in this comparison suggests that diagnostic features extracted from theoretical spectra for inversion purposes may be directly applicable to the field situation.

FEATURE SELECTION

The theoretical diffraction model was used to generate a set of 1890 distinct cases for evaluation. The data set is represented by 14 different

size defects ranging from a .312 by .312 mm disk up to a 2.5 by 2.5 mm disk. Nine polar angles covering the region from 10° to 89° and 15 azimuthal angles from 0° to 350° were considered in developing the theoretical data base. A hexagonal array containing 19 receivers were used in estimating the diffracted spectra for each individual case.

The features selected from these individual spectra involved consideration of the energy level of the amplitude spectrum and a measurement of the ripple period structure inherent in the diffracted spectrum. Estimates of these parameters were made for each element in the array and were then analyzed as a unit to determine the spatial dependence of these features within the array. The spatial characteristics were determined by fitting a surface to the 19 estimates using a least squares criterion. The exact procedures employed in the estimation of the surfaces were identical to those used in the three-dimensional analysis presented earlier. Coefficients representing the best fit surface to the spectral features, other spatial measurements related to the centroid location and angular quantities of the data were made. The steps involved in the estimation of these spectral features are illustrated schematically in Fig. 28. The measurements obtained from the total energy and ripple period features are the same 13 spatial features computed from the spheroidal defects, and a list appears in the section explaining feature extraction.

The total energy feature was computed using the amplitude spectrum at each receiver location over the frequency band of 2.0 to 8.0 MHz. This limited frequency band was selected based on the analysis of the attenuation effects described earlier in this section. The estimation of this feature involved a direct summation of spectral values over this frequency range with a frequency resolution of approximately 0.1 MHz. These values were normalized by dividing the estimate at each receiver by the maximum energy observed at any site in the array before the surface fits were made.

Estimation of the ripple period evident in the diffracted spectra was accomplished by a Fourier transform analysis. The mean value determined from the theoretical spectrum was calculated and removed from the spectrum. The resulting function ideally approximates a trigonometric (sine or cosine) time series of period f^* where f^* is the ripple period measured in MHz. Depending on the duration of this resulting function, a Fourier transform should produce a sharply peaked response at a value of $1/f^*$. The location of the maximum value is determined from the transform output and its inverse equated to the ripple period of the theoretical spectrum. This procedure is outlined schematically in Fig. 29. Surface features are then computed from the ripple period measurements made within the array.

ALN MODEL SYNTHESIS

Adaptive Learning Networks were trained using the 26 spatial values measured from the ripple period and total energy. Four networks were determined corresponding to the four unknown parameters required to define the defect size and orientation (A^* , B^* , α^* , β^*). The connectivity

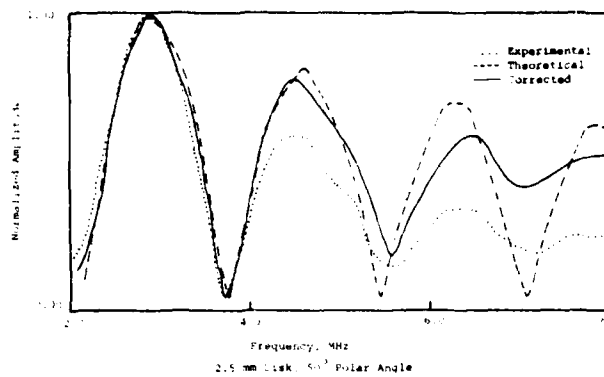


Fig. 26 Illustration of experimental recordings corrected for attenuation effects.

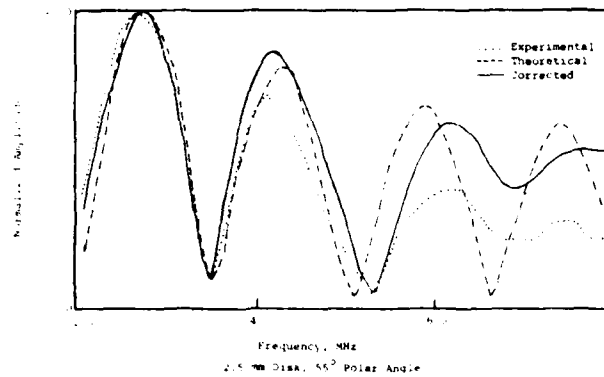


Fig. 27 Illustration of experimental recordings corrected for attenuation results.

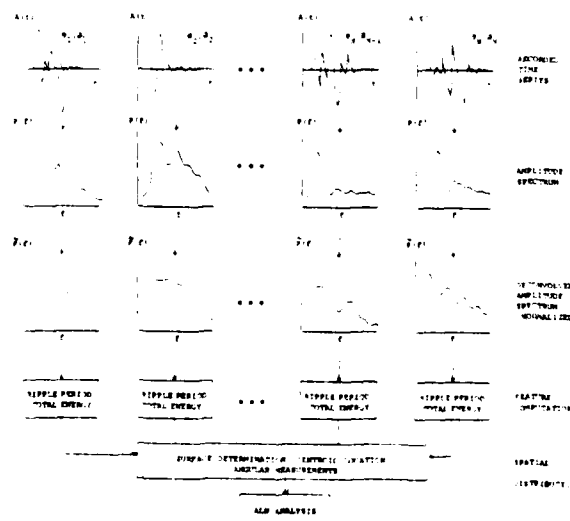


Fig. 28 Schematic illustrating steps involved in the computation of ALN feature inputs.

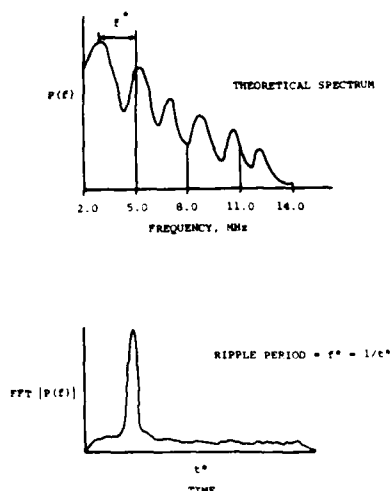


Fig. 29 Schematic illustrating steps involved in the computation of the ripple period feature .

and coefficients determined from the ALN analysis as well as a discussion of how well the resulting model describes the theoretical data will be presented in this section.

The network which resulted from an analysis of the polar angle (α') is presented in Fig. 30. The structure of this network is quite simple and indicates that the estimation of α' depends mainly on the distribution of power within the recording array. Each element in the network consists of a six-term quadratic multinomial of two input variables. The input features shown in this figure were selected by the model from the list of 26 available values. The outputs of the leftmost elements provide inputs to subsequent elements, with the final element providing an estimate of α' . The evaluation set used in this analysis was not incorporated in the network training exercise. The comparison of this independent data set with the model yielded an average relative error of slightly more than 4% and an average absolute error of 4° for the polar angle.

The structure of the ALN for estimating the defect azimuthal angle (β') is presented in Fig. 31. The network is represented by only two input variables and resulted in very good estimates of β' for the independent evaluation data with an average relative error of 2% and an average absolute error of only 3.5° .

The defect size parameters, A' and R' , were subjected to ALN analysis with the resulting structures shown in Figs. 32 and 33, respectively. In general, the structures for the networks for estimating the sizes are more complex than those obtained for the angular orientations. The

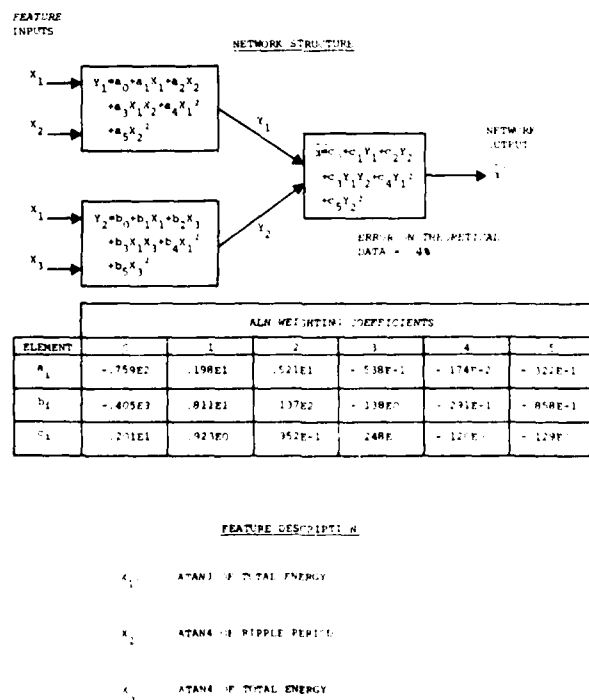


Fig. 30 Adaptive learning network to estimate orientation parameters, α' , for elliptical crack defects.

ELEMENT	ALN WEIGHTING COEFFICIENTS					
	0	1	2	3	4	5
a_1	.180E3	-.271E-1	.101E1	.149E-3	-.189E-4	211E-4

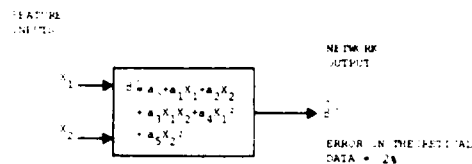
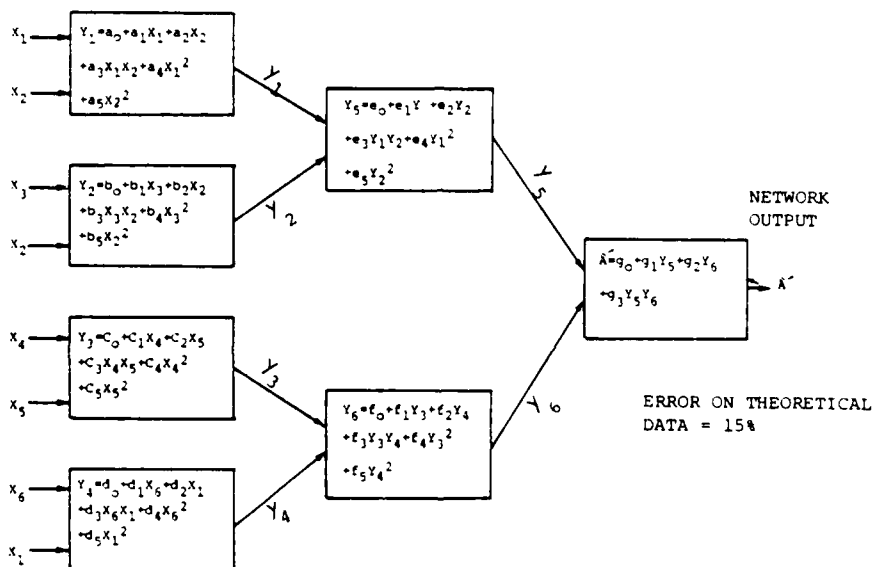


Fig. 31. Adaptive learning network to estimate orientation parameter, β' , for elliptical crack defects.

FEATURE DESCRIPTION

X_1 : W_4 SURFACE COEFFICIENT OF TOTAL ENERGY
 X_2 : ATANI OF TOTAL ENERGY

FEATURE
INPUTS



ELEMENT	ALN WEIGHTING COEFFICIENTS					
	0	1	2	3	4	5
a_1	.372E0	.529E1	-.130E1	.538E1	-.587E1	.150E1
b_1	.361E0	.529E1	-.130E1	.443E1	-.510E1	-.121E1
c_1	-.153E1	-.388E0	.118E0	-.636E-2	.524E-1	-.668E-3
d_1	.641E0	-.474E0	.300E1	-.854E1	-.730E0	.459E0
e_1	.125E0	.278E0	.159E0	.329E0	-.106E-1	.108E-1
f_1	.354E0	-.298E0	.157E0	.540E0	.275E0	-.159E0
g_1	-.122E-1	.639E0	.339E0	.257E-1		

FEATURE DESCRIPTION

X_1 : W_2 SURFACE COEFFICIENT OF RIPPLE PERIOD
 X_2 : W_3 SURFACE COEFFICIENT OF RIPPLE PERIOD
 X_3 : W_1 SURFACE COEFFICIENT OF RIPPLE PERIOD
 X_4 : Z-COMPONENT OF CENTROID OF RIPPLE PERIOD
 X_5 : ATANI OF RIPPLE PERIOD
 X_6 : Z-COMPONENT OF CENTROID OF TOTAL ENERGY

Fig. 32. Adaptive learning network to estimate minor axis, A' , for elliptical crack defects.

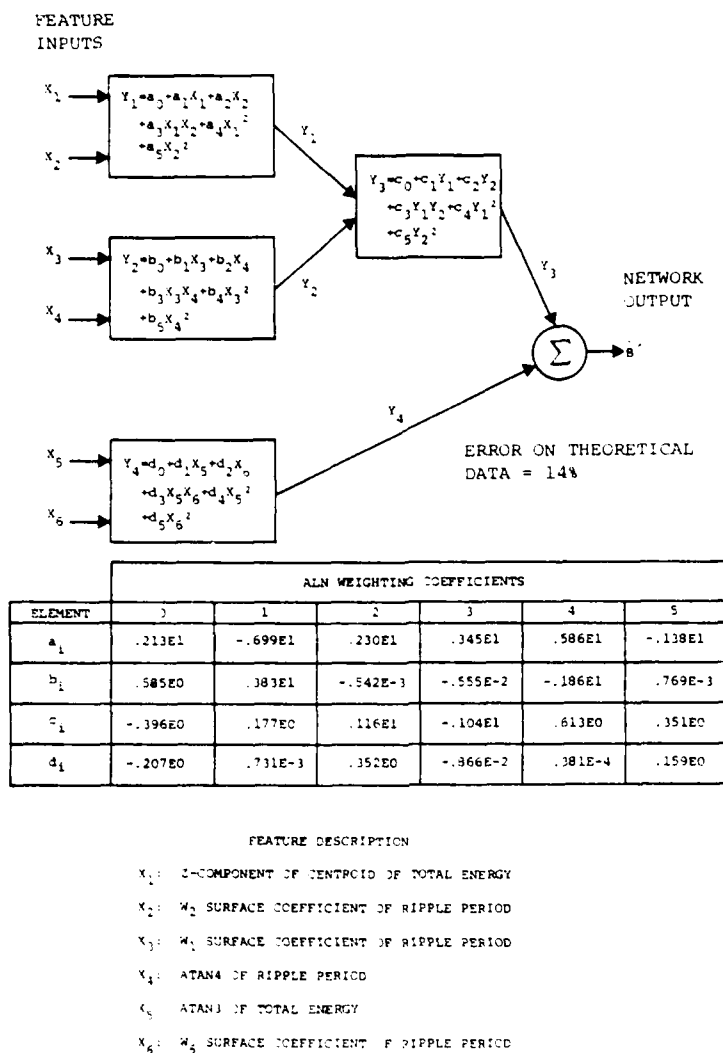


Fig. 33 Adaptive learning network to estimate major axis, B' , for elliptical crack defects.

average relative and absolute errors determined for A' were 26% and 0.17 mm and 14% and 0.18 mm for B' when the network estimates were compared with the evaluation data set. The average errors quoted for these cases appear to be higher than expected; however, a detailed analysis of the individual errors indicates that the amount of error is related to the size of the defect. The small sizes (.312 mm especially) resulted in the most error which leads to a distortion of the average values calculated over all lengths. In fact, the analysis was repeated after all data of length 0.312 mm on the minor axis were removed from the sample and resulted in a significant reduction in the average relative and absolute errors to more acceptable levels of 15% and 0.14 mm. The structure of the ALN obtained from this analysis was quite similar to that obtained from the total sample again indicating the difficulty in estimation of small defect lengths. The majority of the features selected by the ALN model for use in estimation of the defect size are concerned with the ripple period measurements obtained from the diffracted spectra, while those selected for use in estimation of the defect orientation are concerned with energy measurements. The calculation of the diffracted energy at each receiver is a simple task; however, the ripple period calculation involves a more complex set of operations. The larger errors observed in the size estimates may conceivably be a direct result of the larger uncertainty associated with the ripple period estimate. A higher resolution spectral estimate of the ripple period features may result in a considerable reduction in the errors related to the defect size and will be investigated in future work.

In summary, the ALN's trained on the theoretical diffraction data yielded excellent results for estimating the angular orientations of the two-dimensional cracks. Estimates of the size of

the defect also provided good comparisons with data not used in determining the network structures, especially for medium and large length defects. The networks presented in this section are compared with experimental data in the next section to assess the predictive capability of the ALN models in a blind test environment.

EXPERIMENTAL INVERSION RESULTS

The data collected from a set of three known specimens were analyzed to determine how well the ALN models trained on the theoretical data perform under experimental conditions. The various procedures employed in obtaining the diffracted spectra as well as the various features (total energy and ripple period) measured from the spatial distribution of these observations comprising the array structure were discussed in earlier sections of this section. The estimates of the defect size (A' and B') and orientation (α' and β') determined from the appropriate model are shown in Table 9. The agreement obtained between the observed and predicted quantities is excellent for each of the three tests. The best comparison is obtained for the defect orientation characteristics with the maximum deviation being less than 6%. The maximum difference obtained for an estimate of the defect size was about 22%. The average relative error determined for the three evaluations considered in this study is 10% for the minor axis (A'), 5% for the major axis (B'), 3% for the polar angle (α'), and 0% for the azimuthal angle (β').

The results presented here illustrate that ALN models trained on theoretical data bases provide very good estimates of defect size and orientation estimates when the models are used in predicting experimental results. More experimental data, especially at different orientation angles, are required to provide more stringent tests of the developed models.

DISCRIMINATION BETWEEN TWO-DIMENSIONAL AND THREE-DIMENSIONAL DEFECTS

INTRODUCTION

The work presented in this section covers the discrimination between two-dimensional (crack-like) defects and three-dimensional (void-like) defects. This is an important step in the defect characterization process since it determines which of the previously described algorithms will be used to estimate the defect size and orientation parameters as shown in Fig. 2.

Since the geometry is different between cracks and voids, one would expect the scattered ultrasonic field to also be distinguishable. The results shown below indicate this to be true since no difficulty was found in performing the discrimination.

The approach to this problem has been similar to that of the previous two sections in that a theoretical data base was generated, an ALN syn-

Table 9. Size And Orientation Estimates For Three Experimentally Recorded Elliptical Crack Defects Determined by ALN's Trained on Theoretical Data

		A' (mm)	B' (mm)	α'	β'
EXPERIMENT #1	TRUE VALUE	2.50	2.50	90°	0°
	ALN ESTIMATE	2.36	2.32	85°	0°
EXPERIMENT #2	TRUE VALUE	1.25	2.50	90°	0°
	ALN ESTIMATE	0.98	2.40	89°	0°
EXPERIMENT #3	TRUE VALUE	0.625	2.50	90°	0°
	ALN ESTIMATE	0.644	2.41	89°	0°
AVERAGE RELATIVE ERROR		10%	5%	3%	0%

thesized, and the network evaluated on both theoretical and experimental data. One problem was that no pitch-catch data were available for spheroidal defects, and no pulse-echo data were available for cracks. Hence, the final network could only be evaluated on one type of data. It was decided that the 19-element hexagonal array would be used in the pulse-echo mode, since these measurements require only a single roving transducer, plus more experimental data were available for spheroids than for cracks. The ALN discrimination model was evaluated on the nine experiments.

DATA BASE

The theoretical data base for training consisted of the 240 spheroid experiments described earlier, and 360 pulse-echo elliptical crack experiments generated with H. McMaken's GTD crack model. The 10 sizes and 36 orientations of the crack data base appear in Table 10. Features of only the power spectrum were used to perform defect recognition. The crack spectra were generated from 1.0-8.8 MHz, exactly the same bandwidth as the void spectra. The 19-element hexagonal array was used to record the scattered field.

- (1) First Moment (μ_1)
- (2) Second Moment (μ_2)
- (3) Low-to-High Ratio (P)
- (4) Standard Deviation (σ)
- (5) Normalized Total Power (P_T)

All features were computed over the range of 1.0-8.8 MHz. The low-to-high ratio was computed by dividing the power in the 1-4.5 MHz band by the power in the 4.5-8.8 MHz band.

The 13 spatial features (listed in the section on spheroid feature extraction) were computed on each of the five spectral features, yielding a total of 65 candidate features for ALN synthesis.

ALN MODEL SYNTHESIS

The ALN model output was designed to map all crack feature vectors into +1 and all void feature vectors into -1. Therefore, any ALN output greater than the zero threshold are indicative of a crack, and negative outputs are indicative of voids. The resultant network structure is shown in Fig. 34. This ALN selected four power spectral $[P(f)]$ feature inputs:

Table 10. Sizes And Orientations Of The 360 Theoretical Pulse-Echo Elliptical Crack Experiments Used For Crack/Void Discrimination

Defect Sizes		Defect Orientations	
A (μm)	B (μm)	α (degs)	β (degs)
312	312	90	55
312	625	80	140
625	625	70	245
312	1250	60	330
625	1250	50	
1250	1250	40	
312	2500	30	
625	2500	20	
1250	2500	10	
2500	2500		
10 sizes times 9 α 's times 4 β 's = 360 experiments			

FEATURE EXTRACTION

Three basic differences were observed between crack and void power spectra:

- (1) cracks had more energy concentrated at the low-frequency position of the spectrum than did voids;
- (2) dips in the spectrum were more pronounced for cracks than for voids, yielding more spectral "activity," and
- (3) the energy roll-off as a function of polar angle was greater for cracks than for voids.

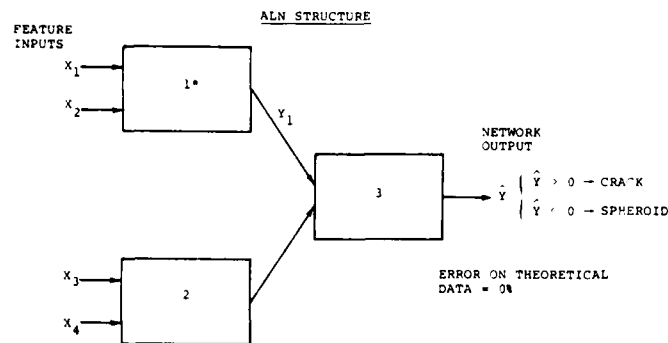
These observations contributed to the proposition of the five following spectral features:

- (1) z-centroid (\bar{C}_z) of the first moment,
- (2) z-centroid (\bar{C}_z) of the low-to-high ratio;
- (3) y-centroid (\bar{C}_y) of the standard deviation; and
- (4) z-centroid (\bar{C}_z) of the standard deviation.

The network correctly classified 100% of the crack and void defects when evaluated on theoretical data.

EXPERIMENTAL RESULTS

The nine pulse-echo spheroidal experiments were processed through the ALN discriminant and



* ELEMENTAL FORM: $Y_1 = W_0 + W_1 X_1 + W_2 X_2 + W_3 X_1 X_2 + W_4 X_1^2 + W_5 X_2^2$

FEATURE DESCRIPTION

- X_1 : \bar{C}_2 of Power Spectral First Moment
 X_2 : \bar{C}_2 of Low to High Power Ratio
 X_3 : \bar{C}_Y of Power Spectral Standard Deviation
 X_4 : \bar{C}_2 of Power Spectral Standard Deviation

NETWORK WEIGHTING COEFFICIENTS

ELEMENT	W_0	W_1	W_2	W_3	W_4	W_5
1	-.592E+02	.305E+02	.112E+03	-.309E+02	-.372E+01	-.431E+02
2	.353E+01	.322E+02	-.324E+03	-.917E+03	.238E+05	.513E+04
3	-.303E+00	.613E+00	.463E+00	-.890E-01	.216E+00	.173E+00

Fig. 34 Adaptive learning network to discriminate two-dimensional (crack-like) defects from three-dimensional (void-like) defects.

the output results are shown in Table 11. Note that eight of the nine defects were classified correctly. Experiment 4, (A = 200 μ m; B = 400 μ m; α = 80°; β = 160°) was incorrectly classified. Low signal-to-noise ratios at many of the receiver positions for this experiment could have contributed to this error. The overall results, however, are very encouraging. A plan for future efforts will include evaluating this model on experimental pulse-echo crack data.

REFERENCES

1. T. J. Ulrych, T. N. Bishop, "Maximum Entropy Spectral Analysis and Autoregressive Decomposition," Review of Geophysics and Space Physics, Vol. 13, 1975, p. 183.
2. N. E. Paton, "Sample Preparation," Interdisciplinary Program for Quantitative Flaw Definition, Special Report Second Year

Table 11. Results Obtained By Processing The Nine Spheroid Experiments Through The ALN Crack/Spheroid Discriminator. Eight Of The Nine Experiments Were Correctly Classified.

Experiment No.	ALN Output	True Class	Estimated Class
1	-.4569	Spheroid	Spheroid
2	-.4869	Spheroid	Spheroid
3	.1685	Spheroid	Crack
4	-.3137	Spheroid	Spheroid
5	-.5138	Spheroid	Spheroid
6	-.2794	Spheroid	Spheroid
7	-.3759	Spheroid	Spheroid
8	-.2455	Spheroid	Spheroid
9	-.4097	Spheroid	Spheroid

- Effort, AFML Contract F33615-74-C-5180, Science Center, Rockwell International, July 1976, pp. 89-101.
3. M. F. Whalen, A. N. Mucciardi, "Inversion of Physically Recorded Ultrasonic Waveforms Using Adaptive Learning Networks Trained on Theoretical Data," Interdisciplinary Program for Quantitative Flaw Definition, Special Report Fourth Year Effort, AFML Contract F33615-74-C-5180, Science Center, Rockwell International, July 1978, pp. 55-80.
 4. J. H. Rose, J. A. Krumhansl, "A Technique for Determining Flaw Characteristics from Ultrasonic Scattering Amplitude," Interdisciplinary Program for Quantitative Flaw Definition, Special Report Fourth Year Effort, AFML Contract F33615-74-C-5180, Science Center, Rockwell International, July 1978, pp. 1-5.
 5. Harry McMaken, Personal Communication, 1979.
 6. J. D. Achenbach, A. K. Gautesen, and H. McMaken, "Diffraction of Elastic Waves by Cracks - Analytical Results," Elastic Waves and Non-Destructive Testing of Materials, AMD-Vol. 29, Edited by Y. H. Pao, 1978.
 7. J. D. Achenbach, A. K. Gautesen, and H. McMaken, "Application of Geometrical Diffraction Theory to QNDE Analysis," Interdisciplinary Program for Quantitative Flaw Definition, Special Report Fourth Year Effort, AFML Contract F33615-74-C-5180, Science Center, Rockwell International, July 1978, pp. 31-38.
 8. L. Adler, "Identification of Flaws by Ultrasonic Spectral Analysis," Interdisciplinary Program for Quantitative Flaw Definition, AFML Contract F33615-74-C-5180, Science Center, Rockwell International, July 1978, pp. 46-54.
 9. W. Maurice Ewing, Wenceslas S. Jardetzky and Frank Press, Elastic Waves in Layered Media, McGraw-Hill, 1957.
 10. L. Knopoff, "Q," Reviews of Geophysics, Vol. 2, 1974, p. 273.
 11. V. V. Varadan, V. K. Varadan, "T-Matrix Calculations for Elastic Scattering from Spheroidal Cavities and Inclusions and Crack-Like Flaws," Interdisciplinary Program for Quantitative Flaw Definition, AFML Contract F33615-74-C-5180, Science Center, Rockwell International, July 1978, pp. 18-30.
 12. P. P. Tittmann, Personal Communication, May 1979.

TESTING THE INVERSE BORN PROCEDURE FOR SPHEROIDAL VOIDS*

J. H. Rose
Physics Department
University of Michigan
Ann Arbor, Michigan 48109

V. V. Varadan and V. K. Varadan
Boyd Laboratory
Ohio State University
Columbus, Ohio 43210

R. K. Elsley and B. Tittman
Rockwell International Science Center
Thousand Oaks, California 91360

ABSTRACT

Previously we have shown that the inverse Born approximation allows an accurate determination of the radius of spherical flaws in Ti. Here we report the results of extending that analysis to spheroidal voids. Both oblate and prolate spheroids are considered. Using scattering amplitude generated by the T-matrix method, we find that both the major and minor axes of 2-1 spheroids are accurately determined. Inversion results using experimental data will be presented for the 2-1 oblate spheroid; a comparison of the experimental and theoretical results will be given.

INTRODUCTION

Recent developments in ultrasonic scattering theory have been strongly motivated by the non-destructive evaluation needs of the structural materials community. Their primary question is: given a set of ultrasonic measurements (e.g. scattering amplitudes) from some industrial component, when will it break? An intermediate step in answering this question is: given the scattering data, what are the characteristics of the flaws in the piece? Here one would like to know if one has a volume flaw such as a void or inclusion, or if one has a crack. Also, one would like to know the size, shape and orientation of the flaw; and, if it is an inclusion, what it is made of. Answering these questions is what I will refer to as the ultrasonic inversion problem.

The current status of the ultrasonic inversion problem depends upon the ratio of the characteristic size of the flaw (a_0) to the wavelength λ ($k = 2\pi/\lambda$). When the size of flaw is much larger than the wavelength, $ka_0 \gg 1$, then imaging techniques can be used, and a good deal of progress has been made. In the opposite limit, $ka_0 \ll 1$, there has been some recent progress, both in terms of describing what information can be extracted in principle and in terms of practical algorithms for simply shaped flaws.¹ Between these two limits we have the intermediate regime, where the wavelength is on the order of the size of the object. This paper focuses on the intermediate regime and studies the geometric features of single voids.

We will review the theoretical development of an inversion algorithm for the intermediate wavelength case. Further, we will summarize the progress of our group effort to empirically verify this algorithm. The need for detailed empirical verification stems from the theoretical justification of the algorithm, which is based on perturbative solutions of the wave equation and is valid only if the scattering is sufficiently weak! However, many of the flaws of interest in NDE are

anything but weak (e.g. a void). It is not clear how to extend our current inversion algorithm formally to the strong scattering case. However, for voids of simple shape, the algorithm yields good results as we will report.

It is in this empirical verification scheme that recent developments in elastic wave scattering theory (such as the T-matrix method²) have a key role to play. For in order to establish the limits of validity of this algorithm and other empirical inversion algorithms, it is desirable to have the scattering amplitudes for a wide range of differently shaped flaws. Particularly interesting for this purpose would be flaws with sharp edges such as cones and pill boxes. Up to the present time we are limited to investigating spherical, and oblate and prolate spheroidal flaws.

The structure of the paper is as follows. In the second section we review the derivation of the algorithm. In section three we indicate how the theory was simplified for the case of ellipsoidally shaped flaws. In the fourth section we report the results of testing the algorithm with experimentally generated data. In the fifth section we report the results of testing the inversion algorithm using scattering amplitudes generated by the T-matrix method for 2-1 oblate and prolate spheroidal voids. Finally, in section six we provide a discussion of our results and conclude.

GENERAL THEORY

The algorithm to be discussed below is a procedure for approximately determining the Fourier transform of the characteristic function, $\chi(r)$, of the flaw. Here $\chi(r)$ is 1 for r inside the flaw, and $\chi(r)=0$ for r outside the flaw. We restrict our review of the theory to the simplest experimental situation. That is we assume a pulse-echo geometry as shown in Fig. 1. Here a longitudinally or shear polarized plane wave is incident on the

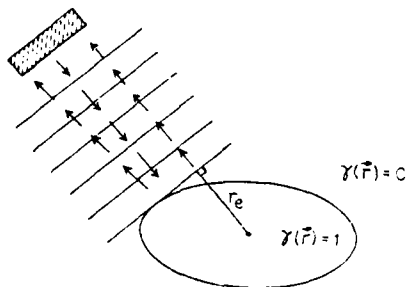


Figure 1. The geometry of a pulse echo experiment. The distance from the center of the flaw to the tangent plane is the effective radius, r_e , discussed in the text.

flaw, and the directly backscattered longitudinal or shear amplitude is determined. The pulse echo scattering amplitudes can be written for an arbitrarily shaped flaw as

$$A(\vec{k}) = a(\vec{k}, \{\mu\}) S(2\vec{k}) k^2 \quad (2-1)$$

Here $S(2\vec{k})$, the shape factor, is the Fourier transform of the characteristic function of the flaw. The wavevector of the incident wave is denoted by \vec{k} and $a(\vec{k}, \{\mu\})$ is a function to be calculated which yields the correct scattering amplitudes A for an arbitrary \vec{k} . Here $\{\mu\}$ denotes the material parameters of the host material.

The virtue of writing the scattering amplitudes in the form of Eq. 2.1 is that several approximate theories^{4,5} yield very simple forms for the factor $a(\vec{k}, \{\mu\})$. In particular we will use the form of $a(\vec{k}, \{\mu\})$ which can be derived from the extended quasi-static approximation. In that approximation one takes account of the long wavelength elastic deformation of the flaw correctly, and hence obtains the angular features of the scattering correctly in this limit. For the extended quasi-static approximation $a(\vec{k}, \{\mu\})$ is assumed to be independent of $|\vec{k}|$ and given by its long wavelength limit which depends only on the direction of \vec{k} , \vec{k} , and $\{\mu\}$. We denote this approximate form of $a(\vec{k}, \{\mu\})$ as $a_{QSA}(\vec{k}, \{\mu\})$. Using this approximation we rewrite equation 2.1 as

$$S(2\vec{k}) = A(\vec{k}) / (k^2 a_{QSA}(\vec{k}, \{\mu\})) \quad (2.2)$$

Experimentally, a_{QSA} can be obtained for an arbitrarily shaped object by measurements of the long wavelength scattering amplitudes. In that limit $S(2\vec{k})$ goes to a constant, and a_{QSA} can be determined from the angularly dependent coefficients of A

$$a_{QSA}(\vec{k}, \{\mu\}) = \lim_{k \rightarrow 0} A(\vec{k}) / k^2 \quad (2.3)$$

Once a_{QSA} is obtained we can determine $S(2\vec{k})$ from Eq. 2.2 via an experimental measurement of the

backscattered amplitudes. Taking the Fourier transform of $S(2\vec{k})$ then allows us to determine the characteristic function of the flaw, and hence its size, shape and orientation. The major approximation in using a_{QSA} is that we assume that it depends only on \vec{k} and not on $|\vec{k}|$. The characteristic function is given explicitly in terms of the shape function as⁶

$$\gamma(\vec{r}) = \text{const.} \int d^3k e^{2i\vec{k} \cdot \vec{r}} R_e(A(\vec{k})) / (k^2 a_{QSA}(\vec{k}, \{\mu\})) \quad (2.4)$$

SIMPLIFIED THEORY FOR ELLIPSOIDALLY SHAPED FLAWS

In the last section we described an approximate procedure for determining the size, shape and orientation of an arbitrary three dimensional flaw. In order to use this inversion technique one requires pulse-echo measurements from all incident directions \vec{k} . The characteristic function is then obtained (Eq. 2.4) as an inverse Fourier transform which involves integrating over both $|\vec{k}|$ and \vec{k} . For the class of ellipsoidally shaped flaws, one can obtain all relevant information about the flaw by inverting each pulse-echo record independently as discussed below. This avoids the angular integration over \vec{k} in the inverse Fourier transform, and significantly simplifies the application of the algorithm.

In order to illustrate how this simplification comes about, let us consider the weak scattering limit. Then the theory of the last section is rigorously valid and Eq. 2.2 becomes

$$S(2\vec{k}) = \text{const.} A_L(\vec{k}) / k^2 \quad (3.1)$$

We have used the fact that $a(\vec{k}, \{\mu\})$ is a constant in the weak scattering limit as a function of \vec{k} . For an ellipsoid we know that $S(2\vec{k})$ is given by the following equations

$$S(2k) = \frac{\sin(2k r_e) - 2k r_e \cos(2k r_e)}{(2k r_e)^3} \quad (3.2)$$

and

$$r_e = (a_x^2 \cos^2 \theta \sin^2 \phi + a_y^2 \cos^2 \theta \cos^2 \phi + a_z^2 \sin^2 \theta) / 2 \quad (3.3)$$

Here the axes of the ellipsoid are $a = (a_x, a_y, a_z)$, and θ and ϕ define the direction of \vec{k} in spherical co-ordinates. The angular dependence of the shape factor comes in strictly through the function which we have called $r_e(\theta, \phi)$. In a pulse-echo measurement, the incident direction \vec{k} is kept fixed, and r_e is a constant for that set of data. We note for a fixed incident direction, Eq. 3.2 has the same form as a Fourier transform of a sphere with an effective radius r_e . For each incident direction \vec{k} , we obtain r_e in the following way. First we obtain $S(2|\vec{k}|)$ from Eq. 3.1. We then extend $S(2|\vec{k}|)$ to be spherically symmetric in k -space. Thus, we obtain the three dimensional Fourier transform of a sphere of radius $r_e(\theta, \phi)$. This Fourier transform is then inverted to yield the effective radius for that direction. The resulting effective radius (Eq. 3.3) has a simple geometric interpretation as shown in Fig. 1. When a wavefront strikes the surface, it is first tangent at some one point (which is an accumulation point for phase). The radius r_e is the distance from the center of the

flaw to the plane of the wavefront. An important consequence of Eq. 3.3 is that pulse-echo measurements along the axis of an ellipsoid yield the axis length directly. For example, a measurement along the a axis yields an effective radius equal to $a/2$. Hence, one can obtain the length of the ellipsoid axes directly from three measurements if one knows the orientation of the ellipsoid.

So far we have been discussing the weak scattering limit for the sake of illustration. The appropriate extension to the strong scattering case is straightforward. Eq. 2.2 is

$$S(2k) = \text{const. } A(k)/(k^2 a_{\text{QSA}}(k, \{\mu\})) \quad (3.4)$$

For a given incident direction $a(k, \{\mu\})$ is just a constant since it doesn't depend on $|k|$ in the quasi-static approximation. With this approximation we recover Eq. 3.1 and can proceed in an approximate way with the entire procedure which was given above. Of course for a strongly scattering flaw, our analysis is only approximate and must be checked empirically. In the next sections we provide some empirical tests of the strong scattering limit.

INVERSION OF EXPERIMENTAL DATA

We summarize the initial results of testing the algorithm, in its simplified form for ellipsoids, with experimental data. More extensive results and a comprehensive treatment of both experiment and data analysis will be given in Ref. 7. We report results for a spherical void with a radius of 400 μ , and an oblate spheroid with a semi-major axis of 400 μ and a semi-minor axis of 200 μ . These were machined flaws in the center of large spheres of Ti-6Al-4V. Details of the construction of the flaws and their use as calibration samples are given in Ref. 8 and 9.

The simplified algorithm allows us to treat each pulse-echo measurement separately, and it yields the distance from the center of the flaw to the tangent plane of the incoming wavefront. For the sphere we obtained a single pulse-echo record which suffices to determine the size of the flaw due to its spherical symmetry. However, for the spheroid we only examined the pulse-echo record for a measurement along the axis of symmetry.

Before presenting the results, we want to discuss two crucial details of the data analysis scheme. First, for sufficiently small wavevector, k , the phase of the scattering amplitudes must be constant and zero. This reflects the fact that the real part of the scattering amplitude rises as k^2 for small k while the imaginary rises much more slowly. This constraint on the phase allows one to establish the phase of the experimental data, which otherwise would not be entirely determined.⁷ The second point concerns the effects of limited bandwidths. A lack of low frequency data would leave the phase of the data undetermined as just indicated. A lack of high frequency data causes the characteristic function to be blurred, and this introduces some uncertainty in determining the size of the flaw. In large part the effects of blurring due to the limited bandwidth can be overcome by an appropriate calibration procedure. For the simplified form of the algorithm, the analysis is carried out in terms of equivalent spheres. The effects of a limited high frequency bandwidth on the characteristic function of a sphere can be determined in the following way. We consider the Fourier transform of a sphere in k -space. We then band-limit it

with a rectangular window extending from $k=0$ to k_{max} . Then we transform it back to r -space. The resulting curves can then be compared to the experimentally determined characteristic functions and thus serve as a calibration for the effects of blurring.

Inverting the pulse-echo data for the sphere ($0 < ka < 4$) where a is the radius. We find a radius of approximately 400 μ with an uncertainty of about 40 μ . This should be compared to the exact value of 400 μ . The inversion of the spheroid data yields an estimate of the semi-minor axis of 220 μ with an uncertainty of about 20 μ . The exact value is 200 μ . We consider these results to be quite encouraging. It is clear however, that considerably more scattering data for other orientations of the spheroids, for other materials and for other types of volume flaws (e.g. inclusions) will be necessary before the algorithm can be considered fully tested. To partially examine these questions we turn to the theoretically generated data of the next section.

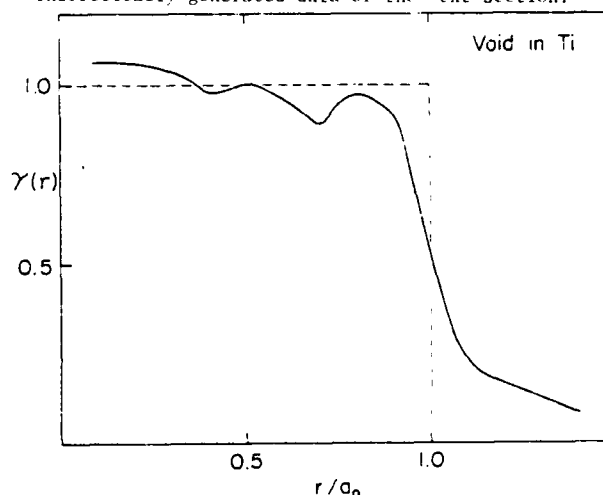


Figure 2. The calculated characteristic function for a spherical void of radius, a , in titanium. The result was obtained by inverting theoretical scattering amplitudes with a bandwidth $0 < ka < 10$.

INVERSION OF THEORETICAL DATA

The inversion algorithm was tested for three different flaws in titanium using data generated from theory. The first flaw was a spherical void with $0 < ka < 10$. The second flaw was a 2-1 oblate spheroid with $0 < ka < 4$ (where a denotes the semi-major axis). The third flaw was a 2-1 prolate spheroid with $0 < kb < 4$ (here we define b as the semi-minor axis). The sphere data was generated using the exact theory of Ying and Truell and isotropic elastic constants for titanium. The T-matrix method was used to obtain the scattering amplitudes for the (400 μ by 200 μ) prolate and oblate spheroidal flaws.

The spherical flaw is considered first. Figure 2 shows the characteristic function obtained from the inversion procedure. Using the 50% point to define the boundary, we find that the radius is determined to within about 5%. We note that the inversion procedure was tested for sensitivity to noise for this spherical flaw and found to be quite

insensitive.⁷

The preliminary analysis of the spheroidal data is confined to an approximate determination of the semi-major and semi-minor axes using the simplified theory of section three. The simplified theory has the feature that a pulse-echo waveform along one of the axes can be used to determine the radius of an equivalent sphere with the radius of that axis. In Fig. 3 we show the characteristic function derived from the pulse-echo waveform measured along the semi-minor axis. Figure 4 is the equivalent

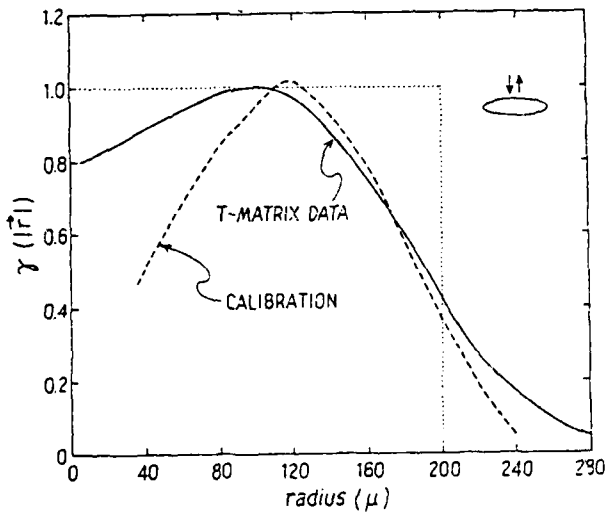


Figure 3. Calculated characteristic function for the semi-minor axis of the prolate spheroid using theory data with a bandwidth of $0 < kb < 4$.

result for the semi-major axis. Using these results we obtain estimates of 420μ and 210μ for these axes compared to the exact results of 400μ and 200μ . Similar results for the oblate spheroids are 360μ and 210μ compared to exact values of 400μ and 200μ .

In section four we calculated the characteristic function for the semi-minor axis of an oblate spheroid from experiment. In this section we computed the same result using scattering amplitudes obtained from the T-matrix method. We now compare both results (with a bandwidth $0 < kb < 2$). The results are shown in Fig. 5, and the agreement is essentially exact.

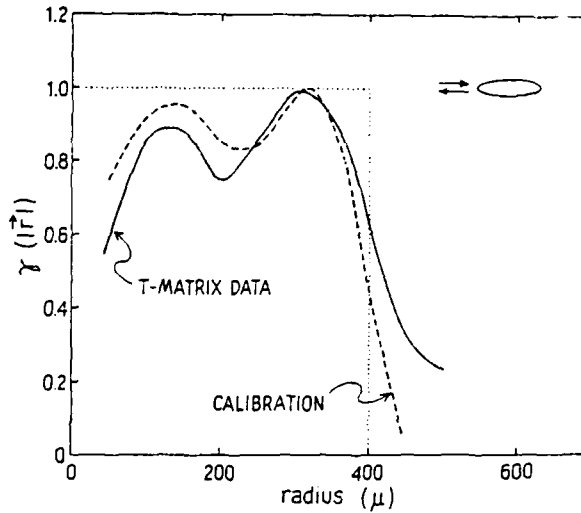


Figure 4. Calculated characteristic function for the semi-major axis of the prolate spheroid using the theory data with a bandwidth of $0 < ka < 4$.

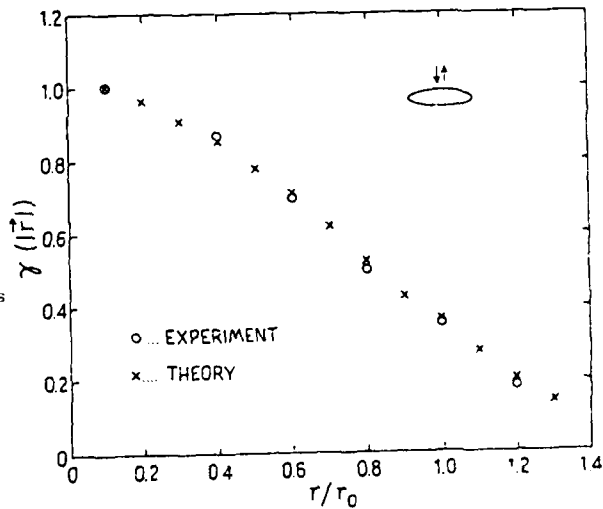


Figure 5. The calculated characteristic functions for the semi-minor axis of the oblate. Theory and experiment are compared.

CONCLUSION

We have presented an inversion algorithm for the intermediate scattering regime when the size of the flaw is comparable to the wavelength of the ultrasound. Tests of the algorithm were performed for the case of spherical and spheroidal voids in Titanium. Good results were obtained for the size and shape of the flaws. These results suggest that this algorithm may be of practical use for the non-

destructive testing community in determining the characteristics of volume type flaws in various solids.

REFERENCES

*This research was supported by the Center for Advanced NDE, Rockwell International Science Center.

1. J. M. Richardson, IEEE Ultrasonics Symposium, Cherry Hill New Jersey 759 (1978).
2. J. H. Rose and J. A. Krumhansl, J. Appl. Phys. 50 2951 (1979).
- 3a. V. V. Varadan and Y. H. Pao J. Acoust. Soc. Am. 60 556 (1976).
- b. V. V. Varadan J. Acoust. Soc. Am. 63 1014 (1978).
- c. V. V. Varadan and V. K. Varadan J. Acoust. Soc. Am., in press.
4. J. E. Gubernatis, E. Domany, J. A. Krumhansl and M. Huberman, J. Appl. Phys. 48 2812 (1977).
5. J. E. Gubernatis, Los Alamos Scientific Laboratories Report LA-UR-771339 (1977), unpublished.
6. The characteristic function, $\gamma(\vec{r})$, is real which we insure by inverting only the real part of the scattering amplitude. This procedure for preserving the reality of γ is discussed in reference 7.
7. J. H. Rose, V. V. Varadan, V. K. Varadan, R. K. Elsley and B. R. Tittman, to be published.
8. B. R. Tittman, E. R. Cohen, J. M. Richardson, J. Acoust. Soc. Am. 63 68 (1978).
9. B. R. Tittman, R. K. Elsley, H. Nadler and E. R. Cohen, to be published.

DETERMINISTIC AND PROBABILISTIC INVERSION AT LONG WAVELENGTHS*

J.M. Richardson
Rockwell International Science Center
Thousand Oaks, California 91360

ABSTRACT

In contrast with the scalar wave case, the scattering of elastic waves in the long wavelength limit yields data containing a surprising amount of information concerning the nature of the scatterer. We will consider both deterministic and probabilistic versions of the inversion problem pertaining to the above scattering problem. The deterministic version provides theoretical insight into the "blindspots" of an optimal inversion procedure in the hypothetical limit of zero measurement error. The probabilistic version is appropriate for the interpretation of real data containing errors and possible inconsistencies. In the former category our discussion will start with a review of earlier results obtained by Kohn and Rice, Gubernatis, and the author. Some new results dealing with ellipsoidal inclusions will be discussed.

INTRODUCTION

Since the low frequency (long wavelength) limit in the scattering of elastic waves represents a situation in which the limit of resolution is many times the size of the scatterer, one expects to obtain very little information about the nature of the scatterer, which is indeed true in the case of scalar wave scattering in quantum mechanics. However, in the case of elastic wave scattering, a surprising amount of information concerning the quasi-stationary elastic behavior of the scatterer can be deduced from scattering data.

Before considering the detailed results, it is important to ask: What advantages would such an approach have relative to other approaches for defect characterization? The following points can be made in its favor:

- 1) The theory of the scattering of elastic waves at low frequencies is well established for the case of ellipsoidal inclusions and voids. Thus, the inverse scattering problem for this class of scatterers is quite tractable. At higher frequencies, this is not the case.
- 2) Low frequency measurements are sensitive only to the overall shape and size of the defect and not to small textural details. This is also the information of importance in fracture (at least in metals).
- 3) Low frequency scattering measurements are particularly sensitive to cracks compared with other scatterers (e.g., inclusions of the same volume or even the same area). In particular, the scattering measurements are significantly more sensitive to a large crack than to a number of small cracks with the same total area.
- 4) The elastic processes involved in low frequency scattering are intimately related to those involved in the early stages of the fracture process (at least in most metals) as has been pointed out

by Budiansky and Rice.¹ A further advantage is that the relevant stress intensity factor is proportional to the $1/6$ power of the scattering amplitude, yielding thereby a substantial reduction of variance in the estimation process, a fact emphasized by Kino.²

Thus the low frequency scattering region has a number of attractive features, particular in the context of NDE.³ The disadvantages of this approach are mainly associated with the extraction of the low frequency scattering amplitude from raw scattering data, a problem that R.K. Elsley will discuss in a later talk at this symposium.

In the present paper, we attempt to give a cursory overview of the inversion problem associated with low frequency elastic scattering with emphasis on both deterministic and probabilistic approaches. A purpose of the deterministic approach is to provide insight into the blindspots that limit what properties can in principle be yielded by an inversion procedure using certain categories of input data, even when these data are assumed to be perfectly accurate and available in any quantity (of course, within the restrictions implied by the definition of each category). In the real world we must deal with noisy data involving incompleteness and near-inconsistencies and here we must use a probabilistic approach. However, in the latter context, the results of the deterministic approach can have substantial value in providing guidance about what kinds of inferences are possible from a given category of data. These considerations provide additional motivation for the talk to be given by Fertig at the end of the present session.

THE DIRECT PROBLEM

We consider a linear, nondissipative elastic medium characterized at each point $\vec{r} = \hat{e}_1 x_1 + \hat{e}_2 x_2 + \hat{e}_3 x_3$ by a mass density $\rho + \delta \rho(\vec{r})$ and an elastic constant tensor $C_{\alpha\beta\gamma\delta} + \delta C_{\alpha\beta\gamma\delta}(\vec{r})$ (we use

*This research was sponsored by the Center for Advanced NDE operated by the Rockwell International Science Center, for the Advanced Research Projects Agency and the Air Force Materials Laboratory under Contract No. F33615-74-C-5180.

Greek subscripts to denote cartesian coordinate directions along with the usual summation convention). We assume that everywhere outside of the scatterer domain D_s (see Fig. 1) the perturbations $\delta\rho(\vec{r})$ and $\delta C_{\alpha\beta\gamma\delta}(\vec{r})$ vanish. Thus, the host material is characterized by the constant density ρ and elastic constant tensor $C_{\alpha\beta\gamma\delta}$ where, in accordance with the assumption of isotropy,

$$C_{\alpha\beta\gamma\delta} = \lambda \delta_{\alpha\beta} \delta_{\gamma\delta} + 2 \mu I_{\alpha\beta\gamma\delta} \quad (2.1)$$

in which λ and μ are the Lamé constants and

$$I_{\alpha\beta\gamma\delta} = \frac{1}{2} (\delta_{\alpha\gamma} \delta_{\beta\delta} + \delta_{\alpha\delta} \delta_{\beta\gamma}) \quad (2.2)$$

the 4th order unit tensor appropriate for elastic processes.

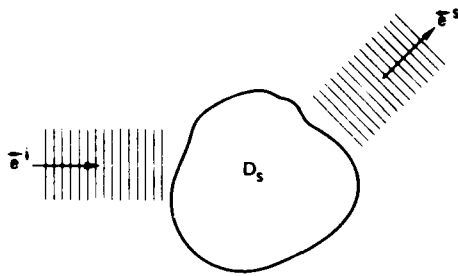


Fig. 1 Scattering geometry.

At a position \vec{r} and frequency ω , the displacement field $\vec{u} = \vec{u}(\vec{r}, \omega)$ can be decomposed into incident and scattered parts in accordance with the relation

$$\vec{u} = \vec{u}^i + \vec{u}^s \quad (2.3)$$

The incident part can be written in the form

$$\vec{u}^i = [\vec{e}^i \vec{e}^i \exp(ik_L \vec{e}^i \cdot \vec{r}) + (\vec{I} - \vec{e}^i \vec{e}^i) \exp(ik_T \vec{e}^i \cdot \vec{r})] \cdot \vec{a} \quad (2.4)$$

where \vec{e}^i and \vec{e}^s are the incident and scattered directions, respectively. \vec{I} is the second order unit tensor, \vec{a} is the incident polarization and where, finally, k_L and k_T are the wave numbers for longitudinal and transverse elastic waves. In the far-field regime, the scattered wave can be written in the form

$$\vec{u}^s_{r \rightarrow \infty} = [\vec{e}^s \vec{e}^s \exp(ik_L r) + (\vec{I} - \vec{e}^s \vec{e}^s) \exp(ik_T r)] \cdot \vec{A}(\vec{e}^s, \vec{e}^i; \omega) \cdot \vec{a} \quad (2.5)$$

where $r = |\vec{r}|$ is the radial distance from an origin assumed to be placed at a point inside the scatterer domain D_s . As usual, the longitudinal and transverse wave numbers are given by

$$k_L = \omega/c_L \quad (2.6a)$$

$$k_T = \omega/c_T \quad (2.6b)$$

where the longitudinal and transverse propagation velocities are given by

$$c_L = [(\lambda + 2\mu)/\rho]^{1/2} \quad (2.7a)$$

$$c_T = (\mu/\rho)^{1/2} \quad (2.7b)$$

Since the scatterer is localized, we can expand the scattering amplitudes in a power series in the frequency, namely

$$\vec{A}(\vec{e}^s, \vec{e}^i; \omega) = \sum_{n=0}^{\infty} \vec{A}_n(\vec{e}^s, \vec{e}^i) \omega^n \quad (2.8)$$

The spatial localization implies that

$$\vec{A}_0 = \vec{A}_1 = 0 \text{ for all } \vec{e}^i \text{ and } \vec{e}^s \quad (2.9)$$

and thus the leading term is $\vec{A}_2 \omega^2$. Since the quantity in the time domain corresponding to \vec{A} in the frequency domain (i.e., the impulse response function) must be real, it follows that the reality condition

$$\vec{A}(\vec{e}^s, \vec{e}^i; -\omega) = \vec{A}^*(\vec{e}^s, \vec{e}^i; \omega) \quad (2.10)$$

must hold and hence A_n is real if n is even and imaginary if n is odd.

The higher order terms beyond $A_2 \omega^2$ are negligible if the frequency ω is sufficiently low or equivalently the relevant wavelengths are sufficiently long. This is called the Rayleigh (or low frequency) regime which is the sole concern of the present discussion.

The main feature of the results of Gubernatis, et al.,⁴ is that the coefficient \vec{A}_2 is a linear function of the mass excess M and the D-tensor $D_{\alpha\beta\gamma\delta}$, collectively representing all of the properties of the scatterer determining the low frequency scattering behavior. If two different scatterers have the same values of M and $D_{\alpha\beta\gamma\delta}$, then the low frequency scattering behavior will be the same. The mass excess is given by

$$M = \int d^3\vec{r} \delta\rho(\vec{r}) \quad (2.11)$$

and the D-tensor by

$$D_{\alpha\beta\gamma\delta} = \int d^3\vec{r} \delta C_{\alpha\beta\gamma\delta}(\vec{r}) \quad (2.12)$$

where $\Gamma_{\alpha\beta\gamma\delta}(\vec{r})$ is the strain proportionality tensor relating the strain $\epsilon_{\alpha\beta}$ at \vec{r} due to a uniform applied (or incident) strain $\epsilon_{\alpha\beta}$ in accordance with the relation

$$\epsilon_{\alpha\beta}(\vec{r}) = \Gamma_{\alpha\beta\gamma\delta}(\vec{r}) \epsilon_{\gamma\delta}^i \quad (2.13)$$

It is understood that the above relation is derived in the quasi-static elastic approximation.

It is of interest to consider the particular forms of \vec{A}_2 for the various mode-to-mode scattering situations. However, for the sake of brevity we will restrict our discussion to the case of longitudinal-to-longitudinal ($L \rightarrow L$) scattering described by the scalar scattering amplitude

$$\begin{aligned} A_{2,L \rightarrow L} &= \vec{e}^s \cdot \vec{A} \cdot \vec{e}^i \\ &= \frac{1}{4\pi\rho} \frac{1}{c_L^2} \epsilon_{\alpha}^s \epsilon_{\alpha}^i M - \frac{1}{4} \epsilon_{\alpha}^s \epsilon_{\beta}^s D_{\alpha\beta\gamma\delta} \epsilon_{\gamma}^i \epsilon_{\delta}^i \end{aligned} \quad (2.14)$$

In deriving the above result we have assumed that $\vec{a} = \vec{e}^i$, i.e., the displacement amplitude of the incident wave is a unit vector pointed in the longitudinal direction.

It is useful to break up the scattering amplitude into parts that are even or odd with respect to the reversal of \vec{e}^i or \vec{e}^s . We accordingly define

$$\begin{aligned} A_{2, \ell+2}(\vec{e}^s, \vec{e}^i) \\ = \frac{1}{2} A_{2, \ell+2}(\vec{e}^s, \vec{e}^i) \pm A_{2, \ell+2}(-\vec{e}^s, \vec{e}^i) \\ = \frac{1}{2} A_{2, \ell+2}(\vec{e}^s, \vec{e}^i) \pm A_{2, \ell+2}(\vec{e}^s, -\vec{e}^i) \quad (2.15) \end{aligned}$$

It is clear from an inspection of Eq. (2.14) that $A_{2, \ell+2}$ depends only on the D-tensor and thus is called the elastic part. On the other hand $A_{2, \ell+2}$ depends only on M and thus is called the inertial part.

We turn finally to a consideration of the properties of $D_{\alpha\beta\gamma\delta}$. It is easily seen from Eq. (2.13) that this tensor must be invariant to the interchange of α and β . Also, Eq. (2.13) implies that it can be assumed, without loss of generality, to be invariant to the interchange of γ and δ . It can be proved with relatively complicated arguments⁵ that it is also invariant to the interchange of $\alpha\beta$ and $\gamma\delta$. Therefore the D-tensor has the same invariance properties as the elastic constant tensor with respect to the interchange of indices.

Thus, the D-tensor has 21 independent elements (i.e., independent as far as the interchange of indices is concerned). Combined with M, this means that there are $21 + 1 = 22$ properties of the scatterer determining low frequency scattering behavior, a fact that has been independently noted by Kohn and Rice⁶ and by the author.⁷

THE DETERMINISTIC INVERSE PROBLEM

There are two kinds of procedures for dealing with the low frequency inverse scattering problem. As shown in scheme below, one procedure is to follow the scheme below, that is,

Scattering + M, D-tensor + Scatterer
Data Parameters

start with scattering data and deduce M and the D-tensor which in turn are used as the basis for deducing whatever scatterer properties (or combinations of properties) are accessible. A second and apparently simpler procedure is to deduce the scatterer parameters (more precisely, the accessible combinations) directly from scattering data. We will use the first procedure in dealing with the deterministic inversion problem in the present section and the second procedure for the probabilistic inversion problem in the next section.

To simplify the treatment of the present section, it is expedient to introduce abbreviated notation. We will let a general 4th order tensor

$B_{\alpha\beta\gamma\delta}$ be represented by the bare symbol B, i.e.,

$$B_{\alpha\beta\gamma\delta} \Leftrightarrow B \quad (3.1)$$

and the product of two such tensors by the correspondence

$$B_{\alpha\beta\gamma'\delta'}^{(1)} B_{\gamma'\delta'\gamma\delta}^{(2)} \Leftrightarrow B^{(1)} B^{(2)} \quad (3.2)$$

An essential part of our formalism is the trace operation (denoted by the symbol "Tr" defined by

$$\text{Tr} B = B_{\alpha\beta\alpha\beta} \quad (3.3)$$

The 4th order tensors involved in our treatment are assumed invariant to the interchange of the first pair of indices and the interchange of the last pair, i.e., $B_{\alpha\beta\gamma\delta} = B_{\beta\alpha\gamma\delta}$, etc. The inverse B^{-1} corresponding to $B_{\alpha\beta\gamma\delta}$ is defined by the relation

$$B B^{-1} = B^{-1} B = I \quad (3.4)$$

where

$$I_{\alpha\beta\gamma\delta} \Leftrightarrow I \quad (3.5)$$

where, in turn, $I_{\alpha\beta\gamma\delta}$ is the 4th order unit tensor defined by Eq. (2.2). In actual computation, special provision must be made to limit the above inverse to the "vector" space of 2nd order symmetric tensors. The strain $\epsilon_{\alpha\beta}$, a typical operand, will be represented by the bare symbol ϵ .

In terms of the abbreviated notation, Eq. (2.13) can be rewritten in the form

$$D = \int d^3r \rho \epsilon \epsilon^T \quad (3.6)$$

where the correspondences to the previous indicial notation are obvious.

It will be convenient to introduce the compression projection tensor P defined by the correspondence

$$\frac{1}{3} \delta_{\alpha\beta} \delta_{\gamma\delta} \Leftrightarrow P \quad (3.7)$$

which projects a general strain $\epsilon_{\alpha\beta}$ into its isotropic or pure compression part, namely

$$P \epsilon \Leftrightarrow \frac{1}{3} \delta_{\alpha\beta} \delta_{\gamma\delta} \epsilon_{\gamma\delta} = \frac{1}{3} \delta_{\alpha\beta} \epsilon_{\gamma\gamma} \quad (3.8)$$

where the scalar quantity $\epsilon_{\gamma\gamma}$ is clearly the dilatation:

$$\epsilon_{\gamma\gamma} = \nabla \cdot \vec{u} \quad (3.9)$$

The complementary projection tensor \bar{P} is, of course, defined by

$$\bar{P} = I - P \quad (3.10)$$

and projects a general strain into its traceless or pure shear part. The elastic constant tensor for an isotropic medium can now be written in a simple form, e.g., in the case of the host medium we have

$$\begin{aligned} C &= 3\bar{P} + 2\mu I \\ &= (3\lambda + 2\mu)P + 2\mu\bar{P} \quad (3.11) \end{aligned}$$

We turn now to the question of how much information concerning M and D can be deduced from various categories of scattering measurements. The determination of the mass excess M is relatively trivial. For example, from Eq. (2.15a), we get

$$A_{2,2+2}^{(-)} = \frac{1}{4\mu\alpha\epsilon} \bar{e}^S \cdot \bar{e}^T M \quad (3.12)$$

and thus, for example, a single pair of $2+2$ scattering measurements with a single incident direction \bar{e} and opposite scattering directions $\bar{e}^S = \pm \bar{u}$ ($|\bar{u}| = 1, \bar{e}^T \bar{u} \neq 0$) will suffice. It has been demonstrated by Kohn and Rice⁵ that a sufficient number of $2+2$ scattering measurements provides enough information to determine the full D -tensor.

We must consider the problem of deducing the values of the scatterer parameters from a knowledge of M and D . We will confine (with exceptions as indicated) this discussion to the case of ellipsoidal inclusions (with the void as a special case) in contrast with the immediately previous discussion which was valid for completely general localized inhomogeneities.

Eshelby⁶ has proved that in the case of an ellipsoidal inclusion a uniform applied strain (i.e., a strain field that would be uniform in the absence of an inhomogeneity) produces a uniform strain in the inclusion. Using this peculiar property of the ellipsoidal geometry, one obtains the simple result

$$D = V(G + \alpha^{-1})^{-1} \quad (3.13)$$

where V is the volume of the inclusion and G is a constant Green's tensor given by the correspondence

$$G \Leftrightarrow V^{-1} \int_{D_S} d^3\bar{r} \int_{D_S} d^3\bar{r}' G_{\alpha\beta\gamma\delta}(\bar{r} - \bar{r}') \quad (3.14)$$

where $G_{\alpha\beta\gamma\delta}(\bar{r} - \bar{r}')$ relates in the host medium the strain at \bar{r} due to a stress applied at \bar{r}' . G is dependent only on the shape and orientation of the inclusion and on the elastic properties of the host medium. It is independent of the size and material properties of the inclusion. It also possesses remarkable contraction properties, namely that $\text{Tr}GP$ and $\text{Tr}G\bar{P}$ are dependent only on the elastic properties of the host medium. The quantity α^{-1} , the inverse of the elastic constant tensor perturbation α , is of course a constant and represents the elastic properties of the inclusion.

In the case of general inclusions (ellipsoidal or otherwise) the mass excess is given by the simple expression

$$M = V\delta\rho \quad (3.14)$$

where now $\delta\rho$ is the uniform value of density deviation within the inclusion. Thus from a knowledge of solely the inertial part $A_{2,2+2}^{(-)}$ one can determine only the product $V\delta\rho$ and nothing about the shape and orientation of the inclusion.

In the case of general inclusions in which the elastic property deviations represented by α are small in some suitable sense the D -tensor is given by

$$D = V\alpha \quad (3.15)$$

Here in this case of small α we encounter a situation that is analogous to the one characterizing the mass excess M regardless of the value of $\delta\rho$. From a knowledge of solely the elastic part $A_{2,2+2}^{(-)}$ we can determine only the product $V\alpha$ and nothing about the shape and orientation of the inclusion. This is the "blind spot" associated with weak inhomogeneities (at least as far as elastic properties are concerned).

However, if we have prior knowledge that the inclusion is a member of a certain finite set of possible inclusions, we can then attempt to match the ratios

$$\frac{\alpha}{\delta\rho} = \frac{D}{M} \quad (3.16)$$

to the corresponding ratios for the members of the above set (with suitable searches over orientations of crystallographic axes if the inclusion is not elastically isotropic).

In the category of strong inhomogeneities, we encounter rather different situations. Here we assume that the elastic properties of the inclusion are not all close to those of the host medium. Here we restrict our attention to inclusions with ellipsoidal boundaries. In the present category, the void is an allowable special case, while in the previous category it was not allowable.

Here, Eq. (3.13) is the fundamental tensor equation, which represents a set of at most 21 independent scalar equations. It is then clear that we cannot determine the scatterer parameters if the inclusion has unrestricted elastic properties, since then α then involves 21 parameters by itself, and when this set is combined with the geometrical parameters there are more unknowns than equations. We are thus led to consider inversion problems involving inclusions with greater elastic symmetry.

In the case of an inclusion with isotropic (locally) material and ellipsoidal geometry, the D -tensor is given by

$$VD^{-1} = (G + \alpha^{-1}) \quad (3.17)$$

where

$$\alpha^{-1} = (3\delta\lambda + 2\delta\mu)^{-1}P + (2\delta\mu)^{-1}\bar{P} \quad (3.18)$$

where, in turn, $\delta\lambda$ and $\delta\mu$ are the perturbations of the Lamé constants and P and \bar{P} are the compression and shear projection tensors defined by Eqs. (3.7) and (3.10). Multiplication of Eq. (3.17) successively by P and \bar{P} followed by the trace operation yields the relations

$$(3\delta\lambda + 2\delta\mu)^{-1} = V\text{Tr}D^{-1}P - \text{Tr}GP \quad (3.19)$$

$$5(2\delta\mu)^{-1} = V\text{Tr}D^{-1}\bar{P} - \text{Tr}G\bar{P} \quad (3.20)$$

Since D is regarded as given and since $\text{Tr}GP$ and $\text{Tr}GP$ depend only on the elastic properties of the host medium, the above relations give the isotropic elastic properties of the inclusion as a function of the volume V , as yet undetermined.

If the inclusion has a spherical boundary, then the G as well as \mathcal{C} must be isotropic, i.e., it must equal a linear combination of P and \bar{P} , and therefore according to Eq. (3.13), D^{-1} must have the same property. It then follows that $\text{Tr}D^{-1}P$ and $\text{Tr}D^{-1}\bar{P}$ represent the only information contained in D and hence there is no additional information for determining V . This is the so-called spherical "blind spot."

We have succeeded⁷ in proving that in the case of a nonspherical ellipsoidal inclusion of isotropic material, the inverse problem can be solved, i.e., from D we can deduce the isotropic elastic properties of the inclusion and the relevant geometrical properties. This statement is valid as long as \mathcal{C} is not too small in some sense. The density deviation $\delta\rho$ can be determined from M via Eq. (3.14) because V is now known.

PROBABILISTIC INVERSION

As stated earlier, the probabilistic approach to inversion is the appropriate one for dealing with real experimental because of the several reasons we have already discussed. In the probabilistic version we will limit our attention to the parametric case, i.e., where each possible defect under consideration is defined by a finite dimensional state vector z .

Let us model the possible results of the n th scattering measurement (assumed in all cases to be longitudinal-to-longitudinal) by the stochastic expression:

$$y_n = f_n(z) + v_n, \quad n = 1, \dots, N \quad (4.1)$$

where y_n is a possible measured value and v_n is a possible measurement error. The function $f_n(z)$ is given by

$$f_n(z) = A_{2L \times L}(\hat{e}_n^s, \hat{e}_n^i; z) \quad (4.2)$$

where $A_{2L \times L}$ is given, except for the inclusion of the vector z , by Eq. (2.14). The subscript n added to \hat{e}^s and \hat{e}^i denotes the configuration used in the n th measurement. In the case in which the included material is known a priori, the vector z represents the geometrical properties of the void. In the spheroidal case, we assumed as shown in Fig. 2 that the semi-axis lengths are denoted by a , b and c and that the axis of symmetry is given by

$$\hat{w} = \hat{e}_1 \gamma_1 + \hat{e}_2 \gamma_2 + \hat{e}_3 \sqrt{1 - \gamma_1^2 - \gamma_2^2} \quad (4.3)$$

where \hat{e}_1 , \hat{e}_2 , and \hat{e}_3 are the unit vectors in the x_1 , x_2 , and x_3 directions and where γ_1 and γ_2 are the direction cosines associated with the x_1 and x_2 directions.

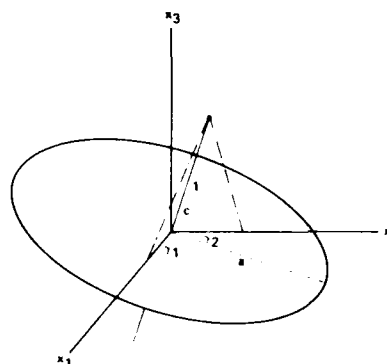


Fig. 2 Characterization of spheroidal geometry.

Thus the vector z is given by

$$z = \begin{pmatrix} z_1 \\ z_2 \\ z_3 \\ z_4 \end{pmatrix} = \begin{pmatrix} a \\ c \\ \gamma_1 \\ \gamma_2 \end{pmatrix}, \quad (4.4)$$

It is to be stressed that the Cartesian coordinates (x_1, x_2, x_3) are defined in the laboratory frame of reference and have no necessary relation to the axis of symmetry of the spheroid.

The definition of the stochastic model is completed by the specification of the a priori statistical properties of z and v_n and is characterized by the probability density (p.d.) $P(z)$. The measurement errors v_n are assumed to be Gaussian random variables with the properties

$$\begin{aligned} E v_n &= 0 \\ E v_n v_n^T &= \sigma_v^2 \delta_{nn}, \end{aligned} \quad (4.5)$$

where E is the averaging (or expectation) operator in the a priori sense. We assume that z and the v_n are statistically independent.

Whatever is chosen for the criterion of performance of the estimation process, we must calculate the observationally conditioned p.d. of z , namely $P(z|y)$ where

$$y = \begin{pmatrix} y_1 \\ - \\ - \\ - \\ y_N \end{pmatrix} \quad (4.6)$$

A convenient estimate $\hat{z}(y)$ is the value of z that maximizes $P(z|y)$.

At the previous meeting of the present symposium series we reported⁸ on the application of this inversion technique to spheroidal voids. Estimates based upon theoretical and experimental test data were in excellent agreement with the known properties of the scatterers.

In the later talk to be presented by Fertig, this methodology will be extended to the case of inclusions (with the void regarded as a special case) in which the inclusion type is not known

a priori. In the case of spheroidal geometry this entails replacing the four-dimensional vector z given by (4.4) by a five-dimensional one in which the fifth component is a discrete-valued variable labelling the inclusion types.

REFERENCES

1. B. Budiansky and J.R. Rice, "On the Estimation of a Crack Fracture Parameter by Long Wavelength Scattering," Trans. ASME, J. Appl. Mech., Vol. 45, pp. 453-454 (1978).
2. G.S. Kino, "Measurement of a Crack Stress Intensity Factor," informal report. Sept. (1977).
3. R.K. Elsley, J.M. Richardson, and R.B. Thompson, "Determination of Fracture Mechanics Parameters from Elastic Wave Scattering Measurements at Low Frequencies," Interdisciplinary Program for Quantitative Flaw Definition, Semi-Annual Report (Jan., 1978).
4. J.E. Gubernatis, J.A. Krumhansl, R.M. Thomson, "Interpretation of Elastic Wave Scattering Theory for Analysis and Design of Flaw Characterization Experiments: I. Long Wavelength Limit," Los Alamos Scientific Laboratory Report, LA-UR-76-2546 (1976).
5. J.M. Richardson, "Scattering of Elastic Waves in the Rayleigh Limit. I. The Direct Problem," to be published.
6. W. Kohn and J.R. Rice, "Scattering of Long Wavelength Elastic Waves from Localized Defects in Solids," submitted to J. Appl. Phys.
7. J.M. Richardson, "The Inverse Problem in Elastic Wave Scattering at Long Wavelengths," 1978 Ultrasonics Symposium Proceedings, IEEE Cat. #78 CH 1344-1SU, pp. 759-766.
8. J.M. Richardson, "Direct and Inverse Problems Pertaining to the Scattering of Elastic Waves in the Rayleigh (Long Wavelength) Regime," Proceedings of the ARPA/AFML Review of Progress in Quantitative NDE (July 1978), pp. 332-340, Jan. 1979.

QUESTIONS AND ANSWERS

Mr. De Facio: We have time for a couple of questions. Be sure to identify yourself and your institution.

James Rice: Yes, Rice, Brown University. John, you talked about some of the weaknesses, the blind spots, but what specifically?

Mr. Richardson: The blind spots are obviously some of the weaknesses. The additional properties that will be discussed by Fertig will compensate for the blind spots. The other weaknesses have to do with experimental problems, i.e., extracting A_2 from the raw data. Elsley will discuss that in some detail tomorrow, but I will mention here that there is a problem of signal-to-noise when you get down to the low frequencies. There is also a problem with spurious propagation effects getting in the way. You need a rather big time window to get enough of your signal in there to get an accurate A_2 out. Those are some of the difficulties.

Jack Cohen: You also listed the insensitivity to surface structures as a strength of the method. It's also a weakness, if the surface structure is what you're after.

Mr. Richardson: Well, it turns out that the fracture is also somewhat insensitive to textural defects.

Mr. Cohen: In ceramics, you worry about the surface area.

Mr. Richardson: Your point is a good one. In fact, in my talk tomorrow I will talk about one case where the failure model for ceramics is one in which peripheral surface cracks are the cause of failure and in the low-frequency measurements you cannot resolve any of this information - and of course, it's very valuable information to have. So, your point is very well taken. I was thinking of ordinary fracture in metals; in ceramics, you're quite right.

Mr. De Facio: Thank you.

SUMMARY DISCUSSION
(J. Richardson)

James Rice (Brown University): John, you talked about some of the weaknesses, the blind spots, but what specifically --

John Richardson: The weaknesses had not -- the blind spots are obviously some of the weaknesses, and the additional properties that will be discussed by Fertig to compensate for the blind spots, but the other weaknesses have to do with experimental problems, extracting A-2 from the data. Of course Elsley will discuss that in some detail tomorrow, but I will mention there is a problem of signal-to-noise when you get down to the low frequencies. There is also a problem with spurious propagation effects getting in the way. You need a rather big time window to get enough of your signal in there to get a reliable A-2 out. Those are some of the difficulties.

Jack Cohen (Denver Applied Analytics): You also listed the insensitivity to surface structures as a strength of the matter. It's also a weakness, if that's what you're after.

John Richardson: Well, it turns out that the fracture is also somewhat insensitive to textural defects.

Jack Cohen: In ceramics, you worry about the surface area.

John Richardson: Your point is a good one. In fact, in my talk tomorrow I will talk about one case where the failure model for ceramics in which peripheral surface cracks are the cause of failure and in the low-frequency measurements you cannot resolve any of this information. And of course it's very valuable information to have. So, your point is very well taken. I was thinking of just ordinary fracture in metal. In ceramics, you're quite right.

#

ULTRASONIC CAUSTICS AND THE INVERSE SCATTERING PROBLEM IN NDE

P. A. Doyle
Aeronautical Research Laboratories
Melbourne, Australia

ABSTRACT

This paper explores theoretically the possibility of using caustics, formed in the ultrasonic field diffracted by defects, as an approach to the inverse scattering problem. The case of crack-like defects is considered in detail, using the geometrical theory of diffraction.

The involute of the far field caustic reproduces the projection of the crack edge in the incident beam direction, for a plane incident wavefront. This purely geometrical inversion is carried out uniquely for the astroid and its involute, the elliptical edge. For a general edge shape, the complete inversion requires one further length measurement, which may be carried out in some cases by further experiments with caustics. Useful limitations on the possible shapes of caustics are explained on the basis of catastrophe theory. Calculations show that the inherent intensity-level change ($\sim 2-3$ dB) and width (\sim wavelength) over which it occurs for a typical ultrasonic caustic are adequate for observation. Some discussion is given of experimental requirements, as well as of caustics formed in the near field of a crack and of those formed by voids and inclusions. The topology of the far field caustic cannot in general distinguish between volumetric and crack-like defects. Studying caustics may prove to be a useful adjunct to ultrasonic imaging systems for the inspection of fatigue cracks.

INTRODUCTION

Recently, attention has been given to the theoretical inversion of ultrasonic scattering data (1-4), so that the characteristics of the scattering singularity can be identified. This paper will explore the possibility of using caustics, which are the envelopes of rays diffracted by the defect, for this inversion. Caustics lie in or near the geometrical shadow of the defect; they also occur, in principle, in the back-scattered field, though this region is not studied here because of the anticipated lower contrast, and the likely experimental complications.

THEORY

The scattering of high frequency ultrasound by defects can be described by the geometrical theory of diffraction (5). This theory gives the asymptotic wave amplitude u diffracted to a field point y from a point x on the edge of a crack as a series in decreasing powers of the wave number k . The first and most important term is

$$u(y) \sim A \left[\frac{Y}{(Y^2 + \epsilon^2)^{3/2}} \right] \exp \left[i k \phi(\sigma, \epsilon) \right] \quad (1)$$

where $\epsilon = |x - y|$ measures arc length along the edge, A is aplitude factor, and Y is the distance from the edge to the caustic along the ray (Fig. 1). If $\phi(\sigma)$ is the phase of the incident wave at σ ,

$$\phi(\sigma, \epsilon) = \phi(\sigma) + \pi \quad (2)$$

If more than one geometrical ray path passes from edge points through y , (1) should be replaced by a sum. When y lies near the caustic, $(Y^2 + \epsilon^2)^{3/2}$ and (1) should be replaced by a superposition of plane waves (6)

$$u(y) = \int_{-\infty}^{\infty} \gamma(\tau) \exp \left[i k \phi(\sigma, \tau) \right] d\tau \quad (3)$$

For large k , (3) can be evaluated by the stationary phase method, which states that the dominant contributions to $u(y)$ come from points on the edge where the derivative $\phi_{\sigma} = 0$. If β is the angle between the incident ray and the tangent to the edge at σ (Fig. 1) the field at y is due to rays which satisfy the condition

$$\beta(\sigma, \epsilon) = \cos \beta - \epsilon / \rho = 0 \quad (4)$$

The envelope of these cones of rays, which is the caustic surface of the singly diffracted rays, satisfies (4) and also the equation

$$\phi_{\sigma\sigma} = \frac{\partial(\cos \beta)}{\partial \sigma} - \frac{\epsilon}{\rho} \frac{\partial n}{\partial \sigma} + \frac{\partial n}{\partial \sigma} \frac{\partial \epsilon}{\partial \sigma} = 0 \quad (5)$$

where n is the principal normal and ρ is the radius of curvature of the edge at σ . Eqn. (5) corresponds to the coalescence of two stationary phase points along the edge. In the far field, Eqns. (4) and (5) (which describe the caustic surface) reduce to those defining the caustic surface produced by the projection of the object in the incident beam direction (5). Using λ to denote this projection, the far field caustic is then defined by

$$\lambda^2 = 0 \quad (6)$$

$$\sigma^2 n^2 = \rho^2 \quad (7)$$

Eqn. (7) shows that the far field caustic contains the evolute of the projection of the edge, i.e. the locus of the centres of curvature of points on this projection. Eqn. (6) shows that the far field caustic surface is a cylinder with generators in the incident beam direction, so that in the classical limit $k \rightarrow \infty$ for which these interpretations strictly hold, all far field cross-sections are identical. Therefore, if the geometry of the far field caustic in ultrasonics

can be observed, the shape and, in some cases, the size (as discussed below) of the crack projection in the incident beam direction can be found simply by constructing the involute of the caustic. Because (6) and (7) are independent of k , the geometries of caustics formed by S and P waves are identical, so that the present scalar wave analysis is adequate for waves in solids as well as in liquids.

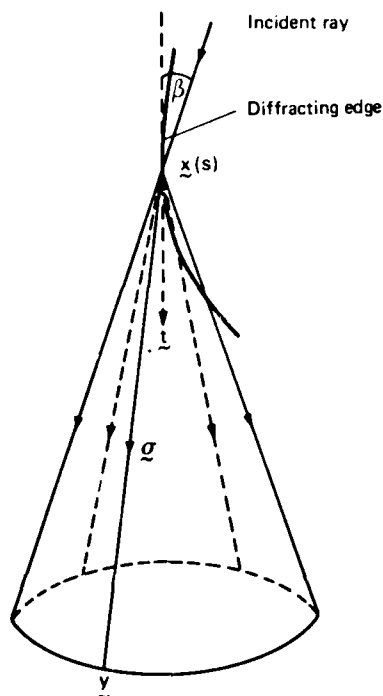


Fig. 1 The cone of rays diffracted from the incident ray at the point $x(s)$ on the edge, and the geometrical definition of parameters used.

Any theoretical limitations that can be placed on the possible shapes of caustics would greatly assist their identification. For this purpose, we adapt the application of the catastrophe theory of THOM (7) to wave phenomena (8). Because the local description of the crack edge requires only one parameter (s), only cuspid catastrophes are generically ('typically') possible for edge diffraction. Since the far field depends on two co-ordinates (control parameters), only elementary folds, which appear as ordinary points of the caustic, and cusps, can occur. It follows that the far field caustic produced by diffraction from a purely convex edge projection consists of a closed line interrupted only by cusps. Departures from this rule can occur by accident or by symmetry, but are unlikely for diffraction by real cracks. In the near field, the next cuspid catastrophe (the so-called 'swallow-tail') is generically possible, though likely to be difficult to observe in ultrasonics because of the compressed form of its near-singular sections.

Cusps correspond to the coalescence of three geometrical ray paths, or three stationary phase points on the edge projection, which occurs when

$\rho_{s, s, s} = 0$. Using (7) with the Fresnel formulae, it follows that $\rho_{s, s, s} = 0$ for cusps in the far field caustic, i.e., cusps occur when the curvature or radius of curvature of the corresponding points on the projected edge is extremal. Also, the cusp is normal to the edge at this corresponding extremal point.

RECONSTRUCTION OF THE DIFFRACTING OBJECT

Consider firstly a diffracting edge whose projection is an ellipse with principal axes $2a$ and $2b$. Then, the cross-section of the far field caustic will be the evolute shown in Fig. 2, which is an astroid. Conversely, when the caustic is observed to be an astroid, it is immediately known that the edge projection is elliptical. If the distances between the two pairs of opposite cusps are measured as 2ξ and 2η , it follows from the equation of the astroid that the major axis of the ellipse is $2a = 2\xi\eta_0/(\eta_0^2 - \xi^2)$, and $b/a = \xi/\eta$. Since the cusps are normal to the tangents at the corresponding extremal points on the edge, the ellipse is oriented as shown in Fig. 2 with its major axis parallel to the line 2ξ between the closer pair of cusps. Thus it is actually not necessary to observe the complete caustic in this simple case—only the positions of the cusps in the rectangular array are required.

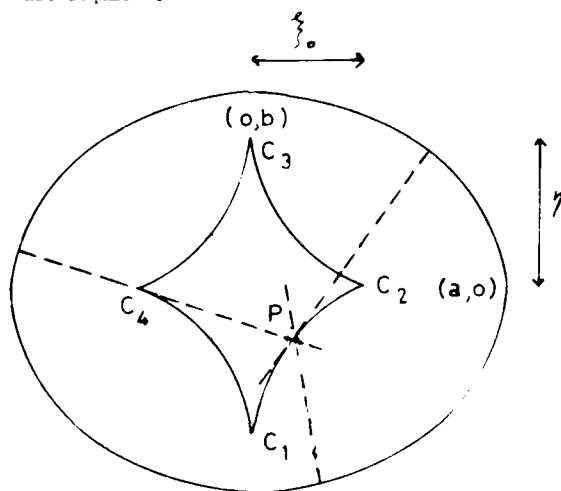


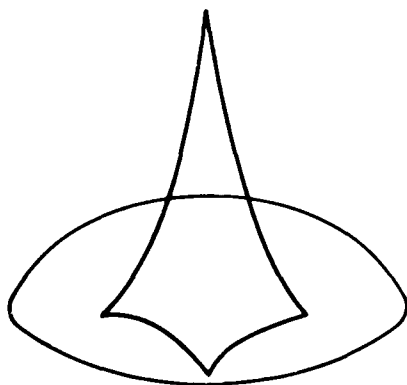
Fig. 2 An elliptical diffracting edge and the corresponding far field caustic. This figure represents a superposition of the spaces of the edge projection and of the far field diffraction pattern, drawn on the same scale. The two cusps lying along the major axis are always inside the geometrical shadow; the other two cusps are outside the shadow for ellipses having eccentricity $> 1/\sqrt{2}$. The dashed lines indicate all rays contributing to the field at point P, as discussed below.

It is useful to construct the involute of the astroid in another way, based on the knowledge that the caustic is the locus of centres of curvature of the edge. Imagine a string set along the inside of the section C_1C_2 of the astroid (Fig. 2)

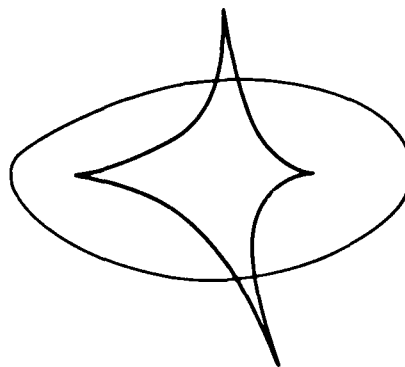
and extending beyond γ_2 in the direction of the cusp by a distance equal to the minimum radius of curvature of the ellipse, which is known from the caustic to be $\frac{1}{2} = \frac{1}{2}(\gamma_1^2 - \gamma_2^2)$. Unwinding this string traces out the first quadrant of the ellipse. Next, wind the string onto the section C_1C_2 of the astroid to produce the second quadrant of the ellipse. Proceeding clockwise around the astroid and alternately winding and unwinding in this way, the complete ellipse is generated in an anticlockwise sense.

Some special cases of the ellipse are of interest. For eccentricity $e \rightarrow 1$, $\gamma_1 \rightarrow \infty$, so that $\gamma_2 \rightarrow \infty$, i.e. one pair of cusps extends laterally to infinity and is not observed. Therefore, tilting the object about the axis of the closer pair of cusps enables direct measurement of the major axis, since the two remaining cusps become coincident with the ends of the narrow shadow boundary. Also, for $e \rightarrow 0$, the edge approaches a circle and $\gamma_1 \approx \gamma_2 \rightarrow 0$, giving the diffracted spot at the centre of the shadow, which is well known in optics to have an intensity equal to that of the incident beam. Observation of such a degenerate caustic immediately gives the projection of the diffracting edge as being circular. This particular case is not described in the classification given by Thom's theorem, because of its high symmetry. The size of a nearly circular defect may be found by tilting the specimen, giving an elliptical projection whose caustic is an astroid of convenient dimensions.

Some other examples of caustic/diffracting edge pairs can be generated from the elliptical case. If one side of a distorted ellipse is flatter than the other, a caustic will result which has two pairs of cusps arrayed at right angles, but not symmetrically (Fig. 3a). Again, if an ellipse is distorted by shifting one turning point from the symmetrical position, the cusps will no longer be directed as two opposing pairs at right angles (Fig. 3b). Nevertheless, the directions of the tangents at the turning points are immediately known by inspection of the caustic.



3(a)



3(b)

Fig. 3 Distorted ellipses with their corresponding caustics.

- (a) One side of the ellipse more eccentric than the other.
- (b) One minimum of curvature shifted from the symmetrical position.

If the edge projection contains a concave part, the caustic will appear discontinuous, since it extends to infinity at points of inflection. Figure 4 shows an ellipse 'pressed in' at one end, and the corresponding caustic. Note that the intensity of the caustic tends to zero far out along those sections which are asymptotic to the normal at the points of inflection, because the density of contributing ray paths then approaches zero. Therefore, only a limited part of the caustic will actually be observed. A less severe depression in the end of the ellipse will produce the cusp marked D further away from the rest of the caustic. A 'flattened end' on an ellipse which is nevertheless convex will give a caustic section as a closed line containing six cusps. Three of these cusps coalesce into one as the distortion of the ellipse is reduced to zero, again producing the simple 4-cusped astroid.

Involuting the far field caustic gives the projection of the diffracting edge in the incident beam direction. The orientation of a planar defect in three dimensions could be inferred from several such measurements involving different projections. Another approach is to examine the variation of the caustic pattern as the plane of observation is moved into the near field: the special case of normal incidence produces no change of the caustic in this region. Identifying this behaviour defines the normal to a planar defect.

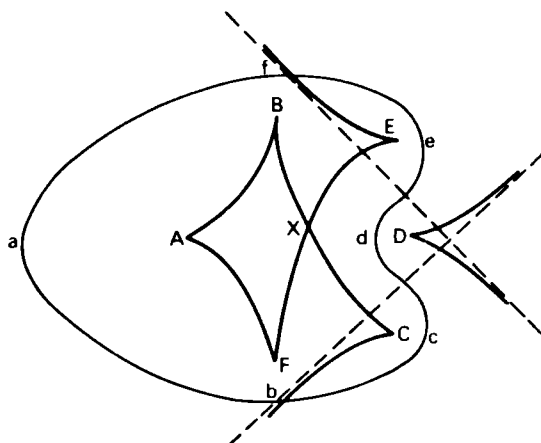


Fig. 4 An ellipse 'pressed in' at one end, and its corresponding caustic. The association between cusps and turning points is indicated by letters. The pattern in the region marked X is a superposition of elementary fold catastrophes, and should not be mistaken for a section of some higher catastrophe.

Any smooth, purely convex closed shape has an even number of turning points, since maxima and minima of curvature must alternate in circuit. Therefore, there is an even number of cusps in the caustic which is itself a partial check on an experiment. The diffracting edge projection is normal to the cusps at the points of extremal curvature, so the orientation of the projection is known by inspection of the cusps. Edge projections corresponding to caustics of four, six, eight or higher even number of cusps can be constructed by alternately folding and unfolding each caustic section in turn, just as was done for the ellipse. For this general case, there is no representation of the caustic in terms of elementary functions as there was for the astroid. Therefore, the radius of curvature at one extremal point cannot be deduced simply from the spacing of cusps, and a different method must be sought to achieve a unique reconstruction.

Since the cusps corresponding to minima of $P(s)$ are less sharp than those corresponding to maxima (e.g. see the ellipse of Fig. 2), it should be possible to identify at least one cusp corresponding to a minimum of $P(s)$, say P_1 . Beginning with this cusp, and assuming particular values for P_1 , a one-parameter family of possible involutes of the caustic can be generated. It then remains to choose the correct involute from this set. One technique suitable for planar defects would be to tilt the object about an axis between two approximately opposite cusps, whose spacing would then be asymptotic to the length of the narrow shadow boundary. This procedure enables direct measurement of one length in the diffracting edge, which is sufficient to select the correct involute. If one length in the edge can be determined by a different technique, as is possible for some objects using ultrasonic spectroscopy, the desired involute can again be chosen from the set of possibilities.

CALCULATED CONTRAST

The ease of observation of caustics in

ultrasonics will depend on their width as well as their intensity relative to the background in their neighbourhood. These properties will be studied by considering a particular but typical case, viz. normal incidence of a plane wavefront on a planar elliptical crack. Calculations will be made for a point on the caustic which lies within the geometrical shadow of the ellipse; the contrast will be low for any part of the caustic which lies outside this shadow in the bright field of the incident wave.

Referring again to Fig. 2, the coalescence of two stationary phase points at $\theta = \pi/4$, for example, contributes to the caustic surface along a line which projects into the astroid segment C_1C_2 at point F. In addition, these rays from $\theta = \pi/4$ contribute as from an isolated stationary point to caustic segments in the first and third quadrants, respectively before and after passing through the caustic. Equivalently, there are two 'isolated' contributions from the fourth and second quadrants to the field at all points along the caustic line through F. The question then reduces to a comparison between the intensity on the 'bright side' of the caustic (the inside of the astroid), to which four rays contribute including two which coalesce, and the intensity on the 'dark side' to which two rays contribute.

Table 1 lists results of calculations which make use of the stationary phase evaluation of the diffraction integral for the isolated contributing rays at point F, and the transitional approximation for the coalescing rays. These results are for the caustic 100 mm behind the ellipse $(a, b) = (10, 7.5)$ mm at 10MHz for water and for typical 1 and 3 wavelengths in steel. C_{\max} is the maximum contrast, defined as the ratio of the intensity at the first peak of the Airy fringes which 'clothe' the caustic on the bright side, to the intensity on the dark side. C_{av} represents the contrast predicted by averaging over the first two fringes. The spacings of these fringes in ultrasonics are of the order of the wavelength λ , which is also an estimate of the resolution that can be achieved in any scanning or imaging system which may be used to observe caustics. Therefore the Airy fringes will not readily be observed in ultrasonics, particularly when broadband transducers are used, so C_{av} gives a more realistic estimate of the expected caustic contrast than C_{\max} . The changes of intensity level $\sim 2-3\text{dB}$ in table 1 are observable. The widths d , over which these changes occur $\sim \lambda$ or slightly greater, which is also suitable for observation.

	Water (mm)	Steel (S) 0.30	Steel (P) 0.60
C_{\max} (dB)	3.12 (4.94)	2.68 (4.28)	2.32 (3.65)
C_{av} (dB)	2.02 (3.04)	1.79 (2.56)	1.64 (2.14)
d_w (mm)	0.24	0.37	0.60

Table 1 Intensity changes across the caustic at point F expressed as a ratio and in dB, and caustic width, listed at 10MHz for the section 100 mm behind an elliptical crack having semi-major axes $(a, b) = (10, 7.5)$ mm.

DISCUSSION

Thus far, this paper has assumed a plane incident wavefront. If this wavefront is curved, as for example from a point source, the interpretation of the caustic is more complicated because its geometry depends on the curvature of the incident wave as well as on that of the edge. Nevertheless, the caustic is just as sharp and easily detected. The most important factor experimentally is to tailor the incident wave to minimize the angular spread of wavelets incident on a single point on the edge, since this spread smears out the caustic.

One approach to forming the incident field would be to use a focused ultrasonic probe, with its minimum spot set at the back focal plane of an acoustical lens to produce the convenient (though not essential) plane wavefront. Alternatively, the minimum spot could be produced by a normal probe together with another acoustical lens, which in practice can reduce the width of the generated sound field to the order of λ (9). Other approaches may be to exploit either the direct production of a plane wavefront from a piezoelectric plate (10), or the low divergence of beams of Gaussian cross-section (11). Ultrasonic point sources of diameter 10 μm or less have been generated using lasers (12) and, at the expense of complexity, these sources appear most promising for observing ultrasonic caustics. An initial demonstration of ultrasonic caustics may be most easily carried out in the near field, since the lateral smearing would increase with distance from the defect. For the actual observation of the diffracted field, any scanning or imaging system with sufficient resolution could be used.

The caustic pattern is found in and near the geometrical shadow, and its dimensions are typically comparable to those of the defect. Therefore, the study of these patterns is not seen as a means of improving the resolution of imaging systems. The advantage may come in dealing with defects which, though sufficiently large, produce images that cannot be easily interpreted. For example, an image of a fatigue crack can be complicated by specular reflection from facets on the crack faces and by penetration through regions of crack closure. However, if the edge itself is opaque to ultrasound, as may be inferred from studies of the crack tip in Al alloys (13), the caustic will still be formed. 'False' edges formed at regions of closure are much smaller than the true edge, and would give caustics which were smaller and either unresolved or else easily distinguished from the caustic from the true edge.

In the near field of rays transmitted by a solid or liquid filled inclusion, it can be shown that the caustic sections described as elliptic or hyperbolic umbilics are expected, though these are likely to be masked by diffraction effects and experimental smearing. In the far field, again only elementary folds and cusps are generically possible. Therefore, the topology of far field caustics cannot distinguish between inclusions and planar defects. This result does not hold if the orientation of the specimen is regarded as an additional accessible control parameter in the sense discussed in (8); then, singular umbilic sections can in principle be produced in the far

field by rotating the specimen.

A situation similar to the above occurs for voids, for which umbilic sections in the near field result from the decay of creeping waves, but these are not likely to be observable. The far field again consists only of elementary folds and cusps. An important singular case is the spherical void, which gives a point caustic at the centre of its shadow for all orientations. This case is not described by THOM's theorem because of its high symmetry.

A more detailed account of this work will be published elsewhere.

ACKNOWLEDGEMENT

The author thanks DARPA and SCRI for support to attend this Review.

REFERENCES

1. Majda A 1976 *Comm. Pure and Appl. Maths.* **29** 261-91
2. Bleistein N and Cohen JK 1977 *J. Math. Phys.* **18** 194-201
3. Whalen MF and Mucciardi AN 1978 ARPA/ARML Review of Progress in Quantitative NDE, to be published
4. Achenbach JD Gantesen AK and McMaken H 1978 in *Elastic Waves and Non-destructive Testing of Materials AMD Vol 29* 33-52
5. Keller JB 1957 *J. Appl. Phys.* **28** 426-44
6. Ludwig D 1966 *Comm. Pure and Appl. Maths.* **19** 215-50
7. Thom R 1975 *Structural Stability and Morphogenesis* (Reading Mass: Benjamin)
8. Berry MV 1976 *Adv. in Physics* **25** 1-26
9. Knollmann GC Carver D and Hartog JJ 1978 *Materials Evaluation* **36** 41-7
10. Lakestani F Baboux JC Fleischmann P and Perdrix M 1976, *J. Phys. D. : Appl. Phys.* **2** 547-54
11. Martin PD and Breazeale RA 1971 *J. Acoust. Soc. Am.* **49** 1668-9
12. Mallozzi FJ Fairand BJ and Golis MJ 1977 *Research Techniques in Non-destructive Testing Vol. 3* ed. Sharpe RS 481-93 (Academic Press)
13. Bowles JO 1978 Delft Univ. of Technology Dept. of Aerospace Engineering Report LR-270

SUMMARY DISCUSSION
(P. A. Doyle)

Brian DeFacio (Session Chairman-Ames Laboratory): We have time for a couple of questions. Let me ask one. I thought I remember there was a dilation or change of scale between the star in the middle and the ellipsoid. Is that wrong?

Peter Doyle: You mean the ellipse, the figure?

Brian DeFacio: And the caustic imposed. Is it unique, or is there a dilatation involved?

Peter Doyle: You're worrying that the caustic is smaller ..

Brian DeFacio: I'm worrying that outside some minimal ellipse I can put some family of ellipse around --

Peter Doyle: We end up with a family of ellipses, or more general shape. We end up with a family starting from the small size right up to the big size, and we have to make it one length. Does that answer your question?

Brian DeFacio: Yes.

J. D. Auchenbach (Northwestern University): I'm not an experimentalist, but I'm a little bit pessimistic because it seems that you would have to scan the whole field to detect the position of these caustics, and particularly since experimentalists work in the time delay, as a wave starts to move back and forth the position of caustics also there is an evolution in time. If you have a crack, of course, the edge diffraction will produce one in three dimensions, the surface in space. If it isn't normal. Then if surface waves start to propagate over the surface of the crack, they produce another system of diffracted waves which in turn produces its caustic. Of course the intensity decreases as time goes on. All this takes place as time evolves. Since you have to be everywhere in space because you have to map out a number of points to get back to this caustic, it all seems to be a difficult problem.

Peter Doyle: It takes too long to date out, but this is the caustic of the singly diffracted wave. And that will turn up in the geometrical shadows. There is no way to look for that. The point is, caustic is not really scattered waves, which is maybe a surface wave in the meantime. They turn up in different directions.

J. Auchenbach: That may well be so, but, see, you don't know in advance where to look.

Peter Doyle: I have a beam coming down here, and whatever orientation is, it's over in the shadow. You don't have to know that. The orientation. It's the projection of the edge that you learn about in the farfield projection of the edge and the incident beam direction.

J. Auchenbach: You don't know in advance where the crack is, and the crack is very small. You know the incident beam, but you don't know the shadows on it.

Peter Doyle: I should have said we assumed we know where the crack is. We're trying to find out how big it is, its shape and size.

K. K. Galveston (SMU): Unless you work at extremely high frequencies, the bright spots on the disk are within the boundary layer of the shadow boundaries, and so the hole will get smeared out unless you're using high frequencies like in the optics range, where they have the class of experiments where you can actually see them. In the elastomagnetic case, you're working at three, four, five -- what is it? Wave number three, four five or something like that. And the boundary is computed from the edge and will smear out the caustics involved. Especially if you have bright spots inside the crack.

Peter Doyle: One particular case of the degenerative caustic is the case of a circular crack.

K. Galveston: But even then the same thing happens, the bright spot gets smeared out of the boundary layers.

Peter Doyle: It's not an easy experiment, but this is a proposal.

(continued)

P. Doyle (continued discussion)

K. Galveston: You have to have a frequency range within (inaudible).

Peter Doyle: These populations are only ten megahertz.

K. Galveston: They are only valid if you include the effect of the boundary layers, the shadows. You have to include the effects of the shadow boundary. That boundary layer also has to be included in the calculation because they coalesce.

Peter Doyle: Most of the caustic won't be at the shadow boundary. The most important feature is the cusp.

J. Auchenbach: I think if you know where the crack is -- I discussed this a couple of years ago with Wolfgang Sachse -- I don't know if he is around here. If you know where the crack is, I think -- I don't know. You were going to try it.

Wolfgang Sachse (Cornell University): I was going to tell that, but I guess I wanted to let them finish. I had a couple undergraduates about three years ago try this experiment of having a circular disk approximately six inches. We also tried four inches, eight inches in diameter. And we were moving a 40 kilohertz transducer. This was in a large room. And they were measuring the amplitude as a function of distance behind the disk. They were mapping out an XY grid behind the disk. And the only configuration of obstacle in which we were able to see some really significant intensity, if you will, variation behind it was the disk. And in that case -- I don't have the slide with me, but in that case I remember that we had a very, very bright spot behind the disk. We also did ellipses, various shapes. In fact, we used the same technique that this 1908 paper used to make the ellipse. But we got some results. But you really had to use your imagination to say there was a bright region in a particular -- behind the disk, behind the ellipse.

Peter Doyle: Could I make one comment to that -- The K.A. value in that case worked out -- as a matter of fact, ten short of some experiment (inaudible).

#

INVERSE SCATTERING AT LOW AND INTERMEDIATE FREQUENCIES

K.W. Fertig and J.M. Richardson
Rockwell International Science Center
Thousand Oaks, California 91360

ABSTRACT

In this paper, we address the inversion problem in the scattering of elastic waves from scatterers using a probabilistic approach. This work extends that of previous efforts in that it considers a wider set of input measurements and a wider class of possible defects. For a given transducer arrangement, the input measurements involve the coefficient A_2 , which characterizes scattering at low frequencies, and a second quantity that is related to the distance from the center of the scatterer to the front face tangent plane perpendicular to the direction of the incident beam. The first property is deducible from low frequency scattering data and the second from low and intermediate frequency scattering data. These properties are determined for a set of transducer configurations. The class of possible scatterers now includes a finite discrete set of possible inclusions as well as a void. The boundary geometry is assumed to be ellipsoidal. In the probabilistic approach we start with a statistical ensemble of scatterer properties and measurement errors and then remove the members inconsistent with the scattering data obtained from the measurements. The best estimates of the geometrical properties and inclusion types (with the void regarded as a special case) are then the average or most probable values of these properties in the resultant reduced ensemble. These estimates are accompanied by several types of confidence measures. The behavior of the inversion algorithm using theoretical test data, both noiseless and noisy, was studied by computer simulation.

INTRODUCTION

In a previous report(1) we discussed the inverse problem in the scattering of elastic waves from voids at low frequencies (i.e., the Rayleigh regime). Here we consider an extended version of the inverse problem in which a wider set of types of measurements and types of scatterers are assumed. Namely, we consider a set of measurements that includes the low frequency scattering amplitudes as before but also the distance from the geometrical centers of the scatterer to the front-face tangent plane, a property deducible from the low and intermediate frequency characteristics of the scattering amplitude. As before a diversity of longitudinal-to-longitudinal scattering measurements are considered but this time attention is limited to the pulse-echo type. The set of possible scatterers has been extended to include a specified discrete set of possible inclusions as well as a void. As before, the boundary geometry is assumed to be ellipsoidal, although the actual calculations were performed for the oblate spheroidal case.

As before we pursue a probabilistic approach in which we start with a statistical ensemble of scatterer properties and measurement errors and then remove the members inconsistent with the scattering data obtained from the measurements. The best estimates of the geometrical properties and inclusion types (with the void regarded as a special case) are then the average or most probable values of these properties in the resultant reduced ensemble.

FORMULATION OF THE PROBLEM

In this section we present an outline of the analysis of the present extended version of the inverse scattering problem. In the next section, a discussion is given of the numerical approach and certain relevant analytical details. In the section following that, a set of preliminary results is presented giving the response of the inversion algorithm to various kinds of synthetic test data.

The possible results of scattering measurements (including post-detection processing) are represented by the stochastic mathematical model

$$y = h_q(x) + \epsilon, \quad (2.1)$$

where y and ϵ are N -dimensional vectors whose components are the possible measured values and measurement errors, respectively. The vector function $h_q(x)$ gives the error-free values of measurements that would be obtained with an ellipsoidal scatterer with inclusion type q ($q = 1, \dots, G$) and geometry defined by the m -dimensional state vector x .

We consider two types of measurements and thus it is appropriate to write

$$y = \begin{pmatrix} y_1 \\ y_2 \end{pmatrix} \quad (2.2)$$

$$x = \begin{pmatrix} 1 \\ 2 \end{pmatrix} \quad (2.3)$$

$$h_q = \begin{pmatrix} h_{q1} \\ h_{q2} \end{pmatrix}, \quad (2.4)$$

where y_1 , y_2 , and h_{q1} are N_1 -dimensional vectors associated with measurements of Type 1 and, similarly, y_2 , y_2 , and h_{q2} are N_2 -dimensional vectors associated with measurements of Type 2. Clearly, we must require $N_1 + N_2 = N$. In the case of Type 1 measurements, we obtain

$$h'_{q1} = (h_{q11}, \dots, h_{q1N_1}) \quad (2.5)$$

where the prime denotes the transpose. The n th component is defined by

$$h_{g_1 n} = h_{g_1 n}(x) = A_2(\vec{e}_n^s, \vec{e}_n^i; x, q), \quad (2.6)$$

where A_2 is the coefficient of ω^2 in the ω -expansion of the theoretical amplitude $A(\vec{e}_n^s, \vec{e}_n^i; x, q)$ for longitudinal-to-longitudinal scattering from an ellipsoidal inclusion of Type q and geometry x . The unit vectors \vec{e}_n^i and \vec{e}_n^s give the incident and scattered directions corresponding to the transducer placement in the n th experiment (in the pulse-echo case $\vec{e}_n^s = -\vec{e}_n^i$).

In the Type 2 measurements, we have

$$h'_{g_2} = (h_{g_{21}}, \dots, h_{g_{2N_2}}) \quad (2.7)$$

in which the n^{th} component is defined by

$$h_{g_{2n}} = h_{g_{2n}}(x) = d(\vec{e}_n^i; x), \quad (2.8)$$

where d is the distance from the geometrical center of the ellipsoidal to a front-face tangent plane perpendicular to \vec{e}_n^i . The experimental value of this quantity is determined from a suitable analysis of the n th pulse-echo scattering measurement in which $\vec{e}_n^s = -\vec{e}_n^i = \vec{e}_n$. It is worthy of note that in this formulation d depends only on x and not on q . A simple extension of this theory allows for dependence of d on q .

With x and q given, the experimental error vector v is assumed to be a Gaussian random vector with the properties

$$E(v|x, q) = 0 \quad (2.9)$$

$$E(vv'|x, q) = C. \quad (2.10)$$

The $N \times N$ covariance matrix C is assumed to be independent of x and q . In the actual computations we assumed that C is diagonal, an assumption corresponding to the statistical independence of experimental errors.

The above stochastic model defines the probability density of y given x and q , namely $P(y|x, q)$ given by Eq. (3.1) of the next section. The statistical description of the measurement model is completed by the specification of the prior probability $P(x, q)$ which is given a more detailed discussion in the next section. The final decision (estimation of defect type and geometry) depends upon the posterior probability density of x and q given y , namely

$$P(x, q|y) = P(y|x, q)P(x, q)/P(y), \quad (2.11)$$

where

$$P(y) = \sum_q \int dx P(v|x, q)P(x, q) \quad (2.12)$$

plays the role of a normalization constant.

The process of making a best decision about the values of x and q from the measurement vector y depends on the global context in which this problem is embedded. At this point it is necessary to focus

the reader's attention on both the immediate as well as the ultimate purpose of the present inversion problem. The ultimate purpose involves the embedding of the inversion problem in a more extensive decision logic terminating in accept/reject decisions, estimation of life-cycle costs, etc. For the time being, however, it is expedient to regard the inversion algorithm as a "free-standing" entity with its own performance criteria.

With this point of view it is appropriate to consider a loss function $L(\hat{x}, \hat{q}; x, q)$ specifying the loss (or penalty) incurred if the algorithm gives the decisions \hat{x} and \hat{q} when the actual values are x and q . A reasonable optimization criterion is to minimize the risk defined by

$$R = EL(\hat{x}(y), \hat{q}(y); x, y), \quad (2.13)$$

where E is the unconditional averaging operator. It should be noted that here \hat{x} and \hat{q} are functions of the random process (2.1). Thus R is a functional of the decision functions $\hat{x}(y)$ and $\hat{q}(y)$ and it is to be minimized on the form of these functions.

Here we will consider two loss functions, namely

$$L(\hat{x}, \hat{q}; x, q) = -\delta(\hat{x} - x)\delta_{\hat{q}q} \quad (2.14)$$

and

$$L(\hat{x}, \hat{q}; x, q) = -\delta_{\hat{q}q}. \quad (2.15)$$

In the first case

$$E(L|y) = -P(x=\hat{x}, q=\hat{q}|y) \quad (2.16)$$

and in the second

$$E(L|y) = -P(q=\hat{q}|y). \quad (2.17)$$

Thus, in the first case the optimal decision functions correspond to the most probable values of x and q given y . The second case will be discussed later.

COMPUTATIONAL APPROACH

As discussed in the last section, the estimation of the inclusion type q and geometry x is performed using standard decision theory. Using either loss function, i.e., Eq. (2.14) or (2.15), we must consider the posterior probability of q and x given the observed measurement vector, y . Using the notation of the last section, we represent the measurement model (2.1) as the probability density

$$P(y|x, q) = \frac{1}{(2\pi)^{N/2}} |C|^{-1/2} \exp \left[-\frac{1}{2} (y - h_q(x))' \cdot C^{-1} (y - h_q(x)) \right]. \quad (3.1)$$

The covariance matrix C was defined in the previous section and $|C|$ is its determinant.

The posterior probability of x and q is obtainable once the prior on x and q is specified. Denoting this prior by $P(x, q)$, the posterior probability is then

$$P(x, q|y) = P(y|x, q)P(x, q)/P(y). \quad (3.2)$$

where $P(y)$ plays the role of a normalizing constant. Maximization of (3.2) with respect to x and g is performed by sequentially maximizing (3.2) on x for each specified $g, g = 1, \dots, G$. This latter maximization is conveniently performed using the International Mathematics and Statistics Library routine ZXMIN. This routine(2) uses a quasi-Newton algorithm to find the minimum of a function of m variables. In the current application, it was found that certain precautionary steps are necessary in order to assure convergence of the iterative scheme. Before discussing these steps, it is desirable to elaborate on the computational procedure to obtain $P(x, g|y)$ in (3.2) near its maximum.

Maximization of (3.2) over x for a given g is equivalent to minimizing the functional $\phi(x, g; y)$ over x for specified y where ϕ is defined by

$$\begin{aligned}\phi(x, g; y) &= -\ln[P(x, g|y)P(y)](2\pi)^{-N/2}|C|^{-1/2} \\ &= \frac{1}{2} (y - h_g(x))' C^{-1} (y - h_g(x)) - \ln P(x, y)\end{aligned}\quad (3.3)$$

Specifically, ϕ is completely known without having to evaluate the normalization constant in (3.2). Let $\hat{x}_g(y)$ be the value of x for which the minimum is obtained. That is

$$\phi(\hat{x}_g, g; y) = \min_x \phi(x, g; y). \quad (3.4)$$

Thus $\hat{x}_g = \hat{x}_g(y)$ gives the geometry of the inclusion that maximizes the posterior density function for inclusion type g . Since the gradient of ϕ with respect to x vanishes at \hat{x}_g , we see that $\phi(x, g; y)$ has the series expansion

$$\phi(x, g; y) = \phi(\hat{x}_g, g; y) + \frac{1}{2} (x - \hat{x}_g)' H_g (x - \hat{x}_g) + \dots, \quad (3.5)$$

where

$$H_{gij} = \left[\frac{\partial^2 \phi}{\partial x_i \partial x_j} \right]_{x=\hat{x}_g}$$

is the Hessian of the function ϕ at $x = \hat{x}_g$. A numerical approximation of H_g is computed in the inversion software using central difference approximations. We note that for ϕ to have a true minimum at $x = \hat{x}_g$, H_g must be positive definite.

The expansion in (3.5) allows for an approximate expression to be developed for $P(x, g|y)$ given in (3.2) using the relation (3.3). In particular, we obtain the expression

$$P(x, g|y) = A(y) \exp \left[-\phi(\hat{x}_g, g; y) - \frac{1}{2} (x - \hat{x}_g)' H_g (x - \hat{x}_g) \right], \quad (3.6)$$

where $A(y)$ is now easily computed as

$$\begin{aligned}A(y) &= \left(\int dx P(x, g|y) \right)^{-1} \\ &= \left[(2\pi)^{m/2} \sum_{g=1}^G |H_g|^{-1/2} \exp(-\phi(\hat{x}_g, g; y)) \right]^{-1}\end{aligned}\quad (3.7)$$

In Eq. (3.7), m is the number of elements in the geometric state vector x . The approximation in (3.6) is used to avoid the multidimensional numerical integration implied in (3.2) to define $P(y)$. The posterior probability of inclusion type can be found by integrating out x in (3.6). The result is

$$\begin{aligned}P(g|y) &= \exp[-\phi(\hat{x}_g, g; y)] |H_g|^{-1/2} \\ &\times \left[\sum_{g'=1}^G \phi(\hat{x}_{g'}, g'; y) |H_{g'}|^{-1/2} \right]^{-1}\end{aligned}\quad (3.8)$$

The maximum value of $P(x, g|y)$ for a specified g is

$$P(\hat{x}_g, g|y) = A(y) \exp[-\phi(\hat{x}_g, g|y)], \quad (3.9)$$

where the normalization factor $A(y)$ is given by Eq. (3.7). A measure of the uncertainty in x for any assumed g is given by the posterior covariance matrix of x for the value of g specified. Using the above approximations, we find this to be just $\text{cov}(x|q, y) = H_g^{-1}$.

Two decision rules are of interest in choosing an inclusion type, g . The first is to choose the value of g that maximizes $P(g|y)$ in (3.8) corresponding to the loss function (2.15) in the last section. The second is to choose that value of g that maximizes $P(\hat{x}_g, g|y)$ in (3.9), which is consistent with the loss function (2.14) in the last section. The former rule has a certain intuitive appeal. If the present inversion procedure is regarded as a "free-standing" entity then either rule can be used, the corresponding loss functions being a matter of taste. However, if the procedure is to be integrated into a larger, more complex, scheme of decision logic yielding optimal accept/reject policies, etc., then no decisions are to be made in the inversion procedure, except as an approximation to simplify the processing in the remainder of decision logic. As an approximation, it is usually sufficient to input into the remaining decision logic the approximation to $P(x, g|y)$ given by (3.6).

At present, the computer program implementing the inversion algorithm reports both $P(g|y)$ and $P(\hat{x}_g, g|y)$ for each g as well as the posterior standard error of each component of x and correlation matrix of these components. The program is written in FORTRAN 5 and is able to run in pseudo real time on a Data General M-600. [Approximately two minutes of CPU time (timeshare mode) is required to estimate the geometry for each inclusion type in a class of five inclusions.] Currently, there are several options available for specification of the prior distribution of x and y . In each of these options, the geometry x is assumed to be distributed independently of the inclusion type, g . This restriction is easily relaxed with a small modification to the computer code. The discrete prior distribution of g is specified in the input. Normally, this will be taken as flat (equal probability over all inclusion types). The flow of the various types of input information is shown in Fig. 1 along with the major output discussed above.

In the case of spheroidal voids or inclusions, the prior distribution of $x = (a, c, r_z, i)$ is assumed factorable into the following three parts:

$$P(a, c, r_z, i) = P(a, c) P(r_z) P(i). \quad (3.10)$$

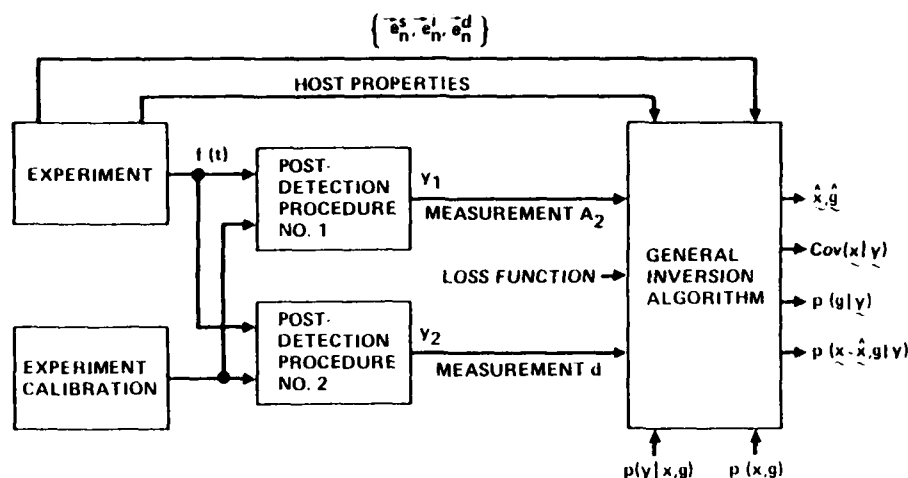


Fig. 1.
Schematic of
Information
Flow for General
Inversion
Algorithm

In the above expression, a and c are the semi-major and semi-minor axis lengths of an oblate spheroid and γ_2 and α define the orientation (i.e., the direction cosine relative to the z -axis and the azimuthal angle, respectively).

The program, as currently implemented, allows for the following parameterization of the prior distribution:

- (1) $\gamma_2 \sim$ Beta with input degrees of freedom ν_{γ_1} and ν_{γ_2} .
- (2) $\alpha/2\pi \sim$ Beta with input degrees of freedom ν_{α_1} and ν_{α_2} .
- (3) (i) $(a, c) \sim$ Bivariate Weibull with input shape and scale parameters.
(ii) $(a, c) \sim$ Bivariate lognormal with input location and scale parameters.
(iii) $(a, c) \sim$ Bivariate extreme value type-I with input location and scale parameters.
(iv) $(a, c) \sim$ Flat.

The joint distribution of a and c is restricted to have positive mass only when $a \geq c$. This is because the current coding of the low frequency scattering algorithm is restricted to oblate spheroidal geometry.

The beta priors on γ_2 and α include the uniform density as a special case ($\nu_{\gamma_1} = \nu_{\gamma_2} = \nu_{\alpha_1} = \nu_{\alpha_2} = 1$).

Specifications of the uniform density for these parameters is equivalent to assuming x and g that the axis of symmetry is uniformly distributed over the unit sphere. If this uniform distribution is assumed and if the distribution of a and c is taken as flat (no x and g bias) the program will automatically produce the maximum likelihood estimate of x for each category g . This is because the loss function being used is the Dirac delta function. The posterior variance reported by the program becomes the conditional covariance matrix of x_g conditioned on x and g . The distributional properties of x_g in this conditional situation are discussed in Appendix C.

The inversion algorithm as currently implemented requires the measurement covariance matrix C as input. This matrix is assumed to be diagonal (independent observations). The program reads in an estimate of the standard error of y_{1n} and y_{2n} for each y_{1n} and y_{2n} input. This estimate will presumably come from replicate experiments or from various comparisons of theory and experiment. The actual estimated x_g depends only on the relative sizes of these standard errors, not their absolute magnitude. The posterior standard error does depend upon their magnitude however. The following is reported for each inclusion type considered:

1. Posterior probability of g : $P(g|y)$.
2. Posterior density of x and g at \hat{x}_g : $P(\hat{x}_g, g|y)$.
3. Residual sum of squares for A_2 measurements: $(y_1 - h_1(\hat{x}_g))' C_1^{-1} (y_1 - h_1(\hat{x}_g))$.
4. Residual sum of squares for d measurements: $(y_2 - h_2(\hat{x}_g))' C_2^{-1} (y_2 - h_2(\hat{x}_g))$.
5. Total residual sum of squares: $(y - h_g(\hat{x}_g))' C^{-1} (y - h_g(\hat{x}_g))$.
6. Convergence information.
7. Estimates of the two major axes (a, a) and the one minor axis (c) and the direction cosines of all axes.
8. Posterior standard errors of all items in (7).
9. Posterior correlation matrix of all items in (7).
10. Observations, predicted values and residuals for each of the A_2 type measurements and each of the d type measurements.

All standard errors and correlations are computed using the usual linear approximation techniques. In particular, if $v = h(u)$ where v and u are random vectors, then the corresponding covariance matrices are related by the approximate expression

$$E_v = J_u J_u'$$

where

$$J = \partial h / \partial u$$

is the Jacobian matrix of the transformation h . This matrix need not be square.

The residual sums of squares in outputs (3) through (5) above allow one to test the statistical model's adequacy. In particular, these sums of squares will be approximately χ^2 distributed when the inclusion type is correctly assumed. They give a direct measure of the experimental uncertainty. In Appendix C, we discuss their distributional form in more detail.

The residuals reported in output (10) provide a further indication of the model's adequacy. Simple run tests performed on these residuals will indicate non-random patterns and thus address the question of goodness-of-fit of the mathematical scattering model to the experimental situation for each postulated inclusion type. Those postulated inclusion types which exhibit non-random residuals should be considered as wrong candidates.

As mentioned earlier, certain precautionary steps are necessary in order to assure convergence of the quasi-Newton algorithm used by ZXMIN. First of all, it is useful to transpose the state vector $x = (a, c, \gamma_z, \alpha)$ into the state vector x^* given by

$$\begin{aligned} x_1^* &= \ln(a/a^*) \\ x_2^* &= \ln(c/(c^*a-c)) \\ x_3^* &= \gamma_x/\gamma_z \\ x_4^* &= \gamma_y/\gamma_z \end{aligned} \quad (3.11)$$

where

$$\gamma_x = \cos \alpha \sin \theta$$

$$\gamma_y = \sin \alpha \sin \theta$$

and

$$\gamma_z = \cos \theta.$$

Here, a^* is an arbitrary scaling constant chosen so that underflows or overflows of digits are avoided. The term c^* is a biasing factor that is used to avoid singularities encountered in the calculation of A_2 when the geometry is too close to a sphere. It represents the maximum allowable ratio of c/a .

The transformation specified by (3.11) maps the original state variable x into an unconstrained state variable x^* . In particular, each component of x^* may range between $-\infty$ and ∞ . This mapping, which is 1-1, greatly facilitates the use of ZXMIN which would otherwise ignore the constraints in the original state space: $0 < \gamma_z < 1$, $0 < \alpha < 2\pi$, and $a > c > 0$.

The inverse transformation is given by

$$\begin{aligned} a_1 &= a^* e^{x_1^*} \\ c &= c^* a^* e^{x_1^*} e^{x_2^*} / (1 + e^{x_2^*}) \\ \gamma_x &= x_3^* / (1 + x_3^{*2} + x_4^{*2})^{1/2} \end{aligned}$$

$$\begin{aligned} \gamma_y &= x_4^* / (1 + x_3^{*2} + x_4^{*2})^{1/2} \\ \gamma_z &= 1 / (1 + x_3^{*2} + x_4^{*2})^{1/2} \end{aligned}$$

In actual implementation of the inversion algorithm, it has been found that convergence is quite sensitive to the first guess. When there is little *a priori* bias, it often turns out that the first guess will be at a place on the response surface $c(x, y)$ where the Hessian is not positive definite. This implies that the surface at a small distance from the minimum has a ridge-canyon behavior that will defeat the algorithm if suitable tactics are not utilized. The iteration scheme used in ZXMIN employs an approximation to the Hessian. At the initiation of the algorithm, any positive definite matrix may be used (not necessarily the true Hessian) for this approximation. The approximation is updated each iteration and converges to the true Hessian as the true minimum is reached. The rapidity of convergence is tied to the difference between the initial approximate Hessian and the true one. If the true Hessian at x_0 is not positive, then it cannot be used as a first guess. The program as implemented, forces this matrix to be positive definite by taking the absolute value of the diagonal portion of the Hessian when it is discovered that the Hessian is not computationally positive definite. In order to reduce computational effort as much as possible, as well as to assure that a local minimum is to be obtained, the program uses a simple, but very robust initial search algorithm to find the approximate location of a local minimum in the four dimensional space of x^* . In the simulation runs performed to date, it was often found that the use of this robust search algorithm before employing ZXMIN was essential to assure convergence when the inclusion type assumed was different from that which was used in the generation of the test data. It is just as important that convergence be reached for incorrect inclusion types as for the correct ones, so that a proper assessment of posterior probabilities can be made.

NUMERICAL RESULTS

In this section, we describe some of the recent numerical testing of the inversion algorithm. The purpose is to determine the robustness of the algorithm to perturbations of the various assumptions in both the statistical model and the physical scattering model. As a minimum, it is necessary to assess the effect on the inversion results of 1) flaw sizes, 2) flaw orientation, 3) flaw type, 4) host property variation, 5) *a priori* distributional assumptions, 6) actual measurement error, 7) assumed rms measurement error, 8) transducer placements, and 9) scattering theory inaccuracies. To date, only some of the numerical experiments addressing items 1 through 7 have been run. It has been found that the inversion algorithm performs quite well over a wide range of experimental errors. Some of the results are reported in Table 1. This table is based on synthetic scattering data generated using a Gaussian random number generator. The standard errors reported as σ_{A_2} and σ_d under the subheading

"Experimental" were used to scale the Gaussian random number. The inversion algorithm used the standard errors reported under the "Analysis" subheading. Three simulations were performed for each case. In point of fact, if the function being minimized

TABLE 1
INVERSION ALGORITHM NUMERICAL RESULTS FOR SELECTED AREAS (MAXIMUM LIKELIHOOD)

Experimental		Analysis								
σ_{A_2}	σ_d	σ_{A_2}	σ_d	a	σ_a	c	σ_c	γ_z	σ_{γ_z}	P(void)
A. Void, a = 0.04, c = 0.02, $\gamma_z = 1.0$										
10%	20%	10%	20%	0.0405	0.0009	0.0203	0.0018	0.993	0.005	0.992
				0.0402	0.0009	0.0200	0.0019	0.982	0.015	0.989
				0.0400	0.0009	0.0205	0.0018	0.997	0.006	0.982
20%	40%	20%	40%	0.0412	0.0017	0.0203	0.0036	0.990	0.021	0.779
				0.0415	0.0020	0.0182	0.0038	0.917	0.064	0.790
				0.0400	0.0017	0.0209	0.0035	0.988	0.025	0.669
10%	20%	10%	10,000%	0.0410	0.0011	0.0196	0.0022	0.982	0.017	0.345
				0.0417	0.0010	0.0168	0.0021	0.977	0.016	0.307
				0.0396	0.0011	0.0212	0.0024	0.997	0.009	0.354
B. Void, a = 0.04, c = 0.038, $\gamma_z = 1$										
10%	20%	10%	10%	0.0409	0.0009	0.0374	0.0018	0.793	0.335	0.995
				0.0422	0.0011	0.0344	0.0019	0.555	0.179	0.911
				0.0405	0.0009	0.0375	0.0018	0.739	0.407	0.997
5%	10%	10%	20%	0.0403	0.0008	0.0380	0.0018	0.937	0.243	0.998
				0.0406	0.0010	0.0370	0.0019	0.692	0.352	0.988
				0.0401	0.0008	0.0380	0.0017	0.921	0.306	0.999
C. Void, a = 0.04, c = 0.038, $\gamma_z = 0.5$										
10%	20%	10%	20%	0.0412	0.0013	0.0367	0.0021	0.443	0.330	0.991
				0.0427	0.0012	0.0334	0.0019	0.428	0.152	0.826
				0.0413	0.0012	0.0359	0.0020	0.444	0.274	0.990
D. Void, a = 0.04, c = 0.020, $\gamma_z = 0.5$, $\alpha = 45^\circ$										
10%	20%	10%	20%	0.0402	0.0012	0.0209	0.0017	0.489	0.079	0.840
				0.0409	0.0012	0.0189	0.0016	0.461	0.068	0.614
				0.0410	0.0012	0.0190	0.0015	0.507	0.068	0.939

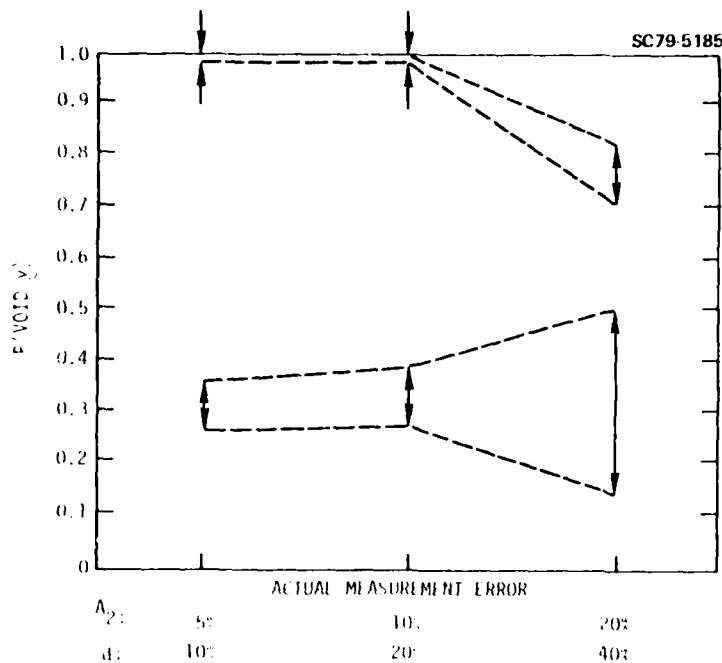
to determine x_g were a pure quadratic form in x , then the posterior variances reported in Table 1 would not be a function of the specific random vector y observed, but only a function of the assumed values of σ_{A_2} and σ_d , the transducer placements, and

the inclusion type. Deviation from quadratic behavior in the functional form of \dagger yields additional variability in the posterior variances.

All of the scattering measurements were taken to be of the pulse-echo type. The transducers were assumed to be placed in a symmetrical array on a spherical test piece with the inclusion at the center. Seventeen transducers were used. One was placed directly above the flaw. The remaining sixteen transducers were placed four each, 90° apart, in four different cones above the inclusion. The four cones had half angles of 15° , 30° , 45° , and 60° , respectively. The optimum number and placement of transducers is still under investigation.

All of the analyses represented in Table 1 assumed *a priori* that the flaw being measured was one of five types: void, BN, Si, SiC, or WC. Given the low frequency scatter coefficients, A_2 , for SiC and WC are negative in a SiN_3 host, these two categories may be eliminated immediately when the true inclusion type is a void. The last column in Table 1 reports the posterior probability that the inclusion type is a void. The only serious contender using the five types allowed was BN. In every case run so far, the posterior probabilities of inclusion other than a void or BN (when a void was used in the test data) were all less than 0.0001. Similar results using a different random seed are plotted in Fig. 2 wherein the actual measurement error ranges from 5% to 20% in A_2 and from 10% to 40% in d .

The results reported in Part A of Table 1 and Fig. 2 indicate two things. First, very large random components of the measurement error may be tolerated before the inversion breaks down. The



INPUT σ_{A_2} TRUTH
 σ_d TRUTH

INPUT σ_{A_2} 10%
 σ_d 10,000%

Fig. 2.
 Effect of
 Random
 Measurement
 Error On
 Classification
 Probability
 (Oblate Void
 200 μ m/400 μ m)

posterior probability of 0.66 to 0.79, with 20% to 40% measurement error per measurement, is quite good. (Note that since 17 observations are being taken for each of the A_2 type measurements, the effective random error in inversion is approximately $17^{-1/2}$ or 0.24 of the individual errors.) The Gaussian approximation to the posterior distributions of a and g for the various flaw types is shown in Fig. 3 for a specific set of random measurement errors. The area under each flaw's curve represents the posterior probability of that flaw type. The spread of the curve indicates the posterior uncertainty in the major semi-axis length. It can be seen that the void is by far the most probable flaw category in the three cases shown. Also, the spread widens as the measurement increases. This is a natural result.

The second item of interest seen from Part A and Fig. 2 is that it appears that the d type measurements are crucial to the inversion procedure in most cases. The run whose σ_d was taken as 10,000 in the analysis stage effectively gives the d measurements zero weight for that inversion. The result is an inversion based on A_2 measurements alone. As can be seen, the posterior probability of a void is only 0.3 to 0.36. In fact, the posterior probability of BN was 0.60 to 0.70 for these runs. On the other hand, it is apparent from the estimate of a , c , and y_2 , that the geometry is still being estimated quite accurately based on the A_2 measurements alone. The unfortunate part is that the BN category seems to fit the noisy A_2 data for a void just as well as a void does. In the actual three simulation runs, the major difference between the BN and void computation was in $|H_2|^{-1/2}$. This is a measure of the curvature of the posterior density of x near its maximum. This curvature was larger for the BN category than for the void category. Interestingly, both categories produced essentially the same residual sum of squares.

Part B of Table 1 represents some of the results obtained when the inclusion becomes nearly spherical. As can be seen, the posterior probability of a void remains high. The posterior standard error, σ , becomes quite large. This is to be expected, $1/2$ since in the limit when the flaw becomes a sphere, the axis of symmetry loses meaning.

Part C of the table demonstrates that tilting a nearly spherical flaw has essentially no effect on the inversion algorithm. However, tilting a more eccentric spheroid does, of course, have an effect. Part D of the table represents the results of the inversion algorithm in the case where the axis of symmetry of a flaw with dimensions $a = 0.04$ cm and $c = 0.02$ cm is 45° off of the vertical with an azimuthal angle of 45° . Further results using a different random seed are presented in Fig. 4. For certain orientations, the classification probability becomes quite poor. Presumably, this difficulty is correlated with the transducer configuration used. Clearly, it is desirable to devote more work to the quantification of the effect of transducer placement.

No runs have been made yet to assess the effect of scattering model error. In particular, it is desirable to determine the effect on inversion of such things as, 1) losses in the host, 2) multiple scatterers, and 3) non-spheroidal scatterer geometry.

REFERENCES

1. R.K. Elsley, J.M. Richardson and R.B. Thompson, "Determination of Fracture Mechanism Parameters from Elastic Wave Scattering at Lower Frequencies," Semi-Annual Report, Interdisciplinary Program for Quantitative Flaw Definition, Report SC595.32SA, pp. 104-14, February 1978.
2. Fletcher, R., "Fortran Subroutine for Minimization by Quasi-Newton Methods," R7125 AFRF, Harwell, UK.

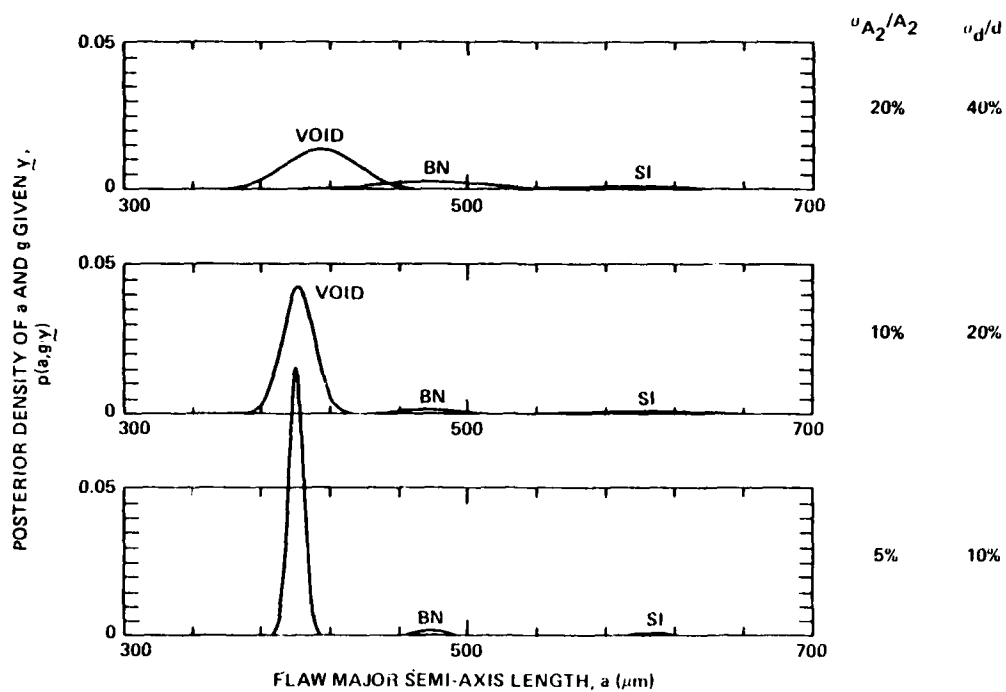


Fig. 3. Effect of Measurement Error on Estimated Geometry of Ellipsoidal Inclusions (Oblate Void 200 μm /400 μm)

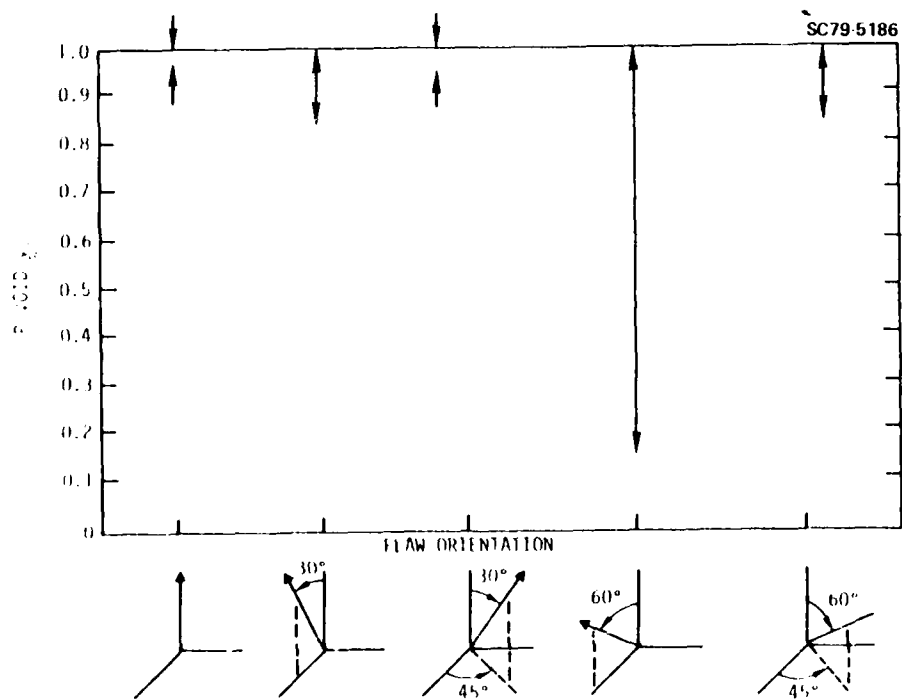


Fig. 4. Effect of Orientation on Classification Probability (Oblate Void 200 μm /400 μm)

APPENDIX A

SCATTERING OF ELASTIC WAVES FROM ELLIPSOIDAL VOIDS AND INCLUSIONS IN THE LOW FREQUENCY (RAYLEIGH) REGIME

It is our purpose here to present further details of the analysis of $A_2 = A_2(\vec{e}^S, \vec{e}^i; x, g)$ for the case of longitudinal-to-longitudinal elastic wave scattering. In this case, we have that

$$A_{2-2}(\vec{e}^S, \vec{e}^i) = \frac{V_S}{4\pi\rho} [\delta\rho c_L^{-2} e_{\alpha\alpha}^S e_{\alpha\alpha}^i - c_L^{-2} t_m^S (G_{mn} + \delta C_{mn}^{-1})^{-1} t_n^i], \quad (A-1)$$

where repeated subscripts imply summation. In the following, the subscripts α, β, γ , and δ will range from one to three, representing the x, y, and z directions in a laboratory coordinate system, while the subscripts m and n range from one to six.

In equation (A-1), V_S is the volume of the ellipsoid and is given by

$$V_S = \frac{4\pi}{3} abc,$$

where a, b and c are the semiaxes lengths of the ellipsoid with principal axes defined by the unit vectors \hat{u} , \hat{v} , and \hat{w} , respectively. The parameter c_L is the velocity of longitudinal waves in the bulk and is given by

$$c_L = [(\lambda + 2\mu)/\rho]^{1/2},$$

where ρ is the density of the bulk and λ and μ are the Lamé constants of the bulk.

We let $\rho + \delta\rho$, $\lambda + \delta\lambda$, $\mu + \delta\mu$ be the density and Lamé constants of the inclusion.

The six vectors t_m^S and t_m^i are obtained via a transformation from the 3×3 matrix representation of strain. Specifically,

$$t_m^S = e_{\alpha}^S e_{\beta}^S s_{m\alpha\beta},$$

$$t_m^i = e_{\alpha}^i e_{\beta}^i s_{m\alpha\beta},$$

where $\vec{e}^S = (e_{\alpha}^S)$ is the unit vector in the scattered direction and $\vec{e}^i = (e_{\alpha}^i)$ is the unit vector in the incident direction of the plane acoustic wave.

Recalling that $\hat{u} = (u_{\alpha})$, $\hat{v} = (v_{\alpha})$, $\hat{w} = (w_{\alpha})$ are the three principal axes of the ellipsoid, we have that the transformation matrix S is given by

$$s_{1\alpha\beta} = u_{\alpha} u_{\beta}$$

$$s_{2\alpha\beta} = v_{\alpha} v_{\beta}$$

$$s_{3\alpha\beta} = w_{\alpha} w_{\beta}$$

$$s_{4\alpha\beta} = \frac{1}{\sqrt{2}} (v_{\alpha} w_{\beta} + w_{\alpha} v_{\beta})$$

$$s_{5\alpha\beta} = \frac{1}{\sqrt{2}} (w_{\alpha} u_{\beta} + u_{\alpha} w_{\beta})$$

$$s_{6\alpha\beta} = \frac{1}{\sqrt{2}} (u_{\alpha} v_{\beta} + v_{\alpha} u_{\beta}),$$

where $\alpha, \beta = 1, \dots, 3$.

The six by six matrix δC_{mn} is given by

$$\delta C_{mn} = s_{m\alpha\beta} \delta C_{\alpha\beta\gamma\delta} s_{n\gamma\delta},$$

where $\delta C_{\alpha\beta\gamma\delta}$ is the elastic constant deviation tensor in the inclusion.

The Green's matrix G_{mn} has very special structure for an oblate spheroid ($a = b > c$). It is given by

$$G_{mn} = \begin{pmatrix} G_{11} & G_{12} & G_{13} & | & 0 & 0 & 0 \\ G_{12} & G_{11} & G_{13} & | & 0 & 0 & 0 \\ G_{13} & G_{13} & G_{33} & | & 0 & 0 & 0 \\ \hline 0 & 0 & 0 & | & G_{44} & 0 & 0 \\ 0 & 0 & 0 & | & 0 & G_{44} & 0 \\ 0 & 0 & 0 & | & 0 & 0 & G_{66} \end{pmatrix},$$

with

$$G_{11} = pI_a - q(2I_a - 3a^2I_{aa})$$

$$G_{33} = p(4\pi - 2I_a) - q(8\pi - 4I_a - 3c^2I_{cc})$$

$$G_{12} = -q(I_a - a^2I_{aa})$$

$$G_{13} = -q(I_a - 3c^2I_{ac})$$

$$G_{44} = \frac{1}{2} p(4\pi - I_a) - \frac{1}{2} q(4\pi - I_a - 6(a^2 + c^2)I_{ac})$$

and

$$G_{66} = pI_a - q(I_a - 2a^2I_{aa}).$$

In the above,

$$I_a = \frac{2\pi a^2 c}{(a^2 - c^2)^{3/2}} \left(\cos^{-1} \frac{c}{a} - \frac{c}{a} \left(1 - \frac{c^2}{a^2} \right)^{1/2} \right)$$

$$I_{aa} = \frac{3}{4(a^2 - c^2)} I_a - \frac{c^2}{a^2(a^2 - c^2)}$$

$$I_{ac} = \frac{4\pi - 3I_a}{3(a^2 - c^2)}$$

and

$$I_{cc} = \frac{2}{a^2 - c^2} I_a + 4\pi \frac{a^2 - 3c^2}{3c^2(a^2 - c^2)},$$

with

$$p = \frac{1}{8\pi\rho} \left(\frac{1}{c_t^2} + \frac{1}{c_l^2} \right)$$

and

$$q = \frac{1}{8\pi\rho} \left(\frac{1}{c_t^2} - \frac{1}{c_l^2} \right).$$

Here c_t is the transverse wave velocity in the host and is given by

$$c_t = (\mu/\rho)^{1/2}.$$

In the special case of a sphere ($a=b=c$), the above is somewhat simpler. Specifically,

$$G_{11} = G_{33} = \frac{3 + \kappa}{15\rho c_l^2}$$

$$G_{12} = G_{13} = \frac{2 - \kappa}{30\rho c_l^2}$$

$$G_{44} = G_{66} = \frac{4 + 3\kappa}{30\rho c_l^2}$$

with

$$\kappa = 2(\lambda + 2\mu)/\mu.$$

APPENDIX B

DISTANCE FROM THE CENTER TO THE FRONT-FACE TANGENT PLANE FOR ELLIPSOIDAL GEOMETRY

We present here a detailed derivation of the distance $d(\vec{e}; x)$ discussed in the second section of the paper. The general equation of an ellipsoid can be written in the form

$$\phi(\vec{r}) \equiv \vec{r} \cdot \vec{Q} \cdot \vec{r} = 1, \quad (B-1)$$

where the tensor \vec{Q} is given by

$$\vec{Q} = a^{-2}\vec{u}\vec{u} + b^{-2}\vec{v}\vec{v} + c^{-2}\vec{w}\vec{w} \quad (B-2)$$

in which a , b and c are the semi-axis lengths and \vec{u} , \vec{v} and \vec{w} are the mutually orthogonal unit vectors giving the directions of the corresponding principal axes. In the case of a spheroid we obtain

$$\begin{aligned} \vec{Q} &= a^{-2}(\vec{u}\vec{u} + \vec{v}\vec{v}) + c^{-2}\vec{w}\vec{w} \\ &= a^{-2}(\vec{1} - \vec{w}\vec{w}) + c^{-2}\vec{w}\vec{w}, \end{aligned} \quad (B-3)$$

where $\vec{1}$ is the unit tensor. It is clear that $\phi(\vec{r})$ depends upon the geometrical state vector x , but only through the tensor \vec{Q} .

Let us consider a plane that is tangent to the ellipsoid at the point r and that has an outward pointing normal \vec{e} . This plane represents a wave-front impinging on the ellipsoid in a pulse-echo experiment in which $-\vec{e}$ is the propagation direction of the incident wave (at the front face of the ellipsoid) and \vec{e} is the propagation of the scattered wave (i.e., the part that will propagate back to the transducer). The vector \vec{e} , corresponding to the position \vec{r} , is given by

$$\vec{e} = \frac{1}{2} h \nabla \phi = h \vec{Q} \cdot \vec{r} \quad (B-4)$$

from which we deduce

$$\vec{r} = \frac{1}{h} \vec{Q}^{-1} \cdot \vec{e}. \quad (B-5)$$

In the above expression h is a normalization factor, as yet undetermined.

The condition that \vec{r} lies on the surface of the ellipsoid is

$$\begin{aligned} 1 &= \phi(\vec{r}) \equiv \vec{r} \cdot \vec{Q} \cdot \vec{r} \\ &= \frac{1}{h^2} \vec{e} \cdot \vec{Q}^{-1} \cdot \vec{e} \end{aligned} \quad (B-6)$$

from which we infer

$$h = (\vec{e} \cdot \vec{Q}^{-1} \cdot \vec{e})^{1/2}. \quad (B-7)$$

It is obvious that the distance from the center of the ellipse to the front-face tangent plane is

$$d = \vec{r} \cdot \vec{e} = h \vec{r} \cdot \vec{Q} \cdot \vec{r} = h. \quad (B-8)$$

Thus we finally obtain the desired result

$$\begin{aligned} d &= d(\vec{e}; x) \\ &= (\vec{e} \cdot \vec{Q}^{-1} \cdot \vec{e})^{1/2}. \end{aligned} \quad (B-9)$$

In the case of the spheroid we obtain

$$d = [a^2 - (a^2 - c^2)(\vec{w} \cdot \vec{e})^2]^{1/2}. \quad (B-10)$$

If we write

$$\vec{w} = \vec{e}_x \gamma_x + \vec{e}_y \gamma_y + \vec{e}_z (1 - \gamma_x^2 - \gamma_y^2)^{1/2}, \quad (B-11)$$

then

$$\vec{w} \cdot \vec{e} = \vec{e} \cdot \vec{e}_x \gamma_x + \vec{e} \cdot \vec{e}_y \gamma_y + \vec{e} \cdot \vec{e}_z (1 - \gamma_x^2 - \gamma_y^2)^{1/2}. \quad (B-12)$$

APPENDIX C

DISTRIBUTIONAL PROPERTIES OF ESTIMATORS WITH RESPECT TO MEASUREMENT ERROR WHEN BAYES RULES ARE EMPLOYED

The estimation rule for \hat{x} and \hat{g} is Bayes in that it minimizes the risk with respect to the joint distribution of x , g , and y . As discussed in the third section of the paper, if the prior on x and g is flat, then $\hat{x}_g(y)$ will be the maximum likelihood estimate of the vector parameter x for each postulated inclusion g . In this situation, the distributional properties of $\hat{x}_g(y)$ are considered with respect to the conditional distribution of y given x and g . Even if the prior is not taken as flat, because $\hat{x}_g(y)$ is a function of y , it is still appropriate to consider its distributional properties with respect to this conditional distribution. To do this we note that \hat{x}_g and y are such that the surface $\phi(x, g; y)$ has a stationary point. Defining the matrix P as the Jacobian matrix of $h_g(x)$ with respect to x , that is

$$[P_{ki}] = \left[\frac{\partial h_{gk}(x)}{\partial x_i} \right]. \quad (C-1)$$

It is easily seen that since

$$0 = \frac{\partial \phi}{\partial x} \bigg|_{\hat{x}_g, y} = \frac{\partial \phi}{\partial x} \bigg|_{x_{0g}, y_0} + \left[\frac{\partial^2 \phi}{\partial x_i \partial x_j} \right] [\hat{x}_g - x_{0g}] + \frac{\partial^2 \phi}{\partial y \partial x} (y - y_0) + \dots, \quad (C-2)$$

then

$$(\hat{x}_g - x_{0g}) = H_g^{-1} P' C^{-1} (y - y_0), \quad (C-3)$$

where x_{0g} is the state that minimizes $\phi(x, g; y_0)$

when $y = y_0$ is observed as measurement error free.

From (C-3) it is seen that, since $y_0 = E(y | x_{0g}, g) = h_g(x_{0g})$, then

$$E(\hat{x}_g | x_{0g}, g) = x_{0g} \quad (C-4)$$

and

$$\text{Cov}(\hat{x}_g | x_{0g}, g) = H_g^{-1} P' C^{-1} P H_g^{-1}. \quad (C-5)$$

We note that the Hessian has the form

$$H_g = \left[\frac{\partial^2 \phi}{\partial x_i \partial x_j} \right] = P' C^{-1} P - Q, \quad (C-6)$$

where

$$[Q_{ij}] = \left[\frac{\partial^2 \ln p(x, g)}{\partial x_i \partial x_j} \right] \quad (C-7)$$

is the Hessian of the log of the prior distribution. In the case that $p(x, g)$ is flat in x , then

$$\text{Cov}(\hat{x}_g | x_{0g}) = (P' C^{-1} P)^{-1}. \quad (C-8)$$

From (C-3) it is seen that since y is multivariate normal with mean $h_g(x_{0g})$ and variance covariance matrix C , $\hat{x}_g(y)$ will also be multivariate normal with mean (C-4) and variance covariance (C-5). This result is independent of any *a priori* bias that is assumed.

Under normality of the measurement errors, the distributional properties of the residual sum of squares may be derived. The residual sum of squares is defined by

$$S = (y - h_g(\hat{x}_g))' C^{-1} (y - h_g(\hat{x}_g)). \quad (C-9)$$

In the case where measurement errors in the A_2 experiments are uncorrelated with those in the d experiments, S has the decomposition

$$S = S_1 + S_2 \quad \text{with} \quad S_1 = (y_1 - h_{g_1}(\hat{x}_g))' C_1^{-1} (y_1 - h_{g_1}(\hat{x}_g)), \quad (C-10)$$

$$S_2 = (y_2 - h_{g_2}(\hat{x}_g))' C_2^{-1} (y_2 - h_{g_2}(\hat{x}_g)). \quad (C-11)$$

The statistics S_1 and S_2 are not independent since they both involve \hat{x}_g .

We now develop an approximate distribution for S . The cases for S_1 and S_2 are done similarly. Assume we know the matrix C up to a scale factor α , and the matrix Q up to the scale factor α^{-1} , that is

$$C = \alpha W, \quad (C-12)$$

$$Q = \alpha^{-1} U \quad (C-13)$$

with both W and U completely known. This is equivalent to knowing the relative weights of the measurement errors among the different experiments as well as relative to the prior information. Equation (C-3) can now be written

$$\hat{x}_g - x_{0g} = (P' W^{-1} P - U)^{-1} P' W^{-1} (y - h_g(x_{0g})). \quad (C-14)$$

Thus,

$$\begin{aligned} y - h_g(\hat{x}_g) &= y - h_g(x_{0g}) - (h_g(\hat{x}_g) - h_g(x_{0g})) \\ &= (y - h_g(x_{0g})) - P(\hat{x}_g - x_{0g}) \\ &= (I - P(P' W^{-1} P - U)^{-1} P' W^{-1})(y - h_g(x_{0g})). \end{aligned} \quad (C-15)$$

Therefore,

$$S = \frac{1}{\alpha} (y - h_g(x_{0g}))' B (y - h_g(x_{0g})), \quad (C-16)$$

with

$$B = (I - W^{-1}P(P'W^{-1}P - U)^{-1}P')W^{-1} \\ \cdot (I - P(P'W^{-1}P - U)^{-1}P'W^{-1}) \quad (C-17)$$

Thus the scalar $R = \theta S$, is independent of θ and thus is computable without its knowledge.

In the case of a flat prior, $U = 0$. Then

$$B = (I - W^{-1}P(P'W^{-1}P)^{-1}P')W^{-1} \quad (C-18)$$

Equation (C-16) represents S as a quadratic form in the multivariate Gaussian variable y . In the following, we assume that the value θ_0 is used in calculation of S , and that this may in general be different from the true scale factor θ . The first two moments of S are

$$E(S|x, g) = \text{tr} \left(\frac{1}{\theta_0} BC \right) = \frac{\theta}{\theta_0} \text{tr} (BW) \quad (C-19)$$

$$\text{var}(S|x, g) = 2 \text{tr} \left[\left(\frac{1}{\theta_0} BC \right)^2 \right] = 2 \left(\frac{\theta}{\theta_0} \right)^2 \text{tr} (BW)^2 \quad (C-20)$$

where we have written θ_0 for the value of the scale factor assumed in the calculations and θ for the true value of the scale factor. Equations (C-19) and (C-20) are valid even if y is not Gaussian. We note that in the case of a flat prior, BW is idempotent with $\text{tr} (BW) = \text{rank} (BW) = N - m$.

Knowledge of (C-19) and (C-20) up to the unknown scale factor θ allows one to develop a chi-square approximation to its distribution. In particular, we have that the random variable

$$\chi_v = \frac{\theta_0}{\theta} \frac{\text{tr} (BW)}{\text{tr} (BW)^2} S \quad (C-21)$$

is approximately a chi-square variate with degrees of freedom

$$v = [\text{tr} (BW)]^2 / \text{tr} [(BW)^2] \quad (C-22)$$

In the case that the prior is flat, the approximation becomes exact. That is,

$$\frac{\theta_0}{\theta} S \sim \chi_{N-m}^2 \quad (C-23)$$

The above results allow one to construct $100(1-\alpha)\%$ confidence intervals for θ/θ_0 . In particular,

$$\frac{S}{\chi_{v, 1-\alpha/2}^2} \leq \frac{\theta}{\theta_0} \leq \frac{S}{\chi_{v, \alpha/2}^2} \quad (C-24)$$

If such a confidence interval does not contain 1, then this is strong evidence that either the assumed measured error scale factor θ_0 is wrong, or that the assumed flaw type is wrong.

In terms of R , (C-24) may be rewritten as a confidence interval for θ as

$$\frac{R}{\chi_{v, 1-\alpha/2}^2} \leq \theta \leq \frac{R}{\chi_{v, \alpha/2}^2} \quad (C-25)$$

Finally, we remark that if an independent estimate of θ is obtained from replicate experiments, then the above distributional properties of R (even when an *a priori* bias is allowed) can be used to test the goodness-of-fit of the scattering model to the data. In particular, if $\hat{\theta}_0$ is an independent estimate of θ based on v_0 degrees of freedom, then the statistic

$$F = (R/v) / \hat{\theta}_0 \quad (C-26)$$

will be an F-statistic with v and v_0 degrees of freedom. Large values of this statistic indicate that either the scattering model is wrong or the postulated inclusion type is wrong.

RADIOGRAPHIC INSPECTION OF WELDS

R. L. Buckrop
U. S. Army Armament Materiel Readiness Command
Rock Island, Illinois 61299

ABSTRACT

This paper addresses the difficult problem of evaluating weld integrity of partial penetration type weld joints. Radiographic standards for partial penetration welds have in the past not been considered feasible due to confusing indications on the radiograph, resulting from the partially welded joint. The Army has developed a technique to offset this problem with suitable radiographic standards for conventional weld defects. This technique will be discussed.

INTRODUCTION

To adequately discuss the inspection of welds, it would be valuable to briefly cover the welding process. After this, since we are to consider the radiographic inspection technique, it will be desirable to cover the basic aspects of radiography. Finally, the adaptation of the radiographic procedure to weld inspection will be made.

Welding as applied to all materials would be much too broad a category for this discussion. To make the subject manageable; only metals will be considered, specifically aluminum and steel.

Weld Bead Material Characteristics⁽¹⁾ - The weld bead is a cast type metal, which is an alloy of the base metal being welded and that of the welding rod or wire added. During the welding process, this alloy is subjected to a very severe thermal environment which affects its metallurgical properties such as ductility, tensile strength, grain size and uniformity, impact qualities and alloy purity. Elements in steel such as sulphur, phosphorous, hydrogen have undesirable effects and every effort is made to eliminate them during the making of the metal and during welding. Base metal used for weldments is limited for practical reasons to compositions that can be readily fabricated without appreciable defects. One major stipulation restricts carbon hardening elements for steel to certain maximum levels. Too often the base material is selected from handbooks without recourse to materials or production engineering assistance. Many times troubles encountered in producing sound, crack free welds is traceable to difficult to weld base material. Filler material required for a weld is basically determined by the welding process. For some welds, no filler metal is required, in which case the weld metal consists of melted base metal. In addition to the restrictions imposed by the welding process, the choice of filler metal is based on mechanical and metallurgical considerations. The first consideration being that the filler metal have sufficient strength and ductility to perform adequately under the stress system imposed. Weld metal is a cast dendritic structure of comparatively low ductility and therefore, it is usually the practice to obtain a weld deposit of equal or greater strength than the base metal. Then in case of overstressing, the deformation will occur in the base metal which can better withstand deformation. This practice may not be desirable since other material properties other than strength and ductility may be needed, such as toughness,

strain aging, creep, corrosion or wear resistance.

Weld Fabrication⁽¹⁾ - The temperature in a weld joint will range from above the melting point to ambient of the section being welded. These temperatures cause expansion and contraction, chemical reactions and extreme mechanical stress in a weldment. The thermal gradient from ambient base material temperature to melting and the associated cooling rates represent a range of heat treating cycles of both good and extremely poor practices, resulting in questionable weld integrity. The molten weld metal may react with constituents of the surrounding atmosphere such as oxygen, hydrogen, nitrogen or gaseous compounds of these elements with carbon, causing degradation of the weld joint. Contamination by gases can be avoided by proper manipulation and utilization of the atmospheric shielding provided for a particular weld process. Most gases evolve from the molten weld metal readily, but time must be allowed for the gases to escape before the weld melt solidifies and entraps them. During the welding process, the operator must manipulate the heat source for two effects, (1) to produce a molten puddle of base material to fuse with the filler metal and (2) to exert control over the rate of solidification.

from this cursory look at the welding process, we see that many of the inherent problems confronted in obtaining a sound casting are also present during the weld process, i.e., material porosity, gas cavities slag inclusions, tears, etc. There are other defects inherent to welding alone, i.e., lack of fusion, incomplete joint penetration, cracking, overlap, weld crater, etc. Most of these defects can be located with good radiographic techniques.

Radiographic Process⁽²⁾ - X-rays are a form of radiant energy similar to visible light. They are of extremely short wave length and it is this characteristic that provides for their ability to penetrate materials which stop ordinary light. X-rays have all of the properties of visible light besides some which are characteristic to themselves, i.e., visible light is refracted by glass and therefore is capable of being focused by a lens made from it, however, for all practical purposes x-rays are not refracted and cannot be focused by a glass lens (their refraction by glass is ever so slight). Since radiography involves exposures made with Gamma radiation as well as x-rays, it is expedient to state that Gamma rays, although similar to x-rays, usually have a shorter wave length and are more

penetrating. They are distinguished from x-rays by their source and not their nature. Gamma rays are emitted from the disintegrating nuclei of radioactive substances of which the quality and intensity of the radiation cannot be controlled by the user. X-rays are produced when electrons, traveling at high speed, collide with matter. In the tube of a conventional static x-ray machine (Fig. 1) an incandescent filament supplies the electrons and forms the cathode (negative electrode). The tube target is made the anode (positive electrode). A high voltage potential is applied across the cathode and anode providing an accelerating force to the electrons produced by the filament. The sudden stopping of these fast moving electrons near the surface of the target anode results in the generation of x-rays. The higher the temperature of the filament, the greater is its emission of electrons and the larger the resulting tube current. Other conditions remaining the same, the x-ray output is proportional to the tube current. Most of the energy applied to the tube is transformed into heat at the focal spot on the target anode, with only a small portion being transformed into x-rays. The focal spot should be as small as feasible so as to obtain the sharpest possible definition (sharpness of image). However, the smaller the focal spot the less energy it will stand without damage. The higher the voltage the greater the speed of the electrons striking the target (increasing focal spot deterioration) with an associated decrease in wave length and a consequent increase in penetrating power (x-ray intensity). It is to be noted that x-rays produced at higher kilovolts contain all of the wave lengths of x-rays that would be produced at a lower kilovoltage plus additional shorter wave lengths having greater penetrating capability. Practical thickness limitations for typical x-ray machines are shown in the attached table. The intensity of gamma radiation (disintegrating nuclei of radioactive substance) is proportional to the source strength in curies, often referred to as "specific activity", expressed in terms of "curies per gram" or "curies per cubic centimeter."

Making A Radiograph⁽²⁾ - A radiograph is a photographic record produced by passing penetrating radiation through a specimen onto a sensitized film, thus producing a shadow graph of the specimen. Penetrating radiation causes an invisible change to occur in the coating on the film. The exposed areas become dark when the film is immersed in a developing solution; the degree of darkening dependent upon the extent of the exposure. After adequate development, the film is rinsed which stops development. Next the film is placed in a fixing bath to dissolve away the unexposed portions of the film emulsion, after which it is washed to remove the fixer. The basic features of a radiographic exposure are shown in Figure 2. The diagram shows the focal spot as a small area in the x-ray tube from which the radiation is emitted. The radiation travels in straight lines to the specimen. Upon entering the specimen, some rays pass through while others are absorbed. The amount which is transmitted depends upon the nature of the material and its thickness. If the specimen contains a void, radiation passing through will be less impeded and more energy will be transmitted than through the surrounding material. This will result in a dark spot on the development film corresponding to the projected position of the void, thus a shadow picture is formed of the specimen. The direct action of x-rays on a sensitized film can

often be enhanced by the use of intensifying screens, which are placed on each side of the film. These are generally of two types, (1) calcium tungstate, which converts x-rays into visible light which aids in the film exposure and (2) lead foil, which when radiated with penetrating radiation gives off free electrons which also benefits the exposure of the radiographic film. Lead foil has still another benefiting action of filtering out scattered radiation which improves the contrast, detail and clarity of a radiograph image. There are several types of radiographic film available, each of which has a special purpose to enhance radiographic results for a particular application, Fig. 3.

Radiographic Inspection - The inspection process is utilized to determine that the work being performed complies with the prescribed job or product requirements. Although there are several ways to inspect or evaluate welds, we will consider only the radiographic technique. It should be remembered however, that radiography may not necessarily be the best choice for all weld inspections and may often need to be verified by other types of tests, i.e., ultrasonics, physical tests. When considering any test there are some fundamental aspects which should be established, i.e., the object of the test, selection of the specimen, cost factor, validity of the test and the usefulness or value of the results. These test fundamentals need to be combined with common sense for satisfactory inspection.⁽¹⁾

Radiography has some inherent limitations which must be considered to obtain satisfactory results. Since a radiograph is a shadow picture of an object placed in the path of an x-ray beam, the forming of an image is influenced by the relative positions of the object and the film, the direction of the beam and the size of the source. For these reasons, familiarity with shadow formations is important for making and interpreting radiographs to assure radiographic image sharpness and minimum distortion. Figure 4 shows the effects of changing the size of the source and of changing the relative positions of source, object and card (film). It can be concluded then that the following conditions are needed to produce sharp, true shadowgraphs:⁽²⁾

- a. The source of x-rays should be as far from the object as practicable.
- b. The source of x-rays should be small as possible.
- c. The recording surface (film) should be as close to the object as possible.
- d. The x-rays should be directed perpendicular to the recording surface.
- e. The plane of the object and the plane of the recording surface should be parallel.

The enlargement of the object shadow will occur if the object is not in close contact with the film the degree of enlargement being dependent upon the relative distance of the object from the film and from the x-ray source.

Radiographic Sensitivity⁽²⁾ - Two factors affecting radiographic visibility are Radiographic contrast and Definition. Radiographic contrast is the difference in film densities for various areas of a radiograph. It depends upon both subject contrast and film contrast. Subject contrast is the relation

of x-ray intensities transmitted by various portions of a specimen. Subject contrast depends upon the characteristics of the specimen, the radiation used and the effects of scattered radiation. Film contrast depends upon the type of film, its processing and density (darkness). Definition is the sharpness of the image outline. It is dependent upon the radiation quality, geometry of radiographic setup and type of film and screens used. A check on the adequacy of a radiograph is made by use of a penetrameter, which is placed on the source side of a specimen. It has a thickness of a definite proportion of the specimen thickness, i.e., 2 percent, 1 percent, 5 percent. If the outline of the penetrameter shows clearly in the radiograph, the technique is considered satisfactory. Penetrameters may contain slots or holes of various sizes and judgement is based upon radiographic display of these holes. It should be pointed out that even if a hole in a penetrameter is visible on a radiograph, a void of the same diameter and thickness may not be visible. The penetrameter holes have sharp edges which give abrupt changes in metal thickness where a natural cavity has a more rounded edge which gives a gradual change. The image of the penetrameter hole will be sharper and more easily seen in a radiograph than will a natural cavity. Also, a fine crack may be quite extensive, however, if the x-rays pass across the thickness of the crack it probably will not be visible. Consequently, a penetrameter is used to check radiographic technique and not as a measure of the size of void which can be shown.

Typical Weld Joint Flaws - In order to utilize any inspection process, realistic standards of acceptability must be established. These standards will depend upon many aspects of the welded component, i.e., its application to the base material, cost, etc. Since the perfect weld has never existed and only degrees of weld imperfection will be obtainable, the following examples of weld joint discontinuities are presented:

Figures 5 and 6 show the recommended radiographic procedures for partial penetration weld joint designs. Partial penetration welds differ from full penetration welds and require more care when being radiographed to assure complete or maximum weld coverage with minimum interference from the normal unfused weld joint land.

Figures 7 and 8 illustrate radiation angles for two typical weld joint designs.

Figure 9 - Gas cavities in aluminum weld.

Figures 10 and 11 - Incomplete penetration in aluminum and steel welds respectively.

Figures 12 and 13 - Lack of fusion in aluminum and steel welds respectively.

Figure 14 - Ungraded conditions in aluminum welds.

Figure 15 - Fine scattered porosity in steel welds.

Figure 16 - Coarse scattered porosity in steel welds.

Figure 17 - Linear porosity in steel welds.

Figure 18 - Clustered porosity in steel welds.

Figure 19 - Scattered slag inclusions in steel welds.

CONCLUSION

Radiographic inspection of welds is a valuable tool which must be utilized with caution, taking into account all of the known technique, hazards and limitations so as not to be fooled by the apparent simplicity of radiography. It is often possible to have a good defect-free radiograph and an associated defective component.

REFERENCES

1. Course Handout and notes from "Special Course in Welding Inspection", U. S. Army Ordnance Corps. - Watertown Arsenal, Watertown, 72, Mass.
2. Radiography in Modern Industry, second edition Eastman Kodak Co., X-ray Division - Rochester 4, New York.
3. Walter F. Wulf, Materials Laboratory, U. S. Army Tank Automotive Command, Warren, Michigan - Technical Report No. 8910 (Phase 11) - Development of Radiographic Procedures and Standards for Partial Penetration Weld Joints on Heavy Aluminum and Steel Plate.

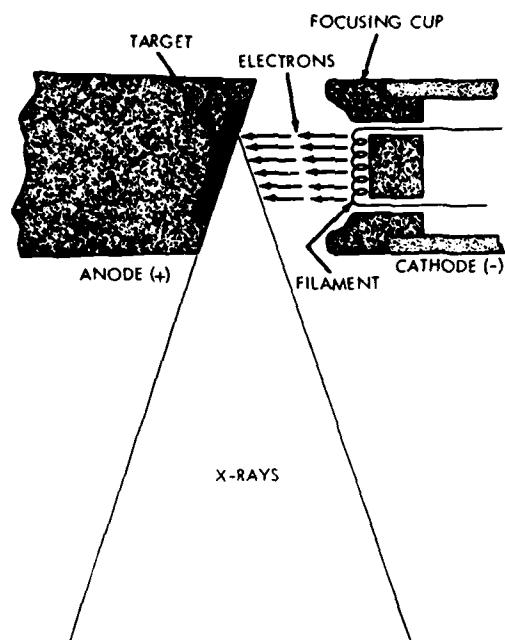


Figure 1. Schematic diagram of an X-ray Tube

Maximum Voltage (K.V.P.)	Screen	Applications and Approximate Part Thickness Limits
50	None	Extremely thin metal sections, wood, plastic, biological specimens, etc.
100	None or lead foil	Thin metal, thin metal, biological specimens, etc.
150	Fluorescent	Thin metal, biological specimens, etc.
200	Lead foil	Thin metal, biological specimens, etc.
250	Fluorescent	Thin metal, biological specimens, etc.
400	Lead foil	Thin metal, biological specimens, etc.
500	Fluorescent	Thin metal, biological specimens, etc.
1000	Lead foil	Thin metal, biological specimens, etc.
1500	Fluorescent	Thin metal, biological specimens, etc.
2000	Lead foil	Thin metal, biological specimens, etc.
24 Mev	Fluorescent	Thin metal, biological specimens, etc.

Figure 3. Typical X-ray Machines and Their Applications

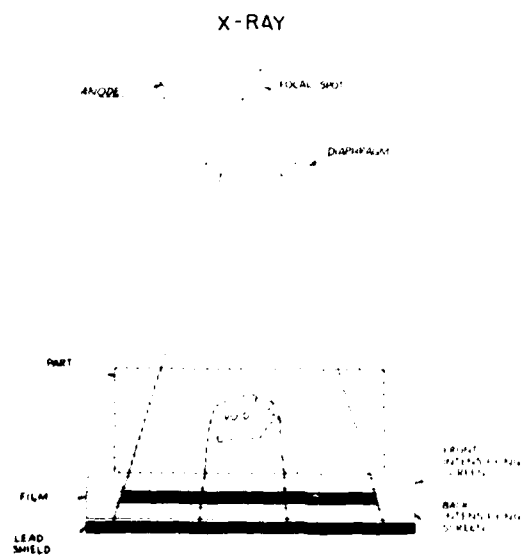


Figure 2. X-ray Tube Schematic

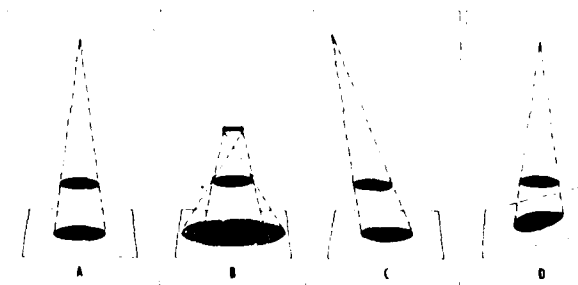


Figure 4. General Geometric Principles of Shadow Formation

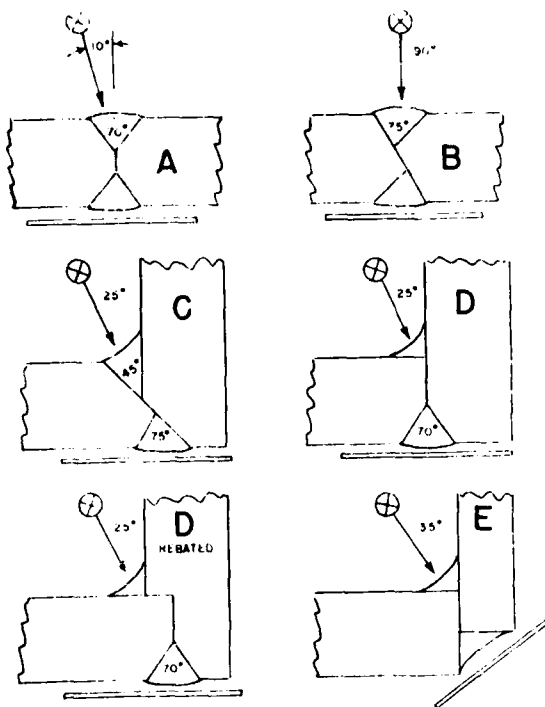


Figure 5. Recommended Radiographic Procedures for Partial Penetration Joint Designs

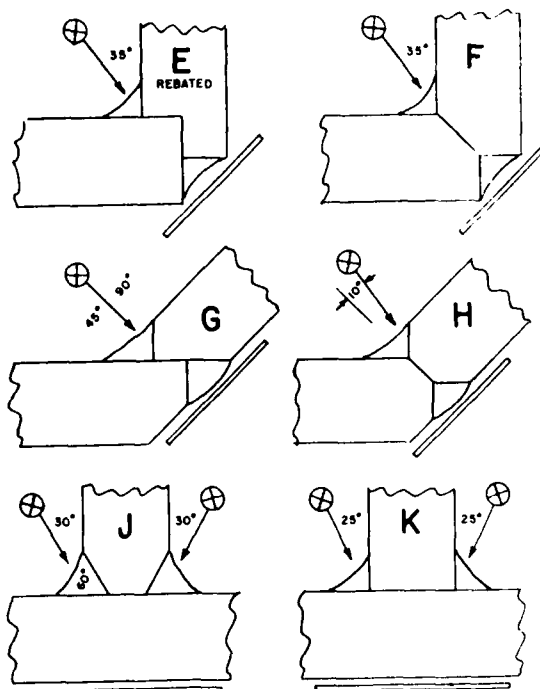


Figure 6. Recommended Radiographic Procedures for Partial Penetration Joint Designs



Figure 7. Correct and Incorrect Radiographic Procedure for Joint Design (C)

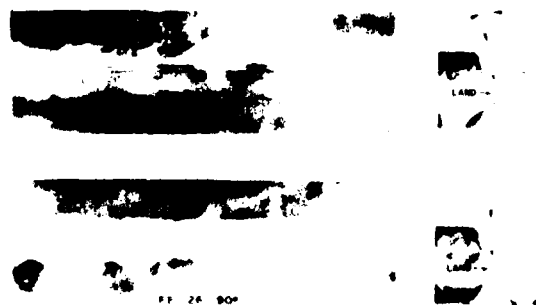


Figure 8. Correct and Incorrect Radiographic Procedure for Joint Design (A)

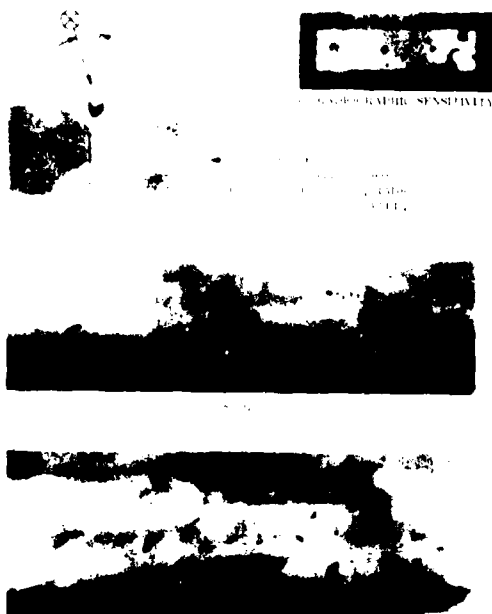


Figure 9. Reference Standards for Gas Cavities - Aluminum Welds

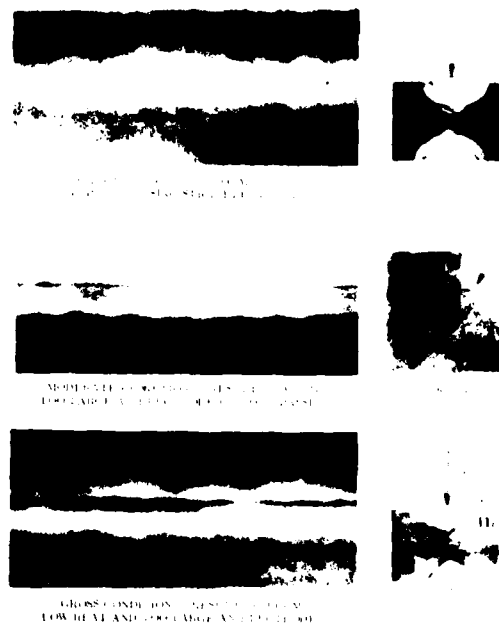


Figure 11. Varying Degrees of Incomplete Penetration in Steel Welds, Correlated with Weld Cross Sections

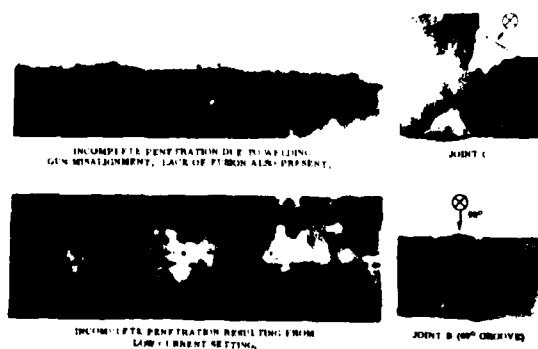


Figure 10. Examples of Incomplete Penetration Correlated with Weld Cross Sections - Aluminum Welds

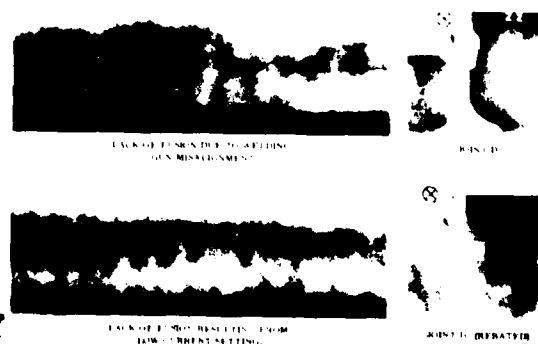


Figure 12. Examples of Lack of Fusion Correlated with Weld Cross Sections - Aluminum Welds

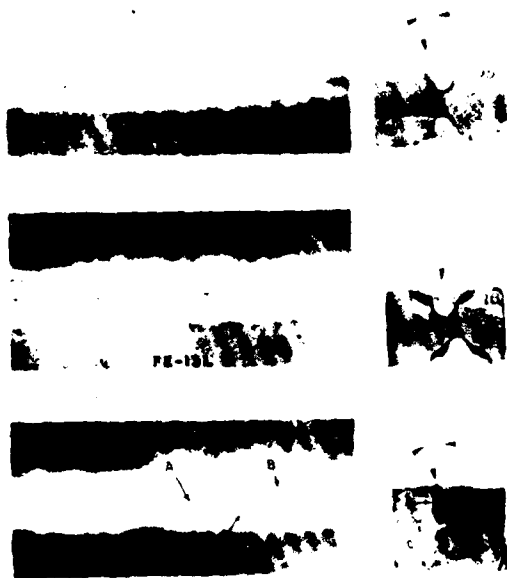


Figure 13. Lack of Fusion in Steel Welds, Correlated with Weld Cross Sections

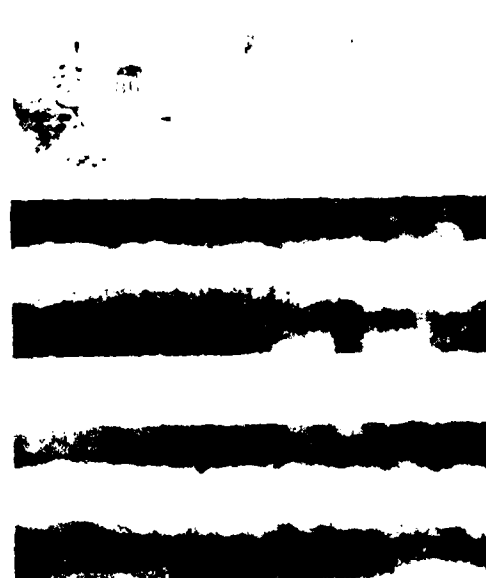


Figure 15. Reference Standards for Fine Scattered Porosity in Steel Welds

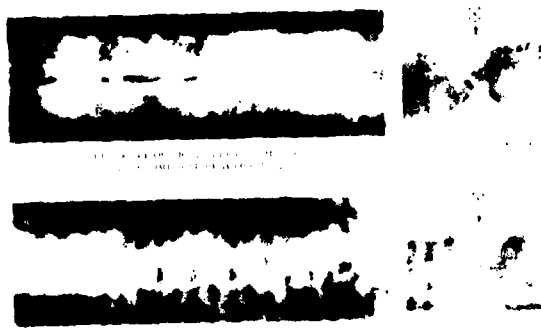


Figure 14. Examples of Ungraded Conditions Correlated with Weld Cross Sections - Aluminum Welds

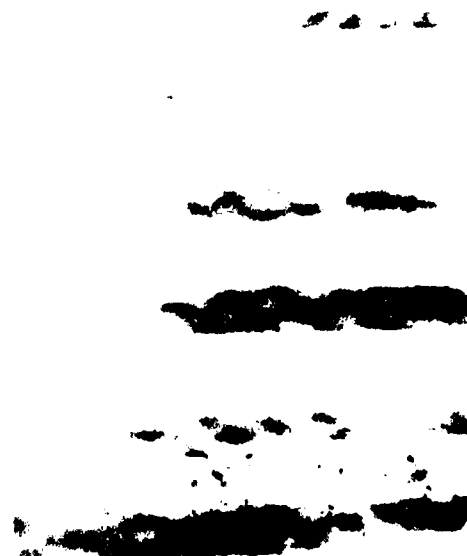


Figure 16. Reference Standards for Coarse Scattered Porosity in Steel Welds

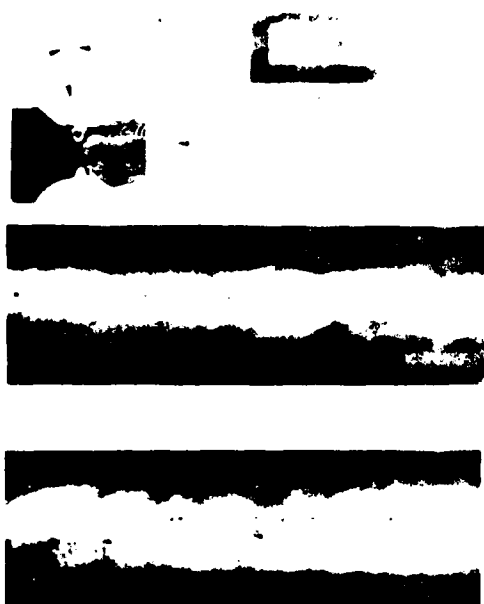


Figure 17. Reference Standards for Linear Porosity in Steel Welds

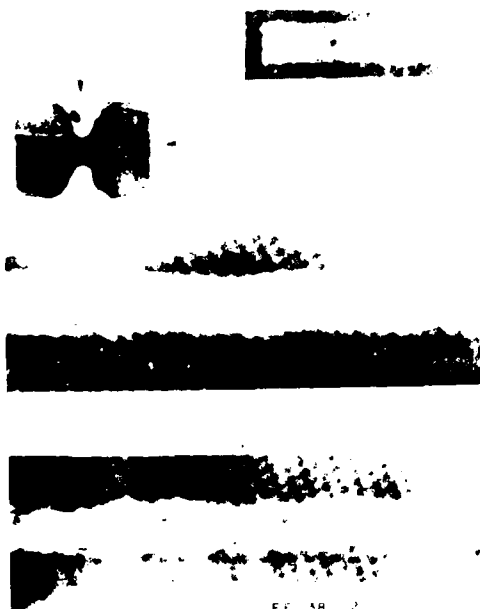


Figure 19. Reference Standards for Scattered Slag Inclusions in Steel Welds

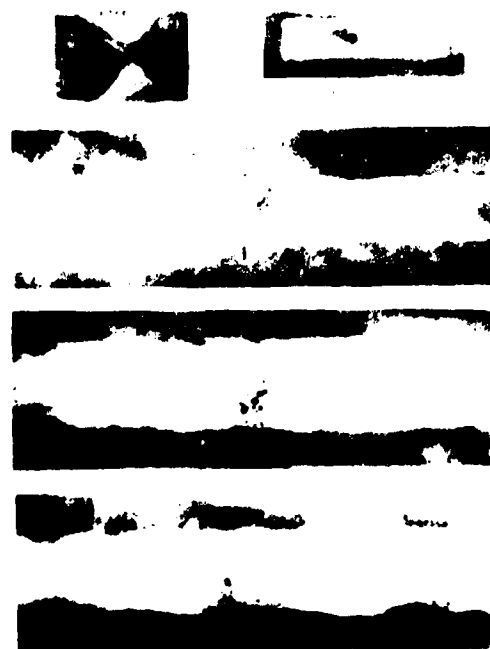


Figure 18. Reference Standards for Clustered Porosity in Steel Welds

WELD INSPECTION WITH SHEAR HORIZONTAL ACOUSTIC WAVES GENERATED BY EMATS

C. M. Fortunko
Albuquerque Development Laboratory-Science Center
Rockwell International
Albuquerque, New Mexico 87106

and
W. E. Lawrence
Science Center
Rockwell International
Thousand Oaks, California 91360

ABSTRACT

The potential advantages of using electromagnetic acoustic transducers (EMATs) for nondestructive evaluation of metal parts have been known for some time. Recently a generically new EMAT has been perfected which can generate and receive horizontally polarized shear (SH) wave angle beams. SH waves offer considerable advantages over SV waves for inspecting metal parts of complex shape: 1) they reflect specularly from planes containing the direction of particle displacement, 2) they can be generated in any direction lying in the sagittal plane with equal efficiency, and 3) SH wave transducers inherently discriminate against Rayleigh, L and SV waves. These advantages make SH waves particularly useful for weldment inspection.

A brassboard system was assembled for locating natural and simulated flaws in thick MIG welds, and a new technology for placing controllable defects in weld deposits was developed. It was then shown that the SH-wave inspection system was capable of producing an accurate map of the controllable defects introduced into the weld deposit. The ultrasonic map compared well with the notes taken by the welder and contained considerably more detail than the radiographic map. The inspection was performed at 1.7 MHz with the SH wave beam axis inclined at approximately 38° with respect to surface normal. Tungsten and alumina rod inclusions as small as 3/32 inch in diameter with localized within the weld deposit with signal-to-noise ratios of better than 10 dB and the inspection was performed on an "as-welded" sample without surfaces preparation through surface grinding or polishing.

INTRODUCTION

Bulk SH waves appear to be better suited than SV waves for ultrasonic inspection of metal parts of complex shape and microstructure. Unless the acoustic beam angle is judiciously selected for a particular application, at each reflection, an SV wave can be split up into shear (SV and SH) longitudinal (L) and surface wave reflections travelling in different directions at different velocities. However, in contrast to SV waves, SH waves are always reflected specularly and the SH wave transducers discriminate against all other polarizations which may be generated within the metal part through mode conversion. These properties of SH waves result in considerably cleaner ultrasonic displays which are usually easier to interpret than ultrasonic displays generated with SV waves.

For weldment inspection the use of SH waves may offer additional advantages: 1.) The horizontal particle polarization may be more suitable for inspecting weld metal deposits which exhibit complicated microstructures and are very anisotropic, 2.) SH wave beam angles may be frequency scanned, allowing a considerably greater flexibility in positioning transducers and selecting beam angles with respect to surface normal, and 3.) since SH wave transducers are non-contact EMATs, inspections at elevated temperatures may be feasible.

In this paper we describe the experimental results obtained with a prototype SH wave system on realistic MIG weld deposit containing many controllable weld defects. We also describe a new technique for introducing controllable weld defects into weld deposits by placing tungsten and alumina rods in the weld puddle.

FABRICATION OF CONTROLLABLE DEFECTS IN MIG WELD DEPOSITS

An in-house capability was developed at the Science Center for producing weld defects in a controllable and reproducible manner. In a production environment this was accomplished by assembling a high quality welding station which could be interfaced with SH wave ultrasonic systems. The system, shown in Poster 1, employs the Gas Metal Arc Welding (GMAW) method using Flux Cord Arc Welding type filler material (FCAW). It is fully motorized and includes an accurate closed loop control system for weld head travel. The welding supply is a Tektron LSC.

Since literature studies and discussions with experienced welding engineers did not reveal a reliable method for generating defects of controllable size, orientation and type (inclusions, voids etc.), it was decided to place tungsten and alumina inclusions, as well as SiC chips from a grinding wheel, at various locations throughout the weld deposit. The method of placement is also illustrated in

Poster 1 which shows a number of Al_2O_3 inclusions placed along the centerline of the weld deposit directly above the root pass. The tungsten and alumina inclusions were 3/32 and 1/4 inch in diameter respectively and interpass grinding was employed to avoid inadvertent slag inclusions. A careful record of the defect types, new and locations was maintained throughout the building up of the weld deposit. A sample of the welder's notes is also included in Poster 1.

The weld preparation consisted of a simple V-groove butt-weld in a 2-1/4% Cr 1% Mo steel, 1" plate stock ordered and certified to meet ASME Boiler and Pressure Vessel Code (B&PVC) SA 387 Grade 22, Class 2 requirements. The 2-1/4% Cr-1% Mo steel base metal was selected primarily because it was found to exhibit particularly high EMAT transduction efficiencies due to magnetostrictive enhancement and because it is in wide commercial use. The completed weld is shown on the left in Poster 2. Also shown in Poster 2 is a weld sample of the same type but 2 1/4 inches in thickness which as obtained from the Energy Systems Group of Rockwell International. This weld did not contain controllable weld defects in the weld deposit, but did contain a number of side holes drilled for the purpose of for transducer calibration.

The method for generating defects of controllable type, size and orientation proved to be very successful. It was found that the tungsten defects held their shape and only showed slight melting of the skin as the molten metal on arc passed over them. On the other hand, the alumina rod showed some melting and edge rounding when the weld puddle was carefully positioned so that its edge cast against the rod. When welding directly over the rod, the material bubbled severely, actually deflecting the arc to one side. Finally the SiC melted into blobs and spheres, but remained essentially in place in the puddle.

In addition to the alumina and tungsten inclusions, a number of simple calibration standards were also prepared by drilling side holes ranging from 3/32 to 5/16 inch in diameter in the 1 inch thick base metal.

DETECTION OF CONTROLLABLE DEFECTS AND SIDE DRILLED HOLES IN THICK MIG WELDS

A brassboard SH wave system was assembled specifically for localizing the naturally occurring and simulated defects described in the preceding section.

The system used a pair of the periodic magnet transducers and a tuned transmitter-receiver electronics package capable of operating either in "pitch-catch" or "pulse-echo" and the transducers were provided with special metal "shutters", which enabled them to be operated on plates of less than 2 inches in thickness. The frequency of operation of the system could be adjusted in the range 1-1.8 MHz; corresponding to a range of acoustic beam entry angles of 90°-30° with respect to surface normal. The electronics package did not include a detector stage. Instead, the received ultra-

sonic signals were displayed directly on a CRT after preamplification. In addition, a digital signal averager was included in the system for added sensitivity. The digital signal averager was used in some of the experiments resulting in a 30 dB signal-to-noise improvement by averaging 1000 frames of data. However, it was unable to follow the RF displays in real-time and could not be transported outside the laboratory. The transducer used a tandem periodic array of Sm-Co permanent magnets with a period of 0.120 inch. The overall usable length of the array was approximately 1.5 inches and the aperture width was approximately .5 inch. a 0.005 inch thick copper foil "shutter" was used in conjunction with the transducer to adjust the acoustic length by shielding an eddy current from the transducer electrode.

Using the EMAT system described above a careful study was made of the weld sample containing the controllable defects. The results of the ultrasonic scan of the weld metal deposit, radiographic data, and the welder's notes were compared and are presented in Poster 3. Ultrasonic data was taken from both directions in order to establish the position of a particular defect within the weld deposit by triangulation and the transducer was operated at approximately 1.7 MHz corresponding to a beam entry angle of approximately 38.5° with respect to surface normal. The frequency of 1.7 MHz and angle of 38.5° were used since it was found that inspection at other beam angles resulted in less sensitivity to flaws or more spurious signals. In particular inspection at 1.5 MHz (45°) was very difficult because of strong masking of the flaw reflections by direct reflections from the 45° weld preparation.

The mapping of the weld deposit was accomplished by moving the transducer along the weld in 1/2 inch increments over a total distance of 12 inches. Concurrently, a number of calibration measurements were also made using the empty side-drilled holes. A comparison of the ultrasonic map with the x-ray data and welder's notes showed that all alumina and tungsten inclusions were positively located with the SH wave system, and their positions corresponded well to x-ray data and welder's notes. In fact, some of the alumina inclusions were not registered in the radiograph because of their low density, but they were easily detected with the SH wave system. Also, detected and localized were the lack of fusion areas generated by adjusting the welding torch. However, defect characterization based on the acoustic data was not attempted although typical signals obtained from the 3/32 and 1/4 inch diameter inclusions had signal-to-noise ratios of better than 10 dB.

The results of the back reflection calibration measurements have been compared to theory of SH wave scattering from cylindrical voids. The results and the experimental arrangement are shown in Poster 4 in which a corner reflection of the signal was used to normalize the back reflected signals from the side drilled holes and a 3/32 inch diameter tungsten inclusion. It is interesting to note that the measured back-reflection from the 3/32 tungsten inclusion in the weld deposit exhibits the same reflection coefficient as that from an

empty cylindrical hole of the same diameter; contrary to the theory. This result may indicate that the tungsten inclusion was not in intimate contact with the weld deposit - possibly due to the presence of "soft" impurities on the surface of the tungsten generated by the welding process.

SUMMARY

An ultrasonic inspection technique using SH waves and a welding procedure for placing controllable weld defects in weld deposits were demonstrated. The results clearly show that SH waves can offer potential advantages for weld inspection. SH waves generate fewer spurious signals and can be frequency scanned. In addition, EMATs offer the advantage of being able to operate at elevated temperatures. However, the advantages of SH systems for weldment inspection must be weighed against the inherently low transduction efficiencies of electromagnetic transducers, which may vary from material to material - depending on composition, heat treatment, etc. Nevertheless, it is believed that new SH wave applications in the area of weldment inspection are in prospect.

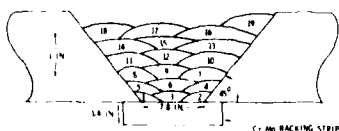
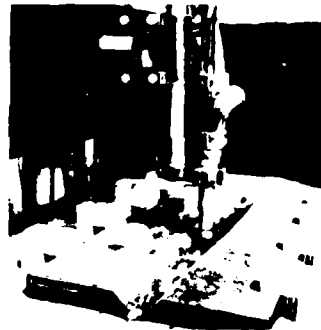


Fig. 13 Pass sequence (left end view).

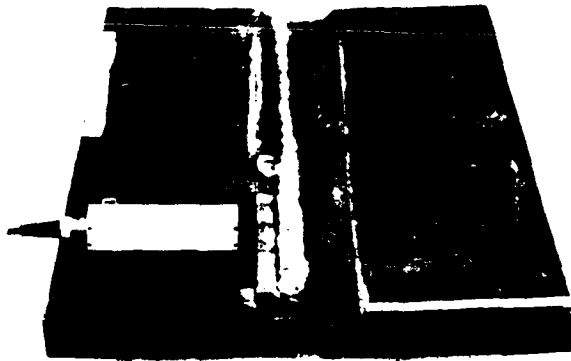
TABLE I
WELD FLAWS

Pass No.	Location (inches)	Type
1		Lack of fusion
2-24		Porosity
4-7, 12-13		Lack of fusion
2-24		Porosity
4-7		3/4 in. Al ₂ O ₃
12		3/4 in. W
13		5/8 in. W
14		3/4 in. Al ₂ O ₃
15		Al ₂ O ₃ slag
16		3/4 in. W
17		3/4 in. W
18		3/4 in. W
19		3/4 in. W

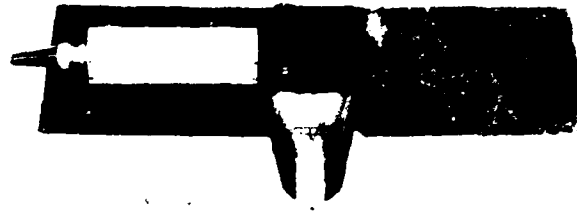
WELD SAMPLES WERE PREPARED AT SCIENCE CENTER USING PRODUCTION WELDING EQUIPMENT.

1/4 INCH DIAMETER ALUMINA AND 3/32 TUNGSTEN RODS WERE PLACED IN WELD PUDDLE AT SELECTED LOCATION.

LACK OF FUSION DEFECTS WERE GENERATED BY STOPPING THE TORCH.

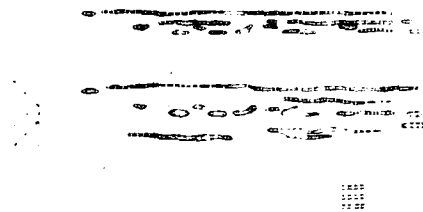
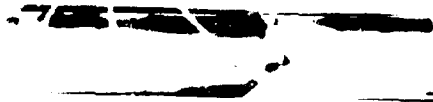


WELD SAMPLE PREPARED AT SCIENCE CENTER
WITH ALUMINA AND TUNGSTEN INCLUSIONS.



WELD SAMPLE PREPARED AT ATOMIC INTERNATIONAL
DIVISION, ROCKWELL INTERNATIONAL.

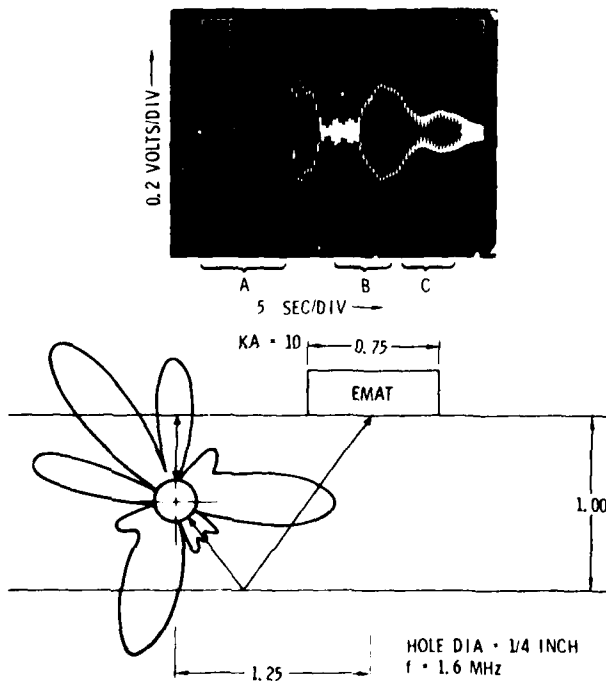
Poster 2



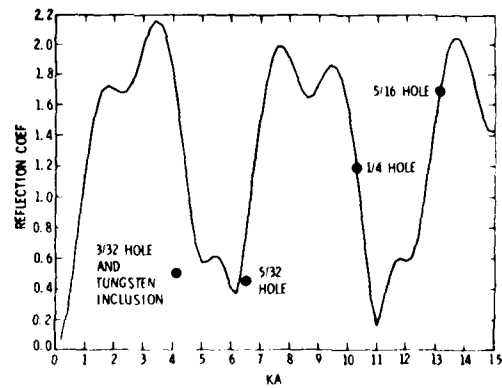
RESULTS OF WELD INSPECTION

- (A) RADIOGRAPH
(B) ULTRASONIC USING SH WAVES AT 1.6 MHz AND INCLINED AT 40° WITH RESPECT TO SURFACE NORMAL

Poster 3



- A. RECEIVER RECOVERY TIME
B. DIRECT BACKSCATTER FROM 1/4 HOLE
C. SIGNAL RERADIATED BY HOLE AFTER REFLECTION FROM TOP SURFACE



Comparison of experimental SH wave back scattering
from cylindrical voids with theory.

RESULTS OF CALIBRATION MEASUREMENTS USING ROUND HOLES

DEMONSTRATION OF THE ALN 4000 MULTI PURPOSE PROCESSING SYSTEM FOR
ULTRASONIC AND EDDY CURRENT QUANTITATIVE NDE*

A. N. Mucciardi
Adaptronics, Inc.
McLean, VA 22102

ABSTRACT

The ALN 4000 Multi Purpose Processing System (MPPS) is a significant new advancement in data acquisition, real time analysis, and control technology. This programmable instrument is ideally suited to high-speed signal processing using the most advanced algorithms, including Adaptive Learning Networks.

INTRODUCTION

The interactive capability of the ALN 4000 greatly reduces the need for operator training. The ALN 4000 MPPS consists of two compact, portable units, the ALN 4040 Controller/Processor and the ALN 4080 Storage/Display Unit.

New developments in semiconductors and the advent of miniature peripherals made the ALN 4000 concept feasible. The foundation of the instrument is a powerful dual microcomputer system with several peripherals and dedicated Nondestructive Evaluation (NDE) software. Highly specialized circuit boards perform NDE functions such as detection, location, and sizing of material flaws.

The ALN 4000 is designed to perform these NDE functions in as simple a manner as possible and with a minimum of equipment. In addition to the ALN 4000, only a transducer, a pulse-amplifier, and a receiver are necessary. When applicable, a positioning mechanism (scanner) for the transducer can be included in the NDE system.

SYSTEM COMPONENTS

The ALN 4000 MPPS is packaged in two cases. As shown in Fig. 1, the front panel of one of the

cases, the 4080 Storage/Display Unit, has all the switches and status lights, the integral mini-printer and two miniature tape cassettes. The panel on the 4040 Controller/Processor Unit is blank except for a power light. There are only three switches, POWER, RESET, and PAUSE; all other functions are controlled via the terminal. There are three status lights to indicate the current operation: RUN, STANDBY, DIAGNOSTICS.

The peripherals consist of a hand-held LCD terminal serving as the control unit and keyboard, and integral miniprinter for hard-copy display results, and a dual mini-cassette system for mass storage. Alternatively, an off-line typewriter terminal may be used for more printing capability as well as for providing a modem to transfer data to another computer system for Adaptive Learning Network (ALN) training or for archival data storage. There is digital-to-analog capability for oscilloscope display of waveforms and analog-to-digital capability for digitizing RF signals from the transducer. A rectified amplitude oscilloscope display is also provided in some models.

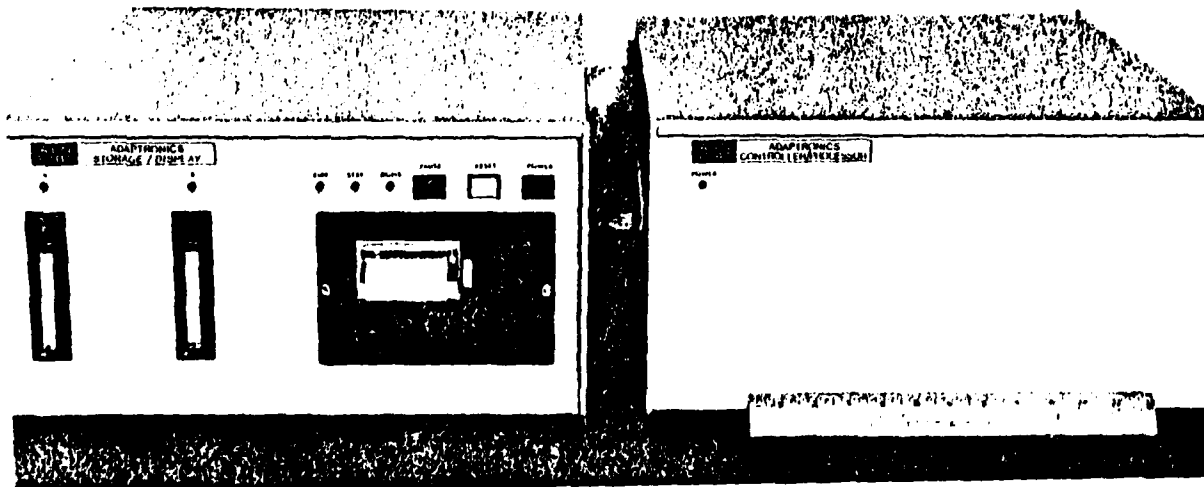


Fig. 1 ALN 4000 multi-purpose processing system.

*This work has been supported in part by the Electric Power Research Institute under Contract RP1125-1.

The MPPS contains, where the application requires it, the hardware and software to control a scanning device. This permits automatic inspection and increases the speed of the inspection as well as decreases the number of operations performed by the operator.

HARDWARE/SOFTWARE

Flexibility of both the system hardware and software has been achieved. The design reflects a desire to minimize the effort required to modify the instrument for different applications. The data acquisition system for ultrasonic applications can be programmed for different sampling rates (up to 20 MHz). To convert the MPPS for use with eddy current applications, the A/D board and associated software are simply replaced. Software changes are made as easily as changing a tape cassette. Data for specific applications can be entered via the keyboard, or prepared at an earlier date and stored on cassette. The software modules that are applicable in any NDE system are

permanently resident in the ALN 4000. These will include supervisory programs, self-test diagnostics, I/O drivers, DMA routines, and signal processing routines. Those routines and data that are application-specific are stored on cassettes and include the transducer scanning protocols, ALN structure and coefficients, and routines to drive and control the scanning device.

OPERATIONAL MODES

Three modes of operation are possible using the ALN 4000.

One is a data collection and digitization mode to store sufficient data to provide a data base necessary for ALN network training, for example. If a scanner is present, it may be controlled by the ALN 4000 in this mode to automate the collection procedure.

The second mode is on-line analysis to be performed at the inspection site. This includes control of the scanning device, signal conversion, and ALN processing to provide NDE diagnosis such as crack detection and sizing on-line and in real-time.

A third mode of operation is off-line analysis to provide an inspector with the capability of selecting waveforms from the mass storage device and to perform signal processing operations as desired. The use of the off-line terminal in this mode will provide printing capability. The modem permits data transfer to another computer. Use of an oscilloscope will provide a display of the waveforms.

ALN 4000 MPPS SIGNAL PROCESSING SOFTWARE

A number of signal processing routines exist in pre-programmed (PROM) form and are supplied with the ALN 4000 MPPS as part of a signal processing library. Each routine has been coded to take full advantage of the high-speed arithmetic processing circuits. The user can incorporate these routines into new programs in a manner similar to the way scientific package sub routines can be incorporated into FORTRAN programs.

- Fast Fourier Transform (FFT):

Complex FFT of any power-of-two length waveform up to 256 points; (the current limit can be extended easily to a larger number of points); routine returns the complex coefficients; arithmetic is performed in 32-bit fixed point form; the routine also incorporates an automatic scaling feature to prevent resolution loss for very low or high level signals.

- Signal Averaging (Temporal Averaging):

Summing of several waveforms while holding a transducer at a fixed position, the random noise components in the received data will cancel but the coherent signal transients will add.

- Beamforming (Spatial Averaging):

Averaging several waveforms recorded at different positions; each waveform is delayed before averaging so the signals add coherently; beamforming reduces coherent noise sources.

- Bandpass Filtering:

Digitally filtering signal components outside of a desired bandwidth; the filter pass band characteristics can be changed easily to accommodate any bandwidth of interest.

- Match Filtering/Convolution:

Convolving a known response with a noise waveform to detect a signal of interest.

- Convolution/Deconvolution:

Adding/eliminating a specific signal to/from a noisy waveform.

- Correlation

Auto-and-cross-correlation of waveforms.

PORTABLE INSTRUMENT FOR DETECTION OF SURFACE
FLAWS USING EMATs

C. F. Vasile, R. B. Houston and E. Pongracz-Bartha
Rockwell International Science Center
1049 Camino Dos Rios
Thousand Oaks, California 91360

R. E. Lee
Albuquerque Development Laboratory
Rockwell International Science Center
2340 Alamo, SE
Albuquerque, New Mexico 87106

ABSTRACT

The work reported here is the development of a first prototype portable ultrasonic inspection instrument based on EMAT (electromagnetic acoustic transducer) technology. The goal was to demonstrate EMAT inspection capabilities for small-size flaws in metal parts and to build a self-contained NDE unit that had a high degree of signal processing on-board so that human interpretation was minimized. The unit also served as a test bed, so that a number of new concepts could be evaluated. This instrument is viewed as an important step in the development of future NDE equipment.

DESCRIPTION OF UNIT AND BASIC CAPABILITIES

The EMAT flaw detector instrument (see Fig. 1) is capable of launching and detecting ultrasonic energy in metal parts using transducers that are physically separate from the specimen under investigation.^{1,2} This operation eliminates the inconvenient and restrictive coupling medium (fluid) that is required by conventional piezoelectric ultrasonic instruments. The prototype is designed to inspect for surface flaws in both ferrous and nonferrous materials using a 1 MHz surface-acoustic-wave launched from a unidirectional EMAT transducer. This single transducer serves both as a generator and detector of straight crested surface waves. The unit is a radical departure from conventional equipment in that all information can be displayed in a digital format using the front panel digital LC (liquid crystal) display. Front panel ports are available if a display of reflected signal amplitude versus time (A-scan) is desired.

The instrument has two modes of operation:

Search Mode - Ultrasonic signals are introduced into the part and reflections monitored automatically. Reflected signals larger than a threshold that is operator-set sound an audio alarm. The distance between transducer and flaw is automatically displayed on the digital meter. Stray reflections are excluded by a range-gate circuit (set according to the size of part under inspection) so that natural part boundaries will not trigger the unit. A number of closely spaced flaws can be separated (resolved) by a "signal select" circuit that allows monitoring of the first, second (etc.) reflections occurring in a given time interval.

Inspection Mode - The instrument measures the magnitude of the signal reflected from the flaw and compares it to a preset signal level. This

preset level is derived from a "standard" used for calibration. The LC meter displays the ratio (in dB) of the signal from the flaw under investigation compared to the standard. Positive readings indicate flaws reflecting more signal than the standard and negative readings less signal than the standard.

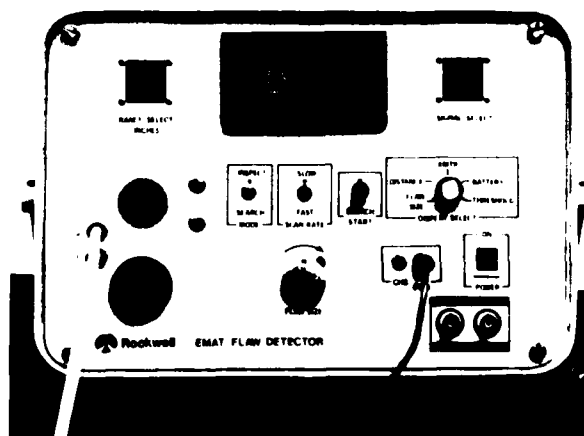


Fig. 1. Photograph of EMAT Flaw Detector Instrument.

The unit is self-testing in that the transmitter signal can be monitored and displayed on the LC meter. Also, the battery (or power supply) condition can be displayed. The threshold level (corresponding to the calibration standard) can be set from a 10-turn potentiometer and is displayable on the digital meter.

The instrument is designed to operate on an internal battery that will allow over 8 hours of continuous operation between recharging cycles. Repetition rates at which ultrasonic pulses are generated can be set at either 100 pulses/sec for fast inspection or

1 pulse/sec for increased battery life. The instrument battery can be fully recharged in about 8 hours through a front panel jack. Alternatively, where dc power is available, an external power port (12 volts at 0.6 amps) can be utilized to supply the required power to the instrument.

An rf output signal is available at the front panel, along with a synchronizing pulse for oscilloscope display of the detected flaw reflection. Signal levels of about 50 to 100 mv are achieved for flaws 0.010 inches deep and 0.25 inches wide on the surface of a ferrous metal (corresponding to a signal-to-noise ratio of better than 20 dB at the 1 MHz frequency of operation).

TRANSDUCER ELEMENT

EMAT transducers rely upon the forces produced in a metal part when eddy currents induced by an excitation coil interact with an applied static magnetic field from a permanent magnet or electromagnet to generate acoustic waves. The resultant surface traction forces, similar to the forces present in an electric motor, are the cross-products of the induced surface current density times magnet field strength. Due to the wide variety of coil and magnet configurations possible, EMATs are capable of producing numerous types of acoustic waves (surface, horizontal and vertical shear and longitudinal waves).

The particular EMAT transducer used here is composed of 2 printed circuit coils with periodicity of ~3.0 mm that are interlaced (using a two-sided PC board and plated-through holes for connection) so that when each coil is driven at 1 MHz and 90 degrees out of phase with respect to each other they produce a unidirectional sound beam about 1 inch wide. As a result, this EMAT is unidirectional with a front-to-back rejection ratio better than 30 dB.

The magnetic field is derived from a pair of adjacent samarium cobalt magnets 1" long by 1/2" wide that are oriented "N-S and S-N" and cover the entire back surface of the EMAT. A soft-iron keeper is used to close the flux path at the rear of the transducer so that the field produced is essentially uniform and normal magnetic fields in the coil region (Br ~4000 Gauss). There is a "scratch protection" layer (of a tough polymer material 5 mils thick) that covers the front of the coils. The entire transducer assembly occupies a volume of about 1-1/2" x 1-1/2" x 1-1/2" and can be easily maneuvered by hand.

As stated above, essentially straight crested surface waves are produced by this probe design. This can be used as an aid for determining the orientation of flaws. "Crack-like" flaws produce maximum reflection when the wave fronts of the incident surface acoustic wave are aligned parallel to the length of the flaw. Thus, by pointing the transducer at the flaw and scanning it about the flaw, a maximum return corresponds to parallel alignment with the flaw. If equal scattering is observed over a broad angular distribution, then a pit-like flaw is indicated. By knowledge of the scattering

properties of different flaws, one can use this instrument to perform flaw characterization.

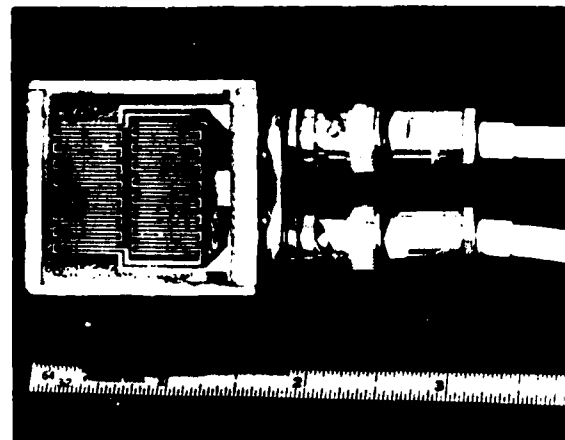


Fig. 2. Photograph of EMAT Transducer Coils for Unidirectional Ultrasonic Generation of Surface Waves.

ELECTRONICS SIGNAL PROCESSING CAPABILITIES

The electronics of the EMAT flaw detector can be subdivided into four functional blocks: (1) a high power transmitter, (2) a low noise receiver, (3) analog signal processing and (4) signal digitization, sampling, and display.

The transmitter is composed of a pulser and a dual 1 MHz bipolar transistor power amplifier circuit, used to drive a high current tone burst of 14-cycles duration, 60 amps peak-to-peak through the coils. The low impedance of the EMAT coil is matched to the transmitter using ferrite core step-up transformers and discrete reactive components.

The dual-channel receiver circuit employs low-noise FET transistors to achieve two purposes. First it amplifies the return signal and establishes the electronic noise figure of the unit. Second, it compensates the phase imbalance of the two signal channels. Since the same EMAT sensor is used to both generate and detect the ultrasonic signal, dual back-to-back diodes and reactive shunting elements are used to protect the receiver from the direct transmitted signal and filter out noise. Matching circuits at the receiver input raise the impedance level to optimize the signal-to-noise performance of the amplifier section. Four stages of amplification produce a gain of -80 dB and a recovery time of about 20 μ sec (from the conclusion of the transmitted signal). This allows flaws of .01" depth and 0.1" width to be easily detected at any range between 1.5" to 18" in front of the EMAT probe.

The analog signal processing performed in this unit is through use of a "correlation receiver", which acts as a nearly matched filter to the triangular-shaped rf waveforms characteristic of flaw reflections in EMAT systems. Figure 3 illustrates the block diagram. To perform the matched filter function and maximize the S/N ratio, the correlation receiver uses two channels: I (in-phase) and Q (quadrature-

phase). Each channel is driven by a separate EMAT coil and 80 dB preamplifier. The two-channel multiplier circuit multiplies the received flaw signals with a suitably delayed square wave burst supplied by the burst generator (at the time delay corresponding to the ultrasonic range element being inspected for flaws). The square wave burst B_1 is phase-shifted 90° from B_0 so that no matter what phase the return flaw signal has, there will be a multiplied output in one channel or the other. This approach essentially removes the phase sensitivity of the measurement technique. The product signals are integrated separately to produce a voltage level corresponding to the signal energy in each channel. The output of the integrator circuit is

$$\int_0^T B(t) S(t) dt,$$

which (except for a time inversion) is the convolution of the flaw signal with the reference which we desire to achieve. The output of the integrators is then sampled individually and stored as analog voltage levels. An additional operation is performed involving the square root of the sum of the square of the two integrator outputs. This operation is required to preserve the linearity of the detection process independent of phase. The output undergoes further signal processing to achieve the ratio which is displayed as an output on the LC display.

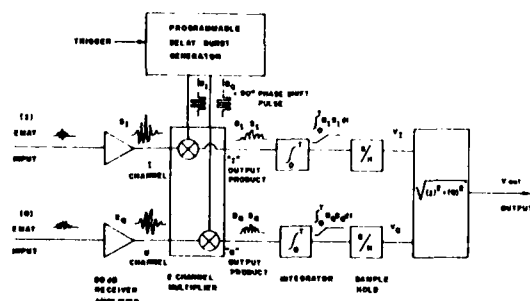


Fig. 3. Block Diagram of Correlation Receiver Portion of EMAT Flaw Detector.

The main advantage of the correlation receiver is the improvement in signal-to-noise performance offered (to within 0.7 dB of exact matched filtering). It offers substantial advantages over narrow band tuned filters for noise reduction, which spread the pulse width (reducing time resolution) and distort the phase linearity. The two-channel approach exhibits a 3 dB noise figure degradation compared to a single-channel approach; however, the two-channel system is phase-insensitive (as required by the detection process).

A full description of the digital circuits which allow display of the various signals and time delays is omitted since it is too detailed to be presented in this paper.

SUMMARY

A prototype portable EMAT instrument has been built which is capable of inspecting metal parts for minute surface flaws. Significant features of the EMAT unit are:

1. Flaw detection demonstrated by detecting EDM notches 0.01" deep by 0.25" wide over a transducer to flaw distance of 1-1/2" to 18" range on a polished steel plate. (15-20 dB S/N ratio).
2. Unidirectional ultrasonic transduction (30 dB front to back isolation).
3. Sonic alert signal when flaws above a certain threshold are found.
4. Automatic readout of distance between the probe and the flaw.
5. Digital output reading that is related to flaw scattering strength.
6. Ability to determine orientation of crack-like surface flaws.
7. Battery operation for field use.

Although the present EMAT transducer head is designed to inspect flat samples, curved or shaped heads will allow inspection of other geometries (pipes or bars). Also, volume (interior) flaws are easily detected using a modified EMAT transducer that emits shear or longitudinal waves into the part under inspection.

Non-contact ultrasonic transduction of this EMAT instrument offers the possibility of very rapid inspection of large area metal parts. This type of equipment is expected to advance the state-of-the-art in NDT inspection over the next few years.

REFERENCES

1. R. B. Thompson "Electromagnetic, Non-contact Transducer", 1973 Ultrasonics Symposium Proceedings, p395 (New York IEEE, 1973).
2. R. B. Thompson "Electromagnetic Generation of Rayleigh and Lamb Waves in Ferromagnetic Materials", 1975 Ultrasonics Symposium Proceedings, p633 (New York IEEE, 1975).
3. R. B. Thompson "Non-contact Transducers", 1977 Ultrasonic Symposium Proceedings, p74 (New York IEEE, 1977).

CODED APERTURE IMAGING IN NDE*

T. M. Cannon and E. E. Fenimore
University of California
Los Alamos Scientific Laboratory
Los Alamos, New Mexico 87545

ABSTRACT

It is sometimes the case in nondestructive evaluation that the position and intensity of a faint radioactive source must be determined. A simple pinhole camera may suffice in many instances, however its small collection efficiency may result in unreasonable exposure times. To correct for the low collection efficiency, a multiple-pinhole (coded) aperture can be substituted for the single pinhole. The result is that many more photons are collected by the camera, however the resulting picture is scrambled beyond recognition and must be somehow decoded. Various coded apertures have been used in the past, including Fresnel zone plates and random arrays.

Recent work at Los Alamos has produced a state-of-the-art advance in coded aperture imaging. The sensitivity of the coded aperture system can be greatly increased by the use of a newly developed uniformly redundant array (URA) as the camera aperture. When coupled with recent advances in computer decoding methods, the URA coded aperture camera can produce images that are totally free of the artifacts that hinder other approaches.

*Work performed under the auspices of the U. S. Department of Energy, Contract No. W7405-ENG-36.

ACOUSTIC EMISSION MONITORING OF IN-FLIGHT CRACK GROWTH
IN AIR CRAFT STRUCTURES

P.H. Hutton and J.R. Skorpik
Battelle Northwest
Richland, Washington 99352

ABSTRACT

Purpose of the program is to evaluate acoustic emission (AE) for in-flight detection of fatigue crack growth in aircraft structure. A special AE system was developed and installed on a RAAF Macchi jet trainer. It has been effectively measuring AE from a fatigue crack since August, 1978. Work is continuing to investigate correlation of AE data with crack growth.

PROGRAM REVIEW

This program was funded by the U.S. Defense Advanced Research Projects Agency for application to a Royal Australian Air Force aircraft. The purpose of the program is to evaluate the use of the acoustic emission (AE) technique to provide a definitive continuous monitor of fatigue crack growth in a critical aircraft structural member.

The program started in September, 1977, with Phase I consisting of defining technical and procedural details and developing and fabricating an AE monitor system. A unique AE monitoring system was fabricated and laboratory tested. (Fig. 1, 2) It utilizes a source isolation feature to distinguish AE signals originating from an identified area of interest. Two parameters of AE information are recorded on one solid state digital memory for later retrieval and analysis. (Fig. 3) Phase I was completed in April, 1978.

Phase 2 was concerned with installing and testing the AE monitoring system in an aircraft. Installation was made in RAAF Macchi 326 aircraft A7-021 during a major maintenance overhaul (Fig. 4, 5) The system is monitoring AE from fatigue cracks in a fastener hole in the tension member of the wing structure center section continuously during flight. (Fig. 6) Installation was completed in August, 1978, with four test flights to evaluate system performance and make necessary adjustments.

Battelle Northwest is providing follow-up support to the Australian Aeronautical Research Laboratory (ARL) on this program under a continuing Phase 3. This support includes assistance in data analysis and correction of any AE system problems. Evaluation of data from the first 25 flights shows that background noise and transient signals are not a problem, that the character of the data is rational and that the AE is influenced by the type of flying--i.e., low level, formation, aerobatics, etc. Sample results from individual flights are shown in Fig. 7, 8, 9. Evaluation of correlation between AE and crack growth will require at least a year of data gathering to assimilate sufficient crack growth data points.

Acknowledgements

The significant contributions made by J. F. Dawson, Battelle, to this program are gratefully acknowledged. Also, Australian ARL and RAAF personnel provided outstanding cooperation and assistance.

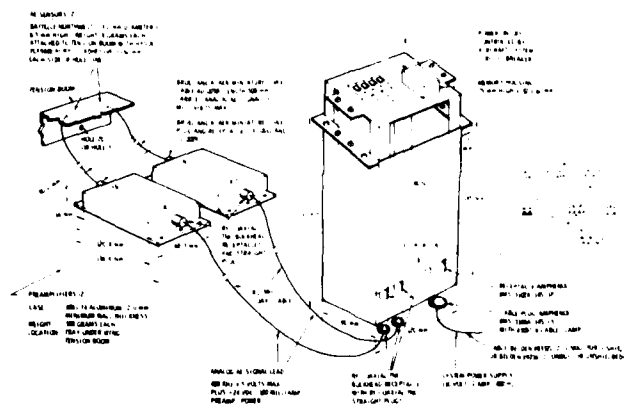


Figure 1. Specifications for Onboard Aircraft Ah System.

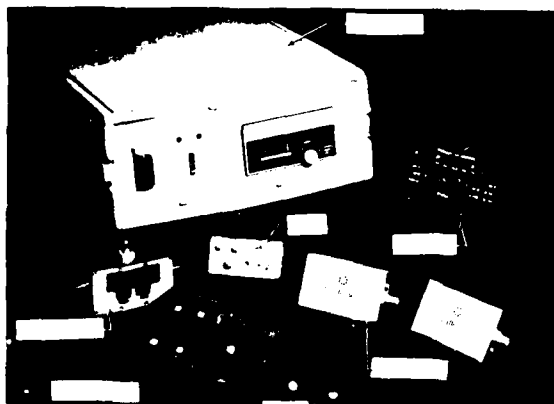


Figure 2. Complete Ah Aircraft System

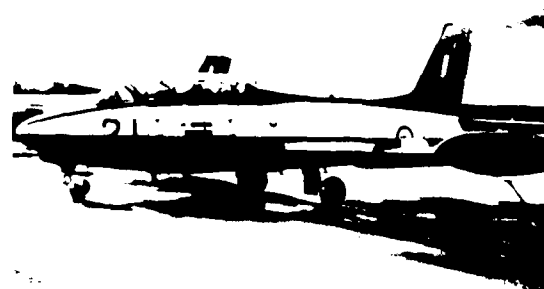


Figure 4. BAAF Machi Jet Two Place Jet Trainer

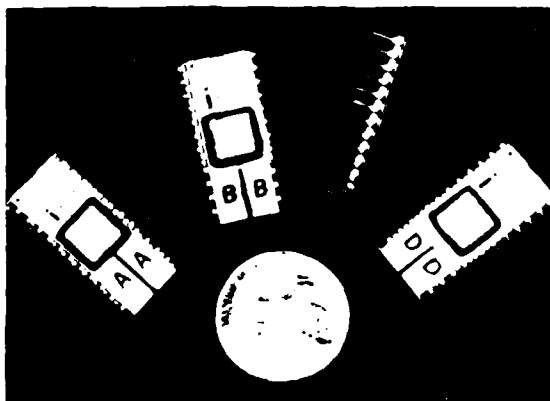


Figure 3. Solid State Digital Monitor



Figure 5. BAAF Machi Jet Two Place Jet Trainer

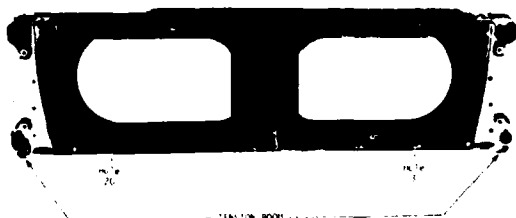


Figure 6. Center Wing Section -
Macchi 326 Aircraft

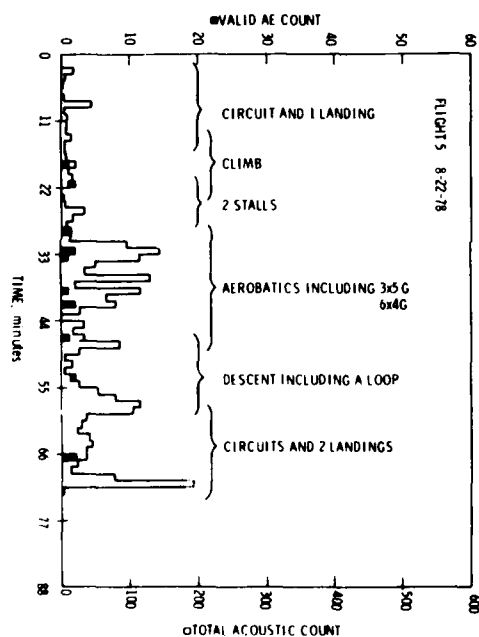


Figure 7. Sample Data - Flight 5

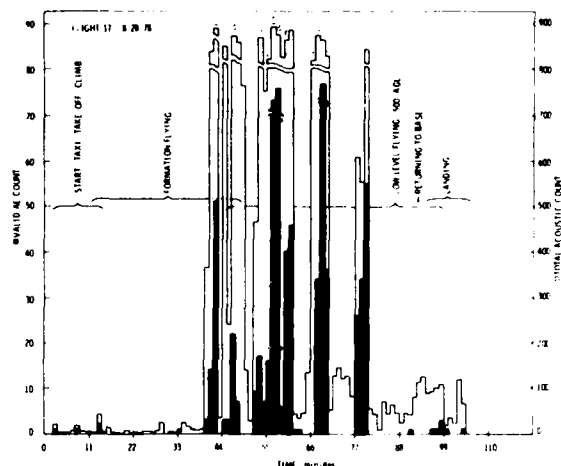


Figure 8. Sample Data - Flight 17

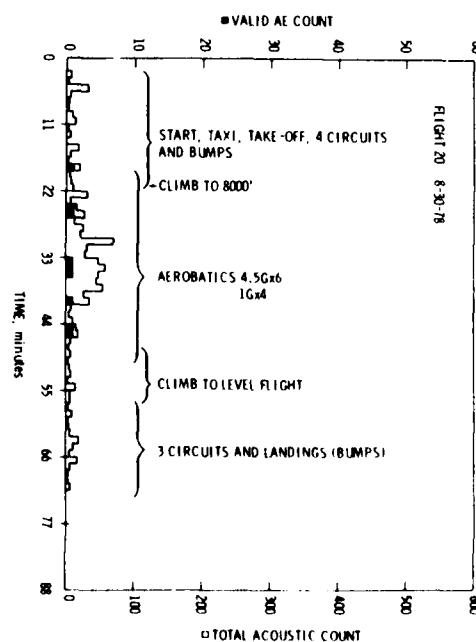


Figure 9. Sample Data - Flight 20

AN EMAT SYSTEM FOR DETECTING FLAWS IN STEAM GENERATOR TUBES*

R.B. Thompson, R.K. Elsley, W.E. Peterson, C.F. Vasile
Rockwell International Science Center
Thousand Oaks, California 91360

ABSTRACT

The detection of flaws in steam generator tubing is often made difficult by environmental considerations. The small diameter, 7/8 inch (2.2 cm), long, 70 feet (21.3m), tubes occur in large bundles with access only being possible from the inside of the end of each tube. Furthermore, inspection must be fully automatic when the steam generator is part of a nuclear power plant because of radiation exposure limits. Consequently, a couplant free probe which can be operated remotely at the end of an automatic probe puller is needed. This paper summarizes the development of an EMAT system for this application. The device uses periodic permanent magnet probes to excite the fundamental torsional mode traveling along the axis of the tube. Included is a discussion of data obtained during a recently completed feasibility study and a description of a prototype system presently under construction.

SUMMARY

Figure 1 presents the problem, which is made difficult by a radioactive environment, difficulty of access, and complexity of flaws.

The ultrasonic approach being developed is summarized in Fig. 2. Ultrasonic waves are excited by an EMAT probe, which has the advantage that no couplant is required. In particular, the periodic permanent magnet geometry is used to excite the fundamental torsional mode of the tube. This will provide new information which is complementary to that obtained by eddy currents, and which experiences less interference in the presence of support plates, dents and other geometrical complexities.

Figures 3 and 4 present data obtained during a previous feasibility study which demonstrated the unique capabilities of the EMAT approach. In Fig. 3, the use of EMATs to detect flaws in dented regions is demonstrated. In these measurements, made at 500 kHz, it was seen that a 2.5% dent produced a weak ultrasonic reflection, but that a partially through hole produced a much larger reflection. Detection of flaws in dented regions thus appears feasible.

Figure 4 shows that flaws in U-bends can be detected by probes placed outside of the U-bend region. In this experiment, the probes were placed at opposite ends of the U-bend for convenience. However, they could easily be placed at the same end. The multiple signals, produced at the ends of the short sample by mode conversion, would not be present in a real steam generator

tube of greater length. The flaw reflection, signal number 2, would then stand out cleanly. These results illustrate the important property that EMATs can detect flaws at a distance.

Figure 5 presents a block diagram, and a photograph, of the system under construction.¹ It will be seen that digital signal processing is used because of its flexibility in implementing matched filtering and other signal processing operations.

Figure 6 is a photograph of a steam generator mock-up in which the system will be evaluated.

Figure 7 presents a summary of the present status, and future direction, of the program.

REFERENCES

1. C.F. Vasile and R.B. Thompson, "Excitation of Horizontally Polarized Shear Elastic Waves by Electromagnetic Transducers with Periodic Permanent Magnets," J. Appl. Phys. 50 2583 (1979).
2. C.F. Vasile and R.B. Thompson, "Evaluation of Electromagnetic-Acoustic Concepts of Inspection of Steam Generator Tubing," EPRI report NP-519 (Electric Power Research Institute, Palo Alto, 1978).
3. B. Thompson, "Development of a Prototype EMAT System for Inspection of Steam Generator Tubing," in Nondestructive Evaluation Program, Progress in 1979, Report EPRI NP-1234-SR (Electric Power Research Institute, Palo Alto, 1979).

*This work was sponsored by the Electric Power Research Institute, Palo Alto, California, under EPRI agreement S101-1.

AUTOMATIC, HIGH SPEED INSPECTION REQUIRED

- RADIOACTIVE ENVIRONMENT
- HIGH NUMBER OF LONG TUBES
- LARGE ECONOMIC COSTS OF REACTOR DOWN TIME
- DIFFICULT ACCESS

FLAW INDICATIONS IN EDDY CURRENT INSPECTION CAN BE OBSCURED BY

- DENTS
- U-BENDS
- SUPPORT PLATES

Pressurized water reactor (PWR)

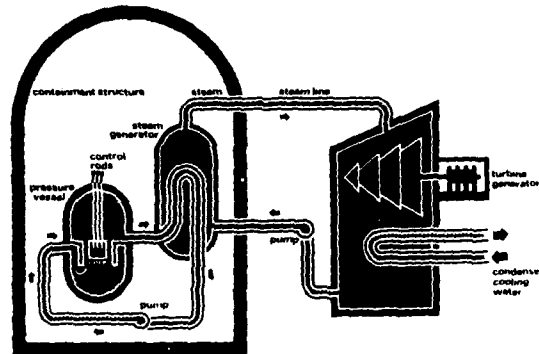
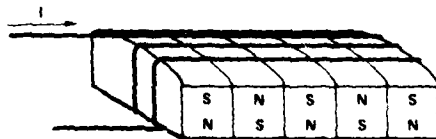


Fig. 1 Statement of problem.

ULTRASONIC WAVES EXCITED BY EMAT'S

- COUPLANT FREE PROBES HAVE OPERATIONAL CHARACTERISTICS COMPATIBLE WITH EXISTENT EDDY CURRENT PROBE PULLERS AND REMOTE CONTROLLERS.
- ULTRASONICS PROVIDES NEW INFORMATION
 - COMPLEMENTARY TO EDDY CURRENT INFORMATION
 - LESS OBSCURED BY SUPPORT PLATES DENTS, ETC.
- LOW LOSS AT 340 KHz ALLOWS WAVES TO RECOVER INFORMATION FROM U-BENDS WITHOUT PROBE ENTERING REGION.
- TRANSDUCERS DESIGNED TO EXCITE SINGLE, TORSIONAL MODE PROPAGATING ALONG TUBE AXIS.

BASIC EMAT ELEMENT



FUNDAMENTAL TORSIONAL MODE

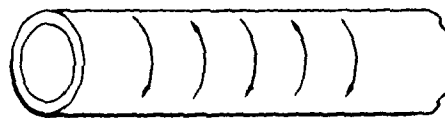


Fig. 2 Summary of EMAT solution.

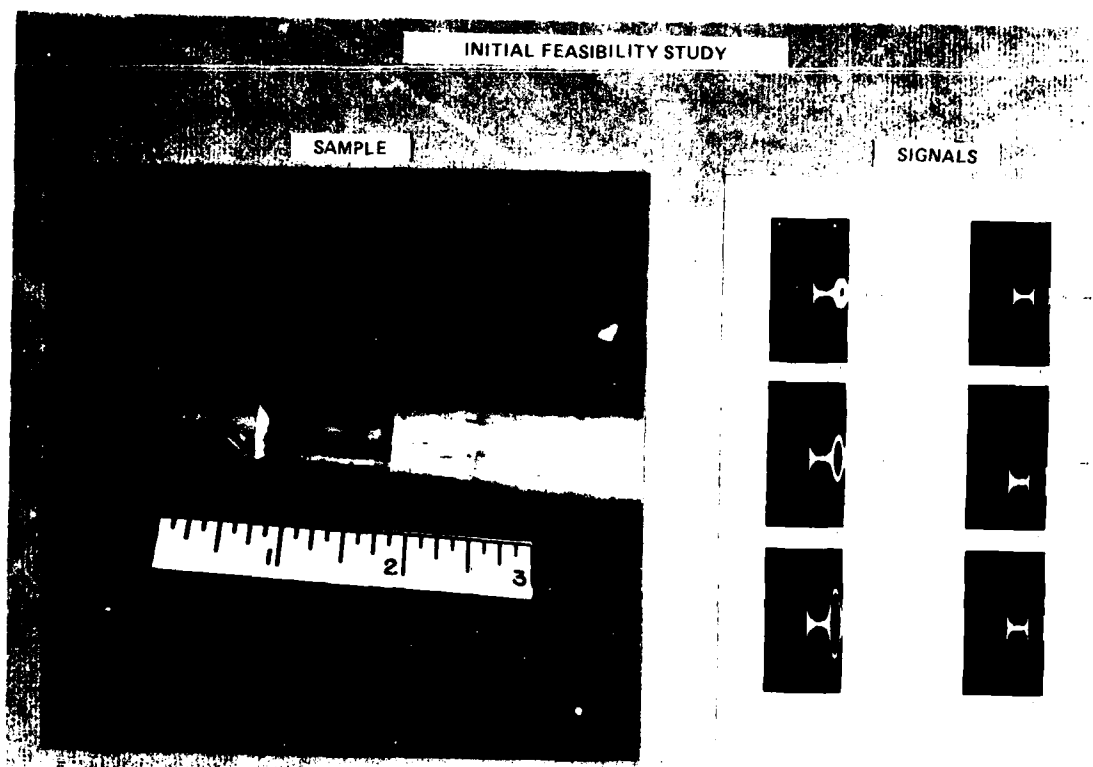


Fig. 3 Detection of flaws in dents.

AD-A094 826

ROCKWELL INTERNATIONAL THOUSAND OAKS CA SCIENCE CENTER F/G 11/2
PROCEEDINGS OF THE DARPA/AFML REVIEW OF PROGRESS IN QUANTITATIVE-ETC(U)
JUL 80 D O THOMPSON, R B THOMPSON F33615-74-C-5180

UNCLASSIFIED

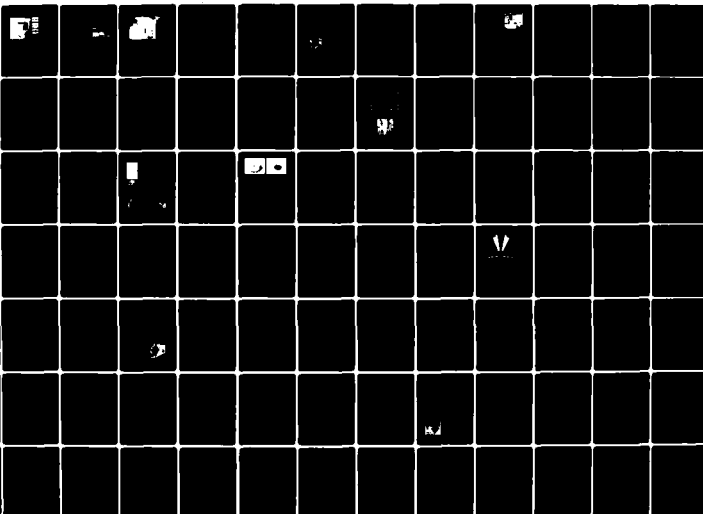
SC595.70AR

AFWAL-TR-80-4078

NL

7 of 8

03 04020



INITIAL FEASIBILITY STUDY

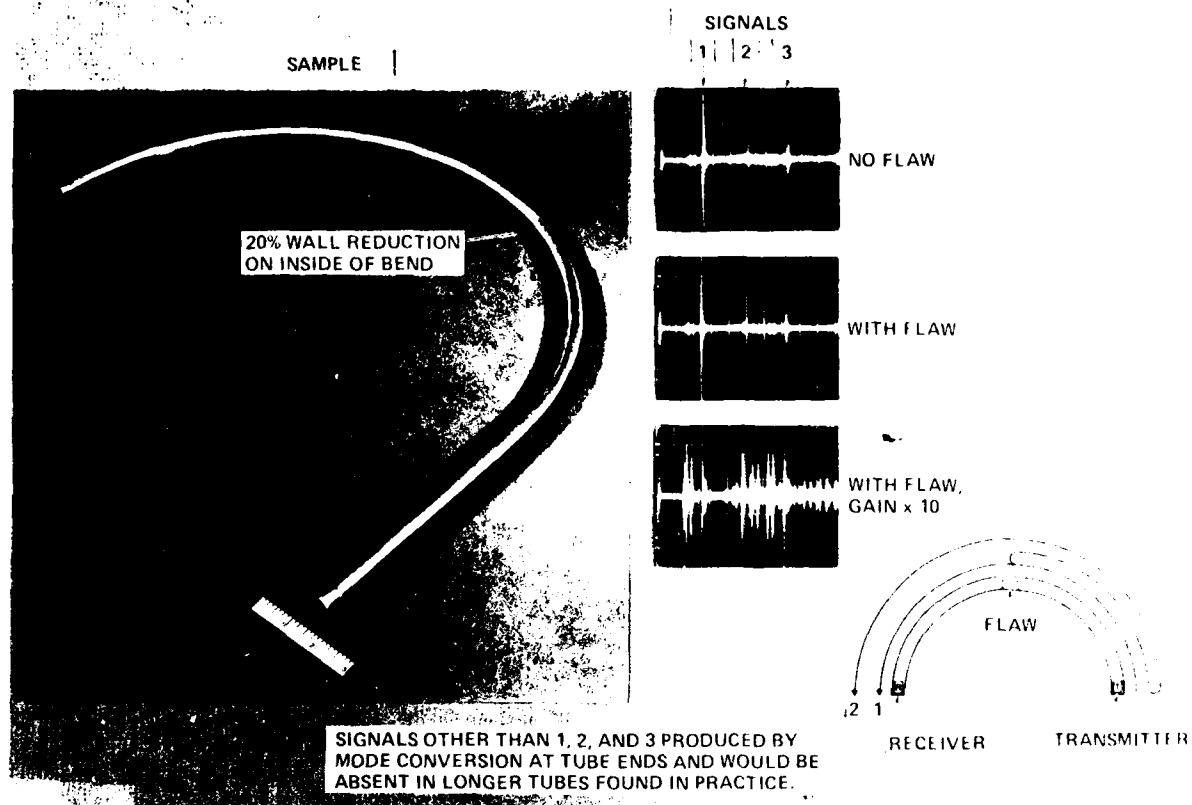


Fig. 4 Detection of flaws in U-bends.

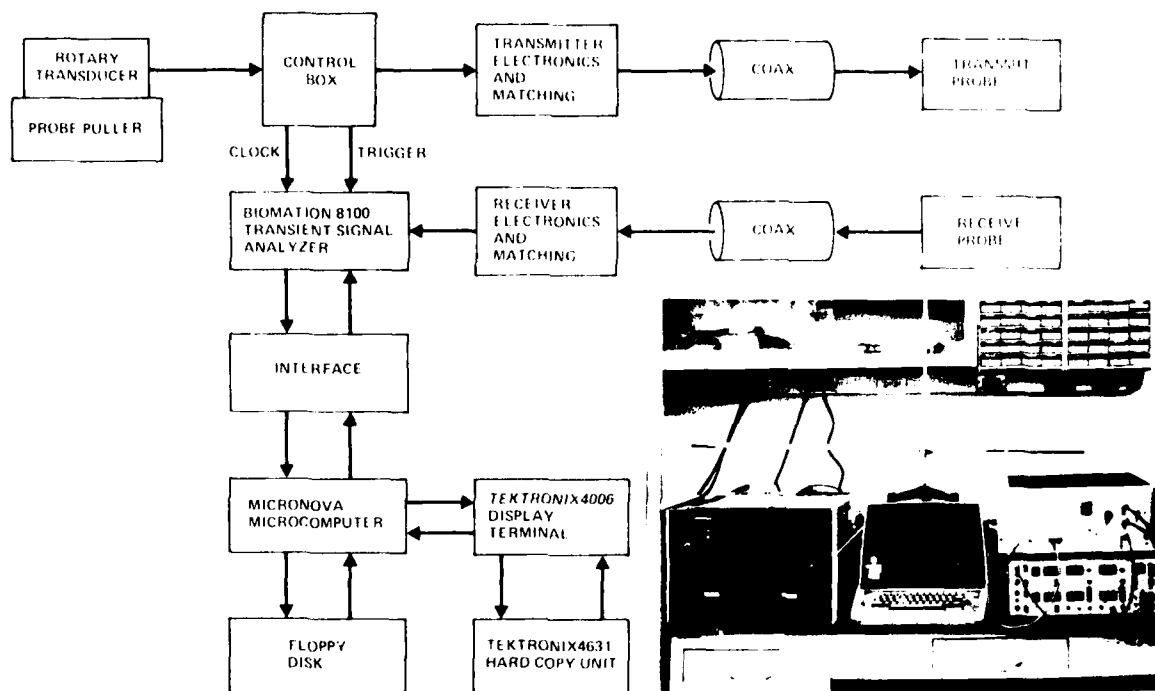


Fig. 5 Prototype system.

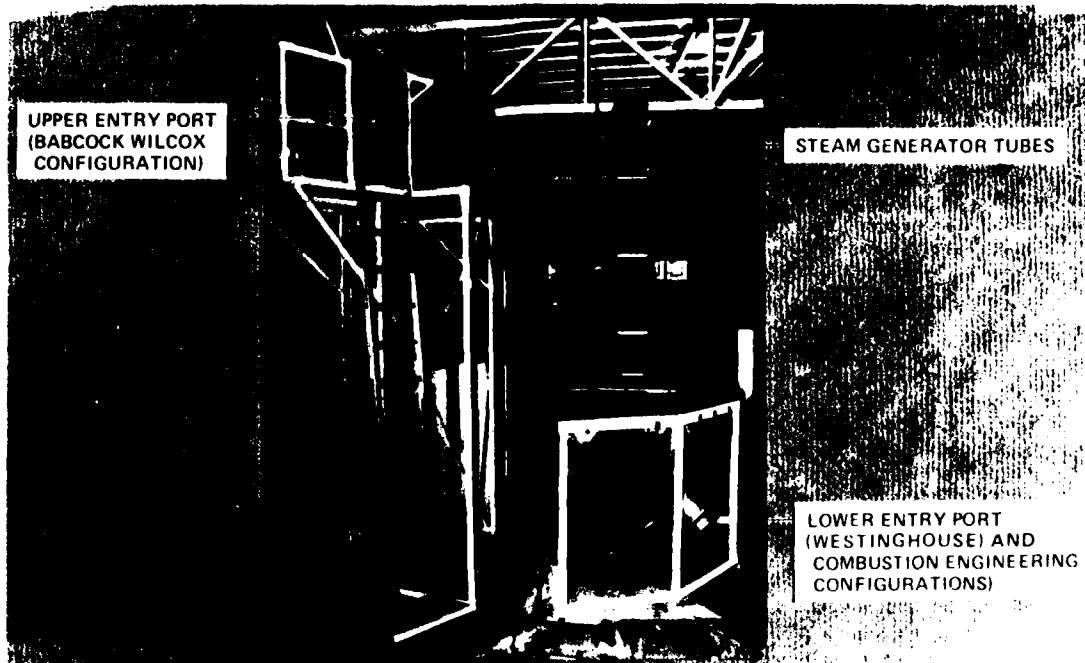


Fig. 6 Evaluation at steam generator mock-up.

- PREVIOUS FEASIBILITY STUDY DEMONSTRATED THAT EMAT'S COULD BE USED TO DETECT FLAWS IN STEAM GENERATOR TUBES.
- PRESENT PROGRAM WILL TEST A PROTOTYPE OF A FULL SYSTEM, COUPLED WITH AUTOMATIC PROBE PULLERS, IN A STEAM GENERATOR MOCK-UP.
- FUTURE EFFORTS WILL DEVELOP FLAW CHARACTERIZATION PROCEDURES AND REDUCE RESULTS TO PRACTICE IN ON-LINE STEAM GENERATORS.

Fig. 7 Conclusions.

INSPECTION OF THE LOWER HALF OF WING LAP JOINTS WITH EMATS*

J.F. Martin, P.J. Hodgetts, R.H. Houston,
R.B. Thompson, and D.O. Thompson
Rockwell International Science Center
Thousand Oaks, California 91360

ABSTRACT

Detection of fatigue cracks at the fastener holes in the lower portion of the C5A wing lap joint is complicated by lack of a direct line of access, and by the presence of fasteners and sealant material. Furthermore, any successful detection procedure must take into account the wide variation in the geometrical features of the joint. In this work, periodic permanent magnet EMATs (electromagnetic-acoustic transducers) have been employed to excite the $n=0$ horizontally polarized shear mode of the skin at 200 kHz and 250 kHz. These modes are partially transmitted into the overlap region joined by the fastener. Spectral analysis of suitably time gated and apodized portions of the reflected waveform have allowed simulated cracks growing out of fastener holes to be detected, and preliminary sizing algorithms have been developed.

SUMMARY

A major problem in aircraft maintenance is the detection of cracks growing from fastener holes in wing lap joints. As shown in Fig. 1, the problem is particularly difficult in the lower half of the joint, where direct measurement is obscured by intervening metallic and sealant layers. The former is opaque to all but low frequency eddy currents, whereas the latter has a variable, and often high, attenuation for ultrasonic waves in the MHz frequency range.

lant free, EMAT (electromagnetic-acoustic transducer) operating at 250 kHz and placed on the right hand exposed portion of the lower half of the joint. The energy propagated around the discontinuities, interrogated the fastener region, and returned to a receiving EMAT probe. An analog-based Fourier transform signal processor analyzed the experimental data. Horizontal shear waves were chosen in order to minimize loss in received ultrasonic energy due to mode conversion.

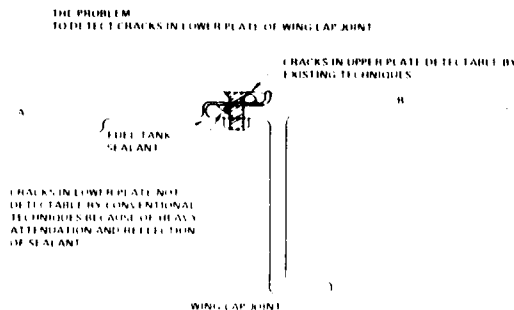
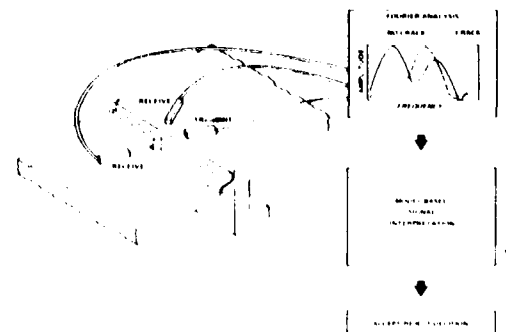


Fig. 1 The problem: to detect cracks in lower plate of wing lap joint.

The work described herein, funded by AFML and DARPA, includes a completed study performed in 1978 (Ref. 1) and a new study in progress.

The 1978 study was done largely with an unassembled mockup of the lower half of the joint. It contained 18 fastener holes, 12 of which were usable for experimental purposes. Four of the holes had a 0.010" wide saw slot of lengths 0.030", 0.11", 0.20", and 0.26", emanating from the hole perpendicular to the lap joint towards the edge of member B of Fig. 1.

Figure 2 illustrates the approach. The waves were injected into the lap joint region by a coup-



• THIN SKIN ACTS AS A WAVEGUIDE WHICH CHANNELS ENERGY TO LOWER JOINT.



• $n=0$ MODE IS MOST USEFUL SINCE THE INTERPRETATION OF THE DATA IS SIMPLEST

Fig. 2 Approach: Detection of cracks under fasteners with EMATs

Figure 3a shows actual transducer positions on the mockup and the received and analyzed waveforms. The initial pulse centered at about 15 us in Fig. 3b is the result of rf leakage from the

*This research was sponsored by the Center for Advanced NDE operated by the Rockwell International Science Center, for the Advanced Research Projects Agency and the Air Force Materials Laboratory under Contract No. F33615-74-C-5180.

transmitter to the receiver. In effect, the receiver acts as a radio antenna. This leakage has been found to be quite useful since it provides a measure of the true zero of time for measurement of acoustic delays. The signal centered near 60 μ s is the reflection from the first step encountered in the wing lap joint. This merges with the reflection from the extreme plate edge, which is centered at approximately 80 μ s. At 110 μ s, the reflection from the end of the stiffening rib (member C) is just beginning. Figure 3c shows the signal after the Hanning apodization function is used to gate out all but the flaw information. Figure 3d is the Fourier transform of the waveform shown in Fig. 3c.

Note that Fig. 3a shows two paths for an acoustic beam to travel: L_1 and L_2 . The concept used to guide the analysis here is that uncracked holes yield a signal which is a sum of the signals from both paths L_1 and L_2 . That sum will show, at some angle θ , an interference null in the Fourier spectrum. The size of the signal due to the path L_2 will decrease as the crack or slot increases in length and therefore the depth of the interference null will correspondingly decrease. A theoretical model of the wing lap joint was constructed based on a single node equivalent circuit. When combined with measurements of the geometry of the mock-up, the calculation of the structure transfer

function for this model affirmed the presence of this interference null within the bandwidth of the EMAT transfer function (Fig. 4b). Figure 4c shows the results when an experiment with $\theta = 45^\circ$ was performed on the wing mock-up. Indeed, there is an interference null, and its depth does decrease as the saw slot length increases. This allows a measurement of the length of the slot based on this null only.

The effort in Ref. 1 also included experiments on a real wing lap joint supplied by AFML into which a 0.100" saw slot was inserted. Both reflection and transmission data was collected and analyzed. Figure 5 shows the experimental setup and the results. With the bolt removed, the 0.100" saw slot definitely decreased the depth of the interference null. Furthermore, the data in transmission indicate that the acoustic energy transmitted through the lap joint was also affected by the presence of the saw slot. Hence, this 1978 work demonstrated the feasibility of using EMATs and horizontally polarized shear waves to detect fatigue cracks growing from fastener holes in the lower half of the joint. Saw slots originating in the fastener holes were successfully detected and the ultrasonic response quantified in terms of slot length. However, the primary limitations of that study included a high noise level, the lack of an opportunity to study

PROCESSED WAVEFORMS

TYPICAL TRANSDUCER POSITIONS

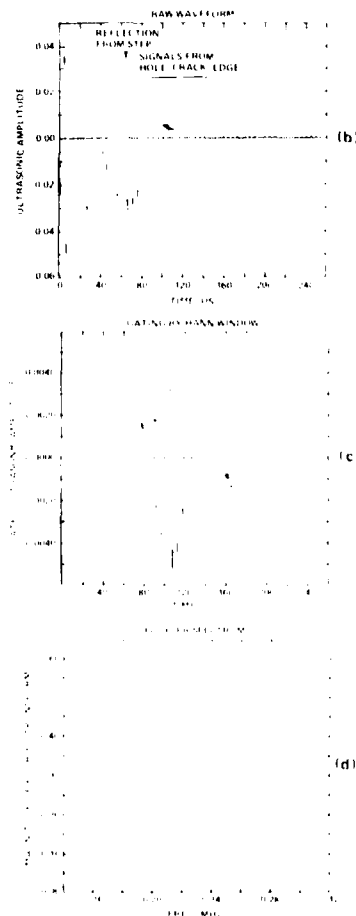
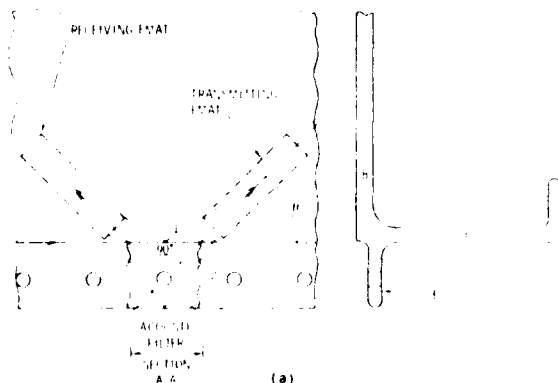


Fig. 3 Signal processing

CRACK DESTROYS INTERFERENCE NULL BY ELIMINATING ONE WAVE PATH

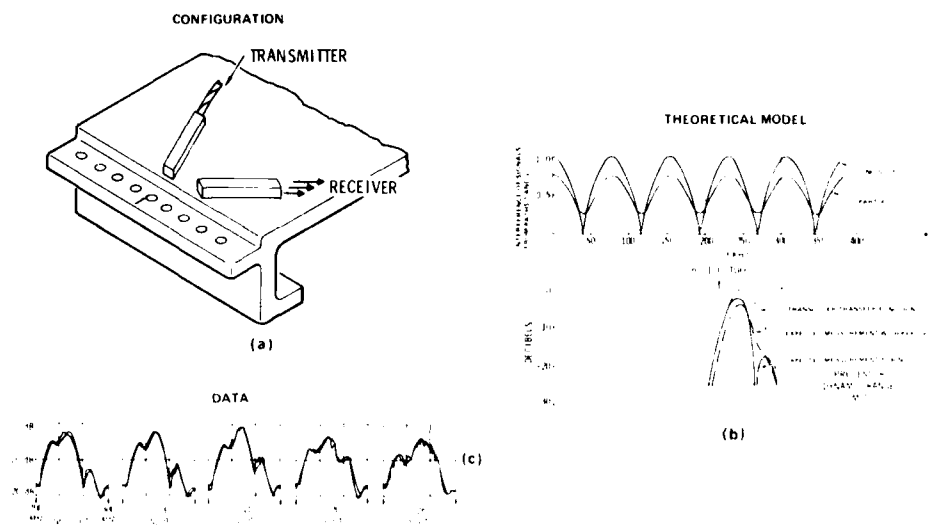


Fig. 4 Data on mock-up sample

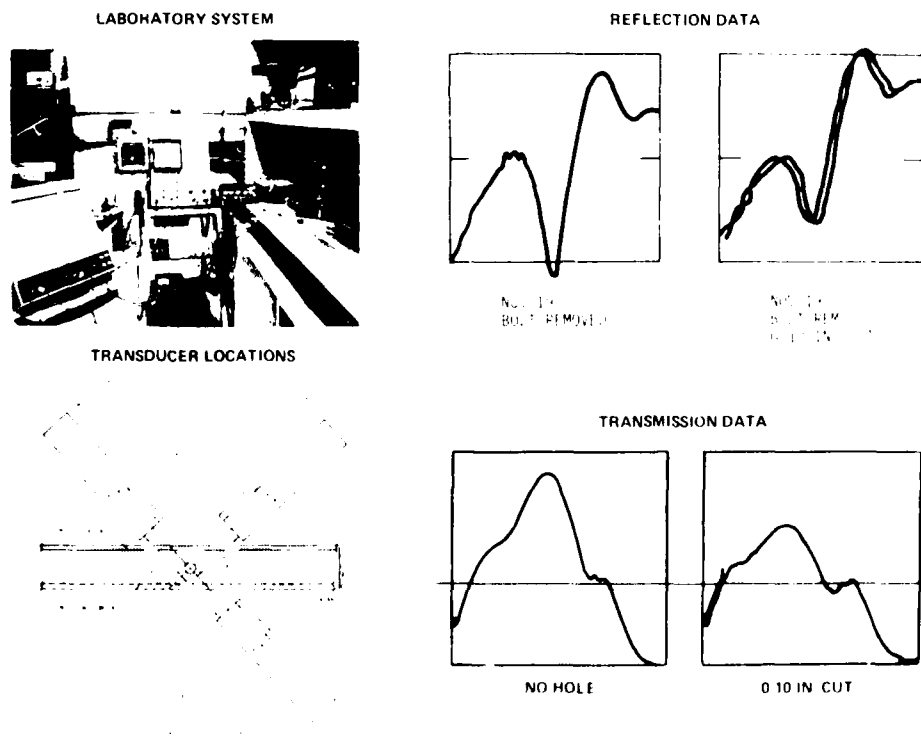


Fig. 5 Data on real wing lap joint

real fatigue cracks in assembled wing joints, and the lack of an opportunity to explore procedures which were adaptable to changes in part geometry.

The new study, in progress now, has as its objectives:

1. to achieve refinement of the system developed in Ref. 1 and to establish procedures to distinguish flaw responses from sample-geometry-determined changes in the ultrasonic response;
2. to prepare, and use in experiments, a minimum of three wing joint specimens, two of which would contain laboratory grown interior layer corner fatigue cracks;
3. to develop a preliminary configuration design of an EMAT system suitable for field inspection of wing lap joints for such cracks.

In order to achieve objective 1., the 250 kHz EMATs were replaced with 200 kHz devices in order to avoid all but the $n=0$ mode of acoustic propagation. The power supplies for the amplifying electronics were replaced. Finally and most important of all, the analog signal processor was replaced by a minicomputer-based data acquisition and analysis system. The computer is used to acquire, gate, and Fourier transform the time waveforms. A few of the resulting advantages are:

1. Averaging of up to 250 signals can be used to improve the signal-to-noise ratio.
2. Data can be collected once, and then the location of the gate and the type of apodization used can be varied for the same data. This allows accurate comparison of the effects of these different parameters.

3. The graphical display capabilities of the computer can be employed for comparison purposes.

Figure 6 shows the results of the first experiments on the original mockup, unassembled. Here θ was varied over 5 angles from 40° to 50° . Notice that the curves generated by the Fourier transform for the hole with no slot are all very similar in shape. However, the same angles for a slotted hole yield curves very dissimilar in shape. This kind of comparison could be easily quantified with appropriate software in the computer for a yes/no decision on whether a crack was present. Furthermore, this technique may prove to be less geometry dependent than the use of data at just one θ .

The current directions of the new study include:

1. detailed mapping of the acoustic energy field in the region of the fastener hole with a special, small area, EMAT probe;
2. preparation of 2 fully assembled specimens with laboratory-induced fatigue cracks;
3. investigations of the effects of the sealant and other geometrical variables;
4. selection of the design parameters of a fieldable instrument.

REFERENCE

1. "Detection of Cracks in the Inaccessible Lower Half of Wing Lap Joints Using EMATs," Air Force Materials Laboratory, Contract No. F33614-74-C-5180, Science Center Report No. SC595.4435A.

COMPUTER USED TO GATE AND ANALYZE SIGNALS

- SIGNAL AVERAGING USED TO IMPROVE SIGNAL TO NOISE RATIO.
- FLEXIBILITY IN SELECTION OF GATE LOCATION AND APODIZATION.

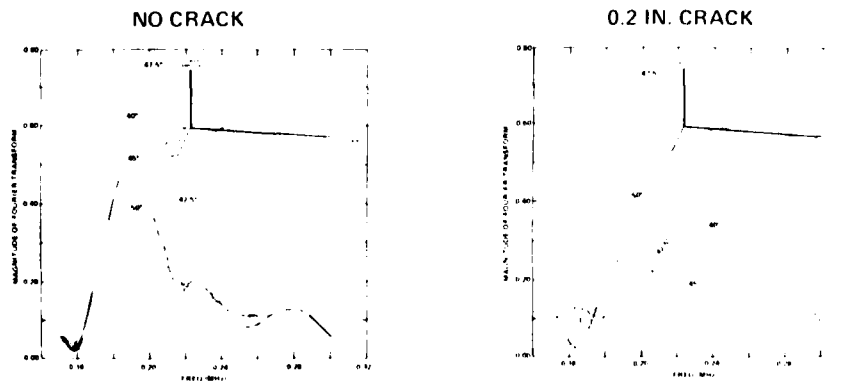


Fig. 6 New results as function of angle.

DETECTION OF BENDING STRESSES IN BURIED PIPELINES

G. A. Alers
Albuquerque Development Laboratory
Rockwell International
2340 Alamo, SE
Albuquerque, New Mexico 87106

R. B. Thompson
Science Center
Rockwell International
1049 Camino Dos Rios
Thousand Oaks, California 91360

ABSTRACT

When gas or oil pipelines must be laid through sand or permafrost or other unstable soils, the pipe walls can be subjected to large bending loads if the soil shifts. In order to detect this condition and correct it, it would be useful to monitor the state of stress along the pipeline at regular time intervals using a vehicle that is moved through the line by the fluid or gas in it. The experiments described here demonstrate that such a vehicle, using EMATs to excite and detect ultrasonic waves in the pipe wall, would be feasible because the transduction efficiency of the EMATs and thus the insertion loss of such a system can be related quantitatively to the stress level in the pipe wall.

INTRODUCTION

Whenever a gas or oil pipeline must be laid in unstable soil (such as in permafrost or on a sandy ocean floor), it may be subjected to earth movements which can bend an entire section of the line. The bending stresses thus induced in the pipe wall when added to the stress arising from the high pressure contents of the pipeline may lead to critical stress levels and possible rupture of the line. To avoid such a catastrophe, the designer must consider the worst case and must specify additional wall thickness along the entire route that is in unstable soil. If a reliable inspection method could be devised to monitor the stress level in the pipe walls, less steel would have to be used because the development of dangerous amounts of bending could be detected and corrective actions taken before the safety of the line becomes questionable.

Several years ago, it was shown that an instrumented vehicle could be sent through a pipeline to inspect it for wall thinning flaws by an ultrasonic Lamb wave technique. The transducers used to excite and detect the Lamb waves were of a noncontacting, electromagnetic type that utilized the magnetostrictive properties of the steel for interconversion of electrical currents and ultrasonic waves. It was later demonstrated in the ARPA/AFML program, that this magnetostrictive mechanism of transduction was very sensitive to the presence of stresses in the metal under the transducer coils. In fact, a measurement of the efficiency of transduction as a function of applied magnetic field could be used to make a quantitative determination of both the direction and magnitude of this stress level. An example of these previous results is shown in Fig. 1 which plots the amplitude of acoustic wave generated by an Electromagnetic Acoustic Transducer (EMAT) as a function of applied, tangential magnetic

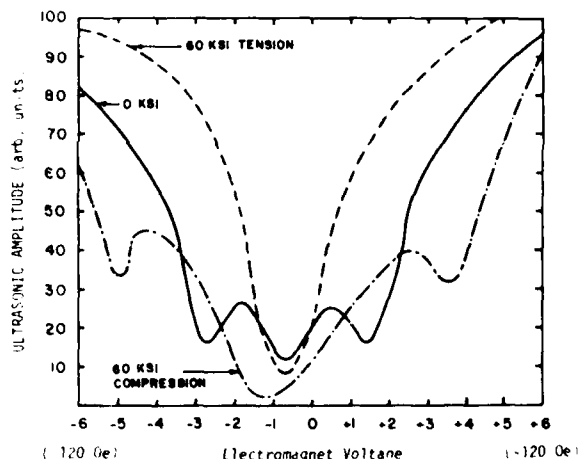


Fig. 1. Experimental demonstration of the effects of stress on the efficiency of electromagnetic, acoustic transducers. See Ref. 3.

field for different states of stress in a bar of iron under the transducer. Clearly, by characterizing the shape of each curve with a single parameter, the value of that parameter could be used to infer the magnitude and sign of the stress level acting on the metal.

The objective of the experiments described in this paper was to demonstrate that by combining the ultrasonic technique for detecting flaws in a buried pipeline with the phenomena of stress dependent transducer efficiency, it would be feasible to monitor bending stresses along a gas or oil pipeline traversing a region of unstable soil. The approach used was to assemble a mechanical device for bending a 36 inch

diameter, 40 foot long piece of gas linepipe at the Science Center and then to measure the magnetic field dependence of the transduction efficiency of a EMAT placed in the region of maximum wall stress. By placing the EMAT at different locations around the circumference of the bent pipe, it should be easily possible to observe the effects of both the compressive and tensile stresses that occur on opposite sides of such a bent structural element.

EXPERIMENTAL APPARATUS

Since an EMAT system for detecting flaws in large diameter pipes was already available at the Science Center, the most serious problem was the construction of a device to subject a large diameter pipe to a bending stress. Figure 2

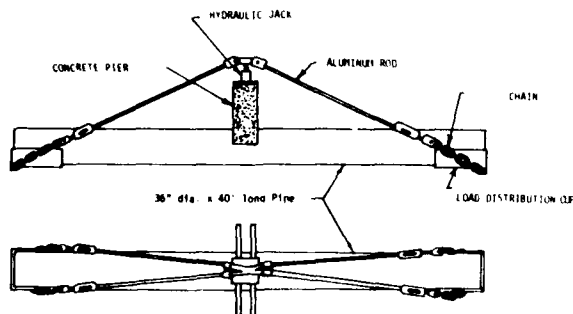


Fig. 2 Drawing of the scheme used to subject a 36 inch diameter, 40 foot long joint of gas pipeline to a bending stress.

displays a drawing of the apparatus designed to convert the force of a 200,000 pound capacity hydraulic jack into a bending moment. If the pipe could be considered as a rigid beam, simple mechanical formulae show that 200,000 pounds of force at the jack should deflect the two ends of the pipe by 1.7 inches and subject the 0.4 inch thick pipe wall directly under the jack to a tensile or compressive stress of 47,000 psi (assuming a 22 degree angle for the pull rods). Figure 3 shows a photograph of the completed mechanical structure which used four, 2 inch diameter aluminum alloy pull rods to transfer the load from the jack to the ends of the pipe.

Electrical resistance strain gages were distributed around the interior circumference of the pipe to make measurements of the actual state of stress in the pipe wall so that the pressure in the hydraulic jack or the end deflection values could be used to deduce the values of stress existing in any given experiment. Figure 4 shows the values of the strain observed at two key locations around the ID of the pipe as a function of the deflection of the end of the pipe and the hydrostatic pressure in the 20:1 intensifier that supplied the jack.

The acoustic measurement apparatus consisted of an electromagnet in the center of the pipe under the jack support with a flexure wave generating EMAT between its pole pieces. This transducer acted as a generator of 130 KHz ultrasonic waves which propagated along the length of the pipe to a receiver EMAT mounted



Fig. 3. Photograph of the apparatus used to bend the pipe.

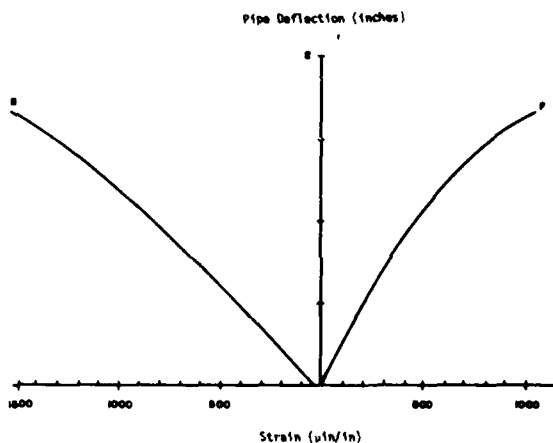


Fig. 4. Strain measured on the ID of the pipe on the bottom (tension) side-Curve F- and on the top (compression) side-Curve B-as a function of deflection of the end of the pipe.

between the pole pieces of a large permanent magnet positioned about five feet away. In this way, the relative signal amplitude generated by the transmitter EMAT could be measured as a function of current in the electromagnet coils. It was very important that this electromagnet be powerful enough to generate a magnetic field sufficient to achieve the maximum in transducer efficiency that characterizes the magnetostrictive mechanism of acoustic wave generation.

EXPERIMENTAL RESULTS

The experiment consisted of recording measurements of the received signal amplitude at many different values of electromagnet current (both positive and negative) for a series of fixed settings for the bending load on the pipe. Figure 5 displays an example of these data for three different stress levels in the

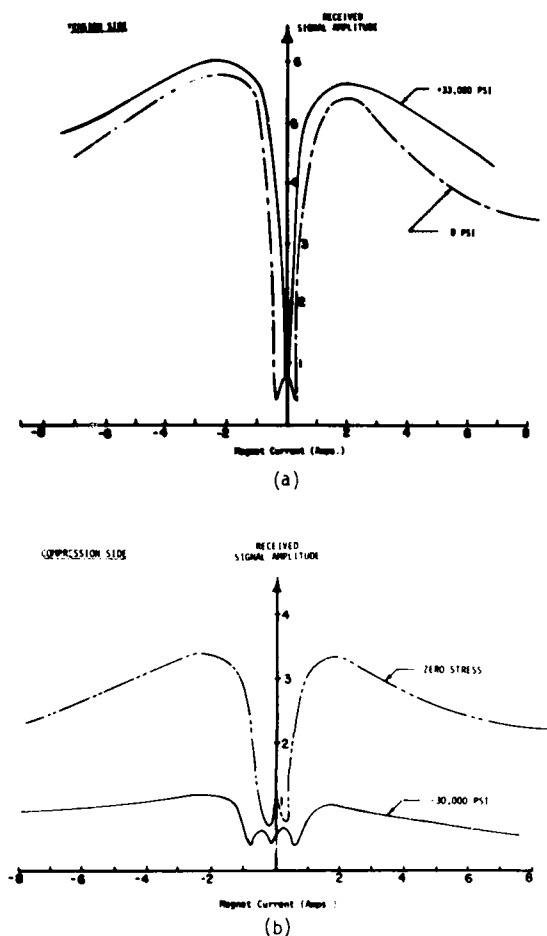


Fig. 5. Experimental results showing the variation of EMAT signal generated by a transmitter EMAT in the gap of an electromagnet whose current was varied from -8 to +8 amperes. (a) Data for the EMATs on the bottom ID of the pipe. (b) Data for the EMATs on the top ID of the pipe.

pipe wall under the transmitter EMAT. Compression was achieved by mounting the electromagnet and EMAT on the top of the ID of the pipe while tension was obtained for the EMAT on the bottom of the ID of the pipe. Obviously, the presence of a stress dramatically changes the shape and magnitude of the signal versus electromagnet current curves. The maxima in transduction efficiency are increased and moved to lower electromagnet currents by a tension while the opposite occurs under compression. In fact, the presence of a compressive load almost eliminates the magnetostrictive enhancement of the transduction process and spoils the response of the entire EMAT system.

In order to use this relationship between stress and EMAT efficiency as a quantitative tool to measure the stress levels in bent pipelines, it is necessary to extract a single

parameter from an observed signal versus electromagnet current curve and to establish a calibration curve for this parameter as a function of stress. Because the signal voltage received in a particular experiment depends upon such uncontrollable variables as the spacing between the transducer coil and the pipe wall as well as on the gain and bandwidth of the particular electronic system used, the measured signal voltages must be normalized to eliminate sensitivity to these variables. Likewise the current in the electromagnet does not fully define the magnetic field at the transducer because variations in the pole-piece to pipe wall gap have a strong influence on the magnetic field distribution. Thus, the electromagnet current must also be normalized. The existence of a maximum in the experimental curves (Fig. 5) provides an excellent normalization opportunity because each curve can be replotted with the signal voltages normalized to the maximum signal voltage and the currents normalized to the electromagnet current needed to achieve the maximum in efficiency. This yields curves with unitless coordinates that are independent of the values of transducer lift-off, receiver gain and electromagnet pole gaps that are characteristic of a particular measurement situation.

The most obvious characteristic of these curves that changes with the stress level is the sharpness or width of the dip in efficiency around zero current. An easily determined parameter that measures this dip width is the difference in current between points at which the signal amplitude has fallen to half its maximum value. For normalization purposes, this difference in current can be divided by the difference in electromagnet current between points at which the maximum in transducer efficiency is observed. Thus a unitless, normalized parameter that qualitatively varies with stress level can be deduced from data such as that shown in Fig. 5 by using the formula

$$\text{Parameter } P = \frac{I^+(V_1) + I^-(V_1)}{I^+(V_0) + I^-(V_0)} \quad (1)$$

where $I^+(V_1)$ is the current at which the signal voltage is half its maximum value for a positive current, $I^-(V_1)$ is the current at which the signal voltage is half of its maximum value for a negative current, $I^+(V_0)$ is the current at the maximum signal for positive currents and $I^-(V_0)$ is the negative current at which a maximum signal occurs.

Figure 6 plots this parameter value as a function of the stress in the pipe under the transducer. It can be seen that a reasonably linear relationship exists so that a measurement of the parameter under unknown stress conditions could be used to deduce the stress level present. The accuracy of this procedure can be assessed by performing a statistical analysis of the data. Such an analysis yielded the result that the line shown in Fig. 6 has a correlation coefficient with the data of 0.96 and that a measurement of the parameter could predict the highest stress level of 50 KSI to an accuracy of ± 15 KSI.

CONCLUSION

Figure 5 shows that the presence of a bending stress in a pipe makes an easily recognized change in the magnetic field dependence of an EMAT's efficiency. By extracting a unitless parameter from the curve of signal voltage

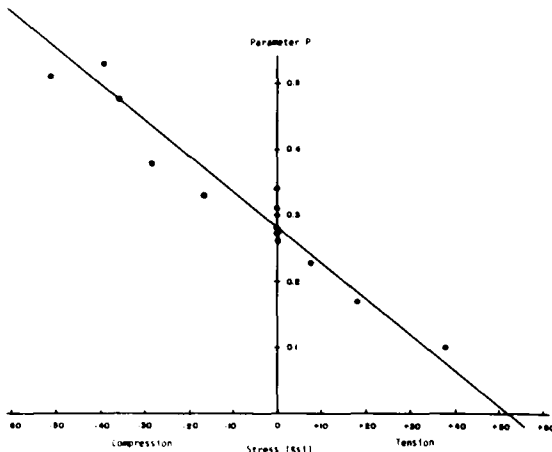


Fig. 6. Dependence of the unitless parameter that characterizes the shape of the EMAT efficiency versus electromagnet current curves (see Eq. 1) upon the stress level in the pipe wall under the EMAT.

versus electromagnet current, a value of the stress and its sign can be deduced from a calibration curve such as shown in Fig. 6. In these initial experiments, an accuracy of ± 15 KSI was achieved. This translates into being able to monitor the bending stress levels in a pipeline to an accuracy of 25% of the yield stress since most line pipe has a yield strength of 60 to 70 KSI.

A measurement device for monitoring stress in a pipeline would consist of an electromagnet powered EMAT on a carriage that is pushed through the pipe by the fluid it carries. At regular intervals the current in the electromagnet could be driven through a programmed cycle while the ultrasonic signals generated by the EMAT were monitored. An on-board microprocessor could then extract the parameter from the electrical measurements and record its value along with the carriage location information on a tape recorder for subsequent analysis. By using four such electromagnet-EMAT systems around the circumference of the pipe, the maximum bending stress could be deduced at any given location.

ACKNOWLEDGMENTS

These feasibility studies were supported by the Flow Control Division of Rockwell International. The authors wish to express their gratitude to the staffs of the Facilities and Machine Shop Departments, particularly Dick Johnson and Al Lewin, for designing and assembling the pipe bending apparatus. They also wish

to thank Mr. Larry Bivins for his efficient assembly of the electronic and ultrasonic devices and his conscientious collection of all the data.

REFERENCES

1. G. A. Alers and R. B. Thompson, "Ultrasonic Inspection of Buried Gas Pipelines", Contract PR-73-57 American Gas Association, 1972-1977.
2. R. B. Thompson "Electromagnetic Noncontact Transducers" Proceedings of the 1973 Ultrasonics Symposium, Monterey, California, p. 385.
3. R. B. Thompson "Strain Dependence of Electromagnetic Generation of Ultrasonic Surface Waves in Ferrous Metals" Applied Physics Letters, 28, 483, (1976).

ON DETERMINING STRESS IN BOLTS ULTRASONICALLY

D. E. MacDonald
Metal Science and Standards Division
National Measurement Laboratory
National Bureau of Standards
Washington, D. C. 20234

ABSTRACT

Several factors affecting the ultrasonic determination of stress in bolts are examined which help to clarify existing problems with the interpretation of certain experiments. To begin with, the use of ultrasonic waves to determine stress inverts the results of experiments used to evaluate third-order elastic constants. Thus, the unambiguous determination of stress must be subject to the same conditions as the experimental measurement of higher-order moduli. For example, Thurston and Brugger's expression for the transit time in terms of the natural velocity and the unstressed length provides an alternative to the usual practice of relating the transit time to the stress dependent true velocity and the stress induced change in length. Using the natural velocity emphasizes the explicit stress dependence of the velocity and avoids the unnecessary corrections for changes in path length and density. Although temperature and dislocation mobility are closely controlled in third-order elastic constant determinations, these factors are rarely considered in ultrasonic stress measurements. It is shown that in steels a stress of 10MPa (1.5Ksi) is equivalent to a 1°C change in temperature. The possible role of defects or temperature in the relaxation phenomena observed in ultrasonic stress determinations is also examined. The effects of constrained thermal stress and unloaded bolt length on the so-called stress-acoustic constant are presented. The correct functional form of the stress and strain dependence of the sound velocity is shown to be crucial to the problem of thermally modified bolt load. The effect of unloaded bolt length is considered for the case where the nut is stationary during loading and where it is tightened to produce the load. Finally, the difficulties caused by longitudinal wave mode conversion upon reflection off the bolt sides are examined.

THIRD-ORDER ELASTIC CONSTANTS

The variation in the elastic modulus with stress is very small. It is not measurable in a standard tensile test. The velocity of ultrasonic waves is coupled to the stress through the higher-order elastic coefficients. In part, the resonant frequency of a solid is changed by the stress the same way a violin string frequency is changed by stretching. Determining the stress from the change in resonant frequency or transit time and the known third-order moduli is the inverse of the usual procedure for measuring third-order moduli. For this reason, the technique is applicable only for elastic deformations.

NATURAL VELOCITY

The repetition frequency can be expressed as either the true velocity over instantaneous length or the natural velocity over original length. This is a direct analogy to expressing the load in a tensile test as either the true stress times instantaneous area or the engineering stress times the original cross-sectional area. This formalism alleviates the need for independently determining the new length and density under stress. This fact appears to have escaped some of the investigators in the field.

TEMPERATURE ACOUSTIC CONSTANT

Care must be taken in interpreting ultrasonic data because many things effect ultrasonic wave propagation. For example, one can introduce a temperature acoustic constant similar to the stress acoustic constant. Unlike the stress case where the break-down between true velocity and length change is two to one; in the case of temperature the effect on true velocity is nine times greater than the

effect on the length. A one degree Kelvin change in temperature produces the same effect as 10MPa (1.5Ksi) change in stress for steel.

STRESS ACOUSTIC CONSTANT

In resonant techniques, the sections of unstressed length in bolts must be treated as parts of a composite resonator. The resultant modifications to the stress acoustic constant are presented for the case of the nut stationary during loading and the case where the nut is turned to produce the load. In addition to a factor which represents the percent of the length that is stressed, there is a term which depends on the harmonic number. An expression for the stress acoustic constant for thermally induced loads in constrained bolts has yet to be developed.

SIDE WALL REFLECTIONS

The frequency spectra of bolts in tension contain nulls which do not track with the change in stress. It is shown that upon reflection off the bolt sides a mode converted transverse wave generates a series of longitudinal pulses. The nulls in the spectrum correspond to the time separation between the pulses, i.e. the time it takes the transverse wave to traverse the bolt from side to side. The spectrum for an initial transverse wave does not contain these nulls. This is because a longitudinal wave is not produced by the reflection at grazing incidence of a transverse wave.

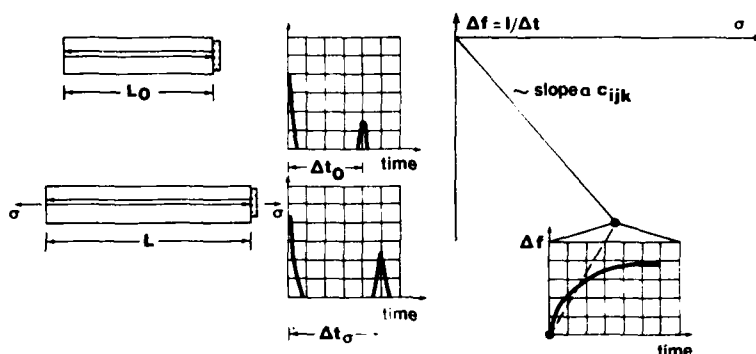
ACKNOWLEDGEMENTS

Much of the work reported on here was done while the author was with the Instrument Research Division of the NASA Langley Research Center, Hampton, VA on an IPA Agreement from Pennsylvania State Univ.

Third-Order

Elastic Constant, C_{ijk} , Experiments \longleftrightarrow Ultrasonic Stress Measurements

The change in the transit time, Δt , or its inverse, the repetition frequency, Δf , is recorded versus an applied stress, σ .



The third-order elastic constants are found by measuring the stress and the repetition frequency. By the inverse operation the stress is determined from the known third-order moduli and measurements of the repetition frequency. Although care is taken to eliminate the contributions from temperature changes and defect motion in finding C_{ijk} , this is not the case for ultrasonic stress measurements.

After rapid loading the repetition frequency is often found to relax asymptotically to a value which depends on the initial load. It has yet to be determined whether this is due to the frictional heat of loading or a thermoelastic effect or stress-induced interstitial ordering.

True Velocity, V \longleftrightarrow Natural Velocity, W

The repetition frequency, f , can be expressed equivalently in terms of either the true velocity, V , over deformed length, L , or the natural velocity, W , over the unstressed length, L_0 .

$$f = \frac{V}{L} = \frac{W}{L_0} = f$$

$$\Delta f = \Delta \left(\frac{V}{L} \right) = \frac{\Delta V}{L_0} + V_0 \Delta \left(\frac{1}{L} \right) = \frac{V_0}{L_0} \left(\frac{\Delta V}{V_0} - \frac{\Delta L}{L_0} \right) \Leftrightarrow \frac{W_0}{L_0} \frac{\Delta W}{W_0} = \frac{\Delta W}{L_0} = \Delta \left(\frac{W}{L_0} \right) = \Delta f$$

$$\frac{\Delta f}{f_0} = \frac{\Delta V}{V_0} - \frac{\Delta L}{L_0} = \frac{\Delta W}{W_0}$$

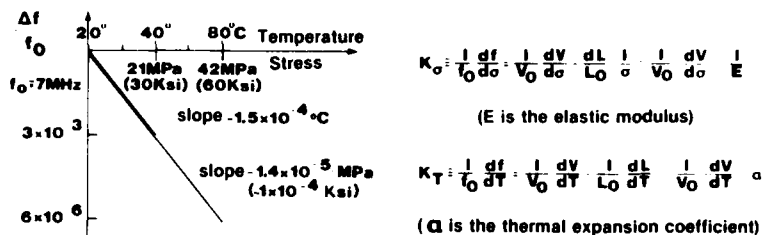
The expression for the change in true velocity contains a term which exactly cancels the strain term. Expressing the change in repetition frequency in terms of the natural velocity, W , avoids the unnecessary* corrections for changes in path length and density.

*See "Change of the Ultrasonic Characteristics with Stress in Some Steels and Aluminum Alloys", S. Takahashi, E. Yamamoto, N. Uetake, R. Motegi, *Journal of Materials Science*, 13 (1978) pp. 843-850.

Stress Acoustic Constant, K_σ / Temperature Acoustic Constant, K_T

The repetition frequency, f , is a relatively stronger function of temperature than it is of stress.

431 Stainless Steel*



The change in repetition frequency produced by a 1°C change in temperature is roughly the same as that produced by a 10MPa (1.5 Ksi) change in stress.

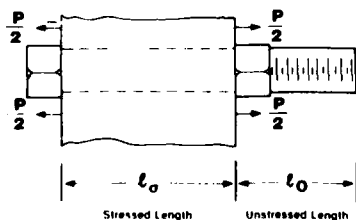
*From "Fastener Load Analysis Method", F.R. Rollins, Jr. NASA Report CR-61354 (1971).

Effect of Unloaded Bolt Length on the Stress Acoustic Constant

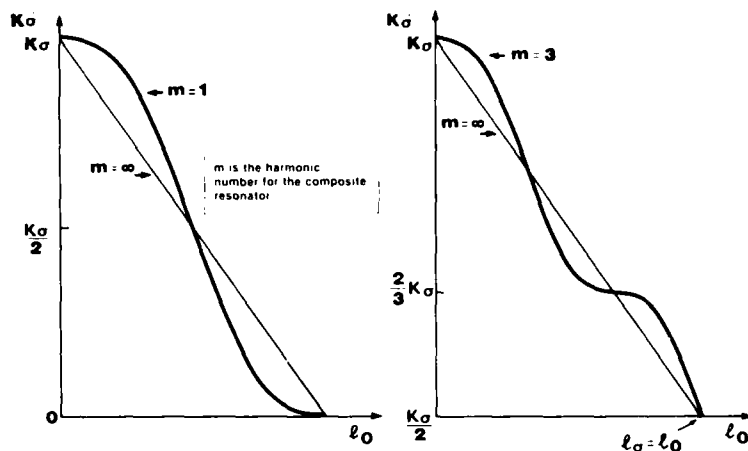
In resonant techniques the stress acoustic constant is expressed in terms of the m^{th} harmonic of the bolt, ω_m .

$$K_\sigma = \frac{1}{\omega_m} \frac{d\omega_m}{d\sigma} = \frac{1}{V_0} \frac{dV}{d\sigma} - \frac{1}{E} = \frac{1}{W_0} \frac{dW}{d\sigma}$$

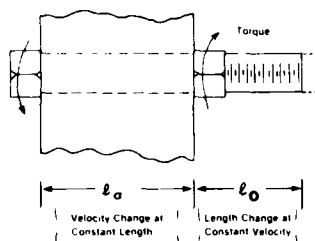
If only a portion of the length is stressed, then the bolt must be treated as a composite resonator. The resonance condition on the system for the case where the nut is stationary during loading yields the effective stress acoustic constant, K_σ .



$$K_\sigma = \frac{1}{\omega_m} \frac{d\omega_m}{d\sigma} = \frac{K_\sigma \left| 1 - \sin c \left(2\pi m \frac{l_\sigma}{l_\sigma + l_0} \right) \right|}{\left(1 + \frac{l_\sigma}{l_\sigma + l_0} \right)}$$



When the nut is tightened to produce the load, the velocity changes in the loaded section whereas the length change occurs in the unloaded section. Shown below is the resulting expression for the effective stress acoustic constant, K_{σ}



$$K_{\sigma} = \frac{l}{\omega_m} \frac{d\omega_m}{d\sigma} = \frac{l}{1 + \frac{l_0}{l_{\sigma}}} \left[K_{\sigma} - \frac{l}{V_0} \frac{dV}{d\sigma} \sin c \left(\frac{2\omega_m l_{\sigma}}{V_0} \right) + \frac{l}{E} \sin c \left(\frac{\omega_m l_0}{V_0} \right) \cos \frac{\omega_m l_0 + 2l_{\sigma}}{V_0} \right]$$

On the Stress Acoustic Constant for Thermal Loading

For thermal loading under constraint, the repetition frequency can be expressed as the stress and temperature dependent velocity over the constant length, L_0 .

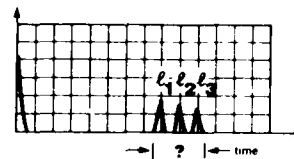
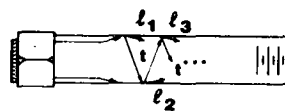
$$f = \frac{V(\sigma, T)}{L_0}, \quad df = \frac{1}{L_0} \left[\frac{\delta V}{\delta T} dT + \frac{\delta V}{\delta \sigma} d\sigma \right], \quad \frac{df}{f_0} = \frac{1}{V_0} \frac{\delta V}{\delta T} dT + \frac{1}{V_0} \frac{\delta V}{\delta \sigma} d\sigma$$

The $\frac{dV}{dT}$ term is straight forward. A difficulty arises with the $\frac{dV}{d\sigma}$ term. Most researchers use the expressions of Hughes and Kelly* which unfortunately incorporate the constitutive relation for unconstrained deformation and are therefore not applicable here. To date a self-consistent analysis for constrained thermal loading has not been published.

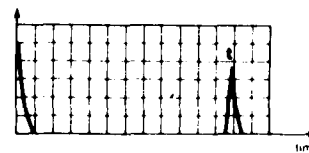
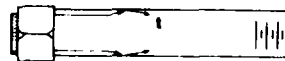
*See "Second-Order Elastic Deformation of Solids", D.S. Hughes and J.L. Kelly, *Physical Review*, 92 (1953) pp. 1145-1149.

Effect of Side Wall Reflections in Measuring Bolt Tension

Reflections off the bolt sides can lead to inaccuracies in determining bolt tension.



Because of the conditions a longitudinal plane wave, ℓ , must satisfy upon reflection off a boundary, a mode converted transverse wave, t , is generated in the bolt. Upon each reflection a portion of the transverse wave is reconverted back to a longitudinal wave giving rise to a series of longitudinal pulses traveling down the bolt. In low attenuation materials a way around this problem is to start with a transverse wave which upon reflection yields only the transverse wave.



RAPID ULTRASONIC INSPECTION OF ARMY PROJECTILES

Len T. Spragins
Albuquerque Development Laboratory
Rockwell International
2340 Alamo, SE
Albuquerque, New Mexico 87106

ABSTRACT

The electromagnetic acoustic transducer (EMAT) is a device of particular interest for rapid non-destructive evaluation (NDE) in assembly line applications because of its noncontact mode of operation. Speed is a crucial factor in the performance of an NDE system designed for the inspection of artillery projectiles where production rates may be on the order of several shells per minute. These requirements severely restrict the reliability of conventional ultrasonic techniques that use fluid couplants.

A fully automated micro-processor based inspection system utilizing multiple EMATs to launch shear vertical acoustic waves traveling at 30 degrees with respect to the surface normal is being assembled to inspect 155 mm projectiles for both ID and OD flaws. The system's ability to detect small defects has been demonstrated by locating semi-elliptical EDM notches having surface lengths of 2.5 mm (0.1 in.) and maximum depths of 0.8 mm (0.03 in.).

INTRODUCTION

The principles of electromagnetic transduction will not be discussed in detail in this paper. It is sufficient to note that a transducer consists of a coil of wire carrying a dynamic current at the desired frequency and a magnet to impress a static bias field. Ultrasonic waves are launched as a reaction to electromagnetic forces exerted when the transducer is placed adjacent to the surface of a metal part, and they are detected by reciprocal processes. Absolutely no physical contact is required, hence transducers and the part can be moved rapidly relative to each other with no fear of disturbing the coupling medium. The approach thus combines the scanning convenience of eddy current techniques with the many advantages of ultrasonics. One of the most important of the latter is the ability to excite directed beams which propagate through the thickness or around the circumference of a projectile and interrogate large volumes of material in a single measurement.

Inspection Technique - The details of the ultrasonic inspection scheme used to detect flaws in the wall of the projectile are shown in figure 1. The EMAT which operates in the "pulse-echo" mode, generates an ultrasonic wave launched at approximately 35° with respect to the surface normal. A flaw that exists in the path of the wave reflects a signal which is then detected by the same EMAT that delivered the transmitted ultrasonic wave.

Shown in figure 2 is an oscilloscope photograph of a typical reflected signal from a 0.020 inch deep EDM notch of the ID surface of an M-549 projectile. The first signal is the electrical feedthrough from the transmitted burst at 1.94 MHz, and the second is the signal reflected from the simulated flaw. The reflected signal, appearing approximately 20 μ sec after the transmission burst, represents a third bounce signal as indicated in figure 1.

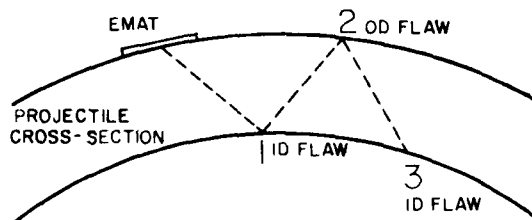


Figure 1. Inspection of projectile wall with shear-vertical acoustic waves.

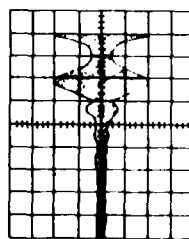


Figure 2. Oscilloscope photograph of reflected signal from ID notch.

The location of the flaw, either ID, bulk or OD, is determined by the elapsed time between transmitted and received signals.

A total of forty EMATs arranged in pairs are located between the projectile and each adjacent pole piece as shown in figure 3. One-half of the EMATs launch ultrasonic waves circumferentially and the other half longitudinally. The EMATs are fired sequentially every 200 μ sec as the projectile is rotated which assures complete inspection. The total inspection time for a single projectile is less than one second.

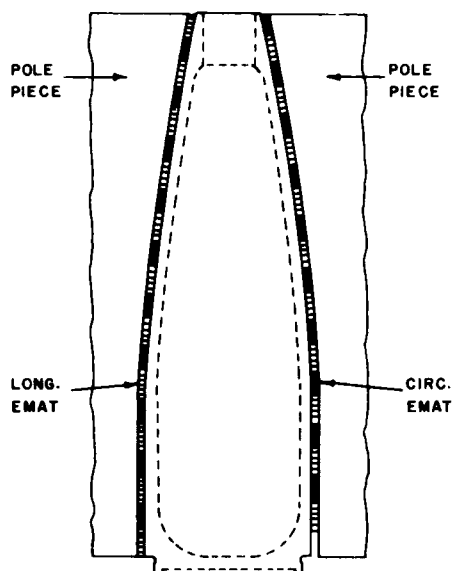


Figure 3. FMAT and pole piece configuration.

System Operation - Shown in figure 4 is a simplified block diagram of the overall inspection system. The system is composed of the following major components:

Hydraulically controlled projectile handling unit which houses the electromagnet, pole pieces and EMATs.

Hydraulic power pack and handling unit control panel.

Electromagnet power supply.

Micro-processor based analog and digital processor.

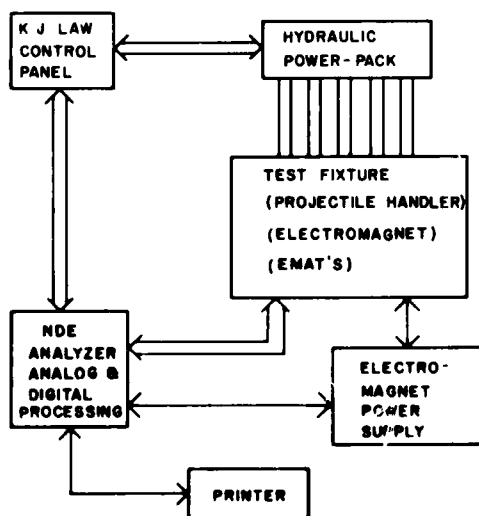


Figure 4. System block diagram.

The handling unit automatically places the projectile between the electromagnet pole pieces and relays a signal to the processor that the inspection mode may begin. The electromagnet power supply is brought up to voltage and approximately forty amperes is delivered to the coils during the short inspection cycle. A 19 kilo-Gauss normal field is generated in the 3/32 inch gap between the projectile and each pole piece. Each EMAT is fired as the shell is rotated and if flaws exist, are recorded by the processor. Flaws may be located to within a one-half inch square area based on information gathered from range-gating and shaft encoding. At the end of the inspection cycle, a print-out of the flaw locations is available for permanent record.

The actual determination as to what constitutes a flaw is based on a set of "standards" generated by the U.S. Army Armament Research and Development Command, Dover, New Jersey. The "standards" are actually a set of projectiles containing calibrated EDM notches with depths ranging from 0.010 in. to 0.030 in. The reflections from these circumferential and longitudinal notches are used to establish accept/reject criteria applicable to production line standards.

CONCLUSIONS

Objectives which have been met as a direct result of this effort have been to demonstrate that an ultrasonic inspection system using noncontact, electromagnetic acoustic transducers can function effectively and is capable of performing inspection of the complete projectile at full production line rates.

STRONG NEED FOR IMPROVED ULTRASONIC STANDARDS FOR INSPECTION OF ARTILLERY SHELL METAL BODIES

J. M. Smith
Army Materials and Mechanics Research Center
Watertown, Massachusetts 02172

ABSTRACT

Ultrasonic standards for artillery shells are made by machining grooves into inert projectile bodies. Current standards are difficult to design and build and do not realistically simulate manufacturing defects. This poster paper will discuss the design process and use of ultrasonic standards and will describe some of their current limitations.

This poster paper describes an Army problem concerned with the design and use of ultrasonic standards for artillery shell inspection. Three aspects of this problem will be addressed: (1) How standards are designed, (2) How standards are used, and (3) Problems with current standards.

(1) How standards are designed:

During the initial design phase, a stress analysis of the projectile for launch and rough handling is made and the critical defect sizes and locations are determined from fracture mechanics. The upper part of Figure 1 shows a stress profile for the M549 155mm Projectile under launch conditions. Fracture mechanics is then applied to determine critical crack sizes. Critical crack sizes for certain locations in the M549 Projectile are shown in the lower section of Figure 1.

Ultrasonic standards for artillery shells are made by machining grooves into inert projectile bodies. In order to determine the required depth of these grooves (for a fixed length) the ultrasonic response from cracked shells and from grooves is compared (Figure 2). From this study, groove depths are determined that give reflection amplitudes nearly equivalent to those expected for "ideal" critical cracks. Because the data (Figure 2) shows a great deal of scatter, the worst case ratio of groove to crack response is chosen in order to be conservative.

The final design of the standards is determined by such factors as the size and location of the critical defects, the correlation study for groove and crack response, machining limitations and cost considerations. Figure 3 shows the placement of the grooves in two standards for the M549 Projectile.

(2) How standards are used:

The inspection procedures and the proper use of the standards are described in the Technical Data Package. A page from such a document is shown in Figure 4. The critical function of the ultrasonic standards is to set the accept/reject thresholds for the ultrasonic inspection. The accept/reject threshold is set at the level of the reflected signal from the standard. This means that the standards play a critical role in determining the overall rejection probability of the ultrasonic inspection.

Ultrasonic standards are also used for setup and calibration of the ultrasonic equipment. Periodically, the inspection system will use the standards to check proper alignment of transducers and threshold level settings. Figure 5 shows an example of a recent ultrasonic inspection station for the M549 Projectile.

(3) Problems with current standards:

The design of current standards is a difficult and costly process. As previously mentioned, standards are made by machining grooves into inert warheads. Unfortunately, as pointed out by expensive empirical studies, there is generally a poor correlation between the ultrasonic response from grooves and real cracks. Therefore, current standards do not closely simulate real cracks. This complicates the design process because it is difficult to determine the proper groove depth and length that best represents the response from a critical defect. Generally, the worst case ratio of groove to crack response is taken in order to be reasonably safe. This approach, however, may be overly conservative and may lead to an unnecessary increase in the false rejection rate (rejection of good shells).

Current standards are expensive to build because machining grooves to tight specifications is difficult and time consuming. Using the best technology available, it is still not possible to machine two standards with identical ultrasonic response. Each standard is truly "unique."

In conclusion, standards are needed that are less costly to design and build and, yet, are more realistic in simulating manufacturing defects.

Acknowledgement: The author would like to thank Mr. Mark Weinberg, ARRADCOM, Dover, New Jersey, for providing some of the Figures shown in this poster paper

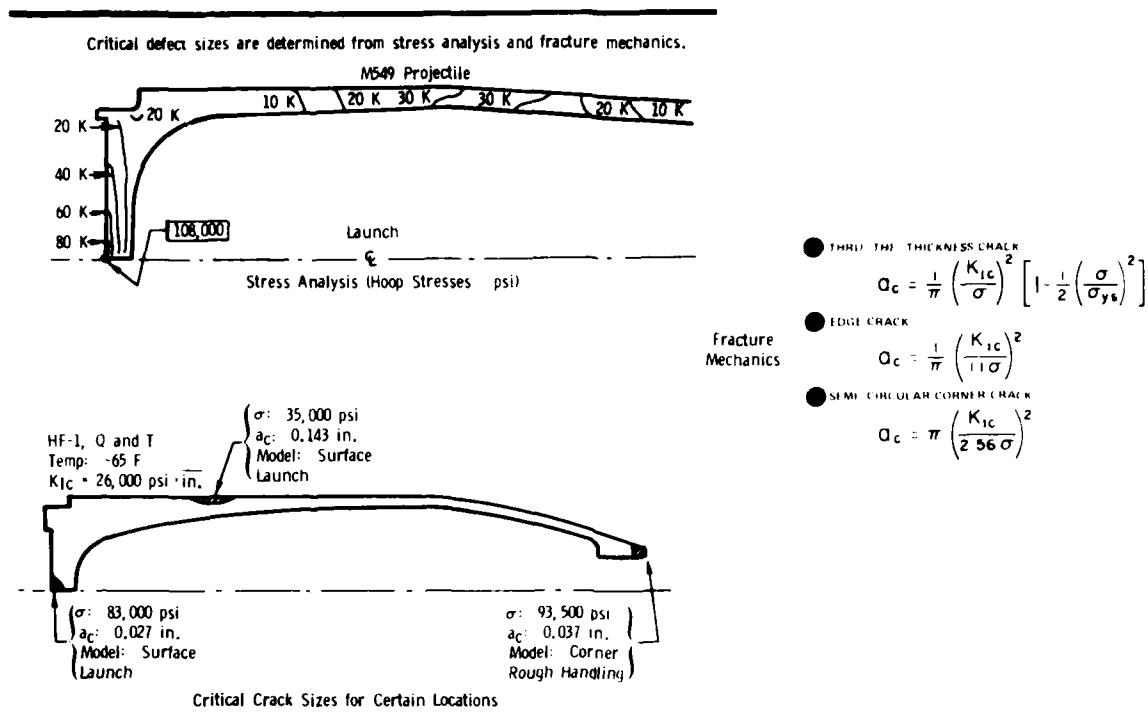


Figure 1. Stress analysis and critical crack sizes for M549 projectile.

Standards consist of grooves machined into an inert warhead.
 Correlation between ultrasonic response of grooves and real cracks is needed.

Sample	Zone	Equivalent Groove Depth	Actual Measured Crack Depth	Groove/Crack
1	Ogive	0.020	0.006	0.30
5	Ogive	0.020	0.020	1.00
10	Ogive	0.030	0.050	1.67
29	Ogive	0.030	0.060	2.00
32	Bourrelet	0.020	0	0
34	Ogive	0.020	0.050	2.50
40	Bourrelet	0.020	0	0
46	Ogive	0.010	0.040	4.00
68	Ogive	0.020	0.040	2.00
74	Bourrelet	0.020	0	0
93	Bourrelet	0.010	0	0
102	Ogive	0.030	0.060	2.00
176	Bourrelet	0.010	0	0

Data taken from ARRADCOM Report QAR-Q-013, "Defect Correlation Analysis for Fixed Channel Ultrasonic Inspection System for Warhead, 155MM, M549A1," R. Scott, April 1979.

Figure 2. Destructive analysis of cracked shells to correlate groove and crack response.

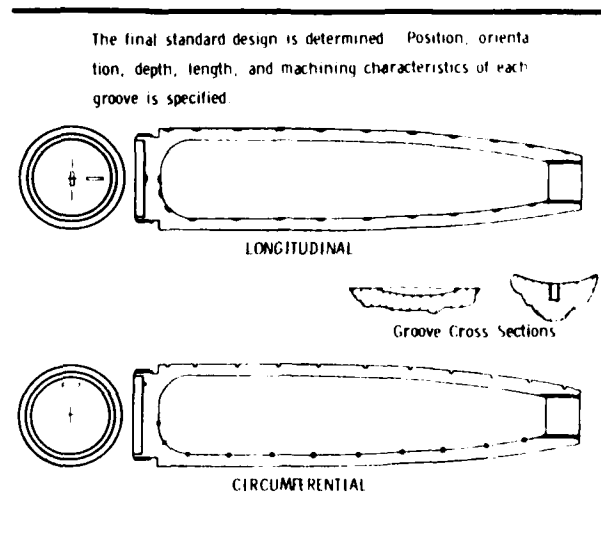


Figure 3. Ultrasonic inspection standards.

Included in a Technical Data Package is a description of the required inspection procedures. This document specifies the NDT methods to be used, the design of the standards, and the inspection equipment parameters. Standards are used to set the accept/reject thresholds, which determine to a great extent how reliable the inspection will be.

<p>2.5 THE SYSTEM SHALL ULTRASONICALLY INSPECT THE ENTIRE PROJECTILE IN BOTH LONGITUDINAL AND CIRCUMFERENTIAL DIRECTIONS. INSPECTION SENSITIVITY MUST BE ADEQUATE TO REJECT ALL SLOTS IN ULTRASONIC INSPECTION STANDARDS.</p>		
<p>2.6 THE SYSTEM MUST CONFORM WITH ALL PLANT, MUNICIPAL, STATE AND NATIONAL CODES AND SAFETY REGULATIONS INCLUDING OSHA REGULATIONS.</p>		
<p>2.7 THE SYSTEM SHALL PROVIDE A MEANS TO AUTOMATICALLY MARK A REJECT AS SHOWN ON BODY. PREFORM DWG 9323969 ONLY ON ACCEPTED BODIES. REJECTS SHALL BE PERMANENTLY STAMPED AND SEGREGATED AND NOT ALLOWED TO RE-ENTER THE PRODUCTION LINE.</p>		
<p>3. A TANK SHALL BE PROVIDED WHICH SHALL:</p>		
<p>3.1 BE FABRICATED OF CORROSION RESISTANT MATERIALS. DISSIMILAR METALS SHOULD NOT BE USED TO AVOID ELECTROCHEMICAL REACTION. JUN 6 1973</p>		
<p>3.2 BE LARGE ENOUGH TO ALLOW EASY INSERTION AND REMOVAL OF THE BODY AND TO CONTAIN THE SUPPORT FIXTURE AND THE TRANSDUCERS WITH THEIR MANIPULATORS, WITH SUFFICIENT ROOM FOR CONVENIENT ADJUSTMENT OF THE TRANSDUCERS.</p>		
<p>STANDARD TANK MUNITIONS</p>		
<p>ENVELOPE DRAWING ULTRASONIC INSPECTION EQUIPMENT OF BODY FOR PROJECTILE 105MM HEAT T, M456A2 METAL PARTS</p>	<p>A 19200</p>	<p>9323972</p>
<p>77-09-07 REVISION LEVEL - 2</p>		

Figure 4. Page from a technical data package.

Standards are used to set up and calibrate the ultrasonic inspection equipment. Periodic calibration of the equipment is specified in the Technical Data Package.



Figure 5. Example of ultrasonic shell inspection system.

A BASIS FOR TRACEABLE NDE STANDARDS

D. G. Eitzen, H. Berger and G. Dirnbaum
National Bureau of Standards
Washington, D. C. 20234

ABSTRACT

The National Bureau of Standards (NBS) is beginning to provide a mechanism for traceability for a number of NDE measurement procedures, an activity that is expected to have a significant, positive impact on the reproducibility and accuracy of NDE measurements. Much of the NDE standards activity has been in ultrasonics and acoustic emission, this effort leading to calibration services for ultrasonic reference blocks and ultrasonic and acoustic emission transducers. Additional NDE standards are also available or are being developed in radiography, eddy currents, magnetic particles, liquid penetrants and visual testing.

INTRODUCTION

The National Bureau of Standards has been involved in improving the reproducibility and quantitative aspects of nondestructive evaluation (NDE) measurements¹ in response to a growing need for improvements in this area. This report is concerned particularly with the development of NDE measurement procedures that incorporate traceability⁺⁺ to National Reference Standards. The work described is due to many NBS workers in addition to the authors. Points of contact for the various technical areas are listed at the end of this paper.

ULTRASONICS

Pulse/echo ultrasonic techniques offer great potential for detecting and evaluating material defects nondestructively. However, these methods are sensitive to measurement equipment characteristics and to the condition of the reference artifacts used. An effort to improve the reliability and diminish the uncertainty of these techniques has focused on the development of measurement services for transducers and reference blocks. The measurement services now available from NBS are described below:

1. Ultrasonic Transducer Power Output versus Frequency. By using a modulated radiation pressure technique, the absolute total power output of ultrasonic transducers versus frequency is measured over any part of a range from about 1-20 MHz. The transducer undergoes swept cw excitation. The uncertainty is frequency dependent but is nominally about ± 5 percent. In addition to this relative power versus frequency information, the measurement provides the value of the radiation conductance used to calculate absolute power output levels. The apparatus, procedure, error analysis and sample results are discussed in reference 2.

2. Ultrasonic Transducer and System Power Output by Calorimetry. By using a twin, series flow ultrasonic calorimetric comparator, the

time-averaged total absolute power output of a transducer system is measured for any voltage input waveform, e.g. pulsed, in the range of 1-15 MHz. The uncertainty is approximately ± 7 percent. The system, procedures, and uncertainties are described in reference 3.

3. Aluminum Ultrasonic Reference Block Calibration. Sets of ASTM E-127 type ultrasonic reference blocks are compared with a block designated as the NBS Interim Reference Standard and associated model by using a well-characterized measurement system. The service provides a mechanism for comparing sets of blocks with the NBS data base and with other reference blocks through the NBS ultrasonic system. The system and detailed procedures are described in reference 4.

4. Loaner Services for Transducers and Transfer Blocks. By arrangement, carefully characterized ultrasonic source transducers and aluminum block transfer standards can be made available for loan. By employing the accurately measured ultrasonic source transducers, a user's power or frequency measurement apparatus can be calibrated *in situ*. The transfer aluminum ultrasonic blocks, which have been carefully compared with the NBS Interim Reference Standard, provide a means for users to compare their reference artifacts with those of NBS on their own ultrasonic system, i.e. they provide a basis for traceability to the NBS Interim Reference Standard. Some of the source transducers are currently being employed in an international intercomparison on ultrasonic power measurement methods. The transfer blocks can provide a means for users to compare their reference artifacts with those of NBS on their own ultrasonic system, i.e. they provide a basis for traceability to the NBS Interim Reference Standard. Some of the source transducers are currently being employed in an international intercomparison on ultrasonic power measurement methods. The transfer blocks can provide the basis for a measurement assurance program. Calibration of users blocks can be accomplished by the user with an uncertainty of a few percent using an NBS developed procedure.

Additional work on ultrasonic measurement systems is in progress. An expansion of the NBS artifact system for ultrasonic reference blocks to steel and titanium reference blocks is being developed. The feasibility of developing improved steel and titanium reference blocks is to be established in 1979. Also under consideration are material-independent reference blocks made of

¹ This paper is to be published in a somewhat expanded version as an NBS report.

⁺⁺ There are several noninterchangeable concepts termed "traceability." The subject is carefully explored in "Traceability - an Evolving Concept" by B. C. Bellmer to appear in *Standardization News*.

amorphous, low-attenuation material; these could replace much of the present multiplicity of reference artifacts.

The influence of changes or adjustments to instrumentation on the variations in the amplitude of response from reflectors has also been studied in some detail. For example, changes in the pulse length adjustment of a flaw detector result in amplitude response changes from a reference block by over 13 percent, even after normalization. A study of the effects of different (but very similar) transducers was also conducted.⁶ The study showed variations of over 26 percent in response due to different transducers. This study has important implications; one of the key issues is: what are the necessary tolerances on the instrumentation in order to obtain the required reliability and uniformity in ultrasonic nondestructive evaluation (NDE)?

Another important area of study is the development of methods for determining the directivity pattern of ultrasonic transducers.⁷ A mathematically vigorous method called planar scanning is being developed as a laboratory method. It is capable of measuring the absolute value of all of the important field point parameters of transducers. Work is also proceeding on the development of techniques more appropriate for the user community.

Additional work on standards for quantitative ultrasonic NDE are being planned. This planning process has been greatly enhanced by a study just completed for DARPA. The objective of the project was to examine the present system of standards for ultrasonic NDE measurements, to assess the standards needs of emerging and more quantitative systems and to present recommendations for the development of an adequate system of standards for quantitative ultrasonic NDE systems. The results of the study have been reported to the sponsor and should soon be available to the public as an NBS report. Other outputs of this project include a separate summary of the open literature on ultrasonic NDE standards and a detailed study of foreign and U.S. standards documents both to be published as NBS reports and a chapter on ultrasonic transducers and their characterization in an upcoming volume of Physical Acoustics.

ACOUSTIC EMISSION

A calibration capability is being developed for acoustic emission (AE) transducers and will shortly be offered as a measurement service.⁸ This activity is partially supported by a larger EPRI/NBS Acoustic Emission Program and by the Office of Naval Research. The objective is to determine the sensitivity versus frequency of AE transducers over the approximate range of 100 to 1000 KHz. This is accomplished by obtaining time histories from the transducer under test and the NBS standard transducer, both mounted on a large (2200 Kg) steel transfer block. The input is a simulated source on the same surface of the block as the transducers. The resulting time histories are digitized and processed in frequency space to obtain the desired measure of spectral response. The simulated source and transfer block produce a vertical surface displacement that is theoretically calculable (Fig. 1). The displacement measured by the first candidate standard transducer is shown to faithfully reproduce the actual displacement as shown in

Fig. 2. A newly designed and constructed standard transducer has resulted in further accuracy; it provides measurements of absolute dynamic displacement of the order of a nanometer with an uncertainty of about 3 percent (Fig. 3).

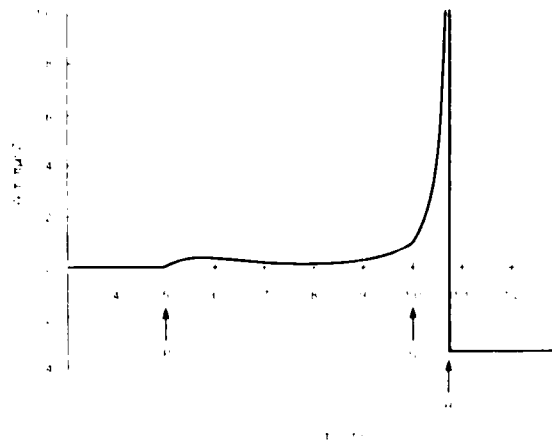


Fig. 1. Theoretical waveform of vertical displacement on the transfer block

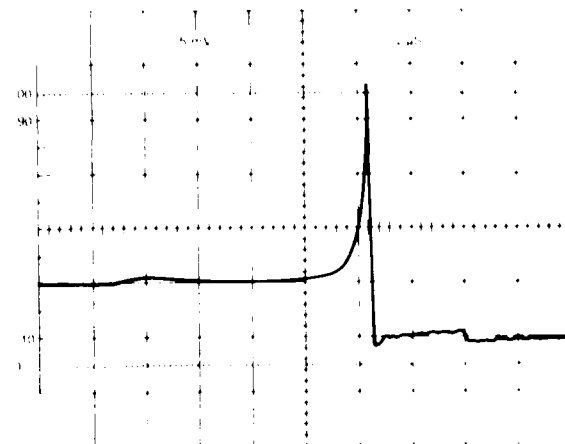


Fig. 2. Displacement of transfer block measured with model 1 NBS transducer. New NBS transducer gives even better agreement (not shown) with theory.

There is also a substantial theoretical effort associated with the ultrasonic and acoustic emission work. Theoretical developments using the scattering matrix description of electroacoustic transducers have impacted work on determining directivity patterns of transducers. Two recent theorems on the nature of the radiated field of generated acoustic sources suggest future calibration techniques for users. A recent theoretical description, which more accurately describes actual transducers, is making possible more realistic standards procedures (NBS and ASTM). Theoretical developments in dynamic elasticity are making possible the development of primary and secondary acoustic emission calibration methods.

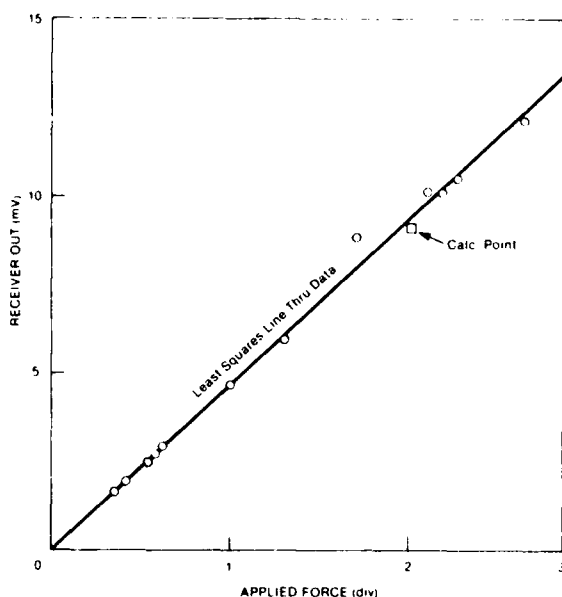


Fig. 3. Plot showing about 3 percent agreement in dynamic surface displacement between theory and measurement using new NBS standard transducer.

RADIOGRAPHY

A Standard Reference Material[†] available from NBS⁹ provides a mechanism for traceability of radiographic film density measurements. This is SRM 1001, a radiographic film step tablet covering the H & D density unit range from 0 to 4.0. Density measurements are reproducible to about 0.02 H & D units.

Additional standards-related work in radiography at NBS includes a recommended practice for thermal neutron radiography (now under consideration by ASTM, Committee E-7) and work to determine important characteristics of x-ray film⁹ (also being done in collaboration with ASTM E-7).

EDDY CURRENT TESTING

Facilities for dc and ac electrical conductivity measurements have been completed. Future work will include establishing measurement procedures for conductivity standards over the range of 1-100 percent of the International Annealed Copper Standard and methods for the calibration of eddy-current test equipment. Initial conductivity calibration services will be offered to accuracies of 0.5%. It is expected, as experience is gained in the measurements, that accuracy can be improved to 0.1%. In addition to the planned calibration facilities for electrical conductivity, the measurement of this characteristic will also be traceable by means of SRM conductivity samples, now under development.

[†]Standard Reference Materials are samples which have been characterized by the National Bureau of Standards for some physical or chemical property and are issued with a certificate that gives the results of the characterization.

Theoretical solutions^{10,11} for the fields and current distributions associated with defects in materials will also provide guidance for eddy current testing and development of artifact standards.

MAGNETIC PARTICLES

Work is under way to measure the brightness of fluorescent magnetic particles. This could lead to a calibration service, or more likely, to an SRM comparison standard for judging brightness.

In addition, studies of magnetic flux leakage are in progress. A recent report¹² described results of investigations of a test ring for judging the effectiveness of magnetic particles (as used in military specification). A model was developed to describe the magnetic response of subsurface defects in the ring; the model showed good correlation with experiment. The work is leading toward suggestions for making the testing more useful for general evaluation of magnetic particles.

LIQUID PENETRANTS

Brightness of fluorescent penetrants would follow the same pattern as indicated above for magnetic particles. In addition, work is under way to prepare a relatively inexpensive, well characterized, crack test plate for evaluating materials and consistency during operation as well as comparing the one product or process against another.

In this approach, alternate layers of copper and nickel are plated. The nickel is merely a separator between well characterized thicknesses of copper (to values as small as 0.3 μm). When these copper layers are etched, they provide well characterized slots or cracks in terms of width. The width can be determined to within 0.15 μm or 10%, whichever is greater. The depths of the cracks, determined by etching, are somewhat more difficult to control. However, for depth to width ratios of about 4, the minimum crack depth can be determined to an uncertainty of about 0.5 μm .

This plated assembly can be etched, measured and cut into small specimens such as indicated in Fig. 4. It is expected that this approach would result in a relatively inexpensive crack sensitivity plate.

PLATED PENETRANT CRACK PLATE

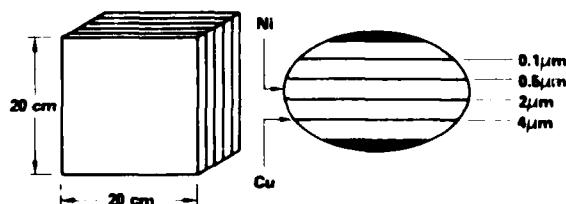


Figure 4. Crack sensitivity plate which is under development for liquid penetrants.

VISUAL TESTING

An important parameter in visual testing is the capability of the inspector to see detail that may be small in size, of low contrast and unsharp. The visual acuity of inspectors is now measured with a Jaeger chart in which the inspector is asked to read small black letters on a white background. This high contrast situation does not always simulate what an NDE inspector may be called upon to observe.¹³ He may be looking for a penetrant indication or a low contrast shading in a radiograph. Therefore, NBS is pursuing the development of a visual acuity measurement procedure that more closely duplicates the inspector's situation. The new procedure will involve varying the contrast as well as varying sharpness and width of indications. A report on this is planned for late 1979.

CONCLUSIONS

Several mechanisms for achieving traceable NDE measurements are now available from NBS. These, along with additional measurement services and improved procedures and techniques will help industry achieve traceability and result in more reproducible and meaningful NDE measurements.

Additional information on the various technical areas may be obtained from:

Ultrasonic Block Calibration and Transfer Blocks	D. Chwirut (301)921-3646 Sound A147 NBS Washington, D.C. 20234
Ultrasonic Transducer Calibration and Transfer Transducers	C. Tschiegg (301)921-3646 Sound A147 NBS
Acoustic Emission Transducer Calibration	F. Breckenridge 921-3646 Sound A147 NBS
Radiography Standards, X-ray	R. Placius (301)921-2201 RADP C216 NBS
Radiography Standards, Neutron	D. Garrett (301)921-3646 Reactor A106 NBS
Eddy Current Conductivity Measurements	G. Free (301)921-2715 MET B146 NBS
Eddy Current Theoretical Solutions	A. Kahn (301)921-2841 MATLS A251 NBS
Magnetic Particle Brightness Measurements	K. Mielenz (301)921-2143 CHEM B222 NBS
Liquid Penetrants Crack Test Plate	F. Ogburn (301)921-2957 POLY B168 NBS
Visual Acuity Measurements	C. Yonemura (301)921-2680 RR A313 NBS

We are indebted to these NBS colleagues for sharing information with us and for their efforts in forming a basis for traceable NDE measurements.

REFERENCES

1. H. Berger and L. Mordfin, editors, Annual Report 1978, Office of Nondestructive Evaluation, National Bureau of Standards report, NBSIR 78-1581, January 1979.
2. M. G. Greenspan, F. Breckenridge and C. Tschiegg, "Ultrasonic Transducer Output by Modulated Radiation Pressure," J. Acoust. Soc. Am., **63**, 1031-1038 (April, 1978).
3. T. L. Zapf, M. E. Harvey, N. T. Larsen and R. E. Stoltenberg, "Ultrasonic Calorimeter for Beam Power Measurements," National Bureau of Standards Technical Note 686 (Sept., 1976).
4. D. J. Chwirut, G. F. Sushinsky and D. G. Eitzen, "Procedures for the Calibration of ASTM E-127-Type Ultrasonic Reference Blocks," National Bureau of Standards Technical Note 924 (Sept., 1976).
5. D. J. Chwirut and G. D. Boswell, "The Evaluation of Search Units Used for Ultrasonic Reference Block Calibrations," National Bureau of Standards report NBSIR 78-1454 (Feb., 1978).
6. E. B. Miller and D. G. Eitzen, "Ultrasonic Transducer Characterization at NBS," IEEE Trans. Sonics and Ultrasonics, Vol. SU-26, No. 1, 28-37 (Jan., 1979).
7. F. R. Breckenridge, C. E. Tschiegg and M. Greenspan, "Some Applications of Lamb's Problem," J. Acoust. Soc. Am., Vol. 57, 626631 (1975).
8. "Catalog of NBS Standard Reference Materials," NBS Special Publication 260 (1979-80).
9. R. C. Placius, "ASTM Activity in Industrial Radiographic Film Characterization," to be presented ASNT Fall Conference, St. Louis, October, 1979.
10. A. H. Kahn, R. Spal and A. Feldman, "Eddy Current Losses Due to a Surface Crack in Conducting Material," J. Appl. Phys., Vol. 48, 4445 (Nov. 1977).
11. S. Spal and A. H. Kahn, Eddy Currents in a Conducting Cylinder with a Crack, J. Appl. Phys., to be published (Sept. 1979).
12. L. J. Swartzendruber, "Magnetic Leakage and Force Fields for Artificial Defects in Magnetic Particle Test Rings," 12th Symp. on NDE, Southwest Research Inst., San Antonio, April 1979, to be published.
13. G. T. Yonemura, "Considerations and Standards for Visual Inspection Techniques," in Nondestructive Testing Standards -- A Review, pp. 220-230, STP 624, American Society for Testing and Materials, Philadelphia, (1977).

TEST BED FOR QUANTITATIVE NDE*

R. C. Addison, R. B. Houston, J. M. Martin, R. B. Thompson
Rockwell International Science Center
Thousand Oaks, CA 91360

ABSTRACT

The ARPA/AFML Interdisciplinary Program for Quantitative Flaw Definition has demonstrated a number of new techniques for quantitatively sizing flaws, as are reported elsewhere in these proceedings. This paper describes a test bed program to assemble and demonstrate these techniques in a single integrated measurement system that will extend them from the idealized geometries that have been considered thus far to geometries that are a better approximation to those that are found in real parts. Included are discussions of the conceptual design of the system, the detailed design and construction of specific modules, and preliminary experimental results. The basic system consists of a Data General Eclipse S/200 minicomputer, a multi-axis microprocessor controller, a Biomation A/D converter, an immersion tank, and a contour following system with six degrees of freedom. A detailed description of the operation of the various components of the system will be given. Included are discussions of the conceptual design of the system, detailed design and construction of specific modules, and preliminary experimental results.

A limitation of mechanically scanned systems is the time required to acquire data. To overcome this, the Test Bed includes a piezoelectric array transducer, to be used both for the imaging of flaws and the gathering of scattering data for use in other flaw characterization algorithms. Such an array has been received, and the construction of the necessary array electronics is in progress. Included in the paper is a discussion of the digital signal processing approach being implemented, which takes advantage of recent advances in A/D converters and array processors to achieve the near real time formation of images with a high degree of flexibility for evaluating various signal processing algorithms.

The extended data gathering capability of the system has been demonstrated with several of the diffusion bonded samples that have been fabricated for the ARPA/AFML program. Preliminary measurements on a sample containing an 800µm spherical void were made. Subsequent analysis of these measurements using the Inverse Born Approximation predict a diameter of 320µm thus demonstrating the validity of the technique.

Conceptual Design

The ultrasonic test bed program has been initiated to complement the ARPA/AFML Interdisciplinary Program for Quantitative Flaw Definition. Specifically, we are implementing the variety of new techniques that have arisen for obtaining quantitative data about flaws such as the size, shape, orientation and stress intensity factor. These will be adapted into procedures for identifying flaws in parts of complex geometry such as turbine disks. The results will serve a twofold purpose. First, a new inspection capability will be demonstrated. Second, in cases where the practical constraints of the part geometry degrade the quality of some of the measured flaw parameters, this information can be fed back into the research program to guide that effort.

In order to implement these techniques, we must establish a protocol for their use. Although we remain quite flexible with regard to the final form of this protocol, the system we are starting with is shown in Fig. 1.

The part is first searched and the locations of all regions that possibly contain flaws are stored in the test bed memory. Each of these

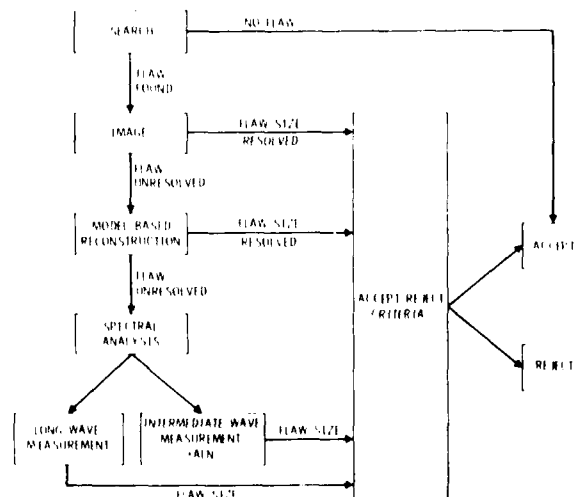


Fig. 1 System protocol.

*This work was supported by the Defense Advanced Projects Agency under Contract F33615-78-C-5164.

Physical Test Bed & Microprocessor Controller

Fig. 2 Test bed laboratory.

In operation, the turbine disk will be rotated at a speed that is selected on the basis of the desired resolution for the inspection as well as the maximum pulse repetition rate of the transducer. The transducer will be moved radially

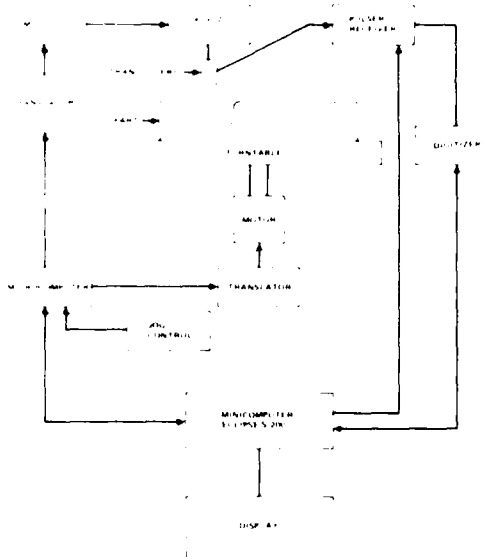


Fig. 3 Test bed block diagram.

It is the task of the microcomputer to accept these data blocks and convert them into interleaved trains of pulses that are sent to the stepping motors controlling the relevant axes. This must be done in such a way that the transducer follows the contour of the part with the required offset and with an accuracy that is within four stepping motor increments of the specified contour. A block diagram of the microcomputer system is shown in Fig. 4. The software for controlling these detailed motions is resident in the 16K PROM memory of the microcomputer and is entirely written in assembly language to make it as compact as possible.

The system has now been delivered to the Science Center. We are just beginning to learn how it operates with all six axes moving. We expect that there will be a period of debugging before the system is fully operational.

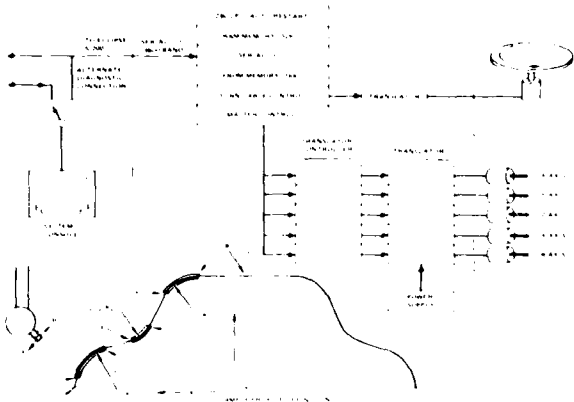


Fig. 4 Sample profile and microcomputer block diagram.

The software for controlling the operation of the Test Bed is resident in the S/200 minicomputer in the form of a multitasking program. A diagram of this program is shown in Fig. 5. The program allows 1) use of a master terminal to send commands to the host CPU (S/200) or the microcomputer (designated controller CPU in Fig. 5). Examples of these commands would be requests for the current coordinates of the transducer, Halt commands, or Continue commands. The microcomputer can 2) send data to the master terminal or to the disk memory. Examples of this would be error messages, confirmation that data was received, or transducer coordinates. Task 3) stores the control blocks for specifying the profile of the part on the disk memory, which can be read by the Host CPU and sent to the microcomputer. Task 4) allows the Host CPU (S/200) to send trigger pulses to the Biomation A/D converter and to the pulser. Task 5) allows the Host CPU to accept digitized data from the A/D converter and stores this data on the disk memory. After accepting the digitized data the host CPU will analyze the data. If it exceeds a predetermined threshold which may be a function of the location within the part, then the host CPU can request the microcomputer to send it the current coordinates of the transducer and, upon receipt, store these on the disk memory.

Ultrasonic Array

One of the objectives of the test bed program is to utilize an ultrasonic array for imaging and scattering measurements. The electronics for driving this array will have a somewhat different objective than some of the array based systems that are currently available. Our chief purpose will be to obtain a waveform that has as little distortion as possible, whereas for many systems the objective is to obtain an image in as little time as possible. In systems of the latter type one depends on the image enhancement ability of the eye/brain system to filter out the effects of the distortion that results. In the system that is being designed and built for the test bed, we would like to be able to display a single frame of an image and be able to recognize the important details of the object under study. In addition the system will be required to collect scattering

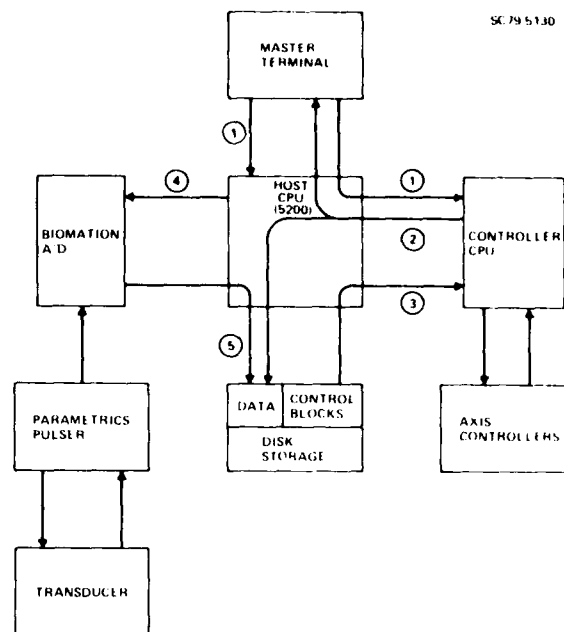


Fig. 5 Test bed multitasking control program.

data that can be used with the various inversion techniques.

The system is based on an ultrasonic array with 240 elements. This array will have a center frequency of 2.5 MHz and will be able to scan an ultrasonic beam over $\pm 25^\circ$. The bandwidth will be adequate to produce pulses that have about 5 half cycles. Only 16 contiguous transmit and 16 contiguous receive elements will be used at one time. Since the particular group of 16 transmit and receive elements will be programmable, it will be possible to scan a beam over a part with a curved surface such as the one shown in Fig. 6. It will be possible to correct for the wavefront distortion caused by refraction at the curved surface of a part by suitably delaying each of the received signals.

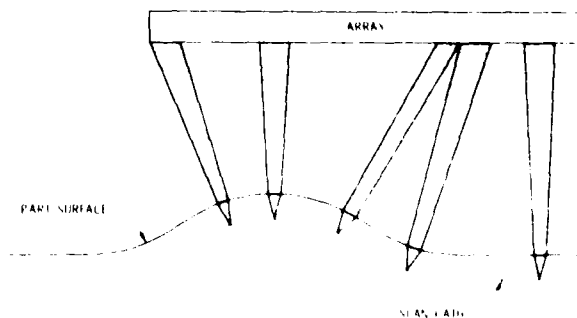


Fig. 6 Linear array used for reflection mode imaging.

The array would be used to collect scattering data by the technique illustrated in Fig. 7 or by other similar techniques. In Fig. 7 one group of

elements is being used to insonify the defect and other groups are being used sequentially to collect scattered signals at various angles. If the array is rotated about an axis passing through the defect, then a complete set of scattering waveforms can be collected for use by the Inverse Born Approximation or by the POFFIS algorithm.

A block diagram of the ultrasonic array system is shown in Fig. 8. The S/200 minicomputer will send out a set of codes that will select the desired set of transmit elements, the desired set of receive elements and the set of time delays that will define the transmit beam direction. These codes will be stored in the control memory. The timing and control block will interpret the codes and activate the transmit and receive multiplexers so that the appropriate array elements are selected. This block will also send

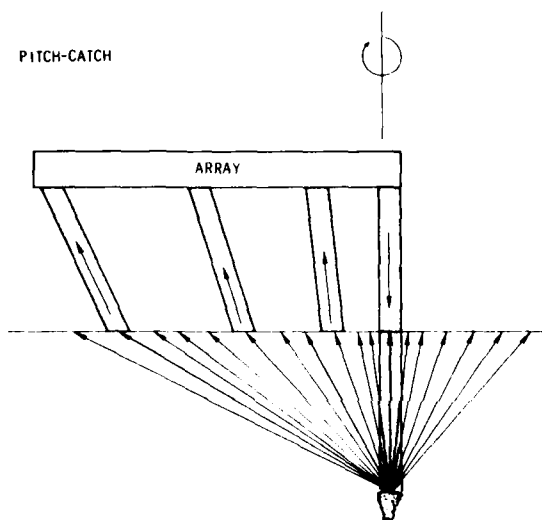


Fig. 7 Linear array used in a pitch catch mode for obtaining scattering data.

suitably delayed trigger signals to each of the 16 selected transmitter elements to synthesize an ultrasonic beam with the desired direction. The trigger signals which are positive going TTL level pulses will activate the pulser and cause a high voltage (200-300V) pulse to be applied to the transducer. The returning ultrasonic signal from the object under investigation will be received by each of the 16 selected receive elements. The received signals will each be amplified by 26 dB by a low noise, low distortion, hybrid preamplifier. They will then pass through the receive multiplexer to a line driver that will send them each to an 8 bit, 19 MHz A/D converter which will digitize the signal and load it into an 8 x 1K bit fast random access memory. All 16 of the A/D converters are started synchronously after a delay corresponding to the round trip time of the ultrasonic signal between the transducer and the front surface of the part. The contents of each of the sixteen memories will be sequentially clocked through the interface to the array processor at a rate compatible with the operation of the array processor and minicomputer (approximately 0.5 MHz). The array processor will have the task of

shifting the waveforms and summing them to synthesize a beam from a specified direction. The array processor will also interpolate between data points in the waveform if the desired shift is not an integral number of clock cycles. This will reduce the sidelobe levels in the array response. The array processor will also be used to correct for amplitude errors in the response of a particular array element. The processed signals will be sent to the S/200 minicomputer for storage on the disk memory and to be displayed on the color display. The raw waveforms can also be sent to the S/200 for storage on the disk memory. The display unit can be programmed in a rather general way to display the data in many different formats. For image data, we anticipate that both B and C scan displays will be useful. For scattering data, other formats will be used to convey the maximum information about the signals. (We are currently exploring various techniques for doing this but have not yet reached any conclusions.) The 240 element array was just recently received. We plan

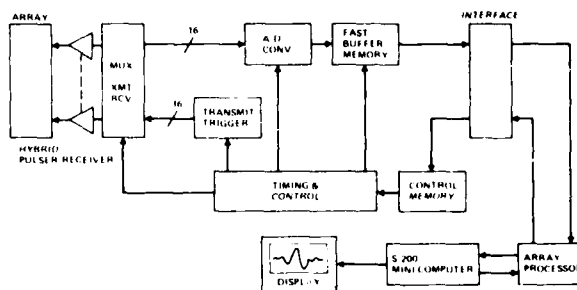


Fig. 8 Ultrasonic array signal processing systems.

to test it out as soon as we can. The documentation received from Battelle Northwest indicates that the acceptance angle for an individual element to the 6 dB level exceeds $\pm 30^\circ$ in water. The 6 dB bandwidth is between 30% and 35% with a center frequency of 2.6 MHz.

We are developing a hybrid pulser/receiver for use with the array. We were fortunate to be able to evaluate a unit furnished to us by William Sturrock of Northrup. This unit was in a 1 cm x 1 cm x 3 mm flat pack that we deemed to be small enough for our application. We are refining the design of the circuitry to have lower power consumption, a wider bandwidth receiver, and a pulser with more reproducible characteristics. Although the design of the receiver is firm, the details of the design of the pulser to accompany the receiver are still being modified. The crux of the problem is to obtain an active element 1) that can be used to generate a sufficiently sharp shock excitation pulse to fully excite the bandpass of the transducer, 2) that will hold off 300 volts and 3) whose characteristics will be virtually identical from one unit to the next. We are currently considering high voltage transistors operated in the linear mode, high voltage transistors operated in the avalanche mode, and silicon controlled rectifiers.

The design of the multiplexer to be used in the system is complete. The multiplexer can be divided into three separate units each of which is a 240 to 16 multiplexer. The first of these is a

digital unit that is used to select the transmit elements. The second is also a digital unit that is used to select the receivers that are to be turned on. The third is an analog unit that will connect the active receivers to the A/D converters. The technique used for multiplexing is shown schematically in Fig. 9. Although each of the numbered rectangles could correspond to a single transducer element, we have decided to have the unit switch four elements at a time to reduce the space required. Consequently each of the numbered rectangles corresponds to four transducer elements. Each of the switches shown has 15 switch positions although only 5 are explicitly shown. This implies that there are 60 distinct groups of transducers that can be selected. The switching is accomplished by initially sending a master code on the line labeled D that selects the same corresponding position for each of the four switches. Note that this automatically selects four contiguous groups of elements or 16 elements. If we want to select a group of 16 elements that corresponds to a shift of an integral multiple of 16 elements (4 groups) then the master code is simply advanced or retarded by n where n is the appropriate integer. If we want to shift by less

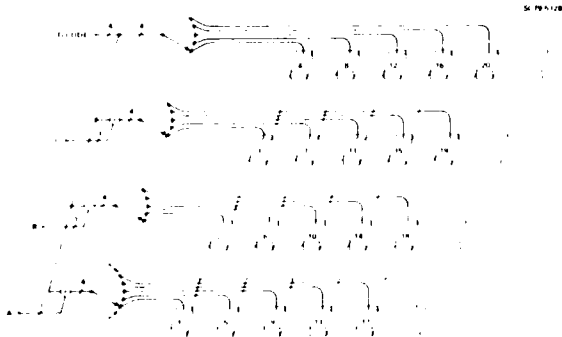


Fig. 9 Ultrasonic array multiplexer.

than an integral multiple of 16 elements, auxiliary codes can be sent on lines A, B, and C. A one on line A will provide a shift of 4 elements. A one on lines A and B will provide a shift of 8 elements. A one on lines A, B, and C will provide a shift of 12 elements. In this way it is possible to select groups of 16 contiguous elements in groups of four at any location on the array. Note that we are not required to have more than one wire connected to each element. Furthermore we only need eight, 8:1 multiplexers for each of the three separate units.

The 16 receiving elements will each be connected to an 8 bit analog to digital converter operating at a clocking rate of 19 MHz. We are using the TRW Model TDC 1007J A/D converter that was mentioned in Interim Technical Report #1. Each of the A/D converters will clock the digitized signals into a fast 1K byte random access memory that will store the signal until it is clocked out to the array processor or the S/200 minicomputer at a rate compatible with their operation. The circuitry for operating the A/D

converter, the circuitry for the interface between the A/D and the RAM, and the circuitry for operating the RAM has to be designed as a unit because of the clocking speeds that are being used and because everything has to work together. To help in optimizing the design, a prototype of the digitizer and memory for a single channel was constructed. A block diagram showing the major elements of this prototype is shown in Fig. 10.

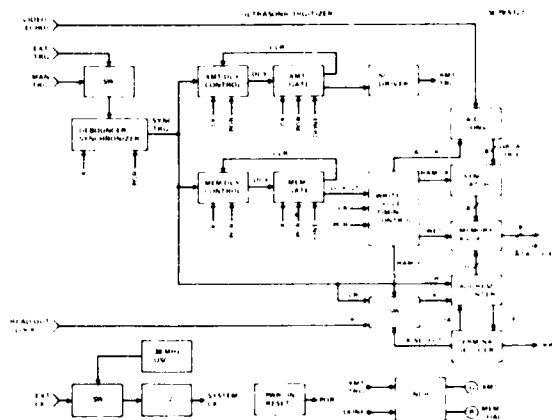


Fig. 10 Ultrasonic digitizer.

Other than the A/D converter and the memory, the important blocks are the latch between the two units, a delay circuit for determining when the memory will start loading after an external trigger is received, and a delay circuit for determining when the transmit trigger will be sent to the pulser.

The performance of the unit was evaluated using the experimental setup shown in Fig. 11. A standard 2.25 MHz transducer was connected to a Panametrics pulser whose output was connected to the digitizer. The memory of the digitizer was

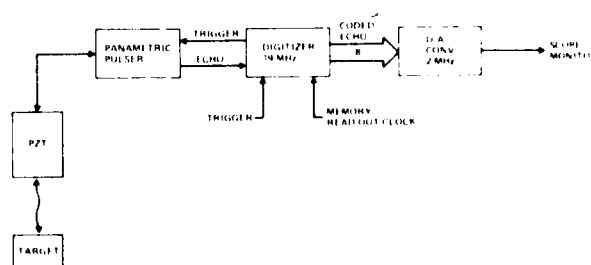


Fig. 11 Ultrasonic digitizer test system.

clocked out to a digital-to-analog converter at a 2 MHz rate. The resulting analog signal showing a quantization due to the sampling was displayed on an oscilloscope. In Fig 12, the upper trace shows the signal sent in to the digitizer while the lower trace shows the signal after being digitized, stored in memory, and reconstructed. The reconstructed signal is a good replica of the input signal with the quantization added. This circuit has been very useful for optimizing detailed design features of the digitizer such as

timing, gain setting circuitry at the input, and grounding techniques for minimizing noise effects. A photograph of the completed unit and the D/A converter is shown at the bottom of Fig. 12.

Simulated Turbine Bore Samples

One of the objectives of the program is to be able to inspect real parts and in particular to be able to inspect the inner bore of a turbine disk. The demonstration of this capability is somewhat difficult since it seems to be virtually impossible to obtain a turbine disk with a known flaw in the bore. To get around this problem we have fabricated some simulated turbine bore samples with known flaws in them. We have done this using the diffusion bonding process that Neil Paton developed earlier in the ARPA/AFML program.

The samples are shown in Fig. 13. Each sample has a cylindrical wall which has a 3.5" radius oriented differently with regard to the diffusion bonded surfaces represented by the bond lines. Each sample contains nine defects at varying depths. These defects range over the whole gamut of defects that have been previously tried. A list of the defects is given in Table 1.

We have been very careful to document all of these flaws as illustrated in Fig. 14 for the case of a prolate ellipsoidal void. Both dimensions of the void have been measured after the cavities were machined into the titanium and a micrograph has been made of the circular cross section. The samples have all been diffusion bonded and we are preparing to machine the cylindrical surfaces into them.

Early Data

The microprocessor controller is not fully operational yet but we have been able to collect some data from one of the diffusion bonded disks containing an 800 μ m spherical void. This can

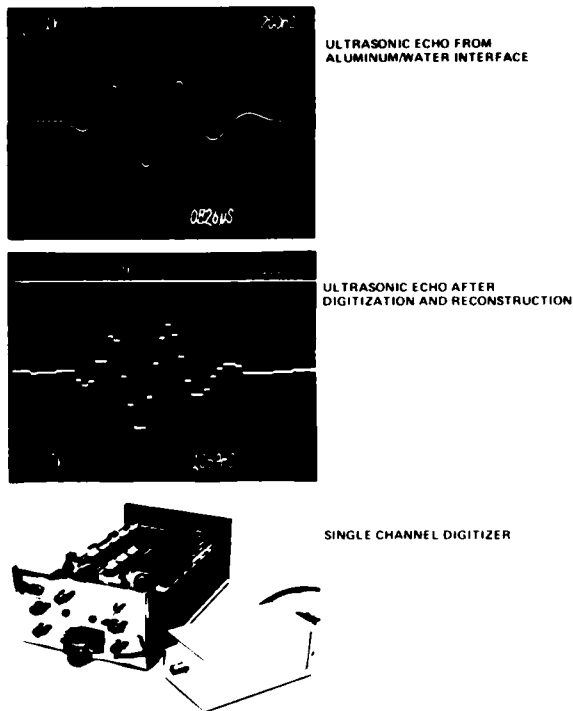


Fig. 12 Performance of single channel digitizer.

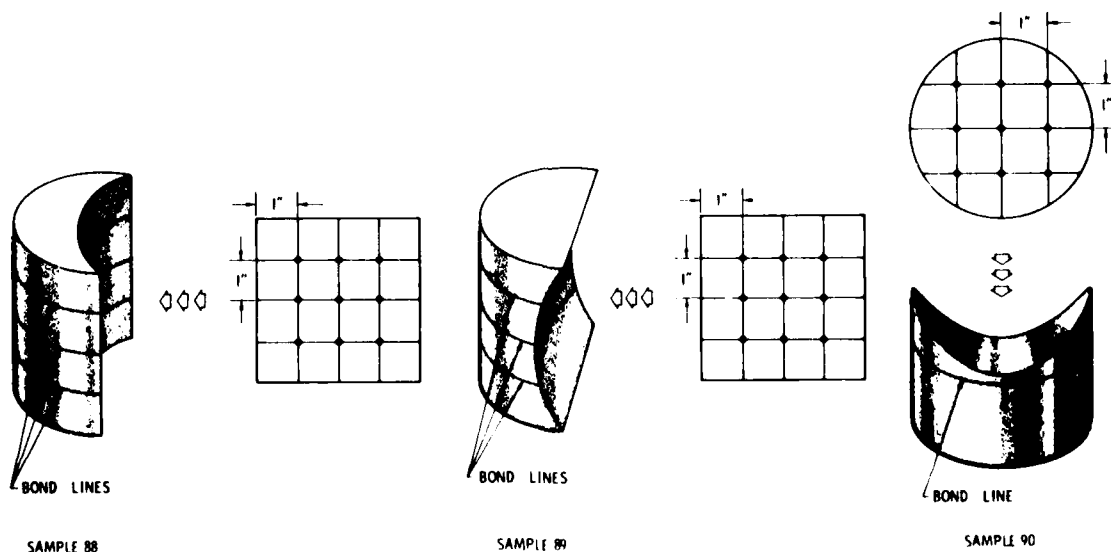


Fig. 13 Simulated turbine bore samples.

TABLE 1
List of Flaws Contained In Simulated Turbine Dore Samples

Sample No.	Defect No.	Defect Type	Distance From Surface (mm)	Diameter (μm)	Height (μm)
88	1	Prolate Spheroidal Void	6.4	800	1600
88	2	Penny Shaped Crack	6.4	800	100
88	3	Oblate Spheroidal Void	6.4	800	300
88	4	Spherical Void	2.5	400	400
88	5	Penny Shaped Crack	6.4	1200	100
88	6	WC Spherical Inclusion	6.4	400	400
88	7	Simulated Fatigue Crack	6.4	1200	---
88	8	Simulated Fatigue Crack	0.4	1200	---
88	9	Al_2O_3 Spherical Inclusion	6.4	400	400
89	1	Al_2O_3 Spherical Inclusion	6.4	800	800
89	2	Penny Shaped Crack	6.4	1200	100
89	3	Spherical Void	6.4	800	800
89	4	Simulated Fatigue Crack	6.4	1200	---
89	5	Simulated Fatigue Crack	0.4	1200	---
89	6	Spherical Void	6.4	1200	1200
89	7	WC Spherical Inclusion	2.5	1200	1200
89	8	Penny Shaped Crack	6.4	800	100
89	9	WC Spherical Inclusion	6.4	800	800
90	1	Oblate Spheroidal Void	9.7	800	200
90	2	Simulated Fatigue Crack	6.4	1200	---
90	3	Spherical Void	9.7	400	400
90	4	Prolate Spheroidal Void	9.7	800	1600
90	5	Penny Shaped Crack	6.4	1200	100
90	6	Spherical Void	9.7	800	800
90	7	Spherical Void	9.7	1200	100
90	8	Penny Shaped Crack	6.4	800	100
90	9	Al_2O_3 Spherical Inclusion	9.7	800	800

serve as an example of the approach described earlier for locating and analyzing a flaw. Initially the sample was scanned in a raster pattern with an unfocused transducer. The signals were digitized and the maximum peak height of the signal for each transducer position was stored in memory. After the scan was completed these peak heights were displayed to form an image of the disk shown in Fig. 15. There is an indication that a flaw is present in the center of the disk. Therefore a focused transducer was substituted for the unfocused one and a small region in the center of the disk was scanned in a raster pattern. The resulting image is shown in Fig. 16. Since the characteristics of the focal spot of the transducer have been previously determined, it is known that the flaw is not resolved and we are only seeing the profile of the focal spot. Subsequent analysis showed that $ka = 2$ for this flaw and it is known that the imaging mode cannot be used for ka values less than 6. The next step was to use the flat transducer and obtain a set of scattering data from the flaw. We chose to analyze this data using the Inverse Born Approximation. The bandwidth of the data extended from 1.8 MHz to 6 MHz. The characteristic function resulting from this analysis is shown in Fig. 17. The predicted radius of the flaw is $410 \mu\text{m}$ which agrees very well with the actual radius of $400 \mu\text{m}$. This analysis was based solely on the scattering data from a single direction. In regular practice one would combine the analysis of many different directions to also obtain an estimate of the shape and orientation of the flaw. As soon as it is feasible to do so we plan to extend our measurements to nonspherical flaws and to parts with complex geometries.

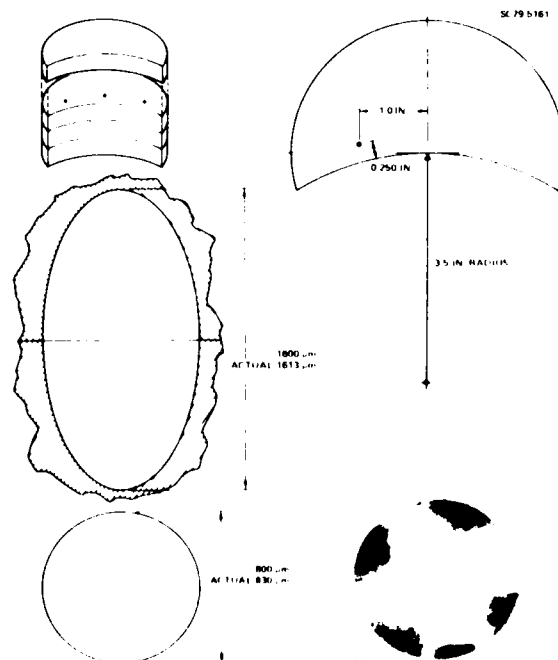


Fig. 14 Sample 88-1 $800 \mu\text{m} \times 1600 \mu\text{m}$ prolate spheroidal void.



Fig. 15 Ultrasonic image of diffusion bonded disk #48.

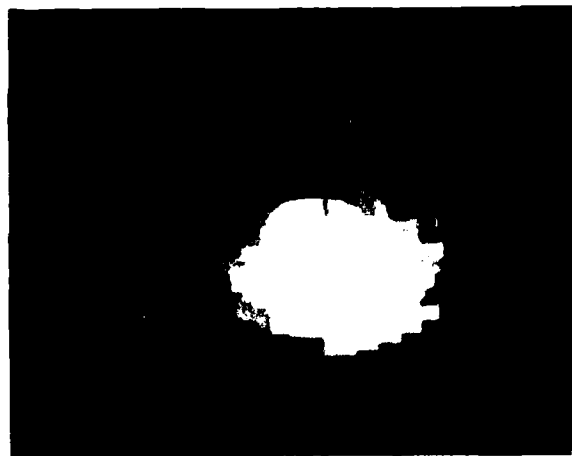


Fig. 16 800 μm diameter spherical void in titanium disk #48.

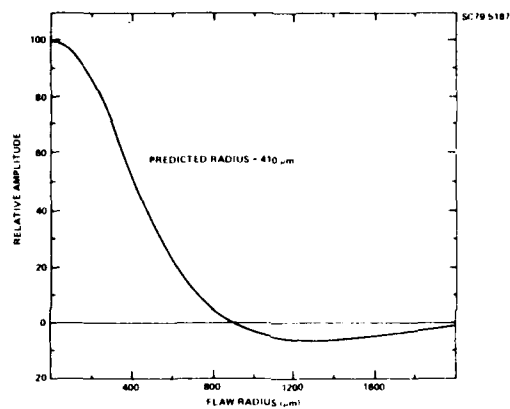


Fig. 17 Inverse born approximation characteristic function for nominal 800 μm diameter flaw.

SUMMARY DISCUSSION
(R. Addison)

John Brinkman (Session Chairman--Rockwell, Albuquerque Development Laboratory)
We have time for a couple of questions.

Paul Holler (Inst. fur Zerstörungsfreie Prüfverfahren): What type of array processor were you using?

Bob Addison: It will be an analogic array processor. I can't give you all the details on it, but there are people here who can. It has been ordered and we anticipate delivery in about a month.

#

AUTOMATIC INTERPRETATION OF ULTRASONIC IMAGING*

Stephen S. Lane
Adaptronics, Inc.
McLean, Virginia 22102

and

Douglas K. Lemon
Battelle-Northwest
Richland, Washington 99352

ABSTRACT

The objective of this work is to develop an advanced automatic ultrasonic inspection system via adaptive learning network signal processing techniques. This system will provide the type, location, and size of defects in metal more quickly and to smaller defect size than current imaging systems, without the need for operator interpretation of the results.

An ultrasonic imaging array constructed for this project has been used to record data from artificial defects in carbon steel test blocks. Software has been written to automatically determine the orientation and size of cracks from these digitized waveforms. Detection of these cracks has been unambiguous down to $1/6$ wavelength or 0.25 mm. Sizing for depth is accurate to 12% down to $1/3$ wavelength.

Further research will extend these results to other defect types and to smaller defects. The significance of this work is that it will demonstrate the feasibility of a totally automatic detection, classification, and sizing system which will work with hardware ordinarily used for imaging. This system will provide a numerical estimate of the defect parameters rather than an image requiring operator interpretation, and it will do so at defect dimensions smaller than the limits set by the resolution of imaging systems.

INTRODUCTION

It is generally recognized that the ultrasonic energy pattern or signature reflected from a given target contains substantially greater information than is being utilized by present ultrasonic nondestructive testing techniques. When an ultrasonic sound beam illuminates a given target, the pattern generated by the target contains reflected, diffracted, and redirected energies which include time, amplitude, and frequency spectral information that uniquely describes the reflector. Linear arrays afford the opportunity of capturing the pattern reflected from a flaw or target.

It was anticipated at the start of this program that parameters of the scattered waveforms, as well as those of the reflected energy, could be used to size defects. This has proven to be the case as will be shown in this paper. Parameters from the mode-converted diffracted adaptive learning networks to classify these cracks as to their orientation and provide estimates of their depth. Furthermore, the work reported here shows that these parameters can be extracted from the raw waveforms automatically. It remains in this project to extend these results to other types of defects and to implement the algorithms developed so far in hardware.

DATA COLLECTION

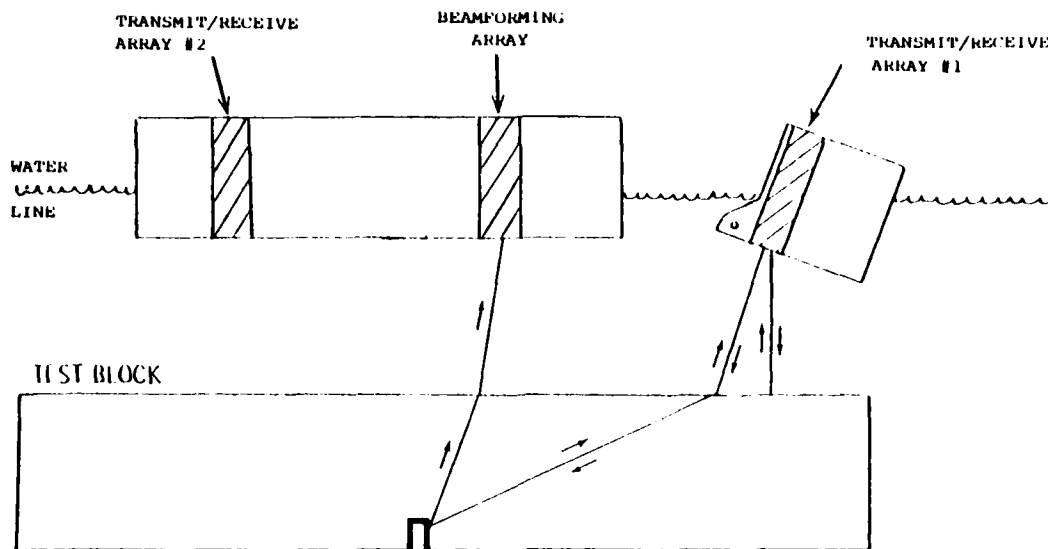
The experimental apparatus has been described in last year's Proceedings of this conference¹ and

only changes in that description will be presented here. All data were collected by D. K. Lemon of Battelle. The outboard array previously referred to was positioned as close as possible to the main receiving array, and receiving elements on the main array were wired as shown in Fig. 1. A shear (S) wave beam at 34° from the vertical was directed into the metal; pulse-echo data from the outboard array and pitch-catch data from receivers on the main array were collected for all EDM notches, both at 0° and 30° from the vertical. This constituted a total of 32 artificial defects. Data were taken on the main array for receivers successively further from the outboard array until no defect-related signal could be observed. Approximately 700 waveforms were recorded in this way. All defects were detected with good signal-to-noise ratio.

SOFTWARE DEVELOPMENT

Software to simulate, as far as possible, the intended functions of the ALN 4000 in this application was written to analyze these data. Since the array was positioned by an operator this function could not be simulated. In the hardware implementation, the ALN 4000 will acquire the desired waveforms by addressing particular receivers. Here, all waveforms were prerecorded and were acquired by searching through a list for the desired receiver. All other functions described below will be implemented in software much as they are here.

*This research is supported by the Defense Advanced Research Projects Agency under Contract No. MDA-903-78-C-0223, DARPA Order No. 3442.



CURRENT

Given: Beam Angles
Two Water Depths, Steel Depth
Receiver-Transmitter Distance

Find: Phase Arrival Time

FUTURE

Given: Beam Angles
Two Water Depths, Arrival Times
Receiver/Transmitter Distance

Find: Defect Depth

Fig. 1 Test block and ultrasonic arrays.

The system performs the following functions in this sequence:

- detect defect in pulse-echo mode;
- acquire pitch-catch waveforms;
- identify defect-related energy;
- extract features; and
- classify and size.

The specific implementation of these steps is shown in Fig. 2. Defect detection is performed by moving the array by a step size as determined by the ultrasonic spot size and acquiring a pulse-echo waveform. This waveform is passed to a signal detector which selects those portions of the waveform where the signal-to-noise ratio is high enough that a signal may be claimed to be present. The detection-association-processor (DAP) determines which, if any, of those signals may be due to a defect of interest. Other signals may be due to geometric reflectors or uninteresting defects such as layers of precipitate. If no defect is present, the array is moved to another nearby position. If a defect-related detection is found, the array is stopped and additional waveforms are acquired.

In the present configuration, eight waveforms from the receivers labeled "beamforming array" in Fig. 1 are recorded and used to form an ordinary time-delay-and-sum beam pointed at the defect at the compressional (P) wave velocity. The mode-

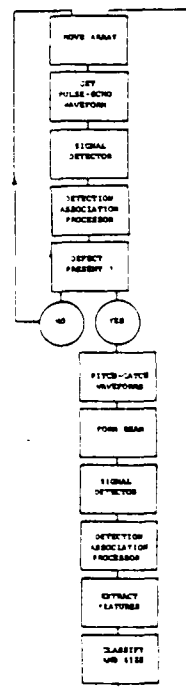


Fig. 2 Inspection system logic.

converted diffracted energy preferentially passed by this beam is expected to provide significant sizing and classification information. This beamed waveform proceeds to the signal detector which locates time windows with signals as before. The detection association processor again finds those signals due to the defect, and these signals provide the features used in classification and sizing, the last step in the process.

Figure 3 shows some details of the signal detector. The only reasonable criterion for the presence of a signal is a signal-to-noise ratio (DET) above some preassigned threshold, so the task of a signal detector is to calculate the noise power and the signal power. This is done by executing the loop shown in Fig. 3 once per time point. The signal power (STA) is simply the average power over some time window, generally about the length of the expected signal. The noise power (LTA) is the average power over some much longer time interval preceding the current time, and chosen so as to exclude any signals. The noise power as well as the signal power must be continually updated in order to account for the inevitable nonstationarity in the noise. Nonstationarity occurs for a variety of reasons in real experiments, and in this case is caused by distance-dependent attenuation and inhomogeneities in the metal, among others.

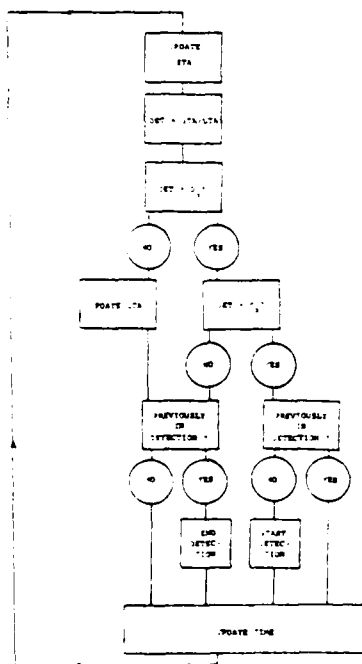


Fig. 3 Signal detector logic.

Bursts of noise of short duration may occur in the data, and these should not be included in the noise estimate. Neither should they be declared to be signals, so separate thresholds are set for freezing the noise estimate and for declaring detections. It is found that setting the detection threshold about 4 dB above the noise-freezing threshold does result in satisfactory

performance. When the signal-to-noise ratio crosses the detection threshold, an entry is made in the detection log, claiming the beginning or ending of a signal, depending on whether the signal-to-noise ratio was increasing or decreasing.

Figure 4 shows a sample waveform from a beam of eight elements directed toward an EDM notch 0.76 mm deep. The waveform with windows where a detection was claimed is shown in the top of the figure, and the signal-to-noise ratio in the bottom. The horizontal line at the bottom corresponds to the detection threshold, about 18 dB in this case. Corresponding arrows on the top figure show detections. The predicted arrival time for the mode converted energy is indicated by "SP time" and is seen to agree well with the actual arrival time of a pulse of energy.

It is the task of the detection-association-processor (DAP) to predict the arrival times of the various phases and decide which, if any, of the actual detections match those times. It therefore must contain a model of the experiment, including distances, geometry, and propagation velocities. Figure 1 shows the relevant ray paths for this experiment.

First, the DAP calculates the water depth. There is sufficient side-lobe energy from the out-board array to give a large response from the front surface, and this enables the calculation of the water depth, given the speed of compressional waves in water. Then the phase arrival time can be found from the metal depth, the shear wave velocity in the metal, and the beam angle in the water bath. In the future when defects at different depths are examined, a depth will be calculated for each arrival time and those in the range of interest accepted as belonging to defects.

When the DAP is entered with a detection log from a pitch-catch waveform, the requirements are somewhat different. The water depth and the defect depth are known, and it is required to find the arrival times of the various phases at a given receiver. Again, from Fig. 1 it can be seen that knowledge of the geometry, the transmitter-receiver distance, and the various velocities may be used to find these times. The signal closest in time to the predicted time, if it is within a preset tolerance, will be claimed to be the phase in question.

FEATURE EXTRACTION

Once the required signals were obtained, parameters were extracted. Previous experience (Shankar, 1979)² has shown that spectral parameters may be used to size cracks ultrasonically. Accordingly, power spectra of all arrivals were calculated and the parameters illustrated in Fig. 5 found. This figure shows the power spectrum of the SP waveform shown in Fig. 4 and is typical of SP phases. The frequency interval between 0.5 and 4.0 MHz has been divided into eight equal intervals, and the fractional power in each interval calculated. These powers are normalized parameters not dependent on gains or pulser settings. The integral of this parameter, i.e., the power in a band up to and including a particular frequency, was also calculated. Finally, the frequency at which the integrated fractional power achieved 1/8, 2/8, ... was found.

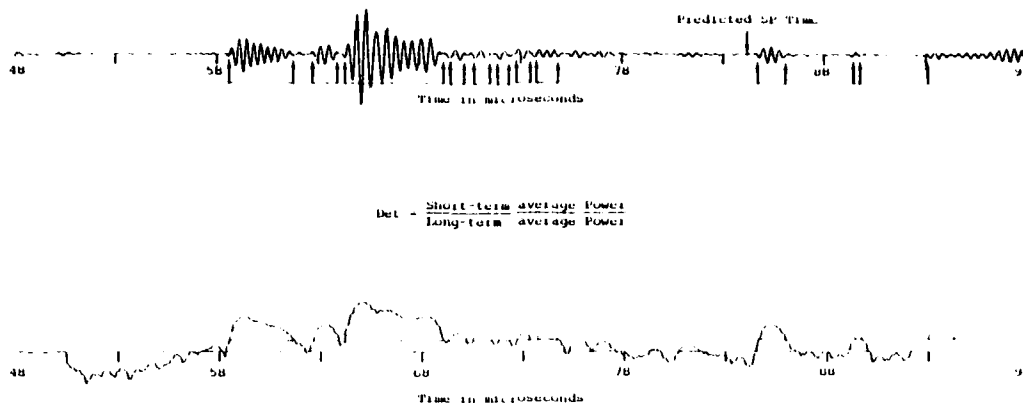


Fig. 4 Beamed waveforms.

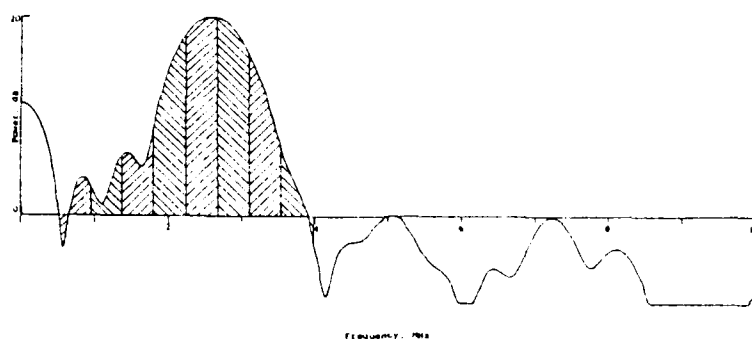


Fig. 5 SP power spectrum.

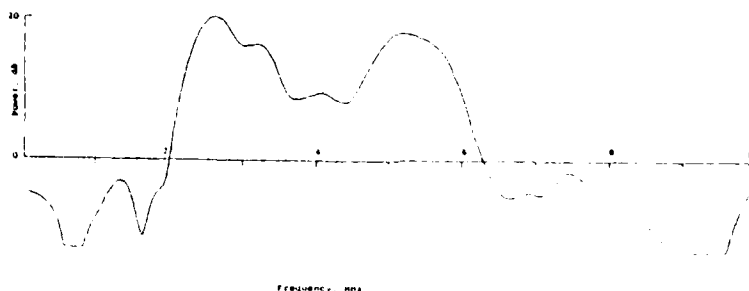


Fig. 6 SS power spectrum.

These parameters describe the shape of the spectrum. The first indicates the location of the spectral peak. The second, the integrated power, gives an idea of how sharply peaked the spectrum is. Rapid variation in this parameter indicates a narrow spectrum. The third has the opposite meaning. Large changes in this parameter indicate a slowly varying spectrum. As a group, they were found satisfactory for parameterizing the spectrum.

Figure 6 shows a typical SS spectrum recorded in the pulse-echo mode. The target was the same as that in Fig. 5, but the spectral shape is dramatically different. There is relatively much more energy in the frequency range above 4.0 MHz in the SS spectrum.

These spectra are as recorded so they contain the effects of the transducer, whose spectrum peaks at about 2.5 MHz and has a minor peak near 5.0 MHz. The energy in this minor peak is relatively less than its contribution in the SS spectrum, suggesting that the processes of mode conversion and diffraction at the target have shifted energy from the incident shear wave into the outgoing compressional wave much more efficiently at low frequencies than at high frequencies. Hence the low frequency SS level is lower than expected and the low frequency SP level higher than expected.

ADAPTIVE LEARNING NETWORKS

The SS spectra were parameterized in the same way as the SP spectra, except that the frequency range used was from 1.0 MHz to 6.5 MHz, reflecting the different distribution of energy in these spectra. All spectral parameters were input to Adaptronics adaptive learning network software which found networks which discriminated between cracks at 30° and 0° from the vertical, and which found the depths of the cracks in each class. Separate networks were necessary for each crack angle, a result that might be expected given the fact that discrimination on angle was possible. Networks for classification and sizing are shown in Figs. 7, 8, and 9, along with the parameters involved in them. In every case, parameters from the SP waveforms were found to be important, showing that mode-converted and diffracted energy is indeed useful in defect characterization. Finally, Fig. 10 shows the model depth as a function of the true depth for both crack orientations. The mean absolute deviation between model and prediction is about 12% here, which is satisfactory agreement.

SUMMARY AND CONCLUSIONS

Using the present array and software, present capability is:

- cracks can be detected automatically and unambiguously as low as 1/6 wavelength;
- cracks at 30° from the vertical can be distinguished from those at 0° from the vertical;
- cracks can be sized with about 12% mean deviation from the true depth as low as 1/3 wavelength; and
- the processes for acquiring the data to train the adaptive learning networks for these functions can be made automatic, as can be actual sizing and classification themselves.

REFERENCES

1. A. N., Mucciardi, S. S. Lane, and G. J. Posakony, "Overview of Planned Ultrasonic Imaging System with Automatic ALN Data Interpretation," DARPA Contract DSA MDA 903-78-C-0223, March 15, 1978 to May 14, 1980.
2. R. S., Shankar, in EPRI NP-964 1979 Interim Report, January 1979, on EPRI Contract RP1125-1, Application of Nonlinear Signal Processing to Pipe and Nozzle Inspection.

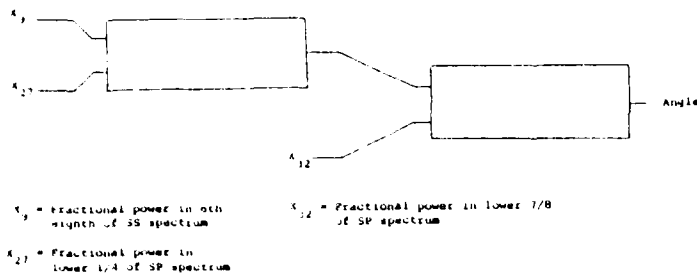


Fig. 7 Network to discriminate crack angle.

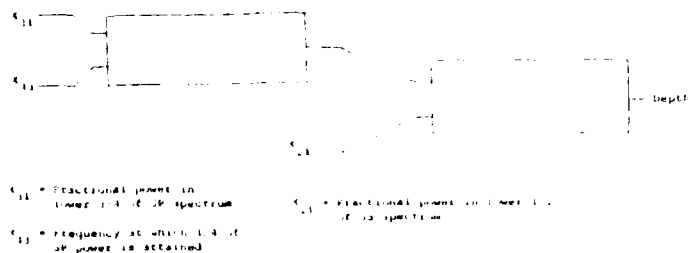


Fig. 9 Network to size 0° cracks.

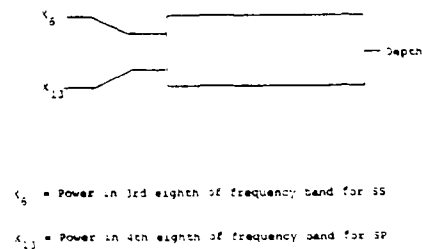


Fig. 8 Network to size 30° cracks.

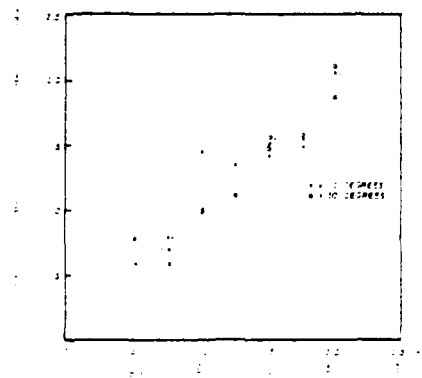


Fig. 10

Predicted versus known crack depths

SUMMARY DISCUSSION
(S. S. Lane)

Mark Weinberg (U.S. Army Armament R&D Command): Were all three transducers fixed in relation to each other in the scan?

Steve Lane: They were in this experiment. There is a capability of moving the transducer array, number one, which is mounted on a goniometer to about five different known positions from the main array.

Mark Weinberg: Do you see any particular difficulty in applying a sequence of this nature to other than a flat plane?

Steve Lane: The detection association processor would have to be modified to correctly predict the mode arrival times. But other than that, no. You would also have to know where you were with respect to the curved front surface, for instance. But presumably the pulse echo shots at the front surface could give you that information.

#

DEVELOPMENT OF ADVANCED NDE ULTRASONIC EQUIPMENT

A.S. Birks and G.J. Posakony
Battelle Pacific Northwest Laboratories
Richland, WA 99352

ABSTRACT

Recent studies to determine the probability of detection of nondestructive examination methods by the Air Force indicate that these capabilities are severely limited. One of the factors contributing to the insufficiency of ultrasonic testing is related to a general lack of versatility and capability of commercial ultrasonic equipment. Inadequate instrument reliability, inconsistent components including transducers, and uncertain calibration standards further compromise the potential utility of this method.

Battelle Pacific Northwest Laboratories, under the sponsorship of the Manufacturing Technology Division of the Air Force Materials Laboratory, is developing an advanced ultrasonic nondestructive testing system directed at resolving these deficiencies. As a result, this program will establish a modular ultrasonic system specification that will prevent near term obsolescence by permitting the addition of new technology such as ARPA developments in the form of additional or replacement modules.

This paper will describe the Phase I and II tasks and objectives which are planned to establish an equipment specification, demonstrate initial prototype systems, and provide a procurement specification and technical manuals. Progress to date will be summarized.

INTRODUCTION

Recent studies¹ by the Air Force to determine the probability of detection of service induced flaws suggests that the capabilities of the ultrasonic examination method is limited to relatively large flaws. A current program² to determine acceptable performance ranges of transducers indicates that these components are highly variable and are suspected of being a major contributor to the unreliability of the examination method. In concert with similar on-going programs to provide more reliable NDE equipment to the USAF field and depot inspection activities and to make this equipment available to the manufacturers of engine/airframe components, a Manufacturing Technology Division program has been initiated under AFSC Contract F33615-78-C-5032 to establish specifications for more reliable, advanced ultrasonic NDE equipment.

The program will utilize current state-of-art opportunities as well as advanced concepts to attain the required performance improvements. The equipment will be established in a modular configuration that will permit future concepts to be added as they are developed and thereby prevent near term obsolescence. The advanced equipment concept is shown in Fig. 1. The functional areas to be addressed in this program includes the basic pulser-receiver elements used in the contemporary pulse-echo technique, the transducers, coaxial cable, electronic "gating" and recording methods, packaging, and system manuals.

Program Objectives - Specific areas of improvement have been identified as a result of reviewing previously conducted studies, surveys of USAFNDI shops and discussions with airframe and engine manufacturers. Typical areas of concern resulting from the survey of AFNDI shops are shown in Fig. 2. Specific areas of the instrumentation portion of the system where improvements will be made are:

1. Optimize pulser/driver
2. Establish transducer performance specs

3. Improve receiver noise figures, gain and bandwidth
4. Improve RF detector sensitivity and linearity
5. Optimize video display
6. Improve gating and recording
7. Optimize packaging for field use
8. Standardization of controls
9. Provide simplified calibration
10. Insure computer interfaceability

Improved technical training and operating maintenance manuals will be developed for the advanced ultrasonic equipment. These manuals will emphasize operation and performance clarity.

The ultrasonic system will then be documented as a final production procurement specification.

Current Activity - Several project teams have been making measurements and collecting data needed to establish performance specifications exemplifying these improvements. Specific areas of study include:

Evaluation of Current Equipment - One task group is evaluating current commercial UT equipment representative of that now in use by the Air Force and their suppliers. Seven instruments manufactured by four commercial UT equipment manufacturers have been selected for these tests. Each instrument will be evaluated at points in the system as shown in Fig. 3. A procedure has been developed to make these measurements in a specific and repeatable manner to provide accurate engineering data. The resulting data will be used to establish a baseline of current equipment performance. In addition, the information will provide a basis for the development of new specifications for the advanced ultrasonic equipment. The procedures used will be further utilized to evaluate the performance of newly manufactured equipment

TABLE 1.

TEST POINT	OASIS CONTROL SETTING	TURNS	PARAMETER				UNITS	TOLERANCE	TEST METHOD	TOLERANCE	TEST METHOD
			LOWER LIMIT	UPPER LIMIT	MIN	MAX					
A. ELECTRICAL POWER	MAN	TRANSITION 10	1.0	1.0	0.0	—	—	—	—	—	—
	MAN	TRANSITION 10	0.0	0.0	0.0	—	—	—	—	—	—
B. GENERATOR OUTPUT VOLTAGE	MAN	TRANSITION 10	0.0	1.0	0.0	0.00	1	—	—	—	—
	MAN	TRANSITION 10	0.00	0.0	0.0	0.00	0	—	—	—	—
C. ELECTRICAL POWER	MAN	TRANSITION 10	0.0	1.0	0.0	0.00	1	—	—	—	—
	MAN	TRANSITION 10	0.0	0.0	0.0	0.00	0	—	—	—	—
D. ELECTRICAL POWER	MAN	TRANSITION 10	0.0	1.0	0.0	0.00	1	—	—	—	—
	MAN	TRANSITION 10	0.0	0.0	0.0	0.00	0	—	—	—	—
E. ELECTRICAL POWER	MAN	TRANSITION 10	0.0	1.0	0.0	0.00	1	—	—	—	—
	MAN	TRANSITION 10	0.0	0.0	0.0	0.00	0	—	—	—	—
F. ELECTRICAL POWER	MAN	TRANSITION 10	0.0	1.0	0.0	0.00	1	—	—	—	—
	MAN	TRANSITION 10	0.0	0.0	0.0	0.00	0	—	—	—	—

TEST OF INSTRUMENT AT 50 mhz

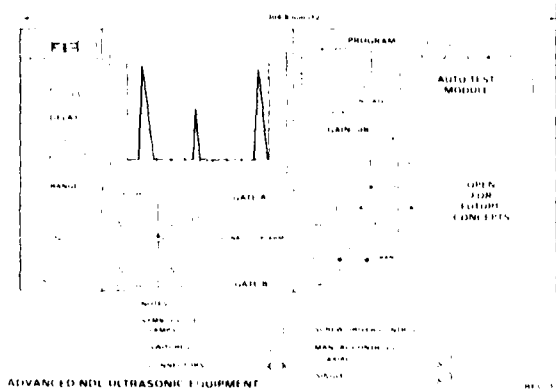


Figure 1. Concept of Advanced Ultrasonic System Control Panel

COMMENT SUGGESTION	RESEARCH	DESIGN	TRAINING	MAINTENANCE
PHYSICAL FACTORS				
LARGE SCOPE				
AUDIBLE ALARM				
RAILS ON CABINET				
EXPLOSION PROOF				
CONNECTOR INTEGRAL WITH S				
ACCESS TO CONNECTORS				
LESS HEIGHT				
TILT ADJUST				
ABLE WIND "D"				
REMOTE TRIP WITH SWEEP GAIN				
CONTROL GAIN AT 100%				
TRIP PROOF				
RT MODE				
ELECTRICAL FACTORS				
HIGHER GAIN				
WIDOUT SCOPE				
BATTERY PROBLEMS				
NON INTERCHANGEABLE				
"NO MAN" ABLES IN ADAPT 10				
REMAINING TIME 100% AFO				
IMPERFECTS: CALIBRATION AND TECHNIQUE				
HART REGENERATE NOT "NO PERMANENT"				
RECORD				
CURRENT QUALITY DEF.				
BUILT IN STANDARD				
VIDEO STORAGE				
THICKNESS READOUT				
MS OPERATION				
MAINTENANCE FACTORS				
AUTOMATIC TROUBLE DETECT				
BATTERY OVER-CHARGE				
WIRING REAR OUT				
SOLDER JOINTS INTERMITTENT OR BRIDGES				
SCOT TRANS STORE				
ABLES RAY				
MAN FACTORS				
POOR TRAINING (MANUAL)				
GAIN CONTROL NOT OPTIMIZATION				
BETTER BL REPRINT TRAINING				
IMPROVED PRACTICAL TRAINING				
ALARM FOR ORBITATING				
AUTOMATIC CONTRA IDENTIFY WITH				
SEVERAL CONTRA				

Figure 2. Current Problems and Recommendations for Advanced NDE Ultrasonic Equipment

and to assess the degree of performance deterioration of the production prototype equipment resulting from a full scale field evaluation.

Evaluation of Transducers - Transducer performance has been concurrently reviewed to determine the variabilities in relative insertion loss, electrical impedance, center frequency, bandwidth and damping.

Several prototypes have been manufactured utilizing current state-of-art developments. Transducers which have been effectively applied to turbine engine components manufactured in support of the near-net-shape program have provided excellent performance and appear to be prime candidates for the advanced systems. Others have been fabricated to arbitrary specifications to determine the parameters which must be specified to provide improved performance.

An intensive study has been conducted into the parameters of pulser/transducer impedance optimization in an effort to maximize acoustic output and minimize distortion. Several designs are now under study as possible candidates for the advanced equipment.

Calibrator Development - A method to permit the operator to conveniently and accurately evaluate the ultrasonic system's performance has been studied. The present concept will be developed at Battelle and incorporated as part of the system specification.

The calibrator envisioned would permit the transducer to be used for a specific application to be placed on the surface of a specifically designed test block. Sound transmitted into the block is detected by fixed wide band transducers located at the center of the incident sound beam. By selecting appropriate delays and gains, the incident pulse would be amplified, transmitted, and redirected back toward the transducer.

The returned pulse will then be viewed on the instrument's oscilloscope to determine if the system is operating within acceptable limits. The exact results of this test could be logged on test reports to indicate that the system had been checked and had maintained the correct level of operation through the test.

Breadboard Design - A breadboard demonstration system is concurrently being designed with the above activities. The breadboard will be built incorporating specific advancements to provide an interim model emulating the design concepts and performance established for the initial production prototype equipment. The breadboard system will

be used to demonstrate improvements of the advanced equipment to users and manufacturers that may be potential bidders for manufacture of six initial production prototype systems.

One of the features of the breadboard model shown in Fig. 4, is the use of a programmed standardization system. A microprocessor will adjust various system parameters to the requirements of a specific Technical Order (T.O.). These procedures describe the calibration adjustments required for testing a specific aircraft structural component. Specifically, the pulse transmission rate, receiver gain, sweep speed, gate interval and position, alarm and record levels will be controlled. To compensate for slight variations in transducers or electronic performance, a small amount of manual override over the nominal microprocessor selected adjustments will be provided. Similar instructions could be programmed for a variety of examinations providing subcomponents of the system are controlled by appropriate specifications.

New State-Of-Art Opportunities - One of the principal objectives of the advanced equipment program is to insure that the system will not be subject to near term obsolescence. To attain this goal, the specifications must consider present and future applications in parameters describing the basic pulser/transducer/receiver, computer architecture and physical structure.

In response to this need, both current and new state-of-art concepts and opportunities are being evaluated. Those which have a good potential of upgrading ultrasonic equipment performance will be developed into breadboard models, as shown in Fig. 5, to determine the specific interface required for adaption. Areas such as digital signal processing, pattern recognition and signal improvement/noise suppression are typical candidates for future upgrading and are currently under study.

Progress to Date

Evaluation of Current Equipment - Data collected to date on the performance of current equipment indicates that:

1. A variety of pulse shapes are used by commercial equipment designers to excite the transducer to create the acoustic pulse burst. The most common pulse is a negative going pulse having a fast rise time and a gradual decay. In almost all cases, the pulser has been designed to work into a 50 Ω resistive load and little concern has been given to:
 - a. Matching the output impedance, consisting of the cable and transducer assembly, thereby eliminating or reducing standing waves and resulting distortions caused by reflections from the trans-

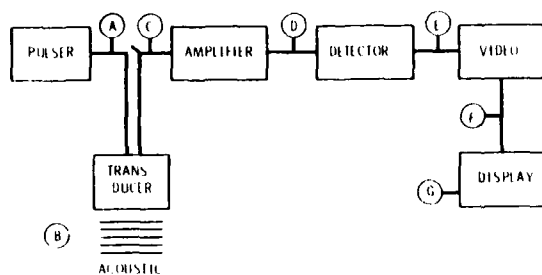


Figure 3. Ultrasonic Test Facility - Evaluating Advanced State-of-Art Concepts

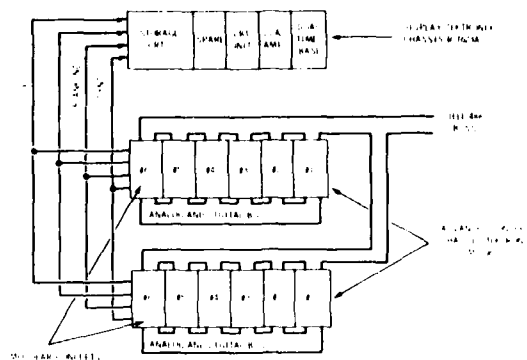


Figure 5. Ultrasonic Test Facility - Evaluating Advanced State-of-Art Concepts

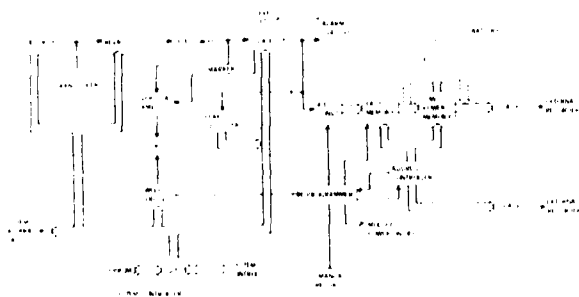


Figure 4. Advanced Ultrasonic Equipment - Breadboard Concept

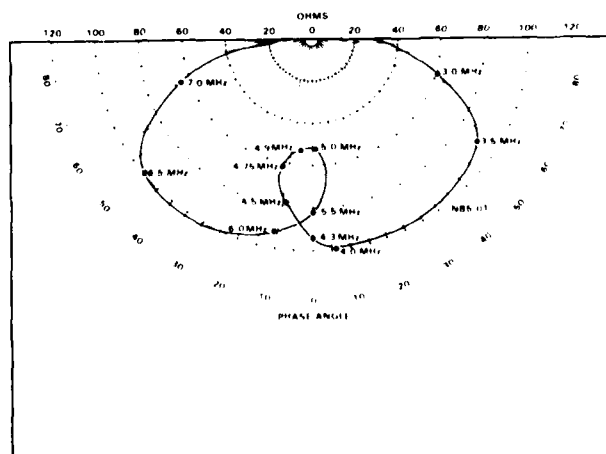


Figure 6. Transducer Complex Impedance as a Function of Frequency

ducer to cable mismatch.

- b. Properly terminating the input to effectively isolate the pulser impedance from the cable after the pulse has ceased
2. A test frequency shift has been measured on most equipment tested from point B to point D, Fig. 3. The frequency change measured on a typical instrument is shown in Table 1, where a variation of 3.0 MHz was observed as a result of merely manipulating the damping control from minimum to maximum setting. The most significant impact of this situation is that the actual center frequency and spectral content of the interrogating acoustic beam at point B varied from 3.0 MHz to 6.25 MHz, while the 6 dB bandwidth of the pulse changed from 1.0 to 6.0 MHz (min. damping) to 4.5 to 7.0 MHz (max. damping) as the signal passed through various stages of the instrument. If flaw characterization by pattern recognition or adaptive learning techniques are to be applied in the future, this uncontrolled variability must be controlled.
3. Commercial transducers evaluated to date appear to be of two basic types, highly damped with limited bandwidth or medium damped with tuned narrow band performance. Large impedance variations have been measured ranging from a few ohms to over 1000 ohms. The phase angle of the impedance can range from highly capacitive to inductive depending on the transducer design. Typical impedance plots in the form of a Smith chart are shown in Fig. 6. Actual frequency of operation is an approximation that nominally indicated, while bandwidths vary widely.

Transducers for future equipment will have to perform in a more predictable manner. However, the method and procedure of measuring the performance of transducers must be simultaneously developed to provide a common ground for evaluation of specified performance. An arbitrary procedure is being established as part of this study.

SUMMARY

The need to resolve the unpredictable performance of ultrasonic nondestructive testing equipment has been treated by the user as a specific and monotonic value in determining examination repeatability, sensitivity and detectability. Reliable flaw characterization using current commercial equipment appears to be unattainable unless tighter equipment specifications are invoked.

The specific contributors to unacceptable

performance are not obvious and perhaps this is the reason they have been retained in current equipment designs. The results of evaluating current commercial equipment indicates that the following areas are the most serious:

1. The availability of transducers that have unspecified wide variations in impedance values and phase angles.
2. The presence of uncalibrated and non-uniform controls which when reset create unpredictable testing parameters.
3. The creation of harmonics and phase distortions by improperly terminating cables and transducer loads.
4. The use of random lengths and types of coaxial cables.
5. Saturation in the receiver amplifier creating response variations that are difficult to relate to the causative source.
6. Noise inherent to the equipment design or other sources within the system that requires the use of "reject" or other noise reduction schemes.

The current program will provide significantly advanced NDE ultrasonic equipment, correctly designed for the user and manufactured to perform in an accurate and predictable manner. The implementation of this equipment by the Air Force and its suppliers will result in improved probability of detection of defects by the ultrasonic nondestructive examination method.

REFERENCES

1. W.H. Lewis, Lockheed Georgia Company, "Non-destructive Inspection Reliability Program - Workshop Notes, USAF-AFLC Contract F41608-73-D-2850-0038, August, 1978.
2. V.D. Smith, C.M. Teller, R.E. Swanson, Southwest Research Institute, "Engineering Services to Determine Acceptance Levels of Ultrasonic Transducers for Nondestructive Testing", Final Engineering Report, USAF Contract F41608-77-C-1381, June, 1978.

SUMMARY DISCUSSION
(A. S. Birks)

Don Thompson (Science Center): Could you describe your calibrator again?

Al Birks: The calibrator we have developed at this point is a delay line, a block of solid piece of material, on which the transducer selected for a particular application would be placed. The sound beam would propagate through the block where the signal would be detected by a wide bandwidth transducer located on the opposite side. The signal would go through an amplifier and a delay line, whose amplification and delay time would be set in accordance with the required transducer. This is required to compensate for the beam geometry which is dependent on the frequency and size of the transducer. This signal is then repropagated back toward the transducer. The returning signal will then be amplified by the instrument's receiver--now you're back into the main instrument--and displayed on the oscilloscope screen. The program could be set up to call for a certain amplitude of signal. The presence of this appropriate signal, as required by the program, would be evaluated by a decision algorithm in the program and advise the technician to proceed with his test. It's kind of a check-out. It's not a true calibration.

Chris Fortunko (Science Center): Could you tell us what the improvements will be to the transmitter and circuitry in this instrument over the current instrumentation?

Al Birks: The improvements are multifold. First of all, we are looking at this present time at a spike pulse, which appears to be a very good selection. We have also looked at other forms of excitation, mainly a square wave, which appears to have very good possibilities. It looks like there may be approximately five db more gain available here over the spike pulse, but it may require quite a bit of temporal adjustment to attain this gain.

Chris Fortunko: The problem with the spike pulse is that it has a lot of energy to get the high frequency. The way you generate it now is by means of an avalanche device, such as a transistor or SCR, where biasing is very sensitive to thermal variations and load characteristics.

Al Birks: You mean like the impedance? That's another problem. The impedance of the cable and terminating load of the transducer is quite a factor in the system. A mismatch introduces quite a bit of standing wave distortion. We're looking at the impedance-matching problems both at the output of the pulse, the receiver input isolation, and transducer load to reduce distortion in the reflected wave coming back from the transducer.

Bob Addison (Science Center): Just a point of clarification. When you were measuring the peak of the frequency response for those variety of pulses, what measurement was that? I wasn't quite clear what you were measuring.

Al Birks: You mean the amplitude?

Bob Addison: You were measuring the peak amp. What frequency did it peak out? The center frequency? The first pulser characteristics? Then you have two dampening control settings, one is two and one is 5.8. What were you looking at there? I just wasn't sure. What are you measuring?

Al Birks: We are measuring the center frequency.

Bob Addison: The center frequency of what?

Al Birks: The electrical pulse which is applied to the crystal or the load. This is the spectrum of the pulse that is applied to the transducer and the maximum response of that spectrum has been labeled "Peak Frequency".

Bob Addison: Fine.

Al Birks: At this time we do not know what good this information is going to be to us, but, obviously, if you don't have the frequency contained in the electrical pulse that is activating the transducer, it's rather difficult to expect to get the acoustic energy at that frequency out later. That's what I mean, this specific interrelationship has not yet been developed--it has been quite interesting observing these variations which form a base line and a basis for preliminary specifications. We will have to convert these specifications into

(continued)

A. Birks (continued discussion)

a production procurement document for the Air Force and procure improved equipment. Therefore, we have got to get a thorough understanding of how current equipment performs.

Unidentified Speaker: Did this instrument have a spike pulse on the transmitter, or was it a switch sort of a thing that went down sharply and then came back?

Al Birks: It was spiked.

Unidentified Speaker: Avalanche-type pulse?

Al Birks: I believe it was, yes.

Roy Buckrop (U.S. Army Armament Matl. Readiness Command): Al, you said you might talk about a logarithmic readout as compared to a linear. Is this a move and an attempt to be able to discriminate more finitely between the background and the usable signal? I'm referring back to our nonmetallic inclusion application where we used computer banks in order to provide signal discrimination out of the "grass" or background noise signals. Will a logarithm help you do this?

Al Birks: It really won't help you. It will amplify the low level signals and actually make your noise a more prominent feature of the display. A problem in the Air Force operation is that they use a lot of "rejects" to remove these unwanted signals. I've seen some operators use an undesirable amount of "rejects" where the dial would be turned to the 75 percent "ON" position. You know, with all the concern about vertical linearity and other instrument performance, we created a monster here where gain and distortion are running rampant without much concern of the compromises to reproducibility or detectability.

Roy Buckrop: So you're still going to make the discriminating factor operator oriented, not trying to put anything in the instrument's gain to remove the operator's characteristics and provide a more finite discrimination of signal information as compared to the background noise? Is the gating going to be adjusted any closer to that signal-to-noise relationship?

Al Birks: Roy, we hope that by making the signal a less-distorted signal and balancing all of the electronics throughout the system, we will get a much cleaner signal. Hopefully then the noise will be minimized and the "noise" that remains is truly representative of acoustic information rather than electronic distortion.

#

AUTOMATED INSPECTION DEVICE FOR EXPLOSIVE CHARGE IN SHELLS - AIDECS*

**Hans Weber, A. P. Trippe, D. Costello, J. C. Young,
L. A. Parks, C. A. Preskitt and Joseph John
IRT CORPORATION
San Diego, California**

ABSTRACT

Certain defects in the explosive charge of an artillery shell can cause the projectile to explode prematurely in the barrel of the launcher from which it is fired. The sensitivity of the radiographic technique presently used is limited by the large influence of the steel shell casing on the transmitted radiation. A filmless radiometric technique utilizing the basic radiation principle of Compton scattering, which will detect cavities in the explosive filler with minimal interference from the steel casing, has been identified and tested.

By scanning the shell with a beam of radiation and observing the Compton scattering through a unique collimating system, it has been possible to detect voids as small as 1/16 inch in cross section. The hardware consists of the source, beam collimator, detector collimator, and a large plastic scintillator detector system. The projectile is inserted into the beam path and moved through a fixed scanning pattern by a mechanical handling system. The scanning sequence is computer controlled and results in a three-dimensional data matrix giving a direct representation of density within the projectile. Voids are identified and classified by computer analysis, and shell acceptability decisions are automatically generated.

An engineering prototype system is currently being assembled and tested. (A production prototype conceptual design is concurrently under development.) This new technique will replace an existing film radiography inspection procedure and eliminate the need for human interpretation of the defects, while providing more consistent and reliable inspections at lower costs.

INTRODUCTION

Experience has shown that certain defects in the explosive charge of an artillery shell can cause the projectile to explode prematurely in the barrel of the launcher from which it is fired. Since such failures are dangerous and costly, their incidence must be reduced to a minimum by ensuring that the defective shells are detected with the highest possible confidence. Therefore, a great need exists for a reliable, nondestructive inspection technique that provides a means of identifying defects inside a shell with a speed compatible with the production rates anticipated in the U.S. Army's Ammunition Base Modernization Program.

Inspection programs currently in use rely primarily on radiographic techniques, utilizing x-ray sources and film radiographs that inspect only a limited sample of the entire output of a given production facility. With the development of new, automated production facilities under the Ammunition Base Modernization Program, the demands on nondestructive inspection programs are becoming considerably more severe, since they must ensure with a high degree of confidence that the high-volume production output is sufficiently free of defects. It is recognized that currently employed radiographic methods do not provide a sufficiently accurate and economical inspection capability for automated production of shells, as evidenced by the Army's current sponsorship of the AIDECS program to develop an engineering prototype for the automated,

filmless, high-speed inspection of 105 mm projectiles.

The inspection technique embodied in this approach is based on the measurement of Compton-scattered radiation. The method was identified as the most suitable method for inspecting explosive charges for cavitation defects. It provides high resolution data in a three-dimensional format which readily lends itself to a completely automated, cost-effective defect analysis. A further major advantage is that the technique is inherently less sensitive to defects in the steel projectile casing than transmission techniques.

After demonstrating the feasibility of the technique in laboratory experiments, an engineering prototype which embodies the scattering technique was fabricated. This prototype is capable of performing a complete three dimensional inspection of the explosive filler charge in 105 mm, M1 projectiles.

Based upon the full scale operation of the 105 mm engineering prototype system, it is projected that with some product improvements required to accommodate larger projectiles, several inspection modules will inspect artillery ammunition production on a 100% basis. The cost for this total inspection service is estimated to be significantly less than radiography costs incurred by the current sampling plan.

COMPTON SCATTERING TECHNIQUE

A review of the basic photon scattering physics and its relationship to artillery projectile inspection is presented below. This is followed by a brief description of an analytical

* Work supported by U.S. Army Materials & Mechanics Research Center, Watertown, Massachusetts, under Contract DAAG-77-C-0009.

model used as an aid in making design tradeoff decisions.

This photon scattering inspection technique is based upon the fact that sufficiently energetic gamma radiation interacts with the material in its path by scattering a portion of the incident beam. This interaction, known as Compton scattering, is the dominant mode of interaction between gamma rays and target materials for gamma-ray energies between approximately 200 keV and several MeV. In this interaction mode, part of the energy of the gamma ray is transferred to a target electron during a collision. Conservation laws require that the photon be deflected in a particular direction as a result of the collision. A small loss of energy is associated with a small angular deflection; while larger energy losses occur at larger deflection angles. The maximum energy loss occurs when photons are scattered 180 degrees, directly back into the incident beam. The probability for a gamma ray to be scattered through a particular angle is a clearly defined function of the incident beam energy and the angle. Also, for gamma-ray energies in excess of about 100 keV the number of scattered photons is independent of the material composition and depends almost wholly on the electron density of the scattering target. In other words, the number of scattering events from a unit volume in the target depends almost entirely upon target density (number of electrons per unit volume) in the volume element.

inspection volume element. The introduction of a void into the volume element means reduction in the amount of material available to scatter gamma rays, and consequently results in a decrease in the detector response. On the other hand, the presence of a higher density inclusion causes an increase in the detector response.

The photon scattering technique collects this scattered radiation over a very large solid angle through the use of a large scintillator which views the projectile through a "focusing" collimator. This is analogous to integrating the output of several detectors, each monitoring the scattered radiation at a different angle about the incident beam. The focusing collimator allows only radiation from a small segment of the incident beam to reach the scintillator; radiation scattered from other regions of the incident beam is blocked by the focusing collimator. The geometric design of the focusing collimator defines the inspection aperture, or one dimension of the inspection volume element. The other two dimensions of the inspection volume are formed by the collimation control of the incident beam.

If the inspection volume element is selected sufficiently small so as to represent only a small fraction of the entire shell volume, the detector response becomes highly localized, and consequently, is less subject to interference from signals from the rest of the shell. It also

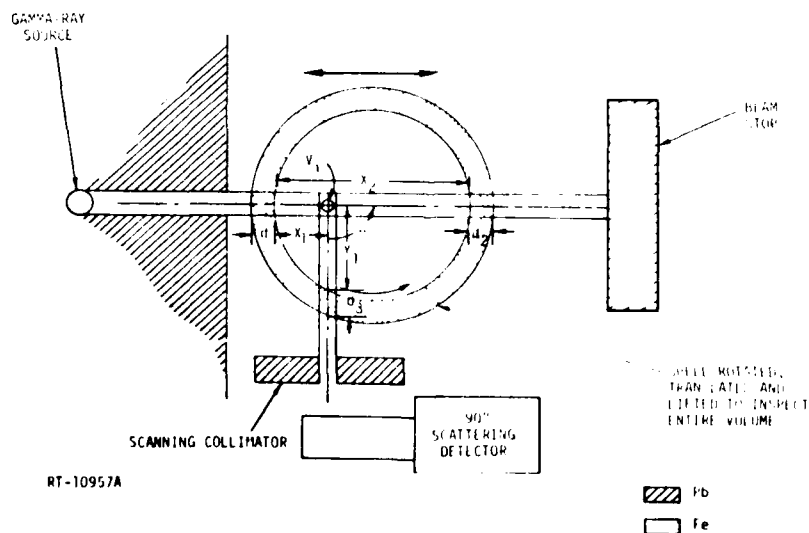


Fig. 1. Basic Compton Scattering Configuration

A selected portion of the scattered radiation can be measured by an appropriately collimated radiation detector placed at a certain angle to the incident beam. The detected scattered radiation results from Compton interactions in the volume element defined by the intersection of the incident beam and the detector collimator. Figure 1 schematically represents the basic measurement technique. The volume element from which the scattered radiation originates appears to the detector like a source of radiation whose intensity depends on the amount of material contained in this

becomes highly sensitive to even minute voids if the ratio of void and inspection volume falls within a suitable range. Detection of large voids, cracks, porosity, annular rings, piping cavities, and base separations is accomplished by software analysis of the defect signals which exhibit themselves throughout several neighboring volume elements.

A complete scan of one projectile is accomplished by rotating the shell about its axis, translating the rotating shell along a line

parallel to the incident beam, and indexing the shell up or down. During a scan these combine into a continuous path covering the entire projectile volume. At discrete positions along this path (~ 0.2 inch), a number proportional to the amount of radiation scattered from the inspection volume is read by the computer from the detector electronics. These data points are stored in a three-dimensional data array representing a discrete volume map of the projectile. Subsequent analysis for variations in the scattering levels for each volume element indicates statistically meaningful deviations of material density. These deviations are then quantitatively analyzed to define size, shape, and orientation of defects.

Thus, the photon-scattering gauge is seen to be an inspection device which provides a high-resolution, three-dimensional scan profile of the entire explosive charge. It performs a differential measurement which, with an appropriately small inspection volume element, not only identifies the presence of discontinuities in the explosive (such as voids, cracks, annular rings, and inclusions), but also provides data about their size, three-dimensional location, and orientation.

In order to make engineering design tradeoff decisions, a model of this technique as it applies to artillery projectile inspection was developed. This analytical model contains two distinct parts. The first part consists of a detailed calculation of the gamma-ray penetration and scattering process within an artillery shell, and the second consists of an analysis of the viewing characteristics of the selected detector collimator. The spatial distribution of multiply scattered gamma rays is a crucial aspect of the analysis, and this is computed using a Monte Carlo technique to track large numbers of gamma-ray histories throughout the shell. The parameters of this distribution are then used by the collimator analysis code to predict the response to specified defects. The model has been validated against experimental data and is currently being used for its intended purpose*.

ENGINEERING DETAILS

A photon scattering inspection system capable of automatically detecting cavitation defects in artillery projectiles consists of six major subsystems:

1. Main Frame Structure
2. Mechanical Scanner
3. Source Collimator and Storage Assembly
4. Detector Collimator and Scintillator
5. Electronic Data Accumulator and Control System
6. Computers and Display Network

A discussion of the functional requirements for each subsystem follows.

The main frame consists of support members

*Details of the model and its validation can be found in IRT Report No. 8188.06 prepared for Contract No. DAAK10-79-C-0062, May 21, 1979

which provide leveling and alignment of the other system components. Safety shielding is also considered to be part of the main frame. The alignment between the collimated source beam, the inspection aperture defined by the focussing collimator, and the scanning mechanism is attained and maintained by the lower frame structural components. The entire frame rests on a steel base plate which is leveled on adjustable jacks. The other components are mounted to this plate by a variety of adjustable fixtures.

The functions performed by the mechanical scanner subsystem are (1) grip the projectile, (2) accurately register the projectile so that its location is always available for use by the computer, and (3) move the projectile through a controlled scan pattern such that the fixed inspection element travels through all of the internal shell volume. The mechanical scanner must be capable of supporting and transporting the total mass of the projectile in a smooth, rapid scan. It receives position commands from the computer and provides computer readable, actual projectile position signals.

A storage and beam collimation cask for the radioactive sources serves the dual role of (1) providing a shielded storage unit which allows personnel to safely work near the inspection system, and (2) collimating the output radiation to form a precisely defined gamma-ray beam. The sources are mounted on a transport slide which allows for movement from a storage position to an inspection position. It is required that the storage shielding be sufficient to reduce the radiation to levels which allow for safe personnel approach. When the source is in the inspection position, personnel are prevented from inadvertently stepping into the radiation zone by means of an interlock circuit which will automatically move the source to the storage location if someone attempts to enter the area. The engineering prototype contains 14,000 curies of Cobalt-60 in the form of three encapsulations similar to those used in commercial irradiators.

The detector collimator selectively transmits gamma radiation from the inspection element to the scintillator while blocking radiation scattered from other points along the incident beam. The effectiveness of the detector collimator is dependent upon its geometric configuration. The optimum geometric configuration is one which provides the largest possible solid angle for viewing the radiation scattered from the inspection volume element, consistent with efficient screening out of all other radiation. The detector collimator design for the engineering prototype consists of 16 coaxial lead cones with each having a 2.25-inch radius hole centered at the cone apex, for 105 mm projectile insertion. This 16-cone assembly as shown in Figure 2, is trimmed so that the final outside dimensions are flat surfaces which mate against the large flat plastic scintillator front faces.

The scintillator geometry is selected to capture most of the incident gamma radiation. The scintillator emits visible light photons proportional to the total incident gamma-ray energy.

The visible light generated in the scintillator by scattered gamma rays is collected by a network of photomultiplier tubes. The individual

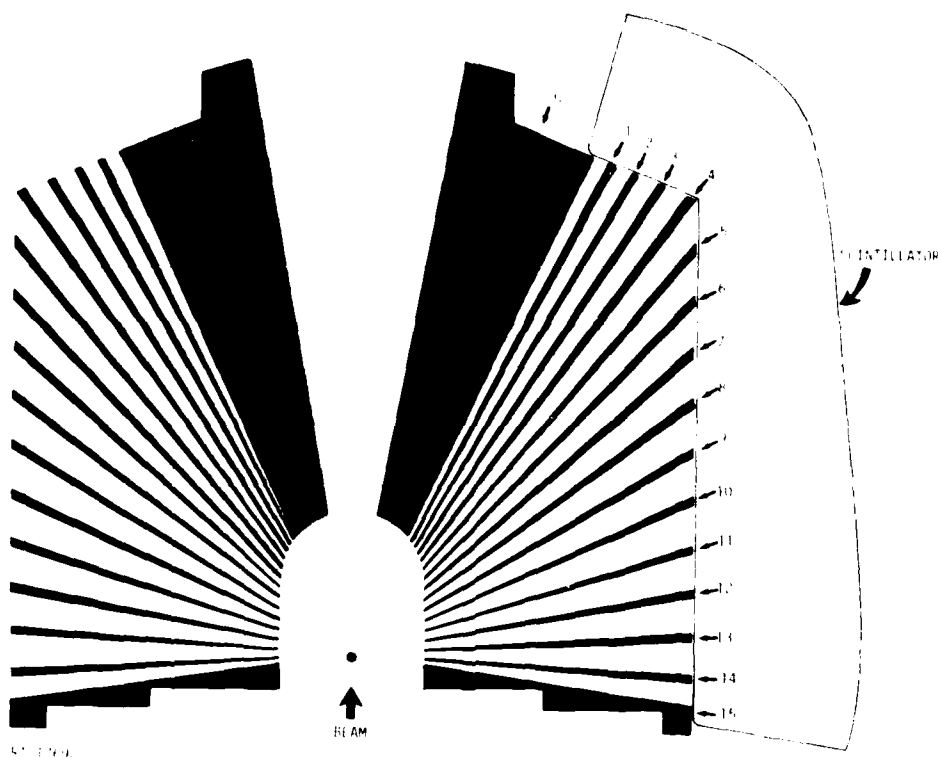


Fig. 2. Cutaway View of the AIDECS Detector Collimator Assembly Looking From the Top Down. The 16 Cones focus to the Black Dot (Focal Point). The Gamma-Ray Beam Direction Corresponds to the Axes of Symmetry of the Cones.

tubes are balanced so that a particular incident gamma-ray energy results in specific electronic charge output. These current pulses are summed by a current integration circuit which generates an analog voltage. The output is tracked by a sample-and-hold device until an analog-to-digital converter outputs a digital number proportional to the amount of gamma radiation observed in the scintillator. The computer input to this signal accumulator controls the timing gates which determine the discrete count times for each volume element. Count periods are controlled by a high frequency crystal oscillator circuit. The computer gates the counting circuit on and off, reads the digital output value, and stores the value along with the three-dimensional coordinate information about the location of the data point in the projectile volume. This control system consists of hardware circuits designed to perform these functions within the designated sampling times.

The control, analysis, and display functions performed by the computer network perform the following tasks:

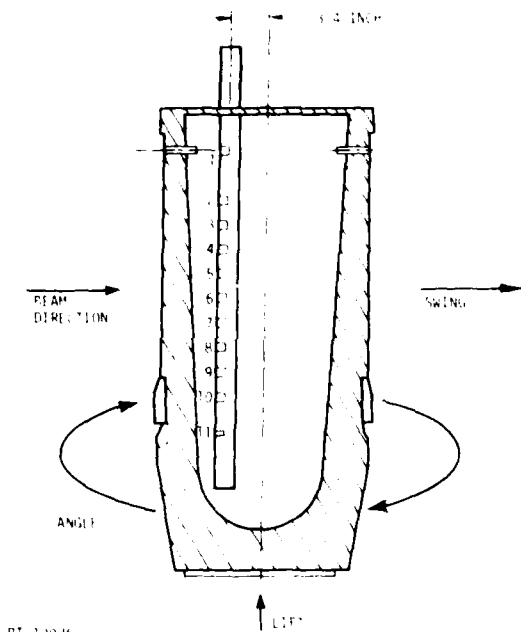
1. Control Mechanical Scanner
2. Start and stop counting periods
3. Read digital element values and coordinate data
4. Store all raw data

5. Analyze three-dimensional segment volumes
6. Classify defects
7. Perform accept/reject decision
8. Provide summary inspection data
9. Display defects
10. Automatic calibration
11. Perform maintenance and test functions

A pipeline, serial approach using several slow speed computers to divide these tasks has been applied to the engineering prototype. Appropriate software to accomplish the above tasks has been compiled.

DEFECT DETECTION CAPABILITIES

Several tests for defect detection capabilities have been performed. Initially data were taken in a laboratory setup using lucite plastic blocks with machined holes to simulate defects. Later a testbed facility was built around a 500 curie Cobalt-60 source. Automated scanning and data collection were finally added to this testbed. Projectiles with inert fillers which contained machined defects in known locations were Government supplied for these tests. Figure 3 shows a



RT-100/6

Fig. 3. Cross-Sectional View of AIDECS Test Projectile Indicating Positions of Various Defects. The Coordinate System Used (Lift, Swing, and Angle) and Beam Direction Are Also Shown

representative test projectile. These standards are now being used to validate the engineering prototype. In all cases, the data collected showed that the Compton scattering technique was feasible for detecting cavitation defects in HE projectiles.

In early June 1979, fabrication of the engineering prototype was completed and data collection and analysis tasks were initiated. Scan data obtained for several long cylindrical voids positioned in the inert filler are shown in Figure 4. These data were taken with the full scale system using all 64 detectors and automatic data collection. It represents the first outputs after all the functional subsystems were assembled and operated together. It must be noted that the data shown in Fig. 4 does represent an optimum system response for geometry of the defects. The scan pattern used during the test was located so as to provide a maximum defect response in the plane for which the data is displayed. The data in Fig. 4 is raw data which has not been filtered to reduce statistical noise. Automatic operations under full software control will eliminate much of the statistical noise by taking advantage of the fact that neighboring data points are correlated by the finite width of the system response which extends over several contiguous finite volume elements.

To illustrate the statistically optimized response of the system to a defect when the statistical noise is reduced, slow speed scans of the test projectile have been made. The results of one of these scans is shown in Figure 5. The signals from two 1/16 inch diameter defects (one 0.2 inch long and located 1.09 inches from the bottom of the filler and the other 0.18 inch long and located

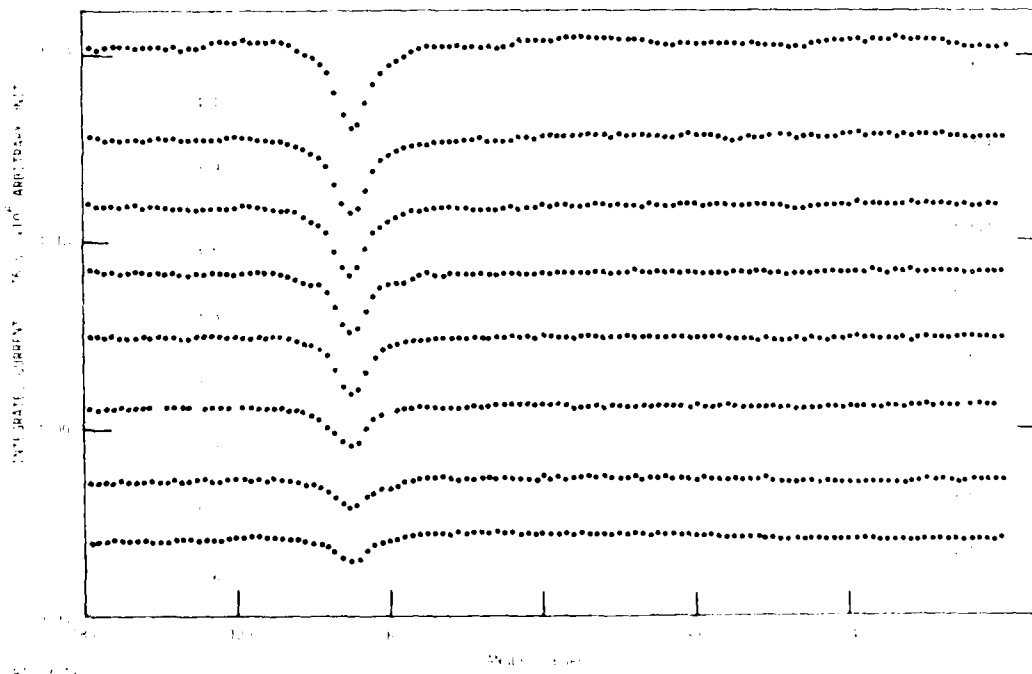


Fig. 4. Response Functions for 1/8 inch diameter defects ranging in length from 0.156 to 0.192 inch at different distances from the bottom of plastic charge

2.09 inches from the bottom) are both clearly discernible. Notice that the system stability aids in allowing the detection of such signals.

SUMMARY

This paper has presented details concerning a Compton scattering inspection technique and the prototype engineering hardware built to provide a fullscale demonstration of the method. The work is directed toward the inspection of 105 mm artillery projectiles and provides a means of detecting cavitation defects. The hardware is automated and filmless. Accept/reject signals can be used to physically segregate the defective projectiles.

Future work will include:

1. Delivery of the engineering prototype system
2. Design and fabrication of a 155 mm production prototype system
3. Production prototype testing at an Army load plant
4. The installation of multiple inspection systems to provide 100% inspection in a near realtime mode.

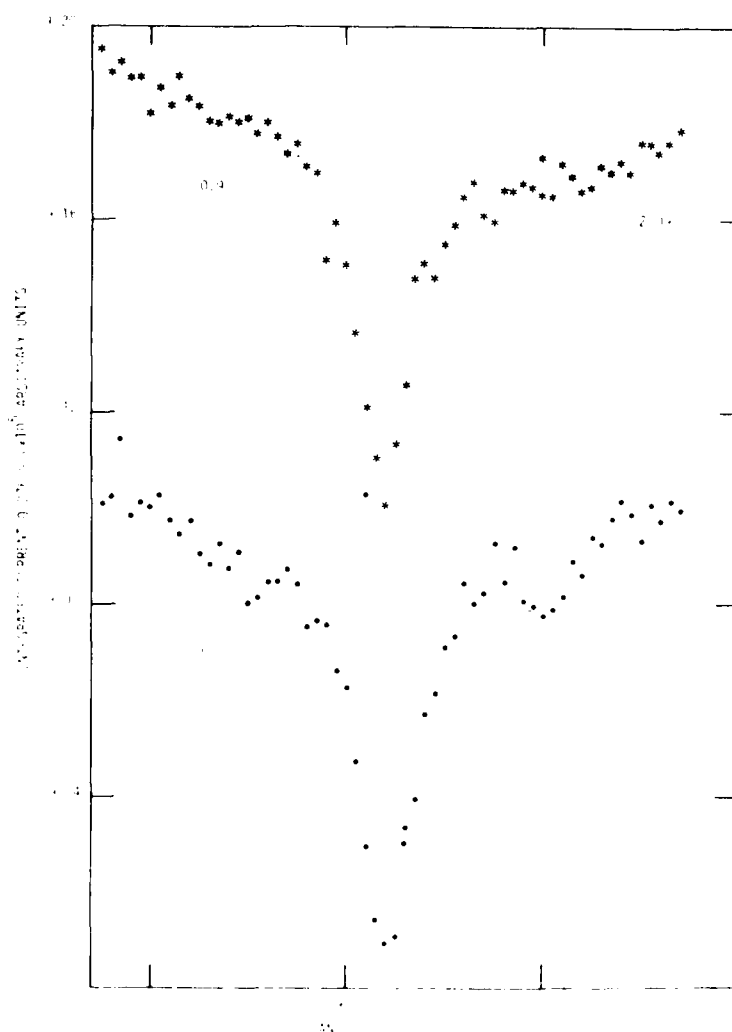


Fig. 5. Response Functions for 1/16 inch Diameter Defects 0.10 and 0.200 inch in length at Different Distances from the Bottom of the Plastic Charge

STATE DISCUSSION
(J. John)

John Derakacs: ... take your statement on there is a one-to-one correspondence between the defect and response?

J. John: ... one-to-one correspondence is that if there is a defect of a specific nature at a specific point in the shell, there is, first of all, a one-to-one correspondence between the coordinates of the defect and the location of the inspection point in the shell when the response is obtained. In addition to that, there is a one-to-one correspondence between the type of defect and the response you get. For example, if you have a void, then you have a negative response. If you have an inclusion, you have a positive response. Now, what we are measuring is the amount of material in the inspection volume. So, if you are trying to, let's say, characterize a long object, then what you want to do is to divide that up into a number of small inspection volumes. And in each inspection volume you measure the amount of material. So that there is no confusion between the results and reality. The effect is very localized.

Sam Snow (Union Carbide): I was impressed by the one-minute inspection time. I think that's very impressive for this type of measurement, which leads me to my question. What type of source?

J. John: The design intensity of the source is about 30,000 curies. The data-taking time is 2.3 milliseconds per data point. Now, the assembly that you saw there is geared for about 50,000 curies. The radiation level on the outside is one-tenth of a milli-roentgen. We have to spin the shell at various speeds, as high as 2,000 RPM.

Tom Derakacs (TRW): What size defect were you looking for?

J. John: In this particular case, it's a collection of things. There is at this stage no absolute, clear connection between the size of defects in the shell and its performance. There is a whole lot of experience. The experience has now been summarized in the form of a set of specs, and the specs are related to X-rays. So, when you really come down to it, the specifications require that the sum of all the defects in the X-ray add up to a certain amount, in one case one-sixty-fourth of a square-inch. Now, we have translated that into some defect size. And for this particular system, the defect that you're looking at is 60 mils by a quarter of an inch. Very large defects. Very macroscopic. What we have done is to lay that requirement on our measurement system. We have a very large collimator, very large inspection volume. Now, in principle, we can look at extremely small defects. We can see one percent variation very easily. And, therefore, you could design your inspection volume such that it is about between ten or twenty times the smallest defect to be detected. So, in principle, there is no limit to the size we can get. There's a practical limit, of course. As you decrease the size of the inspection volume, the inspection time goes up.

#

STRUCTURAL AND MICROSTRUCTURAL DESIGN IN BRITTLE MATERIALS

A.G. Evans
Materials Science and Mineral Engineering
University of California
Berkeley, CA 94720

ABSTRACT

Structural design with brittle materials requires that the stress level in the component correspond to a material survival probability that exceeds the minimum survival probability permitted in that application. This can be achieved by developing failure models that fully account for the probability of fracture from defects within the material (including considerations of fracture statistics, fracture mechanics and stress analysis) coupled with non-destructive techniques that determine the size of the large extreme of critical defects. Approaches for obtaining the requisite information are described in this paper. The results provide implications for the microstructural design of failure resistant brittle materials by reducing the size of deleterious defects and enhancing the fracture toughness.

INTRODUCTION

The design of structural components from brittle solids is, in concept, quite straightforward. It simply requires that the stress level in the component should not exceed the strength of the material, at the permissible level of survival probability. The implementation of this concept is, however, very involved. It requires the combination of information derived from the disciplines of fracture statistics, fracture mechanics and flaw detection (or non-destructive evaluation). The description of the general scientific framework for structural design, utilizing these disciplines, and of the future prospects for this class of materials, are the primary intents of the present paper.

Ultimately, design might take the form of a computer simulation of crack growth in real microstructures, coupled with microstructural characterization techniques (such as acoustic scattering). Presently, however, useful progress is being achieved using a partially decoupled approach. The evolution of failure from defects and the crack extension mechanisms are studied separately, and merge where possible. This approach has influenced the structure of the paper, which includes separate considerations of fracture initiating flaws, crack propagation and defect characteristics.

The character of the design problem is illustrated in Fig. 1a, which plots the probability of fracture of a ceramic (measured, say, in flexure) as a function of stress level. It might be construed that for design purposes, it is simply necessary to superimpose the permissible level of failure onto this figure, to obtain a maximum allowable stress in the component; and then to design the component accordingly. The limitations of this approach are exposed when it is appreciated that the fracture probability curve can be substantially perturbed by a wide variety of phenomena. These include: the incidence of slow crack growth (Fig. 1b), the occurrence of undetected flaw populations in the inevitable region of extrapolation (Fig. 1c), and effects of stress state (Fig. 1d). Because of the problems associated with the direct use of statistical design

procedures, alternate approaches have been sought, which attempt to effectively truncate the strength distribution at a level above the design stress (Fig. 1e). One such approach, involving the characterization of fracture initiating defects and of the evolution of failure, is emphasized in the present paper. Implications for microstructural design are included, as they emerge from the general scheme.

Fracture in brittle solids usually occurs either by direct extension of a single pre-existent flaw (from the large extreme of the flaw population) or by the coalescence of small flaws. The level of stress needed to activate these flaws relates to the size of the flaw in a manner that depends upon the interactions and the resultant strength, flaw size, probability relations are described in the first part of the paper, for each of the prevalent flaw types: inclusions, voids, surface cracks, microcracks. Immediate implications for microstructural design derive from these descriptions of strength.

The formation of flaws (especially extrinsic flaws such as surface cracks, impact damage, thermal cracks), and their extension susceptibility, depends sensitively upon the fracture toughness of the material. The toughness thereby emerges as a critical structural parameter. The fracture toughness of brittle materials and its dependence on microstructure is discussed in the second part of the paper. Implications for improved microstructural and structural design, based on toughness considerations, are then explored.

The ultimate survival of a brittle structural component at an acceptable survival probability requires the use of a flaw characterization technique in conjunction with a failure model. Such techniques involve the detection and analysis of waves scattered or absorbed by defects. The most versatile and sophisticated mode of flaw characterization involves the use of acoustic waves: either bulk waves or surface waves. The utility of acoustic waves for providing the requisite survival information, including the combination of the measurement and fracture results to derive optimum accept/reject decision schemes, is described in the third part of the paper.

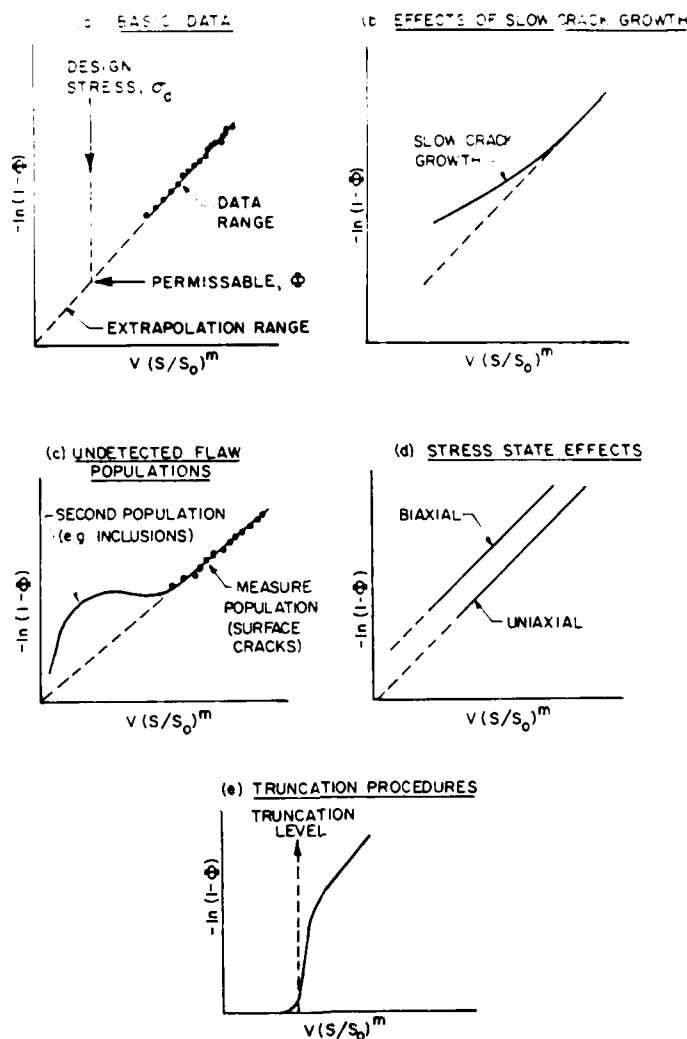


Fig. 1 A schematic illustrating some of the issues that limit the use of a direct statistical approach for structural design. The diagrams relate the fracture probability Φ to the strength level S and the sample volume V .

Finally, some prospects for further advancement of our comprehension of the failure process are discussed.

FRACTURE INITIATING DEFECTS

The flaws that ultimately initiate fracture in brittle solids can be conveniently classified as intrinsic or extrinsic. The intrinsic flaws are introduced during the fabrication and are predominantly inclusions or voids. The extrinsic flaws are stress induced cracks, such as the surface cracks introduced during machining and the microcracks that result from large residual stresses (e.g., due to thermal contraction anisotropy). Each class of defect will be discussed separately.

The only available analyses of fracture from defects that provide a consistent description of effects of defect size, type and shape invoke the

existence of preexistent microflaws, activated by the concentrated stress fields around and within the defects.^{1,2,3} However, the character of these small flaws is not well-defined. It is supposed that the flaws are the small voids (or precipitates) that typically occur at grain boundaries (e.g., at triple points). These flaws are prone to activation at relatively small levels of applied stress because of the large residual stresses that can exist at grain boundaries due to thermal contraction anisotropy⁴ (Fig. 2); such flaws located in high energy boundaries would be particularly susceptible to microcrack formation. Direct evidence of this mode of microcracking has not been obtained, however, and the concept must be treated as phenomenological at this juncture.

The statistical character of the microcracking process can be conveniently posed by

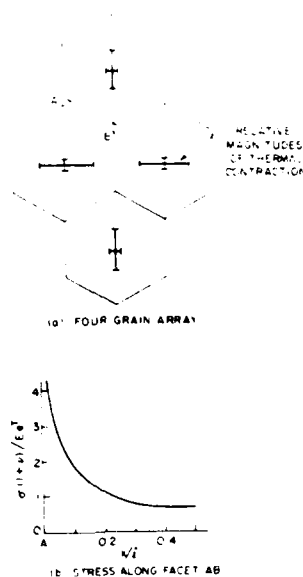


Fig. 2 Stresses caused by thermal expansion anisotropy.

commencing with the premise that the microflaws exhibit an extreme value size distribution that leads to the probabilistic relation;^{5,6}

$$\phi(a) = 1 - \exp[-(A/A_0)(a_0/a)^k] \quad (1)$$

where $\phi(a)$ is the probability of finding a micro-flaw larger than a on a grain boundary of area A , a_0 is a scale parameter, k is a shape parameter and A_0 is a normalizing constant. Noting that a flaw will extend under the condition that the stress intensity factor K reaches the critical value for grain boundary fracture, $K_{g.b.}$ then gives the approximate result;^{7,8}

$$\frac{\pi(K_{g.b.})^2}{4a} = \sigma^2 + \frac{4\tau^2}{(2-\nu)^2} \quad (2)$$

where σ is the total stress (applied plus residual) normal to the boundary and τ is the total in-plane shear stress needed to induce crack extension. Substituting a from Eq. (2) into Eq. (1) gives the probability of microcracking as a function of applied stress (σ_a, τ_a) as;

$$\phi(\sigma_a, \tau_a) = 1 - \exp \left[- \left(\frac{1}{A_0} \right) \left(\frac{4a_0}{\pi} \right)^k \int_A \left(\frac{(2-\nu)^2 \sigma_a^2 + 4\tau_a^2}{K_{g.b.}^2 (2-\nu)^2} \right)^k dA \right] \quad (3)$$

It should be noted that, since the residual stresses and the toughness are variables, the microcrack probability associated with a specific boundary is not uniquely related to the applied stress; rather, a distribution of probabilities generally exists. This effect allows the origination of a crack tip microcrack zone (i.e., microcracks do not necessarily initiate first at the

most highly stressed boundary contiguous with the crack tip). For many other problems, the probability of crack formation averaged over many grains is more pertinent. For this situation, the average residual stress must be zero, and Eq. (3) reduces to the simple form;

$$\phi(\sigma_A) = 1 - \exp \left[- \frac{1}{V_0} \int_V (\sigma_A/S_0)^m dV \right] \quad (4)$$

where σ_A is the applied stress, m is the shape parameter ($=2k$), S_0 is the scale parameter (which includes $K_{g.b.}, a_0$ and ν as well as the coefficient that reflects an averaging of the normal and shear stresses over the grain boundaries) and V is the volume of material. A relation similar to Eq. (4) is also generally assumed to describe microcrack extension, except that S_0 will have a different significance.

Intrinsic Defects

Voids - The probability of fracture from a void can be ascertained by combining the void stress field with the appropriate statistical relation for extension of microcracks existing in the vicinity of the void. If the microcracks are very much smaller than the void radius, a direct statistical analysis using Eq. (4) suffices.^{1,2} For example, when the microcracks predominate at the void surface (Fig. 3), the surface stress field;⁹

$$\sigma_{\theta\theta}/\sigma_A = [3/2(7-5\nu)][(4-5\nu) + 5 \cos 2\theta] \quad (5)$$

$$\sigma_{\theta\theta}/\sigma_A = [3/2(7-5\nu)][5\nu \cos 2\theta - 1]$$

can be combined with Eq. (4), and integrated over the tensile portion of the void surface, to yield;⁷

$$\phi = \exp[1-\phi] = 8r^2(\sigma_A/S_0)^m \exp[0.52m-1.4] \quad (6)$$

where r is the void radius. A stronger dependence on r emerges for volume distributed microflaws, viz., $\phi \propto r^3$, as deduced by Vardar, et al.¹

When the microcracks are not small, vis-a-vis the void radius, a stress gradient correction derived from fracture mechanics solutions must be applied.⁷ This correction arises because the stress intensity factor for a flaw located in a rapidly varying stress field depends sensitively on the exact flaw location and on its size relative to the gradient. The effect is especially manifest for surface located microcracks, which are subject to the following approximate peak stress intensity factor;⁷

$$\hat{K} = \frac{2\sigma_A \sqrt{a}}{\sqrt{\pi[1+0.3(0.2+a/r)]}} \quad (7)$$

This relation for \hat{K} can be used to obtain an effective stress σ_{eff} , that replaces the applied stress in Eq. (16), given by;

$$\sigma_{\text{eff}} = \sigma_A \left\{ 0.3 + 0.7 [(1 + \alpha/2)^2]^{-1} \right\} \quad (8)$$

where $\alpha = 1/r (K_C/\sigma_A)^2$. Typical void size, strength relations at constant probability, predicted by this analysis, are plotted in Fig. 3.

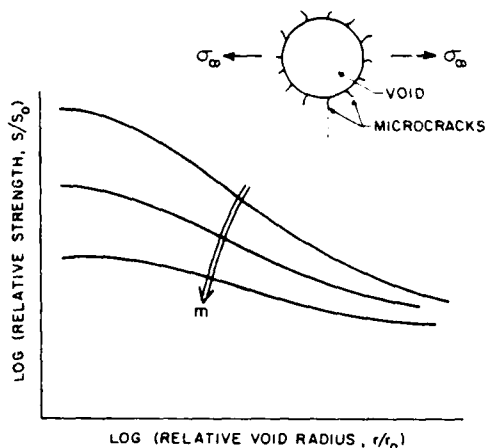


Fig. 3 A schematic illustrating flaws distributed at the void surface, and the fracture strength, void size relation derived at constant probability.

The basic pertinence of the statistical approach for describing strength in the presence of voids, has been substantiated for voids in silicon nitride¹ and in PZT.¹ A detailed statistical analysis was conducted for the experiments performed on silicon nitride. This analysis revealed a maximum likelihood estimate of the void radius dependence of 2.1 and demonstrated that the coefficients m and S_0 were independent of the void radius, with maximum likelihood estimates of $m = 4.6$ and $S_0 = 106$ MPa.

Inclusions - Several modes of failure have been associated with the presence of inclusions. The first distinguishing feature is the tendency for cracking due to thermal contraction mismatch^{10,11} (Fig. 4). If the thermal expansion coefficient of the inclusion is appreciably lower than that for the matrix, radial matrix cracks can initiate when the defect exceeds a critical size. This situation can produce severe strength degradation. This is, however, an unusual condition for structural brittle materials, which must have an intrinsically low thermal expansion coefficient in order to resist thermal shock. Alternately, if the expansion coefficient of the inclusion exceeds that of the matrix, several possibilities can result. Highly contracting, high modulus inclusions will tend to detach from the matrix, tending to produce a defect comparable in character to a void. Inclusions that are more compliant or exhibit smaller relative contractions, remain attached to the matrix. Thereupon, several modes of failure are possible, as exemplified by the results for several types of inclusion in silicon nitride¹ (Fig. 5). The expected failure mode depends upon the elastic modulus and fracture toughness of the inclusion, vis-a-vis the matrix. When

the inclusion has a larger toughness than the matrix (an unusual occurrence) fracture initiates within the matrix, usually from microflaws located within (or adjacent to) the interface. The process then resembles the void fracture problem. However, one additional distinction must be introduced. When the bulk modulus of the inclusion exceeds that of the matrix, the tensile stresses (in a direction suitable for continued extension of the crack due to the applied stress) are confined to a relatively small zone near the poles of the inclusion (Fig. 4). The fracture probability can then be anticipated to be relatively small, as exemplified by the high survival probability for WC inclusions in silicon nitride. Alternatively, when the modulus of the inclusion is smaller than that for the matrix, the maximum tensile stresses occur near the equatorial plane. The fracture condition is then comparable to that for a void, modified by a stress coefficient λ that depends on the modulus ratio;

$$\lambda = 1 + \frac{2[(\kappa/\mu) - 1](1 - 2\nu)}{3(1 - \nu)} \left[\frac{4\mu_m + 3\mu_i}{4\mu_m + \mu_i} \right] \quad (9)$$

where κ is the bulk modulus and μ is the shear modulus. This case is expected to be an important one in ceramics, because the inclusions are often porous¹ (following high temperature mass transport driven by thermal contraction anisotropy) and hence, of low effective modulus.

Most inclusions typically encountered in brittle matrices are of low toughness, because they are usually the friable product of chemical reaction with the matrix (Fig. 6). If such an inclusion also has a relatively high modulus (approaching that of the matrix), the inclusion can fracture sub-critically to create a crack of dimensions comparable to the cross-section of the inclusion. The ultimate fracture strength is then dictated by the usual fracture mechanics relation for an internal crack:¹²

$$\sigma = z(a/c)K_C^M a^{1/2} F(\kappa/\mu, \nu) \quad (10)$$

where a and c are the dimensions of the crack, K_C^M is the effective toughness of the matrix phase neighboring the defect and ν is an exponent (~ 0.5) that depends on the modulus ratio. This type of defect is the most deleterious of the high expansion defects (Fig. 4). Defects in this category are exemplified by Si inclusions in Si₃N₄ (Fig. 5). When the modulus of the defect becomes very small, because of extensive porosity (Fig. 6), the stresses do not attain a sufficient level to induce defect fracture (despite their friability); the situation is then identical to that of low modulus, high toughness inclusions. However, an intermediate condition is also possible; where fracture can initiate within the defect and then propagate directly into the matrix to cause complete failure. In this situation, fracture is dictated by the probability of activating microflaws within the inclusion, and the fracture probability becomes;

$$P = 1 - \exp \left\{ -V_i \left(\frac{\sigma_i}{\sigma_0} \right)^m \right\} \quad (11)$$

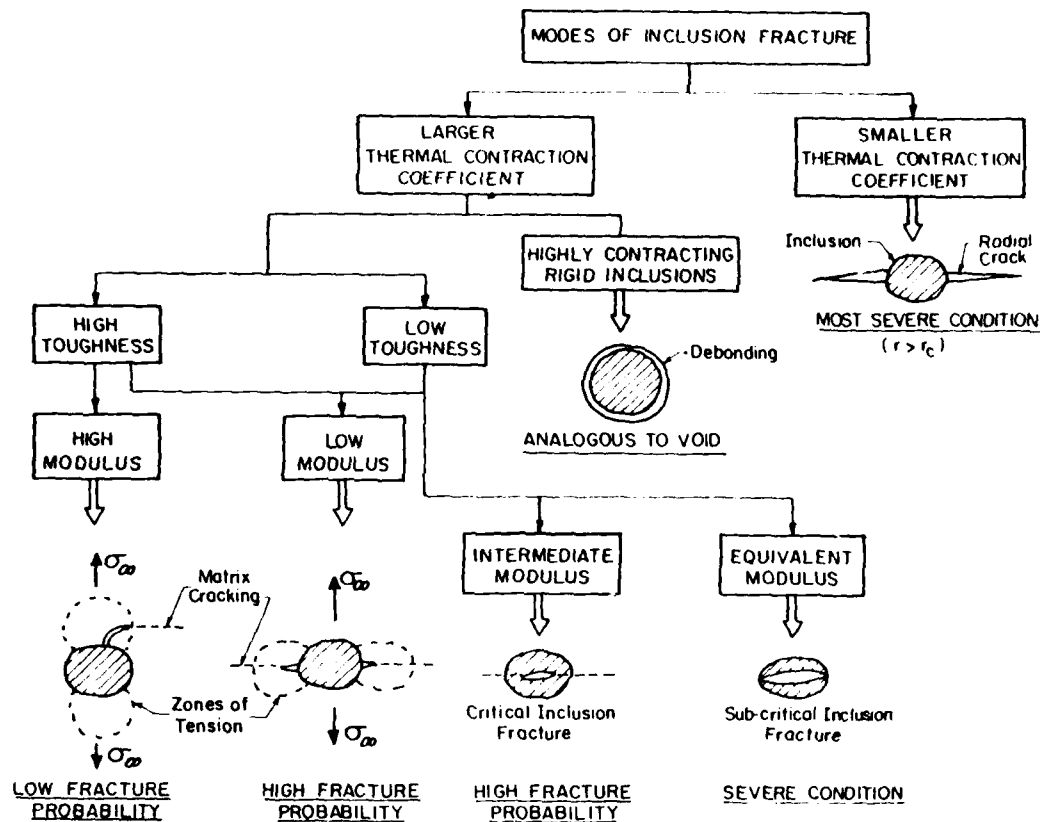


Fig. 4 A schematic indicating the various cracking responses that can occur in the presence of inclusions.

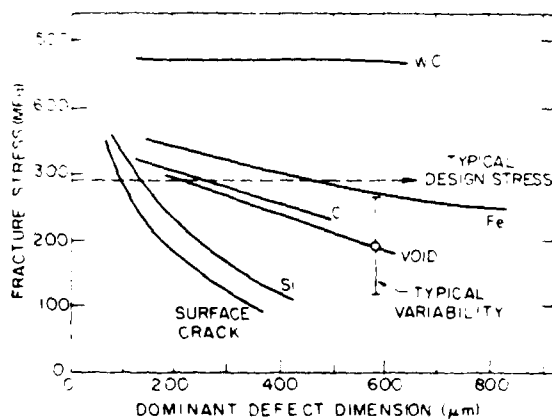


Fig. 5 Strength, size relations for various fracture initiating defects in silicon nitride.

where p_0 is the scale parameter, γ is the shape parameter, and V_i is the inclusion volume. Fracture results obtained for iron silicide inclusions in silicon nitride satisfy a joint fracture relation involving a combination of the critical defect fracture model (Eq. 11) and the matrix fracture model pertinent to low modulus

inclusions.³ This is a plausible situation considering the potential for a transition, with decrease in size, from inclusion initiated fracture (volume dependent) to matrix fracture (area dependent).



Fig. 6 A scanning electron micrograph of an iron silicide inclusion in silicon nitride.

Extrinsic Defects

Extrinsic defects are usually cracks produced by large transient or localized stress states. The most common sources of extrinsic defects are surface cracks produced by machining,¹⁴ impact¹⁵ or thermal shock. The machining induced cracks are the most prevalent (and comparable in character to the cracks introduced by projectile impact.¹⁵ The evolution of the cracks, and their resultant influence on strength, is analogous to the cracking that occurs during indentation¹⁶ (Fig. 7). The ultimate dimensions of the cracks are dictated by the residual indentation field, as controlled by the hardness, H , toughness, K_{IC} , and modulus, E , of the material. A specific relation recently derived for the strength controlling radial cracks is;¹⁶

$$a^{3/2} = 2 \cdot 10^{-2} (\cot^{2/3} \psi) (E/H)^{2/3} K_{IC}^{-1} P_N \quad (12)$$

where ψ is the included angle of the grinding particle and P_N is the normal force applied to the particle. The term E/H arises because fracture is a residual stress dominated process.¹⁷ The radial cracks are usually semi-circular, because of the symmetry of the residual field.

The extension of the surface cracks introduced by grinding is explicable using standard fracture mechanics relations for mode I,¹³

$$K = F(\theta) \frac{2}{\sqrt{\pi}} \sigma \sqrt{a} \quad (13)$$

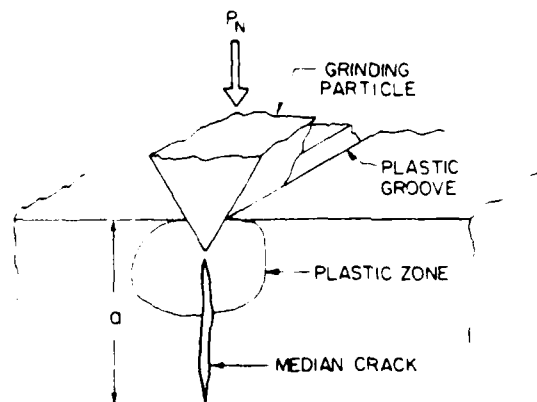


Fig. 7 The median cracking that accompanies the grinding of ceramic surfaces

where $F(\theta)$ is the function, plotted in Fig. 8, that describes the variation in K around the crack periphery. Extension to the mixed mode fracture of inclined cracks appears to be adequately described, over an appreciable angular range, by the simple coplanar strain energy release rate criterion.¹⁸ However, the effective stress that produces crack extension can include a significant residual component; particularly in coarse grinding situations, where the plastic zone is not removed by subsequent fine grinding. Consequently, the applied stress at fracture can exhibit both

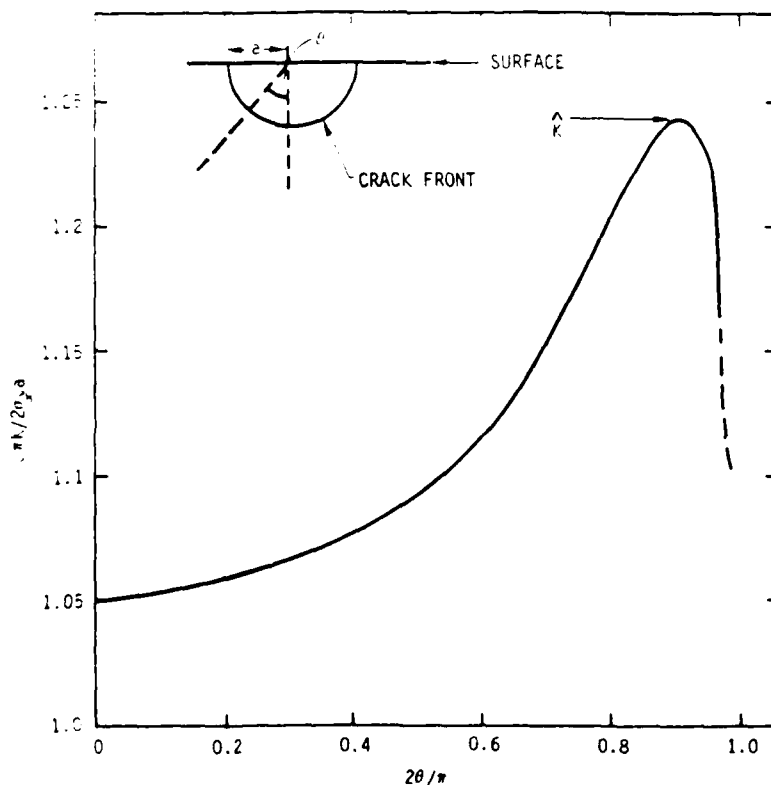


Fig. 8 The variation of the stress intensity factor with peripheral location for a semi-circular surface crack.

systematic and random variations from that anticipated by direct application of Eq. (13) (with the peak stress intensity factor K equated to K_C). Available test results suggest a probability of fracture given by the normal distribution¹⁹

$$\Phi(\sigma_\infty | \sigma_p) = \frac{1}{\omega \sqrt{2\pi}} \int_{-\infty}^{\sigma_\infty} \exp \left[-\frac{(\sigma_\infty - \alpha + \beta \sigma)^2}{2 \omega^2 \nu} \right] d\sigma_\infty \quad (14)$$

where σ_p is the predicted strength obtained from Eq. (13);

$$\sigma_p = \frac{K_C}{F(\theta)} \frac{\sqrt{\pi}}{2\sqrt{a}} \quad (15)$$

$\hat{F}(\theta)$ corresponds to the value at \hat{K} , ν is the variance in σ_p , B is a systematic error coefficient and α is a parameter related to the mean strength.

Microstructural Design

Several direct implications for microstructural design emerge from the fracture models. A reduction in the size of the large extreme of voids and inclusions is the most obvious. Inclusions derive from several different sources, usually in connection with the powder preparation and compaction stages of fabrication. The implementation of more stringent powder handling controls (both chemical and size distribution) provides direct benefits. Voids are more difficult to minimize. Large voids form due to coarsening phenomena (driven by surface diffusion or evaporation/condensation) that can occur concurrent with densification. Their existence can be minimized by avoiding domination of the mass transport by surface diffusion control or evaporation/condensation control: as ascertained by reference to initial stage sintering maps for the material and the sintering environment.²⁰

The formation of extrinsic cracks is determined by those microstructural parameters that influence the toughness and hardness, as indicated by Eq. (12). The relevant issues are described in the following section.

THE FRACTURE TOUGHNESS

Inspection of the above relations for the fracture probabilities from both intrinsic and extrinsic defects indicates that the fracture toughness of the matrix is usually a strength controlling parameter. It is essential, therefore, that the pertinent toughness be understood and, where possible, optimized. For this purpose, it is convenient to introduce the concept of micro-toughness and its relation to the macro-toughness of a material. This concept is necessary because the ultimate fracture of brittle materials (especially those with coarse microstructures) can occur at crack lengths which are sufficiently small, vis-a-vis the important microstructural dimensions, that the macro-toughness of the material is not directly pertinent to the fracture problem.^{21,22,23} The variation of toughness with crack length is still rather ill-defined, because of the difficulties associated both with the conduct of critical experiments and the development of theoretical solutions. The only unequivocal statement currently permissible is that the

effective toughness K_{eff}^C varies from its single crystal value K_s at $a \approx d$ (where d is the grain diameter) to the macroscopic value at $a \gg d$, where ν is the approximate range 5-100 (depending upon the nature of the crack/microstructure interaction), as depicted in Fig. 9. The significance of this variation is illustrated by considering that the effective toughness varies as;²⁴

$$K_{eff}^C = K_s + \frac{K_C - K_s}{1 + d\omega/a} \quad (16)$$

where ω is a constant (≈ 5). The crack extension stress for a circular crack then becomes;

$$\sigma = \left(\frac{\sqrt{\pi}}{2} \right) a^{-1/2} \left[K_s + \frac{(K_C - K_s)}{1 + d\omega/a} \right] \quad (17)$$

which can be rearranged into dimensionless groups to give;

$$\left(2\sqrt{\frac{\omega}{\pi}} \right) \left(\frac{\sigma \sqrt{d}}{K_s} \right) = \frac{1 + \epsilon(1 + \kappa)}{\epsilon^{1/2}(1 + \kappa)} \quad (18)$$

where $\epsilon = a/d\omega$ and $\kappa = (K_C - K_s)/K_s$. Typical stress variations are plotted in Fig. 10a. For $\kappa \gg 8$, the curve shows a maximum. This maximum will control the fracture strength σ_f if the initial crack is in a range that yields an initial crack extension stress less than the maximum, as depicted in Fig. 10b. Differentiating Eq. (18), and setting to zero to obtain the maximum, yields a critical crack length at fracture ($\kappa \gg 8$), given by;

$$\epsilon_c = \frac{[\kappa - 2 + \kappa(1 - 8/\kappa)^{1/2}]}{2(1 + \kappa)} \quad (19)$$

which reduces for large κ to $\epsilon_c \approx 1$, i.e., $a \approx d\omega$. The fracture stress is thus given (for large κ) by;

$$\sigma_f = \frac{K_C}{4\sqrt{d\omega}} \quad (20)$$

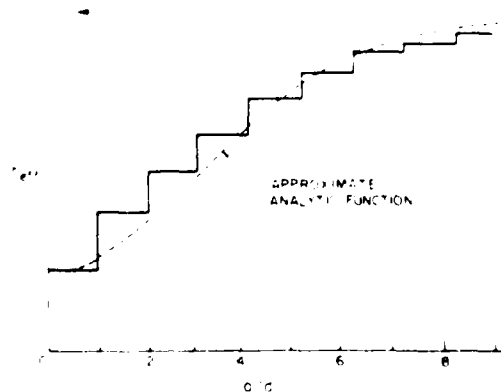


Fig. 9 A typical variation in toughness with relative crack length for small cracks.

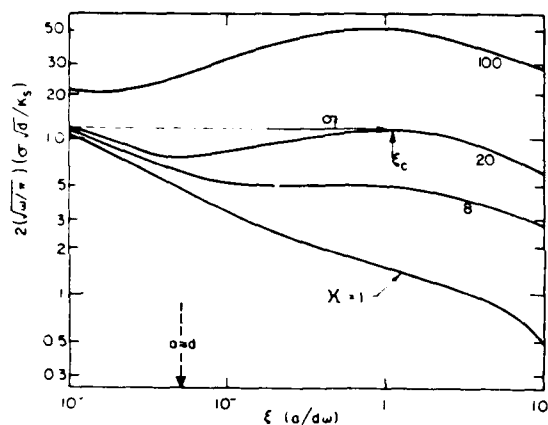


Fig. 10a The variation in the normalized crack extension stress with relation given in Fig. 9.

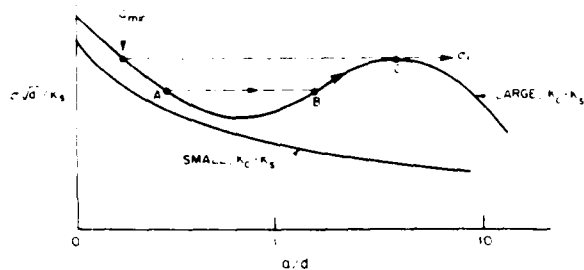


Fig. 10b A schematic indicating the growth of cracks for large $K_{IC} - K_{ICs}$, up to the fracture stress σ_c ; A to B occurs unstably while B to C corresponds to stable growth.

The interesting result thus emerges that the strength is inversely proportional to $d^{1/2}$ (regardless of the function selected for K_{eff}); a behavior typical of coarse grained ceramics,^{21,22} for which the pre-existent cracks are in the microcrack range. Catastrophic crack extension is also noted to occur when $K_{eff} < K_{IC}$. The concept of toughness is thus often a nebulous one for coarse grained materials; and the conventional use of toughness should be confined to materials with fine microstructures (for which strength does not relate systematically to grain size).

The development of theoretical relations between the intrinsic toughness of brittle materials, microstructure and crack length is presently at a very elementary level, primarily because crack extension is a complex three-dimensional problem. Reliance on toughness levels for correlating strength results with defect dimensions (through the fracture models) must presently be placed on measured values, obtained on single crystals and polycrystals. However, a more advanced comprehension of extrinsic toughening has recently emerged. This comprehension provides

useful insights pertinent to microstructural design, and will be presented in some detail.

Microstructural Design

Two important mechanisms of toughening have been subject to recent analysis:^{25,28} toughening induced by martensitic transformations and by microcracking. Both processes involve a zone of dilation and induced around the crack tip, which results in a reduced crack tip tension and hence, an increase in toughness. Also, it is self-evident that the closer the system is to transformation (or microcracking) in the absence of stress, the larger will be the process zone size and hence, the larger the toughness. However, in detail, the processes are quite different.

Martensitic Toughening

A toughening can be induced in brittle materials if particles are introduced that undergo a diffusionless transformation,^{25,26,29} induced by a stress field of combined shear and hydrostatic tension. Typical examples are ZrO_2 , HfO_2 , $BaTiO_3$ and BN. A prerequisite for the toughening is that the particles be incorporated in a relatively stiff elastic matrix. This constrains the transformation strain and thus, permits the thermally induced transformation to be considerably suppressed below M_s . Then, activation by an applied stress becomes viable.

Estimation of the conditions required for toughening can be obtained by examining the free energy of the total system, before and after transformation. Toughening will be permissible if, as noted above, an applied hydrostatic tension and shear are needed to yield an incremental energy decrease due to transformation. The total mechanical energy change of the system following transformation, under applied stress p^A (dilatational) and p_{ij}^A (deviatoric) is:^{6,30}

$$\Delta U = - \left[e^T V_p (p^A + p^I/2) + e_{ij}^T V_p (p_{ij}^A + p_{ij}^I/2) \right] \quad (21)$$

while e^T and e_{ij}^T are the dilatational and deviatoric transformation strains; p^I , p_{ij}^I are the stresses within the inclusion after transformation, given (for a spherical particle) by:³¹

$$p^I = - \frac{(1+\nu_m)/2e_m^T + (1-2\nu_m)/e_p^T}{(1+\nu_m)/2e_m^T + (1-2\nu_m)/e_p^T} \quad (22)$$

$$p_{ij}^I = - \frac{e_{ij}^T}{(1+\nu_m)/2e_m^T + (1-2\nu_m)/e_p^T}$$

By considering the total free energy of the system following transformation,

$$\Delta F = \Delta U + \Delta S - \Delta F_0 \quad (23)$$

where ΔF_0 is the difference in chemical free energy, per unit volume, between the two crystal structures and ΔS is the difference in surface energy, the critical transformation stresses p_c^A , (p_{ij}^A) can be deduced by permitting ΔF to

incrementally decrease; this assumes that the thermodynamic driving force is a sufficient condition for transformation (i.e., appropriate nuclei pre-exist within the particles). Neglecting the difference in surface energy, since this is presumed to be small (at least, for incoherent particles), the critical applied stress for transformation, under uniaxial tension σ_A ($p_A = \sigma_A/3$; $p_{ij} = \sigma_A/2$) becomes

$$\frac{\sigma_A [2+2\epsilon]}{6eT_p E_p} = \frac{1}{\beta(1+\nu_m)+2(1-2\nu_p)} + \frac{(\epsilon^2/2)(7-5\nu_m)}{(1+\nu_p)(7-5\nu_m)+2(1+\nu_m)(4-5\nu_m)} - \Delta F_0/E_p(e^T)^2 \quad (24)$$

where $\epsilon = e^T_{ij}/e^T$ and $\beta = E_p/E_m$. As a first approximation, conditions which yield a positive σ_A are likely to result in transformation toughening.

This approach can be tentatively extended to examine transformation zones around crack tips, by inserting the crack tip field relations for p_A and p_{ij} into Eq. (21). This approach can only be regarded as highly approximate because significant effects are neglected; namely, stress gradient effects, particle interactions, crack surface relaxations and reverse transformations. Nevertheless, some useful insights are provided. The relation for the transformation zone radius r_c at small particle volume fractions (for $\nu_p = \nu_m = 0.2$) is,

$$r_c \left(\frac{e^T E_p}{K_I} \right)^2 = \frac{4.1}{\pi} \quad (25)$$

$$\left[\frac{\cos(\theta/2)[\pm 1 + 1.25\epsilon \sin(\theta/2)\cos(3\theta/2)](1+\beta)}{\beta(1+3\epsilon^2) - 3.6(1+\beta)\Delta F_0/E_p(e^T)^2} \right]^2$$

Some typical zones are plotted in Fig. 11. The transformation zone radius can subsequently be used to estimate the toughening increment

$$\frac{\sigma_T}{\sigma_0} = \frac{V_f(1+\beta)[\beta(1-V_f)+V_f][0.34\epsilon]^2}{[\beta(1+3\epsilon^2) - 3.6(1+\beta)\Delta F_0/E_p(e^T)^2]} \quad (26)$$

where V_f is the volume fraction of particles. The central role of the chemical free energy in the resulting toughening signifies strong effects of temperature and of chemical composition: the toughness decreasing as the temperature increases (Fig. 12). The evident merits of an intrinsically high toughness host (σ_0) and of a large volume fraction of particles also emerge.

Further developments which take specific account of interaction effects and of the particle orientation can be envisaged using computer techniques, analogous to those recently employed for microcracking (see following section). Research on the influence of chemical composition on ΔF_0 (and hence, on σ_0) is also needed; probably involving composition probes within particles, using the scanning transmission electron microscope.

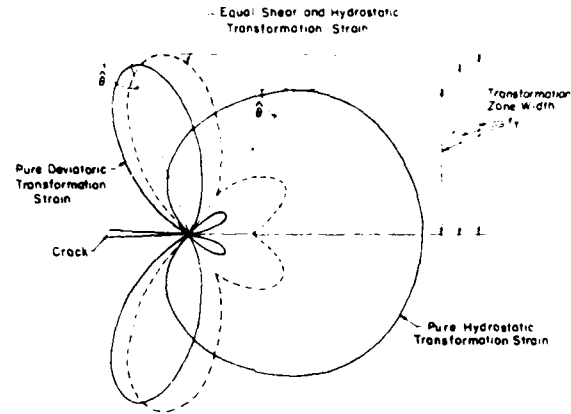


Fig. 11 Calculated transformation zones around crack tips in brittle materials.

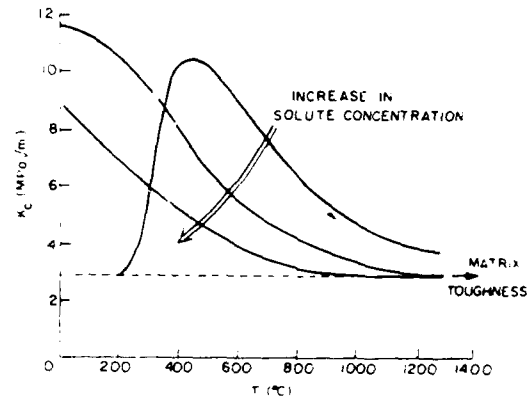


Fig. 12 A schematic illustrating trends in martensitic toughening with temperature and chemical composition.

coupled with toughness measurements. Additionally, the role of twinning, particularly its effect on the shear component of the strain energy, requires clarification: again using electron microscope techniques.

Microcracking

Stable microcracking is presumed to occur in materials that contain stresses (e.g., due to thermal contraction mismatch or transformation), which also have a sufficiently coarse microstructure.¹¹ The induction of stable microcracks within a crack tip process zone (Fig. 13) can be described through probabilistic microcrack formulations (such as Eq. 3) superimposed on the crack tip field equations.¹¹ However, computer techniques are needed to take proper account of the strong interaction of the microcracks with the primary crack. Such an approach has recently been reported by Hoagland and Embury,¹² using a Green's function devised by Hirth, et al.¹³ One important result of this analysis is the realization that

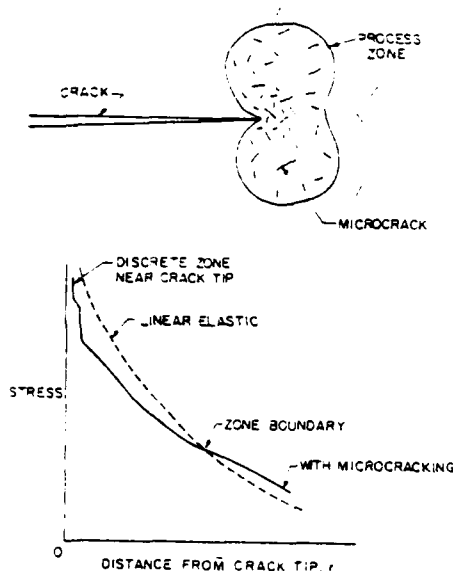


Fig. 13 A microcrack process zone induced in materials with large local residual stresses, indicating that microcrack densities and the resultant crack tip stress field.

the process zone size is not appreciably affected by crack interaction effects.²⁷ However, little has yet been done to explore the influence of the various microcrack parameters on the fracture toughness.

Conceptually it is useful to consider the microcrack process zone as a dilatant, compliant zone that inevitably must yield a reduction of the tensile stress at the primary crack tip²³ (Fig. 13). The effect is typified by solutions for a crack entering a low modulus inclusion.³⁵

One microcrack toughening situation that can be addressed more positively is the toughening in the presence of second phase particles. A typical condition would be the incorporation of small particles that exhibit a larger thermal contraction coefficient than the host. It has previously been established¹¹ that particle microcracking, in this situation, can be reasonably well described by requiring that the strain energy in the particle exceed the surface energy needed to create a circumferential crack (a surprising result that has, nevertheless, been recently substantiated by numerical strain energy release rate calculations).³⁶ Hence, a thermodynamic calculation, analogous to that conducted for martensitic toughening should provide an approximate estimate of the process zone size and hence, of the toughening. The merits of the zone size calculations are reinforced by the Hoagland and Embury²⁷ result (noted above) that interaction effects are of secondary importance. The basic ingredients of the calculation are the strain energy³⁶

$$\Delta U = (4/3)\pi r_p^3 e^T \left[p^A + \frac{e^T E_m}{(1+\nu) + 2\nu(1-2\nu)} \right] \quad (27a)$$

and the surface energy;

$$\Delta S = 4\pi r_p^2 \gamma_{int} \quad (27b)$$

where r_p is the particle radius, e^T is the thermal contraction mismatch strain ($e^T = \Delta\alpha\Delta T$) and γ_{int} is the fracture surface energy for particle microfracture. Note that, in the present approximation, a particle which contracts away from the matrix is necessary, in order that the strain energy of the system can be increased by the crack tip (tensile) stress field. Microfracture will then proceed, according to the present criterion, when $\Delta U > \Delta S$; while toughening can occur when p^A in Eq. (27) is positive (the particles must be intact prior to stress application). Inserting the hydrostatic component of the crack tip stress field,

$$p^A = \frac{2K(1+\nu)\cos\theta/2}{3\sqrt{2\pi}r} \quad (28)$$

the transformation zone size and shape $r_c(\theta)$ can be approximately deduced. For the condition, $\nu = 0.2$, substitution of Eq. (28) into Eq. (27) gives;

$$r_c = \frac{1}{2\pi} \left(\frac{K}{E_m e^T} \right)^2 \frac{\cos^2(\theta/2)(1+\nu)^2}{[3.62(1+\nu)-1]^2} \quad (29)$$

where $\mu = \gamma_{int}/r_p E_m (e^T)^2$. The zone size can be converted into a toughening increment from the residual free energy in the transformation zone

$$\Gamma_T = [\Delta S - \Delta U_0] r_c(\theta) V_f / (4/3)\pi r_p^3 \quad (30)$$

where V_f is the volume fraction of particles, ΔU_0 is the strain energy in the absence of an applied stress and $\theta = \pi/2$. Combining Eqs. (27), (29) and (30), the toughening increment becomes;

$$\frac{\Gamma_T}{\Gamma_0} = \frac{n}{1-n} \quad (31)$$

where

$$n = \frac{3V_f(1+\nu)}{16\pi[3.62(1+\nu)-1]}$$

The maximum toughening clearly occurs when $3\gamma_{int} > r_p E_m (e^T)^2$. The particle size and the mismatch strain exert an influence through the n term in the denominator, in the sense that Γ_T increases as the particle size or the mismatch strain increase, provided that r_p is below the critical value for spontaneous (stress free) microcracking. These results provide useful perspectives for designing optimally tough ceramic systems, based on controlled microcracking.

NON-DESTRUCTIVE DEFECT CHARACTERIZATION

Accept/Reject Criteria

Accept/reject decisions based on a non-destructive measurement of scattering from a defect must recognize the probabilistic character of the problem.¹⁷ At least three probabilities enter the analysis: the failure probability,

given the defect dimensions (discussed above) $\phi(a_{\infty}^C|a)da$; the joint probability of identifying the defect type and of estimating its size, $\phi(a_{es}|a)da_{es}$; the a priori distribution of defect sizes, $\phi(a)da$. These probabilities are combined and integrated to various inspection levels, a_{es}^* , to obtain two interrelated probabilities: the false-accept probability ϕ_A and the false-reject probability, ϕ_R (Fig. 14a):

$$\phi_A = \int_0^A \int_0^{a_{es}^*} \int_0^{\infty} \quad (32)$$

$$\left[\phi(a_{\infty}^C|a)da_{\infty} \right] \left[\phi(a_{es}|a)da_{es} \right] \left[\phi(a)da \right]$$

$$\phi_R = \int_A^{\infty} \int_{a_{es}^*}^{\infty} \int_0^{\infty}$$

$$\left[\phi(a_{\infty}^C|a)da_{\infty} \right] \left[\phi(a_{es}|a)da_{es} \right] \left[\phi(a)da \right]$$

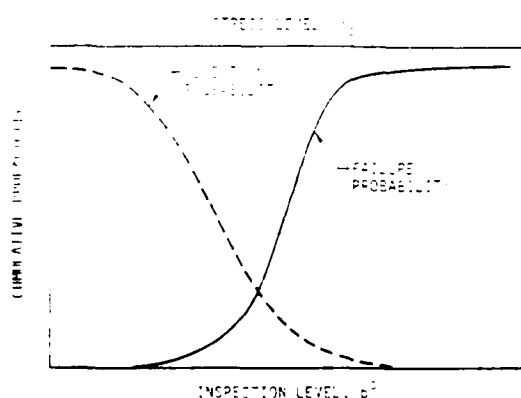


Fig. 14a False-accept, false-reject curves for two hypothetical measurement techniques, A and B.

where a_A is the level of the applied tension in the volume element containing the defect. The inspection level a_{es}^* refers to the estimated defect dimension(s) selected for the rejection or acceptance of the component, e.g., all components with an estimated maximum dimension less than a_{es}^* are accepted and all components with an estimated dimension greater than a_{es}^* are rejected. The false-accept probability ϕ_A is thus the probability that components accepted in accord with the specified inspection level will contain defects more severe than indicated by the estimate, and will actually fail in service (i.e., related to the failure probability). This probability decreases, of course, as the inspection level decreases (Fig. 14b). The false-reject probability ϕ_R is the (related) probability that rejected components would, in fact, have performed satisfactorily in service, because the defect severity has been overestimated by the selected inspection level. This probability increases as a_{es}^* decreases (Fig. 14b). However, it is crucial to recognize that these probabilities are interrelated, i.e., they merely represent different ranges of integration of the same combination of probability functions (Eq. 32). This interdependence is exemplified in Fig. 14a, which is a typical plot relating the false-accept and false-reject probabilities: once one of these probabilities has been selected, the other probability, as well as the associated inspection level, are necessarily defined. It is now apparent from Fig. 14a that the inspection technique, or combination of techniques, that would be preferred is that which yields a curve as close as possible to the probability axes. For example, technique B is preferred over technique A, because the rejection of satisfactory components required to satisfy the failure probability requirements is much lower. Such curves thus represent a quantitative method for characterizing the failure prediction capabilities of various inspection techniques, for a given material and service condition.

Scrutiny of the available inspection methods pertinent to ceramics indicates that acoustic methods are preferred, because acoustic waves are appreciably scattered by all of the critical defect types encountered in structural ceramics. The most promising measurement algorithms and their future potential are thus briefly reviewed.

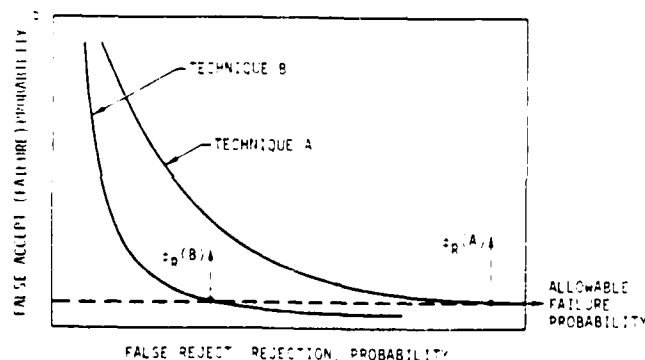


Fig. 14b The variations of failure probability and rejection probability with inspection level.

Acoustic Measurement Algorithms

Surface Waves - The most directly successful method is the use of surface acoustic waves to predict failure from surface cracks; in particular, the use of long wavelength, $\lambda \gg a$, surface waves.^{38,39} In the long wavelength limit, the scattering of an acoustic wave (stress wave) by a crack is closely analogous to the interaction of the crack with an applied stress field. In particular, both the scattering coefficient S_1 and the strain energy release rate G are related to the crack surface integral;³⁸

$$\int_{A_s} \sigma_{ij} \Delta u'_j n_i dA_s$$

where σ_{ij} is the stress across the crack plane in the absence of the crack, $\Delta u'_j$ is the displacement of the crack surfaces and A_s is the crack surface area. Hence, it is straightforward to demonstrate that the scattering coefficient is directly related to the crack extension stress σ_c by;³⁹

$$\frac{K_c}{\sigma_c} = 2 \left[\frac{6(1-\nu)\lambda^2 S_1 w}{\pi f_z^2} \right]^{1/6} \quad (33)$$

where w is the beam width, π is the transducer efficiency and $f_z \sim 0.4$. This result is strictly correct when both the acoustic wave and the applied stress are normal to the crack plane, as exemplified by recent results¹⁹ summarized in Table I. However, since the coplanar criterion also appears to afford a reasonably satisfactory description of surface crack extension in ceramics,¹⁸ at least over the angular range of interest, the approach appears to be of general applicability. Surface waves also have the advantage that they propagate over curved surfaces, so that complex shapes can be readily probed.¹⁹

Table I

Comparison of Measured Surface Crack Sizes With Those Predicted Using Long Wavelength Surface Acoustic Waves

Sample	σ_F Actual MPa	Acoustic a μ m	σ_F Acoustic MPa	z
5kg: 1	338.45	56	350	3.3
2	365	51	367	0.54
10kg: 1	298.5	67	320	6.72
2	275.4	66	322.7	14.6
20kg: 1	159.22	274	158.4	0.52
2	179.13	262	159.7	12.17
3	189	255	154.2	15.1

Bulk Waves - The characterization of bulk defects is more complex. Information over a wide range of frequencies appears to be needed to obtain a highly probable defect type classification and hence, a size estimation. Appropriate techniques are available including: the scanning laser acoustic microscope,⁴⁰ 200 MHz ZnO transducers⁴¹ and conventional (2-50 MHz) transducers. Rapid scanning methods for defect location have also been devel-

oped. The most critical issue, therefore, concerns the appropriate choice of algorithms to obtain the most reliable defect characterization. A typical set of algorithms and their interaction are illustrated in Table II, using low and high frequency information as well as acoustic microscopy. This set has not yet been fully evaluated, so many redundancies may exist. Four algorithms are employed in this scheme: (i) long wave length scattering,⁴² (ii) intermediate wavelength Born approximation,⁴³ (iii) high frequency spectroscopy⁴⁴ and (iv) cross sectional information from acoustic microscopy. The impulse response functions (Fig. 15) are firstly used to determine whether the defect is a void or an inclusion; the void has an impulse response function (Fig. 15a) characteristic of the transducer, while inclusions have more complex functions (Fig. 15b). Thereafter, voids can be analyzed straightforwardly, using a variety of algorithms. For example, a long wavelength algorithm similar to that described for surface cracks may be employed. In the long wavelength limit the scattered amplitude is related to the void volume V by;⁴⁷

$$A = \frac{-V\omega^2}{(4\pi c^2)^2} \left[1 + \frac{1+\nu}{7-2\nu} + \frac{10(1-2\nu)}{7-5\nu} \right]^2 \quad (34)$$

where ω is the frequency and c is the elastic wave speed in the host. Inclusions are more difficult to analyze; the combined use of several algorithms is almost certainly required. For nearly spherical inclusions, the interpretation is relatively straightforward. For example, a combination of the long wavelength algorithm (which contains coupled volume and type information) and the Born approximation (which provides an independent estimate of the distance from the geometric center to the back face of the inclusion) can yield the requisite size and type information. A typical result, obtained for a 100 μ m radius Si inclusion in Si_3N_4 , is illustrated in Fig. 16; wherein the joint probability of the defect type and size is plotted as a function of the estimated size. In order to obtain this result, six possible inclusion types were permitted to exist within the material (selected on the basis of detailed failure analyses conducted on this material). Alternatively, high frequency measurements displayed in the frequency domain would provide close estimates of the defect size and type.

FUTURE PROSPECTS

It is hoped that this paper conveys the impression that a positive start has been made in establishing the scientific framework for microstructural design with brittle materials. Certain rewarding research directions have emerged and several exciting near term, and more remote, prospects seem viable.

Further studies aimed at characterizing models of fracture from defects are very pertinent. The incisive combination of inputs from mechanics, materials and statistics demonstrated on the limited set of problems addressed thus far should provide some direction and scope for continued activity. Important defects not yet considered include: void clusters, sub-surface inclusions, surface crack arrays. Progress toward the comprehension of fracture from these defects could utilize existing (or marginally extended)

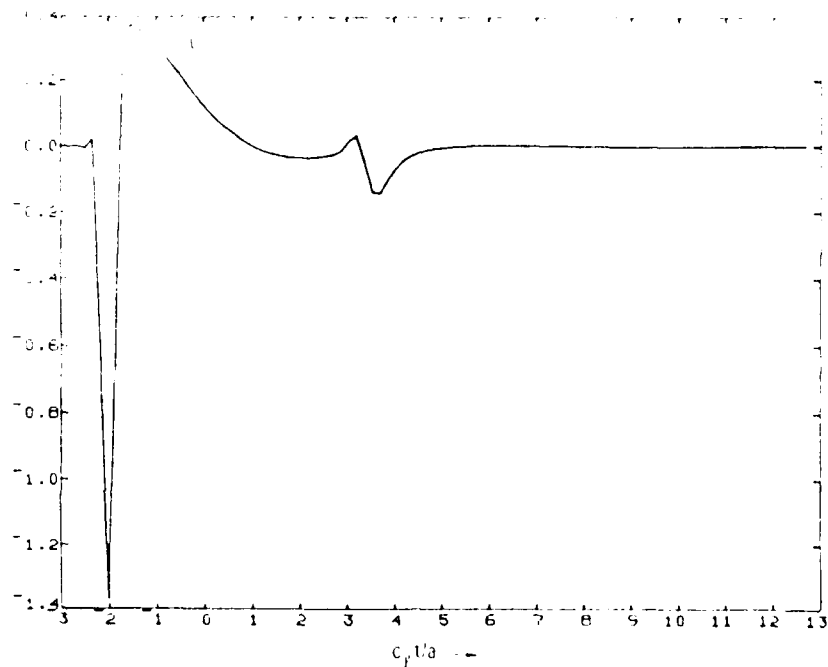


Fig. 15a Impulse response functions for defects in ceramics, a void in Si_3N_4 .

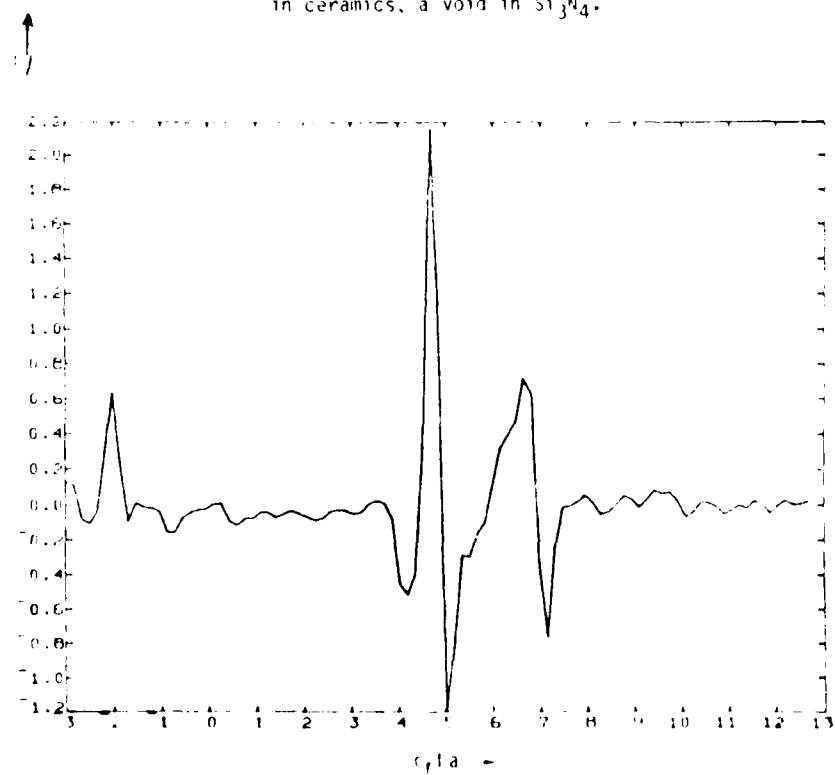


Fig. 15b Impulse functions for defects in ceramics, an inclusion in Si_3N_4 .

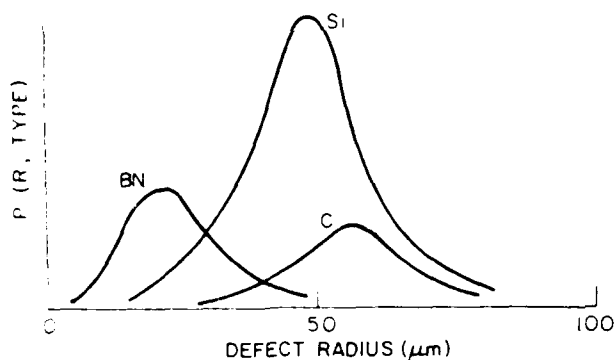


Fig. 16 The joint probability of defect type and size deduced from a coupled long wavelength, Born approximation algorithm.

stress analyses coupled with advanced statistical methods and fracture mechanics solutions.

A very preliminary comprehension of toughening mechanisms has evolved from simplified thermodynamic analyses and computer simulations. Considerable advances could be anticipated through the coupled use of analytic and computer methods. These would include stress (or strain) based transformation or microcracking criteria, statistically distributed in accord with distribution functions inferred from critical experiments (e.g., acoustic emission amplitude distributions). Monte Carlo methods could then be used to study the evolution of process zones, with interaction effects accounted for using image stress solutions.

More immediate advances can be anticipated in ultrasonic flaw characterization. A comprehensive set of inversion algorithms already exist, and initial results imply that good estimates of defect size and type are possible, using combinations of these algorithms. Future prospects for devising effective accept/reject schemes pertinent to ceramics are thus very exciting.

ACKNOWLEDGEMENT

The author wishes to thank the Division of Materials Sciences, Office of Basic Energy Sciences, U.S. Department of Energy under Contract No. W-7405-Eng-48 for funding the work on toughening mechanisms, the Advanced Research Projects Agency for funding the work on fracture models and accept/reject criteria under Contract F33615-74-C-5130, and the Office of Naval Research for supporting the work on surface crack dilation.

REFERENCES

1. O. Vardar, I. Finnie, D.R. Biswas and R.M. Fulrath, *Int'l J. Frac.* **13**, 218 (1977).
2. A.G. Evans, D.R. Biswas and R.M. Fulrath, *J. Amer. Ceram. Soc.* **62**, 101 (1979).
3. A.G. Evans, G. Meyer, K. Fertig, B.I. Davis and H.R. Baumgartner, *J. of Non-Destructive Evaluation*, in press.
4. A.G. Evans, *Acta Met.* **26**, 1845 (1978).
5. A.M. Freudenthal, *Fracture* (Ed. H. Liebowitz) **2**, Academic Press, N.Y., 592 (1969).
6. A.G. Evans, B.R. Tittmann, L. Ahlberg, G.S. Kino, and B.T. Khuri-Yakub, *J. Appl. Phys.* **49**, 2669 (1978).
7. S.B. Batdorf and H.L. Heinisch, *J. Amer. Ceram. Soc.* **61**, 355 (1978).
8. A.G. Evans, *J. Amer. Ceram. Soc.* **61**, 302 (1978).
9. S. Timoshenko and J.M. Goodier, *Theory of Elasticity*, McGraw Hill, N.Y. (1951).
10. A.G. Evans, *J. Mater. Sci.* **9**, 1145 (1974).
11. R.W. Davidge, and T.J. Green, *J. Mater. Sci.* **9**, 629 (1968).
12. H.R. Baumgartner and D. Richerson, *Fracture Mechanics of Ceramics* (Ed. R.C. Bradt, D.P.H. Hasselman and F.F. Lange) **1**, 369 (1974).
13. G.C. Sih, *Handbook of Stress Intensity Factors*, Lehigh Univ. Press (1973).
14. M.V. Swain, *Fracture Mechanics of Ceramics*, *ibid.* **3**, 257 (1978).
15. A.G. Evans, M.E. Gulden and M. Rosenblatt, *Proc. Roy. Soc. A361*, 343 (1978).
16. B.R. Lawn, A.G. Evans and D.B. Marshall, *J. Amer. Ceram. Soc.*, in press.
17. D.B. Marshall and B.R. Lawn, *J. Mater. Sci.*, in press.
18. J.J. Petrovic and M.G. Mendiratta, *J. Amer. Ceram. Soc.* **59**, 163 (1976).
19. B.T. Khuri-Yakub, J. Tien, G.S. Kino and A.G. Evans, *J. Amer. Ceram. Soc.*, to be published.
20. M.P. Ashby, *Acta Met.* **22**, 275 (1974).
21. R.W. Rice, *Fracture Mechanics of Ceramics*, *ibid.* **1**, 323 (1974).
22. R.W. Rice, *Treatise on Materials Science and Technology*, **11** Academic Press, 199 (1977).
23. J.P. Singh, A.V. Virkar, D.K. Shetty and R.S. Gordon, *J. Amer. Ceram. Soc.* **62**, 179 (1979).
24. A.G. Evans, *J. Amer. Ceram. Soc.*, in press.
25. D. Porter, A.G. Evans and A.H. Heuer, *Acta Met.*, in press.
26. A.G. Evans and A.H. Heuer, *J. Amer. Ceram. Soc.*, in press.
27. R.G. Hoagland and D. Embury, *J. Amer. Ceram. Soc.*, in press.
28. A.G. Evans, to be published.
29. R. Garvie, R.H. Hanninck and R.T. Pascoe, *Nature* **258**, 703 (1975).

30. J.D. Eshelby, Proc. Roy Soc. A252 561 (1959).
31. T. Gupta, Bull Amer. Ceram. Soc. 58 330 (1978), Abstract only.
32. F.F. Lange, work performed at Rockwell International Science Center, to be published.
33. A.G. Evans, A.H. Heuer and D. Porter, Fracture 77 (Ed. D.M.R. Taplin) Univ. Waterloo Press 1, 529 (1977).
34. J.P. Hirth, R.G. Hoagland and P.C. Gehlen, Int'l J. Solid Structures 10, 977 (1974).
35. B. Erdogan and G. Gupta, Int'l J. Frac. 11, 13 (1978).
36. Y.M. Ito, M. Rosenblatt, F.F. Lange and A.G. Evans, Int'l J. Frac., in press.
37. J.M. Richardson and A.G. Evans, J. of Non-Destructive Evaluation, to be published.
38. B. Budiansky and J.R. Rice, J. Appl. Mech. 45 2 (1978).
39. B.T. Khuri-Yakub, G.S. Kino and A.G. Evans, J. Amer. Ceram. Soc., in press.
40. L.W. Kessler, work performed at Sonoscan.
41. B.T. Khuri-Yakub and G.S. Kino, J. Phys. Lett. 30, 2 (1977).
42. W. Kohn and J.R. Rice, J. Appl. Phys., to be published.
43. J.H. Rosi and J.A. Krumhansl, Materials Science Center Report 2846, Cornell Univ.
44. R.B. Thompson and A.G. Evans, Sonics and Ultrasonics 23, 292 (1967).

PRELIMINARY DISCUSSION
A. I. Evans

Tom Darken (Ch): I noticed on the slide you had strength versus defect size you didn't have any defect smaller than 100 microns. I also wondered what temperature that data was taken at. Was that room temperature data? And if so, what happens?

Tony Evans: Good question. It turns out that to achieve a strength of about 50,000 psi which is just about the limit of any design stresses for ceramic turbines, 100 micron defects is as small as you can get. 100 microns is about right. But those data were at room temperature. What happens when you take equivalent data at high temperature is that the silicon inclusion becomes less deleterious. Everything else more or less gets in the same category. But the silicon inclusion becomes less deleterious, it becomes more pliable and, therefore, less brittle. So, silicon turns out to be more like a void in really high temperatures. About 1,000 degrees centigrade. So, depending upon where the components see the stresses, because if it's a thermal shock then you need the results pertinent to about 900 degrees centigrade. And those results are incorporated. The (inaudible) rotations in the turbine blade, high temperature is also more appropriate.

John Schallies (Airesearch): Just a general comment from those of us who are out in the industry and who have to use these components. I think perhaps it wouldn't be unrealistic to say in the past we weren't encumbered by too much knowledge, so we went ahead and used some of these things. And in some cases successfully and in other cases not, as we are all aware. I think there is maybe one point that should be made, that you have to look at the stress distribution in the particular component and its geometry. And it turns out in most cases the area of real concern is at or near the surface. And while we may be able to detect very, very small defects in the subsurface, we still got the near surface resolution problem to tackle. And if there was an area that those of us would like to see work being done in, it would be in tackling the near surface resolution problem and defect detection. Obviously, in a size range you have indicated now, that's critical for the blower-size defects.

Tony Evans: You're right about the perturbation of the acoustic wave on the front face of the sample. And therefore, the defect gets obscured by that front face.

John Schallies: That's why we are pursuing things in acoustic microscopy and photo-acoustic spectroscopy. We are interested in learning of the work at Stanford now that detects those things because when you look at the stress distribution in a component and you superimpose thermal and vibration and all that, high stress gradients are at the surface of the part.

Tony Evans: The surface or subsurface. That's right.

Paul Bellert: I was wondering on one of your first slides showing two gaussian distributions for being satisfactory or not, and the abscissa was a defect size. So, I assume you have continuous distribution of your defect size versus some parameter type. Yet, how do you get from these two well-separated gaussian probabilities for satisfactory or unsatisfactory?

Tony Evans: They weren't gaussian. They were somewhat bimodal.

Paul Bellert: They were separated. It doesn't matter, they were --

Tony Evans: I agree with that. This is the slide he is referring to. He is wondering about why there is a separation. The separation comes from the measurement process. It's distinguishing large defects from small ones. And the data relates that distinction. The wider spread there two bimodal become. In fact, to get this, one has to make an assumption for a measurement of the distribution of existing defects. And in this case we took a bell-shaped distribution of defect size. Bell's inequality says rather faintly for the defect size distribution and used that information to compute --

Paul Bellert: That's a uniform distribution of the defects.

Tony Evans: It's a bell-shaped distribution of the defects.

A. J. Evans (discussion continued)

Paul Holler: How do you get a uniform distribution of defects to this very well separated distribution for the probability to be satisfactory or not satisfactory?

Tony Evans: Because of the measurement. The measurement distinguished the very large extreme of the distribution from the intermediate extreme, and the measurement allows those curves to separate out. If there is no measurement, you're right, they all come together in one curve.

John Richardson (Science Center): It also depends on the nature of the failure process. The failure process has a great deal of randomness, so they won't separate.

Tony Evans: What John is saying is if it's an extremely random process. In other words, if you have a defect of size A and a fracture strength associated with that size so broad, then those would also be separated by a very narrow amount. But separation for a given size is not that broad and therefore, that allows you to make those curves.

Paul Holler: I still have not understood, but I don't want to hold you up.

Tony Evans: One more question. I'm afraid we're going to have to get the talks under way.....let's get back to the question that John made about surface versus volume. If you were to use surface wave technique to look at subsurface inclusions, then you concentrate on the distributions that are in the near surface which is sampled by the surface wave. If you look using a bulk wave method, then you use distribution which is pertinent to the bulk wave. It may be the same or it may be different. Anyway, I think we have to conclude. Many answers to these questions are better approached in the actual talks as they occur this morning.

#

PROBABILISTIC MODELS FOR DEFECT INITIATED FRACTURE IN CERAMICS

A. G. Evans
University of California
Berkeley, California 94720

M. E. Meyer, K. W. Fertig and B. I. Davis
Rockwell International Science Center
Thousand Oaks, California 91360

H. R. Baumgartner
Norton Co.
Worcester, Massachusetts 01606

ABSTRACT

Fracture tests on hot-pressed silicon nitride containing voids and several types of inclusions have been conducted. Fracture models pertinent to each defect type have been proposed and correlated with the data. The specificity of the fracture models is emphasized, and the various trends with defect size that result from the models are described. The resultant fracture probability relations are one of the key inputs to accept/reject decisions for nondestructive failure prediction.

INTRODUCTION

Inclusions and voids are important sources of failure in structural ceramics. It is crucial for the structural utilization of these materials that the probability of fracture from typical defects be sufficiently characterized that effective non-destructive failure prediction schemes can be devised. In this study, samples of silicon nitride containing typical defects are subjected to controlled fracture tests to determine both the fracture mechanism and the specific fracture stress at the defect. Fracture models pertinent to each defect type are then developed, and the fracture probabilities (derived from the test data) are related to the parameters of the models. The resultant probability functions constitute one of the three functions required to isolate the accept/reject criterion pertinent to nondestructive failure prediction.¹

Preliminary studies of fracture from defects in ceramics²⁻⁴ have indicated that the fracture process is likely to consist of the activation of small defects (voids, disbonds, grain boundary cracks), occurring within or near the defect, by the ambient local stress field (due to both the thermal expansion mismatch and the applied stress). Usually, the influence of the defect on strength is expected to be less severe than that of a crack of equivalent dimensions.^{5,6} The important exception is an inclusion with both a thermal expansion coefficient and a bulk modulus lower than the host material (then, large radial cracks can develop that substantially reduce the strength). However, the incidence of such inclusions in structural ceramics (such as silicon nitride) is expected to be minimal, because these materials have a low intrinsic thermal expansion coefficient.

The inherent flaws that initiate inclusion fracture are likely to be statistically distributed in size and space. Therefore, the fracture stress should not be expected to relate uniquely to the defect dimensions, but rather, to exhibit a distribution of values for each defect size.^{7,8} The determination of the pertinent fracture distribution functions is the primary objective of the present study.

EXPERIMENTAL

Technique - Samples containing the defect types that predominate in hot-pressed silicon nitride (Table 1) were specially fabricated* in two sets. One set consisted of 2.5 cm diameter discs with the defects approximately located at the disc center. The other set consisted of oversized bars containing inclusions, later to be machined to final dimensions suitable for flexure testing. The samples were inspected using advanced ultrasonic techniques to determine the precise location of the dominant defect. The samples were then machined until the defect was located ~200 μ m from one surface of the sample. This operation was conducted to ensure that the defect would be subjected to an appreciable tensile stress during subsequent flexure testing. Therefore, each sample was annealed, in air at 1000°C for ~20 hr., to minimize the influence of surface cracks introduced during the grinding process. Finally, the samples were subjected to flexural, constant displacement-rate fracture tests conducted at room temperature. Those samples with defects located at the disc center were tested in biaxial flexure.⁶ Samples with defects displaced from the disc center were put into beams (20 cm x 5 mm x 5 mm), such that the defect was located at the beam center, and then tested in three-point flexure. Acoustic emission was monitored on each sample throughout the test. The bar samples were also machined into beams (38 mm x 6 mm x 3 mm), and tested in four-point flexure such that the inclusions were between the inner span supports. After strength testing, fracture faces were examined by microscopy and microprobe to verify the location and nature of fracture origins.

Results - The results of the fracture were used to calculate the stress at the center plane of the defect, at the condition of fracture instability. These defect fracture stresses are summarized in Table 1. The acoustic emission record did not generally indicate well-defined pre-fracture emission, except for the silicon inclusions, which exhibited consistent emission at about one-tenth of the final fracture load.

*The fabrication was conducted by the Norton Co., Worcester, Massachusetts.

The dimensions of the fracture initiating defects on the fracture plane were measured on each sample, as summarized in Table I. Also, for samples in which defect removal could be effected, the defect volumes were measured. The detailed volume measurement technique is described in Appendix II. The results are summarized in Table I. As a general comparison, the present results are combined with other results* to plot trends in the average strength with defect-size (Fig. 1). The strong role of defect type on strength is immediately apparent.

TABLE I

Defect Type	Stress at (MPa) Defect	Defect size		
		z(μ)	x(μ m)	V(m^3)
Silicon	400	50	265	-
	362	100	475	-
	375	75	425	-
	264	125	625	-
	243	250	875	-
	283	125	875	-
	272	250	675	-
	410	75	200	-
	432	75	275	-
	284	175	425	-
	357	100	100	-
	424	75	250	-
	434	50	100	-
	265	175	750	-
	252	125	625	-
Iron	398			2.5×10^{-12}
	323			1.6×10^{-11}
	383			9.1×10^{-12}
	334			2.2×10^{-11}
	355			3.1×10^{-11}
	210			3.9×10^{-10}
	217			3.1×10^{-10}
	404			6.2×10^{-13}
	258			7.0×10^{-11}
	296			6.1×10^{-11}
	333			3.3×10^{-11}
	283			6.5×10^{-11}
	173			2.9×10^{-10}
	281			1.1×10^{-10}
	206			3.2×10^{-10}
	190			3.0×10^{-10}
	268			1.8×10^{-10}
Tungsten Carbide	550	75	175	
	590	125	150	
	560	75	300	
	610	400	675	
	600	100	300	
	480	400	400	
Void	365	250	250	
	317	250	250	
	316	250	250	
	314	250	250	
	302	250	250	
	293	250	250	
	265	250	250	
	365	250	250	
	317	250	250	

*Results obtained from: H.R. Baumgartner, R.H. Brockelman and P.M. Hansen, AMMRC Report TR 78-11 (June 1978) and from: J.J. Petrovic and M.G. Merdiratta, Jnl. Amer. Ceram. Soc., 59 (1976) 163.

TABLE 1 (Cont'd)

Defect Type	Stress at (MPa) Defect	Defect Size		
		z(μ m)	x(μ m)	V(m^3)
Void	316	250	250	
	314	250	250	
	302	250	250	
	293	250	250	
	265	250	250	
	265	250	250	
	248	250	250	
	248	250	250	
	247	250	250	
	246	250	250	
	226	250	250	
	206	250	250	
	191	250	250	
	181	250	250	
	165	250	250	
	234	500	500	
	224	500	500	
	211	500	500	
	210	500	500	
	194	500	500	
	197	500	500	
	185	500	500	
	178	500	500	
	177	500	500	
	176	500	500	
	153	500	500	
	145	500	500	
	140	500	500	
	126	500	500	
	109	500	500	
	100	500	500	
	434	44	48*	

*Result obtained from: F. I. Barratta, G. W. Driscoll and R. N. Katz, Ceramics For High Performance. Applications (Ed., J. J. Burke, A. G. Gorum and R.N. Katz), Brooke Hill, MA (1974) p. 445.

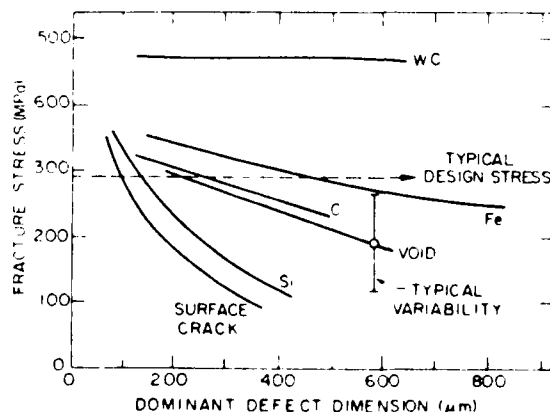


Fig. 1 A plot of trends in the average fracture strength with defect size for several different defect types in silicon nitride.

FRACTURE MODELS

General Considerations - It is instructive to provide a perspective of defect fracture by examining the stress fields associated with defects, and thereby, to identify the possible modes of fracture. (The fracture modes that occur for inclusions with a lower expansion coefficient than the matrix are excluded from consideration, as noted in the Introduction.)

The thermal expansion mismatch introduces hydrostatic tension within inclusions. The magnitude of this stress, σ_{ii} , is given by^{7,8}

$$\sigma_{ii} = \frac{4G_m \Delta \alpha}{1 + [2(1-2\nu_i)/(1+\nu_i)](G_m/G_i)} \Delta T \quad (1)$$

where $\Delta \alpha$ is the differential thermal expansion coefficient, ΔT is the temperature differential, G is the shear modulus, ν is Poisson's ratio and the subscripts m and i refer to the matrix and inclusion, respectively. The equivalent stresses with the matrix are, for a spherical inclusion with radius R ,

$$\sigma_{rr} = \beta * (R/r)^3 \quad (2)$$

$$\sigma_{\theta\theta} = -\beta * (R/r)^3/2$$

The application of a stress σ_{∞} generates additional stresses within the inclusion. For a spherical defect and an applied pressure p_{∞} , the stress in the defect is given by⁸:

$$\frac{p_i}{p_{\infty}} = 1 + \frac{2[(\nu_i/\kappa_m - 1)(1-2\nu)]}{3(1-\nu)} \left[\frac{4G_m + 3\kappa_m}{4G_m + 3\kappa_i} \right] \quad (3)$$

where κ is the bulk modulus.

The significance of these local stresses depends on the distribution of flaws within the defect, matrix and interface; as well as the intrinsic toughness (of inclusion and matrix). When the toughness of an inclusion is appreciably larger than that of the matrix (as might pertain for WC inclusions in Si_3N_4), fracture will tend to initiate within the matrix, from flaws located either at the interface or within the matrix itself (Fig. 2). In this case, the location of fracture and the fracture probability depend primarily on the ratio of the inclusion and matrix elastic constants. Specifically, for inclusions with a smaller modulus than the matrix, the maximum local tensile stress occurs at the equatorial plane, and fracture will initiate from flaws located in this vicinity, as indicated in Fig. 2(a). For inclusions with a higher modulus than the matrix, the maximum local tension (in the appropriate orientation for continued extension into the matrix, i.e., normal to σ_{∞}) occurs at the poles of the inclusion (Fig. 2(b)). However, both the maximum tension and the extent of the

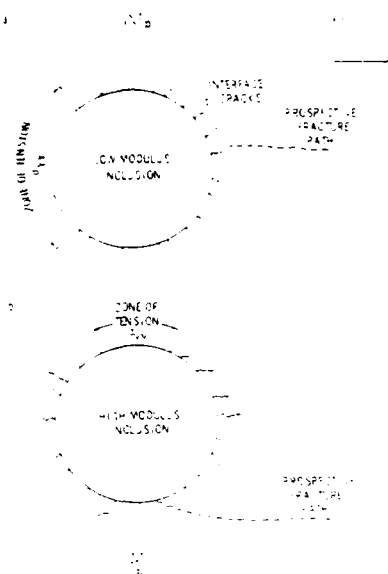


Fig. 2 Schematics indicating fracture initiation within the matrix from interface microcracks for (a) low modulus inclusions and (b) high modulus inclusions.

tensile zone are appreciably smaller (for the same modulus mismatch) than the equivalent quantities for the low modulus inclusions. The probability of fracture from the latter is thus anticipated to be relatively low.

A more typical condition involves inclusions with a lower fracture toughness than the matrix. Then, inclusion fracture may occur. When the inclusion has a relatively high modulus (although not necessarily higher than that of the matrix), so that appreciable stresses develop within the inclusion, the fracture of the inclusion can be subcritical, i.e., an additional stress is required to initiate structural failure. Alternatively, if the inclusion has a low modulus (e.g., a porous inclusion, see Appendix 1), the stress within the inclusion is low and inclusion fracture might then coincide with structural failure.

This multiplicity of fracture modes requires that each inclusion type be evaluated on an individual basis. The subsequent analysis comprises separate sections for each of the defect types listed in Table 1.

Specific Fracture Models

Voids - Previous studies^{9,10} have suggested that fracture from voids occurs by the activation of microcracks located on (or near) the surface of the voids (see Fig. 2a). A combined fracture mechanics, statistical analysis of this problem yielded the following relation for the fracture probability, P , at the stress S :

$$z = 1 - \exp \left\{ [-8R^2 (S/S_0)^m \exp(0.52m - 1.4) D(u)] \right\} \quad (4)$$

where S_0 is the scale parameter, m the shape parameter, R is the void radius; u is given by:

$$u = (1/R) (K_c/S)^2 \quad (5)$$

where K_c is the effective microcrack extension resistance and $D(u)$ has the approximate form,

$$D(u) = 0.3 + 0.7[1 + (u/2)^2]^{-1} \quad (6)$$

The conformance of the test data to the predictions of this model is assessed by separately estimating the dependence of the data on the radius R of the void and on the stress level S . This is achieved through a generalization of Eq. (4);

$$\begin{aligned} \varphi(x|r) &= P[S < x | R = r] \\ &= 1 - \exp[-g(r, \beta) \int_0^x \lambda_0(u) du] \quad (7) \end{aligned}$$

where $g(r, \beta)$ is of known functional form (except for the parameter β) and independent of the value of S , while $\lambda_0(u)$ is independent of the value of R . For the present problem Eq. (7) can be written as

$$\varphi(x|r) = 1 - \exp[-r^\beta \int_0^x \lambda_0(u) du] \quad (8)$$

We commence the analysis by supposing that the term $D(u)$ is relatively invariant within the range of the test data. Then, the hypotheses of the fracture model are:

$$\beta = 2$$

$$\lambda_0(u) = \frac{m}{S_0} \left(\frac{u}{S_0} \right)^{m-1} \quad (9)$$

The influence of the radius is examined first, by comparing the formal statement of the null hypothesis, $H_0: \beta = 2$, with the alternative, $H_1: \beta \neq 2$. A procedure devised by Cox³, which is independent of the functional form of $\lambda_0(u)$, is used for this purpose. Let the observed failure stresses for samples k_1, k_2, \dots, k_n be, $0 < u_1 < u_2 < \dots < u_n$, where no ties are allowed. Let $R(u_j)$ be the set of all items surviving until just before the j 'th failure. Then, the partial likelihood function L_p is;

$$L_p = \prod_{j=1}^n \frac{r_{k_j}}{\sum_{i \in R(u_j)} r_{k_i}} \quad (10)$$

Under the null hypothesis H_0 that $\beta = 2$, the statistic $(-2 \ln L_p / \partial \beta) / (-2 \ln L_p / \partial \beta) \sim \chi^2_1$ is asymptotically distributed as a chi-square random variable with one degree of freedom. Hence, for large samples, it can be used as a test statistic for the null hypothesis, H_0 . For the test data pertinent to void initiated fracture summarized in Table 1, application of the above result yields a test statistic of 1.80. This value has an asymptotic significance level of 0.18 and, therefore, the null hypothesis that $\beta = 2$ appears to be supported by the data. The maximum likelihood estimate of β was also obtained from

$$\frac{\partial \ln L}{\partial \beta} = 0 \quad (11)$$

yielding a value, $\hat{\beta} = 3.03$.

The consistency of the test data with the simplified model, $\beta = 2$, does not exclude the possibility that for small (or large) voids an additional dependence on R may emerge from $D(u)$. Additional data will be required to examine this possibility.

The analysis can now proceed, by testing the hypothesis that the parameters m and S_0 do not depend on the radius r_i , through the restated model

$$-\ln[1 - \varphi(x_i | r_i)] = r_i^2 \left| \frac{x_i}{S_0(r_i)} \right|^m (r_i) \quad (12)$$

where r_i is fixed for each data sample. Since there are two samples ($r_1 = 125 \mu\text{m}$ and $r_2 = 250 \mu\text{m}$), the intent is to test the null hypothesis

$$H_0 : \begin{cases} m(125) = m(250) = m \\ S_0(125) = S_0(250) = S_0 \end{cases}$$

versus the alternate hypothesis

$$H_1 : \begin{cases} m(125) \neq m(250) \text{ or} \\ S_0(125) \neq S_0(250) \end{cases}$$

To test the relative merits of H_0 versus H_1 , the likelihood ratio statistic λ was obtained. Noting that $-2 \ln \lambda$ is distributed as a chi-square random variable (with two degrees of freedom), the analysis yielded the result, $-2 \ln \lambda = 2.709$, which is not significant at the 0.25 level. Hence, on the basis of this test, the data support the null hypothesis H_0 , that m and S_0 are independent of

the void radius. A Weibull goodness of fit test also strongly supports the hypothesis. Maximum likelihood estimates obtained for the scale and shape parameters are;

$$\hat{S}_0 = 106.3 \text{ MPa}$$

$$\hat{m} = 4.57$$

As a final assessment of the model, the fracture probability associated with the test result obtained for the 44 μ m diameter void is, derived from the above estimates of \hat{R} , \hat{m} and \hat{S}_0 . This analysis provides a fracture probability of 0.25, which is quite reasonable.

The application of the test results to the prediction of failure or survival ideally requires that a maximum likelihood estimate be derived. This estimate, described in Appendix III, is given by;

$$\hat{P}[S > x | R = r] \quad (13)$$

$$= \prod_{k=1}^N \left[1 - \frac{r_k^2}{\sum_{k=1}^N r_k^2} \right]^{(r/r_k)^2}$$

Inclusions

Silicon Inclusions - The silicon inclusions observed on the fracture surface are characterized by a lack of porosity, signifying (see Appendix I) that there is little thermal expansion mismatch at temperatures above ~1000°C (the temperature at which stress relaxation by mass transport becomes slow). This can be rationalized by noting that the large thermal contraction of the silicon between 1000 and 1800°C is counteracted by the unusual volume expansion that occurs during solidification. Between 1000°C and 30°C the total contraction of the silicon is very similar to that of silicon nitride; indicating that the thermal mismatch stresses in the silicon inclusions should be small.

Dense silicon has elastic properties appreciably lower than those of silicon nitride (Young's moduli of 110 and 320 GPa, respectively). These relative properties lead to a stress in the inclusion $\sigma_i \sim 0.64 \sigma_\infty$ (see Eq. 3). However, silicon has a very low fracture toughness (0.6 MPa \sqrt{m}) compared with the silicon nitride matrix (5 MPa \sqrt{m}); so that, despite the low stress level in the inclusion, the inclusion is liable to subcritical fracture. This interpretation is consistent with the acoustic emission measurements (Section 2).

The subcritical fracture of the silicon inclusion introduces a crack with dimensions dictated by the boundaries of the inclusion. The cracked inclusion produces a complex stress intensification of the type¹¹:

$$K_I = Z(a/c)F(G_I/G_m)\sigma_\infty a^b \quad (14)$$

where Z is a function of the crack shape, F is a function of the relative elastic moduli and b is a constant ranging from 0.3 to 0.7. The present fracture model is developed on the premise that the modulus mismatch is small and that the cracked inclusion can be treated as a crack in a homogeneous body. (This simplification is necessary at the present level of comprehension of the crack/inclusion problem, and will evidently introduce an error into the fracture characterization.) Then, introducing the macro-toughness of silicon nitride and the inclusion dimensions (on the fracture surface), the predicted fracture stress σ_p becomes

$$\sigma_p = \frac{K_c}{Z(a/c)^{1/b} a} \quad (15)$$

The predicted stress for each sample is plotted in Fig. 3 as a function of the measured fracture stress. A reasonable correlation is apparent.

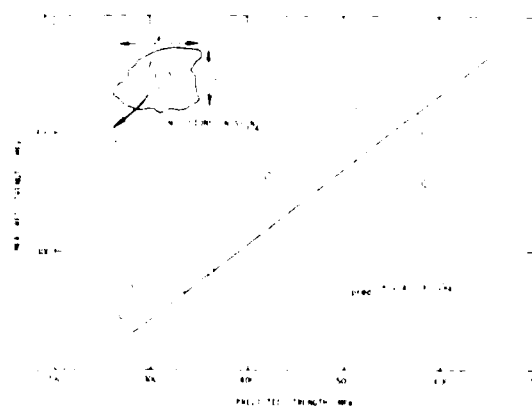


Fig. 3 A plot of the measured fracture strength of silicon inclusions as a function of the strength predicted by the subcritical crack-inclusion model.

A detailed statistical analysis has also been conducted to determine the level of correlation between the test data and the model. For this purpose, it has been supposed that the primary source of variability in the measured strength is the variation in fracture toughness of the matrix circumventing the inclusion (which could be very different from that of the remote matrix, because of an interaction zone). The inclusion/crack size is appreciably larger than the grain size. Hence, the variability in toughness is assumed to be normal. The fracture data are thus analyzed to determine their conformance to the normal distribution. (An alternative hypothesis attributes the strength variability to variations in the shape of the crack at the criticality; this possibility is not examined in the present analysis.)

The hypothetical model can be formally expressed as:

$$P_r[S \leq x | \sigma_p = x] = \frac{1}{\sigma_p \sqrt{2\pi}} \int_{-\infty}^x \exp \left[-\frac{1}{2} \left(\frac{y - (\alpha + \beta x)}{\sigma_p} \right)^2 \right] dy \quad (16)$$

where σ_p^2 is the variance of the strength S for any given σ_p and P_r is the conditional distribution of strengths S ; note that the conditional expectation of S , given σ_p , is assumed to be a linear function of σ_p .

$$(S | \sigma_p = x) = \alpha + \beta x + e \quad (17)$$

where e is a random variable having mean zero and variance σ_p^2 . Applying the usual null hypothesis tests to the available data is complicated by the fact that the fracture data comprise 15 observations of 12 random variables. Specifically, only the residual

$$e = (S | \sigma_p = x) - \hat{\alpha} - \hat{\beta}x \quad (18)$$

can be observed, where $\hat{\alpha}$ and $\hat{\beta}$ are the maximum likelihood estimates of α and β .

The normality of the fracture data are thus analyzed using two approaches: (a) by disregarding the variance-covariance structure of the residuals and (b) by obtaining independent residual observations using an orthogonal transformation of the fracture data.

The first method of analysis assumes that these residuals are independent. The variation in the magnitude of the residuals with the magnitude of the observation can then be obtained directly, as plotted in Fig. 4. There does not appear to be a systematic trend in the residuals (as verified by values of α_1 (skewness) = 0.04 and α_2 (excess) = -0.93), indicating that the normality hypothesis may be reasonable. Further, the residuals are arranged in increasing order of magnitude and plotted against the expected value of the i 'th order statistic (Fig. 5). The good linearity of the plot tends to support the contention that the residuals are observations of a random variable having a normal distribution. Separate analysis of the data at large and small σ_p , using a procedure proposed by Goldfeld and Quandt¹⁰, indicates that the residuals exhibit a systematic increase with increasing magnitude of the observation. This does not invalidate the normality of the distribution, but suggests a variance that increases as σ_p increases; a result that can be tentatively rationalized, as discussed below. However, it should be noted that the data may also conform with similar confidence to alternate models. The data analysis does not, therefore, provide a unique confirmation of the proposed fracture model.

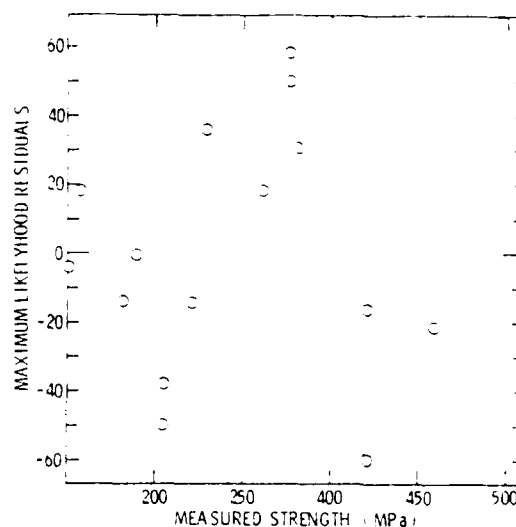


Fig. 4 A plot of the maximum likelihood residuals as a function of the measured strength.

The second method of analysis uses a procedure proposed by Henry Theil.¹¹ It involves an orthogonal transformation through an identity matrix. Only 13 residuals can be obtained because 2 degrees of freedom (slope and intercept) are sacrificed in the estimation procedure. The residuals obtained in this fashion exhibit precisely the same trends as the maximum likelihood residuals, as exemplified in Fig. 5.

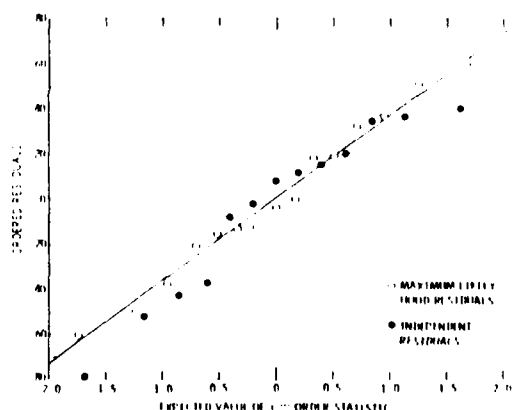


Fig. 5 A plot of the ordered residuals as a function of the estimate of the order statistic for both the maximum likelihood and the independent residuals.

It may be concluded, therefore, that the hypothesized fracture model, modified to allow for an increase in variance with increase in strength level, cannot be rejected by the data. However, this does not discount the possibility that the data might be also be consistent with an alternate fracture model. If the assumed fracture model is indeed valid, the parameters of the model implied by the data are: $\alpha = 99.655 \text{ MPa}$, $\beta = 0.541$. The deviation of β from unity suggests, within the context of the model, that the local toughness of the matrix may be lower than the remote macro-toughness of the matrix (i.e., $\sim 3 \text{ MPa}\sqrt{\text{m}}$ instead of $5 \text{ MPa}\sqrt{\text{m}}$). This effect can be justified on the basis of a matrix locally degraded by interaction with the inclusion. The relative extent of the degradation may also be supposed to increase as the inclusion size decreases: accounting for the observed increase in variance with increase in strength level.

Iron Inclusion - Examination of the iron inclusions (Fig. 6) indicates that the inclusions contain several open cracks and/or porosity. The cracks and pores are presumably formed by diffusion within the inclusion (while at elevated temperatures) to relieve the stresses introduced by thermal expansion mismatch (Appendix I). An unrelieved thermal expansion mismatch strain ϵ_{α} will, of course, still develop at temperatures below those capable of sustaining rapid mass transport. The presence of the open cracks reduces the effective bulk modulus of the inclusion. The stresses within the inclusion, induced by the applied stress (Eq. 3) and the thermal expansion mismatch (Eq. 1), should thus be appreciably lower than would be anticipated from the intrinsic modulus of the iron silicide that comprises the inclusion. The low effective modulus also results in relatively large stresses in the matrix adjacent to the inclusion, comparable in form and magnitude to the stresses around a void. One possible failure model thus involves the activation of microcracks in the matrix, at the interface, by the enhanced tensile stress near the equatorial plane. The probability of fracture for this mode of failure can thus be expressed by the void fracture relation (Eq. 4), modified by a coefficient that depends upon the ratio of the inclusion modulus to the matrix modulus (c.f., Eq. 3).



Fig. 6 A scanning electron micrograph of a fractured iron inclusion in hot-pressed silicon nitride.

An alternate, or coupled, failure model supposes that a critical fracture condition is attained when the stress within the inclusion reaches the level required to extend one of the internal cracks: thereby excluding a subcritical inclusion fracture event. This hypothesis would be consistent with the lack of detectable acoustic emission prior to final fracture. The stress within the inclusion is a relatively uniform, hydrostatic tension p_i (or exactly uniform for an ellipsoidal inclusion) given by:

$$p_i = \psi \sigma_{\infty} + \sigma_{\alpha} \quad (19)$$

A weakest link model of inclusion fracture for a state of uniform tension would indicate a fracture probability:

$$\phi_i = 1 - \exp \left[-V_i \int_0^{p_i} g(S) dS \right] \quad (20)$$

where V_i is the volume of the inclusion ($= (4/3)\pi r^3$) and $g(S)dS$ is the distribution of flaw strengths that relates to the distribution of cracks within the inclusion (and the toughness of the inclusion). If we adopt the Weibull assumption, that $g(S)$ is given by:

$$\int_0^{p_i^C} g(S) dS = \left(\frac{p_i^C}{p_0^C} \right)^k \quad (21)$$

where p_0^C is a scale parameter and k a shape parameter, the inclusion fracture probability becomes:

$$\phi_i = 1 - \exp \left[(4/3)\pi r^3 \left(\frac{\psi \sigma_{\infty}^C + \sigma_{\alpha}}{p_0^C} \right)^k \right] \quad (22)$$

where σ_{∞}^C is the applied stress at fracture.

Statistical analysis of the fracture results for iron inclusions, according to the procedure described above for void fracture, indicates that the maximum likelihood estimate of the radius coefficient, β is ~ 7 . This value is larger than predicted by either of the above fracture models and thus excludes the existence of a single fracture model over the complete range of test results. A transition from one mechanism to another, as a function of defect size, may thus be occurring. The results can be rationalized by this hypothesis, but are too sparse to verify the existence of such a transition.

Tungsten Carbide Inclusions - The relatively minor effect of tungsten carbide inclusions on the fracture strength of silicon nitride precludes the need for a detailed statistical analysis of strength. The innocuous nature of these inclusions derives from a combination of relatively high toughness and modulus, as noted above. The analysis of fracture would involve considerations

of the distribution of microcracks located with the matrix in the small zone of tension near the poles of the inclusion.⁶ The mode of analysis would be essentially similar to that conducted for fracture from voids^{4,5}, as modified by the different distribution of matrix stress and the presence of a high toughness inclusion.

IMPLICATIONS AND CONCLUSIONS

Good physical models of the probability of fracture from defects can greatly enhance the ability to predict failure from a nondestructive assessment of the defect type and size. Models pertinent to specific defect types have been presented, and correlations with fracture data have been attempted. The data are essentially consistent with the fracture models. However, to obtain good statistical confidence in the models, additional data are required, for well-controlled defect morphologies. Specifically, data sets are required for defects of a given size, taken at several different size values.

The present results can be used directly, within the probabilistic range encompassed by the data, even though the applicability of the models has not been substantiated (in each case) with good statistical confidence. The confident substantiation of the present (or alternative) models of fracture from defects would have the advantage of permitting the reliability predictions to be extended beyond the range of the data. Additionally, with self-consistent models and ample data, the variance would be minimized; thereby reducing the rejection probability for a given method of nondestructive analysis.⁷

The strong influence of the defect type on the fracture strength is re-emphasized. Specifically, tungsten carbide inclusions can be regarded as almost innocuous, while silicon inclusions are extremely deleterious (at least at low temperatures); iron inclusions and voids are of intermediate severity. It is interesting to note that surface cracks in hot-pressed silicon nitride produce about the same strength degradation as silicon inclusions with the same equivalent diameter. However, it should be noted that silicon develops appreciable toughness above ~1000°C, and melts at 1420°C. Silicon inclusions are thus likely to become less deleterious at elevated temperatures (> 900°C) tending to approach the behavior of voids of equivalent size.

Finally, the appreciable dependence of the fracture probability on the inclusion type clearly emphasizes the importance of defect type classification for effective nondestructive failure prediction schemes.

APPENDIX I STRESSES PRODUCED BY THERMAL EXPANSION MISMATCH

The magnitude of the thermal expansion mismatch stress depends on the cooling temperature ΔT (Eq. 1). An exact definition of this temperature differential presents several problems. The stress within the inclusion is purely hydrostatic (i.e., no shear stresses), and stress relaxation can only occur by mass transport processes. By contrast, the stress within the matrix has a zero hydrostatic component, $p(\sigma_{rr} + 2\sigma_{\theta\theta}) = 0$, but a very

large shear component, $\sigma_{r\theta}$ ($\sim 3\sigma/4$); relaxation in the matrix can thus only occur by shear induced processes (e.g., grain boundary sliding accommodated by diffusive transport). The chemical potential that acts as the driving force for atom migration within the inclusion is dictated primarily by the hydrostatic pressure

$$\mu_i = -p\Omega \quad (A1)$$

where Ω is the atomic volume. The incidence of atom transport will modify the chemical potential and the stress distribution. This will occur primarily by vacancy transport to the interface. However, if the stress within the inclusion is tensile, cavities may nucleate by vacancy condensation.¹¹

Once a cavity has nucleated, the stress at the cavity surface and the local chemical potential must be maintained at their equilibrium values

$$p = 2\gamma_s/r \quad (A2)$$

$$\mu = -\gamma_s/r$$

where r is the cavity radius. The chemical potential gradient now favors vacancy diffusion into the cavity, and cavity growth can be anticipated. Hence, if several cavities nucleate, the stresses within the inclusion remain at a moderate level, while mass transport is occurring. It should also be noted that the formation of cavities decreases the modulus of the inclusion. This tends to minimize the stresses which develop on cooling below the temperature at which mass transport eventually ceases.

APPENDIX II A POSTERIORI MEASUREMENTS OF INCLUSION VOLUME

Most of the naturally occurring inclusions in structural ceramics develop cracks during temperature excursions. Consequently, the inclusions are relatively friable after fracture, and can be readily separated from the matrix by suitable etchants. The remaining void space can then be filled with a low density wax and the density of the ceramic/wax system measured in a density column. This density is directly related to the inclusion volume, v , the density of the ceramic host, ρ_c , and the density of the wax, ρ_w , as indicated below.

The measured density ρ' is:

$$\rho' = (M + m)/(V + v) \quad (A3)$$

where M is the mass of the ceramic, V its volume and m the mass of the wax contained within the void space. The parameters in Eq. (A3) that cannot be easily measured are m and V , these can be eliminated from the measurement process by substituting the densities ρ_w and ρ_c .

$$v = \left(\frac{M}{c} \right) \left| \frac{\rho_c - \rho'}{\rho' - \rho_w} \right| \quad (A4)$$

The densities ρ_c and ρ' can be obtained directly from density column studies, before and after the wax has been inserted into the void space.

APPENDIX III MAXIMUM LIKELIHOOD ESTIMATE OF SURVIVAL FUNCTION

Assume the survival function;

$$P[S \geq x | R = r] = \exp \left[- \int_0^x \lambda(u; r) du \right] \quad (A5)$$

where

$$\lambda(u; r) = \lambda_0(u) g(r, \beta),$$

and $g(r, \beta)$ is of known form, except for β . Take

$$\lambda_0(u) = \sum_{k=1}^{\infty} a_k \delta(u - \epsilon_k), \quad (A6)$$

where $0 < \epsilon_1 < \epsilon_2 < \dots$ is a net defined on R^+ (the positive real axis) that is dense enough to include all possible observations, and $\delta(\cdot)$ is the Dirac δ function which is defined to be zero everywhere except at the point $x = 0$. In particular

$$\delta(x) = 0 \quad \text{for } x \neq 0$$

and

$$\int_{-\infty}^{\infty} \delta(x) dx = 1$$

It therefore follows that

$$P[S \geq x | R = r] = \exp \left[- \int_0^x \lambda_0(u) g(r, \beta) du \right]$$

$$= \exp \left[-g(r, \beta) \int_0^x \sum_{k=1}^{\infty} a_k \delta(u - \epsilon_k) du \right]$$

$$= \exp \left[-g(r, \beta) \sum_{\{k | \epsilon_k \leq x\}} a_k \right] \quad (A7)$$

Hence the survival function is given as

$$P[S \geq x | R = r] = \prod_{\{k | \epsilon_k \leq x\}} \exp[-a_k g(r, \beta)] \quad (A8)$$

Now, let F_i be the set of all test samples failing at epoch ϵ_i , and R_i be the set of all test samples surviving up to $(\epsilon_i - 0)$. Then

$$P[F_i | R_i] = \prod_{j \in F_i} (1 - \exp[-a_j g(r_j, \beta)])$$

$$\prod_{j \in R_i \setminus F_i} \exp[-a_j g(r_j, \beta)] \quad (A9)$$

where r_j is the radius of the void in the j^{th} test sample. The total likelihood is then

$$L = \prod_{i=1}^{\infty} \left\{ \prod_{j \in F_i} (1 - \exp[-a_j g(r_j, \beta)]) \prod_{j \in R_i \setminus F_i} \exp[-a_j g(r_j, \beta)] \right\} \quad (A10)$$

If no failures occur at epoch $j = k$, then the contribution to the total likelihood is

$$\prod_{j \in R_k \setminus F_k} \exp[-a_k g(r_j, \beta)]$$

which is maximum whenever $a_k = 0$ (since $g(\cdot)$ is a positive function). Therefore, restricting attention to those epochs at which failures do occur,

$$L = \prod_{k=1}^N \left\{ (1 - \exp[-a_k g(r_{(k)}, \beta)]) \prod_{k \leq \ell \leq N} \exp[-a_k g(r_{(\ell)}, \beta)] \right\} \quad (A11)$$

$$\frac{\partial \ln L}{\partial a_k} = 0 \quad \text{for } k = 1, 2, \dots, \text{ or } N,$$

and denoting the estimate of a_r by \hat{a}_r , we have

$$\exp[-\hat{a}_k g(r_{(k)}, \beta)] = 1 - \sum_{k \leq \ell \leq N} \frac{g(r_{(k)}, \beta)}{g(r_{(\ell)}, \beta)} \quad (A12)$$

From (A8),

$$\hat{P}[S \geq x | R = r] \quad (A13)$$

$$= \prod_{k \leq x} \left[1 - \frac{g(r_{(k)}, \beta)}{\sum_{k \leq x \leq N} g(r_{(k)}, \beta)} \right]^{g(r, \beta) / g(r_{(k)}, \beta)}$$

for arbitrary radius r . If, in particular,

$$g(r, \beta) = r^\beta,$$

then,

$$P[S \geq x | R = r]$$

$$= \prod_{k \leq x} \left[1 - \frac{r_{(k)}^\beta}{\sum_{k \leq x \leq N} r_{(k)}^\beta} \right]^{(r/r_{(k)})^\beta} \quad (A14)$$

ACKNOWLEDGMENT

This research was sponsored by the Center for Advanced NDE, operated by the Science Center,

Rockwell International, for the Defense Advanced Research Projects and the Air Force Materials Laboratory under Contract F33615-74-5180 and by the Army Materials and Mechanics Research Center under Contract DAAG46-76-0022.

REFERENCES

1. J.R. Richardson and A.G. Evans, to be published.
2. A.G. Evans, J. Mater. Sci., 9 (1976) 1145.
3. F.F. Lange, Fracture Mechanics of Ceramics (Ed. R.C. Bradt, D.P.H. Hasselman, F.F. Lange) Plenum, NY (1978) Vol. 4, p. 799.
4. O. Vardar, I. Finnie, D.R. Biswas and R.M. Fulrath, Int'l. J. Frac., 13 (1977) 215.
5. A.G. Evans, D.R. Biswas and R.M. Fulrath, J. Amer. Ceram. Soc., 62 (1979) 101.
6. J.B. Wachtman, W. Capps and J. Mandel, J. Materials, 7 (1972) 188.
7. J. Selsing, J. Amer. Ceram. Soc., 44 (1961) 149.
8. J.D. Eshelby, Proc. Roy. Soc., 241A (1958) 376.
9. D.R. Cox, Proc. Roy. Stat. Soc., 34B (1972) 187.
10. S.M. Goldfield and R.E. Quandt, J. Amer. Statistical Assoc., 60 (1965) 539.
11. H. Theil, J. Amer. Statistical Assoc., 60 (1965) 1067.
12. J.R. Matthews, F.A. McClintock and W.J. Shack, J. Amer. Ceram. Soc., 59 (1976) 304.
13. A.G. Evans, J.R. Rice and J.P. Hirth, J. Amer. Ceram. Soc., in press.

CONDITIONAL PROBABILITY OF FAILURE AND ACCEPT/REJECT CRITERIA

J. M. Richardson and E. W. Fertig
Rockwell International Science Center
Thousand Oaks, CA 91360

A. G. Evans
University of California
Berkeley, CA 94720

ABSTRACT

A discussion is given of a general probabilistic approach to the derivation of the failure probability conditioned by nondestructive (ND) measurements and of an optimal accept/reject procedure. This approach involves the use of explicit stochastic models of both the ND measurement process and the failure process (including a postulated stress environment). The overall decision logic involves a number of on-line and off-line inputs and outputs which will be described in detail with some indications of the kinds that are of interest to various categories of users. Particular emphasis will be placed upon the operating characteristic curve (i.e., the false-rejection probability vs. the false-acceptance probability) representing a broad spectrum of optimal decision procedures) and its significance as a measure of the performance and cost-effectiveness of NDE systems. Explicit results will be given for the case of ceramic NDE with acoustical scattering measurements and two alternative failure models. The first is one in which the fracture process originates at a void surrounded by peripheral microcracks and the second involves fracture originating in a subcritical inclusion. Particular attention will be devoted to limiting situations in which the unconditional failure probability is small and/or in which the ND measurements are accurate and sufficiently diverse.

INTRODUCTION

The purpose of this paper is to present a description of progress made since the last review of quantitative NDE on the subject of probabilistic failure prediction and optimization of accept/reject criteria. This work goes beyond other work on reliability theory by making use of explicit physical models of both the failure and measurement processes. The resultant formalism enables one to bridge the gap between the ND measurements and the concerns of the ultimate user.

Although our methodology applies in principle to any material, our explicit applications will be made to structural ceramics. We will make the following simplifying assumptions:

1. The ND measurement, or set of such measurements, will be performed at a single time and a single accept/reject decision will be made on the basis of the result.
2. Only the most significant (e.g., the largest defect in a first-piece causes failure, if any, and the less significant defects in aggregate have a negligible probability of causing failure.
3. The applied stress is spatially uniform. The probability of failure depends only on the maximum stress and is independent of the stress history up to that time.

In the following sections we discuss first the general theory of failure prediction and accept/reject decisions. In later sections, we discuss the applications to failure in ceramics due to voids and subcritical inclusions, respectively. Various output properties are considered with particular emphasis on plots of false-reject vs false-accept probabilities. Although the failure models have been validated with real data on fracture and the associated causative defect in each

of a number of test pieces, the assessments of the overall decision formalisms have been carried out only with artificial theoretical data based upon the relevant models of the measurement and failure processes.

GENERAL PROBABILISTIC THEORY OF FAILURE PREDICTION AND ACCEPT/REJECT DECISIONS

In this section we discuss the formalism that is required to derive an optimal accept/reject decision procedure using the results of nondestructive measurements as input data. The major part of the formalism deals with the calculation of the probability of failure (or survival) of the test piece (under an assumed stress environment) based upon the nondestructive measurements. The decision to be considered involves a single inspection before the component is put into service. In the case of a brittle ceramic, failure is defined as the inability to avoid catastrophic fracture under a specified time-invariant uniform applied stress (1,2). The procedure outlined here applies to any material subject to a single inspection.

As shown in Fig. 1 the input information to the decision process is composed of nondestructive measurements on the test piece. The output is a

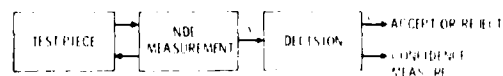


Fig. 1 Operational NDE decision process.

binary decision either to accept or to reject the piece. An ancillary output is the confidence measure connected with the decision. In Fig. 2 we show many of the elements of the off-line decision process that require more detailed discussion in the analysis of an NDE system--in particular those

that are connected with the physical model of the failure process and with the model of the non-destructive measurements.

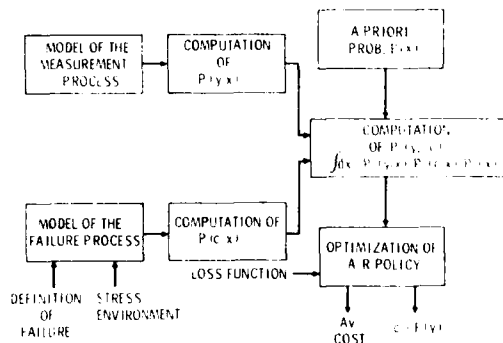


Fig. 2 Analysis and optimization of NDE decision process.

In this discussion we limit our attention to the case in which each test-piece contains only one defect that is significant contribution to failure. We can assume, for example, that the largest defect in a given test piece has a much larger probability of causing failure at a given applied stress than the probability due to the combined effect of all of the smaller defects. With this assumption, we can formulate our problem as though only one defect were present.

Further discussion is necessary to clarify the meaning of failure, in particular what kind of event constitutes failure and under what conditions. In all cases in this paper, failure means fracture (e.g., the propagation of a crack across the component with resultant division into two or more pieces) and not some relatively benign occurrence such as a small amount of irreversible bending. The conditions under which failure occurs must be specified and the nature of this specification depends on the kind of material involved. For example, in the case of a brittle material one need only specify the stress environment (e.g., a static applied stress in the simplest case) since here the elapsed time is irrelevant (within wide limits) since fatigue and aging processes do not occur to a significant extent. In the case of fatigue of metals under a cyclic stress of constant amplitude, it is necessary to specify this amplitude and the number of cycles. However, here the elapsed time (for a given number of cycles) is not important since the fatigue process is almost independent (within wide limits) of the rate with which the stress cycles are executed. There is also the problem of stochastic stress environments which we will not discuss here. Failure depends not only on the stress environment but depends on the thermal and chemical elements (e.g., the temperature and humidity); in the ensuing discussion we will assume a constant temperature and a chemically inert environment.

Non-destructive measurements are a random process represented by the non-deterministic variable y . In the specific examples to be given, the measurement consists of a cross-sectional to-longitudinal

scattering of elastic waves in the Rayleigh regime (i.e., low frequency or, equivalently, long wave length) with various combinations of transmitter and receiver positions. Then, one scalar quantity represents the final result of measurement for each combination.

We next introduce a binary variable c describing the structural performance of the test piece. The variable c takes the value 0 if the test piece fails under a specified applied stress and the value 1 if it survives. Although the variable c is deterministically defined, it is only probabilistically related to the variable y . In simple cases, the binary variable c can be related to more conventional variables (e.g., the failure stress σ_f or the time to failure t_f). The variable c can still be given a precise meaning when one considers cases with more subtle definitions of failure and/or with random stress environments.

The final stage of the decision process requires a knowledge of the joint probability function $P(y,c)$. It is also of interest to consider two derived probability functions, namely

$$P(c) = \int dy P(y,c) \quad (1)$$

and

$$P(y|c) = P(y,c)/P(c) \quad (2)$$

The first function, $P(c)$ is the unconditional probability of performance (failure or survival). The second function, $P(y|c)$, is the probability density of y given the performance c . It describes the normalized populations of test pieces in y -space of objects that are going to survive ($c = 1$) and fail ($c = 0$), respectively. The nature of $P(y|c)$ is illustrated in Fig. 3 for the case in which y is scalar.

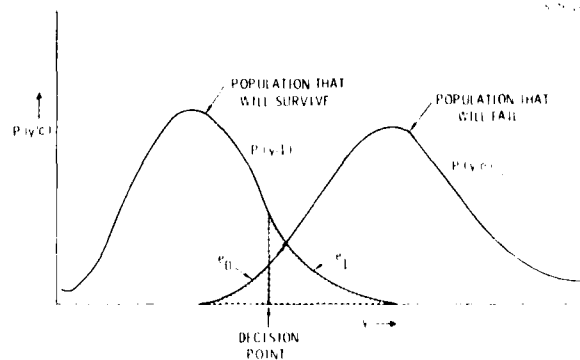


Fig. 3 The nature of failing and surviving populations and classification errors.

Two additional probability functions are also of interest, i.e.,

$$P(y) = \sum_c P(y,c) \quad (3)$$

and

$$P(c|y) = P(y,c)/P(y) \quad (4)$$

The function $P(y)$ is the unconditional probability density of y and it represents the total population of test pieces, i.e., the combination of the surviving and failing sub-populations. The function $P(c|y)$ is the probability of performance c given the measurements y .

To carry out an optimization of the accept/reject decision in terms of minimum cost, we need two kinds of inputs: (a) the probability function $P(y, c)$ discussed above and (b) an optimality criterion that assigns an average cost to each candidate decision procedure. To formulate the optimality criterion we start with the introduction of the loss (or cost) function $L(\hat{c}, c)$, which is the loss incurred if we decide the performance is $\hat{c}(y)$ when it is actually c . For a given y the decision $\hat{c} = 1$ (i.e., future survival) leads to acceptance and conversely $\hat{c} = 0$ (future failure) leads to rejection. Thus the losses $L(0, 1)$ and $L(1, 0)$ are associated with false rejection and false acceptance, respectively. In the present analysis, the nature of the NDE measurement is assumed to be given and hence its cost is not explicitly considered. Typically the cost of false rejection is the cost of the test piece. On the other hand, the cost of false acceptance can be very high and clearly involves product-liability considerations. The optimality criterion to be considered here is the average loss (which is called risk, R , in the decision theory literature) given by

$$R \approx \sum_c \int dy L(\hat{c}(y), c) P(y, c) \\ = w_0 e_0 + w_1 e_1 + b \quad (5)$$

The parameters w_0 , w_1 and b are dependent solely on the loss function $L(\hat{c}, c)$ and the unconditional performance probability $P(c)$. The quantities e_0 and e_1 are the two types of misclassification probabilities (or rates). Specifically, e_0 is the probability that we decide $c = 1$ (survival) when actually $c = 0$ (failure) and will call it the false-acceptance probability. Similarly, e_1 is the probability that we decide $c = 0$ (failure) when actually $c = 1$ (survival) and correspondingly we will call this the false-rejection probability. The nature of e_0 and e_1 is illustrated in Fig. 3.

With a given loss function a short calculation (2) leads to the result that the optimal decision rule is given by the scheme:

$$\Lambda(y) > \lambda \text{ implies } \hat{c} = 1 \text{ (i.e., accept);} \\ \Lambda(y) < \lambda \text{ implies } \hat{c} = 0 \text{ (i.e., reject);} \quad (6)$$

where

$$\Lambda(y) = P(y|1)/P(y|0), \quad (7)$$

and where

$$\lambda = w_0/w_1 \quad (8)$$

The senses of the inequalities in (6) are based upon the assumption that the coefficients w_0 and w_1 are positive.

*Here the local stress is defined as the stress that would be induced at the point in question by the applied stress if no microcracks were present.

In order to deal separately with the models of failure and measurement, it is necessary to introduce a state vector x having the property

$$P(y, c|x) = P(y|x)P(c|x), \quad (9)$$

i.e., when x is specified y and c become statistically independent. From (1) we infer the relations

$$P(y|x, c) = P(y|x) \quad (10)$$

$$P(c|x, y) = P(c|x) \quad (11)$$

In words, (10) means that the probability density of y given x and c does not depend on c because the specification of x represents sufficiently comprehensive knowledge that the additional specification of c is irrelevant. A similar statement can be applied to (11).

Up to now we have not discussed how the state vector is to be related to the underlying physical realities. It is important to emphasize at this point that, although the physicists concept of state (at least in the classical case) is a possible realization of our concept, our likely choice is far cruder than that of the physicist. For example, in the case of ceramics, the state of a spherical voids with peripheral microcracks would be given by its radius. The nature of the microcracks would not be included in the state vector because there is no ND measurement procedure presently available for detecting them.

In any case, with the introduction of the state variable x , defined in terms of the decorrelation of failure and measurement processes (i.e., by Eq. (1)), we can write the joint probability of measurement and performance in the form

$$P(g, c) = \int dx P(y, c|x) P(x) \\ = \int dx P(y|x) P(c|x) P(x) \quad (12)$$

where (9) was used in obtaining the last line of (12). The integration on x is assumed to span the entire domain of definition of state space, unless otherwise specified.

The schematic illustration in Fig. 2 of the analysis and optimization of the NDI decision process reflects the advantages of the separate modelling of measurement and failure achievable through the introduction of the state vector x .

FAILURE DUE TO A VOID WITH PERIPHERAL MICROCRACKS

It is known that voids, which are almost always present in ceramics, are frequently the sites for the initiation of catastrophic crack growth under sufficiently large applied stresses. We consider a model of this process involving a random set of microcracks the periphery of the void with each crack having an independent probability of propagating to failure. We present a detailed treatment of the perhaps over-simplified case in which it is assumed that the propagation probability depends only on the local stress* at the void surface. Later, a brief analysis will be given of

the use in which it is assumed that the stress gradient also influences the propagation probability. For the same of simplicity, the voids are assumed to be spherical.

Three independent considerations are involved in the assembly of a decision framework; the estimate of the pertinent defect dimensions from the inspection measurement y given the defect state x ; the probability of performance c at a specified stress level $\sigma_{\alpha\beta}$ given the defect state x ; and the *a priori* probability density of the state x corresponding to the distribution of defects. Each of these inputs is examined separately and then combined to provide the optimal accept/reject decision rule and associated decision performance measures.

Measurement Process. The relevant conditional probability density $P(y|x)$ is implied by the stochastic measurement process

$$y = \eta a^3 + r$$

where y is a possible measured value of $A(\omega)/\omega^2$, i.e., the scattering amplitude for longitudinal-to-longitudinal backscatter divided by the square of the frequency ω , evaluated at a sufficiently small value of ω . The quantity ηa^3 is the theoretical value of the above quantity when the state $x = a$ (the void radius) is assumed to be known. The coefficient η depends only on the known properties of the host material and is given by the expression

$$\eta = \frac{1}{3} \frac{1}{c_L^2} \left(1 + \frac{1}{2} \frac{1 + \nu}{1 - 2\nu} + \frac{10(1 - 2\nu)}{7 - 5\nu} \right) \quad (1a)$$

where c_L is the propagation velocity of longitudinal elastic waves and ν is Poisson's ratio. The experimental error r is assumed to be a Gaussian random variable with zero mean and covariance C_r .

Failure Process. This subsection deals with the calculation of $P(c|x)$, the probability of the performance c , given the state $x (=a)$ of the significant defect. In the present model the only type of defect that is significant in the context of structural failure is a spherical void. As illustrated in Fig. 4 this void has randomly positioned cracks distributed at its surface. With a specified applied stress, each crack has the potential of propagating into a large crack, subsequently causing structural failure. The probability of this happening is a function of the

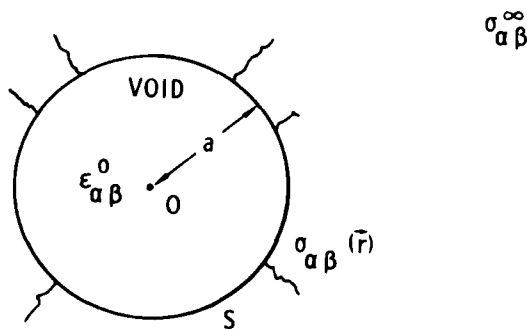


Fig. 4 Failure model geometry.

local stress $\sigma_{\alpha\beta}(\vec{r})$ in the neighborhood of the crack. The cracks are, in this instance, considered to be much smaller than the void diameter, so that the effects of stress gradients into the host can be neglected. The modifications that pertain when this condition is not satisfied will be discussed later.

Based upon this model, the probability of survival, given that the state $x = a$ is specified, is

$$P(1|a) = 1 - P(0|a) = \exp(-4\pi n_s a^2 \langle Q \rangle_A) \quad (2)$$

where n_s is the average surface density of cracks on the surface of the spherical void and $Q = Q(\sigma_{\alpha\beta}(\vec{r}))$ is the probability that a crack at the position \vec{r} on the surface will propagate to failure. The symbol $\langle Q \rangle_A$ denotes the area average of Q over the surface of the void.

The A Priori Probability Density of Defects. Studies of defect densities in ceramics indicate that the large value extreme, of interest to fracture problems, can frequently be characterized by the cumulative distribution

$$F(a) \equiv \int_0^a P(a) da = 1 - \exp\left[-\left(\frac{a}{a_c}\right)^k\right] \quad (3)$$

where a_c is a characteristic radius and k is a constant exponent.

Results. Here we combine the outputs of the last three subsections to yield $P(y,c)$ from which we deduce $P(y|c)$ and the classification errors e_0 and e_1 .

It is desirable to introduce the dimensionless variables $z = y/C_r^{1/2}$, $\xi = a/a_c$, and an additional dimensionless parameter $\kappa = \eta a_c^3/C_r^{1/2}$, which is signal-to-noise ratio characterizing the observation of elastic waves scattered from a spherical void of radius a_c . Another useful quantity is the dimensionless failure parameter

$$\zeta = 4\pi n_s a_c^2 \langle Q \rangle_A \quad (4)$$

whose significance is given by $P(1|x) = P(1|a) = \exp(-\zeta)$ when $a = a_c$ (i.e., the void has the critical radius defined by (9)). We actually compute $P(z|c)$ instead of $P(y|c)$ with a scale factor introduced into the normalization.

In Fig. 5 we present plots of $P(z|0)$ and $P(z|1)$ vs. z for $k = 3$, $\kappa = 10$ and $\zeta = 0.01$. These figures show the structure of the $c = 0$ class (i.e., the normalized population of objects that are going to fail) and $c = 1$ class (i.e., the normalized complementary population of objects that are going to survive). Moreover, they show the nature of the overlap of the two classes.

In Fig. 6 we also give a plot of e_1 vs. e_0 for the same parameter values. This is the so-called "operating characteristic" of the system. It is to be emphasized again that e_0 is the falsely accepted fraction of objects that are actually going to fail. Conversely, e_1 is the falsely rejected fraction of objects that are actually going to survive.

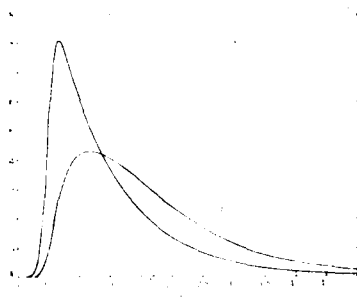


Fig. 5 Nature of surviving and failing populations.

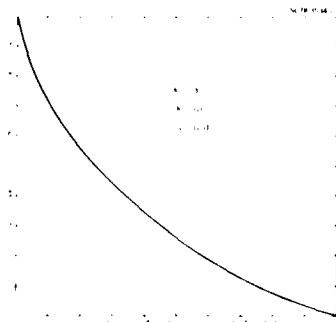


Fig. 6 NDE operating characteristics.

The above results indicate a rather poor NDE performance due, of course, to an excessive overlap of surviving and failing populations. This overlap is due almost entirely to inherent randomness in the failure process remaining even when the state $x = a$ is known with precision. However, one must measure the width of the overlap region relative to the width of the combined populations. The latter width depends upon the form of $P(x)$. The quantitative nature of these considerations is partially clarified in the ensuing decision.

Effect of Stress Gradients. A preliminary investigation has been made of the influence of the stress gradient effect on NDE performance. We take this effect into account by assuming that $\langle Q \rangle_A$ depends upon the spherical void radius a . Proceeding on a phenomenological level, let us assume that

$$\langle Q \rangle_A = f(\sigma_{ab}^m) a^{m-2} \quad (5)$$

giving

$$P(c = 1|a) = \exp(-\zeta(a/a_c)^m) \quad (6)$$

where ζ is defined now by

$$\zeta = 4\pi n_s a_c^m f(\sigma_{ab}^m) \quad (7)$$

Clearly, many other modifications of $\langle Q \rangle_A$ may have greater physical justification, i.e., the case discussed by Evans, Piswas and Fulrath.³ However, the above modification enables us to obtain relatively simple results without difficulty.

We now obtain with $\kappa \gg 1$ and $\zeta \ll 1$ (i.e., large signal-to-noise ratio and low a priori failure probability) the results

$$p(c = 0) = \zeta \Gamma(1 + \frac{m}{k}) \quad (8)$$

$$P(c = 1) = 1 - \zeta \Gamma(1 + \frac{m}{k}) \quad (9)$$

$$e_1 = \exp(-u^*) \quad (10)$$

$$e_0 = \frac{\gamma(1 + \frac{m}{k}, u^*)}{\Gamma(1 + \frac{m}{k})} \quad (11)$$

where

$$\Gamma(\alpha) = \int_0^\infty dt t^{\alpha-1} \exp(-t) \quad (12)$$

is the gamma function and where

$$\gamma(\alpha, x) = \int_0^x dt t^{\alpha-1} \exp(-t) \quad (13)$$

is the incomplete gamma function. The variable u^* is defined by

$$u^* = (\gamma^* / n a_c^3)^{k/3} \quad (14)$$

We now consider the quantitative determination of the dependence of the operating characteristic upon the ratio m/k . In Fig. 7 we present a plot of the false acceptance probability e_0 vs. m/k for a fixed false-rejection probability $e_1 = \exp(-1) = 0.368$ corresponding to $u^* = 1$. This result strongly suggests that this e_1 vs. e_0 curve moves closer to the horizontal and vertical axes as m/k increases, i.e., the performance of the NDE system improves as this ratio increases. It is clear that with $m = 2$ the previous case with no stress

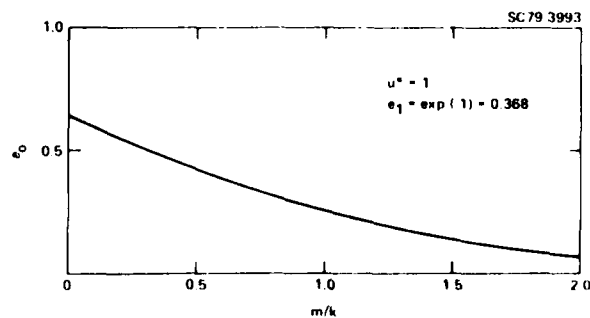


Fig. 7 Dependence of false acceptance probability on the stress gradient effect.

gradient effect is obtained. In this case the improvement can be due only to the decrease of k . This corresponds to an increase of the width of the combined populations of surviving and failing components relative to the width of the overlap region. On the other hand, with k fixed, the improvement can be brought about only by the increase of m . This corresponds to the converse of the situation just discussed, i.e., the decrease of the overlap region relative to the width of the combined populations.

FAILURE DUE TO A SUBCRITICAL INCLUSION

We turn now to the consideration of failure due to a subcritical inclusion. An example of such a system is an Si inclusion in Si_3N_4 . The work reported here is largely due to Fertig and Meyer.⁴ Here, it is assumed that a crack is first nucleated in the interior of an inclusion of lower toughness than the host. The "bottleneck" in the failure process is the propagation of the crack through the inclusion boundary into the host, a process requiring a substantially higher level of applied stress than that required to produce the earlier stages of crack development within the inclusion.

The geometrical nature of the model of the defect and its observation by elastic wave scattering is depicted in Fig. 8. We assume a semi-infinite specimen with known host material. With Cartesian coordinate system partially shown, the boundary of the specimen is parallel to the xy-plane and the outward pointing normal lies in the positive z-direction. We assume that the defect is an ellipsoidal inclusion (although the subsequent analysis is limited for the sake of brevity to the spheroidal case) with a known included material. We explicitly show a pulse-echo (i.e., backscatter) measurement with the incident wave pointed in the negative z-direction. However, additional transducer configurations will be considered later.

CS80-8285

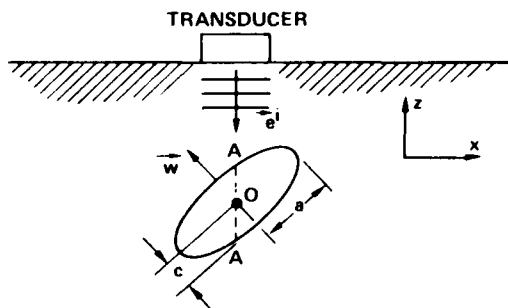


Fig. 8. Subcritical inclusion geometry.

State. If the inclusion boundary is assumed to be spheroidal then the state vector x need only be spheroidal then the state vector x need only be the four-dimensional representation of the geometry since the included material is assumed known. For the four-dimensional state vector, we will find it expedient to use the form

$$x = \begin{pmatrix} a \\ c \\ \theta \\ \gamma_z \end{pmatrix} \quad (1)$$

where θ is the azimuthal angle (in the xy-plane) of the symmetry axis defined by the unit vector \vec{w} and where γ_z is the direction cosine of \vec{w} relative to the z-axis. The vector \vec{w} can be expressed in terms of θ and γ_z as follows

$$\vec{w} = (1 - \gamma_z^2)^{1/2} (\vec{e}_x \cos \theta + \vec{e}_y \sin \theta) + \gamma_z \vec{e}_z \quad (2)$$

where \vec{e}_x , \vec{e}_y and \vec{e}_z are the unit vectors in the Cartesian coordinate directions.

Measurement Process. We assume that the measurements consist of an arbitrary number of low-frequency longitudinal-to-longitudinal backscatter processes. These are collectively represented by a standard stochastic model of the generic form

$$y = f(x) + r \quad (3)$$

where y , $f(x)$, and r are N-dimensional vectors (but considerable attention will be devoted to the case $N = 1$). The exact theoretical measurement $f(x)$ contains an nth component given by

$$f_n(x) = A_{2,L \times L} (\vec{e}_n^S, -\vec{e}_n^I; x) \quad (4)$$

where it is assumed that $\vec{e}_n^S = -\vec{e}_n^I = \vec{e}_n$.

The conditional probability density $P(y|x)$ is then given by

$$P(y|x) = G(y - f(x), C_r) \quad (4a)$$

where $G(\dots)$ is the N-dimensional Gaussian probability density given by

$$G(u, C) = (2\pi)^{-N/2} (\text{Det } C)^{-1/2} \exp(-\frac{1}{2} u^T C^{-1} u) \quad (4b)$$

Failure Process. It is assumed that a uniaxial stress is applied in the x-direction. At sufficiently high levels the stress causes the initiation of processes described earlier. An interior defect thus causes a crack to propagate through the inclusion. We make the rather crude assumption that this crack forms, as represented by the dashed line AA' in Fig. 8, a plane intersecting the geometrical center of the spheroid and having an orientation perpendicular to the axis of the applied stress, i.e., the x-axis. At a sufficiently higher value of the applied stress the crack will propagate from the lower toughness inclusion (e.g., Si) into the higher toughness host material (e.g., Si_3N_4). We assume that the condition for this event can be adequately represented by an empirically recalibrated version of simple fracture mechanics with a Gaussian random additive variable representing the inherent variability in the fracture process.

In explicit mathematical terms, we assume that the performance variable c is given by

$$c = H(\sigma_f - \sigma_\infty) \quad (5)$$

where $H(\cdot)$ is the Heaviside unit step function, σ_∞ is the applied stress, and σ_f is the failure stress. The latter quantity is a random variable by the random process

$$\sigma_f = \alpha + \beta \sigma_p + s \quad (6)$$

where σ_p is the failure stress predicted according to simple fracture mechanics, α and β are empirical recalibration constants, and s is a Gaussian random variable with zero mean and variance C_s . The application of simple fracture mechanics (i.e., the computation of yield stress under the assumption that the ellipsoidal crack is surrounded solely by host material) gives

$$\sigma_p = \frac{K_C}{Z(c'/a') \sqrt{\pi c'}} \quad (7)$$

where K_C is the fracture toughness, a' and c' are the major and minor semi-axis lengths of the fully developed inclusion crack, and $Z(\cdot)$ is a function defined by

$$Z(u) = \left[\int_0^{\pi/2} d\psi (1 - (1 - u^2) \sin^2 \psi)^{1/2} \right]^{-1} \quad (8)$$

As stated earlier, we assume that the fully developed crack inside the inclusion is represented by the cross section formed by a plane, perpendicular to the x -axis, passing through the center of the spheroid. A straightforward geometrical analysis yields the result

$$a' = a \quad (9)$$

$$c' = (a^{-2} + (c^{-2} - a^{-2}) w_1^2)^{-1/2} \quad (10)$$

where w_1 is the length of the projection of \hat{w} (the unit vector defining the axis of symmetry of the spheroid) onto the crack plane. Using (2) we obtain

$$w_1^2 = 1 - (1 - r_z^2) \cos^2 \theta \quad (11)$$

Equations (7)-(11) thus give σ_p as a function of the state vector x defined by (1).

We turn finally to the calculation of $P(c|x)$. First we observe that, according to the stochastic model (b), the conditional probability density of σ_f is given by

$$P(\sigma_f|x) = G(\sigma_f - \alpha - \beta \sigma_p(x), C_s) \quad (12)$$

where $G(\cdot, \cdot)$ is the Gaussian function defined by (4b) which in the present case is specialized to a case of a scalar variable, i.e.,

$$G(u, C) = (2\pi C)^{-1/2} \exp\left(-\frac{1}{2} C^{-1} u^2\right) \quad (13)$$

Using (5) we obtain

$$\begin{aligned} P(c = 0|x) &= \int_{-\infty}^{\sigma_\infty} d\sigma_f P(\sigma_f|x) \\ &= \phi(C_s^{-1/2}(\sigma_\infty - \alpha - \beta \sigma_p(x))) \end{aligned} \quad (14)$$

where the function $\phi(u)$ is the error integral

$$\phi(u) = \frac{1}{\sqrt{2\pi}} \int_{-\infty}^u dt \exp\left(-\frac{1}{2} t^2\right) \quad (15)$$

Clearly, the conditional probability $P(c = 1|x)$ is given by

$$P(c = 0|x) + P(c = 1|x) = 1, \quad (16)$$

the normalization condition.

A Priori Probability Density. In the next several paragraphs, we discuss the *a priori* probability density $P(x)$, which is more complicated than that assumed in the previous section because the state vector x is now four-dimensional in order to characterize the spheroidal geometry.

We assume that the semi-axis lengths are independent of the angle variables. Furthermore, we assume that the latter are distributed with axial symmetry about the z -axis. These assumptions imply that

$$\begin{aligned} P(x) &= P(a, c, \theta, r_z) \\ &= P(a, c) P(\theta) P(r_z) \end{aligned} \quad (17)$$

with

$$P(\theta) = \frac{1}{2\pi} \quad (18)$$

If the axis of symmetry (represented by the unit vector \hat{w}) is completely isotropically distributed, then we obtain

$$P(r_z) = 1 \quad (19)$$

under the assumption that r_z is constrained to be positive. If the axis of symmetry is preferentially nearly parallel to the z -axis—then we could assume a probability density of the form

$$P(r_z) = (1 + \nu) r_z^\nu \quad (20)$$

with $\nu > 0$.

Here the distribution of semi-axis lengths is constrained by the inequality $a > c$ in order to limit the class of spheroids to the oblate case. In order to imitate the *a priori* probability density used in the last section, we assume

$$P(a, c) = B g(a) h(c) \quad (21)$$

where

$$g(a) = \left(\frac{a}{a_c}\right)^{k-1} \frac{k}{a_c} \exp\left(-\left(\frac{a}{a_c}\right)^k\right) \quad (22)$$

$$h(c) = \left(\frac{c}{c_c}\right)^{k-1} \frac{k}{c_c} \exp\left(-\left(\frac{c}{c_c}\right)^k\right) \quad (23)$$

The normalization factor B is given by

$$B = 1 + \left(\frac{c}{a}\right)^k \quad (24)$$

The exponent k determines the sharpness of the decline of $g(a)$ or $h(c)$ when a or c exceeds the characteristic values a_c or c_c , respectively.

Combination of Probabilities. In order to compute the probability functions $P(y, c)$, $P(c|y)$, etc., we must first combine the various results of the previous paragraphs according to the relation

$$P(c, y) = \int dx P(c|x) P(y|x) P(x) \quad (25)$$

The calculation of $P(c|y)$, $P(y)$, and $P(c)$ have been discussed earlier.

In terms of the functions pertaining explicitly to the present case of failure due to subcritical inclusions, we obtain

$$P(y) = \int dx G(y-f(x), C_r) \quad (26)$$

where $G(\cdot, \cdot)$ is the Gaussian probability density defined by (4b), and $f(x)$ is given by (4). In the case of $P(c, y)$ we need consider only $P(c=0, y)$ now given by

$$P(c=0, y) = \int dx \phi(C_z^{-1/2}(\sigma_\infty - \alpha - \beta \sigma_p(x))) G(y-f(x), C_r) P(x) \quad (27)$$

where $\phi(\cdot)$ is defined by (15). We can use the relation

$$P(c=0, y) + P(c=1, y) = P(y) \quad (28)$$

to obtain other functions of interest.

Computations. In the numerical computations, we have used a Monte Carlo technique in which quantities of the type $\int dx(\cdot)P(x)$ are replaced by $\sum_{x \in S} (\cdot) / N$ where the samples of the state vector in the set S have been drawn at random in accordance with the probability density $P(x)$.

Throughout the computations we have employed the centimeter-gram-microsecond (c-g-us) system of physical units except in the case of stress or pressure which is expressed in pascals (Pa). This exception entails no difficulty because stresses will always be divided by other quantities involving the same units.

In all computations we will uniformly use the following assumptions and parameter values.

1. A priori statistics are partly defined by the assumption that the angular distribution of the axis of symmetry, defined by w , is isotropic, i.e., (18) and (19) hold. It is further defined by assuming the distribution of semi-axis lengths are given by (21)-(24) with $k = 1$, $a_c = 0.0325$, and $c_c = 0.0075$.
2. The material properties of the host (Si_3N_4) are assumed to take the values $\rho = 3.200$, $\lambda = 1.586$, and $\mu = 1.250$

(ρ , λ , and μ are the density and the two Lamé constants). The corresponding properties of the inclusion (Si) are assumed to take the values $\rho' = 2.340$, $\lambda' = 0.527$, and $\mu = 0.680$.

3. In the failure process the empirical recalibration constants take the values $\alpha = 0.997 \times 10^8$ Pa and $\beta = 0.541$. For the fracture toughness constant we assume $K_c = 0.500 \times 10^4$ Pa cm^{1/2}.

The purely statistical parameters C_r and C_c and the applied stress σ_∞ will be discussed later.

In the following paragraphs we present numerical results for three cases to illustrate the separate effects of randomness and completeness in the measurement process and randomness in the failure process.

Case 1. One Measurement. Random Measurement and Failure Processes. In this case we consider a single ND measurement, i.e., a pulse-echo, longitudinal-to-longitudinal scattering of elastic waves with the incident propagation in the negative z -direction. The random experimental error is represented by the standard deviation $C_r^{1/2} = 10^{-6}$ corresponding to a signal-to-noise ratio of about 10, using as a signal standard the return from a scatterer with $a = a_c$, $c = c_c$, $r_z = 1$ and θ irrelevant. It is to be stressed that the single measurement assumed here represents a decidedly incomplete set of measurements since the state vector is four-dimensional. In the failure process, we assume the applied stress $\sigma_\infty = 2.5 \times 10^8$ Pa, and a standard deviation of σ_f given by $C_s^{1/2} = 0.367 \times 10^8$ Pa.

In Fig. 9 we show the computed curves of $P(y|c=0)$ and $P(y|c=1)$ representing the failing and surviving populations. It is clear that the severe overlap will yield a rather poor NDE

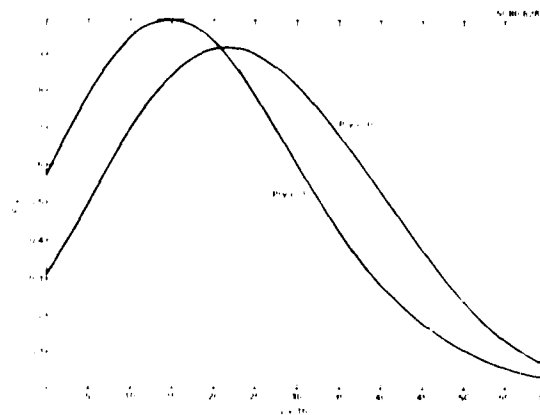


Fig. 9 Probability densities of failing ($c=0$) surviving ($c=1$) populations vs. ND measurement y .

performance as indicated by the plot of false rejection probability e_f vs. false acceptance probability e_a shown in Fig. 10. The poor performance is associated with three factors.

incompleteness in the set of measurements, randomness in the measurement process, and randomness in the failure process. The two remaining cases will throw some light on this matter.

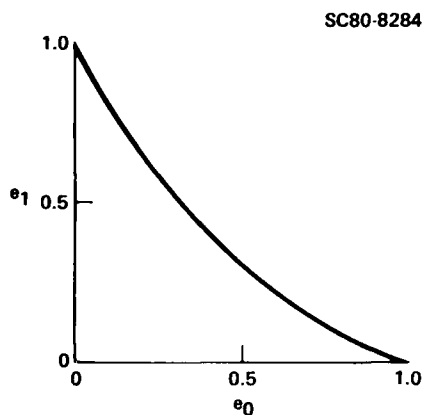


Fig. 10 NDE operating characteristics.

Case 2. One Measurement. Deterministic Measurement and Failure Processes. Here we consider again a single measurement of the same kind as in the last case. However, for the sake of understanding we eliminate the randomness from the measurement and failure processes by setting the variances $C_e = C_s = 0$. The resultant NDE performance (hypothetical) is given by the e_1 vs. e_0 plot in Fig. 11. Although there is a marked improvement in the performance, i.e., the curve has moved closer to the horizontal and vertical axes, the performance is hardly what one would expect from a perfect system. This is due, as one might expect, to the serious incompleteness of the measurement set. Incidentally, the lack of smoothness of the curve is due to the relatively small fraction of Monte Carlo samples that actually affect the final answer.

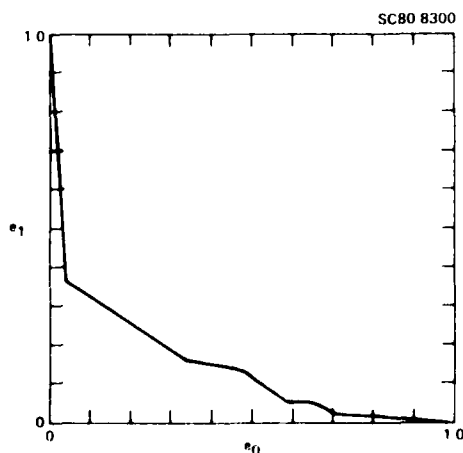


Fig. 11 NDE operating characteristic.

It is desirable to add a few clarifying remarks concerning the effect of an incomplete measurement set. A deterministic measurement model implies that the relation

$$P(y|x) = \delta(y-f(x)) \quad (29)$$

holds, i.e., a given value of the vector x implies a unique value of y . This result holds regardless of the dimensionality of y relative to the dimensionality of x and it is obviously valid when y is scalar. However, in the present case of an incomplete measurement set one cannot make analogous statements concerning $P(x|y)$. Here a given value of the scalar y does not imply a unique value of the four-dimensional vector x , but only a unique three-dimensional subspace. Thus here $P(x|y)$ is approximately proportional to $P(x)$ with a constraint that x lies in this subspace. More precisely $P(x|y)$ is given by

$$\begin{aligned} P(x|y) &= P(y|x) P(x)/P(y) \\ &= \delta(y-f(x)) P(x)/P(y) \end{aligned} \quad (30)$$

with $P(y)$ playing the role of a normalization constant. It is obvious that if $P(x)$ is sharply peaked in this subspace (defined by $f(x) = y$) then the lack of completeness in the measurement set does not lead to a serious degradation of NDE performance.

Case 3. Complete Measurement Set. Deterministic Measurement Process but a Random Failure Process. In this case, we assume a significantly large diversity of very accurate measurements that the measurement vector y implies a unique estimate of x , namely $\hat{x}(y)$, with a negligible a posteriori variance (more precisely, a covariance matrix $\text{Cov}(x|y)$, whose eigenvalues are sufficiently small in an appropriate sense). This means that we can write

$$P(c|y) = P(c|x = \hat{x}(y)), \quad (31)$$

or, in more explicit terms

$$P(c=0|y) = \phi(C_2^{-1/2}(\sigma_\infty - \alpha - \psi \sigma_p(x(y)))) \quad (32)$$

where $\phi(\cdot)$ is defined by (15). In the damage process, we assume the same standard deviation as in Case 1, i.e., $C_1^{1/2} = 0.367 \times 10^6$ Pa, but with a somewhat higher applied stress, i.e., $\sigma_\infty = 3.5 \times 10^8$ Pa.

The resultant plot of e_1 vs. e_0 , the NDE operating characteristic, is presented in Fig. 12. This highly satisfactory result demonstrates clearly that randomness in the present failure process (failure initiated in subcritical inclusions) is not a significant contributor to the degradation of NDE performance. In order to understand the relative contributions of incompleteness and randomness in the measurement process, it would be interesting to investigate the case in which the measurement set is complete but randomness in the form of measurement error remains. Because of excessive computational labor, this has not yet been done.

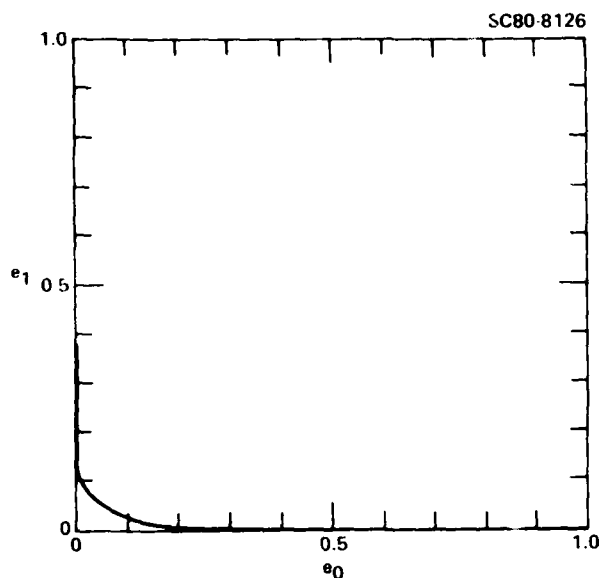


Fig. 12 Operating characteristic.

DISCUSSION

We have set up a complete formalism for the calculation of $P(c|y)$, the probability of performance (failure or survival) of a structural component given the results of ND measurements. With the definition of a suitable loss function giving the costs of wrong decisions, an optimal accept/reject decision procedure was derived. With the inclusion of $P(y)$, the probability density of ND measurement results on the entire population of failing and surviving components, it was possible to calculate the so-called operating characteristic, the plot of the probability of false-rejection vs. the probability of false-acceptance for all possible loss functions. This curve provides a unique characterization of the behavior of the NDI system independently of the loss function and a priori component performance probability.

The discussion here involves a basic approximation, namely that the most significant (from the standpoint of the probability of causing failure) defect is considerably more significant than the combined effect of all of the remaining defects. The specific application of this formalism was to the case of brittle fracture in ceramics. We considered two kinds of defects: voids and subcritical inclusions. In the first case, failure is associated with peripheral microcracks, any one of which may propagate to failure. In the second case the failure is connected with the possibility

of a crack propagating from a lower-toughness inclusion into a higher-toughness host. In each case we assumed that the ND measurements consisted of a set of low-frequency, L-to-L, pulse-echo scattering measurements (it is understood that a set composed of a single measurement is an admissible special case). The analysis of failure in ceramics is especially simple because to a high degree of approximation there is no slow evolution of failure (e.g., like fatigue in metals) before rapid catastrophic failure occurs. Thus, here the probability of failure depends, in the case of a uniaxial applied stress, only upon the maximum positive (i.e., tensile) stress applied during an appropriate time interval. In present treatment, we regarded this maximum stress as a parameter with an arbitrarily specified value.

The problem of estimating the conditional probability of failure for the two kinds of failure mechanisms in ceramics has been investigated with the aid of synthetic (i.e., theoretical) ND measurement data. The operating characteristic (i.e., the plot of false rejection probability vs false-acceptance probability) was determined for various combinations of parameter values. It is noteworthy that the unconditional failure probability (i.e., the fraction of the total population that would fail under the assumed applied stress) had very little influence on the operating characteristics, thereby reinforcing the notion that these curves reflect the incremental value of NDI. Calculations conducted for the case of voids with peripheral microcracks, without stress gradient effects taken into account, yielded operating characteristics that were rather disappointing, a feature that was due in most cases almost entirely to randomness inherent in the failure model. However, the calculations carried out for the case of subcritical inclusions yield very different results. We obtained poor and good operating characteristics depending on the degree of completeness of the set of ND measurements. In all cases, the degradation due to randomness in the failure model was very minor.

ACKNOWLEDGEMENT

This research was sponsored by the Center for Advanced NDI operated by the Science Center, Rockwell International, for the Advanced Research Projects Agency and the Air Force Materials Laboratory under Contract No. F33615-74-C-5180.

REFERENCES

1. A. G. Evans and J. M. Richardson, "Non-destructive Failure Prediction in Ceramics," talk given at the 80th Annual Meeting of the American Ceramic Society, Detroit, Michigan, May 1978.
2. J. M. Richardson and A. G. Evans, "Accept/Reject Decisions and Failure Prediction for Structural Ceramics: Application to Failure from Voids," to be published in *Nondestructive Evaluation*.
3. A. G. Evans, D. P. Biswas and P. M. Fuhrath, "Since Effects of Cavities on the fracture of ceramics," *J. Am. Ceramic Soc.*, in press.
3. I. W. Fertig and M. I. Meyer, private communication, 1978.

LONG WAVELENGTH ULTRASONIC CHARACTERIZATION OF INCLUSIONS IN SILICON NITRIDE

L. A. Ahlberg, R. K. Elsley, L. J. Graham, and J. M. Richardson
Rockwell International Science Center
Thousand Oaks, California 91360

ABSTRACT

The size and material content of Fe and Si inclusions in Si_3N_4 have been measured by means of pulse-echo scattering of elastic waves in the frequency range 5 to 100 MHz. The inclusions were of 100 μm and 400 μm nominal diameters and were located 3 mm deep in the Si_3N_4 . The electronic noise was reduced by signal averaging and, in some cases, the noise due to grain scattering was reduced by averaging over transducer position. The scattering amplitude $A(\omega)$ and the impulse function $R(t)$ were obtained by a desensitized deconvolution of the reference waveform obtained by reflecting the transmitted pulse from the back surface of the sample in a defect-free region. Comparison of theory and experiment are given for $A(\omega)$ and estimates of flaw size and material content are presented.

INTRODUCTION

Silicon nitride and other ceramics have a greater fracture strength at high temperatures than do metals. They are, therefore, candidates for use as turbine blades in new high temperature turbofan engines. The fracture strength of silicon nitride is known^(1,2) to depend not only on the size, shape and orientation of inclusions it contains, but also on the material an inclusion is made of. For example, the critical flaw size for an Si inclusion in hot pressed Si_3N_4 is 40 μm whereas for an Fe inclusion it is 150 μm and a WC inclusion reduces the fracture strength of the bulk Si_3N_4 hardly at all.

The most promising method for detecting and characterizing these defects is ultrasonics. There are two experimental ultrasonics tasks being performed in parallel under this program. These tasks are roughly divided into the two frequency regimes where the ultrasonic wavelength is small compared to the defect size (Stanford, described elsewhere in the proceedings) and comparable to or large compared to the defect size (Science Center, reported here). This is natural division both in terms of the experimental techniques required and the wave scattering theories used to interpret the ultrasonic waveforms. The same set of silicon nitride specimens containing defects of various known sizes and types are being studied in each task as well as by acoustic microscopy (Sonosan, also described in this proceedings). It may turn out that elements of all of these measurements are required to characterize the defects.

A third task (also described elsewhere in this proceedings) considers the statistical aspects of the ultrasonic flaw characterization, flaw distribution, component stress history and the consequences of falsely accepting or rejecting a component in formulating a probabilistic accept/reject criterion.

EXPERIMENTAL PROCEDURE

The overall experimental approach, described in Fig. 1, required obtaining and characterizing seeded specimens, developing measurement capabilities, and using the experimental data to

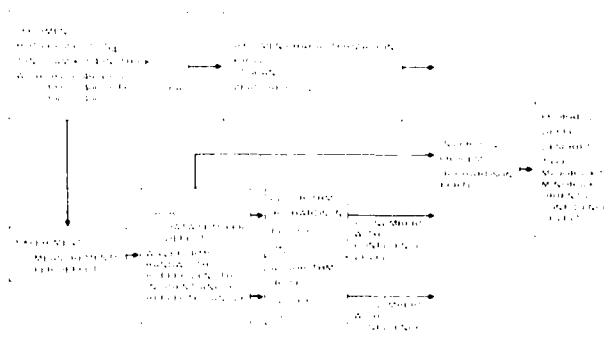


Fig. 1 Elements of the experimental program.

extract features which are a consequence of the characteristics of the defect and then using these features in an inversion formalism to obtain a probabilistic defect description.

Specimen Characterization. Hot pressed Si_3N_4 specimens containing specified inclusions were ordered from Norton Co. for use in developing the ultrasonic defect characterization techniques. Ten each of 1 in. diam. x 1/4 in. thick specimens containing Si, Fe and C inclusions 100 μm and 400 μm in diameter were ordered but 16 of each type were delivered. Only a few specimens of each type met the specified density of $\pm 3.20 \text{ gm/cm}^3$ as seen in Fig. 2. Each of the 96 specimens was carefully packaged and labeled to retain its individual identity. Master lists were maintained showing the correspondence between specimen numbers and the specimen density, thickness, wave velocities, and defect locations as this information became available.

Instrumentation. Some instrumentation development was required to extend present ultrasonic capabilities to higher frequency and greater sensitivity. First, a scanning liquid bath system was designed and constructed to accommodate two transducers, both of which are able to be positioned at an angle with respect to the specimen surface. Also, the specimen is mounted in a goniometer so all sides of the defect may be observed. Secondly, new techniques have been devised util-

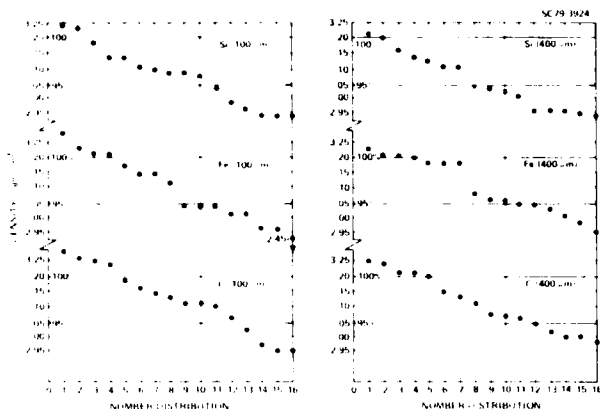


Fig. 2 Distribution of densities among the hot pressed Si_3N_4 test specimens.

izing unfocussed broadband pulser-transducer-buffer combinations using lithium niobate transducers and fused silica or 6061-T6 Al (aluminum) buffer rods, and pulsers using transistors operating in the avalanche mode to deliver high voltage delta function pulses to the transducers.

Scanning Bath System. The x, y scanning system is shown schematically in Fig. 3. The specimen is placed in the immersion tank (A) which is mounted

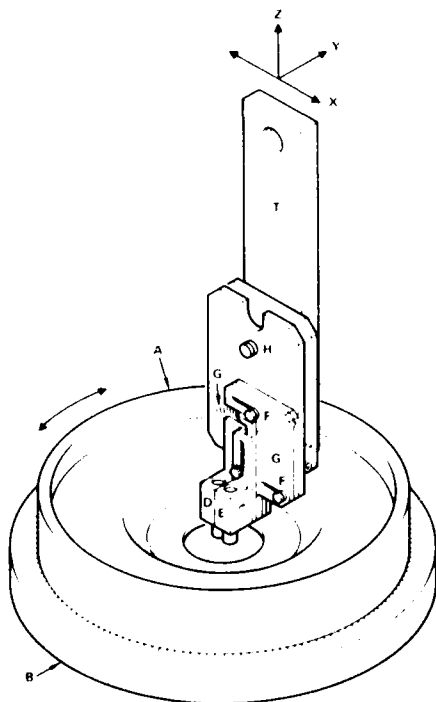


Fig. 3 Ultrasonic goniometer for one or two transducer immersion testing on the x-y scanning table.

on a goniometer (B). Transducer holders (D, E) are able to be positioned at an angle with respect to the specimen. These angles are measured with the

transducer goniometers (G). Transducer holder E can also be moved away from holder "D" by its own separate holder, goniometer device (F). Knob "H" is a positioning knob to insure that the transducers are normal to the specimen in that plane. "T" is the arm which is mounted on the x, y scanning device and is able to move in the "z" direction. Computer controlled scanning in raster steps as small as 25 μm can be accomplished using focused or unfocussed transducers in either the pulse-echo or pitch-catch modes. This system was prepared for use in the 100% volume inspection of the critical regions of Si_3N_4 turbine blades. The present measurements on the seeded specimens were made, however, using only contact transducers in pulse-echo at 0° and 15° incidence angles.

Broadband Transducer System. In the past, a modified Panametrics pulser-receiver was used for the detection of the defects. This system, however, has characteristics which can be greatly improved upon. First, the receiver amplifier has an upper cutoff frequency of 35 MHz which does not allow the characterization of flaws < 275 microns; secondly, the transmitter pulser has restrictions on its rise time; and third, the use of long, unmatched (up to 4 ft.) coaxial cables can result in unwanted reverberations in the transducer signal at higher frequencies which can give erroneous results in the characterization of the defects.

To solve these problems, pulser-transducer-buffer systems were constructed that were mounted in a manner to minimize circuit inductance and designed to match 50 ohm coaxial cable with 50 ohm attenuators and broadband amplifiers. The pulser is a transistor operating in the avalanche mode whose circuit layout construction uses high frequency strip line techniques (i.e., all leads are very close to ground planes and have parallel plate construction). The lead to the transducer is kept as short as possible and is the major source of system inductance. However, the resonant circuit consisting of the transducer-system capacitance and inductance is heavily damped and does not seem to cause any problems (Fig. 4).

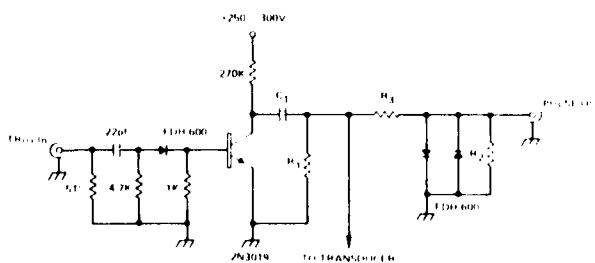


Fig. 4 Pulser-TR switch schematic.

The pulser can be tuned to the transducer by changing the discharge capacitor (C_1) and the resistors R_1 , R_2 , R_3 are altered to give a 50 ohm output impedance. The attenuators and amplifiers are wide band (attenuators have 0-1 GHz bandwidth and the amplifiers are 5 MHz to 1 GHz with ~ 30 db gain) with low noise figures (4.5 db).

Because of the limited bandwidth of any single transducer, several had to be constructed to cover the required frequency range. The reason for this can be seen in Table I where the range of frequencies corresponding to $0.2 < ka < 3$ are shown for various defect sizes within the range of interest. Because ka , rather than frequency determines the nature of scattering from a defect, transducers suitable for a 400 μm diameter defect are unsuitable for characterizing a 40 μm diameter defect.

Table I
Frequency (MHz) - ka Correspondence
For Typical Defect Diameters

d (μm)	VALUES OF ka		
	0.2	1	3
400	1.6	8	24
200	3.2	16	48
100	6.4	32	96
40	15.5	78	235

Table II lists the transducer-buffer combinations which were constructed and used in making the measurements. In most cases they were made by bonding a longitudinal lithium niobate crystal onto the end of the buffer rod, lapping the crystal to the desired thickness (resonance frequency), then providing an electrode and backing material for critical damping to increase its bandwidth. The buffer length and electrode diameter were chosen so that the defects in the seeded specimens would be in the far-field radiation pattern of the transducer over its frequency bandwidth. Figure 5 shows the characteristics of two of these transducers, obtained by a pulse echo measurement of a plane reflector. A matching 15° aluminum wedge was bonded to the face of the 40 MHz LiNbO₃-buffer combination to get the plane surface reflection shown in Fig. 5.

Table II
Transducers and Buffers Which
Have Been Constructed

TRANSDUCER			BUFFER		
TYPE	DIAMETER (mm)	FREQUENCY (MHz)	DIAMETER (mm)	MATERIAL	LENGTH (mm)
PARAMETRIC	0.64	15	1.27	Al	254
PZT	0.62	25	0.95	FeS	1.27
LiNbO ₃	0.62	40	0.95	Al	1.27
LiNbO ₃	.12	50	0.95	Al	1.27
LiNbO ₃	0.12	40	0.95	FeS	1.27
LiNbO ₃	0.1	80	0.95	FeS	1.27
LiNbO ₃	0.12	40	15.5	Al	1.27

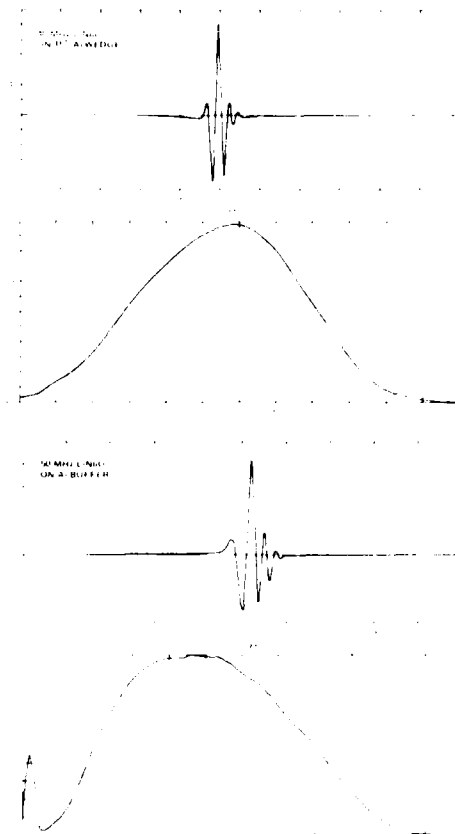


Fig. 5 Examples of Transducer characteristics.

Measurements. Several specimens of each type were scanned and the coordinates of any ultrasonic indications above the noise level were compiled. The number of indications range from 0 - 14 per specimen. No indications were observed in the samples containing carbon inclusions. This could be due to conversion (during the hot pressing) of the carbon seed to silicon carbide which has a similar acoustic impedance to the host material.

For the strongest indications, a variety of measurements were conducted. The measurements include normal incidence pulse-echo scans across the defect at close-spaced intervals (< 0.1 mm), and measurements at 30° incidence with the sample being rotated to 0, 90, 180, and 270 degree azimuthal angles using the Al wedge transducer buffer system. Experiments were conducted on both sides of the sample. Figure 6 shows the raw waveforms for a 100 μm Si inclusion and a 400 μm Fe inclusion, respectively. Note that, as expected, the echo for the larger flaw has a longer time duration.

Data Analysis. Two features were extracted from each waveform: A_2 (3,4) and d (5-7). They are derived from the low and intermediate frequency portion of the scattering spectrum. The reason for this choice is that for flaws which are as

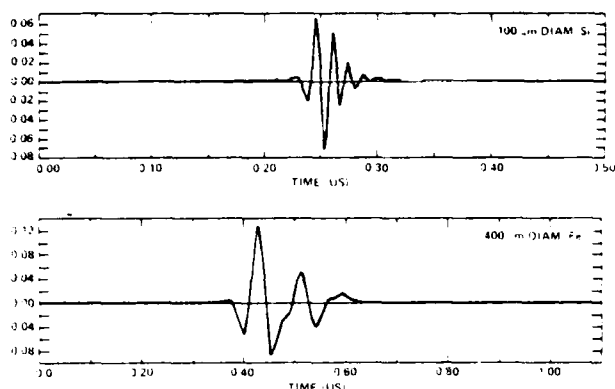


Fig. 6 Measured waveforms for 2 inclusions in Si_3N_4 .

irregular and spatially and chemically inhomogeneous as inclusions in Si_3N_4 are known to be; the high frequency portion of the spectrum will be dominated by fine structural details of the flaw whereas the overall size and material properties of the flaw will be easily accessible at lower frequencies.

A_2 is the coefficient of frequency squared in the long wavelength ($ka \ll 1$) regime. In this regime, A_2 completely defines the scattering of ultrasound from the flaw in a given direction. Therefore, by combining the values of A_2 for a variety of directions, it has been demonstrated that it is sometimes possible to obtain estimates of the size, shape and orientation of the defect.⁽³⁾ In addition, the sign of A_2 indicates whether the acoustic impedance of the flaw is greater or less than that of the host material.

The second feature which is extracted from the data is "d" which is an estimate of the defect radius in a given direction obtained using the one dimensional Born inversion algorithm. The Born inversion uses the intermediate frequency ($ka \sim 1$) part of the data as well as the low frequency phase data.

The extraction of A_2 and d was performed in the frequency domain, although equivalent time domain algorithms⁽⁴⁾ can be written and may prove more efficient computationally. The raw waveforms have had a reference waveform from a flaw-free region of the sample subtracted from them, and have then been Fourier transformed. The spectrum of the incident pulse was then divided out of the measured spectrum, yielding the normalized spectrum. A_2 was extracted by plotting the spectrum in a log-log manner and finding the intercept of the slope-of-2 region. d was extracted by time centering the spectrum using the low frequency flaw center,⁽⁴⁾ applying the Born inversion, and estimating radius as the area of the characteristic function divided by its peak.

Inversion. The inverse problem of finding the flaw properties given the measured features is handled by a statistical inversion algorithm.⁽⁸⁾ The input data consists of one or more pairs of A_2 and d. By making use of the ability to calculate A_2 for any spheroidal geometry, the algorithm

iteratively arrives at best estimates of the scatterer geometry and type given the input data. Appropriate confidence measures are also included in the output.

The inversion algorithm can be used in either of 2 different methods. In the first, only one normal incidence pulse echo measurement of the flaw is performed. This is the data that would be available if a part were being rapidly scanned. In the inversion algorithm, the assumption is made that the flaw is spherical and the algorithm estimates the radius and the material content of the flaw. In the second method of using the algorithm, a set of pulse echo measurements from various angles are made, as would be done in a detailed inspection of a suspected flaw. The resulting set of A_2 and d pairs is input to the inversion algorithm and estimates are made of the size, shape, orientation and material content of the spheroid which best fits the flaw. Generalization of the algorithm from spheroidal to ellipsoidal geometry would be straightforward.

RESULTS

Comparison of Measurements with Theory. Figure 7 shows theoretically calculated frequency (ka) spectra and impulse response functions for spherical inclusions of Si and Fe in Si_3N_4 , respectively. A_2 describes the parabolic region of the frequency curves below $ka = 0.5$. In each case, the impulse response function shows a front surface echo as well as miscellaneous later echoes. In the case of Fe, the front surface echo is small and the late arriving echoes extend well beyond the right edge of the figure.

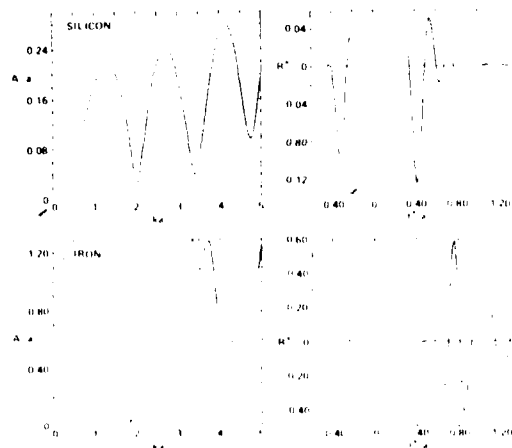


Fig. 7 Scattering calculations in the frequency (ka) and time domains for spherical inclusions in Si_3N_4 .

The first notable observation about the data is that for 2 different 400 μm Fe inclusions, there is no detectable front surface echo. Although the expected front surface echo is small for an Fe inclusion, it should still have been detectable. A likely explanation of this is that the very irregular front surface of the flaw will not specularly reflect the high frequency

components of which the front surface echo is largely composed. This should not appreciably affect the low frequencies for which the wavelength is larger than the scale of the irregularities. The complete absence of a front surface echo suggests that some other as yet not understood mechanism may also be present. For the 100 μ m Si inclusion studied, the incident sound pulse is not quite short enough to allow us to determine if the front surface echo is missing. However, if it were missing, this would have larger effect than in the case of Fe.

In order to explore the implications of a missing front surface echo, we have calculated the frequency spectra expected for spherical inclusions if the front surface echo is windowed out of the impulse response of the flaw. Figure 8 is a composite presentation of these comparisons. It shows, for 100 μ m Si and 400 μ m Fe inclusions, various frequency spectra and, below them, the deconvolved impulse response of the measured data. The solid curve in the frequency spectra is the normalized spectrum of the measured waveform. The dashed curve in each case is the calculated spectrum for a spherical inclusion (including front surface echo). The dotted curve is the calculated spectrum with the front surface echo windowed out.

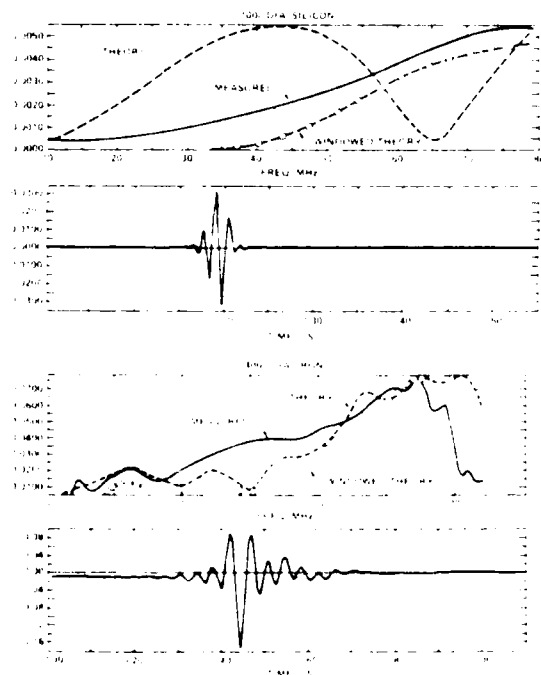


Fig. 8 Comparison of measured and theoretical spectra (with and without front surface echo windowed out); deconvolved impulse response functions of measured data.

For the case of Fe, the small size of the front surface echo means there is little difference between the two theory curves. The measured spectrum agrees reasonably with the theory. In the case of Si, the spectrum is greatly affected since about half of the impulse response has been windowed out. In particular, the windowed spectrum looks like the unwinded spectrum of a

smaller flaw. The measured flaw spectrum seems to be more like the windowed (front surface echo missing) spectrum. However, remember that the theory curves are based on the nominal size of the flaw. The photomicrograph of this flaw after sectioning (see Fig. 11 and accompanying discussion) leaves open the question of whether there is a systematic lack of front surface echos in the low frequency regime. In the absence of more definitive evidence, we have done the flaw characterizations assuming the presence of the front surface echo.

Determination of Flaw Size and Material. The inversion algorithm requires as inputs the set or sets of A_2 and d , a priori error estimates for them and the list of candidate inclusion materials to be considered. By observing the sign of A_2 , the algorithm can immediately limit its consideration to those candidate materials whose acoustic impedance is on the same side of the host material's acoustic impedance as that of the flaw being measured.

The output of the inversion algorithm is presented graphically in Fig. 9 and 10. These figures show the joint probability of flaw radius and flaw material plotted vs radius. Therefore, each curve is the probability of the flaw having a given radius assuming that the flaw is made of the given material. The area under each curve is therefore the probability of the flaw being made of the corresponding material. These probabilities are listed for each curve and are the basis for deciding which material the flaw is made of. The results obtained from these plots are summarized in Table III.

Table III
Results

APPROACH	FLAW	NOMINAL RADIUS (μ m)	MATERIAL	PROBABILITY	PROBABILITY
I	Fe	200	Fe	0.23	2.39
			Wc	0.2	
			Sn	0.04	
I	Si	50	Si	0.60	26
			C	0.22	
			BN	0.18	
II	Si	50	Si	0.40	21.33
			BN	0.24	
			C	0.4	
			Wc/B	0.17	

AD-A094 826

ROCKWELL INTERNATIONAL THOUSAND OAKS CA SCIENCE CENTER F/8 11/2
PROCEEDINGS OF THE DARPA/AFML REVIEW OF PROGRESS IN QUANTITATIV--ETC(U)
JUL 80 D O THOMPSON; R B THOMPSON F33615-74-C-5180
SC595.70AR

UNCLASSIFIED

AFWAL-TR-80-4078

NL

8 of 8

084926

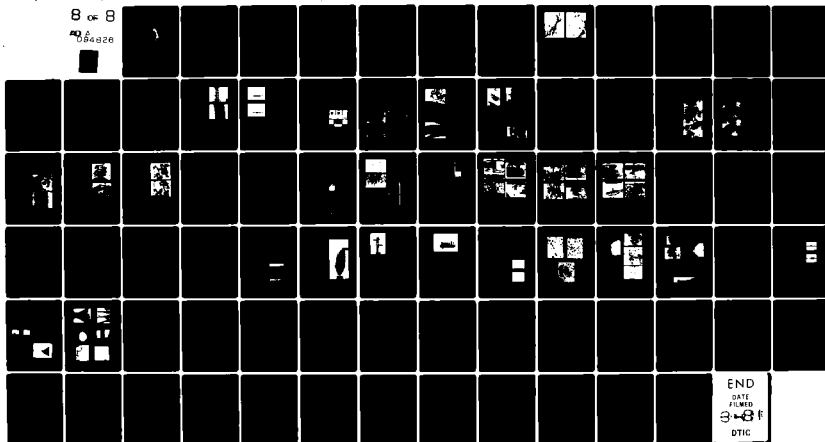


Figure 9 contains the results for a nominally 400 μm diameter Fe inclusion. Method 1 (one pulse echo waveform, assumed sphericity) was used. The probability of the flaw being Fe is 71% and the most likely diameter is 410 μm . This estimate is within 3% of size determined by destructive examination.

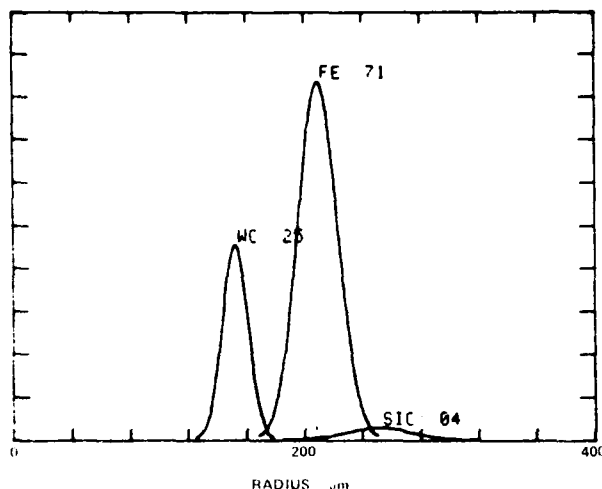


Fig. 9 Joint probability of flaw type and radius for nominal 200 μm radius Fe inclusion.

Figure 10 shows the probability curve for a nominal 100 μm diameter Si inclusion treated by method 1. The probability of it being Si is 60% and the most likely diameter is 52 μm .

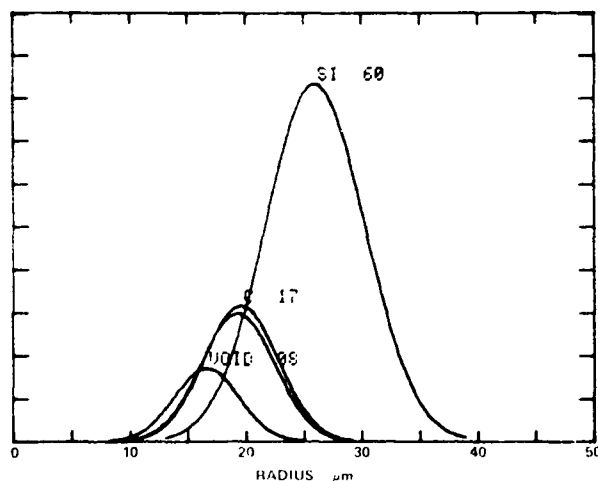


Fig. 10 Joint probability of flaw type and radius for nominal 50 μm Si inclusion.

Another set of results for the same Si flaw are given in the table, this time using method two (several measured waveforms). The flaw is again called Si and it is estimated to be slightly oblate (26 μm x 33 μm) and slightly tilted (4°) from the surface normal.

Figure 11 shows a photomicrograph of this Si flaw after sectioning. It is revealed to be 2 very inhomogeneous regions close to one another. The observed radii are seen to be less than the nominal 50 radius of the Si seed, due no doubt to the dispersing of the original spherical seed which occurred during hot pressing. Both methods of analysis estimate a 26 μm radius in the direction perpendicular to the plane of the photograph, where an exact measurement is not available. However, judging by the lateral radii visible in the photograph, these estimates, together with the 33 μm lateral radius estimate, are somewhat low, but are probably within 40% of the correct values. This result is gratifyingly good, considering how much the actual flaw differs from the simple model flaws upon which the analysis is based.



Fig. 11 Photomicrograph of nominal 50 μm radius Si inclusion showing 2 separate and very inhomogeneous flaw regions.

Two comments are in order here. First, for a pair of flaws interrogated together, a radius estimate based on A_2 alone should increase only by the sixth root of 2. Also, the radius estimate from the Born inversion for normal incidence should be little bigger than for each of individual regions alone because of their positioning next to one another. Secondly, recall the lack of measurable front surface echo mentioned above and the large effect it had on the frequency spectrum of Si inclusions. Because the spectral features are offset to higher frequencies when there is no front surface echo, this would lead to underestimation of A_2 and d and therefore to underestimation of flaw size. It is possible that this is occurring here.

CONCLUSIONS

It has been shown that we can determine the size and material content of inclusions in silicon nitride with reasonable accuracy by using as few as one low frequency pulse echo ultrasonic waveform. The material of which the inclusion is made is identified correctly from among a small set of likely candidates. The flaw size was accurately estimated for a large (400 μm) Fe inclusion and somewhat underestimated for a small (100 μm) Si inclusion. The causes of this underestimation are under investigation.

These results provide a significant advancement in the state-of-the-art of characterizing flaws in ceramics, especially in determining the material content of the flaw.

ACKNOWLEDGEMENT

This research was sponsored by the Center for Advanced NDE operated by the Rockwell International Science Center for the Advanced Research Projects Agency and by the Air Force Materials Laboratory under Contract No. F33615-76-C-5180 and by the Rockwell International Independent Research and Development Program.

REFERENCES

1. A. G. Evans, H. R. Baumgartner, to be published.
2. A. G. Evans, "Accept/Reject Decisions for Ceramics Based on Ultrasonic Measurements," Proceedings of the ARPA/AFML Review of Progress in Quantitative NDE, Fifth Annual Report, in press.
3. J. M. Richardson, "The Inverse Problem in Elastic Wave Scattering at Long Wavelengths," Proceedings of the 1978 IEEE Ultrasonics Symposium, 78CH 1334-1 SU, pp. 759-766 (1978).
4. J. M. Richardson, R. K. Elsley, "Extraction of Low Frequency Properties from Scattering Measurements," This Proceedings.
5. J. H. Rose, J. A. Krumhansl, "A Technique for Determining Flaw Characteristics from Ultrasonic Scattering Amplitudes," Proceedings of the ARPA/AFML Review of Progress in Quantitative NDE, Fourth Annual Report, AFML-TR-78-205 pp. 368-372 (1979).
6. J. H. Rose, J. A. Krumhansl, "Determination of Flaw Characteristics from Ultrasonic Scattering Data," J. Appl. Phys. 50, 2951 (1979).
7. J. H. Rose, V. V. Varadan, V. K. Varadan, R. K. Elsley, B. R. Tittmann, "Testing the Inverse Born Procedure for Spheroidal Voids," Recent Developments in Classical Wave Scattering, Pergamon Press, in press.
8. K. Fertig, J. Richardson, "Unified Inversion Algorithms and Computer Simulation," Proceedings of the ARPA/AFML Review of Progress in Quantitative NDE, Fifth Annual Report, in press.

C. H. Chou, B. T. Khuri-Yakub, K. Lian, and G. S. Kino
Stanford University
Stanford, CA 94305

ABSTRACT

A 50 MHz C-scan imaging system is under construction for fast defect detection. A high-frequency (150-450 MHz) A-scan system is used for host material evaluation, and defect characterization. Several signal processing schemes such as time and space averaging, Wiener filtering, diffraction and propagation loss corrections are used in the process of defect characterization. Further modifications of the exact theory of scattering from spherical inclusions are made to ease the process of defect identification.

C-SCAN SYSTEM

A C-scan imaging system is being built to scan ceramics for interior defects. Initially, the device will operate at 50 MHz with a partially focused transducer to produce a beam approximately 1 cm in diameter. The device will be capable of scanning in both the x and y directions along the surface of a ceramic. By operating in a reflection mode, it should be possible to determine both the depth and the transverse position of a flaw. Eventually, it is intended to operate at frequencies as high as 400 MHz and to use the same system to evaluate the size and nature of the flaw. By using a moveable point source as a synthetic aperture system, i.e., a focused beam focused on the surface of the ceramic, we expect eventually to be able to reconstruct an image of the flaw on the computer.

The mechanically-scanned system being designed for this purpose has to satisfy the following requirements:

(1) the system should be computer compatible, and it should be possible to control the whole system operation from a computer terminal; and

(2) the mechanical scans should be accurate to about 10 μ m or less (i.e. at 100 MHz).

Thus, defect location and evaluation could be eventually carried out on one system. We believe that such a system will combine the advantages of A-scan with those of the acoustic microscope, but be able to examine internal as well as surface defects. For this application, steps of the order of one or two wavelengths in the X and Y directions are usually required.

System Design - The system has been designed to operate in one or any combination of the following modes:

Slow Mode - Scanning is at constant velocity. The maximum scan velocity is 5 cm/sec. set by thumb-wheel switches.

Increment Mode - Scanning is carried out by stepping from one point to the next. The step size can be varied from 50 μ m to 1 cm with an accuracy of $\pm 8 \mu$ m. The mechanical settling time per step is 3 msec. In this mode, the number of rf samples taken per step is settable from 10-999. The speed of the scan is controlled by the operator.

Go-To Mode - In this mode, the transducer can be moved to any location of interest on the fuel. The position is dialed on thumb-wheel switches and is found with an accuracy of ± 0.1 mm. The scan can be continued from this location in any of the modes previously described.

Flaw-stop Mode - In this mode, the scan stops when a defect is located. A thumb-wheel switch on the thumb-wheel switches is used to decide at what level a signal is considered to be due to a defect. The discriminator also gives out a signal to turn the z -axis (pen up, pen down) of an oscilloscope.

A combination of these modes is expected to be the best way to use the system. For example, a slow scan at a moderate speed can be used to determine the rough location of the defect. Then to come and followed by a fine-scan scan to determine the correct location of the defect. A flaw-stop can be used to stop the scan even the defect location when the signal is coming up. The x - y location of the defect is displayed on oscilloscope display in the main panel and/or the plot of an x - y recorder. The A-scan display is continuously monitored on a cathode ray oscilloscope which can be used to determine the location of the defect in the depth of the sample.

HIGH-FREQUENCY A-SCAN SYSTEM

A schematic diagram of the A-scan system used in our study is shown in Fig. 1. The bottom end of the buffer rod is polished with a radius of curvature of 20 cm. Contact to the ceramic under study is made by pushing the upper end of the buffer rod against the ceramic without using a contacting layer such as gold. The transducer is excited with a 40 V, 2 msec. electric pulse in order to obtain broad bandwidth operation (15-450 MHz).¹

The received signal at the transducer is passed into a sampling oscilloscope which yields an output that is a slowed down version of the pulse. A Brookan analog-to-digital converter digitizes the slowed down pulse for insertion into a PDP11-23 minicomputer. The computer is used to take fast Fourier transform and correct the received signal.

Signal Processing Methods - The signal processing schemes we use to correct and improve the signal from the defects are:

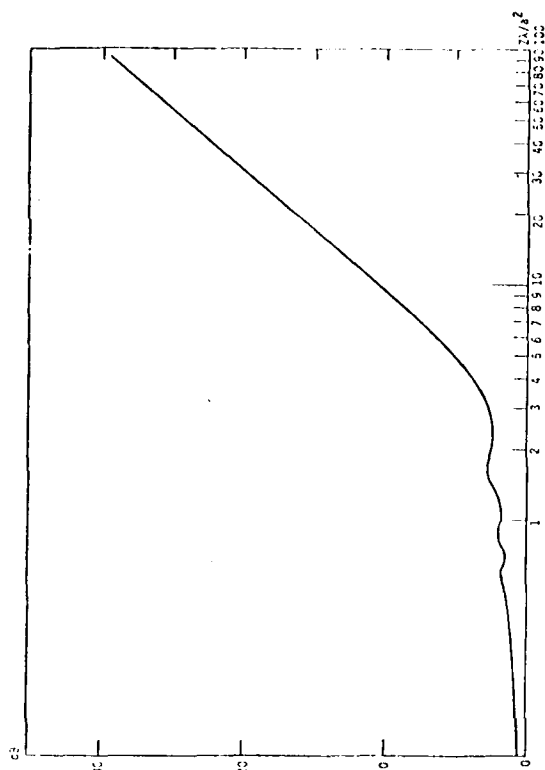


Fig. 1. Loss of power due to diffraction between two identical piston transducers of radius a as a function of their distance apart in units of a^2/z .

1. Time domain averaging.
2. Space domain averaging.
3. Wiener filtering.
4. Propagation loss correction.
5. Diffraction loss correction.

Time domain averaging consists of reading the signal N times at a certain location, then taking the average of the sum of the N signals. The amplitude of the signal from a defect relative to random noise is improved by \sqrt{N} . Space domain averaging consists of reading the signal at N different locations on the sample, then taking the average of the N signals. The criteria for the maximum step over the sample is to keep the signal from a defect almost constant, i.e., the defect is kept within the radius of the beam. This type of averaging improves the signal-to-grain scattering noise level.³ Wiener filtering is a deconvolution scheme used to remove the effect of the transducer response. This technique, which has been described in the previous report, consists mainly of dividing the received signal by the impulse response of the transducer while taking account of the presence of noise in the system.¹ Propagation and diffraction loss corrections take care of acoustic beam spreading and propagation loss through the host material itself. By using the techniques described, we have been able to improve the signal-to-noise ratio in the system, and look at the impulse response of defects separated from the effect of the transducer and the propagation media.

Propagation Loss Measurements - One important step in the NDE of ceramics is to evaluate the quality of

the host material itself. If the host material is porous or has large grains and does not meet fracture strength requirements, there is no point in looking for isolated defects and attempting to characterize them. For this test, we carry out a propagation loss measurement vs. frequency, as described in an earlier publication.⁴

The most important development in the last year has been to calculate the exact diffraction loss for all ranges of normalized distances from the transducer. This loss can be written as

$$\frac{\langle p \rangle}{\langle p_0 \rangle} = 2e^{-jkz} \int_0^{\infty} \frac{J_1^2(y)}{y} e^{js^2 y/4\pi dy} \quad (1)$$

where $\langle p \rangle$, $\langle p_0 \rangle$ are the average values of the pressure over the area of the output transducer at a distance z , and at the input transducer, respectively. $S = z/a^2$ where a is the transducer radius, k is the wave number, and $J_1(y)$ is a Bessel function of the first kind and first order.

The diffraction loss L is therefore

$$L = 20 \log \frac{\langle p \rangle}{\langle p_0 \rangle} \quad (2)$$

Fig. 1 shows a plot of the diffraction loss versus S , for S varying from 1 to 100. When the medium is anisotropic, the loss can be found simply by changing S to $(1-2b)S$ where b is an anisotropy coefficient defined as

$$b = \frac{(C_{33} - C_{13} - 2C_{44})(C_{33} + C_{13})}{2C_{33}(C_{33} - C_{44})} \quad (3)$$

for a material with hexagonal symmetry,⁵ such as sapphire (the buffer rod), $b = .16$. For isotropic materials, these formulae are reliable for $S \ll 1$, provided $ka \gg 10$. For anisotropic materials, however, the accuracy of the formula is better for $S \gg 1$.

We repeated our measurements of propagation loss in hot pressed NC 132 silicon carbide and at different locations in the same sample. Fig. 2 shows the results of some of these measurements. The loss is about 3 dB/cm at 300 MHz and follows an f^4 dependence, as would be expected from Rayleigh scattering theory. The value of the propagation loss at 300 MHz and the f^4 dependence were consistent for good hot-pressed silicon nitride samples. In a later section, we will discuss our results on some "bad" or lossy samples. It will be noted that, especially in the lower frequency range, it is vital to correct for diffraction.

Scattering Theory - The type and size of defects is determined by comparing their back-scattered power spectra to theory. The theoretical calculations for various types of spherical inclusions in a silicon nitride host matrix were calculated using the theory developed by Ying and Truett,⁶ and Johnson and Truett,⁷ using techniques similar to those of Richardson and Cohen.⁸ A PDP 11-34 mini-computer was used to carry out the calculations.

We found that the time taken to calculate the back-scattered signal versus ka (where $k = 2\pi/\lambda$, and a is the radius of the defect) took about 8 min for $9 < ka < 20$. For $0 < ka < 100$, the time taken per inclusion was roughly about 1 hr. The results for such calculations are shown in Figs. 3a, b, and c.

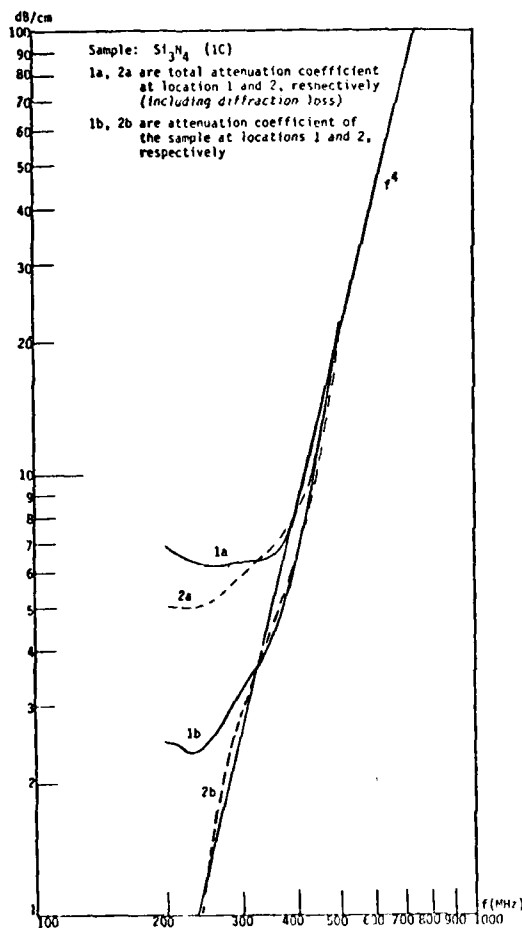


Fig. 2. Attenuation measurement at two different locations.

It is convenient to plot the theoretical scattering versus $\log ka = \log k + \log a$. Then, $\log a$ is unknown, as it would be in an experiment. The comparison between theory and experiment can be made by directly overlapping the experimental and theoretical curves, and finding a from the position where they overlap.

It will be noted that the scattering signal variation with frequency, denoted by the full line curves, is much simpler in form for a vacancy than for an inclusion. The reason is that the inclusion has associated with it several types of resonances. Put another way, the vacancy gives rise to a back-scattered echo from its front surface, and a wave which can propagate around the surface and interfere with the echo from the front surface, thus giving rise to the quasi-

periodic back-scattering structure. On the other hand, a wave can propagate through the middle of the inclusion and be scattered from its back surface as either a shear or a longitudinal wave. The return echoes interfere with each other, thus giving rise to a far more complicated form for the scattering cross-section as a function of frequency.

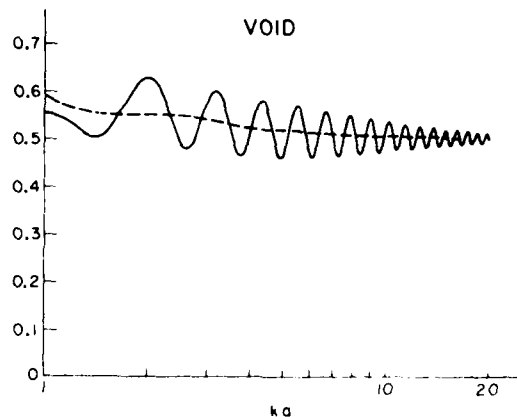


Fig. 3a. The scattering cross-section σ from a void in Si_3N_4 as a function of ka .

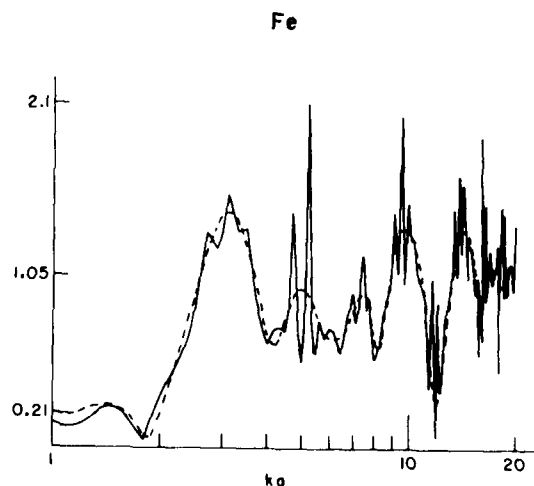


Fig. 3b. The scattering cross-section σ for Si_3N_4 as a function of ka .

The time domain impulse response of the defects has been calculated by inverse Fourier transforming the calculations of Fig. 3 into the time domain. A cosine squared window centered at $ka = 10$ and equal to zero at $ka = 0$ and $ka = 20$ was multiplied by the frequency response before inverse Fourier transforming in order to limit the time domain response, and give the pulses a shape like a real transducer response. The results of the calculations are shown in Figs. 4a, b, and c.

By examining the time domain responses in detail, it is possible to compare the results with simple optical ray tracing concepts, and determine the types of waves that contribute to the

impulse responses of the defects.⁹ The various waves are shown schematically in Fig. 4. It is obvious from Figs. 3 and 4 that different inclusions give rise to different return echo responses in both the frequency and time domains, thus making it possible to differentiate between different types of defects. It is also obvious that a void can be directly differentiated from inclusions because its spectrum is very flat with frequency, i.e., there is only a strong return echo from its front surface. Thus, it is simple to classify defects as to whether they are voids or inclusions.

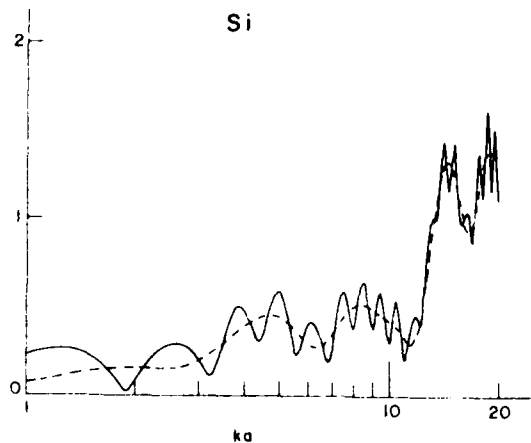


Fig. 3c. The scattering cross-section from Si in Si_3N_4 as a function of ka .

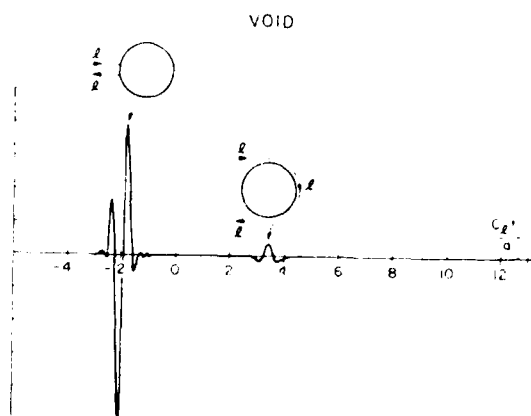


Fig. 4a. Relative scattering cross-section from a void as a function of time.

If a defect is a void, it is typically not possible to detect the second echo due to the leaky wave propagating around it. This we believe is due to the fact that the inside surface of the void is rough and scatters the circumferential wave before it reaches the transducer. The size of a void is then determined from a measurement of the echo amplitude. Another distinction to be made is whether a void is a "volumetric" void or a flat crack. This is typically done by measuring the thickness of the void either by measuring its location from the two sides of the sample, or by

measuring the distance from the back wall to the mirror image of the defect with respect to the back wall.

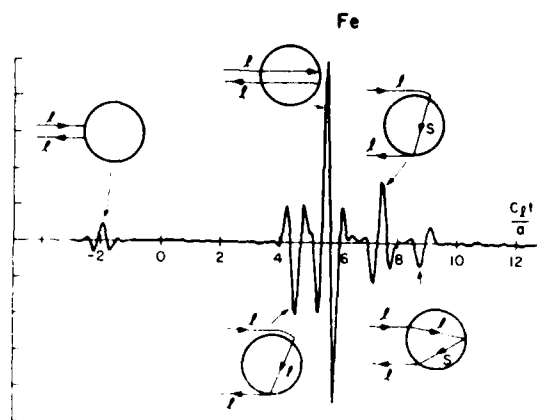


Fig. 4b. Relative scattering cross-section from Fe as a function of time.

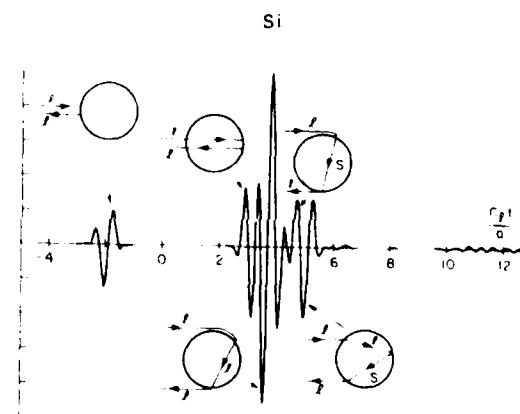


Fig. 4c. Relative scattering cross-section from Si as a function of time.

If the defect is an inclusion, we may use the signal processing schemes described above to compare the back-scattered spectrum of the flaw to theory and decide on its type and size. In our efforts to confirm the theory with samples having seeded defects, a new problem arose: the seeded samples are usually porous resulting in a large amount of back-scattering from grain boundaries and, of course, a large amount of propagation loss in certain cases. The effect of this grain scattering is that the resultant noisy signal tends to obscure the front face echo, which is relatively weak compared to the back face echo. In some cases space averaging enabled us to reduce the effect of grain scattering and isolate the front face echo. In many other cases, this was not possible, and we had to decide on the type and size of inclusions using the defect back-face echoes only.

We simulate this case in the theory by gating out the specular reflection from the front face in

the time domain, then Fourier transforming the remainder of the signal into the frequency domain. The results of this calculation are shown as dashed lines in Figs. 3a, b and c. Notice that as there is no longer interference between the back-face and front-face echoes, the high-frequency ripples (as a function of ka) are removed. The modified spectra differ for each material, and so allow flaw identification.

Results - We used a number of seeded NC 132 silicon nitride disks to confirm our theory on detection and characterization of defects. The samples were seeded with iron (Fe), silicon (Si) and carbon (C) inclusions. The sizes of the inclusions were either 100 μm or 400 μm in diameter. We tested seven of these samples and the results are shown in Table I.

Type & Size of Seeded Defect	ρ , g/cm ³	V_L , km/sec	V_T , km/sec	No. of Defects	No. of Voids	No. of Cracks	Hard Type of Identified Inclusions	No. of Identified Inclusions	Remarks
67 C-400 μm	3.12	10.11	7.5	5	2	1	0	2	30 dB Inhomogeneous
66 Fe-400 μm	3.2	10.3	12	3	0	2	1 Fe	0	7dB Inhomogeneous
93 Si-400 μm	2.95	9.24	80	2	0	1	1 Si	0	>30 dB Inhomogeneous
27 C-100 μm	3.24	10.8	7	18	9	6	0	1	Very Porous
1 Si-100 μm	3.23	10.7	11	10	1	4	3 Si 100 μm	2	...
2 Fe-100 μm	3.28	10.9	9	23	0	20	1 Fe	2	High Density of Small Cracks
23 C-400 μm	3.27	10.67	8	4	0	4	0	0	...

Measured Parameters

TABLE I

Results of measurements carried out on various seeded samples.

From Table I, the following conclusions can be made.

Some of the samples exhibited a large amount of localized inhomogeneity. In sample #67, the echo from the back side of the sample changed by 30 dB when the transducer was moved from one location to another, 1 or 2 mm away.

The density of the samples varied dramatically from one to the other. Sample #93 had a 10% lower density than fully dense silicon nitride. The densities of the rest of the samples are also lower by lesser amounts.

The longitudinal wave velocity measured at a frequency of 300 MHz is lower than expected for fully dense silicon nitride (11.0 km/sec). The longitudinal wave velocity seems to roughly be proportional to the density of the material. This indicates that the stiffness of the material decreases dramatically when the density decreases. The estimated stiffness of sample #93 is 36% lower than theoretically predicted for fully dense silicon nitride (NC 132).

The propagation loss measurement ties in very well with the density and longitudinal velocity measurements. We note that the less dense and correspondingly slower velocity materials have more propagation loss due to scattering from pores in the samples. From these

results, we can clearly conclude that measurements of density, velocity, and propagation loss give direction information on the quality of the material and could be used to improve the manufacturing process before proceeding to look for isolated defects.

Many isolated defects were found in the samples tested. In sample #2, 23 defects were found in an area of only 2mm x 3mm. In the lossy, inhomogeneous samples (#67, 86 and 93), far fewer defects were found because of the excessive propagation loss. This limits our sensitivity and obscures the back-scattered signal from defects in the back-scatter signal from the pores. In all the samples tested, a large amount of scattering from porosity was observed. The level of this scattering was comparable in amplitude to the reflection from the front side of the inclusions. Using the processing schemes described previously, we were able to separate the front face echo of the defect, and thus decide on its type and size, as tabulated. In other cases, we were able to decide on the type and size of an inclusion without using the front-face echo, as we have described. However, there were still some inclusions that we could not identify because of the large amount of scattering from porosity.

Judging by the number of defects found in the seeded samples, we observe that over 90% of all defects found were either voids or appeared to be cracks, which in fact were later found to be BN discs. Thus, many voids may not occur in unseeded samples and certainly do not in high quality NC 132 material.

We concentrated our detailed quantitative interpretation on the measurements of sample #1, the sample with isolated inclusions. After processing all the signals from the defects, as described, we found that three of the defects in the sample were Si inclusions 100 μm in diameter. This result is in good agreement with the type and size of inclusions with which the sample was said to be seeded.

At the time of writing, the sample had been partially polished to the locations of some of the defects we found. The results indicate that we were able to detect every defect present in the portion of the sample examined. Moreover, all the cracks we detected were found at the prescribed locations. They were in reality thin disks of BN, a material used in the pressing operation, which is relatively harmless as far as its effect on fracture is concerned. Flat empty cracks do not occur in hot pressed Si_3N_4 , and hence when "cracks" are detected by our acoustic method, they must be expected to be thin disks filled with a low acoustic impedance material such as BN. Hence, for hot pressed Si_3N_4 , all the detected cracks are thin disks of BN.

In another example, we decided that one of the voids we detected was actually two voids separated by 50 μm in depth. This decision was made because two echoes of equal amplitude were detected with 10 nsec separation in time. The actual defect is shown in Fig. 5a. The defects consist of two voids, as predicted, the two voids being connected by a porous region.

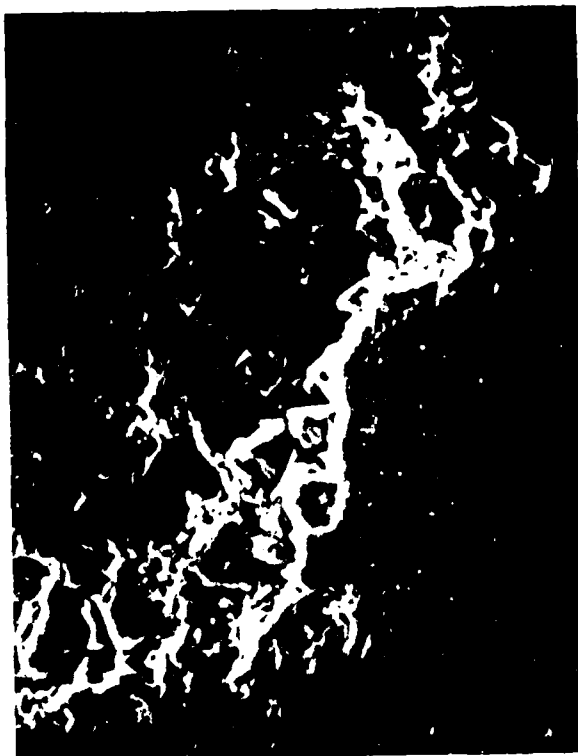


Fig. 5a. S.E.M. picture of two voids, 50 μ apart.

Some of the defects detected were of a new and unexpected type. They corresponded to a series of echoes with a short time separation between them (10-15 nsec), as would be expected from granular scattering. One such defect is shown in Fig. 5b. This defect turned out to consist of regions of concentrated MnO inclusions, a material used in the hot pressing operation to increase the density of the ceramic. It was thought that this material would disperse and not give rise to any problems; however, it obviously does not always do so. This unexpected defect, which was first detected clearly by acoustic techniques, is likely to have an important effect on the fracture characteristics of these ceramics.

There are a few more defects present in the samples, namely Si . We are presently awaiting the results of the polishing to compare with our acoustic measurements. At the present time, the polishing process has reached only one defect. The results obtained on this one defect are not encouraging, because the Si seed turned out to be porous, and of a larger size than had been predicted by our theory. This would be expected because the theory was based on the supposition that the defect was a sphere of Si . Here it was not spherical, nor was it pure Si . It remains to be seen whether the other Si seeds have changed in the same way.



Fig. 5b. S.E.M. picture of MnO rich defect region.

CONCLUSIONS

We have developed two systems to locate and characterize defects in ceramics. We have used a set of signal processing schemes to improve the signal-to-noise (electronic noise and grain-scattering noise) ratio and to correct the signals received from defects. We believe that our theoretical and experimental techniques have not been fully tested yet, because the seeded samples we had were inferior to hot pressed, unseeded silicon nitride. However, we feel confident that our technique will work well on high quality samples of the type that should be used in real turbines. One difficulty is that artificially seeded materials always appear to be far worse in quality than the natural unseeded samples with naturally occurring defects present.

It appears from our initial results that the seeded defects which occur are not always spherical or simple in nature. This presumably will be the case with naturally occurring defects. Thus, although there are acoustic signatures associated with the different types of defects that are present, it will be necessary to develop further acoustic methods to provide a complete unequivocal quantitative identification of the size and type of all defects present. Naturally occurring inclusions of biphasic materials of awkward shape are the most difficult to identify. For a complete analysis, it will probably be necessary to resort to the imaging techniques which we are presently developing.

REFERENCES

1. B. T. Khuri-Yakub, G. S. Kino, A.P.L., Vol. 31, No. 2 (15 Jan. 1977).
2. Y. Murakami, B. T. Khuri-Yakub, G. S. Kino, J. M. Richardson, A. G. Evans, A.P.L., Vol. 33, No. 8 (15 Oct. 1978).
3. K. Goebbels, P. Höller, Proceedings of the First International Symposium on Ultrasonic Material Characterization, Gaithersburg, Md., June, 1978.
4. A. G. Evans, B. R. Tittmann, L. Ahlberg, B. T. Khuri-Yakub, G. S. Kino, J.A.P., Vol. 49, No. 5, May, 1978.
5. P. C. Waterman, Phys. Rev. 113, 1240 (1959).
6. C. F. Ying, R. Truett, J. Appl. Phys., 27, 1086 (1956).
7. G. Johnson, R. Truett, J. Appl. Phys., 36, 3466 (1965).
8. J. M. Richardson, D. Cohen, Rockwell Science Center (Private Communication).
9. Y. H. Pao, W. Sachse, J. Acoust. Soc. Am. Vol. 56, No. 5, Nov. 1974.

ACKNOWLEDGMENT

This work was supported by the Advanced Research Projects Agency under Rockwell International sub-contract R174-20773.

SUMMARY DISCUSSION
(F. Khuri-Yakub)

Wolfgang Sachse (Cornell University): One comment and a question. It's nice to see that someone else has found Weibull useful for classifying certain defects, but my question is: you said you made the diffraction correction. You mean to say that you found what is the diffraction of a sound wave as it leaves the buffer rod into the sample?

F. Khuri-Yakub: No. When you want to make a correction loss, if you're at high TS, and if you look at all the published data, you find it goes up to four or five.

Wolfgang Sachse: That's for a piston radiator?

F. Khuri-Yakub: That is a piston transducer, too.

Wolfgang Sachse: I'm not sure, but anyhow --

F. Khuri-Yakub: We just took it farther because we needed to get that right correction there.

Jim Rose (Univ. of Michigan): You cut off your theory of KA of 1. Does that imply in your data analysis you don't use the low-frequency information?

F. Khuri-Yakub: It depends on the size of the transducer (inaudible), the only reason why we did that was because we plotted on a log-log scale (inaudible).

#

ACOUSTIC SURFACE WAVE PROBING OF CERAMICS

J. Tien, B. Khuri-Yakub, and G. S. Kino
Stanford University
Stanford, California 94305

ABSTRACT

We have developed a low frequency theory for scattering from surface cracks. For the case of half-penny shaped surface cracks, we are able to relate the reflection coefficient of a Rayleigh wave incident on the crack with the crack size as well as the fracture stress of a sample with the crack in it. Comparisons of the theoretical predictions for the fracture stress with the actual fracture stresses for silicon nitride samples containing cracks with estimated radii ranging from 51 μm to 274 μm show excellent agreement, with less than 16% error. A qualitative study in the high frequency regime of the reflected echoes from surface cracks in silicon nitride turbine blades has also been made.

INTRODUCTION

Our aim in this work has been to establish qualitative and quantitative procedures for identifying cracks in the surface of structural ceramics. The basic technique we have been employing is to excite a Rayleigh wave on the surface of the ceramic and observe reflections of the acoustic surface wave from the crack. Accordingly, we have developed techniques for exciting acoustic waves in the low frequency range below 10 MHz and another range of experimental methods for exciting acoustic waves at frequencies above 50 MHz. As we are interested in cracks ranging in size from 25 μm upwards and the wavelengths at 10 MHz and 50 MHz are typically 600 μm and 120 μm , respectively, both these low and high frequency techniques are important.

Currently, most of the quantitative studies have been carried out in the low frequency regime because here we have been able to develop in detail a theory to associate our experimental measurements with not only the crack size but also with the fracture stress of a sample with a crack present. Such an association can be made because the stress field due to a Rayleigh wave has a component of longitudinal stress parallel to the surface for penetration depths much less than an acoustic wavelength and consequently, the fields in the neighborhood of a crack are distorted in the same way as they would be for an applied static stress (i.e., a bending stress) where the acoustic wavelength is much larger than a typical crack dimension. It is thus possible to establish a relation between the reflection coefficient of the Rayleigh wave (which we can obtain via acoustic measurements) and the stress intensity factor. Knowing the stress intensity factor then allows us to predict the fracture stress of a sample when the crack is present.

THEORETICAL DEVELOPMENTS

The theory we describe here has its restrictions in that it requires the depth to which the crack extends below the sample surface to be less than a tenth of the acoustic wavelength. This, however, implies that the signal reflected back from the crack is very weak. The simple theory we will begin with is based on the idea that the fields in the neighborhood of a half-penny shaped surface crack can be calculated by assuming that they are distorted in approximately the same way as the

fields in the neighborhood of a circular volume crack. This, in fact, is not an entirely adequate assumption because the stresses are changed near the surface for a semi-circular crack, and the stress intensity factor tends to be higher near the surface of a material than in its interior. Furthermore, the Rayleigh wave fields are not uniform across the plane of the crack, but rather, fall off with depth into the sample. We will take these modifications into account in a later part of our theory. Lastly, we will discuss briefly the effect on the results should the crack be semi-elliptical rather than semi-circular.

Kino and Auld have worked out a general theory of scattering from flaws.^{1,2} The situation considered is illustrated in Fig. 1. Transducer 1 transmits a signal with amplitude A_1 . This signal is reflected off the flaw and the reflected wave is received by transducer 2. The reflection coefficient S_{21} is defined as the amplitude ratio of the reflected signal A_2 to the incident signal A_1 at the terminals of the transducers and is given by the relation

$$S_{21} = \frac{A_2}{A_1} = \frac{i}{4P_1} \int_S \frac{u_1^{(2)} A_1^{(1)}}{u_1^{(1)} u_1^{(2)}} u_1^{(2)} ds \quad (1)$$

Here, P_1 is the input power to the transmitting transducer, $u_1^{(2)}$ is the Rayleigh wave displacement field when the receiving transducer is used as the transmitter, and $u_1^{(1)}$ is the applied stress in the vicinity of the flaw before the flaw has been introduced. The integral here is taken over the entire surface of the flaw, S . When the same transducer is used to both transmit and receive, we write $S_{21} = S_{11}$.

We will begin by considering the case of a Rayleigh wave normally incident on a half-penny shaped crack located in the $x-y$ plane (Fig. 2). The reflection coefficient then may be written as

$$S_{11} = \frac{i}{4P_1} \int_S \Delta u_1^{(1)} \frac{A_1}{u_1^{(1)}} ds \quad (2)$$

where now $\Delta u_1^{(1)}$ is the discontinuity in the Rayleigh wave displacement field across the crack, and

σ_{zz}^A is the applied stress. The integral is taken over just the semi-circular area, S . To evaluate the displacement discontinuity, Δu_z , we initially use the theory for a penny-shaped crack of radius a .³ This gives the result

$$\Delta u_z = k_I \sigma_{zz}^A \frac{4}{(\pi a)^{1/2}} \frac{1 - \nu^2}{E} (a^2 - r^2)^{1/2} \quad (3)$$

where $k_I = 2(a/\pi)^{1/2}$ is the normalized mode I stress intensity factor, E is Young's modulus, ν is Poisson's ratio, and r is the distance from the center of the crack. Using Eq. (3) in Eq. (2) and approximating the stress σ_{zz}^A by its value at the sample surface, namely $\sigma_{zz}^A|_{\text{surf}}$, we find for the reflection coefficient

$$S_{11} = \frac{2}{3} j\omega \frac{(\sigma_{zz}^A|_{\text{surf}})^2}{P_1} a^3 \frac{(1 - \nu^2)}{E} \quad (4)$$

Note the cubic dependence of the reflection coefficient on the crack radius a . Evaluating $\sigma_{zz}^A|_{\text{surf}}$ in terms of the input power P_1 gives then for the modulus of S_{11}

$$|S_{11}| = \frac{16\pi^2}{3} \frac{f_z n_a^3}{\lambda^2 w (1 - \nu)} \equiv R \quad (5)$$

In Eq. (5), f_z is a material's parameter tabulated by Auld,⁴ n is a loss term, λ is the acoustic wavelength, and w is the width of the incident beam. Typically, for a ceramic with a Poisson's ratio $\nu \approx 0.2$, $f_z \approx 0.4$.

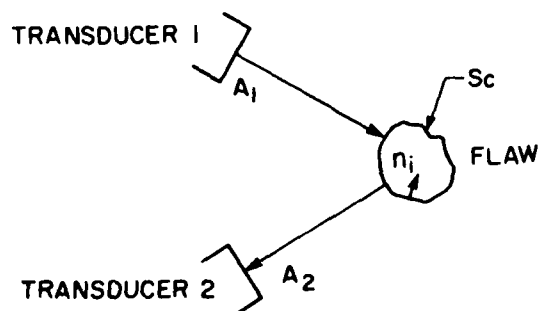


Fig. 1. A schematic of the geometry considered in the derivation of the reflection coefficient, S_{21} , for a flaw.

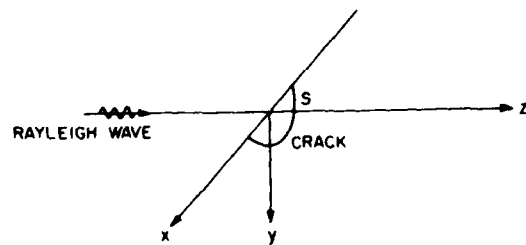


Fig. 2. Scattering geometry for Rayleigh wave normally incident on a half-penny shaped crack.

For a crack located on the central axis of the beam, the loss term n can be written as

$$n = n_T n_D \quad (6)$$

where n_T is the transducer power loss in converting the input electrical signal to an acoustic surface wave and n_D is a diffraction loss term. For a crack a distance z from the transducer located in the far field of the transducer, i.e., for $z \gg w^2/\lambda$, n_D can be expressed as

$$n_D = w^2/\lambda z \quad (7)$$

More generally, an effective value for n_D can be calculated by averaging the stress field over the width of the transducer. The result is shown in Fig. 3. We observe that for $z \gg w^2/\lambda$ (far field region), the formula given for n_D in Eq. (7) is indeed accurate.

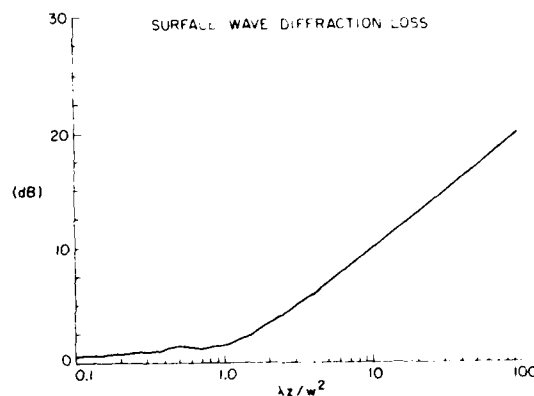


Fig. 3. Surface wave diffraction loss as a function of the normalized distance from the transducer, $\lambda z/w^2$.

We next modify the theory to take into account scattering from the crack at an angle. We consider the case where the transmitting transducer 1 produces an acoustic wave incident on the crack at an angle θ with respect to the crack normal and the receiving transducer 2 receives the reflected wave at an angle $-\theta$ (Fig. 4A). A simplification of this situation occurs when a single transducer is used to both transmit and receive along a line at an angle θ with respect to the crack normal (Fig. 4B). This second configuration is of interest in considering backscatter from a crack at an arbitrary angle. One problem, however, that we have encountered experimentally when using the same transducer to both transmit and receive is that spurious signals are produced by the transducer which tend to interfere with the reflected signals received. This is especially troublesome when the reflected signals are very weak. In such situations, the first configuration (Fig. 4A) becomes useful as the receiving transducer then receives only the acoustic wave reflected off the crack and none of the spurious signals produced by the transmitting transducer.

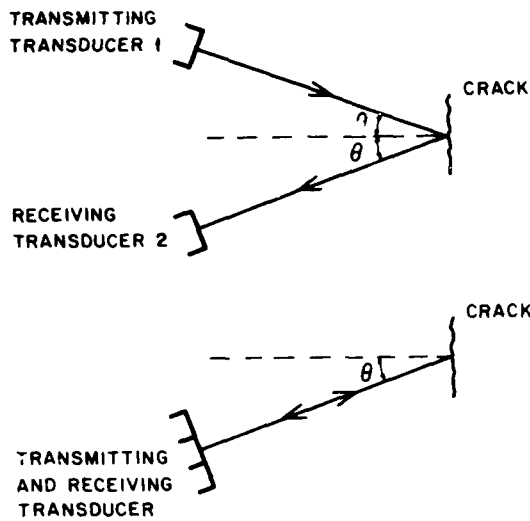


Fig. 4. (A) Two-transducer configuration and (B) single transducer configuration for scattering from the crack at an angle.

For each of these configurations, we find that the reflection coefficients are given by

$$|S_{21}| = R|G(\theta)| \quad \text{two-transducer configuration} \quad (8A)$$

$$|S_{11}| = RF(\theta) \quad \text{single transmitting and receiving transducer} \quad (8B)$$

where

$$\frac{|G(\theta)|}{|F(\theta)|} = \frac{(\cos^2 \theta - \nu \sin^2 \theta)^2}{2(2 - \nu)} = \frac{(1 + \nu)^2}{2(2 - \nu)} \sin^2 2\theta \quad (9)$$

and R is defined in Eq. (5). Examples of the angular variation of $F(\theta)$ and $|G(\theta)|$ for the case of silicon nitride are shown in Figs. 5 and 6. Note that neither $F(\theta)$ nor $|G(\theta)|$ vanish at $\theta = 90^\circ$.

We now discuss how imaging forces at the surface, which affect the value of the stress intensity factor near the surface, and the variation with depth of the Rayleigh wave stress fields can be taken into account for the case of scattering at normal incidence from a half-penny shaped crack. Again, the reflection coefficient is given by Eq. 5 (2). It has been shown by Budiansky and O'Connell that the surface integral given in Eq. (2) is related to the crack formation energy, E , by

$$E = (1/2) \int_S \Delta u_z \sigma_{zz}^A ds \quad (10)$$

Alternatively, E may be written as

$$E = \frac{1 - \nu^2}{3E} \int_C a K_I^2(\tilde{\theta}) d\ell \quad (11)$$

where C is the crack circumference shown in Fig. 7. Due to the surface imaging forces, the stress intensity factor is a function of the angle $\tilde{\theta}$, taken to be the angle from the normal to the sample surface passing through the crack center. To evaluate the angular dependence of K_I , we make use of a theory by Smith, Emery, and Kobayashi.⁶ Smith, et al. considered the case of a half-penny shaped crack in a plate of thickness $2c$, to which a bending stress was applied. The applied stress then has a linear form given by

$$\sigma_{zz}^A(y) = A(1 - y/c) \quad (12)$$

where A is a constant, and y is the distance from the surface of the substrate. The stress intensity factor is consequently given by

$$K_I(\tilde{\theta}) = 2\sqrt{a/\pi} A [\psi_0(\tilde{\theta}) - (a/c)\psi_1(\tilde{\theta})] \quad (13)$$

where $\psi_0(\tilde{\theta})$ and $\psi_1(\tilde{\theta})$ were numerically evaluated by Smith et al. and are shown in Fig. 8. Here, the function $\psi_0(\tilde{\theta})$ determines the increase in the stress intensity factor near the sample surface and the quantity $-(a/c)\psi_1(\tilde{\theta})$ governs the fall-off in the Rayleigh wave stress field with depth. To evaluate the effective values for the constants A and c for our case where the stress, is due to the Rayleigh wave and not a bending stress we determine the exact variation of the stress field with depth y , following the work of Viktorov,⁷ and make a linear approximation. The result for silicon nitride is shown in Fig. 9. Note that the linear approximation follows the exact curve very well for $y/\lambda < 0.1$. With this approximation, we can find A and c in terms of the surface value of the stress σ_{zz}^A and the slope of the linear approximation. Evaluating $K_I(\tilde{\theta})$, substituting the results into Eq. (11), and using Eqs. (2) and (10) then gives for the reflection coefficient

$$|S_{11}| = RH\left(\frac{2\pi a}{\lambda}\right) \quad (14)$$

where $H(2\pi a/\lambda)$ must be numerically evaluated and is plotted in Fig. 10 for the case of silicon nitride. Observe that there is a considerable reduction in the scattering amplitude as the value of the parameter $2\pi a/\lambda$ increases. In view of the linear approximation we have made, we normally would expect this theory to be accurate for values of $2\pi a/\lambda$ less than unity; however, we have found that the theory does surprisingly well even for much larger values of this parameter.

The theory by Smith et al. has also been used by us in collaboration with Resch⁸ to predict the maximum measured stress intensity factor for semi-elliptical cracks, using a formulation very similar to that already given. In the interests of brevity, we will not go into the details of these results here. Suffice it to say that the measured stress intensity factor varies by a factor of 1.22 to .8 as the ratio of the minor to major axes varies from 1 to 0.1. Thus, the variation is somewhat larger than that predicted by Budiansky and Rice.⁹ On the other hand, when considering surface cracks in brittle materials such as ceramics or glasses, the variation of the ratio of minor to major axes typically ranges only from 1.0 to 0.5, with the corresponding variation in the stress intensity factor going from 1.22 to 1.05.

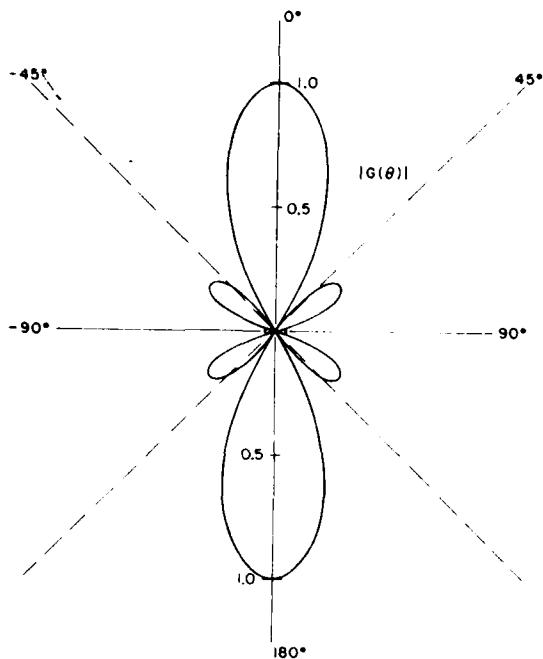


Fig. 5. Angular variation of $|G(\theta)|$, which determines the angular dependence of the reflection coefficient for the two-transducer configuration, for the case of silicon nitride.

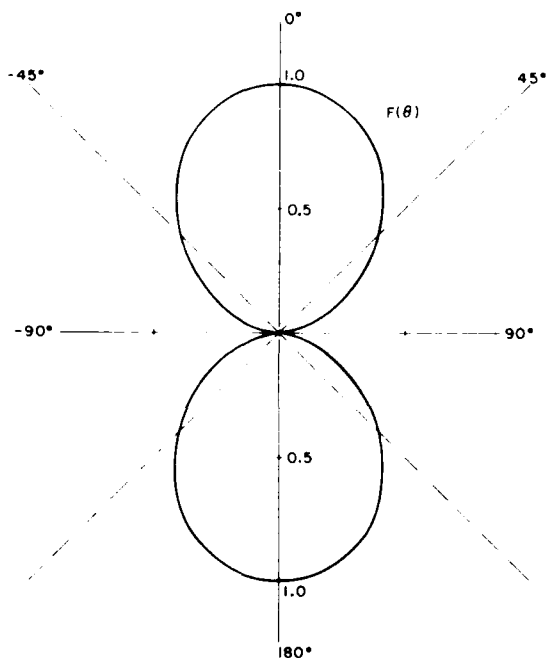


Fig. 6. Angular variation of $F(\theta)$, which determines the angular dependence of the reflection coefficient for the single transducer configuration, for the case of silicon nitride.

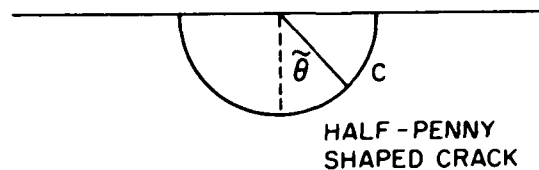


Fig. 7. Schematic of half-penny shaped crack geometry.

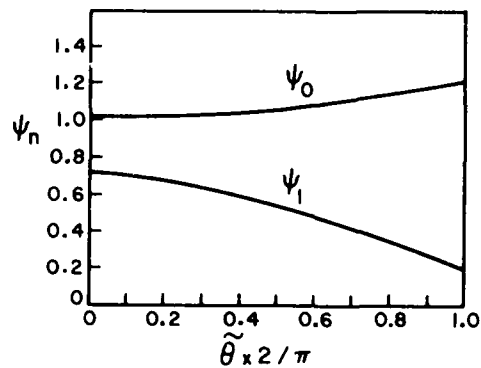


Fig. 8. Functions $\psi_0(\tilde{\theta})$ and $\psi_1(\tilde{\theta})$ vs. $\tilde{\theta}$ numerically evaluated by Smith, Emery, and Kobayashi.⁶

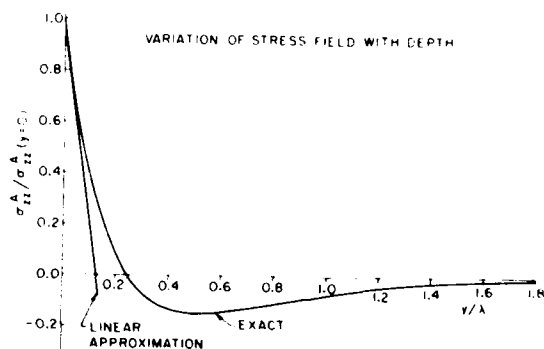


Fig. 9. Variation of stress field with depth in both exact form and in linear approximation for the case of silicon nitride.

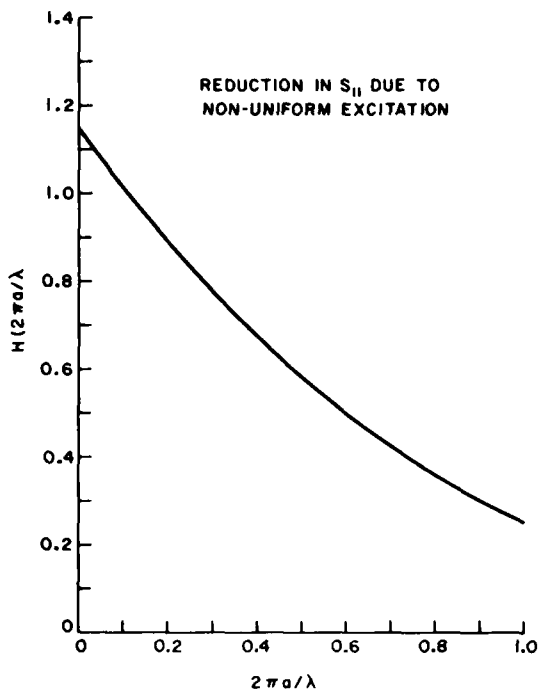


Fig. 10. Reduction in $|S_{11}|$ due to surface imaging forces and depth variation in the Rayleigh wave stress field for the case of silicon nitride.

QUANTITATIVE MEASUREMENTS ON FLAT SURFACES

We discuss here the quantitative measurements we have made in the low frequency regime. The ceramic selected for this study was a commercial hot-pressed silicon nitride (NC-132). Plate specimens ($7.6 \times 2.6 \times .64$ cm) were machined from an as-pressed billet and the surfaces optically polished. Cracks were introduced into each sample using a Knoop hardness indenter by Evans at Berkeley and Resch at Stanford.

In our experiments, we used a wedge transducer to excite a Rayleigh wave on the surfaces of the samples as shown in Fig. 11. We carried out a series of measurements on different sizes of cracks using both the technique of direct backscatter to a single transducer acting as both the transmitter and receiver as well as the technique employing two different transducers, one to transmit and the other to receive. Our measurements were made at a frequency of about 9 MHz, which corresponds to an acoustic wavelength of about $650 \mu\text{m}$. The results are shown in Table I. Note that the parameter $2\pi a/\lambda$ is well within the range we expect our theory to be accurate for the smaller 5 kg and 10 kg cracks but is well out of this range for the larger 20 kg cracks. From our estimates for the crack radii, we were able to predict a value for the fracture stress $\sigma_F^{\text{Acoustic}}$ by using the relation

$$\sigma_F^{\text{Acoustic}} = \frac{K_{IC}}{k_I|_{\text{surf}}} \quad (15)$$

where

$$k_I|_{\text{surf}} = 1.22 k_I|_{\text{bulk}} = 1.22 [2(a/\pi)^{1/2}] \quad (16)$$

and $K_{IC} = 3.55 \text{ MPa}\sqrt{\text{m}}$.¹⁰ We then broke the samples and measured the actual fracture stress. The deviations between the predicted values and the actual values of the fracture stress are shown in the last column of Table I. In all cases, the error in our measurements is less than 16%, with the measurements on the smaller cracks having the best accuracy, as anticipated.

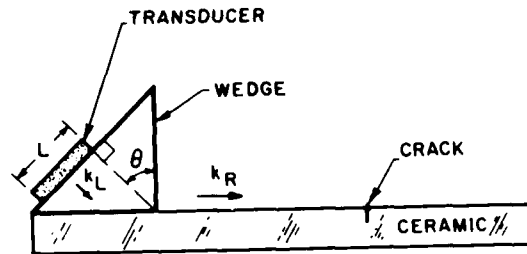


Fig. 11. Schematic of surface crack and experimental set up.

TABLE I

Sample	Acoustic a (μm)	$2\pi a/\lambda$	Acoustic σ_F (MPa)	Actual σ_F (MPa)	%
5 kg: 1	56	.5391	350	338.45	3.3
2	51	.4960	367	365	.54
10 kg: 1	67	.6493	320	298.5	6.72
2	66	.6396	322.7	275.4	14.6
20 kg: 1	274	2.650	158.4	159.22	.52
2	262	2.539	159.7	179.13	12.17
3	255	2.470	164.2	189	15.1

We also made a preliminary study to determine whether the cracks in our samples might be partially closed. To do this, we applied a calibrated bending stress to the sample while simultaneously measuring the reflected signal from the crack. We found that our estimate of the crack radius tended to increase by about 10% from its unstressed value under the application of a bending stress. We thus conclude that the cracks in our samples were indeed partially closed when the samples were in an unstressed state.

MEASUREMENTS ON TURBINE BLADE ROOTS

The silicon nitride turbine blades used in this study were manufactured by Airesearch Manufacturing Co. and provided to us by H. G. Graham from AFML. A schematic of a turbine blade and the experimental set-up is shown in Fig. 12. Our aim in this study was to detect and locate cracks in the neck region of the turbine blades. In Fig. 12, the LiNbO_3 transducer was used as both the transmitter and the receiver. Experiments were carried out at both

64 MHz and 100 MHz. In our initial study, all six turbine blades supplied to us gave indications that either cracks or machining marks were present in the neck region. In Fig. 13A, we show a picture taken with an optical microscope of the neck region. Here, the presence of machining marks with a periodicity of about $20\text{ }\mu\text{m}$ is clearly indicated. As we expect the depth b of the machining marks to be no greater than about $25\text{ }\mu\text{m}$, we can determine the reflection coefficient from these marks by assuming $\lambda \gg b$ and using a long wavelength theory. Making assumptions regarding the stress fields similar to those initially made in our simple theory for the half-penny shaped crack and approximating the geometry of a machining mark by a long slit crack, we find that

$$|S_{11}| = C(v) \eta \frac{b^2}{\lambda^2} \quad (17)$$

Here, η is again a loss term and $C(v) \approx 8.694$ for silicon nitride.

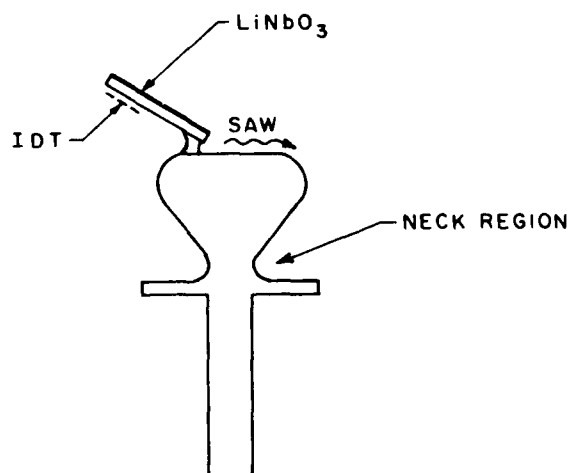


Fig. 12. Schematic of turbine blade and experimental set-up.

To determine whether there were cracks present under the machining marks, we had the neck region of the blade polished and then re-did the acoustic measurements. A picture of the neck region after polishing is shown in Fig. 13B. The subsequent acoustic study did indeed indicate the presence of cracks in the blade neck regions. Examples of the reflected echoes received in the presence and absence of cracks are shown in Figs. 14A and 14B, respectively.

CONCLUDING REMARKS

In the low frequency regime, we have found that we can detect and size cracks on flat surfaces down to crack radii of about $50\text{ }\mu\text{m}$. From our estimates of the crack dimensions, we are then able to predict the fracture stress of a sample with a crack in it to well within 16% of the actual value.

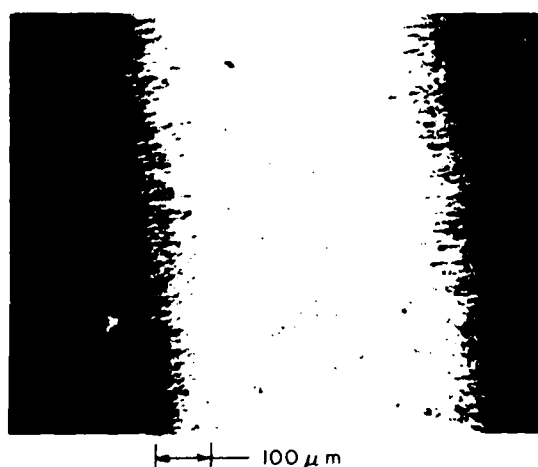
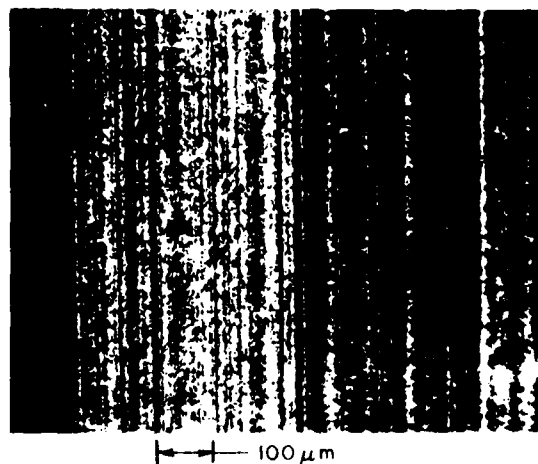


Fig. 13. Optical microscope photographs of turbine blade neck (A) before and (B) after polishing.

Cracks with radii smaller than $50\text{ }\mu\text{m}$ we find can easily be detected with higher frequency transducers. In regard to our measurements on turbine blades in this frequency regime, we are not yet able to make a good quantitative estimate of the crack size due to the presence of machining marks and corners along the propagation path as well as the complications of propagation along a curvilinear surface. To aid in quantifying our measurements here, we thus propose to introduce in the neck region of the blades half-penny shaped cracks of known size using a Knoop hardness indenter. The reflected signals from these known cracks can then be used to calibrate the reflected signals from the cracks originally present in the neck region. In our future work, we aim to apply this calibration technique as well as to extend our theory into the high frequency regime.

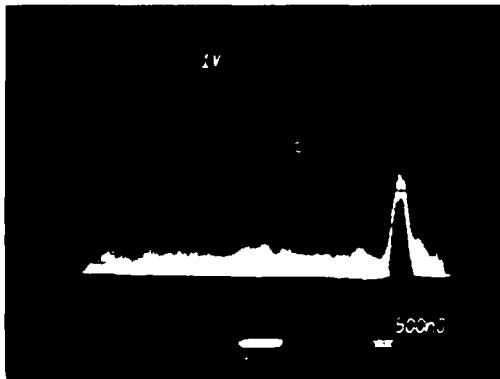
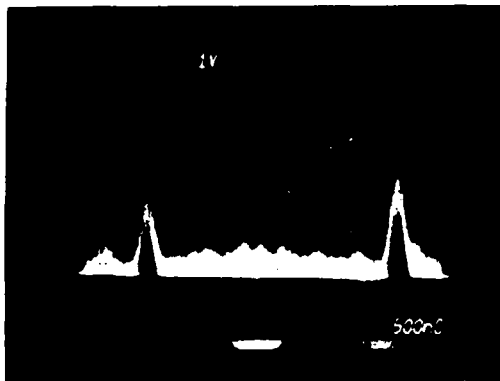


Fig. 14. Reflected echoes observed in measurements of turbine blades (A) in the presence and (B) in the absence of a crack.

ACKNOWLEDGMENT

This work was supported by the Office of Naval Research under Contract No. N00014-78-C-0283.

REFERENCES

1. G. S. Kino, "The Application of Reciprocity Theory to Scattering of Acoustic Waves by Flaws," *J. Appl. Phys.*, vol. 49, no. 6, June 1978, pp. 3190-3199.
2. B. A. Auld, "General Electromechanical Reciprocity Relations Applied to the Calculation of Elastic Wave Scattering Coefficients," *Wave Motion*, vol. 1, no. 1, January 1979, pp. 3-10.
3. I. N. Sneddon, *Proc. Cambridge Philos. Soc.*, vol. 61, 1965, p. 609.
4. B. A. Auld, *Acoustic Fields and Waves in Solids*, vol. II, Wiley-Interscience, New York, 1973.
5. B. Budiansky and R. J. O'Connell, "Elastic Moduli of a Cracked Solid," *Int. J. Solid Structures*, vol. 12, pp. 81-97, Pergamon Press, 1976.

6. F. W. Smith, A. F. Emery, and A. S. Kobayashi, "Stress Intensity Factors for Semicircular Cracks: Part 2, Semi-Infinite Solid," *J. Appl. Mech.*, vol. 34, no. 4, pp. 953-959, December 1967.
7. I. A. Viktorov, *Rayleigh and Lamb Waves, Physical Theory and Applications*, Chap. I, Plenum Press, New York, 1967.
8. M. T. Resch, B. T. Khuri-Yakub, G. S. Kino, and J. C. Shyne, "The Acoustic Measurement of Stress Intensity Factors," *Appl. Phys. Lett.*, vol. 34, no. 3, pp. 182-184, 1 February 1979.
9. B. Budiansky and J. R. Rice, "On the Estimation of a Crack Fracture Parameter by Long-Wavelength Scattering," *J. Appl. Mech.*, vol. 45, no. 2, pp. 453-454, June 1978.
10. J. J. Petrovic, L. A. Jacobson, P. K. Talty, and A. K. Vasudevan, "Controlled Surface Flaws in Hot-Pressed Si_3N_4 ," *J. Amer. Ceramic Soc.*, vol. 58, pp. 113-116, March/April 1975.

DIFFERENTIATION OF VARIOUS FLAW TYPES IN CERAMICS USING THE SCANNING LASER ACOUSTIC MICROSCOPE

D. E. Yuhas, T. E. McGraw and L. W. Kessler
Sonoscan, Inc.
Bensenville, Illinois 60106

ABSTRACT

High frequency acoustic imaging represents a powerful technique for the nondestructive evaluation of optically opaque materials. In this report the Scanning Laser Acoustic Microscope (SLAM) is used to detect and characterize flaws in ceramics. SLAM micrographs showing typical examples of cracks, laminar flaws, porosity and solid inclusions are presented. The various flaw types are easily differentiated on the basis of their characteristic acoustic signatures. The importance of an imaging approach to the nondestructive evaluation of ceramics is demonstrated.

INTRODUCTION

This report is the first in a series of two papers describing high frequency (100 MHz) acoustic imaging of ceramics. The current investigation deals primarily with the recognition and interpretation of a variety of different flaw types. In this and other studies the Scanning Laser Acoustic Microscope has been used to investigate cracks, delaminations, porosity, machine damaged surfaces and solid inclusions¹⁻⁵. Examples of these are presented to provide a general overview of acoustic micrographs obtained with the SLAM and to gain an appreciation for the unique features of the various flaws. In a companion paper, attention is focused on implanted solid inclusions in silicon nitride discs⁶. The differentiation of solid inclusions from cracks, delaminations and porosity is based on comparison of the characteristics of flaws found in these discs with those observed in other samples where the exact nature of the flaw type has been confirmed by destructive analysis. A SLAM catalogue of flaws is presented in this paper in order to provide the necessary background for the results presented on solid inclusions (companion paper).

EXPERIMENTAL APPARATUS AND TECHNIQUE

Figure 1 is a photograph of the SONOMICROSCOPE 100⁷. The principles of operation have been described in the literature⁸. Briefly, the instrument produces full grey scale acoustic images at frequencies from 30-500 MHz. The results appearing in this paper are all at 100 MHz where the field of view is 2x3 mm, resolution is about 1/2 wavelength, or 30 microns in silicon nitride (shearwaves), and images are produced in real time. The transmitting transducer is a piezoelectric element. A focused laser scans the insulated zone and acts as the receiving transducer. By synchronizing the laser scan with a television monitor, real-time acoustic images are obtained.

As a by-product of the technique, an optical image of the scanned surface is produced on a separate TV monitor. This image is quite useful in documenting the location of flaws.

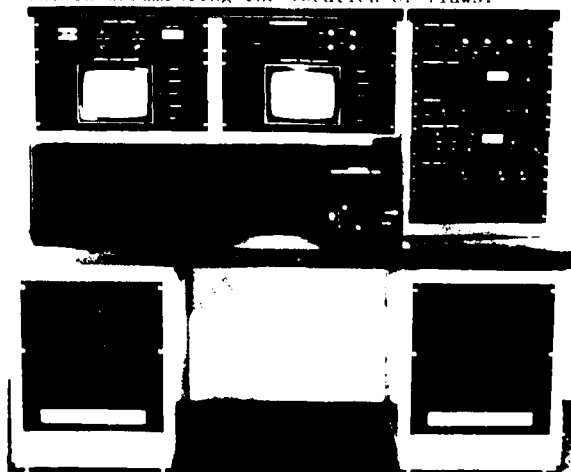


Figure 1 - Scanning Laser Acoustic Microscope (SLAM) used in this investigation⁽⁷⁾.

SLAM DATA

Two types of acoustic micrographs, amplitude images and interferograms are commonly used. They are easy to distinguish and both are useful for defect characterization. Figure 2 shows an amplitude image (top) and interferogram (bottom) obtained in the same silicon nitride test sample. The amplitude image shows the relative transmission level over the field of view. In the amplitude mode, bright areas correspond to zones in the sample with good acoustic transmission, whereas the darker areas are attenuating. The interferogram has a characteristic set of vertical fringes which are produced by electrical

Figure 1 shows a high-magnification micrograph of a surface with a periodic, wavy pattern. The pattern consists of alternating dark and light vertical bands. A scale bar at the bottom center indicates a length of 1mm.

1 2 3

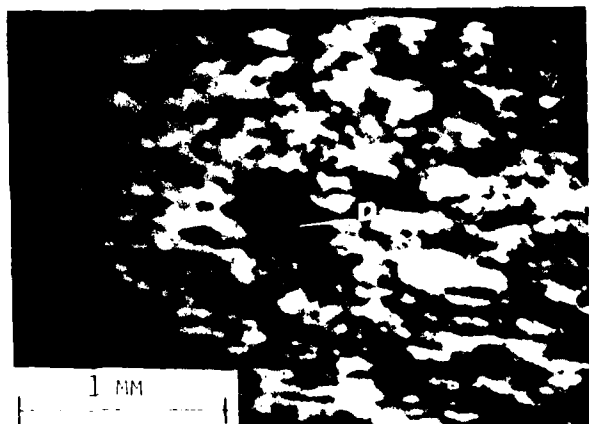


Fig. 4 - Acoustic amplitude micrograph of laminar flaw found in a ceramic turbine airfoil.

Figure 5 is an optical reflection micrograph confirming the acoustic results presented in Figure 4. The most apparent feature is a 100 micron diameter pore located near the center of the section (see arrow). Contiguous with the pore is a laminar crack-like flaw running horizontal in the micrograph. Both the crack and pore lead to high sound attenuation thus producing a dark region in the acoustic micrograph (see Fig. 4). The length of pore and crack is approximately 600 microns which is comparable dimensionally with the dark zone imaged acoustically. Remember that the acoustic micrograph provides a two-dimensional projection image of the defect. Several serial sections would be required to map the entire flaw optically.



Fig. 5 - Optical reflection micrograph on turbine airfoil section confirming the flaw found in Figure 4.

Crack Detection (Acoustic Shadow) - The fracture characteristics revealed by acoustic microscopy depend on the crack orientation relative to the direction of sonic propagation, the size of the crack opening, the roughness of the fracture interface, and the extension of the fracture beneath the surface. The acoustic transmission level across the fracture interface may vary from almost total attenuation (evidenced by a shadow, as shown schematically in Fig. 6) to only slight variations in acoustic contrast. Similarly, the perturbation of the interferogram fringe spacing may range from complete disruption to an almost imperceptible fringe shift.

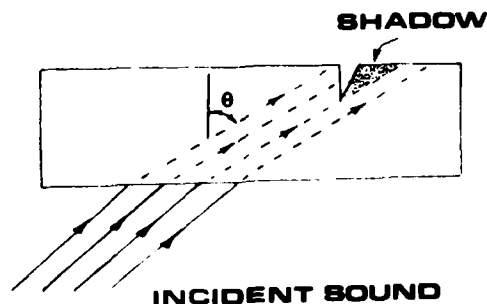


Fig. 6 - Schematic illustrating the effect of crack shadowing observed in the SIAM.

Figure 7 shows acoustic micrographs of a fracture opening to the surface of an alumina sample. The micrographs are oriented such that the sound field propagates out of the plane of the paper at an angle of 45° from left to right across the field of view. Sound propagating through the sample is attenuated at the fracture interface resulting in a shadow to the right of the fracture. The primary feature that distinguishes a surface opening crack is the abrupt and sharply defined onset of the shadow region. This is seen as a sharp boundary separating the light and dark portions of the micrographs in Figure 7. The interferogram fringes are almost obliterated in this area, indicating almost total sound attenuation. By measuring the length of the shadow and using the known propagation angle, measurement of crack extension beneath the surface is made. In Figure 7 the propagation angle was 45° , the shadow is approximately 1 mm in length, thus the crack extends 1 millimeter below the surface.

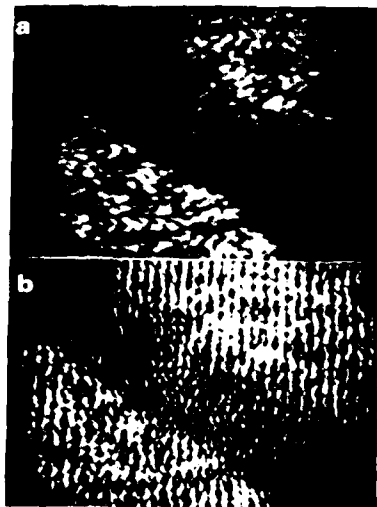


Fig. 7 - a) amplitude micrograph
b) acoustic interferogram showing
a crack in an alumina substrate.

Micro Cracks - Mode Conversion - For large cracks which extend several wavelengths below the surface (greater than 200 microns) the primary micrograph feature is the shadow zone. Smaller cracks are rendered visible due to easily detected mode conversion at the flaw site.

Figure 8 shows a micrograph obtained in the vicinity of a Vickers indent in a hot-pressed silicon nitride test bar¹. The presence of the mode-converted surface-skimming bulk wave leads to the characteristic cone-shaped ripple pattern observed in the vicinity of the flaw. Explanation of the detection phenomenon and the image characteristics have been reported elsewhere².

A nice feature of the intrinsic mode conversion at the site of small cracks is that it is easy to detect flaws at low magnification. Waves generated at the flaw site propagate several millimeters beyond the flaw site, thus leading to enhanced detection sensitivity and remote sensing capability.

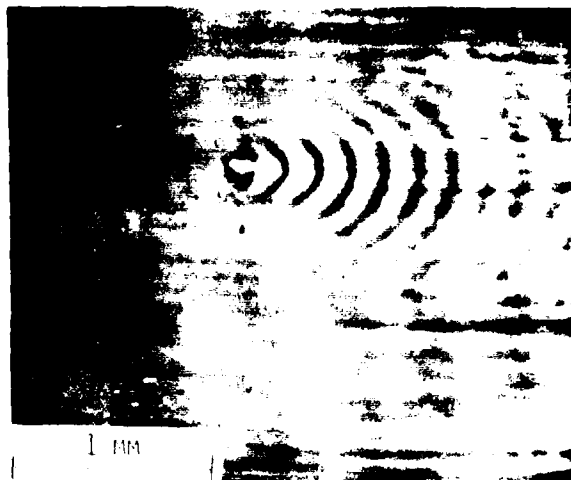


Fig. 8 - SLAM detection of mode conversion
at the site of a flaw produced by a Vicker's
indenter. (5Kg load)

Characteristics of Inclusions - Figure 9 shows a typical silicon nitride sample with an implanted solid inclusion. The primary features which distinguish this flaw type from other defects are the - 1) bright center with acoustic transmission greater than or equal to the background structure, 2) ring pattern due to diffraction of sound by the inclusion, 3) and the well-defined boundary of the flaw. These image characteristics seem to be prevalent for solid inclusions observed so far and they are quite different type from porosity variations in laminar flaws. The micrograph was obtained on a sample containing an implanted 400 micron diameter silicon inclusions. The image size, the diameter of the first ring, is 160 microns and the flaw is 900 microns below the surface. To obtain the relationship between SLAM image size and the actual flaw size, it may be necessary to account for the effects of diffraction and beam spreading. This point is investigated in greater detail in the companion paper⁶. The flaw is presented to illustrate the unique morphology of solid inclusions.

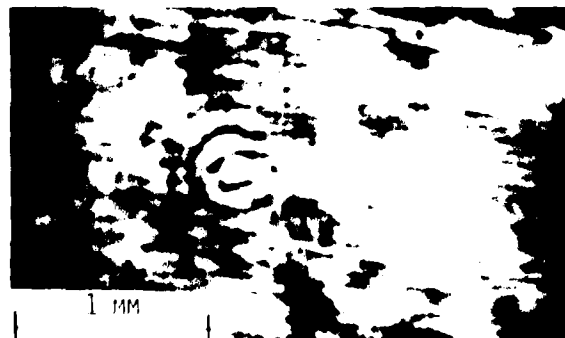


Fig. 9 - Acoustic amplitude micrograph showing
a flaw with image characteristic indicative
of a solid inclusion.

SUMMARY

Examination of a variety of different flaws in ceramics has led to the development of a series of unique image characteristics. These acoustic signatures can be used to differentiate various flaw types. Many of the interpretations rely on defect morphology. Thus, underscoring the utility of the imaging approach. This is particularly important, for example, in detecting solid inclusions in porous ceramics. Acoustic images also provide a handle on the determination of flaw sizes. The extension of cracks below the surface are directly obtainable from micrographs. Estimates of the size of solid inclusions are also obtainable. However, in this case, it may be necessary to correct recorded image size for beam spreading and diffraction effects.

REFERENCES

1. D. S. Kupperman, C. Sciammarella, N. P. Lapinski, A. Sather, D. Yuhas, L. Kessler, and N. F. Fiore, "Preliminary Evaluation of Several NDE Techniques for Silicon Nitride Gas-Turbine Rotors," Argonne National Laboratory Report ANL-77-89, January 1978.
2. D. F. Yuhas, Characterization of Surface Flaws by Means of Acoustic Microscopy, First International Symposium on Ultrasonic Materials Characterization, June 7-9, 1978, National Bureau of Standards, Gaithersburg, MD., (In Press) ed by: H. Berger (1979).
3. D. S. Kupperman, I. Pabis, D. Yuhas, and T. McGraw, Acoustic Microscopy for Structural Ceramics, submitted Journal of American Ceramic Society, 1979.
4. D. F. Yuhas and L. W. Kessler, Scanning Laser Acoustic Microscope Applied to Failure Analysis; Proc. ATFA - 78 IEEE Inc., New York, N. Y. Catalog No. 78CH1407-6 REG6., pp. 25-29 (1978).
5. Acoustic Microscopy, SEM and Optical Microscopy: Correlative Investigations in Ceramics, Scanning Electron Microscopy 1979, 1, SEM Inc., AMF O'Hare, IL 60666, pp. 103-110.
6. D. F. Yuhas, T. E. McGraw, and L. W. Kessler, Scanning Laser Acoustic Microscope Visualization of Solid Inclusions in Silicon Nitride, Proc. ARPA/AFML Conf. on Quantitative NDE., LaJolla, CA, 1979.
7. Commercially available under trade name SONOMICROSCOPE™ 100, Sonoscan, Inc., Bensenville, Illinois 60106.
8. L. W. Kessler and D. F. Yuhas, Acoustic Microscopy 1979, Proc. IEEE, 67, (4) pp. 526-536 (1979).
9. S. A. Goss and W. D. O'Brien, Direct Ultrasonic Velocity Measurements of Mammalian Collagen Threads.; J. Acoust. Soc. Amer. 65(2) pp. 507-511 (1979)
10. G. S. Kino, Nondestructive Evaluation, Science, Vol. 206, pp 173-180, Oct. 1979.
11. Micrograph Courtesy of J.J. Schuldies, Airesearch Mfg. Co., Phoenix, AR.

SCANNING LASER ACOUSTIC MICROSCOPE VISUALIZATION OF SOLID INCLUSIONS IN SILICON NITRIDE

D. E. Yuhas, T. E. McGraw and L. W. Kessler
Sonoscan, Inc.
Bensenville, Illinois 60010

ABSTRACT

The Scanning Laser Acoustic Microscope (SLAM) operating at a frequency of 100 MHz is used to characterize solid inclusions in silicon nitride. Ten, seven millimeter thick discs, with 100 and 400 micron implanted inclusions are analyzed. We find that the images of a solid inclusion are characterized by a bright high transmission central zone, a well defined dark boundary and a characteristic diffraction ring pattern. These image features differentiate solid inclusions from pores and voids which may also be encountered in the samples. The images of the implanted flaws were generally found to be larger than anticipated. This can be understood in terms of the divergence of the sound due to diffraction and due to lens action of the curved boundary of the flaw. Our initial observations suggest that accurate estimates of defect size may be obtainable from a more complete analysis of SLAM micrographs.

INTRODUCTION

The acoustic signatures of a variety of flaw types, e.g. cracks, delaminations, solid inclusions, etc. were presented in a companion paper¹. This paper concentrates on characterizing solid inclusions, specifically, silicon, carbon and iron inclusions within hot pressed silicon nitride.

The approach adopted is empirical. Image features of flaws found in these discs are compared with those found in other samples where the flaw type was confirmed by destructive analysis. The image features derived in this manner were subsequently found to compare well with those predicted based on elementary scattering theory².

THE TECHNIQUE AND SAMPLES

All samples were analyzed using a commercially available scanning laser acoustic microscope operating at a frequency of 100 MHz. Introductory material describing acoustic micrographs and the SLAM are presented elsewhere¹.

A total of 10 samples were investigated using the Scanning Laser Acoustic Microscope. Each sample was in the form of a disc approximately 25 mm in diameter and ranging from 6 to 7 mm thick. The sample identification, the bulk density and size and type of implanted inclusion are listed in Table I. Although the intended size and type of each inclusion was known prior to the investigation, its actual size and location were not. This led to some confusion since in many samples, several inclusions were found; not all of them were intended. Furthermore, several samples contained inhomogeneous porosity distributions which may have been inadvertently introduced in the "bedline" process.

TABLE I

Sample ID #	Density g./cc	Presumed Flaw type	Presumed Flaw type (Diameter-Microns)
65	3.01	Iron	100
88	3.03	Iron	100
29	3.21	Iron	100
90	-	Iron	100
32	2.94	Silicon	100
31	2.94	Silicon	100
49	-	Silicon	100
63	3.10	Carbon	100
5	3.04	Carbon	100
73	3.21	Carbon	100

NOTE: Fully dense Si₃N₄ has a density of 3.21 g./cc³.

MATERIAL CHARACTERIZATION

From Table I, we see that the density of the sample discs varies over a percent range from a high density of 3.21 g./cc³ to a low of 2.94 g./cc³. The density of the sample correlates with the observed ultrasonic attenuation and the structural features in the micrographs. Figure 1 shows three acoustic micrographs obtained on samples with measured densities of 3.11, 3.10, and 2.94 g./cc³ respectively. The variation in the micrograph characteristics with density is quite dramatic and can be readily recognized. Most samples were investigated "as supplied" with a fairly coarse surface grind finish. Although the grind marks are visible in the micrographs, they do not preclude location and identification of the buried flaws. Some of the samples reported here using the SLAM were subsequently examined by Kino, et al at Stanford University with a higher

frequency pulse echo system¹. For this examination, however, the samples had to be surface lapped and polished in order to make them compatible. After the pulse echo work, one of the samples (#70) was again returned to Sonoscan for a repeat SLAM investigation. The surface polish made the SLAM micrographs prettier but it did not alter the findings.

Figure 1a is an amplitude micrograph of Sample 73 illustrating the typical acoustic microstructure encountered in the high density samples ($\rho = 3.21 \text{ gm/cm}^3$). The intensity across this 2 mm field of view is "relatively" uniform exhibiting only low contrast features. The vertical linear structures are the result of the surface texture.

Figure 1b is an amplitude micrograph of Sample 45 ($\rho = 3.10 \text{ gm/cm}^3$), illustrating the typical acoustic microstructure. Notice the non-uniformity in acoustic transmission observed in this 3 mm field of view. Some of the larger regions of decreased transmission are noted with arrows. The regions of low transmission are attributable to energy losses at embedded clusters of pores. The non-uniform distribution of porosity of this sample, relative to the high density samples, lends the acoustic image a characteristic visual texture. Note the surface texture is also evident in this micrograph (vertical, linear structures).

Figure 1c is an amplitude micrograph of Sample 51, $\rho = 2.94 \text{ gm/cm}^3$, the typical acoustic microstructure encountered in the low density samples is illustrated in this 3 mm field of view. The substantial transmission variation is attributed to the non-uniform distribution of porosity (relative to Sample 73). Relative to Sample 45, the porosity is segregated in larger zones. Attenuating zones, indicative of increased porosity are typically 1.0 to 2.5 millimeters (largest dimension).



Fig. 1 - SLAM micrographs showing typical silicon nitride for a range of bulk densities.

- (a) $\rho = 3.21 \text{ gm/cm}^3$
- (b) $\rho = 3.10 \text{ gm/cm}^3$
- (c) $\rho = 2.94 \text{ gm/cm}^3$

The particularly regular growth changes from round to Sample 11 (is illustrated in Figure 1) with the amplitude micrograph (D) and the interference (A) are presented. (Three, large, alternating zones are evident in this view.) A large number of these changes were found in a rectangular zone 1 cm by 1.5 cm in size.

Depth determination of the three flaws in Figure 1 indicate that they are located in a zone 1 cm in diameter near the center of the sample (3 cm in diameter) on the surface. Although the presence of the three flaws leads to a complex background in the center, they are morphologically distinct over a wide field and can be differentiated easily.

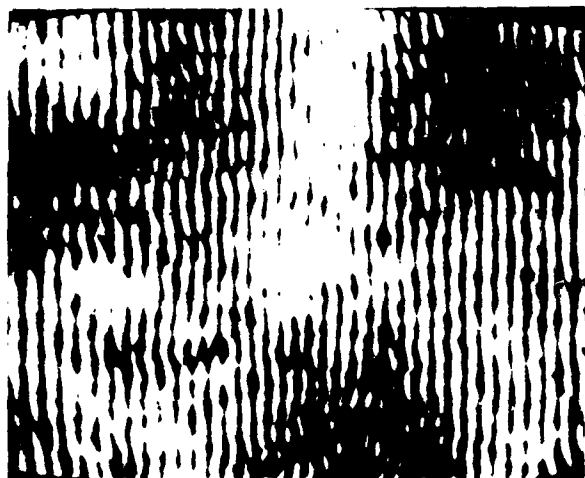
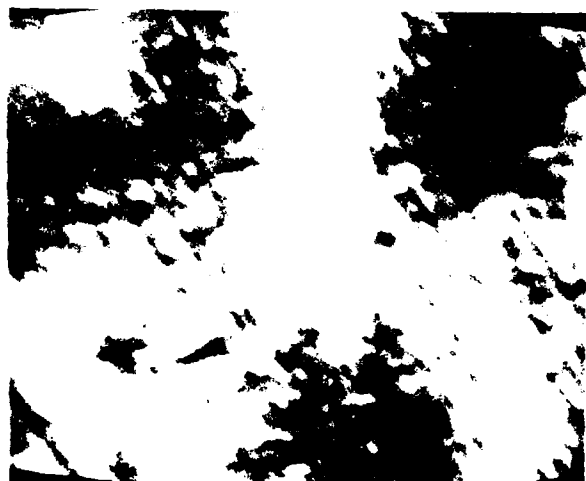


Fig. 1. Interference (A) and amplitude (D) micrographs of the surface of Sample 11.

Fig. 1. Interference (A) and amplitude (D) micrographs of the surface of Sample 11.

Fig. 1. Interference (A) and amplitude (D) micrographs of the surface of Sample 11.

CONCLUSIONS

As will be seen from the results obtained in the above analysis, the data illustrate the flaws and their interpretation. In conclusion, the detection of the flaws in the central zone where the transverse direction of the growth is parallel to the surface of the sample is well illustrated. The results obtained in the above analysis indicate that the flaws are located in a zone 1 cm in diameter near the center of the sample (3 cm in diameter) on the surface. Although the presence of the three flaws leads to a complex background in the center, they are morphologically distinct over a wide field and can be differentiated easily.

It is to be noted that the above results are presented in a form which is not a direct representation of the data. The data are presented in the form of a micrograph, where the flaws are indicated. The results are presented in the form of a micrograph, where the flaws are indicated. The results are presented in the form of a micrograph, where the flaws are indicated.

TABLE II

Sample Number	Defect Identification	Image Size (Microns)	Depth (mm)	Shear Wave Image	Compressional Wave Image	Comment	Intended Flaw
5	a	640	4.7	Best	Yes	Circular, medium contrast	400 micron carbon
5	b	200	-	No	Yes	Circular, low contrast	
73	a	690	4.9	Best	Yes	Circular, high contrast	400 micron carbon
73	a	490	2.1	Best	Yes	Same flaw from other side	
45	a	150	-	Best	No	Circular, low contrast, near edge	100 micron carbon
90	a	625	-	Yes	Yes	High contrast elliptical	400 micron Iron
29	a	530x370	3.5	Best	Yes	Irregular shape, med. contrast	
29	b	165x350	-	No	Yes	Irregular, med. contrast	400 micron Iron
88	a	550	3.6	Best	Yes	Circular low contrast	
88	b	100	Near Surface	No	Yes	Circular low contrast	400 micron Iron
65	a	280x190	-	Yes	No	Irregular, difficult to distinguish from porosity	100 micron Iron
51	a	175	0.9	Yes	Yes	Very high contrast circular	400 micron silicon
51	a	750	6.0	Yes	Yes	Same flaw from other side	
51	b	Two Flaws 60	Near Surface	Yes	Yes	Two close lying 60 micron flaws	
51	c	225	Near Surface	No	Yes	Bright, circular, low contrast	
51	d	250	-	Yes	No	Low contrast, circular	
51	e	450	-	No	Yes	Triangular, Low contrast	
49	a	780	-	No	Yes	Very low contrast circular	400 micron silicon
32	a	225	-	Yes	No	Circular, very low contrast	100 micron silicon

Thus, the recorded image size may differ from the actual flaw size and will also depend on depth below the observation plane. In general, we expect the soundfield to diverge from the flaw site which leads to image sizes typically larger than the actual flaw size. This would be true for any imaging technique.

Column 4 lists depth determinations. This is determined by stereoscopy which is illustrated in Figure 3. Stereoscopy involves imaging the same flaw at two different angles of insonification. By measuring the shift in the projected image position of the flaw (relative to a fixed point on surface) the flaw depth can be determined. Because the depth determination by stereoscopy uses the acoustic images, the accuracy is governed by image resolution (30 microns for shear waves).

The fifth and sixth columns refer to flaw "visibility" for different methods of examination. Two methods were employed. For shearwave investigation, a plane wave is incident on the sample at an angle of 4.4° from the normal through a water couplant. This is beyond the compressional wave critical angle; only shearwaves propagate and are responsible for the image. For compressional wave investigations, an acoustic plane wave is normally incident, only compressional waves are incident upon the flaw. Experimentally, we have found definite preferences for shear or compressional insonification to optimize visibility of defect. Three levels of flaw visibility are listed: "yes" - detectable; "no" - non-detectable and "best" - optimum flaw visualization. For those flaws where visibility was similar for both methods, both columns are marked "yes".

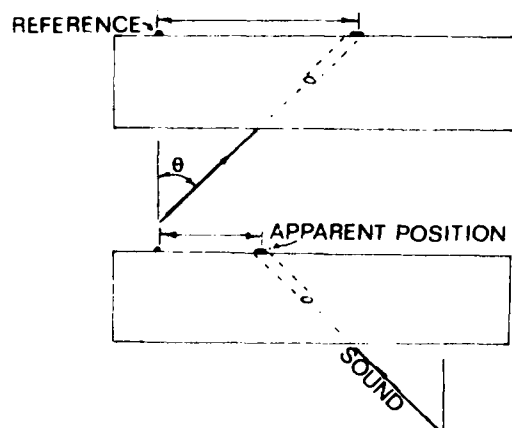


Fig. 3 - Schematic illustrating depth determination by stereoscopy.

Carbon Inclusions - Three samples were investigated which contained implanted carbon inclusions, #5, #73, and #45). In each case the images (Flaws 5a, 73a and 45a) were circular. Visibility was optimum with shear wave insonification, however, each of the 400 μ flaws were detectable with either compressional or shear waves. On the other hand, the 100 micron carbon flaw was only detected with shear waves. Of this group, the flaw implanted in Sample 73 exhibits the highest contrast and is most easily detected. Acoustic micrograph of this flaw is given in Figure 4a. The smaller flaw found in Sample #45 is presented in Figure 4b.

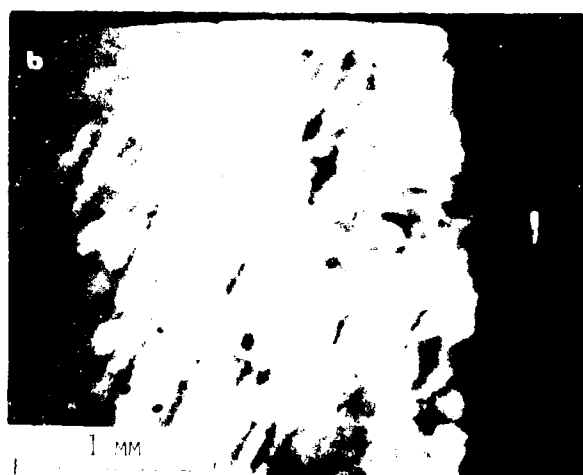


Fig. 4 - SLAM images of implanted carbon inclusion in silicon nitride disc.

- a) Sample 73
- b) Sample 45

In order to accurately estimate flaw dimensions from acoustic images, proper account must be taken of beam spreading and possible focusing. To illustrate the magnitude of the effects, a single flaw was imaged at two different depths in a sample. Sample 73 was convenient since the flaw is located 2.1 mm below one surface and 4.9 mm below the other. The difference in image size was found to be 490 microns compared with 690 microns as the flaw is observed from opposite surfaces. After destructive analysis of this sample to reveal the actual flaw size, an accurate formula can be obtained for flaw size determination from the image dimensions and depth.

Iron Inclusions - Four samples analyzed contained implanted iron inclusions, 3 contained 400 micron flaws, the other contained a 100 micron flaw. The detected flaws showed considerable variation in both degree of contrast and morphology. For example, the flaw detected in Sample #90 shows a symmetric circular pattern surrounded by several well-developed diffraction rings. The flaw found in #88 (flaw 88a) is also circular but exhibits lower contrast and was more difficult to detect. In Sample #29 (400 u Fe) the contrast is similar to that of Sample #90, however, the shape is quite irregular and a well-developed diffraction ring pattern was not observed. Similarly, the smaller flaw detected in Sample #65 (100 u, Fe) has an irregular shape. Flaw found in Sample #90 is compared with that of #29 in Figure 5.

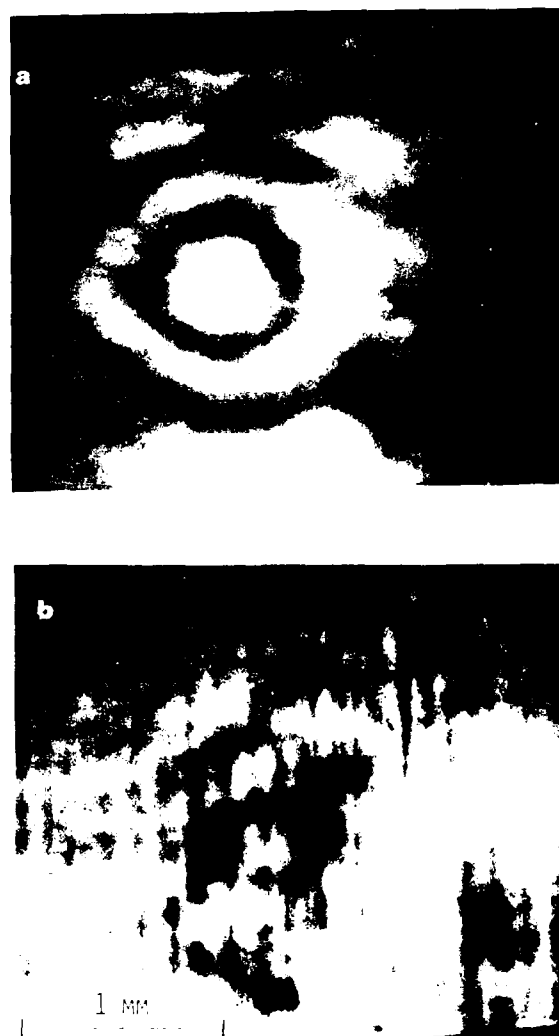


Fig. 5 - SLAM micrograph of implanted iron inclusions in Samples 90 and 29 respectively.

Silicon Inclusions - Three samples were analyzed which had implanted silicon inclusions. A complete analysis was carried out on Sample #51 where five flaws, with features characteristic of solid inclusions, were found. This sample was a low density sample ($\rho = 2.94 \text{ gm/cm}^3$) and substantial acoustic transmission variations (attributed to increased porosity) were found. Four of the flaws were relatively low contrast features and one exhibited high contrast with a well developed diffraction ring pattern. Visibility of this high contrast flaw was similar using shear and compressional waves. The image of this high contrast flaw is shown in Figure 6. Both a compressional (6a) and shear wave (6b) images are presented for comparison.

For silicon inclusions, the visibility is comparable for both insonification modes. The elliptical characteristic of the flaw in Figure 6b is attributable to the angular insonification. A sphere will project an elliptical image using angle beam shear wave insonification. Another point to be made with regards to this flaw is the large increase in image size with flaw depth. In Figure 6, the flaw lies 0.9 mm below the observation plane. This flaw is also detectable at the opposite surface of the disc where it is 6 mm below the observation plane. The image sizes are 175 and 750 microns respectively.

Flaws found in samples number 49 and 42 exhibit some anomalous behavior. Although circular, like flaw image 51a, they show much less contrast. Additionally, the large circular flaw in #49 was detectable only with compressional insonification while the flaw in Sample #42 was found only with shear waves.

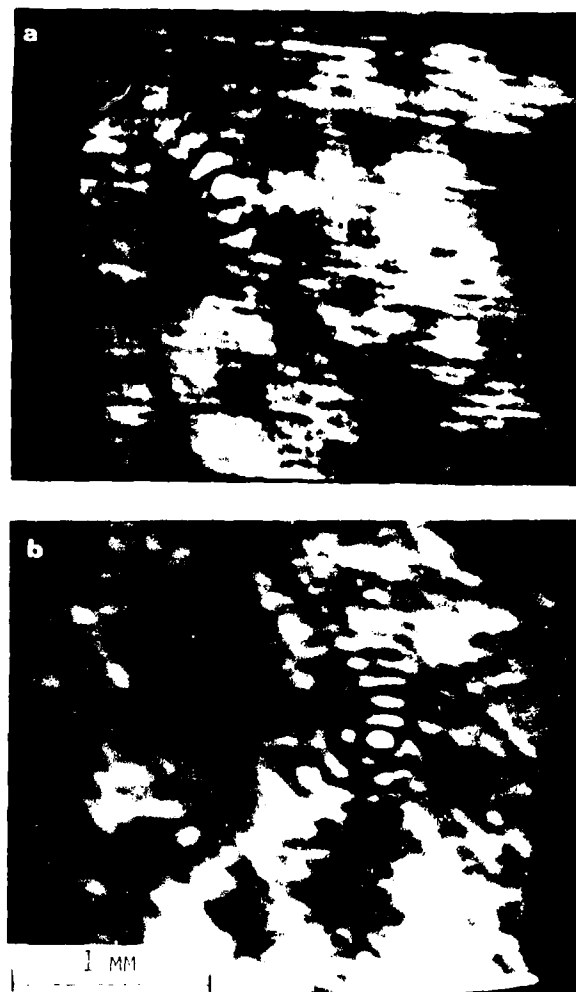


Fig. 6 - Comparison of compressional (a) and shear wave (b) images of inclusion 51a.

SUMMARY

This investigation represents only the initial step in delineating the characteristics of solid inclusions in hot-pressed silicon nitride. The imaging capability is found to be essential for the recognition and differentiation of flaws. The unique characteristics of these implanted inclusions were found to be: 1) the presence of high acoustic transmission centers, 2) well defined boundaries and, 3) diffraction ring patterns. These features serve to distinguish solid inclusion from laminar flaws, cracks and porosity variations. Solid inclusion characteristics observed in this study have subsequently been shown to have obvious similarities with those predicted by elementary scattering theory². Although qualitative agreement exists between theory and experiment, direct analysis, the same flaw analyzed experimentally, theoretically and destructively, has yet to be done.

Detect size estimates can be made by measuring the image sizes recorded on the acoustic micrographs. However, it is clear that such determinations need to be corrected for defect depth. Additionally, qualitative observations of variations in defect contrast as well as shape may prove to be useful in identifying specific types of solid inclusions. Unfortunately, definitive conclusions cannot be made because of a great uncertainty in the actual size and type of inclusions in the samples investigated. Our observations demonstrating a multiplicity of flaws when only one was intended, coupled with the discovery of complex chemical reactions between the implanted inclusions and the host silicon nitride³ make interpretation of some of our observations to be somewhat speculative. Validation of flaw dimensions and type by destructive analysis needs to be done.

We anticipate that a detailed image analysis using either scattering theory or direct holographic reconstruction will take full advantage of all the information available in SAM micrographs. This approach coupled with adequate destructive analysis will lead to accurate defect sizing and differentiation of the various solid inclusion types. Furthermore, in other studies involving the SAM, we have shown that results obtained on samples with simple shapes are similar to those found on complex production components^{4,5}. The SAM is the only high frequency ultrasonic technique which has demonstrated the capability to deal with complex shapes. In these studies, where the primary interests involved detection of cracks and porosity routine non-destructive testing procedures have been developed. The same should be true for the SAM analysis of production components containing solid inclusions.

REFERENCES

1. D. E. Yuhas, T. E. McGraw, and L. W. Essler, Differentiation of Various Flaw Types in Ceramics Using the Scanning Laser Acoustic Microscope, Proc. ARPA/AFM Conf. on Quantitative NDE, LaBolla, CA, 1979.
2. R. T. KHURI-YAKUB, Nondestructive Evaluation of Structural Ceramic Component, Proc. 1979 Ultrasonics Symposium New Orleans, Sept. 1979.
3. J. S. Kino, Nondestructive Evaluation, *Acoustic*, Vol. 1996, pp 173-180, Oct. 1979.
4. D. E. Yuhas, T. E. McGraw, and L. W. Essler, Non-Destructive Evaluation of Stainless Steel Ball and Rod Components by Means of Scanning Laser Acoustic Microscopy (SLAM), *Transactions of ASME*, Vol. 101, Oct. 1979.
5. D. S. Ruppert, Jr., S. L. Farnsworth, A. E. Lankford, A. G. Eber, D. Yuhas, L. Essler, and A. L. Hanson, "Preliminary Evaluation of Several NDE Techniques for Silicon Nitride Gas Turbine Components," *General Motors Research Laboratories Report* GM-84-149, January 1984.
6. J. S. Farnsworth, L. Farnsworth, D. Yuhas, and T. E. McGraw, Acoustic Microscopy for Structural Materials, *Subject: Journal of American Ceramic Society*, 1979.
7. D. E. Yuhas, and L. W. Essler, Scanning Laser Acoustic Microscopy Applied to Ball and Rods, Proc. AME 79-8-1101, Inc., New York, New York, Top No. 199910, Vol. 110, pp. 1099-1100, 1979.
8. Private communication from James S. Farnsworth, General Motors, Warren, Mich., 1984.

ULTRASONIC DETECTION OF SURFACE FLAWS IN GAS TURBINE CERAMICS

T. Derkacs and I. M. Matay
TRW, Inc.
TRW Materials Technology
Cleveland, OH 44117

ABSTRACT

This paper presents the results of a program sponsored by NADC for NASC to develop an ultrasonic surface wave technique for detection of small flaws, $<100\text{ }\mu\text{m}$ ($<0.004\text{ inch}$), in gas turbine quality ceramics. A 45 MHz ultrasonic surface wave inspection technique is described, which employs immersion scanning and C-scan recording. Inspection results are presented using this technique on specimens of hot pressed silicon nitride and silicon carbide, from two sources each, and reaction bonded silicon nitride. Results are also presented of four-point-bend tests and scanning electron micrography, which were used to identify defect sizes and types and to correlate flexural strength with inspection results. The flexural strength is shown to correlate, at least qualitatively, with the extent of ultrasonic response from machining damage. The sensitivity to individual defects is shown to be limited primarily by the extent of machining damage and the spot size of the ultrasonic beam.

INTRODUCTION

This paper describes a program sponsored by the NADC for the NASC to develop a very high frequency (VHF) surface wave inspection technique for gas turbine ceramics. In earlier programs we developed a longitudinal wave technique (Ref. 1) capable of detecting defects down to at least 0.001 inches (25 μm) in size with a near-surface deadband of 0.0063 inches (160 μm), and a shear wave technique (Ref. 2) that improved the sensitivity so that 0.0004 inch (10 μm) defects can be detected, and reduced the near-surface deadband to 0.0016 inches (40 μm). The purpose of this program (Ref. 3) was to develop a near-surface inspection technique in order to eliminate the remaining deadband. As in the earlier programs, our approach for surface defects was to develop a technique that would allow scanning of a reasonable volume of material in a practical period of time. Our goal was to develop an immersion technique in order to allow rapid scanning and automatic data recording so that the combination of the three techniques, longitudinal, shear and surface waves, would allow an automated inspection providing complete part coverage.

TECHNIQUE

Ultrasonic surface wave inspection at conventional frequencies is normally a manual, contact operation in which no provision is made to automatically correlate defects with their locations in the part. This is necessary because immersion testing is not usually possible. A surface wave traveling on a part submerged in water radiates energy into the water and quickly dissipates. The method used in this program to overcome this limitation is illustrated in Fig. 1. The transducer used was an Aerotech Laboratories 45 MHz alpha transducer with a focal length of 1.8 inches in water and a beam spot size at half-amplitude of .023 inches (580 μm). The transducer and part were submerged in water and the transducer was tilted at an angle to the entry surface of about 18° in order to generate surface waves in the specimen by mode conversion. The water path was set so that the beam was focused in the material a short distance past the point of entry. This provides the shortest possible path length and therefore the minimum possible loss in a reflected pulse from a surface defect. The ultrasonic defect gate was set to encompass only the transducer focal point, so that as the

transducer was scanned over the part a defect indication was recorded only when the beam was focused on the defect.

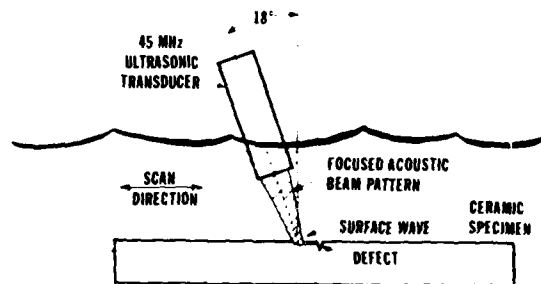


Fig. 1 Immersion 45 MHz Ultrasonic Surface Wave Technique.

INSPECTIONS

Initial evaluations were performed to demonstrate that the technique does indeed generate surface waves. A simple test was to make a recognizable mark, such as a number or letter, on the surface of a ceramic specimen with a grease pencil. Then when the part was inspected, the mark showed up as a defect indication. This technique points out the importance of cleanliness. Any air bubble or dust particle on the part surface shows up as a defect indication. We adopted the policy of individually checking significant defect indications by brushing the surface to make sure the "defect" could not be removed. A more sophisticated technique for ensuring the presence of surface waves was to inspect a billet to locate surface flaws and then to machine off a thin layer and re-inspect the part. Figures 2 and 3 show an example of this technique. Figure

2 shows a C-scan recording of a 45 MHz ultrasonic surface wave inspection of a 7 1/2 inch (19 cm) diameter billet of NC-350 reaction bonded silicon nitride (RBSN). After inspection the billet was cut to remove the three numbered specimens and the left hand side was machined to remove 0.0006 inches (15 μ m) in the shaded area. The machining was done to split the linear indication in that portion of the billet. The grinding was perpendicular to the cut edge. Figure 3 shows the same portion of the billet after machining. The linear indication was removed in the machined area while remaining in the unmachined area. It is apparently less than 0.0006 inches (15 μ m) deep. The defect indication labelled F was reduced in size but not removed. This defect is apparently greater than 0.0006 inches (15 μ m) deep. The inspection technique was also found to be sensitive to machining damage. Figure 4 shows a scan of the same part made parallel to the cut edge and therefore perpendicular to the machining direction. In this case the entire machined area appears defective. This is a significant fact, since it is known that flexural strength specimens ground parallel to their major axis are stronger than those ground perpendicular to their major axis. Figures 3 and 4 indicate that the surface wave technique is sensitive to this difference in grinding direction and therefore to strength.

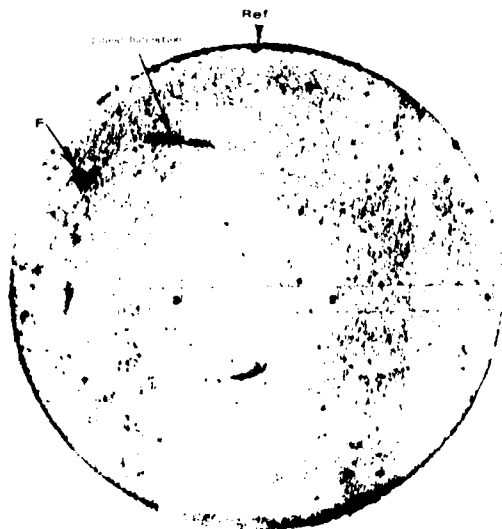


Fig. 2 Machined (Shaded) Area Overlayed on C-Scan Recording of 45 MHz, 18° Surface Wave Inspection of Top Surface of Billet of NC-350 RBSN.

Figures 5, 6 and 7 show another billet that was used to verify the presence of surface waves. This is a billet of Ceralloy 147A hot pressed silicon nitride (HPSN) which was received in the as-pressed condition and then was machined to remove a total of about 0.040 inches (1000 μ m) to provide smooth surfaces on both sides. The areas of heavy concentrations of indications in Fig. 5 correspond to the areas shown in the photomicrographs (7X) of Fig. 6 which contain surface ridges left by the pressing operation. After machining these ridges away, the indications in areas A and B disappeared. The billet of Ceralloy 147A HPSN was inspected by both shear and surface waves before machining and by surface waves after machining. A comparison of the before and after surface wave inspections shows no significant correlation in indications. This is to be expected given the amount of material removed. A comparison of the shear wave

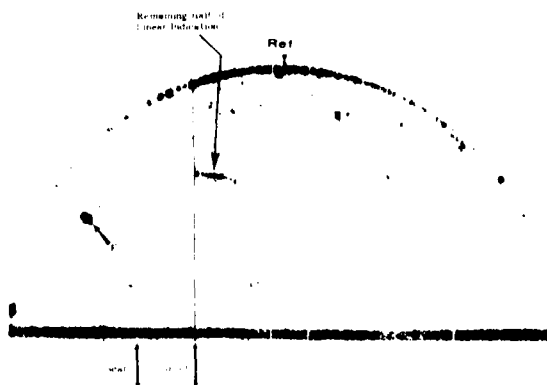


Fig. 3 C-Scan Recording of 45 MHz, 18° Surface Wave Inspection of Top Surface of Segment of Billet of NC-350 RBSN Containing Machined Area (Scan Parallel to Grinding Direction).

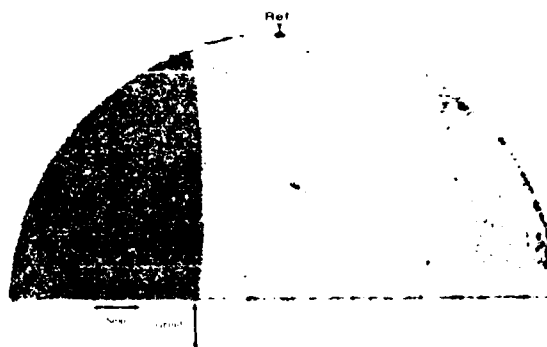


Fig. 4 C-Scan Recording of 45 MHz, 18° Surface Wave Inspection of Top Surface of Segment of Billet of NC-350 RBSN Containing Machined Area (Scan Perpendicular to Grinding Direction).

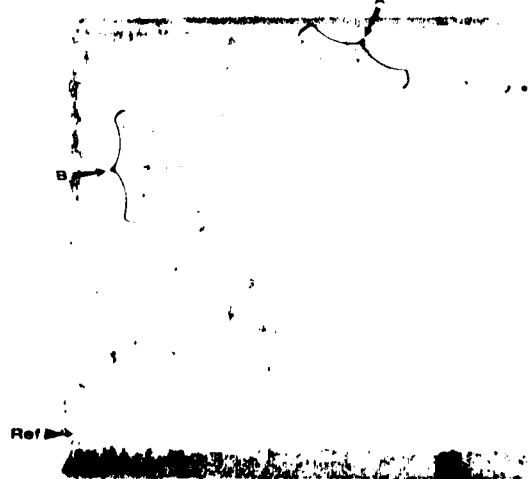
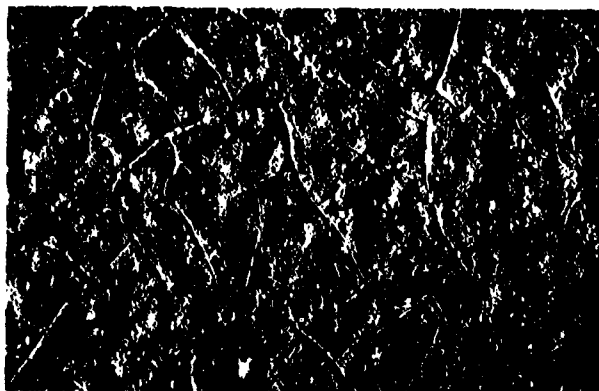


Fig. 5 C-Scan Recording of 45 MHz, 18° Surface Wave Inspection of Billet of Ceralloy 147A Hot Pressed Silicon Nitride (notch up).



Area A

7X



Area B

7X

Fig. 6 Photomicrographs Showing Surface Condition of Two Typical Areas of As-Pressed Billet of Ceralloy 147A HPSN Where Large Numbers of Surface Wave Indications Were Detected.

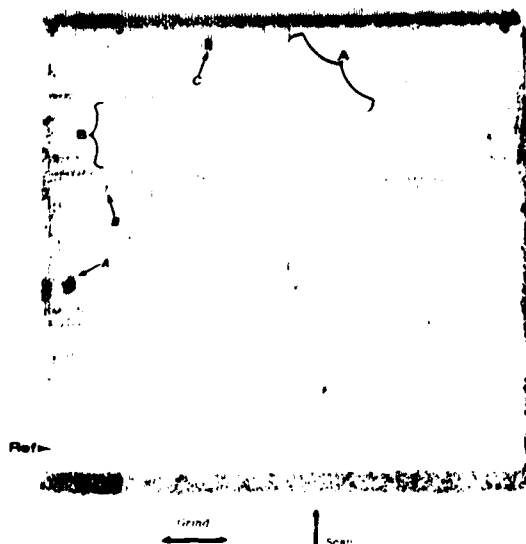


Fig. 7 C-Scan Recording of 45 MHz, 18° Surface Wave Inspection of Top Surface of Billet of Ceralloy 147A HPSN After Machining (Scan Perpendicular to Grinding Direction).

results before machining and the surface wave inspections after machining show a number of corresponding indications. The defects labelled A, B and C in Fig. 7, for example, correspond to defect indications in the corresponding shear wave scan.

Billets of NC-132 and Ceralloy 147A HPSN, NC-350 RBSN, NC-230 and Ceralloy 146 hot pressed silicon carbide (HPSiC) and boron doped sintered SiC were inspected using the surface wave technique. In each case inspections were made on both major surfaces both parallel and perpendicular to the grinding direction. Fig. 7 is the result of a scan made perpendicular to the grinding direction in the billet of Ceralloy 147A HPSN. In this case the sensitivity was reduced so only the most severe grinding damage was detected, thereby allowing the individual defects to also be seen. Figures 8 and 9 show the inspection results for one surface of the billet of NC-132 HPSN. The rectangles in these figures represent four-point-bend specimens machined from this billet. Figure 8 shows a defect-free billet except for very tiny indications in specimens 1, 2 and 3. Figure 9 shows a scan of the same surface perpendicular to the grinding damage. Figure 10 shows the nine bend specimens after machining. This scan was made parallel to the major axis so as to be sensitive to strength controlling defects. The contrast between grinding directions is readily apparent. Similar results were obtained for the other materials tested.

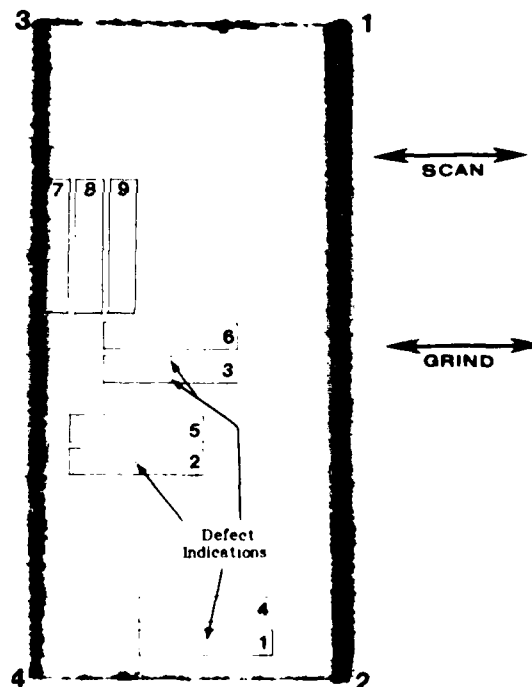


Fig. 8 C-Scan Recording of 45 MHz Ultrasonic Surface Wave Inspection of Bottom of Billet of NC-132 HPSN (Scan Parallel to Grinding Direction).

MECHANICAL TESTING

Four-point-bend specimens were made from each of the billets inspected. Specimens were made from defect free areas machined parallel to the major axis, from areas showing grinding indications as a result of being machined perpendicular to the grinding damage, and from areas containing only individual defect indications. The specimens were machined with a 320 grit diamond wheel

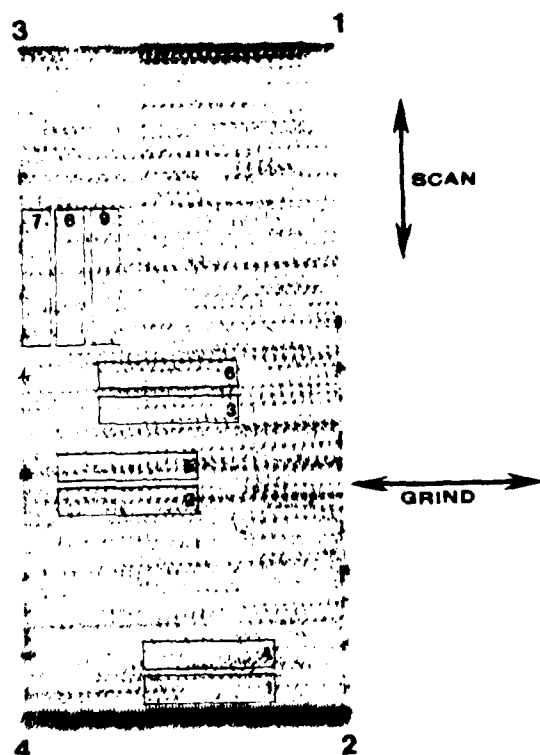


Fig. 9 C-Scan Recording of 45 MHz Ultrasonic Surface Wave Inspection of Bottom Surface of Billet of NC-132 HPSN (Scan Perpendicular to Grinding Direction).

parallel to the major axis on all surfaces except the tensile surface, which was left as inspected. The specimens were also chamfered 0.005 inches (125 μ m) at 45° on the edges. One specimen of each material machined parallel to the major axis was given a 1 kg Vicker's indentation and one specimen of each machined perpendicular to the major axis was given a 50 kg Vicker's indentation. With the quality of surfaces involved (all billets had originally been machined with a 320 grit diamond wheel) only the 50 kg Vicker's could be resolved ultrasonically.

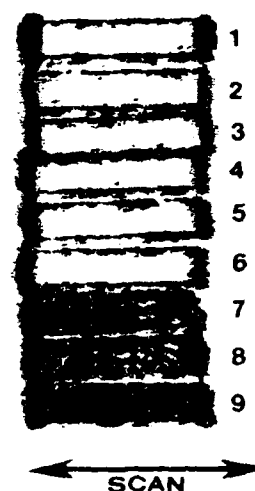
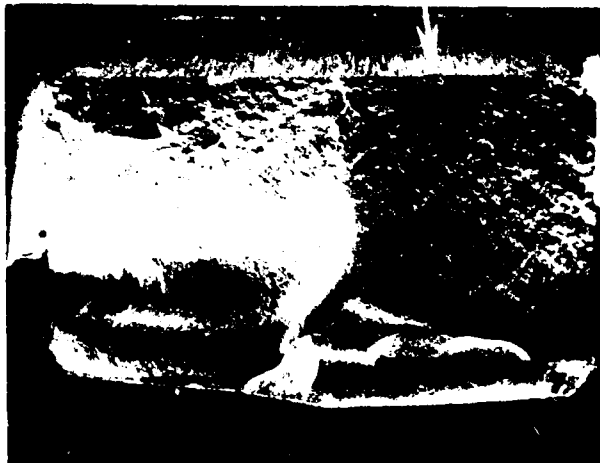


Fig. 10 C-Scan Recording of 45 MHz Ultrasonic Surface Wave Inspection of Tensile Surfaces of NC-132 HPSN Four-Point-Bend Specimens.

The four-point-bend tests along with SEM fractography provided data on material strength, fracture origin location with respect to indication location and the nature and size of fracture origins. From this data it was possible to correlate a number of strength limiting defects with their ultrasonic responses. Figures 11 through 16 show some typical ultrasonically detected fracture origins. Figure 11 shows a surface pit in specimen #2 of Ceralloy 147A HPSN. It is about 0.0072" (180 μ m) across and 0.0030" (75 μ m) deep. Figure 12 shows a typical 50 kg Vicker's indentation; a pit about the same size as in the previous specimen with a crack extending over 0.020 inches (500 μ m) deep in the part. Figure 13 shows the 1 kg Vicker's indentation in the same material, an approximately 0.002 inch (60 μ m) deep crack. Figure 14 shows a 0.020 inch (500 μ m) wide by 0.012 inch (300 μ m) deep area of very large grains in specimen #3 of Ceralloy 147A HPSN. Figure 15 shows a flake-like inclusion about 0.0004" (10 μ m) thick and 0.0028" (70 μ m) wide located 0.0008" (20 μ m) below the surface. This is defect A in Fig. 7. Figure 15 shows the smallest defect correlated with an ultrasonic indication, a 0.0006" (16 μ m) wide by 0.0008" (20 μ m) deep area of large grains at the surface in specimen #1 of NC-132 HPSN (see Fig. 8 for the indication). A defect of about this same size was the largest one found at a fracture origin that could not be correlated with an ultrasonic indication. This suggests that this size defect may not have a high probability of being detected.



100X



100X

Fig. 11 Fracture Surface of Ceralloy 147A Specimen No. 2 Showing Ultrasonically Detected Surface Pit at Fracture Origin.

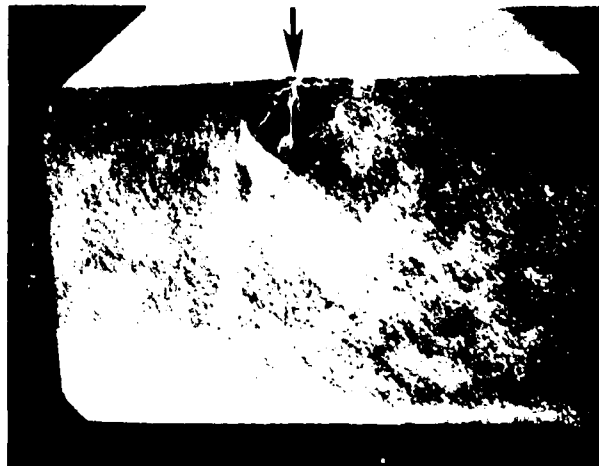
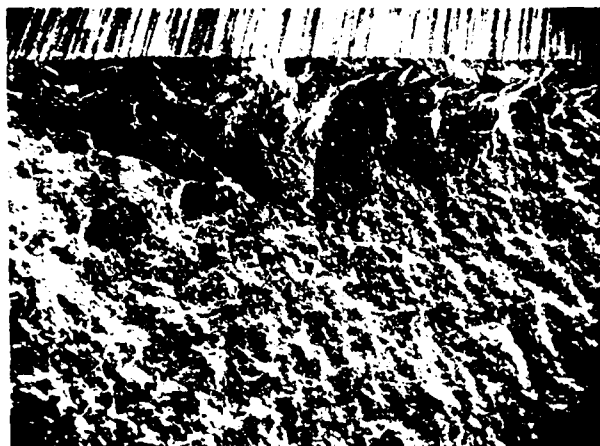
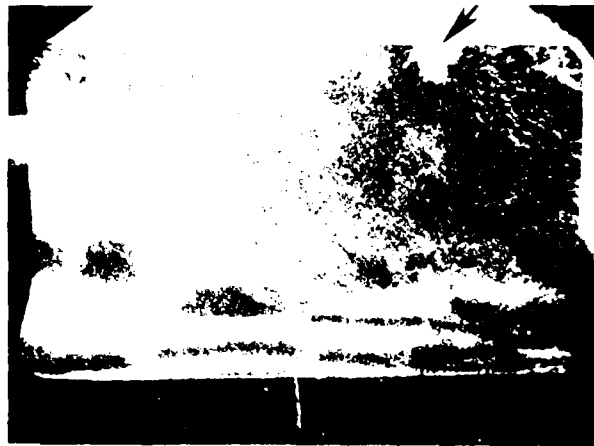


Fig. 12 Fracture Surface of Ceralloy 147A HPSN Specimen No. 9 Showing Fracture Origin at 50 kg Vicker's Indentation

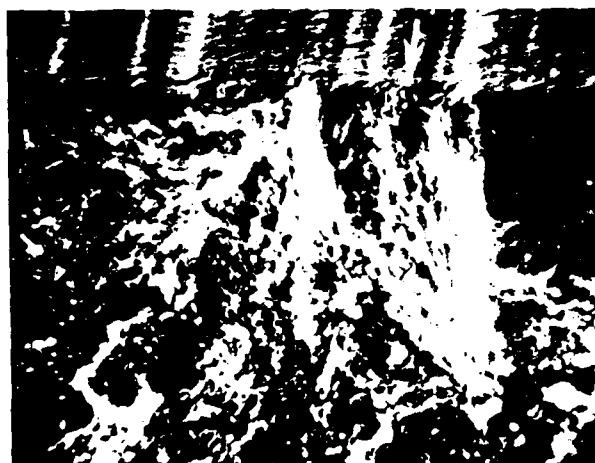
located in the strength measurements, and SEM analysis, a graph was made of strength versus defect size for the two types of HPSN. This is shown in Fig. 17. The largest defects in the graphs are, of course, Vicker's indentations. The zero defect size is defect free material ground parallel to the major specimen axis. The points in between are, of course, detected defects. A graph was also made based on measured strengths parallel and perpendicular to grinding. This is shown in Fig. 18 for two types of HPSN and two types of HPSN. The ultrasonic response is designated light damage (below a certain threshold) or heavy damage (above a certain threshold). Although the correlation shown in this graph is only qualitative, these results indicate that by assigning a numerical value to the magnitude of ultrasonic response, it may be possible to measure the material strength associated with a given surface finish.



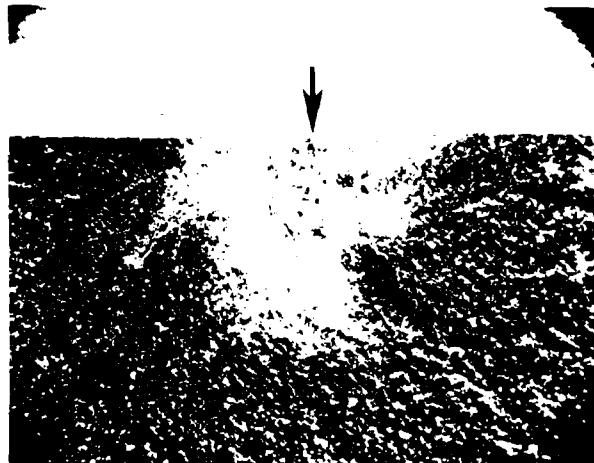
100X



10X



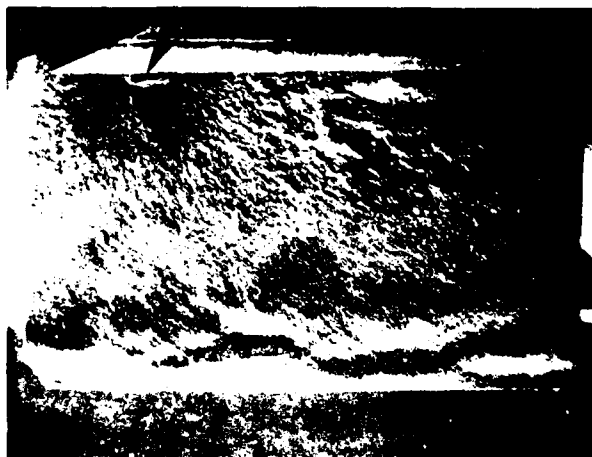
1000X



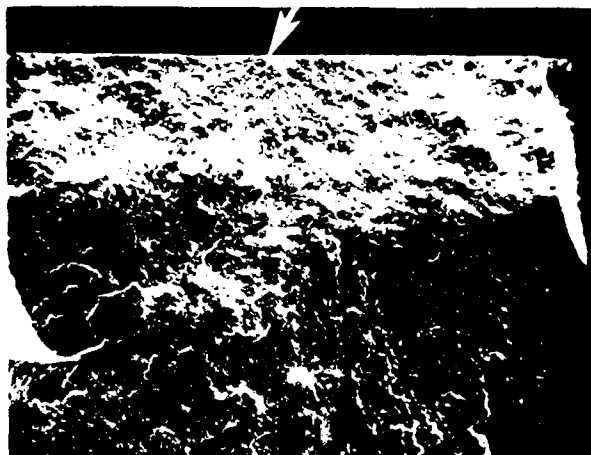
40X

Fig. 13 Fracture Surface of Ceralloy 147A HPSN Specimen No. 6 Showing Fracture Origin at 1 kg Vicker's Indentation.

Fig. 14 Fracture Surface of Ceralloy 147A HPSN Specimen No.3 Showing Ultrasonically Detected Fracture Origin.



16X



500X



500X

Fig. 15 Fracture Surface of Ceralloy 147A HPSN Specimen No. 4 Showing Ultrasonically Detected Fracture Origin.

Fig. 16 Fracture Surface of NC-132 HPSN Specimen No. 1 Showing Ultrasonically Detected Fracture Origin.

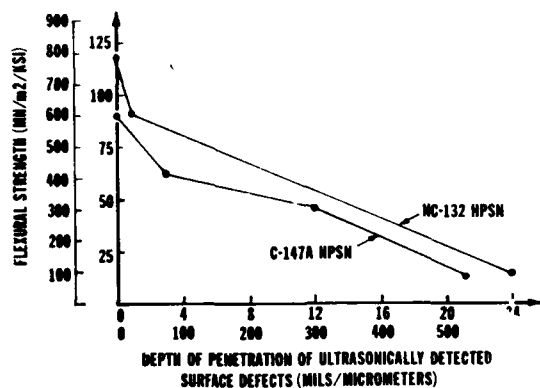


Fig. 17 Flexural Strength as a Function of the Depth of Penetration of Ultrasonically Detected Surface Defects.

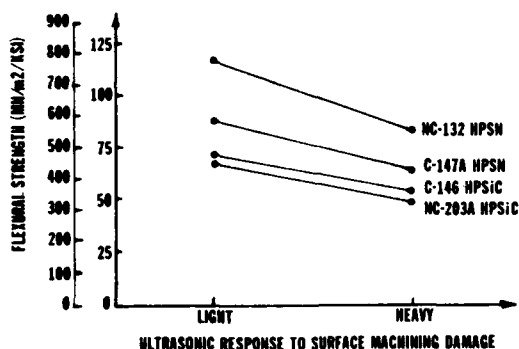


Fig. 18 Flexural Strength as a Function of Ultrasonically Detected Surface Damage in HPSN and HPSiC.

DISCUSSION

The results indicate that, in general, a part may have a general background of machining damage and also individual larger defects. If an individual defect is large enough to be strength limiting, then the inspection technique must be capable of distinguishing it from the background caused by surface damage. A good example of such a defect is the 1 kg Vicker's indentation used in this program. Although the 1 kg indentations could not be detected against the machining background, the specimens containing these indentations were weaker than the other specimens cut parallel to the grinding direction and in some cases were weaker than those cut perpendicular to the grinding direction. Therefore improved discrimination capability is needed to allow detection of the strength limiting defect.

A simple model for estimating discrimination sensitivity is to assume that the reflected pulse from a defect is proportional to the percentage of the beam that it intercepts. Using this assumption, surface damage 0.0006 inches (15 μ m) deep would limit defect detection with a 0.023 inch (580 μ m) diameter beam to a semi-circular crack 0.0043 inches (108 μ m) deep. This assumes that a 3 to 1 signal-to-noise ratio is required for reliable detection. This situation can be improved by either reducing the depth of the machining damage or the diameter of the beam. If the machining damage is reduced to a depth of 0.0002 inches (5 μ m), the minimum detectable defect becomes 0.0025 inches (63 μ m). If the beam diameter is reduced to 0.005 inches (125 μ m), a defect 0.0028 inches (70 μ m) deep can be detected. If both are done a defect 0.0016 inches (40 μ m) deep can be detected. Although the size of defects calculated may not be accurate because of the simplified assumptions used to calculate them, the numbers illustrate the order of magnitude improvement that is possible.

CONCLUSIONS

Based on the experimental results, the following conclusions can be drawn:

1. A very high frequency (VHF) immersion ultrasonic surface wave inspection technique has been successfully developed;
2. The technique is capable of detecting small defects, penetrating less than 0.001 inch (25 μ m) deep in the material;
3. A quantitative correlation has been shown between flexural strength and the depth of ultrasonically detected strength controlling defects;
4. A qualitative correlation has been shown between flexural strength and ultrasonically detected surface damage; and,
5. Sensitivity to individual strength controlling defects is limited by the extent of the machining damage and the ultrasonic beam diameter.

REFERENCES

1. Derkaes, T., Matay, I.M. and Brentnall, W.D., "Nondestructive Evaluation of Ceramics," Final Report, Contract N00019-75-C-0238, Naval Air Systems Command, July 1976, TRW Internal Report No. ER-7798-F.
2. Derkaes, T., Matay, I.M., and Brentnall, W.D., "Ultrasonic Inspection of Ceramics Containing Small Flaws," Final Report, Contract N62269-76-C-0148, Naval Air Development Center for Naval Air Systems Command, August 1977, Internal Report No. ER-7867-F.
3. Derkaes, T. and Matay, I. M., "Detection of Surface Flaws in Gas Turbine Ceramics," Final Report, Contract N62239-C-0136, Naval Air Development Center for Naval Air Systems Command, June 1979, Internal Report No. ER-7980-F.

SUMMARY DISCUSSION
-T. Derkaes-

Wolfgang Sachse (Cornell University): The transducer you used is 45 megahertz?

Tom Derkaes: Yes.

Wolfgang Sachse: Is that a commercial device, or did you --

Tom Derkaes: We bought it commercially. I'm not sure whether it's still available. It was.

John Irati (Teledyne CAE): The C scans you showed, there was a lot of background or things that you didn't pick out and mark as defects. Is this --

Tom Derkaes: In the case of the reaction bonded silicon nitride when you buy it, it has lines in the surface that are caused by cutting in the green state, and these lines are about 15 microns deep. And you do get a background indication from those. If you were to turn it so it actually lines up perpendicular to the beam these lines would cause a black background at this sensitivity. In the scan shown in the slide it was turned at an angle, so we're not getting a strong reflection. It does give a problem of background.

#

NONDESTRUCTIVE EVALUATION TECHNIQUES FOR SILICON CARBIDE HEAT-EXCHANGER TUBING*

D.S. Kupperman, W.D. Deininger, N.P. Lapinski, C. Sciammarella**, and D. Yuhas[†]
Materials Science Division, Argonne National Laboratory
Argonne, IL 60439

ABSTRACT

The adequacy of various nondestructive evaluation (NDE) techniques for inspecting silicon carbide heat-exchanger tubing is discussed. These methods include conventional ultrasonics, acoustic microscopy, conventional and dye-enhanced radiography, holographic interferometry and infrared scanning techniques. On the basis of current test results and an examination of the discussions in available literature, these techniques were compared with respect to (a) effectiveness in detecting cracks, pitting, inclusions, and voids, (b) effectiveness in characterizing detected flaws, (c) adaptability to tube geometry, (d) adaptability to in-service inspection, (e) reliability, and (f) extent of development required for commercialization.

INTRODUCTION

The production of reliable and long-lived structural ceramic components depends on the development of effective nondestructive evaluation (NDE) techniques. Since structural ceramics such as silicon carbide and silicon nitride have a critical flaw size an order of magnitude smaller than that of metals (e.g., on the order of 100 μm for silicon carbide), NDE methods that are adequate for metals may not be appropriate for ceramic materials. This paper describes an Argonne National Laboratory-Materials Science Division program to assess the effectiveness of various NDE methods applicable to silicon carbide heat-exchanger tubes, develop promising techniques, and establish a strategy for tube inspection. The techniques currently under evaluation include conventional ultrasonic testing, dye-enhanced radiograph, acoustic microscopy, infrared scanning (IR), and holographic interferometry. (The latter three techniques can also measure elastic properties, thermal conductivity and stress-intensity factors, respectively.) Techniques previously evaluated but no longer under study include acoustic impact testing, acoustic emission and internal friction. These techniques, although useful for evaluating the overall quality of components, have not been found practical for detecting very small defects. Overload proof testing has also been considered as an NDE method; however, this technique is very expensive and time-consuming and does not necessarily reproduce stresses encountered in the field environment. References 1-4 describe other techniques applicable to silicon carbide.

The tube specimens investigated in the present study were fabricated from siliconized, sintered and chemical-vapor-deposited (CVD) silicon carbide. (As will be shown later, the variation in microstructure among these three types of silicon carbide affects the sensitivity of ultrasonic inspection techniques. The tubes, obtained from Carborundum, Norton and Materials Technology Corporation

(MTC), are approximately 200 mm in length and 25 mm in diameter and have wall thicknesses ranging from 1 to 3 mm. The flaws sought were cracks, inclusions, voids and free silicon. Several of the techniques are discussed below and compared for effectiveness in detecting flaws.

DYE-ENHANCED RADIOGRAPHY

The dye-enhanced radiographic method is based on the filling of surface defects with a substance that will absorb penetrating radiation more effectively than the base material. Thus, surface defects, such as cracks and pitting, which are not generally revealed by ordinary radiography may become detectable when a dye is present. Dye enhancement has been most successfully used in conjunction with neutron radiography.⁵ However, x-radiography is a more convenient technique. For x-radiography, the most effective doping agent found in the present investigation was a solution of silver nitrate and water (equal parts by weight). Figure 1 shows the ratio of mass absorption coefficients for silver nitrate and silicon nitride as a function of x-ray energy and wavelength. Silver nitrate absorbs x-rays approximately 20 times more strongly than silicon nitride; the ratio for silver nitrate and silicon carbide is similar. The absorption edge for silver results in a peak in the ratio of mass absorption coefficients at an energy of about 25 keV. The best contrast for silicon carbide was obtained at an x-ray energy of about 50 keV. The results obtained with a CVD silicon carbide tube approximately 1 mm thick, examined by radiography and subsequent metallographic sectioning, are typical. The largest crack (50 through the wall) found after sectioning was revealed by ordinary radiography, but four other cracks were revealed only by dye-enhanced radiography. Since good photographic reproductions of these radiographs were not obtainable, a similar result obtained from a cracked Plexiglass rod x-rayed with and without silver nitrate penetrant is shown in Fig. 2. The x-ray with the doping agent clearly shows numerous cracks that are not otherwise visible.

This technique has also been used to reveal dents in hot-pressed silicon carbide bars. For example, a dent 25 μm and 700 μm across was not indicated in conventional radiographs; however,

*Work supported by the U.S. Department of Energy

**Illinois Institute of Technology, Chicago, IL 60616

[†]Sonoscan, Inc., Bensenville, IL 60106

when filled with the silver nitrate doping agent, it was clearly seen by radiography.

HOLOGRAPHIC INTERFEROMETRY

The specific objective of the holographic interferometry effort is to assess the applicability of this technique to the detection of cracks in ceramic heat-exchanger tubing. Figure 3 shows a schematic representation of the optical system. Lens techniques are utilized to facilitate the application of double-beam holography and to allow for reconstruction with a less coherent source when a reduction of the speckle noise is needed.

1. Thermal Stress - The introduction of a temperature gradient can produce very high stresses on a tube. Heat-exchanger tubes were subjected to thermal gradients by means of a linear heating element located in the center of the tube, producing cracks. The outer-wall temperature was measured with a thermistor. Discontinuities in the interference pattern, produced by the cracks, were observed in real time and photographed. Examples are shown in Figs. 4 and 5. Figure 5 is particularly interesting because although the saw-cut crack is very shallow, the discontinuity produced by the presence of the crack is clearly visible in the fringe system.

2. Method for Obtaining the Stress-intensity Factor from the Interference Pattern - No rigorous solution exists for a stress-intensity factor associated with a surface crack on a cylinder, which is subjected to a 3-D state of stress. However, an approximate solution may be derived as follows: If the v -displacement field is projected on a plane tangent to the cylinder, the displacement field parallel to the tube axis is given by

$$v = \frac{K_1}{G} \sqrt{\frac{r}{2\pi}} (2 - 2\nu) \sin \frac{\theta}{2}, \quad (1)$$

where r is the distance from the crack tip, K_1 is the stress-intensity factor, G is the shear modulus, ν is Poisson's ratio, and θ is the angle with the tube axis. From the holographic moiré pattern obtained by pressurizing the tube, we can obtain the displacement and the distance from the crack tip, and thus K_1 . For example, if the displacement field is represented by Eq. 1, the fringe orders in the y -direction (perpendicular to the crack plane) should vary with \sqrt{r} ; consequently, in a log-log plot, the fringe orders should plot as straight lines with a slope of 0.5. By inserting the appropriate values in Eq. 1, we obtain

$$v = 0.0243 \sqrt{r} K_1 \times 10^{-4} \quad (2)$$

or

$$K_1 = \frac{41.09v}{\sqrt{r}} \times 10^4 \quad (3)$$

From a given order in the hologram, r and v are determined and thus K_1 .

INFRARED SCANNING

This program evaluated the use of thermographic techniques to detect flaws and measure heat-transport properties in silicon carbide heat-exchanger tubing. In these investigations, the

tubing (sprayed with graphite to ensure uniform emissivity) was heated at one end and simultaneously monitored with an IR camera to record temperature distributions due to axial heat flow. Computer modeling was used to help interpret the results, and thermocouples were placed on the silicon carbide tubes to establish the accuracy of quantitative IR scanning data.

1. Computer Modeling - A solution of the heat-conduction equation was used in a model for axial heat flow to aid in interpreting temperature-distribution data in silicon carbide tubing. Assume the tubes are finite rods of length L , and their initial temperature distribution is $f(x)$. If there is no flow of heat at $x = L$, and the temperature (as a function of time) at $x = 0$ is $\theta_2(t)$, the temperature distribution along the tube is given by⁶

$$T(x,t) = \frac{2}{L} \sum_{n=0}^{\infty} e^{-t(\nu + \beta_n^2)} \cos(\beta_n x) \left\{ \beta_n (-1)^n + \int_0^t e^{-(\nu + \beta_n^2)\lambda} \theta_2(t) d\lambda \right\} + \int_0^L f(x') \cos(\beta_n x') dx' \quad (5)$$

where $\beta_n = (2n + 1)\pi/2L$, $\nu = K/\rho c$ (thermal diffusivity), $\rho = H\rho/cw$, room temperature is taken as the zero point, K is the thermal conductivity, p is the circumference, c is the specific heat, H is the coefficient of heat transfer, ρ is the density, and w is the cross-sectional area of the rod.

Assume the rod is initially at room temperature (therefore $f(x) = 0$ for all x), and after immersion of the end of the tube in a water bath, $\theta_2(t) = T_b$ (the bath temperature). Then for all $t \geq 0$, we get

$$T(x,t) = \frac{2}{L} \sum_{n=0}^{\infty} e^{-t(\nu + \beta_n^2)} \cos(\beta_n x) \left\{ \beta_n (-1)^n \int_0^t T_b e^{-(\nu + \beta_n^2)\lambda} d\lambda \right\} \quad (6)$$

After we evaluate the integral and simplify, the temperature distribution becomes

$$T(x,t) = \frac{2T_b}{L} \sum_{n=0}^{\infty} \frac{\beta_n (-1)^n}{\nu + \beta_n^2} \cos(\beta_n x) \left[1 - e^{-t(\nu + \beta_n^2)} \right] \quad (7)$$

Equation (7) is valid for all $t \geq 0$ and for all x where $0 \leq x \leq L$.

Two computer programs were written to evaluate Eq. (7). The first one calculated temperature vs position, along the rod as a function of time with various values of the thermal constants k and α . The significant parameter was the thermal conductivity. As an example, when one end of the tube is at $\sim 60^\circ\text{C}$, a 10% variation in the thermal conductivity results in a change in the tube temperature (as a function of position) of up to 1.5°C during heating and 0.8°C after equilibrium is reached at $\sim 50^\circ\text{C}$. The curves allow prediction of ΔT , the difference in temperature between equivalent points on two different rods. The other program calculated temperature vs time as a function of position along the rod for various thermal-conductivity values. Here again, with all other parameters unchanged, a 10% variation in the thermal conductivity resulted in a temperature variation of up to 1.5°C during heating and 0.8°C after equilibrium was reached. The experimental data may be compared directly with the calculated curves. A combination of the results allows the prediction of $\Delta T(\Delta x)$, the difference in temperature between two points on the same rod, as a function of time.

2. Experimental Measurements - Axial heat flow was examined in samples of silicon carbide heat-exchanger tubing to determine whether flaws in the tubes could be detected and to compare the thermal properties of different tubes. The experimental apparatus is shown in Fig. 6. Water flows into the basin and circulates freely to maintain a uniform temperature. A Styrofoam block holds the tubes in an upright position, with one end of each tube immersed in the water bath to a depth of ~ 3 cm. This allows simultaneous comparison of the temperature distributions produced by axial heat flow in several tubes. Data were obtained by making thermograms with an AGA Thermovision 750 IR camera, which is capable of resolving temperature differences of 0.2°C , and reading isotherm units from the color IR monitor. When quantitative measurements were made using the isotherm controls, a thermometer, with the mercury bulb sprayed with graphite, was heated with a heat gun to provide a reference temperature. Figure 7 shows a typical thermogram (initially in color) of the transient temperature distribution during axial heat flow. The different colors can be related to the surface temperature. As shown in Fig. 7, each tube had a unique heating rate. The temperature distribution in tube 4, which was severely cracked by thermal quenching, differs markedly from that of tube 3, which was not cracked. (Before tube 4 was cracked, the temperature distribution patterns in the two tubes were similar.) To examine the differential heating of the tubes more thoroughly, a series of thermograms were made with the tubes in different sequences. It was found that the Norton NC430 tubes always conducted heat better than the Carborundum Super KT tubes. To estimate the actual temperature differences between the tubes, ΔT (tube), the scale on the left side of the thermogram in Fig. 7 was divided into 10 isotherm steps, each represented by a different color. The calibration curve for isotherm units vs temperature is linear in the 30 - 50°C temperature region. This implies that the color scale in the thermogram covers a 2°C temperature range. Analysis of Fig. 7 indicates that the NC430 tubes are $\sim 1^\circ\text{C}$ hotter at midheight than the KT tubes. According to data supplied by the manufacturers, the thermal conduc-

tivity of the NC430 tubing is 10% greater than that of KT. For tubes differing by this amount in thermal conductivity, Eq. (7) predicts an average temperature difference of $\sim 1^\circ\text{C}$ during heating. Thus, the data are in reasonable agreement with the model prediction.

Three thermocouples were attached to tube 1 to obtain temperature-vs-time data at specific points along the tube. One thermocouple was attached to the top of the tube and the others 7.3 and 12.4 cm below the top using Hysol K20 conductive epoxy cement. Quantitative measurements made with the IR camera were compared with the thermocouple data as well as with the computer-model predictions to determine the adequacy of the IR camera in measuring temperature gradients. Figure 8 shows a plot of $\Delta T(\Delta x)$ for the top and middle thermocouples as a function of time. There was fair agreement among the computer-model predictions, the IR data, and the thermocouple data for elapsed times of 60-250 s. For example, the value of $\Delta T(\Delta x)$, according to the thermocouples, is 3.8°C at 120 s. The IR data gave a value of 2.2°C and the computer model predicted a value of 3.3°C . However, as shown in Fig. 8, the IR scanning data show consistently smaller ΔTs than the thermocouple and computer-modeling predictions. This can be attributed to inaccuracies in reading the calibration curves and the isotherm marker scale. The deviations from the model predictions for $t < 60$ s and $t > 250$ s are probably due to the inadequacy of approximating a hollow tube as a small-diameter rod and the difficulty in accounting for convective cooling (i.e., accurately determining h).

INSPECTION OF SiC TUBES WITH AN ULTRASONIC BORE-SIDE PROBE

Efforts are underway to develop a bore-side ultrasonic probe for silicon carbide tubes. The conceptual design for the ultrasonic interrogation of straight tubes is shown in Fig. 9. A transducer frequency higher than that conventionally used for metal tubes is chosen in order that flaws as small as ~ 100 μm can be resolved. The transducer is oriented parallel to the water-filled tube to generate waves axially down the tube. An acoustic mirror is placed below the probe to deflect the longitudinal beam to the wall for detection of wall thinning or delaminations. For crack detection, the angle of incidence is adjusted so that longitudinal waves incident on the inner surface are mode converted to shear waves traveling axially down the tube. The beam would have to be offset about 1 mm to generate circumferential shear waves. In all cases, a motor rotates the mirror so that a 360° scan can be made at each axial location. It is anticipated that the axial motion of the probe will be controlled by a microprocessor and stepping motor and that data on signal amplitude versus position in the tube will be stored and displayed via a computer. In Fig. 10, the resolution achievable by the scheme described above is shown for longitudinal waves. Figure 10a shows the radio-frequency inner-wall reflection and backwall echo seen when a 20-MHz, 1/8-in.-diameter probe is used from the bore side with a 45° reflector. An "impulse"-type initial pulse is used. With a "tuned" initial pulse (Fig. 10b) and a different pulser-receiver used in the video-output mode, many more echos can be seen. The latter scheme may be more sensitive than the former for locating defects. The evalu-

uation of these two systems is continuing.

Electric-discharge-machined reference notches were made in a sintered silicon carbide tube. The tube was radiographed to confirm the notch size and depth, and was then interrogated ultrasonically from the outside to estimate the sensitivity of this inspection method. A 20-MHz, 6-mm-dia transducer and Sonic Mark III pulser-receiver were employed. The large notches (50 x 250 μ m deep) were clearly evident in the video mode; the smaller notches (250 x 125 μ m) could also be resolved, but not as readily. Searching for the notches from the OD is hampered by the curvature of the tube, which results in a defocussing of the beam as it passes through the wall. When the tube is inspected ultrasonically from the bore side, however, the opposite occurs; the refraction tends to focus the beam.

ACOUSTIC MICROSCOPY

1. Effect of Microstructure - Several types of silicon carbide samples with different microstructures were interrogated, employing through-transmission acoustic microscopy techniques. Hot-pressed, sintered, siliconized, and CVD samples were examined. The effect of the variation in microstructure on the acoustic-microscopy results is discussed below.

Two types of siliconized tubes (Norton NC430 and Carborundum KT) were electrolytically etched in the solution described in Ref. 7 to reveal the microstructural differences between them. Figure 11a shows an etched sample of CVD silicon carbide tubing supplied by MTC, with grains up to 50 μ m in size and some porosity. The KT material (Fig. 11b) has small grains, with a maximum size of \sim 20 μ m. NC430 (Fig. 11c) has a bimodal distribution of grain sizes, with a maximum size of \sim 100 μ m. The light areas seen in both materials are free silicon. Figures 12a and b show optical micrographs of hot-pressed (Norton) and sintered (Carborundum) silicon carbide samples, respectively. Pores (dark areas), generally less than 10 μ m in size, are more prevalent in the sintered material.

Acoustic micrographs of two siliconized silicon carbide tube samples (NC430 and SKT) and one CVD sample are shown in Fig. 13. The NC430 material (Fig. 13a) shows higher levels of acoustic noise than the smaller-grained SKT material (Fig. 13b), despite the fact that the SKT sample is thicker (3 vs 1 mm). The lines in the latter micrograph are curved because of the curvature of the sample. The 1-mm-thick CVD specimen (Fig. 13c) has a higher acoustic noise level than either siliconized specimen. Figure 14 shows acoustic micrographs of a 6-mm-thick bar of hot-pressed silicon carbide and a 1-mm-thick tube section of sintered silicon carbide. Although it is much thinner, the sintered specimen (Fig. 14b) is acoustically much noisier than the less porous hot-pressed specimen (Fig. 14a). However, the sintered specimen is less noisy than either of the siliconized samples (Figs. 13a and b). In summary, the hot-pressed SiC had the lowest level of acoustic noise of any of the materials examined and would be the easiest to inspect with through-transmission acoustic microscopy techniques, followed in increasing order of difficulty by the sintered, siliconized and CVD materials.

2. Defect Confirmation - This section discusses the localization, by destructive examination, of defects indicated by acoustic microscopy techniques. A piece of siliconized silicon carbide tubing (SKT), 25 mm in diameter with a 3-mm wall thickness, serves as an example. A flaw indication is evident in the acoustic micrograph of Fig. 15. Axial and radial radiographs of the intact tube section showed no flaw indications. The tube was cut down in size until an axial-view radiograph indicated a circumferential delamination about 1 mm across (in agreement with the acoustic-micrograph result) and approximately 0.3 mm below the surface. The sample was then ground down circumferentially to determine the axial length of the defect. Figure 16 shows the result. A delamination approximately 1.5 mm long was revealed, again in agreement with the acoustic-microscopy result.

As a result of the initial success in using the acoustic microscope to detect natural flaws in silicon carbide tube sections, a stage was developed to interface with the Sonoscan acoustic microscope so that a helical scan of a tube could be made. This stage is currently being evaluated.

COMPARISON OF TECHNIQUES

Clearly, there are many considerations in selecting an NDE technique for silicon carbide heat-exchanger tubes. One must consider the adaptability of the technique to the tube geometry, rate of inspection, applicability to in-service inspection, reliability, effectiveness of flaw detection and characterization and the development required for commercial use of the technique. Table I summarizes the results to date of the present investigation, in terms of these criteria. Table II gives the estimated sensitivities of some of the methods under ideal laboratory conditions. Among the techniques investigated, acoustic microscopy has been shown to be the most sensitive for detecting defects in silicon carbide tubing; this technique can also reveal the character of the defect. A surface defect of 100 μ m long and 50 μ m deep in a silicon carbide bar has been revealed by holographic interferometry techniques, using a 4-point bending fixture. The sensitivity of radiography has been improved through the use of dye-enhancement techniques. Infrared scanning has been shown to be useful for detecting variations in heat-transport properties, and conventional ultrasonic testing has been shown to be capable of detecting reflectors on the order of 100 μ m in size using frequencies of 20 MHz or possibly higher, which are well above the frequencies normally used for metal tubes. At this time, the three most useful techniques for NDE of silicon carbide tubes appear to be acoustic microscopy, conventional ultrasonic testing from the bore side, and dye-enhanced radiography.

REFERENCES

1. A.G. Evans, G.S. Kino, P.T. Khuri-Yakub and B.R. Tittman, "Failure Prediction in Structural Ceramics," Mater. Eval. 35 (4), 85 (April 1977).
2. A.J. Bahr, "Microwave Techniques for Non-destructive Evaluation of Ceramics," Final Report AMMRC-CTR-77-29, SRI International, Menlo Park, CA (Nov. 1977).
3. B.T. Khuri-Yakub, "Acoustic Surface Wave Scattering: The Detection of Surface Cracks in Ceramics," Report SC5064-2TR, Rockwell International Science Center, Thousand Oaks, CA (Dec. 1977).
4. Y.H. Wong and R.L. Thomas, "Laser Photo-acoustic Techniques for NDE," presented at the ARPA/AFML Review of Progress in Quantitative NDE, Scripps Institution of Oceanography, La Jolla, CA, July 17-21, 1978.
5. H. Berger, "Practical Applications of Neutron Radiography and Gauging," ASTM Special Technical Publication 586, American Society for Testing and Materials, Philadelphia (1975).
6. V.S. Arpaci, Conduction Heat Transfer, Addison/Wesley, Reading, MA (1966) p. 51.
7. G.W. Robinson and R.E. Gardner, "Ceramographic Preparation of Silicon Carbide," J. Am. Ceram. Soc. 47 (4) (April 1964).

Table I. Comparison of Several NDE Techniques for Flaw Detection in Silicon Carbide Heat-exchanger Tubing^a

Method	Relative Effectiveness for Flaw Detection										Relative Rate at Which Tubes Could Be Inspected		
	Surface						Effectiveness for Characterization of Detected Flaws	Adaptability to Tube Geometry	Adaptability to Preservice Examination	Adaptability to In-service Examination		Relative to Conventional Technique	Extent of Development Required for Commercialization
	Cracks	Pitting	OD	Subsurface Inclusions	Voids								
Acoustic Microscopy	G ^b	E	G	E	G/A	E	E	F	G	P	GA	high	slow
Dye-enhanced Radiography	G	G	G	G		G	G	G	E	E	G	some	slow
Conventional Radiography	F	F	G	G	G	G	G	G	E	P	G	some	slow
Conventional Ultrasonic Testing	G	G	G	G	G	G	F	F/A	E	G	G	some	fast
Overload Proof Testing	G	G	P	P	P	P	P	P	P	P	F	some	fast
Holographic Interferometry	P	G/A	P/A	P/P		E	F/A	G	G	F	E	very high	fast
Infrared Scanning	P	P	P	P	P	P	P	E	F	G	G	some	fast
effective measure of heat transport properties													
Internal friction Measurement	F	F	P	P	P	P	P	P	P	P	P	very high	slow
Fluorescent Dye Penetrant Testing	G		G			F	F	E	E	P	G/A	none	slow

^aFor tubes with wall thickness > 1 mm.
^bGA = excellent, G = good, F = fair, P = poor, - = not applicable

Table II. Estimated Sensitivity of NDE Methods for Flaw Detection in Silicon Carbide Heat-exchanger Tubing

Technique	Smallest Anomalies Detectable
Acoustic Microscopy	Flaws $\leq 100 \mu\text{m}$ long
Holographic Interferometry	Flaws $\sim 100 \mu\text{m}$ long (with lens techniques)
Dye-enhanced Radiography	Surface flaws with depth = 0.5λ t
Infrared Scanning	2% variation in thermal conductivity
Conventional UT	Surface flaws $\sim 100 \mu\text{m}$ deep

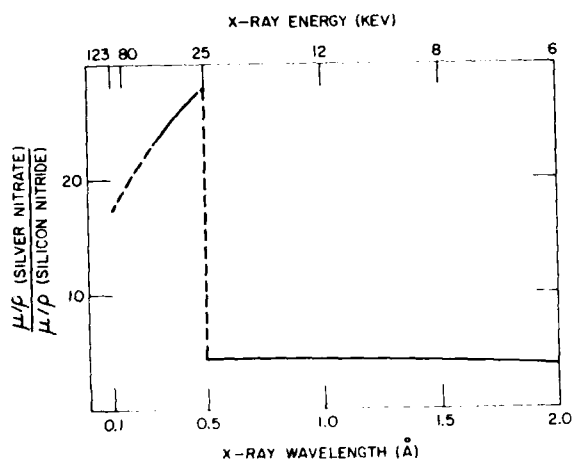


Fig. 1. Ratio of Mass Absorption Coefficients for Silver Nitrate and Silicon Nitride.



Fig. 2. Cracked Plexiglass Rod Radiographed Without and With Dye Enhancement.

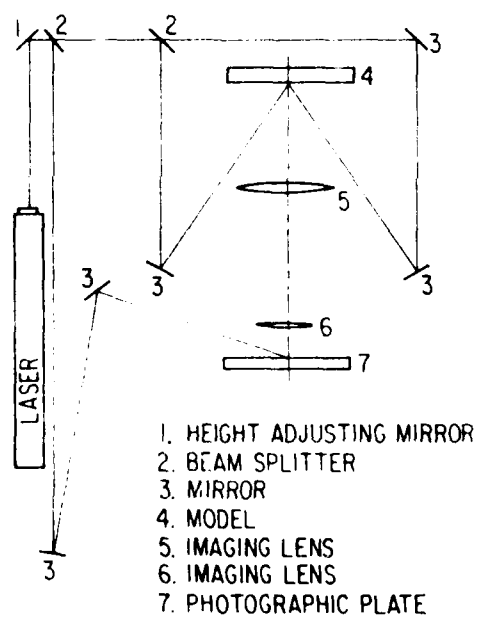


Fig. 3. Schematic Representation of Holographic Interferometry System.

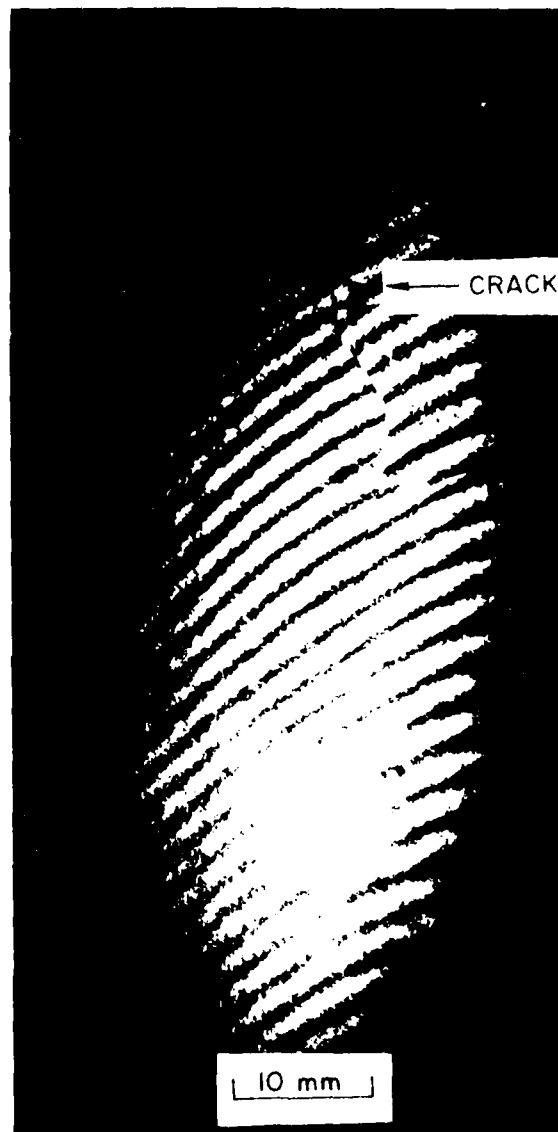


Fig. 4. Holographic Interferogram of Silicon Carbide Tube Showing Crack.

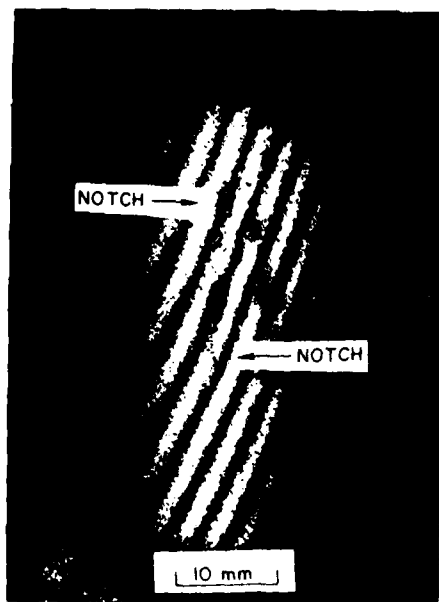


Fig. 5. Holographic Interferogram of Silicon Carbide Tube Showing Saw Cut (maximum depth 500 μ m).

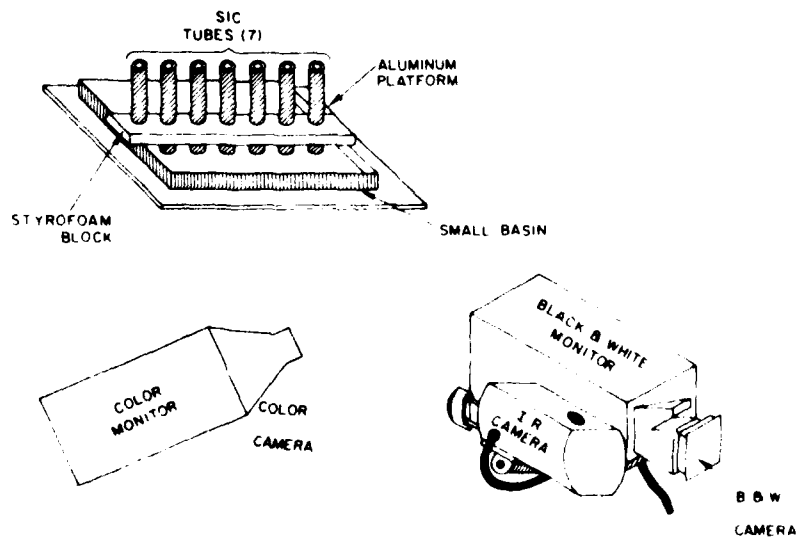


Fig. 6. Schematic of Infrared Scanning Apparatus

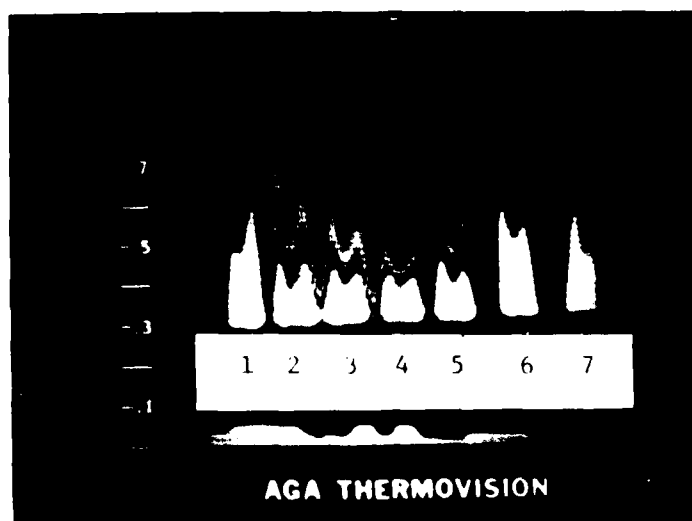


Fig. 7. Thermogram of Silicon Carbide Heat-exchanger Tubes. Tubes 1, 6 and 7 are Norton NC430; The others are Carborundum KT. Tube 4 was cracked by thermal quenching.

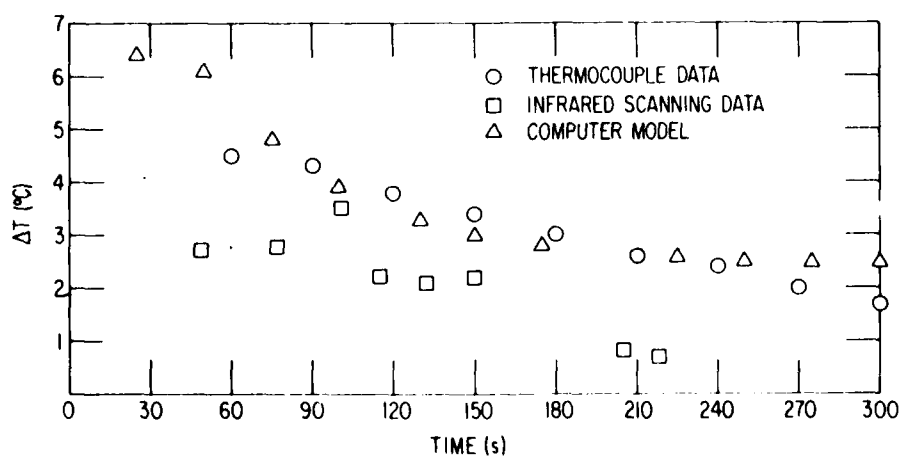


Fig. 8. Plot of $\Delta T(\Delta X)$ vs Time for Top and Middle Thermocouples, IR Data and Computer Model.

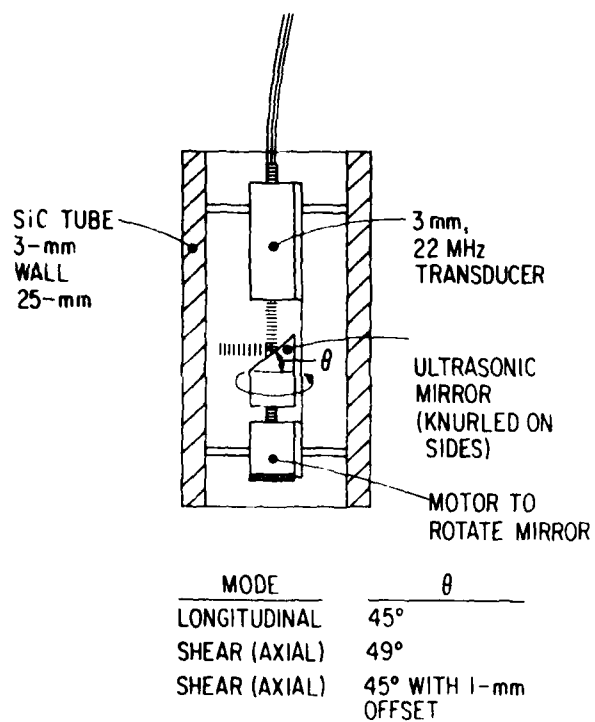


Fig. 9. Conceptual Design for Ultrasonic Bore-side Inspection of Silicon Carbide Tubes.

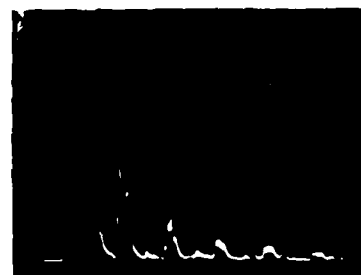
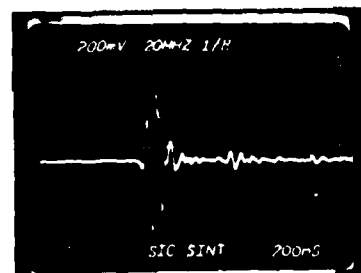


Fig. 10. Resolution of Normal-incidence longitudinal waves (20 MHz) from the bore side of a Silicon Carbide tube with a 3-mm wall thickness. (a) Radio-frequency signal, (b) video output.

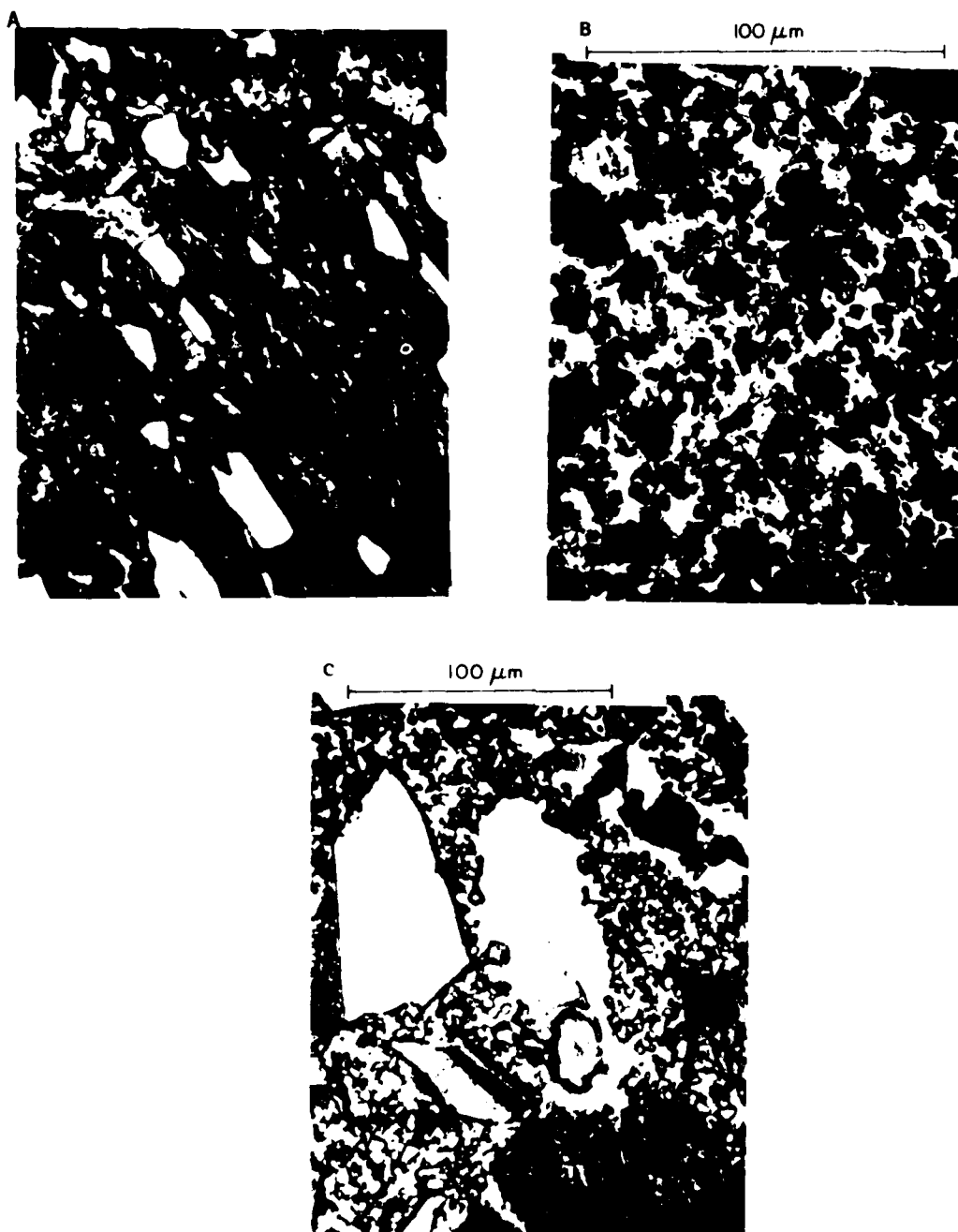


Fig. 11. Optical Micrographs of (a) CVD (Materials Technology Corporation), (b) Siliconized (Carborundum KT), and (c) Siliconized (Norton NC430) Silicon Carbide.



Fig. 12. Optical Micrographs of (a) Hot-pressed and (b) Sintered Silicon Carbide.

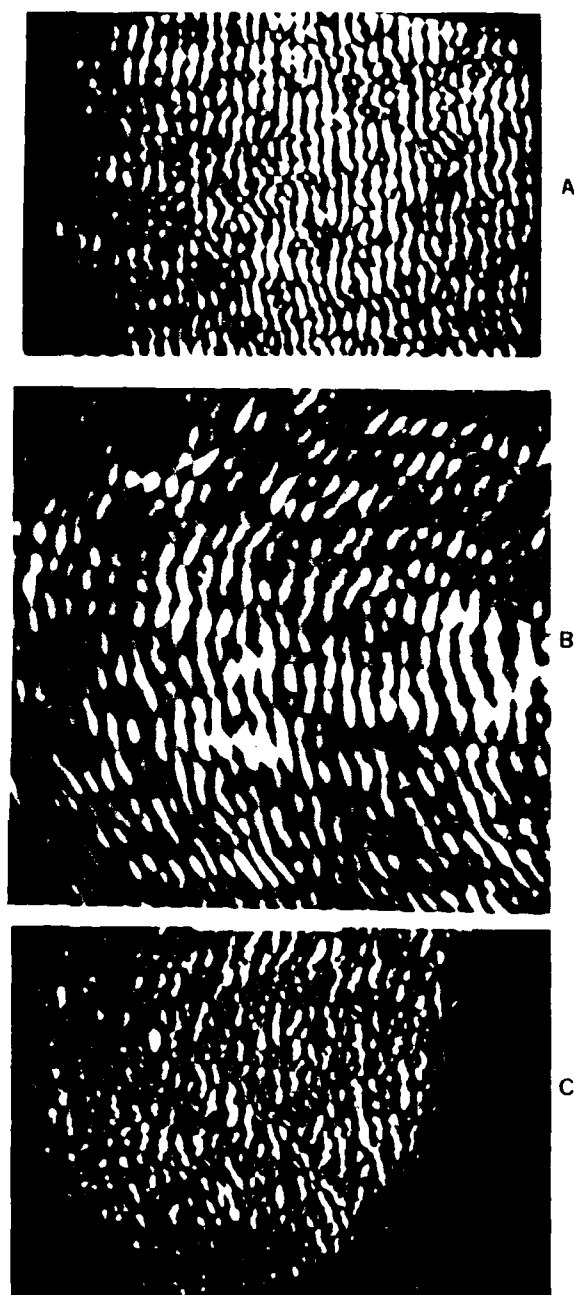
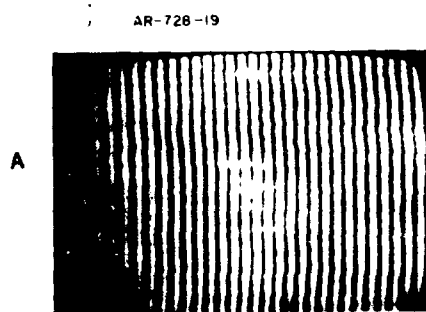


Fig. 13. Acoustic Micrographs of (a) Norton NC430, (b) Carborundum SKT, and (c) CVD Silicon Carbide.



SR2-26

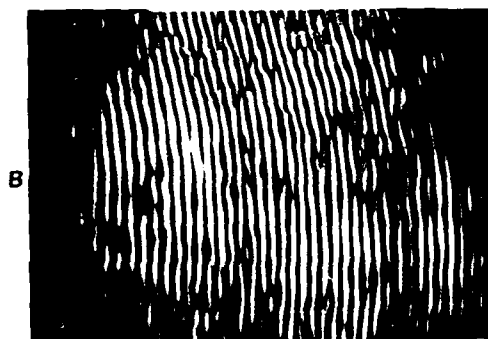


Fig. 14. Acoustic Micrograph of (a) Hot-pressed and (b) Sintered Silicon Carbide. Area shown is $\sim 3 \times 2$ mm

KPII-19



Fig. 15. Acoustic Micrograph of SKT Tubing Showing Flaw. Area shown is $\sim 3 \times 2$ mm.



Fig. 16. Destructive Examination Results Showing Defect Seen by Acoustic Microscopy in Fig. 15. Length of defect is ~ 1.5 mm.

CHARACTERIZATION OF DEFECTS AND HETEROGENEITIES IN SILICON NITRIDE AND SILICON CARBIDE
BY DIFFERENT NDE METHODS

K. Goebbels, H. Reiter
Fraunhofer-Institut für zerstörungsfreie Prüfverfahren
D-6600 Saarbrücken 11, Germany

ABSTRACT

The brittleness of ceramic materials like silicon nitride and silicon carbide makes it necessary to fabricate homogeneous structures and to detect small defects in the region of 10 to 100 microns diameter. In the German program on NDE for the gas turbine therefore a study was made to compare different NDE methods and to develop new techniques. Tests were made with ultrasonics, microradiography, vibration analysis, acoustic emission and optical-holographical interferometry on test samples and real components of the gas turbine (rotor, stator, combustor). The results show that especially

- microradiography with projection technique and X-ray focus of $\approx 10 \mu\text{m}$ diameter.
- ultrasonics with different kind of transducers, equipment and wave modes in the frequency range until about 150 MHz

are well suited to detect the small defects and to characterize structure heterogeneities.

- Vibration analysis seems to be a good method to compare many samples of the same kind and to detect scatter of the fabrication process data.

The comparison between UT, vibration analysis, acoustic emission and destructive tests (fracture strength) indicates that there are more or less correlations between NDE and the destructive analysis.

INTRODUCTION

Two problems have to be solved according to the nondestructive evaluation of ceramics like Si_3N_4 and SiC for gas turbine components: characterization of materials structure (i.e. description of homogeneity, analysis of heterogeneities) and detection of smallest defects (dimensions $< 10 \mu\text{m}$ for surface regions, $\geq 10 \mu\text{m}$ below the surface). Two methods primarily are suited to solve these problems: high frequency ultrasonic waves and microfocus radiography. Both will be discussed in detail below. Several other methods were studied in the German program for the NDE of ceramics. From these the vibration analysis (determination of the main resonance frequency) seems to be the best way to characterize by an integral way a lot of components with the same geometry (e.g. turbine blades). In Fig. 1 two series of one hundred 4-point-bending-test specimens (RBSN) were analyzed by ultrasonic longitudinal wave velocity (v_L) measurements and the resonance frequency (measured parameter: $2T$ = two wavelengths in the free domain). It is easily to see that for the second series the fabrication process resulted in a more uniform structure than for the first series, for the first series the measurements were completed by shear wave velocity (v_T) measurements, density (ρ) measurements and acoustic emission during the destructive strength (σ_B) determination (4-point-bending fracture). The correlation between these data and derivations is shown in Fig. 2. Drawing the data in a row with increasing fracture strength shows the result to be expected: there is no clear correlation. But with further analysis of these data a linear regression analysis points out that with increasing strength the Poisson ratio ν and the wavelength of resonance vibration λ are decreasing while the ultrasonic wave velocities v_L ,

v_T and the elastic modulus E are increasing, too. We think that this should be analysed further in new experimental series. For the acoustic emission measurement (by Motoren-Turbinen-Union, Munich) no significant results could be obtained. Additional destructive tests together with acoustic emission energy measurements on 50 RBSN specimens with and without Knoop-indented microcracks did not show any promising results.

Studies with optical-holographical interferometry from homogeneous and inhomogeneous (microcracks) RBSN samples were able to distinguish between the types of specimens (Institute for Applied Ray Technique, Bremen) but the ultrasonic and radiographic detection and location of the defects were more effective [1].

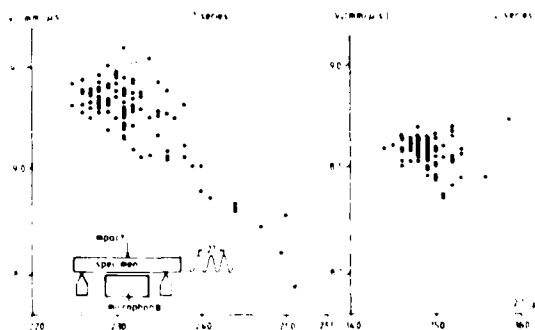


Fig. 1 Longitudinal wave velocity and vibration analysis of two series of 4-point-bending-test specimens from RBSN

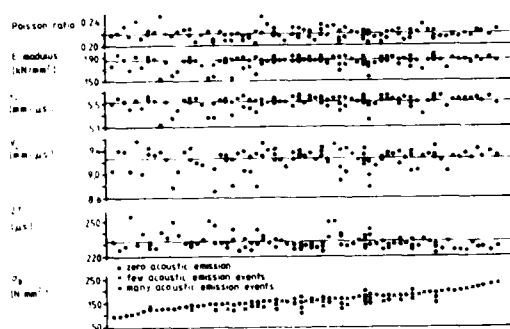


Fig. 2 Analysis of 100 RBSN 4-point-bending-test specimens with ultrasonic waves, vibration analysis, acoustic emission in correlation to the fracture strength.

ULTRASONICS

Structure heterogeneities can be detected with ultrasonic attenuation, scattering and velocity measurements. Because of the high accuracy of velocity determinations - e.g. by pulse-echo-overlap techniques - they were used for the analysis of many turbine components and samples of hot pressed and reaction bonded silicon carbide and silicon nitride [1/]. In Fig. 3 two pictures are reproduced from a HPSN disc with 36 mm thickness and 136 mm diameter. In the outer region residual stresses could be detected with 5 MHz polarized shear waves (Fig. 3 above): double reflection arising for two directions of vibration (45° to the radial direction) and vanishing for the other two (radial and tangential) is a strong reference to residual stresses in circumferential orientation. The quantitative stress determination needs the knowledge of the elastic higher order constants l, m, n [2/]. The inner region of the disc shows a sharp boundary of change of density (Fig. 3 below): three high damped backwall echoes (10 MHz longitudinal waves) followed by 20 μ s without any echo and then many echoes created by a sequence of mode conversion processes are obtained if the pulse-echo transducer position is exactly on the boundary region.

Single defects generally are easier to detect with high frequency ultrasonic waves [2,4/] than with low frequencies. In special cases low frequencies can be used, too. Figure 4 shows the detection of small saw cuts (width 150 μ m) of different depths with 17 MHz shear waves. The 6 μ m cut also can be resolved with the 300 μ m wavelength. In Fig. 5 natural surface defects in turbine blades are analysed with 8 MHz Rayleigh waves: the amplitude of the signal reflected at the rotor ring is a measure for the influence of the defects on the wave propagation. For high frequency ultrasonic waves (10 MHz to > 100 MHz) a new technique was adopted, recommended by Arnold [5/]. LiTaO_3 single crystals ($\rho = 7.5 \text{ g/cm}^3$, $v_l = 5.5 \text{ mm/\mu s}$, 5 mm diameter, 10 mm length) excited with high frequency bursts (cf. Fig. 6) can be used for a wide frequency region. The piezoelectric crystals do not need any evaporated

thin films of metallic (e.g. Au) and piezoelectric (e.g. CdS) materials. Frequency and pulse width are given by the electric excitation. Figure 6 shows (left) more than 600 backwall echoes for $\approx 90 \text{ MHz}$ and the first backwall echo followed by three backwall echoes from a 3.5 mm thick HPSN bending test specimen (right) for 20 MHz.



5 MHz shear waves, 20 μ s



10 MHz longitudinal waves, 10 μ s

Fig. 3 Detection of residual stresses (above) and inhomogeneity regions (below) with 5 MHz shear and 10 MHz longitudinal waves, respectively in a disc of HPSN.

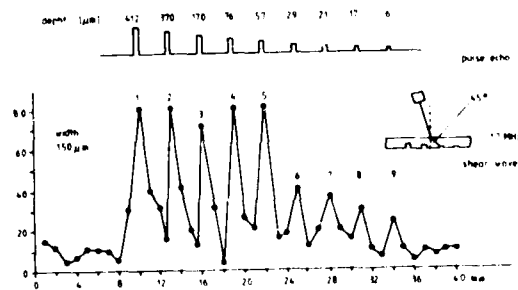


Fig. 4 Detection of 150 μ m width slots of different depths in RBSN with 17 MHz shear waves

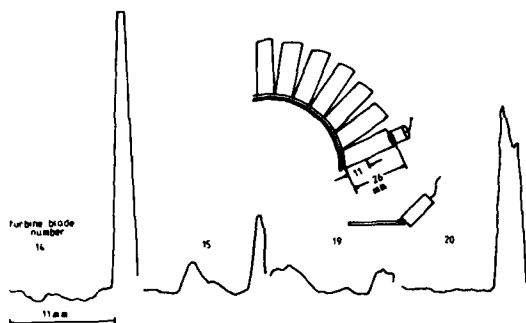


Fig. 5 Detection of surface defects in turbine blades with 8 MHz Rayleigh waves.

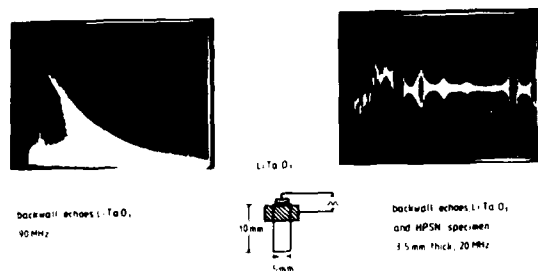


Fig. 6 High frequency ultrasonic waves from a LiTaO₃-transducer (5 mm diameter, 10 mm length). Left: backwall echoes for 90 MHz. Right: backwall echoes from 3.5 mm thick 4-point-bending-test specimen of HPSN (20 MHz).

MICRORADIOGRAPHY

Microfocus X-ray units enable the imaging of greater sample areas ($\approx 25 \times 25 \text{ mm}^2$), for curved shapes, too, with microscopic resolution ($\approx 25 \text{ }\mu\text{m}$). The projection technique used (WARDRAY E12 Unit, developed by the NDT Centre Harwell) is sketched in Fig. 7. Electrostatic focussing of the electron beam results in a $\approx 15 \text{ }\mu\text{m}$ diameter X-ray focus inside the tube. The specimen directly is attached at the window (distance to the focal spot $\approx 130 \text{ mm}$) while the film has a distance of several meters (2 - 3) to the specimen. The X-rays ($\leq 80 \text{ kV}$ Voltage, $\approx 0.5 \text{ mA}$ current) are propagating with a diverging beam of 18° . By separating the sample and film in projection radiography first a natural magnification of about $\times 10$ to $\times 20$ is achieved. Secondly a very significant 'clean up' in the microradiograph is effected because a very large fraction of the secondary radiation dissipates it-

self by attenuation before it reaches the film. Heterogeneities as well as single defects are reproduced on the film. The exposure time depending on the kind of film and the sample thickness lies between $< 1 \text{ sec}$ and $> 1 \text{ hour}$. Density variations in HPSN and HPSC are shown in Fig. 8a and Fig. 8b. The disc described in Fig. 3 is reproduced by microradiography in Fig. 9, showing clearly the inner inhomogeneous zone. The slots in RBSN ($150 \text{ }\mu\text{m}$ width) analysed with ultrasonic waves in Fig. 4 are imaged in Fig. 10. The resolution of the X-ray technique allows to see the $21 \text{ }\mu\text{m}$ slot. The smaller ones (17 and $6 \text{ }\mu\text{m}$ deep) cannot be resolved. Surface defects in original turbine blades (Fig. 5 for ultrasonic waves) and pores in an original stator are shown in Fig. 11a and Fig. 11b, respectively. Some seeded defects (inclusions of Fe and C) in HPSN and HPSC specimens are imaged in Fig. 12.

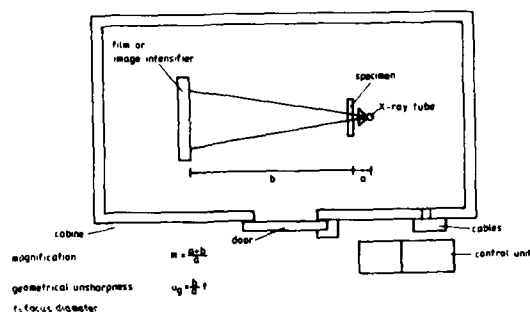


Fig. 7 Microfocus X-ray equipment with projection technique

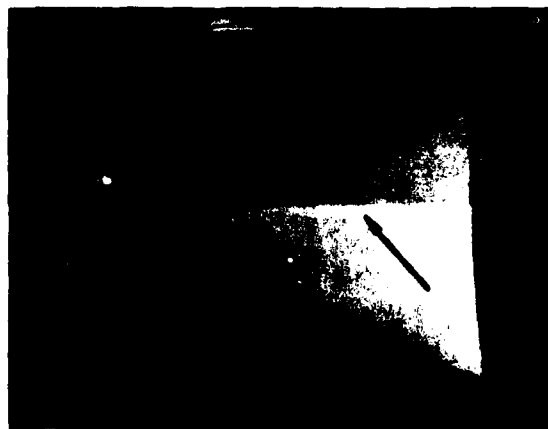


Fig. 8a Microradiography image of a HPSN specimen with density variation. Irradiated thickness: 9.5 mm.



Fig. 8b Microradiography image of a HPSC specimen with density variations. Irradiated thickness: 4 mm

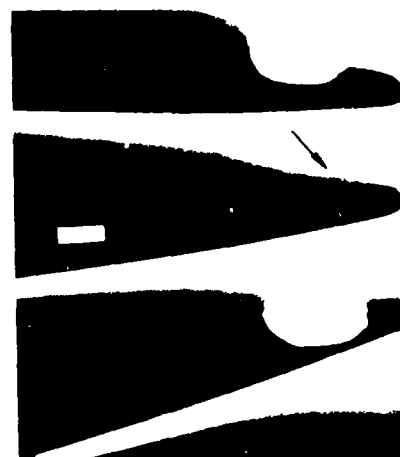


Fig. 11a Surface defects in RBSN turbine blades



Fig. 9 Microradiograph of a 36 mm thick HPSN disc with density variation.

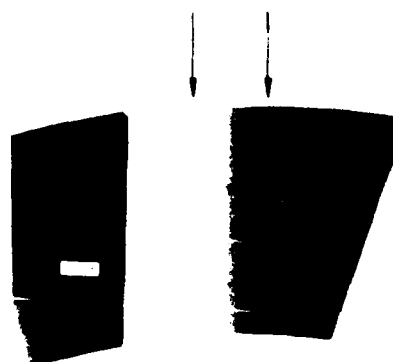


Fig. 11b Pores in a RBSN stator, diameter of the marked wire: 30 μ m



Fig. 10 Detection of 150 μ m width slots of different depths in 5 mm thick RBSN with microradiography. Greatest depth: 412 μ m, lowest depth detected: 21 μ m (cf. Fig. 4)

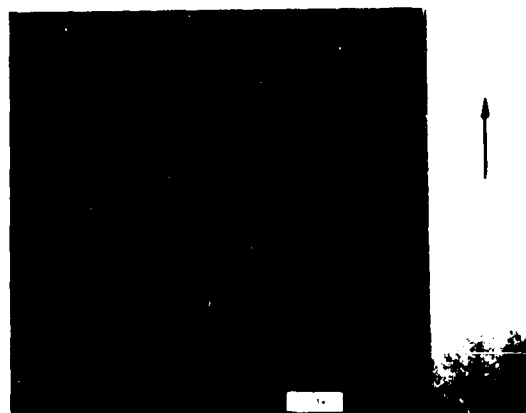


Fig. 12 Microradiographs of seeded defects in HPSN (Fe, C) and HPSC (Fe) (from left to right). Sample thickness = 3.5 mm.

DISCUSSION

For the analysis of structure heterogeneities and single defects in ceramics like Si_3N_4 and SiC different NDE methods are well suited. Original parts of the gas turbine (e.g. stator, rotor, combustor) with partly complicated shapes and varying thicknesses create difficulties for the application in practice. Ultrasonic free and guided waves and especially microfocus X-rays have advantages over other methods. At the moment the most advanced technique with at the same time high resolution and greater specimen volume analysed in a relatively short time seems to be the micro-radiography. High resolution image intensifier instead of films should enable an easier imaging of defect areas. Additionally, stereo-micro-radiography (with two photographs from two different positions) should enable to locate the defect inside the component.

Some advantages can be seen, too, for the characterization of the homogeneity of the fabrication process if lots of specimens are analysed with vibration measurements. For one of the most interesting points, the correlation between strength and NDE results, more experiments have to be done.

ACKNOWLEDGEMENTS

The work described above was done with financial support of the Bundesministerium für Forschung und Technologie. We have to thank all the companies which delivered the specimens and especially Mr. A. McLean (FORD) and Dr. E. Lenoir (AMMRC) for original turbine components and samples with seeded defects, respectively.

REFERENCES

- /1/ H. Reiter, K. Goebbels, W. Deuble:
ZfP von Hochtemperatur-Keramikbauteilen für
Kfz-Turbinen.
IzFP-Bericht Nr. 790204-TW, Saarbrücken 1979
- /2/ D.S. Hughes, J.L. Kelly: Physical Review 92
(1953) 1145-1149
- /3/ B.T. Khuri-Yakub, G.S. Kino: 1976 Ultrasonics
Symposium Proceedings IEEE, p. 564-566
- /4/ A.G. Evans, B.R. Tittmann, L. Ahlberg,
B.T. Khuri-Yakub, G.S. Kino:
J. Appl. Phys. 49 (1978) 2669-2679
- /5/ W. Arnold: private communication.

SUMMARY DISCUSSION
(K. Goebels)

John Schuldies (Airresearch): Could you comment on why you think vibrational resonance testing of a rod is better than just absolute velocity measurements?

Klaus Goebels: It is better. I think only it is easy if you have several hundred samples from the same propagation process from the same material out from the beginning, and then you are making easy impact testing and measurements, and if there are some samples that are lying outside the scatter of most of the data, I think that you can then take them away and concentrate further on the others.

John Schuldies: I guess the purpose of my comment was that you still got to make a translation later on from the test bar to the real piece. If so, if you came up with a means of velocity very accurately, you could immediately make that transition to the actual piece and confirm that the properties of the test bar are the same as the components that you are using. What was the reason for my comment.

#

PLANNING ACTIVITY REPORT FOR NDE OF ADHESIVE BONDED STRUCTURES

F.N. Kelley
University of Akron

W.G. Knauss
California Institute of Technology

D.H. Kaelble
Rockwell International Science Center

ABSTRACT

Following a workshop held at the Rockwell International Science Center, Thousand Oaks, California in January, 1979, an ad hoc planning activity was undertaken to set forth a program plan to address the needs in NDE for adhesive bonded structures. The objectives of the planning activity were to develop a program rationale and strategy, determine the existence of reasonable approaches, and to propose a detailed plan of action for review at the annual DARPA/AF meeting in September, 1979. The plan encompasses the basic elements of an accept/reject methodology based on fracture mechanics, expected developments of valid flaw growth models, stress analysis, and non-destructive measurement techniques. A central issue is the prospect for determining a valid non-destructive measure of strength for the bonded joint as might be reflected in the tendency for preexistent flaws to propagate under environmental loads.

I. PROGRAM SCOPE AND STRATEGY

This program plan is directed toward methods of establishing the reliability of adhesive bonds as may be employed in primary aircraft structures. Similar approaches may be inferred for fiber-reinforced resin matrix composites in particular instances where matrix-dominated failure modes and delaminations are involved. The central strategy for the plan is based on the concept that the structural design process for bonded joints must be well-established and validated in order that accept/reject decisions might be made from non-destructive measurements information. The plan is presented in the context of a decision methodology, characterized by a systems approach, which is expected to provide a useful framework regardless of the state of development of the various system elements. An essential prerequisite is the knowledge of primary failure initiating defects.

A search of field repair information reveals that a very high percentage of adhesive bond failures experienced on aircraft structures to date have been associated with local damage and intrusion of the environment (usually moisture). While the most experience has been gained on bonded aluminum honeycomb secondary structure, it may be reasonably assumed that damage and environmental intrusion may occur at the edges of bonded panels or more highly loaded primary structural joints. A note of caution which should be added on possible inferences from field experience concerns the more recent developments in pre-bonding surface preparations and their relationship to bond durability. Prior to the PABST^(6,7) program, limited information existed on newer surface treatments, such as phosphoric acid anodization, which promises vast improvements in durability. If future bonded joints incorporate these treatments, it is possible that the modes of joint failure may differ from those shown by prior field experience. In any case, flaws are likely to occur from a variety of sources and are likely to grow under operational loads.

Defects, as considered in this plan, are assumed to include a range of geometrical or bounded

defects such as cracks and inclusions, as well as boundaryless defects such as uncured or moistured-softened adhesives. The interaction of these "extrinsic" or bounded flaws with the "intrinsic" material state is often a necessary consideration in the use of failure models involving polymeric materials.

One of the more perplexing issues in the evaluation of bonded joint reliability is a determination of the relative importance of the interface between adherend and adhesive and the condition of the adhesive itself. In recent years the designation "interphase" is often employed, since the transition from adherend to adhesive is frequently a material combination of finite thickness, however, ill-defined for analytical purposes. While some program suggestions for the assessment of the structural capability of the interphase in a manufactured joint might be made, it is most likely that measurements and interpretation of failure in this region will continue to be a doubtful undertaking. The structural reliability of the interphase may be enhanced by the careful and complete monitoring of prepared adherend surfaces and adhesives before the joint is formed in the manufacturing process.

An operational definition of strength for adhesive bonds is needed to provide a figure of merit for non-destructive evaluation. At present no single strength characteristic may be uniquely defined. As an operational premise, however, failure will be defined as that condition in which the structure has lost its ability to support the required load. Failures, therefore, may occur due to growth of cracks, and due to geometric instabilities. The growth of a crack (disbond) is presumed to be the principal failure mechanism of concern in adhesive bonded joints, and fracture mechanics should provide material factors most likely to be rated as measures of strength.

As a point of initial departure, the summary statements from the ARPA/AFM workshop held on January 19, 1979, will be used. Six areas of investigation were listed as encompassing the needed, and potentially fruitful, program

activities leading to the goal of reliable adhesive bonded structures. These areas were identified as follows:

1. Flaw growth models (plus nucleation).
2. Stress and fracture analysis.
3. Quality control for bond preparation.
4. Adhesive bulk property measurement correlatable with strength.
5. Cure state monitor.
6. Development and refining of an integrated methodology.

An attempt at providing a methodology as required by item 6 above was made in the form of a logic flow for a structural reliability system as shown in Fig. 1.

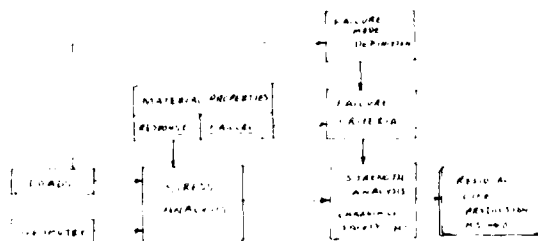


Fig. 1 Elements of a life prediction methodology for structural adhesives.

The diagram shown in Fig. 1 is a simplified schematic system showing the principal elements of the structural design process. Central to the entire methodology is a stress analysis which accepts input in terms of part geometry, environmental loads and a quantitative description of the material properties which encompass those material characteristics necessary to define the distribution of stresses throughout the part. We define this set of material properties by the term response. A second set of properties of equal importance in the strength analysis is referred to simply as failure. A proper definition of a failure "property" would fit the requirement for an operational figure-of-merit for material strength.

The failure criteria as specified in the diagram is an analytical statement of exceedance in which the intrinsic failure limit of a material is compared with the stress and strain requirements generated by the stress analysis. A failure model is implied in which critical stresses and/or strains are incorporated along with relevant material properties.

The output of the strength analysis is presumed to be a structural margin of safety (M.S.) and the life prediction is then based upon the timewise projection of the margin in zero. Life prediction assumes that the mode of failure is known and has been incorporated in the failure criteria. Each structural part subjected to the analysis is expected to demonstrate particular failure modes under the operating loads when the capability of the structure is exceeded. Failure may be the result of an overload or of degraded material properties. Exaggerated loads are sometimes used to fail parts intentionally in order to more clearly define potential failure modes. This procedure is called overtesting.

The methodology outlined in Fig. 1 may be used to examine the non-destructive evaluation process for adhesively bonded structures in terms of needed advances in measurement, analysis and interpretation of extrinsic and intrinsic flaws. As described thus far the process has not accounted for elements related to the inspection process other than a need for quantified material properties, loads and geometries. It was stated earlier that fracture mechanics holds promise as an approach for providing figures of merit for accept/reject decisions. In the context of the elements shown in Fig. 1, the application of fracture mechanics may lead to a failure criterion based on flaw growth to a critical size. Using for present discussion a viscoelastic analog of the Griffith energy balance relationship, i.e.,

$$\sigma_c = k \sqrt{\frac{E(t) \gamma_c(t)}{d}} \quad (1)$$

where σ_c is the critical stress required for crack growth, $E(t)$ is a time dependent modulus, $\gamma_c(t)$ is a time dependent cohesive fracture energy, a is a crack length, and k is a geometrical factor, we find that several of the necessary elements for non-destructive evaluation are specified. The material property $E(t)$ representing the response and $\gamma_c(t)$ representing the failure characteristics indicated in Fig. 1 are incorporated in the expression, as well as crack length which could be the object of definition by non-destructive inspection methods. Both $E(t)$ and $\gamma_c(t)$ may be considered material properties which manifest the existence of intrinsic flaws as discussed earlier, as possibly related to poor cure or moisture softening. While Eq. (1) may not be a sufficiently general or correct statement of the conditions necessary for flaw growth, it is illustrative of the kind of relationship needed for this study. Accepting for the moment that non-destructive investigation methods are available to characterize the geometric flaw, the intrinsic property $E(t)$ should be measurable as well since it reflects a small deformation response. Dielectric cure monitors are typical of the measurements which provide information on the intrinsic state of a material, non-destructively. Unfortunately, the determination of $\gamma_c(t)$ requires a series of destructive tests. Since, however, both $E(t)$ and $\gamma_c(t)$ are apparently linked by the same physical mechanisms which determine their time-dependent character, there is some hope that indirect assessments of $\gamma_c(t)$ may be made from a knowledge of $E(t)$.

The discussion to this point has been based entirely on a deterministic approach to failure prediction. In any real case the bonded joint will contain distributed flaws, and both material properties and loads must be interpreted by probabilistic considerations. Accept/reject decisions will be based on measurable conditions of crack size, load history and material state, all viewed against a backdrop concerned with the probability of failure. The generation of a data base on the distribution of naturally occurring flaws forms a part of the program methodology.

11. TECHNICAL DISCUSSION

This brief discussion treats the central aspects of reliability in adhesive bonded structures which are displayed in Fig. 1. In each of these

areas considerable advances in design concepts and property utilization are evident. One issue in any newly proposed program in reliability and life assessment of adhesive bonded structures is how to implement already available analytical tools. This section describes an approach to achieving this important objective.

A. Background

Load transfer between the adherend and adhesive elements of a bonded structure is accomplished by minute differential displacements between these elements.^(1,2) Bonded joints cannot be designed on the basis of a uniformly stressed adhesive over the entire bonded area. In regions of high stress, typically at the bond edges and in the immediate vicinity of a damaged area the adhesive may be loaded beyond its elastic yield stress and display high damping and fracture energy due to viscous flow processes. In regions of low stress normally removed some distance from edges and damage zones the adhesive layer is below its yield stress and displays a high elastic modulus and creep resistance with low damping. Figure 2a shows a profile view of a long overlap shear joint with plastic stress of higher magnitude at the bond edges and elastic stresses of lower magnitude in the center region of the bond. Figure 2b shows a short overlap shear joint in which the stresses are essentially uniform due to high adherend stiffness and uniform plastic shear stresses are displayed by the adhesive interlayer over the entire joint. The oversimplified stress profiles of Fig. 2 ignore the cleavage (tension-compression) stress distributions which are highly localized at the bond edges and the stress distributions through the thickness of the adhesive layer which are known to strongly affect fatigue life of an adhesively bonded structure.^(3,4)



Fig. 2 Influence of lap length on bond stress distribution.

Recent studies of the structural properties of adhesives by Renton⁽⁴⁾ provide new recommendations for adhesive test specimens and procedures for

defining the engineering structural property of adhesive interlayers using low cost test methods. A thick adherend single-lap shear test, a rectangular butt joint tensile test, and a rectangular scarf joint test were selected and analyzed by Renton.⁽⁴⁾ The stress-strain properties of FM73 and FM400 (NARMCO Div., Celanese Corp.) structure adhesives were evaluated using these three test geometries. Based on limited data a promising correlation between adhesive free film properties and thick adherend shear test data was shown.

Studies by Clark and coworkers⁽⁵⁾ show that the most prevalent critical bond line defects are crack like voids, circular voids, and porosity, and that these voids can be detected by state-of-the-art NDE (non-destructive evaluation). Defects not detected by state-of-the-art NDE such as weak bonds due to surface contamination, and improper adhesive cure state were excluded from study. These studies show that flaw growth initiates in the regions of high stress concentration near bond edges and flaws and that this growth can be detected by available NDE methodology. Hot-humid environments and low cyclic fatigue rate which lower the adhesive elastic yield stress promote higher flaw growth rates. This study also showed that regions of very thin bond line act to produce adhesive stress concentrations and sites of selective crack initiation and growth.

The Primary Adhesive Bonded Structures Technology Program (PABST) was initiated by the Air Force^(6,7) to demonstrate adhesive bonding in highly loaded, primary aircraft structures. In the PABST program the actual stress-strain response of the adhesive was represented by an elastic-plastic idealization of the actual shear stress-strain curve^(3,5) as shown in Fig. 3. The idealized stress-strain response (dashed curve, Fig. 3) describes the actual failure stress and strain of the adhesive and the same strain energy to failure which fixes the effective initial elastic modulus, as shown in Fig. 4 different adhesives can show substantially different strength, extensibility and strain energy at room temperature due to differing curve structure and chemistry. At different temperatures, as shown in Fig. 5, a ductile adhesive will display significant changes in stress-strain response as will also occur with changes in moisture content and strain rate. The data summary of Table 1 shows that two to three fold changes in ductile adhesive strength and deformation properties are encountered over the service temperature range encountered in the PABST design and test program.

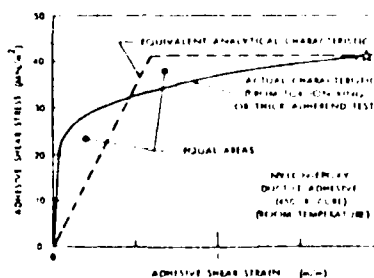


Fig. 3 Elastic-plastic idealization of adhesive shear stress-strain response.

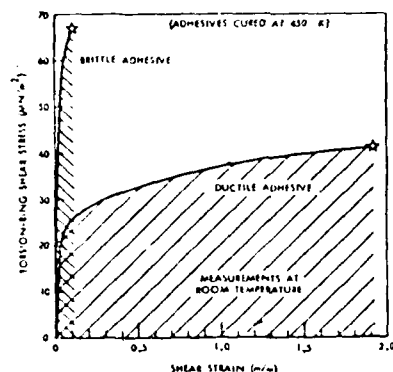


Fig. 4 Comparison between typical shear stress-strain responses of brittle and ductile structural adhesives.

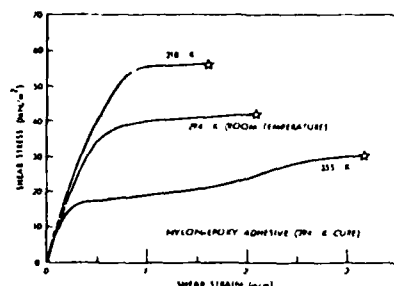


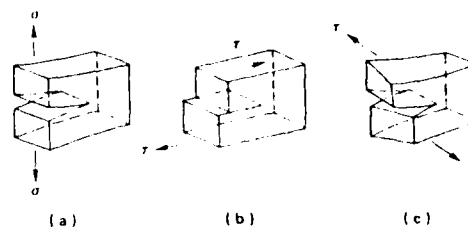
Fig. 5 Typical effects of temperature on ductile adhesive stress-strain response.

Table 1
Typical Adhesive Properties Used in PABST
Bonded Joint Analysis⁽⁵⁾

Temperature (°F)	-50	70	140
Effective Shear Modulus (psi)	80,000	70,000	40,000
Shear Strength (psi)	6,000	5,000	2,500
Yield Strain (in/in) = (m/m)	0.075	0.071	0.063
Fracture Strain (in/in) = (m/m)	0.50	1.00	1.50

As mentioned earlier, the failure of ductile adhesives is localized at the regions of high stress at bond edges and near defect regions. Fracture mechanics recognizes and treats three macroscopic modes of crack tip loading as shown in the upper view of Fig. 6. These pure modes of crack tip loading usually appear in combined form in the usual fracture tests used to evaluate adhesive bond strength as shown in the lower view of Fig. 6.

Assuming an idealized fracture mode of loading, the microscopic process by which adhesives undergo failure may be highly heterogeneous as illustrated by the schematic diagram of crazing as shown in the views of Fig. 7. Structural adhe-



(a) Tension (mode I)
(b) In-plane shear (mode II)
(c) Out-of-plane shear (mode III)

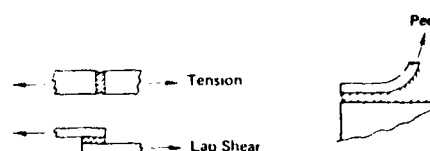


Fig. 6 Schematic diagram of tension, lap shear, and peel tests (lower view) and principal fracture mechanics modes for crack propagation analyses (upper view).

sives are microscopically heterogeneous with even unmodified epoxy networks showing evidence of two phase structure as evidenced by a modular fracture surface. Fracture mechanics analysis is only recently becoming interested in the role of adhesive morphology on fracture energy, fatigue life and structural reliability. The intrinsic scatter in fatigue lifetimes may be dominantly influenced by the small scale micromorphology of the adhesive phase which is known to dramatically influence fracture energy of adhesive joints.

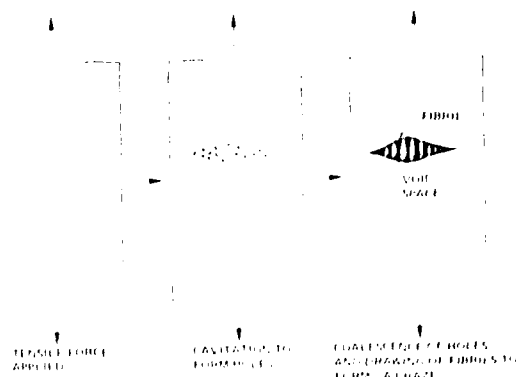
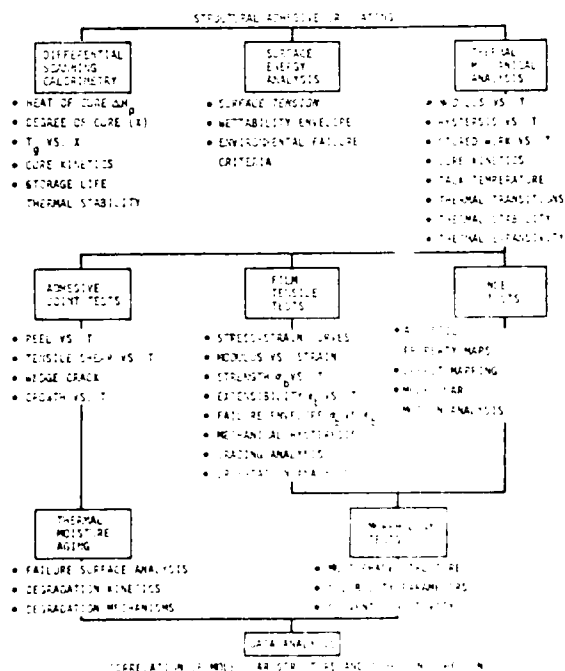
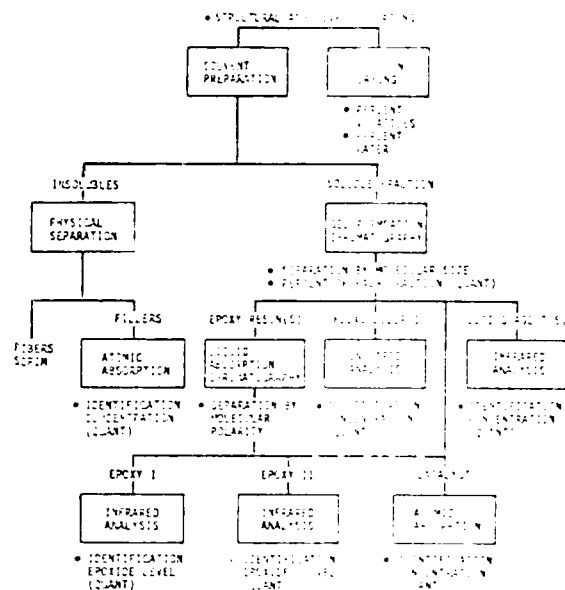


Fig. 7 Schematic diagram of crazing induced by applying tensile force to a polymer. Crazes form at right angles to the direction of stress.

The statistical distribution of adhesive joint strengths (failure load per bonded area) has been shown in a number of studies^(8,9) to follow the

Joint strength and the distribution of joint strengths needs to be directly related to microdefect properties (size, structure, molecular force character, etc.) and the intrinsic distribution of these properties. In other words, the lack of a fundamental materials and process related understanding and control of intrinsic craze zone initiators (see Fig. 7) will continue to lower confidence in high reliability performance of adhesive bonded structures.

Materials selection and process optimization which occurs in preliminary structural design makes extensive use of the above characterizations. This type of quantitative information is only recently being utilized in the nondestructive evaluation (NDE) and life assessment of bonded structures.^(10,11) Key detailed materials and process characterization road maps are already developed and available for material and process characterization. Figure 8 presents a detailed flow chart and methodology for quantitative chemical characterization of adhesives, coatings, and composite matrix materials based upon epoxy resin chemistry. In Fig. 9 a detailed flow chart for physical and mechanical response is presented. The flow chart of Fig. 9 includes studies of hydrothermal aging, failure surface analysis (lower section Fig. 9) which is combined with data from manufacturing simulation (upper section Fig. 9). These data are combined in a data analysis (lower box Fig. 9) which draws upon available structure property relations to replace empirical correlations with failure data defined by discrete physical or chemical processes.



During laboratory investigations of a research or development nature it is customary, if not mandatory, to deal with relatively simple loading situations. Before embarking on a research effort such as is before us, it is important, however, to

classify the types of loads and their possible effects on bond (strength) performance.

We distinguish two ingredients in the description of loads or forces acting on bond geometries: a spatial distribution of forces or tractions and their time history. The simplest case arises in situations leading to what one refers to as proportional loading: this type of loading results when the distribution of forces remains invariant in time but the magnitude of the forces or tractions vary. For example, the time-varying pressurization of a fuselage would fall into this category. A special case results when constant loads are applied to a bonded structure. Most laboratory tests fall in this category.

Problems associated with Non-proportional loading are more difficult to deal with, both analytically and experimentally: applied force distributions vary with time and must be reckoned within realistic use environments. An example of this type of loading is given by a (bonded) shaft that is first loaded in axial tension and then subjected to twist.

With regard to loading histories (under proportional or non-proportional loading) one distinguishes monotonic loading (continuously increasing or decreasing loads with time-constant loads as limit cases) and non-monotonic loads. The latter are either of a cyclic or of a purely random nature. Cyclic loads are relatively easily applied in most laboratory environments when they are of the purely sinusoidal type but require less readily available equipment if arbitrarily varying proportional loading histories are required. The latter comprises the cases of random loading which are particularly difficult to deal with whenever one is confronted with history-dependent material behavior such as results with the use of polymeric bonding agents.

If and when our predictive capability of bonded joint behavior progresses to the point where we can predetermine failure behavior for arbitrary load distributions and histories, such distinctions are not necessary. However, in parallel to the failure response of metal structures and monolithic polymer structures, we anticipate that we shall lack this complete capability for more time to come; as a result we shall have to be continuously aware of the possibility of different deformation and failure responses as a result of different load histories.

So far, we have dealt here with applied mechanical forces. It is equally important to consider forces induced in bonded joints during exposure to varying environment. Normal dilation, either as a result of polymer-cure or of normal changes during use; cure-shrinkage; and swelling due to weather or other solvent infusion are factors that give rise to mechanical forces acting on the bond line. To date little more than lip-service has been given to the recognition of these facts, but we think that the time is here when the latter, seemingly less important factors in bond loading, are assessed, particular attention being given to their effect on the long-range performance of bonds.

3. Stress Analysis

As for the performance analysis of any load-bearing structure, a stress and deformation analysis is a necessary ingredient to a life and

failure estimate. Today all fracture and deformation failures are based on concepts evaluated within frameworks of solid mechanics analyses of varying degrees of refinement. The degrees of analysis sophistication is often a somewhat debatable issue. Most often it is clear that a simple P-over-A analysis does not form a sufficient criterion and an extremely refined fracture analysis with microstructural material refinements at the crack tip would represent "over-kill." While it has become obvious that a simple P-over-A analysis is insufficient for design purposes, the question as to what constitutes sufficient analysis procedures is yet being debated. No doubt that question will be answered progressively and through trial-and-error procedures in an engineering way.

We distinguish historically two types of analyses: those that deal with stress components averaged over the thickness of the bond, termed for present purposes "thickness-averaged stress analyses," and those in which attention is paid to the detailed distribution that is resolved throughout the bond thickness. It is our opinion that only the latter type of analysis has promise of aiding in the formulation of a framework of predictive failure analysis. That this is so is readily apparent when one inspects newly bonded test samples which have been loaded without inducing gross failure. Fractures are observed readily in regions of stress concentrations which are clearly not identified by a thickness-averaged analysis.

There are several high stress regions that figure prominently in a bonded joint: edges and corners at adherend-to-adhesive interfaces develop high stresses due to material discontinuities. Within the assumptions underlying linearly (visco)-elastic analyses, the stresses may become unbounded at certain points. While the unboundedness is a consequence of the linearity assumption and does not exist in reality, to ignore the location of these excessively high stress regions as the thickness-averaged analysis would do would be folly.

When failure proceeds by the propagation of crack, the stresses at the tip of that crack are again very high and, again within the framework of linearly (visco)-elastic stress analysis, their character depends on whether the crack tip is located at the interface or is embedded in the adhesive. Interface (or interphase) cracks exhibit an oscillatory crack tip stress field that is not supported by physical reasoning and is due to the linearization of the problem. At any rate, the domain in which this anomalous stress-field behavior acts is so small that, from a practical point of view, it is most probably unimportant.

Most practical bonded joints employ adhesive on a carrier or scrim cloth. The adhesive interlayer is thus really a composite and inhomogeneous material, and it is not clear at this time under which circumstances this fact can be neglected or must be accounted for.

In connection with cracked bond lines a way of structural failure analysis has developed which we term, for lack of a better term, "thickness-averaged fracture mechanics." We mention this here because of the implication for the requisite stress analysis. In this approach to the bond

failure problem, the adhesive layer and its response is ignored. The attendant stress analysis is thus confined to adherends and the adhesive layer merely serves as a guide for the propagation of the crack.

In opposition to this simplification we must recognize that the stress fields in bonded joints have three-dimensional character. No more is this obvious than when one observes the distinct failure patterns in laboratory specimens which arise from these three-dimensional stress fields. Such facts notwithstanding, one is most likely forced to extract maximal information out of two-dimensional analyses, be they of a closed form or other analytical nature or derived from finite element loads.

In most engineering fields drawing on structural or continuum stress analyses, there exists a body of information on characteristics of stress distributions. Stress analysis of bonded joints has been a stepchild of bond strength investigators, primarily because their background did not point up the need for an improved understanding of that aspect in joint failure prediction. As a result we are, at present, short of a body of stress analysis results. It is not that we lack the capability; it is merely that that capability has not been exercised enough. No doubt that deficiency will be removed as time goes on.

It may be illustrative to relate experience in this regard that comes from our early experience with engineering of solid propellant rocket motors. Analysis tools were being developed or were available as they are now. However, we learned that for certain configurations involving high volume constraint, standard notions of stress distributions were rather inadequate (for nearly incompressible solids). Bonded joints place similarly high deformation constraints on the adhesive; the consequences of this are not explored nor understood. Recent results in failure studies simulating long-time endurance failure indicate that such effects are important. In another instance the common notion of what constitutes "rigid" adherends relative to the adhesive has been questioned.

These isolated examples of deviations in stress distribution from an apparently accepted norm make us believe that attention needs to be focused on this area.

A discussion of stress analyses and their application to bonded joint failure prediction would not be complete without calling attention to the need for stress analysis validation. Specifically, one is here concerned with examining in which respect, and by how much, any assumptions underlying currently available analysis codes (linearly elastic, elastic-plastic) violate or corroborate the physical situation. In particular, our visco-elastic stress analysis capability is very limited and assumptions in this regard are even more in need of checking than those already mentioned.

Since stresses cannot be measured directly, any validation procedure must involve the comparison of a displacement field resulting from theory and experiment. Strain gages are, in general, of little usefulness because they are large compared

to the thickness of the bond; they may be useful in verifying the surface strain distribution in thin adherends. Other than that, one is bound to rely on displacement measurements. These may be checked at particular points with various displacement gages, or possibly in limited regions, by optical interferometry or speckle interferometry. Verification of deformation in highly stressed domains promises to be very difficult in realistically dimensioned joints because the regions in which they occur are so small.

4. Failure Modelling

We consider two basic types of structural failure: (a) loss of ability of a structure to carry an assigned load and (b) excessive deformation. The latter failure mode is analyzed and predicted completely by a component stress analysis (probably not a linear analysis) and we therefore point out once more the need for advances in our capability to successfully deal with deformation analyses of structural bonds. We shall not concern ourselves with this aspect of failure in this section.

The loss of load carrying ability of a bond is (apart from problems derived from extreme flow of the adhesive) clearly tied to fracture. Therefore an analysis of failure in bonded joints is almost synonymous with the steady fracture progression in a special class of structures.

The problem of bond strength has been investigated for a long time. Most of that effort in the past has been spent on developing "better adhesives"⁽¹²⁻¹⁴⁾ or studying the interface problem.⁽¹⁴⁻¹⁷⁾ Less attention has been directed towards the mechanics of the failure process in the bond-joint geometry.⁽¹⁸⁻²⁰⁾ Because of its promise as an effective and efficient construction method and because of a basic lack of understanding of joint strength in spite of the extensive chemistry related research, the mechanics aspects of the problem are now being exercised more intensively. In that connection several basic problems have been posed, none of which are resolved in a satisfactory manner though ongoing work is making strides towards practical solutions. Today, the failure of bonded joints is approached largely through the problem of peel testing on the one hand⁽²¹⁾ and through what we have referred to as thickness-averaged fracture mechanics on the other. Peel is often associated with soft adhesives and thickness-averaged fracture mechanics with rigid adhesives, although that distinction is not systematically adhered to, since peel tests are also used to evaluate rigid adhesives.

The two approaches differ primarily with respect to the choice of the test geometry. Peel approaches the adhesion problem by specifying relatively thin adherends which undergo large (elastic or elasto-plastic) deformations (see Fig. 10). Test results or analyses are concerned with net forces acting on the adhesive system and the resulting deformations with no or a minimum of attention paid to the detailed process in the adhesive. Thickness-averaged fracture mechanics deals primarily with (two-dimensional) plate or beamlike geometries, two pieces of plate being joined along a line by an adhesive layer (see Fig. 11). Since the adhesive layer is usually thin compared to the thickness of the plates the

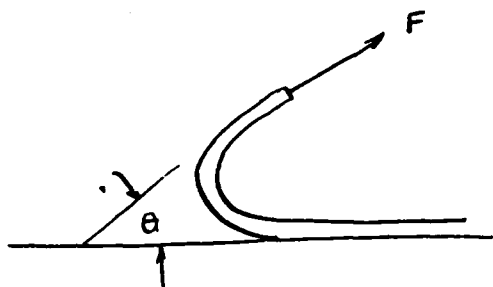


Fig. 10 Peel test geometry

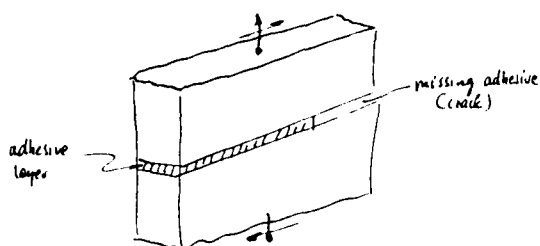
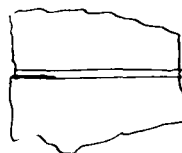


Fig. 11 Standard test geometry used for thickness-averaged fracture mechanics.

thickness of the adhesive layer is deemed negligible, thus reducing the plate problem to the fracture of a homogeneous plate containing a weak internal material plane. The problem is then further analyzed by fracture mechanics concepts developed for homogeneous solids and defining average properties for the adhesive layers. While this appears on first sight a very reasonable approach to a complicated problem, we shall see later that there are pitfalls inherent in this approach. Suffice it to say here that thickness-averaged fracture mechanics makes certain fracture parameters a function of bond thickness whereas in ordinary fracture mechanics such quantities are interpreted as material constants. This limitation poses special difficulties in a technology where bond thickness variations are a fact of life, and where the variations may have to be carefully measured post facto (by ultrasonics?). If time-dependent adhesive properties must be considered, such parameters become rate- or time-dependent quantities which, in the context of thickness-averaged fracture mechanics, would be functions of the bond line thickness also. Both the approaches of peel and of thickness-averaged fracture mechanics to bond fracture have in common that they neglect, by and large, the details of the processes in the adhesive itself. Beyond this similarity there has apparently not been established any quantitative relation between peel and thickness-averaged fracture mechanics. In fact, we are not aware of that question being raised. Instead we experience laboratory tests employing either approach and application of the resulting data to design problems that involve geometries somewhat intermediate to those characteristics of peel and thickness-averaged fracture mechanics. Since the peel mode involves large deformations, in particular much larger than those involved in thickness-averaged fracture mechanics, it is clear

that such indiscriminate use of bond strength test results is potentially dangerous. In other words, since bonding is applied to structural adherends of widely varying thicknesses neither the conditions commensurate with peel nor thickness-averaged fracture mechanics prevail. It appears mandatory therefore to examine the conditions that lead to joint fracture in more detail than either the peel mode or thickness-averaged fracture mechanics can portray.

In order not to mislead the reader, we should mention here that mathematical analyses are being made for layered elastic systems wherein one or more layers contain cracks. Such problems are intended to model the formation and propagation of cracks in adhesive layers and thus the part of the initial process of the adhesion failure. For analytical reasons the geometries are simple and of the type shown in Fig. 12. While these geometries appear reasonable choices, they are not necessarily based on observations preceding joint fracture. What concerns us is not so much the necessary simplicity in the analytical modelling but the prospect that this assumed simplicity prejudices the interpretation of the fracture process which interpretation should be derived from direct observation preceding any modelling and analysis.



Interface unbond
two-dimensional
or penny-shaped
unbond



Embedded crack
two-dimensional
or penny-shaped
crack on bond midplane

Fig. 12 Two-dimensional bond fracture geometries.

Connected with this concern is the observation that virtually all information on the fracture process is derived from the post facto appearance of the fractured joint. Reconstruction of the fracture process is thus often made ambiguous because the source of fracture surface features are second-guessed. The need to intensify work on fractographic studies is pointed out later.

There does not exist to date a nearly comprehensive theory of bond fracture. However, once one decides that a quantitative account of the failure process is imperative for a predictive failure theory, one needs to cope with the fact that cracks exist in many shapes and forms and can respond in different ways, depending on the applied loads.

Flaws or cracks may pre-exist in a bond as manufacturing defects or may develop under loading. Cracks located in the interior of a bond area are less detrimental than those located near edges or in stress singularities. Apparently interior flaws have little effect on the strength of a new or intact joint. This is so because by far

most of the load transfer in bond-parallel loading is effected near the bond ends. The severity of flaws in a structural integrity sense depends thus on its location relative to the (current) bond end. If cracks grow from the edge, an interior flaw becomes thus more critical.

In principle the ideas of fracture mechanics are equally applicable to bonded joints as they are to monolithic structures. The differences enter through the materials, in particular polymers, which are not part of a standard engineering repertoire, and through difference in geometries. The latter, especially through the ubiquitous interface boundaries in joint geometries, complicate matters.

Some other features, not normally observed in monolithic fractures, need to be pointed out. In terms of a standard test geometry, a smooth crack front is expected as depicted in Fig. 13. However, it can be shown that in slow model tests a crack may not propagate with a smooth front. Instead the crack front appears (in plain view) as in Fig. 14. It appears thus that present test methods, which are geared to relatively short-term data gathering, could easily (and probably will) misrepresent failure modes encountered under long-time loading. The interaction of the crack tip stress field with the bond interfaces gives rise to changes in the crack path direction, especially when coupled with non-proportional loading. For example, depending on the loading on an adhesive bond, a centrally located crack may grow to the interface. An understanding of whether it stops or grows along the interface requires a fracture criterion that is more general than those developed for cracks propagating along their original axis or in their original plane.

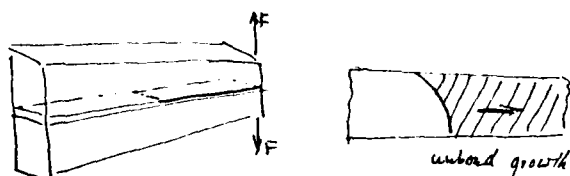


Fig. 13 Crack front in standard test



Fig. 14 "Finger" development at front of unbond "Finger" spacing is very regular, shown approximately to scale.

The (two-dimensional) problem of crack extension under loads such that the extension makes some angle with the original crack has been solved for the homogeneous solid. Figure 15 shows the geometry before (a) and after (b) crack extension by a small amount Δc . The criterion for the critical load at which the crack extends as well as the direction is based on an argument of maximal energy release in the crack propagation process. The ratio of difference in the (negative)

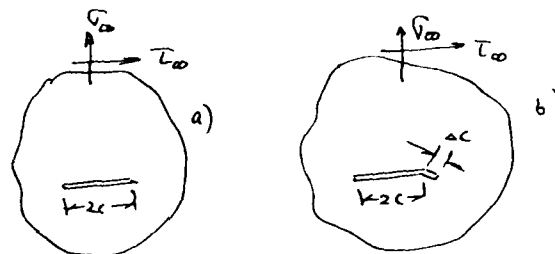


Fig. 15 Non-linear crack growth.

potential energy between the original and crack-extended geometry and the extension Δc is maximized to determine the orientation of the crack extension for a limit $\Delta c \rightarrow 0$. The crack is judged to propagate when this maximal energy release rate was just equal to the (constant) intrinsic fracture energy of the material.⁽²²⁾

The interesting result of such a rather difficult energy analysis is that the much simpler approximate stress criterion gave closely the same result: The stress criterion⁽²³⁾ asserts that fracture occurs along that ray emanating from the crack tip normal to which the tensile stress attains a maximum value with respect to angular orientation of the ray. Crack growth starts when the stress intensity associated with this maximum stress reaches a critical value. As a result of this favorable comparison, an extension of the stress criterion for brittle fracture can be made to crack extension under arbitrary loading. A key development in that extension to fracture development in a three-dimensional context rested heavily on the experimental findings⁽²⁴⁾ that under a mode III (antiplane shear) loading a crack does not propagate along its original plane but develops crack extensions that spiral from one of the initial crack surfaces around the crack front to the other crack surface in a somewhat helical path (see Fig. 16). The resulting crack-extended geometry is distinctly three-dimensional.

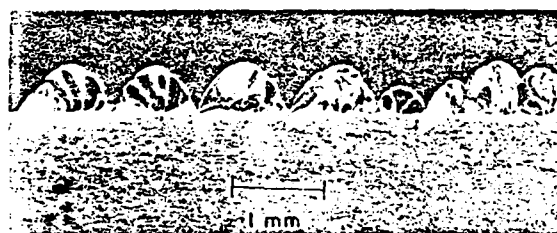


Fig. 16 Cracks generated in antiplane shear.

It follows from the two-dimensional energy analysis results -- which compare well with careful experiments -- and from the just-mentioned findings in mode III failure, that the extension of cracks under general loading should not be analyzed by methods which assume the growth process to occur in the plane of the original crack.

We turn now to a discussion of phenomena in fracture modelling that are concerned with time dependence of the process.

1) Time dependent fracture. The time dependence of the failure process may have several causes. Among these the

a) Viscoelastic properties of the adhesive certainly play a dominant role. While to date "rigid" adhesives are treated (almost?) invariably as time independent, recent tests on typical (supposedly rate-insensitive) adhesives have been shown to exhibit a surprising amount of stress relaxation (on the order to 10 - 20%) within minutes of test start.⁽²⁵⁾ In the same vein it is known that bonds lose a significant amount of load-carrying ability in a few days' loading; this observation points to significant viscoelastic influence, too. For this reason it is necessary to characterize the viscoelastic behavior of any adhesive.

b) Rate dependence influenced by the geometry. It is a well-documented fact⁽²⁶⁾ that in peel experiments the path of fracture moves from an intra-adhesive location at high rates of failure propagation (low temperature) to an (apparent?) interface failure at low rates of failure growth (high temperature). Beyond the suggestion that intra-adhesive failure is the result of void formation and coalescence (when uncrosslinked adhesives are used), which void formation does not occur in near-interface failure, this phenomenon is not understood. Gent and Petrich⁽²⁷⁾ even contend that cavitation may not be responsible for the change in failure mode.

A plausible explanation of this phenomenon in connection with relatively rigid adhesives appears to be related to a combination of non-linear material behavior and the geometry.

The high stresses at the tip of a crack or unbond cause a local mechanical degradation. This irreversible damage occurs in a limited zone, say a typical dimension λ . If the crack is embedded in a solid with all geometric dimensions large compared to λ we speak of small-scale damage (in metals: small-scale yielding). For small-scale damage fracture characterization can be accomplished in terms of a single parameter, the stress intensity factor, say, without reference to the size of λ of the damage zone. This is so because in a characterization test the geometry is taken so that λ does not enter the considerations. As long as the critical stress intensity factor criterion is applied to geometries in which λ is small compared to all other dimensions, this parameter need not be considered.

In this connection we need to mention a phenomenon observed in fatigue failures. When a bond is subjected to "small" cyclic loads (fatigue), fracture occurs along an interface; but when the crack has grown to sufficiently large dimensions so that "catastrophic" failure sets in, then crack propagation occurs through the center of the bond (scrim area). What happens apparently is that during the (low level) fatigue loading, the zone at the crack front is small enough not to play a significant role in the stress distribution. When the load transmitted to the crack-tip in the final stages becomes large as catastrophic fracture approaches, that is no longer the case.

c) Initial propagation and other transient histories of growth. To date, problems in visco-

elastic fracture and unbonding have been considered primarily in the context of steady crack-ing rates. From this viewpoint the rate of crack growth is essentially a function of the instantaneous stress intensity factor. Cracks and unbonds are observed to start propagating with time delay after load application. In some highly crosslinked materials this delay can be interpreted simply as the time required to increase the stress intensity to the point where the flaw growth accelerates to a measurable rate. On the other hand, the deformation and degradation of the material at the crack tip is time dependent so that some of the delay is attributable to deformation without flaw growth. Similar phenomena must occur under (transient) cyclic loading when the flaw grows, on the average, less than the length of the damage zone (long-time fatigue). We thus face a question, the answer to which is important in structural life prediction: Is a substantial portion of the structural life taken up by processes to get the flaw to a growth stage or is the life determined (almost entirely?) by its growth rate? The answer is vitally important in connection with fatigue of polymers. Resolution of that question requires experimental methods that provide high resolution of the deformations at the front of a flaw.

d) Effect of moisture on time-dependent fracture. The observation that cracks can propagate slowly (10^{-7} to 10^{-2} mm/sec) in inorganic (silicate) glasses is often attributed to the influence of moisture. This influence is greatest in the highly stressed region around the tip of the flaw. We would expect that the same is true where polymers are concerned, as long as they are not totally inert to moisture. We know that moisture ingress is a form of plasticization and results in a shortening of the material relaxation times. Due to the highly dilated molecular structure at the crack tip, the diffusion process should be accelerated, and it is just in this critical domain where the creep behavior is accelerated by moisture. One would expect therefore, a dominant effect of moisture on failure rates in some polymers; among these we count the epoxies and polyurethanes, polymers which are used structurally in large quantities.

e) Effect of temperature on fracture and unbonding. For thermorheologically simple elastomers (above the glass transition temperature) it is well established that the rate of failure propagation and temperature are connected by the time-temperature superposition scheme. This is true with respect to both cohesive and adhesive failure. While the sensitivity of viscoelastic relaxation to temperature changes decreases notably as a polymer is cooled down through the glass transition temperature, there is every reason to believe that a time-temperature superposition is valid in rigid polymers (below the glass transition temperature). Problems may arise for filled polymers (hard particulate filler, scrim cloth, "toughened" with rubber particles) which are usually not thermorheologically simple.

We consider next in more detail phenomena associated with crack geometries:

2) Load Criterion for Fracture. It follows from the discussion of the influence of temperature on the time history of the fracture process

that temperature changes also induce stresses in a composite structure. Often a temperature increase is used to model the speed-up of the viscoelastic responses (accelerated testing). If this is done it is also necessary to understand the effect of temperature on the mechanical state of stress. For "rigid" polymers this problem leads certainly to dealing with polymer behavior near the glass transition.

The (possibly) thermally induced stresses combine with those due to mechanical loading. We have discussed these already jointly in connection with the stress analysis.

a) Mode interaction.* We shall consider next the response of a crack or cracklike flaw in a bonded joint or composite to mechanical loads. This we do initially without reference to time dependence. We first define some terminology: With reference to Fig. 17, let point A lie on the smooth periphery of a planar crack and establish a Cartesian coordinate system with z tangent to the periphery at point A and x contained in the plane of the crack. With reference to this coordinate system we define the three primary modes of crack deformation, modes I, II and III in standard fracture terminology. These modes describe the relative motion of the upper and lower crack surfaces respectively parallel to the y , x and z directions. We speak of a mode-interaction problem if the loading is such that fracture propagation results in the presence of more than one deformation mode.

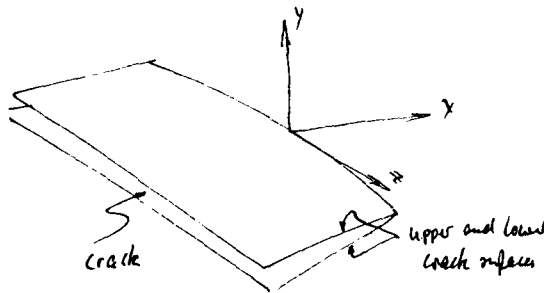


Fig. 17 Local coordinate system at crack front.

In monolithic cracked structures the mode-interaction problem has been considered recently by several authors; a fairly comprehensive review of that problem is documented in Ref. 22. However, in connection with bonded joints the motion of a crack is inhibited by the proximity of the relatively rigid and infrangible adherends. One will therefore have to re-examine the mode-interaction problem for the bond problem. Specific questions arising in this context relate to: the fracture path(s) as a function of the relative magnitude of modes I, II and III; how does this

path depend on the relative strength of the interface adhesion and the cohesive strength of the adherend; what is the functional relation between the three modes of deformation at fracture; is such a relation invariant under time-dependent failure processes?

The next question that needs to be considered relates to the fracture path. Fracture in bonded joints is observed to occur along (or near) the interface or in the adhesive. There is no documented criterion that relates the path of fracture to the loads acting on a joint apart from the general criterion that the crack follows a path requiring minimum energy expenditure.

In this connection it is pertinent to discuss the problem of proper test data interpretation for design applications. Suppose an adhesive layer between two relatively rigid adherends is subjected to a general loading up to fracture initiation in a geometry such as is shown in Fig. 18. This type of geometry is a standard way to evaluate the strength of adhesion by thickness-averaged fracture mechanics. Fractures appear (not necessarily visible on the surface) such as indicated in Fig. 18 by solid lines without total failure of the specimen. Upon further loading these cracks may join along the dotted lines in Fig. 18. Generally, cracks open initially so that the newly created fracture surfaces separate. However, as the cracking process continues, a complicated fracture pattern may result.

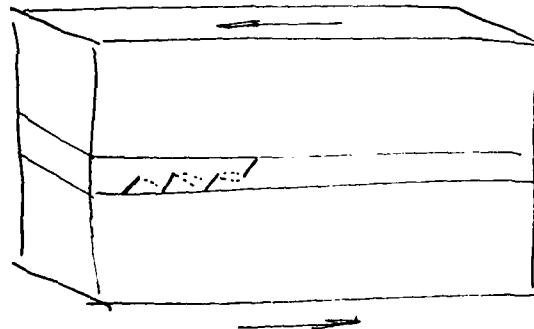


Fig. 18 Fracture path and sequence in shear test.

b) Initiation. Opinions seem to diverge on the importance of initiation in the failure or cracking process. There are those who hold that a "properly designed" bonded joint should never develop a crack and others who claim that cracking cannot be avoided at bond terminations and that bond-life depends on suppression or retardation of continued growth through suitable bonding agents. Apparently observations diverge on this point because we do not understand sufficiently well the interaction of bond geometry, stress field and material properties.

*The definition of the interaction problem is often sloppy. When writers have in mind thickness-averaged fracture mechanics only the deformation of the adherends in the bond-termination region is considered. Therefore, motion of the adherends apart and normal to the bondline is interpreted as a "crack opening" model (mode I). However, if we consider the detailed stress distribution around the front of a disbond between adherend and adhesive, then the deformation under the same loading on the adherends produces both mode I and II motions, the mode II being induced through Poisson coupling from mode I.

Of dominant concern in this regard are the high discontinuity stresses acting almost invariably at the bond termination. Some studies are available that deal with shaping the adherends near to bond termination (tapering) to minimize these stresses. However, the interactions of such geometric variables with bond material characteristics such as nonlinear or "plastic" deformations need to be explored. Standard fracture mechanics principles do not apply for the initiation phase as long as a crack or disbond cannot be identified. Only at the end of this initiation phase can this be done so that time dependent fracture mechanics processes apply. It may be possible, however, to explore the initiation problem through energetics involving appearance of cracks or disbonds of discrete length or size.

5. Fractography. Fracture of homogeneous bodies involves characteristics of the fracture surface features which allow often the reconstruction of the fracture process. These features have been studied completely empirically and constitute an important body of information in fracture analysis.

Similar observations are in progress in the study of bonded joints, most of them presumably as an adjunct in ongoing failure studies. It would be advantageous, however, to structure a program more systematically about fractographic questions, in particular in connection with NDI type investi-

gations. Such a program should comprise NDI of bonded joints subjected to various load histories and (etched) removal of the metal adherends for examination of the fracture feature in the adhesive, probably a painstaking task.

III. PROGRAM PLAN

The program plan is described in the "roadmap" format common to Air Force planning documentation. This format allows the program content to be viewed in context, with interrelationships among the separate work units to be displayed against a time-line. Since there are programs currently underway and in planning by the agencies, it is particularly important to discover those which provide necessary or complementary activity to the main thrust of this plan. These programs will be shown as well with their output contributing at specific time periods in the plan. The most pertinent ongoing effort is indicated on the first block of the roadmap entitled Fatigue Behavior or Adhesive Bonds (Contractor: General Dynamics/Fort Worth). Each block on the roadmap diagram indicates a logical work package with its own objective; however, combinations or further subdivision may be appropriate as the implementation of the plan proceeds. A work package description is included for each block on the roadmap, in which the objective, scope, approach and resource needs are outlined. Finally, a funding summary by fiscal year is provided.

ATTENDEE LIST
REVIEW OF PROGRESS IN QUANTITATIVE NDE
SCRIPPS INSTITUTION OF OCEANOGRAPHY
July 8-13, 1979

J. D. Achenbach (Dr.)
Department of Civil Engineering
Northwestern University
The Technical Institute
Evanston, IL 60201

Robert C. Addison, Jr. (Dr.)
Rockwell International Science Center
1049 Camino Dos Rios
Thousand Oaks, CA 91360

Laszlo Adler (Assoc. Prof.)
Department of Physics
University of Tennessee
Knoxville, TN 37916

Lloyd Ahlberg
Rockwell International Science Center
1049 Camino Dos Rios
Thousand Oaks, CA 91360

George A. Alers (Dr.)
Rockwell International -
Albuquerque Development Laboratory
2340 Alamo, SE - Suite 200
Albuquerque, NM 87106

Eric A. Ash (Prof.)
Department of Electronics & Elec-
trical Engineering
University College London
Torrington Place, London, England
WC1E 7JE

Abdulah Atalar
Department of Applied Physics
Stanford University
Stanford, CA 94305

Bert A. Auld (Prof.)
Edward L. Ginzton Laboratory
Stanford University
Stanford, CA 94305

Sevig Ayter (Dr.)
W. W. Hansen Laboratory of Physics
Stanford University
Stanford, CA 94305

Alfred J. Bahr (Dr.)
SRI International
333 Ravenswood Avenue
Menlo Park, CA 94025

G. D. Barcus
General Electric Company
100 Plastics Avenue (2224)
Pittsfield, MA 01201

N. K. Batra (Dr.)
Systems Research Laboratory, Inc.
2800 Indian Ripple Road
Dayton, OH 45440

Paul M. Beckham
Rockwell International Science Center
1049 Camino Dos Rios
Thousand Oaks, CA 91360

Albert L. Bertram
Naval Surface Weapons Center
White Oak Laboratory Code R31
Silver Spring, MD 20910

Robert Birchak
NL Drilling Systems Technology
Division of NL Petroleum Service
P.O. Box 1473
Houston, TX 70001

Albert S. Birks
Battelle Northwest Laboratories
P.O. Box 999
Richland, WA 99352

Robert A. Blake, Jr. (Dr.)
MAE Department
University of Delaware
Newark, DE 19711

Norman Bleistein (Dr.)
Denver Applied Analytics
2555 S. Ivanhoe Place
Denver, CO 80222

David B. Bogy
Department of Mechanical Engineering
University of California, Berkeley
Berkeley, CA 94720

Leonard J. Bond (Dr.)
Department of Physics
The City University
Northampton Square, London
England EC1V 0HM

Naser Bozorg Grayeli
Department of Electrical Engineering
W. W. Hansen Laboratory of Physics
Stanford University
Stanford, CA 94305

James R. Brink
David Taylor Naval Ship R&D Center
Carderock, MD 20084

John A. Brinkman
Rockwell International -
Albuquerque Development Laboratory
2340 Alamo, SE - Suite 200
Albuquerque, NM 87106

Robert A. Brooks
Magnetic Analysis Corporation
535 S. 4th Avenue
Mt. Vernon, NY 10550

Joseph W. Brophy
Babcock & Wilcox Company
Lynchburg Research Center
Lynchburg, VA 24505

William Bruckley
U.S. Army Ballistic Research
Aberdeen Proving Ground, MD

Otto Buck (Dr.)
Rockwell International Science Center
1049 Camino Dos Rios
Thousand Oaks, CA 91360

Michael J. Buckley (Dr.)
Defense Advance Research Projects Agency
Materials Science Office
1400 Wilson Boulevard
Arlington, VA 22202

Roy L. Buckrop (Commander)
U.S. Army Armament Materials
Readiness Command
Rock Island, IL 61299

O'Neill J. Burchett
Sandia Laboratories
Division 1552
Albuquerque, NM 87185

Harris M. Burte (Dr.)
Metals & Ceramics Division
Air Force Materials Laboratory
Wright Patterson AFB, OH 45433

Spencer H. Bush
Battelle Northwest Laboratories
Richland, WA 99352

T. M. Cannon (Dr.)
University of California
Los Alamos Scientific Laboratory
Los Alamos, NM 87545

Steve H. Carpenter
University of Denver
Denver, CO 80208

James M. Carson
Air Force Office of Scientific Research
Bolling AFB, DC
904 Atlanta Circle
Seaford, DE 19973

F. H. Chang
General Dynamics/Fort Worth Division
P. O. Box 748
Fort Worth, TX 76101

Dale E. Chimenti
U.S. Air Force Materials Laboratory
NDE Branch/11F
Wright Patterson AFB, OH 45433

K. Choi
James Electronics, Inc.
4050 N. Rockwell Street
Chicago, IL 60618

Chou Ching-Hua (Mrs.)
Edward L. Ginzton Laboratory
Stanford University
Stanford, CA 94305

Kent Chuang
University of California, Berkeley
Berkeley, CA 94720

S. Chung
General Electric Company
Mail Drop E45
Cincinnati, OH 45215

Jack K. Cohen (Dr.)
Denver Applied Analytics
2555 S. Ivanhoe Place
Denver, CO 80222

J. C. Collingwood
Material Physics Division
AERE Harwell
Didcot, Oxfordshire
England

Dale H. Collins (Dr.)
Battelle Northwest Laboratories
P. O. Box 999
Richland, WA 99352

Thomas C. Collins
Air Force Office of Scientific Research/NI
Building 410
Bolling AFB, DC 20332

William D. Cook (Dr.)
University of Houston
Houston, TX 77004

John I. Cook
Hughes Aircraft Company
Building 6, M/S D129
Culver City, CA 90230

Kenneth J. Cook
The Valeron Corporation
32380 Edward Street
Madison Heights, MI 48071

Douglas Corl (Dr.)
Edward L. Ginzton Laboratory
Stanford University
Stanford, CA 94305

Clifford D. Coulbert
Jet Propulsion Laboratory
4800 Oak Grove Drive
Pasadena, CA

Robert L. Crane (Dr.)
Air Force Materials Laboratory/11F
Wright Patterson AFB, OH 45433

Benjamin T. Cross
Rockwell International -
Rocky Flats Division
P. O. Box 464
Golden, CO 80401

Z. J. Csendes
General Electric Company
Building 37, Room 373
P. O. Box 43
Schenectady, NY 12301

Isaac M. Daniels (Dr.)
IIT Research Institute
10 West 35th Street
Chicago, IL 60616

T. J. Davis
Battelle Northwest Laboratories
P. O. Box 999
Richland, WA 99852

W. E. Deeds (Prof.)
Department of Physics
University of Tennessee
Knoxville, TN 37920

Brian DeFazio (Dr.)
Department of Physics
Ames Laboratory
U.S. Space-Dept. of Energy
Ames, IA 50011

Richard C. Deitrich
Naval Air Engineering Center
Code 92724
Lakehurst, NJ 08733

Richard V. Denton
Systems Control, Inc.
1801 Page Mill Road
Palo Alto, CA 94304

Thomas Derkacs
TRW, Inc. T/M2429
23555 Euclid Avenue
Cleveland, OH 44117

Ronald R. DeSpain
Rocketdyne Division
Rockwell International
6633 Canoga Avenue
Canoga Park, CA 91304

John M. Deutch
Department of Energy
1000 Independence Avenue, SW
Washington, DC 20585

Gary W. DeYoung
Electric Power Research Institute
3412 Hillview Avenue
Palo Alto, CA 94303

Thomas Dickinson (Dr.)
Department of Physics
Washington State University
Pullman, WA 99164

Steven R. Doctor
Battelle Northwest Laboratories
P. O. Box 999
Richland, WA 99352

Eytan Domany (Dr.)
Department of Electronics
Weizmann Institute of Science
Rehovot, Israel

Peter Doyle (Dr.)
Aeronautical Research Laboratories
Box 4331, PO Melbourne 3001
Australia

Bernard E. Droney (Dr.)
Homer Research Lab - Building A
Bethlehem Steel Corporation
Bethlehem, PA 18016

John C. Duke, Jr. (Dr.)
Virginia Polytechnic Institute
& State University
Blacksburg, VA 24061

Robert Dukes (Dr.)
Admiralty Marine Technology Establishment
Holton Heath, Poole
Dorset, England

E. F. Eals
EG&G Idaho, Inc.
P. O. Box 1625
Idaho Falls, ID 83401

Jeffrey W. Eberhard
Building K1, Room 3A42
General Electric Res & Dev.
Schenectady, NY 12309

John R. Edson
Boeing Aerospace Company
P. O. Box 3999
Seattle, WA 98124

Donald G. Eitzen (Dr.)
National Bureau of Standards
Sound B106
Washington, DC 20234

J. Kiefer Elliott
General Electric Res. & Dev.
P. O. Box 8
Schenectady, NY 12301

Richard K. Elsley (Dr.)
Rockwell International Science Center
1049 Camino Dos Rios
Thousand Oaks, CA 91360

Robert C. Erwin
Northrop Corporation
3901 W. Broadway
Hawthorne, CA 90250

Anthony G. Evans (Dr.)
Dept. of Materials Science &
Mineral Engineering
University of California, Berkeley
Berkeley, CA 94720

Edward Fenimore
Los Alamos Scientific Laboratory
Los Alamos, NM 87545

Michael Fernandez
Lawrence Livermore Laboratory
P. O. Box 808
Livermore, CA 94550

Kenneth W. Fertig (Dr.)
Rockwell International Science Center
1049 Camino Dos Rios
Thousand Oaks, CA 91360

Donald M. Forney
Air Force Materials Laboratory/LLP
Wright Patterson AFB, OH 45433

Christopher M. Fortunko (Dr.)
National Bureau of Standards
325 Broadway
Boulder, CO 80303

Ellis L. Foster
Battelle Columbus Laboratories
505 King Avenue
Columbus, OH 43201

Charles L. Frederick
NORTEC
3001 George Washington Way
Richland, WA 99352

Paul M. Gammell
Jet Propulsion Laboratory
4800 Oak Grove Drive
Pasadena, CA 91103

Arthur K. Gautesen
Department of Engineering Science
Northwestern University
Evanston, IL 60601

Klaus Goebbels (Dr.)
Fraunhofer-Institut für Zerstörungsfreie
Prüfverfahren, Universität, Geb. 37
6600 Saarbrücken 11,
Germany

James F. Goff
NSWS
Silver Spring, MD 20910

Alicia Golebiewska
Division of Applied Mechanics
Stanford University
Stanford, CA 94305

Ulrich Gonser (Dr. Prof.)
Universität des Saarlandes
Fachbereich 12.1
66 Saarbrücken, Bau 22
West Germany

J. E. Gordon (Dr.)
Department of Engineering
University of Reading
Whiteknights
Reading, England RG6 2AY

Lloyd J. Graham
Rockwell International Science Center
1049 Camino Dos Rios
Thousand Oaks, CA 91360

R. S. Graham
Rockwell International Automotive Oper.
2135 W. Maple Road
Troy, MI 48064

W. Grandia
Grandia Laboratories
1001 West 17th Street
Costa Mesa, CA 92627

N. Grayelli
Department of Electrical Engineering
W. W. Hansen Laboratory of Physics
Stanford University
Stanford, CA 94305

Robert E. Green, Jr. (Dr.)
Mechanics & Materials Science Dept.
The Johns Hopkins University
Baltimore, MD 21218

George J. Gruber
Southwest Research Institute
8500 Culebra Road
San Antonio, TX 78228

James Gubernatis (Dr.)
Los Alamos Scientific Laboratory
P. O. Box 1663 (T-11, MS457)
Los Alamos, NM 87544

John F. Gudas
DTNSRDC
Annapolis, MD 21402

Marvin Hamstad (Dr.)
Lawrence Livermore Laboratory
Livermore, CA 94550

Stephen D. Hart
Naval Research Laboratory, Code 8435
4555 Overlook Avenue
Washington, DC 20375

Robert Hay (Dr.)
Centre de Développement Technologique
Campus de l'Université
de Montréal, CF 6079
Succursale à Montréal, Québec H3C3A7
Canada

Donald B. Heckman
AMF Electronics Research Laboratory
3001 Centreville Road
Herndon, VA 22070

George Herrmann (Dr.)
Division of Applied Mechanics
Stanford University
Stanford, CA 94305

B. F. Hildebrand
Spectron Development Laboratories
3303 Harbor Boulevard
Costa Mesa, CA 92626

Phil Hodgetts
Los Angeles Division
Rockwell International
5701 West Imperial Highway
Los Angeles, CA 90009

Paul Holler (Prof. Dr.)
Institut für Zerstörungsfreie
Prüfverfahren
Universität, Gebäude 37
6600 Saarbrücken
West Germany

Masaru Igarashi
Department of Mechanical &
Industrial Engineering
University of Utah
Salt Lake City, UT 84112

D. Ilic (Dr.)
Edward L. Ginzton Laboratory
Stanford University
Stanford, CA 94305

Richard Inman
Rockwell International Science Center
1049 Camino Dos Rios
Thousand Oaks, CA 91360

M. H. Jacoby
Lockheed Missiles & Space Company
(84-34 B154)
Sunnyvale, CA 94088

George E. Jahn
Varian Associates
611 Hansen (K102)
Palo Alto, CA 94303

Michael R. James
Rockwell International Science Center
1049 Camino Dos Rios
Thousand Oaks, CA 91360

S. Johar (Dr.)
Ontario Research Foundation
Sheridan Park Research Community
Mississauga, Ontario
Canada L5K 1B3

Joseph John (Dr.)
IRT Corporation
7650 Convoy Court
San Diego, CA 92101

Wendell B. Jones (Dr.)
Sandia Laboratories
Division 5835,
P. O. Box 5800
Albuquerque, NM 87185

Julia Ju-Wen Tien
Edward L. Ginzton Laboratory
Stanford University
Stanford, CA 94305

David H. Kaelble (Dr.)
Rockwell International Science Center
1049 Camino Dos Rios
Thousand Oaks, CA 91360

Arnold H. Kahn
Solid State Materials, A255 Matls.
A251/223 - Div. 565
National Bureau of Standards
Washington, DC 20234

Frank N. Kelley
Institute of Polymer Science
University of Akron
Akron, OH 44325

Larry Kessler (Dr.)
Sonoscan, Inc.
752 Foster Avenue
Bensenville, IL 60106

Framod Khandelwai
Detroit Diesel Allison
P. O. Box 894
Indianapolis, IN 46224

B. T. Khuri-Yakub
Edward I. Ginzton Laboratory
Stanford University
Stanford, CA 94305

T. G. Kincaid
Building 37, Room 523
General Electric Company
Schenectady, NY 12345

Gordon S. Kino (Dr.)
Edward I. Ginzton Laboratory
Stanford University
Stanford, CA 94305

Richard King
Applied Mechanics
Stanford University
Stanford, CA 94305

Timothy E. Kinsella
General Dynamics, Ft. Worth Div.
P. O. Box 748, MZ 6472
Fort Worth, TX 76101

Wolfgang G. Knauss
Graduate Aeronautical Laboratory, 105-50
California Institute of Technology
Pasadena, CA 91125

Edgar A. Kraut (Dr.)
Rockwell International Science Center
1049 Camino Dos Rios
Thousand Oaks, CA 91360

V. Krstic
Ontario Research Foundation
Sheridan Park Research Community
Mississauga, Ontario
Canada L5K 1B3

James A. Krumhansl (Dr.)
National Science Foundation
1800 6th Street, NW
Washington, DC 20550

David Kupperman
Argonne National Laboratory
9700 W. Cass
Argonne, IL 60439

Kenneth Lakin (Dr.)
Department of Electrical Engineering
University of Southern California
Los Angeles, CA 90007

Robert Landel
Jet Propulsion Laboratory
4800 Oak Grove Drive
Pasadena, CA 91103

Stephen Lane
Adaptronics, Inc.
7700 Old Springhouse Road
McLean, VA 22102

William Lankelis
General Dynamics - Convair
Mail 41-3100
F. C. Box 80847
San Diego, CA

Melvin E. Lapites (Dr.)
Electric Power Research Institute
F. C. Box 10412
Falo Alto, CA 94303

Adrian Lee
University of California, Berkeley
Berkeley, CA 94720

David A. Lee (Dr.)
U.S. Air Force Institute of Technology
AFIT/ENC Building 640
Wright-Patterson AFB, OH 45431

Robert E. Lee
Albuquerque Development Laboratory
Rockwell International
2340 Alamo SE, Suite 200
Albuquerque, NM 87106

John Leffler
Systems Research Laboratories
2800 Indian Ripple Road
Dayton, OH 45440

Douglas K. Lemon
Battelle Northwest Laboratory
P. C. Box 999
Richland, WA 99352

Chuk L. Leung
Rockwell International Science Center
1049 Camino Dos Rios
Thousand Oaks, CA 91360

Kenneth Liang
Stanford University
228 Lexington Drive
Menlo Park, CA 94025

Dean Lingenfelter
Dept. 84-34, Bldg. 182
Lockheed Missiles & Space Co. Inc.
Sunnyvale, CA 94088

G. J. London (Dr.)
Code 6063
Naval Air Development Center
Warminster, PA 18974

Stuart A. Long
Department of Electrical Engineering
University of Houston
Houston, TX 77004

Douglas E. MacDonald (Dr.)
Room B-118, Materials Bldg.
National Bureau of Standards
Washington, DC 20234

Harris Marcus (Dr.)
Mechanical Engineering Department
University of Texas
Austin, TX 78712

James F. Martin
Rockwell International Science Center
1049 Camino Dos Rios
Thousand Oaks, CA 91360

I. Matay
Thompson-Ramo-Woolridge
23555 Euclid Avenue
Cleveland, OH 44117

George A. Matzkanin
Southwest Research Institute
P. C. Drawer 28510
San Antonio, TX 78240

Bruce Maxfield (Dr.)
Lawrence Livermore Laboratory
Mail Code 1333
Livermore, CA 94550

B. J. McKinley
Lawrence Livermore Laboratory
P. C. Box 808
Livermore, CA 94550

Harry McMaken
Northwestern University
Technological Institute
Evanston, IL 60220

M. Eugene Meyer
Rockwell International Science Center
1049 Camino Dos Rios
Thousand Oaks, CA 91360

David T. Mih
Northrop Corporation
3901 W. Broadway Street
Hawthorne, CA 90250

Jovan Moacanin (Dr.)
Jet Propulsion Laboratory
4800 Oak Grove Drive, M/S 122-123
Pasadena, CA 91103

Joseph B. Moore
Pratt & Whitney Aircraft Group
P. C. Box 2691 (loc. B-150)
West Palm Beach, FL 33402

Thomas J. Moran (Dr.)
Air Force Materials Laboratory/111
Wright Patterson AFB, OH 45433

Frederick Morris (Dr.)
Rockwell International Science Center
1049 Camino Dos Rios
Thousand Oaks, CA 91360

Roger A. Morris
Group M-1
Los Alamos Scientific Laboratory
Los Alamos, NM 87545

Alastair J. S. Morton
Code 2803 - Annapolis Laboratory
David W. Taylor Naval Ship R&D Center
Annapolis, MD 21402

Wesley A. Mowrer
Pratt & Whitney Aircraft, G.P.D.
P. O. Box 2691, M/S B-95
West Palm Beach, FL 33402

Joseph Moyzis
Air Force Materials Laboratory/111
Wright Patterson AFB, OH 45440

Anthony N. Mucciardi (Dr.)
Adaptronics, Inc.
7700 Old Springhouse Road
McLean, VA 22102

Kathie Newman
Physics Department, FM-15
University of Washington
Seattle, WA 98195

Leo J. O'Brien
Adaptronics, Inc.
7700 Old Springhouse Road
McLean, VA 22102

Louis Odor (Dr.)
Rockwell International
4300 E. 5th Avenue
Columbus, OH 43216

David W. Cliver
General Electric
Building K-1, Room C531
P. O. Box 8
Schenectady, N. Y. 12345

Jon I. Opsal
Lawrence Livermore Laboratory
Livermore, CA 94550

V. Orphan (Dr.)
Science Applications, Inc.
4030 Sorrento Valley Blvd.
San Diego, CA 92121

R. Palanisamy
Department of Electrical Engineering
Colorado State University
Fort Collins, CO 80523

Derek J. Palmer
Defense Equipment Staff
British Embassy
3100 Massachusetts Avenue, NW
Washington, DC 20008

S. Panchandeerswaran
Department of Materials Science
University of Utah
Salt Lake City, UT 84112

Vicki E. Panhuse (Dr.)
Applied Research-NDT
General Electric Company
Schenectady, NY 12345

Rod Panos (Dr.)
Rockwell International Science Center
1049 Camino Dos Rios
Thousand Oaks, CA 91360

P. Patricelli
Science Applications, Inc.
4030 Sorrento Valley Boulevard
San Diego, CA 92121

William J. Jardee (Dr.)
Rockwell International Science Center
1049 Camino Dos Rios
Thousand Oaks, CA 91360

Malcolm Perry
Holls Royce Ltd.
P. O. Box 3
Silton, Bristol
England

B. Frank Peters (Dr.)
Defence Research Establishment Pacific
Forces Mail Office
Victoria, BC V8S 1B0
Canada

Mark Peterson
U.S. Army Aviation R&D Command
P. O. Box 209, Attn: DRDAV-CH
St. Louis, MO 63166

Donald W. Pettibone
Edward L. Ginzton Laboratory
Stanford University
Stanford, CA 94305

R. Byron Pipes
MAE Department
University of Delaware
Evans Hall
Newark, DE 19711

William M. Fless
Lockheed-Georgia Company
86 S. Cobb Drive
Marietta, GA 30063

R. Polichar (Dr.)
Science Applications, Inc.
4030 Sorrento Valley Boulevard
San Diego, CA 92121

J. J. Posakony
Battelle Northwest Laboratories
P. O. Box 999
Richland, WA 99352

John Prati
Teledyne CAE - Turbine Engines
1330 Lasky Road
Toledo, OH 43612

Jaul K. Predecki
Space Science Bldg - Room 218
University of Denver
Denver, CO 80208

William S. Prince (Lt.)
AF Aeropropulsion Laboratory
Turbine Engine Division
Wright-Patterson AFB, OH 45432

Paul M. Kropp
SAMSO/YC/AFML
P. O. Box 92960
Worldway Postal Center
Los Angeles, CA 90009

C. Quate (Dr.)
Department of Applied Physics
Stanford University
Stanford, CA 94305

Mark Raglin
U. S. Army R&D Command
P. O. Box 209
St. Louis, MO 63166

Charles A. Rau, Jr.
Failure Analysis Associates
750 Welch Road
Falo Alto, CA 94304

Michael T. Resch
Department of Materials Science
Stanford University
Stanford, CA 94305

James Rice (Dr.)
Division of Engineering
Brown University
Providence, RI 02912

John M. Richardson (Dr.)
Rockwell International Science Center
1049 Camino Dos Rios
Thousand Oaks, CA 91360

James Rose (Dr.)
Physics Department
University of Michigan
Ann Arbor, MI 48109

Dov Rosenfeld
S.L.I. International
333 Ravenswood
Menlo Park, CA 94025

Corinne Ruokangas
Rockwell International Science Center
1049 Camino Dos Rios
Thousand Oaks, CA 91360

Wolfgang Sachse (Dr.)
Department of Theoretical and
Applied Mechanics
Cornell University
Ithaca, NY 14853

Armit Sagar
Westinghouse Electric Corporation
Forest Hills Site
Pittsburgh, PA 15230

Kamel Salama
Mechanical Engineering Department
University of Houston
Houston, TX 77004

Albert I. Schindler
Assoc. Director of Research (Code 6000)
Naval Research Laboratory
Washington, DC 20375

Lester W. Schmerr
Laboratory of Mechanics - 202A
Ames Laboratory
Iowa State University
Ames, Iowa 50011

Scott W. Schramm
ITT Research Institute
10 West 35th Street
Chicago, IL 60616

John J. Schuldies
Airesearch Manufacturing Company
Dept. 93-393/503-4Y
111 S. 34th Street
Pheonix, AZ 85010

Martin I. Scott
Department of Materials Science
& Engineering
Stanford University
Stanford, CA 94305

Emanuel Segal
Drexel University
32nd & Chesnut Streets
Philadelphia, PA 19104

Patrick Serad
U.S. Army Armaments R&D Command
Dover, NJ 07801

Nisar Shaikh
Department of Applied Mechanics
Stanford University
Stanford, CA 94305

Clinton L. Shank
Vought Corporation
Unit 2-42210
P. O. Box 225907
Dallas, TX 75265

W. H. Sheldon
Northrop Aircraft
3901 Broadway
Hawthorne, CA 90250

Larry Shepherd
General Electric - CR&D
Building K1, Room 5C19
P. O. Box 8
Schenectady, NY 12301

William Sheppard
Department of Electrical Engineering
University of Southern California
Los Angeles, CA 90007

John Shyne (Dr.)
Department of Materials Science
& Engineering
Stanford University
Stanford, CA 94305

M. Simaan
Department of Electrical Engineering
University of Pittsburgh
Pittsburgh, PA 15261

Wilbur C. Simmons (Dr.)
Air Force Office of Scientific Research/NE
Building 410
Bolling Air Force Base, DC 20334

James Skorpik
Battelle Northwest Laboratory
P. O. Box 999
Richland, WA 99352

James Smith (Dr.)
Army Materials & Mechanics
Research Center
Watertown, MA

Ora E. Smith (Dr.)
Rockwell International Science Center
1049 Camino Dos Rios
Thousand Oaks, CA 91360

Richard Smith
Southwest Research Institute
6220 Culebra Road
San Antonio, TX 78284

Sam Snow
Union Carbide - M/S 003
P. O. Box Y
Oakridge, TN 37830

Leonard T. Spragins
Albuquerque Development Laboratory
Rockwell International
2340 Alamo S.E. - Suite 200
Albuquerque, NM 87106

M. Srinivasan
High Performance SiC Division
The Carborundum Company
P. O. Box 832
Niagra Falls, NY 14302

Frederick E. Stanke
Edward L. Ginzton Laboratory
Stanford University
Stanford, CA 94305

Louis Fred Steele
Brunswick Corporation
4300 Industrial Avenue
Lincoln, NE 68504

Robert Steskal
Code 5163B
Naval Air Systems Command
Washington, DC 20375

Ronald D. Strong
Los Alamos Scientific Laboratory
P. O. Box 1663, MS 912
Los Alamos, NM 87545

Thomas W. Strouble
The Timken Company
1835 Dueber Avenue, SW
Canton, OH 44706

William R. Sturrock
Northrop Corporation
3901 W. Broadway
Hawthorne, CA 90250

Thomas L. Szabo
RADS 1LFA
Hanscom Air Force Base, MA 01731

Graham H. Thomas
Drexel University
32nd & Chestnut Streets
Philadelphia, PA 19104

K. Bruce Thompson (Dr.)
Rockwell International Science Center
1049 Camino Dos Rios
Thousand Oaks, CA 91360

Donald O. Thompson (Dr.)
Ames Laboratories
Spedding Hall, Room 231
Iowa State University
Ames, IA 50011

Robb Thomson (Dr.)
Institute of Material Research, Room B354
National Bureau of Standards
Washington, DC 20234

Bernard R. Tittmann (Dr.)
Rockwell International Science Center
1049 Camino Dos Rios
Thousand Oaks, CA 91360

Chen S. Tsai (Dr.)
Department of Electrical Engineering
Carnegie-Mellon University
Pittsburgh, PA 15213

R. W. Ure
Department of Materials Science
& Engineering
The University of Utah
Salt Lake City, Utah 84112

Owen Van Manning
General Dynamics
Mail Zone 41-3100
P. O. Box 80847
San Diego, CA 92138

Marvin C. VanWanderham (Dr.)
Pratt & Whitney Aircraft Group
Location B-08
P. O. Box 2691
West Palm Beach, FL 33402

V. K. Varadan (Dr.)
Department of Engineering Mechanics
The Ohio State University
Columbus, OH 43210

William M. Visscher
Theoretical Division
Los Alamos Scientific Laboratory
Los Alamos, NM 87544

F. A. Wedgwood
Material Physics Division
AERE Harwell
Oxfordshire OX11 0RA
England

R. D. Weglein
Hughes Research Laboratories
3011 Malibu Canyon Road
Malibu, CA 92065

Mark Weinberg
U. S. Army Armament R&D Command
Dover, NJ 07860

David Weinstein
Edward L. Ginzton Laboratory
Stanford University
Stanford, CA 94305

Michael F. Whalen
Adaptronics Inc.
7700 Old Springhouse Road
McLeon, VA 22102

J. K. White
Westinghouse Research Laboratory
Beulah Road - 4012B30
Pittsburgh, PA 15235

R. M. White (Dr.)
Department of Electrical Engineering
Electronics Research Laboratory
University of California, Berkeley
Berkeley, CA 94720

H. K. Wickramasinghe
University College London
Torrington Place
London W.C. 1
England

Richard H. Williams
EECS Department
University of New Mexico
Albuquerque, NM 87131

Alec R. Willis
Sandia Laboratories
Division 8444
Livermore, CA 94550

D. K. Winslow
Edward L. Ginzton Laboratory
Stanford University
Stanford, CA 94305

Harry Wugalter
Albuquerque Development Laboratory
Rockwell International
2340 Alamo SE - Suite 200
Albuquerque, NM 87106

Philip Yarnall, Jr.
David W. Taylor Naval Ship R&D Center
Bethesda, MD 20084

C. Yates
School of Engineering
University of Pittsburgh
Pittsburgh, PA 15261

D. Yuhas
Sonoscan, Inc.
752 Foster Avenue
Bensenville, IL 60106

John Zukauskis
Panametrics
221 Crescent Street
Waltham, MA 02154

DATE
L MED
-8